

Graduate Texts in Physics

Steven L. Garrett

# Understanding Acoustics

An Experimentalist's View of Sound  
and Vibration

*Second Edition*



OPEN ACCESS

Springer

---

# **Graduate Texts in Physics**

## **Series Editors**

Kurt H. Becker, NYU Polytechnic School of Engineering, Brooklyn, NY,  
USA

Jean-Marc Di Meglio, Matière et Systèmes Complexes, Bâtiment Condorcet,  
Université Paris Diderot, Paris, France

Sadri Hassani, Department of Physics, Illinois State University, Normal, IL,  
USA

Morten Hjorth-Jensen, Department of Physics, Blindern, University of Oslo,  
Oslo, Norway

Bill Munro, NTT Basic Research Laboratories, Atsugi, Japan

William T. Rhodes, Department of Computer and Electrical Engineering and  
Computer Science, Florida Atlantic University, Boca Raton, FL, USA

Susan Scott, Australian National University, Acton, Australia

H. Eugene Stanley, Center for Polymer Studies, Physics Department, Boston  
University, Boston, MA, USA

Martin Stutzmann, Walter Schottky Institute, Technical University of  
Munich, Garching, Germany

Andreas Wipf, Institute of Theoretical Physics, Friedrich-Schiller-University  
Jena, Jena, Germany

## **The ASA Press**

ASA Press, which represents a collaboration between the Acoustical Society of America and Springer Nature, is dedicated to encouraging the publication of important new books as well as the distribution of classic titles in acoustics. These titles, published under a dual ASA Press/Springer imprint, are intended to reflect the full range of research in acoustics. ASA Press titles can include all types of books that Springer publishes, and may appear in any appropriate Springer book series.

### *Editorial Board*

Mark F. Hamilton (Chair), University of Texas at Austin

James Cottingham, Coe College

Timothy F. Duda, Woods Hole Oceanographic Institution

Robin Glosemeyer Petrone, Threshold Acoustics

William M. Hartmann (Ex Officio), Michigan State University

Darlene R. Ketten, Boston University

James F. Lynch (Ex Officio), Woods Hole Oceanographic Institution

Philip L. Marston, Washington State University

Arthur N. Popper (Ex Officio), University of Maryland

Christine H. Shadle, Haskins Laboratories

G. Christopher Stecker, Boys Town National Research Hospital

Stephen C. Thompson, The Pennsylvania State University

Ning Xiang, Rensselaer Polytechnic Institute



---

Steven L. Garrett

# Understanding Acoustics

An Experimentalist's View of Sound  
and Vibration

Second Edition



Steven L. Garrett  
Pine Grove Mills, PA, USA

ISSN 1868-4513                    ISSN 1868-4521 (electronic)  
Graduate Texts in Physics         ISBN 978-3-030-44786-1         ISBN 978-3-030-44787-8 (eBook)  
ISBN 978-3-030-44786-1         <https://doi.org/10.1007/978-3-030-44787-8>

© The Editor(s) (if applicable) and The Author(s) 2020  
Jointly published with ASA Press

This book is an open access publication.

**Open Access** This book is licensed under the terms of the Creative Commons Attribution 4.0 International License (<http://creativecommons.org/licenses/by/4.0/>), which permits use, sharing, adaptation, distribution and reproduction in any medium or format, as long as you give appropriate credit to the original author(s) and the source, provide a link to the Creative Commons license and indicate if changes were made.

The images or other third party material in this book are included in the book's Creative Commons license, unless indicated otherwise in a credit line to the material. If material is not included in the book's Creative Commons license and your intended use is not permitted by statutory regulation or exceeds the permitted use, you will need to obtain permission directly from the copyright holder.

The use of general descriptive names, registered names, trademarks, service marks, etc. in this publication does not imply, even in the absence of a specific statement, that such names are exempt from the relevant protective laws and regulations and therefore free for general use.

The publisher, the authors, and the editors are safe to assume that the advice and information in this book are believed to be true and accurate at the date of publication. Neither the publisher nor the authors or the editors give a warranty, expressed or implied, with respect to the material contained herein or for any errors or omissions that may have been made. The publisher remains neutral with regard to jurisdictional claims in published maps and institutional affiliations.

This Springer imprint is published by the registered company Springer Nature Switzerland AG  
The registered company address is: Gewerbestrasse 11, 6330 Cham, Switzerland

*For Izzy, Moe,  
Seth, and Greg*

---

## The Acoustical Society of America

On 27 December 1928 a group of scientists and engineers met at Bell Telephone Laboratories in New York City to discuss organizing a society dedicated to the field of acoustics. Plans developed rapidly, and the Acoustical Society of America (ASA) held its first meeting on 10–11 May 1929 with a charter membership of about 450. Today, ASA has a worldwide membership of about 7000.

The scope of this new society incorporated a broad range of technical areas that continues to be reflected in ASA's present-day endeavors. Today, ASA serves the interests of its members and the acoustics community in all branches of acoustics, both theoretical and applied. To achieve this goal, ASA has established Technical Committees charged with keeping abreast of the developments and needs of membership in specialized fields, as well as identifying new ones as they develop.

The Technical Committees include acoustical oceanography, animal bio-acoustics, architectural acoustics, biomedical acoustics, engineering acoustics, musical acoustics, noise, physical acoustics, psychological and physiological acoustics, signal processing in acoustics, speech communication, structural acoustics and vibration, and underwater acoustics. This diversity is one of the Society's unique and strongest assets since it so strongly fosters and encourages cross-disciplinary learning, collaboration, and interactions.

ASA publications and meetings incorporate the diversity of these Technical Committees. In particular, publications play a major role in the Society. *The Journal of the Acoustical Society of America* (JASA) includes contributed papers and patent reviews. *JASA Express Letters* (JASA-EL) and *Proceedings of Meetings on Acoustics* (POMA) are online, open-access publications, offering rapid publication. *Acoustics Today*, published quarterly, is a popular open-access magazine. Other key features of ASA's publishing program include books, reprints of classic acoustics texts, and videos. ASA's biannual meetings offer opportunities for attendees to share information, with strong support throughout the career continuum, from students to retirees. Meetings incorporate many opportunities for professional and social interactions, and attendees find the personal contacts a rewarding experience. These experiences result in building a robust network of fellow scientists and engineers, many of whom become lifelong friends and colleagues.

From the Society's inception, members recognized the importance of developing acoustical standards with a focus on terminology, measurement procedures, and criteria for determining the effects of noise and vibration. The ASA Standards Program serves as the Secretariat for four American National Standards Institute Committees and provides administrative support for several international standards committees.

Throughout its history to present day, ASA's strength resides in attracting the interest and commitment of scholars devoted to promoting the knowledge and practical applications of acoustics. The unselfish activity of these individuals in the development of the Society is largely responsible for ASA's growth and present stature.

---

## Preface to the Second Edition

I was very pleased by the reviews<sup>1,2</sup> of *Understanding Acoustics* and by the positive reception that it received from many of my colleagues and former students. The textbook was written to preserve the perspective that I adopted from four of the greatest physicists working in acoustics and vibration during the second-half of the twentieth century: Isadore Rudnick and Seth Putterman at UCLA, Martin Greenspan at the National Bureau of Standards, and Greg Swift at Los Alamos National Laboratory.

Several of my colleagues taught courses from the first edition and were kind enough to provide me with feedback that included lists of errors and recommendations for improvements. My initial pleasure was tempered by my remorse for letting so many errors slip into the first edition that could only be designated as “sloppy.” This second edition is particularly indebted to errors identified by Brian Anderson who has used the first edition to teach more than one acoustics class at Brigham Young University, to Guillaume Dutilleux at the Norwegian University of Science and Technology, to S. Hales Swift at Argonne National Laboratory, to Mark Hamilton who corrected some historical errors in Chap. 15 on nonlinear acoustics, and to Greg Swift who made a critical reading of Chaps. 7, 8, 9 and 10 that not only identified errors but also updated the material on the use of the DELTAEC software. Greg also suggested the major revision in the mathematical notation that appears in the second edition explicitly distinguishing among scalars, vectors, functions, complex variables, and linear acoustic amplitudes that are now designated by phasors.

The structure and content of the first edition have been preserved, but the second edition includes some new topics (e.g., the unbaffled piston in Sect. 12.9), new references, new problems, and some improved figures and tables. Also, the index to the first edition, which was generated “automatically,” was deemed nearly useless, so I took it upon myself to write my own index for the second edition, which has the two-level structure that was common among earlier textbooks. I hope this will improve my textbook by making it more useful as a reference book, especially for those who used it in classes.

I am grateful to the ASA for providing content editors to improve my manuscript for this second edition. I am honored by the fact that the chairman

---

<sup>1</sup> P. Joseph, Physics Today **70**(10), 61 (2017).

<sup>2</sup> M. Kleiner, J. Audio Eng. Soc. **65**(11), 972 (2017).

of the ASA Books Committee, Mark Hamilton, agreed to edit my final chapter on nonlinear acoustics himself and approved three other members to edit the remaining chapters: Julian (Jay) D. Maynard covered the first six chapters, Greg Swift covered Chaps. 7, 8, 9 and 10, and Preston Wilson covered Chaps. 11, 12, 13 and 14. Of those four, three have received the Silver Medal in Physical Acoustics; the ASA's highest honor for scientific achievement, and Preston was just awarded the ASA's Rossing Prize in Acoustics Education. All four made significant and valuable contributions to the manuscript and identified many of my errors and ambiguities. I don't think any other author of any acoustics textbook ever had the benefit of input from such an accomplished and knowledgeable quartet. Thank you, gentlemen!

As with the first edition, I am grateful for the support of the Paul S. Veneklasen Research Foundation, in Santa Monica, California. Their support for this textbook is not unrelated to the fact that the home office of Veneklasen Associates is a short distance from the Physics Department on the campus of UCLA. When I was considering writing this textbook, two of the Veneklasen Foundation Board Members, John LoVerde and David Lubman, were most encouraging. They felt that an acoustics text with the UCLA "West Coast" perspective would provide an interesting and potentially valuable alternative to the more theory-based, mid-Atlantic view of the traditional East Coast and British authors.

The generosity of the Veneklasen Foundation has allowed Springer to make this second edition an "open-access" textbook—it is available for free download worldwide, and printed versions will be available at a substantially reduced price. Their timing could not have been better since this second edition will be published during the International Year of Sound 2020<sup>3</sup>.

Pine Grove Mills, PA, USA

Steven L. Garrett

---

<sup>3</sup>L. K. Jones, "Preparing for the International Year of Sound 2020," *Acoustics Today* 15(4), 68–69 (2019).

---

## Preface to the First Edition

The concepts and techniques that form the basis of the discipline known as “acoustics” are critically important in almost every field of science and engineering. This is not a chauvinistic prejudice but a consequence of that fact that most matter we encounter is in a state of stable equilibrium; matter that is disturbed from that equilibrium will behave “acoustically.” The purpose of this textbook is to present those acoustical techniques and perspectives and to demonstrate their utility over a very large range of system sizes and materials.

Starting with the end of World War II, there have been at least a dozen introductory textbooks on acoustics that have been directed toward students who plan to pursue careers in fields that rely on a comprehensive technical understanding of the generation, propagation, and reception of sound in fluids and solids and/or the calculation, measurement, and control of vibration. What is the point of adding another textbook to this long list? One may ask a more direct question: what has changed in the field and what appears missing in other treatments?

The two most obvious changes that I have seen over the past 40 years are the rise in the availability and speed of digital computers and the abdication of research and teaching responsibilities in acoustics and vibration by physics departments to engineering departments in American universities. This academic re-alignment has resulted in less attention being paid to the linkage of acoustical theory to the fundamental physical principles and to other related fields of physics and geophysics.

*Beauty is in the eye of the beholder.*

The same can be said for “understanding.” We all know the wonderful feeling that comes with the realization that some new phenomenon can be understood within the context of all previous education and experience. I have been extraordinarily fortunate to have been guided throughout my career by the wisdom and insights of Isadore Rudnick, Martin Greenspan, Seth Puttermann, and Greg Swift. Those four gentlemen had similar prejudices regarding what constituted “understanding” in any field of science or technology. Briefly, it came down to being able to connect new ideas, observations, and apparatus to the fundamental laws of physics. The connection was always

made through application of (usually) simple mathematics and was guided by a clear and intuitively satisfying narrative.

*Understanding Acoustics* is my attempt to perpetuate that perspective. To do so, I felt it necessary to include three chapters that are missing from any other acoustics treatments. In Part I – Vibrations, I felt this necessitated a chapter dedicated to elasticity. In my own experience, honed by teaching introductory lecture and laboratory classes at the graduate level for more than three decades, it was clear to me that most students who study acoustics do not have sufficient exposure to the relationship between various elastic moduli to be able to develop a satisfactory understanding of the vibrations of bars and plates nor the propagation of waves in solids. It was also an opportunity to provide a perspective that encompassed the design of springs that is critical to understanding vibration isolation.

In Part II – Waves in Fluids, there are two chapters that also do not appear in any other acoustics textbook. One covers thermodynamics and ideal gas laws in a way that integrates both the phenomenological perspective (thermodynamics) and the microscopic principles that are a consequence of the kinetic theory of gases. Both are necessary to provide a basis for understanding of relations that are essential to the behavior of sound waves in fluids.

I have also found that most acoustics students do not appreciate the difference between reversible and irreversible phenomena and do not have an understanding of the role of transport properties (*e.g.*, thermal conductivity and viscosity) in the attenuation of sound. Most students have been exposed to Ohm’s law in high school but do not appreciate the similarities with shear stresses in Newtonian fluids or temperature in the Fourier Diffusion Equation. Without the concept of thermal penetration depth, the reason sound propagation is nearly adiabatic will never be understood at a fundamental level.

After reading the entire manuscript for this textbook, a friend who is also a very well-known acoustician, told me that this textbook did not start its treatment of acoustics until Chap. 10. Although I disagreed, I did see his point. It is not until Chap. 10 that the wave equation is introduced for sound in fluids. In most contemporary acoustics textbooks (at least those that do not initially address vibration), the wave equation appears early in Chap. 1 (*e.g.*, Blackstock on pg. 2 or Pierce on pg. 17). Again, my postponement is a consequence of a particular prejudice regarding “understanding.” From my perspective, combining three individually significant equations to produce the wave equation makes no sense if the student does not appreciate the content of those equations before they are combined to produce the wave equation.

*If you learn it right the first time, there’s a lot less to learn.*

I will readily admit that I’ve included numerous digressions that I think are either interesting, culturally significant, or provide amusing extensions of the subject matter that may not be essential for the sequential development of a specific topic. For example, it is not necessary to understand the construction of musical scales in Sect. 3.3.3, to understand the dynamics of a stretched string. Such sections are annotated with an asterisk (\*) and can be skipped without sacrifice of the continuity of the underlying logical development.

With the availability of amazingly powerful computational tools, connecting the formalism of vibration and acoustics to fundamental physical principles is now even more essential. To paraphrase P. J. O'Rourke, “without those principles, giving students access to a computer is like giving a teenage boy a bottle of whisky and the keys to a Ferrari.” The improvements in computing power and software that can execute sophisticated calculations, sometimes on large blocks of data, and display the results in tabular or graphical forms, raises the need for more sophisticated understanding of the underlying mathematical techniques whose execution previously may have been too cumbersome. More importantly, it requires that the understanding of the user be sufficient to discriminate between results that are plausible and those which cannot possibly be correct. A computer can supply the wrong result with seven-digit precision a thousand times each second.

There are many fundamental principles, independent of the algorithms used to obtain results, which can be applied to computer-generated outputs to test their validity. That written, there is no substitute for physical insight and a clear specification of the problem. One goal of this textbook is to illuminate the required insight both by providing many solved example problems and by starting the analysis of such problems from the minimum number of fundamental definitions and relations while clearly stating the assumptions made in the formulation.

Unfortunately, some very fundamental physical principles that can be used to examine a seemingly plausible solution have vanished from the existing textbook treatments as the teaching of acoustics has transitioned from physics departments to engineering departments. In some sense, it is the improvement in mathematical techniques and notation, as well as rise of digital computers that have made scientist and engineers less reliant on principles like adiabatic invariance, dimensional analysis (*i.e.*, similitude or the Buckingham  $\Pi$ -Theorem), the Fluctuation-Dissipation Theorem, the Virial Theorem, the Kramers-Kronig relations, and the Equipartition Theorem. These still appear in the research literature because they are necessary to produce or constrain solutions to problems that do not yield to the current suite of analytical or numerical techniques. This textbook applies these approaches to very elementary problems that can be solved by other techniques in the hope that the reader starts to develop confidence in their utility. When solving a new problem, such principles can be applied to either check results obtained by other means or to extract useful results when other techniques are inadequate to the task.

For example, the Kramers-Kronig relations can be applied to a common analogy for the behavior of elastomeric springs (consisting of a series spring-dashpot combination in parallel with another spring). The limiting values of the overall stiffness of this combination at high and low frequencies dictate the maximum dissipation per cycle in the dashpot. Although for springs and dashpots these results can be obtained by simple algebraic methods, when measuring the frequency dependence of sound speed and attenuation in some biological specimen or other complex medium, the Kramers-Kronig relations can expose experimental disagreement between those two measurements that might call the results into question.

Traditionally, the analysis of the free-decay of a damped simple harmonic oscillator generates an exponential amplitude decay that results in the mass eventually coming to rest. Since energy is conserved, the energy that is removed from the oscillator appears as heating of the resistive element which exits “the system” to the environment. It is important to recognize that the route to thermal equilibrium is a two-way street. It also allows energy from the environment to excite the oscillator in a way that ensures a minimum (non-zero!) oscillation amplitude for any oscillator in thermal equilibrium with its environment. Simple application of the Equipartition Theorem provides the statistical variance in the position of the oscillating mass and can elucidate the role of the resistance in spreading the spectral distribution of that energy, leading to an appreciation of the ubiquity of noise introduced by all dissipative mechanisms. The origin of fluctuations produced by dissipation is known in physics as “Onsager Reciprocity.” In acoustics, it is much more likely that our “uncertainty principle” is dominated by Boltzmann’s constant, rather than by Planck’s constant. In an era of expanding application of micromachined sensors, thermal fluctuations in those tiny oscillators can be the dominant consideration that determines their minimum detectable signal.

The calculation of the modal frequencies of a fluid within an enclosure whose boundaries cannot be expressed in terms of the eleven separable coordinate systems for the wave equation is another example. These days, the normal approach is to apply a finite-element computer algorithm. Most enclosure shapes are not too different from one of the separable geometries that allow the mode shapes and their corresponding frequencies to be determined analytically. Adiabatic invariance guarantees that if one can deform the boundary of the separable solution into the desired shape, while conserving the enclosure’s volume, the modal frequencies will remain unchanged, and, although the mode shape will be distorted, it will still be possible to classify each mode in accordance with the separable solutions. (Adiabatic invariance assumes that “mode hopping” does not occur during the transformation.) Needless to say, this provides valuable insight into the computer-generated solutions while also checking the validity of the predicted frequencies. In this textbook, adiabatic invariance is first introduced in a trivial application to the work done when shortening the length of a pendulum.

Another motivation for taking a new approach to teaching about waves in fluids is fundamentally pedagogical. It comes from an observation of the way other textbooks introduce vibrational concepts that are focused on Hooke’s law (a primitive constitutive relation) and Newton’s Second Law of Motion. These are first combined to analyze the behavior of a simple harmonic oscillator. This is always done before analyzing waves on strings and in more complicated (*i.e.*, three-dimensional) solid objects. This is not the approach used in other textbooks when examining the behavior of waves in fluids. Typically, the fundamental equations of thermodynamics and hydrodynamics (*i.e.*, the equation-of-state, the continuity equation, and Euler’s equation) are linearized and combined to produce the wave equation and much later the subject of “lumped element” systems (*e.g.*, Helmholtz resonators, bubbles) that are the fluidic analogs to masses and springs are addressed.

The fact that the continuity equation leads directly to the definition of fluid compliance (*e.g.*, the stiffness of a gas spring) and the Euler equation defines fluid inertance should be introduced before these equations are combined (along with the equation-of-state) to produce the wave equation. In my experience, the wave equation is of rather limited utility since it describes the space-time evolution of a particular fluid parameter (*e.g.*, pressure, density, or particle velocity) but does not relate the amplitudes and phases of those parameters to each other. The “lumped element first” approach is adopted in Greg Swift’s *Thermoacoustics* textbook, but that book is intended for specialists.

Having mentioned Greg Swift’s name, I gladly admit that much of the content of this textbook has been based on an approach that was taught to me by my Ph.D. thesis advisors, Isadore Rudnick and Seth Putterman, at UCLA, in the 1970’s. Their perspective has served me so well over the past four decades, in a variety of applications, as well as in teaching, that I feel an obligation to future generations to record their insights. Unfortunately, neither Rudnick nor Putterman have written acoustics textbooks, but as a student, I had the foresight to make detailed notes during their lectures in courses on acoustics and on continuum dynamics.

As I hope I have expressed above, this textbook is an attempt to synthesize a view of acoustics and vibration that is based on fundamental physics while also including the engineering perspectives that provide the indispensable tools of an experimentalist. This preface closes with a table of quotations that have guided my efforts. Unfortunately, I must take full responsibility for both the errors and the ambiguities in this treatment, though hopefully they will be both minor and rare.

## List of Recurring Symbols

### Roman Lower Case

Symbol	Units	Meaning	First use
a, b,		Arbitrary scalars	(1.31)
a, b,		Exponents used for dimensional analysis	(1.78)
c	m/s	Sound speed	(10.4)
e		2.71828182846...	(1.4)
f	Hz	Frequency	(1.79)
g	m/s <sup>2</sup>	Acceleration due to gravity	(1.26)
g	s <sup>-1</sup>	Sound speed gradient, $dc/dz$	(11.25)
j		Unit imaginary number $j \equiv \sqrt{-1}$	(1.52)
k	m <sup>-1</sup>	Wavenumber	(3.15)
m	kg	Mass	(2.1)
p	Pa	Pressure	(1.17)
z	Pa·s/m	Specific acoustic impedance	(10.26)

### Roman Upper Case

Symbol	Units	Meaning	First use
A*		Complex conjugate of A	(1.67)
A, B, C	Pa	Virial coefficients	(15.16)
$\vec{B}$	T	Magnetic induction	(2.88)
B	Pa	Bulk modulus	(4.8)
C	m <sup>3</sup> /Pa	Acoustical compliance	(8.26)
D	Pa	Modulus of unilateral compression	(4.14)
E	Pa	Young's modulus	(4.1)
G	Pa	Shear modulus	(4.17)
$\vec{I}$	W/m <sup>2</sup>	Acoustic intensity	(10.36)
KE	J	Kinetic energy or kinetic energy density [J/m <sup>3</sup> ]	(2.15)
L	kg/m <sup>4</sup>	Acoustical inertance	(8.47)
M	kg/mol	Molecular or atomic weight	(7.4)
PE	J	Potential energy or potential energy density [J/m <sup>3</sup> ]	(1.22)
Pr		Prandtl number	(9.61)
Q		Resonance quality factor	(2.44) App. B
T	s	Period	(2.3)
T	K	Temperature	(2.49)
U	m <sup>3</sup> /s	Volume flow rate ( $=\dot{m}/\rho$ )	(8.24)
V	m <sup>3</sup>	Volume	(4.8)
V	V	Voltage	(2.89)
W	J	Work	(2.14)

## Greek Lower Case

Symbol	Units	Meaning	First use
$\alpha$	$\text{m}^2/\text{s}$	Thermometric conductivity	(9.11)
$\alpha$	$\text{Pa}\cdot\text{m}$	Surface tension	(12.26)
$\beta$		Wakeland number	(10.100)
$\gamma$		Polytropic coefficient ( $= c_p/c_V$ )	(7.19)
$\delta$		Logarithmic decrement	(2.46)
$\epsilon$		Strain	(4.1)
$\zeta$	$\text{Pa}\cdot\text{s}$	Bulk viscosity, second viscosity	(14.12)
$\eta$	$\text{m}$	Normal coordinate	(2.111)
$\theta$	$\text{rad}$	Angle	Fig. 1.5
$\kappa$	$\text{m}$	Radius of gyration	(4.26)
$\kappa$	$\text{W}/\text{m}\cdot\text{K}$	Thermal conductivity	(9.3)
$\lambda$	$\text{m}$	Wavelength	(3.17)
$\mu$	$\text{Pa}\cdot\text{s}$	Shear viscosity	(9.2)
$\nu$	$\text{m}^2/\text{s}$	Kinematic viscosity	(9.32)
$\nu$		Poisson's ratio	(4.2)
$\pi$		3.14159265359...	(1.42)
$\rho$	$\text{kg}/\text{m}^3$	Mass density	(7.3)
$\sigma$	Various	Standard deviation	(1.88)
$\tau$	$\text{s}$	Exponential damping time	(2.41)
$\omega$	$\text{rad}/\text{s}$	Angular frequency	(2.3)

## Greek Upper Case

Symbol	Units	Meaning	First use
$\Gamma$		Grüneisen parameter	(15.9)
$\Delta$	$\text{m}$	Gravitational offset	(2.28)
$K$	$\text{N}/\text{m}$	Spring stiffness	(1.25)
$\Pi(t)$	$\text{W}$	Instantaneous power	(1.73)
$\langle \Pi \rangle_t$	$\text{W}$	Time-averaged power	(1.75)
$T$	$\text{N}$	Tension	(3.1)
$\Omega$	ohm	Unit of electrical resistance	Fig. 2.24
$\Xi$	$\text{Pa}$	Complex elastic modulus	(4.76)

## Subscripted Upper-Case Roman

Symbol	Units	Meaning	First use
$B_s$	$\text{Pa}$	Adiabatic bulk modulus	(10.20)
$C_n$	various	Standing wave modal amplitude	(3.30)
$C_p$	$\text{J}/\text{K}$	Heat capacity at constant pressure	(7.14)
$C_V$	$\text{J}/\text{K}$	Heat capacity at constant volume	(7.11)
$I_n(x)$		Modified Bessel function of the first kind	Fig. 6.20
$J_n(x)$		Bessel function	Fig. 6.8
$K_n(x)$		Modified Bessel function of the second kind	Fig. 6.20
$N_n(x)$		Neumann function	Fig. 6.9
$R_m$	$\text{kg}\cdot\text{s}$	Mechanical resistance	(2.39)
$\mathbf{M}_o$	$\text{V}/\text{Pa}$	Open circuit microphone sensitivity	(10.67)
$\mathbf{M}_s$	$\text{A}/\text{Pa}$	Short-circuit microphone sensitivity	(10.68)
$P_{II}$		Power reflection coefficient	(10.106)
$R_I$		Resistive coefficient of a piston's radiation impedance	(12.124)
$S_o$	$\text{Pa}/\text{A}$	Current-driven source strength	(10.69)
$S_s$	$\text{Pa}/\text{V}$	Voltage-driven source strength	(10.70)
$T_m$	$\text{K}$	Mean temperature	Sect. 8.6.2
$T_{II}$		Power transmission coefficient	(10.106)
$X_I$		Reactive coefficient of a piston's radiation impedance	(12.125)
$Z_{ac}$	$\text{Pa}\cdot\text{s}/\text{m}^3$	Characteristic impedance	(10.27)
$Z_{el}$	$\Omega$	Electrical impedance	(2.90)
$Z_m$	$\text{N}\cdot\text{s}/\text{m}$	Mechanical impedance	(2.58)

## Subscripted Lower-Case Roman

Symbol	Units	Meaning	First use
$c_p$	J/kg-K	Specific heat at constant pressure	(7.11)
$c_v$	J/kg-K	Specific heat at constant volume	(7.14)
$(\Delta f)_{EQNB}$	Hz	Equivalent noise bandwidth	Fig. 2.8
$k_B$	J/K	Boltzmann's constant	(2.49), App. A
$p_m$	Pa	Mean pressure	(8.1)

## Subscripted Lower-Case Greek

Symbol	Units	Meaning	First use
$\alpha_i$		Surface absorption coefficient	(13.23)
$\epsilon_o$	F/m	Permittivity of free space	(6.63), App. A
$\beta_p$	K <sup>-1</sup>	Volume coefficient of thermal expansion	(14.22)
$\delta_\kappa$	m	Thermal penetration depth	(9.14)
$\delta_\nu$	m	Viscous penetration depth	(9.33)
$\delta_{m,n}$		Kronecker delta	(1.38)
$\rho_L$	kg/m	Linear mass density	(2.12)
$\rho_m$	kg/m <sup>3</sup>	Mean mass density	(8.2)
$\rho_S$	kg/m <sup>2</sup>	Surface mass density	(6.2)
$\sigma_{ij}$	Pa	Shear stress	(4.17)
$\tau_R$		Exponential relaxation time	(4.58)
$\omega_o$	rad/s	Pendulum or Helmholtz angular frequency	(2.32), (8.51)
$\omega_d$	rad/s	Damped free-decay angular frequency	(2.45)

## Phasors

Symbol	Units	Meaning	First use
$\hat{C}$	m	Oscillator displacement amplitude	(2.7)
$\hat{p}$	Pa	Acoustic pressure amplitude	(8.6)
$\hat{u}$	m/s	Acoustic particle velocity amplitude	(8.18)
$\hat{U}$	m <sup>3</sup> /s	Acoustic volume velocity amplitude	Fig. 8.3
$\hat{v}$	m/s	Velocity amplitude	(2.57)

## Other

Symbol	Units	Meaning	First use
$\forall$	m <sup>-2</sup>	Reciprocal (k-space) area	(6.15)
$\varsigma$		Gas stiffness enhancement factor	(6.51)
dB		Decibel	(2.69)
$\hat{e}_x, \hat{e}_y, \hat{e}_z$		Unit vectors in the three Cartesian directions	(1.33)
$\Im m[ ]$		Imaginary part	(1.70)
$\bar{l}$	m	Mean free path	(9.52)
$\mathfrak{M}$	N-m	Bending moment	(4.26)
$\Re e[ ]$		Real part	(1.69)
$\mathfrak{R}$	J/K	Universal gas constant	(1.16), (7.3)
$\mathfrak{T}$	N/m	Membrane tension per unit length	(6.1)
$\bar{x}$		Statistical mean value	(1.87)

*If you learn it right the first time, there's a lot less to learn.*

R. W. M. Smith

*One measure of our understanding is the number of different ways we can get to the same result.*

R. P. Feynman

*An acoustician is merely a timid hydrodynamicist.*

A. Larraza

*Thermodynamics is the true testing ground of physical theory because its results are model independent.*

A. Einstein

*Superposition is the compensation we receive for enduring the limitations of linearity.*

Blair Kinsman

*If your experiment needs statistics, you should have done a better experiment.*

E. Rutherford

*A computer can provide the wrong result with seven-digit precision.*

Dr. Nice Guy

*I have often been impressed by the scanty attention paid even by original workers in physics to the great principle of similitude. It happens not infrequently those results in the form of 'laws' are put forward as novelties on the basis of elaborate experiments, which might have been predicted a priori after a few minutes of consideration.*

J. W. Strutt (Lord Rayleigh)

*Given today's imperfect foundations, additional approximations are useful whenever they improve computational ease dramatically while only slightly reducing accuracy.*

G. W. Swift

*Each problem I solved became a rule which served afterward to solve other problems.*

R. Descartes

*The industrial revolution owes its success to the fact that the computer hadn't been invented yet. If it had, we would still be modeling and simulating the cotton gin, the telegraph, the steam engine, and the railroad.*

D. Phillips

*The best science doesn't consist of mathematical models and experiments. Those come later. It springs fresh from a more primitive mode of thought, wherein the hunter's mind weaves ideas from old facts and fresh metaphors and the scrambled crazy images of things recently seen. To move forward is to concoct new patterns of thought, which in turn dictate the design of models and experiments. Easy to say, difficult to achieve.*

E. O. Wilson

*In no other branch of physics are the fundamental measurements so hard to perform and the theory relatively so simple; and in few other branches are the experimental methods so dependent on a thorough knowledge of theory.*

P. M. Morse

---

## Acknowledgments

As mentioned in both the Dedication and the Preface, this textbook is my attempt to repay the intellectual generosity of Isadore (Izzy) Rudnick (1917–1996), Martin (Moe) Greenspan (1912–1987), Seth Puttermann, and Greg Swift. Oddly, all four started their careers as theorists and ended up becoming extraordinarily competent experimentalists.

I am also indebted to the Acoustical Society of America (ASA). It has been my professional home since 1972. In all of my experience with professional scientific societies, I have never found any similar organization that was more welcoming to students or more focused on meeting the needs of their members. I would not have begun this effort had I not been contacted by Allan Pierce, then the Society's Editor-in-Chief, who sent an e-mail message to several members saying that the ASA's Books+ Committee was going to expand from selling affordable reprints of classic acoustics textbooks to production and distribution of first editions that would be useful to ASA members.

I am glad to thank the Paul S. Veneklasen Foundation and particularly Foundation board members David Lubman and John LoVerde. When they heard that I was writing an acoustics textbook with a distinctively West Coast perspective, they offered the Foundation's support to cover my editorial and graphic expenses.

Once I had completed my manuscript, the ASA assigned two technical content editors. I am very grateful to Prof. Peter Rogers, now retired from Georgia Tech, and Asst. Prof. Brian Anderson for accepting that assignment. Pete is one of the most accomplished acousticians of my generation, and Brian is a recent addition to the Physics Department of Brigham Young University. I am indebted to the both of them for their careful consideration of my manuscript and for their insightful comments and corrections. I am also grateful to my Penn State colleagues, Anthony Atchley, Tom Gabrielson, Jay Maynard, and Dan Russell, who have allowed me to use some figures from their class notes in this textbook.

After enjoying a 40-year career as an academic acoustician, there are many others who have helped me refine and expand my understanding of sound and vibration. I have supervised more than 70 master's and Ph.D. thesis students, and each has challenged me in different ways that ultimately led to deeper understanding. That said, I must explicitly acknowledge David A. Brown and

David L. Gardner who were my Ph.D. students in the Physics Department at the Naval Postgraduate School and Matthew E. Poese and Robert W. M. Smith who received their Ph.D. degrees from the Graduate Program in Acoustics at Penn State under my supervision. All four were gifted scientists and engineers before they joined my research group, and all have continued to collaborate with me for decades. Besides benefiting from their ingenuity, perseverance, and wise counsel, I also have been continually amused and bolstered by their amazing sense of humor.

In addition to students, the perspectives reflected in this textbook benefit from longtime collaborations with some outstandingly knowledgeable and creative colleagues. I enjoyed working with Richard Packard both as the F. V. Hunt Fellow of the Acoustical Society of America while at the University of Sussex and following that year as a Miller Institute Postdoctoral Fellow at UC-Berkeley for two more years, where Prof. Packard was a member of the Physics Department and where I first met Greg Swift, who was one of Packard's many distinguished Ph.D. students. (Packard is shown on his fishing boat, *The Puffin*, in Alaska, in Fig. 4.13.) Oscar B. Wilson took me under his wing, both figuratively and literally (at one time he owned at least four aircraft and encouraged me to get my pilot's license), when I started my academic career at the Naval Postgraduate School. At the Naval Postgraduate School and later at Penn State, I benefited from collaborations with Thomas B. Gabrielson and Robert M. Keolian. In addition to their extraordinary competence as experimentalists, both are very gifted teachers, as are Matt Poese, Bob Smith, and David Brown.

The effort required to produce a textbook is significant, and I required hundreds of daylong sessions that required uninterrupted concentration. Thanks to the Penn State library's online journal access and a year of sabbatical leave, I was able to write anywhere in the world that provided decent Internet access. I thank my son, Adam, who let me write in his Brooklyn apartment; my dear cousin, Karen Rothberg, who let me write from her beautiful home in Santa Barbara, California; my friends Susan Levenstein and Alvin Curran who let me write in their wonderful apartment in the heart of ancient Rome; and Anne-Sophie and Bernard Thuard who rented me an apartment above their bookstore in the center of Le Mans, France, where the largest portion of this book was written. I must also thank Guillaume Penelet, Pierrick Lotton, and Gaëlle Poignand, all associated with the Laboratoire d'Acoustique de l'Université du Maine. They made me feel at home in Le Mans, where I was also a member of their "Acoustics HUB" program that provided both a laboratory and office space in their acoustics program.

The Internet also made it possible to write from Los Angeles and Venice, California; Puerto Escondido, Mexico; and Haifa, Israel, where I was able to rent apartments and enjoy great weather and indigenous cuisines that were perfect for textbook writing. If you are considering writing a book, I will certify that there is nothing wrong with any of the venues I've mentioned that can also provide excellent weather.

The ASA made a very wise choice by teaming with Springer to publish their first editions. Springer's representative to the ASA during this entire

process has been Sara Kate Heukerott. She has always responded to my multiple queries about mechanics and style quickly, completely, and with good humor. As of this date, the ASA has received over 30 book proposals from members interested in producing first editions. I look forward to reading many of them.

I close by thanking my daughter and son, Wendy and Adam, for their support during this process and for making sure that their father was amused and well fed. Thanks (in advance) to the students, teachers, and researchers who will contact me to let me know how this textbook might have better served their needs.

---

# Contents

<b>1</b>	<b>Comfort for the Computationally Crippled . . . . .</b>	<b>1</b>
1.1	The Five Most Useful Math Techniques . . . . .	2
1.1.1	Taylor Series . . . . .	2
1.1.2	The Product Rule or Integration by Parts . . . . .	4
1.1.3	Logarithmic Differentiation . . . . .	5
1.2	Equilibrium, Stability, and Hooke's Law . . . . .	6
1.2.1	Potentials and Forces . . . . .	8
1.2.2	A Simple Pendulum . . . . .	10
1.3	The Concept of Linearity . . . . .	12
1.4	Superposition and Fourier Synthesis . . . . .	13
1.5	Convenience (Complex) Numbers . . . . .	16
1.5.1	Geometrical Interpretation on the Argand Plane . . . . .	18
1.5.2	Phasor Notation . . . . .	19
1.5.3	Algebraic Operations with Complex Numbers . . . . .	19
1.5.4	Integration and Differentiation of Complex Exponentials . . . . .	21
1.5.5	Time Averages of Complex Products (Power) . . . . .	21
1.6	Standard (SI) Units and Dimensional Homogeneity . . . . .	22
1.7	Similitude and the Buckingham $\Pi$ -Theorem (Natural Units) . . . . .	23
1.7.1	Three Simple Examples . . . . .	24
1.7.2	Dimensionless $\Pi$ -Groups . . . . .	25
1.7.3	Windscreens Noise* . . . . .	26
1.7.4	Similitude Summary . . . . .	29
1.8	Precision, Accuracy, and Error Propagation . . . . .	29
1.8.1	Random Errors (Noise) and Relative Uncertainty . . . . .	30
1.8.2	Normal Error Function or the Gaussian Distribution . . . . .	32
1.8.3	Systematic Errors (Bias) . . . . .	34
1.8.4	Error Propagation and Covariance . . . . .	35
1.8.5	Significant Figures . . . . .	37

1.9	Least-Squares Fitting and Parameter Estimation . . . . .	37
1.9.1	Linear Correlation Coefficient . . . . .	39
1.9.2	Relative Error in the Slope . . . . .	42
1.9.3	Linearized Least-Squares Fitting . . . . .	43
1.9.4	Caveat for Data Sets with Small $N^*$ . . . . .	46
1.9.5	Best-Fit to Models with More Than Two Adjustable Parameters . . . . .	46
1.10	The Absence of Rigorous Mathematics . . . . .	47
	References . . . . .	54

## Part I Vibrations

2	The Simple Harmonic Oscillator . . . . .	59
2.1	The Undamped Harmonic Oscillator . . . . .	60
2.1.1	Initial Conditions and the Phasor Representation . . . . .	61
2.2	The Lumped-Element Approximation . . . . .	63
2.2.1	Series and Parallel Combinations of Several Springs . . . . .	64
2.2.2	A Characteristic Speed . . . . .	65
2.3	Energy . . . . .	66
2.3.1	The Virial Theorem . . . . .	67
2.3.2	Rayleigh's Method . . . . .	68
2.3.3	Gravitational Offset . . . . .	69
2.3.4	Adiabatic Invariance . . . . .	71
2.4	Damping and Free-Decay . . . . .	73
2.4.1	Viscous Damping and Mechanical Resistance . . . . .	73
2.4.2	Free-Decay Frequency and Quality Factor . . . . .	75
2.4.3	Critical Damping . . . . .	76
2.4.4	Thermal Equilibrium and Fluctuations . . . . .	76
2.4.5	Frictional (Coulomb) Damping* . . . . .	82
2.5	Driven Systems . . . . .	83
2.5.1	Force-Driven SHO . . . . .	83
2.5.2	Power Dissipation, the Decibel, and Resonance Bandwidth . . . . .	87
2.5.3	Resonance Tracking and the Phase-Locked Loop* . . . . .	90
2.5.4	Transient Response . . . . .	92
2.5.5	The Electrodynamic Loudspeaker . . . . .	95
2.5.6	Electrodynamic (Moving-Coil) Microphone . . . . .	99
2.5.7	Displacement-Driven SHO and Transmissibility . . . . .	100
2.6	Vibration Sensors . . . . .	102
2.7	Coupled Oscillators . . . . .	105
2.7.1	Two Identical Masses with Three Identical Springs . . . . .	105
2.7.2	Coupled Equations for Identical Masses and Springs . . . . .	106

---

2.7.3	Normal Modes and Normal Coordinates . . . . .	107
2.7.4	Other Initial Conditions . . . . .	108
2.7.5	General Solutions for Two Masses and Three Springs . . . . .	109
2.7.6	Driven Oscillators, Level Repulsion, and Beating . . . . .	110
2.7.7	String of Pearls . . . . .	112
2.8	The Not-So-Simple (?) Harmonic Oscillator . . . . .	115
	References . . . . .	130
<b>3</b>	<b>String Theory . . . . .</b>	<b>133</b>
3.1	Waves on a Flexible String . . . . .	134
3.2	Pulse Reflections at a Boundary and the Utility of Phantoms . . . . .	138
3.3	Normal Modes and Standing Waves . . . . .	141
3.3.1	Idealized Boundary Conditions . . . . .	141
3.3.2	Consonance and Dissonance* . . . . .	144
3.3.3	Consonant Triads and Musical Scales* . . . . .	145
3.4	Modal Energy . . . . .	147
3.4.1	Nature Is Efficient . . . . .	149
3.4.2	Point Mass Perturbation . . . . .	152
3.4.3	Heavy Chain Pendulum (Nonuniform Tension)* . . . . .	153
3.5	Initial Conditions . . . . .	155
3.5.1	Total Modal Energy . . . . .	157
3.6	"Imperfect" Boundary Conditions . . . . .	158
3.6.1	Example: Standing Wave Modes for $M/m_s = 5$ . . . . .	161
3.6.2	An Algebraic Approximation for the Mass-Loaded String . . . . .	161
3.6.3	The Resistance-Loaded String* . . . . .	163
3.7	Forced Motion of a Semi-Infinite String . . . . .	165
3.8	Forced Motion of a Finite String . . . . .	166
3.8.1	Displacement-Driven Finite String . . . . .	167
3.8.2	Mass-Loaded String in the Impedance Model . . . . .	169
3.8.3	Force-Driven Finite String . . . . .	170
3.8.4	An Efficient Driver/Load Interaction . . . . .	170
3.9	"I've Got the World on a String . . . . .": Chapter Summary . . . . .	171
	References . . . . .	177
<b>4</b>	<b>Elasticity of Solids . . . . .</b>	<b>179</b>
4.1	Hooke, Young, Poisson, and Fourier . . . . .	180
4.2	Isotropic Elasticity . . . . .	181
4.2.1	Bulk Modulus . . . . .	182
4.2.2	Modulus of Unilateral Compression . . . . .	183
4.2.3	Shear Modulus . . . . .	185
4.2.4	Two Moduli Provide a Complete (Isotropic) Description . . . . .	187

4.3	Real Springs . . . . .	187
4.3.1	Solids as Springs . . . . .	188
4.3.2	Flexure Springs . . . . .	193
4.3.3	Triangularly Tapered Cantilever Spring* . . . . .	198
4.3.4	Buckling . . . . .	200
4.3.5	Torsional Springs . . . . .	202
4.3.6	Coil Springs . . . . .	203
4.4	Viscoelasticity . . . . .	206
4.4.1	The Maxwell (Relaxation Time) Model . . . . .	207
4.4.2	Standard Linear Model (SLM) of Viscoelasticity . . . . .	210
4.4.3	Complex Stiffnesses and Moduli* . . . . .	211
4.4.4	Kramers-Kronig Relations . . . . .	213
4.5	Rubber Springs . . . . .	216
4.5.1	Effective Modulus . . . . .	217
4.5.2	Rubber-to-Glass Transition (Type I and Type II Rubbers) . . . . .	218
4.5.3	Transmissibility of Rubberlike Vibration Isolators . . . . .	220
4.6	Anisotropic (Crystalline) Elasticity* . . . . .	225
4.7	There Is More to Stiffness Than Just “K” . . . . .	227
	References . . . . .	232
5	<b>Modes of Bars . . . . .</b>	235
5.1	Longitudinal Waves in Thin Bars . . . . .	236
5.1.1	Longitudinal Waves in Bulk Solids . . . . .	240
5.1.2	The Quartz Crystal Microbalance . . . . .	240
5.1.3	Bodine’s “Sonic Hammer” . . . . .	242
5.2	Torsional Waves in Thin Bars . . . . .	245
5.3	Flexural Waves in Thin Bars . . . . .	246
5.3.1	Dispersion . . . . .	247
5.3.2	Flexural Wave Functions . . . . .	249
5.3.3	Flexural Standing Wave Frequencies . . . . .	250
5.3.4	Flexural Standing Wave Mode Shapes . . . . .	252
5.3.5	Rayleigh Waves* . . . . .	256
5.4	Resonant Determination of Elastic Moduli . . . . .	256
5.4.1	Mode-Selective Electrodynamic Excitation and Detection . . . . .	258
5.4.2	Bar Sample Size and Preparation . . . . .	259
5.4.3	Measured Resonance Spectra . . . . .	260
5.4.4	Effective Length Correction for Transducer Mass . . . . .	263
5.4.5	Modes of a Viscoelastic Bar . . . . .	266
5.4.6	Resonant Ultrasound Spectroscopy* . . . . .	270
5.5	Vibrations of a Stiff String* . . . . .	274
5.6	Harmonic Analysis . . . . .	277
	References . . . . .	280

---

<b>6</b>	<b>Membranes, Plates, and Microphones . . . . .</b>	283
6.1	Rectangular Membranes . . . . .	284
6.1.1	Modes of a Rectangular Membrane . . . . .	286
6.1.2	Modal Degeneracy . . . . .	288
6.1.3	Density of Modes . . . . .	291
6.2	Circular Membranes . . . . .	294
6.2.1	Series Solution to the Circular Wave Equation . . . . .	295
6.2.2	Modal Frequencies and Density for a Circular Membrane . . . . .	299
6.2.3	Mode Similarities Illustrating Adiabatic Invariance . . . . .	300
6.2.4	Normal Modes of Wedges and Annular Membranes* . . . . .	302
6.2.5	Effective Piston Area for a Vibrating Membrane . . . . .	304
6.2.6	Normal Mode Frequencies of Tympani . . . . .	306
6.2.7	Pressure-Driven Circular Membranes . . . . .	308
6.3	Response of a Condenser Microphone . . . . .	310
6.3.1	Optimal Backplate Radius . . . . .	313
6.3.2	Limits on Polarizing Voltages and Electrostatic Forces . . . . .	315
6.3.3	Electret Condenser Microphone . . . . .	317
6.4	Vibrations of Thin Plates . . . . .	321
6.4.1	Normal Modes of a Clamped Circular Plate . . . . .	322
6.5	Flatland . . . . .	324
	References . . . . .	329

## Part II Waves in Fluids

<b>7</b>	<b>Ideal Gas Laws . . . . .</b>	333
7.1	Two Ways of Knowing—Phenomenology and Microscopies . . . . .	334
7.1.1	Microscopic Models . . . . .	336
7.1.2	Phenomenological Models . . . . .	338
7.1.3	Adiabatic Equation of State for an Ideal Gas . . . . .	341
7.1.4	Adiabatic Temperature Change . . . . .	342
7.2	Specific Heats of Ideal Gases . . . . .	343
7.2.1	Monatomic (Noble) Gases . . . . .	344
7.2.2	Polyatomic Gases . . . . .	344
7.3	The Fundamental Equations of Hydrodynamics . . . . .	347
7.3.1	The Continuity Equation . . . . .	348
7.3.2	The Navier-Stokes (Euler) Equation . . . . .	349
7.3.3	The Entropy Equation . . . . .	350
7.3.4	Closure with the Equation of State . . . . .	352
7.4	Flashback . . . . .	352
	References . . . . .	356

<b>8</b>	<b>Nondissipative Lumped Elements . . . . .</b>	357
8.1	Oscillations About Equilibrium . . . . .	359
8.2	Acoustical Compliance and the Continuity Equation . . . . .	361
8.2.1	The Continuity Equation . . . . .	361
8.2.2	Linearized Continuity Equation . . . . .	363
8.2.3	Acoustical Compliance . . . . .	366
8.2.4	The Gas Spring . . . . .	366
8.3	Hydrostatic Pressure . . . . .	367
8.4	Inertance and the Linearized Euler Equation . . . . .	369
8.4.1	The Venturi Tube . . . . .	369
8.4.2	The Linearized Euler Equation . . . . .	370
8.4.3	Acoustical Inertance . . . . .	372
8.4.4	Acoustical Mass . . . . .	373
8.5	The Helmholtz Resonance Frequency . . . . .	373
8.5.1	Helmholtz Resonator Network Analysis . . . . .	377
8.5.2	A 500-mL Boiling Flask . . . . .	378
8.6	DELTAECC Software . . . . .	381
8.6.1	Download DELTAECC . . . . .	382
8.6.2	Getting Started with DELTAECC (Thermophysical Properties) . . . . .	382
8.6.3	Creating planewave.out . . . . .	384
8.6.4	Running planewave.out . . . . .	388
8.6.5	Finding the Resonance Frequencies of planewave.out . . . . .	389
8.6.6	State Variable Plots (*.sp) . . . . .	391
8.6.7	Modifying planewave.out to Create Flask500.out . . . . .	392
8.6.8	Interpreting the *.out File . . . . .	392
8.6.9	The RPN Segment . . . . .	394
8.6.10	Power Flow and Dissipation in the 500 mL Boiling Flask . . . . .	396
8.6.11	An “Effective Length” Correction . . . . .	396
8.6.12	Incremental Plotting and the *.ip File . . . . .	397
8.6.13	So Much More Utility in DELTAECC . . . . .	401
8.7	Coupled Helmholtz Resonators . . . . .	402
8.8	The Bass-Reflex Loudspeaker Enclosure . . . . .	405
8.8.1	Beranek’s Box Driven by a Constant Volume Velocity . . . . .	406
8.8.2	Loudspeaker-Driven Bass-Reflex Enclosure* . . . . .	409
8.9	Lumped Elements . . . . .	412
References . . . . .		418
<b>9</b>	<b>Dissipative Hydrodynamics . . . . .</b>	421
9.1	The Loss of Time Reversal Invariance . . . . .	422
9.2	Ohm’s Law and Electrical Resistivity . . . . .	424

---

9.3	Thermal Conductivity and Newton's Law of Cooling . . . . .	425
9.3.1	The Thermal Boundary Layer . . . . .	427
9.3.2	Adiabatic Compression Within a Bounded Volume . . . . .	430
9.3.3	Energy Loss in the Thermal Boundary Layer . . . . .	432
9.3.4	Adiabatic vs. Isothermal Propagation in an Ideal Gas . . . . .	433
9.4	Viscosity . . . . .	434
9.4.1	Poiseuille Flow in a Pipe of Circular Cross-Section . . . . .	435
9.4.2	The Viscous Boundary Layer . . . . .	436
9.4.3	Viscous Drag in the Neck of a Helmholtz Resonator . . . . .	438
9.4.4	Quality Factors for a Helmholtz Resonator . . . . .	440
9.5	Kinetic Theory of Thermal and Viscous Transport . . . . .	443
9.5.1	Mean Free Path . . . . .	443
9.5.2	Thermal Conductivity of an Ideal Gas . . . . .	444
9.5.3	Viscosity of an Ideal Gas . . . . .	446
9.5.4	Prandtl Number of an Ideal Gas and Binary Gas Mixtures* . . . . .	447
9.6	Not a Total Loss . . . . .	449
	References . . . . .	451
<b>10</b>	<b>One-Dimensional Propagation . . . . .</b>	<b>453</b>
10.1	The Transition from Lumped Elements to Waves in Fluids . . . . .	454
10.2	The Wave Equation . . . . .	456
10.2.1	General Solutions to the Wave Equation . . . . .	458
10.3	The Dispersion Relation (Phase Speed) . . . . .	459
10.3.1	Speed of Sound in Liquids . . . . .	460
10.3.2	Speed of Sound in Ideal Gases and Gas Mixtures . . . . .	460
10.4	Harmonic Plane Waves and Characteristic Impedance . . . . .	463
10.5	Acoustic Energy Density and Intensity . . . . .	464
10.5.1	Decibel Scales . . . . .	465
10.5.2	Superposition of Sound Levels (Rule for Adding Decibels) . . . . .	468
10.5.3	Anthropomorphic Frequency Weighting of Sound Levels . . . . .	468
10.6	Standing Waves in Rigidly Terminated Tubes . . . . .	470
10.6.1	Quality Factor in a Standing Wave Resonator . . . . .	472
10.6.2	Resonance Frequency in Closed-Open Tubes . . . . .	474

<b>10.7</b>	Driven Plane Wave Resonators . . . . .	474
10.7.1	Electroacoustic Transducer Sensitivities . . . . .	476
10.7.2	The Principle of Reciprocity . . . . .	477
10.7.3	In Situ Reciprocity Calibration . . . . .	478
10.7.4	Reciprocity Calibration in Other Geometries . . . . .	481
10.7.5	Resonator-Transducer Interaction . . . . .	482
10.7.6	Electrodynamic Source Coupling Optimization* . . . . .	488
<b>10.8</b>	Junctions, Branches, and Filters . . . . .	490
10.8.1	Abrupt Discontinuities and the Acoustic Admittance . . . . .	490
10.8.2	Tuned Band-Stop Filter . . . . .	492
10.8.3	Stub Tuning . . . . .	494
<b>10.9</b>	Quasi-One-Dimensional Propagation (Horns) . . . . .	495
10.9.1	Semi-infinite Exponential Horns . . . . .	495
10.9.2	Salmon Horns* . . . . .	499
10.9.3	Horns of Finite Length* . . . . .	500
	References . . . . .	510
<b>11</b>	<b>Reflection, Transmission, and Refraction . . . . .</b>	<b>513</b>
11.1	Normal Incidence . . . . .	514
11.2	Three Media . . . . .	518
11.2.1	A Limp Diaphragm Separating Two Gases . . . . .	520
11.2.2	An Impedance Matching Antireflective Layer . . . . .	520
11.2.3	The “Mass Law” for Sound Transmission Through Walls . . . . .	520
11.2.4	Duct Constriction/Expansion Low-Pass Filters . . . . .	521
11.3	Snell’s Law and Fermat’s Principle . . . . .	523
11.3.1	Total Internal Reflection . . . . .	526
11.3.2	The Rayleigh Reflection Coefficient . . . . .	528
11.4	Constant Sound Speed Gradients . . . . .	529
11.4.1	Constant Gradient’s Equivalence to Solid Body Rotation . . . . .	531
11.4.2	Sound Channels . . . . .	534
11.4.3	Propagation Delay* . . . . .	536
11.4.4	Under Ice Propagation . . . . .	537
11.4.5	Sound Focusing . . . . .	538
	References . . . . .	541
<b>12</b>	<b>Radiation and Scattering . . . . .</b>	<b>543</b>
12.1	Sound Radiation and the “Causality Sphere” . . . . .	546
12.2	Spherically Diverging Sound Waves . . . . .	548
12.2.1	Compact Monopole Radiation Impedance . . . . .	550
12.2.2	Compact Monopole Acoustic Transfer Impedance . . . . .	553
12.2.3	General Multipole Expansion* . . . . .	554

---

12.3	Bubble Resonance . . . . .	555
12.3.1	Damping of Bubble Oscillations . . . . .	557
12.4	Two In-Phase Monopoles . . . . .	560
12.4.1	The Method of Images . . . . .	564
12.5	Two Out-Of-Phase Compact Sources (Dipoles) . . . . .	567
12.5.1	Dipole Radiation . . . . .	571
12.5.2	Cardioid (Unidirectional) Radiation Pattern . . . . .	574
12.5.3	Pressure Gradient Microphones . . . . .	575
12.5.4	The DIFAR Directional Sonobuoy . . . . .	578
12.6	Translational Oscillations of an Incompressible Sphere . . . . .	578
12.6.1	Scattering from a Compact Density Contrast . . . . .	580
12.6.2	Scattering from a Compact Compressibility Contrast . . . . .	583
12.6.3	Scattering from a Single Bubble or a Swim Bladder . . . . .	584
12.6.4	Multiple Scattering in the “Effective Medium” Approximation . . . . .	586
12.7	N-Element Discrete Line Array . . . . .	588
12.7.1	Beam Steering and Shading . . . . .	591
12.7.2	Continuous Line Array . . . . .	593
12.8	Baffled Piston . . . . .	595
12.8.1	Rayleigh Resolution Criterion . . . . .	599
12.8.2	Directionality and Directivity . . . . .	599
12.8.3	Radiation Impedance of a Baffled Circular Piston . . . . .	602
12.8.4	Radiation Impedance of a Baffled Rectangular Piston* . . . . .	604
12.8.5	On-Axis Near-Field Pressure from a Circular Baffled Piston* . . . . .	604
12.9	Radiation Impedance of an Unbaffled Piston . . . . .	607
12.10	Linear Superposition . . . . .	610
	References . . . . .	618
13	<b>Three-Dimensional Enclosures</b> . . . . .	621
13.1	Separation of Variables in Cartesian Coordinates . . . . .	622
13.1.1	Rigid-Walled Rectangular Room . . . . .	623
13.1.2	Mode Characterization . . . . .	624
13.1.3	Mode Excitation . . . . .	625
13.1.4	Density of Modes . . . . .	626
13.2	Statistical Energy Analysis . . . . .	627
13.2.1	The Sabine Equation . . . . .	630
13.2.2	Critical Distance and the Schroeder Frequency . . . . .	633
13.3	Modes of a Cylindrical Enclosure . . . . .	635
13.3.1	Pressure Field Within a Rigid Cylinder and Normal Modes . . . . .	635

---

13.3.2	Modal Density Within a Rigid Cylinder . . . . .	641
13.3.3	Modes of a Rigid-Walled Toroidal Enclosure* . . . . .	644
13.3.4	Modal Degeneracy and Mode Splitting . . . . .	646
13.3.5	Modes in Non-separable Coordinate Geometries . . . . .	648
13.4	Radial Modes of Spherical Resonators . . . . .	651
13.4.1	Pressure-Released Spherical Resonator . . . . .	652
13.4.2	Rigid-Walled Spherical Resonator . . . . .	653
13.5	Waveguides . . . . .	654
13.5.1	Rectangular Waveguide . . . . .	655
13.5.2	Phase Speed and Group Speed . . . . .	656
13.5.3	Driven Waveguide . . . . .	658
13.5.4	Cylindrical Waveguide . . . . .	659
13.5.5	Attenuation from Thermoviscous Boundary Losses . . . . .	660
	References . . . . .	670
<b>14</b>	<b>Attenuation of Sound . . . . .</b>	<b>673</b>
14.1	An Almost Correct Expression for Viscous Attenuation . . . . .	674
14.2	Bulk Thermoviscous Attenuation in Fluids . . . . .	677
14.3	Classical Thermoviscous Attenuation . . . . .	681
14.4	The Time-Dependent Equation of State . . . . .	682
14.5	Attenuation due to Internal Relaxation Times . . . . .	684
14.5.1	Relaxation Attenuation in Gases and Gas Mixtures . . . . .	687
14.5.2	Relaxation Attenuation in Fresh and Salt Water . . . . .	688
14.6	Transmission Loss . . . . .	692
14.6.1	Short and Very Short Wavelengths . . . . .	692
14.6.2	Very Long Wavelengths . . . . .	693
14.7	Quantum Mechanical Manifestations in Classical Mechanics . . . . .	693
	References . . . . .	697

### Part III Extensions

<b>15</b>	<b>Nonlinear Acoustics . . . . .</b>	<b>701</b>
15.1	Surf's Up . . . . .	703
15.1.1	The Grüneisen Parameter . . . . .	705
15.1.2	The Virial Expansion and $B/2A$ . . . . .	707
15.1.3	Anomalous Distortion* . . . . .	708
15.1.4	The Gol'dberg Number . . . . .	711
15.1.5	Stable Sawtooth Waveform Attenuation . . . . .	712
15.2	Weak Shock Theory and Harmonic Distortion . . . . .	714
15.2.1	The Order Expansion . . . . .	714
15.2.2	Trigonometric Expansion of the Earnshaw Solution . . . . .	715
15.2.3	Higher Harmonic Generation . . . . .	716

15.3	The Phenomenological Model . . . . .	718
15.3.1	The (Nondissipative) Nonlinear Wave Equation . . . . .	719
15.3.2	Geometrical Resonance (Phase Matching) . . . . .	720
15.3.3	Intermodulation Distortion and the Parametric End-Fire Array . . . . .	721
15.3.4	Resonant Mode Conversion . . . . .	725
15.4	Non-zero Time-Averaged Effects . . . . .	729
15.4.1	The Second-Order Pressure in an Adiabatic Compression . . . . .	729
15.4.2	The Bernoulli Pressure . . . . .	731
15.4.3	The Rayleigh Disk . . . . .	734
15.4.4	Radiation Pressure . . . . .	735
15.4.5	Acoustic Levitation in Standing Waves . . . . .	737
15.4.6	Adiabatic Invariance and the Levitation Force . . . . .	738
15.4.7	Levitation Superstability ("Acoustic Molasses") . . . . .	743
15.5	Beyond the Linear Approximation . . . . .	746
	References . . . . .	751
	<b>Appendices . . . . .</b>	755
	<b>Index . . . . .</b>	765

---

## About the Book

The materials in Part I (Vibration) and Part II (Waves in Fluids) were developed for introductory first-year graduate courses that were offered in the Physics Department at the Naval Postgraduate School (NPS) in Monterey, CA, from 1982 through 1995, then for two similar courses offered in the Graduate Program in Acoustics at Penn State (PSU), in State College, PA, from 1996 through 2015. At both institutions, the students taking my introductory courses were planning to take other acoustics courses, like electro-acoustic transduction, noise and vibration control, underwater acoustics, signal processing, nonlinear acoustics, architectural acoustics, and biomedical acoustics, and to go on to a variety of careers in acoustics after completing a masters or Ph.D. degree. Some students who were already employed in fields requiring acoustics took these classes as “distance education” students (over the Internet) to upgrade their skills while on the job.

**Introductory Graduate-Level Course** At both NPS and PSU, the materials in Parts I and II were covered in 30 weeks. At NPS, the material was presented sequentially in three 10-week quarters, and at PSU the material was presented in two 15-week semesters that were offered concurrently during the resident students’ first semester. In both cases, students attended about 3 h of lecture each week during each course.

**Weekly Problem Sets** A critical component in such courses are the students’ solutions to weekly problem sets. This textbook contains many end-of-chapter problems. Most were created to encourage the student to combine several concepts and/or techniques to arrive at a final result. Many were structured with multiple parts to help lead the students to that desired final result. This more closely approximates what is required in actual practice than the plug ‘n’ chug substitution problems.

**Laboratory Exercises** In both institutions, teaching laboratory exercises were provided in addition to the lectures, weekly problem sets, and exams. At NPS, the labs were included as part of all three 10-week quarters. At PSU, the labs were included as a separate course that was usually taken after the two concurrent 15-week semesters were completed.

The laboratory exercises I used when I offered the lab class at Penn State are available at the Springer web site for this textbook: <https://www.springer.com/gp/book/9783319499765>. Suitable laboratory experiences will vary among different institutions because of the availability of instrumentation and other infrastructural support, but structured hands-on data collection, analysis, and reporting of results are strongly recommended for students who will go on to careers in acoustics.

For that reason, many parts of this textbook are based on measurements that could be made in a teaching laboratory. Several of the end-of-chapter problems are also based on teaching laboratory experiments. The characterization of electrodynamic loudspeaker parameters in Chap. 2 and the resonant determination of elastic moduli in Chap. 5 are two obvious examples, as are exercises like the loudspeaker equivalent piston area and Rüchardt's determination of the polytropic coefficient in Chap. 7; the 1.0-liter flask and Helmholtz resonator in Chap. 8; the thermophone and reciprocity calibration problems in Chap. 10; the electrodynamic loudspeaker performance calculations in Chap. 12; the Golden Temple's room modes and reverberation time, cylindrical resonator, and pressure-released waveguide in Chap. 13; and waveform distortion and levitator design in Chap. 15.

**Advanced Undergraduate Course** The material in this textbook has also been used in several upper-division elective courses, primarily in physics departments. Such courses are typically only one semester long and thus require significant selectivity in the choice of material that can be covered. Each instructor will have a different emphasis, but a reasonable one-semester course can cover most of Chap. 2 on simple harmonic oscillators and Chap. 3 on the vibration of strings. Rectangular membranes in Chap. 6 might also be worthwhile if modes of three-dimensional enclosures are to be covered in Chap. 13.

For fluids, a review of ideal gas laws in Chap. 7 is a good starting point, followed by lumped element interpretation of the lossless hydrodynamic equations and Helmholtz resonators in the first half of Chap. 8. From there, one-dimensional propagation and resonators, as well as energy and the decibel, are fundamental topics in Chap. 10. Some of the early material in Chap. 11 on reflection is recommended along with monopole radiation in Chap. 12. Most students enjoy exposure to modes of rectangular rooms and statistical energy analysis for architectural applications in Chap. 13. It is doubtful to me that a one-semester course, as just outlined, would have time to cover attenuation at the level presented in Chap. 14, although some exposure to the material in Chap. 15 on nonlinear acoustics, harmonic distortion, and acoustic levitation could stimulate student interest.

**Acoustics Students' Diversity** One of the reasons that I enjoyed teaching acoustics for more than four decades is the diversity of backgrounds that motivated students to seek careers in fields that require acoustical expertise. Although many students who start a graduate program in acoustics come from traditional undergraduate programs in physics, applied mathematics, and

electrical or mechanical engineering, there are a significant number of students with undergraduate majors in music, biology, or architecture.

This textbook is different from others because it includes three chapters that I have not seen in other acoustics textbooks at this level: Chap. 4 (Elasticity of Solids), Chap. 7 (Ideal Gas Laws), and Chap. 9 (Dissipative Hydrodynamics). In addition, the math chapter, Chap. 1 (Comfort for the Computationally Crippled), has a different emphasis than most introductory math chapters in traditional acoustics textbooks.

In my experience, even physics majors have not had much exposure to elastic moduli or to topics in mass and heat transport that require an understanding of viscosity or thermal conductivity. For almost all students who chose to study acoustics, the last time they had any exposure to ideal gas laws might have been in their high school or freshman chemistry classes. It is also unlikely that students other than the ones with undergraduate degrees in mechanical engineering ever used any formal techniques to apply dimensional analysis (i.e., similitude or the Buckingham  $\Pi$  theorem).

At both NPS and PSU, first-year acoustics graduate students were required to take at least one engineering mathematics course. Unfortunately, what I found is that such courses stress solutions to differential equations but do not address more elementary topics, and none talk about the analysis of experimental data using techniques such as linearized least-squares fitting to extract parameters and their statistical uncertainties from experimental results, or to propagate those uncertainties when a result requires the combination of results from two or more experiments. Recognition of the difference between statistical errors and systematic errors (e.g., calibration errors, signal-conditioner gains, and frequency response) rarely receives the emphasis it deserves.

Chapter 1 reviews many important (though elementary) techniques like Taylor series, potentials and forces, Fourier analysis, and complex numbers. I do not recommend teaching from Chap. 1 but using it, as necessary, to make students aware of its content as a resource for the topics and problems in the rest of this textbook.

***Optional Sections*** Almost every chapter includes some sections that are indicated by an asterisk (\*) meaning that they can be skipped without harming the continuity of that chapter's subject development. Some address "cultural" topics, like consonance and dissonance in musical intervals and the construction of musical scales or the application of the kinetic theory of gases to derive the pressure and temperature variation of transport coefficients. Some provide extensions that may be more mathematically challenging like the general multipole expansion and the heavy chain modes, or of specialized interest, like crystalline elastic constants or the extension of a bass-reflex cabinet design to incorporate a real electrodynamic loudspeaker.

I hope that students who use *Understanding Acoustics* as a textbook in an acoustics course will return to this book throughout their careers. As time goes on, some of these optional sections may become interesting or more relevant to their evolving interests. There is no question in my mind that the extensive list of references at the end of each chapter should also serve them well over time.

---

## About the Author



**Steven L. Garrett** received his Ph.D. in Physics from UCLA in 1977. He continued research in quantum fluids at the University of Sussex in England as the first F. V. Hunt Fellow of the Acoustical Society of America, followed by 2 years in the Physics Department at the University of California, Berkeley, as a fellow of the Miller Institute for Basic Research in Science. Prof. Garrett joined the physics faculty of the Naval Postgraduate School in 1982 where his research efforts were concentrated on the

development of fiber-optic sensors and thermoacoustic refrigerators. Prof. Garrett left NPS in 1995 to become a professor of acoustics in the Graduate Program in Acoustics at Penn State and retired in 2016. In 2001, he was a Fulbright Fellow at the Danish Technical University and in 2008 a Jefferson Fellow in the US State Department. Prof. Garrett is a fellow of the Acoustical Society of America and recipient of their Interdisciplinary Medal in Physical and Engineering Acoustics. He received the *Popular Science Magazine* Award for Environmental Technology, the Helen Caldecott Award for Environmental Technology, and the Rolex Award for Enterprise (environment category). He has been issued over two dozen patents.



# Comfort for the Computationally Crippled 1

## Contents

1.1	<b>The Five Most Useful Math Techniques</b> .....	2
1.1.1	Taylor Series .....	2
1.1.2	The Product Rule or Integration by Parts .....	4
1.1.3	Logarithmic Differentiation .....	5
1.2	<b>Equilibrium, Stability, and Hooke's Law</b> .....	6
1.2.1	Potentials and Forces .....	8
1.2.2	A Simple Pendulum .....	10
1.3	<b>The Concept of Linearity</b> .....	12
1.4	<b>Superposition and Fourier Synthesis</b> .....	13
1.5	<b>Convenience (Complex) Numbers</b> .....	16
1.5.1	Geometrical Interpretation on the Argand Plane .....	18
1.5.2	Phasor Notation .....	19
1.5.3	Algebraic Operations with Complex Numbers .....	19
1.5.4	Integration and Differentiation of Complex Exponentials .....	21
1.5.5	Time Averages of Complex Products (Power) .....	21
1.6	<b>Standard (SI) Units and Dimensional Homogeneity</b> .....	22
1.7	<b>Similitude and the Buckingham <math>\Pi</math>-Theorem (Natural Units)</b> .....	23
1.7.1	Three Simple Examples .....	24
1.7.2	Dimensionless $\Pi$ -Groups .....	25
1.7.3	Windscreen Noise* .....	26
1.7.4	Similitude Summary .....	29
1.8	<b>Precision, Accuracy, and Error Propagation</b> .....	29
1.8.1	Random Errors (Noise) and Relative Uncertainty .....	30
1.8.2	Normal Error Function or the Gaussian Distribution .....	32
1.8.3	Systematic Errors (Bias) .....	34
1.8.4	Error Propagation and Covariance .....	35
1.8.5	Significant Figures .....	37
1.9	<b>Least-Squares Fitting and Parameter Estimation</b> .....	37
1.9.1	Linear Correlation Coefficient .....	39
1.9.2	Relative Error in the Slope .....	42

1.9.3	Linearized Least-Squares Fitting .....	43
1.9.4	Caveat for Data Sets with Small $N^*$ .....	46
1.9.5	Best-Fit to Models with More Than Two Adjustable Parameters .....	46
1.10	<b>The Absence of Rigorous Mathematics</b> .....	47
	<b>References</b> .....	54

“The discussion of any problem in science or engineering has two aspects: the physical side, the statement of the facts of the case in everyday language and of the results in a manner that can be checked by experiment; and the mathematical side, the working out of the intermediate steps by means of the symbolized logic of calculus. These two aspects are equally important and are used side by side in every problem, one checking the other.” [1]

The difference between engineering and science, and all other human activity, is the fact that engineers and scientists make quantitative predictions about measurable outcomes and can specify their uncertainty in such predictions. Because those predictions are quantitative, they must employ mathematics. This chapter is intended as an introduction to some of the more useful mathematical concepts, strategies, and techniques that are employed in the description of vibrational and acoustical systems and the calculations of their behavior.

It is not necessary to master the content of this chapter before working through this textbook. Other chapters will refer back to specific sections of this chapter as needed. If you are unsure of your competence or confidence with mathematics, it may be valuable to read through this chapter before going on.

## 1.1 The Five Most Useful Math Techniques

Below is a list of the five most useful mathematical techniques for the study of acoustics and vibration based on my experience. Techniques number one and number five are self-explanatory. The other three will be introduced in more detail in this section.

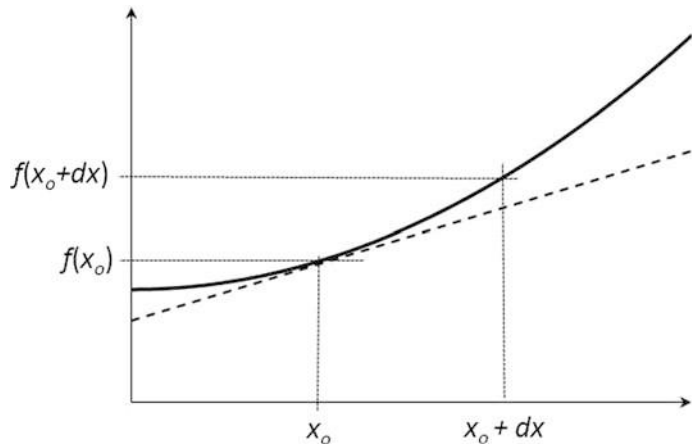
- Substitution
- Taylor series
- The product rule or integration by parts
- Logarithmic differentiation
- Garrett’s First Law of Geometry: “Angles that look alike are alike.”

### 1.1.1 Taylor Series

Acoustics and vibration are the “sciences of the subtle.” Most of our attention will be focused on small deviations from a state of stable equilibrium. For example, a sound pressure level<sup>1</sup> of 115 dB<sub>SPL</sub> is

<sup>1</sup> Do not worry if “sound pressure level” is not yet a familiar term. It will be defined in the fluid part of this textbook when intensity is explained in Sect. 10.5.1. For this example, it is only meant to specify a very loud sound.

**Fig. 1.1** Graph of an arbitrary function of position,  $f(x)$ . The straight dashed line is tangent to  $f(x)$  at  $x_o$ . It represents the first derivative (slope) of  $f(x)$  evaluated at  $x_o$



capable of creating permanent damage to your hearing with less than 15 min of exposure per day [2]. That acoustic pressure level corresponds to a peak excess pressure of  $p_1 = 16 \text{ Pa}$  ( $1 \text{ Pa} = 1 \text{ N/m}^2$ ). Since “standard” atmospheric pressure is  $p_m = 101,325 \text{ Pa}$  [3], that level corresponds to a relative deviation from equilibrium that is less than 160 parts per million (ppm) or  $p_1/p_m = 0.016\%$ .

If we assume that any parameter of interest (e.g., temperature, density, pressure) varies smoothly in time and space, we can approximate the parameter’s value at a point (in space or time) if we know the parameter’s value at some nearby point (typically, the state of stable equilibrium) and the value of its derivatives evaluated at that point.<sup>2</sup> The previous statement obscures the true value of the Taylor series because it is frequently used to permit substitution of the value of the derivative, as we will see throughout this textbook.

Let us start by examining the graph of some arbitrary real function of position,  $f(x)$ , shown in Fig. 1.1. At position  $x_o$ , the function has a value,  $f(x_o)$ . At some nearby position,  $x_o + dx$ , the function will have some other value,  $f(x_o + dx)$ , where we will claim that  $dx$  is a small distance without yet specifying what we mean by “small.”

The value of  $f(x_o + dx)$  can be approximated if we know the first derivative of  $f(x)$  evaluated at  $x_o$ .

$$f(x_o + dx) \cong f(x_o) + \left. \frac{df}{dx} \right|_{x_o} dx \quad (1.1)$$

As can be seen in Fig. 1.1, the approximation of Eq. (1.1) produces a value that is slightly less than the actual value  $f(x_o + dx)$  in this example. That is because the actual function has some curvature that happens to be upward in this case. The differential,  $dx$ , is used to represent both finite and infinitesimal quantities, depending upon context. For approximations,  $dx$  is assumed to be small but finite. For derivation of differential equations, it is assumed to be infinitesimal.

We can improve the approximation by adding another term to the *Taylor series expansion* of  $f(x)$  that includes a correction proportional to the second derivative of  $f(x)$ , also evaluated at  $x_o$ . For the example in Fig. 1.1, the curvature is upward so the second derivative of  $f(x)$ , evaluated at  $x_o$ , is a positive number, so  $(d^2f/dx^2)_{x_o} > 0$ .

<sup>2</sup>What I am calling a “smooth” function is specified by mathematicians as being “infinitely differentiable,” meaning that all of the function’s derivatives are finite, remembering that zero is also finite.

If the curve had bent downward, the second derivative would have been negative. A more accurate approximation than Eq. (1.1) is provided by the following expression containing a correction proportional to  $(dx)^2$ :

$$f(x_o + dx) \cong f(x_o) + \frac{df}{dx} \Big|_{x_o} dx + \frac{d^2f}{dx^2} \Big|_{x_o} \frac{(dx)^2}{2} \quad (1.2)$$

Since  $(dx)^2$  is intrinsically positive and the upward curvature makes  $d^2f/dx^2$  positive, we can see that this *second-order correction* improves our estimate of  $f(x_o + dx)$ . Had the curvature been downward, making  $(d^2f/dx^2)_{x_o} < 0$ , then the second-order correction would have placed the estimated value of  $f(x_o + dx)$  the first-order (linear) estimate, as required, since  $(dx)^2$  would still be positive.

In principle, we can continue to improve the Taylor series approximation by adding higher and higher-order derivatives, although it is rare to extend such a series extended beyond the first three terms in Eq. (1.2). The full generic form of the Taylor series is provided in Eq. (1.3).

$$f(x_o + dx) = f(x_o) + \sum_{n=1}^{\infty} \frac{f^n(x)}{(dx)^n} \Big|_{x_o} \frac{(dx)^n}{n!} = f(x_o) + \sum_{n=1}^{\infty} f^{(n)}(x_o) \frac{(x - x_o)^n}{n!} \quad (1.3)$$

The Taylor series approach of Eq. (1.3) can be used to express continuous functions in a *power series*. Below are some functions that have been expanded about  $x_o = 0$ . As we will see, they will be particularly useful when  $|x| \ll 1$ .

$$e^x = 1 + x + \frac{x^2}{2!} + \frac{x^3}{3!} + \dots = 1 + x + \frac{x^2}{2} + \frac{x^3}{6} + \dots \quad (1.4)$$

$$\sin(x) = x - \frac{x^3}{3!} + \frac{x^5}{5!} - \dots = x - \frac{x^3}{6} + \frac{x^5}{120} - \dots \quad (1.5)$$

$$\cos(x) = 1 - \frac{x^2}{2!} + \frac{x^4}{4!} - \dots = 1 - \frac{x^2}{2} + \frac{x^4}{24} - \dots \quad (1.6)$$

$$\tan(x) = x + \frac{x^3}{3} + \frac{2x^5}{15} + \frac{17x^7}{315} + \frac{62x^9}{2835} \dots \quad (1.7)$$

$$\ln(1+x) = x - \frac{x^2}{2} + \frac{x^3}{3} - \frac{x^4}{4} + \dots \quad (1.8)$$

$$(1+x)^\alpha = 1 + \alpha x + \frac{\alpha(\alpha-1)}{2!} x^2 + \frac{\alpha(\alpha-1)(\alpha-2)}{3!} x^3 + \dots \quad (1.9)$$

## 1.1.2 The Product Rule or Integration by Parts

If we have two functions of  $x$ , say  $u(x)$  and  $v(x)$ , the *product rule* tells us how we can take the derivative of the product of those functions.

$$\frac{d(uv)}{dx} = \frac{du}{dx} v + u \frac{dv}{dx} \quad (1.10)$$

This rule can be extended, for example, to the product of three functions of a single variable, where we have now added  $w(x)$ .

$$\frac{d(uvw)}{dx} = \frac{du}{dx}vw + u\frac{dv}{dx}w + uv\frac{dw}{dx} \quad (1.11)$$

Although it is not the intent of this chapter to derive all the quoted results, it is instructive, in this context, to introduce the concept of a *differential*.<sup>3</sup> If we say that a small change in  $x$ , by the amount  $dx$ , produces a small change in  $u(x)$ , by the amount  $du$ , and that  $|du/u| \ll 1$ , then we can show that Eq. (1.10) is correct by taking the product of the small changes.

$$d(uv) = (u + du)(v + dv) - uv = u(dv) + v(du) + (du)(dv) \quad (1.12)$$

Since both  $du$  and  $dv$  are small, the product of  $du$  times  $dv$  must be much less than  $u(dv)$  or  $v(du)$ . If we make the changes small enough, then  $(du)(dv)$  can be neglected in Eq. (1.12). Throughout this textbook, we will make similar assumptions regarding our ability to ignore the products of two very small quantities [4].

The *Fundamental Theorem of Calculus* states that integration and differentiation are inverse processes. By rearranging Eq. (1.10) and integrating each term with respect to  $x$ , we can write an expression that allows for integration of the product of one function and the derivative of another function.

$$\int u(x) \frac{dv}{dx} dx = u(x)v(x) - \int v \frac{du}{dx} dx \quad (1.13)$$

This result is known as the method of *integration by parts*.

### 1.1.3 Logarithmic Differentiation

The natural logarithm can be defined in terms of the integral of  $x^{-1}$ .

$$\int \frac{dx}{x} = \ln(x) + C \quad (1.14)$$

$C$  is a constant. If we again apply the Fundamental Theorem of Calculus, we can write an expression for the differential,  $dx$ , in terms of the derivative of  $\ln(x)$ , remembering that the derivative of any constant must vanish.

$$d(\ln x) = \frac{dx}{x} \quad (1.15)$$

We will frequently be confronted by mathematical expressions that contain products and exponents. We can simplify our manipulations of such terms by taking the natural logarithms of those expressions and then differentiating. One typical example is the determination of the temperature change,  $dT$ , that accompanies a pressure change,  $dp$ , in a sound wave propagating under adiabatic conditions based on the Ideal Gas Law in Eq. (1.16) and the Adiabatic Gas Law in Eq. (1.17).

<sup>3</sup> Because the concept of a “differential” is so useful, it has multiple definitions that correspond to its usage in different contexts. For this discussion, the definition of the differential as a “small change” is adequate. In thermodynamic contexts, there are “inexact” differentials that produce changes in functions that are dependent upon the “path” of the change taken by the variable. A detailed discussion of the difference is presented by F. Reif, *Fundamentals of Statistical and Thermal Physics* (McGraw-Hill, 1965), Ch. 2, §11.

$$pV = n\mathfrak{R}T \quad (1.16)$$

$$pV^\gamma = \text{constant} \quad (1.17)$$

If we substitute the Ideal Gas Law into the Adiabatic Gas Law, we can write the absolute (kelvin) temperature,  $T$ , and pressure,  $p$ , in terms of a constant,  $C$ , related to the initial pressure and volume; the universal gas constant,  $\mathfrak{R}$ ; and the polytropic coefficient,  $\gamma$ . (Do not worry if none of this is familiar at this point, it is only meant to illustrate the mathematics and will be treated explicitly in Sect. 7.1.4.)

$$pV^\gamma = (n\mathfrak{R}T)^\gamma p^{1-\gamma} \Rightarrow T^\gamma p^{1-\gamma} = \frac{p_o V_o^\gamma}{(n\mathfrak{R})^\gamma} \equiv C \quad (1.18)$$

Again,  $C$  is just a constant that depends upon the initial conditions. The natural logarithm of both sides of the right-hand version of Eq. (1.18) produces Eq. (1.19).

$$\gamma \ln T + (1 - \gamma) \ln p = \ln C \quad (1.19)$$

Using *logarithmic differentiation*, as expressed in Eq. (1.15),

$$\gamma \frac{dT}{T} + (1 - \gamma) \frac{dp}{p} = 0 \Rightarrow \frac{dT}{T} = \frac{(\gamma - 1)}{\gamma} \frac{dp}{p} \quad (1.20)$$

Rearranging terms and recalling that we substituted into the Adiabatic Gas Law, this result provides an expression for the change in the temperature of an ideal gas in terms of the change in the pressure due to a sound wave that is propagating under adiabatic conditions.

$$\left( \frac{\partial T}{\partial p} \right)_s = \frac{(\gamma - 1)}{\gamma} \frac{T}{p} \quad (1.21)$$

The subscript “s” has been placed along the partial derivative to remind us that the change in temperature with pressure is evaluated for an adiabatic process in which the specific entropy (per unit mass),  $s$ , is held constant. As will be illustrated in our investigations of the coupling between sound waves and temperature changes, this is a particularly useful result. It has only been previewed here to illustrate how simple it is to do some calculations by taking a logarithm of an expression before differentiation. This will also be a rather convenient approach for calculation of the uncertainty of a result based on the uncertainty in the parameters that were used to calculate the result (i.e., “error propagation”; see Sect. 1.8.4).

## 1.2 Equilibrium, Stability, and Hooke’s Law

Pause for a moment as you are reading and look around. Close your eyes, count to ten, and then open your eyes. Probably not much has changed. This is because most of the material we observe visually is in a state of *stable equilibrium*.<sup>4</sup> For an object to be in equilibrium, the vector sum of all the forces acting on that body (i.e., the net force) must be zero, and the first derivative of the object’s *potential energy* with respect to its position must be zero. For that equilibrium state to be stable, the second derivative of the object’s potential energy must be positive.

<sup>4</sup> Here, we are referring to what is known as Lyapunov stability, which applies to dynamical systems in the vicinity of their equilibrium configuration.

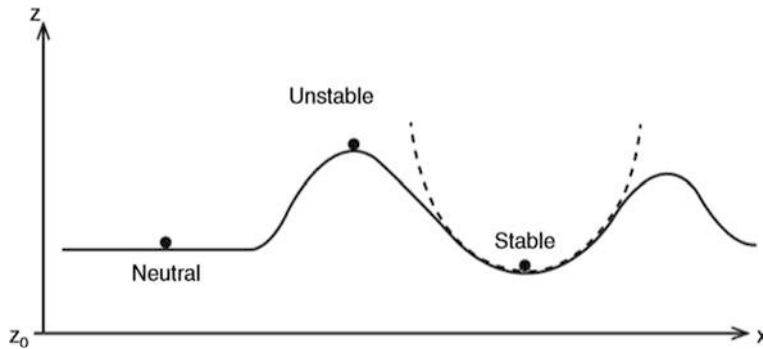


**Fig. 1.2** Potential energy (proportional to height) is shown as a function of position for three objects that are at rest in an equilibrium state within a gravitational field. The ball at the left is in a state of *neutral equilibrium*, since it can move to the left or the right by a small distance and not change its potential energy. The ball at the center is in a state of *unstable equilibrium*. Although the net force (gravitational downward and the force of the surface upward) is zero, if it is displaced by an infinitesimal distance to either the right or the left, it will leave its equilibrium position. The ball at the right is in a position of *stable equilibrium*. If it is displaced by an infinitesimal distance to either the *right* or to the *left*, the net force on the ball will tend to return it toward its equilibrium position. The dashed line is a parabola that is fit to match the curvature of the line near the position of stable equilibrium corresponding to the quadratic contribution in the Taylor series expansion of Eq. (1.23)

Figure 1.2 illustrates three possible equilibrium conditions based on the rate of change of a body's potential energy with position. For this illustration, let us assume that the solid curve represents the height,  $z$ , above some reference height,  $z_o$ , in a uniform gravitational field. The (gravitational) potential energy,  $PE(z)$ , of each of the three balls shown in Fig. 1.2 is therefore proportional to their height,  $z$ , where the mass of each ball is  $m$  and  $g$  is the acceleration due to gravity that is assumed to be independent of  $z$ :  $PE(z) = mg(z - z_o)$ .

The three balls in Fig. 1.2 each respond to a small displacement from their equilibrium positions differently. We can think of the solid curve as representing a flat surface on the left, two peaks at the center and the right, and a valley between two peaks. All three balls are in a state of mechanical equilibrium because the vector sum of the force of gravity (down) and of the surface (up) is zero. In all three cases, the first derivative of the potential energy vanishes at all three locations:  $d(PE)/dx = 0$ . The ball on the left is in a state of *neutral equilibrium* because it can be moved to the left or to the right by a small distance and it will still be at equilibrium, even at its displaced position. The curve at that location is flat and horizontal.

The other two balls are located at local extrema. The slopes of the tangents to the curves at those extrema are just both as horizontal and as the flat region on the left.<sup>5</sup> The ball near the center of Fig. 1.2

<sup>5</sup> The inability of some to connect mathematics with reality is illustrated by this short story told by Richard Feynman in his most entertaining autobiography entitled *Surely You're Joking, Mr. Feynman!* (W. W. Norton, 1985); ISBN 0-393-01921-7.

"I often liked to play tricks on people when I was at MIT. Once, in mechanical drawing class, some joker picked up a French curve (a piece of plastic for drawing smooth curves – a curly, funny-looking thing) and said 'I wonder if the curves on this thing have some special formula?'"

"I thought for a moment and said, 'Sure they do. The curves are very special curves. Lemme show ya,' and I picked up my French curve and began to turn it slowly. 'The French curve is made so that at the lowest point on each curve, no matter how you turn it, the tangent is horizontal.'"

"All the guys in the class were holding their French curve up at different angles, holding their pencil up to it at the lowest point and laying it along, and discovering that, sure enough, the tangent is horizontal. They were all excited by this 'discovery' – even though they had already gone through a certain amount of calculus and had already 'learned' that the derivative (tangent) of the minimum (lowest point) of any curve is zero (horizontal). They did not put two and two together. They didn't even know what they 'knew.'"

is at the top of the “hill,” so  $d(PE)/dx = 0$  and  $d^2(PE)/dx^2 < 0$ . The ball near the right in that figure is at the lowest point in the valley, so  $d(PE)/dx = 0$ , but down in the valley,  $d^2(PE)/dx^2 > 0$ .

The ball at the top of the peak is in a state of *unstable equilibrium* because if it is displaced by an infinitesimal amount in either direction, it will run away from its equilibrium position. In general, objects in states of unstable equilibrium do not remain in those states for very long.

The ball at the lowest point in the valley is in a state of stable equilibrium. If it is displaced in either direction, the potential energy increases, and the ball can reduce its energy by returning to its position of stable equilibrium. A dashed parabola has been drawn which matches the second derivative of the actual potential energy curve. The greater the distance from the point of stable equilibrium, the greater the difference between the actual curve representing the potential energy and the dashed parabola, but for small displacements from equilibrium, the real potential energy curve and the dashed parabola will be indistinguishable. The dashed parabola represents the second-order term in a Taylor series expansion of the potential energy about the equilibrium position provided in Eq. (1.23).

With this understanding of equilibrium and stability, we are in a position to formalize the application of potentials and forces to develop the formalism that is used to characterize the oscillations of systems that obey Hooke’s law.

### 1.2.1 Potentials and Forces

The relationship between forces and potential energy can be extended beyond our simple stability example. In general, the net (vector) force,  $\vec{F}_{net}$ , is the negative of the gradient of the (scalar) potential energy:  $\vec{\nabla}(PE) = -\vec{F}_{net}$ .<sup>6</sup> This is consistent with the definitions of work and energy.

$$W_{1,2} \equiv \int_1^2 \vec{F} \cdot d\vec{x} = (PE)_1 - (PE)_2 = -\Delta(PE) \quad (1.22)$$

The right-hand side assumes that  $\vec{F}$  is a conservative force<sup>7</sup> and the work,  $W_{1,2}$ , done in moving an object from position 1 to position 2, over some distance along the direction of the force (indicated by the “dot product” under the integral), leads to a change in potential energy,  $-\Delta(PE)$ . Again, application of the Fundamental Theorem of Calculus leads to the desired relationship between the gradients of the potential energy and the net force:  $\vec{\nabla}(PE) = -\vec{F}_{net}$ .

If we limit ourselves to the current example of a ball in the valley, we can expand the potential energy about the stable equilibrium position that is identified as  $x_o$ .

---

<sup>6</sup>The sign convention becomes obvious if we consider work against a gravitational field. In that case, if we raise an object,  $\vec{F}$  and  $d\vec{x}$  are antiparallel, and the integral is negative, although we have increased the mass’s potential energy by lifting it.

<sup>7</sup>The work done against a “conservative” force depends only upon the endpoints so that no work is done if the path brings the body back to its original position. The application of Stokes’ Theorem converts the closed path integral into a requirement that  $\text{curl}(\vec{F}) = \vec{\nabla} \times \vec{F} = 0$ , so conservative forces can be derived from the gradient of a scalar potential,  $U$ :  $\vec{F} = -\text{grad}(U) = -\vec{\nabla}U$ . For a more complete discussion, see H. Goldstein, *Classical Mechanics* (Addison-Wesley, 1950).

$$PE(x_o + dx) = PE(x_o) + \frac{d^2(PE)}{dx^2} \Big|_{x_o} \frac{(dx)^2}{2} + \frac{d^3(PE)}{dx^3} \Big|_{x_o} \frac{(dx)^3}{6} + \dots \quad (1.23)$$

Note that the first derivative of  $PE$  is missing from Eq. (1.23) because it is zero if  $x_o$  is the equilibrium position.<sup>8</sup> The term proportional to  $(dx)^3$  corresponds to the contribution to the difference between the actual curve and the dashed parabola in Fig. 1.2. If the deviation between the two curves is symmetric, then the leading correction term would be proportional to  $(dx)^4$ . If the deviation is not symmetric, the leading correction term will be proportional to  $(dx)^3$ .

In our one-dimensional example, the gradient of the potential energy will simply be the derivative of Eq. (1.23) with respect to  $x$ .

$$F_{net}(dx) = -\frac{d(PE)}{dx} = -\frac{d^2(PE)}{dx^2} \Big|_{x_o} (dx) - \frac{d^3(PE)}{dx^3} \Big|_{x_o} \frac{(dx)^2}{2} - \dots \quad (1.24)$$

For sufficiently small displacements from equilibrium, the parabolic approximation to the potential energy curve (i.e., the dashed parabola in Fig. 1.2) provides an adequate representation, and therefore the series of Eq. (1.24) that describes the force can be truncated after the first term.

$$F_{net}(dx) \cong -\frac{d^2(PE)}{dx^2} \Big|_{x_o} (dx) \equiv -K(dx) \quad (1.25)$$

The result in Eq. (1.25) is known as *Hooke's law*.<sup>9</sup> It states that the net force is proportional to the displacement from equilibrium,  $dx$ . Because of the minus sign, the net force is directed opposite to that displacement if  $K > 0$ . The new constant,  $K$ , is known as the "stiffness" when the potential energy is created by the extension or compression of a spring. It is equal to the negative of the second derivative of the potential energy, evaluated at the equilibrium position,  $x_o$ .

In this form, it is obvious that a positive curvature in the potential energy (i.e.,  $d^2(PE)/dx^2 > 0$ ) leads to a stable equilibrium but that a negative curvature in the potential energy causes the system to become unstable. In an unstable state of equilibrium, a small displacement from equilibrium creates a force that causes a small displacement to grow, regardless of the sign of the original displacement; at a position of unstable equilibrium, the stiffness constant,  $K$ , is a negative number.

The approximation represented by Hooke's law leads to a *linear relationship* between net force on a body and the displacement of that body from its position of stable equilibrium. It is normally introduced in elementary mechanics courses as the law which describes the force exerted by a spring when the spring is displaced from its equilibrium length,  $x_o$ . Two such springs are showed schematically in Fig. 1.3.

Both of the springs in Fig. 1.3 obey Hooke's law if the displacements,  $dx$ , from the equilibrium position at  $x_o$  are small:  $(dx)/x_o \ll 1$ . In both cases, large displacements from equilibrium will lead to nonlinear behavior. For the coil spring, excess compression will cause the coils to close up, and the force necessary for further compression will be much larger than predicted by Hooke's law. Similarly, for excess extension, the coils will straighten out, again requiring excess force, until the material fractures and the broken end can be moved an infinite distance without requiring any additional force.

<sup>8</sup> Any constant added to the potential energy has no effect on any observable quantity. This independence of any constant offset in the potential is known as "gauge invariance."

<sup>9</sup> This law is named after Robert Hooke, FRS, who first stated it as a Latin anagram in 1660 and then published the solution in 1678 as *Ut tensio, sic vis*; literally translated, it means "As the extension, so the force."

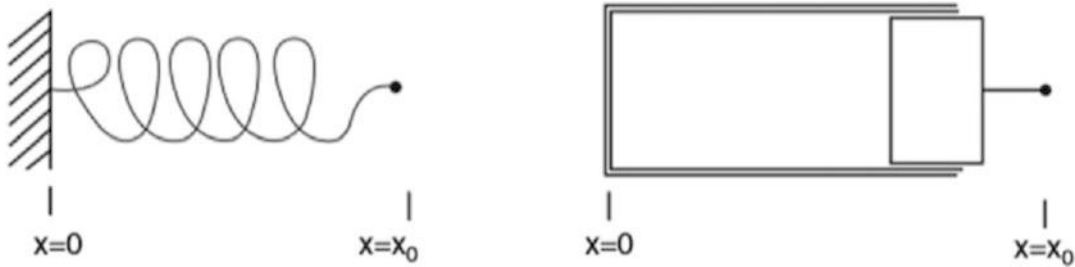


**Fig. 1.3** Schematic representation of two springs that obey Hooke's law for small displacements from their equilibrium positions,  $x_o$ . The spring at the left represents a coil of wire with one end fixed (represented by the hatched wall) at  $x = 0$  and an equilibrium length of  $x_o$ . The spring at the right represents an air-filled cylinder that is closed at the end located at  $x = 0$  and is sealed at the opposite end by a close-fitting, frictionless piston. (It is possible to purchase a piston and cylinder combination that behaves very much like this leak-tight, frictionless idealization. It is called an Airpot® and consists of a glass cylinder and a matched graphite piston: [www.airpot.com](http://www.airpot.com). One such Airpot® is shown in Prob. 4 at the end of Chap. 7, in Fig. 7.6.) The equilibrium position of the gas spring at  $x_o$  occurs when the mean gas pressure inside the cylinder is equal to the mean gas pressure outside the cylinder

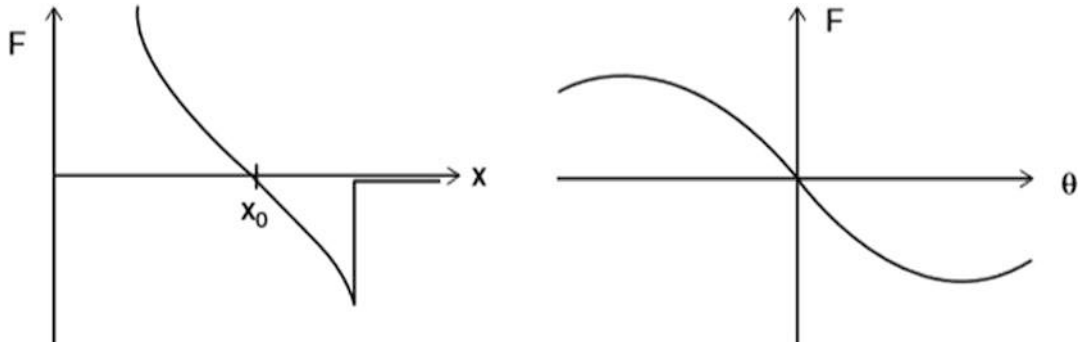


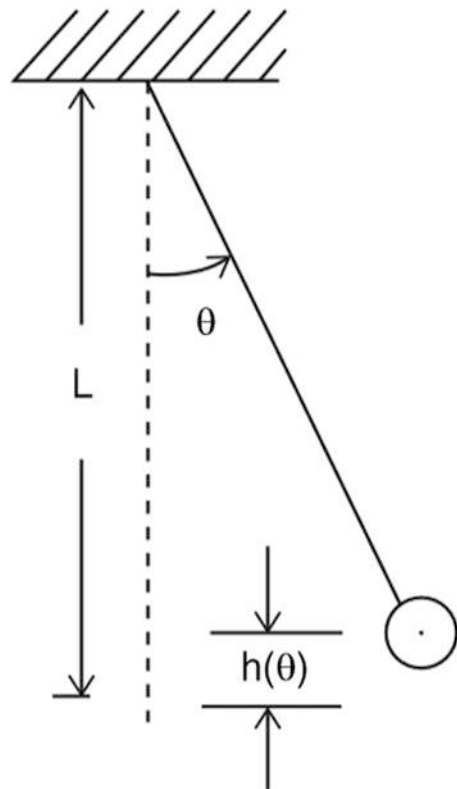
**Fig. 1.4** Two graphs of force vs. displacement which illustrate deviations from linear Hooke's law behavior for two systems that each possess a position of stable equilibrium. At the left is a graph representing springs like those shown in Fig. 1.3. For small displacements from the equilibrium position,  $x_o$ , the force is a linear function of displacement. As  $x$  becomes significantly smaller than  $x_o$ , the spring "stiffens," producing significantly larger forces for a given displacement, presumably because adjacent coils have made contact. As  $x$  becomes significantly greater than  $x_o$ , the spring again stiffens. In this limit, the coils have begun to uncoil, and the force is increasing due to the tensile strength of the coil spring's material. Eventually, the material fractures or the piston is removed from the cylinder, and the force goes to zero. The graph at the right might represent the restoring force of a pendulum that is displaced from its equilibrium vertical position hanging down at  $\theta_o = 0$  (see Fig. 1.5). Again, there is a linear portion of the force vs. angular displacement for small values of  $\theta \ll 1$ , but as the angle increases, less force is required for each increment of angle. This nonlinear spring behavior is called "softening."

Similar deviations from the linear behavior predicted by Hooke's law occur for the gas spring. Two examples of the force vs. displacement that go beyond the linear regime are illustrated in Fig. 1.4.

## 1.2.2 A Simple Pendulum

To emphasize the fact that "linear" behavior is not restricted to linear motion, consider the spherical mass suspended from a rigid ceiling by a (massless) string of length,  $L$ , in a uniform gravitational field, as shown schematically in Fig. 1.5. Its position of stable equilibrium corresponds to the mass hanging

**Fig. 1.5** The pendulum consists of a sphere of mass,  $m$ , which is supported by a massless string. The distance from the point of support to the center of mass of the sphere is  $L$ . When the sphere is displaced from its equilibrium position,  $\theta_0 = 0$ , this angular displacement,  $\theta$ , causes the sphere's center of mass to rise above its equilibrium height by a vertical distance,  $h$ . The associated increase in the gravitational potential energy of the sphere is given by Eq. (1.26). The restoring torque on the pendulum is given by the gradient in the potential energy and is shown schematically in the graph of Fig. 1.4 (right)



vertically downward beneath the point of suspension; hence  $\theta_0 = 0$ . In this case, the gravitational potential energy is a function of the angular displacement corresponding to the change in vertical height of the sphere's center of mass,  $h(\theta)$ , within a gravitational field that is presumed to produce a constant gravitational acceleration,  $g$ . The relationship between the displacement angle,  $\theta$ , and the height change,  $h(\theta)$ , can be calculated from trigonometry.

$$PE(\theta) = mgL[1 - \cos \theta] \cong mgL\left[\frac{\theta^2}{2} - \frac{\theta^4}{24} + \dots\right] \quad (1.26)$$

The above approximation uses a power (Taylor) series expansion of the cosine function from Eq. (1.6). The magnitude of the corresponding restoring torque,  $N(\theta)$ , is given by the negative of the gradient of the potential energy with respect to angle.

$$N(\theta) = -\frac{\partial [PE(\theta)]}{\partial \theta} \cong -mgL\left[\theta - \frac{\theta^3}{6} + \dots\right] \quad (1.27)$$

For  $\theta \ll 1$ , the restoring torque is proportional to the angular displacement from stable equilibrium. In this limit, this results in a torsional stiffness that is a constant. For larger displacements from equilibrium, additional effects generated by the  $\theta^3$  term in Eq. (1.27) reduce the torque producing the “softening” behavior shown in Fig. 1.4 (Right).

### 1.3 The Concept of Linearity

At least 95% (by weight?) of the systems analyzed in this textbook will assume that the dynamical processes occur within the linear regime. This assumption brings with it amazing mathematical and physical simplifications. As will be discussed here, linearity guarantees that:

1. The frequency of oscillation of a “free” system is amplitude-independent (*isochronism*).
2. The steady-state response of a driven linear system occurs only at the driving frequency.
3. We can superimpose an infinite number of responses to simple stimuli to determine the linear system’s response to a very complicated stimulus and vice versa.

The founder of modern science, Galileo Galilei (1564–1642), was the first to record his observation that the period of a pendulum was independent of the amplitude of its displacement. Legend has it that he made that observation in the Cathedral of Pisa when he was a student living in that city. Being bored in church, he noticed that when the wind moved the chandeliers, the period of oscillation, measured against his own pulse rate, was independent of the amplitude of chandeliers’ swing. Although Galileo recognized the value of this amplitude independence for time-keeping devices, it was not until 17 years after Galileo’s death that the great Dutch physicist, Christiaan Huygens (1629–1695), described his “pendulum clock” and other time pieces with errors of less than 1 min/day (later, less than 10 s/day) whose accuracy relied on the amplitude independence of the period of the pendulum.

The behavior of nonlinear springs is dramatically different than the Hooke’s law behavior [5]. When driven at a frequency,  $\omega$ , the system can respond at multiples, or sub-multiples of the driving frequency [6], and can produce non-zero time-averaged changes in the equilibrium position. Nonlinear elastic behavior in solids is responsible for the fact that the thermal expansion coefficient of solids is non-zero. As temperature increases, the thermal vibrational amplitude of the solid’s atoms causes their equilibrium separation to change [7].

Although we have thus far only considered the behavior of systems displaced a small distance from their position of stable equilibrium (thus producing a linear restoring force), we will combine that result with the behavior of masses and dampers in the next chapter on simple harmonic oscillators. The dynamics of masses and dampers also exhibit a substantial linear regime. Newton’s Second Law of Motion,  $\ddot{\vec{F}} = m\ddot{\vec{x}}$ , is linear because it relates the acceleration of a mass to the net force acting on that mass. Acceleration is the second time derivative of displacement and does not involve higher powers of displacement. Similarly, there is a regime where the damping force can be linear in velocity,  $v(t) = \dot{x}(t) \equiv dx(t)/dt$ , which is the first time derivative of displacement. Although we will investigate the behavior of the damped simple harmonic oscillator in the next chapter, we can write down the equation for a linear operator,  $\underline{L}(x)$ , that describes the response of such an oscillator to an externally applied time-dependent force,  $F(t)$ .

$$\underline{L}(x) = m \frac{d^2x}{dt^2} + R_m \frac{dx}{dt} + Kx = F(t) \quad (1.28)$$

To simplify our discussion of linear response, we can lump all of these linear operations performed on  $x$  into a general linear operator,  $\underline{L}(x)$ , where  $\underline{L}$  is underlined to remind us that it is an “operator,” not a function.<sup>10</sup> That operator defines a combination of mathematical procedures that are applied to an independent variable,  $x$  in this case. The operator in Eq. (1.28) is a second-order linear differential

---

<sup>10</sup>This “linear operator” approach is taken from *The Feynman’s Lectures on Physics*, R. P. Feynman, R. B. Leighton, and M. Sands (Addison-Wesley, 1963), Vol. I, Ch. 25.

equation with constant coefficients, those coefficients being the mass,  $m$ ; the mechanical resistance,  $R_m$ ; and the stiffness,  $K$ .

By substitution into Eq. (1.28), it is easy to demonstrate that all linear operations exhibit both an additive and a multiplicative property where  $a$  is an arbitrary scalar.

$$\underline{L}(x + y) = \underline{L}(x) + \underline{L}(y) \quad (1.29)$$

$$\underline{L}(ax) = a\underline{L}(x) \quad (1.30)$$

In fact, these two properties of linear operators can be extended indefinitely.

$$\underline{L}(ax + by + cz + \dots) = a\underline{L}(x) + b\underline{L}(y) + c\underline{L}(z) + \dots \quad (1.31)$$

These properties demonstrate that if we have a solution to Eq. (1.28), that any scalar multiple of that solution is also a solution; if we double the force, we double the response. Similarly, if both  $x_a(t)$  and  $x_b(t)$  are two responses to two forces,  $F_a(t)$  and  $F_b(t)$ , possibly acting at two different frequencies, then their sum is the response to the sum of those forces.

$$\underline{L}(x_a + x_b) = \underline{L}(x_a) + \underline{L}(x_b) = F_a(t) + F_b(t) \quad (1.32)$$

## 1.4 Superposition and Fourier Synthesis

*“Superposition is our compensation for enduring the limitations of linearity”.* [8]

The ability exhibited by Eq. (1.31) to combine solutions to linear equations is so significant that it has its own name: *The Principle of Superposition*. It guarantees that if we can decompose a complicated excitation into the sum of simpler excitations, we can calculate the responses to the simple excitations, and then we can combine those simple solutions to determine the response to the more complicated excitation.

We all have experience with this concept when we locate a point on a two-dimensional surface using Cartesian coordinates. The  $x$  and  $y$  axes form an orthogonal basis that specifies the horizontal and vertical directions. When we want to specify a particular point on that surface, we draw a vector,  $\vec{r}$ , from the origin of the coordinate system to the point and project that vector on to our orthogonal axes by taking the dot product of the vector,  $\vec{r}$ , with the unit vectors,  $\hat{e}_x$  and  $\hat{e}_y$ , along each axis.

$$(x, y) = (\vec{r} \cdot \hat{e}_x, \vec{r} \cdot \hat{e}_y) \quad (1.33)$$

In that way, the ordered sequence of two numbers,  $(x, y)$ , produced by those two operations, uniquely specifies a point on the plane.

This simple concept can be extended to a representation of a function as a superposition of *orthogonal functions*. A general  $n^{\text{th}}$ -order, linear differential equation with constant coefficients,  $a_i$ , will have the form expressed below:

$$a_n \frac{d^n x}{dt^n} + a_{n-1} \frac{d^{n-1} x}{dt^{n-1}} + \dots + a_1 \frac{dx}{dt} + a_0 = F(t) \quad (1.34)$$

There will be  $n$  linearly independent solutions to such an equation, where we mean that the solutions are “independent” if it is not possible to express one of the linearly independent solutions in terms of

linear combinations of the others.<sup>11</sup> With a few minor exceptions (such as flexural waves on bars and plates), our focus in this textbook will be on systems described by second-order differential equations with constant coefficients. For that case  $n = 2$ , so there will be two linearly independent solutions. One convenient choice of independent solutions for vibration and acoustics is the sine and cosine functions.

The representation of periodic functions as the sum of simple oscillating functions dates back to the third century BC when ancient astronomers proposed models of planetary motion based on epicycles. The first use of trigonometric functions as a basis for solving a linear differential equation was made by Jean-Baptiste Joseph Fourier (1768–1830). In his *Treatise on the Propagation of Heat in Solid Bodies*, published in 1807, he used the technique that now bears his name to analyze the diffusion of heat through a metal plate.

As we will see, the solutions to equations describing vibration and sound are particularly simple if the disturbances are sinusoidal in space and/or time. For more complicated disturbances, which are periodic with period,  $T_1$ , it is possible to decompose the disturbance into the sum of sinusoidal disturbances with the same period as the complicated waveform. If the complicated waveform is a continuous function, the periodic waveform can be represented by an infinite number of sines and cosines, each with the correct amplitude, that have frequencies that are integer multiples of the fundamental frequency of the complicated waveform,  $f_1 = T_1^{-1} = \omega/2\pi$ .

$$f(t) = \frac{A_o}{2} + \sum_{n=1}^{\infty} [A_n \cos(n\omega t) + B_n \sin(n\omega t)]. \quad (1.35)$$

The coefficients,  $A_n$  and  $B_n$ , are determined in the same way we selected the  $x$  and  $y$  coordinates for a point on a Cartesian plane; we take the equivalent of the dot product of the complicated function with the linearly independent basis functions over an entire period,  $T$ . Such a “dot product,” also known as the “inner product,” is represented by the following integrals:

$$A_0 = \frac{1}{T} \int_0^T f(t) dt \text{ and } A_n = \frac{2}{T} \int_0^T f(t) \cos(n\omega t) dt \text{ for } n \geq 1 \quad (1.36)$$

$$B_n = \frac{2}{T} \int_0^T f(t) \sin(n\omega t) dt \quad (1.37)$$

Since  $\sin(0) = 0$ , there is no need for  $B_o$ . Since  $\cos(0) = 1$ ,  $A_o$  is just the average of  $f(t)$  over one period,<sup>12</sup> divided by the period,  $T$ . The sine and cosine functions are linearly independent, and the orthogonality of the harmonics of the individual sine and cosine functions can be expressed in terms of the *Kronecker delta* function,  $\delta_{m,n}$ , which is zero if  $m \neq n$  and one if  $m = n$ .

$$\begin{aligned} \frac{2}{T} \int_0^T \cos(m\omega t) \cos(n\omega t) dt &= \delta_{m,n} \\ \frac{2}{T} \int_0^T \sin(m\omega t) \sin(n\omega t) dt &= \delta_{m,n} \end{aligned} \quad (1.38)$$

Depending upon the nature of  $f(t)$ , it is possible that many of the  $A_n$  and  $B_n$  coefficients may be zero. If  $f(t)$  is symmetric about the time axis, then  $A_o = 0$ . If  $f(t) = f(-t)$ , then  $f(t)$  is an even function of  $t$  and

---

<sup>11</sup> For our example of a Cartesian coordinate system, the  $x$  and  $y$  axes are independent because it is impossible to specify some non-zero location on the  $y$  axis using any  $x$  value.

<sup>12</sup> In the parlance of electrical engineers,  $A_o$  is the “DC offset.”

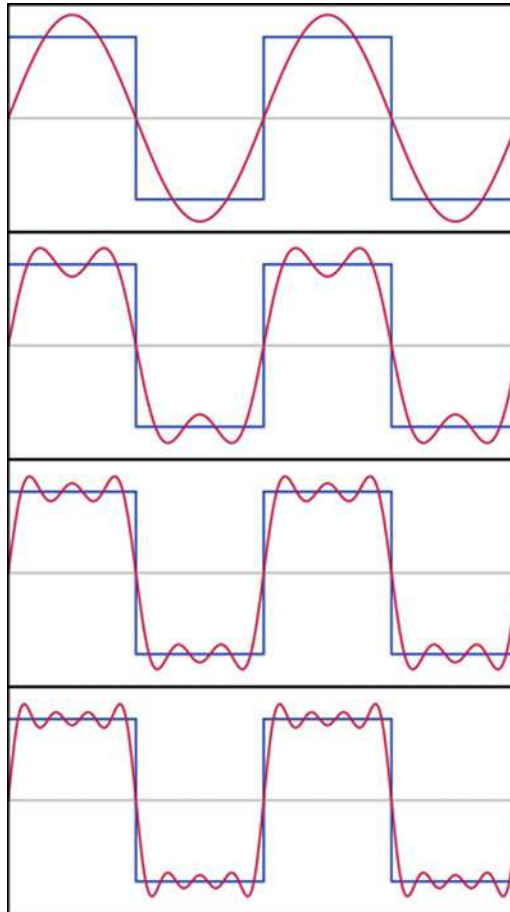


**Fig. 1.6** The square wave defined in Eq. (1.39) is shown along with the sum of the first through fourth non-zero Fourier components. The first term is simply a sinusoidal waveform that is synchronized with the square wave. The third harmonic contribution starts to deform the sum into a shape that more closely resembles the square wave. Addition of the fifth harmonic, and then the seventh harmonic, improves the fidelity of the superposition and makes the slope of the zero-crossing transitions more nearly vertical. Clearly superposition of an infinite number of harmonics would be required to simulate the infinite slope of those transitions and reduce the “ripple” on the plateaus, although the small (9%) overshoot will remain. It does not disappear as more terms are added; it simply becomes narrower [10]. Since the square wave is not a “continuous” function but has a discontinuous slope, its Fourier series representation will have an “overshoot” (known as “ringing”) about those transitions. This is known as the “Gibbs phenomenon”

$B_n = 0$  for all  $n$ , since sine is an odd function. Similarly, if  $f(t) = -f(-t)$ , then  $f(t)$  is an odd function of  $t$ , and  $A_n = 0$  for all  $n$ , since cosine is an even function.

The process of assembling a “complex” waveform from simpler sinusoidal components is known as *Fourier synthesis*. To illustrate Fourier synthesis, let us represent a square wave,  $f_{\text{square}}(t)$ , of unit amplitude and period,  $T$ , that is defined for one period below and is shown in Fig. 1.6:

$$f_{\text{square}}(t) = \begin{cases} +1 & 0 \leq t < T/2 \\ -1 & T/2 \leq t < T \end{cases} \quad (1.39)$$

Since  $f_{\text{square}}(t)$  is symmetric,  $A_o = 0$  and because it is an odd function of  $t$ , only the  $B_n$  coefficients will be non-zero. Substitution of Eq. (1.39) into Eq. (1.37) breaks the integral into two parts.

$$B_n = \frac{2}{T} \left[ \int_0^{T/2} \sin(n\omega t) dt - \int_{T/2}^T \sin(n\omega t) dt \right] \quad (1.40)$$

The integral of the  $\sin(ax)$  over  $x$  is available from any table of integrals. My favorite is the Russian compilation by Gradshteyn and Ryzhik [9].

$$\int \sin(ax) dx = \frac{-1}{a} \cos(ax) + C \quad (1.41)$$

For this problem  $\omega = 2\pi/T$ , so  $a = 2\pi n/T$ .

$$B_n = \frac{1}{n\pi} \left[ -\cos\left(\frac{2\pi n t}{T}\right) \Big|_0^{T/2} + \cos\left(\frac{2\pi n t}{T}\right) \Big|_{T/2}^T \right] \quad (1.42)$$

For odd values of  $n$ ,  $B_n = (4/n\pi)$ , and for even values of  $n$ ,  $B_n = 0$ , so the Fourier series representation of our unit symmetric square wave can be written as an infinite sum.

$$f_{\text{square}}(t) = \frac{4}{\pi} \left[ \sin\left(\frac{2\pi t}{T}\right) + \frac{1}{3} \sin\left(\frac{6\pi t}{T}\right) + \frac{1}{5} \sin\left(\frac{10\pi t}{T}\right) + \dots \right] \quad (1.43)$$

Again, the fact that  $\omega = 2\pi/T$  allows us to rewrite this result in terms of angular frequencies.

$$f_{\text{square}}(t) = \frac{4}{\pi} \left[ \sin(\omega t) + \frac{\sin(3\omega t)}{3} + \frac{\sin(5\omega t)}{5} + \dots \right] \quad (1.44)$$

The sum of the first four terms is shown in Fig. 1.6, illustrating that the addition of successive terms makes the Fourier series superposition an ever more faithful representation of  $f_{\text{square}}(t)$ .<sup>13</sup>

We could repeat the process to determine the Fourier representation of a triangle wave  $f_{\text{triangle}}(t)$ , but if we simply recognize that a triangular wave is the integral of a square wave, then we can integrate Eq. (1.44) term by term.

$$f_{\text{triangle}}(t) = \frac{4}{\pi^2} \left[ \cos(\omega t) + \frac{\cos(3\omega t)}{9} + \frac{\cos(5\omega t)}{25} + \dots \right] \quad (1.45)$$

Since the shape of the triangle wave is much closer to that of a sine or cosine, the high-frequency components decay more quickly (as  $n^{-2}$ ) than those of the square wave (as  $n^{-1}$ ).

---

## 1.5 Convenience (Complex) Numbers

*“The most beautiful formula in mathematics:  $e^{j\pi} + 1 = 0$ .” [11]*

---

<sup>13</sup> Since the square wave is not a “continuous” function but has a discontinuous slope, its Fourier series representation will have an “overshoot” of about 9% with oscillations (known as “ringing”) about those transitions, even with the inclusion of an infinite number of terms. This is known as the “Gibbs phenomenon.”

Calculus is a set of rules that allow us to convert expressions that involve integrals and derivatives into algebraic equations. The simplest of these rules are those which allow us to write down the integrals and derivatives of polynomials and exponentials:

$$\frac{d(ax^n)}{dx} = anx^{n-1} ; \quad \int ax^n dx = \frac{ax^{n+1}}{n+1} + C \quad (1.46)$$

$$\frac{d(ae^{bx})}{dx} = abe^{bx} ; \quad \int ae^{bx} dx = \frac{ae^{bx}}{b} + C \quad (1.47)$$

We have already exploited the simplicity of Eq. (1.46) because our Taylor series expansions resulted in polynomial representations of various functions (see Sect. 1.1.1). In this section, we will exploit the simplicity of Eq. (1.47) in a way that allows us to encode the two linearly independent solutions to a second-order differential equation into a single function by simply multiplying one of those two solutions by the square root of  $(-1)$ . That special linear coefficient will be designated as  $j \equiv \sqrt{-1}$ .

The fact that  $j$  allows us to combine (i.e., superimpose) the solutions to differential equations of interest in a way that permits the use of Eq. (1.47) to do our calculus is the reason I call  $j$  the “convenience number.” Unfortunately, I am the only person who calls  $j$  the convenience number. Everyone else calls  $j$  the unit “imaginary number.”<sup>14</sup> Numbers that contain an imaginary component are called “complex numbers.” This poor historical choice of nomenclature suggests that there is something “complex” about the use of  $j$  when the contrary is true;  $j$  makes computations simpler.

To appreciate the convenience of  $j$ , we can start by examining the solution to the simplest homogeneous second-order differential equation with a constant coefficient that has been designated  $\omega_o^2$  for reasons that will become obvious in the next chapter.

$$\frac{d^2x}{dt^2} + \omega_o^2 x = 0 \quad \text{or} \quad \frac{d^2x}{dt^2} = -\omega_o^2 x \quad (1.48)$$

When written as the right-hand version of Eq. (1.48), it is clear that we seek a solution which produces the negative of itself when differentiated twice. Sine and cosine functions have exactly that property, being linearly independent.<sup>15</sup>

$$\frac{d \sin(at)}{dt} = a \cos(at) ; \quad \int \sin(at) dt = -\frac{\cos(at)}{a} + C \quad (1.49)$$

$$\frac{d \cos(at)}{dt} = -a \sin(at) ; \quad \int \cos(at) dt = \frac{\sin(at)}{a} + C \quad (1.50)$$

Double differentiation of either sine or cosine regenerates the negative of the original function, as required by Eq. (1.48).<sup>16</sup> Superposition allows us to write the complete solution to Eq. (1.48) by introducing two arbitrary scalar constants,  $A$  and  $B$ :

<sup>14</sup> This textbook uses  $j$  to designate the unit imaginary number. That choice is more common among engineers. Physicists and mathematicians prefer to let  $i = (-1)^{1/2}$ . Of course, the choice is arbitrary.

<sup>15</sup> The orthogonality of the sine and cosine functions can be expressed by integrating their product over one period,  $T$ :  $\int_0^T \cos(mt) \sin(nt) dt = 0$ , where  $m$  and  $n$  are any integers, including zero.

<sup>16</sup> We could have obtained the same result in a more general way by assuming an infinite-order polynomial solution and then identifying the resulting series using the Taylor series expansions of Eqs. (1.5) and (1.6). For this approach, see P. M. Morse, *Vibration and Sound* (Acoustical Society of America, 1976); ISBN 0-88318-287-4.

$$x(t) = A \cos(\omega_o t) + B \sin(\omega_o t) \quad (1.51)$$

Using our definition of  $j \equiv \sqrt{-1}$  and the rules for differentiating exponentials in Eq. (1.47), we see that an exponential with an imaginary exponent will also obviously satisfy Eq. (1.48), where again  $A$  and  $B$  are scalar constants that facilitate superposition of the two solutions.

$$x(t) = Ae^{j\omega_o t} + Be^{-j\omega_o t} \quad (1.52)$$

Thanks to our earlier investment in the Taylor series expansions of sine, cosine, and exponential functions, we see that these solutions are identical if we use Eq. (1.4) to expand  $e^{j\theta}$  in a power series and group together terms that are multiplied by  $j$ .

$$e^{j\theta} = 1 - \frac{\theta^2}{2!} + \frac{\theta^4}{4!} - \cdots + j \left[ \theta - \frac{\theta^3}{3!} + \frac{\theta^5}{5!} - \cdots \right] = \cos \theta + j \sin \theta \quad (1.53)$$

This result is known as *Euler's formula* named after Swiss mathematician and physicist Leonhard Euler (1707–1783). By similar means, we see that  $e^{-j\theta} = \cos \theta - j \sin \theta$ . It is also easy to demonstrate the relationship between exponential functions of imaginary arguments and trigonometric functions by taking sums and differences of these expressions of Euler's identity.

$$\cos \theta = \frac{e^{j\theta} + e^{-j\theta}}{2}; \quad \sin \theta = \frac{e^{j\theta} - e^{-j\theta}}{2j} \quad (1.54)$$

These algebraic manipulations certainly build confidence in the equivalence of the two solutions of Eq. (1.48), but for our purposes, a geometric interpretation will have significant utility in our study of both vibrations and waves.

### 1.5.1 Geometrical Interpretation on the Argand Plane

To develop and exploit this geometric interpretation of exponential functions, which contain complex numbers within their arguments (hereafter referred to as *complex exponentials*), we can represent a complex number on a two-dimensional plane known as the “complex plane” or the *Argand plane*. In that representation, we define the  $x$  axis as the “real axis” and the  $y$  axis as the “imaginary axis.” This is shown in Fig. 1.7. In this geometric interpretation, multiplication by  $j$  would correspond to making a “left turn” [12], that is, making a  $90^\circ$  rotation in the counterclockwise direction. Since  $j*j = j^2 = -1$  would correspond to two left turns, a vector pointing along the real axis would be headed backward, which is the equivalent of multiplication by  $-1$ .

In this textbook, complex numbers will be expressed using **bold** font. A complex number,  $\mathbf{z} = x + jy$ , where  $x$  and  $y$  are real numbers, would be represented by a vector of length,  $|\vec{r}| = \sqrt{x^2 + y^2}$ , from the origin to the point,  $\mathbf{z}$ , on the Argand plane, making an angle with the positive real axis of  $\theta = \tan^{-1}(y/x)$ . The complex number could also be represented in polar coordinates on the Argand plane as  $\mathbf{z} = Ae^{j\theta}$ , where  $A = |\vec{r}|$ . The geometric and algebraic representations can be summarized by the following equation:

$$\mathbf{z} = x + jy = |\mathbf{z}|(\cos \theta + j \sin \theta) = |\mathbf{z}|e^{j\theta} \quad (1.55)$$

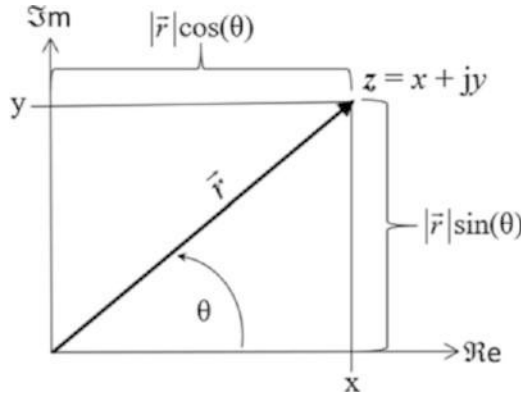


**Fig. 1.7** Representation of a complex number,  $z$ , on the Argand plane. The projection of  $z$  on the Cartesian  $x$  axis represents the real part of  $z$ , and the  $y$  axis projection represents the imaginary part of  $z$ . The projections of the vector,  $\vec{r}$ , onto the real and imaginary axes provide  $\Re(z) = x = |\vec{r}| \cos \theta$  and  $\Im(z) = y = |\vec{r}| \sin \theta$ . The ordinary rules of plane geometry and trigonometry apply. For example,  $|\vec{r}| = (x^2 + y^2)^{1/2}$  and  $\theta = \tan^{-1}(y/x)$

### 1.5.2 Phasor Notation

In this textbook, much of our analysis will be focused on response of a system to a single-frequency stimulus. We will use complex exponentials to represent time-harmonic behavior by letting the angle  $\theta$  increase linearly with time,  $\theta = \omega_o t + \phi$ , where  $\omega_o$  is the frequency (angular velocity) which relates the angle to time and  $\phi$  is a constant that will accommodate the incorporation of initial conditions (see Sect. 2.1.1) or the phase between the driving stimulus and the system's response (see Sect. 2.5). As the angle,  $\theta$ , increases with time, the projection of the uniformly rotating vector,  $\vec{x} = |\vec{x}| e^{j\omega_o t + j\phi t} \equiv \hat{\mathbf{x}} e^{j\omega_o t}$ , traces out a sinusoidal time dependence on either axis. This choice is also known as *phasor* notation. In this case, the phasor is designated  $\hat{\mathbf{x}}$ , where the “hat” reminds us that it is a phasor and its representation in **bold** font reminds us that the phasor is a complex number.

$$\hat{\mathbf{x}} = |\hat{\mathbf{x}}| e^{j\theta} \quad (1.56)$$

Although the projection on either the real or imaginary axis generates the time-harmonic behavior, the traditional choice is to let the real component (i.e., the projection on the real axis) represents the physical behavior of the system. For example,  $x(t) \equiv \Re[\hat{\mathbf{x}} e^{j\omega_o t}]$ .

### 1.5.3 Algebraic Operations with Complex Numbers

The rectangular representation and the polar representation have complementary utility, as the following review of algebraic operations will demonstrate. Addition and subtraction of two complex numbers allow a vector operation to be converted to an algebraic operation, as it would if our concern were analytic geometry instead of complex arithmetic. Starting with two complex vectors,  $\mathbf{A}_1 = a_1 + jb_1 = |\mathbf{A}_1| e^{j\theta_1}$  and  $\mathbf{A}_2 = a_2 + jb_2 = |\mathbf{A}_2| e^{j\theta_2}$ , where  $a$  and  $b$  are real scalars, their sum and difference are just the sums and differences of their real and imaginary components:

$$\mathbf{A}_1 + \mathbf{A}_2 = (a_1 + a_2) + j(b_1 + b_2) \quad \text{and} \quad \mathbf{A}_1 - \mathbf{A}_2 = (a_1 - a_2) + j(b_1 - b_2) \quad (1.57)$$

The utility of the polar representation becomes manifest for operations involving multiplication and division. In terms of their real and imaginary components,  $a$  and  $b$ , multiplication of two complex numbers proceeds just as in the case of the multiplication of two binomials.

$$\mathbf{A}_1 \mathbf{A}_2 = (a_1 + jb_1)(a_2 + jb_2) = (a_1 a_2 - b_1 b_2) + j(a_1 b_2 + b_1 a_2) \quad (1.58)$$

Multiplication by anything other than a scalar is not a linear process, so the real and imaginary components become mixed by multiplication. The equivalent operation expressed in polar coordinates is both simpler to execute and easier to visualize.

$$\mathbf{A}_1 \mathbf{A}_2 = |\mathbf{A}_1| e^{j\theta_1} |\mathbf{A}_2| e^{j\theta_2} = |\mathbf{A}_1| |\mathbf{A}_2| e^{j(\theta_1 + \theta_2)} \quad (1.59)$$

The division of two complex numbers in component form introduces the procedure known as *rationalization*. This is accomplished by multiplying both the numerator and denominator by the *complex conjugate* of the denominator. The complex conjugate of a complex number is just that number with the sign of the imaginary part changed. The complex conjugate is usually designated by an asterisk:  $z^* = x - jy$ ; hence,  $\Im[(z)(z^*)] = \Im[(z^*)(z)] = 0$  (see Sect. 1.5.5). When faced with division by a complex number, the rationalization process makes the denominator a real number and allows the result to be separated into its real and imaginary components.

$$\frac{\mathbf{A}_1}{\mathbf{A}_2} = \frac{(a_1 + jb_1)}{(a_2 + jb_2)} = \frac{(a_1 + jb_1)}{(a_2 + jb_2)} \frac{(a_2 - jb_2)}{(a_2 - jb_2)} = \frac{(a_1 a_2 + b_1 b_2)}{a_2^2 + b_2^2} + j \frac{b_1 a_2 - a_1 b_2}{a_2^2 + b_2^2} \quad (1.60)$$

Again, the process of division is nonlinear, so the real and imaginary components are comingled. The polar representation provides both greater insight and simplified execution.

$$\frac{\mathbf{A}_1}{\mathbf{A}_2} = \frac{|\mathbf{A}_1| e^{j\theta_1}}{|\mathbf{A}_2| e^{j\theta_2}} = \frac{|\mathbf{A}_1|}{|\mathbf{A}_2|} e^{j(\theta_1 - \theta_2)} \quad \text{if } |\mathbf{A}_2| \neq 0 \quad (1.61)$$

Raising a number to a real power or extracting a real root is also simplified using a polar representation.

$$\mathbf{A}^n = (|\mathbf{A}| e^{j\theta})^n = |\mathbf{A}|^n e^{jn\theta} \quad (1.62)$$

Since the extraction of the  $n^{\text{th}}$  root generates  $n$  solutions, it is helpful to include the periodicity of the complex exponential explicitly, since addition of integer multiples of  $2\pi$  to the angle  $\theta$  does not change its value.

$$\sqrt[n]{\mathbf{A}} = \mathbf{A}^{(1/n)} = \left( \mathbf{A} e^{j(\theta + 2\pi\nu)} \right)^{(1/n)} = |\mathbf{A}|^{(1/n)} e^{j[(\theta/n) + 2\pi(\nu/n)]} \quad (1.63)$$

This will generate  $n$  roots with  $\nu = 0, 1, 2, \dots, (n-1)$ . Inclusion of larger integer values of  $\nu \geq n$  just regenerates the same roots. For example, if we calculate the square root of 4,

$$\sqrt{4} = 2e^{j(0/2)} = 2 \quad \text{and} \quad \sqrt{4} = 2e^{j(2\pi/2)} = 2e^{j\pi} = -2. \quad (1.64)$$

The cube root of 8 has three solutions:

$$\begin{aligned} \sqrt[3]{8} &= 2e^{j(0/3)} = 2e^{j0} = 2 \\ \sqrt[3]{8} &= 2e^{j(2\pi/3)} = 2[\cos(2\pi/3) + j\sin(2\pi/3)] = -1 + j\sqrt{3} \\ \sqrt[3]{8} &= 2e^{j(4\pi/3)} = 2[\cos(4\pi/3) + j\sin(4\pi/3)] = -1 - j\sqrt{3} \end{aligned} \quad (1.65)$$

In polar representation, the three roots are three two-unit-long vectors separated by  $120^\circ$ , with the first of those three solutions aligned along the real axis.

The calculation of the natural logarithm of a complex number is also simplified by the use of the polar form.<sup>17</sup>

$$\ln[\mathbf{A}] = \ln[|\mathbf{A}|e^{j\theta}] = \ln[|\mathbf{A}|] + j\theta \quad (1.66)$$

As for the usual case with real numbers,  $\log_{10}[\mathbf{A}] = (\log_{10}e) \ln[|\mathbf{A}|e^{j\theta}] \cong 0.4343 \ln[\mathbf{A}]$ .

### 1.5.4 Integration and Differentiation of Complex Exponentials

The primary motivation for the introduction of complex exponentials is the ease with which it is possible to write their integrals or derivatives as was expressed in Eq. (1.47).

### 1.5.5 Time Averages of Complex Products (Power)

Two complex numbers are said to be complex conjugates if the imaginary parts are negatives of each other.

$$\text{If } \mathbf{A} = a + jb = |\mathbf{A}|e^{j\theta}, \text{ then } \mathbf{A}^* = a - jb = |\mathbf{A}|e^{-j\theta} \quad (1.67)$$

The polar version shows that the complex conjugate,  $\mathbf{A}^*$ , of a complex number,  $\mathbf{A}$ , is just the reflection of  $\mathbf{A}$  about the real axis. The complex conjugate provides a direct method for calculation of the modulus  $|\mathbf{A}|$  of a complex number as well as for the extraction of the real and imaginary parts of a complex number..

$$|\mathbf{A}| \equiv \sqrt{\mathbf{A}\mathbf{A}^*} = [(a + jb)(a - jb)]^{1/2} = (a^2 + b^2)^{1/2} \quad (1.68)$$

$$\Re e[\mathbf{A}] = \left(\frac{1}{2}\right)(\mathbf{A} + \mathbf{A}^*) = \left(\frac{1}{2}\right)[(a + jb) + (a - jb)] = a \quad (1.69)$$

$$\Im m[\mathbf{A}] = (1/2j)(\mathbf{A} - \mathbf{A}^*) = (1/2j)[(a + jb) - (a - jb)] = b \quad (1.70)$$

Complex conjugates are particularly useful for the calculation of time-averaged power,  $\langle \Pi \rangle_t$ , since that calculation requires evaluation of the “dot product” between two variables that characterize a potential and a flow. For a simple harmonic oscillator, those complex variables are force,  $\mathbf{F}$ , and velocity,  $\mathbf{v}$ ; for a fluid, they are pressure,  $\mathbf{p}$ , and volume flow rate,  $\mathbf{U}$ .<sup>18</sup> The dot product guarantees that only the components of the two variables which are in-phase contribute to the result.

It is important to realize that the product of the real parts of two variables is not equal to the real part of their product.

$$\Re e[\mathbf{F}] \times \Re e[\mathbf{v}] \neq \Re e[\mathbf{Fv}] \quad (1.71)$$

Using the definition of the complex conjugate in Eq. (1.67),

---

<sup>17</sup>The natural logarithm of a complex number is not unique, as was the case for roots, but for the applications addressed in this textbook, it can be expressed as shown in Eq. (1.66) and can be treated as being unique.

<sup>18</sup>In electrical circuit theory, the potential and flow are the voltage and the electrical current, respectively.

$$\Re e[\mathbf{F}] = \frac{1}{2} \Re e[\mathbf{F} + \mathbf{F}^*] \quad \text{and} \quad \Re e[\mathbf{v}] = \frac{1}{2} \Re e[\mathbf{v} + \mathbf{v}^*] \quad (1.72)$$

The instantaneous power,  $\Pi(t)$ , can be written using the results of Eq. (1.72).

$$\begin{aligned} \Pi(t) &= \mathbf{F} \bullet \mathbf{v} = \frac{1}{4} (\mathbf{F} + \mathbf{F}^*) (\mathbf{v} + \mathbf{v}^*) = \frac{1}{4} [(\mathbf{F}\mathbf{v} + \mathbf{F}^*\mathbf{v}^*) + (\mathbf{F}\mathbf{v}^* + \mathbf{v}\mathbf{F}^*)] \\ \Pi(t) &= \frac{1}{2} (\Re e[\mathbf{F}\mathbf{v}] + \Re e[\mathbf{F}\mathbf{v}^*]) = \frac{1}{2} \Re e \left[ |\mathbf{F}| |\mathbf{v}| e^{j(2\omega t + \phi_F + \phi_v)} + |\mathbf{F}| |\mathbf{v}| e^{j(\phi_F - \phi_v)} \right] \end{aligned} \quad (1.73)$$

The second version of the instantaneous power assumes simple harmonic time variation of both  $\mathbf{F}$  and  $\mathbf{v}$  at frequency,  $\omega$ , with a phase difference of  $\phi_F - \phi_v$ . If we take the real part of the term in square brackets, the instantaneous power can be expressed in terms of two cosines.

$$\Pi(t) = \frac{1}{2} |\mathbf{F}| |\mathbf{v}| [\cos(2\omega t + \phi_F + \phi_v) + \cos(\phi_F - \phi_v)] \quad (1.74)$$

The time-averaged power is determined by integration of Eq. (1.74) over a complete cycle with period,  $T = 2\pi/\omega$ , or if the integral is over a time much longer than one period. The first term is oscillatory, so the time average is zero. The second term is just a constant, so the time integral over the second term is non-zero.

$$\langle \Pi(t) \rangle_t \equiv \frac{1}{T} \int_0^T \Pi(t) dt = \frac{1}{2} |\mathbf{F}| |\mathbf{v}| \cos(\phi_F - \phi_v) = \frac{1}{2} \Re e[\mathbf{F}^* \mathbf{v}] \quad (1.75)$$

Taking the complex conjugate of the argument on the right-hand side of Eq. (1.75) does not change the result, since we are extracting only the real part.

$$\langle \Pi(t) \rangle_t = \frac{1}{2} \Re e[(\mathbf{F}^* \mathbf{v})^*] = \frac{1}{2} \Re e[\mathbf{v}^* \mathbf{F}] \quad (1.76)$$

## 1.6 Standard (SI) Units and Dimensional Homogeneity

We take for granted that every term in any equation must have the same units as all the other terms in that same equation. This concept is known as *dimensional homogeneity*. From the time of Isaac Newton (1642–1727) through the early nineteenth century, mathematical theories representing physical phenomena were expressed as ratios. For example, Ohm's law was expressed by Georg Ohm as “The force of the current in a galvanic circuit is directly as the sum of all the tensions (i.e., voltages), and inversely as the entire reduced length of the circuit.” Similarly, Hooke's law was expressed as “Stress is proportional to strain.” The idea that laws could be written as equations with consistent units for all terms was introduced by Jean-Baptiste Joseph Fourier. He had to fight for 20 years before this radical concept gained widespread acceptance [13].

By advocating this approach, Fourier also necessarily introduced dimensional constants. At that time, his concentration was on the transfer of heat, so he introduced both the thermal conductivity,  $\kappa$  [W/m-K], and the convective heat transfer coefficient,  $h$  [W/m<sup>2</sup>-K].<sup>19</sup> Not only did this make it possible to express physical laws as equations, such “constants” characterized the properties of specific materials. The American Society of Metals publishes the *ASM Handbook* that has 23 volumes that are

<sup>19</sup> In this textbook, when it is appropriate to designate units, they will be shown within square brackets [ ].

filled with such constants for a variety of metals, alloys, and composites. The printed version of the *ASM Handbook* takes over a meter of shelf space, although it is now also available in electronic form.

Throughout this textbook, we will use the *SI System of Units* exclusively.<sup>20</sup> Although this system is also commonly known as “MKS” units, because it uses meter [m], kilogram [kg], and second [s], it is actually based on seven units, of which those are just the first three. The remaining “base units” that complete the system are ampere [A], kelvin [K], mole [mol], and candela [cd].<sup>21</sup> These seven form the basis of other “derived” units, many of which are commonly used in acoustics and vibration: hertz, Hz [ $s^{-1}$ ]; newton, N [ $kg\cdot m/s^2$ ]; pascal, Pa [ $N/m^2$ ]; joule, J [ $N\cdot m$ ]; watt, W [ $J/s$ ]; coulomb, C [ $A\cdot s$ ]; volt, V [ $W/A$ ]; farad, F [ $C/V$ ]; ohm,  $\Omega$  [ $V/A$ ]; siemens, S [ $\Omega^{-1}$ ]; weber, Wb [ $V\cdot s$ ]; tesla, T [ $Wb/m^2$ ]; and henry, H [ $Wb/A$ ]. Although I was not pleased by the change of “cycles per second” to Hz and the conversion of the conductance unit from mho [ $\mathcal{O}$ ] (the inverse of ohm) to siemens [S], this system is very convenient because it is easy to integrate mechanical and electrical effects, an important feature for acoustical transduction systems (e.g., speakers, microphones, accelerometers, geophones, seismometers, etc.).

As of the date this book is being written, only the United States, Liberia, and Burma (Myanmar) have yet to accept SI as their national standard.<sup>22</sup> We are frequently required either to accept data that is expressed in other systems of units or to report results in other units. This textbook includes problems that require results reported in “customary units,” but it is recommended that all computations be done using SI units and then converted as required. It follows that any result that is not a pure number must be reported along with its units.

The other recommendation regarding units is that any equation should be checked to ensure dimensional homogeneity before any numerical values are placed into that equation. An equation that is dimensionally homogeneous may be wrong, but one that is not dimensionally homogeneous is meaningless. An equation that is not dimensionally homogeneous is not even wrong!

---

## 1.7 Similitude and the Buckingham $\Pi$ -Theorem (Natural Units)

*“I have often been impressed by the scanty attention paid even by original workers in physics to the great principle of similitude. It happens not infrequently that results in the form of ‘laws’ are put forward as novelties on the basis of elaborate experiments, which might have been predicted a priori after a few minutes of consideration.”* (J. W. Strutt (Lord Rayleigh) [14])

I will be the first to admit that “a few minutes of consideration” by Lord Rayleigh might be the equivalent of many hours of my personal effort, but the idea that physical units can dictate the form of mathematical expressions describing physical laws is important at a very fundamental level. Those of you who have studied Mechanical Engineering and/or Fluid Mechanics can attest to the significance of dimensionless groups like the Reynolds number for description of viscous fluid flow and the Nusselt number for description of convective heat transfer.

Although most attention to the discussion of units focuses on the topics in the previous section and we rely on the “standard” SI System of Units to report results and execute calculations, there is an equally important role played by the use of “natural units” that is often overlooked. Because its

---

<sup>20</sup> The International System of Units is designated “SI” from the French *Le Système international d’unités*.

<sup>21</sup> When the names of units are spelled out, they are not capitalized, even though many are based on proper names. When used as abbreviations, the first letter of those abbreviations are capitalized.

<sup>22</sup> The United States is proceeding to the metric system inch by inch.

exploitation is rather subtle, it will be introduced first by example; then it will be generalized within a more formal (and powerful) structure.

### 1.7.1 Three Simple Examples

The simplest vibratory system is the mass-spring oscillator. Although that topic will be covered in detail in the next chapter, there are significant results that can be obtained without even writing down the equations governing the oscillations of a mass on a spring (i.e., Newton's Second Law of Motion and Hooke's law). Following Fourier's introduction of dimensional constants, we assume that the "mass" that is attached to the spring is characterized only by its mass,  $m$ . We also know that the spring is characterized by its "stiffness,"  $K$ , as defined in Eq. (1.25). Mass happens to be one of the SI base units. According to Eq. (1.25), the dimensions of  $K$  must be force divided by displacement.

$$[K] = \frac{[\text{Force}]}{[\text{displacement}]} = \left[ \frac{N}{m} \right] = \left[ \frac{kg - m}{s^2 - m} \right] = \left[ \frac{kg}{s^2} \right] = \left[ \frac{M}{T^2} \right] \quad (1.77)$$

For the discussions that employ dimensional analysis to extract functional relations (a part of a process called *similitude*), it is common to abbreviate the "base units" as  $M$  for mass,  $L$  for length or distance,  $T$  for time, and  $\Theta$  for temperature.

Instead of thinking of this problem in terms of SI units, we can use  $m$  and  $K$  as our "natural units." First, notice that the definitions of  $m$  and  $K$  involve two base units,  $M$  and  $T$ , and that both  $M$  and  $T$  appear in  $K$ . Let's say we are interested in the calculation of the frequency of oscillation,  $f$ , of this simple mass-spring combination. Since frequency has the units of reciprocal time ( $1/T$ ), we can ask what combination of  $K$  and  $m$ , the natural units for the description of this specific system, will have the units of frequency? Although it is not too difficult to simply guess the correct result, let's employ a more formal procedure that will become useful when we analyze more complicated applications.

To express the natural frequency of vibration,  $f_o$ , in terms of  $K$  and  $m$ , we can let  $a$  and  $b$  be exponents and write an equation to guarantee dimensional homogeneity:

$$m^a K^b = \frac{M^a M^b}{T^{2b}} = \frac{1}{T} = T^{-1} M^0 \quad (1.78)$$

The term at the far right is just included to emphasize that we are seeking a result that does not include  $M$ . Now the values of  $a$  and  $b$  can be determined by inspection:  $a + b = 0$  so  $a = -b$ . Equating the time exponents,  $b = 1/2$  so  $a = -1/2$ . Based solely on the units of  $K$  and  $m$ , we can write the required functional form of our desired result.

$$f_o \propto \sqrt{\frac{K}{m}} \quad (1.79)$$

This approach cannot determine the numerical constant that would change this proportionality into an equation. As we will see in the next chapter, if we choose to use the radian frequency,  $\omega_o = 2\pi f_o$ , then no numerical constant is required:  $\omega_o = \sqrt{K/m}$ . If we were deriving this relationship for a more complicated system, for which an analytic solution may not exist, then an experiment or a numerical calculation could be used to determine the constant. Even more importantly, if the experiments or the numerical calculations did not obey Eq. (1.79), then there must be other parameters required to specify the dynamics, or the experiments or calculations are flawed.

What if we added damping to the mass-spring system? The damping is characterized by a mechanical resistance,  $R_m$ , that has units of [kg/s]. Now we have three parameters ( $m$ ,  $K$ , and  $R_m$ ), but those parameters still only involve two base units. When the number of parameters exceeds the number of base units, it is then possible to combine those parameters to form *dimensionless groups*.

Using the same approach as employed in Eq. (1.78), we can identify this dimensionless group.

$$m^a K^b R_m^c = \frac{M^a M^b M^c}{T^{2b} T^c} = M^0 T^0 \quad (1.80)$$

The resulting equations for the exponents show that  $a + b + c = 0$  and  $2b + c = 0$ , so  $c = -2b$ ; thus  $a = b$ . These dimensionless groups are called  $\Pi$ -groups, based on the classic paper by Buckingham [15]. In this case, we have created one  $\Pi$ -group that is designated  $\Pi_1$ .

$$\Pi_1 = \frac{Km}{R_m^2} = \frac{\omega_o^2 m^2}{R_m^2} \equiv Q^2 \quad (1.81)$$

Substitution for  $K$ , using  $\omega_o^2 = (K/m)$ , produced an expression for  $\Pi_1$  that will appear frequently in the next chapter as the dimensionless quality factor,  $Q$ . When damping is present, our result for frequency can only depend upon  $R_m$  through some function of  $Q^2$ , hence the damped frequency,  $\omega_d = f(K, m, Q^2)$ . Again, that function  $f(K, m, Q^2)$  can be determined either by experiment or by solution of the fundamental Eq. (1.28) with  $F(t) = 0$ .

One additional simple example might be helpful before introducing the general result. Equation (1.27) expresses the torque on a simple pendulum. The parameters in that expression are the mass of the bob,  $m$ ; the length of the string,  $L$ ; and the acceleration due to gravity,  $g \approx 9.8 \text{ m/s}^2$ . We have three parameters and three “base units,” so there are no dimensionless groups. As before, recognizing that frequency, either  $f_o$  or  $\omega_o$ , has units of  $T^{-1}$ , the dimensional equation below can be solved for the appropriate exponents.

$$m^a L^b g^c = \frac{M^a L^b L^c}{T^{2c}} = \frac{1}{T} = T^{-1} M^0 L^0 \quad (1.82)$$

The first result is that  $a = 0$ , so the frequency is independent of the mass of the bob. Since time only enters through the acceleration due to gravity,  $2c = 1$  and  $b + c = 0$ , so  $c = -b = \frac{1}{2}$ .

$$f_o \propto \sqrt{\frac{g}{L}} \quad (1.83)$$

Even though we included the mass of the pendulum bob as a parameter, that turned out to have no effect on the pendulum’s frequency; our dimensional analysis was able to exclude that parameter from the final result even if our intuition did not.

## 1.7.2 Dimensionless $\Pi$ -Groups

The general idea can be summarized by expressing some dependent variable,  $q_o$ , in terms of the independent variables,  $q_1$  through  $q_m$ . Those independent variables characterize the physical process that defines the dependent variable through some function,  $F$ , of the independent variables.

$$q_o = F(q_1, q_2, \dots, q_m) \quad (1.84)$$

$q_1$  through  $q_m$  define  $m$  independent parameters. If those independent parameters can be expressed with  $n$  “base units,” then there will be  $(m - n)$  dimensionless groups. If we rearrange Eq. (1.84) into a different function,  $G$ , which includes all the variables and set  $G$  equal to zero, then we obtain one more dimensionless group that results in a homogeneous expression.

For our simple oscillator examples, we solved for  $q_o$  ( $f_o$  or  $\omega_o$  in our examples) based on the independent parameters. If we would have included  $f_o$ , then we would have generated one dimensionless group that would have been equal to zero. With either approach, we would have arrived at the same result.

Those three examples that dictated the functional dependence of the frequencies for three oscillators were particularly simple. We will be able to obtain these results (including the required numerical pre-factor) by solving the differential equations directly. In acoustics and vibration, there are problems for which we cannot obtain closed-form analytical solutions, even when we know the fundamental governing equations [16]. There are occasions when a numerical answer for a particular case can be obtained using digital computation, but an “answer” for a single case is not the same as a “solution.” The use of dimensional analysis can provide an independent check on an “answer” and can provide the functional form of a solution (where the “answer” might be used to produce the numerical pre-factor). Also, our dimensional solution can be used to test answers for different cases (e.g., flow velocity, object sizes, etc.), since the parameters in the numerical solution have presumably been identified.

### 1.7.3 Windscreen Noise\*

We will complete this section by examining an acoustical example that does not easily yield to conventional mathematical analysis. Windscreens are placed around microphones to reduce the noise that such microphones detect when they measure sound in the presence of flowing air (wind). Figure 1.8 shows measurements of the sound pressure levels in one-third octave bands,  $p_{1/3}$ , as a function of the band-centered frequencies for air flow velocities from 2 m/s to 14 m/s.

To apply our dimensional analysis, we first need to determine the relevant parameters. Some thought is required to select a physically significant set. Obviously, frequency,  $f$ ; one-third octave-band pressure level,  $p_{1/3}$ ; flow velocity,  $v$ ; and windscreen diameter,  $D$ , seem to be potentially relevant. We also might include the properties of the fluid. Three possible candidates are the density,  $\rho$ ; the sound speed,  $c$ ; and the shear viscosity,  $\mu$ , of the flowing air. As we saw with the pendulum frequency, we can choose the wrong (or suboptimal) parameter set and still end up with a valid solution. Our practical interest is in understanding the noise pressure levels.

If we examine the first four parameters that are identified in Table 1.1, we notice that there is no other parameter that includes mass other than  $p_{1/3}$ . To nondimensionalize  $p_{1/3}$ , we have to include a fluid parameter that has units of mass. Since the flow speeds are much less than the sound speed (which does not contain units of mass) and we expect that the windscreen noise is generated by turbulence around the screen, I will select density rather than viscosity.<sup>23</sup>

We have identified five parameters that can be expressed using three basic units, so we will be able to form two dimensionless  $\Pi$ -groups:  $(m - n) = 5 - 3 = 2$ . Again, since our interest is in the pressure levels at different frequencies, the choice suggested by the raw data plotted in Fig. 1.8 is to create a

---

<sup>23</sup> Here I have used my knowledge that the effects of density dominate those of viscosity for turbulent solutions to the Navier-Stokes equation (which presumably generate the turbulent flow noise the windscreens are intended to suppress). The success of dimensional analysis is frequently enhanced by what Rayleigh called “a few minutes of consideration” [14], which I interpret as the application of additional physical insight related to the specific problem.

**Fig. 1.8** Measured one-third octave-band levels of noise generated by a microphone with a 9.5-cm-diameter spherical windscreens in air flows that ranges from 2 m/s to 14 m/s [18]. The band center frequencies of the one-third octave-band levels are plotted on a logarithmic horizontal axis. The magnitudes of the one-third octave bands are plotted as dB re: 20  $\mu\text{Pa}_{\text{rms}}$

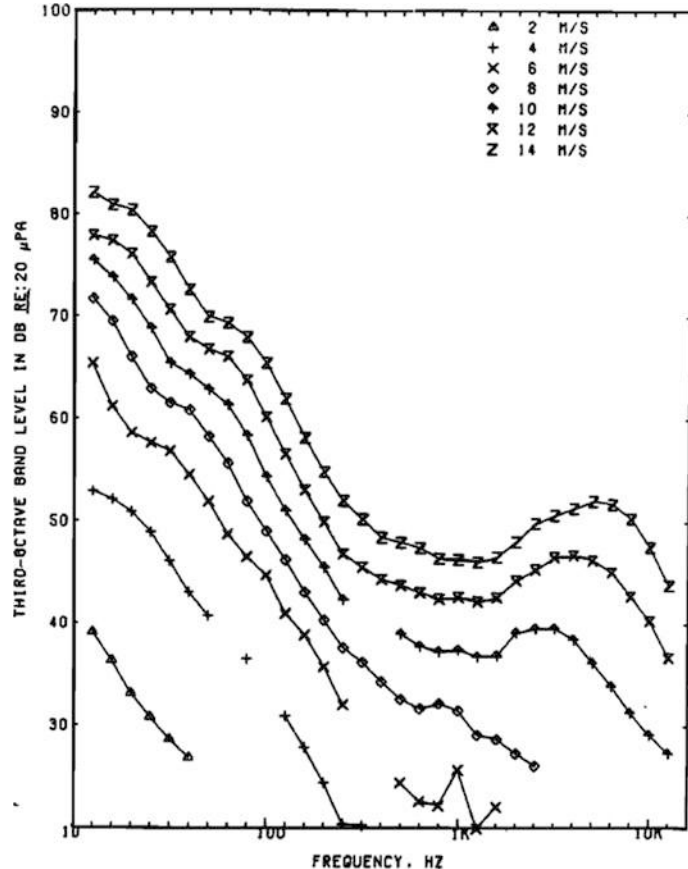


**Table 1.1** Five parameters that are being tested to determine the dimensionless groups that will characterize the one-third octave-band pressure,  $p_{1/3}$ , detected by a microphone protected by a windscreens of characteristic diameter,  $D$ , in air of density,  $\rho$ , that is flowing past the microphone with a velocity,  $v$ , as a function of the band center frequency,  $f$ , of each one-third octave band

Parameter	$f$	$p_{1/3}$	$\nu$	$D$	$\rho$
Basic units	$\text{s}^{-1}$	$\text{N/m}^2 = \text{kg/m} \cdot \text{s}^2$	$\text{m/s}$	$\text{m}$	$\text{kg/m}^3$
Dimensions	$\text{T}^{-1}$	$\text{ML}^{-1}\text{T}^{-2}$	$\text{LT}^{-1}$	$\text{L}$	$\text{ML}^{-3}$

With five parameters selected and three base units, there will be two dimensionless  $\Pi$ -groups

dimensionless frequency,  $\Pi_f$ , and a dimensionless pressure,  $\Pi_p$ . For the calculation of  $\Pi_f$ , we know that the units for  $f$  do not include mass, so we can eliminate  $\rho$  from the  $\Pi_f$  group.

$$\Pi_f = f^a v^b D^c = \frac{1}{T^a} \frac{L^b}{T^b} L^c = T^0 L^0 \quad (1.85)$$

The length terms suggest  $b + c = 0$ , or  $b = -c$ , and the time terms make  $a + b = 0$ , so  $a = -b = c = 1$ ; hence  $\Pi_f = fD/v$ . This dimensionless group is known as the Strouhal number.

The  $\Pi$ -group for pressure will not include the frequency, since  $\Pi_p$  will be used to replace the results plotted with reference to the vertical axis of the graph in Fig. 1.8 with the dimensionless axis in Fig. 1.9.

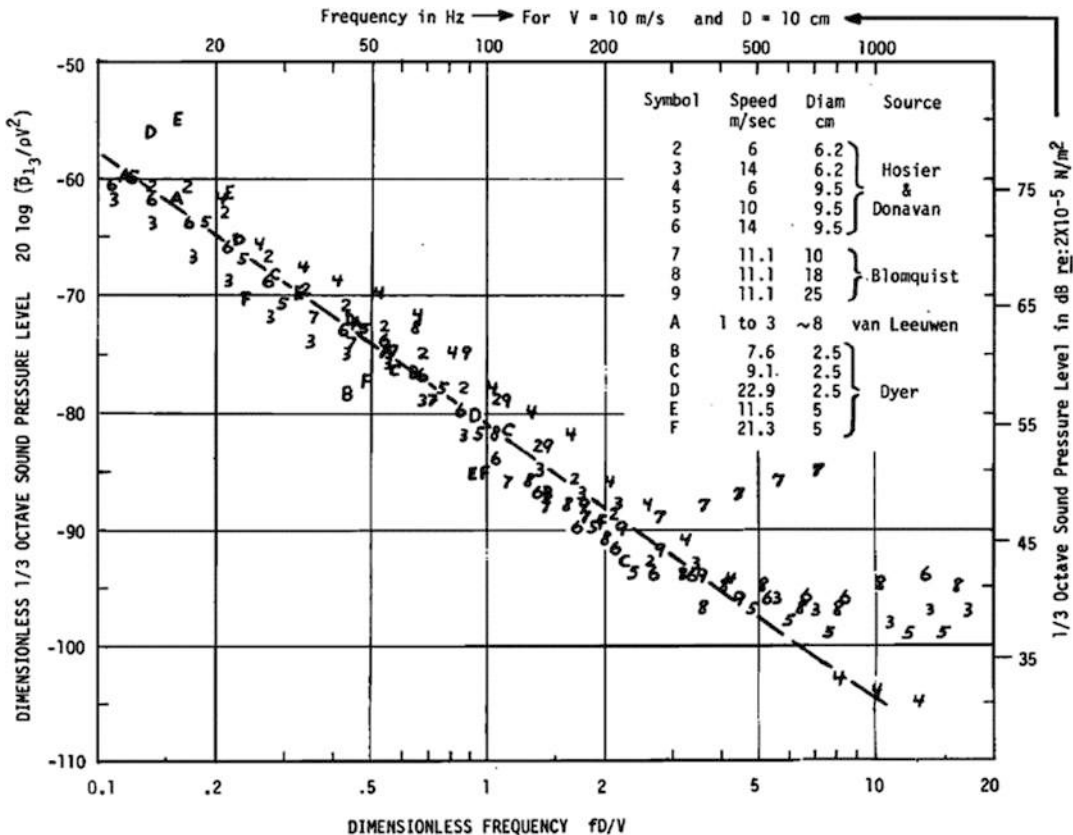


**Fig. 1.9** Plot of the dimensionless one-third octave-band pressures,  $\Pi_p = p_{1/3}/\rho v^2$ , versus the dimensionless frequencies,  $\Pi_f = fD/v$  (Strouhal number), for four different groups of measurements, performed by four different researchers, using windscreens of diameters ranging from 2.5 cm to 25 cm, in air flows with velocities ranging from 1 m/s to 23 m/s [17]. The vertical axis at the left is  $\Pi_p$ , scaled in decibels. The vertical axis at the right is the one-third octave-band sound pressure levels in dB re:  $20 \mu\text{Pa}_{\text{rms}}$ , if  $v = 10 \text{ m/s}$ . The lower horizontal axis is logarithmic in dimensionless frequency,  $\Pi_f$ , and the upper axis is scaled in frequency for  $v = 10 \text{ m/s}$  and  $D = 10 \text{ cm}$ . The systematic deviation of some data points from the dashed best-fit straight line above  $\Pi_f > 2$  indicates that another parameter may have become important, possibly the windscreen pore size

$$\Pi_p = \left( p_{1/3} \right)^a v^b D^c \rho^d = \frac{M^a}{L^a T^{2a}} \frac{L^b}{T^b} L^c \frac{M^d}{L^{3d}} = M^0 L^0 T^0 \quad (1.86)$$

The mass terms require  $a + d = 0$ , so  $a = -d$ ; the time terms require  $2a + b = 0$  or  $b = -2a$ ; and the length terms require  $-a + b + c - 3d = 0$ . Substituting time and mass results into length, we obtain  $-a - 2a + c + 3a = 0$ , so  $D$  did not need to be part of  $\Pi_p = p_{1/3}/\rho v^2$ ; one-third octave-band pressure levels are therefore normalized by the kinetic energy density of the fluid.

Strasberg has taken the windscreen noise data from Fig. 1.8 and plotted it, along with measurements made by three other investigators in three other laboratories, as  $p_{1/3}/\rho v^2$  versus  $fD/v$  in Fig. 1.9 [17]. This choice of nondimensional variables causes all of the data in Fig. 1.8, which were represented by seven different curves, to fall on a single straight line along with three other sets of measurements made by three other researchers using windscreens of eight different diameters in Fig. 1.9.

The fact that Fig. 1.9 shows systematic deviation of some data sets from the best-fit straight line for  $\Pi_f > 2$  could indicate that some other parameter that was not included in the dimensional analysis has

become important in that regime. For these measurements, the windscreen pore size might start to play a role at higher frequencies.

### 1.7.4 Similitude Summary

Fourier's requirement for dimensional homogeneity introduced dimensional constants that can provide sets of "natural units." Such "derived units" lead to important restrictions on the functional form (to within a multiplicative constant) of mathematical expressions for the behavior of physical systems. We have used a formalism introduced by Buckingham [15] to extract those functions and to determine how many independent dimensionless groups can be formed that control the behavior of the physical system under the assumption that we have identified all the controlling parameters correctly. Although we may not be able to derive or even guess the form of the functions, we know that those functions can only depend on those dimensionless  $\Pi$ -groups.

Figure 1.9 demonstrated how the use of  $\Pi$ -groups as the plotting variables can produce a universal relationship that unifies seemingly diverse sets of data, like those in Fig. 1.8, to produce a single correlation across a large variation of experimental parameters.

The  $\Pi$ -groups also provide guidance in the design and planning of experiments. Using the  $\Pi_r$ -group, we could select flow velocities and windscreen diameters to optimize our variation of Strouhal number. The  $\Pi_p$ -group introduces the option of using gases of different densities to further increase the range of an experimental investigation, either by using less dense gases like H<sub>2</sub> or He or a denser gas like SF<sub>6</sub> (sulfur hexafluoride), in addition to air, or by changing the mean pressure to modify the density of a single gas.

Experiments are expensive! It is very valuable to be able to span the largest range of parameters with the fewest measurements.

Since the use of similitude is not commonly taught as a powerful technique for acoustics and vibration (although it is indispensable to the education of mechanical engineers in fields like fluid flow and heat transfer), the steps in determining  $\Pi$ -groups will be summarized again below:

1. List all of the parameters involved and their SI "base units." An arrangement like Table 1.1 can be useful.
2. The difference between the number of parameters,  $m$ , and the required number of SI units,  $n$ , needed to express the  $m$  parameters will determine the number of dimensionless  $\Pi$ -groups. The resultant number of  $\Pi$ -groups equals  $(m - n)$ .
3. Select  $n$  of the  $m$  parameters you will use as the "natural units," keeping in mind that you cannot use parameters that differ by only an exponent, for example, a base unit like length,  $L$ , and the volume,  $L^3$ .
4. Express the other  $(m - n)$  parameters, one at a time, in terms of the "natural units" using the requirement of dimensional homogeneity (e.g., Eqs. (1.78), (1.80), (1.81), (1.82), (1.85), and (1.86)) to produce  $(m - n)$  dimensionless  $\Pi$ -groups.
5. Check to be sure that the  $\Pi$ -groups you have formed are dimensionless.

---

## 1.8 Precision, Accuracy, and Error Propagation

*"The best instrument for detecting systematic error is between your ears." [19]*

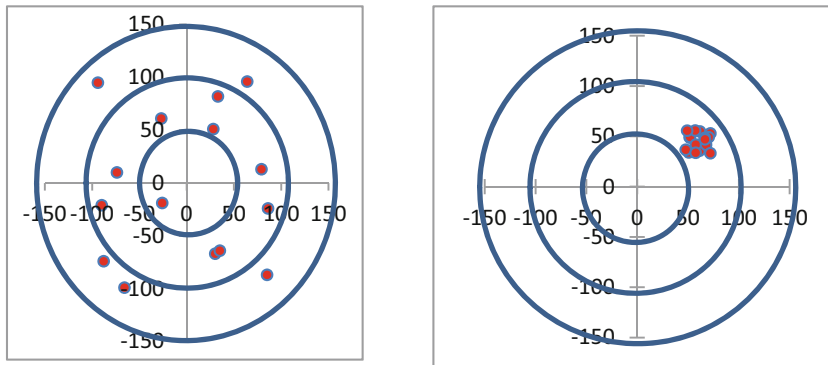


**Fig. 1.10** The target patterns created by 16 bullets fired from two hypothetical guns illustrating the difference between random error and systematic (bias) error. If we assume that the numbering on the targets corresponds to centimeters, the holes in the target at the left have an average position at the exact center of the target, but the standard deviation of the distance of those holes from the center is 94 cm. The average distance of the 16 holes in the target at the right is 60 cm to the right of the center and 45 cm above the center, corresponding to an average “miss” distance from the center of 75 cm, but the standard deviation about that average is 12 cm. The target on the left exhibits large random error (possibly due to large fluctuations in the wind), and the target on the right is dominated by systematic error, possibly due to a misaligned gun sight

This textbook will dedicate a lot of space to the development and derivation of mathematical results that summarize the behavior of vibratory and acoustical systems. All of these equations will contain parameters that either specify the properties of a material or component (e.g., stiffness, mass density, elastic modulus, sound speed, heat capacity, thermal conductivity, viscosity, etc.) or the value of some geometric feature of the system under consideration (e.g., length, perimeter, diameter, surface area, volume, etc.). Each of these parameters will have some uncertainty in its specification and those uncertainties will be reflected in the error estimate of the result. For that reason, this section as well as the subsequent section of this chapter will address some basic concepts that are used to quantify those uncertainties and to combine them to provide an estimate of the uncertainty in the final result.

It is important to first recognize that there are two distinct types of errors (other than blunders): (1) *random errors* due to noise-induced statistical fluctuations and (2) *systematic errors*, also known as *bias errors*, which arise because of calibration errors or an oversimplification of the equation that connects the measurements to the desired result. The reason that it is important to distinguish between those errors is that they need to be addressed in two very different ways. Figure 1.10 illustrates this difference.

### 1.8.1 Random Errors (Noise) and Relative Uncertainty

We are usually able to quantify random errors by making  $N$  measurements of a scalar quantity,  $x_i$ , under (presumably!) identical conditions and then using the average (mean) of those measurements,  $\bar{x}$ , as the best estimate of the value of the parameter being measured.

$$\bar{x} = \frac{\sum_{i=1}^N x_i}{N} \quad (1.87)$$

The variability of such a collection of  $N$  measurements can be quantified by defining the deviation of each individual measurement from the mean value:  $\delta x_i = x_i - \bar{x}$ . Based on the definition of the

mean, the sum of all the deviations will be zero, being equally positive and negative. If all of the deviations,  $\delta x_i$ , are squared, then the square root of the sum is an indication of the *statistical fluctuations* about the mean value.

The square root of the sum of the squares of the deviations is generally not used as a statistical measure of the fluctuation since it is widely recognized that if the measurement were repeated and another set of  $N$  measurements were collected, both the average,  $\bar{x}$ , and the deviations from the average,  $\delta x_i$ , would be different, although both samples would represent the same phenomenon.<sup>24</sup> Careful statistical analysis distinguishes between the “population” and the “sample” and suggests that the *standard deviation*,  $\sigma_x$ , be slightly larger than the root-mean-squared deviation [20]. Since our values of  $N$  are usually fairly large, the difference is usually not significant.

$$\sigma_x = \sqrt{\frac{\sum_{i=1}^N (x_i - \bar{x})^2}{N-1}} = \sqrt{\frac{\sum_{i=1}^N \delta x_i^2}{N-1}} \quad (1.88)$$

This variability can be attributed to a number of different sources depending upon the experimental conditions, sensors, signal-conditioning electronics, cabling, connectors, and instrumentations. Since many measurements today are made with instruments that employ an analog-to-digital conversion, some variability (noise) might be due to digitization errors, round-off errors, or simple truncation.

Electronic measurements are also susceptible to electromagnetic interference (EMI) that may be correlated to the power line frequency (e.g., 60 Hz in the North America, 50 Hz in Europe) and its harmonics<sup>25</sup> or higher-frequency radiation from switch-mode power supplies, motor controllers, or other power electronics. Sometimes the fluctuations in the readings might be due to fluctuating conditions such as background noises and vibrations, wind, etc. For our purposes, the sources of these fluctuations are not the immediate concern, although recognizing the magnitude and importance of such fluctuations is the reason for introducing a standard means of quantifying such random influences.

In this textbook (and in my own research), we will use the ratio of the standard deviation to the mean to define a *relative uncertainty* of the mean value. This normalization of the standard deviation is convenient both because the relative uncertainty is dimensionless and because it makes it very easy to combine errors from different sources to produce an uncertainty in a result that depends upon simultaneous errors in the measurement of several different parameters (see Sect. 1.8.4). I designate this relative uncertainty as  $\delta x / |\bar{x}|$ . In this simple case, involving a single variable,  $x$ ,  $\delta x / |\bar{x}| \equiv \sigma_x / |\bar{x}|$ . We typically use the relative uncertainty to specify the *precision* of a measurement.

This concept is extended to two dimensions in Fig. 1.10, which simulates randomness using a pattern of  $N = 16$  bullets fired at targets by two different weapons. The holes in the target on the left were produced by generating two columns of uncorrelated random numbers between  $-100$  and  $+100$  representing the  $x_i$  and  $y_i$  for  $i = 1$  through  $16$ . The average values of both components were zero:  $\bar{x} = \bar{y} = 0$ . If the numbers on the axes in Fig. 1.10 represent centimeters, the standard deviations of both variables are also nearly equal:  $\sigma_x \cong \sigma_y \cong 66$  cm. The average of those 16 shots is a “bull’s-eye,” although only one of the bullets landed within 50 cm of the origin. Only 11 of the 16 bullets (69%) were within  $|\vec{r}| = (\sigma_x^2 + \sigma_y^2)^{1/2} = 94$  cm of the center.

<sup>24</sup> The *ergodic hypothesis* is a statement of the assumption that the average of a parameter over time in a single system and the average of the same parameter at a single time in a number of similarly prepared systems yield the same average value.

<sup>25</sup> The best modern electronic instruments are designed to integrate the measured signal over an integer number of power line cycles so that any variations that are synchronized to the line frequency will average to zero.

The target on the right-hand side of Fig. 1.10 has a much smaller variation in the positions of the bullets,  $\sigma_x \approx \sigma_y \approx 8$  cm and  $(\sigma_x^2 + \sigma_y^2)^{1/2} = 12$  cm, but the average position is displaced;  $\bar{x} = 60$  cm and  $\bar{y} = 45$  cm, so the center of the distribution is located = 75 cm from the origin of the coordinates at an average angle of  $37^\circ$  above the horizontal to the right of center.

### 1.8.2 Normal Error Function or the Gaussian Distribution

“Everyone believes that the Gaussian distribution describes the distribution of random errors; mathematicians because they think physicists have verified it experimentally, and physicists because they think mathematicians have proved it theoretically.” [21]

When we think about random processes, a common example is the coin toss. If we flip a fair coin, there is a 50% probability that the coin will land “heads” up and an equal probability that it will land “tails” up. If we toss  $N$  coins simultaneously, the probability of any particular outcome, say  $h$  heads and  $t = N - h$  tails, is given by a binomial distribution. The average of that distribution will still be  $\bar{h} = \bar{t} = N/2$ , but the likelihood of getting exactly  $N/2$  heads in any given toss is fairly small and grows smaller with increasing  $N$ .

The probability,  $P_B(h, p, N)$ , of obtaining  $h$  heads and  $t = N - h$  tails is given by a binomial distribution where the probability of obtaining a head is  $p = 0.5$ . Of course, the probability of a tail is  $q = 0.5$ .

$$P_B(h, p, N) = \frac{N!}{h!(N-h)!} p^h q^{(N-h)} \quad (1.89)$$

For the binomial distribution, the average outcome with the largest probability is the mean,  $\bar{h} = Np$ , and the standard deviation about that mean is  $\sigma = [Np(1-p)]^{1/2}$ . It is worthwhile to recognize that  $\bar{h}$  is proportional to the number of trials  $N$ , whereas  $\sigma$  is proportional to  $\sqrt{N}$ . Therefore, the relative width of the distribution function,  $\sigma/\bar{h}$ , decreases in proportion to  $\sqrt{N}$ . This “sharpening” of the distribution with increasing  $N$  is evident in Fig. 1.11.

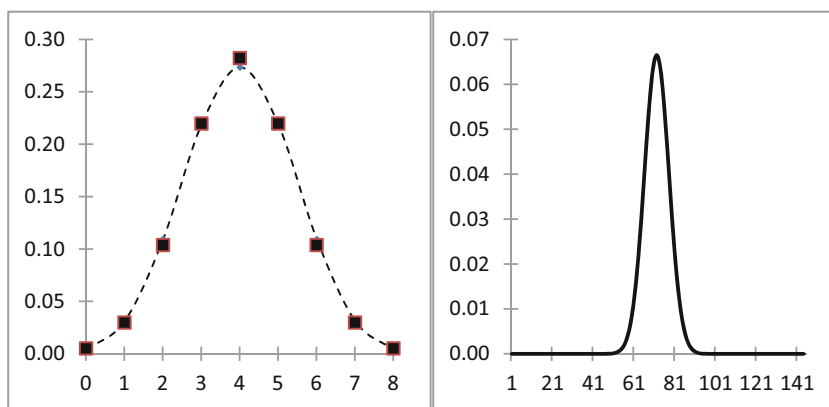


**Fig. 1.11** (Left) The squares are the probabilities of obtaining a number of heads when tossing  $N = 8$  coins. The highest probability is for  $h = 4$  heads,  $P_B(4, 0.5, 8) = 0.273$ . The standard deviation is  $\sigma = \sqrt{2}$ . Superimposed over the discrete results obtained from the binomial distribution is the dashed line representing a Gaussian distribution with the same mean and standard deviation,  $P_G(4, 4, \sqrt{2}) = 0.282$ . (Right) With  $N = 144$ , the probabilities determined by both the Gaussian and the binomial distribution functions are indistinguishable. Here the highest probability  $P_G(72, 72, 6) = 0.0665$  is for  $h = 72$  heads, and the standard deviation is  $\sigma = 6$

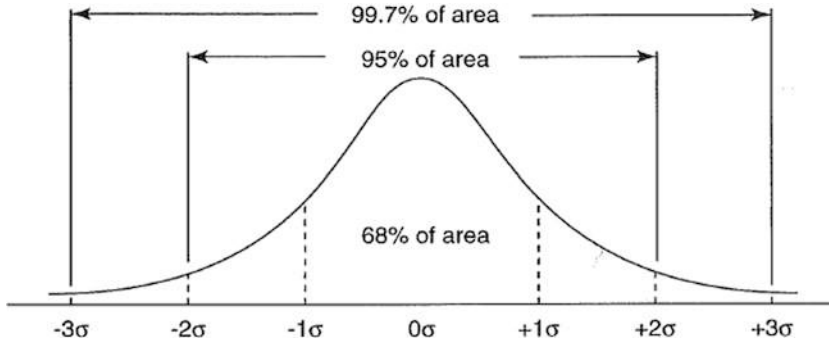


**Fig. 1.12** Integration of the Gaussian distribution makes it possible to determine the area corresponding to the probability of a measurement being within a chosen distance from the mean in terms of the standard deviation of the distribution

If we are interested in a continuous variable instead of a variable with a discrete number of possible outcomes, we can use a Gaussian distribution that provides the probability  $P_G(x, \bar{x}, \sigma)$  of obtaining a value,  $x$ .

$$P_G(x, \bar{x}, \sigma) = \frac{1}{\sigma\sqrt{2\pi}} e^{-\frac{1}{2}(\frac{x-\bar{x}}{\sigma})^2} \quad (1.90)$$

Both of these distribution functions are normalized. The sum of the probabilities for the binomial distribution must equal one, and the integral under the Gaussian distribution must also equal one. These two probability distribution functions are superimposed in Fig. 1.11 for  $N = 8$  coins and  $N = 144$  coins.

The purpose of introducing these distribution functions is to provide some convenient interpretation of the standard deviation. If the measurement errors are truly random, then it is probable that 68% of the measurements will fall within one standard deviation from the mean. For a normal (Gaussian) distribution, 95% of the results will be within two standard deviations from the mean. This is illustrated in Fig. 1.12. In the “target” example on the left of Fig. 1.10, we have already shown that 69% of the holes were within one standard deviation of the distance from the center of the target, so that example quite accurately exhibits Gaussian “randomness.”<sup>26</sup>

In the two cases treated in Fig. 1.11, the relative uncertainty for the  $N = 8$  case is  $\delta x/\bar{x} = (2)^{1/2}/4 = 0.354$  and for the  $N = 144$  case is  $\delta x/\bar{x} = 6/72 = 0.083$ . Their ratio is 4.243, which is  $\sqrt{144}/8$ . This is not a coincidence. For random errors, the relative uncertainty decreases as the square root of the number of measurements. This is a result that is worth keeping in mind when you have to decide whether to reduce the random error by increasing the number of measurements or trying to improve the measurement in a way that reduces the noise (e.g., provide better shielding against EMI, use differential inputs to provide common-mode rejection, etc.).

<sup>26</sup>This is only a rough check of the “Gaussianity” of the distribution. More sophisticated statistical tests, such as the Kolmogorov-Smirnov test, can be applied to determine a quantitative estimate of the distribution’s similarity to a Gaussian distribution.

### 1.8.3 Systematic Errors (Bias)

Systematic error is not reduced by increasing the number of measurements. In the “target” example on the right-hand side of Fig. 1.10, taking more shots will not bring the average any closer to the bull’s-eye. On the other hand, an adjustment of the sighting mechanism could produce results that are far better than those shown in the left-hand side of Fig. 1.10 by bringing the much tighter cluster of holes on the right-hand side toward the center of the target.

The right-hand side of the target example in Fig. 1.10 represents a type of systematic error that I call a “calibration error.” These can enter a measurement in a number of ways. If a ruler is calibrated at room temperature but used at a much higher temperature, the thermal expansion will bias the readings of length. In acoustic and vibration experiments, often each component of the measurement system may be calibrated, but the calibration could be a function of ambient pressure and temperature. The “loading” of the output of one component of the system by a subsequent component can reduce the output or provide a gain that is load-dependent.

For example, a capacitive microphone capsule with a capacitance of 50 pF has an electrical output impedance at 100 Hz of  $Z_{el} = (\omega C)^{-1} = 32 \text{ M}\Omega$ . If it is connected to a preamplifier with an input impedance of 100 MΩ, then the signal amplified by that stage at 100 Hz is reduced by  $(100/132) \cong 0.76$ . Even though the capsule may be calibrated with a sensitivity of 1.00 mV/Pa, it will present a sensitivity to the preamplifier of 0.76 mV/Pa. At 1.0 kHz, the capsule’s output impedance drops to 3.2 MΩ, so the effective sensitivity at that higher frequency will be  $(100/103) \times 1.00 \text{ mV/Pa} = 0.97 \text{ mV/Pa}$ . A typical acoustic measurement system may concatenate many stages from the sensor to its preamplifier, through the cabling, to the input stage of the data acquisition system, through some digital signal processing, and finally out to the display or some recording (storage) device.

As important as it is to know the calibration or gain (i.e., transfer function) of each stage in the measurement system, it is also imperative that the entire system’s overall behavior be tested by an *end-to-end calibration* that can confirm the calculation of the overall system’s sensitivity. This is usually accomplished by providing a calibrated test signal to the sensor and reading the output at the end of the signal acquisition chain. Commercial calibrators are available for microphones, hydrophones, and accelerometers. If a commercial calibrator is not available for a particular sensor, some end-to-end calibration system should be designed as part of the test plan for every experiment.

Another common source of systematic error is an oversimplification of the equation that is employed to relate the measured quantities to the determination of the parameter of interest. For example, let us say that we wanted to determine the local value of the acceleration due to gravity,  $g$ , by measuring the period,  $T$ , of a pendulum that suspends a bob of mass,  $m$ , from a string of length,  $L$ . The simplest expression relating those parameters to the gravitational acceleration involves only the length of the pendulum and its period of oscillation,  $T$ .

$$g = \frac{4\pi^2 L}{T^2} \quad (1.91)$$

It is very easy to make a precise determination of the period,  $T$ , by timing 100 cycles of the pendulum and dividing by 100. The length,  $L'$ , of the string, between the support and the mass is also easy to determine accurately, but the length that appears in Eq. (1.91) should be the distance from the support point to the center of mass of the pendulum bob. Also, Eq. (1.91) does not include the effects of air that provides some buoyancy and also must accelerate and decelerate to get out of the path of the bob’s motion. Since the amplitude of the oscillations is not zero, there are nonlinear effects that are introduced because Eq. (1.91) assumes the small angle approximation by truncating all higher-order terms in the potential energy of Eq. (1.26). Because of the viscous drag of the air, the amplitude of

**Table 1.2** There are several physical effects that influence the period of a pendulum which are not captured by Eq. (1.91) relating the gravitational acceleration,  $g$ , to the period,  $T$ , of a pendulum. Several of the sources of these systematic errors are listed that shift the period by an amount  $\Delta T$  and are comparable to the statistical uncertainty of  $\pm 170 \mu\text{s}$  in the determination of the period [22]

Effect	$\Delta T(\mu\text{s})$
Non-zero amplitude (i.e., second order)	596
Buoyancy	292
Added mass due to air acceleration	346
Mass of the wire	-463
Decay of oscillations	-77
Moment of inertia of the bob	72

those swings decrease over time and that damping increases the period (see Sect. 2.4). Table 1.2 summarizes some of these systematic errors for a pendulum experiment that had  $L \cong 3.00 \text{ m}$  and a spherical bob with diameter  $D \cong 6.01 \text{ cm}$  and  $m \cong 0.857 \text{ kg}$ . The pendulum had an average period of  $T \cong 3.47880 \pm 0.00017 \text{ s}$  [22]. Although the statistical uncertainty in the determination of the period is only  $\pm 170 \mu\text{s}$ , there are several systematic errors, listed in Table 1.2, that have a comparable effect on the relationship between the period and the gravitational acceleration that are not captured by Eq. (1.91).

Finally, there are errors that are just simply blunders. If you are writing results in a laboratory notebook or typing them into a computer, it is possible to enter the wrong number, skip an entry, lose count, forget to write down the model and serial number of a sensor, or transcribe a number incorrectly from the notebook into your calculator or into a spreadsheet or other data analysis software package. The best defense against blunders is to be well-prepared before actually taking the data and be sure you have arranged a place that will be comfortable and well-lit and affords easy access to the knobs that need twisting, the displays that must be read, and the keyboard if you are entering data or observations directly into a computer.

You are really not ready to start an experiment if you have not labeled the columns into which the data will be entered and included the units with that label. Before taking data, you should have a good idea of how the data will be plotted, at least to the level that you have identified the axes and their units. Plotting some data early in an experiment and calculating results based on that early data are always a good way to be sure you are not wasting hours or days acquiring data that will later be recognized as useless.

### 1.8.4 Error Propagation and Covariance

Our interest in the quantification of errors is motivated by the need to specify the uncertainty in our measurement results. Since most calculations require more than a single input parameter, we also need a means to combine those errors in a way that provides the overall uncertainty. The critical question for making such a combination is whether the errors in the determination of the parameters are *correlated* or *uncorrelated*. In the previous example, which used Eq. (1.91) to determine  $g$  from measurements of  $L$  and  $T$ , it is obvious that the errors in determination of  $T$  were uncorrelated to the errors in the determination of  $L$ . If a stopwatch was used to determine  $T$  and a ruler was used to determine  $L$ , then errors introduced by the stopwatch do not have any influence on errors made in reading the length of the string using a ruler.

The correlation, or lack of correlation, between sources of error can be formalized by the introduction of the *covariance*. If a particular parameter,  $x$ , is a function of several other variables,  $x = f(u, v,$

...), we assume that the most probable value of the dependent variable,  $\bar{x}$ , is the same function of the most probable values of the independent variables:  $\bar{x} = f(\bar{u}, \bar{v}, \dots)$ . Using Eq. (1.88) in the limit of very large  $N$ , it is possible to approximate the variance,  $\sigma_x^2$ .

$$\sigma_x^2 \cong \lim_{N \rightarrow \infty} \frac{\sum (x_i - \bar{x})^2}{N} \quad (1.92)$$

Limiting ourselves to only two independent variables,  $u$  and  $v$ , and using a Taylor series, the deviation (also known as the *residual*),  $\delta x_i = x_i - \bar{x}$ , can be expanded in terms of the deviations of those two independent variables.

$$\delta x_i = x_i - \bar{x} \cong \left( \frac{\partial x}{\partial u} \right) (u_i - \bar{u}) + \left( \frac{\partial x}{\partial v} \right) (v_i - \bar{v}) \quad (1.93)$$

Substitution of Eq. (1.93) into Eq. (1.92) generates three contributions to  $\sigma_x^2$ .

$$\begin{aligned} \sigma_x^2 &\cong \lim_{N \rightarrow \infty} \frac{1}{N} \sum \left[ \left( \frac{\partial x}{\partial u} \right) (u_i - \bar{u}) + \left( \frac{\partial x}{\partial v} \right) (v_i - \bar{v}) \right]^2 = \\ &\lim_{N \rightarrow \infty} \frac{1}{N} \sum \left[ \left( \frac{\partial x}{\partial u} \right)^2 (u_i - \bar{u})^2 + \left( \frac{\partial x}{\partial v} \right)^2 (v_i - \bar{v})^2 + 2 \left( \frac{\partial x}{\partial u} \right) \left( \frac{\partial x}{\partial v} \right) (u_i - \bar{u})(v_i - \bar{v}) \right] \end{aligned} \quad (1.94)$$

The last term introduces the covariance  $\sigma_{uv}^2$ .

$$\sigma_{uv}^2 \equiv \lim_{N \rightarrow \infty} \frac{\sum (u_i - \bar{u})(v_i - \bar{v})}{N} \quad (1.95)$$

This allows Eq. (1.94) to be re-written in a more compact and intuitive form.

$$\sigma_x^2 \cong \left( \frac{\partial x}{\partial u} \right)^2 \sigma_u^2 + \left( \frac{\partial x}{\partial v} \right)^2 \sigma_v^2 + 2 \left( \frac{\partial x}{\partial u} \right) \left( \frac{\partial x}{\partial v} \right) \sigma_{uv}^2 \quad (1.96)$$

If the fluctuations  $\delta u_i = u_i - \bar{u}$  and  $\delta v_i = v_i - \bar{v}$  are uncorrelated, then  $\sigma_{uv}^2 = 0$ , and the standard deviation of the dependent variable,  $x$ , is related to the variances in the individual independent variables.

$$\sigma_x \cong \left[ \left( \frac{\partial x}{\partial u} \right)^2 \sigma_u^2 + \left( \frac{\partial x}{\partial v} \right)^2 \sigma_v^2 \right]^{1/2} \quad (1.97)$$

We can apply this formalism directly to a weighted sum. If  $x = au \pm bv$ , then  $(\partial x/\partial u) = a$  and  $(\partial x/\partial v) = \pm b$ , so Eq. (1.96) becomes

$$\sigma_x^2 \cong a^2 \sigma_u^2 + b^2 \sigma_v^2 \pm 2ab \sigma_{uv}^2. \quad (1.98)$$

For products, ratios, and powers of independent variables that are uncorrelated, it is more convenient to deal with the relative uncertainties and to combine the uncertainties using logarithmic differentiation (see Sect. 1.1.3). We can take the natural logarithm of Eq. (1.91).

$$\ln g = \ln 4\pi^2 + \ln L - 2 \ln T \quad (1.99)$$

Using Eq. (1.15), differentiation of that expression leads to a relationship between the relative uncertainties.

$$\frac{\delta g}{g} = \frac{\delta L}{L} - 2 \frac{\delta T}{T} \quad (1.100)$$

Since we have already established the statistical independence of the errors in  $L$  and  $T$  (i.e.,  $\sigma_{LT}^2 = 0$ ), Eq. (1.97) dictates that the relative uncertainty in  $g$  becomes the Pythagorean sum of the individual contributions of the relative uncertainties of the independent variables.

$$\frac{\delta g}{g} = \left[ \left( \frac{\delta L}{L} \right)^2 + \left( -2 \frac{\delta T}{T} \right)^2 \right]^{1/2} \quad (1.101)$$

### 1.8.5 Significant Figures

It is important that the overall uncertainty in a result is part of the number that reports that result. The first consideration should be the number of significant digits used to report the result. For example, if my calculation of sound speed produces a result of 1483.4 m/s and my uncertainty in that result is  $\pm 30$  m/s, it makes no sense to report the result as  $c = 1483.4 \pm 30$  m/s. In that example, only three significant digits are justified, so the result should have been reported as  $c = 1480 \pm 30$  m/s.<sup>27</sup>

The specification of the expected uncertainty in a result differs among users. In my laboratory notebook, my publications, and my technical reports, I usually report a result as the mean plus or minus one standard deviation, thus indicating that I have a 68% confidence in the accuracy of the result. Standards organizations, such as the National Institutes of Standards and Technology (formerly the National Bureau of Standards) in the United States, the National Research Council in Canada, or the National Physical Laboratory in the United Kingdom, customarily specify their uncertainties with errors that are  $\pm 2\sigma$  to provide a 95% confidence level in the result. In every case, it is the responsibility of the experimentalist to specify the meaning of his or her stated uncertainty.

---

## 1.9 Least-Squares Fitting and Parameter Estimation

To this point, our discussion of measurement error has focused on repeated measurement of individual parameters. A more common occurrence in the determination of parameters in an acoustical or vibrational experiment is the measurement of some response,  $y$  (the dependent variable), that is a function of some stimulus,  $x$  (the independent variable). In that case, the goal is to find the function,  $f$ , such that  $y = f(x)$ . Of course, this can be extended to functions of several variables. Instead of measuring  $y$  several times for a given value of  $x$ , we would like to treat the measurement of  $y_i$  values corresponding to  $x_i$  inputs, where  $i = 1, 2, \dots, N$ , to produce  $N$  data pairs  $(x_i, y_i)$ . These pairs are typically displayed graphically [23].

---

<sup>27</sup> There are different standards for the number of significant digits that should be included in the representation of a measurement. For example, the ASTM International (known prior to 2001 as the American Society for Testing and Materials) publishes “Standard Practice for Using Significant Digits in Test Data to Determine Conformance with Specifications,” ASTM Designation E 29 – 08. For certain applications, there are legal ramifications associated with misrepresenting a result by supplying more significant figures than are justified.

The simplest possible relationship between the pairs of data is the linear relationship:  $y = mx + b$ . In a graphical representation,  $m$  corresponds to the slope of the line, and  $b$  is the  $y$ -axis intercept. This section will address the question of how one chooses  $m$  and  $b$  so that the line specified by those two parameters minimizes the deviations (residuals),  $\delta y_i$ , between the experimental measurements,  $y_i$ , and the values generated by the equation for the straight line when  $x_i$  is substituted into that equation:  $\delta y_i = y_i - y(x_i) = y_i - (mx_i + b)$ .

As before, the line that is considered a “best-fit” to the data will minimize the sum of squares of the residuals. If we assume that the values of  $x_i$  are known exactly, then the Gaussian probability of measuring a value  $y_i$  is given by  $P_i(y_i)$ .

$$P_i(y_i) = \frac{1}{\sigma_i \sqrt{2\pi}} \exp \left[ \frac{1}{2} \left( \frac{y_i - y(x_i)}{\sigma_i} \right)^2 \right] \quad (1.102)$$

For  $N$  measurement pairs, the overall probability will be the product of the probability of the individual measurements.

$$P(m, b) = \prod_{i=1}^N P_i(y_i) = \prod_{i=1}^N \left( \frac{1}{\sigma_i \sqrt{2\pi}} \right) \exp \left[ \sum_{i=1}^N \frac{1}{2} \left( \frac{\delta y_i}{\sigma_i} \right)^2 \right] \quad (1.103)$$

We can abbreviate the argument in the sum as  $\chi^2$ .

$$\chi^2 = \sum_{i=1}^N \left( \frac{\delta y_i}{\sigma_i} \right)^2 = \sum_{i=1}^N \left[ \frac{(y_i - mx_i - b)^2}{\sigma_i^2} \right] \quad (1.104)$$

Determination of the best values of  $m$  and  $b$  is therefore equivalent to finding the minima of  $\chi^2$  by setting the derivatives of  $\chi^2$  with respect to  $m$  and  $b$  equal to zero.

$$\frac{\partial(\chi^2)}{\partial m} = 0 \quad \text{and} \quad \frac{\partial(\chi^2)}{\partial b} = 0 \quad (1.105)$$

Using these criteria, it is possible to express the best values of  $m$  and  $b$  in terms of various sums of the measurements.

$$b = \frac{\left( \sum_{i=1}^N x_i^2 \right) \left( \sum_{i=1}^N y_i \right) - \left( \sum_{i=1}^N x_i \right) \left( \sum_{i=1}^N x_i y_i \right)}{N \left( \sum_{i=1}^N x_i^2 \right) - \left( \sum_{i=1}^N x_i \right)^2} \quad (1.106)$$

$$m = \frac{N \left( \sum_{i=1}^N x_i y_i \right) - \left( \sum_{i=1}^N x_i \right) \left( \sum_{i=1}^N y_i \right)}{N \left( \sum_{i=1}^N x_i^2 \right) - \left( \sum_{i=1}^N x_i \right)^2} \quad (1.107)$$

Although the expressions look intimidating, they are exactly the types of expressions that a digital computer can evaluate nearly instantaneously. Practically any software package will automatically determine  $m$  and  $b$  and several other features of such a *least-squares fit*.

### 1.9.1 Linear Correlation Coefficient

*“If your experiment needs statistics, you should have done a better experiment.”* (E. Rutherford, F.R.S [24])

The calculation of  $m$  and  $b$  assumed that the values,  $x_i$ , were known exactly and all of the statistical fluctuations were due to the  $y_i$  values. In some experimental circumstances, that assumption might be valid. For mathematically perfect data (i.e., values of  $y_i$  that are generated by substitution of  $x_i$  into an equation like  $y_i = mx_i + b$ ), we could just as well describe the line which fits  $x = m'y + b'$ , where  $m'$  and  $b'$  would be different from  $m$  and  $b$  in both their numerical values and their units.

Solving the inverse relation,  $x = m'y + b'$  for  $y$ , we obtain the relationships between the primed quantities and the unprimed fit parameters,  $m$  and  $b$ .

$$y = \frac{x}{m'} - \frac{b'}{m'} = mx + b \quad \Rightarrow \quad b = \frac{-b'}{m'} \quad \text{and} \quad m = \frac{1}{m'} \quad (1.108)$$

For mathematically perfect data,  $(m)(m') \equiv R^2 = 1$ ; the product of the slope for a line that plots  $y$  vs.  $x$  is the reciprocal of the slope for the plot of  $x$  vs.  $y$ . By reversing the plotting axes, we are now also assuming that the  $y_i$  values are exact and all of the uncertainty is caused by the  $x_i$  values. If there are errors, the value of  $R^2$  will be less than unity.  $R^2$  is called the square of the *correlation coefficient* that can also be calculated in terms of the same sums used in Eqs. (1.106) and (1.107).

$$R = \sqrt{mm'} = \frac{N \sum x_i y_i - (\sum x_i)(\sum y_i)}{\left[ N \sum x_i^2 - (\sum x_i)^2 \right]^{1/2} \left[ N \sum y_i^2 - (\sum y_i)^2 \right]^{1/2}} \quad (1.109)$$

If the  $(x_i, y_i)$  data pairs are uncorrelated, then  $R = 0$ ; if the data are perfectly correlated and noise-free, then  $R^2 = 1$ . If we use this formalism to fit the data that produced the left-hand “target” in Fig. 1.10, the best-fit gives the following equation for the  $y_i$  values in terms of the  $x_i$  values:  $y = 0.0393x + 0.397$ . The square of the correlation coefficient for that fit is  $R^2 = 0.0015$ . We expect that slope and  $R^2$  for a truly random set of points should both be very close to zero. It is difficult to say how close is “close enough” to declare that the data are truly random and that the slope is zero, since the answer to such a question is inherently probabilistic.

A strict interpretation of the meaning of the correlation coefficient as a measure of randomness and the relationship between the correlation coefficient and the relative uncertainty in the slope,  $\delta m/m$ , requires the evaluation of a two-dimensional Gaussian distribution with careful attention to the distinction between the population and the sample, especially if  $N$  is small (see Table 1.4) [25]. Again, it is the type of result that can be generated by the proper software or by consulting Table 1.3. That table provides the smallest value of  $R$  that would rule out randomness with some specified level of confidence. For example, there is a 10% chance that a set of  $N = 8$  data pairs would produce a correlation coefficient of  $R \geq 0.621$ , even if the data were uncorrelated. At the 1% probability level,  $R \geq 0.834$  would be required to imply causality and  $R \geq 0.925$  to ensure a 0.1% confidence level.

For the least-squares fit to the data plotted on the left-hand side of Fig. 1.10, the correlation coefficient  $R = (0.0015)^{1/2} = 0.039$ . Linear interpolation within Table 1.3 for  $N = 16$  points requires that  $R \geq 0.428$  to rule out, with a 10% probability, that the data were not random and  $R \geq 0.744$  for a 0.1% probability that the data were not random. Those data appear to be truly random, as claimed.

Before leaving this subject, it is important to recognize that in physical and engineering acoustics, controlled experiments that are supposed to be represented by a linear relationship routinely produce  $R^2 > 0.99$ , while in areas like community response to noise or other environmental, architectural, psychological, or physiological acoustical investigations, the square of the correlation coefficients can

**Table 1.3** Values of the correlation coefficient,  $R$ , that would have to be exceeded for  $N$  data pairs to have the probability, given in the top row of the table, that the correlation coefficient,  $R$ , was produced by  $N$  causally related pairs

$N$	Probability				
	0.10	0.05	0.02	0.01	0.001
3	0.988	0.997	0.999	1.000	1.000
4	0.900	0.950	0.980	0.990	0.999
5	0.805	0.878	0.934	0.959	0.992
6	0.729	0.811	0.882	0.917	0.974
7	0.669	0.754	0.833	0.874	0.951
8	0.621	0.707	0.789	0.834	0.925
10	0.549	0.632	0.716	0.765	0.872
12	0.497	0.576	0.658	0.708	0.823
15	0.441	0.514	0.592	0.641	0.760
20	0.378	0.444	0.516	0.661	0.679
30	0.307	0.362	0.423	0.464	0.572
40	0.264	0.312	0.367	0.403	0.502
60	0.219	0.259	0.306	0.337	0.422
80	0.188	0.223	0.263	0.291	0.366
100	0.168	0.199	0.235	0.259	0.327

Adapted from Fisher and Yates [26]

For the example on the left-hand side of Fig. 1.10, linear interpolation for  $N = 16$  points requires that  $R \geq 0.428$  to guarantee with a 10% probability that the data were not random and  $R \geq 0.744$  for a 0.1% probability that the data were not random

**Table 1.4** Comparison of the error estimate in slope and intercept using Eq. (1.112) or their Higbie equivalents in Eqs. (1.113) and (1.114)

Topic	$N$	$R^2$	Higbie slope (%)	Small $N$ slope (%)	Higbie intercept (%)	Small $N$ intercept (%)
Language test	24	0.254	36.9	37.2	18.3	18.6
Frequency	8	0.999937	0.32	0.35		
Decay time	7	0.99973	0.77	0.80		
Phase speed	10	0.99989	0.37	0.40	0.30	0.20
Bevington [24]	9	0.9437	9.23	9.88	101.6	108.6
Beers [28]	6	0.99988	0.55	0.63	239	281

The examples include Fig. 1.14 (language), Fig. 1.15 (frequency and decay time), and Fig. 1.17 (phase speed), as well as the example in Table 6.1 of Bevington [25] and Table XI in Beers [29]. The very large (i.e., >100%) relative errors in the intercepts from the Bevington and Beers examples arise because the value of the intercept,  $|b|$ , is very close to zero. For all entries, the reported errors are based on  $\pm 1\sigma$

be one-half or less (see Fig. 1.14). This is not the result of inferior scientific methods but a consequence of the inability to control the large number of *confounding variables* that influence specific responses of animals and particularly humans.

Recognition of this challenge is not a valid justification for the reliance solely on statistical tests, particularly when a stated “result” can trigger regulatory remediation that may require enormous financial burdens.

The four graphs shown in Fig. 1.13 are all fit with a best-fit straight line. All four lines have the same slope and intercept, and all four have the same squared correlation coefficient. The fit designated “ $y_1$ ” (upper left) is what is usually assumed when we think of a linear relationship that describes fairly noisy data. The data in the graph fit by “ $y_2$ ” (upper right) is much smoother but clearly would be better represented by a quadratic equation rather than a linear one. In fact, those points were generated by the following equation:  $y_2 = -0.127 x^2 + 2.78 x + 6$ .

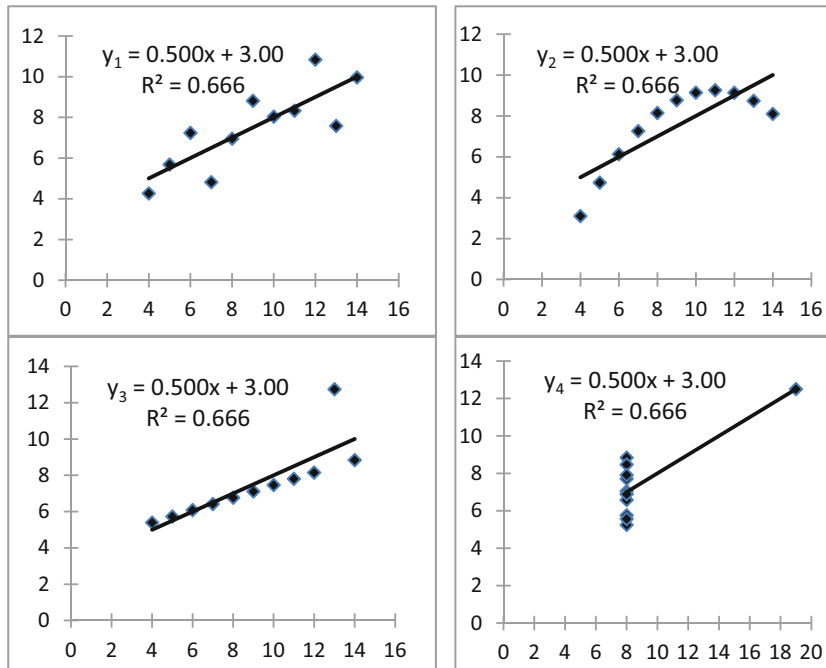


**Fig. 1.13** These four data sets each contain  $N = 11$  data pairs that are plotted and include solid lines that were determined by a best-fit to each data set. All lines have the same slope,  $m = 0.500$ ; intercept,  $b = 3.00$ ; and (diabolical) squared correlation coefficient,  $R^2 = 0.666$ . (Data taken from Anscombe [23].)

The third and fourth examples in Fig. 1.13 are intentionally pathological. The fit designated “ $y_3$ ” (lower left) is dominated by one “outlier,” but all the other points were generated by a linear equation with a different slope and intercept:  $y_3 = 0.346x + 4$ . Similarly, the slope of the line that is the best-fit to produce “ $y_4$ ” is entirely dominated by one “outlier” which, if removed, would leave the remaining points with an infinite slope since the variety of all  $y_i$  values corresponds to a single value for all the remaining  $x_i = 8$ .

Although I’ve called “ $y_3$ ” and “ $y_4$ ” least-squares fits in the lower half of Fig. 1.13 “pathological,” they are not uncommon. Figure 1.14 is taken from Fig. 9 in an article on the relationships between unoccupied classroom acoustical conditions and a metric for elementary school student achievement [27]. The authors fit their data to a straight line and claim “a significant negative correlation between the Terra Nova language test score and the temperature-weighted average BNL [background noise level] . . . .”

Using the analysis of Table 1.3, it is true that there is only about a 5% probability that such a data set incorporating those 24 points would have been generated by a random set of ordered pairs, but if only the 21 points, corresponding to  $L_{eqA} \leq 45 \text{ dB}_A$ ,<sup>28</sup> are fit to a straight line, then percentile rank [from Fig. 1.14] =  $-0.135 L_{eqA} + 70.95$  with  $R^2 = 0.0014$ . Using techniques introduced in the next section, that “best-fit” slope of  $m = -0.135$  could range anywhere from  $m = -0.97$  to  $m = +0.70$  if the fit were good to  $\pm 1\sigma$ . This correlation coefficient is just as “random” as the intentionally random data set on the left of Fig. 1.10 (i.e.,  $R^2 = 0.0015$ ). The reported “effect” is due only to the three additional points corresponding to  $45 \leq L_{eqA} \leq 52 \text{ dB}_A$ .

<sup>28</sup>The unit  $\text{dB}_A$  is a version of a sound pressure level (see footnote 1) that compensates for the frequency dependence of the sensitivity of human hearing.

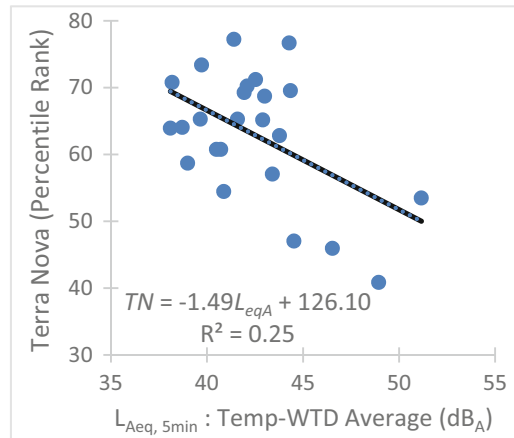


**Fig. 1.14** Graph taken from an article that claims a “statistically significant” relationship between background noise levels and language test achievement scores [27]. The line is the authors’ least-squares fit to a straight line with a squared correlation coefficient  $R^2 = 0.25$ . A fit to all the data with  $L_{Aeq} \leq 45$  dB<sub>A</sub> has a slope of  $-0.135$  and  $R^2 = 0.0014$ . The addition of those three “outliers” produces a result similar to that shown as the “y<sub>3</sub>” fit in the lower-left quadrant of Fig. 1.13

The message that I hope these examples provide is that both graphical and statistical interpretations of data, and the models used to fit data, must be applied simultaneously to avoid erroneous conclusions. Once confidence in the analysis that might involve a least-squares fit is established, there are further techniques that are invaluable in the determination of the uncertainty of the slope and intercept that are generated by such a fit.

### 1.9.2 Relative Error in the Slope

For most data sets generated by experiments in physical or engineering acoustics, causality is not in question. In such cases, it is far more important to determine the relative error in the slope  $\delta m/m$  and the intercept  $\delta b/b$ . These error estimates are related to the variance determined by the squared sum of the residuals,  $\delta y_i$ , produced by the fitting function.

$$\sigma^2 \cong \frac{\sum (y_i - mx_i - b)^2}{N - 2} \quad (1.110)$$

Unlike the definition of the standard deviation in Eq. (1.88), the denominator above is  $N - 2$  instead of  $N - 1$ . This is due to the fact that the best-fit straight line had two adjustable parameters,  $m$  and  $b$ , whereas the standard deviation had only one:  $\bar{x}$ .

The estimate of the error in  $m$  and  $b$  is related to Eq. (1.110) through combinations of sums for the  $x_i$  and  $y_i$  measurements like those in Eqs. (1.106), (1.107), and (1.109).

$$\Delta = N \left( \sum_{i=1}^N x_i^2 \right) - \left( \sum_{i=1}^N x_i \right)^2 \quad (1.111)$$

The relative errors in the slope and the intercept can be expressed in terms of  $\Delta$ .

$$\begin{aligned}\frac{\delta m}{|m|} &= \frac{\sigma_m}{|m|} = \frac{N}{|m|} \frac{\sigma}{\Delta} \\ \frac{\delta b}{|b|} &= \frac{\sigma_b}{|b|} = \frac{\sqrt{\sum x_i^2}}{|b|} \frac{\sigma}{\Delta} = \frac{N^{1/2} x_{rms}}{|b|} \frac{\sigma}{\Delta} = x_{rms} \frac{\sigma_m}{|b|}\end{aligned}\quad (1.112)$$

Again, these combinations are commonly provided automatically by many software packages when data is fit to a straight line.

I have found an expression suggested by Higbie [28] to be a convenient way to calculate the relative uncertainties in slope,  $\delta m/|m|$ , and intercept,  $\delta b/|b|$ , directly from the  $R^2$  obtained by a straight-line least-squares fit, which is usually available even when data are analyzed on a handheld calculator in the laboratory.

$$\frac{\delta m}{|m|} = \frac{\tan(\cos^{-1} R)}{\sqrt{N-2}} = \sqrt{\frac{\frac{1}{R^2}-1}{N-2}} \quad (1.113)$$

The relative uncertainty in the intercept,  $\delta b/|b|$ , can be calculated from substitution of Eq. (1.113) into Eq. (1.112) where  $x_{rms}$  is the root-mean-squared value of the  $x_i$  values.

$$\frac{\delta b}{|b|} = \delta m \frac{x_{rms}}{|b|} = \left( \frac{\delta m}{|m|} \right) \frac{|m|}{|b|} x_{rms} \quad (1.114)$$

### 1.9.3 Linearized Least-Squares Fitting

The formalism developed in the previous section can easily be extended to many other models that have two adjustable parameters but are not plotted as straight lines. Most books on the data analysis demonstrate that exponential growth or decay, power law relationships, and logarithmic relaxation can be transformed into straight lines. These will be demonstrated, along with more specific applications, in acoustic problems that will be analyzed later in this textbook that also fix the values of two adjustable parameters.

The first example is the envelope of an exponentially decaying damped simple harmonic oscillator (Sect. 2.4). For a damping force that is proportional to velocity, we expect the amplitude to decay with time according to  $V(t) = V_o e^{-t/\tau}$ , where  $\tau$  is the characteristic exponential decay time (i.e., the time required for the amplitude to decrease by a factor of  $e^{-1} \approx 36.8\%$ ). By taking the natural logarithm of that expression, we can see that the expected behavior can be plotted as a straight line if the natural logarithm of the amplitude envelope is plotted against time as shown in Fig. 1.15.

$$\ln[V(t)] = \ln[V_o] - \frac{t}{\tau} \quad (1.115)$$

Sample data taken from the recording of a digital oscilloscope is shown in Fig. 1.15 along with the least-squares line fit to those data. The use of Eq. (1.113) provides the relative uncertainty in the slope:  $\delta\tau/|\tau| = \pm 0.73\%$ . The slope of the line it provides is the negative reciprocal of the characteristic exponential decay time:  $\tau = 22.18 \pm 0.17$  s. For this type of measurement, we are not interested in the intercept,  $V_o$ , since it is just a measure of the amplitude extrapolated back to an arbitrary time designated  $t = 0$ .

The reverse of the transformation in Eq. (1.115) can be used to fit a straight line to a logarithmic decay. This is illustrated in Fig. 1.16 showing the creep of an elastomeric loudspeaker surround. The

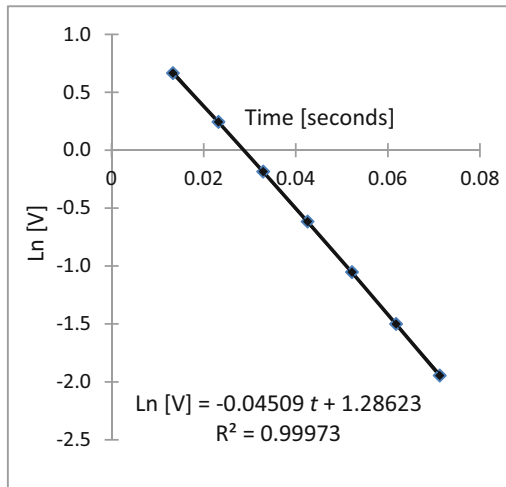


**Fig. 1.15** Free-decay data that plots the natural logarithm of the peak-to-peak amplitude of the waveform vs. the average time between successive peaks and troughs. The slope of the line provides the negative reciprocal of the characteristic exponential decay time,  $\tau = (22.18 \pm 0.17) \times 10^{-3}$  s, with the uncertainty determined from  $R^2$  by way of Eq. (1.113). A plot of the time for zero-crossings vs. the cycle number provides  $f_d = 51.82 \pm 0.17$  Hz

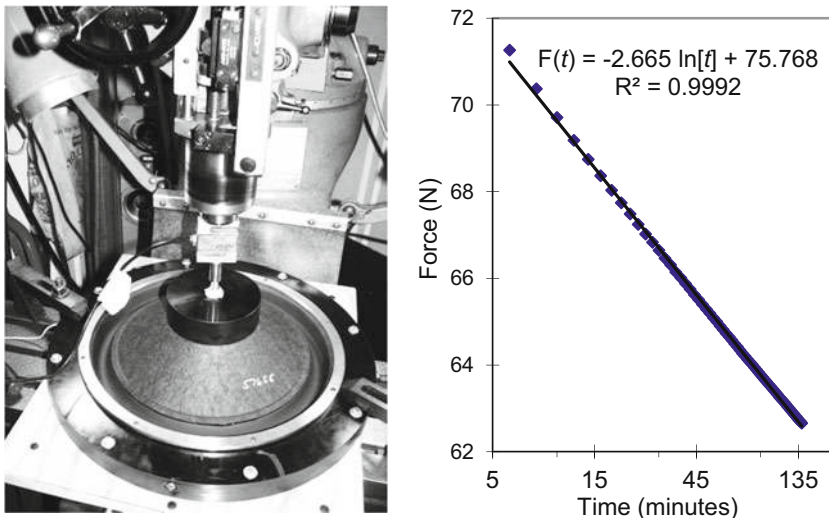


**Fig. 1.16** (Left) The force necessary to displace a loudspeaker cone from its equilibrium position is applied by the quill of a milling machine. Between the quill and the fixture applying the force to the loudspeaker cone is a load cell that measures the force. (Right) Plot of the force necessary to displace an elastomeric loudspeaker surround as a function of the logarithm of the time it was held in a fixed position. The least-squares fit to the force vs. the logarithm of the holding time yields a straight line. The force decreases by 10% from its value at the first second for each multiple of 17.2 s. The force is reduced by 20% at  $(17.2)^2 = 295$  s and by 30% at  $(17.2)^3 = 5060$  s = 1.4 h and would reach half its value after  $1.49 \times 10^6$  s = 17.3 days

surround was displaced from its equilibrium position, and the force needed to hold it in that position is plotted vs. the logarithm of the holding time.

The same approach can be used to transform power-law expressions,  $V(t) = bt^m$ , where  $b$  and  $m$  can be determined by again taking logarithms, typically using base 10 to make it easy to read a graph.

$$\log_{10}[V(t)] = \log_{10}[b] + m \log_{10}[t] \quad (1.116)$$

This linearization technique should not be limited only to the two-parameter fits that are treated in the data analysis textbooks. There are several instances in this textbook where proper plotting of the results of acoustical or vibrational measurements simplifies the extraction of important parameters and their uncertainties. I will use one example that occurs when we investigate the propagation of sound in waveguides and introduce the concepts of group speed,  $c_{gr}$ , and phase speed,  $c_{ph}$ , and their relationship to the square of the thermodynamic sound speed,  $c_o^2 = c_{ph}c_{gr}$ . In the following equation,  $f$  is the frequency of the sound propagating within the waveguide in a mode with a cut-off frequency,  $f_{co}$ .

$$c_{ph} = \frac{c_o}{\sqrt{1 - \left(\frac{f_{co}}{f}\right)^2}} \quad (1.117)$$

It is possible to make very accurate measurements of phase speed, and with a synthesized function generator, the frequency can be selected with relative accuracies on the order of a few parts per million. Equation (1.117) has two adjustable parameters:  $c_o$  and  $f_{co}$ . By squaring Eq. (1.117) and inverting the result, it can be cast into the form of a straight line.

$$\frac{1}{c_{ph}^2} = \frac{1}{c_o^2} - \frac{f_{co}^2}{c_o^2} \frac{1}{f^2} = \frac{1}{c_o^2} - \frac{f_{co}^2}{c_o^2} T^2 \quad (1.118)$$

The results of measurements of phase speed vs. frequency in a water-filled waveguide are shown on the left-hand side of Fig. 1.17 (also see Prob. 5 in Ch. 13). One could attempt to locate a vertical asymptote to determine the cut-off frequency,  $f_{co}$  (where the phase speed would have become infinite), and a horizontal asymptote that would intersect the y axis at a value of  $c_{ph} = c_o$ . Plotting the same data using Eq. (1.118) makes such guesswork totally unnecessary. The right-hand side of Fig. 1.17 shows a plot of the reciprocal of the square of the phase speed ( $c_{ph}$ )<sup>-2</sup> vs. the square of the period of the sound,

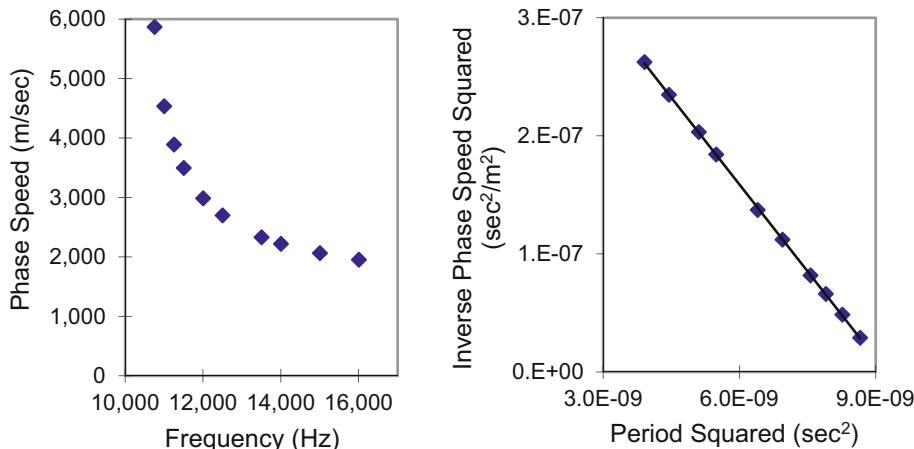


**Fig. 1.17** The same data plotted in two different ways. (Left) The raw data consisting of phase speed,  $c_{ph}$ , in a waveguide vs. the frequency of the sound propagating through the waveguide. (Right) The same data plotted using Eq. (1.118) that is fit with the straight line:  $c_{ph}^{-2} = -49.04 T^2 + 4.531 \times 10^{-7} \text{ s}^2/\text{m}^2$ . The correlation coefficient of the fit is  $R = -0.999944$ , corresponding to an uncertainty in the slope of  $\delta m/m_l = 0.37\%$ . The uncertainty in the intercept is  $\delta b/b_l = 0.30\%$ . The combined uncertainty gives  $c_o = 1485.6 \pm 2.2 \text{ m/s}$  and  $f_{co} = 10,404 \pm 25 \text{ Hz}$

$T^2$ . The thermodynamic sound speed,  $c_o$ , is the square root of the y axis intercept of the best-fit straight line. The square root of the ratio of the slope to the intercept is the cut-off frequency,  $f_{co}$ .

### 1.9.4 Caveat for Data Sets with Small $N^*$

The uncertainties in the slopes and intercepts reported for the graphs in the previous section were based on Eq. (1.112) or the Higbie equivalents of Eq. (1.113) and Eq. (1.114). For smaller data sets, these estimated uncertainties are not exactly correct, even though those estimates incorporate the number of measurements through the  $(N - 2)^{1/2}$  in the denominator of Eq. (1.113). In fact, the error estimates are not necessarily symmetric (i.e., instead of  $\pm$ , the + and – errors may differ slightly). Most software packages that can calculate least-squares fits can also provide estimates for the errors. Table 1.4 provides a comparison between those simpler error estimates and the correct estimates that incorporate the actual number of points. In general, those error estimates are slightly larger than obtained by use of the Higbie expression. In both cases, the quoted errors correspond to variation by  $\pm 1\sigma$ .

### 1.9.5 Best-Fit to Models with More Than Two Adjustable Parameters

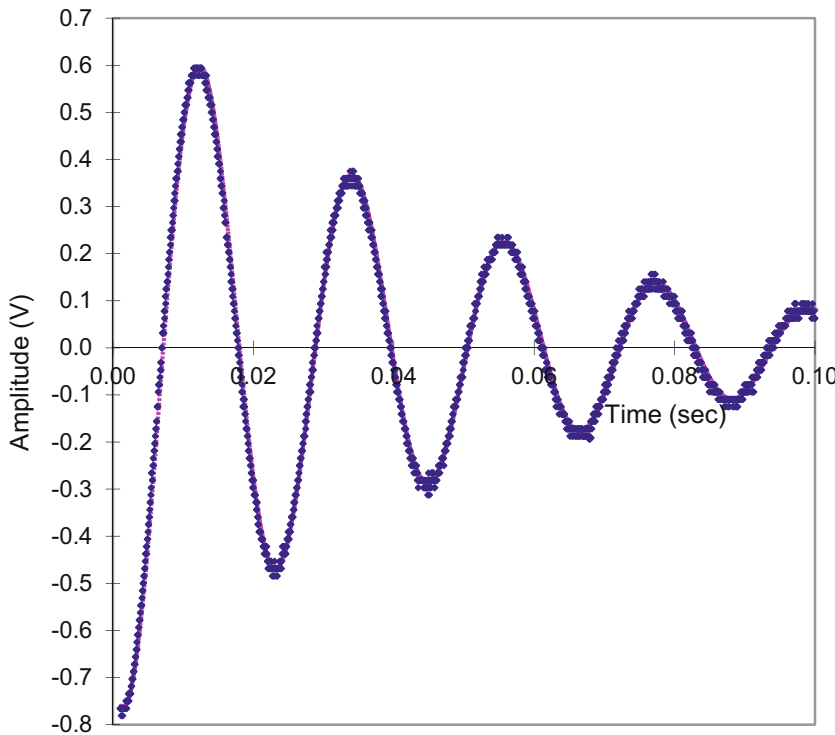
The availability of digital computers makes it rather easy to optimize the fit of nearly any function to a data set, although it should always be remembered that the number of fitting (free) parameters must be less than the number of data points. The extension of the least-squares fitting to a polynomial of arbitrary order is deterministic but algebraically messy [29]. Again, most software packages are capable of executing a fit to an  $n^{th}$ -order polynomial automatically if the number of data pairs  $N \geq n + 1$ .

Figure 1.18 shows 2000 data points acquired by a digital oscilloscope and imported to a spreadsheet program. The goal was to fit the entire data set to a free-decay expression that is related to Eq. (1.115) used to produce the fit shown in Fig. 1.15. Since all the measurements were used, instead of just the amplitudes of the peaks and the troughs, the equation had also to incorporate the time dependence explicitly.

$$V(t_i) = V_o e^{-t_i/\tau} \sin(2\pi f_d t_i + \phi) \quad (1.119)$$

This expression has four adjustable parameters:  $V_o$ ,  $\tau$ ,  $f_d$ , and  $\phi$ . Those parameters have to be adjusted simultaneously to minimize the sum of the square of the residuals.

The fit shown in Fig. 1.18 was made by taking the time and amplitude data columns and creating a column that took each time and plugged it into Eq. (1.119) using guesses for the values of each parameter that seemed reasonable based on inspection of the plot of  $V(t)$  vs.  $t$ . For example, the initial amplitude was approximately  $|V(t)| \cong 0.8$  volts, so one initial guess was  $V_o = 0.8$  volts. We see approximately three complete cycles between  $t \cong 0.018$  s and  $t \cong 0.082$  s, so a reasonable guess for frequency is  $f_d \cong 3$  cycles/0.064 s = 47 Hz. Just considering the first four peaks, it appears that amplitude decreases by about  $e^{-1} \cong 37\%$ , from about 0.6 volts to about 0.2 volts, and also in about 0.064 s, so  $\tau = 0.064$  s is a reasonable guess. Finally, we assumed sinusoidal time dependence, but a sine wave starts from zero amplitude at  $t = 0$ . If the data in Fig. 1.18 were actually a sine wave, we would have to translate the origin of our time axis backward by about 0.007 s. Using the period based on the frequency guess,  $T = f_d^{-1} \cong 0.021$  s, this means we need to retard the phase by about one-third



**Fig. 1.18** The 2000 plotted points were acquired by a digital oscilloscope and were imported to a spreadsheet program. By allowing the program to vary the four parameters in Eq. (1.119), the program attempted to minimize the sum of the squared residuals,  $(\delta V_i)^2 = (V_i - V(t_i))^2$ , based on the initial guesses provided. The result is the characteristic exponential decay time,  $\tau = 0.0445$  s, with a root-mean-squared relative error of  $\pm 0.15\%$ . The quality of that fit is so good that the line representing Eq. (1.119) is almost entirely obscured by the individual data points. The other parameters that were optimized by the program are  $f_d = 46.141$  Hz,  $V_o = 0.788$  volts, and  $\phi = -2.032$  radians

of a cycle or advance it by two-thirds of a cycle corresponding to  $\phi \cong -2\pi/3$  or  $+4\pi/3$  radians. I choose to use  $\phi \cong -2$  radians.

With those initial guesses, it is possible to calculate the residuals,  $\delta V_i = V_i - V(t_i)$ , square those residuals, and add them together for all 2000 points. (Ain't computers wonderful!) To create the fit shown in Fig. 1.18, I used MS Excel's "solver," which I let vary those four adjustable parameters from their guessed values in an attempt to minimize the sum of the squared residuals. The final values are provided in the caption of Fig. 1.18.

## 1.10 The Absence of Rigorous Mathematics

"In the mathematical investigations I have usually employed such methods as present themselves naturally to a physicist. The pure mathematician will complain, and (it must be confessed) sometimes with justice, of deficient rigor. But to this question there are two sides. For, however important it may be to maintain a uniformly high standard in pure mathematics, the physicist may occasionally do well to rest content with arguments which are fairly satisfactory and conclusive from his point of view. To his mind, exercised in a different order of ideas, the more severe procedures of the pure mathematician may appear not more but less demonstrative. And further, in many cases of difficulty, to insist upon the

highest standard would mean the exclusion of the subject altogether in view of the space that would be required.” [30]

### Talk Like an Acoustician

In addition to thinking like an acoustician and calculating like an acoustician, you need to be able to speak like an acoustician. You should understand the meaning of the technical terms below that have been introduced in this chapter. (Note: The first time a significant new term is introduced in the notes, it is *italicized*.) If a term is descriptive, you should have your own definition (e.g., isotropic medium → a medium whose properties are the same in every direction). If it is a physical quantity, you should know its definition and its units (mechanical work,  $dW = F \cdot dx$  or  $dW = P \cdot dV$ [Joules]).

Taylor series expansion	Phasor notation
Second-order correction	Rationalization
Power series	Complex conjugate
Product rule	Dimensional homogeneity
Differential	SI System of Units
The Fundamental Theorem of Calculus	Similitude
Integration by parts	$\Pi$ -groups
Logarithmic differentiation	Dimensionless groups
Stable equilibrium	Random errors
Potential energy	Systematic (bias) errors
Neutral equilibrium	Statistical fluctuations
Unstable equilibrium	Relative uncertainty
Linear relationship	Precision
Hooke’s law	Standard deviation
Isochronism	Ergodic hypothesis
Harmonic generation	Residual
The Principle of Superposition	End-to-end calibration
Orthogonal functions	Correlated or uncorrelated errors
Fourier synthesis	Covariance
Kronecker delta	Least-squares fit
Euler’s identity	Correlation coefficient
Complex exponentials	Confounding variables
Argand plane	

## Exercises

1. **Taylor series.** It is easy to evaluate trigonometric functions using a handheld calculator. In this exercise, you will estimate the value of  $\sin 1.10 = 0.8921$  using a Taylor series based on the value at  $x_0 = 1.0$  radians,  $\sin 1.0 = 0.8415$ , and  $dx = 0.10$  radians.
  - (a) Using Eq. (1.1) and the fact that  $d(\sin x)/dx = \cos x$ , evaluate the first approximation to  $\sin(1.10)$ , and compare that result to the exact result. Express that difference as a percentage relative to the exact result.
  - (b) Using Eq. (1.2) and the fact that  $d^2(\sin x)/dx^2 = -\sin x$ , evaluate the second approximation to  $\sin(1.10)$ , and compare that result to the exact result. Express that difference as a percentage relative to the exact result.

- (c) Using the Taylor series expansion of  $\sin x$  about  $x_o = 0$  in Eq. (1.5), approximate  $\sin$  (1.10) using the first three terms. Express the difference between the exact result and the result using the  $x$ ,  $x^3$ , and  $x^5$  terms as a percentage relative to the exact result.
2. **Product rule.** For a simple mass-spring system, the sum of the kinetic energy of the mass,  $m$ , and the potential energy of the spring having a spring constant,  $K$ , is conserved.

$$\frac{1}{2}m\left(\frac{dx}{dt}\right)^2 + \frac{1}{2}Kx^2 = \text{constant} \quad (1.120)$$

Use the product rule to show that time differentiation of Eq. (1.120) leads to Newton's Second Law of Motion.

$$\left[m\frac{d^2x}{dt^2} + Kx\right]\frac{dx}{dt} = 0 \quad \Rightarrow \quad m\frac{d^2x}{dt^2} + Kx = 0$$

3. **Logarithmic differentiation.** The volume of a cylinder is  $V = \pi a^2 h$ , where  $a$  is the cylinder's radius and  $h$  is its height. Calculate the relative change in the volume of the cylinder,  $\delta V/V$ , in terms of the relative change in radius,  $\delta a/a$ , and the relative change in height,  $\delta h/h$ .
4. **Complex roots.** Find the value of  $z$  that solves the following equation:

$$e^{2z} = 2j$$

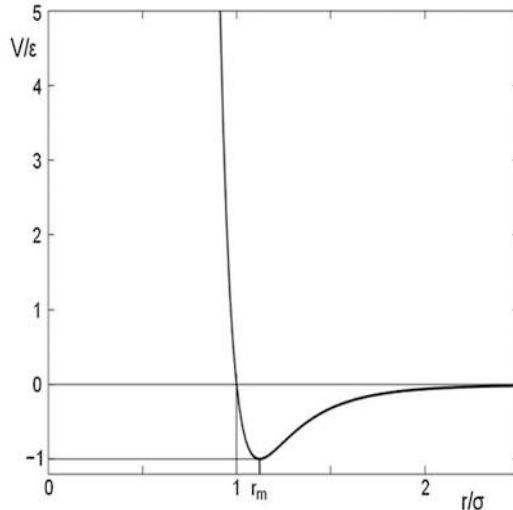
5. **Convenience numbers.** Evaluate the following expressions where  $j = (-1)^{1/2}$ :

- (a)  $\sqrt[3]{-j}$
- (b)  $(32)^{1/5}$
- (c)  $\ln[3 + 4j]$
- (d)  $\left|\frac{a-jb}{b-ja}\right|$
- (e)  $\Re e\left[\frac{e^{-jx}}{1+e^{a+jb}}\right]$
- (f)  $\Re e\left[\frac{1}{1-j}\right]$
- (g)  $(j + \sqrt{3})^2$
- (h)  $(1 - j\sqrt{3})^{1/2}$
- (i)  $\left|\frac{\sqrt{5}+3j}{1-j}\right|$

6. **Lennard-Jones potential.** This potential function, sometimes known as the “6–12 potential,” describes the interaction of two inert gas atoms as a function of their separation and is useful in calculations of scattering or determination of the temperature of condensation from a gas to a liquid. It was first proposed by John Lennard-Jones in 1924 [31] (Fig. 1.19).

$$V(r) = 4\epsilon \left[ \left(\frac{\sigma}{r}\right)^{12} - \left(\frac{\sigma}{r}\right)^6 \right]$$

**Fig. 1.19** Lennard-Jones interatomic potential



The term proportional to  $r^{-12}$  represents an empirical fit to the hard-core repulsion produced by the Pauli exclusion at short ranges when the atoms are close enough that the electron orbital overlaps. The  $r^{-6}$  term represents the van der Waals attraction due to the mutual interactions of the fluctuating dipole moments. Determine the equilibrium separation of two atoms,  $r_m$ , in terms of  $\sigma$  and  $\epsilon$ .

7. **Work.** Determine the work done by the specified force over the specified paths where  $e_x$  is the unit vector in the  $x$ -direction and  $e_y$  is the unit vector in the  $y$ -direction. The units of  $F$  are newtons and  $x$  and  $y$  are in meters.

$$\vec{F} = x\hat{e}_x + 3y\hat{e}_y \quad \text{and} \quad W = \int_S \vec{F} \bullet d\vec{s}$$

- (a) Evaluate the work done by the force along Path  $S_1$ ,  $(0, 0)$  to  $(2, 0)$  to  $(2, 1)$ , with all motion along straight lines.  
 (b) Evaluate the work done by the force along Path  $S_2$ , which is one straight line directly from  $(0, 0)$  to  $(2, 1)$ .  
 (c) Evaluate the work along the straight-line Path  $S_3$ :  $(0, 0)$  to  $(2, 0)$  to  $(2, 1)$  to  $(0, 0)$ .
8. **Similitude.** Use dimensional analysis to determine the functional dependence of the variables that describe the following physical systems:
- (a) *Boleadoras.* A mass,  $m$ , at the end of a string of length,  $\ell$ , is swung overhead. Its tangential velocity is  $v$ . Determine the tension in the string. (You may neglect gravity.)  
 (b) *Droplet oscillations.* A liquid drop of radius,  $a$ , and mass density,  $\rho$  [ $\text{kg}/\text{m}^3$ ], may oscillate with its shape being restored to a sphere if the liquid has a surface tension,  $\sigma$  [ $\text{N}/\text{m}$ ]. Determine how the period of oscillation could depend upon these three parameters.  
 (c) *Deep water ocean waves.* Waves on a very deep ocean travel with a speed,  $v$ , that depends upon their wavelength,  $\lambda$ , but not upon their amplitude. How should this speed depend upon the wavelength,  $\lambda$ ; the acceleration due to gravity,  $g$  [ $\text{m}/\text{s}^2$ ]; and the density of water,  $\rho$  [ $\text{kg}/\text{m}^3$ ]?  
 (d) *Shallow-water gravity waves.* If the wavelength of a disturbance on the surface of water is much greater than the depth of the water,  $h_o \ll \lambda$ , the speed of the surface wave depends only upon depth and the acceleration due to gravity. How does the shallow-water gravity wave speed depend upon  $h_o$  and  $g$ ?

- (e) *Capillary waves.* At very short wavelengths,  $\lambda$ , the speed of surface waves on water depends upon wavelength; the fluid mass density,  $\rho$ ; and the surface tension,  $\sigma$  [N/m].
- (f) *Piano string.* How should the frequency of a string depend upon its tension,  $T$  [N]; its length,  $\ell$ ; and its linear mass density,  $\rho_L$  [kg/m]?
9. **Oscillator output impedance.** One way to determine the output impedance of an electronic oscillator or an amplifier is to measure the output voltage as a function of load resistance. The oscillator's internal resistance,  $R_{int}$ , and the load resistance,  $R_{load}$ , form a voltage divider circuit that relates  $V_{out}$  to  $V_{osc}$ , as shown in Fig. 1.20.

$$V_{out} = V_{osc} \left( \frac{R_{load}}{R_{int} + R_{load}} \right) \Rightarrow \frac{1}{V_{out}} = \frac{R_{int}}{V_{osc}} \frac{1}{R_{load}} + \frac{1}{V_{osc}}$$

Table 1.5 provides values of the load resistance,  $R_{load}$ , and the measured output voltage,  $V_{out}$ , corresponding to that load. Linearize the equation, and make a least-squares plot to determine the oscillator's internal resistance,  $R_{int}$ , and the oscillator's internal voltage,  $V_{osc}$ .

**Fig. 1.20** An oscillator which produces a constant output voltage,  $V_{osc}$ , will produce voltage,  $V_{out}$ , across a load resistor,  $R_{load}$ , that depends upon the load resistance and the oscillator's own internal output resistance,  $R_{int}$

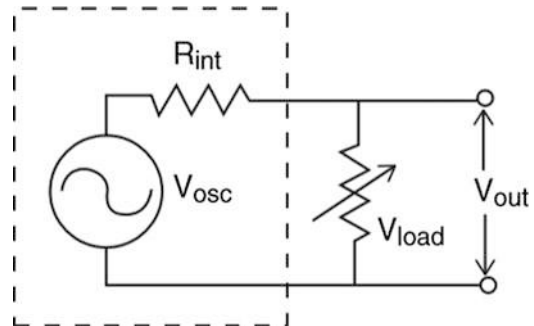
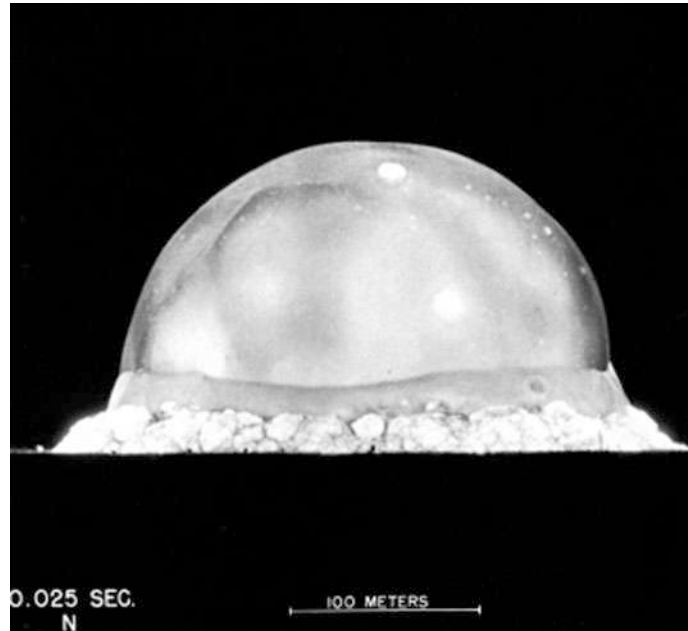


**Table 1.5** Measured values of output voltage,  $V_{out}$ , vs. load resistance,  $R_{load}$

$R_{load}$ [kΩ]	$V_{out}$ [V <sub>ac</sub> ]
∞	1.97650
11.0	1.81276
9.0	1.77892
8.0	1.75779
7.0	1.73038
6.0	1.69524
5.0	1.64860
4.0	1.58302
3.0	1.48438
2.0	1.32063
1.0	0.99272
0.9	0.94760
0.8	0.88300

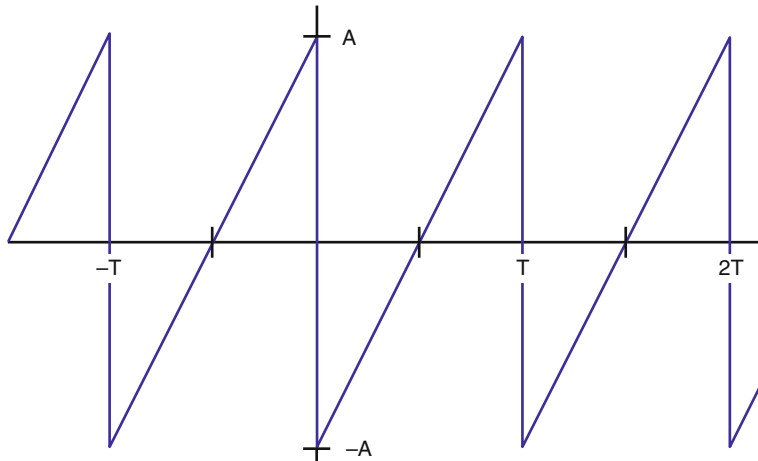
- 10. Pendulum data analysis.** An experiment proceeds as follows: The pendulum is clamped at the 50th mark, approximately 1 m from the attachment point between wire and the pendulous mass. The oscillation period of the pendulum is recorded. The attachment point is raised by  $2.00 \pm 0.01$  cm to the 49th mark (so the wire is shortened by 2.00 cm), and the period of oscillation is measured again. This same procedure is repeated nine more times, producing an 11-element data set containing the approximate wire length,  $\ell_i$ , and oscillation period,  $T_i$ , for  $i = 1, 2, 3, \dots, 11$ .
- Write an algebraic expression for the acceleration due to gravity,  $g$ , in terms of the period,  $T_i$ ; the wire length,  $\ell_i$ ; and an undetermined constant,  $a$ , that accounts for the unknown distance between the last mark on the wire and the center of gravity of the mass.
  - Rearrange the equation you wrote in part (a) so that the data set can be plotted as a straight line and the slope and intercept of the line can be used to determine the local acceleration due to gravity,  $g$ , and the undetermined offset distance,  $a$ . Write expressions for  $g$  and for  $a$  in terms of the slope and the intercept of the straight line.
- 11. Energy released by the first atomic bomb.** The first atomic bomb was detonated in Alamogordo, New Mexico, on 16 July 1945. The explosion was captured in a series of photographs like the one shown in Fig. 1.21. Using these photos, G. I. Taylor [32] was able to use similitude to estimate the energy released by the blast based on the rate at which the fire ball expanded, assuming that the fire ball was hemispherical and that the physical size of the source of the energy was very small.
- Use dimensional analysis to determine the radius of the hemisphere if that radius depends upon time,  $t$ ; the energy released by the explosion,  $E$ ; and the density,  $\rho$ , of the air. You may assume that the proportionality constant is unity.
  - The blast radius (in meters) as a function of time (in milliseconds) is given in Table 1.6. Plot the radius vs. time using log-log axes, and determine the power law of the best-fit to those data. How close was the exponent that relates time to radius to the value predicted in part (a)?
  - Express your result in part (a) in terms of the energy release,  $E$ .
  - Plot  $R^5$  vs.  $t^2$  and set the intercept to zero.

**Fig. 1.21** Photo of the first atomic bomb explosion 25 milliseconds after detonation. The diameter of the blast hemisphere is approximately 260 m



**Table 1.6** Blast radius

Time[ms]	Radius [m]
0.38	25.4
0.52	28.8
0.66	31.9
0.80	34.2
0.94	36.3
1.08	38.9
1.22	41.0
1.36	42.8
1.50	44.4
1.65	46.0
1.79	46.9
1.93	48.7
3.26	59.0
3.53	61.1
3.80	62.9
4.07	64.3
4.34	65.6
4.61	67.3
15.00	106.5
25.00	130.0
34.00	145.0
53.00	175.0
62.00	185.0

**Fig. 1.22** Sawtooth waveform

- (e) Using the slope determined in part (d), estimate the energy released by the explosion assuming the density of air is  $1.2 \text{ kg/m}^3$ . Report your result in joules and in kilotons of TNT. (1 kiloton of TNT =  $4.184 \times 10^9 \text{ J}$ .)

12. **Fourier synthesis of a sawtooth waveform.** The sawtooth waveform occurs when nonlinear effects distort a sinusoidal sound wave into a fully developed shock wave (Fig. 1.22).

One cycle of a sawtooth wave, with period  $T$  and amplitude  $A$ , be expressed algebraically.

$$y(t) = \frac{2At}{T} - A \quad (1.121)$$

Write an expression for the sawtooth as a superposition of Fourier components with frequencies  $f_n = n/T$ , where  $n = 1, 2, 3, \dots$

## References

1. P.M. Morse, K.U. Ingard, *Theoretical Acoustics* (McGraw-Hill, New York, 1968); ISBN 07-043330-5
2. U.S. Department of Labor, Occupational Safety & Health Administration (OSHA), Standard No. 1910.95(b)(2): [https://www.osha.gov/pls/oshaweb/owadisp.show\\_document?p\\_table=standards&p\\_id=9735](https://www.osha.gov/pls/oshaweb/owadisp.show_document?p_table=standards&p_id=9735)
3. U.S. Standard Atmosphere (National Oceanic and Atmospheric Administration, National Aeronautics and Space Administration, and United States Air Force, Washington, DC); NOAA-S/T 76-1562. U.S. Gov't. Printing Office, Stock No. 003-17-00323-0 (1976)
4. R. Courant, *Differential & Integral Calculus*, 2nd edn. (Blackie & Son, Glasgow, 1937), Ch. 2, §3.9
5. J. J. Stoker, *Nonlinear Vibrations in Mechanical and Electrical Systems* (Interscience, New York, 1950); ISBN 978-04-71570-332
6. A. B. Pippard, *The Physics of Vibration* (Cambridge University Press, Cambridge, 1989). See Ch. 9; ISBN 0 521 37200 3
7. L.D. Landau, E.M. Lifshitz, *Theory of Elasticity*, 2nd edn. (Pergamon, Oxford, 1970). See §7; ISBN 0 08 006465 5
8. B. Kinsman, *Wind Waves* (Prentice-Hall, Englewood Cliffs, 1965)
9. I.S. Gradshteyn, I.M. Ryzhik, *Tables of Integrals, Series, and Products*, 4th edn. (Academic, New York, 1980); ISBN 0-12-294760-6
10. M.L. Boas, *Mathematical Methods in the Physical Sciences*, 2nd edn. (Wiley, New York, 1983). See Ch. 7; ISBN 0-471-04409-1
11. D. Wells, Are these the most beautiful? *Math. Intell.* **12**(3), 37–41 (1990)
12. H. Lamb, *Dynamical Theory of Sound*, 2nd edn. (Edward Arnold & Co., London, 1931) or (Dover, 1960), pg. 54
13. E.F. Adiutori, *Fourier. Mech. Eng.* **127**(8), 30–31 (2005)
14. J.W. Strutt (Lord Rayleigh), The principle of similitude. *Nature* **95**, 66–68 (1915)
15. E. Buckingham, On physically similar systems; illustrations of the use of dimensional equations. *Phys. Rev.* **4**(4), 345–376 (1914)
16. J.R. Olson, G.W. Swift, Similitude in thermoacoustics. *J. Acoust. Soc. Am.* **95**(3), 1405–1412 (1994)
17. M. Strasberg, Dimensional analysis of windscreen noise. *J. Acoust. Soc. Am.* **83**(2), 544–548 (1988)
18. N.R. Hosier, P.R. Donovan, “Microphone Windscreen Performance,” National Bureau of Standards Report NBSIR 79-1559 (Jan. 1979)
19. Private communication from Thomas J. Hofler
20. S. Rabinovich, *Measurement Errors: Theory and Practice* (American Institute of Physics, New York, 1995); ISBN 1-56396-323-X
21. H.D. Young, *Statistical Treatment of Experimental Data* (McGraw-Hill, New York, 1962); ISBN 07-072646-9.
22. R.A. Nelson, M.G. Olsson, The pendulum – Rich physics from a simple system. *Am. J. Phys.* **54**(2), 112–121 (1986). A better, though less readily accessible treatment, is that of G. G. Stokes, *Mathematical and Physical Papers* (Macmillan, 1905)
23. F.J. Anscombe, Graphs in statistical analysis. *Am. Stat.* **27**(1), 17–21 (1973)
24. Ernest Rutherford, F.R.S., 1st Baron Rutherford of Nelson (1871–1937)
25. P.R. Bevington, *Data Reduction and Error Analysis for the Physical Sciences* (McGraw-Hill, New York, 1969)
26. R.A. Fisher, F. Yates, *Statistical tables for biological, agricultural and medical research*, 6th edn. (Oliver and Boyd, London, 1963)
27. L.M. Ronse, L.M. Wang, Relationships between unoccupied classroom acoustical conditions and elementary student achievement in eastern Nebraska. *J. Acoust. Soc. Am.* **133**(3), 1480–1495 (2013)
28. J. Higbie, Uncertainty in the linear regression slope. *Am. J. Physiol.* **59**(2), 184–185 (1991)
29. Y. Beers, *Introduction to the Theory of Error*, 2nd edn. (Addison-Wesley, Reading, 1957)

30. J. W. Strutt (Lord Rayleigh), *The Theory of Sound*, vol I, 2nd edn. (Macmillan, London, 1894) reprinted (Dover, 1945)
31. J.E. Lennard-Jones, On the determination of molecular fields. Proc. R. Soc. Lond. A **106**, 463–477 (1924)
32. G.I. Taylor, The formation of a blast wave by a very intense explosion. II. The atomic explosion of 1945. Proc. Roy. Soc. Lond **201**(1065), 175–186 (1950)

**Open Access** This chapter is licensed under the terms of the Creative Commons Attribution 4.0 International License (<http://creativecommons.org/licenses/by/4.0/>), which permits use, sharing, adaptation, distribution and reproduction in any medium or format, as long as you give appropriate credit to the original author(s) and the source, provide a link to the Creative Commons license and indicate if changes were made.

The images or other third party material in this chapter are included in the chapter's Creative Commons license, unless indicated otherwise in a credit line to the material. If material is not included in the chapter's Creative Commons license and your intended use is not permitted by statutory regulation or exceeds the permitted use, you will need to obtain permission directly from the copyright holder.



---

**Part I**

**Vibrations**



# The Simple Harmonic Oscillator

2

## Contents

2.1	<b>The Undamped Harmonic Oscillator</b> .....	60
2.1.1	Initial Conditions and the Phasor Representation .....	61
2.2	<b>The Lumped-Element Approximation</b> .....	63
2.2.1	Series and Parallel Combinations of Several Springs .....	64
2.2.2	A Characteristic Speed .....	65
2.3	<b>Energy</b> .....	66
2.3.1	The Virial Theorem .....	67
2.3.2	Rayleigh's Method .....	68
2.3.3	Gravitational Offset .....	69
2.3.4	Adiabatic Invariance .....	71
2.4	<b>Damping and Free-Decay</b> .....	73
2.4.1	Viscous Damping and Mechanical Resistance .....	73
2.4.2	Free-Decay Frequency and Quality Factor .....	75
2.4.3	Critical Damping .....	76
2.4.4	Thermal Equilibrium and Fluctuations .....	76
2.4.5	Frictional (Coulomb) Damping* .....	82
2.5	<b>Driven Systems</b> .....	83
2.5.1	Force-Driven SHO .....	83
2.5.2	Power Dissipation, the Decibel, and Resonance Bandwidth .....	87
2.5.3	Resonance Tracking and the Phase-Locked Loop* .....	90
2.5.4	Transient Response .....	92
2.5.5	The Electrodynamic Loudspeaker .....	95
2.5.6	Electrodynamic (Moving-Coil) Microphone .....	99
2.5.7	Displacement-Driven SHO and Transmissibility .....	100
2.6	<b>Vibration Sensors</b> .....	102
2.7	<b>Coupled Oscillators</b> .....	105
2.7.1	Two Identical Masses with Three Identical Springs .....	105
2.7.2	Coupled Equations for Identical Masses and Springs .....	106
2.7.3	Normal Modes and Normal Coordinates .....	107

---

2.7.4	Other Initial Conditions .....	108
2.7.5	General Solutions for Two Masses and Three Springs .....	109
2.7.6	Driven Oscillators, Level Repulsion, and Beating .....	110
2.7.7	String of Pearls .....	112
2.8	<b>The Not-So-Simple (?) Harmonic Oscillator</b> .....	115
	<b>References</b> .....	130

This chapter will introduce a system that is fundamental to our understanding of more physical phenomena than any other. Although the “simple” harmonic oscillator seems to be only the combination of the most mundane components, the formalism developed to explain the behavior of a mass, spring, and damper is used to describe systems that range in size from atoms to oceans.

The treatment of the harmonic oscillator in this chapter goes beyond the “traditional” treatments found in the elementary physics textbooks. For example, the introduction of damping will open a two-way street: a damping element (i.e., a mechanical resistance,  $R_m$ ) will dissipate the oscillator’s energy, thus reducing the amplitudes of successive oscillations, but it will also connect the oscillator to the surrounding environment (where the dissipated energy must go to “leave” the system). That surrounding environment will also return energy into the oscillator. The oscillation amplitude does not decay to zero but to a value that represents the oscillator’s thermal equilibrium with its surroundings.

The excitation of such a harmonic oscillator by an externally applied force, displacement, or combination of the two will result in a response that is critically dependent upon the relationship between the frequency of excitation and the natural frequency of the oscillator, which is the oscillation of the undamped free oscillations. We will pay special attention to both the magnitude and phase of the driven response and will introduce the critical concepts of mechanical impedance, resonance, and quality factor.

Finally, the harmonic oscillator model will be extended to coupled oscillators that are represented by combinations of several masses and several springs. As the number of coupled masses and springs increases, several new features of such combinations will preview the behavior of continuous systems (like strings, bars, membranes, and plates). Ultimately, solid matter consists of a nearly infinite number of masses (atoms and molecules) that are coupled together by three times that number of stiffnesses arising from their mutual attraction or repulsion.

---

## 2.1 The Undamped Harmonic Oscillator

We begin this exploration by simply joining one *point mass* (meaning we neglect the spatial distribution of the mass which might require the specification of a moment of inertia),  $m$ , to one end of a spring with stiffness constant,  $K$ , where the concept of a stiffness constant was addressed in Sect. 1.2.1 and the stiffness was related to potential gradients that produced forces or vice versa. The other end of the spring is assumed to be rigidly immobilized (i.e., fixed, as shown in Fig. 1.3). We further restrict the junction of the spring and the mass to move only along a single direction: the  $x$  axis. This system is called a one-dimensional, single degree-of-freedom, undamped simple harmonic oscillator. (Damping will be added in Sect. 2.4.) Why does such a simple combination of two idealized components have such a complicated designation? It is an indication that there will be numerous variations on this theme.

At this stage, we will assume that the spring is massless,  $m_s = 0$ , but we will see soon that a non-zero spring mass can be easily accommodated under some simplifying assumptions. Our analysis of the motion of this simple mass-spring system will begin by combining a *dynamical equation* with an *equation of state*. The dynamical equation is Newton’s Second Law of Motion. It relates the

acceleration of the mass to the net external force acting on the mass. The net force will be that which the spring exerts on the mass, determined by the displacement of the spring,  $x$ , from its equilibrium extension,  $x_o$ , according to Hooke's law in Eq. (1.25). You may be more familiar with thermodynamic equations of state that relate the pressure of a gas to its density or temperature, but Hooke's law is a simple example of an equation of state that relates some deformation of the system (a stimulus) to its response (the net force). The dynamical equation is generic (i.e., system independent), but the equation of state is particular to a specific system, the spring in this case. To simplify subsequent calculations, we will define the origin of our one-dimensional coordinate system to be located at  $x_o = 0$ , the equilibrium length of our spring:

$$F = ma = m \frac{d^2x}{dt^2} = -Kx \quad \text{or} \quad \frac{d^2x}{dt^2} + \frac{K}{m}x = 0 \quad (2.1)$$

There is an assumption that is built into Hooke's law that will be examined in the next section. We are assuming that the restoring force produced at the spring's moveable end depends only on the position of that end. That is true for a static extension or compression (e.g., weighing bananas on a spring scale in a market or the Gerber scale in Fig. 2.2). It might not be exact in a dynamical situation since we have assumed that the entire spring is instantaneously aware of the end's location. For that to be true, information about the end's position would have to propagate along the spring with an infinite speed, as discussed in Sect. 2.2.

Equation (2.1) is a second-order, homogeneous, linear differential equation with constant coefficients, and therefore there are two linearly independent solutions. As discussed in Sect. 1.5, we could solve that equation to provide the entire time history of the mass-spring system's response,  $x(t)$ , using a superposition of sine and cosine functions or complex exponentials, where we have set  $\omega_o^2 = K/m$ .

$$x(t) = A \cos(\omega_o t) + B \sin(\omega_o t) \quad (2.2)$$

This solution is periodic and repeats when  $\omega_o T = 2\pi$  or integer multiples of  $2\pi$ , so the *frequency* of oscillation,  $f_o = (1/T) = \omega_o/2\pi$ , is the reciprocal of the *period*,  $T$ .

$$\omega_o = 2\pi f_o = \frac{2\pi}{T} = \sqrt{\frac{K}{m}} \quad (2.3)$$

We call  $\omega_o$  the *angular frequency* or the *radian frequency*. The radian frequency simplifies calculations by eliminating the need to explicitly include factors of  $2\pi$ . It is important to remember that instrumentation and most software typically report frequencies in cycles per second [Hz], not radians per second.

### 2.1.1 Initial Conditions and the Phasor Representation

It is worthwhile to re-emphasize the fact that the “natural frequency” of oscillation,  $\omega_o$ , for this simple linear system (see Sect. 1.3) is amplitude independent. As shown in Sect. 1.7.1, simple dimensional arguments require that the frequency be proportional to  $\sqrt{K/m}$ . The general solution for the motion of our simple undamped mass-spring oscillator in Eq. (2.2) contains two amplitude-dependent constants:  $A$  and  $B$ . These constants are determined by the conditions that initiate the system's motion at the instant that defines  $t = 0$ . We will first consider two ways that could set the system into motion: an initial displacement,  $x_1$ , or an initial impulse that propels the mass with an initial velocity,  $v_1 \equiv (dx/dt)_o$ , where the subscript on the derivative indicates that it is to be evaluated at  $t = 0$ .

If we hold the mass at position  $x_1$  and then release it at  $t = 0$ , the sine term vanishes, and the cosine term in Eq. (2.2) will equal one, so  $A = x_1$ . The instantaneous velocity of the mass is determined by differentiating Eq. (2.2):

$$v(t) = \dot{x}(t) = \frac{dx(t)}{dt} = -\omega_o A \sin(\omega_o t) + \omega_o B \cos(\omega_o t) \quad (2.4)$$

At  $t = 0$ , the sine term again vanishes and  $v(0) = \omega_o B$ . Since the mass is at rest at  $t = 0$ ,  $v(0) = 0$ , so  $B = 0$ . For this initial displacement, the subsequent motion of the mass is given by  $x(t) = x_1 \cos(\omega_o t)$ . Initially, the mass moves closer to its equilibrium position; one-quarter period later, it passes through its equilibrium position,  $x_o = 0$ , reaching its maximum negative position,  $-x_1$ , a time,  $T/2$ , after starting, and returns to its initial position,  $x_1$ , at  $t = T$ . In principle, this motion repeats forever with period,  $T$ .

If instead the mass is initially at rest at  $x(0) = 0$  and the motion is initiated by impulsively striking the mass to impart an initial velocity  $v(0) = v_1$ , then Eq. (2.4) sets  $B = v_1/\omega_o$ , while Eq. (2.2) sets  $A = 0$ . The subsequent motion is given by  $x(t) = (v_1/\omega_o) \sin(\omega_o t)$ ; we have given the mass an initial velocity in the  $+x$  direction, and it moves off in that direction until reversing its direction one-quarter cycle later, after coming to rest for an instant at  $x_1 = |v_1/\omega_o|$ .

Of course, those two exemplary initial conditions are not the only possibilities. In fact, we could impose both of the previous initial conditions simultaneously by displacing the mass by a distance,  $x_1$ , and then striking it at  $t = 0$  to produce a velocity  $v_1$ . The procedure to determine the amplitudes,  $A$  and  $B$ , is the same and produces the same results.

$$x(t) = x_1 \cos(\omega_o t) + \frac{v_1}{\omega_o} \sin(\omega_o t) \quad (2.5)$$

For an initial displacement in the  $+x$  direction, combined with an initial velocity in the same direction, the amplitude of the oscillation will be larger than if either condition was imposed individually, as was done previously. A geometrical interpretation will be useful.

In Fig. 2.1, we imagine the position of the mass being represented by the projection on the  $x$  axis of a vector that rotates counterclockwise at an angular velocity,  $\omega_o$ . The superposition of the two initial conditions produces a vector of length  $|\vec{x}| = \sqrt{x_1^2 + (v_1/\omega_o)^2}$ . At  $t = 0$ , the vector makes an angle  $\phi = -\tan^{-1}[(v_1/\omega_o)/x_1]$ , which is below the  $x$  axis in the fourth quadrant. As time increases, the vector rotates, and its projection along the  $x$  axis increases until  $t = \phi/\omega_o$  when the displacement reaches its maximum positive value.

Another way of expressing the solution provided in Eqs. (2.2) and (2.5) is to express  $x(t)$  in terms of a single amplitude  $C = \sqrt{x_1^2 + (v_1/\omega_o)^2}$  and the same phase angle,  $\phi$ , as diagrammed in Fig. 2.1.

$$x(t) = C \cos(\omega_o t + \phi) \quad (2.6)$$

The value of  $\phi$  allows a mixture of the appropriate proportion of the sine and cosine terms in Eq. (2.2) to meet the specific initial conditions. It also is ideally suited to the expression of  $x(t)$  as the real part of a complex exponential.

$$x(t) = \Re e[\hat{\mathbf{C}} e^{j\omega_o t}] = \Re e[|\hat{\mathbf{C}}| e^{j\phi} e^{j\omega_o t}] = \Re e[|\hat{\mathbf{C}}| e^{j(\omega_o t + \phi)}] \quad (2.7)$$

Now  $\hat{\mathbf{C}}$  is treated as a complex number (phasor) with magnitude  $|\hat{\mathbf{C}}|$  and phase  $\phi$ . Taking the real part of Eq. (2.7) regenerates Eq. (2.6) and allows the use of the complex exponential to simplify the calculation of integrals and derivatives as shown in Eq. (1.47).

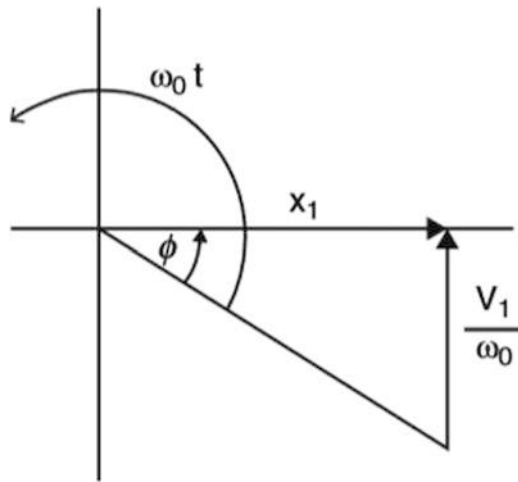


**Fig. 2.1** Geometrical representation for the combination of an initial displacement,  $x_1$ , and initial velocity,  $v_1$ , for a single degree-of-freedom, undamped, simple harmonic oscillator. The vector of length  $|\vec{x}| = \sqrt{x_1^2 + (v_1/\omega_0)^2}$  starts at an angle  $\phi = -\tan^{-1}[(v_1/\omega_0)/x_1]$  and rotates in the counterclockwise direction at angular velocity,  $\omega_0$ . The projection of that vector on the horizontal axis represents the position of the mass as a function of time

For example, we can produce the velocity in complex notation, as we did for the trigonometric expression of Eq. (2.4), by simple multiplication of Eq. (2.7) by  $j\omega_0$ . Similarly, double differentiation of Eq. (2.7) produces the acceleration  $a(t)$  by multiplication of Eq. (2.7) by  $(j\omega_0)(j\omega_0) = -\omega_0^2$ .

$$\begin{aligned} v(t) &= j\omega_0 x(t) = \Re e[j\omega_0 \hat{\mathbf{C}} e^{j\omega_0 t}] \\ a(t) &= -\omega_0^2 x(t) = \Re e[-\omega_0^2 \hat{\mathbf{C}} e^{j\omega_0 t}] \end{aligned} \quad (2.8)$$

These expressions indicate that there is a  $+90^\circ$  phase shift (in the counterclockwise sense) between displacement and velocity and  $180^\circ$  phase shift between displacement and acceleration.

The use of complex exponentials is so convenient and ubiquitous in the treatment of problems involving acoustics and vibration that it is customary to simply drop the explicit reference to “taking the real part of the complex expression” and treat the complex expressions as the “result” with the tacit understanding that the behavior of the physical system corresponds to only the projection of the complex vectors onto the real axis.

## 2.2 The Lumped-Element Approximation

The previous analysis of the undamped simple harmonic oscillator used a spring constant,  $K$ , to relate the motion of the end of the spring to the force it imposed on the attached mass. The fact that the force depended only upon the position of the end of the spring implied a *quasi-static approximation* that is equivalent to saying that each location along the spring’s entire length had instantaneous “knowledge” of the current location of the end of the spring. Said another way, information about the end position was instantaneously accessible at every location along the entire length of the spring, or the speed at which such information could propagate is infinite. In the quasi-static approximation, the displacement of each “coil” of the spring is linearly proportional to its distance from the fixed end. Figure 2.2 shows an adjustable scale (i.e., ruler) which exploits that proportionality.

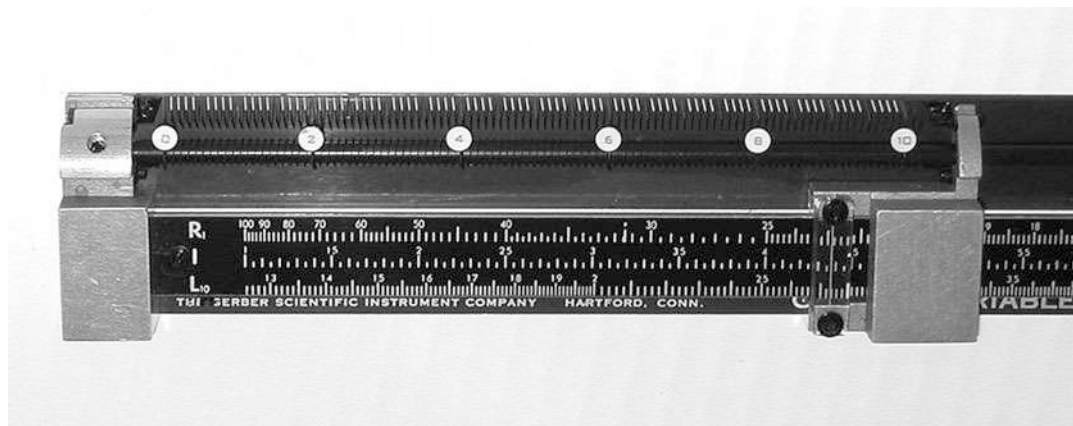


**Fig. 2.2** The Gerber scale (H. Joseph Gerber (1924–1996) was a prolific inventor and able businessman who had been granted more than 650 patents over his lifetime) makes use of the quasi-static approximation to produce a ruler with equally spaced markings but adjustable overall length. At the top of the photograph is a triangular spring that has every tenth coil painted red, every fifth coil blue, and the other coils white. Even-numbered labels are mounted on a second spring to keep track of the red marks. Since these are linear springs, which obey Hooke's law, the coils will be equally spaced with respect to any stop position of the slider. Consequently, in the days before computerized plotting and data analysis, this scale could be used for linear interpolation or extrapolation of plotted data points without any computation. The logarithmic scale on the base plate allows it to be used on graphs with logarithmic coordinates

In reality, as the end of the spring is moved, there will be a wave launched from the moving end. Since we will not be addressing wave motion until the next chapter, we can make an estimate of the limitations of the quasi-static assumption using dimensional arguments (i.e., using similitude as discussed in Sect. 1.7). Before doing so, we need to consider the net stiffness of combinations of two or more springs.

### 2.2.1 Series and Parallel Combinations of Several Springs

If two springs are connected from a fixed mounting to the same load, as illustrated schematically on the left in Fig. 2.3, their individual stiffnesses will add. Springs combined in such an arrangement are said to be “springs in parallel.” Since the ends of both springs will be displaced by the same amount,  $x$ , the magnitude of the net force,  $F_{\text{parallel}}$ , will be the sum of their forces.

$$-F_{\text{parallel}} = -(F_1 + F_2) = K_1x + K_2x = (K_1 + K_2)x = K_{\text{parallel}}x \quad (2.9)$$

The parallel combination of the two springs of stiffness  $K_1$  and  $K_2$  will have an effective spring constant of  $K_{\text{parallel}} = K_1 + K_2$ . The extension to the parallel combination of several springs will result in an effective parallel spring constant that is just the sum of their individual stiffnesses.

If the same two springs are joined end to end, then we say the springs are combined “in series.” Their effective series spring constant will be less than that of either spring acting alone. If the position of the free end of the combination is at  $x$  and the junction is at  $x_a$ , then the forces at  $x_a$  produced by either spring must be equal, since that intermediate position is neither accelerating nor decelerating.

$$-F_a = K_1x_a = K_2(x - x_a) \Rightarrow x_a = \frac{K_2}{K_1 + K_2}x \quad (2.10)$$

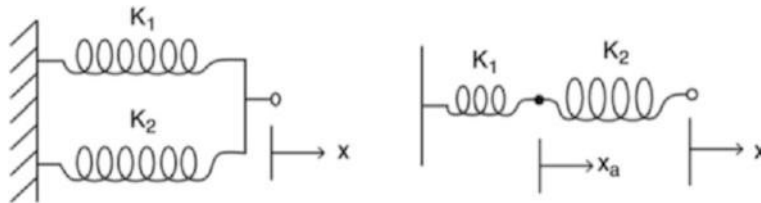


**Fig. 2.3** (Left) Two springs combined in parallel will exhibit a net effective spring constant that is the sum of the individual spring constants. (Right) For the series combination, the forces at the junction between the two springs must be equal and opposite, as dictated by Newton's Third Law of Motion, and the net stiffness will be smaller than the stiffness of either spring

This result makes sense in the limit that  $K_2 \gg K_1$ , making  $K_2$  effectively rigid, since only  $K_1$  would be extended if  $x$  was increased so  $x_a \cong x$ . Similarly, in the opposite limit, if  $K_1 \gg K_2$ , then only  $K_2$  would be extended, so  $x_a \cong 0$ . The other obvious check would be to let  $K_1 = K_2$ . In that case, we expect each spring to provide half the displacement, i.e.,  $x_a = x/2$ , and the force would be half that of a single spring displaced from its equilibrium position by the same amount.

The force of the series combination can be obtained by substitution of  $x_a$  back into the expression for the force.

$$\begin{aligned} -F_a = -F_{\text{series}} &= K_1 x_a = \frac{K_1 K_2}{K_1 + K_2} x = \left( \frac{1}{K_1} + \frac{1}{K_2} \right)^{-1} x = K_{\text{series}} x \\ \frac{1}{K_{\text{series}}} &= \frac{1}{K_1} + \frac{1}{K_2} \end{aligned} \quad (2.11)$$

Again, the extension to a series concatenation of several springs is also simple. Readers with exposure to the basics of electrical circuit theory will recognize that these expressions for the stiffnesses of series and parallel combinations of springs are the exact reverse of those for the series and parallel combinations of electrical resistors or inductors, although the same as for series and parallel combinations of capacitors. This is because for electrical resistors in series, the flow (i.e., electrical current) is continuous and the potentials (i.e., voltages) are additive. For springs in series, the potential (i.e., force) is continuous, and the flow (i.e., displacement) is additive.

## 2.2.2 A Characteristic Speed

To determine an estimate for the limits of validity of the assumption that we can use the static stiffness of a spring for calculation of the dynamical behavior of a mass-spring oscillator, we can use a dimensional argument to calculate a characteristic speed for a spring of stiffness,  $K$ , and length,  $L$ . Since such a characteristic speed should be a property of the spring and not any particular application, we need to identify spring properties that are not a function of the spring's length.

The spring's mass,  $m_s$ , can be divided by the spring's length,  $L$ , to produce a linear mass density,  $\rho_L$ , which is a characteristic of the spring and independent of length:  $\rho_L = m_s/L$ . For a uniform spring,  $\rho_L$  will be a constant. Based on our calculation of the overall stiffness of a series combination of springs, the product of the stiffness,  $K$ , of a spring with its length,  $L$ , is independent of the spring's length and only a property of the spring's construction (i.e., shape and materials). If two identical springs are attached in series, the overall stiffness of the combination is half that of either spring individually, and the overall length is doubled. For a uniform spring material, the product, ( $LK$ ), is a constant.

We can now use similitude (see Sect. 1.7) to combine  $\rho_L$  [kg/m] and  $(LK)$  [(N/m)m = N = kg·m/s<sup>2</sup>] to produce a speed,  $c$  [m/s], based on the units required to specify those two parameters that are characteristics of the spring and independent of its length.

$$\rho_L^a (LK)^b = \frac{M^a}{L^a} \frac{M^b L^b}{T^{2b}} = \frac{L}{T} = c \quad (2.12)$$

Since  $c$  does not require any mass units,  $a + b = 0$ . Since only  $(KL)$  involves  $T$ ,  $2b = 1$ , so  $b = \frac{1}{2}$ , and therefore  $a = -\frac{1}{2}$ . Equating the terms involving  $L$  requires  $-a + b = 1$ , which is also satisfied.

$$c \propto \sqrt{\frac{LK}{\rho_L}} = L \sqrt{\frac{K}{m_s}} \quad (2.13)$$

To determine whether it was appropriate to use a static spring stiffness to solve a dynamical problem, we can now simply compare the period,  $T$ , of our simple harmonic oscillator given by Eq. (2.3) to the time,  $t_s$ , it takes for information to propagate back and forth along a spring of length,  $L$ , at speed  $c$ :  $t_s = 2L/c$ . If  $T \gg t_s$ , then there is plenty of time for the entire spring to be influenced by the changing position of its point of attachment to the mass [1].

The dimensional argument that produced Eq. (2.13) cannot provide any multiplicative numerical constant. For now, we will simply express the criterion,  $T \gg t_s$ , as  $m \gg m_s$ . Once we are able to calculate the speed of compressional wave propagation along the spring, we will see that our “lumped-element” approximation, used to derive Eq. (2.3), is equivalent to saying that the spring length,  $L$ , is much less than the wavelength,  $\lambda$ , of a compressional wave of frequency,  $f_o$ . That criterion also leads to the requirement that  $m \gg m_s$  to justify neglecting dynamical effects that would alter the effective stiffness of the spring from its static value.

To reiterate, under certain circumstances (usually at lower frequencies), it is possible to treat our mass as having no stiffness and our stiffness as having no mass, allowing us to neglect wavelike behavior associated with the spring’s length. Under those assumptions, these components are specified at a point and are called “lumped elements” in the same way that inductors, capacitors, and resistors are considered lumped elements in electrical circuit theory.

## 2.3 Energy

Just as the definition of work was used to establish the relationship between a restoring force and its associated potential energy, Eq. (1.22) can be used to calculate the work done against the inertia of a particle with mass,  $m$ , based on Newton’s Second Law of Motion:  $\vec{F} = m(\vec{d}\vec{v}/dt)$ .

$$W = - \int \vec{F} \cdot d\vec{x} = -m \int \frac{dv}{dt} dx = -m \int v dv = -\frac{1}{2}mv^2 + \text{constant} \quad (2.14)$$

A particle of mass,  $m$ , has an energy associated with its velocity,  $v$ , which is called its kinetic energy.

$$KE = \frac{1}{2}mv^2 \quad (2.15)$$

The relationship between the work done by a conservative force and the change in potential energy created by such a vector force,  $\vec{F}$ , operating over a vector displacement,  $\vec{x}$ , was described in Sect. 1.2.1. If the force is produced by a linear spring that obeys Hooke’s law, and the force and the displacement are co-linear, then the potential energy takes a particularly simple form.

$$PE = \frac{1}{2}Kx^2 \quad (2.16)$$

In that expression, the displacement,  $x$ , is assumed to be the deviation from the spring's equilibrium position,  $x_o$ , so Eq. (2.16) also assumes a coordinate system with its origin making  $x_o = 0$ .

If the origin of our time coordinate is defined so that we can eliminate the cosine term from the position of the mass,  $x(t)$ , expressed in Eq. (2.2), then we can write  $x(t) = B \sin(\omega_o t)$  and  $v(t) = \omega_o B \cos(\omega_o t)$ . Substitution of these into the expressions for the potential and kinetic energy of a mass-spring system will provide an expression for the total instantaneous energy,  $E_{Tot}(t)$ .

$$E_{Tot}(t) = KE(t) + PE(t) = \frac{m\omega_o^2 B^2}{2} \cos^2(\omega_o t) + \frac{KB^2}{2} \sin^2(\omega_o t) \quad (2.17)$$

Since  $\omega_o^2 = K/m$ , and  $\cos^2 x + \sin^2 x = 1$ , the total energy is time-independent. The energy oscillates between being entirely kinetic, as the mass moves through  $x(t) = 0$ , to entirely potential when  $x(t) = \pm B$ .

$$E_{Tot} = \frac{KB^2}{2} = \frac{m\omega_o^2 B^2}{2} = (PE)_{\max} = (KE)_{\max} \quad (2.18)$$

Furthermore, the time-averaged values of both the kinetic and potential energies are equal.

$$\begin{aligned} \langle KE \rangle_t &= \frac{m\omega_o^2}{2T} \int_0^T B^2 \cos^2(\omega_o t) dt = \frac{m\omega_o^2 B^2}{4} \\ \langle PE \rangle_t &= \frac{K}{2T} \int_0^T B^2 \sin^2(\omega_o t) dt = \frac{KB^2}{4} \end{aligned} \quad (2.19)$$

Conservation of energy can be used to demonstrate the equivalence to the Newtonian formulation of Eq. (2.1).

$$\frac{1}{2}m\left(\frac{dx}{dt}\right)^2 + \frac{1}{2}Kx^2 = \text{constant} \quad (2.20)$$

Differentiation of this expression with respect to time regenerates Eq. (2.1).

$$\left[ m \frac{d^2x}{dt^2} + Kx \right] \frac{dx}{dt} = 0 \quad \Rightarrow \quad m \frac{d^2x}{dt^2} + Kx = 0 \quad (2.21)$$

### 2.3.1 The Virial Theorem

The fact that the sum of the kinetic and potential energies is time-independent is a consequence of energy conservation, since no components have been introduced (yet!) in the system that can dissipate energy. The fact that the maximum and the time-averaged kinetic and potential energies are equal also seems plausible, but it is not universal. This equality is a consequence of the assumed Hooke's law behavior where the power law exponent,  $b = 1$ :  $F \propto x^b$ .

For "central forces" (i.e., those forces that act along a line connecting the force with the object acted upon by that force) that obey a power law, the *virial theorem* guarantees that the time-averaged kinetic and potential energies are dependent upon that exponent [2].

$$\langle KE \rangle_t = \frac{b+1}{2} \langle PE \rangle_t \quad (2.22)$$

The equality of the time-averaged potential and kinetic energies is a consequence of our assumption of the linear behavior of our spring. It is useful to remember that this equality does not hold for a nonlinear spring.

A simple counterexample is planetary motion under the influence of gravity. In the simplest case of circular orbits, the centripetal force,  $F_{cent}$ , on a planet of mass,  $m$ , is provided by Newton's universal law of gravitation<sup>1</sup> due to a larger central body of mass  $M \gg m$ . Their centers of mass are separated by a distance,  $R$ .

$$F_{cent} = mv^2/R = GMm/R^2 \Rightarrow \omega^2 = GM/R^3 \quad (2.23)$$

This is a result known as Kepler's third law of planetary motion: the square of the orbital period is proportional to the cube of the radius of the orbit.<sup>2</sup> The planet's kinetic energy is determined by its tangential velocity,  $v_t = \omega R$ .

$$KE = \frac{1}{2}mv_t^2 = \frac{m}{2}(\omega R)^2 = \frac{1}{2}\frac{GMm}{R} \quad (2.24)$$

The gravitational force,  $F_{grav} = GMm/R^2$ , is the negative gradient of the gravitational potential energy.

$$PE = -\frac{GMm}{R} \quad (2.25)$$

For this simple example, both the  $KE$  and  $PE$  are time-independent, so the average  $PE$  is twice the average  $KE$  in accordance with Eq. (2.22) for  $b = -2$ .

### 2.3.2 Rayleigh's Method

*"The object being to approach the truth as nearly as can be done without too great a sacrifice of simplicity."*  
(J. W. Strutt (Lord Rayleigh) [3])

We can take advantage of the equality of the time-averaged values of the kinetic and potential energy that is unique to the vibration of a system whose restoring force is linear in the displacement from equilibrium. The magnitude of the oscillatory velocity,  $|v|$ , for a simple harmonic oscillator is equal to the product of the magnitude of the displacement times the oscillatory frequency:  $|v| = \omega_o |x|$ . Setting  $KE$  in Eq. (2.15) equal to  $PE$  in Eq. (2.16) leads to the same expression for  $\omega_o$  that was derived in Eq. (2.3).

This equality facilitates calculation of the correction to the natural frequency of the mass-spring oscillator when  $m_s \neq 0$ . The displacement of each coil of a spring that is extended from its equilibrium position,  $x_o$ , by an amount  $x_1$  is proportional to its distance,  $x$ , from the fixed end at  $x = 0$ , in the quasi-static approximation (as it was for the Gerber scale in Fig. 2.2). The magnitude of the displacement of

<sup>1</sup> The value of  $G = 6.6738 \times 10^{-11} \text{ N}/(\text{m/kg})^2$  is the most poorly known physical constant, having a relative uncertainty of  $8G/G = \pm 1.4 \times 10^{-4}$ ; P. J. Mohr, B. N. Taylor, and D. B. Newell, "The 2010 CODATA Recommended Values of the Fundamental Physical Constants," <http://physics.nist.gov/constants>

<sup>2</sup> Kepler's third law applies to elliptical orbits. The assumed circular orbit is just a special case for an ellipse without eccentricity. For an elliptical orbit, the square of the period is proportional to the cube of the semi-major axis.

any point on the spring can be expressed as  $\xi(x) = x_1(x/L)$ . The magnitude of the velocity of the spring at that location is  $v(x) = \omega_o \xi(x)$ .

Again, defining the linear mass density,  $\rho_L = m_s/L$ , of the spring in terms of the spring's mass,  $m_s$ , and its length,  $L$ , as in Eq. (2.13), the kinetic energy of the spring  $KE_s$  can be calculated by the mass density of the spring times the square of its maximum local velocity,  $v^2(x)$ , integrated over the entire length of the spring.

$$(KE_s)_{\max} = \frac{1}{2} \int_0^L \rho_L v_1^2 \left(\frac{x}{L}\right)^2 dx = \frac{\omega_o^2 x_1^2}{6} (L\rho_L) = \frac{1}{3} \left(\frac{1}{2} m_s \omega_o^2 x_1^2\right) \quad (2.26)$$

That result for the maximum kinetic energy of the spring can be added to the maximum kinetic energy of the mass attached to the mobile end of the spring. By Eq. (2.18), the total kinetic energy can be equated to the maximum potential energy of the spring.

$$\begin{aligned} (PE)_{\max} &= \frac{1}{2} K x_1^2 = (KE)_{\max} = (KE_{\text{mass}})_{\max} + (KE_s)_{\max} \\ \frac{1}{2} K x_1^2 &= \frac{1}{2} \omega_o^2 x_1^2 \left(m + \frac{m_s}{3}\right) \Rightarrow \omega_o = \sqrt{\frac{K}{m + \frac{m_s}{3}}} \end{aligned} \quad (2.27)$$

In the quasi-static approximation, which we have shown in Sect. 2.2.2 requires that  $m \gg m_s$ , the effect of the spring's mass on the frequency of oscillation is to add one-third of the spring's mass to the moving mass,  $m$ , that is attached to the moving end of the spring and then calculate the resonance frequency using Eq. (2.3). This technique of using the calculation of the kinetic energy of a distribution of masses to determine the natural frequency of a linear vibratory system is known as *Rayleigh's method* [4]. In Sect. 3.4.3 we will use Rayleigh's method to approximate the natural frequency by integrating both the potential and the kinetic energies and then taking the square-root of their ratio. Rayleigh's method is used throughout this textbook because it can "improve computational ease dramatically while only slightly reducing accuracy" [5].

### 2.3.3 Gravitational Offset

To this point, the effects of gravity on our mass-spring system have been neglected. There has been a tacit assumption that our mass has been constrained to move in only a single direction by some frictionless guide. Mass-spring systems are used as scales for weighing, whether it is a traditional grocer's spring scale, a sport fishing spring scale, or a digital scale which incorporates an elastic load cell and some electronic system for measuring and displaying the deflection caused by the weight of a load.

If our  $z$  axis is defined as increasing in the upward direction, then Hooke's law provides the static downward deflection,  $\Delta$ , from the spring's unloaded equilibrium position,  $z_o$ , as shown at the left in Fig. 2.4:  $\Delta = -(mg)/K$ .

The right side of Fig. 2.4 is a plot of the gravitational potential energy,  $(PE)_{\text{grav}} = mg(z - z_o)$ , represented as the dotted line, and the elastic potential energy,  $PE = (\frac{1}{2})K(z - z_o)^2$ , represented as the dashed parabola; and their sum is shown as the solid line. The origin of the  $z$  axis in that figure has been translated to place the equilibrium position of the unloaded spring at  $z_o = 0$ .

The minimum of the sum of those two potential energies is shifted to a negative  $z$  value, indicating that the addition of the mass has produced  $\Delta < 0$ . Using the formalism developed in Sect. 1.2, the net

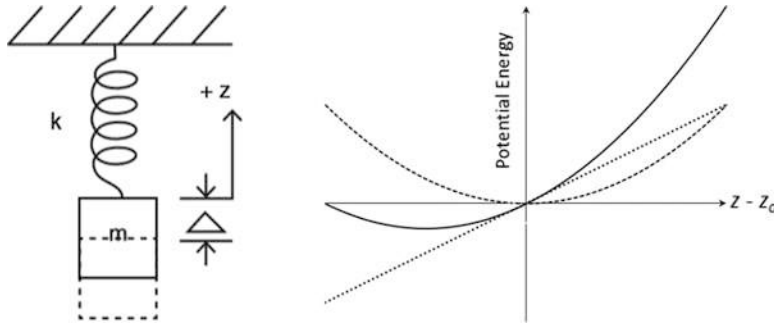


**Fig. 2.4** (Left) A spring of equilibrium length,  $L$ , is suspended from a rigid support, and a mass,  $m$ , is hung from the spring causing a static deflection,  $\Delta$ , from its unloaded equilibrium position,  $z_0$ . (Right) The solid line represents the total potential energy on the vertical axis as a function of position,  $(z - z_0)$ , plotted on the horizontal axis. The dotted line represents the gravitational potential energy,  $(PE)_{grav} = mg(z - z_0)$ . The dashed parabola represents the elastic potential energy,  $PE = (\frac{1}{2}) K(z - z_0)^2$

force at the new position of equilibrium will be given by the first derivative of the potential energy. When the net force is zero, the mass will be at its equilibrium position,  $-\Delta$ .

$$\frac{d(PE)}{dz} = -Kz - mg = 0 \quad \Rightarrow \quad \Delta = -mg/K \quad (2.28)$$

As shown in Eq. (1.25), the second derivative of the potential energy provides the stiffness, which is unaltered by the displacement produced by the attachment of the weight,  $mg$ .

$$\left( \frac{d^2(PE)}{dz^2} \right)_{z=\Delta} = -K \quad (2.29)$$

The fact that the spring stiffness is unaltered by the displacement produced by the attachment of the weight is a consequence of the linearity of Hooke's law. As long as the weight does not take the spring beyond its linear regime (see Fig. 1.4), the oscillation frequency,  $\omega_o = (K/m)^{1/2}$ , will be the same as in the previous case where we neglected gravity and assumed that the one-dimensional displacements were maintained by some frictionless constraint.

It can be useful to recognize that the natural frequency of the mass-spring system subject to the force of gravity can be expressed in terms of the magnitude of the static displacement,  $|\Delta|$ , produced when a mass,  $m$ , is added to the spring of stiffness,  $K$ . From Eq. (2.28), we see that  $K = |mg/\Delta|$ . Substitution of that result into Eq. (2.3) allows the natural frequency,  $\omega_o$ , to be specified in terms of the gravitational acceleration,  $g$ , and the magnitude of the static displacement,  $\Delta$ .

$$\omega_o = \sqrt{\frac{g}{\Delta}} \quad (2.30)$$

This form of the result can be convenient for the design and analysis of vibration isolation systems discussed in Sect. 2.5.7.

The pendulum is a simple harmonic oscillator with a natural frequency that is explicitly dependent upon gravity. In this case, there is no “spring” and gravity provides the restoring force. Using the coordinate system of Fig. 1.5, the angular equivalent of Eq. (2.1) is obtained by equating the moment of inertia of the suspended mass,  $I = mL^2$ , times its angular acceleration,  $\ddot{\theta} = d^2\theta/dt^2$ , to the angle-dependent torque,  $N(\theta)$ , derived in Eq. (1.27).

$$(mL^2) \frac{d^2\theta}{dt^2} + mgL \left[ \theta - \frac{\theta^3}{6} + \dots \right] = 0 \quad (2.31)$$

Restricting the angular displacements to small values,  $\theta \ll 1$ , the nonlinear term in the restoring force can be neglected. If we restrict the maximum deflection to  $\theta_1 \leq 0.10 \text{ rad} = 5.7^\circ$ , the ratio of the nonlinear contribution to the linear contribution will be less than  $\theta_1^2/6 = 0.17\%$ .

After cancellation of common terms, the expression can be cast into the same form as Eq. (2.1) with  $\theta$  as the independent variable and  $\omega_o^2 = g/L$ .

$$\ddot{\theta} + \frac{g}{L}\theta = \ddot{\theta} + \omega_o^2\theta = 0 \quad \Rightarrow \quad \omega_o = \sqrt{\frac{g}{L}} \quad (2.32)$$

Unlike the natural frequency,  $f_o$ , of the mass-spring system, the natural frequency of the pendulum is independent of the mass at the end of the string but is explicitly dependent upon the acceleration due to gravity,  $g$ .

This is not because the mass is not important to the motion of the pendulum. The disappearance of mass from Eq. (2.32) is a consequence of the fact that the inertia and the restoring force are both directly proportional to the mass,  $m$ . Since the natural frequency depends upon the ratio of the restoring force (or restoring torque, in this case) to the inertia, the mass cancels out of the expression that provides the natural frequency. It is worthwhile to compare Eq. (2.32) for the frequency of the pendulum to Eq. (2.30) for the frequency of a mass-spring system in a gravitational field. In Eq. (2.30), the explicit dependence on the mass has also disappeared, again due to the fact that the stiffness is being expressed in terms of the static displacement,  $\Delta$ , caused by the gravitational force on the mass.

### 2.3.4 Adiabatic Invariance

The pendulum provides a simple system that will allow us to demonstrate an additional useful relationship between the energy of a simple harmonic oscillator and its frequency. If we change a constraint on our oscillator, and if we make that change gradually on the time scale set by the period of oscillation,  $T$ , then the relative change in the energy is equal to the relative change in the natural frequency.

$$\delta\left(\frac{E}{\omega}\right) = 0 \quad \text{or} \quad \frac{\delta E}{E} = \frac{\delta\omega}{\omega} \quad (2.33)$$

For slow transitions,<sup>3</sup> the ratio of the energy to the frequency is a constant. Although this general relationship can be derived from a Lagrangian mechanical perspective [6], it is much better known by its quantum mechanical manifestation as Planck's law for the emission of electromagnetic radiation,  $E = \hbar\omega$ , where  $\hbar \equiv 1.05457182 \times 10^{-34} \text{ J} \cdot \text{s}$  is Planck's constant,  $h$ , divided by  $2\pi$ . In that application, the ratio of energy to frequency is determined by Planck's constant.

---

<sup>3</sup>It is the “slowness” of the transition that gives rise to the “adiabatic” designation. If a transition is abrupt, that is, taking place during much less than one period of oscillation, then energy is deposited in a variety of modes other than the original single mode of oscillation. In our pendulum example, a rapid change in the length of the string attached to the pendulum's mass will launch transverse waves of wavelength,  $\lambda < L$ , along the string, putting the energy into modes of vibration other than the pendulum mode, as illustrated in Fig. 3.8. (If the length is changed at twice the natural frequency, then it is possible to excite a parametric resonance.) If the change is slow compared to  $T$ , then the pendulum will continue to swing in the same way but at a frequency that is altered by the slow change in length,  $\delta L$ .

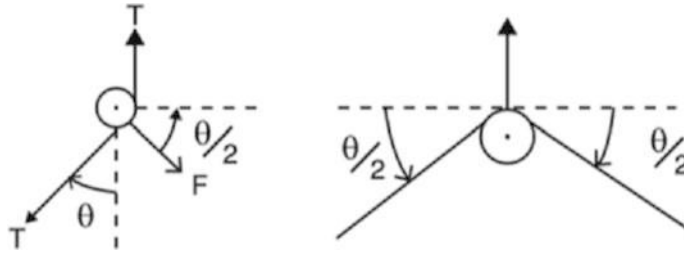


**Fig. 2.5** (Left) The support point for the pendulum of Fig. 1.5 is replaced by a pair of frictionless pinch-rollers. Only one roller is shown. The string that supports the pendulum's mass has a tension,  $T$ . The left pinch-roller must exert a force  $F = 2T \sin(\theta/2)$  on the string to keep it from moving the attachment point. The vertical component of that force is  $F_z = F \sin(\theta/2) = 2T \sin^2(\theta/2) \cong T\theta^2/2$ . (Right) This rotated view of the figure on the left simplifies the identification of the angle,  $\theta/2$ , used in the diagram of the movable pendulum support. The pinch-rollers must do work against this vertical force to move the attachment point lower and shorten the string

The classical relationship can be applied to the simple pendulum. Logarithmic differentiation of Eq. (2.32) relates the relative change in the pendulum's frequency to the relative change in length by assuming that  $g$  is constant.

$$\frac{\delta\omega_o}{\omega_o} = -\frac{1}{2} \frac{\delta L}{L} \quad (2.34)$$

To demonstrate that this result is consistent with *adiabatic invariance*, we can imagine that the suspension point for the string that supports the pendulum's mass is squeezed between a pair of frictionless pinch-rollers, as shown in Fig. 2.5. Those rollers can be moved downward to reduce the length of the pendulum by an amount  $\delta L$ . We will calculate the work required to move the pinch-roller along the string. That should be equal to the amount of energy added to the system by the slow variation of this constraint.

Before calculating that force, it is important to recognize that whether the pendulum moves to the right or to the left, the force on the pinch-rollers is always upward. If we let that force move the pinch-rollers, then the pendulum would be doing work on the pinch-rollers, and energy would be removed from the pendulum as the length of the string increases. For the following calculation, we will move the pinch-rollers down, doing work on the pendulum against this force, although either choice would produce a confirmation of adiabatic invariance.

Figure 2.5 shows the force exerted by the pinch-rollers on the string. When the string moves to the left, the pinch-rollers have to exert a force,  $F$ , that is downward and to the right:  $F = 2T \sin(\theta/2)$ . The vertical component of that force in the direction of the motion is  $F_z = F \sin(\theta/2) = 2T \sin^2(\theta/2) \cong T\theta^2/2$ .

The tension,  $T$ , in the string is due to the weight of the mass,  $mg$ , and the centripetal acceleration of that mass as it swings to and fro at the natural frequency,  $\omega_o$ , and with an angular displacement amplitude,  $\theta_1$ . Selecting the origin of our time coordinate to make  $\theta(t) = \theta_1 \sin \omega_o t$  eliminates the need for a phase,  $\phi$ , that appears in Eq. (2.6).

$$T = mg + mL\dot{\theta}^2 = mg + mL\omega_o^2\theta_1^2 \cos^2 \omega_o t = mg(1 + \theta_1^2 \cos^2 \omega_o t) \quad (2.35)$$

This expression can be integrated to calculate the work done by slowly sliding the pulley down by a distance,  $\delta L$ .

$$\delta E = W = \int_0^{\delta L} F_z dz = mg \int_0^{\delta L} (1 + \theta_1^2 \cos^2 \omega_o t) \frac{\theta_1^2}{2} \sin^2(\omega_o t) dz \quad (2.36)$$

Since we are moving the pulley slowly by a distance,  $\delta L$ , over a time corresponding to many cycles of period,  $T = 2\pi/\omega_o$ , we can take the time-average of the trigonometric functions:  $\langle \sin^2(\omega_o t) \rangle_t = \frac{1}{2}$  and  $\langle \cos^2(\omega_o t) \sin^2(\omega_o t) \rangle_t = \frac{1}{8}$ .

$$\delta E = \frac{\theta_1^2}{2} mg \left( \frac{1}{2} + \frac{\theta_1^2}{8} \right) \delta L \cong \frac{\theta_1^2}{4} mg(\delta L) \quad (2.37)$$

The energy of the pendulum can be written as the maximum kinetic energy which equals the total energy as the pendulum swings through  $\theta = 0$ :  $E(\theta = 0) = \frac{1}{2} mv^2 = \frac{1}{2} mL^2 \theta_1^2 \omega_o^2$ .

$$\frac{\delta E}{E} = \frac{\frac{1}{4} mg(\delta L)}{\frac{\theta_1^2}{2} mL^2 \omega_o^2} = \frac{1}{2} \frac{g(\delta L)}{L^2 \omega_o^2} = \frac{1}{2} \frac{\delta L}{L} = -\frac{\delta \omega_o}{\omega_o} \quad (2.38)$$

Since we are shortening the pendulum by doing work on it,  $\delta L < 0$ , and this result is identical to our expectation based on Eq. (2.34). Although this result only reconfirms our understanding of the relationship between the pendulum's frequency and its length, as we will see in Sect. 6.2.3 and Sect. 6.2.4, and subsequently in Part II as well, adiabatic invariance will allow us to calculate normal mode frequencies of systems that have complicated geometries in Sect. 13.3.5 or will allow us to determine forces when the frequency changes as system constraints are varied in Sect. 15.4.6.

## 2.4 Damping and Free-Decay

With only a mass and a spring, there is no mechanism by which the vibrational energy can be dissipated. Once set in motion, the mass-spring system has a total energy that is conserved, with the energy being transformed from kinetic to potential forms and vice versa as expressed in Eq. (2.17) throughout each cycle. In principle, the amplitude of oscillation will remain unchanged forever. In this section, we will add a third lumped element that will be able to convert a portion of that energy to heat, thereby reducing the amplitude of the oscillations, until the mass-spring-damper system comes to thermal equilibrium with its environment. As will be demonstrated, all of the energy is initially localized in the kinetic and potential energy of the mass and spring, but the damping element will dissipate this ordered energy, converting it to the disordered form known as heat.

### 2.4.1 Viscous Damping and Mechanical Resistance

Although damping can be introduced through a variety of physical mechanisms (e.g., friction or sound radiation), the most common and useful dissipative element is the viscous damper, represented in Fig. 2.6 as a *dashpot*. A dashpot is typically envisioned as consisting of a cylinder filled with a viscous fluid in which the motion of a movable vane is resisted by viscous drag, like a spoon being moved slowly through honey. The force of that viscous damping element is proportional to the velocity difference between its ends and is directed opposite to that velocity. Assuming that one end of the dashpot is immobilized, then the force,

$$F_{vis} = -R_m v,$$

where  $R_m$  [kg/s] is called the *mechanical resistance*. Adding the viscous force to the previous equation, which included inertia and stiffness, produces the equation of motion for a viscously damped simple harmonic oscillator.

$$m \frac{d^2x}{dt^2} + R_m \frac{dx}{dt} + Kx = 0 \quad \text{or} \quad \ddot{x} + \frac{R_m}{m} \dot{x} + \omega_o^2 x = 0 \quad (2.39)$$

The solution of this second-order differential equation with constant coefficients highlights the extraordinary utility of complex exponentials. We will postulate that the (complex) solution will have the form  $\mathbf{x}(t) = \hat{\mathbf{C}} e^{\eta t}$ , substitute into Eq. (2.39), and determine the form of our (as yet) undetermined exponent,  $\eta$ .

$$\left( \eta^2 + \frac{R_m}{m} \eta + \omega_o^2 \right) \hat{\mathbf{C}} e^{\eta t} = 0 \quad (2.40)$$

To satisfy this equation, the term in parentheses must vanish, since the value of  $\hat{\mathbf{C}} e^{\eta t}$  varies with time. This requirement is met by use of the quadratic formula to specify those two roots corresponding to the two values of  $\eta$ .

$$\eta = \frac{-\frac{R_m}{m} \pm \sqrt{\left(\frac{R_m}{m}\right)^2 - 4\omega_o^2}}{2} = -\frac{1}{\tau} \pm \sqrt{\left(\frac{1}{\tau}\right)^2 - \omega_o^2} \quad (2.41)$$

The choice of  $\tau = 2 m/R_m$  makes sense since  $\tau$  has the units of time, as required for dimensional homogeneity.

As with any new result, it is always valuable to examine the limiting case that corresponds to a previous solution (i.e., no damping). If we let  $R_m$  go to zero, making  $\tau$  go to infinity, we should recover the earlier result in Eq. (2.7).

$$\lim_{R_m \rightarrow 0} \eta = \pm j\omega_o \quad (2.42)$$

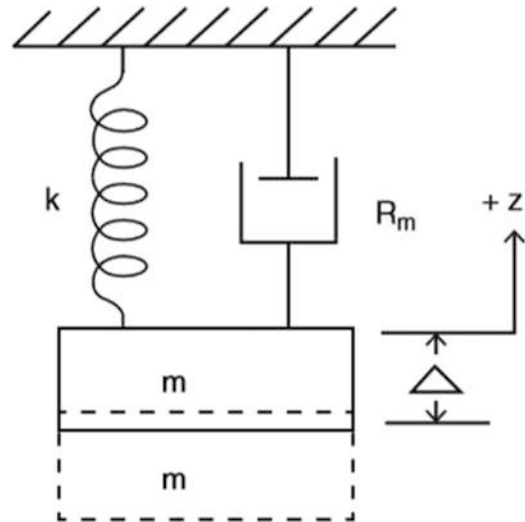
After taking the real part of the assumed exponential solution,  $\mathbf{x} = \hat{\mathbf{C}} e^{\eta t}$ , once Eq. (2.41) has been substituted for  $\eta$ , we see that  $\tau$  corresponds to the exponential decay time for the amplitude of the oscillation.

$$x(t) = \Re[\hat{\mathbf{C}} e^{\eta t}] = |\hat{\mathbf{C}}| e^{-t/\tau} \cos(\omega_d t + \phi) \quad (2.43)$$

The damped natural frequency,  $\omega_d$ , is provided in Eq. (2.45).

Figure 1.18 shows the time evolution of one such damped harmonic oscillator. The motion is no longer strictly periodic. The peak amplitude of each cycle is less than the amplitude of the previous cycle by an amount known as the *logarithmic decrement*. As in the undamped case, the frequency is still amplitude independent. In the damped case, we can define the frequency as the reciprocal of the time between upward or downward zero-crossings, since zero is not amplitude dependent. Equation (2.41) has also led to the introduction of the damped oscillation frequency,  $\omega_d$ , that will be discussed further in the next section. For the undamped case, where  $R_m = 0$ ,  $\tau \rightarrow \infty$ ,  $\omega_d = \omega_o$ . When  $R_m \neq 0$ , the period of the oscillatory portion described by Eq. (2.43) becomes longer.

**Fig. 2.6** A dashpot representing the viscous resistance,  $R_m$ , has been added to the mass and spring system of Fig. 2.4. The dashpot symbol is meant to represent a vane in an oil bath that will provide a viscous force that is proportional and opposite to the velocity of the vane:

$$F_{vis} = -R_m v$$


## 2.4.2 Free-Decay Frequency and Quality Factor

In the previous chapter's discussion of similitude (see Sect. 1.7.1), the addition of  $R_m$  as a third parameter that is required to specify a damped harmonic oscillator introduced a dimensionless group which was labeled  $Q^2$  at that time in Eq. (1.81), without justification.

$$Q^2 = \frac{Km}{R_m^2} = \frac{\omega_o^2 m^2}{R_m^2} = \frac{\omega_o^2 \tau^2}{4} \quad (2.44)$$

Similitude analysis suggests that the square root of this dimensionless group,  $Q = (\omega_o \tau)/2$ , known as the *quality factor*, must provide the only combination of parameters that can control the system's response, even if it is impossible to specify the exact functional form of that control from only dimensional arguments. To see this, we write  $\tau = 2Q/\omega_o = Q/(\pi f_o) = QT/\pi$ . This shows that  $Q$  corresponds to  $\pi$  times the number of cycles it takes for the amplitude of a damped harmonic oscillator to decay to  $e^{-1} \cong 36.8\%$  of its initial amplitude. Similarly, substitution into Eq. (2.41) shows that the damped oscillation frequency,  $\omega_d$ , is related to the undamped *natural frequency*,  $\omega_o$ .

$$\omega_d = 2\pi f_d = \sqrt{\omega_o^2 - \left(\frac{1}{\tau}\right)^2} = \omega_o \sqrt{1 - \frac{1}{4Q^2}} \cong \omega_o \left(1 - \frac{1}{8Q^2}\right) \quad (2.45)$$

The expression on the far right is an approximation (using the binomial expansion of Eq. 1.9), which is valid for lightly damped oscillators if  $Q^2 \gg 1$ . A related expression can be written for the *logarithmic decrement*,  $\delta$ , where  $T_d = 2\pi/\omega_d$  is the period of the damped sinusoid.

$$\begin{aligned} \delta &= \ln \left[ \frac{e^{-t/\tau}}{e^{-(t+T_d)/\tau}} \right] = \ln \left[ e^{-T_d/\tau} \right] = -\frac{T_d}{\tau} = \frac{2\pi}{\omega_d \tau} \\ \delta &= \frac{\pi}{Q} \left(1 - \frac{1}{4Q^2}\right)^{-1/2} \cong \frac{\pi}{Q} \left(1 + \frac{1}{8Q^2}\right) \end{aligned} \quad (2.46)$$

We can use the parameter values determined by the fit of Eq. (1.116), which is identical in form to Eq. (2.43), to develop some intuition about the results just obtained for a damped harmonic oscillator.

$$V(t_i) = V_o e^{-t_i/\tau} \sin(2\pi f_d t_i + \phi) \quad (1.119)$$

The fit values provided in the caption of Fig. 1.18 are  $f_d = 46.141$  Hz and  $\tau = 0.0445$  s. Based on Eq. (2.45), let's assume that  $\omega_d \cong \omega_o$  and use the measured  $\tau$  to calculate  $Q = (\omega_o \tau)/2 = \pi f_d \tau = 6.45$ . Substitution of that result back into Eq. (2.45) suggests that  $\omega_d/\omega_o = 0.997$ , so treating the natural and damped frequencies as being equal for the initial calculation of the quality factor,  $Q$ , was a most reasonable choice.

### 2.4.3 Critical Damping

The solution to the quadratic formula for  $\eta$  in Eq. (2.41) has three regimes. If  $\omega_o \tau = 2Q \gg 1$ , then the solutions are oscillatory and exhibit an exponentially decaying amplitude with time, as described in Eq. (1.119) and illustrated in Fig. 1.18. Such solutions are called *underdamped*.

In the opposite limit, the system is *overdamped*. That means that  $R_m/\omega_o \gg m$  or equivalently  $R_m/\omega_o m = Q^{-1} \gg 1$ . In that limit, the behavior of the system is governed by a first-order differential equation, where the inertial term,  $m(d^2x/dt^2)$ , in Eq. (2.39), can be ignored.

$$R_m \frac{dx}{dt} + Kx = 0 \quad (2.47)$$

Being a first-order differential equation, it possesses only one solution corresponding to exponential relaxation.

$$\int \frac{dx}{x} = -\frac{K}{R_m} \int dt \quad \Rightarrow \quad x(t) = C e^{-(K/R_m)t} \quad (2.48)$$

If the mass is displaced from equilibrium by an amount  $x_1$ , it is dragged back to equilibrium by the spring and  $x(t) = x_1 e^{-t/\tau}$ , where  $\tau = R_m/K$ .

An intermediate case can produce *critically damping*. If  $\omega_o \tau_{crit} = 1$  (i.e.,  $Q = 1/2$ ), the term under the radical in Eq. (2.41) is zero:  $\tau_{crit} = \omega_o^{-1} = (m/K)^{1/2}$ . If the system is initially displaced from equilibrium by an amount  $x_1$ , then the position decays exponentially to zero, like the solution in Eq. (2.48). Critical damping brings the mass back to its equilibrium position in the least amount of time without crossing zero. For the mass to approach the equilibrium position in the minimum time, the damping should be about 60% of the critical value, although when “critically underdamped,” the mass will cross zero before coming to rest.

### 2.4.4 Thermal Equilibrium and Fluctuations

*“The phase (or interferometric) sensor,<sup>4</sup> whether for magnetic, acoustic, rotation, etc., sensing, theoretically offers orders of magnitude increased sensitivity over existing technologies. In the case of the acoustic sensor*

---

<sup>4</sup> The fact that these authors are discussing a fiber-optic interferometric sensor is irrelevant, in this context. Such a sensor uses optical interference to detect changes in the difference of the length of two optical fibers. For our purposes, the interferometric sensor only provides a long “optical lever” like the mirrored galvanometer, shown in Fig. 2.6, that will be analyzed later in this section.

*constructed utilizing optical fiber interferometers, these theoretical predictions have been verified to the limit of state of the art in acoustic measurements... In the case of the magnetic sensor, it appears that fiber sensors operating at room temperature offer detection sensitivities comparable to or exceeding cryogenic SQUID technology, which normally operate between 4 and 10 K.” [7]*

The claims in the above quotation are completely wrong (and cost the US taxpayer millions of dollars as those authors chased this “impossible dream”). That quote epitomizes the problem that is encountered if we neglect the fact that the addition of our resistive element to the mass-spring harmonic oscillator opens a two-way street for the exchange of energy with the environment. Before the inclusion of  $R_m$ , the total energy of the system was determined by the initial conditions and that total energy remained constant, although the energy shuttled back and forth between its kinetic and potential forms. With a dissipative element, there was a path for energy to leave the oscillator, in this case as heat.<sup>5</sup> That path also connects the oscillator to “the environment” that must share energy with the oscillator by virtue of the fact that the absolute (kelvin) temperature of the environment and  $R_m$  is both non-zero. Temperature is a measure of the average kinetic energy of the particles that make up matter. Given sufficient time, every degree of freedom will get its “fair share.” This result is known as the *Equipartition Theorem* and can be thought of as a definition of thermal equilibrium, being the condition where, on average, each degree of freedom has the same average energy.

For degrees of freedom that have energies that are quadratic in their position or momentum coordinates,<sup>6</sup> that “fair share” is  $(\frac{1}{2}) k_B T$ , where the Boltzmann’s constant<sup>7</sup> is  $k_B \equiv 1.380649 \times 10^{-23} \text{ J/K}$  and  $T$  is the absolute (kelvin) temperature.

Before examining the consequences of thermal equilibrium on the limiting behavior of a damped harmonic oscillator due to thermal fluctuations, it may provide some comfort to reflect on the history of science, since it demonstrates that our understanding of heat and temperature took a relatively long time to develop. By comparison, our classical understanding of gravity and dynamics of particles from Newton’s falling apple to the orbits of the planets in the solar system, seemingly a far more arcane problem, was completely understood two centuries before we had a fundamental understanding of temperature and the mechanical equivalence of heat.

The year 1642 was an important milestone on the path to our current scientific understanding of the physical world. Galileo died in January of that year and Newton was born on December 25 of the same year, which turned out to be our guarantee that the scientific method would survive the death of Galileo.<sup>8</sup> Kepler (1571–1630) published his first two laws of planetary motion in 1609 and his third (see Sect. 2.3.1) in 1619, based on the observations of Tycho Brahe (1546–1601). Newton’s *Philosophiae Naturalis Principia Mathematica* was first published in 1687. It unified the dynamics of falling bodies on earth with the orbital motion of the planets in our solar system through Newton’s laws of motion and his law of universal gravitation.

---

<sup>5</sup> As will be shown in Chap. 12, energy can also leave by radiation of sound, but the thermodynamic consequences of energy being shed to the environment by any means are identical.

<sup>6</sup> The potential energy of a spring,  $(\frac{1}{2}) Kx^2$ , is quadratic in displacement. Kinetic energy,  $(\frac{1}{2})mv^2 = (\frac{1}{2})p^2/m$ , is quadratic in the momentum,  $p$ . For degrees of freedom that have energies that are quartic in the generalized coordinate, each degree of freedom gets  $(\frac{1}{4}) k_B T$  in thermal equilibrium.

<sup>7</sup> The most accurate value of Boltzmann’s constant is determined by a sound speed measurement, e.g., M. de Podesta et al., “A low-uncertainty measurement of the Boltzmann constant,” *Metrologia* **50**, 354–376 (2013). As of 20 May 2019, the value of  $k_B$  that is used here is taken to be exact (see Appendix A), and other practical units, such as the kilogram, the second, the meter, and the kelvin, are defined in terms of those “exact” fundamental physical constants.

<sup>8</sup> During the winter holiday season, some godless Humanists (commonly called atheists) celebrate “Continuity Day” to commemorate the continuity of the scientific method.

One would think that the concepts of heat and temperature, which are familiar to us through our own senses, would have been understood much earlier, but exactly the opposite is true. James Prescott Joule (1818–1889) measured the mechanical equivalence of heat (now incorporated into the First Law of Thermodynamics) in 1845,<sup>9</sup> nearly 160 years later than Newton's *Principia*. In fact, the connection between molecular motion and temperature was not established until the work of James Clerk Maxwell (1831–1879) and Ludwig Boltzmann (1844–1906) introduced the kinetic theory of gases and statistical mechanics (see Chaps. 7 and 9). Boltzmann went to his grave defending his theory against opposition within the scientific community at that time, and his gravestone has  $S = k \ln W$  at its top, where  $S$  is entropy,  $k = k_B$  is Boltzmann's constant, and  $W$  (for *Wahrscheinlichkeit*) is the number of microscopic states (i.e., combinations of positions and velocities) that correspond to the macroscopic equilibrium state of the system.

The first recorded observation of the mechanical consequences of thermal fluctuations was the microscopic observation in 1827 by botanist Robert Brown (1773–1858) of the motion of pollen particles suspended in water.<sup>10</sup> The theoretical explanation for this random motion was published by Albert Einstein (1879–1955) in 1905 [8] and was the reason, along with the photoelectric effect, that he was awarded the Nobel Prize in 1921.<sup>11</sup> The generalization of the role of thermal fluctuation to mechanical and electrical dissipation did not really start to develop until the 1920s. Most relevant to our immediate interests are thermal fluctuations in simple harmonic oscillators, which started with the observation of random motion in the mirrored galvanometer.

The mirrored galvanometer was patented by William Thompson (Lord Kelvin) in 1858.<sup>12</sup> It consists of a coil of wire, placed in a magnetic field, acting as an electrical meter that uses a mirror to reflect a beam of light to a scale, usually several meters away on a wall. That long “optical lever” provided a sensitive indication of the current passing through the coil. A torsion fiber provided the restoring force for the mirror-coil combination. (A similar arrangement is shown in Fig. 15.33.)

It was noticed that the spot of light reflected from the mirror underwent random motion. At first, it was assumed that the random motions were due to the collision of air molecules with the mirror, and a study was undertaken to measure the fluctuating position of the light spot as air was pumped out of the galvanometer [9]. Even without air, the random motions were still observed. In 1929, Uhlenbeck and Goudsmit were able to show that those fluctuations “depend on the properties of the observed system and on the temperature only”<sup>13</sup> [10]. At the same time, Nyquist was able to demonstrate that electrical

---

<sup>9</sup> That was the date when he presented his results at a scientific meeting. Those results were not published until 1850: J. P. Joule, “On the mechanical equivalent of heat,” Phil. Trans. Roy. Soc. **140**(Part I), 61–82 (1850).

<sup>10</sup> The fact that such motions were not biological in origin was confirmed when similar motion was observed in a drop of water trapped in amber (i.e., fossilized tree sap). No living creature could have survived that long in a water droplet isolated since antiquity.

<sup>11</sup> Einstein's Nobel Prize in Physics did not mention his theory of relativity since it was still too controversial in 1921.

<sup>12</sup> Thompson played a significant role in the laying of the first transatlantic telegraph cable between Ireland and Newfoundland that was successfully completed in 1865. He traveled on the cable-laying ship, the *Great Eastern*, as scientific advisor for all electrical matters. The mirrored galvanometer allowed detection of the weak electrical signals that made it through the cable. He set up two companies to sell these galvanometers and provide engineering consulting services to submarine cable companies. Those endeavors made him a wealthy man. The fascinating story of this first transatlantic cable is told by J. S. Gordon in *A Thread Across the Ocean* (Perennial, 2003): ISBN 978-0060524463.

<sup>13</sup> It is worth mentioning that these two Dutch physicists were also responsible for postulating that the electron had an internal degree of freedom that became known as the “electron spin.”

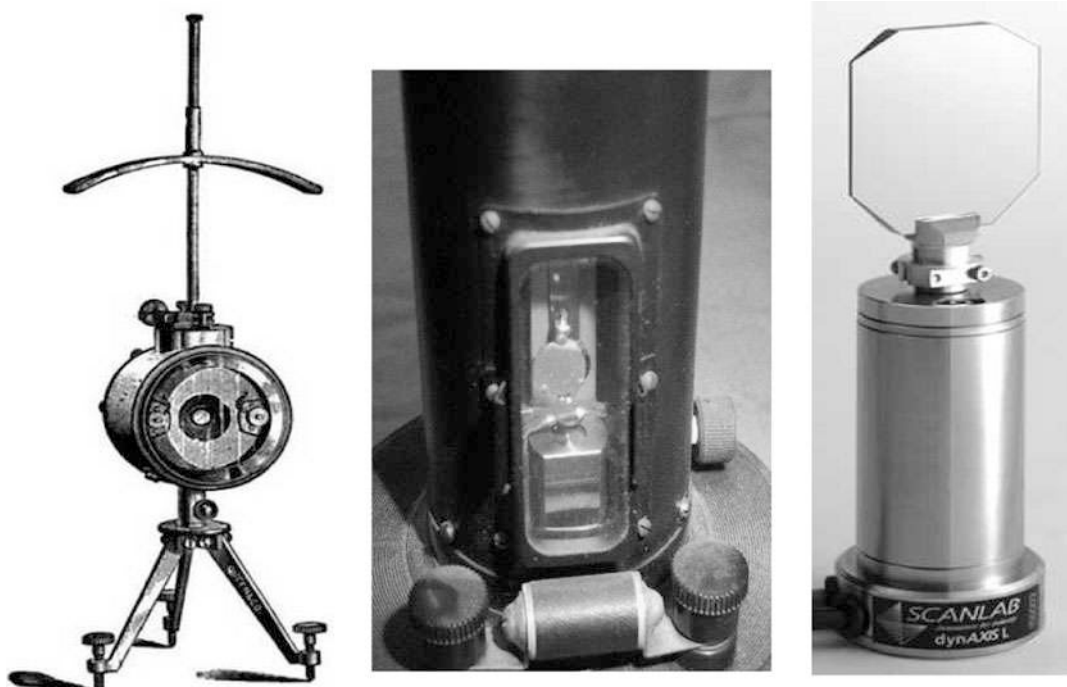


**Fig. 2.7** (Left) Drawing of Lord Kelvin’s patented mirrored galvanometer. (Center) Photograph of a mirrored galvanometer from the author’s collection. (Right) Although such instruments are no longer used to measure electrical currents, the same type of device is used to deflect laser beams for optical scanning purposes. (Photo courtesy of Scanlab, <http://www.scanlab.de>)

noise was generated by electrical resistors (Johnson noise [11]) based on their temperature [12] (Fig. 2.7).

Again, this very long historical digression is intended to point out that the connection between temperature and thermal fluctuations took a very long time before it was understood, along with its consequences for setting a minimum detectable signal for sensors [13]. The absurdity of the quote that started this section by claiming that “fiber sensors operating at room temperature offer detection sensitivities comparable to or exceeding cryogenic SQUID technology, which normally operate between 4 and 10 K” [7] is simply a reflection (no pun intended) of those authors’ ignorance of the fluctuations that had been observed in the 1920s with mirrored galvanometers [14]. In effect, their “optical lever” was 1–1000 m of optical fiber. The first fiber-optic interferometric sensor that was limited by thermal fluctuations was demonstrated experimentally in 1987 [15].

The Equipartition Theorem contradicts the result in Eq. (2.43), which claims that the amplitude of the motion of the mass connected to the spring and damper will decay to as small a value as you like, if you are willing to wait long enough for the exponential factor,  $|\hat{\mathbf{C}}| e^{-t/\tau}$ , to reduce the oscillatory amplitude. In thermal equilibrium, the mean value of each independent quadratic term in the energy will contain an average amount of energy that is  $(\frac{1}{2}) k_B T$  [16].

This result can be applied to the kinetic energy of the pollen particle that Brown observed jittering under his microscope in 1827. Today, it is easier to observe the motion of colloidal gold suspensions that are made with particle diameters of  $5 \times 10^{-6}$  cm [17]. The mass of each gold particle is about  $10^{-15}$  g. If we equate their kinetic energy per degree of freedom to  $(\frac{1}{2}) k_B T$ , and account for the fact that the

particles move in three dimensions (hence, there are three quadratic degrees of freedom corresponding to the velocities  $v_x$ ,  $v_y$ , and  $v_z$ ), we can solve for the gold particles' root-mean-squared velocity,  $v_{rms}$ .

$$v_{rms} = \langle v^2 \rangle^{1/2} = \left\langle v_x^2 + v_y^2 + v_z^2 \right\rangle^{1/2} = \sqrt{\frac{3k_B T}{m}} \quad (2.49)$$

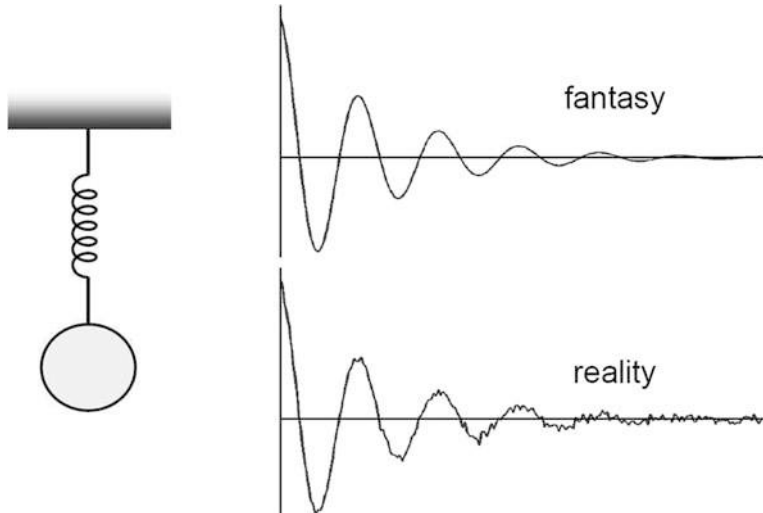
For such a colloidal suspension at  $T = 300$  K,  $v_{rms} \cong 10$  cm/s, which is what is observed [17]. If we make the same calculation for a 1 g sphere at 300 K,  $v_{rms} \cong 3.5 \times 10^{-9}$  m/s = 11 cm/year, which is why we don't see such small (but macroscopic) particles moving about randomly.<sup>14</sup>

The same approach can be applied to our single degree-of-freedom mass-spring-damper system to calculate the steady-state motion of the mass by equating the thermal energy per degree of freedom ( $\frac{1}{2} k_B T$ ) to the potential energy,  $(\frac{1}{2}) Kx^2$ .

$$x_{rms} = \langle x^2 \rangle^{1/2} = \sqrt{\frac{k_B T}{K}} \quad (2.50)$$

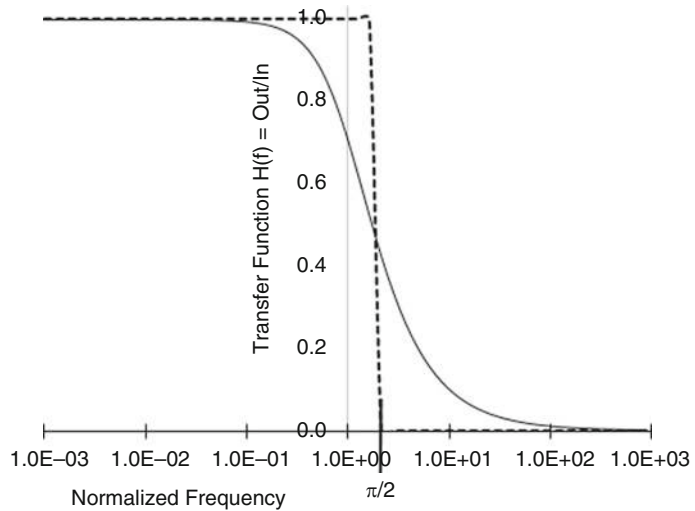
For the mirrored galvanometer, we would get the same result for  $\theta_{rms}$  except that K would be the torsional stiffness instead of the linear stiffness. Again, for macroscopic masses and ordinary temperatures, the fluctuations in the position of the mass are insignificant, but with the recent ubiquity of micro-electro-mechanical sensors (MEMS) (e.g., accelerometers and microphones), thermal fluctuations can be the dominant noise source [18] (Fig. 2.8).

**Fig. 2.8** The decay of a mass-spring system due to damping given by the time history in Eq. (2.43) is only true for displacements that are substantially larger than the thermal fluctuation amplitude,  $x_{rms}$ , given in Eq. (2.50). In reality, the motion of the mass does not decay to zero but will fluctuate randomly about its equilibrium position indefinitely due to its thermal energy. (Diagram courtesy of T. B. Gabrielson)



<sup>14</sup> The precise measurements of Brownian motion that were used to test Einstein's theory were made by Harvey Fletcher (1884–1981) with oil droplets as part of his Ph.D. thesis under the supervision of R. A. Millikan. His advisor chose to publish the charge quantization demonstrated by that oil drop experiment under his own name and received the Nobel Prize in Physics in 1923. Fletcher published the Brownian motion measurements under his name and went on to a very successful career in acoustics at Bell Labs: M. F. Perry, “Remembering the oil-drop experiment,” Phys. Today **60**(5), 56–60 (2007).

**Fig. 2.9** The transfer function,  $H(\Omega)$ , of a single-stage low-pass filter (solid line) is plotted against the normalized frequency.  $\Omega = f/f_{-3 \text{ dB}}$ , where  $f_{-3 \text{ dB}}$  is the frequency at which the amplitude of the transfer function has decreased to  $\sqrt{2}$  of its low-frequency limit. The dashed rectangle has the value one up to  $\Omega = \pi/2$  and zero for  $\Omega > \pi/2$ , giving it the same area as that under the solid line. For that reason,  $(\Delta f)_{EQNB} = \pi f_{-3 \text{ dB}}/2$



This random motion can be interpreted as the response to a fluctuating force,  $F_{noise}$ . Its root-mean-squared value is related to the square root of the product of the absolute (kelvin) temperature,  $T$ ; the mechanical resistance,  $R_m$ ; and the *equivalent noise bandwidth*,  $(\Delta f)_{EQNB}$ , of the system.

$$F_{rms} = \langle F_{noise}^2 \rangle^{1/2} = \sqrt{4k_B T R_m (\Delta f)_{EQNB}} \quad (2.51)$$

The part of this expression which may be unfamiliar at this point is  $(\Delta f)_{EQNB}$ . At the simplest level, that bandwidth specifies the range of frequencies over which the fluctuating force will preferentially excite the system's response. The “equivalence” is a way to hide the fact that one needs to integrate over the entire system's frequency response function then choose an equivalent “rectangular” filter response function that has a frequency width of  $(\Delta f)_{EQNB}$  and unity gain, as shown in Fig. 2.9. We will calculate this *effective bandwidth* for a damped driven harmonic oscillator in Sect. 2.5.

At this point, the attentive reader (hopefully, you!) might become a little anxious. (S)he might reflect thusly: “This section started off claiming that the addition of a mechanical resistance opened a ‘two-way street’ that let ordered vibrational energy leave the system but also created a path for the random thermal motion to enter the system. I can see in Eq. (2.51) that the fluctuating force is related to that mechanical resistance, but the results for  $x_{rms} = \langle x^2 \rangle_t^{1/2} = \sqrt{k_B T / 2K}$  and  $v_{rms} = \langle v^2 \rangle_t^{1/2} = \sqrt{k_B T / 2m}$  do not involve the mechanical resistance at all. What gives?”

The lazy textbook author would provide the following response: “Do you remember our calculation of the frequency of the pendulum? The result,  $\omega_o^2 = g/L$ , does not involve the mass, yet it is the mass of the pendulum that provided the inertia and the mass of the pendulum that was proportional to the gravitational restoring force. In the final result for frequency, which depends upon the ratio of the restoring force to the inertia, the mass cancelled out. The same is true here, though at this point it is not at all obvious. For a simple harmonic oscillator,  $(\Delta f)_{EQNB} \propto R_m/m$ , so  $R_m$  comes out of the square-root in Eq. (2.51). At the frequency of peak response,  $\omega_o$ , the velocity of the mass is proportional to  $F/R_m$ , thus cancelling  $R_m$  out of the final result for  $v_{rms}$ . A similar argument holds for  $x_{rms}$ .”

The thermal noise of any mechanical system that is in thermal equilibrium with its surroundings, no matter how complex, can be analyzed by including this fluctuating force combined with the resistance;

just as in electrical circuits, a fluctuating voltage source,  $V_{noise}$ , can be included with the electrical resistance,  $R_{el}$  [11].

$$V_{rms} = \langle V_{noise}^2 \rangle^{1/2} = \sqrt{4k_B T R_{el} (\Delta f)_{EQNB}} \quad (2.52)$$

That expression is the “Johnson noise” [11] that is familiar to electrical engineers.

### 2.4.5 Frictional (Coulomb) Damping\*

Most of us are first exposed to friction in high school physics classes where the frictional force,  $F_d$ , is the sliding friction between two dry surfaces. That frictional force is characterized by a coefficient of sliding friction,  $\mu$ , assumed to be velocity independent and proportional to the force (usually gravitational) that is squeezing the two surfaces together.

$$F_d = -\mu mg \quad (2.53)$$

To determine the amplitude decay for frictional damping, we can calculate the work done by the frictional force during one half-cycle and equate that to the change in the potential energy. Figure 2.10 shows the first few cycles that will be used to calculate the amplitude decrease for successive oscillations.

Starting with an initial displacement of  $x_1 = x(t = 0)$ , the mass will come to rest instantaneously at the other extreme of the motion,  $x_{-1} = x(T/2)$ , where it changes direction. Since there will be frictional losses,  $|x_1| > |x_{-1}|$ .

$$\frac{1}{2}K(x_1^2 - x_{-1}^2) = \frac{1}{2}K(x_1 - x_{-1})(x_1 + x_{-1}) = W_d = F_d(x_1 + x_{-1}) \quad (2.54)$$

This results in an expression for the amplitude decrease for the first half-cycle:  $(x_1 - x_{-1}) = 2F_d/K$ . Repeating the procedure for the next half-cycle, we again see that the amplitude is decreased by the same amount resulting in a loss of  $\Delta x(T) = x_1 - x_2 = 4F_d/K$ . This will continue, as illustrated in

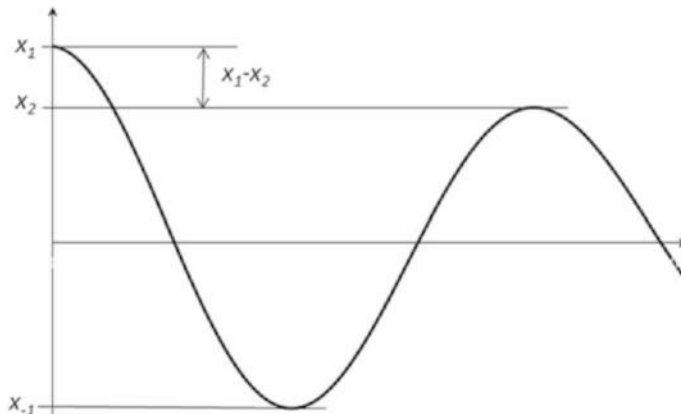


**Fig. 2.10** Decay of the amplitude of a simple harmonic oscillator that is subject to sliding friction can be calculated by examination of the losses that occur during each half-cycle. The time history at the right starts with a positive displacement,  $x_1$ , at time,  $t = 0$ , and at the end of the first half-cycle the mass has moved to  $x_{-1}$ . The energy dissipation guarantees  $|x_1| > |x_{-1}|$ . During the second half-cycle, the mass moves from  $x_{-1}$  to  $x_2$ , with  $|x_{-1}| > |x_2|$ , etc.

**Fig. 2.11** (Left) A viscous damping force,  $F_{vis} = -R_m v$ , produces an exponentially decaying amplitude. (Right) A frictional (Coulomb) damping force,  $F_d = -\mu (mg)$ , produces an amplitude that decays linearly with time. (Figures from Pippard [19])

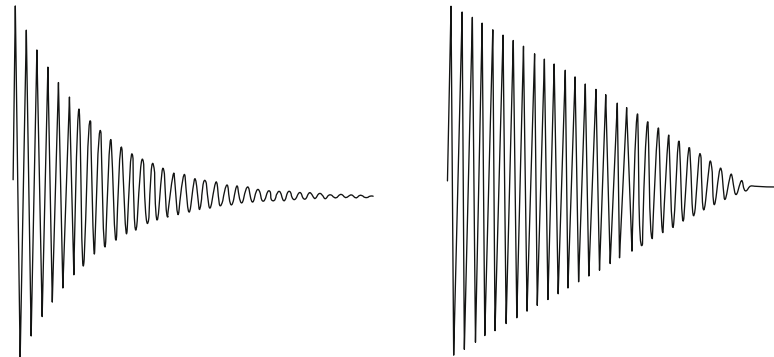


Fig. 2.11, until the mass comes to rest. The decay per cycle is a constant, so the amplitude decreases linearly with time, not exponentially with time [19].

## 2.5 Driven Systems

Thus far, we have only analyzed the response of a harmonic oscillator that is provided with an initial displacement, an initial velocity, or both. Those solutions, like that shown in Eq. (2.43), are allowed to evolve in time without any further energy input. We have also demonstrated that the imposition of a steady gravitational force will displace the equilibrium position but not influence the oscillator's dynamical response. In this section, we will examine the response of a viscously damped simple harmonic oscillator to a periodic force applied to the mass or to a periodic displacement applied to the end of the spring not attached to the mass. The steady-state solution that supplies the response to both of those driven systems will be provided through the calculation of a *mechanical impedance*. Also, important will be the concept of *resonance*. When the drive occurs at the natural frequency,  $\omega_o$ , of the undriven system, the steady-state (velocity) response at resonance is only limited by the damping. Resonance is one of the most valuable tools available to the acoustician, and this section will provide our first exposure to its wonders.

### 2.5.1 Force-Driven SHO

We start by assuming that a sinusoidally varying force of amplitude,  $F_1$ , is applied to the mass in a mass-spring-damper system. The force amplitude,  $F_1$ , can be chosen to be a real number without any loss of generality since that choice indicates that any phase shifts will be referenced to the phase of the force, which has now been chosen to define the origin of our phase reference (i.e.,  $\phi = 0$ ), so  $F(t) = F_1 \cos(\omega t)$ . When that sinusoidally time-varying force is applied to the mass, then Eq. (2.39) is no longer homogeneous.

$$m \frac{d^2x}{dt^2} + R_m \frac{dx}{dt} + Kx = m \frac{dv}{dt} + R_m v + K \int v dt = F(t) \equiv F_1 e^{j\omega t} \quad (2.55)$$

Instead of writing our differential equation in terms of the displacement of the mass, it is entirely equivalent to write it in terms of the velocity of the mass.

Although the above equation assumes a force is applied to the mass-spring-damper system at a single driving frequency,  $\omega$ , our discussion of Fourier synthesis (see Sect. 1.4) indicated that, for such a

linear system (see Sect. 1.3), we could produce the response to a more complicated periodic driving force by superposition of forces that are applied with other frequencies, amplitudes, and phases.

It is also important to remember that a driven linear system can only respond at the driving frequency, once any transient behavior dies out (see Sect. 2.5.4). Since Eq. (2.39) is homogeneous, solutions to the homogeneous equation, like that in Eq. (2.43), can be added to the solution of Eq. (2.55) in amounts determined by the initial conditions. Because  $\tau < \infty$ , those transient solutions will eventually die out leaving only the steady-state response.

Again, convenience (complex) numbers (see Sect. 1.5) make the solution to Eq. (2.55) straightforward. Since we know that the linear system's steady-state response occurs only at the driving frequency,  $\omega$ , we will postulate a solution for the velocity of the mass's response of the form,  $v(t) = \Re[\mathbf{C}e^{j\omega t}]$ , with the understanding that  $\mathbf{C}$  is a phasor (complex number) that can introduce a phase shift between the applied force and the velocity, as well as determine the amplitude of the response. We again revert to phasor notation that allows us to combine both the amplitude and phase into a single complex symbol,  $\hat{\mathbf{v}}e^{j\omega t} = \hat{\mathbf{C}}e^{j\omega t}$ , and substitute that solution into Eq. (2.55) and factor out the common term.

$$\left(j\omega m + R_m + \frac{K}{j\omega}\right)\hat{\mathbf{C}}e^{j\omega t} = F_1 e^{j\omega t} \quad (2.56)$$

The amplitude and the phase of the velocity response, as represented by the velocity phasor,  $\mathbf{v}$ , to the applied force of amplitude,  $F_1$ , at frequency,  $\omega$ , can be written directly.

$$\hat{\mathbf{v}}e^{j\omega t} = \frac{F_1 e^{j\omega t}}{j(\omega m - \frac{K}{\omega}) + R_m} \quad (2.57)$$

The entire response of the driven system is characterized by the complex denominator. By analogy with electrical circuit theory, that denominator is identified as the complex mechanical impedance,  $\mathbf{Z}_m$ .

$$\mathbf{Z}_m \equiv \frac{F}{\hat{\mathbf{v}}} = j\left(\omega m - \frac{K}{\omega}\right) + R_m \quad (2.58)$$

The imaginary component of the mechanical impedance is  $\Im[\mathbf{Z}_m] \equiv X_m = \omega m - (K/\omega)$ . It is called the *mechanical reactance* and represents the storage of energy as either elastic stiffness or inertia. It is important to recognize that the reactance vanishes,  $X_m(\omega_o) = 0$ , when the forcing frequency equals the natural frequency,  $\omega = \omega_o = \sqrt{K/m}$ .

We recognized  $\Re[\mathbf{Z}_m] = R_m$  as the mechanical resistance that represents the dissipation of energy. At resonance, when  $X_m(\omega_o) = 0$ , the response is controlled entirely by the resistance; hence it is referred to as the *resistance-controlled* response regime. The steady-state solution for the displacement,  $x(t)$ ; the velocity,  $v(t)$ ; or the acceleration,  $a(t)$ , in response to the driving force,  $F(t)$ , can be written compactly in terms of  $\mathbf{Z}_m$ . The transient response is included in Eq. (2.80).

$$x(t) = \Re\left[\frac{1}{j\omega} \frac{F_1 e^{j\omega t}}{\mathbf{Z}_m}\right], \quad v(t) = \Re\left[\frac{F_1 e^{j\omega t}}{\mathbf{Z}_m}\right], \quad \text{and } a(t) = \Re\left[j\omega \frac{F_1 e^{j\omega t}}{\mathbf{Z}_m}\right] \quad (2.59)$$

As with any new result, it is prudent to interpret the consequences and compare them to our assumptions. The fact that the mechanical impedance has singled out a specific frequency,  $\omega_o = \sqrt{K/m}$ , makes it easy to define what is meant by the low- and high-frequency limits. In the low-frequency limit,  $\omega \ll \omega_o$ , the stiffness is dominant, and substitution of Eq. (2.58) into the above

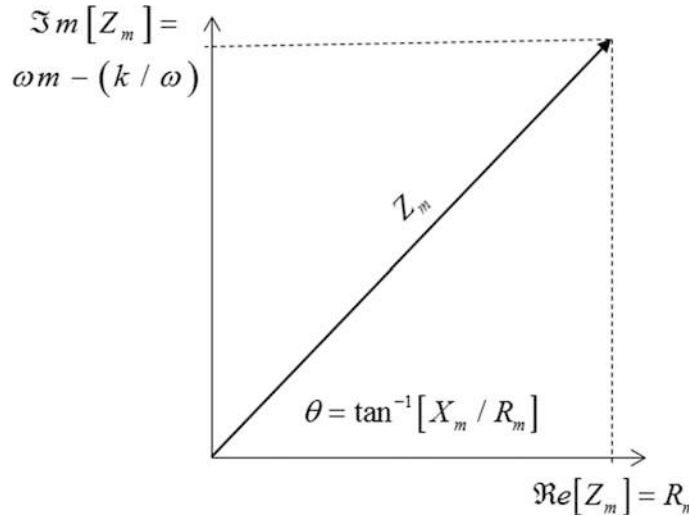


**Fig. 2.12** The complex mechanical impedance can be represented in polar form with the frequency-independent real component,  $\Re e[Z_m] = R_m$ , and the imaginary component,  $\Im m[Z_m] = X_m = \omega m - (K/\omega)$ . The magnitude of the mechanical impedance,  $|Z_m|$ , is given by the length of the hypotenuse, and the phase angle between the force and the velocity is  $\Theta = \tan^{-1}[X_m/R_m]$ . That phase angle can vary between the “stiffness-controlled limit,”  $-90^\circ$ , well below the resonance frequency (i.e., displacement  $x(t) = v(t)/(j\omega)$  out-of-phase with force), and  $+90^\circ$ , the “mass-controlled limit,” well above the resonance frequency (i.e., acceleration,  $a(t) = (j\omega) v(t)$ , is in-phase with the force)

expression,  $x(t) \cong -F_1/K$ , results in the cancellation of the frequency and the recovery of Hooke’s law. For that reason, the low-frequency limit is referred to as the *stiffness-controlled* response regime.

In this high-frequency limit,  $\omega \gg \omega_o$ , the  $j\omega m$  term in the mechanical impedance is dominant, so  $a(t) \cong F_1/m$  is frequency-independent, and Newton’s Second Law is recovered. For that reason, the high-frequency limit is referred to as the *mass-controlled* response regime.

It is useful to have a polar representation of the mechanical impedance magnitude and phase:  $|Z_m| = (Z_m Z_m^*)^{1/2}$  and  $\Theta = \arctan(X_m/R_m)$ . The geometric interpretation is provided in Fig. 2.12.

$$|Z_m| = \sqrt{Z_m Z_m^*} = \left[ R_m^2 + \left( \omega m - \frac{K}{\omega} \right)^2 \right]^{1/2} = \omega_o m \left[ \left( \frac{\omega}{\omega_o} - \frac{\omega_o}{\omega} \right)^2 + \frac{1}{Q^2} \right]^{1/2} \quad (2.60)$$

$$\Theta = \tan^{-1} \left( \frac{X_m}{R_m} \right) = \tan^{-1} \left[ \frac{\omega m - \frac{K}{\omega}}{R_m} \right] = \tan^{-1} \left[ Q \left( \frac{\omega}{\omega_o} - \frac{\omega_o}{\omega} \right) \right] \quad (2.61)$$

Figure 2.13 shows the magnitude and phase of the velocity response to the sinusoidal force,  $F(t) = F_1 e^{j\omega t}$ . The complex velocity response can be written in a more symmetric form by using  $Q = \omega_o m / R_m$  to substitute for  $R_m$  in Eq. (2.57).

$$\mathbf{v}(t) = \frac{F_1 e^{j(\omega t - \Theta)}}{|Z_m|} = \frac{\frac{F}{R_m Q} e^{j(\omega t - \Theta)}}{\left[ \left( \frac{\omega}{\omega_o} - \frac{\omega_o}{\omega} \right)^2 + \frac{1}{Q^2} \right]^{1/2}} = v_1(\omega) e^{j(\omega t - \Theta)} \quad (2.62)$$

Expressions with the form of Eq. (2.62) show up for all driven resonance behavior, not just the driven simple harmonic oscillator. As will become apparent throughout this book, this *Rayleigh line*

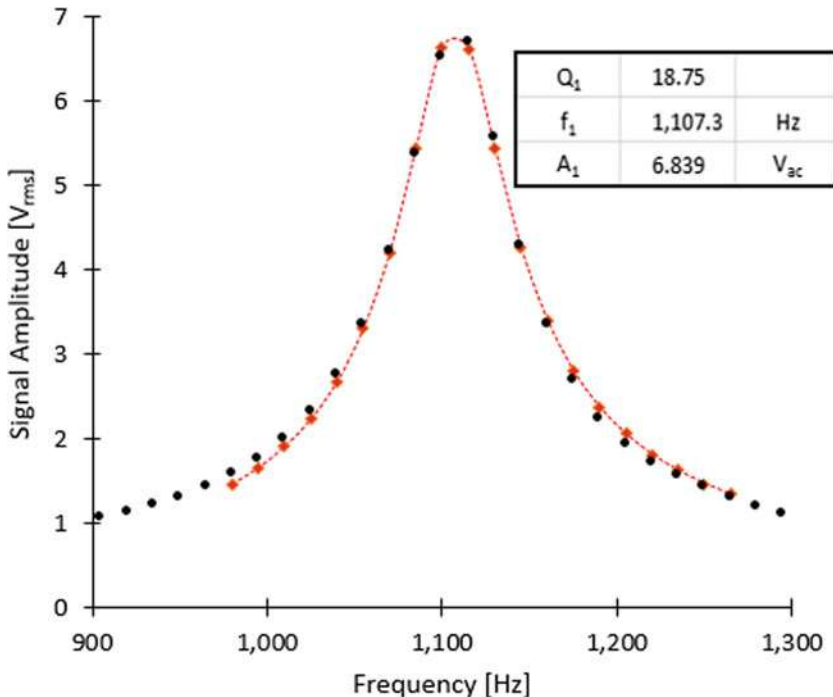


**Fig. 2.13** Response of the  $n = 1$  torsional resonance of a bar similar to the fundamental mode shown in Fig. 5.16. The measured amplitudes,  $A_{exp}(f)$ , are shown as the 27 black dots plotted for  $900 \leq f \leq 1300$  Hz. The red diamonds are values of  $A_1(f/f_1)$  from Eq. (2.63) that have been joined by a smooth dotted line to illustrate the Rayleigh line shape. The parameter values in the box are those adjusted by a nonlinear curve-fitting algorithm (i.e., “solver”) that minimized sum of the squared difference between  $A_{exp}(f)$  and  $A_1(f/f_1)$

*shape* (aka Lorentz line shape) will describe systems with multiple resonances, like the modes of a long thin cylindrical bar in Fig. 5.16 or the modes of a gas-filled plane wave resonator driven by a loudspeaker in Figs. 10.12 and 10.14, as long as the individual modal frequencies are well-separated.

We can rewrite Eq. (2.62) in a more general form where the subscript,  $n$ , refers to the mode number. For the single-degree-of-freedom simple harmonic oscillator that has just been analyzed (or for the Helmholtz resonator discussed in Sect. 8.5),  $n = 0$ . For the torsional resonance in Fig. 5.16, there are five resonances that would be designated  $1 \leq n \leq 5$ . At resonance, the amplitude of the response has its maximum value,  $A_n(1)$ .

$$A_n(f/f_n) = \frac{A_n(1)/Q_n}{\sqrt{\left(\frac{f}{f_n} - \frac{f_n}{f}\right)^2 + \frac{1}{Q_n^2}}} \quad (2.63)$$

Here  $Q_n$  is the quality factor of the  $n$ th mode, and  $f_n$  is the resonance frequency of that  $n$ th mode. With  $A_n(1)$ , the frequency response function (i.e., line shape) created by Eq. (2.63) is characterized by three parameters:  $A_n(1)$ ,  $f_n$ , and  $Q_n$ .

We have already marveled at the ability of modern digital instrumentation and mathematical software to make it possible to acquire an array of data and fit those measurements to a chosen functional form. In Fig. 1.18, 2000 data points were acquired, and a nonlinear curve-fitting algorithm (i.e., “solver”) was used to extract the five parameters necessary to characterize the free-decay of a

loudspeaker that were specified in Eq. (1.119) by minimizing the sum of the squared difference between those measurements and the fitted function.

In Fig. 2.13, we executed a similar procedure to select the values of the three parameters in Eq. (2.63) that minimize the sum of the squared difference between the measured amplitude values,  $A_{exp}(f)$  and  $A_n(f/f_n)$ , as was done for the least-squares fit to a straight line in Sect. 1.9. In this example, the response amplitudes were generated by the measurement of the fundamental ( $n = 1$ ) resonant torsional modes of a spectrum like that in Fig. 5.15 but for a different bar. The best-fit values are shown in the boxed inset within Fig. 2.13. The slight asymmetry between the fit and the data is due to electromagnetic cross talk (see Sect. 5.4.3) that could be included within the model to improve the fit.

## 2.5.2 Power Dissipation, the Decibel, and Resonance Bandwidth

The time-averaged power dissipated in the mechanical resistance can be calculated using Eq. (1.73), and the mechanical impedance can be used to provide  $v(t)$ .

$$\langle \Pi \rangle_t = \frac{1}{2} \Re e[\mathbf{F}^* \hat{\mathbf{v}}] = \frac{F_1^2}{2} \Re e[\mathbf{Z}_m^{-1}] = \frac{F_1^2 R_m}{2 | \mathbf{Z}_m^2 |} = \frac{1}{2} \frac{F_1^2 R_m}{X_m^2 + R_m^2} \quad (2.64)$$

At resonance,  $X_m(\omega_o) = 0$ , and the power dissipated in the mechanical resistance has its maximum time-averaged value,  $\langle \Pi_{max} \rangle_t$ . The equation is analogous to the power dissipated in an electrical resistor with a potential difference amplitude,  $V_1$ , across an electrical resistance,  $R_{el}$ .

$$\langle \Pi(\omega_o) \rangle_t = \langle \Pi_{max} \rangle_t = \frac{1}{2} \frac{F_1^2}{R_m} \quad (2.65)$$

If instead we had used  $\mathbf{Z}_m$  to eliminate  $\mathbf{F} = \mathbf{Z}_m \hat{\mathbf{v}}$  in Eq. (2.64), then we would have produced the analog to the electrical power dissipation which is proportional to the square of the current through the resistor.

$$\langle \Pi(\omega_o) \rangle_t = \frac{1}{2} \Re e[\mathbf{F}^* \hat{\mathbf{v}}] = \frac{v_1^2}{2} \Re e[\mathbf{Z}_m] = \frac{1}{2} R_m v_1^2 \quad (2.66)$$

It is easy to see from Eq. (2.64) that the power is reduced to half of the maximum value when  $R_m = \pm X_m$ . There are two frequencies at which the power is half the maximum:  $\omega_+$  and  $\omega_-$ . Those two frequencies can be determined by solution of Eq. (2.58).

$$m\omega_+ - (K/\omega_+) = R_m \quad \text{and} \quad m\omega_- - (K/\omega_-) = -R_m \quad (2.67)$$

Substituting K from the expression for  $\omega_-$  into the expression for  $\omega_+$  produces an equation that can be factored to determine the required frequency difference.

$$\omega_+^2 - \omega_-^2 = (\omega_+ - \omega_-)(\omega_+ + \omega_-) = \frac{R_m}{m} (\omega_+ + \omega_-) \quad (2.68)$$

The expression for the quality factor from Eq. (2.44) generates another useful relation for  $Q$  that emphasizes the fact that  $Q$  is a dimensionless measure of the sharpness of a resonance.

$$Q = \frac{\omega_o m}{R_m} = \frac{\omega_o}{\omega_+ - \omega_-} = \frac{f_o}{f_+ - f_-} = \frac{\sqrt{f_+ f_-}}{f_+ - f_-} = \frac{f_o}{(\Delta f)_{-3 \text{ dB}}} \quad (2.69)$$

Due to the symmetry of Eq. (2.62) with respect to  $\omega/\omega_0$  and  $\omega_0/\omega$ ,  $f_o$  is the geometric mean of  $f_+$  and  $f_-$ , not their arithmetic average.

The right-hand expression introduces the “down 3 dB” bandwidth of the resonance,  $(\Delta f)_{-3 \text{ dB}} = f_+ - f_-$ . This is the full bandwidth of the resonance between the two half-power frequencies and is also known as the *full width at half maximum*,  $(\Delta f)_{FWHM}$ . The use of the decibel for expression of power ratios will be discussed further in Part II – Fluids, particularly for the specification of sound levels in air in Sect. 10.5. Briefly, the *decibel* (abbreviated “dB”) was introduced in the early days of telephony as a means for using addition and subtraction to multiply transducer sensitivities, amplifier gains, and transmission losses in the calculation of the overall response of telephone systems in the century before digital computers became available to engineers and scientists.

$$\text{dB} \equiv 10 \log_{10} \left( \frac{\Pi_1}{\Pi_2} \right) \quad (2.70)$$

In our case,  $\Pi_2 = \langle \Pi_{\max} \rangle_t$ , the time-average power at resonance, and  $\Pi_1 = (\frac{1}{2}) \langle \Pi_{\max} \rangle_t$  is the half-power point:  $10 \log_{10}(\frac{1}{2}) = -3.01$ , hence, the “down 3 dB” designation.

Figure 2.14 plots the velocity amplitude response (above) and phase response (lower right) vs. frequency ratio,  $f/f_o$ , for a driven harmonic oscillator with three different values of quality factor,  $Q$ . Those amplitude response curves never cross. Driven with the same force, the system with the higher-quality factor will have larger displacement, velocity, and acceleration responses at all drive frequencies. The peak in the velocity response always occurs at  $f_o$ . If we were to plot the displacement response, the peak would occur slightly below  $f_o$  since  $\hat{x} = \hat{v}/(j\omega)$ . Similarly, the peak in the acceleration response,  $\hat{a} = (j\omega)\hat{v}$ , would occur at a slightly higher frequency than  $f_o$ .

The relative power delivered to the mechanical resistance vs. the frequency ratio,  $f/f_o$ , is shown at the lower left of Fig. 2.14. The dashed lines, which intersect  $(\frac{1}{2}) \langle \Pi_{\max} \rangle_t$ , occur at  $f_-$  and  $f_+$ .

At this point, it is useful to derive still another expression for the quality factor, this time in terms of the energy stored in the spring and the mass at resonance,  $E_{Stored}$ , and the energy dissipated in the mechanical resistance during one cycle,  $\langle \Pi_{\max} \rangle_t T$ .

$$\frac{E_{Stored}}{\langle \Pi_{\max} \rangle_t T} = \frac{\omega_o E_{Stored}}{2\pi \langle \Pi_{\max} \rangle_t} = \frac{\frac{m}{2} v_1^2 \omega_o}{2\pi \frac{R_m v_1^2}{2}} = \frac{Q}{2\pi} \quad (2.71)$$

This form can be convenient for calculation of  $Q$  since  $E_{Stored}$  and  $\langle \Pi_{\max} \rangle_t$  are both scalars.

Now that we have an expression for the power dissipated in the mechanical resistance of a damped driven simple harmonic oscillator, it is possible to calculate the equivalent noise bandwidth,  $(\Delta f)_{EQNB}$ , as shown in Eq. (2.73), that was required for our reconciliation of the consequences of the Equipartition Theorem in Eqs. (2.49) and (2.50), and the fluctuating force in Eq. (2.51), by working backward to create an expression for the fluctuating force from the results of the Equipartition Theorem.

$$\frac{1}{2} k_B T = \left\langle \frac{1}{2} m v^2 \right\rangle = \frac{m}{2} \left\langle \frac{|F|^2}{|\mathbf{Z}_m|^2} \right\rangle = \frac{m F_{noise}^2}{2} \int_0^\infty \frac{df}{|\mathbf{Z}_m|^2} \quad (2.72)$$

Using the form of mechanical impedance from Eq. (2.60) and defining a dimensionless frequency ratio,  $\Omega = f/f_o$ , so  $df = f_o d\Omega$ , that definite integral can be evaluated using integral tables [20] or numerically [14].

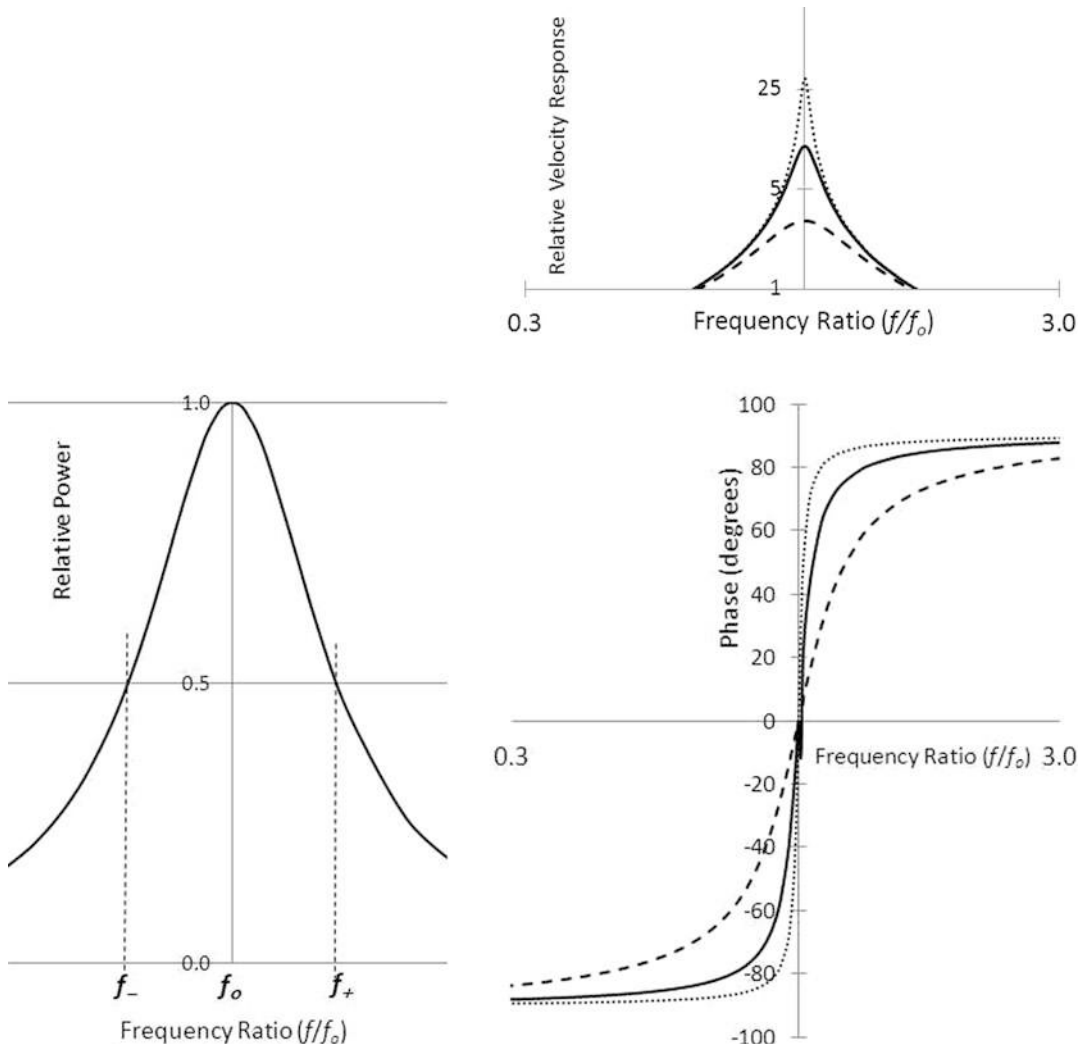


**Fig 2.14** (Top right) Velocity amplitude response of a driven damped harmonic oscillator with  $Q = 3$  (dashed line),  $Q = 10$  (solid line), and  $Q = 30$  (dotted line) vs. the ratio of the drive frequency to the resonance frequency,  $f/f_0$ . Note that none of these lines cross. (Bottom right) Phase response vs. frequency ratio for the same three values of  $Q$ . (Bottom left) Relative power for  $Q = 3$  showing the resonance frequency,  $f_o$ ; the lower  $-3$  dB frequency,  $f_-$ ; and the upper  $-3$  dB frequency,  $f_+$ :  $Q = f_o/(f_+ - f_-)$

$$\int_0^\infty \frac{d\Omega}{\frac{1}{Q^2} + (\Omega - \frac{1}{\Omega})^2} = \frac{\pi Q}{2} \quad (2.73)$$

Substitution of the integral back into Eq. (2.72) results in an expression for the average kinetic energy that is independent of  $R_m$ .

$$\left\langle \frac{1}{2} m v_1^2 \right\rangle = \frac{m}{2} \frac{4k_B T R_m}{\omega_o^2 m^2} f_o \frac{\pi Q}{2} = \frac{1}{2} k_B T \quad (2.74)$$

The equivalent noise bandwidth,  $(\Delta f)_{EQNB}$ , of the resonance can also be related to the integral in Eq. (2.73):  $(\Delta f)_{EQNB} = (\pi/2)(\Delta f)_{-3 \text{ dB}}$ . Once again, as we saw in Sect. 2.3.3, we have a final result that

is dependent upon a particular parameter (i.e., the noise introduced by the dissipative component,  $R_m$ ) but which hides the explicit dependence on the parameter that governs that phenomenon.

### 2.5.3 Resonance Tracking and the Phase-Locked Loop\*

Typically, we think of the peak in the amplitude response of a damped driven harmonic oscillator as being the primary characteristic of a resonator driven at its resonance frequency. There is certainly good reason for this prejudice, since resonance can be used to optimize the coupling of an oscillatory force to a useful load, for example, the coupling of an electrodynamic loudspeaker to a thermoacoustic resonator [21]. But we are well aware (see Sect. 1.2) that the slope of the amplitude vs. frequency at that response maximum (or any extremum) is zero. For that reason, if the drive is de-tuned from resonance (e.g., by a change in temperature or some other environmental effect that alters  $\omega_o$ ), the amplitude of the response will decrease whether the de-tuning is either “flat” (i.e., drive frequency below resonance) or “sharp” (i.e., drive frequency above resonance). For that reason, a control system that monitors amplitude cannot determine whether to increase or to decrease the drive frequency to maintain the system on resonance based only on this change in amplitude.

A casual inspection of the resonance response curves in Fig. 2.14 shows that the rate of change of the phase difference with frequency, between the driving force and the velocity response,  $d\Theta/d\omega$ , is maximum at resonance, where  $\Theta = 0$ . Because  $\Theta \cong 0$  near the resonance frequency,  $\omega_o$ , it is easy to calculate that derivative,  $(d\Theta/d\omega)_{\omega_o}$ , using only the first term in the Taylor series for  $\tan^{-1} x \cong x$ .<sup>15</sup>

$$\left. \frac{d\Theta}{d\omega} \right|_{\omega_o} = \frac{d(\tan^{-1} X_m/R_m)}{d\omega} \Big|_{\omega_o} = \frac{1}{R_m} \frac{d}{d\omega} \left( \omega m - \frac{K}{\omega} \right) \Big|_{\omega_o} = \left[ \frac{m + \frac{K}{\omega^2}}{R_m} \right]_{\omega_o} \quad (2.75)$$

Evaluation of that derivative at  $\omega = \omega_o$ , and substitution of  $Q = \omega_o m / R_m$  and  $K = \omega_o^2 m$ , relates the rate of change of phase with respect to frequency to the quality factor.

$$\left. \frac{d\Theta}{d\omega} \right|_{\omega_o} = \frac{2m}{R_m} = \frac{2Q}{\omega_o} \quad \text{or} \quad \left. \frac{d\phi}{df} \right|_{f_o} = \frac{360^\circ}{\pi} \frac{Q}{f_o} \cong 114.6^\circ \frac{Q}{f_o} \quad (2.76)$$

The right-hand version uses  $\phi$  to indicate the phase difference in degrees, rather than  $\Theta = \pi\phi/180^\circ$ , which was in radians, since the phase angle is more commonly reported in degrees by instrumentation or in computer models. This also produces another valuable expression for the quality factor in terms of the rate of change of phase difference with frequency at resonance.

$$Q = \left| \frac{\pi f_o}{360^\circ} \frac{d\phi}{df} \right|_{f_o} \cong \left| \frac{f_o}{114.6^\circ} \frac{d\phi}{df} \right|_{f_o} \quad (2.77)$$

The absolute value is specified since the sign of the slope can be either positive or negative, depending upon the parity of the resonances, in systems with multiple resonances that occur for standing waves in continuous vibrators, like strings (see Sect. 3.3) or plane wave resonators (see Sect. 10.6).

In many circumstances, it is much easier to fit a straight line (see Sect. 1.9) to the phase difference vs. frequency, close to the zero-crossing (near resonance), to determine  $Q$  than it is to use the  $-3$  dB bandwidth of Eq. (2.69). One such example is provided for the Helmholtz resonator in Sect.

<sup>15</sup> It is easy to see that  $\tan^{-1} x \cong x$  by inspection of the first term in the Taylor series expansion of  $\tan x \cong x$  in Eq. (1.7) for small values of  $x \ll 1$ .

[8.5.2.](#) The phase vs. frequency for that resonance is plotted near the resonance frequency in Figs. [8.32](#) and [8.33](#).

Returning to the control question, we see that phase difference between the drive and the response generates an “error signal” proportional to the de-tuning that provides the information required by a control system to correct deviations between the drive frequency,  $\omega$ , and the natural frequency,  $\omega_o$ . It provides a parameter that has one sign if the system is driven sharp and the opposite sign if the system is driven flat. That error signal is nearly linear in its deviation for small frequency shifts away from the resonance frequency.

The extraction of such an error signal, proportional to the phase difference, can be accomplished by multiplication of the drive and response signals followed by a low-pass filtering of the product.<sup>16</sup> The drive signal will be our “reference,” having constant amplitude and a frequency,  $\omega$ . The reference waveform could include a phase shift,  $\phi_r$ , due to the response of electronics, cables, etc., but we will allow  $\phi_r$  to have an adjustable component as well:  $F(t) = F_1 \sin(\omega t + \phi_r)$ . The steady-state response (signal) will have an amplitude given by Eq. [\(2.62\)](#) and must also have the same frequency,  $\omega$ , since we assume a linear response, but it will have a different phase,  $\phi_s$ , that will combine  $\Theta$  of Eq. [\(2.61\)](#) and any electronic phase shifts:  $v(t) = v_1 \cos(\omega t - \phi_s)$ . The following trigonometric identity will simplify the resulting product.

$$(\sin x)(\cos y) = \frac{1}{2} [\sin(x+y) + \sin(x-y)] \quad (2.78)$$

$$F(t)v(t) = \frac{F_1 v_1}{2} \{ \sin[2\omega t + (\phi_r + \phi_s)] + \sin(\phi_r - \phi_s) \} \quad (2.79)$$

Both signals are assumed to be electrical waveforms generated by the driving force and some velocity transducer, and their product is also an electrical waveform.<sup>17</sup> If the product is passed through a low-pass filter with a cut-off frequency,  $2\pi f_{-3 \text{ dB}} \ll \omega$ , then the component at twice the drive frequency will be strongly attenuated, and only a signal proportional to the sine of the phase difference will remain. If the electronically induced phase shifts are adjusted to make the phase difference  $(\phi_r - \phi_s) \cong 0$  at resonance, then the output of the low-pass filter will be just the error signal that was sought for control of the drive frequency.<sup>18</sup>

The low-pass filtered signal can be fed back to a voltage-controlled oscillator<sup>19</sup> to drive the system at its resonance frequency. This strategy, known as a *phase-locked loop*, is used in many applications outside of acoustics [\[22\]](#).

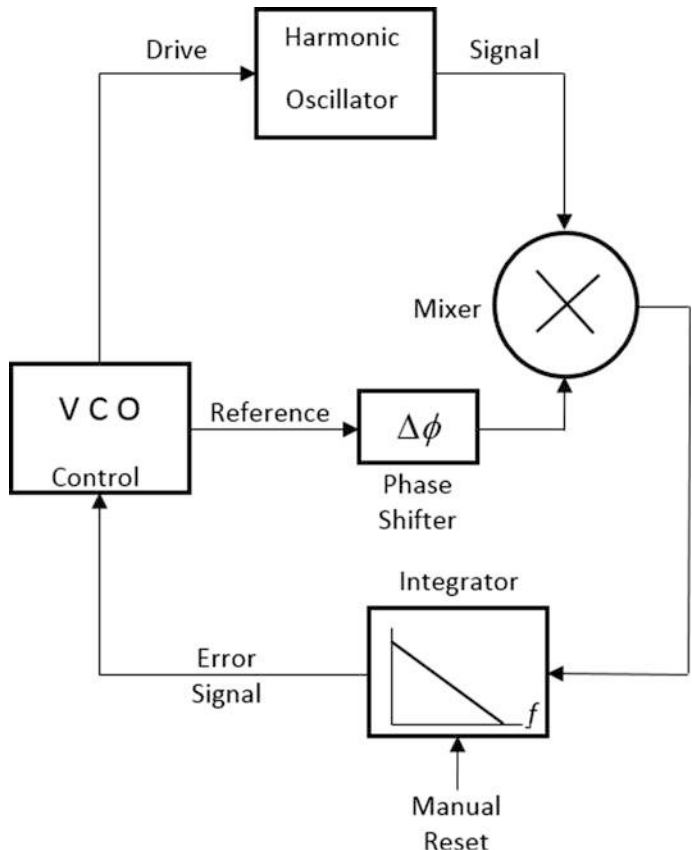
<sup>16</sup> The “multiplication” can be done either digitally or using analog electronics. Various analog schemes can be implemented ranging from a simple “optional inverter” [\[11\]](#) that synchronizes a square waveform with the reference to multiply the signal by  $\pm 1$  to the use of a four-quadrant analog multiplication integrated circuit (e.g., Analog Devices AD633).

<sup>17</sup> Of course, it is possible that those signals were digitized prior to multiplication, and the operation of Eq. [\(2.79\)](#) was executed in a computer. For now, I will continue to treat the signals as analog electrical waveforms (“cause I’m an “old guy”).

<sup>18</sup> An integrator is often used instead of a low-pass filter since it can provide a non-zero output to the voltage-controlled oscillator that forces the phase difference to zero. If a low-pass filter is used, then a non-zero phase difference is required to provide the correction to the voltage-controlled oscillator, so the system will have to be driven slightly off-resonance to provide an adequate error signal. As the gain is increased to minimize the offset, the electronic system can become oscillatory (i.e., unstable).

<sup>19</sup> Analog integrated circuits that are voltage-controlled oscillators are readily available and very inexpensive for a wide variety of frequency ranges. For audio applications, I have used an Exar XR2206 that provides both a square-wave and low-distortion sine wave output and also includes a voltage-controlled amplifier to facilitate automatic gain control.

**Fig. 2.15** This block diagram illustrates the signal flow in a phase-locked loop frequency tracking circuit meant to maintain a driven harmonic oscillator at its resonance frequency by generation of an error signal proportional to the phase difference between the drive and the response. In this diagram, an integrator is used as the low-pass filter, since it can provide a non-zero output to control the VCO when the phase difference has been driven to zero. The mixer executes the multiplication in Eq. (2.79)



It is not the intention of this textbook to provide detailed electronic strategies for tracking resonances, but it is very important to appreciate the utility of the phase difference between the drive and response of a simple harmonic oscillator, as well as the frequency dependence of the amplitude. Such feedback control systems have to be designed carefully to avoid instabilities, but the combination of digital or analog electronics that can provide phase detection and stability at a level of  $\pm 0.01^\circ$  at very modest cost, combined with the high rate of change of phase with frequency shown in Eq. (2.76) for resonators with even modest quality factors, is a very powerful tool in a variety of acoustical control applications. A block diagram of one possible implementation of such a frequency tracking phase-locked loop (PLL) is shown in Fig. 2.15.

## 2.5.4 Transient Response

Thus far, in our analysis of the damped driven simple harmonic oscillator, we have focused on the steady-state solution that is determined entirely by the oscillator's mechanical impedance, given in Eq. (2.58) or Eqs. (2.60) and (2.61). As mentioned earlier, the equation that describes the dynamics of the undriven system is identical to Eq. (2.55) but homogeneous. The solution to Eq. (2.39) can be added to the steady-state solution to incorporate the initial conditions at the time the harmonic forcing

function,  $F(t) = \Re e[\hat{\mathbf{F}}e^{j\omega t}]$ , is applied to the mass through the specification of the undetermined amplitude,  $|\hat{\mathbf{C}}|$ , and phase,  $\phi$ , or at the time the excitation is removed.

$$x(t) = |\hat{\mathbf{C}}| e^{-t/\tau} \cos(\omega_d t + \phi) + \frac{|\hat{\mathbf{F}}|}{\omega |\mathbf{Z}_m|} \sin(\omega t - \Theta) \quad (2.80)$$

The contribution of the transient term can initially interfere with the steady-state solution, but eventually the transient solution will diminish after a number of periods that spans any interval longer than  $\tau$ .

Possibly more important are the consequences of the transient term which follow the removal of the forcing function. The reason is that it is possible that the amplitude of the steady-state solution can become quite large, especially if the system is being driven at a frequency that is close to its natural (resonance) frequency,  $\omega_o$ . When the forcing ceases, the system will *ring down*, decaying at its damped frequency,  $\omega_d$ . The acoustic radiation from this ring down is a serious problem for sound reproduction systems at low frequencies producing undesirable “boominess in the bass.”

An accomplished musician, playing an electric bass guitar, will frequently damp the motion of a string, abruptly cutting off the force that the instrument (through the pick-up and amplifier) applies to the loudspeaker. If the loudspeaker (in its enclosure) is significantly under-damped, the sound radiated after the electric bass’s string has stopped vibrating will be dominated by the decay of the loudspeaker’s motion. That sound will decay at  $\omega_d$ , independent of the note played by the bassist. In certain high-power automotive sound systems, this effect, caused by the ring down, can be particularly unpleasant.

The effects of the transient term in Eq. (2.80) provide insights into the growth and decay of the response of a damped, driven harmonic oscillator that are particularly useful when that system is driven at the resonance (natural) frequency,  $\omega_o$ . At  $t = 0$ , the response is zero, so  $C$  equals the steady-state amplitude and the transient term is  $180^\circ$  out-of-phase with the steady-state solution. As the transient portion decays with an exponential time constant,  $\tau$ , the response amplitude grows. For early times,  $t < \tau$ , after the application of the force, the sum of the transient and the steady-state solution creates a maximum amplitude envelope,  $|A(t)|$ , that initially grows linearly with time.

$$|A(t)| = A_1 \left( 1 - e^{-t/\tau} \right) \quad (2.81)$$

In this expression,  $A_1$  is the steady-state amplitude response to the driving force. For times that are less than  $\tau$ , the exponential can be approximated by the first two terms in the Taylor series expansion of Eq. (1.4), so the initial growth of the amplitude envelope will be approximately a linear function of time after the application of the driving force, as shown in Fig. 2.16.

$$|A(t)| = A_1 \left( 1 - e^{-t/\tau} \right) \cong A_1 \left[ 1 - \left( 1 - \frac{t}{\tau} + \dots \right) \right] \cong A_1 \frac{t}{\tau} \quad \text{for } t \leq \tau \quad (2.82)$$

Using this linear approximation for the initial growth of the resonance, we can approximate the time,  $t_{1/2}$ , it takes for the amplitude of the resonance to grow to one-half of its steady-state value, since initially  $dA/dt \cong (A/\tau)$ .

$$\frac{|A(t_{1/2})|}{A_1} = \frac{1}{2} \cong \frac{t_{1/2}}{\tau} = \frac{Q}{2\pi f_o} = \frac{Q}{2\pi} T \quad (2.83)$$

It takes approximately  $(Q/2\pi)$  cycles for the response of a system driven at its resonance frequency to reach half its steady-state amplitude.

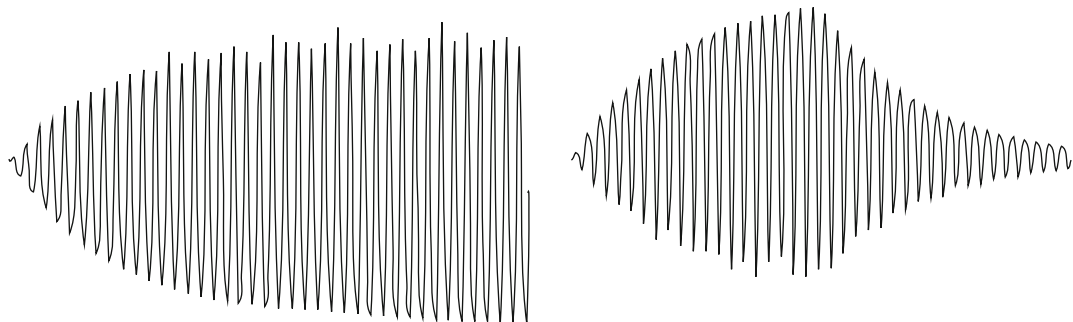


**Fig. 2.16** The growth and decay of a damped harmonic oscillator driven at its natural frequency  $\omega_o$ . In this example,  $Q \cong 25$ . The response grows to about half of its steady-state value after about five cycles. Once the drive is cut off, the freely decaying sinusoid has a frequency,  $\omega_d$ , which has a relative difference from  $\omega_o$  of only 0.02%. (Figures courtesy of J. D. Maynard [23])

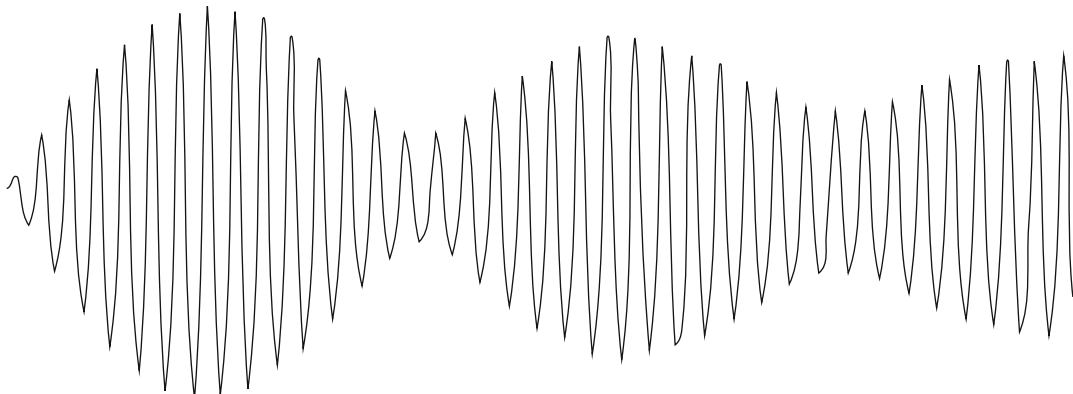


**Fig. 2.17** This response is generated by an oscillator with  $Q = 80$  driven slightly off resonance. The transient solution beats against the steady-state solution. Forty cycles are shown, but after about 80 cycles, the transient contribution would be negligible. (Figures courtesy of J. D. Maynard [23])

Since the drive frequency is  $\omega_o$  and the frequency of the transient contribution is  $\omega_d \neq \omega_o$ , one might ask whether those two solutions might not maintain the phase relation we assumed to fit the initial condition of zero amplitude as time increases. As calculated in Eq. (2.45), the relative differences in those two frequencies are small and are related to the square of the quality factor.

$$\frac{\omega_o - \omega_d}{\omega_o} \cong \frac{1}{8Q^2} \quad (2.84)$$

By the time the resonance has grown to one-half its steady-state amplitude, the phase difference,  $\varphi(t_{1/2})$ , between the transient and steady-state solutions, will equal  $\varphi(t_{1/2}) = \delta\omega \cdot t_{1/2} = (8Q)^{-1} = 45^\circ/Q$ , so de-phasing of those two terms of slightly different frequencies is insignificant for high- $Q$  systems.

If the driving frequency is slightly different from the natural frequency, the transient and the steady-state solutions can “beat” against each other until the transient solution has decayed. This behavior is illustrated in Fig. 2.17. When slightly off resonance, the transient and the steady-state solutions can destructively interfere to nearly zero; if the drive is turned off at that time, the ring-down is nearly eliminated.

### 2.5.5 The Electrodynamic Loudspeaker

The moving-coil electrodynamic loudspeaker is a nearly perfect example of a force-driven, damped, simple harmonic oscillator. It is particularly useful because passing an alternating electrical current through the loudspeaker's voice coil provides an easy method to control the magnitude and frequency of the force applied to the moving mass,  $m_o$  (i.e., cone, voice coil, and former). The parts of such a loudspeaker are shown schematically in Fig. 2.18 (right). The voice coil can also be used as a velocity transducer since it will produce an open-circuit voltage that is directly proportional to the velocity of the moving mass.

In this section, we will use data taken from a “typical” electrodynamic loudspeaker<sup>20</sup> to determine the parameters that characterize the behavior of this simple harmonic oscillator:  $m_o$ ,  $K$ , and  $R_m$ . The “ $B\ell$  – product” is the transduction coefficient that connects the alternating electrical current,  $I(t) = \Re e[\hat{\mathbf{I}}e^{j\omega t}]$ , to the force on the voice coil:  $F(t) = (B\ell)I(t)$ . In this case,  $(B\ell)$  is the product of the magnitude of the magnetic induction,  $|\vec{B}|$  [T],<sup>21</sup> times the length,  $\ell$  [m], of the wire wound around the “former” to create the voice coil. Of course, we want to determine all of these parameters as accurately as possible without causing any damage to the loudspeaker.

The accurate determination of a loudspeaker’s parameters is crucial for the design of a speaker system or headphones that are intended to reproduce music and/or speech. It also can provide important insight into the consistency of the manufacturing processes. In this section, one measurement method is described that exploits the description that was developed in this chapter to understand the damped driven harmonic oscillator. Although this approach may not be appropriate for production-line testing, it can provide “ground truth” to certify the validity of a production-line testing procedure.

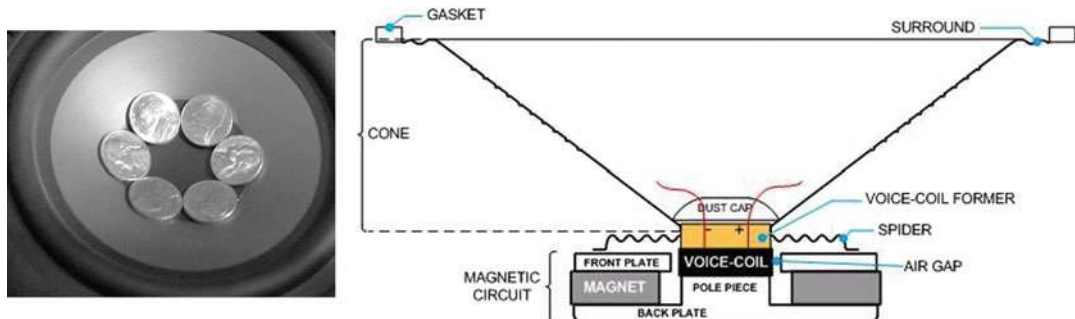


**Fig. 2.18** (Left) Photograph looking down on a loudspeaker with six nickels resting on the cone surrounding the dust cap. (Right) Schematic representation of a moving-coil electrodynamic loudspeaker. The surround and spider center the voice coil in the air gap and provide the restoring stiffness,  $K$ , to center the voice coil in the magnet gap. The mass of the voice coil, voice coil former, dust cap, and a portion of the masses of the surround and spider all contribute to the moving mass,  $m_o$ . The magnetic circuit, consisting of the permanent magnet material in a high magnetic permeability fixture (back plate, front plate, and pole piece), provides a radial magnetic flux,  $|\vec{B}|$ , in the air gap that is everywhere perpendicular to the wire of length,  $\ell$ , wound around the voice coil former

<sup>20</sup> Axon model 6S3 Mid-Bass Woofer with a cone diameter of about 6" (16 cm)

<sup>21</sup> The tesla [T] is the SI unit of magnetic induction. The older c.g.s. unit is the gauss, which still appears in some of the loudspeaker literature: 1.0 T = 10,000 gauss.

The stiffness,  $K$ , and moving mass,  $m_o$ , can be determined by adding known masses,  $m_i$ , to the cone and measuring the loudspeaker's resonance frequencies,  $f_i$ , with each added mass. When the voice coil is driven by a constant current source (i.e., the current is independent of the electrical load presented by the voice coil),<sup>22</sup> the voltage across the voice coil has its maximum value at resonance. This is a direct consequence of *Lenz's Law*, which is responsible for the minus sign in *Faraday's law of induction*:  $V = - (d\Phi/dt)$ . The magnetic flux,  $\Phi$ , is the product of the magnitude of the magnetic induction,  $|\vec{B}|$ , and an area with a normal that is perpendicular to the direction of  $\vec{B}$ . The "back electromotive force (*emf*)," represented by the induced voltage,  $V$ , will have its maximum value at resonance since the rate of change of the flux is proportional to the velocity of the voice coil.

Convenient masses to use for such an experiment are the US nickel, which weighs exactly 5.000 g.<sup>23</sup> Care must be taken to keep the electrical current through the voice coil at a low enough level that the peak acceleration of the loudspeaker cone never exceeds the acceleration due to gravity. At greater accelerations, the coins will "bounce," since they cannot fall back fast enough to track the displacement of the cone. The data acquired for measurement of the resonance frequencies,  $f_i$ , corresponding to the addition of  $m_i = (0.005 \text{ kg}) i$ , is tabulated on the left side of Fig. 2.19 for  $i = 0, 1, 2, 3, 4$ , and 5.

The natural frequency of the loudspeaker, with the added masses, is given simply by the square root of the ratio of the suspension stiffness,  $K$ , and the total moving mass,  $m_o + m_i$ .

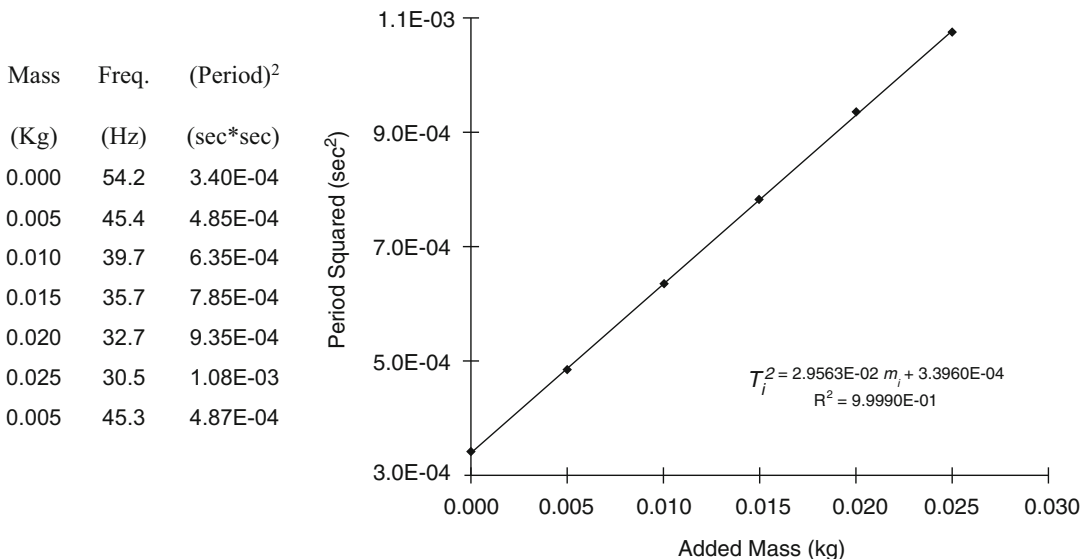


**Fig. 2.19** (Left) Table of frequencies and squared periods for an electrodynamic loudspeaker's resonance with between zero and five US nickels placed on the cone (see Fig. 2.18). (Right) Plot of period squared,  $T_i^2$ , vs. added mass,  $m_i$ .  $R^2$  is the square of the correlation coefficient (see Sect. 1.9.1)

<sup>22</sup> In practice, it is easy to approximate a constant current source by placing an electrical resistor,  $R_c$  (commonly referred to as the "current limiting resistor"), in series with the output of a signal (voltage) generator that is large compared to the largest magnitude of the loudspeaker's input electrical impedance  $|Z_{el}| \ll R_c$ . For these measurements,  $|Z_{el}| < 100 \Omega$ , so  $R_c \cong 1 \text{ k}\Omega$  was adequate to keep the current sufficiently constant.

<sup>23</sup> The US Mint website provides mass specifications for US coinage: [www.usmint.gov](http://www.usmint.gov). The US penny is 2.500 gm.

$$f_i = \frac{1}{2\pi} \sqrt{\frac{K}{m_o + m_i}} \quad (2.85)$$

That equation has only two unknown parameters:  $m_o$  and K. The technique of linearized least-squares fitting, introduced in Sect. 1.9.3, can be used to transform Eq. (2.85) into a linear relationship between the square of the period,  $T_i^2 = (f_i^2)^{-1}$ , and the added masses,  $m_i$ .

$$\frac{1}{f_i^2} = T_i^2 = \frac{4\pi^2}{K} (m_0 + m_i) = \frac{4\pi^2}{K} m_0 + \frac{4\pi^2}{K} m_i \quad (2.86)$$

In this form, the slope of the line plotted in Fig. 2.19 (Right) is  $4\pi^2/K$ . The value of the intercept divided by the value of the slope provides the moving mass,  $m_o$ .

Visual inspection of the graph in Fig. 2.19 suggests that the tabulated measurements are well-represented by Eq. (2.86). The techniques described in Sect. 1.9.2 relate the square of the correlation coefficient,  $R^2$ , to the relative uncertainty in the slope, providing the following value for the measured suspension stiffness and its uncertainty based on those six measured resonance frequencies:  $K = 1335 \pm 7 \text{ N/m}$  ( $\pm 0.5\%$ ). Here, the reported uncertainty corresponds to one standard deviation ( $\pm 1\sigma$ ).

The relative uncertainty in the intercept is  $\pm 0.6\%$ . Since the moving mass involves the ratio of the intercept to the slope, the relative uncertainties in both the slope and the intercept need to be combined in a Pythagorean sum, as discussed in Sect. 1.8.4.

$$\frac{\delta m_o}{|m_o|} = \left[ \left( \frac{\delta(\text{slope})}{|\text{slope}|} \right)^2 + \left( \frac{\delta(\text{intercept})}{|\text{intercept}|} \right)^2 \right]^{1/2} = \sqrt{(0.5\%)^2 + (0.6\%)^2} = 0.8\% \quad (2.87)$$

This results in an experimental value for the loudspeaker's moving mass:  $m_o = (11.5 \pm 0.1) \times 10^{-3} \text{ kg}$ . Again, the estimated error reflects an uncertainty of one standard deviation ( $\pm 1\sigma$ ).

The mechanical resistance can be determined from a simple free-decay experiment. I find it convenient to build a simple switching circuit<sup>24</sup> that allows me to drive the speaker near its resonance frequency and then cut the drive while simultaneously triggering a digital oscilloscope and recording the voltage generated by the voice coil that is then connected to the input of that oscilloscope (see Fig. 1.18), which is directly proportional to the velocity of the voice coil.

The data from the free-decay measurement on this loudspeaker were used as the example for fitting an exponentially decaying signal to a straight line by taking the logarithm of the output voltage differences between successive peaks and troughs of the damped sinusoidal waveform. The natural log of these voltage differences is plotted in Fig. 1.15. The linearized least-squares fit produced an exponential decay time of  $\tau = (22.18 \pm 0.17) \times 10^{-3} \text{ s}$ . A fit to the cycle number vs. the time for the voltage zero-crossings, using the same data, provided a measurement of the free-decay frequency and its uncertainty:  $f_d = 51.82 \pm 0.17 \text{ Hz}$ .

The mechanical resistance is related to both the decay time,  $\tau$ , and the moving mass,  $m_o$ ,  $R_m = 2m_o/\tau$ , so the relative uncertainties for both quantities have to be combined in a Pythagorean sum, as was done previously in Eq. (2.87). This results in a measured value of  $R_m = 1.04 \pm 0.01 \text{ kg/s}$ .

<sup>24</sup> Such a switch can be as simple as a double-pole double-throw toggle switch with one pole controlling a battery that provides a triggering voltage to the oscilloscope and the other pole used to move the voice coil from the output of the signal generator to the input of the oscilloscope that acquires and stores the free-decay time history, like the one shown in Fig. 1.18 and analyzed in Fig. 1.15.

Having determined  $R_m$ , it is possible to measure the  $B\ell$ -product if the DC electrical resistance of the voice coil,  $R_{dc}$ , is known, and the magnitude of the electrical impedance at resonance,  $|\mathbf{Z}_{el}(f_o)| = V_{ac}(f_o)/I_{ac}(f_o)$ , is measured. At resonance, the voltage and current are in-phase (thus allowing use of the rms values of  $V$  and  $I$ ), if the voice coil's inductance,  $L$ , can be neglected:  $\omega_o L \ll R_{dc}$ . At resonance,  $X_m = 0$ , and the expression for the velocity of the voice coil is very simple in the resistance-controlled regime.

$$v(f_o) = \frac{F}{R_m} = \frac{(B\ell)I}{R_m} \quad (2.88)$$

A voltage across the voice coil will be produced, in accordance with Faraday's law, by the back-emf,  $V_{emf}$ , generated by the velocity,  $v$ , of the voice coil of length,  $\ell$ , moving in the magnetic field of magnetic induction,  $|\vec{B}|$ .

$$V_{emf}(f_o) = (B\ell)v = \frac{(B\ell)^2 I}{R_m} \quad (2.89)$$

The ohmic voltage across the voice coil,  $V_\Omega$ , is due to the current through  $R_{dc}$ :  $V_\Omega = R_{dc} I$ . Since both voltages are in-phase with the current, the magnitude of the total electrical impedance measured at resonance,  $|\mathbf{Z}_{el}(f_o)|$ , is just the sum of those two voltages divided by the electrical current,  $I$ .

$$|\mathbf{Z}_{el}(f_o)| = \left| \frac{V}{I} \right|_{f_o} = \frac{(B\ell)^2}{R_m} + R_{dc} \quad \Rightarrow \quad (B\ell) = \sqrt{R_m(|\mathbf{Z}_{el}(f_o)| - R_{dc})} \quad (2.90)$$

This method for measurement of the  $B\ell$ -product will not have the same accuracy as the mechanical measurements for  $m_o$ ,  $K$ , and  $R_m$ , since  $R_m$  was measured when the voice coil was an open circuit and there is a non-zero current passing through the voice coil when  $|\mathbf{Z}_{el}|$  is being measured. This introduces other losses related to eddy currents induced in the metallic portions of the magnetic circuit and hysteresis in the orientation of the domains of the permanent magnetic materials [24], but with a reasonably large current-limiting resistor, these additional error sources can be minimized.

All of the moving-coil loudspeaker's mechanical parameters have been determined with a relative uncertainty of  $\pm 1\%$  or less using a few coins, an electrical resistor to hold current constant, a signal generator, an AC voltmeter, and a digital storage oscilloscope. This approach is so simple it can be used as a teaching laboratory exercise for college freshmen in a first-year seminar [25]. The fact that such simple, inexpensive, and highly accurate determinations of the parameters that characterize the linear behavior of electrodynamic loudspeakers are not widely appreciated, as evidenced by the following quotation [26]:

The added mass technique, discussed by Beranek [27] and others, requires a known, appreciable mass to be carefully attached to a diaphragm with appropriate distribution and driver orientation. The enclosed volume technique,<sup>25</sup> discussed by Thiele [28] and others, requires the use of an airtight box with known enclosed volume after a driver has been mounted to it. Both approaches can be time consuming and problematic in implementation, with relative bias errors often reaching 10% or higher.

---

<sup>25</sup>The “enclosed volume technique” is similar to the added mass technique just described except instead of adding masses; the gas stiffness of the enclosure is used to measure the resonance frequency while changing the total stiffness. See Problem 4 at the end of this chapter.

## 2.5.6 Electrodynamic (Moving-Coil) Microphone

The electrodynamic loudspeaker is a *reversible transducer*. Sound is generated by placing an alternating electrical current through the loudspeaker's voice coil. If the same speaker is placed into a sound field, the oscillating pressure difference (assuming the back of the speaker's cone is isolated from the oscillating pressure) of the sound will cause the speaker's diaphragm to vibrate.

If we start the analysis by assuming that the flow resistance shown in Fig. 2.20 (Left) is infinite, then the air inside the microphone remains at a constant pressure,  $p_m$ , and the excess pressure due to one frequency component of a sound wave that impinges on the microphone's diaphragm can be represented as  $p(t) = \Re[\hat{\mathbf{p}} e^{j\omega t}]$ . If the microphone has an area,  $A_{mic}$ , then the force on the diaphragm is  $F_1(t) = A_{mic} \Re[[\hat{\mathbf{p}} | e^{j\omega t}]$ . The microphone's moving mass (i.e., diaphragm and coil); suspension stiffness,  $K$ ; and mechanical resistance,  $R_m$ , determine the microphone's (complex) mechanical impedance,  $\mathbf{Z}_m$ , so that the velocity of the coil is given by Eq. (2.62). Again, by Faraday's law,  $V_{emf}(t) = (B\ell)v_1(t)$ .

Operating as just described, such an electrodynamic microphone would have very uneven frequency response. During the second half of the twentieth century, small loudspeakers were used as both a sound source and a microphone in intercommunication systems for multistory dwellings. A resident could listen to someone at the front door and then press a switch that changed the mode of operation of the loudspeaker into a microphone and hear the voice of the visitor. In such an application, the fidelity was adequate for speech intelligibility.

The success of the electrodynamic microphone in both sound reinforcement and recording applications was due to Benjamin Baumzweiger (who later changed his name to Bauer), in 1937, who added the flow resistance shown in Fig. 2.20 (left) [29]. As just described, if the oscillating acoustic pressure is only applied to the outer surface of the microphone diaphragm, then the response of the microphone will be omnidirectional, if the wavelength of the sound is greater than the size of the diaphragm. If the acoustic pressure could reach both sides of the diaphragm, then the microphone would have a figure-eight (bi-directional) response pattern [30]. Bauer realized that a resistive element, in combination with the internal volume of the microphone, would provide access for the pressure at a small distance from the front of the microphone which could produce an intermediate (cardioid)

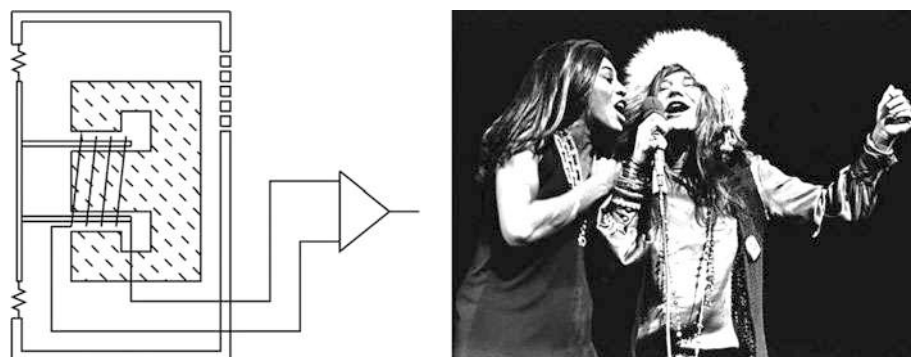


**Fig. 2.20** (Left) Schematic diagram of an electrodynamic (moving-coil) microphone. An oscillatory pressure difference between the outside and the inside of the microphone's case exerts an oscillating force on the diaphragm causing the coil (shown connected to the input of an amplifier) to vibrate within the radial magnetic field produced by the hatched magnet structure. At the upper right of the microphone's enclosure is a porous medium that provides a flow resistance. Silk cloth is commonly used to provide the required flow resistance (see Sect. 12.5.3) (Diagram courtesy of J. D. Maynard). (Right) An electrodynamic microphone is shared by Tina Turner and Janis Joplin (Photo by Amalie R. Rothschild from the collection of Susan Levenstein and Alvin Curran)

**Fig. 2.21** The Shure Model 55 “Unidyne®,” (right) was the first product to incorporate the electrodynamic microphone strategy diagrammed schematically in Fig. 2.19 (left). (Left) The later model SM58 used a similar capsule. It is shown in use (with windscreens) in Fig. 2.19 (right). (Images used by permission, Shure, Inc.)



directivity pattern and that making the mechanical system resistance-controlled, the frequency response would be fairly uniform over a large range of frequencies.<sup>26</sup>

The first such single-element unidirectional electrodynamic microphone that used a single diaphragm, back-vented through a flow resistance, is the iconic Shure “Unidyne®” Model 55 shown in Fig. 2.21 (right) [31]. Later models, with the same type of microphone capsule, appeared in other packages like the Model SM58, shown in Fig. 2.21 (left), which has been the best-selling vocal microphone for the past 30 years.

### 2.5.7 Displacement-Driven SHO and Transmissibility

The decision to first analyze a damped simple harmonic oscillator, driven by a single-frequency sinusoidal force of constant amplitude,  $\mathbf{F}$ , that is applied to the mass, was an arbitrary choice. In this section, the response of the same system will be analyzed but driven by a constant amplitude displacement,  $x_o(t) = \Re[\hat{\mathbf{x}}e^{j\omega t}]$ , applied at the end of the spring that is not attached to the mass. Since the driving frequency,  $\omega$ , is determined, the effects of a constant displacement, constant velocity, or constant acceleration that is applied to the end of the spring will be similar, differing only by one or two factors of  $j\omega$ .

This situation is diagrammed schematically in Fig. 2.22. Such an arrangement is fairly typical of a vibration isolation system that is intended to support a sensitive instrument (phonograph, microphone, disk drive, atomic force microscope, etc.) and isolate it from the vibrations of the foundation on which it is supported.

The mass will be accelerated due to the force applied by the spring and by the dashpot.

$$K(x_o - x_2) - R_m \dot{x}_2 = m \ddot{x}_2 \quad \text{or} \quad Kx_o = m \ddot{x}_2 + R_m \dot{x}_2 + Kx_2 \quad (2.91)$$

Dividing this equation by  $m$  and letting  $x_o(t) = \Re[\hat{\mathbf{x}}e^{j\omega t}]$  transforms the above differential equation into an algebraic equation

<sup>26</sup>A systematic analysis of the directivity pattern of acoustic sensors will be provided in Sect. 12.5.

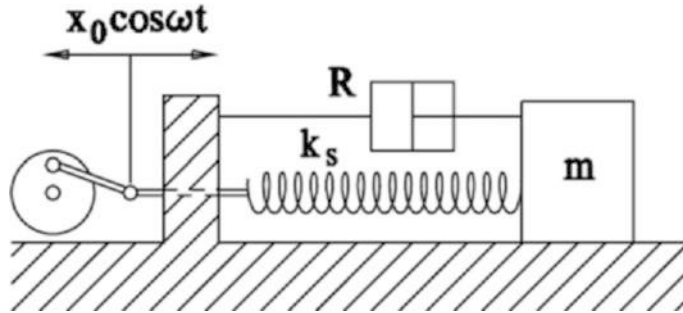


**Fig. 2.22** In this configuration, a sinusoidal displacement is applied to the end of the spring located at  $x_o$ . A mass is attached to the other end of the spring with the junction between the mass and spring defining the position  $x_2(t)$ . One terminal of a dashpot, having a mechanical resistance,  $R_m$ , is attached to the mass, and the other terminal is rigidly fixed so the dashpot exerts a resistive force,  $F = -R_m(dx_2/dt)$ . (Diagram courtesy of J. D. Maynard)

$$\omega_o^2 x = -\omega^2 x_2 - j\omega \frac{R_m}{m} x_2 + \omega_o^2 x_2 \quad (2.92)$$

The steady-state solution for the mass's displacement,  $x_2(t)$ , is then rather reminiscent of our force-driven solution in Eq. (2.57).

$$x_2(t) = \Re e \left[ \frac{\omega_o^2 \hat{x}_2 e^{j\omega t}}{(\omega_o^2 - \omega^2) + j\omega \frac{R_m}{m}} \right] = \Re e \left[ \frac{m\omega_o^2 \hat{x}_2 e^{j\omega t}}{j\omega [R_m + j(\omega m - \frac{k}{\omega})]} \right] \quad (2.93)$$

If the mass's response is expressed in terms of its complex velocity,  $\mathbf{v}_2(t) = \dot{\mathbf{x}}_2(t) = j\omega \mathbf{x}_2(t)$ , then the steady-state solution that was expressed in terms of our complex mechanical impedance,  $\mathbf{Z}_m$ , is recovered, as though  $m\omega_o^2 x_o$  had been substituted for  $F_1$  in Eq. (2.57).

$$\hat{\mathbf{v}}_2 = \hat{\mathbf{x}}_2 = \frac{m\omega_o^2 x_o}{\mathbf{Z}_m} \quad (2.94)$$

Many features of this solution should now be familiar. When driven at the resonance frequency,  $\omega_o$ , the displacement amplitude of the mass,  $x_2$ , is “amplified” by the quality factor of the oscillator.

$$|\frac{\hat{\mathbf{x}}_2}{\hat{\mathbf{x}}}|_{\omega_o} = \frac{\omega_o^2 m}{\omega_o R_m} = \frac{\omega_o m}{R_m} = Q \quad (2.95)$$

If the frequency of the drive,  $\omega$ , is much greater than  $\omega_o$ , the oscillator operates in its mass-controlled regime, so that the motion of the mass is reduced from that of the foundation.

$$\lim_{\omega \gg \omega_o} |\frac{\hat{\mathbf{x}}_2}{\hat{\mathbf{x}}}| = \lim_{\omega \gg \omega_o} |\frac{\hat{\mathbf{v}}_2}{\hat{\mathbf{x}}}| = \lim_{\omega \gg \omega_o} |\frac{\hat{\mathbf{a}}_2}{\hat{\mathbf{x}}}| = \frac{\omega_o^2}{\omega^2} \quad (2.96)$$

In this mass-controlled limit, the displacement, velocity, or acceleration decreases by a factor of four for each reduction in  $\omega_o$  by a factor of two. Of course, it is possible to stack multiple harmonic oscillator stages in series and produce even larger reductions in the transmissibility of a vibration isolator.

The similarity between the force-driven and displacement-driven cases means that the same strategy can be used to reduce the force generated by a vibrating piece of machinery. In the case of a *vibration isolator*, the foundation moves both the spring and the damper. This is not the same as Fig. 2.22, where

one end of the resistance is fixed but is mechanically identical to the driven foundation of Fig. 2.23, where the mass is connected to the foundation through both the stiffness and the resistance elements.

As discussed in the following treatment of vibration sensors, our interest is in the relative motion of the mass and its foundation,  $\mathbf{z} \equiv \mathbf{x}_1 - \mathbf{x}_2$ . Equation (2.91) can be rewritten by substituting  $\mathbf{z} = \mathbf{x}_1 - \mathbf{x}_2$ .

$$m\ddot{\mathbf{z}} + R_m\dot{\mathbf{z}} + K\mathbf{z} = -m\ddot{\mathbf{x}}_1 = m\omega^2\hat{\mathbf{x}}_1 e^{j\omega t} \quad (2.97)$$

The complex *transmissibility*,  $T$ , is defined as the ratio of the motion of the mass, relative to the foundation,  $\mathbf{z}$ , divided by the motion of the foundation,  $\mathbf{x}_1$ , or the ratio of the force on the mass,  $\mathbf{F}_2$ , to the force on the foundation,  $\mathbf{F}_1$  [32]. If the drive frequency,  $\omega$ , is written in terms of the natural frequency,  $\omega_o$ , so  $\Omega = \omega/\omega_o$ , and the mechanical resistance is written in terms of the quality factor,  $R_m = \omega_o m/Q$ , then the magnitude of the transmissibility,  $|T|$ , and the phase angle between the displacements or forces,  $\theta_T$ , based on Eq. (2.93), can be put in a general form.

$$|T| = \left| \frac{\mathbf{z}}{\mathbf{x}_1} \right| = \left| \frac{\mathbf{F}_2}{\mathbf{F}_1} \right| = \frac{\sqrt{1 + (\Omega/Q)^2}}{\sqrt{(1 - \Omega^2)^2 + (\Omega/Q)^2}} \quad (2.98)$$

$$\theta_T = \tan^{-1} \left[ \frac{-\Omega^3/Q}{1 - \Omega^2 + (\Omega/Q)^2} \right] \quad (2.99)$$

A plot of  $|T|$  and  $\theta_T$  will look identical to those for the driven harmonic oscillator in Fig. 2.14. Similarly, the frequency dependence of the transmissibility of a damped harmonic oscillator (DHO) is compared to the transmissibility for vibration isolators using rubber springs is presented in Sect. 4.5.3 in Figs. 4.30, 4.31, and 4.33.

## 2.6 Vibration Sensors

The displacement-driven one-dimensional simple harmonic oscillator provides the basis for most common vibration sensors. Typically, such a sensor is housed in a case that will be mounted on a vibrating surface. A schematic diagram of such a sensor is shown in Fig. 2.23. Since the transduction

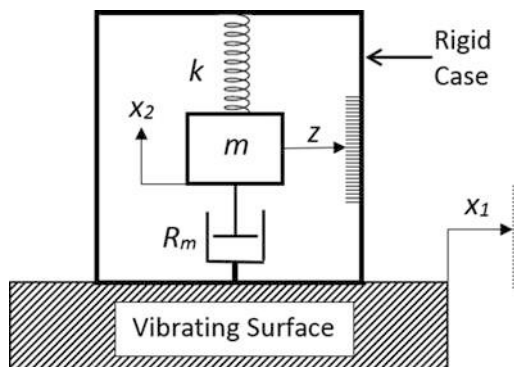


**Fig. 2.23** Generic vibration sensor contained within a rigid case that is attached to a vibrating surface. The displacement of the vibrating surface is given by  $\mathbf{x}_1(t)$  and the motion of the mass,  $\mathbf{m}$ , is given by  $\mathbf{x}_2(t)$ . The displacement of the mass, relative to the case, is given by  $\mathbf{z}$ , where the scale inside the case represents the sensor's transduction mechanism. Scales are provided for  $\mathbf{x}_1$  and for  $\mathbf{z}$ , where  $\mathbf{x}_1$  and  $\mathbf{x}_2$  are measured relative to a fixed coordinate system

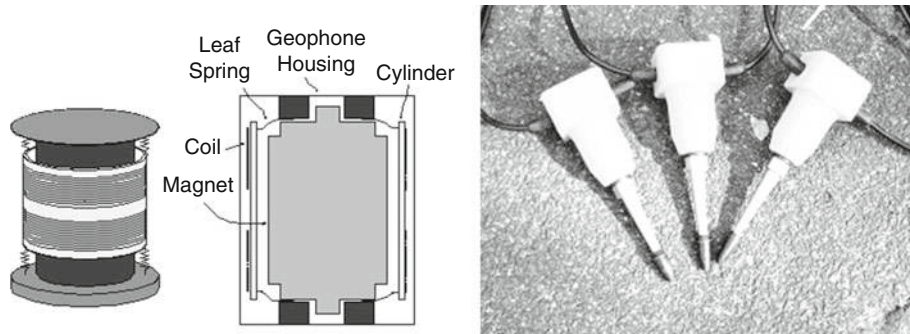


**Fig. 2.24** (Left) Schematic representation of a geophone containing a permanent magnet surrounded by a coil of wire wound around a cylinder. The leaf spring has a very small stiffness making the natural frequency much lower than the frequencies of interest. The weak suspension means that the coil is effectively stationary and the magnet, attached rigidly to the case, moves with the ground. The relative motion of the coil and magnet generates the electrical signal in the same way as the electrodynamic microphone. (Right) Three commercial geophones with spikes that facilitate their insertion into the ground

mechanism (e.g., piezoelectric or electrodynamic) is contained within the sensor, it can only measure the motion of the mass relative to the motion of the case, just as was done for the vibration isolator. The solution is identical to Eqs. (2.98) and (2.99).

Such vibration sensors are called seismic sensors (*seismometers*) or *geophones* if the sensor is operated in its mass-controlled regime where  $\Omega \gg 1$ . For that circumstance, the mass remains nearly at rest, and the transduction mechanism senses the relative motion of the case. If the transduction mechanism measures the relative displacement, then the sensor is a seismometer. If the transduction mechanism is a coil and magnet (i.e., electrodynamic), then the sensor's output is proportional to the relative velocity of the (nearly stationary) mass and the case, and the sensor is called a geophone.

Seismometers are used to measure earthquake activity, and geophones are usually used for exploration geophysics (e.g., finding sub-surface fossil fuel deposits). Frequently, dozens of geophones will be placed in the ground, and an explosive or vibratory mechanical source will be used to create seismic waves. The outputs of the geophones' response will be processed to create images of sub-surface features. Figure 2.24 shows the typical construction of a geophone.

It is easy to control the damping of the geophone by adjusting the electrical resistance across the output of the coil. The coil's motion, relative to the magnet, will generate the voltage,  $V_{emf} = (B\ell)v_{coil}$ , in accordance with Faraday's law. As shown in Fig. 1.20, the coil will have some electrical resistance,  $R_{int}$ , but if the load resistance,  $R_{load}$ , is infinite, no current will flow,  $I_{out} = 0$ , and the voltage across the coil's terminals will be  $V_{emf}$ .

If a load resistance is placed across the geophone's terminals, then the geophone's output voltage,  $V_{out}$ , will be reduced, and the current flowing through the coil and the load will be  $I_{out}$ , assuming the coil's inductance,  $L_{coil}$ , can be ignored (i.e.,  $\omega L_{coil} \ll [R_{int} + R_{load}]$ ).

$$V_{out} = \frac{R_{load}}{R_{int} + R_{load}} V_{emf} \quad \text{and} \quad I_{out} = \frac{V_{out}}{R_{load}} \quad (2.100)$$

The time-averaged power dissipated in the electrical circuit,  $\langle \Pi_{el} \rangle_t$ , will produce an equivalent mechanical dissipation that can be represented as an equivalent mechanical resistance,  $R_{eq}$ .

$$\langle \Pi_{el} \rangle_t = \frac{V_{emf} I_{out}}{2} = \frac{1}{2} \frac{V_{emf}^2}{R_{int} + R_{load}} = \frac{1}{2} \frac{(B\ell)^2 v_{coil}^2}{R_{int} + R_{load}} = \frac{1}{2} R_{eq} v_{coil}^2 \quad (2.101)$$

$$R_{eq} = \frac{(B\ell)^2}{R_{int} + R_{load}} \quad \Rightarrow \quad Q_{eq} = \frac{\omega_o m}{R_{eq}} \quad \Rightarrow \quad \frac{1}{Q_{total}} = \frac{R_m}{\omega_o m} + \frac{1}{Q_{eq}}$$

A geophone that gets quite a bit of use in our laboratory is the Geo Space GS-14-L3. It is contained within a small cylindrical capsule about 17 mm in both height and diameter. It has a natural frequency of  $f_o = \omega_o/2\pi \cong 28$  Hz. The coil has an internal resistance,  $R_{int} = 570 \Omega$ , and a moving mass of  $m = 2.15$  g. The inductance of the coil,  $L_{coil} = 45$  mH, so even at 1.0 kHz,  $\omega L_{coil}/R_{int} < \frac{1}{2}$ . Its output voltage as a function of frequency and electrical load resistance,  $R_{load}$ , is shown in Fig. 2.25.

If the vibration sensor is operated in its stiffness-controlled regime,  $\Omega \ll 1$ , then it is called an accelerometer. The motion of the case and the mass are nearly equal, and the transduction mechanism measures the force necessary to maintain their spacing. Two typical piezoelectric accelerometers are shown in Fig. 4.6 and are analyzed in Sect. 4.3.1.

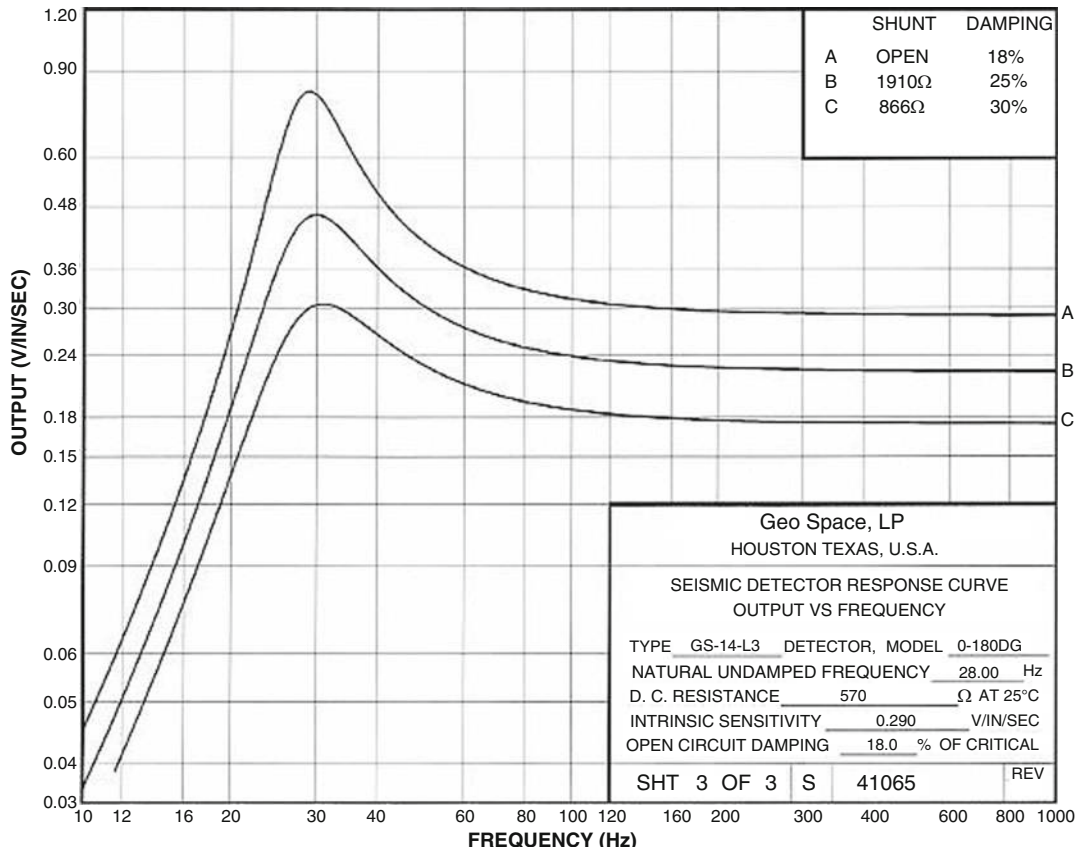


**Fig. 2.25** Output sensitivity [V/(in/s)] for a Geo Space GS-14-L3 geophone capsule as a function of frequency for load resistances of  $R_{load} = \infty$  (open circuit sensitivity),  $R_{load} = 1.91$  k $\Omega$ , and  $R_{load} = 866 \Omega$ . The external load resistance adds damping, lowering  $Q$ , and reducing the sensitivity but making the sensitivity more uniform over a larger range of frequencies. (In the words of Prof. S. J. Puttermann, “The flattest response is no response at all.”)

## 2.7 Coupled Oscillators

The techniques developed for our understanding and analysis of the one degree-of-freedom simple harmonic oscillators can be extended to multiple masses joined by multiple springs. This problem is important because we frequently couple one harmonic oscillator to another resonator to drive that system (which may have multiple resonances) as discussed in Sect. 10.7.5 and illustrated in Figs. 10.12 and 10.14. In fact, for closely coupled oscillators, the distinction between the driven system and the driver becomes blurred. Coupled harmonic oscillators are also an important subject because it provides a logical transition to continuous systems as the number of individual masses and springs becomes very large. Since all matter is composed of atoms, it is possible to treat solids as a three-dimensional array of masses joined to their nearest neighbors by springs.

The treatment in this section will again be restricted to motions that are constrained to occur in only one dimension, although we will let the number of degrees of freedom increase to two or more, with the number of coordinates specifying the position of the masses increasing accordingly. In general, for motion restricted to a single dimension, the number of natural frequencies for vibration will also be equal to the number of degrees of freedom, but simple harmonic motion of the coupled system will only be periodic at a single frequency if the system is excited in one of its *normal modes*. If those normal mode frequencies are related by the ratio of integers, then the motion of the coupled system, when disturbed from equilibrium, will be periodic; otherwise the motion will never repeat itself.

Some characteristics of the behavior of coupled systems will be unfamiliar to many readers. For that reason, we will begin our study of coupled oscillators with a very simple pair of coupled undamped oscillators that can be understood intuitively prior to developing the mathematical formalism necessary to write down solutions to the general case.

### 2.7.1 Two Identical Masses with Three Identical Springs

Thus far we have analyzed the dynamics of a single mass, joined to a spring and damper, that is either oscillating freely or driven by some externally imposed periodic force or displacement. At this point, that development has generated one-hundred numbered equations as well as many others that are contained within the text. Now that we are going to extend this analysis to several such oscillatory systems that are coupled in ways that permit them to exchange their energy of vibration, we might expect the solutions to be even more complex mathematically. That expectation will soon be fulfilled.

There is a simple case that can be understood intuitively. It will give us some basis to test the results of a more rigorous treatment of the general problem. It will also introduce simple behaviors that will be characteristic of the more general case illustrated schematically in Fig. 2.26.

We start by letting  $m_1 = m_2 = m$  and  $K_1 = K_2 = K_3 = K$ . We can then guess the two frequencies that will make the combined motion simple and harmonic and identify the periodic displacements of

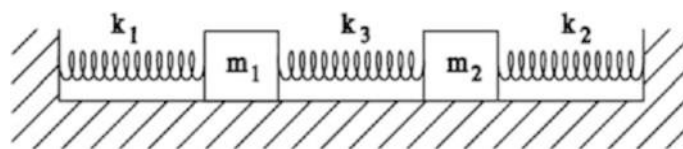


**Fig. 2.26** One-dimensional, two degree-of-freedom, coupled harmonic oscillators. The  $x_1$  coordinate measures the displacement of  $m_1$  from its equilibrium position, and  $x_2$  is the measure of  $m_2$ 's displacement from equilibrium. (Figure courtesy of J. D. Maynard [23])

those two masses that correspond to those two frequencies of oscillation. If  $x_1(t) = x_2(t)$ , the motion is symmetric, and the middle spring that couples their motion,  $K_3$ , is neither compressed nor extended. The frequency of oscillation is just that of either mass oscillating in isolation,  $\omega_s = \sqrt{K/m}$ , where the subscript “s” has been chosen because it corresponds to the *symmetric mode* of oscillation.

In the *antisymmetric mode*, the masses move 180° out-of-phase with each other,  $x_1(t) = -x_2(t)$ . In that case, the center of the  $K_3$  spring is fixed. From the perspective of either mass, it appears as though the  $K_3$  spring has been cut in half and attached to a rigid boundary. The coupling spring, appearing half as long, is now twice as stiff (see Sect. 2.2.1), so the total effective stiffness experienced by either mass oscillating in the antisymmetric mode is  $K_a = K + 2K = 3K$ . The frequency of that antisymmetric mode is therefore  $\omega_a = \sqrt{3K/m}$ .

If the masses are initially displaced by either  $x_1(t) = x_2(t)$  or  $x_1(t) = -x_2(t)$  and then released, the pair will both oscillate at  $\omega_s$  or  $\omega_a$  with the same amplitudes forever. Any other combination of initial displacements will lead to motion that is entirely aperiodic; in fact, the motion, though deterministic, will appear chaotic. The reason for this lack of periodicity is that the ratio of the two normal mode frequencies is an irrational number:  $\omega_a/\omega_s = \sqrt{3}$ .

## 2.7.2 Coupled Equations for Identical Masses and Springs

It is not very difficult to write down the equations of motion for each mass using Newton’s Second Law of Motion. It is also simple to convert those coupled differential equations to coupled algebraic equations by substituting a time-harmonic solution, just as we have been doing for our single degree-of-freedom oscillators. We will do this first for our simple case of  $m_1 = m_2 = m$  and  $K_1 = K_2 = K_3 = K$ .

$$m\ddot{x}_1 + Kx_1 + K(x_1 - x_2) = m\ddot{x}_1 + K(2x_1 - x_2) = 0 \quad (2.102)$$

By symmetry, the equation of motion for the second mass will interchange the subscripts on the coordinates.

$$m\ddot{x}_2 + K(2x_2 - x_1) = 0 \quad (2.103)$$

Since we seek normal modes, where all parts of the coupled system oscillate at the same frequency, substitution of  $x_1 = B_1 \cos \omega t$  and  $x_2 = B_2 \cos \omega t$  converts Eqs. (2.102) and (2.103) into two coupled algebraic equations for the two amplitude coefficients, after dividing through by  $\cos \omega t$ .

$$\begin{aligned} -m\omega^2 B_1 + K(2B_1 - B_2) &= 0 \\ -m\omega^2 B_2 + K(2B_2 - B_1) &= 0 \end{aligned} \quad (2.104)$$

That equation can be rearranged to compute a solution for  $B_1$  and  $B_2$ .

$$\begin{aligned} (2K - \omega^2 m)B_1 - KB_2 &= 0 \\ -KB_1 + (2K - \omega^2 m)B_2 &= 0 \end{aligned} \quad (2.105)$$

For these coupled linear equations to have a nontrivial solution, the determinant of their coefficients must vanish.

$$\begin{vmatrix} (2K - \omega^2 m) & -K \\ -K & (2K - \omega^2 m) \end{vmatrix} = 0 \quad (2.106)$$

Evaluation of that determinant leads to a *characteristic equation*<sup>27</sup> that can be solved to determine the values of  $\omega$  that satisfy the original equations.

$$(2K - \omega^2 m)^2 - K^2 = 0 \Rightarrow (2K - \omega^2 m) = \pm K \quad (2.107)$$

The two solutions correspond to the two modes we guessed in Sect. 2.7.1.

$$\omega = \sqrt{\frac{2K \pm K}{m}} \quad \text{so} \quad \omega_s = \sqrt{\frac{K}{m}} \quad \text{and} \quad \omega_a = \sqrt{\frac{3K}{m}} \quad (2.108)$$

Substitution of those frequencies back into either of the algebraic equations for the coefficients of  $B_1$  and  $B_2$  in Eq. (2.104) will provide expressions for  $x_1(t)$  and  $x_2(t)$  corresponding to those two *normal mode frequencies*,  $\omega_s$  and  $\omega_a$ . Starting with the symmetric mode frequency,  $\omega_s$ ,

$$-m\omega_s^2 B_1 + K(2B_1 - B_2) = -KB_1 + K(2B_1 - B_2) = K(B_1 - B_2) = 0. \quad (2.109)$$

Since  $K \neq 0$ , the result for the symmetric mode has  $B_1 = B_2$ . Making the similar substitution using the antisymmetric normal mode frequency  $\omega_a$ ,

$$-m\omega_a^2 B_1 + K(2B_1 - B_2) = -3KB_1 + K(2B_1 - B_2) = -K(B_1 + B_2) = 0 \quad (2.110)$$

For the antisymmetric mode,  $B_1 = -B_2$ .

These results will allow us to write the solution for motions of the individual masses if they are oscillating at one of those two normal mode frequencies.

$$\begin{aligned} x_1(t) &= B_s \cos(\omega_s t + \phi_s) \quad \text{and} \quad x_2(t) = B_s \cos(\omega_s t + \phi_s) \\ &\quad \text{or} \\ x_1(t) &= B_a \cos(\omega_a t + \phi_a) \quad \text{and} \quad x_2(t) = -B_a \cos(\omega_a t + \phi_a) \end{aligned} \quad (2.111)$$

An arbitrary phase has been introduced to accommodate any choice of the time corresponding to  $t = 0$ .

### 2.7.3 Normal Modes and Normal Coordinates

Having identified the two frequencies for our simple case and the corresponding motions of both masses at those two frequencies, we will now see that a coordinate transformation yields further simplifications. We can introduce the new coordinates,  $\eta_s(t)$  and  $\eta_a(t)$ , that combine the coordinates of the two masses,  $x_1(t)$  and  $x_2(t)$ , in a way that makes  $\eta_a(t) = 0$  for the symmetric mode and  $\eta_s(t) = 0$  for the antisymmetric mode.

$$\left. \begin{array}{l} \eta_s = x_1 + x_2 \\ \eta_a = x_1 - x_2 \end{array} \right\} \Rightarrow \begin{cases} x_1 = \frac{1}{2}(\eta_s + \eta_a) \\ x_2 = \frac{1}{2}(\eta_s - \eta_a) \end{cases} \quad (2.112)$$

Those transforms allow substitution of  $\eta_a(t)$  and  $\eta_s(t)$  for  $x_1(t)$  and  $x_2(t)$  into Eq. (2.103).

---

<sup>27</sup> In older treatments, the characteristic equation is often called the *secular equation*.

$$\begin{aligned}\frac{1}{2}[m(\ddot{\eta}_a + \ddot{\eta}_s) + K(\eta_s + 3\eta_s)] &= 0 \\ \frac{1}{2}[m(\ddot{\eta}_a - \ddot{\eta}_s) + K(-\eta_s + 3\eta_s)] &= 0\end{aligned}\tag{2.113}$$

Adding and subtracting the above equations from each other produces two uncoupled equations for the *normal coordinates*,  $\eta_s$  and  $\eta_a$ .

$$m\ddot{\eta}_s + K\eta_s = 0 \quad \text{and} \quad m\ddot{\eta}_a + 3K\eta_a = 0\tag{2.114}$$

The solutions for the time dependence of these normal coordinates are now trivial, since the above equations are isomorphic to our undamped simple harmonic oscillator equations.

$$\eta_s(t) = C_s \cos(\omega_s t + \phi_s) \quad \text{and} \quad \eta_a(t) = C_a \cos(\omega_a t + \phi_a)\tag{2.115}$$

These normal coordinates provide a complete basis that can be used to express the time dependence of the motion of both masses. The normal coordinates can express initial conditions, for example, those in Eq. (2.116), that do not correspond to initial conditions that produce the simple harmonic motion when the system is displaced from equilibrium into a configuration corresponding to one of those normal modes. Before looking at the time evolution of the positions of the masses for other initial conditions, it will be worthwhile to summarize the results of our simple example that will be present in the solutions to the more general case:

- There will be a number of normal modes that is equal to the number of degrees of freedom.
- A normal mode will have a frequency at which all of the masses will exhibit simple harmonic motion at that frequency.
- Each normal mode will provide a transformation of coordinates that can decouple the equations of motion.
- The normal modes provide a complete set of *basic functions* that can be combined to describe the subsequent motion of the masses for initial conditions that are not those which produce the simple harmonic oscillations characteristic of the normal modes.

## 2.7.4 Other Initial Conditions

To develop an appreciation for the behavior of our simple system of two identical masses connected by three identical springs, we can construct a solution for a very simple initial condition that does not correspond to one of the normal modes by fixing  $m_2$  at its equilibrium position,  $x_2(0) = 0$ , and displacing  $m_1$  by an amount  $x_1(0) = \alpha$ , with both masses initially at rest,  $\dot{x}_1(0) = \dot{x}_2(0) = 0$ . Those initial conditions can be expressed in terms of the normal modes and their frequencies.

$$x_1(t) = \frac{\alpha}{2} \cos \omega_s t + \frac{\alpha}{2} \cos \omega_a t \quad \text{and} \quad x_2(t) = \frac{\alpha}{2} \cos \omega_s t - \frac{\alpha}{2} \cos \omega_a t\tag{2.116}$$

Upon release of both masses at  $t = 0$ , the evolution of their positions can be interpreted by use of the following trigonometric identity:

$$\begin{aligned}\cos x \pm \cos y &= \cos \left[ \frac{1}{2}(x+y) + \frac{1}{2}(x-y) \right] \pm \cos \left[ \frac{1}{2}(x+y) - \frac{1}{2}(x-y) \right] \\ &= \begin{cases} 2 \cos \frac{1}{2}(x+y) \cos \frac{1}{2}(x-y) \\ -2 \sin \frac{1}{2}(x+y) \sin \frac{1}{2}(x-y) \end{cases} \quad (2.117)\end{aligned}$$

The ratio of the frequencies of our normal modes is an irrational number:  $\omega_a/\omega_s = \sqrt{3}$ . Their sum and difference can be expressed in terms of the symmetric mode frequency:  $\omega_a + \omega_b = (\sqrt{3} + 1)\omega_s \cong 2.732 \omega_s$  and  $\omega_a - \omega_b = (\sqrt{3} - 1)\omega_s \cong 0.732 \omega_s$ .

$$\begin{aligned}x_1(t) &= \alpha \cos(1.366\omega_s t) \cos(0.366\omega_s t) \\ x_2(t) &= -\alpha \sin(1.366\omega_s t) \sin(0.366\omega_s t) \quad (2.118)\end{aligned}$$

Although this result is deterministic, it is not periodic. As will be demonstrated for the case of weak coupling, the identity in Eq. (2.117) only leads to periodic solutions if the ratio of the frequencies is the ratio of two integers.

## 2.7.5 General Solutions for Two Masses and Three Springs

Now that the behavior of two coupled harmonic oscillators has been demonstrated for the simplest case, we can progress to the solution of the more general case where the same techniques will allow us to write equations for  $m_1 \neq m_2$  and  $K_1 \neq K_2 \neq K_3$ . For this more general case, Eqs. (2.102) and (2.103) have to be re-written to include the features of Fig. 2.26.

$$m_1 \ddot{x}_1 = -(K_1 + K_3)x_1 + K_3 x_2 \quad \text{and} \quad m_2 \ddot{x}_2 = -(K_2 + K_3)x_2 + K_3 x_1 \quad (2.119)$$

We expect that the lighter mass will experience greater displacements than the heavier mass. The above equations of motion can be simplified if we re-scale the coordinates by introducing the new primed coordinates.

$$x_1(t) = \frac{x_1(t)'}{\sqrt{m_1}} \quad \text{and} \quad x_2(t) = \frac{x_2(t)'}{\sqrt{m_2}} \quad (2.120)$$

Substitution into Eq. (2.119) provides a pair of equations that resemble those of a driven harmonic oscillator where the coupling spring's stiffness,  $K_3$ , is proportional to the driving force due to the motion of the other mass.

$$\frac{d^2 x'_1}{dt^2} + \omega_1^2 x'_1 = \kappa^2 x'_2 \quad \text{and} \quad \frac{d^2 x'_2}{dt^2} + \omega_2^2 x'_2 = \kappa^2 x'_1 \quad (2.121)$$

The new frequencies which appear above are related to the individual masses and springs or to the spring which couples their motion.

$$\omega_1^2 = \frac{(K_1 + K_3)}{m_1}; \quad \omega_2^2 = \frac{(K_2 + K_3)}{m_2}; \quad \kappa^2 = \frac{K_3}{\sqrt{m_1 m_2}} \quad (2.122)$$

If we seek the normal modes for this more general system, as before, those modes must correspond to simple harmonic motion of both masses oscillating harmonically at the same frequency. For that reason, we can substitute harmonic solutions of the same frequency,  $\omega$ , for  $x'_1(t) = \Re e[\tilde{x}'_1 e^{j\omega t}]$  and

$x'_2(t) = \Re e[\hat{\mathbf{x}}'_2 e^{i\omega t}]$ . This substitution again converts the coupled differential expressions in Eq. (2.121) to coupled algebraic equations.

$$\begin{aligned} (\omega_1^2 - \omega^2)x'_1 - \kappa^2 x'_2 &= 0 \\ -\kappa^2 x'_1 + (\omega_2^2 - \omega^2)x'_2 &= 0 \end{aligned} \quad (2.123)$$

As before, we impose the requirement that the determinant of the coefficients for the coupled equations vanish so that nontrivial solutions can be identified.

$$\begin{vmatrix} (\omega_1^2 - \omega^2) & -\kappa^2 \\ -\kappa^2 & (\omega_2^2 - \omega^2) \end{vmatrix} = 0 \quad (2.124)$$

Evaluation of the determinant results in a secular (characteristic) equation for the frequencies which is biquadratic.

$$\omega^4 - (\omega_1^2 + \omega_2^2)\omega^2 + \omega_1^2\omega_2^2 - \kappa^4 = 0 \quad (2.125)$$

The solution can be obtained using the quadratic formula to determine  $\omega^2$  in terms of the oscillators' parameters as defined in Eq. (2.122).

$$\begin{aligned} \omega &= \left[ \frac{1}{2}(\omega_1^2 + \omega_2^2) \pm \frac{1}{2}\sqrt{(\omega_1^2 - \omega_2^2)^2 + 4\kappa^4} \right]^{1/2} \\ &= \frac{1}{\sqrt{m_1 m_2}} \left[ \frac{1}{2}[(K_1 + K_3)m_2 + (K_2 + K_3)m_1] \pm \frac{1}{2}\sqrt{[(K_1 + K_3)m_2 - (K_2 + K_3)m_1]^2 + 4K_3^2 m_1 m_2} \right]^{1/2} \end{aligned} \quad (2.126)$$

As before, we have identified the two unique frequencies that allow both masses to oscillate harmonically at the same frequency. If those frequencies are substituted back into the algebraic expressions of Eq. (2.123), the ratios of  $x'_1$  to  $x'_2$  can be determined.

Since the masses and springs are now different, the normal mode displacements will be more complex than the simple solutions of Sect. 2.7.2. The normal mode descriptions for  $x_1(t)$  and  $x_2(t)$  will still be classified as symmetric and antisymmetric, but the amplitudes will no longer be identical. The reader is referred to the treatment by Morse for those solutions in their full algebraic ugliness [33].

## 2.7.6 Driven Oscillators, Level Repulsion, and Beating

In the limit that  $K_3 = 0$ , so that there is no coupling between the two masses, it is comforting that Eq. (2.126) regenerates the frequencies of the two isolated oscillators. It is instructive to consider the case of two oscillators of the same frequency,  $\omega_1 = \omega_2$ , that are weakly coupled so that  $\kappa \ll \omega_1$ . Under those circumstances, we can use a Taylor series to expand Eq. (2.126) and provide the symmetric and antisymmetric modal frequencies.

$$\begin{aligned} \omega_s &= \sqrt{\omega_1^2 - \kappa^2} = \omega_1 \sqrt{1 - \frac{\kappa^2}{\omega_1^2}} \cong \omega_1 - \frac{\kappa^2}{2\omega_1} \\ \omega_a &= \sqrt{\omega_1^2 + \kappa^2} = \omega_1 \sqrt{1 + \frac{\kappa^2}{\omega_1^2}} \cong \omega_1 + \frac{\kappa^2}{2\omega_1} \end{aligned} \quad (2.127)$$

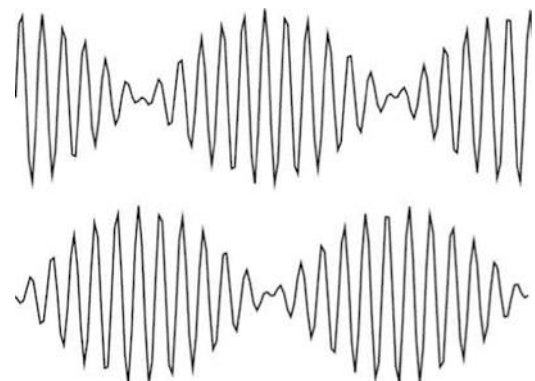
The fact that even weak coupling results in a shift of the natural frequencies of the two uncoupled oscillators is known as *level repulsion*. That term is motived by analogy to splitting of energy levels in atomic systems when such levels become coupled, possibly by electromagnetic interactions.<sup>28</sup> At first glance, the symmetric frequency,  $\omega_s$ , should not be shifted, based on the normal modes of the simpler system of equal masses and springs analyzed in Sects. 2.7.1 and 2.7.2. The fact that  $\omega_s$  is downshifted is a consequence of the assumption that the motion of our simpler system was initiated by making two identical displacements. If one of the masses is driven, then the coupling spring must be displaced initially to permit the transfer of energy from the driven mass to the other mass.

It is easy to visualize this periodic energy transfer in the weak-coupling limit, with  $\omega_s \cong \omega_a$ , and  $n(\omega_s - \omega_a) = (\omega_s + \omega_a)$ , where  $n$  is chosen to be an integer. Using the identities of Eq. (2.117), and assuming the oscillations start with  $x_1(0) = \alpha$  and  $x_2(0) = 0$ , the subsequent evolution of  $x_1(t)$  and  $x_2(t)$  can be written as the product of two trigonometric functions.

$$\begin{aligned} x_1(t) &= \alpha \left[ \cos \frac{(\omega_a - \omega_s)}{2} t \right] \left[ \cos \frac{(\omega_a + \omega_s)}{2} t \right] \\ x_2(t) &= \alpha \left[ \sin \frac{(\omega_a - \omega_s)}{2} t \right] \left[ \sin \frac{(\omega_a + \omega_s)}{2} t \right] \end{aligned} \quad (2.128)$$

The second term in both products represents a simple harmonic oscillation at a frequency which is the average of  $\omega_a$  and  $\omega_s$ . The first terms define an amplitude modulation envelope that closes (i.e., goes to zero) with a period that is integer multiples of  $\pi/(\omega_a - \omega_s)$ . Since the peaks in the envelopes for  $x_1$  and  $x_2$  are  $90^\circ$  out-of-phase, it is apparent that all of the energy starts in  $m_1$ , but at a time  $\pi/2(\omega_a - \omega_s)$ ,  $m_1$  has come to rest, and all of the energy has been concentrated in  $m_2$ , with the situation reversing itself with a period  $\pi/(\omega_a - \omega_s)$ . This periodic modulation is known as *beating* and is illustrated in Fig. 2.27, where  $n = 12$ .

**Fig. 2.27** Time evolution of two weakly coupled oscillators, described by Eq. (2.128), is plotted to illustrate the periodic exchange of energy. The upper plot is  $x_1(t)$  and the lower is  $x_2(t)$ . In this figure, the oscillation frequency  $(\omega_a + \omega_s)/2$  is 12 times the frequency difference  $(\omega_a - \omega_s)$ . Initially, all of the motion is in  $m_1$



<sup>28</sup> As mentioned in Sect. 2.3.3, the atomic energy levels are related to the frequencies of light radiated during a level transition through Planck's equation:  $E/\omega = \hbar$ .

### 2.7.7 String of Pearls

We can now extend this analysis of coupled oscillators to more than two masses. To make it easier to visualize the motion of several coupled masses, we will first solve the problem of an undamped, single degree-of-freedom oscillator consisting of a single mass suspended at the center of a taught string. The location of the mass on the string will be specified by the  $x$  axis, and the displacement of the mass from its position of static equilibrium will be given by its  $y$  coordinate. A point mass,  $m$ , is shown in Fig. 2.28, attached to the center of a limp string<sup>29</sup> of length  $L = 2a$ , and is subject to a tension,  $T$ . Both ends of the string are immobilized:  $y(0) = y(2a) = 0$ . If the mass is displaced from equilibrium by a distance,  $y_1$ , at the center of the string, there will be a net force on that mass that will be opposite to  $y$ ; hence, the mass will obey Hooke's law. We assume that the string is massless,  $m_s = 0$ , and that the tension in the string has a value,  $T$ .

It is easy to demonstrate that tension,  $T$ , in the string exerts a linear restoring force on the mass if the vertical displacement from equilibrium,  $y_1$ , is small enough that  $y_1/a \ll 1$ . As shown in Fig. 2.28, a displacement,  $y_1$ , creates an angle,  $\theta = \tan^{-1}(y_1/a)$ , between the displaced mass and the former equilibrium position of the string. If the displacement,  $y_1$ , is small, the change in the length of the string  $\delta L$  will be second-order in the displacement,  $y_1$ , so the increase in tension due to the stretching of the string can be ignored in a first-order (Hooke's law) analysis.

$$\delta L = 2\sqrt{(a^2 + y_1^2)^{1/2} - a^2} = 2a\sqrt{\left(1 + \frac{y_1^2}{a^2}\right)^{1/2} - 1} \cong a\left(\frac{y_1}{a}\right)^2 \quad (2.129)$$

The restoring force will be linear in the displacement for small enough displacements that  $\theta = \tan^{-1}(y_1/a) \cong y_1/a$ . From Fig. 2.28, Garrett's First Law of Geometry can be used to calculate the vertical component of the force,  $F_v$ , due to the tension,  $T$ , of the string.

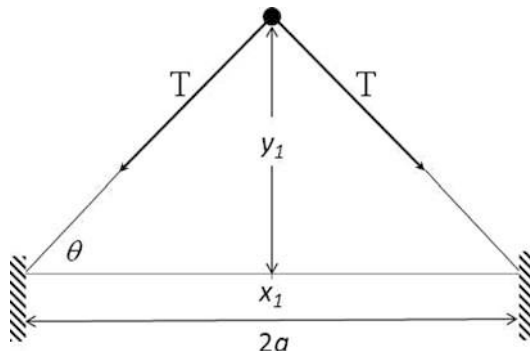


**Fig. 2.28** A limp, massless string of length,  $L = 2a$ , is under tension,  $T$ , and has a point mass,  $m$ , attached at its center and is fixed at both ends. The mass has been displaced from its equilibrium position by a distance  $y_1$ , so the string makes an angle,  $\theta = \tan^{-1}(y_1/a)$ , with the horizontal. The two vertical components of the tension provide a linear restoring force:  $F_y = -2T \sin \theta \cong -(2T/a)y_1$

<sup>29</sup> For this case, we will assume that the string has no flexural rigidity and that the restoring force is entirely due to the tension applied to the string. In Sect. 5.5, we will examine the stiff string, which is under tension but also exhibits flexural rigidity.

$$F_v = -2T \sin \theta \cong -\left(\frac{2T}{a}\right)y_1 \quad (2.130)$$

This “mass on a string” is another example of a simple harmonic oscillator that moves in one dimension, along the  $y$  axis, and has an effective stiffness constant,  $K_{eff} = (2T/a)$ . To demonstrate the utility of this configuration for the representation of coupled oscillators, Fig. 2.29 duplicates the normal mode displacements for masses and springs from Eq. (2.111).

In Fig. 2.30, we extend this mass and string model to multiple masses. At equilibrium, each mass is separated from its adjacent masses by a horizontal distance,  $a$ . The position of the  $i$ th mass is  $x_i = ai$ , where  $1 \leq i \leq N$ . For  $N$  masses, the total length of the string is  $L = (N + 1) a$ . Since the string is rigidly fixed at both ends,  $y(0) = y(x_{N+1}) = 0$ .

The vertical component of the force,  $F_i$ , on any mass,  $m_i$ , depends only upon the position of that mass with respect to its nearest neighbors.

$$F_i = T(\sin \phi - \sin \theta) \cong T\left(\frac{y_{i+1} - y_i}{a} - \frac{y_i - y_{i-1}}{a}\right) = -\frac{2T}{a}y_i + \frac{T}{a}(y_{i+1} + y_{i-1}) \quad (2.131)$$



**Fig. 2.29** The same two normal modes for the simple coupled oscillators with two identical masses and three identical springs that were calculated in Eq. (2.111) are reproduced here as two masses on a tensioned string. The symmetric mode is shown on the left, and the antisymmetric mode, with frequency that is  $\sqrt{3}$  greater than the symmetric mode, is shown at the right

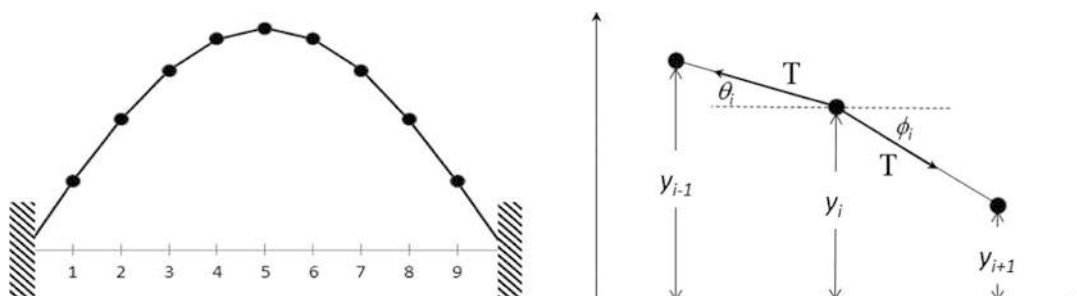


**Fig. 2.30** (Left)  $N = 9$  masses are spaced uniformly on a string of length,  $L = (N + 1) a$ . The coordinate of each mass is specified by its position along the  $x$  axis when the string is at its equilibrium position. Each mass is constrained to move only in the vertical direction, and each mass is displaced from its equilibrium position by an amount  $y_i$ . (Right) The net vertical force on each mass,  $m_i$ , is determined by the vertical displacements of its nearest neighbors,  $y_{i-1}$  and  $y_{i+1}$ , relative to the displacement,  $y_i$ . The vertical component of the force on the  $i$ th mass is determined by the tension in the string,  $T$ , and by the angles  $\theta_i = \tan^{-1} [(y_i - y_{i-1})/a]$  and  $\phi_i = \tan^{-1} [(y_{i+1} - y_i)/a]$

If we assume all masses are equal,  $m_i = m$ , and we apply Newton's Second Law of Motion to the  $i$ th mass, abbreviating  $(T/a)$  as  $K$ , the dynamical equations describing the vertical motion of each of the  $N$  masses can be written in a compact form.

$$m\ddot{y}_i + 2Ky_i - K(y_{i+1} + y_{i-1}) = 0 \quad \text{for } i = 1, 2, \dots, N \quad (2.132)$$

This set of coupled differential equations could be solved by the techniques used previously in Sects. 2.7.3 and 2.7.5. If we define  $\lambda \equiv 2 - (m\omega^2 a/T)$ , then the  $N \times N$  determinant of the coefficients,  $D_N$ , for the algebraic equations, which resulted from the assumption that all masses vibrating in any normal mode must oscillate at the same frequency,  $\omega$ , has the following form that is characteristic of *nearest-neighbor interactions*:

$$D_N = \begin{vmatrix} \lambda & -1 & 0 & 0 & 0 & \cdots & 0 \\ -1 & \lambda & -1 & 0 & 0 & \cdots & 0 \\ 0 & -1 & \lambda & -1 & 0 & \cdots & 0 \\ \vdots & \vdots & \vdots & \vdots & \vdots & \ddots & \vdots \\ 0 & 0 & 0 & 0 & 0 & \lambda & -1 \\ 0 & 0 & 0 & 0 & 0 & -1 & \lambda \end{vmatrix} \quad (2.133)$$

Fetter and Walecka solve this system of linear equations by development of a recursion relation for the minors [34], but we will take a different approach that anticipates our transition to continuous systems in the next chapter.

Since we have chosen our masses to be equal and to be equally spaced from each other along the string, it is possible to treat the vertical displacements of the masses as a function of the  $x$  coordinate:  $y_i = y(x_i)$ , where  $x_i = ai$ . Again, we seek normal mode solutions that require that every mass oscillates with the same frequency,  $\omega$ , but now we will keep track of the amplitudes of vibration of the individual masses by introducing a constant,  $\beta$ , which has the units of inverse length [ $\text{m}^{-1}$ ].

$$y(x_i, t) = Ae^{j(\beta x_i - \omega t)} \quad (2.134)$$

Substitution of that expression for displacements into Eq. (2.132) produces the algebraic Eq. (2.135) after cancellation of common exponential time factors.

$$-m\omega^2 + 2K - K(e^{j\beta a} + e^{-j\beta a}) = 0 \quad (2.135)$$

The resulting equation can be solved for the normal mode frequencies and simplified by use of the trigonometric identity,  $2\sin^2(x/2) = (1 - \cos x)$ , where  $2 \cos x = (e^{jx} + e^{-jx})$ .

$$\omega^2 = \frac{2K}{m}(1 - \cos \beta a) = \frac{4K}{m} \sin^2\left(\frac{\beta a}{2}\right) \quad (2.136)$$

Although the frequencies,  $\omega$ , are a continuous function of  $\beta$ , the normal mode frequencies will become discrete when we impose the end conditions that  $y(0) = y(x_{N+1}) = 0$ . To satisfy the condition at  $x = 0$ , we will subtract a solution with the form of Eq. (2.134), but with a negative  $\beta$ , since both the  $\beta$  and  $-\beta$  parts will be zero when multiplied by  $x = 0$ .

$$y(x_i, t) = \Re e[A(e^{j\beta x_i - j\omega t} - e^{-j\beta x_i - j\omega t})] \quad (2.137)$$

That form of Eq. (2.134) is clearly zero for  $x_o = 0$ . For  $x_{N+1}$ , making  $y_{N+1} = y[(N+1)a] = 0$  results in a condition that discretizes the values of  $\beta$ , simultaneously satisfying both boundary conditions.

$$e^{j\beta(N+1)a} - e^{-j\beta(N+1)a} = 2j[\sin \beta(N+1)a] = 0 \quad (2.138)$$

Only discrete values of  $\beta_n$  are now acceptable.

$$\beta_n(N+1)a = n\pi \quad \Rightarrow \quad \beta_n = \frac{n\pi}{a(N+1)}; \quad n = 1, 2, 3, \dots, N \quad (2.139)$$

Substitution of the quantized values of  $\beta_n$  into Eq. (2.136) provides the normal mode frequencies.

$$\omega_n = 2\sqrt{\frac{k}{m} \sin^2\left(\frac{\beta_n a}{2}\right)} \quad (2.140)$$

Plugging the  $\beta_n$  back into Eq. (2.134) provides the time-dependent displacements for each mass.

$$y(x_i, t) = y_i(t) = A_n \sin\left(\frac{in\pi}{N+1}\right) \sin \omega_n t \quad (2.141)$$

This equation provides  $N$  solutions for each mass corresponding to the  $n$ th normal mode with normal mode frequency,  $\omega_n$ . Each normal mode has an amplitude,  $A_n$ , that would depend upon the strength of the excitation of the  $n$ th mode. The vertical displacements of each mass for each mode are exaggerated for all nine modes in Fig. 2.31, with  $N = 9$  and  $A_n = 1$  for all  $n$ . The ratio of the frequency of each normal mode to the frequency of the  $n = 1$  mode,  $\omega_n/\omega_1$ , is tabulated and plotted as a function of mode number,  $n$ , in Fig. 2.32.

The lowest-frequency modes correspond to in-phase motion of adjacent masses. The highest-frequency mode,  $n = N$ , corresponds to out-of-phase motion of the adjacent masses. By increasing the number of masses and decreasing the spacing to hold the overall length constant,  $L = (N+1)a$ , the number of modes becomes infinite, and the string with masses attached has a uniform linear mass density,  $\rho_L = (m/a)$ . The modal frequencies are those given by Eq. (2.142) in this limit.

$$\lim_{N \rightarrow \infty} \omega_n^2 = \frac{4T}{ma} \left[ \frac{n\pi}{2(N+1)} \right]^2 = \frac{T}{\rho_L} \left( \frac{n\pi}{L} \right)^2 \quad (2.142)$$

The quantity  $(T/\rho_L)^{1/2} \equiv c$  (for *celerity*) has the dimensions of speed [m/s]. As we will see when we transition to continuous systems in the next chapter,  $c$  is just the speed of transverse wave propagating on a uniform string. The low-frequency normal mode frequencies,  $f_n = \omega_n/2\pi$ , correspond to integer numbers,  $n$ , of half-wavelengths fitting between the fixed ends.

For the discrete case with  $N = 9$ , it is easy to imagine that the lowest-frequency mode at the top left in Fig. 2.31 approximates a half-sine waveform fit between the two fixed ends, i.e.,  $\lambda_1 = 2 L$ , and the second mode corresponds to two half-wavelengths (i.e., one entire wavelength) between the fixed ends,  $\lambda_2 = L$ .

## 2.8 The Not-So-Simple (?) Harmonic Oscillator

After 60 pages of discussion, 32 figures, and over 140 numbered display equations, the reader would be justified in requesting an explanation for why “simple” is used as a descriptor for the harmonic oscillator. The mass and the spring that are shown to function in its quasi-static limit are simple components. The description of the time history of the motion of a mass connected to a spring involves only simple trigonometric functions with constants that could be fit to specific initial conditions. The expressions for the kinetic energy stored by the mass,  $KE = (\frac{1}{2})mv^2$ , and the potential energy stored by

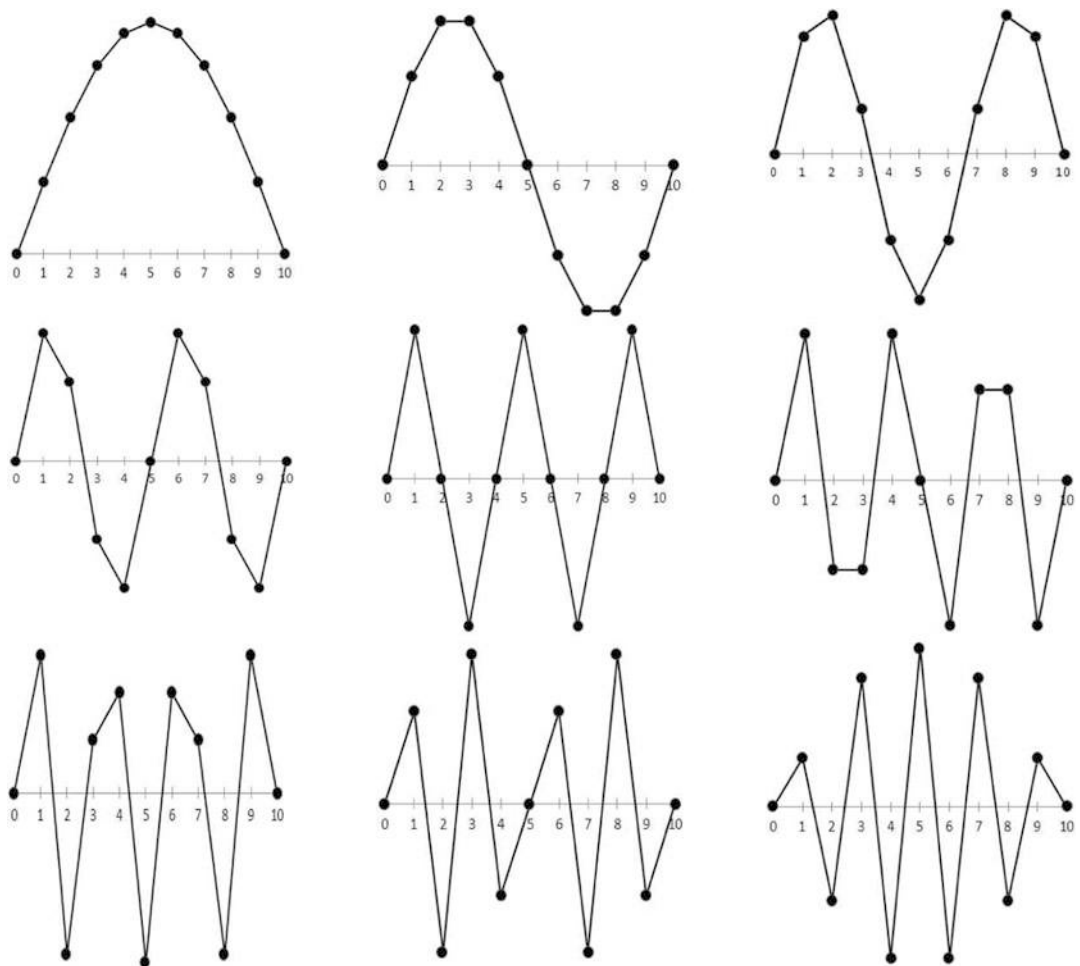
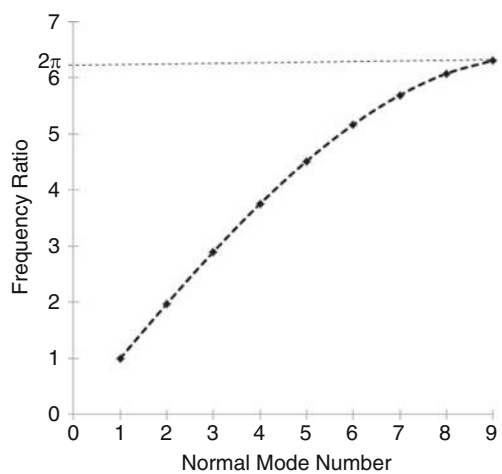


**Fig. 2.31** Mode shapes for the normal modes for the nine equal masses (solid circles) on a taught string (straight lines). The solid circles at  $N = 0$  and  $N = 10$  represent the fixed ends of the string. The amplitudes are greatly exaggerated for clarity. Please remember these results are only valid for  $y \ll a$ . The number of zero-crossings increases with increasing mode number. The fundamental ( $n = 1$ ) mode has no zero-crossings, and each subsequent mode has a number of zero-crossings that is one less than the mode number,  $n$ . The frequencies of these normal modes are tabulated and plotted in Fig. 2.32

**Fig. 2.32** The normalized modal frequencies,  $\omega_n$ , based on Eq. (2.140), for nine equal masses, are tabulated at the left and plotted vs. mode number,  $n$ , at the right

Mode	Freq.
1	1.000
2	1.975
3	2.902
4	3.757
5	4.520
6	5.172
7	5.696
8	6.080
9	6.238



the spring,  $PE = (\frac{1}{2})Kx^2$ , are equally simple, and a gravitational offset had no influence on the dynamical behavior. Even Rayleigh's exploitation of the virial theorem for calculation of oscillatory frequencies would have to be judged "simple," at least in hindsight.

Once the mechanical resistance was added as a means to dissipate energy, the analysis of the oscillator's behavior left the purely mechanical perspective and entered the realm of thermodynamics – the dissipated energy had to leave "the system" and make contact with "the environment." Although such calculations may be unfamiliar, their result incorporated the Equipartition Theorem, which is also quite simple – each quadratic degree of freedom, on average, gets its  $(\frac{1}{2})k_B T$  share of energy at thermal equilibrium. The steady-state response to systematic injection of energy into the oscillator, by either forcing the mass or jiggling the attachment point of the spring, turned out to be determined entirely by the oscillator's mechanical impedance. The approach to steady state involved addition of solutions to the freely decaying oscillator.

The experimental determination of the stiffness and moving mass for the electrodynamic loud-speaker example was achieved by simply adding some pocket change (i.e., nickels) and recording the frequency shift due to the mass loading. The mechanical resistance was determined by the free-decay time. All three parameters were determined simply to an accuracy of better than  $\pm 1\%$  by least-squares fitting, while the force factor (i.e., the  $B\ell$ -product that determined the force produced by the electrical current flowing in the voice coil) required only a DC electrical resistance measurement and an electrical impedance measurement at the resonance frequency.

When two or more (undamped) oscillators were coupled together, the mathematical description became more complicated, but the simplest case could be analyzed intuitively, based on the previous understanding of individual harmonic oscillators. The identification of the normal modes and their frequencies could be algebraically messy when different masses are joined by springs with different stiffnesses. The time histories of the motion might appear chaotic if the normal mode frequencies were not commensurate (i.e., related by the ratio of integers). One must admit those systems constitute a fairly complicated combinations of otherwise simple harmonic oscillators. Although the coupled solutions were the most complicated results derived in this chapter, the next chapter will simplify the situation once again by treating large numbers of coupled oscillators as a continuum, so an overall "shape" is described instead of the individual displacements of point masses.

### Talk Like an Acoustician

Point-mass	Mechanical reactance
Dynamical equation	Resistance-controlled regime
Equation of state	Stiffness-controlled regime
Frequency	Mass-controlled regime
Period	Rayleigh line shape
Angular frequency	Lenz's law
Radian frequency	Faraday's law of induction
Quasi-static approximation	Decibel
Virial theorem	Phase-locked loop
Rayleigh's method	Ring down
Adiabatic invariance	Reversible transducer
Dashpot	Vibration isolator
Mechanical resistance	Transmissibility
Quality factor	Seismometer
Logarithmic decrement	Geophone
Natural frequency	Normal modes

Free-decay frequency	Normal mode frequencies
Underdamped	Symmetric mode
Overdamped	Antisymmetric mode
Critical damping	Characteristic equation
Equipartition Theorem	Secular equation
Half-power bandwidth	Normal coordinates
Full width at half maximum	Basis functions
Equivalent noise bandwidth	Level repulsion
Effective bandwidth	Beating
Mechanical impedance	Nearest-neighbor interactions
Resonance	Celerity

## Exercises

Each problem that I solved became a rule which served afterwards to solve other problems. (Rene Descartes)

1. **U-tube oscillations.** The tube shown in Fig. 2.33 is filled with a liquid that has a uniform mass density,  $\rho$ . The total length of the fluid column is  $L$ , and the cross-sectional area of the tube,  $S$ , is constant. When the fluid is displaced from its equilibrium position by a distance,  $x$  (as shown), the column of liquid executes simple harmonic motion under the influence of a constant gravitational acceleration,  $g$ .
  - (a) *Period.* Calculate the period,  $T$ , of the oscillations, neglecting damping.
  - (b) *Quality factor.* If the oscillations are observed to decrease by 20% during each cycle, calculate  $Q$ .
2. **Coefficient of friction oscillator.** Two cylindrical rollers are located a distance  $2a$  apart. Their bearings are anchored. The rollers rotate at an angular speed  $\omega_r$  in opposite directions, as shown in Fig. 2.34. On the top of the rollers rests a bar of length,  $l$ , and weight,  $W = mg$ .

**Fig. 2.33** Liquid-filled U-tube

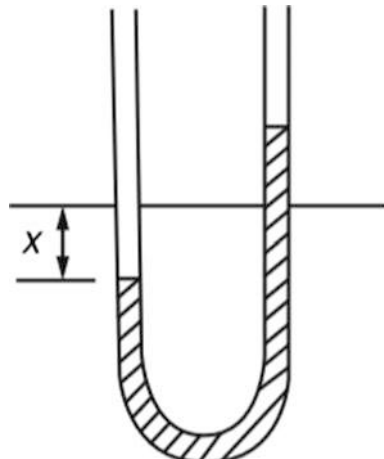
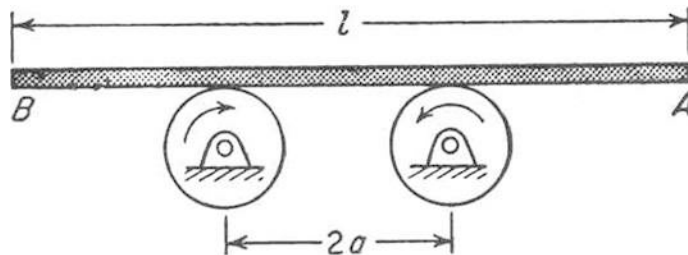


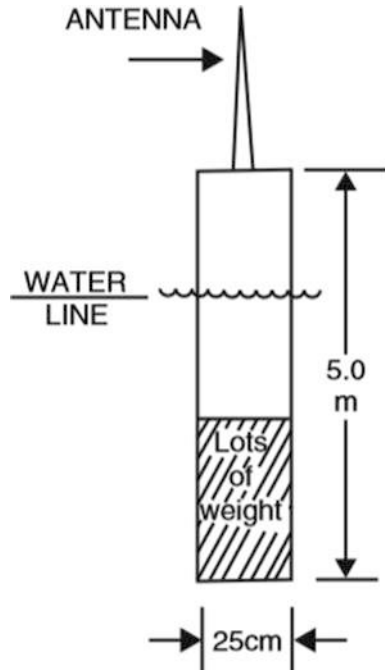
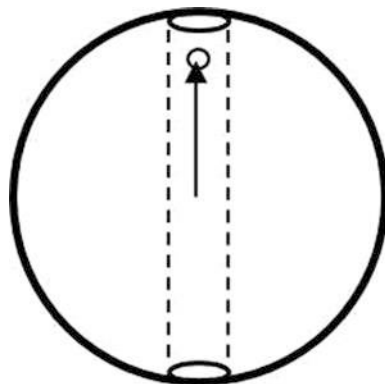
**Fig. 2.34** Bar supported on two counter-rotating wheels with centers separated by  $2a$



Assuming a dry coefficient-of-friction  $\mu$  between the rollers and the bar, the bar will oscillate back and forth longitudinally executing simple harmonic motion.<sup>30</sup> The restoring force will be the *difference* between the frictional forces in the  $x$  direction,  $F_y$  (along the bar), due to the weight (normal force) of the bar in the  $y$  direction,  $F_y = \mu mg$ , of the bar on each roller. (Note that if the end of the bar is closer to one roller, the weight of the bar on the other roller will be larger and will push the bar back toward the center.) Calculate the frequency of the bar's oscillations when the wheels rotate as shown in Fig. 2.34.

3. **Mass loading frequency shift.** A mass-spring system is observed to have a natural frequency of 10.0 Hz. When a mass of 10.0 grams is added to the original mass,  $m_o$ , the frequency decreases to 8.0 Hz. Determine the original mass and the spring's stiffness constant, K.
4. **Loudspeaker in an enclosure.** A loudspeaker has a free cone resonance frequency of 55.5 Hz. If a US nickel (mass = 5.00 g) is placed on the speaker's dust cap, the resonance frequency is reduced to 46.3 Hz. After the nickel is removed, the speaker is installed in a sealed enclosure, and the frequency increases to 80.0 Hz. What is the equivalent stiffness (in Newtons/meter) provided by the elasticity of the air contained within the loudspeaker enclosure?
5. **Spar buoy oscillations.** An oceanographic instrument package is placed at the bottom of a spar buoy shown in Fig. 2.35. The mass (in air) of the entire buoy (instruments, batteries, tube, and antenna) is 150 kg. The tubular portion (5 m long and 25 cm diameter) is partially submerged. You may assume the density of the water,  $\rho = 1000 \text{ kg/m}^3$ , and the acceleration due to gravity,  $g = 9.8 \text{ m/s}^2$ .
  - (a) *Equilibrium depth.* How far from the surface of the water is the **top** of the 5.0 m long tubular section when it is in equilibrium (at rest)?
  - (b) *Frequency.* What is the natural frequency of vibration of the buoy if it is displaced (vertically) from its equilibrium position and released?
  - (c) *Damping.* When the buoy is displaced from equilibrium, the oscillations decay to  $1/e$  of their initial value in 30 s. Determine the viscous (mechanical) resistance,  $R_m$ , which the water provides to damp the oscillations.
  - (d) *Hydrodynamic mass correction.* The water increases the buoy's inertia by adding a mass that is about half that of a sphere, with density  $\rho$  (see Sect. 12.5.1) and with the same diameter as the buoy. Recalculate your result for the frequency from part (b) including the effective mass of the water that is driven by the motion of the cylinder.
  - (e) *Relative motion.* Assume that there is a "ring" drawn at the static (calm) water level on the tubular section at the normal equilibrium position which you calculated in part (a) of this problem. If a sinusoidal swell with peak-to-trough amplitude of 1.0 m passes the buoy position every 20 s (i.e., a wave with a 20 s period), what is the greatest (peak) distance which the ring

<sup>30</sup>The operation of such an oscillator is provided by Dan Russell in a YouTube video: <http://www.youtube.com/watch?v=46lk2FXzwT8>

**Fig. 2.35** Spar buoy**Fig. 2.36** The Earth with a hole passing through its diameter

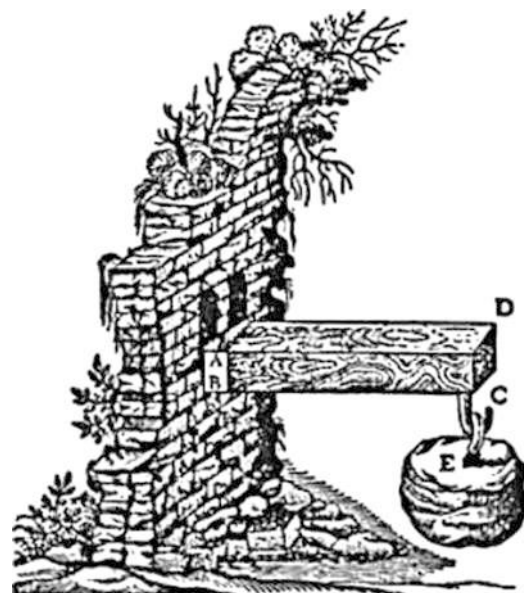
will be above or below the instantaneous (moving) air-sea interface? Report the amplitude of the motion of the buoy **relative** to the moving water surface, not with respect to the static (calm) water level.

6. **Balls to Bunbury.** Assume the Earth is the large diameter solid sphere of uniform mass density,  $\rho_{\oplus}$ , shown in Fig. 2.36. A small-diameter cylindrical hole has been bored through the sphere along a diameter. A ball of mass,  $m$ , with a diameter smaller than the hole, is dropped from the surface of the sphere down the hole.

At a distance,  $r$ , from the center of the Earth, the magnitude of the gravitational potential energy of the ball,  $|U(r)|$ , is determined by the mass of the Earth,  $M(r) = 4\pi\rho r^3/3$ , which is included within a radius less than  $r$ . (Note the net force on the small mass due to the mass of the Earth that is at a radius greater than  $r$  is completely cancelled. Why?)

- (a) *Effective stiffness.* Use Newton's Law of Universal Gravitation, as expressed in either Eq. (2.23) or Eq. (2.25), to determine an effective stiffness constant. Newton's Universal Gravitation Constant,  $G = 6.6726 \pm 0.0005 \times 10^{-11} \text{ m}^3/\text{s}^2\text{-kg}$ . For the planet Earth,  $R_{\oplus} = 6371 \text{ km}$ , the average mass density is  $\rho_{\oplus} = 5520 \text{ kg/m}^3$ .
- (b) *Oscillation period.* Find the period of oscillation. Express your answer in minutes.
- (c) *Orbital period.* Using Eq. (2.23), show that the period you calculated in part (b) is identical to the period of the same mass (or any mass!) in a circular orbit around Earth at a height above the surface  $h \ll R_{\oplus}$ .
- (d) *Superposition.* How is the linear motion of the mass through the Earth related to the orbital motion around the Earth?
7. **An asymmetrically placed mass on a taut string.** A mass,  $m$ , is attached on a string of tension,  $T$ , and length,  $L$ . The mass is located a distance,  $b$ , from the left-side rigid support (hence  $L-b$  from the right rigid support).
- (a) *Natural frequency.* What is natural frequency if we assume that the string is massless,  $m_s = 0$ ?
- (b) *String mass correction.* Using Rayleigh's method, calculate the natural frequency if  $m_s = m/10$ , and report the result as a ratio with respect to the natural frequency you calculated in part (a).
8. **Vibration isolator.** A large air conditioning unit is loaded on to a vibration isolation platform. The platform that supports the chiller, which is attached to the isolators, sinks by 2.0 cm when the air conditioner is placed on it.
- (a) *Natural frequency.* What is the natural frequency (in Hz) of the chiller-isolator system? (You may assume that the acceleration due to gravity is  $9.8 \text{ m/s}^2$ .)
- (b) *Transmissibility.* If the unbalance in the chiller's motor produces an oscillating force in the vertical direction of  $F_1 = 1000 \text{ N}_{\text{peak}}$  at 60 Hz, what is the reduction in the force that the platform applies to the rigid foundation on which it mounted? Report the result as both a decimal ratio and as a dB reduction.
9. **Cantilever spring.** The beam in Fig. 2.37 was drawn by Galileo. When the 50 kg mass "E" was placed on the hook "C," the hook was displaced downward by  $\Delta = 4 \text{ cm}$ .

**Fig. 2.37** Beam supported by a wall with mass "E" attached at the end



- (a) *Frequency.* Neglecting the mass of the beam, what is the frequency of vibration?  
 (b) *Beam mass correction.* The deflection of the beam,  $y(x)$ , as measured from the rigid support at  $x = 0$  is given by the following curve (from Eq. (4.36)):

$$y(x) = \frac{3\Delta}{2L^3} \left( Lx^2 - \frac{x^3}{3} \right)$$

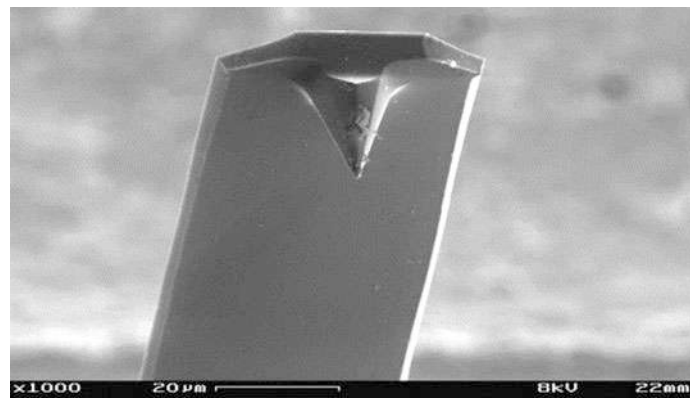
If the mass of the beam is 10 kg, use Rayleigh's method to recalculate the vibration frequency.

10. **Atomic force microscopy.** The beam in Fig. 2.38 is the sensing element of an atomic force microscope.<sup>31</sup> The cantilever is fabricated from silicon nitride ( $\text{Si}_3\text{N}_4$ ) and is  $w = 30 \mu\text{m}$  wide,  $L = 100 \mu\text{m}$  long, and  $t = 3 \mu\text{m}$  thick. For this problem, the mass of the tip can be neglected. The stiffness of this cantilever can be related to the Young's modulus of the  $\text{Si}_3\text{N}_4$ ,  $E = 310 \text{ GPa}$ , by Eq. (2.143).

$$K = \frac{F}{\Delta} = \frac{Ew}{4} \left( \frac{t}{L} \right)^3 \quad (2.143)$$

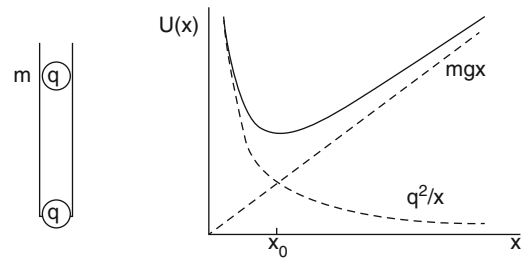
- (a) *Units.* Show that the units on the right-hand side of Eq. (2.143) correspond to the units of stiffness.  
 (b) *Stiffness.* What is the value of the stiffness of the  $\text{Si}_3\text{N}_4$  micromachined cantilever?  
 (c) *Thermal noise.* What is the root-mean-square displacement,  $x_{rms} = \langle x^2 \rangle^{1/2}$ , of the tip if the cantilever is at a temperature of  $20^\circ\text{C} = 293 \text{ K}$ ?  
 (d) *Minimum detectable force.* What force on the tip would be required to produce a static deflection,  $\Delta$ , that is equal to the root-mean-square thermal fluctuation in the position of the tip,  $x_{rms}$ , that you calculated in part (c).

**Fig. 2.38** Silicon cantilever with spike



<sup>31</sup> Image courtesy of *SecretDisk* under their Creative Commons Attribution-Share Alike 3.0 license.

**Fig. 2.39** Two electrically charged spheres are constrained to move only in the vertical direction. The potential energy,  $U(x)$ , of the upper sphere is due to the combination of the force of gravity and the force of electrostatic repulsion. (Figure courtesy of J. D. Maynard [23])



11. **Electrostatic levitation.** Two spheres, made of an electrically insulating material, are contained within a frictionless insulating tube as shown in Fig. 2.39. (You can imagine this as two tiny Styrofoam balls in a drinking straw.) The lower sphere is rigidly attached to the bottom of the tube, and the upper sphere is free to move up or down, without significant damping, only in the vertical direction.

The mass of each sphere is 0.10 g. The electrostatic force,  $F$ , between the spheres is determined by the charges on the spheres,  $Q_{upper}$  and  $Q_{lower}$ ; the separation between their centers,  $x$ ; and a constant,  $\epsilon_o = 8.85 \times 10^{-12}$  Farads/meter, known as the permittivity of free space. In this case, the force between the spheres is repulsive, since the charge on both spheres is positive.

$$F = \frac{1}{4\pi\epsilon_o} \frac{Q_{upper} Q_{lower}}{x^2} \quad (2.144)$$

At equilibrium, the centers of the spheres are separated by 1.0 cm. What is the frequency of oscillation of the upper sphere if it is displaced from its equilibrium position by a very small amount? (Let the acceleration due to gravity,  $g = 9.8 \text{ m/s}^2$ .)

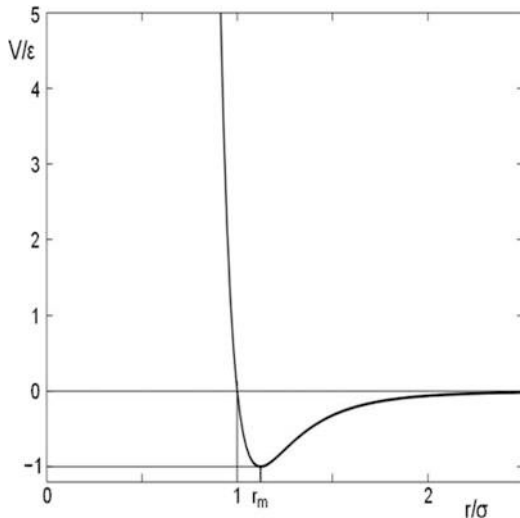
12. **Lennard-Jones potential.** This potential function, sometimes known as the “6–12 potential” of Eq. (2.145), is plotted in Fig. 2.40. It describes the interaction of two inert gas atoms as a function of their separation and is useful in calculations of scattering or determination of the temperature of condensation from a gas to a liquid. It was first proposed by John Lennard-Jones in 1924 [35].

$$V(r) = 4\epsilon \left[ \left( \frac{\sigma}{r} \right)^{12} - \left( \frac{\sigma}{r} \right)^6 \right] \quad (2.145)$$

The term proportional to  $r^{-12}$  represents an empirical fit to the hard-core repulsion produced by Pauli exclusion at short ranges when the atoms are close enough that the electron orbitals overlap. The  $r^{-6}$  term represents the van der Waals attraction due to the mutual interactions of the fluctuating dipole moments.

- (a) *Equilibrium separation.* Determine the equilibrium separation of two atoms,  $r_m$ , in terms of  $\sigma$  and  $\epsilon$ .
- (b) *Argon separation.* For argon,  $\sigma = 3.42 \text{ \AA}$  ( $1 \text{ \AA} = 10^{-10} \text{ m}$ ) and  $\epsilon = 124 \text{ K}$  ( $1 \text{ K} = 1.38 \times 10^{-23} \text{ J}$ ). Determine the equilibrium separation of two argon atoms.

**Fig. 2.40** Lennard-Jones interatomic potential as a function of scaled atomic spacing,  $r/\sigma$



- (c) *Antisymmetric vibrational frequency.* The atomic mass of an argon atom is 39.948 amu (1 amu =  $1.66 \times 10^{-27}$  kg). Determine the stiffness constant,  $K = d^2V/dr^2$ , and use that result to calculate the vibrational frequency of two isolated argon atoms about their equilibrium separation.
13. **Ionic bonding.** Hydrogen chloride (HCl) is a diatomic molecule that forms an ionic bond. The force that bonds the  $H^+$  ion to the  $Cl^-$  is the electrostatic attraction between the oppositely charged ions. Of course, Pauli repulsion will separate the two ions if they are drawn too close together. The potential,  $V(r)$ , for this interaction is the sum of the electrostatic attraction and the Pauli repulsion.

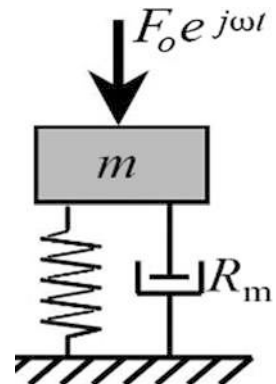
$$V(r) = -\frac{e^2}{4\pi\epsilon_0 r} + \frac{B}{r^9} \quad (2.146)$$

The permittivity of free space is  $\epsilon_0 = 8.85 \times 10^{-12}$  Farads/meter [F/m], and the charge on a single electron is  $e = 1.602 \times 10^{-19}$  C.

- (a) *Repulsion constant.* If the equilibrium separation of centers of the two ions is  $r_m = 1.30$  Å (1 Å =  $10^{-10}$  m), determine the value of the constant,  $B$ , in Eq. (2.146).
- (b) *Effective stiffness.* What is the effective stiffness,  $K$ , of the bond about the equilibrium separation,  $r_m$ ?
- (c) *Vibrational frequency.* The mass of the chlorine ion is about 35 times greater than the hydrogen ion. Assume that the position of chlorine atom is fixed, and determine the frequency of oscillation of the hydrogen ion if it is displaced by a small distance,  $x_1 \ll r_m$ .
- (d) *Reduced mass.* Since the mass of the chlorine ion is not infinite, the oscillation actually takes place about the center of mass, which remains at rest. This can be accounted for by using the reduced mass,  $\mu$ , given in Eq. (2.147), rather than using the mass of the hydrogen ion, so  $f_o = (K/\mu)^{1/2}/2\pi$ .

$$\mu = \frac{M_{Cl^-} M_{H^+}}{M_{Cl^-} + M_{H^+}} \quad (2.147)$$

**Fig. 2.41** Damped, driven harmonic oscillator



By what percentage is this frequency shifted from the value that assumed the chlorine atom had infinite mass?

14. **Damped driven SHO.** The system in Fig. 2.41 has a mass,  $m = 0.100 \text{ kg}$ , that is attached to a rigid foundation with a spring of stiffness,  $K = 1000 \text{ N/m}$ , and a dashpot with mechanical resistance,  $R_m$ , that is to be determined in part (b) of this problem.
  - (a) *Natural frequency.* What is the natural frequency of the mass-spring system, in hertz, if the damper is not present ( $R_m = 0$ )?
  - (b) *Mechanical resistance.* After an impulsive excitation, it is found that amplitude of free vibration of the mass decays to  $e^{-1}$  of its value in 2.0 s. Determine the value of  $R_m$  and report your results in kg/s.
  - (c) *Driven response.* If the mass is driven with a time-harmonic force of amplitude 10 N, at a frequency of 20 Hz,  $F(t) = 10e^{j40\pi t}$ , what is:
    - (i) The magnitude of the time-harmonic displacement of the mass?
    - (ii) The phase of the mass's velocity with respect to that of the driving force?
    - (iii) The time-averaged power dissipated in  $R_m$ ?
15. **Damped harmonic oscillator.** A 1.00 kg mass is suspended from a spring. A 0.40 kg mass is hung by a string below the 1.00 kg mass. The additional mass causes the spring to be extended by an additional 4.0 cm. The string is cut at  $t = 0$  and the additional mass drops to the floor. The resulting harmonic oscillations of the 1.00 kg mass are observed to decay by  $e^{-1}$  in 1 s.
  - (a) *Spring stiffness.* What is the spring's stiffness?
  - (b) *Mechanical resistance.* What is the oscillator's mechanical resistance,  $R_m$ ?
  - (c) *Displacement.* Equation (2.43) provides an expression for the motion of the mass,  $x(t)$ . Determine the values of the constants  $C$ ,  $\tau$ ,  $\omega_d$ , and  $\phi$  that describe the motion for  $t \geq 0$ .
16. **Five identical masses.** Determine the five modal frequencies, and sketch the corresponding five mode shapes (like Fig. 2.31) for five masses, each with mass,  $m$ , that is equally spaced along a massless string of total length,  $L = 6a$ , that is fixed at both ends (i.e.,  $y(0) = y(6a) = 0$ ) and is stretched to a tension,  $T$ . You may assume that the vertical displacements of all of the masses are small compared to their separation (i.e.,  $y \ll a$ ). The normal mode frequencies can be reported in terms of  $T$ ,  $a$ , and  $m$ .
17. **Coupled oscillators.** Nine objects of equal mass are joined by ten identical springs to two rigid boundaries as shown in Fig. 2.42. The masses are constrained to move along the line joining them. In Fig. 2.42, the equilibrium positions of the numbered masses are indicated by the equally spaced tick marks. In that diagram, the nine masses are shown at a particular phase of their collective

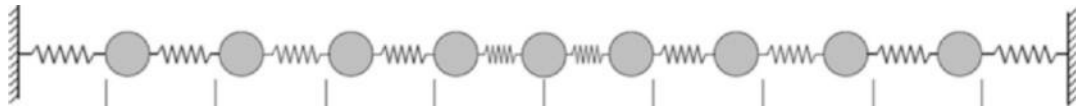
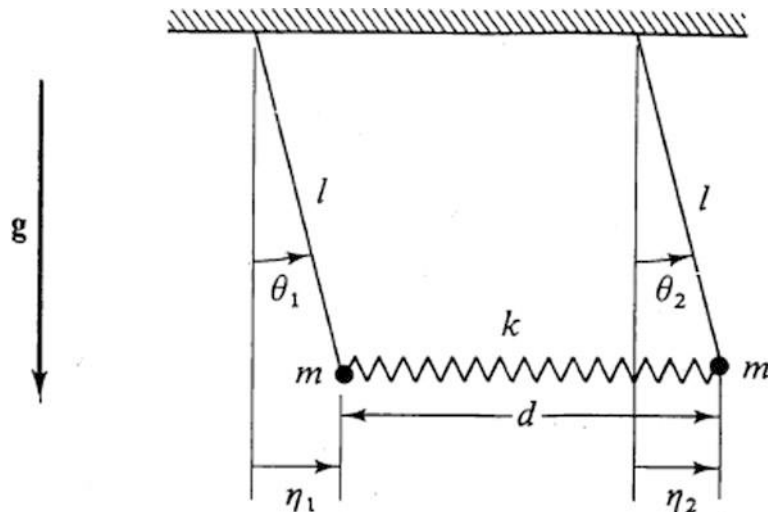


**Fig. 2.42** Nine identical masses connected to rigid boundaries by nine identical springs

**Fig. 2.43** Two pendula coupled by a spring



oscillation corresponding to a normal mode frequency of 20 Hz. What is the frequency of the fundamental (lowest-frequency) mode of oscillation?

18. **Two coupled pendula.** Consider the two identical pendula with masses,  $m$ , and lengths,  $\ell$ , which are joined by a spring of stiffness,  $K$ , diagrammed in Fig. 2.43.
  - (a) *Coupled equations.* Assume that the angular displacements,  $\theta_1$  and  $\theta_2$ , are both small enough that  $\sin \theta \cong \theta$ . Write the coupled differential equations that relate  $d^2\theta/dt^2$  to the angular displacements.
  - (b) *Modal frequencies.* After making the harmonic substitution, calculate the determinate-of-coefficients of the resulting coupled algebraic equations to determine the symmetric and antisymmetric normal mode frequencies in terms of  $\ell$ ,  $m$ ,  $K$ , and gravitational acceleration,  $g$ .
19. **Electrodynamic loudspeaker.** In this exercise, you will characterize a 5" electrodynamic loudspeaker (Morel MW 142, S/N 0496). You may neglect all acoustic loading and assume that the speaker measurements in Table 2.1 are made in a vacuum. Figure 2.44 contains the catalog description of the speaker (Right) and a diagram of its parts (Left) taken from Hunt's *Electroacoustics* [36].
 

You are to determine the values of the loudspeaker's parameters and their uncertainty using least-squares curve fitting and error propagation using the measurements summarized in Table 2.1.

  - (a) *Stiffness and moving mass.* Determine the original moving mass,  $m_o$ , and dynamic stiffness,  $K$ , of the loudspeaker and the uncertainties in those values based on the data in the first two columns of data at the left end of Table 2.1.
  - (b) *Mechanical resistance.* If the driver is driven at its resonance frequency and then the power is cut and the voice coil ( $R_{dc} = 5.1 \Omega$ ) is connected to a high impedance load, the exponential free-decay time,  $\tau$ , can be related to the mechanical resistance,  $R_m = 2m_o / \tau$ , of the loudspeaker. The columns labeled "Time" and "V(peak)" in Table 2.1 are the results of

**Table 2.1** (Left to right) Measured frequency vs. added mass (shaded), free-decay amplitude vs. time, LVDT output vs. position (shaded), and LVDT output vs. DC electrical current through the voicecoil

Mass (gm)	Freq. (Hz)	Time (ms)	V(peak) (mV <sub>dc</sub> )	Position (in.)	V <sub>out</sub> (mV <sub>dc</sub> )	I <sub>dc</sub> (mA <sub>dc</sub> )	V <sub>out</sub> (mV <sub>dc</sub> )
0	55.5	29.25	-823	0.700	947.7	-253.3	388
0.877	53.6	35.50	0	0.650	728.3	-202.1	343
2.877	49.9	39.55	+318	0.600	512.4	-153.6	301
5.877	45.6	45.32	0	0.550	296.3	-101.4	256
10.877	40.2	49.40	-144	0.500	81.4	-54.6	216
20.877	33.4	54.97	0	0.450	-133.5	0	169.1
		59.00	+69	0.400	-247.3	+49.8	136.0
		64.47	0			+102.6	91.3
		68.75	-33			+151.4	46.1
						+202.5	1.6

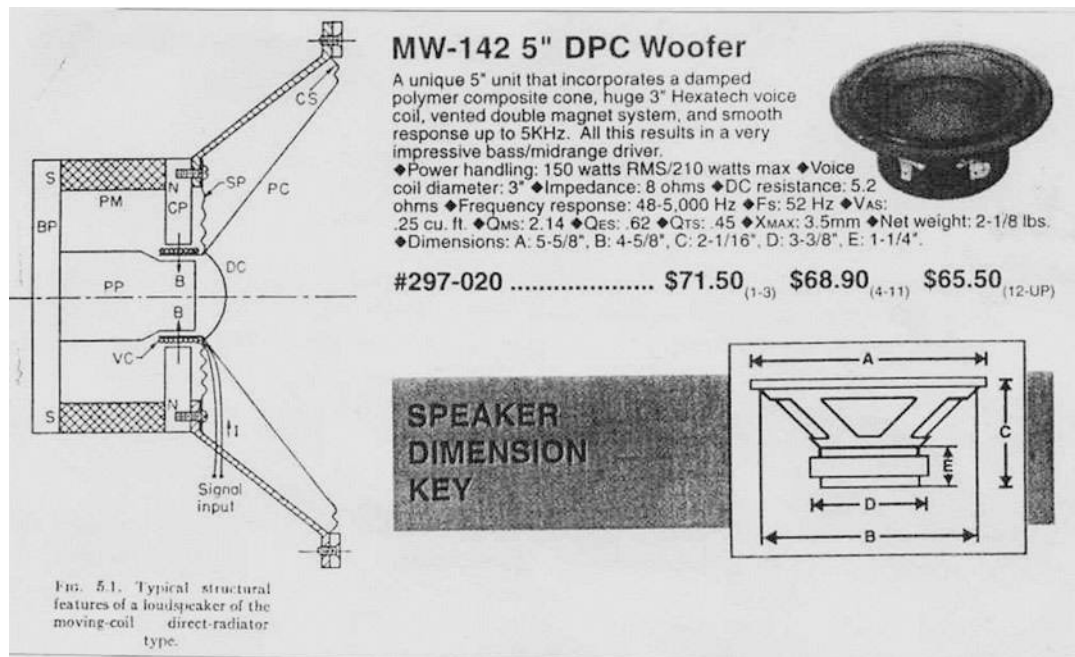


**Fig. 2.44** Electrodynanic loudspeaker used to produce the results summarized in Table 2.1

such a free-decay measurement.  $V(\text{peak})$  is the value of the voltage at the peak (or trough) of each cycle. The peaks occur at integer multiples of the period  $T$ ,  $n = 0, 1, 2, \dots$ . The troughs occur at half-odd integer values of  $n = \frac{1}{2}, \frac{3}{2}, \frac{5}{2}, \dots$

$$V(\text{peak}) = V_1 e^{-nT/\tau} \quad (2.148)$$

Take the natural log of that expression to convert to a linear relation, and find  $R_m$  and its uncertainty by creating a plot like Fig. 1.15.

- (c) *LVDT calibration.* To determine the transduction coefficient,  $B\ell$ , the displacement of the loudspeaker cone has been measured as a function of DC current,  $I_{dc}$ , through the voice coil:

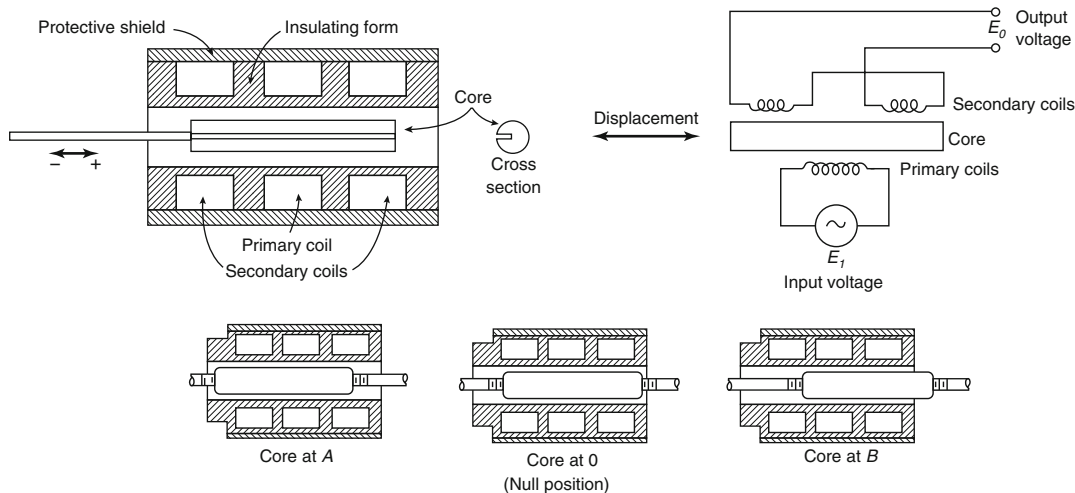


**Fig. 2.45** (Above) Cross-sectional diagrams of an LVDT at the left and electrical schematic diagram of the astatic transformer showing the (driven) primary and (output) secondary coils. (Below) Position of the LVDT core displaced to the left, centered, and displaced to the right. (Courtesy of Lucas-Schaevitz)

$F = -Kx = -(Bl)I_{dc}$ . The displacement is measured by a linear variable differential transformer (LVDT) shown in Fig. 2.45.

The LVDT output (secondary) consists of two coils that are connected (electrically) in series but are wound in opposite directions. The movable core has a high magnetic permeability. When the core is exactly at the center (null position), it couples an equal amount of the oscillating magnetic flux (produced by an AC current applied to the primary coil) to both secondary coils resulting in zero output voltage. When the core is in position *A*, more flux is coupled into the left-hand core which produces a waveform that has an amplitude that is proportional to the distance from the null position and is in-phase with the signal driving the primary. When the core is in position *B*, more flux is coupled into the right-hand core, producing a waveform amplitude that is also proportional to the distance from the null position but is out-of-phase with the signal driving the primary. The voltage output of one such LVDT as a function of position is tabulated in columns labeled "Position" and " $V_{out}$ ." Plot  $V_{out}$  vs. Position to determine the sensitivity of the LVDT,  $dV_{out}/dx$ , and its uncertainty.

- (d) *Bl-product.* After calibration of the LVDT, the  $Bl$ -product can be determined from the fit to " $I_{dc}$ " and " $V_{out}$ ," the LVDT calibration, and the measured stiffness constant,  $K$ , from part (a). Find the value of  $Bl$  and its uncertainty.<sup>32</sup>
- (e) *Constant current response.* Assume the loudspeaker is driven by a constant sinusoidal current of 100 mA<sub>rms</sub> at all the frequencies of interest in this exercise.<sup>33</sup> Plot the magnitude and phase of the voice coil's velocity,  $v$ , as a function of frequency between 10 Hz and 1 kHz. Use a log<sub>10</sub> axis for frequency.
- (f) *Power dissipation.* Determine the power dissipated in the speaker's mechanical resistance,  $R_m$ , at the resonance frequency,  $\omega_o$ .

<sup>32</sup>This calculation assumes that the dynamic stiffness constant measured in the added mass experiment is the same as the static stiffness constant that is used in this part of the exercise to convert the displacement of the cone to the force produced by the current in the voice coil. Due to the viscoelastic behavior of the cone's surround, those two stiffnesses can differ due to relaxation of the elastomeric surround (see Fig. 1.16). For this exercise, that difference can be neglected.

<sup>33</sup>In normal operation, speakers are usually driven at constant voltage, but the variation in the speaker's electrical impedance with frequency makes that calculation more difficult.

20. **Jug hustlers.** One of the most common tools in the oil exploration business is the geophone. It is used for seismic surveys, and the surveyors who plant and recover this ground vibration velocity sensors are known as “jug hustlers,” since the geophones look like little jugs (see Fig. 2.24). In this problem, you will calculate the response of a GeoSpace® Corp. Model GS-30 CT geophone. The moving mass (mostly the coil and bobbin),  $m_o = 11.2 \text{ gm } (\pm 3.5\%)$ , and the natural frequency,  $f_o = \omega_o/2\pi = 10 \text{ Hz}$ .
- Damping.* The open-circuit damping factor,  $\zeta_o = 0.316 = (2Q)^{-1}$ . Find the mechanical resistance,  $R_m$ , of the moving coil and its relative uncertainty.
  - Sensitivity.* The electrodynamically generated, open-circuit voltage,  $V_{emf} = (B\ell)v$ , where  $v$  is the relative velocity of the coil with respect to the case. If the transduction coefficient,  $(B\ell) = 70 \text{ N/A}$ , calculate the root-mean-squared (rms) open-circuit voltage,  $V_{rms}$ , generated by the geophone if the peak-to-peak ground motion is  $10.0 \mu\text{m}$  at  $20, 50, 100$ , and  $200 \text{ Hz}$ .
  - Thermal noise.* Use the Equipartition Theorem to determine the value of  $V_{rms}$  due to the thermal motion of the coil if the temperature,  $T = 20^\circ \text{C}$ .
21. **Rayleigh line-shape fit.** The data in Table 2.2 provides the measured amplitude at 22 frequencies around resonance for the third (i.e.,  $n = 3$ ) torsional mode of a cylindrical rod made from Eastman Tritan® Copolyester TX1001. Using the Rayleigh line-shape of Eq. (2.63), determine the best values for  $f_3$ ,  $A_3(1)$ , and  $Q_3$  by minimizing the squared difference between the measurements and the values produced by Eq. (2.63) by using your choice of “solver” software.
- Parameter estimates.* The convergence of any solver’s results will depend upon the quality of the initial guess for the parameters that the solver is allowed to vary. Estimate  $f_3$  and  $A_3(1)$  by choosing the largest amplitude value in Table 2.2 and its corresponding frequency. Estimate  $Q_3 \cong f_3/(f_+ - f_-)$  where  $f_+$  and  $f_-$  are the “down 3 dB” frequencies, as in Eq. (B.3).

**Table 2.2** Resonance amplitude vs. frequency

Frequency [Hz]	Amplitude [mV <sub>ac</sub> ]
3245	682.5
3260	714.9
3275	749.7
3290	787.1
3305	827.4
3320	870.1
3335	915.3
3350	957.1
3365	997.2
3380	1034.1
3395	1059.0
3410	1073.0
3425	1074.7
3440	1063.6
3455	1036.4
3470	998.0
3485	953.3
3500	905.1
3515	855.9
3530	806.1
3545	758.7
3560	713.8

- (b) *Plot.* On a single graph with properly labeled axes (including units), plot the data in Table 2.2 as “points” and the Rayleigh line shape as a smooth line using the parameter estimates of part (a).
- (c) *Optimize fit.* Have your solver software optimized the values of  $f_3$ ,  $A_3(1)$ , and  $Q_3$  by minimizing the squared difference between the measurements in Table 2.2 and the values produced by Eq. (2.63). Report the optimized values, and update your plot in part (b) using the best-fit parameter values.
- (d) *Error estimate.* How could you try to estimate the uncertainty in the fit parameters? Use your scheme to report your estimate in the relative uncertainty ( $\pm 1\sigma$ ) for your optimized values of  $f_3$ ,  $A_3(1)$ , and  $Q_3$ .

## References

1. R.C. Cross, M.S. Wheatland, Modeling a falling slinky. *Am. J. Phys.* **80**(12), 1051–1060 (2012)
2. H. Goldstein, *Classical Mechanics* (Addison-Wesley, Reading, 1950), pp. 69–71
3. J.W. Strutt (Lord Rayleigh), *The Theory of Sound*, vol. I, 2nd edn. (Macmillan, London, 1894), pp. 112; reprinted (Dover, 1945); ISBN: 486-60292-3
4. J.W. Strutt (Lord Rayleigh), *The Theory of Sound*, vol. I, 2nd edn. (Macmillan, London, 1894), pp. 109–110; reprinted (Dover, 1945); ISBN: 486-60292-3
5. G.W. Swift, *Thermoacoustics: A Unifying Perspective for Some Engines and Refrigerators*, 2nd edn. (ASA Press/Springer, Cham, 2017); ISBN: 978-3-319-66932-8
6. M. Greenspan, Simple derivation of the Boltzmann-Ehrenfest adiabatic principle. *J. Acoust. Soc. Am.* **27**(1), 34–35 (1955)
7. T.G. Giallorenzi, J.A. Bucaro, A. Dandridge, G.H. Sigel Jr., J.H. Cole, S.C. Rashleigh, P.G. Priest, Optical fiber sensor technology. *IEEE J. Quantum Electron.* **QE-18**(4), 626–665 (1982)
8. A. Einstein, Über die von der molekularkinetischen Theorie der Wärme geforderte Bewegung von in ruhenden Flüssigkeiten suspendierten Teilchen (On the motion of small particles suspended in a stationary liquid, as required by the molecular kinetic theory of heat). *Ann. Phys.* **17**(8), 549–560 (1905)
9. W. Gerlach, E. Lehrer, Über die Messung der rotatorischen Brownschen Bewegung mit Hilfe einer Drehwage. *Naturwiss* **15**(1), 15 (1927)
10. G.E. Uhlenbeck, S. Goudsmit, A problem in Brownian motion. *Phys. Rev.* **34**, 145–151 (1929)
11. P. Horowitz, W. Hill, *The Art of Electronics*, 2nd edn. (Cambridge University Press, Cambridge, 1989). §7.11; ISBN: 0-521-37095-7
12. H. Nyquist, Thermal agitation of electric charge in conductors. *Phys. Rev.* **32**, 110–113 (1928)
13. C.W. McCombie, Fluctuation theory in physical measurements. *Rep. Prog. Phys.* **16**, 266–319 (1953)
14. T.J. Hofler, S.L. Garrett, Thermal noise in fiber optic sensors. *J. Acoust. Soc. Am.* **84**(2), 471–475 (1988)
15. D.L. Gardner, T. Hofler, S.R. Baker, R.K. Yarber, S.L. Garrett, A fiber optic interferometric seismometer. *J. Lightwave Technol.* **LT-5**(7), 953–960 (1987); S.L. Garrett, D.L. Gardner, Multiple axis fiber optic interferometric seismic sensor. U.S. Patent No. 4,893,930 (January 16, 1990)
16. F. Reif, *Fundamentals of Statistical Mechanics and Thermal Physics* (McGraw-Hill, New York, 1965), §7.5
17. W.P. Allis, M.A. Herlin, *Thermodynamics and Statistical Mechanics* (McGraw-Hill, New York, 1952)
18. T.B. Gabrielson, Mechanical-thermal noise in micromachined acoustic and vibration sensors. *IEEE Trans. Electron Devices* **40**(3), 903–909 (1993)
19. A.B. Pippard, *The Physics of Vibration* (Cambridge University Press, Cambridge, 1989); ISBN: 0-521-37200-3
20. I.S. Gradshteyn, I.M. Ryzhik, *Tables of Integrals, Series, and Products* (Academic, London, 1980). isbn:0-12-294760-6. See equation 3.264(2)
21. R.S. Wakeland, Use of electrodynamic drivers in thermoacoustic refrigerators. *J. Acoust. Soc. Am.* **107**(2), 827–832 (2000)
22. R.E. Best, *Phase-Locked Loop: Design, Simulation, and Applications*, 6th edn. (McGraw-Hill, New York, 2007); ISBN: 9780079375-8
23. J.D. Maynard, Topics in physics, Part IV-Acoustics, Penn State Lecture Notes, 2012
24. P. Campbell, *Permanent Magnet Materials and Their Application* (Cambridge University Press, Cambridge, 1994); ISBN: 0 521 56688 6
25. S.L. Garrett, J.F. Heake, Hey kid! Wanna build a loudspeaker? The first one’s free. Audio Engineering Society Convention Paper 5882 (2003 October 10–13, New York, NY); S.L. Garrett, Two-way loudspeaker enclosure

- assembly and testing as a freshman seminar. Paper #526, 17th International Congress on Sound and Vibration, 18–22 July 2010, Cairo, Egypt
26. T.W. Leishman, B.E. Anderson, Evaluation of moving-coil loudspeaker and passive radiator parameters using normal-incidence sound transmission measurements: Theoretical developments. *J. Acoust. Soc. Am.* **134**(1), 223–236 (2013)
27. L.L. Beranek, *Acoustics* (Acoustical Society of America, Woodbury, 1996). pp. 185–188, 211–230; ISBN: 0-88318-494-X
28. A.N. Thiele, Loudspeakers in vented boxes: Parts I and II. *Proc. Inst. Radio Eng. (Australia)* **22**, 487–502 (1961); reprinted in *J. Audio Eng. Soc.* **19**, 382–392, 471–483 (1971)
29. B. Baumzweiger (a.k.a., Bauer), Microphone apparatus, U.S. Patent No. 2,184,247 (December 19, 1939)
30. W.L. Dooley, Ribbon microphones. *J. Acoust. Soc. Am.* **136**, 2130 (2014)
31. M.S. Pettersen, 75th anniversary of the Shure Unidyne® microphone. *J. Acoust. Soc. Am.* **136**, 2129 (2014)
32. J.C. Snowdon, *Vibration and Shock in Damped Mechanical Systems* (Wiley, London, 1968)
33. P.M. Morse, *Vibration and Sound*, 2nd edn. (McGraw-Hill, New York, 1948). Reprinted (Acoustical Society of America, 1976). isbn:0-88318-287-4. The normal mode displacement are given in Eqs. (7.3) though (7.5), pp. 55–58
34. A.L. Fetter, J.D. Walecka, *Theoretical Mechanics of Particles and Continua* (Dover, Mineola, 2003); ISBN: 0-486-43261-0
35. J.E. Lennard-Jones, On the determination of molecular fields. *Proc. R. Soc. Lond. A* **106**, 463–477 (1924)
36. F.V. Hunt, *Electroacoustics: The Analysis of Transduction and Its Historical Background* (Wiley, New York, 1954); reprinted (Acoust. Soc. Am., 1982). ISBN: 0-88318-401-X

**Open Access** This chapter is licensed under the terms of the Creative Commons Attribution 4.0 International License (<http://creativecommons.org/licenses/by/4.0/>), which permits use, sharing, adaptation, distribution and reproduction in any medium or format, as long as you give appropriate credit to the original author(s) and the source, provide a link to the Creative Commons license and indicate if changes were made.

The images or other third party material in this chapter are included in the chapter's Creative Commons license, unless indicated otherwise in a credit line to the material. If material is not included in the chapter's Creative Commons license and your intended use is not permitted by statutory regulation or exceeds the permitted use, you will need to obtain permission directly from the copyright holder.





# String Theory

3

## Contents

3.1	<b>Waves on a Flexible String</b> .....	134
3.2	<b>Pulse Reflections at a Boundary and the Utility of Phantoms</b> .....	138
3.3	<b>Normal Modes and Standing Waves</b> .....	141
3.3.1	Idealized Boundary Conditions .....	141
3.3.2	Consonance and Dissonance* .....	144
3.3.3	Consonant Triads and Musical Scales* .....	145
3.4	<b>Modal Energy</b> .....	147
3.4.1	Nature Is Efficient .....	149
3.4.2	Point Mass Perturbation .....	152
3.4.3	Heavy Chain Pendulum (Nonuniform Tension)* .....	153
3.5	<b>Initial Conditions</b> .....	155
3.5.1	Total Modal Energy .....	157
3.6	<b>“Imperfect” Boundary Conditions</b> .....	158
3.6.1	Example: Standing Wave Modes for $M/m_s = 5$ .....	161
3.6.2	An Algebraic Approximation for the Mass-Loaded String .....	161
3.6.3	The Resistance-Loaded String* .....	163
3.7	<b>Forced Motion of a Semi-Infinite String</b> .....	165
3.8	<b>Forced Motion of a Finite String</b> .....	166
3.8.1	Displacement-Driven Finite String .....	167
3.8.2	Mass-Loaded String in the Impedance Model .....	169
3.8.3	Force-Driven Finite String .....	170
3.8.4	An Efficient Driver/Load Interaction .....	170
3.9	<b>“I’ve Got the World on a String . . .”:</b> Chapter Summary .....	171
	<b>References</b> .....	177

The vibrating string has been employed by nearly every human culture to create musical instruments. Although the musical application has attracted the attention of mathematical and scientific analysts since the time of Pythagoras (570 BC–495 BC), we will study the string because its vibrations are easy to visualize and it introduces concepts and techniques that will recur throughout our study of vibration

and the acoustics of continua. A retrospective of these concepts and techniques is provided in Sect. 3.9, near the end of this chapter. You might want to skip ahead to read that section to understand the plot before you meet the characters.

In the analyses of the previous chapter, we sought equations that would specify the time histories,  $x(t)$ , of the displacement of discrete masses constrained to move only along one dimension, focusing particularly on single-frequency time-harmonic motion. At the end of that chapter, we examined the limit as the number of masses became infinite and the inter-mass spacing decreased in a way that held constant the linear mass density,  $\rho_L$ , of our “string of pearls” in Sect. 2.7.7. In this chapter, we will develop continuous mathematical functions of position and time that describe the shape of the entire string. The amplitude of such functions will describe the transverse displacement from equilibrium,  $y(x, t)$ , at all positions along the string.<sup>1</sup>

### 3.1 Waves on a Flexible String

We begin this exploration, as we did with the simple harmonic oscillator, by seeking an equation-of-state (i.e., a relationship between forces and displacements), but now we will examine an infinitesimal segment of string, with length,  $dx$ , acted upon by the tension applied at both ends. As we did with the “string of pearls” in Sect. 2.7.7, we will assume that the string has a constant linear mass density,  $\rho_L$ , and that the string has no flexural rigidity (i.e., no bending stiffness); thus the string can only apply forces produced by the tension,  $T$ , to influence the string’s motion. We will also assume that the string’s displacements from equilibrium are small enough that the displacements create length changes that only contribute modifications to the tension that are second-order in the ratio ( $y/L$ ), as shown in Eq. (2.129), and can be neglected in a linear (i.e., first-order) analysis.

Figure 3.1 shows the infinitesimal length of string as just described. It is acted upon by the vertical components of the tension at either end,  $F_v(x)$  and  $F_v(x + dx)$ . As will be demonstrated, if the string does not have any curvature, there will be no net transverse force. We can apply Newton’s Second Law to that segment of length,  $dx$ , once we calculate the net transverse force,  $dF_{net}$ .

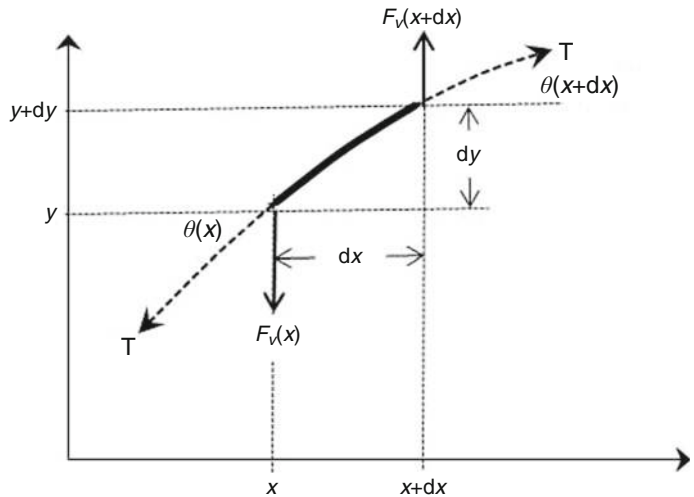
Since  $x$ ,  $y$ , and  $t$  are all independent variables, partial derivatives are used to remind us to hold the other two variables constant when we take a derivative with respect to the third variable.

$$dF_{net} = (T \sin \theta)_{x+dx} - (T \sin \theta)_x \cong \left[ (T \sin \theta)_x + \frac{\partial(T \sin \theta)}{\partial x} \Big|_x dx + \dots \right] - (T \sin \theta)_x \quad (3.1)$$

This approximate expression utilizes the first two terms in the Taylor series of Eq. (1.2). After cancellation of the two leading  $(T \sin \theta)_x$  terms of opposite sign, we are left with an expression for the net transverse force that can be expanded by the product rule of Eq. (1.10).

<sup>1</sup> Since we are discussing transverse waves, it is necessary to recognize that we have two orthogonal options for the specification of the plane of the polarization for those displacements. We will let the  $x$  axis designate the direction of propagation, determined by the undisturbed stretched string. The string’s displacements from equilibrium could be in the  $y$  direction, the  $z$  direction, or some superposition of both. Since we are starting with the assumption of perfect azimuthal symmetry around the axis of the string, the choice is irrelevant. When we apply periodic external forces (see Sect. 3.8) and/or displacements, the polarization plane will be specified. If the string is “twisted,” that symmetry might become broken and the plane of polarization could change with time.

**Fig. 3.1** An infinitesimal length,  $ds = \sqrt{dx^2 + dy^2} \cong dx$ , of a string with uniform linear mass density,  $\rho_L$ , that is acted upon by the tension,  $T$ , exerting a force along the direction of the string. The angle that the string makes with the horizontal at  $x$  is  $\theta(x)$ , and the angle at  $x + dx$  is  $\theta(x + dx)$ . If these angles are different, there will be a net transverse force on that segment, causing it to accelerate



$$dF_{net} = \frac{\partial(T \sin \theta)}{\partial x} \Big|_x dx \cong \frac{\partial\left(T \frac{\partial y}{\partial x}\right)}{\partial x} \Big|_x dx = \left( \frac{\partial T}{\partial x} \Big|_x \frac{\partial y}{\partial x} \Big|_x + T \frac{\partial^2 y}{\partial x^2} \Big|_x \right) dx \quad (3.2)$$

We have again imposed the assumption that  $\partial y / \partial x \ll 1$ , so  $\sin \theta \cong \tan \theta \cong dy/dx$ , where these two differential lengths,  $dx$  and  $dy$ , are shown in Fig. 3.1.<sup>2</sup> For now, we will assume that the tension along the string is independent of position, so  $\partial T / \partial x = 0$ , although we will reconsider this restriction later in Sect. 3.4.3, when we consider the oscillations of a heavy chain that has a tension that decreases as we recede from its point of suspension (since the lower links are supporting less mass than the upper links).

For our simplified case, our equivalent of an equation-of-state for the string shows that the net transverse force,  $dF_v$ , on an infinitesimal string segment is the product of the constant tension,  $T$ , and the curvature of the string.<sup>3</sup> This is consistent with our intuition. Strings that are displaced but remain straight, like those strings attached to the discrete masses shown in Figs. (2.23) through (2.26), only apply forces at the “kinks” produced at the positions of the discrete masses or at the fixed boundaries.

Once again, we will use Newton’s Second Law to provide the dynamical equation that describes the acceleration of that infinitesimal string segment with mass,  $\rho_L dx$ , acted upon by  $dF_{net}$ .

$$(\rho_L dx) \frac{\partial^2 y(x, t)}{\partial t^2} = T \frac{\partial^2 y(x, t)}{\partial x^2} dx \quad (3.3)$$

After cancellation of the common differential, this solution is written in a form known as the *wave equation* where we identify the *speed of transverse waves*,  $c = \sqrt{T/\rho_L}$ .

<sup>2</sup> In Fig. 3.1,  $dy$  has been exaggerated to make the drawing easier to read.

<sup>3</sup> The exact mathematical definition of “curvature,”  $\kappa$ , involves both the second and first derivatives:  $\kappa = \left( \frac{\partial^2 y}{\partial x^2} \right) / \left[ 1 + \left( \frac{\partial y}{\partial x} \right)^2 \right]^{3/2}$ . In our first-order analysis, we can neglect the square of the first-order term  $(\partial y / \partial x)^2$ , since it is second-order, and let  $\kappa \cong \partial^2 y / \partial x^2$ .

$$\frac{\partial^2 y(x,t)}{\partial t^2} - \left(\frac{T}{\rho_L}\right) \frac{\partial^2 y(x,t)}{\partial x^2} = \frac{\partial^2 y(x,t)}{\partial t^2} - c^2 \frac{\partial^2 y(x,t)}{\partial x^2} = 0 \quad (3.4)$$

Such a second-order homogeneous partial differential equation must have two independent solutions. As demonstrated below, those solutions can have any functional form so long as the arguments of those functions only involve two particular combinations of the space and time coordinates.

$$y(x,t) = f_-(x - ct) + f_+(x + ct) \quad (3.5)$$

At this point, the form of the two functions,  $f_-$  and  $f_+$ , is entirely arbitrary, but the requirement imposed by the wave equation suggests that after some time  $t$ ,  $f_-(x - ct)$  will be identical to its shape at  $t = 0$ , except at a distance,  $x = ct$ , farther to the right. Similarly,  $f_+(x + ct)$  will be identical to its shape at  $t = 0$ , except at distance,  $x = -ct$ , farther to the left. Because these functions propagate with speed,  $c$ ,  $f_-(x - ct)$  and  $f_+(x + ct)$  are called *traveling wave* solutions.

The wave equation can be written in a “linear operator” form (see Sect. 1.3) represented by the *d'Alembertian operator*.

$$\begin{aligned} \frac{1}{c^2} \frac{\partial^2 y(x,t)}{\partial t^2} - \frac{\partial^2 y(x,t)}{\partial x^2} &\equiv \square y(x,t) \\ &= \left( \frac{1}{c} \frac{\partial y(x,t)}{\partial t} - \frac{\partial y(x,t)}{\partial x} \right) \left( \frac{1}{c} \frac{\partial y(x,t)}{\partial t} + \frac{\partial y(x,t)}{\partial x} \right) = 0 \end{aligned} \quad (3.6)$$

In the lower expression, the operator has been factored to make it easy to see that the solutions shown in Eq. (3.5) satisfy the wave equation one or the other term in the rightmost version of Eq. (3.6) vanish.

The proof that Eq. (3.5) is a solution to the wave equation of Eq. (3.4) or Eq. (3.6) is simplified by the introduction of a new variable,  $w_{\pm} = x \pm ct$ , and the use of the chain rule.

$$\frac{\partial y}{\partial x} = \frac{\partial f_{\pm}}{\partial w_{\pm}} \frac{\partial w_{\pm}}{\partial x} = \frac{\partial f_{\pm}}{\partial w_{\pm}} \quad (3.7)$$

The same transformation can be applied to the partial derivative with respect to time.

$$\frac{\partial y}{\partial t} = \frac{\partial f_{\pm}}{\partial w_{\pm}} \frac{\partial w_{\pm}}{\partial t} = \pm c \frac{\partial f_{\pm}}{\partial w_{\pm}} \quad (3.8)$$

Substituting Eqs. (3.7) and (3.8) into the factored version of Eq. (3.6) shows that  $f_-$  makes the operator,  $\square$ , with the sum identically zero.

$$\square = \left( \frac{1}{c} \frac{\partial y}{\partial t} - \frac{\partial y}{\partial x} \right) \left( \frac{1}{c} \frac{\partial f_-}{\partial t} + \frac{\partial f_-}{\partial x} \right) = \left( \frac{1}{c} \frac{\partial y}{\partial t} - \frac{\partial y}{\partial x} \right) \left( \frac{-c}{c} \frac{\partial f_-}{\partial w_-} + \frac{\partial f_-}{\partial w_-} \right) = 0 \quad (3.9)$$

Since the second operator is now identically zero, the first operator has no effect. Since the order of application of the factored linear (differential) operators is irrelevant, we could apply the operator with the minus sign to  $f_+$  to obtain the same result. The factorization of the second-order partial differential equation we called the wave equation in Eq. (3.4) into the product of two one-way first-order linear differential operators can be useful in problems where the propagation is only in one direction (i.e., for situations where there is no reflected wave).

The validity of the solutions in Eq. (3.5) to the wave equation in Eq. (3.4) can be established directly by calculation of the second partial derivative with respect to position,  $x$ , or with respect to time,  $t$ , produced by a second application of the chain rule.

$$\frac{\partial^2 y}{\partial x^2} = \frac{\partial}{\partial x} \left( \frac{\partial y}{\partial x} \right) = \frac{\partial}{\partial x} \left( \frac{\partial f_{\pm}}{\partial w_{\pm}} \right) = \frac{\partial^2 f_{\pm}}{\partial w_{\pm}^2} \frac{\partial w_{\pm}}{\partial x} = \frac{\partial^2 f_{\pm}}{\partial w_{\pm}^2} \quad (3.10)$$

$$\frac{\partial^2 y}{\partial t^2} = \frac{\partial}{\partial t} \left( \frac{\partial y}{\partial t} \right) = \frac{\partial}{\partial t} \left( \pm c \frac{\partial f_{\pm}}{\partial w_{\pm}} \right) = \pm c \frac{\partial^2 f_{\pm}}{\partial w_{\pm}^2} \frac{\partial w_{\pm}}{\partial t} = c^2 \frac{\partial^2 f_{\pm}}{\partial w_{\pm}^2} \quad (3.11)$$

In the limit of small displacements, it is important to appreciate that any disturbance will propagate along the string at a constant speed forever without reducing its amplitude or changing shape. That would not be true if our analysis had incorporated dissipation or if nonlinear (i.e., second-order) contributions had not been suppressed.

The result would have been identical if we had chosen to exchange the order of the space and time coordinates. The reader should be convinced that replacing the solution in Eq. (3.5) by the form in Eq. (3.12) still satisfies Eq. (3.4) or Eq. (3.6).

$$y(x, t) = f_{-}(ct - x) + f_{+}(ct + x) \quad (3.12)$$

The function with the minus sign in its argument still corresponds to a right-going wave, and the plus sign corresponds to the left-going wave. As will be shown later in this chapter, the choice of Eq. (3.12) or of Eq. (3.5) might simplify a particular calculation.

Figure 3.2 illustrates the propagation of a Gaussian pulse with the form of Eq. (1.87) but with an argument which is proportional to  $x \pm ct$ .

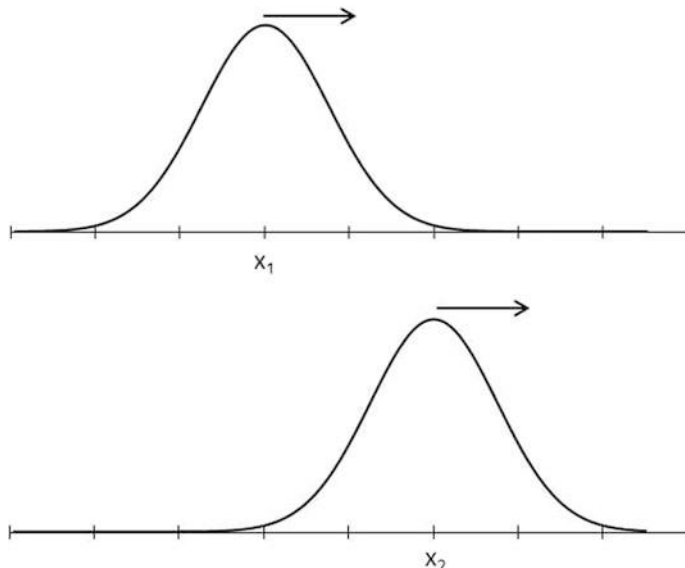


**Fig. 3.2** (Above) A Gaussian pulse with displacement,  $y(x, t)$ , given by Eq. (3.13), is propagating to the right. The pulse is shown at an instant,  $t_1$ , where it has its maximum displacement centered at position,  $x_1$ . (Below) At a later time,  $t_2 > t_1$ , the center of the pulse has moved to a new position,  $x_2$ . The change in position is related to the change in time by the speed of transverse waves on a string of uniform linear mass density,  $\rho_L$ , and uniform tension,  $T$ ,  $c = \sqrt{T/\rho_L} \Rightarrow (x_2 - x_1) = c(t_2 - t_1)$

$$y(x, t) = \frac{1}{\sigma\sqrt{2\pi}} e^{-\frac{1}{2}(\frac{x+ct}{\sigma})^2} \quad (3.13)$$

For Fig. 3.2, I have chosen the right-going argument,  $x - ct$ . The upper plot of Fig. 3.2 captures the pulse at an instant,  $t_1$ , with the pulse centered at  $x_1$ . The lower plot shows the same pulse at a later instant,  $t_2$ , after the center of the pulse had advanced to  $x_2$ . Over that time interval,  $\Delta t = t_2 - t_1$ , all portions of the pulse have advanced by a distance,  $\Delta x = x_2 - x_1$ . The speed of such a transverse disturbance, whatever the shape, is defined by the usual kinematic relation:  $c = \Delta x / \Delta t$ .

### 3.2 Pulse Reflections at a Boundary and the Utility of Phantoms

Infinite strings are hard to come by, and a method for applying a uniform tension to such a beast is even harder to imagine. A string of finite length will be terminated by two boundaries. To initiate our analysis of the reflection of a pulse from such a boundary, we will examine two limiting cases: A rigid (“fixed”) boundary will suppress the transverse motion of the string by providing whatever vertical force,  $F_y = -T \sin(\theta) \cong -T(\partial y / \partial x)_{\text{boundary}}$ , that would be required to keep the string’s attachment point immobile.<sup>4</sup> The opposite limit is a *free boundary*. Such a termination will maintain the tension in the string but will allow the end of the string to move up or down without constraint.<sup>5</sup> Since no vertical forces are produced by the boundary, the pulse must arrive at such a free boundary and leave without any slope,  $F_y = T(\partial y / \partial x)_{\text{boundary}} = 0$ . The common “textbook” way to envision such a boundary is to picture the string attached to a massless ring that slides along a frictionless pole.

Of course, these are only idealized limits that simplify calculations and help to develop our intuition. (If the bridge on a guitar or violin did not move, then the body would not radiate sound.) In this chapter, we will be able to analyze the consequences of a broad range of termination conditions that may be massive (e.g., a mass at the end of a pendulum), elastic (e.g., a string attached to a flexible cantilevered beam), resistive (e.g., a string tensioned by our massless ring but with the ring connected to a dashpot), or a combination of all three.

We will begin by analyzing a pulse that is impinging upon a rigid boundary. This situation is shown schematically in Fig. 3.3 for a Gaussian pulse of the same kind that was displayed in Fig. 3.2. The point of rigid attachment is indicated by the hatched barrier located at  $x = 0$ . At that boundary,  $y(0, t) = 0$  for all times. We also know that the linearity of our general solution to the homogeneous wave equation, given in Eq. (3.5) or Eq. (3.12), allows superposition of any number of such right- and left-going pulses that may be required to satisfy the initial conditions or the boundary constraints.

One fact that is not intuitively obvious is that we can choose to imagine the string extending beyond the termination, as long as the superposition of the pulses coming from that nonexistent extension can be combined with pulses on the physical portion of the string to satisfy the requirements imposed at the boundary. In Fig. 3.3, the pulse at the extreme left, with the arrow above pointing to the right, indicates the real pulse on the real string that is approaching the boundary at  $x = 0$ . We will satisfy the boundary

<sup>4</sup> It is useful to consider that two expressions have been introduced for the vertical force on a string. At a “point,” like that where the string is attached to a boundary or where an harmonic force or displacement is applied to the string (see Sect. 3.7), that vertical force is proportional to the slope of the string at that location:  $F_y = -T \sin(\theta) \cong -T(\partial y / \partial x)_{\text{boundary}}$ . For an infinitesimal segment of string with length,  $dx$ , where the vertical forces on two nearby ends are due to the string’s tension, the net vertical force is proportional to the string’s curvature:  $dF_{\text{net}} \cong T(\partial^2 y / \partial x^2)dx$ .

<sup>5</sup> A “free” boundary condition for a string under uniform tension rarely occurs in realizable physical systems, although a string whose tension is provided by centripetal acceleration can have such a boundary condition (see Problem 9) as does the “heavy chain” described in Sect. 3.4.3. The purpose for introduction of the free condition on a string at this point is only to preview the appearance of free boundary conditions at the ends of vibrating bars that will be examined in Chap. 5.

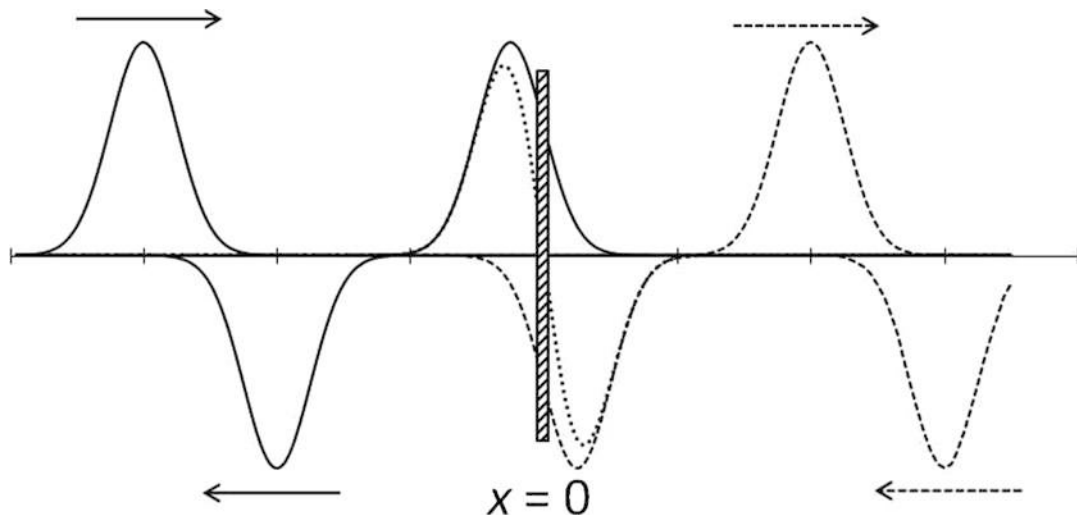


**Fig. 3.3** The positive Gaussian pulse (solid line) at the far left is shown approaching a rigid boundary at  $x = 0$ , represented by the *hatched rectangle*. To satisfy the fixed boundary condition,  $y(0, t) = 0$ , an inverted phantom (dashed line), shown at the far right, is launched along an imaginary extension of the string. The phantom is approaching the boundary from an equal distance, but propagating in the opposite direction, as indicated by the dashed arrow below the phantom pulse. The superposition of those two pulses (dotted line) makes  $y(0, t) = 0$ . As the two pulses leave the boundary, the phantom propagates along the actual string, and the original pulse becomes the phantom

condition,  $y(0, t) = 0$ , by imagining a pulse that is identical to that initial pulse but inverted, approaching from an equal distance behind the boundary. That phantom is shown at the extreme right with a dashed line and a dashed arrow below it. Both pulses are propagating at the transverse wave speed,  $c$ , although in opposite directions.

Since the real pulse and the phantom are always equidistant from the boundary, they reach it at the same time and superimpose linearly within their regions of overlap. One instant during that overlapping time interval is illustrated in the vicinity of the boundary in Fig. 3.3 by the dotted line. At that instant, the “real” pulse has started to excite the nonexistent portion of the string, and the phantom has started to appear on the real string. Because of the equality of their amplitude and the congruency of their shape, at  $x = 0$  their sum, indicated by the dotted line, will be zero. At the instant during overlap, shown in Fig. 3.3, the sum exhibits a greater slope and decreased amplitude. We have assumed an infinitely rigid termination, so the vertical force,  $F_y(x, t) = -T(\partial y/\partial x)_x = 0$ , required to immobilize the string at the boundary, is available to enforce the complete immobilization.

At the instant the two pulses completely overlap, their superposition will mean that the real string (and the fictitious extension) will be flat everywhere. Subsequently, the vertical force which immobilized the string at the boundary will launch the inverted pulse traveling in the opposite direction in the real portion of the string. At a later time, the inverted pulse is shown propagating away from the barrier along the real string, and the original pulse has crossed the barrier and has become the phantom.

We should pause momentarily to reflect (no pun intended) on the process that was used to satisfy the conditions at the real string’s rigid termination. The invention of the phantom provided a simple method to satisfy the boundary condition by trading a semi-infinite string for an infinitely long one. We should remember that there are only real strings and real forces. On the other hand, we would be remiss if we did not also marvel at the human imagination and intelligence that produced such a simple way to understand such a complex combination of wave–barrier interactions.

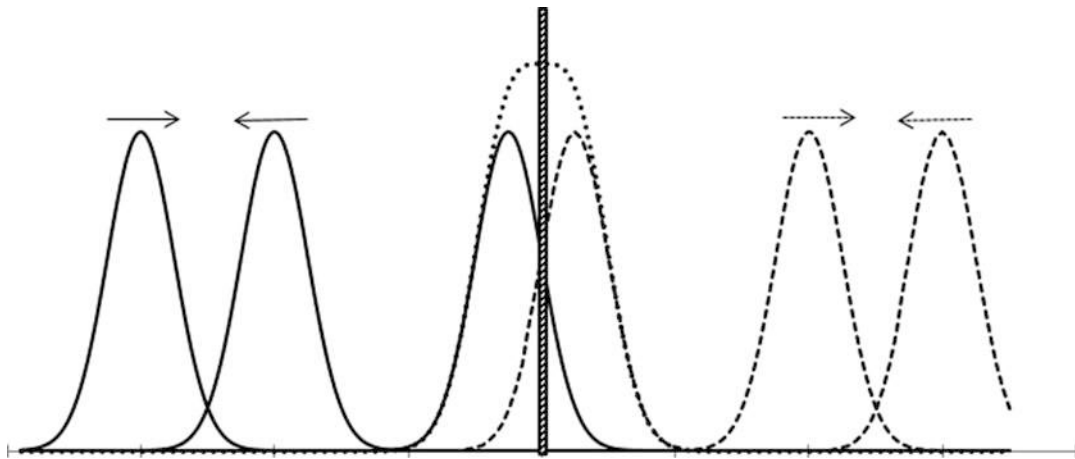


**Fig. 3.4** The positive Gaussian pulse (solid line) at the far left is shown approaching a force-free boundary at  $x = 0$ , represented by the hatched rectangle. To satisfy the boundary condition,  $(\partial y / \partial x)|_{x=0} = 0$ , a phantom (dashed line), shown at the far right, is launched along an imaginary extension of the string, approaching the boundary from an equal distance, but propagating in the opposite direction. The superposition of those two pulses (dotted line) maintains the slope of their sum to be zero at  $x = 0$  and doubles their amplitude at the instant of complete overlap. As the two pulses leave the boundary, the phantom propagates along the actual string, and the original pulse becomes the phantom

It is easy to repeat this analysis for the other limiting case, a boundary that applies no vertical forces on the string. In that case, we require that the slope of the pulse vanishes for all times at  $x = 0$  (i.e.,  $-T(\partial y / \partial x)|_{x=0} = 0$ ). Figure 3.4 is identical to Fig. 3.3 except that the phantom is not inverted. Near the region of the boundary, where the pulses overlap, their superposition always maintains zero slope. At the exact instant of overlap, the pulse has twice its original amplitude.

This approach to the solution of boundary-value problems is common in acoustics and other fields of physics (e.g., electrostatics, optics). It is known as the *method of images*. When we study sound sources in near boundaries (see Sect. 12.4.1 and Figs. 12.13 and 12.14) or in rooms (see Sect. 13.1.1), or underwater in proximity to an air–water interface, we will sprinkle image sources about in regions that are outside those spaces that are physically accessible to the waves to satisfy boundary conditions.

The same results, for both the fixed and free boundaries, can be expressed mathematically by the appropriate choice of functions, with  $w_{\pm}$  in their arguments. If we again choose a Gaussian pulse and abbreviate the waveform of Eq. (3.13) as  $y(x, t) = G_{\pm}(x \pm ct)$ , then the rigid boundary condition at  $x = 0$  is satisfied by a solution  $y(x, t) = G_-(x - ct) - G_+(x + ct)$ . With the additional restriction that when  $x \leq 0$ , we need not concern ourselves with the nonexistent portions of the string.

To satisfy the free boundary condition, we require that the slope vanishes at the boundary  $x = 0$ .

$$\left( \frac{\partial y}{\partial x} \right)_{x=0} = \left( \frac{\partial G_-}{\partial x} \right)_{x=0} + \left( \frac{\partial G_+}{\partial x} \right)_{x=0} = \left( \frac{\partial G_-}{\partial w_-} \right)_{x=0} + \left( \frac{\partial G_+}{\partial w_+} \right)_{x=0} = 0 \quad (3.14)$$

Evaluation of those expressions at  $x = 0$ , with  $w_- = -ct$  and  $w_+ = ct$ , leads to the requirement that both  $G_-$  and  $G_+$  be positive pulses.

### 3.3 Normal Modes and Standing Waves

We will now examine the free vibrations of a uniform string of length,  $L$ , and will start by rigidly fixing both ends of the string so that  $y(0, t) = y(L, t) = 0$ . Those boundary conditions would provide a close approximation to a guitar, violin, *erhu* (二胡), *sitar* (सातिर), harp, ukulele, Balkan tambura, or piano string. Recalling that a normal mode is a particular displacement that results in all parts of the system oscillating at a single frequency, we will seek the normal mode vibration frequencies for a uniform string by again assuming a right- and left-going solution to the wave equation and then combining those solutions in a way that satisfies both boundary conditions simultaneously. This will produce a theoretically infinite set of normal mode frequencies. It should come as no surprise that the mode shapes for the lower-frequency modes will resemble the lower-frequency modes of our “string of pearls” that were diagrammed in Fig. 2.30.

The solutions to the wave equation provided in Eq. (3.5) or Eq. (3.12) involve arguments that have the dimensions of length. The arguments of any mathematical function (e.g., sines, cosines, or exponentials) must be dimensionless. To provide dimensionless arguments that simplify our mathematics, we will scale the argument of the wave functions by a scalar constant,  $k$ , which has the dimensions of an inverse length [ $\text{m}^{-1}$ ] that is known as the *wavenumber*.

$$k(ct \pm x) = kct \pm kx = \omega t \pm kx \quad (3.15)$$

As before, the minus sign indicates propagation in the direction of increasing  $x$  (to the right), and the plus sign corresponds to propagation in the direction of decreasing  $x$  (to the left). The rightmost version of Eq. (3.15) imposes the requirement that  $kc = \omega$ . Since we seek time-harmonic normal modes at radian frequency,  $\omega = 2\pi f$ , we can choose either a complex exponential or a sinusoidal expression as our function of the (now dimensionless) argument required of solutions to the linear wave equation.

$$\begin{aligned} y(x, t) &= \Re e \left[ \hat{\mathbf{y}} e^{j(\omega t \pm kx)} \right] = |\hat{\mathbf{y}}| \Re e \left[ e^{j\phi} e^{j(\omega t \pm kx)} \right] \\ \text{or } y(x, t) &= |\hat{\mathbf{y}}| \cos(\omega t \pm kx + \phi) \end{aligned} \quad (3.16)$$

These solutions are periodic in both space and time. We can define the wavelength,  $\lambda$ , of the disturbance that propagates to the right along the string as  $y(x, t) = y(x + n\lambda, t)$ , where  $n$  can be any positive or negative integer or zero. Based on that definition, the wavelength can be related to the wavenumber.

$$\lambda = \frac{2\pi}{k} = \frac{2\pi}{(\omega/c)} = \frac{c}{f} \Rightarrow c = \lambda f = \frac{\omega}{k} \quad (3.17)$$

Similarly,  $y(x, t) = y(x, t + nT)$ , where  $T = (1/f) = (2\pi/\omega)$  is the period of the oscillation. Fig. 3.5 illustrates the propagation of the harmonic (i.e., single frequency) disturbance along the string as a function of both position and time.

#### 3.3.1 Idealized Boundary Conditions

Our experience with the reflection of pulses from fixed and free boundaries in Sect. 3.2 suggests that we will be able to satisfy the boundary conditions on this string by superposition of left- and right-going waves and letting the displacement amplitude,  $\mathbf{y}(x, t)$ , be a complex function of  $x$  and  $t$ .

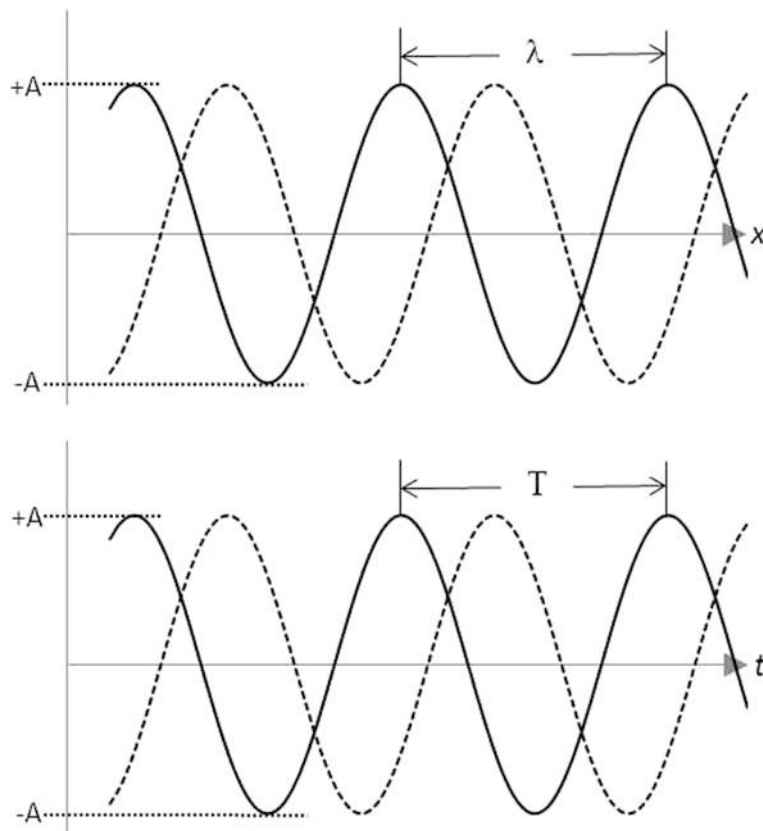


**Fig. 3.5** A time-harmonic wave that propagates to the right along a uniform string. (*Above*) The solid line is the wave at time,  $t_1$ , and the dashed line is the same wave at slightly later time,  $t_2 > t_1$ . The distance between successive peaks or troughs is the wavelength,  $\lambda = (2\pi/k)$ , where  $k$  is the wavenumber. (*Below*) The solid line is the time history of a wave passing a point,  $x_1$ , and the dashed line is the same wave passing a point,  $x_2 > x_1$ , that is farther to the right. The wave repeats itself after a time,  $T = (1/f) = (2\pi/\omega)$ , that is, the period of the harmonic disturbance. The unit of frequency,  $f$ , is given in hertz [Hz], and the unit of angular frequency,  $\omega$ , is in radian/second [rad/s] or just [ $s^{-1}$ ]

$$\mathbf{y}(x, t) = Ae^{j(\omega t - kx)} + Be^{j(\omega t + kx)} \quad (3.18)$$

The boundary condition at  $x = 0$  is  $|\mathbf{y}(0, t)| = 0$ . Evaluation of this restriction on Eq. (3.18) requires that  $A = -B$ .

$$\mathbf{y}(x, t) = B \left( e^{j(\omega t + kx)} - e^{j(\omega t - kx)} \right) = Be^{j\omega t} (e^{jkx} - e^{-jkx}) = \hat{\mathbf{C}} e^{j\omega t} \sin(kx) \quad (3.19)$$

In this expression, we have used the fact that  $2j \sin x = (e^{jx} - e^{-jx})$  and have absorbed  $2jB$  into the new complex amplitude constant (phasor),  $\hat{\mathbf{C}}$ .<sup>6</sup> The imposition of the boundary condition at  $x = 0$  has provided a rather satisfying form for our solution since  $\sin(0) = 0$ , as required.

<sup>6</sup> At this point, the specification of the amplitude constant,  $C$ , is irrelevant. As with the simple harmonic oscillator, or any other linear system (see Sect. 1.3), that constant will be determined by the initial conditions which determine the values of  $C_n$  for each of the  $n$  normal modes.

The imposition of the boundary condition at  $x = L$  now produces the quantization of the frequencies that represent the normal modes of the fixed-fixed string. To make  $|y(L, t)| = 0$ , only those discrete values of  $k_n$  that make  $\sin k_n L = 0$  will satisfy this second boundary condition.

$$\begin{aligned} \sin k_n L = 0 &\Rightarrow k_n L = n\pi ; \quad n = 1, 2, 3, \dots \\ \Rightarrow 2\pi f_n = \omega_n = k_n c &= \frac{n\pi c}{L} \Rightarrow \lambda_n = \frac{2L}{n} \quad \text{or} \quad L = n \frac{\lambda_n}{2} \end{aligned} \quad (3.20)$$

The physical interpretation of this result is simple: the normal mode shapes of a uniform fixed-fixed string correspond to placing  $n$  sinusoidal half-wavelengths within the overall length,  $L$ , of the string. Substitution of these normal mode frequencies,  $\omega_n$ , and wavenumbers,  $k_n$ , into the functional form of Eq. (3.19) provides the description of the mode shapes,  $y_n(x, t)$ , for each of the normal modes.

$$y_n(x, t) = \Re e \left[ \hat{\mathbf{C}}_n e^{j\omega_n t} \sin \left( n \frac{\pi x}{L} \right) \right]; \quad n = 1, 2, 3, \dots \quad (3.21)$$

These solutions are called *standing waves*. It is worthwhile to remember that these standing waves are equivalent to the superposition of two counter-propagating traveling waves of equal amplitude that were our starting point in Eq. (3.18). The term “standing wave” refers to the fact that the amplitude envelope is fixed in space (i.e., standing), although the transverse displacement varies sinusoidally in time. The locations where the  $\sin k_n x$  term vanishes are called the displacement *nodes* (or just nodes) of the standing wave. In this case, there are always two nodes located at the rigid boundaries. As the mode number,  $n$ , increases,  $(n - 1)$  additional nodes appear along the string and are equally spaced from each other for a string of uniform mass density and constant tension.

The locations where  $\sin k_n x = 1$  are designated *anti-nodes* and are the location of the largest amplitudes of harmonic motion. Those anti-nodes are equidistant from the nodes for a string of uniform density and tension. The separation distance of adjacent nodes and anti-nodes for a uniform string is  $\lambda_n/4$ .

This result also accounts for the ubiquity of musical instruments that are based on the tones produced by the vibrations of a fixed-fixed string.

$$f_n = \frac{c}{\lambda_n} = n \left( \frac{c}{2L} \right); \quad n = 1, 2, 3, \dots \quad (3.22)$$

The lowest-frequency mode,  $n = 1$ , is known as the *fundamental frequency*,  $f_1 = c/2L$ . The higher normal mode frequencies are known as the *overtones*. The second mode,  $f_2 = c/L$ , is called the “first overtone.” I find this “overtone” terminology to be needlessly confusing and do not use it in this textbook.

The frequencies in Eq. (3.22) form a *harmonic series*. The frequency of each normal mode is an integer multiple of the fundamental mode:  $f_n = nf_1$ . Pythagoras recognized the intervals produced by a string that was shortened by ratios of integers produced tonal combinations that were pleasing to the ear. A string whose length was halved produced the same note as the full-length string but one octave higher in frequency. A string that is one-third as long as the original produces a note that is a “perfect fifth” above the octave. (See Table 3.1 for the frequency ratios of musical frequency intervals.) Keeping the string length constant but fitting integer numbers of half-wavelengths into the string produces the same frequency as the fundamental of the shorter string.

Although I know of no physical manifestation for the normal modes of a fixed-free string (unless the mass of the string provides its tension, as for the “heavy chain” in Sect. 3.4.3),<sup>5</sup> it is easy to calculate those normal mode frequencies. Those frequencies will provide some useful insights that are

**Table 3.1** The ratios (intervals) between the frequencies of two tones that are judged to be “consonant” are written as a fraction and as a decimal

Interval	Frequency ratio		Equal temperament	
	Fractional	Decimal	Semitones	Ratio
Octave	2:1	2.0000	12	2.0000
Perfect fifth	3:2	1.5000	7	1.4983
Perfect fourth	4:3	1.3333	5	1.3348
Major sixth	5:3	1.6667	9	1.6818
Major third	5:4	1.2500	4	1.2599
Minor sixth	8:5	1.6000	8	1.5874
Minor third	6:5	1.2000	3	1.1892

To avoid difficulties that arise in the transposition of musical keys, an “equal temperament” scale was created (see Sect. 3.3.3) so that the two tones, which are separated by an integer number of “semitone” intervals, have a frequency ratio that is a multiple of  $2^{1/12} = 1.05946$ . In terms of the equal temperament scale, those intervals can be represented by  $2^{1/12}$  raised to the number of semitones between the intervals

applicable to acoustic resonators or vibrating bars.<sup>7</sup> Leaving the boundary condition at  $x = 0$  fixed, so  $y(0, t) = 0$ , we can start with Eq. (3.19). Since the end at  $x = L$  is free,  $(\partial y / \partial x)|_{x=L} = 0$ . This second condition again quantizes the values of  $k_n$  that simultaneously satisfy both boundary conditions.

$$\mathbf{F}_y(L, t) = -T \left( \frac{\partial \mathbf{y}}{\partial x} \right)_{x=L} = -T \hat{\mathbf{C}}_n e^{j\omega_n t} k_n \cos k_n L = 0 \quad (3.23)$$

This can only be satisfied for all times if  $\cos k_n L = 0$ .

$$\begin{aligned} \cos k_n L = 0 &\Rightarrow k_n L = \left( \frac{2n-1}{2} \right) \pi \Rightarrow \omega_n = \left( \frac{2n-1}{2} \right) \frac{\pi c}{L} \\ &\Rightarrow \lambda_n = \frac{4L}{2n-1} \quad \text{or} \quad L = (2n-1) \frac{\lambda_n}{4} \quad \text{for } n = 1, 2, 3, \dots \end{aligned} \quad (3.24)$$

Again, the simple interpretation is that odd-integer multiples of one-quarter wavelengths are fit within the overall length of the fixed-free string of length  $L$ . This produces a harmonic series that includes only odd-integer multiples of the fundamental,  $f_1 = c/4 L$ ,  $f_2 = 3c/4 L$ ,  $f_3 = 5c/4 L$ , etc.

### 3.3.2 Consonance and Dissonance\*

“Agreeable consonances are pairs of tones which strike the ear with a certain regularity; this regularity consists in the fact that the pulses delivered by the two tones, in the same time, shall be commensurable in number, so as not to keep the eardrum in perpetual torment.” Galileo Galilei, 1638 [1]

The perception of musical (and nonmusical) tones has been an interesting topic for experimental psychologists long before the term “experimental psychologist” came into existence. A perceptual feature of hearing that seems to span many cultures is that of the *consonance* or *dissonance* when two notes with different fundamental frequencies are presented simultaneously to a listener. The ratio of the frequency of the higher-frequency tone to the frequency of the lower-frequency tone is known as the *interval* between the two notes. The intervals that are judged to be “harmonious” are called consonant, while other ratios are judged to be “annoying” (producing “perpetual torment”) or dissonant. Table 3.1

<sup>7</sup>For example, the modes of a clarinet behave like those of a fixed-free string because the reed behaves as a closed (fixed) end and the bell behaves as an open (free) end.

**Table 3.2** This is the harmonic sequence produced by a uniform string that has its fundamental normal mode frequency ( $n = 1$ ) set to “Concert A,”  $A_4 = f_1 = 440$  Hz

Mode	1	2	3	4	5	6	7	8
Freq. [Hz.]	440	880	1320	1760	2200	2640	3080	3520
Note	$A_4$	$A_5$	$E_5$	$A_6$	$C_7^{\#}/D_7^b$	$E_7$	$F_7^{\#}/G_7^b$	$A_7$
Intervals	Root	Octave	Fifth	2nd Oct.		Fifth		3rd Oct.
	Octave (2:1)			Major Third (5:4)				
	Fifth (3:2)				Minor Third (6:5)			
		Fourth (4:3)						
			Major Triad (4:5:6)					

The subscripted musical designation of the notes are based on middle-C  $\equiv C_4 = 263.61$  Hz. The first four harmonics consist only of octaves and a perfect fifth. The fifth and seventh harmonics are not exact musical intervals, but the sixth and eighth are again a perfect fifth and an octave. The lower intervals shown in this table are between adjacent harmonics. With the exception of the seventh mode frequency,  $f_7 = 3080$  Hz, they are all intervals deemed “consonant,” as listed in Table 3.1

lists several consonant frequency intervals and the “musical” designation of that interval (e.g., octave, perfect fourth, minor third, etc.).

A harmonic series is not produced for a nonuniform string or for a uniform string subject to nonuniform tension (e.g., a hanging chain), or a uniform string that has some stiffness (in addition to the restoring force provided by the tension, as discussed in Sect. 5.5), or a uniform string subject to boundary conditions that are not perfectly rigid or perfectly free (see Sect. 3.6).

There are various physical explanations for humans finding some intervals pleasing (consonant) and others unpleasant (dissonant), but a few simple arguments can be based upon the relationships between the harmonics of the two tones either being identical, or creating a consonant interval, or being separated by a sufficient frequency difference that the superposition of the overtones do not produce perceptible beating (i.e., a high rate of amplitude modulation due to the interference between the two tones).

Helmholtz concluded that dissonance occurred when the difference between any overtones of the two tones produced between 30 and 40 beats per second [2]. Later investigations have shown that the dissonance caused by the beat rate will depend upon frequency [3]. Table 3.2 lists a series of harmonics that start with “Concert A<sub>4</sub>,” a frequency defined as 440 Hz. A<sub>4</sub> = 440 Hz is used to set the tuning of pitch for most Western musical instruments. As can be seen, the overtones for a single string produce mostly octaves and perfect fifths.

### 3.3.3 Consonant Triads and Musical Scales\*

As we have just seen, the normal modes of a perfect string generate a harmonic series with relationships that are mostly judged to be pleasing to the ear (i.e., consonant). That is a good start, but music is made by a succession of notes that produce a melody within some rhythmic (i.e., temporal) structure. The construction of a series of musical notes (i.e., a musical scale) that is also pleasant is rather complicated. It is possible to construct a musical scale, suitable for Western music (as well as country music), which is based on the consonant intervals in Table 3.1. As will be illustrated briefly [4], it is not possible to create such scales for which all intervals are consonant and which can be readily transposed so that a melody which is written in a particular key signature (i.e., based on a scale

**Table 3.3** Frequency ratios for notes and intervals for the just intonation musical scale constructed from three major triads based on the root (in this case C), the perfect fourth (F), and the perfect fifth (G)

Note	C	D	E	F	G	A	B	C
Root ratio	1:1	9:8	5:4	4:3	3:2	5:3	15:8	2:1
Interval ratio	9:8	10:9	16:15	9:8	10:9	9:8	16:15	

The intervals between adjacent notes are only major whole tones (9:8), a minor whole tone (10:9), or semitones (16:15)

that starts on a specific note) can be played in some other key. A compromise that has been found acceptable, called the scale of *equal temperament* (also known as the tempered scale), places 12 semitones within an octave, all of which have a constant frequency ratio of  $2^{1/12} = 1.05946$ .

A musical scale that has eight notes within an octave can be constructed based on three major triads. Such a scale is called the *scale of just intonation*. As seen in Table 3.2, a three-note major chord is built from a minor third (6:5) above a major third (5:4), producing a frequency ratio of 4:5:6 that is perceived to have a particularly pleasant sound. Those of you familiar with American blues and rock music will recognize that many melodies are based on a succession of three such major chords based on a first (root) note, the perfect fourth, and the perfect fifth. These are known as the tonic (I chord), the subdominant (IV chord), and the dominant (V chord).

If we choose C as our root, then the tonic is {C, E, G}. The dominant (V) major chord is built on the perfect fifth G to produce {G, B, D}, thus introducing B as a major third above the perfect fifth,  $(5/4)(3/2) = 15:8$ , and D which is a perfect fifth above a perfect fifth,  $(3/2)(3/2) = 9/4$ . Reducing the frequency of D by an octave places it within the original octave where we are building the scale, thus producing the interval 9:8, known as a major whole tone. The process is repeated one last time for the subdominant (IV) chord rooted on the perfect fourth, {F, A, C}. A is a major third above a perfect fourth  $(5/4)(4/3) = 5:3$ , and C is the octave. The intervals between the notes and the root, as well as the intervals between adjacent notes, are shown in Table 3.3.

The scale of just intonation introduces two other triads with frequency ratios of 10:12:15 that are known as minor triads. Like the major triad, they are constructed from a major third (5:4) and a minor third (6:5), but with the major third above the minor third.

It all sounds good until we examine two of the new fifths that were generated in this process. Five of the fifths are perfect: G:C = B:E = C:F = D:G = E:A = 3:2, but the ratio of B:F is not actually a fifth,  $B:F = (8/3)/(15/8) = (64/45) = 1.422 \neq 3:2 = 1.500$ . Similarly D:A which should be a fifth is D:A =  $(10/3)/(18/8) = (40/27) = 1.481 \neq 3:2 = 1.500$ . Examination of the perfect fourth reveals two more problematic intervals. Again, five of the fourths are perfect: F:C = G:D = A:E = C:G = E:B = 4:3 = 1.333, but two are not. F:B =  $(15/8)/(4/3) = 45:32 = 1.406 \neq 1.333$  and D:A =  $(18/8)/(5/3) = 27:20 = 1.350 \neq 1.333$ .

If we try to construct a major triad other than I, IV, and V, used to produce the just scale, we see that sharps and flats must be added that correspond to the “black keys” on a piano. Those sharps and flats do not necessarily have the same frequencies. For example, if we construct the major triad with D as its root, then to produce the major third, we need to introduce F<sup>#</sup> that has a ratio of 5:4, so  $F^{\#} = (9/8)(5/4) = (45/32) = 1.406:C$ . If we construct the minor third below A, we introduce G<sup>b</sup> =  $(5/3)/(6/5) = (25/18) = 1.389:C$ . On the piano, F<sup>#</sup> and G<sup>b</sup> are the same note.

Instead of building a scale on major triads, it is possible to construct a scale that attempts to preserve the perfect fifth and perfect fourth by noticing that the octave is produced by the combination of a perfect fifth and a perfect fourth:  $(4/3)(3/2) = 2$ . All 12 notes of the *chromatic scale* can be produced by increasing frequency by a perfect fifth or decreasing it by a perfect fourth and then bringing the note

**Table 3.4** Comparison of the frequency ratios of intervals produced by a just intonation scale, a Pythagorean scale, and an equally tempered scale

Interval	Just		Pythagorean		Equal temperament	
	Ratio	Cents	Ratio	Cents	Ratio	Cents
Octave	2:1	1200	2:1	1200	2:1	1200
Perfect fifth	3:2	702	3:2	702	1.498	700
Perfect fourth	4:3	498	4:3	498	1.335	500
Major sixth	5:3	884	1.687	906	1.682	900
Major third	5:4	386	1.265	408	1.260	400
Minor sixth	8:5	814	1.580	792	1.587	800
Minor third	6:5	316	1.184	294	1.189	300

The frequency ratios are also given in “cents,” corresponding to a frequency ratio of  $2^{1/1200} = 1.0005778$ , to simplify the intercomparison of the intervals among the three scales

back within a single octave to create the *Pythagorean scale*. This approach unfortunately detunes the major and minor thirds from their just intervals, as shown in Table 3.4. Also problematic is the fact that 12 multiplications should return to an octave above the root, except that  $(3/2)^{12} = 129.75$ , but  $2^7 = 128$ . That means the Pythagorean process (also known as the “circle of fifths”) misses the octave by just under one-quarter semitone.

A workable compromise is achieved by constructing a scale based on a definition of a semitone that is a frequency ratio of  $2^{1/12} \cong 1.0595$ . There is an octave between each note that is separated by 12 semitones, and a whole step is two semitones:  $2^{1/6} = 1.1225 \cong 9/8 = 1.125$ . The major scale consists of five notes that are separated by one whole step and two separated by one semitone. The equal temperament now allows musical instruments with fixed pitch to be played in any key (e.g., keyboard instruments like the piano or organ and fretted string instruments like the guitar, banjo, and mandolin). This also eliminates the problems we encountered when major triads generated sharps and flats that had different frequencies but corresponded to the same black keys on a piano keyboard. Of course, the price is that none of the just intervals other than the octave retain their exact frequency ratios.

Table 3.4 provides a comparison between the just, Pythagorean, and equally tempered scales. To make that comparison easier, a frequency ratio that is called a “cent” is introduced. One cent is one one-hundredth of an equal-temperament semitone (in the logarithmic sense), or  $2^{1/1200} = 1.000578$ .

Although the focus of this textbook is not musical acoustics, the harmonicity of the fixed-fixed modes of an idealized string expressed in Eq. (3.22) is culturally significant, as is the psychological perception of consonance and dissonance. Also, an understanding of the difficulties introduced by the scales used by musicians to specify frequencies, and the compromise provided by equal temperament, should be appreciated by anyone who would call themselves an acoustician.

Moreover, this digression provides the opportunity to marvel at the skill of the professional musicians. They are able to exploit the strong feedback between their sense of pitch and their playing technique in a way that allows them to “tune” their notes to enhance the melody if their instrument permits the “bending” of a note by breath control and/or fingering, thus escaping the limitations otherwise imposed by the convenience of equal temperament.

## 3.4 Modal Energy

Just as we were able to calculate the kinetic and potential energy stored in undamped harmonic oscillators (consisting of discrete masses and springs) in terms of their amplitudes of excitation, we can

calculate the energy stored in a normal mode of a continuous system like the string. Instead of summing the kinetic energies of the discrete masses and potential energies of springs, we will integrate over the length of the string to calculate these energies. As before, Rayleigh's method (Sect. 2.3.2) can be used to approximate the natural frequencies of the system, even if we perturb the modes by adding discrete masses, or analyze the modes of a string having a nonuniform mass density distribution, or a variable tension.

Before doing so, we need to consider the process we used to calculate our results by linearizing our equation-of-state relating forces to displacements (or in fluids, pressure changes to volume changes). We imposed an assumption that  $\partial y/\partial x \ll 1$ , so  $\sin \theta \cong \tan \theta \cong dy/dx$ , as illustrated in Fig. 3.1. This is equivalent to neglecting the nonlinear terms in the Taylor series expansions of the sine and tangent functions, given in Eqs. (1.5) and (1.7). We did this by eliminating the terms proportional to  $\theta^3$  and higher powers while retaining the term that is linear.

Because the lowest-order term in both the kinetic and potential energies is quadratic in the displacements from equilibrium, there is no first-order term that will dominate the result and which would let us neglect second-order terms. As was the case for the simple harmonic oscillator, where the expressions for the kinetic energy stored by the mass,  $KE = (\frac{1}{2})mv^2$ , and the potential energy stored by the spring,  $PE = (\frac{1}{2})Kx^2$ , were both quadratic in the amplitudes, we need to produce similar expressions for the vibration of strings.

The maximum kinetic energy of the  $n^{th}$  standing wave normal mode is easy to calculate from Eq. (3.21) since it provides an expression for the transverse displacement of a fixed-fixed string. We also know that all parts of the string must oscillate at the same frequency,  $\omega_n$ , when excited in the  $n^{th}$  normal mode. To simplify our notation, we'll let  $C_n^2 = |\hat{\mathbf{C}}_n|^2$ .

$$(KE)_n = \frac{1}{2} \int_0^L \rho_L \left( \frac{\partial y}{\partial t} \right)^2 dx = \frac{\rho_L C_n^2 \omega_n^2}{2} \int_0^L \sin^2 \left( n \frac{\pi x}{L} \right) dx = \frac{1}{4} \rho_L L C_n^2 \omega_n^2 = \frac{m_s}{4} v_1^2 \quad (3.25)$$

The integral of  $\sin^2 x dx$  or  $\cos^2 x dx$  over an integer number of half-wavelengths is  $L/2$ , since  $\sin^2 x + \cos^2 x = 1$ . This is shown explicitly also for the orthogonality condition expressed in Eq. (3.54). The result in Eq. (3.25) is one-half the value of the maximum kinetic energy that the string would have if all of its mass,  $m_s = \rho_L L$ , were oscillating at the maximum velocity amplitude,  $v_n = \omega_n C_n$ .

The maximum potential energy can be calculated from the work done against the tension due to the change in the length of the string caused by the vertical displacements produced along the string by the wave. In our earlier linearization process for masses on strings, we neglected the time-dependent changes in the total length of the string due to the transverse displacement, because those length changes,  $\delta L$ , approximated in Eq. (2.129), were second-order in the displacement from equilibrium,  $\delta L \cong a(y/a)^2$ . Since we now want to calculate the intrinsically second-order potential energy, that second-order length change is no longer negligible. The Pythagorean theorem can be used to approximate the arc length,  $ds$ , of each differential element, as pictured in Fig. 3.1. To determine the local extension,  $\delta L(x)$ , that is, the difference between the arc length,  $ds$ , and the length of the undisturbed string,  $dx$ , the Pythagorean sum can be simplified using a binomial expansion.

$$\delta L(x) = ds - dx = \sqrt{dx^2 + dy^2} - dx = dx \left[ \sqrt{1 + \left( \frac{\partial y}{\partial x} \right)^2} - 1 \right] \cong \frac{1}{2} \left( \frac{\partial y}{\partial x} \right)^2 dx \quad (3.26)$$

The result is again second-order in the displacement from equilibrium, but now it will not be ignored, as it was previously in the calculation of the string's effective tension. That length change becomes the dominant contribution to the potential energy, since there are no first-order contributions.

The potential energy will be the integral of this length change times the tension.<sup>8</sup> Equation (3.21) can be used to calculate the string's slope.

$$\frac{\partial y_n(x, t)}{\partial x} = C_n k_n \cos(k_n x) e^{j\omega_n t}; \quad n = 1, 2, 3, \dots \quad (3.27)$$

Substitution into the expression for  $\delta L(x)$  in Eq. (3.26) produces a result that is analogous to Eq. (3.25) for the potential energy of the  $n^{\text{th}}$  standing wave mode.

$$(PE)_n = \frac{T}{2} \int_0^L \left( \frac{\partial y}{\partial x} \right)^2 dx = \frac{TC_n^2 k_n^2}{2} \int_0^L \cos^2(k_n x) dx = \frac{C_n^2 c^2 \rho_L L}{4} \frac{\omega_n^2}{c^2} = \frac{m_s}{4} v_1^2 \quad (3.28)$$

We take comfort in the equality of the maximum kinetic and potential energies (and hence their time-averaged values), since it is consistent with the virial theorem (Sect. 2.3.1), under the assumption that our restoring force is linear in the displacement from equilibrium (i.e., obeying Hooke's law).

To calculate the total energy, the time phasing of the kinetic and potential energy contributions must be taken into account. If we take the real part of the normal mode solution in Eq. (3.21), then  $y(x, t)$  is proportional to  $\cos(\omega_n t)$ . Since the kinetic energy includes the square of the transverse velocity,  $(\partial y / \partial t)^2$ , the kinetic energy is proportional to  $\sin^2(\omega_n t)$ . The potential energy involved  $(\partial y / \partial x)^2$ , so it will be proportional to  $\cos^2(\omega_n t)$ . As shown below, the total energy,  $E_{\text{tot}}(t)$ , in the  $n^{\text{th}}$  normal mode, with maximum velocity,  $v_1$ , is a constant.

$$E_{\text{tot}}(t) = (KE)_n + (PE)_n = \frac{1}{4} m_s v_1^2 [\sin^2(\omega_n t) + \cos^2(\omega_n t)] = \frac{1}{4} m_s v_1^2 \quad (3.29)$$

When the string is passing through its equilibrium position,  $y(x, t) = 0$ , all of the energy is kinetic. When it is at its extreme displacement and momentarily at rest, all of the energy is potential. Since no loss mechanisms have been included in the model thus far and the attachment points are rigid, the total energy must be conserved.

### 3.4.1 Nature Is Efficient

*"Nature uses as little as possible of anything."* Johannes Kepler [5]

As before (see Sect. 2.3.1), we can still use the energy to approximate the normal mode frequencies, even for continuous systems, if we equate the maximum kinetic and potential energies. To illustrate this approach and to develop confidence that will empower us to apply Rayleigh's method to attack problems that might be difficult to solve exactly, we will apply his method to the calculation of the fundamental mode frequency of the fixed-fixed string. Since we have already found the exact solution, provided in Eq. (3.22), we can easily determine the error introduced by making such an approximation.

We know that the exact shape of the uniform fixed-fixed string vibrating in its  $n^{\text{th}}$  normal mode consists of  $n$  half-sine functions between the two rigid supports:  $\lambda_n = 2L/n$ . Using Eq. (3.25), we can write the kinetic energy of the  $n^{\text{th}}$  mode.

---

<sup>8</sup> We can ignore the product of the length change and the tension change since that would be the product of two second-order quantities making it fourth-order in the relative displacement from equilibrium.

$$(KE)_n = \frac{\rho_L L}{4} (\omega_n C_n)^2 \quad (3.30)$$

Using Eq. (3.28), and writing  $k_n = 2\pi/\lambda_n$ ,

$$(PE)_n = \frac{\pi^2 TL}{\lambda_n^2} C_n^2 = \frac{n^2 \pi^2 TL}{4L^2} C_n^2. \quad (3.31)$$

I like to call the coefficient of  $C_n^2$  in Eq. (3.31) the *stability coefficient* (see Sect. 1.2) and the coefficient of  $(\omega_n C_n)^2$  in Eq. (3.30) the *inertia coefficient*, although those designations are somewhat archaic [6]. The radian frequency of the  $n^{th}$  normal mode,  $\omega_n$ , is then given by the square root of the ratio of the stability coefficient to the inertia coefficient.

$$\omega_n = \sqrt{\frac{\text{stability}}{\text{inertia}}} = \left[ \frac{n^2 \pi^2 TL}{4L^2} \frac{4}{\rho_L L} \right]^{1/2} = \left[ \frac{n^2 \pi^2 c^2}{L^2} \right]^{1/2} = \frac{n\pi c}{L} \quad (3.32)$$

This regenerates the result of Eq. (3.20) for the normal mode frequencies of a uniform fixed-fixed string.

Now let us imagine that we cannot solve Eq. (3.4) exactly for a fixed-fixed string. To use Rayleigh's method to approximate the fundamental frequency,  $f_1$ , we need to postulate a mode shape that satisfies the boundary conditions, has no zero-crossing (since we want the fundamental mode frequency), and can be easily used to evaluate the kinetic and potential energies of vibration. If we define the center of the string at  $x = 0$ , then the following function will clearly make  $y(-L/2) = y(+L/2) = 0$ .<sup>9</sup>

$$y_1(x, t) = C_1 \left[ 1 - \left( \frac{2x}{L} \right)^m \right] \cos \omega_1 t \quad (3.33)$$

If the exponent  $m = 1$ , then our trial function is just a triangle with its peak in the center. If  $m = 2$ , then the trial function becomes a parabola. These trial functions are plotted in Fig. 3.6. Since the fundamental mode is symmetric about  $x = 0$ , we can calculate the energies for only half of the string.

$$(KE)_1 = \frac{\rho_L}{2} \int_0^{L/2} \left( \frac{\partial y}{\partial t} \right)^2 dx = \frac{\rho_L m^2 L}{2(m+1)(2m+1)} (C_1 \omega_1)^2 \quad (3.34)$$

$$(PE)_1 = \frac{T}{2} \int_0^{L/2} \left( \frac{\partial y}{\partial x} \right)^2 dx = \frac{T m^2}{(2m-1)L} C_1^2 \quad (3.35)$$

Application of Eq. (3.32), using the inertia and stability coefficients calculated above, determines  $\omega_1$  for any value of the exponent,  $m$ .

$$\omega_1^2 = \frac{2(m+1)(2m+1)}{2m-1} \frac{T}{\rho_L L^2} \quad (3.36)$$

For  $m = 1$ ,  $\omega_1^2 = 12(T/\rho_L L^2)$ . The exact answer is  $\pi^2(T/\rho_L L^2) = 9.87(T/\rho_L L^2)$ , so this approximation, using a “triangular” trial function, overestimates the frequency by about 11%. For the parabolic

---

<sup>9</sup> We will be generating non-integer values for the exponent  $m$ , so we should have two expressions for Eq. (3.33), one for positive values of  $x$  and one for negative values. Since the problem is symmetric about  $x = 0$ , we avoid writing the second expression by only integrating over  $0 < x \leq L/2$  when we calculate the stability and inertial coefficients.

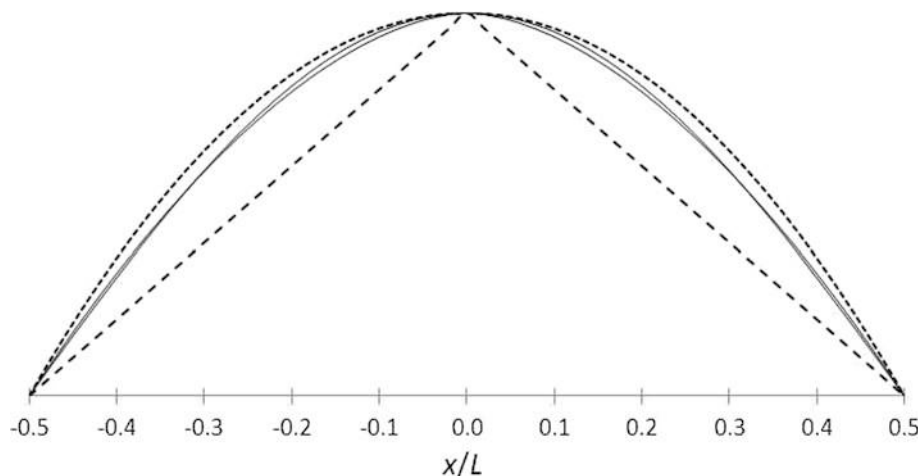


**Fig. 3.6** The four trial functions used to approximate the frequency,  $f_1$ , of the fundamental normal mode of a uniform fixed-fixed string using Rayleigh's method are shown. The *inner* and *outer dashed curves* represent Eq. (3.33) for  $m = 1$  (*triangle*) and  $m = 2$  (*parabola*). The two fine solid lines between them are nearly indistinguishable. They represent the exact sinusoidal solution and Eq. (3.33) with the optimized value of the exponent from (3.37) with  $m \cong 1.725$

trial function, with  $m = 2$ ,  $\omega_I^2 = 10(T/\rho_L L^2)$ , which provides an overestimate of the frequency by less than 0.7%.

As Lord Rayleigh pointed out, “When therefore the object is to estimate the longest proper period of a system by means of calculations founded on an assumed type [the ‘type’ is what we have called the trial function], we know a priori that the result will come out too small.” [7] Said another way, Rayleigh is acknowledging the fact that nature minimizes the total energy by using the exact “trial function,” hence minimizing the normal mode frequency (or equivalently, maximizing the period).

Unless we select nature’s shape function as our trial function, the frequency obtained from Eq. (3.32) will always be an overestimate, as we saw with our  $m = 1$  and  $m = 2$  solutions for the fundamental mode of a fixed-fixed string. The parabolic trial function was closer to nature’s sinusoidal mode shape, so its frequency error was smaller, but the parabolic trial function still predicted a frequency that was slightly greater than the exact solution.

Rayleigh was able to exploit this fact by realizing that he could improve the trial function by minimizing the frequency (or the square of the frequency, if that is more convenient) by adjusting a trial function’s parameter. Taking the derivative of Eq. (3.36) with respect to the exponent,  $m$ , and setting that derivative to zero,<sup>10</sup> we can find the value of  $m$  that provides the lowest frequency that can be obtained with an assumed trial function of the form in Eq. (3.33).<sup>11</sup>

<sup>10</sup> When the fraction is written as the ratio of two quadratic functions in the form  $u = (A + 2Hm + Bm^2)/(a + 2hm + bm^2)$ , then the minimum or maximum value is given by the solution of the following quadratic equation:  $(ab - h^2)u^2 - (aB + bA - 2hH)u + (AB - H^2) = 0$ .

<sup>11</sup> If you are too lazy to work out the derivative (or want an independent check), it is possible to use an equation solver, like that available in many mathematical software packages, to determine the value of  $m$  which minimizes Eq. (3.36). The result from such a solver is  $m = 1.724745$ , producing a coefficient of 9.89898.

$$\frac{d}{dm} \left[ \frac{2(m+1)(2m+1)}{(2m-1)} \right] = 0 \quad \Rightarrow \quad m = \frac{1}{2} (\sqrt{6} + 1) \cong 1.72474 \quad (3.37)$$

Substitution of that optimized exponent into Eq. (3.36) gives  $\omega_I^2 = 9.899 (T/\rho_L L^2)$  which only overestimates the normal mode frequency by less than 0.15%.

Figure 3.6 shows the four trial functions used for this exercise. It is reassuring that the triangular shape produced a modal frequency that was only slightly greater than 10% higher than the exact result. The parabolic trial function is quite close to the exact solution, so an error of 0.7% seems reasonable. In Fig. 3.6, the difference in the shapes between the exact sinusoidal function and Eq. (3.33) with  $m = \frac{1}{2}(\sqrt{6} + 1)$  is nearly imperceptible and produces an approximate frequency that is less than 0.15% greater than the exact result.

### 3.4.2 Point Mass Perturbation

Let us calculate the shift in the normal mode frequencies produced by the addition of a small mass,  $m_o$ , to the string at some location,  $0 < x < L$ , between the rigid supports using Rayleigh's method. We know the exact string shapes for the unloaded uniform string, so if we assume that  $m_o \ll \rho_L L = m_s$ , the unloaded normal mode shapes should provide excellent trial functions. The result will provide a useful check when we calculate the exact solution for a mass-loaded string.

The stability coefficient is unchanged by the addition of a point mass. The inertia coefficient must now include the sum of the kinetic energy contribution made by the added mass,  $m_o$ , located at  $x$ , and the kinetic energy of the uniform string as given by Eq. (3.25). Since we are using the unperturbed normal mode shapes, the velocity of the mass will be  $v(x) = C_n \omega_n \sin(n\pi x/L)$ .

$$(KE)_n = \frac{1}{4} \rho_L L C_n^2 \omega_n^2 + \frac{m_o}{2} C_n^2 \omega_n^2 \sin^2\left(\frac{n\pi x}{L}\right) = \frac{C_n^2 \omega_n^2}{4} \left[ m_s + 2m_o \sin^2\left(\frac{n\pi x}{L}\right) \right] \quad (3.38)$$

Since the “interesting” change produced by the added mass occurs in the denominator of Eq. (3.32), we will write the expression for the square of the period,  $T_n^2$ , instead of the square of the radian frequency,  $\omega_n^2$ .

$$T_n^2 = \frac{4\pi^2}{\omega_n^2} = 4\pi^2 \frac{\text{inertia}}{\text{stability}} = \frac{4\pi^2 m_s}{TLk_n^2} \left[ 1 + 2 \frac{m_o}{m_s} \sin^2\left(\frac{n\pi x}{L}\right) \right] \quad (3.39)$$

Recognizing that  $c^2 = (TL/m_s)$ , the combination,  $(ck_n)^2 = \omega_n^2$ , is just the square of the unperturbed radian frequency.

$$f_n = \frac{1}{T_n} = \frac{\omega_n}{2\pi} \cong \frac{nc}{2L} \left[ 1 - \frac{m_o}{m_s} \sin^2\left(\frac{n\pi x}{L}\right) \right] \quad \text{for } m_o \ll m_s \quad (3.40)$$

As expected, the addition of the mass has decreased the normal mode frequencies. That decrease depends both on the location of the added mass and the mode number, as well as the magnitude of the perturbation,  $m_o$ .

If we designate the perturbed modal frequencies as  $f_n'$ , and the unperturbed frequencies given in Eq. (3.22) as  $f_n$ , application of the binomial expansion to Eq. (3.39) allows us to invert the expression in square brackets and take its square root under the assumption that  $m_o \ll m_s$ .

**Table 3.5** The effect on the modal frequency shift of Eq. (3.41) caused by a small mass,  $m_o$ , placed at  $x = L/4$  on a string of mass,  $m_s \gg m_o$ , is determined by  $\sin^2(n\pi x/L)$ . Since  $x = L/4$  is a location of a node for the  $n = 4$  mode, the added mass has no effect on that normal mode frequency. That position is the location of maximum displacement for the  $n = 2$  and  $n = 6$  modes, producing the largest frequency shifts

Mode	$\sin^2(n\pi x/L)$
1	0.5
2	1.0
3	0.5
4	0.0
5	0.5
6	1.0

$$\frac{f_n - f'_n}{f_n} = \frac{\delta f_n}{f_n} \cong \frac{m_o}{m_s} \sin^2\left(\frac{n\pi x}{L}\right) \quad \text{if } m_o \ll m_s \quad (3.41)$$

Table 3.5 lists the values of  $\sin^2(n\pi x/L)$  for a small mass located one-quarter of the way from one rigid support of a uniform string,  $x = L/4$ . Because the  $n = 4$  normal mode shape has a node at the location of the added mass, the mass has no effect on the normal mode frequency,  $f_4$ , or on any other mode that has a mode number which is an integer multiple of four,  $f_j, j = 4, 8, 12$ , etc.

### 3.4.3 Heavy Chain Pendulum (Nonuniform Tension)\*

As one final example of Rayleigh's method applied to a string, we will obtain an approximate solution to a problem which actually was the first problem to necessitate the use of what are now known as Bessel functions to produce the exact solution [8]: a fixed-free string with a tension that is a linear function of position along the string. We will consider a chain (or string) with a constant linear mass density,  $\rho_L$ , but hung under the influence of gravity, so that the tension decreases linearly with the distance from the fixed attachment point.

To remind ourselves that the string's vertical orientation is central to the definition of this problem, we will choose the  $z$  axis to specify position along the string in its equilibrium (straight) state. If the (fixed) top end of the string is defined as  $z = 0$  and we let  $z$  increase as we go downward, then the tension in the string, as a function of position,  $T(z)$ , is a linear function of distance from the support point.

$$T(z) = g\rho_L(L - z) \quad (3.42)$$

At the top, the entire weight,  $\rho_L g L$ , must be supported, causing the tension to be greatest at the attachment point,  $z = 0$ . We will still let the transverse displacement of the string from its equilibrium state be  $y(z, t)$ .

Returning to our definition of the net vertical force on an infinitesimal length of string, given in Eq. (3.2), we see that we can no longer treat  $T$  as a constant, although we will still make the small-amplitude (linear) approximation.

$$dF_y = \frac{\partial(T \sin \theta)}{\partial z} \Big|_y dz \cong \frac{\partial\left(T \frac{\partial y}{\partial z}\right)}{\partial z} \Big|_y dz \quad (3.43)$$

Application of Newton's Second Law produces an equation of motion that is not the wave equation of Eq. (3.4).

$$\rho_L \frac{\partial^2 y}{\partial t^2} = \frac{\partial}{\partial z} \left[ T(z) \frac{\partial y}{\partial z} \right] = \rho_L g \frac{\partial}{\partial z} \left[ (L - z) \frac{\partial y}{\partial z} \right] \quad (3.44)$$

Having no desire to attempt a solution to this new equation, we will use Rayleigh's method to approximate the fundamental normal mode frequency,  $\omega_o$ .

The first step will be to choose a trial function that satisfies the boundary condition for the fundamental mode,  $y_o(0, t) = 0$ , while providing sufficient flexibility that we are able to minimize the resulting frequency. Of course, a polynomial trial function is preferred to simplify the necessary differentiations and integrations. An adjustable mix of a linear and quadratic dependence upon  $z$  is a reasonable choice. The adjustable parameter,  $\beta$ , will be used to optimize the trial function.

$$y_o(z, t) = C_o \cos(\omega_o t) \left( \frac{z}{L} + \beta \frac{z^2}{L^2} \right) \quad (3.45)$$

Calculation of the kinetic energy will involve the square of the velocity.

$$\dot{y}_o^2 = \omega_o^2 C_o^2 \sin^2(\omega_o t) \left( \frac{z}{L} + \beta \frac{z^2}{L^2} \right)^2 \quad (3.46)$$

Substitution into the equation for kinetic energy is straightforward but a little messy.

$$(KE)_o = \frac{\rho_L \omega_o^2 C_o^2}{2} \int_0^L \left( \frac{z^2}{L^2} + 2\beta \frac{z^3}{L^3} + \beta^2 \frac{z^4}{L^4} \right) dz \quad (3.47)$$

Having chosen a polynomial trial function, integration is simple.

$$(KE)_o = \frac{\rho_L \omega_o^2 C_o^2 L}{2} \left( \frac{1}{3} + \frac{\beta}{2} + \frac{\beta^2}{5} \right) = \frac{\rho_L \omega_o^2 C_o^2 L}{60} (10 + 15\beta + 6\beta^2) \quad (3.48)$$

The calculation of the potential energy requires the square of the derivative of  $y$  with respect to  $z$ .

$$\left( \frac{\partial y}{\partial z} \right)^2 = C_o^2 \cos^2(\omega_o t) \left( \frac{1}{L} + 2\beta \frac{z}{L^2} \right)^2 = C_o^2 \cos^2(\omega_o t) \left( \frac{1}{L^2} + 4\beta \frac{z}{L^3} + 4\beta^2 \frac{z^2}{L^4} \right) \quad (3.49)$$

Since the potential energy must include the dependence of tension on position, the integral contains more terms but is just as easy to evaluate.

$$(PE)_o = \frac{\rho_L g C_o^2}{2} \int_0^L (L - z) \left( \frac{1}{L^2} + 4 \frac{\beta z}{L^3} + 4 \frac{\beta^2 z^2}{L^4} \right) dz = \frac{\rho_L g C_o^2}{12} (3 + 4\beta + 2\beta^2) \quad (3.50)$$

As before, the ratio of the stability coefficient to the inertia coefficient provides an estimate of the upper limit to the square of the normal mode frequency,  $\omega_o^2$ , for the fundamental mode of an oscillating chain with a free end as a function of our adjustable parameter,  $\beta$ .

$$\omega_o^2 \leq \frac{5(3 + 4\beta + 2\beta^2)}{10 + 15\beta + 6\beta^2} \frac{g}{L} \quad (3.51)$$

The use of the “ $\leq$ ” sign in Eq. (3.51) is an acknowledgment of Rayleigh’s recognition that this method never underestimates the modal frequency. If we let  $\beta = 1$ , thereby making the linear and quadratic combinations in Eq. (3.45) be equal,  $\omega_o^2 = (45/31)(g/L) = 1.4516(g/L)$ . We should be able to reduce this result, bringing it closer to the exact value, if we minimize the fractional coefficient of  $(g/L)$  in Eq. (3.51). That can be done analytically<sup>11</sup> or by use of an equation solver. I chose the latter and found  $\beta = 0.6385$ , making  $\omega_o^2 = 1.4460(g/L)$ .

The exact solution is given by the first zero-crossing of the zeroth-order Bessel function of the first kind,  $J_0$ , and produces a result which is identical to Rayleigh’s method (after optimization) to within four decimal places:  $\omega_o^2 = 1.4460(g/L)$ .

Since the fundamental mode corresponds to the motion of the chain staying nearly straight and moving almost like a rigid pendulum, the frequency could have been approximated from the moment of inertia of the chain, treated as a rigid rod:  $I = (m_s L^2)/3$ . The linear restoring torque, given by Eq. (1.25), acting as though all of the mass were concentrated at the chain’s midpoint produces a torsional stiffness:  $K_{torq} = m_s g L/2$ , resulting in  $\omega_o^2 = 1.500(g/L)$ . The actual fundamental frequency is 1.8% lower than this “rigid pendulum” approximation (i.e.,  $\beta = 0$ ).

### 3.5 Initial Conditions

Thus far, the amplitude coefficients,  $C_n$ , for the normal modes have remained undetermined. As was the case with the vibrational amplitudes of the simple harmonic oscillator, the values of these coefficients are determined by the initial conditions. For the excitation of the normal modes of a string, the two limiting cases are a plucked or a struck string. A plucked string (e.g., guitar or harp) is pulled away from its equilibrium position so that the string forms two legs of a triangle with the separation between the fixed ends as its base. It is then released at  $t = 0$ . For a struck string (e.g., piano or dulcimer), a hammer is usually “bounced” off the string at  $t = 0$ , imparting an initial velocity at the instant of contact.<sup>12</sup> The bowed instruments of the violin family or the Chinese *erhu* (二胡) are better described as driven strings that include a complex feedback system of the slip-stick friction produced by the bow that is mode-locked to the modal frequency of the string [9].

The imposition of the initial conditions on a string is facilitated by the use of the Fourier series (see Sect. 1.4). The harmonic modes of the fixed-fixed string in Eq. (3.21) form a complete set of orthogonal basis functions that allow any initial displacement or velocity to be expressed as the superposition of normal modes.<sup>13</sup>

$$y(x, t) = \sum_{n=1}^{\infty} y_n(x, t) = \sum_{n=1}^{\infty} C_n e^{j\omega_n t} \sin\left(n \frac{\pi x}{L}\right) \quad (3.52)$$

An initial displacement,  $y_o(x, 0)$ , or an initial velocity,  $v_o(x, 0)$ , can then be written in terms of that series.

<sup>12</sup> This is the physicists’ definition of the striking process. In reality, there are many other factors that influence the excitation of a struck string including the curvature of the hammer’s face as well as the compliance (e.g., hard wood or soft felt) of the material on the hammer’s face.

<sup>13</sup> It is worth pointing out that the orthogonality of these basis functions for standing waves on a string is a special case that is only true for idealized (rigid) Dirichlet boundary conditions (after P. G. L. Dirichlet, 1805–1859) or (free) Neumann boundary conditions (after Carl G. Neumann, 1832–1925). For other boundary conditions, the normal modes are not orthogonal. See, for example, Fig. 3.8 where the integral of the product of the lowest (pendulum) mode (dashed line) and the first nearly half-wavelength mode (solid line), when integrated over the length of the string, is clearly non-zero.

$$\begin{aligned} y(x, 0) &= y_o(x) = \sum_{n=1}^{\infty} C_n \sin\left(n \frac{\pi x}{L}\right) \\ \dot{y}(x, 0) &= v_o(x) = j \sum_{n=1}^{\infty} \omega_n C_n \sin\left(n \frac{\pi x}{L}\right) \end{aligned} \quad (3.53)$$

As in Sect. 1.4, we exploit the orthogonality of the basis functions (i.e., normal modes) to determine the values of the coefficients,  $C_n$ .

$$\int_0^L \sin\left(n \frac{\pi x}{L}\right) \sin\left(m \frac{\pi x}{L}\right) dx = \begin{cases} L/2 & \text{if } n = m \\ 0 & \text{if } n \neq m \end{cases} \quad (3.54)$$

Multiplication of Eq. (3.53) by  $\sin(m\pi x/L)$  and integration over the length of the string extracts the amplitude coefficients,  $C_n$ .

$$\begin{aligned} \int_0^L y_o(x) \sin\left(m \frac{\pi x}{L}\right) dx &= \sum_{n=1}^{\infty} C_m \int_0^L \sin\left(m \frac{\pi x}{L}\right) \sin\left(n \frac{\pi x}{L}\right) dx = \left(\frac{L}{2}\right) C_m \\ C_n &= \frac{2}{L} \int_0^L y_o(x) \sin\left(n \frac{\pi x}{L}\right) dx \end{aligned} \quad (3.55)$$

The same procedure will also produce the coefficients for an initial velocity distribution.

$$C_m = \frac{2}{\omega_m L} \int_0^L v_o(x) \sin\left(m \frac{\pi x}{L}\right) dx \quad (3.56)$$

For the plucked case, the solution for the  $C_n$  coefficients that describe the subsequent (i.e.,  $t > 0$ ) motion of a string of length,  $L$ , initially displaced from its straight condition by a transverse distance,  $y_o(x_o, 0) = h$ , at a distance,  $x_o$ , from one attachment point can be determined if the initial shape of the string is expressed by the function in Eq. (3.57). Values of the  $C_n$  coefficients can be calculated by breaking the integral of Eq. (3.55) into two parts. Following the terminology used for most Western stringed instruments, we will designate  $x = 0$  as the location of the “bridge” and  $x = L$  as the location of the “nut,” which is typically the end closest to the tension adjusters (e.g., tuning pegs, machine heads).

$$y_o(x, 0) = \begin{cases} h\left(\frac{x}{x_o}\right) & \text{for } 0 \leq x < x_o \\ h\left(\frac{L-x}{L-x_o}\right) & \text{for } x_o \leq x < L \end{cases} \quad (3.57)$$

The initial shape will look much like the dashed triangle in Fig. 3.6, though that figure would pertain to  $x_o = L/2$ , with the amplitude being greatly exaggerated, since  $h \ll L$  is required to ensure the assumed subsequent linear behavior.

$$C_n = \frac{2h}{L} \int_0^{x_o} \frac{x}{x_o} \sin\left(\frac{n\pi x}{L}\right) dx + \frac{2h}{L} \int_{x_o}^L \frac{(L-x)}{(L-x_o)} \sin\left(\frac{n\pi x}{L}\right) dx \quad (3.58)$$

The usual formulas for the integration of sine functions are provided below:

$$\int \sin ax dx = -\frac{1}{a} \cos ax + C; \quad \int x \sin ax dx = \frac{1}{a^2} \sin ax - \frac{1}{a} x \cos ax + C \quad (3.59)$$

After repeated applications of Eq. (3.59) and collection of like terms, the amplitude coefficients for a string plucked at  $x_o$  are obtained.

**Table 3.6** The amplitude coefficients,  $C_n$ , for a plucked string are given in Eq. (3.60)

$x_o/L$	2:1	3:1	4:1	5:1	6:1	7:1	8:1
0.500	0	-0.111	0	0.040	0	-0.020	0
0.400	0.155	-0.069	-0.063	0	0.028	0.013	-0.010
0.333	0.250	0	-0.062	-0.040	0	0.020	0.016
0.200	0.405	0.180	0.063	0	-0.028	-0.033	-0.025
0.143	0.450	0.250	0.140	0.072	0.028	0	-0.016
0.125	0.462	0.268	0.163	0.097	0.051	0.020	0
0.100	0.476	0.291	0.192	0.129	0.085	0.053	0.030
0.050	0.494	0.322	0.235	0.181	0.144	0.116	0.095

In this table, the plucking position is given by  $x_o/L$ . The ratios of the subsequent harmonic amplitudes,  $C_n/C_1$ , are provided in the other columns. A negative ratio indicates that the harmonic has a phase that is opposite that of the fundamental. It can be seen that any harmonic which has a node at the plucking position has zero amplitude (e.g., every other column for  $x_o/L = \frac{1}{2}$  is zero). For the central plucking position,  $x_o/L = 0.50$ , the non-zero ratios decrease in proportion to  $n^{-2}$  as expected for the (isosceles) triangular wave in Eq. (1.45). For the plucking position closest to the bridge,  $x_o/L = 0.05$ , the relative amplitudes decrease nearly in proportion to  $n^{-1}$  as expected from Eq. (3.61)

$$C_n = \frac{2}{\pi^2} \frac{h}{n^2} \frac{L^2}{x_o(L - x_o)} \sin\left(\frac{n\pi x_o}{L}\right) \quad (3.60)$$

For any given plucking displacement,  $h$ , no modes will be excited that would have had nodes at the plucking location, since  $\sin(n\pi x_o/L) = 0$  if  $n = L/x_o$ , or any integer multiple of that ratio, as shown in Table 3.6. For example, if the string is plucked at its center, then none of the even harmonics will be excited, since all such modes have nodes at the string's center,  $x_o = L/2$ .

The result of Eq. (3.60) for the amplitude coefficients of a plucked string has a strong influence on the tonality of the resulting vibrations. This is illustrated in Table 3.6 where it is obvious that the relative strength of the higher harmonics becomes greater as the plucking position approaches the bridge. In the limit that  $x_o/L$  is very small, the relative amplitude of the harmonics falls off as  $n^{-1}$ .

$$\lim_{x_o/L \rightarrow 0} [C_n] = \frac{2h}{\pi n} \quad (3.61)$$

This limiting behavior is approached in the last row of Table 3.6, where  $x_o/L = 0.05$ .

The sound is more “mellow” if the string is plucked near the center and is “twangy” when plucked near the bridge. This is also the reason that many electric guitars have multiple pickup locations (e.g., the Fender Stratocaster has three pickups located between the bridge and the place where the neck joins the body). An electromagnetic guitar pickup will be less sensitive to any mode that has a node that is close to the pickup location. The closer the pickup is to the bridge, the smaller the amplitude of any mode will be, but also the less likely that any mode will have a node near the pickup location. Again, the pickup closer to the position where the neck joins the body will produce a more “mellow” sound and the one near the bridge will sound more “twangy.”

### 3.5.1 Total Modal Energy

Having calculated the behavior of a plucked string that is released at  $t = 0$ , we can now calculate the work it took to displace the string by a transverse distance,  $h$ , at a position,  $x_o$ , before it was released (i.e., at times  $t < 0$ ). Energy conservation guarantees that the work done to displace the string before release must be equal to the sum of the energies of the individual normal modes of vibration that were excited. Since we have shown that the total energy of any mode is the sum of the kinetic and potential

energies and that the maximum value of the kinetic and potential energies is equal, we can simplify this calculation by summing the maximum kinetic energies,  $(KE)_n$ , expressed in Eq. (3.30).

This can be demonstrated easily for a string plucked at its center  $x_o = L/2$ , although it must also be true for any plucking position. Substitution of  $x_o = L/2$  into the general result of Eq. (3.60) provides the amplitude coefficients for the fixed-fixed string plucked at its center.

$$C_n(x_o = \frac{1}{2}L) = \frac{1}{n^2} \frac{8h}{\pi^2} \sin\left(\frac{n\pi x_o}{L}\right); \quad n = 1, 3, 5, \dots \quad (3.62)$$

Since the string is plucked at the center, excitation of all even harmonics is suppressed. The maximum kinetic energy stored in each mode is proportional to the square of the maximum velocity,  $v_n^2 = \omega_n^2 C_n^2$ , of that mode, where we have used Eq. (3.20) to relate  $\omega_n$  to the mode number,  $n$ .

$$v_n^2 = \omega_n^2 C_n^2 = \left(\frac{n\pi c}{L}\right)^2 \left(\frac{1}{n^2} \frac{8h}{\pi^2}\right)^2 = \left(\frac{8hc}{\pi n L}\right)^2 \quad (3.63)$$

The total energy of all of the modes is then expressed as a summation over the odd values of mode number,  $n$ .

$$E_{tot} = \frac{m_s}{4} \sum_{n=odd}^{\infty} \left(\frac{8hc}{\pi n L}\right)^2 = m_s c^2 \left(\frac{4h}{\pi L}\right)^2 \sum_{n=0}^{\infty} \frac{1}{(2n+1)^2} = \frac{2T}{L} h^2 \quad (3.64)$$

The final expression on the right-hand side of Eq. (3.64) uses the fact that the sum of that infinite series is  $\pi^2/8$  [10] and  $m_s c^2 = \rho_L L c^2 = LT$ .

We have already calculated the total vertical component of the force that the tension of a fixed-fixed string exerts when its center is displaced from equilibrium by a distance,  $y$ , in Eq. (2.129). The total work done to displace the center by a distance,  $h$ , is therefore given by the integral of the vertical component of that force,  $F_y(y)$ , times the displacement,  $y$ , in the vertical direction.

$$W = - \int_0^h F_y y dy = \int_0^h \left(\frac{4T}{L}\right) y dy = \frac{2T}{L} h^2 \quad (3.65)$$

The equality of the results of Eqs. (3.64) and (3.65) can be viewed as a confirmation of our faith in the conservation of energy or as an interesting way to find the sum of the infinite series in Eq. (3.64).

### 3.6 “Imperfect” Boundary Conditions

The harmonic series produced by a string that is rigidly immobilized at both ends is a special case.<sup>14</sup> If the boundary conditions are more general, we will see that the standing wave frequencies no longer form a harmonic series and the mode shapes are no longer orthogonal. Also, for the case of a mass-loaded string, a new “lumped-element” mode (i.e., the pendulum mode) appears. That additional normal mode frequency is not harmonically related to the standing wave modes. The wavelength of that pendulum mode may be many times greater than the length of the string joining the rigid attachment point to the mass that provides the termination at the other end.

The analytical “tools” we’ve developed thus far are entirely adequate to treat a string that is terminated by a mass that is not infinite (i.e., a nonrigid termination). If the end of the string at  $x = 0$  is rigidly fixed, then we already know that the form of the solution imposed by that end condition must be given by Eq. (3.19). We can use Newton’s Second Law to impose the boundary condition at

the point of attachment of the mass,  $M$ , located at  $x = L$ , which will result in the quantization of the allowable normal mode frequencies.

$$F_y(L, t) = -T \left( \frac{\partial y}{\partial x} \right)_{x=L} = M \left( \frac{\partial^2 y}{\partial t^2} \right)_{x=L} = j\omega M \left( \frac{\partial y}{\partial t} \right)_{x=L} \quad (3.66)$$

The right-hand version expresses the force which the string applies to the mass (and by Newton’s Third Law of Motion that must be the negative of the force that the mass exerts on the string) in terms of the mechanical impedance of the terminating mass,  $j\omega M$ . Substitution of Eq. (3.19) into the above expressions is straightforward.

$$\left( \frac{\partial y}{\partial x} \right)_L = C_n k_n \cos(k_n L) e^{j\omega_n t} \quad \text{and} \quad \left( \frac{\partial y}{\partial t} \right)_L = j\omega_n C_n \sin(k_n L) e^{j\omega_n t} \quad (3.67)$$

Plugging these expressions into Eq. (3.66) provides an equation that will yield the quantized values of the normal mode frequencies,  $\omega_n$ , and wavenumbers,  $k_n$ .

$$\frac{\cos k_n L}{\sin k_n L} = \cot(k_n L) = \frac{M}{T} \left( \frac{\omega_n}{k_n} \right)^2 k_n = \frac{M}{T} c^2 k_n = \frac{M}{m_s} (k_n L) \quad (3.68)$$

This is a *transcendental equation* for  $(k_n L) \equiv x$ . It does not have a closed-form algebraic solution. Figure 3.7 provides the quantizing solutions for  $(k_n L) \equiv x$ , which occur at the intersections of  $\cot x$  and the straight line of slope  $(M/m_s)$  passing through the origin. Thus far, we have assumed that the tension,  $T$ , is not a function of the string’s mass,  $m_s$ , as it was for the “heavy chain” with variable tension analyzed in Sect. 3.4.3.

Before examining the solutions in some important limits, it is worthwhile to consider the general type of normal modes that arise for this fixed mass-loaded string. If  $M = 0$ , then our current analysis should regenerate the modes of the fixed-free string, given in Eq. (3.24), which correspond to odd-integer multiples of a quarter wavelength fitting within the overall length of the string,  $L$ . If

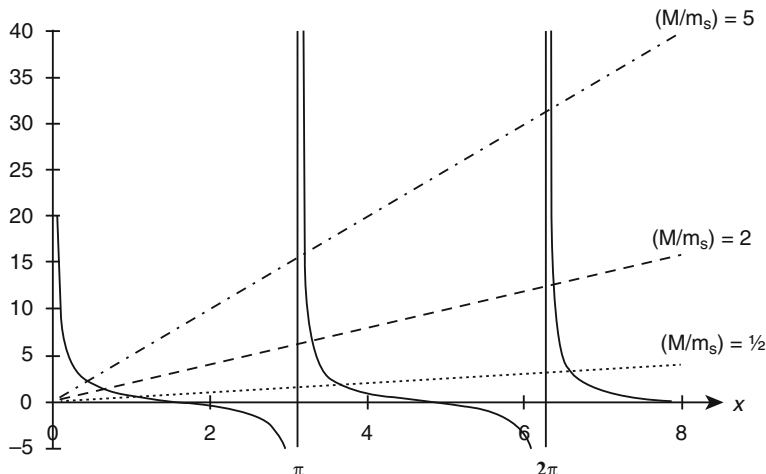


**Fig. 3.7** A graphical solution of Eq. (3.68):  $\cot x = (M/m_s) x$ , hence both axes are dimensionless. If  $M = 0$ , the intersection of  $\cot x$  with the  $x$  axis defines the modes of a fixed-free string with  $(k_n L) = (2n-1)(\pi/2)$ . The dotted line corresponds to  $M/m_s = 1/2$ , the dashed line  $M/m_s = 2$ , and the dash-dot line  $M/m_s = 5$ . As  $M/m_s$  becomes very large, the intersections approach  $(k_n L) = n\pi$ . In that limit, the modes become those of a fixed-fixed string. Intersections of the lines with  $x < \pi/2$  correspond to the lumped-element “pendulum” mode

$M = 0$ , those modes are defined by the intersections of  $\cot(k_n L)$  with the  $x$  axis of the graph in Fig. 3.7. Those intersections occur at  $(k_n L) = (2n - 1)(\pi/2)$ , so  $\omega_n = ck_n = c(k_n L/L) = (2n - 1)(\pi c/2L)$ , or  $f_n = (2n - 1)(c/4L)$ , in agreement with Eq. (3.24), where  $n = 1, 2, 3$ , etc.

As the terminating mass,  $M$ , increases, the slope of the straight line increases, and the values of  $(k_n L)$  for all normal modes decrease. If the terminal mass is much greater than the mass of the string,  $M \gg m_s$ , the intersection of the straight line and the cotangent start to approach the cotangent's asymptotes, so that the standing wave modes approach  $(k_n L) = n\pi$  for  $n = 1, 2, 3$ , etc. This limit produces the (nearly) harmonic series we expect for a fixed-fixed string, since a very large mass approximates a second rigidly fixed end condition.

The one-quarter wavelength mode for the  $n = 0$  case becomes the pendulum mode when  $M > 0$ . The pendulum frequency is given by the intersection of the straight line with the cotangent function and occurs for  $(k_n L) < \pi/2$ . Since we seek solutions for small values of  $x$  when  $M \gg m_s$ , those solutions can be approximated if the cotangent function is expanded in a Taylor series.

$$\lim_{x \rightarrow 0} [\cot x] = \frac{1}{x} - \frac{x}{3} - \frac{x^3}{45} - \frac{2x^5}{945} - \dots \quad (3.69)$$

If we retain only the first term, substitute into Eq. (3.68), and let  $T = Mg$ , then

$$\frac{1}{x} \cong \frac{M}{m_s} x \quad \Rightarrow \quad x^2 = (k_o L)^2 = \frac{\omega_o^2 L^2}{c^2} \cong \frac{m_s}{M} \quad \Rightarrow \quad \omega_o^2 \cong \frac{g}{L} \quad (3.70)$$

The frequency of that pendulum mode is subscripted as  $n = 0$ , a convention we imposed without justification when specifying the natural frequency of a simple (mass-spring) harmonic oscillator in Chap. 2. We will use this designation again for the normal mode frequency of a Helmholtz resonator in Chap. 8 (e.g., the resonance frequency of an ocarina or the frequency generated when blowing over beverage bottles like those shown in Fig. 8.1).

Equation (3.70) has recovered the pendulum frequency calculated for the first time in this textbook using similitude, resulting in Eq. (1.80), and then again from the solution of the differential equation, yielding Eq. (2.32). In both cases, we assumed that “information” could pass along the entire string in time intervals that are short compared to the oscillation period. This is equivalent to saying that the wavelength along the string, when the system oscillates in the pendulum mode, is much greater than the physical length of the string,  $\lambda_o = c/f_o \gg L$ . That allowed us to treat the pendulum as a “lumped-element” system in which all of the mass was concentrated at the pendulum bob.

If we include the second term in the Taylor series expansion of  $\cot x$ , then we see the effects of the string's mass,  $m_s$ , coming into play in just the same way as when we used energy considerations to incorporate the mass of a spring in our calculation of the mass-spring natural frequency given in Eq. (2.27).

$$\frac{1}{x} \cong \left( \frac{M}{m_s} + \frac{1}{3} \right) x \quad \Rightarrow \quad x^2 = \frac{\omega_o^2 L^2}{c^2} \cong \frac{1}{\left( \frac{M}{m_s} + \frac{1}{3} \right)} \cong \frac{m_s}{M} \left( 1 - \frac{m_s}{3M} \right) \quad (3.71)$$

The second term in the expansion of  $\cot x$  tells us that we can improve the accuracy of our solution by adding one-third the mass of the string to the mass of the bob.

$$\omega_o^2 = \left( \frac{g}{L} \right) \left( 1 - \frac{1}{3} \frac{m_s}{M} \right) \quad (3.72)$$

### 3.6.1 Example: Standing Wave Modes for $M/m_s = 5$

Let's examine the modes corresponding to the wavelength being a significant fraction of the string's length. As an example, let's do the calculation for the case of  $M = 0.10 \text{ kg}$  and  $m_s = 0.020 \text{ kg}$ . We will neglect the fact that the tension is a function of the position along the string, but we will use the average tension,  $T = (M + \frac{1}{2}m_s)g = 1.078 \text{ N}$ , to calculate the speed of transverse wave motion. The string's linear mass density is  $\rho_L = m_s/L = 0.020 \text{ kg/m}$ , if we let  $L = 1.00 \text{ m}$ . The speed of transverse waves on that string will be  $c = (T/\rho_L)^{1/2} = 7.34 \text{ m/s}$ .

For this example, we need to solve Eq. (3.68) for  $M/m_s = 5$ . I employed an equation solver to find  $k_o L = 0.4328$ ,  $k_1 L = 3.204$  (2% greater than  $\pi$ ), and  $k_2 L = 6.315$  (0.5% greater than  $2\pi$ ). With the value of the wave speed, and  $L = 1.00 \text{ m}$ , those solutions correspond to  $\omega_n = ck_n$ , so  $\omega_o = 3.18 \text{ rad/s}$ ,  $\omega_1 = 23.52 \text{ rad/s}$ , and  $\omega_2 = 46.36 \text{ rad/s}$ . The displacement amplitudes for the three lowest-frequency normal modes,  $y_o(x)$ ,  $y_1(x)$ , and  $y_2(x)$ , are exaggerated in Fig. 3.8.

### 3.6.2 An Algebraic Approximation for the Mass-Loaded String

*“One measure of our understanding is the number of independent ways we are able to get to the same result.”*  
R. P. Feynman

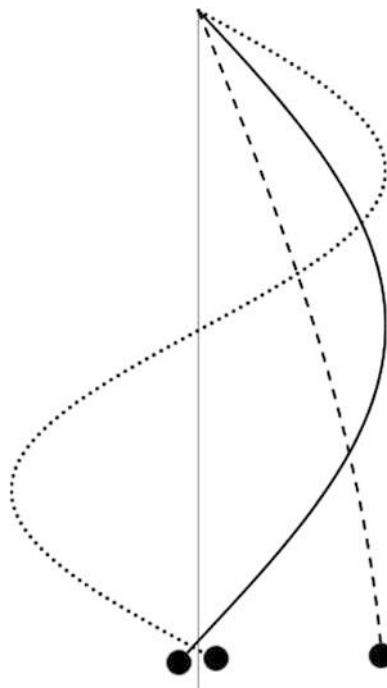


**Fig. 3.8** Greatly exaggerated displacement amplitudes of the three lowest-frequency normal modes of a mass-loaded string with  $M/m_s = 5$ . The (lumped element) “pendulum” mode is shown by the dashed line. The corresponding wavelength,  $\lambda_o \gg L$ , and the normal mode frequency,  $\omega_o = 3.18 \text{ rad/s}$ , based on the example in the text (i.e.,  $c = 7.34 \text{ m/s}$  and  $L = 1.00 \text{ m}$ ). The fundamental mode ( $n = 1$ ) is shown by the solid line which puts just over one full wavelength on the string and produces a frequency  $\omega_1 = 23.52 \text{ rad/s}$ . The second standing wave mode ( $n = 2$ ) is shown by the dotted line which puts just over one wavelength on the string and produces a frequency,  $\omega_2 = 46.36 \text{ rad/s}$ . The ratio,  $\omega_2/\omega_1 \cong 2$ , as it would be for a fixed-fixed string, but the frequency of the pendulum mode has no simple integer relation to the standing wave modes

Equation (3.72) provides a good approximation for the frequency of the pendulum mode obtained by using the first two terms in the Taylor series approximation to  $\cot x$ . We can approximate the standing wave normal modes,  $n \geq 1$ , if we remember that the normal mode is a solution where all parts of the system oscillate at the same frequency.

Careful inspection of Fig. 3.8 shows that a short section of the string connected to the mass is moving out-of-phase with the adjacent section of the string that oscillates with an integer multiple of half-wavelengths. There are nodes very close to the mass for the  $n \geq 1$  modes. We can think of those modes as having exactly an integer number of half-wavelengths above the node connected to a very short pendulum below the node, since the node is equivalent to a rigid termination. Since the normal mode frequency of the pendulum part must be the same as the frequency of the standing wave part, we can use that understanding to approximate the normal mode frequencies without resorting to the solution of a transcendental equation.

Figure 3.9 is an exaggeration of the maximum amplitude for the  $n = 1$  mode that divides the length of the string into two very unequal parts. The longer segment of the string, which contains a fixed-fixed standing wave mode, is designated  $L_s$ . The short pendulum portion is designated  $L_p$ . Based on Eq. (3.70),  $L_p \cong g/\omega_n^2$ . Fitting  $n$  half-wavelengths of a fixed-fixed normal mode between the support and the node makes  $L_s = nc/2f_n = n\pi c/\omega_n$ . The sum of those two segments must equal the total equilibrium length of the string (since we are assuming small displacements),  $L$ , resulting in a quadratic equation for  $\omega_n$ .

$$L = \frac{n\pi c}{\omega_1} + \frac{g}{\omega_1^2} \Rightarrow L\omega_1^2 - n\pi c\omega_1 - g = 0 \quad (3.73)$$

This equation has a well-known algebraic solution.

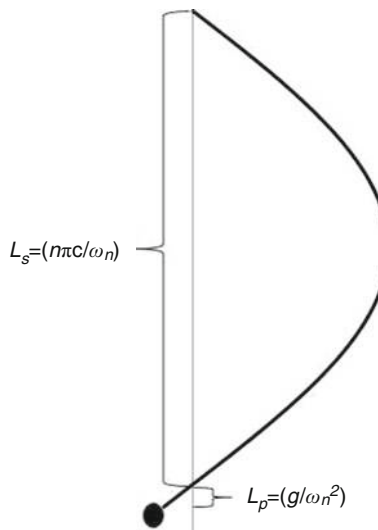


**Fig. 3.9** The exaggerated maximum transverse displacement of a mass-loaded string oscillating in its  $n = 1$  mode shows that the longer segment of the string, above the displacement node (the node close to the mass), is oscillating in the  $n = 1$  fixed-fixed standing wave mode. The length of that segment is  $L_s = \lambda/2 = \pi c/\omega_n$ . The distance between the node and the pendulum bob, based on Eq. (3.70), is  $L_p = g/\omega_n^2$ . The sum of those lengths must equal the equilibrium length of the string,  $L = L_s + L_p$ , leading to a quadratic equation (3.73) for  $\omega_n$ . The frequencies for this example from Eq. (3.68) are  $\omega_{exact}$ , and the frequencies from the quadratic approximation are  $\omega_{quad}$ . Comparison of these frequencies for the first four standing wave modes,  $1 \leq n \leq 4$ , are provided in Table 3.7

**Table 3.7** The radian frequencies for the first four standing wave modes,  $1 \leq n \leq 4$ , of the example in Fig. 3.9 using Eq. (3.68) are  $\omega_{exact}$ . The frequencies from the quadratic approximation of Eq. (3.74) are  $\omega_{quad}$

$n$	1	2	3	4
$\omega_{exact}$	23.5169	46.3510	69.3333	92.3538
$\omega_{quad}$	23.4843	46.3311	69.3195	92.3434
$\omega_{exact} - \omega_{quad}$	0.0326	0.0199	0.0137	0.0104
Diff/ $\omega_{exact}$	0.14%	0.04%	0.02%	0.01%

$$\omega_n = \frac{n\pi c \pm \sqrt{n^2\pi^2c^2 + 4Lg}}{2L} \cong \frac{n\pi c}{L} + \frac{g}{n\pi c} \quad (3.74)$$

The right-hand expression exploits the fact that  $(4Lg/\pi^2c^2) = (4/\pi^2)(m_s/M) \ll 1$  in our example, so the radical can be approximated using the binomial expansion.

The results for the first four standing wave modes are provided in Table 3.7. The frequency,  $\omega_{exact}$ , is obtained from the numerical solutions of the transcendental equation, Eq. (3.68), and  $\omega_{quad}$  comes from the solutions to the quadratic approximation of Eq. (3.74). The ratio of their difference,  $\omega_{exact} - \omega_{quad}$ , to the exact frequency,  $\omega_{exact}$ , is reported as a percentage.

### 3.6.3 The Resistance-Loaded String\*

The calculation of the normal modes of a stiffness-loaded string is left to the exercises (see Problem 11), since it can be treated in a way that is very similar to the mass-loaded string. If we want to consider a pure resistance attached to the string at  $x = L$ , our previous strategy runs into an interesting complication. Since the boundary at  $x = 0$  is still rigidly fixed, Eq. (3.19) must still be valid. The vertical component of the force that a pure resistance would apply to the string is proportional to the velocity of the string at the point of attachment.

$$F_v(L) = -R_m \dot{y}(L) = -j\omega R_m C \sin(kL) e^{j\omega t} \quad (3.75)$$

By Newton’s Third Law, that force must be equal and opposite to the force the string applies to the resistance.

$$F_v(L) = T \left( \frac{\partial y}{\partial x} \right)_L = k_n T C_n \cos(k_n L) e^{j\omega t} = j\omega_n R_m C_n \sin(k_n L) e^{j\omega t} \quad (3.76)$$

This equation can be re-written in the form of Eq. (3.68), but with an interesting difference.

$$\cot k_n L = \frac{j\omega_n R_m}{k_n T} = j \frac{cR_m}{T} = j \frac{c^2 R_m}{cT} = j \frac{R_m}{\rho_L c} \quad (3.77)$$

If  $k_n$  is a real number, then  $\cot k_n L$  must be a real number. In that case, Eq. (3.77) cannot be satisfied since the right-hand side of the equation is purely imaginary. On the other hand, if  $k_n$  were a complex number, say  $k_n = k_n + j\alpha_n$ , then the following identity would produce the necessary imaginary pre-factor.

$$\cot z = j \coth(jz) \quad (3.78)$$

Returning to the form of Eq. (3.77), but allowing  $\mathbf{k}_n$  to be a complex number, we can use the following identities to separate that equation into two individual equations for its real and imaginary components [10].

$$\begin{aligned}\sin(x \pm jy) &= \sin x \cosh y \pm j \cos x \sinh y \\ \cos(x \pm jy) &= \cos x \cosh y \mp j \sin x \sinh y\end{aligned}\quad (3.79)$$

Equating the real parts of Eq. (3.76) produces one equation.

$$-\cos(k_n L) \sinh(\alpha_n L) = \frac{\rho_{LC}}{R_m} \cos(k_n L) \cosh(\alpha_n L) \quad (3.80)$$

Equating the imaginary parts produces another.

$$-\sin(k_n L) \cosh(\alpha_n L) = \frac{\rho_{LC}}{R_m} \sin(k_n L) \sinh(\alpha_n L) \quad (3.81)$$

One solution would be to let  $\sin k_n L = 0$ , automatically satisfying Eq. (3.81), producing the real component of the wavenumber,  $k_n$ , that yields fixed-fixed standing wave solutions (if  $\alpha_n L$  could be neglected), while simultaneously requiring that  $\cos k_n L = 1$ . With  $\cos k_n L = 1$ , the real part, given by Eq. (3.80), becomes the quantizing condition on  $\alpha_n L$ .

$$\frac{\sinh(\alpha_n L)}{\cosh(\alpha_n L)} = \tanh(\alpha_n L) = \frac{\rho_{LC}}{R_m} \leq 1 \quad (3.82)$$

For all values of  $x$ ,  $|\tanh x| \leq 1$ . Our use of this expression requires that the terminal resistance be large compared to the string's characteristic resistance,  $R_m/\rho_{LC} > 1$ . This is certainly true in the limit where  $R_m$  becomes nearly infinite, since that would approximate an immobile boundary resulting in fixed-fixed normal modes, as required by  $\sin k_n L = 0$ , so  $k_n L = n\pi$ , for  $n = 1, 2, 3$ , etc. Also, with  $R_m/\rho_{LC} \gg 1$ , we can make a Taylor series expansion of  $\tanh(\alpha_n L) \cong (\rho_{LC}/R_m) \ll k_n L = n\pi$ . This makes the real portion of the wavenumber dominate the imaginary component, and we have solutions that are now familiar.

If  $(R_m/\rho_{LC}) = 1$ , corresponding to the “matched” impedance case, discussed in the subsequent section describing a driven semi-infinite string (Sect. 3.7), then  $\alpha_n L$  must be infinite; all of the energy will be absorbed. There will be no reflected wave, hence, no normal mode standing wave solution.

The real part of the transcendental equation, given in Eq. (3.80), can be satisfied if  $\cos k_n L = 0$ , producing values of  $k_n L$  corresponding to the odd-integer half-wavelengths that we expect for a fixed-free string, and forcing  $\sin k_n L = 1$ . This leads to the quantizing condition on  $\alpha_n L$  for values of mechanical resistance that are small compared to the string's characteristic impedance,  $R_m < \rho_{LC}$ .

$$\frac{\sinh(\alpha_n L)}{\cosh(\alpha_n L)} = \tanh(\alpha_n L) = \frac{R_m}{\rho_{LC}} < 1 \quad (3.83)$$

If the damping produced by the mechanical resistance is very small relative to the string's characteristic impedance, then  $(R_m/\rho_{LC}) \ll 1$ , again prompting a Taylor series expansion of  $\tanh \alpha_n L \cong \alpha_n L = (R_m/\rho_{LC})$  and making the real component of the wavenumber times the length,  $k_n L$ , again be dominant. Substituting these values back into our assumed solution for a fixed condition at  $x = 0$ , given in Eq. (3.19), describes the resulting normal mode shapes for small damping.

The transition between the fixed-free limit and the fixed-fixed limit is not abrupt. Even when  $\alpha_n L \cong k_n L \cong n\pi$ , which is approximately true in either limit, the amplitude of the function decays to  $e^{-\pi} \cong 0.04$  within one wavelength. Effectively, any standing wave behavior disappears between the fixed-free and fixed-fixed transition.

To complete the substitution back into the mode shape equation, we also need the complex frequency. Since the resistance only dictates a boundary condition, the entire string is still characterized by a uniform value of the linear mass density and a constant tension. The vibrations of the string must still be described by the wave equation as written in Eq. (3.4), so  $c$  is a real scalar constant. This demonstrates that  $k_n c = ck_n + j\alpha_n = \omega_n \equiv \omega_n + j/\tau$ , where we have chosen the imaginary part of the angular frequency to be consistent with our choice for the exponential decay time used with the damped simple harmonic oscillator in Eq. (2.43). Equating the imaginary parts,  $1/\tau = \alpha_n$ .

$$\begin{aligned} y_n(x, t) &= \Re e \left[ \hat{\mathbf{C}} \sin(k_n x) e^{j\omega_n t} \right] \cong \Re e \left[ \hat{\mathbf{C}} e^{-t/\tau_n} e^{j\omega_n t} \right] \sin(k_n x) \\ &= |\hat{\mathbf{C}}| e^{-t/\tau} \sin(k_n x) \cos(\omega_n t + \varphi) \end{aligned} \quad (3.84)$$

### 3.7 Forced Motion of a Semi-Infinite String

Our desire to examine the behavior of a string in response to a time-harmonic excitation should come as no surprise. As before, the steady-state response will be characterized by the string's mechanical impedance. We start that analysis by driving a semi-infinite string that is excited by the time-harmonic transverse vibration of the end of the string at fixed amplitude,  $y(0, t) = y_o \cos(\omega t)$ .

As before, for any linear system (see Sect. 1.3), the steady-state response of the string can only occur at the driving frequency,  $\omega$ . We also assume that our displacement source is sufficiently robust that it can provide whatever force is required to maintain the specified amplitude of oscillation,  $y_o$ . Although semi-infinite strings under uniform tension are rare commodities, this analysis will demonstrate that a string of finite extent can behave as though it were semi-infinite if the undriven end is terminated by a mechanical resistance equal to the *radiation resistance* that was derived for the resistance-loaded uniform string in Sect. 3.6.3.

The behavior of the entire string can be specified by matching the imposed time-harmonic end displacement to a right-going solution to the wave equation. Since the string is assumed to be infinite in length as we go away from the driver, there will be no need for a left-going solution that would represent reflections moving back toward the source. To simplify our mathematics, we will multiply the argument of the wave function by a constant,  $k$ , that has the dimensions of an inverse length [ $\text{m}^{-1}$ ] and is known as the *wavenumber*.

$$k(x \pm ct) = kx \pm kct = kx \pm \omega t \quad (3.85)$$

As before, the  $-$ -sign indicates propagation in the direction of increasing  $x$  (i.e., to the right), and the  $+$ -sign corresponds to propagation in the direction of decreasing  $x$  (i.e., to the left). The rightmost version of Eq. (3.85) imposes the requirement that  $kc = \omega$ , since we know that a time-harmonic driving force at radian frequency,  $\omega = 2\pi f$ , must create a steady-state response only at  $\omega$ . We chose either a complex exponential or a sinusoidal expression as our function of  $x - ct$  or  $ct - x$ .

$$\begin{aligned} y(x, t) &= \Re e \left[ \hat{\mathbf{y}}_o e^{j(kx - \omega t)} \right] = \Re e \left[ |\hat{\mathbf{y}}_o| e^{j\phi} e^{j(\omega t - kx)} \right] \\ \text{or } y(x, t) &= |\hat{\mathbf{y}}_o| \cos(\omega t - kx + \phi) \end{aligned} \quad (3.86)$$

Matching the drive at  $x = 0$  to either right-going solution in Eq. (3.86) requires that  $\phi = 0$ . These solutions are periodic in both space and time.

The vertical component of the force that must be provided by our constant displacement drive to the point of attachment can be calculated from Eq. (3.2) where we again assume a constant tension, T.

$$\mathbf{F}_y(0, t) = -T \left( \frac{\partial y}{\partial x} \right)_{x=0} = jkT |\hat{\mathbf{y}}_o| e^{j\omega t} = F_o e^{j\omega t} \quad (3.87)$$

As with the case of the driven simple harmonic oscillator, it is useful to define the steady-state response of a driven system in terms of its mechanical impedance, as was done in Eq. (2.58), that is, the ratio of the force,  $F_o e^{j\omega t}$ , to the velocity,  $\dot{y}(0, t) = (\partial y / \partial t)_{x=0} = j\omega y(0, t) = j\omega |\hat{\mathbf{y}}_o| e^{j\omega t}$ . In this case, we will designate this impedance as the string's *input mechanical impedance*,  $Z_{m,0}$ , since it is the impedance of the string where the displacement is imposed by the driver at  $x = 0$ .

$$Z_{m,0} = \frac{\mathbf{F}_y(0, t)}{\dot{y}(0, t)} = \frac{jkT |\hat{\mathbf{y}}_o| e^{j\omega t}}{j\omega |\hat{\mathbf{y}}_o| e^{j\omega t}} = \frac{T}{c} = \frac{\rho_L c^2}{c} = \rho_L c \quad (3.88)$$

It is useful to think about the fact that  $Z_{m,0} = \rho_L c$  is a real number. In our analysis of the driven simple harmonic oscillator, the only real part of the mechanical impedance was the mechanical resistance,  $R_m$ , which was also our only means for absorbing power. As yet, no “resistance” has appeared in our model of the flexible string, so we have included no mechanism that would dissipate energy.

For our driven string, this input mechanical resistance is a *radiation resistance*. In terms familiar to the microwave engineer, it would be known as the *characteristic impedance* of the transmission line (i.e., our string). What appears as a “dissipation mechanism” is merely an accounting anomaly—the instantaneous power,  $\Pi(t)$ , delivered to the string, propagates along the string. (Warning: Do not attempt to use this “accounting” argument with the Internal Revenue Service.)

$$\langle \Pi(t) \rangle_t = \frac{1}{T} \int_0^T F_y \cdot \dot{y} dt = \frac{1}{T} \int_0^T \frac{F_o^2}{\rho_L c} \cos^2 \omega t dt = \frac{F_o^2}{2\rho_L c} = \frac{\rho_L c}{2} \dot{y}_o^2 \quad (3.89)$$

Again, the similarity of the above result to the expressions for the Joule heating,  $\Pi_{el}$ , of an electrical resistor,  $R_{dc}$ , is useful:  $\langle \Pi_{el} \rangle_t = (VI/2) = (V^2/2R_{dc}) = (I^2 R_{dc}/2)$ .

It is possible to avoid the issues introduced by a string that must be infinitely long in the  $+x$  direction. If the string is terminated at a free boundary, but the “massless ring” to which the string is attached is joined to a mechanical resistance (e.g., a dashpot) with  $R_m = \rho_L c$ , then all of the energy that is propagating along that string will be dissipated in  $R_m$ , and there will be no reflections, even though the string is not infinitely long.

This “matched load” strategy is very common in electrical engineering. To avoid reflections along a cable attached to a measuring instrument (e.g., oscilloscope, spectrum analyzer), an electrical resistance with a value equal to the cable's characteristic impedance is placed across the input terminals of the instrument. For common co-axial cables, this resistance is typically  $50 \Omega$ . This *nonreflecting termination* technique is so common that many instruments have a built-in, switch-selectable input resistance with the option of providing a  $1 M\Omega$  or  $50 \Omega$  input electrical resistance.

### 3.8 Forced Motion of a Finite String

If the termination of our uniform string is anything besides the characteristic impedance,  $\rho_L c$ , then there will be reflections. Those reflections will influence the driver and can make the amplitude of the input mechanical impedance take values from zero to  $\pm\infty$ . If the termination provides no dissipation

and there are no mechanisms to create propagation losses along the string, the input mechanical impedance will be entirely imaginary.

For that lossless case, with either a fixed or free termination, if we were to launch a pulse of duration,  $\Delta t$ , from the driven end of a string (like those shown in Fig. 3.2 through Fig. 3.5) of total length,  $L$ , the pulse would be reflected and return to the driver after a time,  $t = 2 L/c$ .<sup>14</sup> Being reflected from the driven end, the process would repeat indefinitely with a period,  $T = 2 L/c$ , and there would be no superposition if  $\Delta t < L/c$ . Such multiple reflections would be periodic, but not harmonic.

### 3.8.1 Displacement-Driven Finite String

We can calculate the steady-state behavior for a string of length,  $L$ , which is terminated by a fixed boundary and excited by a single-frequency time-harmonic displacement. Instead of placing our drive at  $x = 0$ , as we did for the semi-infinite case, the calculations are greatly simplified if we let the fixed end be located at  $x = 0$  and drive from the end at  $x = L$ , in this case with a forced displacement amplitude,  $y(L, t) = y_o \cos(\omega t)$ . By letting  $y_o$  be a real scalar, we are only requiring that the phase of the string's response will be referenced to the phase of the displacement drive. This simplification arises from the fact that we already have an exact expression for the string's displacement if  $y(0, t) = 0$ , given in Eq. (3.19), so we can just equate the displacement of the string at  $x = L$  to the imposed harmonic displacement,  $y(L, t) = y_o \cos(\omega t)$ .

$$\begin{aligned} y(L, t) &= y_o \cos(\omega t) = \Re e \left[ \hat{\mathbf{C}} \sin(kL) e^{j\omega t} \right] \\ \Rightarrow |\hat{\mathbf{C}}| &\equiv C = \frac{y_o \cos(\omega t)}{\sin(kL)} \end{aligned} \quad (3.90)$$

Substitution of  $C$  into Eq. (3.19) produces the steady-state response of the entire string to the displacement drive at  $x = L$ .

$$y(x, t) = y_o \frac{\sin(kx)}{\sin(kL)} \cos(\omega t) \quad (3.91)$$

The displacement of the string is infinite everywhere whenever  $kL = n\pi$ . This corresponds to placing an integer number of half-wavelengths between the driver and the rigid termination. We call this condition *resonance*. It will be easy to understand what is happening in this critically important circumstance if we calculate the mechanical input impedance that the string presents to the displacement drive located at  $x = L$ .

At any point along the string, the vertical component of the force can be calculated from Eq. (3.91). By Newton's Second Law, the vertical force,  $F_y$ , on the string will be equal and opposite to the force applied at  $x = L$ .

$$F_y(x, t) = -T \left( \frac{\partial y}{\partial x} \right) = -y_o T k \frac{\cos(kx)}{\sin(kL)} e^{j\omega t} \quad (3.92)$$

The velocity of the string at any location is just as simple to calculate.

---

<sup>14</sup>The termination could be lossless but possibly be mass-like or stiffness-like. In that case, the apparent distance,  $L_{eff}$ , between the driver and termination, might be slightly different than the physical length,  $L$ .

$$\dot{\mathbf{y}}(x, t) = j\omega y_o \frac{\sin(kx)}{\sin(kL)} e^{j\omega t} \quad (3.93)$$

Their ratio gives the mechanical impedance of the string at any location.

$$\mathbf{Z}_m(x) = \frac{F_y(x)}{\dot{\mathbf{y}}(x)} = -\frac{Tk}{j\omega} \frac{\cos kx}{\sin kx} = j\frac{T}{c} \cot kx = j\rho_L c \cot kx \quad (3.94)$$

In this case, the complex mechanical impedance,  $\mathbf{Z}_m(x)$ , anywhere along the string, is a purely imaginary quantity since force and velocity are  $90^\circ$  out-of-phase with respect to each other. The fixed boundary condition and the absence of any loss mechanisms means that none of the input energy can be dissipated.

Before using this result to explain the resonance, it is always prudent to examine a new result in a limit that we have already analyzed by other means (after checking that the units make sense, of course). Back in Chap. 2, we calculated the vertical component of the force exerted on a mass by a string with tension,  $T$ , that was displaced from equilibrium by a distance,  $y$ . In the small-amplitude limit,  $y \ll a$ , the result was given in Eq. (2.124). That expression provided the vertical component of the force due to two taut strings of length,  $a = L/2$ . In this case there is only one string of length,  $L$ , so  $F_y(x = L) = -(T/L)y$ , producing an equivalent stiffness constant,  $(T/L)$ . At very low frequency (i.e.,  $L \ll \lambda$ ), Eq. (3.69) guarantees that  $\cot(kx) = (kx)^{-1}$  in the limit that  $kx \rightarrow 0$ . Also, since the motion is simple harmonic in time,  $\mathbf{y} = \dot{\mathbf{y}}/\omega = -j\dot{\mathbf{y}}/\omega$ . Using all of these assumptions to evaluate Eq. (3.94) shows that the input impedance at  $x = L$  is consistent with the static limit producing a stiffness,  $K = T/L$ .

$$\lim_{\omega \rightarrow 0} [-j\rho_L c \cot(kL)] = \frac{-j\rho_L c}{kL} = \frac{-j}{\omega} \frac{T}{L} = \frac{1}{j\omega} \frac{T}{L} \quad (3.95)$$

Returning now to the question of the resonance of a finite string driven by a constant amplitude harmonic displacement,  $y(L, t) = y_o \cos(\omega t)$ , we see from the mechanical impedance in Eq. (3.94) that the string applies a force to the displacement driver that is infinite when  $kL = n\pi$ . Therefore, the required magnitude of the vertical force is  $|F_y| = |\mathbf{Z}_m(L)|(|dx/dt|) = \infty$ ; an infinite force is required to produce infinite displacements at all locations.

Of course, a real string, driven by a real displacement drive, will not produce infinite displacements. Long before the displacements become infinite, we will have exceeded the limitations of our linear approximation, and the average tension in the string will start to increase with increasing amplitude, causing the speed of the transverse vibrations to increase, thus de-tuning the resonance condition [11]. Also, practical considerations, including the effective output mechanical impedance of the driver and dissipation in the string, radiation of sound from the string, and losses introduced by motion at the “fixed” end, will all limit the transverse displacement amplitudes.

Another useful perspective on this resonance behavior is provided if we consider the string as an *impedance transformer*. This perspective is diagrammed schematically in Fig. 3.10. Movement away from the fixed end at  $x = 0$  by an integer number of half-wavelengths transforms the impedance by  $1:\pm 1$ . Odd-integer numbers of half-wavelengths provide a  $1:-1$  transformation and displacements by full wavelengths correspond to a  $1:1$  transformation. Since resonance occurs when an integer number of half-wavelengths is interspersed between the fixed end at  $x = 0$  and the driven end at  $x = L$ , the resonance corresponds to the transformation of the infinite impedance of the fixed end to an infinite impedance at the driving location.

At the nodal locations, both the displacement and the velocity vanish, but the slope of the line at that location (and hence the vertical component of force at that location) has its maximum value. The mechanical impedance of the string at those nodal points is therefore infinite. Said another way, a

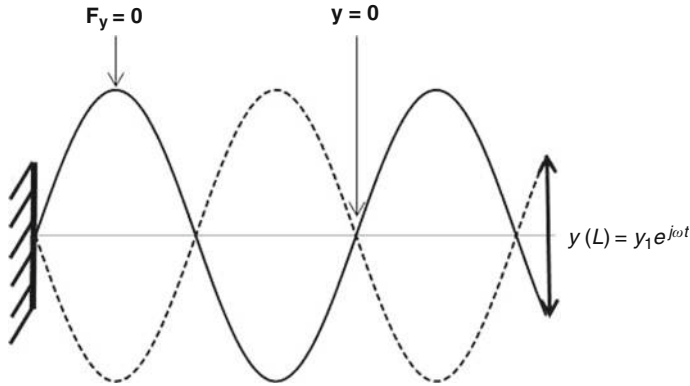


**Fig. 3.10** Displacement amplitude envelope of a uniform string, fixed at  $x = 0$ , driven by a constant displacement drive at  $x = L$  indicated by the *solid double-headed arrow*. At the locations of maximum displacement, the vertical component of the force,  $F_y$ , is zero, as is the string's mechanical impedance. At the nodal locations, both the string's displacement and its velocity are zero. At such nodal locations, the string's mechanical impedance is infinite. In this figure, the constant displacement drive is not located at a node so the string's displacements are finite, though grossly exaggerated in this figure

quarter wavelength displacement corresponds to a  $1:\pm\infty$  transformer. At an anti-node, the impedance is zero, but a quarter wavelength away in either direction is infinite if the string is lossless.<sup>15</sup>

### 3.8.2 Mass-Loaded String in the Impedance Model

The expression for the mechanical impedance of the string in Eq. (3.94) is not a function of the drive but only of the string's properties (i.e., tension and linear mass density) and the fact that its end at  $x = 0$  is rigidly fixed. For that reason, we should be able to use Eq. (3.94) to calculate the normal modes of a string that is fixed at one end and has a mass attached to the other end. An impedance-matching analysis must yield the same results as did our Newtonian analysis in Sect. 3.6.

The mechanical impedance of a mass,  $M$ , is  $Z_m = j\omega M$ . By Newton's Third Law, the force that the string applies to that mass must be equal and opposite to the force that the inertia of the mass applies to the string. Setting the impedance of the mass to the negative of the impedance of the string produces the same transcendental equation as derived before in Eq. (3.68).

$$\begin{aligned} j\omega_n M &= j\rho_L c \cot(k_n L) \\ \Rightarrow M &= \frac{m_s}{k_n L} \cot(k_n L) \quad \text{or} \quad \frac{M}{m_s} (k_n L) = \cot(k_n L) \end{aligned} \quad (3.96)$$

Each successive value of  $n$  corresponds to the mass being transformed another half-wavelength away from the rigid termination at  $x = 0$ . The same approach can be used to solve for the normal modes of a string fixed at  $x = 0$  and terminated by a spring at  $x = L$ .

<sup>15</sup> This results again highlights the difference between the vertical force applied to a point,  $F_v$ , vs. the net force,  $dF_{net}$ , on an infinitesimal string segment of length,  $dx$ , provided in Eq. (3.2) and used to derive the wave equation in Eq. (3.4). The imposition of a fixed displacement or fixed force drive is equivalent to specification of a boundary condition. When this imposed force or displacement is applied to the string at a location other than one of the string's boundaries, it can be thought of as making the string into two independent segments with the drive being applied at a point to two loads corresponding to the two impedances that represent those two separate string segments.

### 3.8.3 Force-Driven Finite String

Having an expression for the mechanical impedance of a string that is attached rigidly at  $x = 0$ , we can easily calculate the behavior of the same string driven by a time-harmonic vertical force of fixed amplitude applied at  $x = L$ :  $F_y(L) = F_o \cos(\omega t)$ . By letting  $F_o$  be a real scalar, we are only requiring that the phase of the string's response will be referenced to the phase of the driving force. In that case, whenever the constant force drive encounters an impedance that is zero, the vertical force produced by the string will be zero. Imposition of a non-zero force at that location implies that the vertical force everywhere else on the string must be infinite.

The mechanical impedance of the string goes to zero whenever  $k_n L = (2n - 1)(\pi/2)$ , where  $n = 1, 2, 3, \dots$ . This resonance condition corresponds to an odd-integer number of quarter-wavelengths between the rigid point of attachment at  $x = 0$  and the constant force driver location at  $x = L$ . It is exactly the opposite of the resonance condition for a constant displacement (or constant velocity) drive.

Although a constant displacement drive is easy to visualize, it may be helpful to provide an example of how a constant amplitude force drive can be applied to a string. With a constant displacement drive, we are assuming that the driving mechanism can provide whatever force is necessary to keep the amplitude of the displacement constant. With a constant force drive, we assume that the force can produce whatever displacement is required to hold the amplitude of the vertical component of the force constant.

Such a fixed amplitude time-harmonic force drive can be created by placing a magnetic field of magnetic induction,  $\vec{B}$ , perpendicular to the direction of the string and running an alternating electrical current,  $I(t) = \Re e[\vec{I} e^{i\omega t}]$ , through the string, assuming that the string is made of a material that conducts electricity. The vertical force on the string is given by the Lorentz equation:  $F_y(t) = (B\ell)I(t)$ , where it is assumed that the magnetic induction,  $\vec{B}$ , is constant over a length,  $\vec{\ell}$ , of the string and that  $\vec{F}_v$ ,  $\vec{B}$ , and  $\vec{\ell}$  are all mutually perpendicular [11].

If the electrically conducting string is fixed at both ends and driven by the current,  $I(t)$ , applied at a frequency that would excite one of the fixed-fixed string's normal modes (i.e.,  $f_n = nc/2L$ ), then if  $|\vec{\ell}| \ll LL$ , and if the magnetic field is centered over a displacement anti-node, where  $|Z_m| = 0$ , the string would be excited at resonance. Being a displacement maximum, the driven anti-node point has zero slope, hence zero force, but the electromagnetic force created by the magnetic field's interaction with the current is non-zero, so the force everywhere else on the string must become infinite. If the magnetic field were placed over a displacement node, then  $|Z_m| = \infty$ , and the string would remain at rest.

### 3.8.4 An Efficient Driver/Load Interaction

There are no displacement drivers that can produce infinite forces, and there are no force drivers that can produce the required unlimited displacements. As with our “perfect” boundary conditions, the idealized force and displacement drives are useful because they inform our intuition and because there are circumstances where the loads which the string (or any “driven” system) places on the driver are far less demanding than the infinite or zero impedances that led to infinite responses. Although conceptually convenient, the cases where the driver overpowers the load are cases where the transfers of energy from the driver to the load are extraordinarily inefficient. In fact, it is this inefficiency that allows the load and driver to be treated independently—the effects of one upon the other are minimal.

The efficient coupling of a driver to an acoustic load requires the matching of the driver’s impedance to the load’s impedance. Since only resistive loads can absorb power, optimization of this matching process requires first that the reactive components (i.e., the stiffness and moving mass) of the combined system cancel. With that cancellation, the power of the driving mechanism (e.g., electrodynamic or piezoelectric forces) is not consumed by the acceleration and deceleration of masses nor the compression or extension of stiffness elements. Here we must recognize that the load and the driver can also provide stiffness or mass (e.g., see Sect. 2.5.5 or Sect. 10.7.5), depending upon the driving frequency.

Matching of the resistive components of the driver and load is also required for high-efficiency power transfer. Since power is proportional to the product of force and velocity, a load resistance,  $R_{load}$ , that is much greater than the drive’s internal mechanical resistance,  $R_m$ , will require greater forces to generate time-averaged power transfer since  $\langle \Pi \rangle_t = F^2/2R_{load}$ . Since no drive mechanism is 100% efficient, the required force will result in some energy loss within the transduction mechanism. Similarly, if  $R_{load}$  is too small relative to the mechanical resistance of the driver,  $R_m$ , then larger velocities,  $v$ , will be required to provide the required time-averaged power to the load,  $\langle \Pi \rangle_t = R_{load}v^2/2$ . If the velocity of the drive is equal to that of the load, then the power dissipated internally within the driver will be proportional to  $R_m v^2/2$ . One solution is provided by the use of some nearly lossless “lever” system that allows the velocity of the driver to differ from the velocity of the load<sup>16</sup> [12].

The cancellation of the reactive components suggests operation at resonance; hence the highest efficiency can only be achieved over a limited range of frequencies. The matching of the driver’s resistance and the resistance of the load may be limited by the available “leverage.” A very large “piston” (e.g., speaker cone) that improves the matching of the resistive components might also be so massive that the piston’s mass requires too much of the motor’s force to accelerate and decelerate it. An exponential horn is a common method used to increase the radiation loading on a smaller piston, but that solution may require the horn to be large (i.e., expensive), particularly for matching at low frequencies (see Sect. 10.9).

This discussion of efficient driving strategies is only meant to raise awareness for subsequent applications that do not involve strings and to emphasize that the idealized concepts introduce practical limitations. Also, there are situations where efficiency is not the primary objective. In sound reproduction systems, sometimes the primary objective is uniform output power (i.e., “flatness”) over the broadest possible bandwidth (i.e., frequency range). In those cases, Professor Puttermann’s perspective is worthy of consideration:<sup>17</sup> “The flattest response is no response at all.” One can trade efficiency for bandwidth just as the sensitivity of a geophone was traded for increased bandwidth, as shown in Fig. 2.24. The “art” is in knowing how to make an optimal trade-off based on the specified design goals.

---

### 3.9 “I’ve Got the World on a String . . .”: Chapter Summary

The physical system that has been the focus of this chapter is an idealized string that is “limp” in the sense that any displacement of the string from its equilibrium condition is restored only by tension and that the string itself has no stiffness (i.e., the string has no flexural rigidity). Although the musical

<sup>16</sup> In acoustical systems, this “lever” might be the area of the piston driving the acoustic load. The piston transforms the velocity of the driver (e.g., the voice coil velocity) to the volume velocity (i.e., oscillatory mass flow rate) of the fluid driven by the piston. Calculations to determine the piston area that optimizes the efficiency of the coupling between an electrodynamic linear motor (e.g., moving-coil loudspeaker) and a standing wave resonator are provided in Sect. 10.7.5.

<sup>17</sup> S. J. Puttermann is a Professor of Physics at the University of California, Los Angeles.

consequences of the string's normal modes of vibration have been briefly noted, the goal of this chapter has been to introduce many of the perspectives and mathematical techniques that will appear repeatedly throughout this textbook to analyze the vibrations of continua (i.e., fluids and solids). It is much easier to illustrate the transverse motion of a string in a textbook than it is to visualize the local concentrations of air molecules that are excited by the passage of a sound wave consisting of longitudinal expansions and compressions. Because these ideas are so important, we will close this chapter by reviewing some of the most significant results.

As stated in Sect. 1.1, two of the most useful techniques in mathematics, substitution and Taylor series, have been employed throughout. As with our analysis of the simple harmonic oscillator, we began by identifying the relationship between forces and displacements (i.e., an equation-of-state), in this case, a transverse force and a slope,  $F_y = -T (\partial y / \partial x)$ . Newton's Second Law of Motion then provided the connection between the acceleration of an infinitesimal segment of the string and the net force produced by the tension acting on both ends of that segment, determined by a Taylor series expansion of the force at one end of the segment relative to the force at the other end. We assumed small displacements from equilibrium so that the Taylor series expansion could be truncated beyond the linear term.

This process led us to combine those tensile and inertial effects into a homogeneous second-order partial differential equation that related transverse displacements to position along the string and to time. That equation is called "the wave equation." The first thing we used that wave equation to reveal was that it could be satisfied by any two functions,  $f_+(w_+)$  and  $f_-(w_-)$ , as long as the argument of those functions had the form  $w_{\pm} = x \pm ct$ , where  $c$  was the speed of propagation for the transverse displacements. It was also the last thing that the wave equation revealed.

Although claiming that "the wave equation is the least useful equation in acoustics" is considered a heresy by many acousticians, the wave equation did not make any further contribution to the investigations within this chapter, nor will it play a more significant role in our other analyses. In this chapter, when we considered a string that had a variable tension,  $T(z)$ , in Sect. 3.4.3, Eq. (3.44) set up the wave equation for that case. We did not bother to solve it.<sup>18</sup> Instead, we employed a plausible solution that satisfied the boundary conditions and calculated the corresponding potential and kinetic energies of vibration to determine the normal mode frequencies from their ratio. When the "trial function" contained an "adjustable parameter," we improved the accuracy of our approximation by minimizing the frequency with respect to variation of the adjustable parameter, an approach known as "Rayleigh's method."<sup>19</sup>

It might seem strange to use an approximate solution when the exact solution is known, but an approximate solution can be a better choice in many circumstances. For example, the use of a polynomial approximation can be much more computationally efficient than the use of exact solutions when simultaneous solution of many coupled equations is performed by a computer [13]. In our case, I had no interest in slowing the development of our investigation of string vibrations by having to introduce Bessel's equation, although it will be introduced in Chap. 6, when Bessel functions will be required to analyze two-dimensional vibrating systems that possess circular symmetry.

With the functional dependence on  $w_{\pm}$  established, the concept of "ideal" boundary conditions was introduced, and the reflection of an arbitrary pulse from such boundaries was explained in terms of the superposition of that pulse and an "image" pulse that approached the boundary traveling in the opposite direction, along a string that did not exist in the real world. We then went on to impose

<sup>18</sup>The solution to Eq. (3.44) can be obtained by a clever change of variables resulting in the spatial dependence being described by a Bessel function (see Fig. 6.8) of the transformed coordinates rather than a trigonometric or exponential function. Execution of this approach is a standard problem in many textbooks on mathematical physics.

<sup>19</sup>In quantum mechanical applications, this is commonly called the Rayleigh-Ritz method.

two such boundary conditions to define a string of finite length. The imposition of one boundary condition restricted the form of the solutions, and the imposition of the second boundary condition quantized the frequencies and wavenumbers of the normal modes of a finite string’s vibrations.

Although no physical boundary condition is an exact match to the idealized cases (e.g., fixed-fixed or fixed-free), it is a good enough approximation in many cases that we could use the normal mode frequencies, and their harmonic relationships, to develop a rudimentary appreciation for the sounds produced by stringed musical instruments and combine those results with our understanding of the psychological concepts of consonance and dissonance. This led to a brief consideration of the difficulties that are encountered when we attempt to preserve consonance while creating the notes of a musical scale that will be both pleasing and practical.

Again, the fundamental equations relating stiffness and inertia to displacements and accelerations (and not the wave equation!) allowed us to develop an understanding of the energy content of the string’s vibration. Those energies were exploited to calculate normal mode frequencies in cases where the exact solution was known, as well as cases where the linear mass density of the string was either perturbed at a point or was a continuous function of position. The use of energy methods to calculate the normal mode frequencies for the case where tension was a function of position has already been mentioned in this summary.

As for any linear system, the solutions for the string’s motion always involved arbitrary amplitudes that could not be determined until the initial conditions were specified. We found that the Fourier series was an ideal method to project such initial conditions (at  $t = 0$ ) onto a linear superposition of normal mode shapes that formed a complete orthogonal basis describing the spatial and temporal evolution of the system for all  $t > 0$ . The relative amplitudes of the normal modes provided some insight into the tonality produced by the location where a string was plucked, as well as explaining the difference in the sound produced by an electrodynamic pickup as a function of its distance from the electric guitar’s bridge.

Although this provides an important piece of our understanding of the physics involved in the production of musical sounds by plucked or hammered strings, it is by no means a complete understanding. The attack and decay of the sound of a plucked string, though related to the harmonic structure, are dependent upon other effects (e.g., damping and motion of the bridge that couples the string’s energy to the radiating surface of the instrument’s body). The attack and the decay are equally important to our perception of musical sounds and our ability to differentiate the sounds produced by specific musical instruments or to identify the individual musicians playing those instruments by the sounds they produce.

Techniques for the calculation of normal mode solutions (i.e., mode shapes and frequencies) for “imperfect” boundary conditions demonstrated that such imperfections (e.g., an end that was “fixed” by a finite mass or a “free” end that was attached to a stiffness or resistance) used the same matching of the wave’s motion to the boundary’s mechanical impedance but produced equations for quantized modal frequencies and wavenumbers that had no closed-form algebraic solutions and produced normal mode frequencies that were not exact integer multiples of the fundamental ( $n = 1$ ) mode’s frequency,  $f_1$ . Again, a small amount of physical insight was leveraged into approximate solutions that did have simple algebraic forms and impressive accuracy. In addition, for the case of a fixed, mass-loaded string, an additional “lumped-element mode” was identified that had a frequency,  $f_o < f_1$ , and did not exhibit any harmonic relationship to the fundamental frequency,  $f_1$ . That normal mode is the pendulum mode.

A brief investigation of the resistance-loaded string introduced behavior that was more complicated to compute, but that approached the expected fixed-free behavior when the resistance was very small (i.e.,  $R_m/\rho_L c \ll 1$ ) and fixed-fixed behavior in the opposite limit. That problem also introduced the need to treat both the wavenumber and the frequency as complex numbers to incorporate dissipative behaviors associated with the connection to a mechanically resistive element.

The last topic was the driven string. For a semi-infinite string, the characteristic impedance,  $\rho_L c$ , was derived as the solution to the steady-state problem. For the string of finite length, the steady-state response was shown to be critically dependent upon both the frequency of the drive and the nature of the driver's excitation. A constant displacement drive produced a very different steady-state response than a constant force drive when applied at the same location and at the same frequency. In the absence of any dissipation, there were frequencies for either driver type that resulted in an infinite response at all points along the string. We identified this behavior as "resonance."

In this chapter and the previous one, we have accumulated a rather impressive arsenal of concepts and mathematical techniques. Although others will be forthcoming, those accumulated thus far should serve us well throughout this textbook.

### Talk Like an Acoustician

Wave equation	Interval
d'Alembertian operator	Equal temperament
Transverse wave speed	Scale of just intonation
Traveling wave	Pythagorean scale
Fixed boundary	Chromatic scale
Free boundary	Stability coefficient
Method of images	Inertia coefficient
Wavenumber	Transcendental equation
Fundamental frequency	Nonreflecting termination
Overtones	Input mechanical impedance
Harmonic series	Radiation resistance
Standing waves	Characteristic impedance
Nodes	Resonance
Anti-nodes	Impedance transformer
Consonance and dissonance	

### Exercises

1. **Mersenne's Laws.** Marin Mersenne wrote the following three laws that govern the frequency of a vibrating string in his 1637 work, *Traité de l'harmonie universelle* [14]:

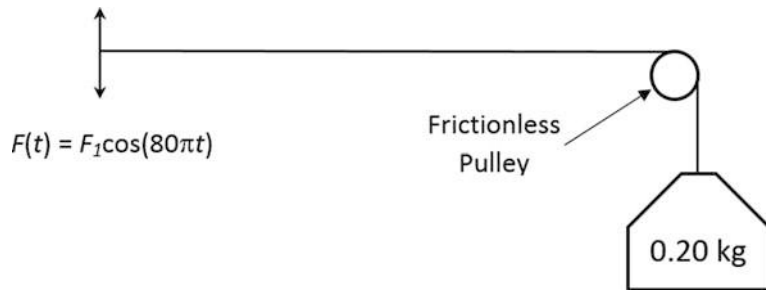
- (i) For a given string and a given tension, the time [period] varies as the length.
- (ii) When the length of the string is given, the time varies inversely as the square root of the tension.
- (iii) Strings of the same length and tension vibrate in times which are proportional to the square root of the linear density.

Show that all three of Mersenne's Laws are a direct consequence of the fact that there is only one combination of tension, length, and linear mass density that have the units of time [15].

2. **Traveling wave.** The transverse displacement of a wave propagating to the right on an infinite string of linear mass density,  $\rho_L = 1.00 \times 10^{-4}$  kg/m, is given by  $y(x, t) = (0.05) \cos(4t - 3x)$ , where  $y$  and  $x$  are in meters and  $t$  is in seconds.

- (a) *Amplitude.* What is the peak-to-peak amplitude of the wave?
- (b) *Transverse wave speed.* Determine the propagation speed of the wave.
- (c) *Tension.* What is the tension in the string?
- (d) *Wavelength.* What is the wavelength of the wave?
- (e) *Transverse string speed.* What is the maximum speed of the string's motion in the transverse direction?

**Fig. 3.11** Force-driven string tensioned by a mass hung from a frictionless pulley



3. **Driven semi-infinite string.** A string of constant linear mass density,  $\rho_L = 0.10 \text{ kg/m}$ , is stretched to a tension of  $T = 10.0 \text{ N}$ . It is excited by a constant displacement generator which produces a transverse displacement of  $y(0, t) = 0.020 \cos(20t)$ , where the amplitude is expressed in meters and the time in seconds.
- Wavelength.* What is the wavelength of the wave that is being generated?
  - Wave function.* Write a wave function which describes the transverse displacement of the string caused by the wave for all positions,  $x > 0$  and all times  $t > 0$ .
  - Power.* How much time-averaged power does the generator have to deliver to the string to maintain the wave?
4. **Force-driven fixed string.** A uniform string is driven at one end at 40 Hz, and the other end runs over a pulley and is attached to a mass of 0.20 kg as shown in Fig. 3.11. You may consider the pulley to provide a rigid termination and let  $g = 9.8 \text{ m/s}^2$ .
- String mass.* In a distance 1.20 m from the pulley, there are three loops (i.e., half-wavelengths). If the distance between the drive and the pulley is 2.00 m, what is the mass of that 2.00 m length of string?
  - Water absorption.* If the string should absorb some water and become heavier but is still driven at 40 Hz, for each of the following quantities, indicate whether they would increase, decrease, or remain the same.
    - Linear mass density,  $\rho_L$ . \_\_\_\_\_
    - Tension,  $T$ . \_\_\_\_\_
    - Propagation speed,  $c$ . \_\_\_\_\_
    - Wavenumber,  $k$ . \_\_\_\_\_
    - Period,  $T = f^{-1}$ . \_\_\_\_\_
    - Wavelength,  $\lambda$ . \_\_\_\_\_
    - Radian frequency,  $\omega$ . \_\_\_\_\_
5. **Plucked string.** A string of length,  $L$ , rigidly constrained at both ends, is displaced by a transverse distance,  $h$ , at a distance,  $(1/3)L$ , from one end and released at  $t = 0$ .
- Harmonic amplitudes.* Determine the amplitude of the first four standing wave modes in terms of the initial displacement,  $h$ .
  - Frequency of vibration.* If  $L = 0.25 \text{ m}$ ,  $T = 10.0 \text{ N}$ , and  $\rho_L = 1.0 \times 10^{-4} \text{ kg/m}$ , determine the frequency of the fundamental ( $n = 1$ ) mode of vibration.
  - Energy of vibration.* What is the total energy of all the modes excited by plucking the string with an initial displacement of  $h = 1.0 \text{ cm}$ ?
6. **Initial velocity harmonic amplitude coefficients.** Calculate the values of  $C_n$  for a string that is excited by the following triangular velocity distribution applied to one-half of the string's length.

$$v_o(x, 0) = \begin{cases} \frac{v_1 x}{L} & \text{if } 0 < x < \frac{L}{4} \\ \frac{v_1}{L} \left( \frac{L}{2} - x \right) & \text{if } \frac{L}{4} < x < \frac{L}{2} \\ 0 & \text{if } x > \frac{L}{2} \end{cases}$$

7. **Nonuniform mass distribution.** Use Rayleigh's method to calculate the normal mode frequencies of a string which has the following parabolic variation linear mass density,  $\rho_L(x)$ , where  $m_s$  is the mass of the string before the parabolic contribution is added. The expression below places  $x = 0$  at the center of the string with length,  $L$ , so  $-L/2 \leq x \leq +L/2$ . Assume  $m_o = m_s/5$  and report your frequencies in terms of the exact frequencies for a uniform string of the same length with constant linear mass density,  $\rho_L(x) = m_s/L$ .

$$\rho_L(x) = \frac{m_s}{L} \left[ 1 - \frac{m_o}{L^2 m_s} \left( x^2 - \frac{L^2}{4} \right) \right]$$

- (a) *Uniform density trial functions.* Calculate the approximate normal mode frequencies using the exact shapes for the uniform string given in Eq. (3.21).
  - (b) *Quadratic polynomial trial function.* Calculate the frequency of the fundamental ( $n = 1$ ) normal mode using the power law shape function of Eq. (3.33) with  $m = 2$ .
  - (c) *Optimized power law trial function.* Write the frequency of the fundamental mode in terms of  $m$ , as was done in Eq. (3.36), and minimize the frequency with respect to  $m$ , to determine the best value for  $m$ . Use that result to calculate a new approximation to the frequency of the fundamental mode.
8. **An “inverse” problem.** The data summarized in Table 3.8 provides the location of the nodes on a string that is 1 m long and tensioned with a force of 3.948 N. For both parts, the string is driven at its tenth standing wave mode.
- (a) *Uniform density.* A string of uniform density is driven at  $f_{10} = 31.4159$  Hz. Determine the linear mass density,  $\rho_L$ , of that string for the node spacing above.
  - (b) *Nonuniform density.* The uniform string is replaced with one of nonuniform density,  $\rho_L(x)$ , and the frequency of the 10<sup>th</sup> mode is found to be  $f_{10} = 31.7565$  Hz. Use the “half-wavelength” of each segment between adjacent nodes (length  $x_i - x_{i-1}$ ), to approximate the mean linear mass density at the mean location,  $(x_i + x_{i-1})/2$ . Write an expression for the linear mass density as a function of position along the string [16].

**Table 3.8** The position of the nodes of the tenth mode of a fixed-fixed string with total length,  $L = 1.00$  m, is provided. For the uniform string, the nodes are equally spaced. For the nonuniform string, the spacing between the nodes decreases monotonically from the end at  $x = 0$  to the end at  $x = L$

	Uniform (m)	Variable (m)
End	0	0
1	0.1	0.1315
2	0.2	0.2505
3	0.3	0.3607
4	0.4	0.4642
5	0.5	0.5625
6	0.6	0.6564
7	0.7	0.7467
8	0.8	0.8338
9	0.9	0.9181
End	1	1

- 9. Whirling string.** The tension in a string that is rotated at a constant angular frequency,  $\omega_a$ , is produced by the centripetal acceleration of the string's mass. For a string with a uniform linear mass density,  $\rho_L$ , the tension,  $T(x)$ , is given by the integral of the centripetal force from  $x$  to the end of the string at  $x = L$ .

$$T(x) = \int_x^L \rho_L \omega_a^2 x dx = \left( \frac{\rho_L \omega_a^2}{2} \right) (L^2 - x^2)$$

Use the parabolic trial function of Eq. (3.45) to approximate the lowest-frequency mode of the whirling string by Rayleigh's method. Compare your result to the pendulum frequency for a pendulum bob of mass,  $M = \rho_L L$ , on a massless string and an equivalent acceleration,  $g = \omega_a^2 L$ .

- 10. Mass-loaded string.** A mass,  $M = 0.20$  kg, is hung from a string that has a mass,  $m_s = 0.05$  kg, and length (measured from the fixed end to the center of mass of the end mass),  $L = 1.00$  m. Neglect the fact that the tension in the string is a function of position and approximate the tension as being constant,  $T = g(M + m_s/2)$ . Let the acceleration due to gravity be  $g = 9.8$  m/s<sup>2</sup>.
- (a) *Pendulum frequency.* Assuming  $m_s = 0$ , what is the pendulum frequency,  $f_o$ , for small oscillations of the terminal mass,  $M$ .
  - (b) *Transverse wave speed.* Assuming a constant tension,  $T = g(M + 1/2m_s)$ , what is the speed of transverse waves on the string?
  - (c) *Pendulum mode.* Determine the frequency of the mode which has only one node located at the fixed attachment point of the string.
  - (d) *(Nearly) Half-wavelength mode.* Determine the frequency of the mode which has one node located at the fixed attachment point of the string and one other node close to the mass.
  - (e) *Transverse displacements.* For the (nearly) half-wavelength mode, determine the ratio between the largest transverse displacement of the string and the transverse displacement of the terminal mass,  $M$ .
- 11. Stiffness-loaded string.** A string of length,  $L$ , is rigidly fixed at one end and terminated at the other end by a spring with spring constant,  $K_{sp}$ , so that  $F_y(L) = -K_{sp}y$ .
- (a) *Normal mode frequencies.* Write a transcendental equation similar to Eq. (3.68) for the mass-loaded string that can be solved for the normal mode frequencies of the stiffness-loaded string.
  - (b) *Stiff spring limit.* Show that your equation for the normal modes in part (a) reduces to those of a fixed-fixed string if  $K_{sp} = \infty$  and for those of a fixed-free string if  $K_{sp} = 0$ .
  - (c) *Normal mode frequencies.* Calculate the lowest three normal mode frequencies,  $f_n$ , where  $n = 1, 2$ , and  $3$ , in terms of the lowest-frequency "idealized" fixed-free normal mode frequency,  $f_{\text{fix-free}} = c/4L$ , if  $K_{sp} = T/L$ .

## References

1. G. Galilei, *Discorsi e dimostrazioni matematiche, intorno à due nuove scienze*, 1638; translated by H. Crew and A. de Salvi, *Dialogs Concerning Two New Sciences* (McMillan, 1914), reprinted (Dover, 1954); ISBN 486-60099-8.
2. H.L.F. von Helmholtz, *On the Sensations of Tone as a Philosophical Basis for the Theory of Music* (Longmans, 1885), reprinted (Dover, 1954); ISBN 0-486-60753-4.
3. R. Plomp, W.J.M. Levelt, Tonal consonance and critical bandwidth. J. Acoust. Soc. Am. **38**, 548–560 (1965)
4. A more complete discussion of scales, as well as other topics related to musical acoustics, is available in T. D. Rossing, *The Science of Sound* (Addison-Wesley, 1982); ISBN 0-201-06505-3.
5. M.J. Kepler, *De Fundamentis Astrologiae Certioribus* [On the more Certain Fundamentals of Astrology or On Giving Astrology Sounder Foundations], 1601

6. H. Lamb, *The Dynamical Theory of Sound* (E. Arnold, London, 1931), pg. 87. Reprinted (Dover, 1960).
7. J.W. Strutt (Lord Rayleigh), *The Theory of Sound*, 2nd ed. (Macmillan, 1894), Vol. I, pg. 112; reprinted by Dover, 1945; ISBN 486-60292-3
8. D. Bernoulli, 1732.
9. L. Cremer, *The Physics of the Violin*, translated by J. S. Allen (MIT Press, 1984); ISBN 0-262-03102-7.
10. I.S. Gradshteyn, I.M. Ryzhik, *Tables of Integrals, Series, and Products* (Academic, 1980); ISBN 0-12-294760-6.
11. G. Penelet, S. Garrett, Periodic self-modulation of an electrodynamically-driven heated wire near resonance. *J. Acoust. Soc. Am.* **145**(2), 998–1017 (2019)
12. E. Mitchell, *Development of a thermoacoustic refrigerator inline model to assist in design*, Master of Science in Acoustics, Penn State (Dec 2012).
13. A. Migliori and J.L. Sarrao, *Resonant Ultrasound Spectroscopy* (Wiley, 1997); ISBN 978-0471123606.
14. M. Mersenne, *Traité de l'harmonie universelle; où est contenu la musique théorique & pratique des anciens & modernes, avec les causes de ses effets* (Guillaume Baudry, Paris, 1627). For a complete discussion of Mersenne's contributions see F. V. Hunt, *Origins in Acoustics* (Yale, 1978); ISBN 0-300-02220-4, reprinted (Acoust. Soc. Am., 1992).
15. J.W. Strutt (Lord Rayleigh), *The Theory of Sound*, 2nd ed. (Macmillian, 1894), Vol. I, pg. 182; reprinted (Dover, 1945); ISBN 486-60292-3.
16. J.R. McLaughlin, Inverse spectral theory using nodal points as data - a uniqueness result. *J. Differ. Equ.* **73**, 354–363 (1988). Good vibrations, *Am. Sci.* 86, 342–349 (1998)

**Open Access** This chapter is licensed under the terms of the Creative Commons Attribution 4.0 International License (<http://creativecommons.org/licenses/by/4.0/>), which permits use, sharing, adaptation, distribution and reproduction in any medium or format, as long as you give appropriate credit to the original author(s) and the source, provide a link to the Creative Commons license and indicate if changes were made.

The images or other third party material in this chapter are included in the chapter's Creative Commons license, unless indicated otherwise in a credit line to the material. If material is not included in the chapter's Creative Commons license and your intended use is not permitted by statutory regulation or exceeds the permitted use, you will need to obtain permission directly from the copyright holder.





# Elasticity of Solids

4

## Contents

4.1	<b>Hooke, Young, Poisson, and Fourier</b> .....	180
4.2	<b>Isotropic Elasticity</b> .....	181
4.2.1	Bulk Modulus .....	182
4.2.2	Modulus of Unilateral Compression .....	183
4.2.3	Shear Modulus .....	185
4.2.4	Two Moduli Provide a Complete (Isotropic) Description .....	187
4.3	<b>Real Springs</b> .....	187
4.3.1	Solids as Springs .....	188
4.3.2	Flexure Springs .....	193
4.3.3	Triangularly Tapered Cantilever Spring* .....	198
4.3.4	Buckling .....	200
4.3.5	Torsional Springs .....	202
4.3.6	Coil Springs .....	203
4.4	<b>Viscoelasticity</b> .....	206
4.4.1	The Maxwell (Relaxation Time) Model .....	207
4.4.2	Standard Linear Model (SLM) of Viscoelasticity .....	210
4.4.3	Complex Stiffnesses and Moduli* .....	211
4.4.4	Kramers-Kronig Relations .....	213
4.5	<b>Rubber Springs</b> .....	216
4.5.1	Effective Modulus .....	217
4.5.2	Rubber-to-Glass Transition (Type I and Type II Rubbers) .....	218
4.5.3	Transmissibility of Rubberlike Vibration Isolators .....	220
4.6	<b>Anisotropic (Crystalline) Elasticity*</b> .....	225
4.7	<b>There Is More to Stiffness Than Just “K”</b> .....	227
	<b>References</b> .....	232

If we take a piece of solid matter that is initially at rest and apply equal and opposing forces to the sample, Newton's Second Law of Motion guarantees that the sample will remain at rest because the net force on the sample is zero. If the sample is an elastic solid, then those forces will cause the solid to deform by an amount that is directly proportional to the applied forces. When the forces are removed,

the sample will return to its original shape and size. These are the characteristics that are required if we say the behavior of the solid is “elastic.”

Most solids will behave elastically if the forces and their resulting deformations are sufficiently small. If the forces are larger, it is possible to fracture the solid or to cause it to yield so that it does not return to its original shape after the forces are removed. Most metals will fracture if the forces that are applied to them cause deformations that change the length relative to the original length by a few percent. Glass will fracture at less than 1% change in relative length, and rubber can behave elastically for relative deformations that exceed 100%. Different solid materials exhibit a very wide range of behaviors, but most exhibit elastic behavior over some range of deformations.

This chapter will quantify the elastic behavior of solids by introducing the concepts of stress and strain and expressing their linear relationship through the definition of elastic moduli that depend only upon the material and not the shape of the sample. Those concepts will allow us to generalize Hooke’s law. As before, the combination of a linear equation of state, like Hooke’s law, with Newton’s Second Law of Motion, will allow us to describe the wave motion in solids in the next chapter. Further insight will be gained by analyzing vibrational modes of bars, both through the understanding of those modes and by the measurement of those modal frequencies to accurately determine the elastic moduli of the materials.

## 4.1 Hooke, Young, Poisson, and Fourier

We begin our investigation into the elasticity of solids by considering the rectangular block of material shown in Fig. 4.1. Since the material is elastic, the force is proportional to the extension,  $F \propto \Delta l$ ; this is the relationship we have called Hooke’s law in previous chapters. If two such pieces are joined end to end to create a piece twice as long, but with the same cross-sectional area,  $S = wh$ , then the same force would create twice the extension,  $2\Delta l$ . We have analyzed this behavior before with springs joined in series, as shown in Fig. 2.3 (right), and also observed twice the extension for the same force. We can therefore write the proportionality of Hooke’s law to exploit this dimensionless measure of deformation as  $F \propto (\Delta l/l)$ . That dimensionless ratio is the *strain* and it is commonly represented by  $\epsilon$ .

Following our analysis of springs in Chap. 2, we can also combine the two solid blocks in parallel so that the overall length of the combination is still  $l$  but the cross-sectional area is doubled. To create the same stretch,  $\Delta l$ , the force would have to be doubled. We can combine the dependence on length,  $l$ , and on cross-sectional area,  $S$ , into a single expression, which is a generalization of Hooke’s law, that introduces a new constant,  $E$ , called *Young’s modulus*. Young’s modulus depends only on the material used to make the block (and its temperature). We will ignore the small difference between the adiabatic

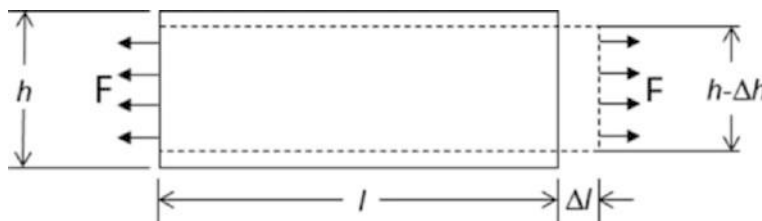


**Fig. 4.1** In the absence of any applied forces, the volume of this rectangular bar is  $V = lhw$ . The bar is shown being stretched by equal and opposite forces,  $F$ , applied to the ends having cross-sectional area,  $S = wh$ . The bar responds elastically to the applied force by increasing its length an amount,  $\Delta l$ . In this two-dimensional representation, we see that the height of the bar is reduced by  $\Delta h$ . The width is also reduced by an amount,  $\Delta w$ .

and isothermal moduli [1].<sup>1</sup> The ratio of the force,  $F$ , to the area,  $S$ , over which it is applied,  $\sigma = F/S$ , is called the *stress* and has the units of pressure [Pa].

$$\sigma = \frac{F}{S} = E \frac{\Delta l}{l} = E\varepsilon \quad (4.1)$$

We read Eq. (4.1) as “stress is proportional to strain.” In this case, the constant of proportionality is Young’s modulus,  $E$ . Our introduction of this dimensional constant, which is a property of the material, preserves dimensional homogeneity in a way that would please Mr. Fourier (see Sect. 1.6). Since strain,  $\varepsilon$ , is dimensionless, the units of Young’s modulus are also pressure [Pa].

In Fig. 4.1, we see that in addition to the elongation of  $l$ , the height,  $h$ , of the rectangle is simultaneously reduced, as is the width,  $w$  (not shown). We can introduce another constant to relate the lateral contraction to the longitudinal extension.

$$\frac{\Delta h}{h} = \frac{\Delta w}{w} = -\nu \frac{\Delta l}{l} \quad (4.2)$$

That constant of proportionality,  $\nu$ , is called *Poisson’s ratio*<sup>2</sup> and is clearly dimensionless.

If the volume of the sample is conserved, when it is strained along its length, as shown in Fig. 4.1, then logarithmic differentiation (see Sect. 1.1.3) can be used to determine the volume-conserving value of Poisson’s ratio.

$$\frac{\Delta V}{V} = \frac{\Delta l}{l} + \frac{\Delta h}{h} + \frac{\Delta w}{w} = (1 - 2\nu) \frac{\Delta l}{l} = 0 \Rightarrow \nu = \frac{1}{2} \quad \text{if } \Delta V = 0 \quad (4.3)$$

The deformation of rubber is nearly volume conserving (see Sect. 4.5.1), so its value of Poisson’s ratio is very close to  $\frac{1}{2}$ , but for most common solid construction materials, like metals and plastics,  $\frac{1}{3} \gtrsim \nu \gtrsim \frac{1}{4}$ . Poisson’s ratio for cork is nearly zero. This makes it a convenient material for sealing wine bottles since it does not expand as force is being applied to push the cork into the neck of a bottle. As we continue our investigation of elasticity, we will determine the fundamental limits on the values of Poisson’s ratio that are imposed by material stability and energy conservation.

## 4.2 Isotropic Elasticity

If the elastic material is homogeneous and isotropic, its elastic behavior is completely specified by  $E$  and  $\nu$ . Our introduction of  $E$  and  $\nu$  was convenient, since our sample had a rectangular shape and was unconstrained along the sides and the forces were normal to the ends where they were applied. The choice of  $E$  and  $\nu$  is not our only option for the two independent constants required to specify the elastic behavior of an isotropic solid. As we are about to demonstrate by the use of the principle of

<sup>1</sup> For gases, this is an important distinction (e.g., the adiabatic bulk modulus of air is 40% larger than the isothermal bulk modulus). The difference between the adiabatic and isothermal Young’s modulus can be expressed in terms of the material’s absolute (kelvin) temperature,  $T$ ; the (volumetric) coefficient of thermal expansion,  $\alpha = (1/V)(\partial V/\partial T)_p$ ; mass density,  $\rho$ ; and specific heat (per unit mass) at constant pressure,  $c_p$ .

$$E_{ad} = \frac{E_{iso}}{1 - E_{iso} T \alpha^2 / 9 \rho c_p}$$

In most solids, this is a small effect. At room temperature,  $E_{iso} T \alpha^2 / 9 \rho c_p$  is about 0.44% for aluminum and 340 ppm for copper.

<sup>2</sup> Simeon Denis Poisson (1781–1840).

superposition (see Sect. 1.4), we can relate  $E$  and  $\nu$  to other moduli that are convenient for the specification of an isotropic material's response to different combinations of stresses.

### 4.2.1 Bulk Modulus

We can use Young's modulus,  $E$ , and Poisson's ratio,  $\nu$ , to calculate the deformation of a solid that is subject to a hydrostatic compression. If we imagine our solid being submerged in a fluid, as the fluid pressure increases, the volume of the solid will decrease, but its shape will remain the same. Pascal's law guarantees that the hydrostatic pressure will be the same on all faces if the sample is at rest and the size of the sample is small enough that any gradients in the gravitational field can be ignored. This situation is shown schematically in Fig. 4.2. We can combine Pascal's law with the principle of superposition to calculate the change in length of any side and combine those changes using Eq. (4.3) to compute the relative change in volume of the sample,  $\Delta V/V$ .

We start by calculating the change in length,  $\Delta l_l$ , due to the force,  $F_l$ , on the ends normal to the  $l$ -direction. The pressure,  $P$ , provides the stress,  $\sigma = P$ .

$$\frac{\Delta l_l}{l} = -\frac{\sigma}{E} \quad (4.4)$$

The minus sign reminds us that the increased pressure decreases the length of the sample. At the same time, the pressure,  $P$ , should produce the same strain in the height,  $(\Delta h_h/h) = -(\sigma/E)$ . Poisson's ratio determines the influence this change in height will have on the change in length.

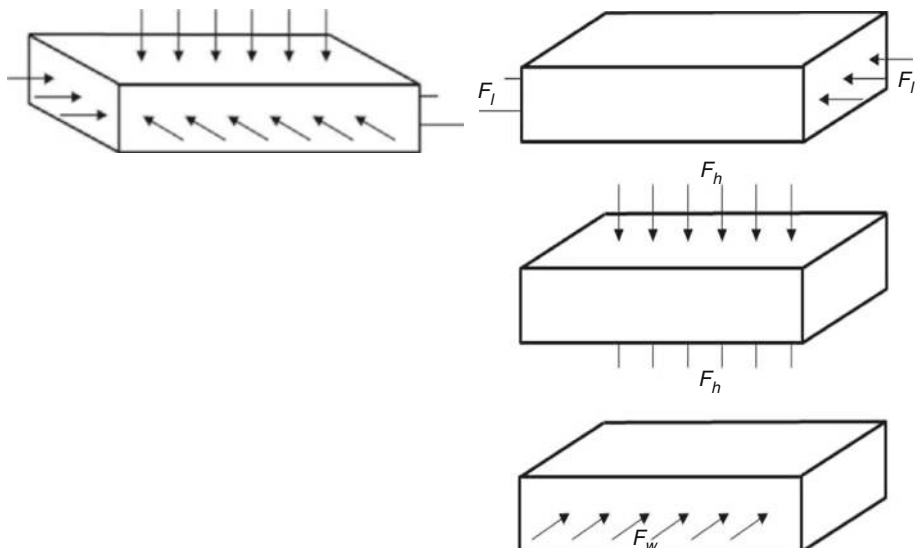


**Fig. 4.2** The deformation of a rectangular object subject to hydrostatic pressure (above) can be analyzed by the superposition of the pressures applied to the orthogonal faces shown at the right. Assuming unit area for all forces, the pressure applied along the  $l$ -direction is  $F_l$ . It causes  $l$  to become shorter while  $h$  and  $w$  become longer, as dictated by Poisson's ratio. At the same time,  $F_h$  reduces  $h$  and increases  $l$  and  $w$ , and  $F_w$  decreases  $w$  and increases  $l$  and  $h$ . The overall change in volume can be calculated by the superposition of the three individual deformations

$$\frac{\Delta l_h}{l} = -\nu \frac{\Delta h_h}{h} = \nu \frac{\sigma}{E} \quad (4.5)$$

Since both the pressure and the material are isotropic, there is an equal change in length,  $\Delta l_w/l$ , caused by  $\Delta w/w$  and Poisson's ratio,  $\nu$ . The total strain in length,  $\Delta l/l$ , must be the sum (i.e., superposition) of these three contributions.

$$\frac{\Delta l}{l} = \frac{\Delta l_l}{l} + \frac{\Delta l_h}{l} + \frac{\Delta l_w}{l} = -\frac{\sigma}{E}(1 - 2\nu) \quad (4.6)$$

This result now allows us to relate the *volumetric strain*,  $\Delta V/V$ , to the hydrostatic pressure,  $P = \sigma$ , again using logarithmic differentiation, as in Eq. (4.3), and recognizing that the strain along all three of the sample's axes must be the same.

$$\frac{\Delta V}{V} = \frac{\Delta l}{l} + \frac{\Delta h}{h} + \frac{\Delta w}{w} = -3(1 - 2\nu) \frac{\sigma}{E} \quad (4.7)$$

We can now define a third elastic modulus, known as the *bulk modulus*,  $B$ , to relate changes in hydrostatic pressure to volumetric strain.

$$P = \sigma = -B \frac{\Delta V}{V} = -\frac{E}{3(1 - 2\nu)} \frac{\Delta V}{V} \quad (4.8)$$

In addition to providing the relationship between the bulk modulus, Young's modulus, and Poisson's ratio, Eq. (4.8) restricts Poisson's ratio to being less than one-half. To guarantee the stability of matter, the bulk modulus can never be negative. If the bulk modulus were negative, then the application of a small amount of pressure would cause the volume of the material to increase rather than decrease. The product of that change in pressure and the change in volume would do work on the surroundings. This would allow us to get useful work out of any material with  $B < 0$  and would violate energy conservation. Similarly, if the solid were immersed in a fixed volume of liquid and the pressure of the liquid decreased (due to a change in temperature?), then the solid would become smaller, decreasing the fluid pressure further, and ultimately the solid would disappear [2].

### 4.2.2 Modulus of Unilateral Compression

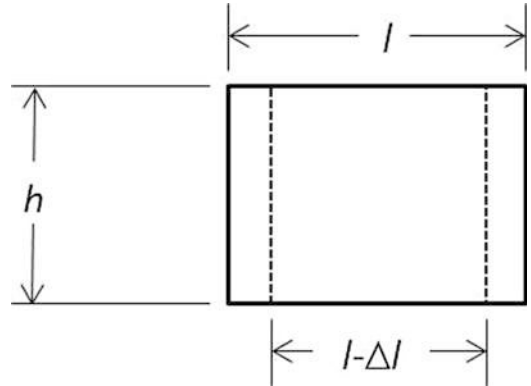
The same use of superposition that allowed us to relate the bulk modulus, Young's modulus, and Poisson's ratio can be exploited again to calculate the *modulus of unilateral compression*, sometimes also known as the *dilatational modulus*. We will use  $D$  to designate this modulus. The modulus of unilateral compression is similar to Young's modulus except that the cross-section is not allowed to change, that is,  $\Delta h_l/h = \Delta w_l/w = 0$ , when  $\Delta l_l/l \neq 0$ . An example of a deformation due to a unilateral compression is shown in Fig. 4.3. This combination of pressure and strain is important for the propagation of plane longitudinal waves in solids.<sup>3</sup>

We would expect the modulus of unilateral compression to be greater than Young's modulus, since it should be more difficult to compress a sample if the walls are not permitted to bulge out. As before, we will superimpose three contributions to the strain in the length.

---

<sup>3</sup> If the diameter of a sound beam is much greater than its wavelength, the associated compressions and expansions do not allow the material to "squeeze out" because there is a compression both above and below that is trying equally hard to squeeze the material in the transverse direction.

**Fig. 4.3** A plane wave of sound in a solid will cause a square element of the solid to be deformed into a rectangle. The height (and also width) of the element remains constant, while the length is changed. The undeformed element is shown as a *solid line*, and the unilaterally compressed element is shown by the *dashed lines*



$$\frac{\Delta l_l}{l} = \frac{1}{E} \frac{F_l}{S_l} - \frac{\nu}{E} \frac{F_h}{S_h} - \frac{\nu}{E} \frac{F_w}{S_w} = \frac{1}{E} \left[ \frac{F_l}{S_l} - \nu \left( \frac{F_h}{S_h} + \frac{F_w}{S_w} \right) \right] \quad (4.9)$$

$$\frac{\Delta l_h}{h} = \frac{1}{E} \left[ \frac{F_h}{S_h} - \nu \left( \frac{F_l}{S_l} + \frac{F_w}{S_w} \right) \right] \quad (4.10)$$

$$\frac{\Delta l_w}{w} = \frac{1}{E} \left[ \frac{F_w}{S_w} - \nu \left( \frac{F_l}{S_l} + \frac{F_h}{S_h} \right) \right] \quad (4.11)$$

Imposition of the constraint that  $\Delta h/h = \Delta w/w = 0$  dictates the required stress needed to keep the cross-section constant. Those stresses can be determined by simultaneous solution of Eqs. (4.10) and (4.11).

$$\frac{F_h}{S_h} = \frac{F_w}{S_w} = \frac{\nu}{1-\nu} \frac{F_l}{S_l} = \left( \frac{\nu}{1-\nu} \right) \sigma \quad (4.12)$$

Substitution of this result back into Eq. (4.9) relates the strain in  $l$  to the stress in the direction normal to  $l$ .

$$\frac{\Delta l_l}{l} = \frac{1}{E} \left( 1 - \frac{2\nu^2}{1-\nu} \right) \frac{F_l}{S_l} = \left( \frac{(1+\nu)(1-2\nu)}{1-\nu} \right) \frac{\sigma}{E} \quad (4.13)$$

By inverting this expression, we can write the modulus of unilateral compression,  $D$ , in terms of Young's modulus and Poisson's ratio.

$$\sigma = D \frac{\Delta l}{l} = \frac{(1-\nu)}{(1+\nu)(1-2\nu)} E \frac{\Delta l}{l} \quad (4.14)$$

Figure 4.4 shows that  $D/E > 1$ , if  $\nu > 0$ , as expected, since the sample is “stiffened” if the cross-section is constrained to remain unchanged.

The appearance of  $(1 + \nu)$  in the denominator of Eq. (4.14) implies that if Poisson's ratio is negative, it cannot be more negative than  $-1$  without violating the stability requirement, so  $-1 < \nu \leq \frac{1}{2}$ .

**Fig. 4.4** The modulus of unilateral compression,  $D$  (also known as the dilatational modulus), is always greater than Young's modulus,  $E$ , if Poisson's ratio,  $\nu$ , is greater than zero. The ratio,  $D/E$ , is plotted for  $0 < \nu < \frac{1}{2}$

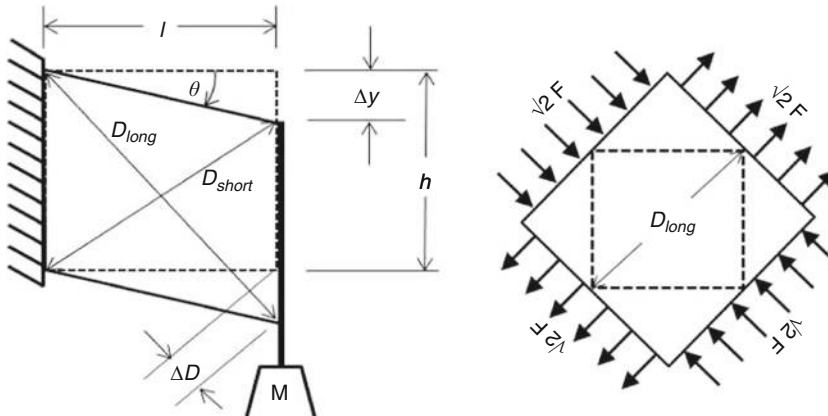
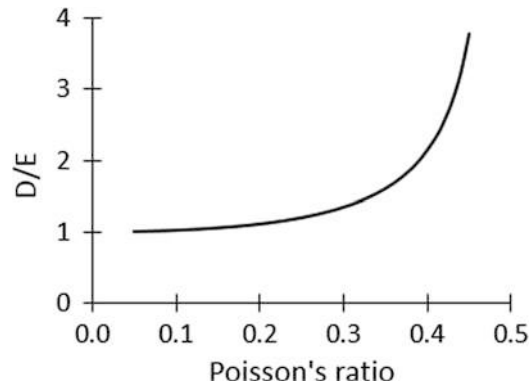


**Fig. 4.5** (Left) A cube of initially square cross-section,  $l = h = w$ , is rigidly attached along one face and is loaded by a shear force,  $F = Mg$ , on the opposite face. This shear stress causes the square to deform into a rhombus with no changes to the cube's width,  $\Delta w = 0$ . The area is conserved by the shearing, but the shape has changed. The two diagonals that were initially of equal length are now unequal. (Right)  $D_{long}$  has been rotated by  $90^\circ$  in this figure. The same deformation can be achieved by applying a force  $F' = F\sqrt{2}$  to a cube with sides  $l' = h' = l\sqrt{2}$  that circumscribes the original cube and is rotated by  $45^\circ$ . The normal force compresses the larger square along two parallel faces and expands it when applied in the opposite direction along the orthogonal faces

### 4.2.3 Shear Modulus

A hydrostatic compression changes the volume of a sample but not its shape. A shear deformation, shown in Fig. 4.5, changes the shape of a sample but not its volume. Figure 4.5 shows one face of an initially cubical sample,  $l = h$ , which is rigidly supported along its left face and has a shearing force,  $F = Mg$ , applied along the opposite face by a suspended mass,  $M$ . The resulting shear strain will deform the square into a rhombus. Since  $h$  has not changed, the areas of the square and rhombus are equal, as are the volumes of their corresponding solids, the cube and rectangular parallelepiped (sometimes referred to as a rhomboid).

We can again use superposition to express the shear modulus in terms of Young's modulus and Poisson's ratio. This process is simplified if we examine Fig. 4.5 and realize that the shear deformation

has taken the two diagonals of the square, which were originally of equal length, and made one diagonal shorter and the other longer,  $D_{long} > D_{short}$ . The cube is represented in Fig. 4.5 by a two-dimensional cross-section that ignores the width,  $w$ , since it is not changed by the shearing. The compression and expansion of the two diagonals can be reproduced if the original square is circumscribed by a larger square that is rotated by  $45^\circ$  with respect to the original. The larger square has edge lengths,  $l' = h' = l\sqrt{2}$ .

If we apply compressive forces,  $F' = F\sqrt{2}$ , to parallel faces, then the applied stress would be unchanged, since the surface area of the larger cube is  $\sqrt{2}$  greater than that of the original cube. Those compressive forces will make one of the diagonals shorter. Similarly, if an equal tensile stress is applied to the cube's orthogonal faces, then the other diagonal is lengthened. The net forces and the net torque are zero, so the cube remains at rest during deformation. Also, we see that a pure shear is equivalent to the superposition of equal compressive and tensile stresses applied at right angles to each other and at  $45^\circ$  to the original faces of the cube.

We again superimpose the two orthogonal stresses to calculate the change in the length and the height of the deformed cube.

$$\frac{\Delta l'}{l'} = \frac{\Delta D_{long}}{D} = -\frac{\Delta h'}{h'} = -\frac{\Delta D_{short}}{D} = \frac{1}{E} \frac{F}{S} + \nu \frac{1}{E} \frac{F}{S} = \left(\frac{1+\nu}{E}\right) \frac{F}{S} \quad (4.15)$$

In Fig. 4.5, the strain is a dimensionless quantity, as is the angle,  $\theta$ , by which the cube is sheared. (Keep in mind that in these calculations,  $D$  is the unstrained diagonal, not the modulus of unilateral compression.)

$$\tan \theta \cong \theta = \frac{\Delta y}{l} = \sqrt{2} \frac{\Delta D}{l} = 2 \frac{\Delta D}{D} = 2 \left(\frac{1+\nu}{E}\right) \quad (4.16)$$

The far-right term takes advantage of the fact that we are assuming linear elastic behavior, so  $\Delta y \ll l$ . Inverting this result leads to the definition of the shear modulus,  $G$ , that again allows us to assert Hooke's law as "stress is proportional to strain," this time for shearing stresses.

$$\sigma_{yx} = \frac{F_y}{S_x} = G\theta = \frac{E}{2(1+\nu)} \theta \quad (4.17)$$

In this version of Hooke's law, a new nomenclature has been introduced that is convenient for the description of stress.  $\sigma_{yx}$  represents a force,  $F_y$ , that is applied in the  $y$  direction on a surface of area,  $S_x$ , which has its normal in the  $x$  direction. In this notation, the normal hydrostatic stresses would be  $\sigma_{xx} = \sigma_{yy} = \sigma_{zz} = P$  and  $\sigma_{xy} = \sigma_{yz} = \sigma_{zx} = 0$ , since fluids cannot sustain static shearing forces.<sup>4</sup>

Again, for stability, we must insist that  $G > 0$ , so  $\nu > -1$ . Combined with the similar restriction imposed by the bulk modulus, the values of Poisson's ratio are therefore restricted:  $-1 < \nu < \frac{1}{2}$ . Most materials have Poisson's ratios that are between zero (e.g., cork) and  $\frac{1}{2}$  (e.g., rubber). *Auxetic materials*, which have negative values of Poisson's ratio, are uncommon. Love reported  $\nu = -0.14$  for single-crystal pyrite [3]. Most auxetic materials are anisotropic, have very low mass densities, and usually involve some complicated internal structure, like solid foams. A Poisson's ratio as small as  $\nu = -0.7$  has been reported for solid foam with a tetrakaidecahedral (14-sided) unit cell [4].

<sup>4</sup> In fluids, shearing forces diffuse; they are not restored elastically. See Sect. 9.4.

**Table 4.1** For any isotropic solid, two elastic constants are sufficient to completely specify the solid's elastic behavior. Given any two known elastic moduli, listed in the left-hand column, equations are provided for the calculation of the other three isotropic elastic moduli

Given	Young's ( $E$ )	Poisson's ( $\nu$ )	Bulk ( $B$ )	Dilatational ( $D$ )	Shear ( $G$ )
$E, \nu$	$E$	$\nu$	$\frac{E}{3(1-2\nu)}$	$\frac{(1-\nu)E}{(1+\nu)(1-2\nu)}$	$\frac{E}{2(1+\nu)}$
$B, E$	$E$	$\frac{1}{2} - \frac{E}{6B}$	$B$	$\frac{3B+E}{9B-E}$	$\frac{3BE}{9B-E}$
$B, \nu$	$3B(1-2\nu)$	$\nu$	$B$	$\frac{3B(1-\nu)}{1+\nu}$	$\frac{3B(1-2\nu)}{2(1+\nu)}$
$G, E$	$E$	$\frac{E}{2G} - 1$	$\frac{EG}{3(3G-E)}$	$G \frac{(4G-E)}{(3G-E)}$	$G$
$G, B$	$\frac{9BG}{3B+G}$	$\frac{3B-2G}{6B+2G}$	$B$	$B + \frac{4G}{3}$	$G$
$G, \nu$	$2G(1+\nu)$	$\nu$	$\frac{2G(1+\nu)}{3(1-2\nu)}$	$\frac{2G(1-\nu)}{1-2\nu}$	$G$

#### 4.2.4 Two Moduli Provide a Complete (Isotropic) Description

If a solid is isotropic and homogeneous, then two moduli provide a complete description of the solid's elastic behavior. The results of the calculations that relate Young's modulus, Poisson's ratio, the bulk modulus, the modulus of unilateral compression (or dilatational modulus), and the shear modulus are summarized in Table 4.1.<sup>5</sup>

---

### 4.3 Real Springs

In Chap. 2, we defined a spring constant that provided a parameter,  $K$ , to relate forces and displacements governed by Hooke's law. That definition allowed us to explore the behavior of simple harmonic oscillators consisting of masses, springs, and dashpots. Having developed a system for understanding the elastic behavior of solids, we can now explore a small amount of the vast territory that is dedicated to the design of a highly engineered product that has a very significant impact on the design or isolation of vibrating systems – the spring.

Real springs are much more complicated than Hooke's law may lead one to believe. Our analysis of the simple harmonic oscillator, in Chap. 2, represented the spring through a single parameter, the spring stiffness,  $K$ , which concealed the multiple design trade-offs that must be made to approach optimum performance for any spring. In addition to stiffness, attention must also be paid to the spring's moving mass; to limitations on the tensile stresses that might cause the material to yield or fracture, thus exceeding the elastic limit (see Fig. 1.4); or to application of compressive stresses that would cause buckling (see Sect. 4.3.4), as well as issues related to fatigue life in a material that is subjected to fully reversing cyclic loading for millions or billions of cycles [5].

In this section, we will explore only a few strategies for shaping materials in ways that make them suitable for applications where they are intended to store (and in some cases, absorb) elastic energy using the spring materials efficiently. We will start with simple use of the bulk material to provide stiffness, but then look at how shapes such as cantilevered beams, tubes in torsion, and helical coils

---

<sup>5</sup> The Lamé constants,  $\lambda$  and  $\mu$ , also are taken as the two isotropic moduli in some elasticity calculations, although they are not listed in Table 4.1. The shear modulus,  $G$ , and  $\mu$  are identical and  $\lambda = \frac{E\nu}{(1+\nu)(1-2\nu)} = \frac{G(E-2G)}{3G-E} = \frac{2G\nu}{1-2\nu}$ .

produce acceptable and convenient trade-offs in a few applications and how rubberlike materials are used as springs for vibration isolation where they simultaneously provide both elasticity and damping.

### 4.3.1 Solids as Springs

Although the majority of spring applications require forming and shaping of the elastic material, as well as surface treatments (e.g., shot peening, tumble deburring) and heat treatments (e.g., precipitation hardening, quick quenching) [6], there are a few circumstances where the material is used “in bulk,” as a block, rod, or tube to provide compressional or shear stiffness. This is most common with rubber springs used as vibration isolators. We will postpone discussion of rubber springs until later in this chapter because the viscoelastic behavior of those elastomeric materials can simultaneously contribute damping as well as stiffness. Here we will examine two piezoelectric accelerometer designs and a resonant piezoelectric underwater sound source that use the elasticity of the bulk materials to provide stiffness.<sup>6</sup>

An accelerometer is a vibration measurement sensor that converts mechanical accelerations into an electrical signal that can be displayed and/or recorded by some electronic measurement instrument. The base of an accelerometer is usually attached to some vibrating structure using a threaded stud, a magnet, an adhesive or wax, etc., that attempts to ensure that the motions of the sensor and of the vibrating structure are identical. As we have seen from our study of the displacement-driven simple harmonic oscillators in Sect. 2.5.6, if the driving frequency,  $\omega$ , is less than the natural frequency,  $\omega < \omega_o = \sqrt{K/m}$ , then the displacement of the spring is directly proportional to the force produced by the acceleration,  $a$ , of the mass,  $m$ :  $xe^{j\omega t} = -mae^{j\omega t}/K$ .

Figure 4.6 shows cross-sectional diagrams of two types of piezoelectric accelerometers. We start by calculating the stiffness of the version (Fig. 4.6, right) that compresses a *test mass* (sometimes also called a *seismic mass* or a *proof mass*) against a hollow cylinder made of a *ferroelectric ceramic* material<sup>7</sup> using a steel “preload stud.” Since ceramic materials are much stronger in compression than under tension, static compression provided by the preload stud guarantees that the piezoelectric spring never goes into tension, as well as holding the mass-spring “sandwich” together. The total stiffness of the cylinder and stud will be the sum of their stiffnesses:  $K_{total} = K_{stud} + K_{piezo}$ .

If we treat the pre-load stud as a thin rod, then its stiffness,  $K_{stud}$ , will be related to its geometry and Young’s modulus of the material that is used to make the stud. We will let the length of the stud (between the mass and the base) be  $l$ , let its diameter be  $D_{stud}$ , and assume the stud is made of some generic steel. The stiffness of the piezoelectric tube will depend upon its Young’s modulus and its inner and outer radii,  $a_{in}$  and  $a_{out}$ . Its elastically active length,  $l$ , is the same as the stud’s length. Using the appropriate cross-sectional areas, the stiffnesses are given by

<sup>6</sup>I will apologize for indulging in a bit of a fraud at this point by introducing piezoelectric solids. So far, we have addressed the elastic behavior of isotropic solids that require only two independent moduli to completely specify their elastic behavior. Piezoelectric solids are intrinsically anisotropic crystalline materials that not only require more than two elastic constants but also require specification of the electrical impedance that provides the load across their electrodes,  $Z_{load}$ . For example, a piezoelectric material’s stiffness will be different if the electrodes are electrically shorted together (i.e.,  $Z_{load} = 0$ ) or left as an “open circuit” (i.e.,  $Z_{load} = \infty$ ). Anisotropic elasticity will be addressed later in this chapter (see Sect. 4.6), but for more complex crystalline substances, there are necessarily more than two independent elastic constants. In practice, once the relevant constants have been identified for a specific deformation, they are incorporated into Hooke’s law in the same way as the elastic constants of an isotropic solid.

<sup>7</sup>A ferroelectric ceramic behaves like a piezoelectric crystal. The difference is the piezoelectric behavior of the crystal is intrinsic, and a ferroelectric material (usually a ceramic or polymer) only exhibits piezoelectric behavior after the material has been “polarized,” usually by application of a large electric field at elevated temperatures [7].



**Fig. 4.6** (Left) Cross-sectional schematic diagram of an accelerometer that uses the shear stiffnesses of multiple piezoelectric elements (called “piezotronic” in this drawing) to both determine the natural frequency,  $\omega_o = (K/m)^{1/2}$ , of the mass-spring combination and to generate an electrical signal that can be used to display and/or record those accelerations (Center) Photograph of an accelerometer that uses three blocks of piezoelectric material in shear and three masses. All of the masses are joined by a retaining ring so that the sensor behaves as a single mass-spring oscillator. At the top center of the photograph, on the post supporting the three shear elastic elements, there is a small integrated electronic circuit that acts as an impedance transforming amplifier to electrically buffer the output of the piezoelectric elements. (Right) Cross-sectional schematic diagram of an accelerometer that uses a tubular piezoelectric cylinder as the spring to support a “test mass,” also known as the “seismic mass.” That spring is compressed and relieved by the forces produced by the accelerations of the supported (seismic) mass. In that design, the “preload stud” is a threaded rod that squeezes the mass and piezoelectric spring together so that the piezoelectric element never experiences tensile strains. (Figures courtesy of PCB Piezotronics, Inc.)

$$K_{stud} = \frac{E_{steel}(\frac{\pi}{4}D_{stud}^2)}{l} \quad \text{and} \quad K_{piezo} = \frac{\pi E_{piezo}(a_{out}^2 - a_{in}^2)}{l} \quad (4.18)$$

Let's assign some nominal values to those one dimensions and to the elastic moduli. For the stud, let  $D_{stud} = 2.0$  mm (about the correct value for a 4–40 machine screw) and let  $l = 6.0$  mm. Representative values for steel<sup>8</sup> are  $E_{steel} = 195$  GPa and  $\rho_{steel} = 7700$  kg/m<sup>3</sup>. We'll choose lead zirconium titanate (PZT) as our piezoelectric (ferroelectric) ceramic, with representative values of  $E_{PZT} = 50$  GPa and  $\rho_{PZT} = 7500$  kg/m<sup>3</sup>. The ceramic tube will have the same length as the stud with an outer radius  $a_{out} = 4.0$  mm and an inner radius  $a_{in} = 2.0$  mm. To be relatively consistent with the dimensions in Fig. 4.6, the test mass will be a steel cylinder with  $D_{mass} = 12.0$  mm and a height  $h = 4.0$  mm. Plugging these values into Eq. (4.18) makes  $K_{stud} = 1.02 \times 10^8$  N/m and  $K_{piezo} = 3.14 \times 10^8$  N/m for a total stiffness of  $K_{total} = 4.16 \times 10^8$  N/m.

For the test (seismic) mass,  $m_{test} = \rho_{steel} (\pi/4) D_{mass}^2 h = 3.5 \times 10^{-3}$  kg. Based on Eq. (2.27), we should add one-third of the mass of the springs to the test mass to approximate the dynamic mass,  $m_o$ .

$$m_o = m_{test} + \left( \frac{m_{PZT} + m_{stud}}{3} \right) = m_{test} + \frac{\pi}{12} [4\rho_{PZT}(a_{out}^2 - a_{in}^2)l + \rho_{steel}D_{stud}^2 l] \quad (4.19)$$

Using the same values for the dimensions and the mass densities,  $m_o = 4.10 \times 10^{-3}$  kg, so  $f_o = (\omega_o/2\pi) = \sqrt{K_{total}/m_o}/2\pi = 50.7$  kHz.

To demonstrate that these numbers are not unrealistic, Fig. 4.7 shows the calibration card for a typical accelerometer of this type that has been in use in my laboratory for decades. The relative

<sup>8</sup>It is important to remember that in a textbook example, it is convenient to define “some generic steel,” but properties of steel (e.g., modulus, yield strength, endurance limit, heat capacity, thermal conductivity, electrical conductivity, etc.) vary with alloy composition and temper. In a commercial design, the choice of the material is very important.

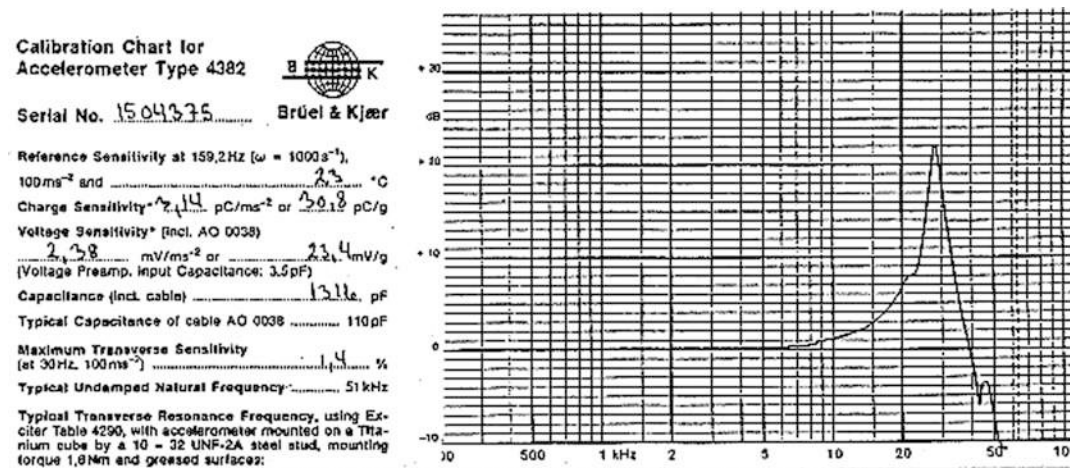


**Fig. 4.7** Calibration card for a Brüel and Kjær Type 4382 piezoelectric accelerometer. The graph provides the response relative to its low-frequency sensitivity, which is “flat” (i.e., frequency independent) to about 6 kHz. The mass-spring resonance frequency occurs just below 30 kHz

response (in dB) as a function of frequency shows a peak at just below 30 kHz. The response is constant with an increase of 1.0 dB in the sensitivity at 10 kHz but is “flat” (frequency independent) below that frequency where the sensor is operating well within its stiffness-controlled frequency regime,  $\omega < \omega_o$ .

Let’s repeat the analysis for the “shear mode” accelerometer shown in Fig. 4.6 (left and center). It consists of three flat quartz ( $\text{SiO}_2$ ) plates supported along their inside surfaces by a post attached to the accelerometer’s case and along their outside surfaces by three masses that are attached to each other by a retaining ring. As the case moves upward, the masses exert a downward shear force on the quartz plates in much the same way as the suspended mass exerts a static shear force on the sample diagrammed in Fig. 4.5 (left). We will use  $G_{\text{quartz}} = 2.23 \times 10^{10} \text{ Pa}$  as the shear modulus of quartz and  $\rho_{\text{quartz}} = 2650 \text{ kg/m}^3$ . We’ll let  $m_{\text{test}} = 5$  grams for the test mass (0.005 kg) and choose plausible dimensions for the quartz plates:  $l = 2.0 \text{ mm}$ ,  $h = 4.0 \text{ mm}$ , and  $w = 5.0 \text{ mm}$ . Using the appropriate cross-sectional areas, the stiffnesses are given by

$$K_{\text{quartz}} = -\frac{F_y}{\Delta y} = G_{\text{quartz}} \frac{wh}{l} \quad (4.20)$$

Remembering that the stiffnesses,  $K_{\text{quartz}}$ , of each of the three plates are additive,  $K_{\text{total}} = 3K_{\text{quartz}} = 6.7 \times 10^8 \text{ N/m}$ . The total mass for the three quartz plates is  $3m_{\text{quartz}} = 0.318$  gram, one-third of which is added to the test mass to make  $m_o = 5.11 \times 10^{-3} \text{ kg}$ . Again,  $f_o = (\omega_o/2\pi) = \sqrt{K_{\text{total}}/m_o}/2\pi = 57.6 \text{ kHz}$ .

The piezoelectric effect will produce an alternating electrical output based on the alternating stresses in the piezoelectric elements in either accelerometer design. This is not the time to belabor the differences between the two designs or their electrical transduction mechanisms, since these accelerometers were introduced primarily as vibration sensors and simple examples of the direct use of the elastic properties of solids to provide stiffness in real (i.e., useful) physical systems.

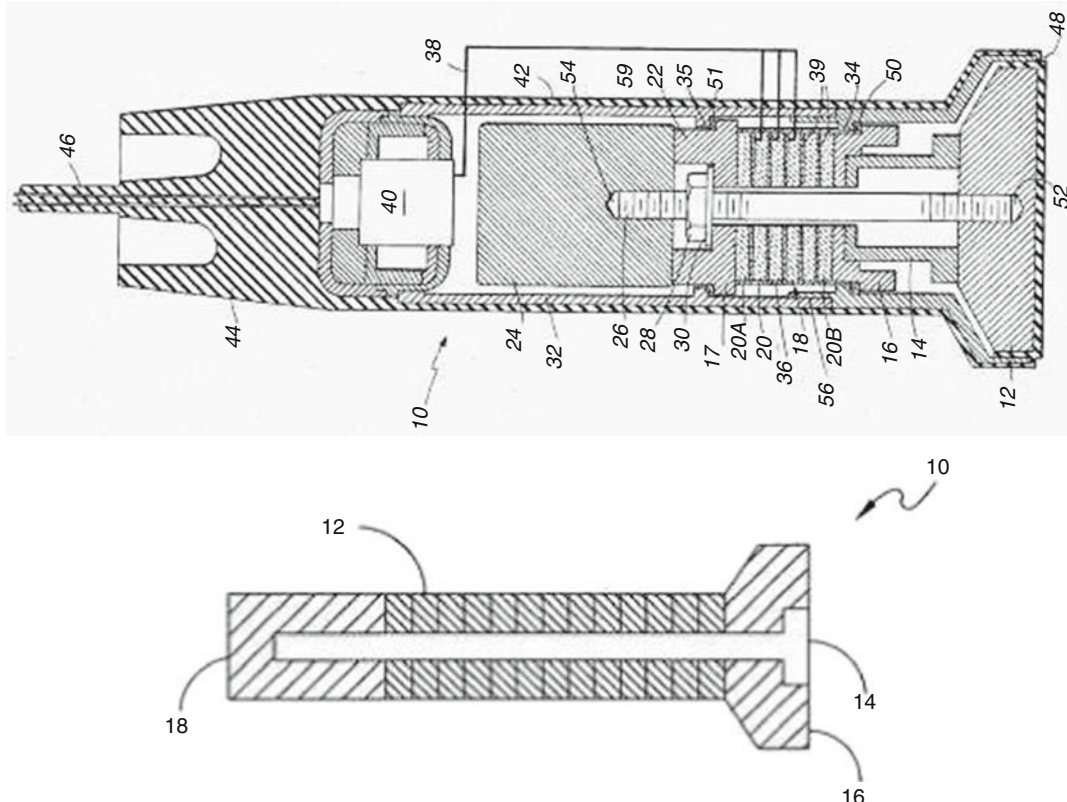


**Fig. 4.8** These cross-sectional diagrams represent a *Tonpilz* transducer [7]. (Above) This figure was taken from a patent [8] that shows many details of a projector intended for efficient production of sound under water. A tensioning rod (52) and nut (28) compress a stack of piezoelectric rings (20, 20A, 20B) between the radiating surface, known as the “head mass” (12), and a “tail mass” (24) that acts as an inertial counter balance. The mechanically active components (i.e., head mass, tail mass, and stack) are contained within the waterproof housing (44) and are resiliently supported (17 and 34) near a node in the oscillatory motion. That node occurs at a position within the piezoelectric stack. Other parts, such as an electrical impedance matching transformer (40), are not related to our calculations. (Below) A simplified cross-section (10) that focuses on only the critical vibrating components [9]: tail mass (18), head mass (16), tensioning rod (14), and the stack of piezoelectric elements (12) that provide both the stiffness and the “motor mechanism” to drive the simple harmonic oscillator at its resonance frequency in the asymmetric mode

Since the piezoelectric effect is both linear and reversible, it is also possible to drive the piezoelectric elements as “motors.” The next example is a *Tonpilz*<sup>9</sup> transducer that is common in naval SONAR systems and torpedo guidance systems [7].

Figure 4.8 shows a detailed drawing of such an underwater projector on the top [8] and a simplified cross-sectional diagram on the bottom [9]. We will further simplify our analysis by treating this transducer as two masses joined by a spring. As with the coupled harmonic oscillators in Sect. 2.7, this transducer is a one-dimensional oscillator that has two degrees of freedom corresponding to the positions of the head and tail masses. It will therefore possess two normal mode frequencies: a lower-frequency symmetric mode (both masses moving in-phase) and a higher-frequency antisymmetric mode. In this case, the symmetric mode corresponds to a uniform translation with both masses

<sup>9</sup> *Tonpilz* is from the German *ton* (tone) and *pilz* (mushroom). Apparently, the piezoelectric stack is the stem and the head mass is the “singing mushroom” cap.

moving at the same velocity in the direction joining their centers. The frequency of that mode is zero because there is no restoring force. Our interest is in the antisymmetric mode, where the head and tail masses move in opposite directions, thus compressing or expanding the spring that joins them.

The modal frequency for such a combination is well-known (see Sects. 2.7.1, 2.7.2, and 2.7.3) because it is analogous to the vibration of a diatomic molecule [10]. If the spring were massless, then the frequency of the antisymmetric mode is  $\omega_a = \sqrt{K/\mu}$ , where  $\mu = (m_1 m_2)/(m_1 + m_2)$  is known as the *reduced mass*.

This result is easy to visualize for  $m_1 = m_2$ . In that case, we know that the amplitude of the motions of both masses must be equal and opposite, so the midpoint of the spring will be a node. The normal mode frequency corresponds to all parts of the system oscillating at the same frequency. We can exploit that fact to calculate  $\omega_a$  by calculating the motion of one mass and one spring of twice the spring constant that has half the total length:  $\omega_a = \sqrt{2K/m_1} = \sqrt{K/\mu}$ . We will use the same approach to calculate the resonance frequency of our *Tonpilz* transducer that has different values for masses,  $m_1 \neq m_2$ , and a spring, being the piezoelectric stack and tensioning rod, which will also contribute non-negligible mass.

First, let's choose some reasonable values for the components in our *Tonpilz* example. Since the objective of this design is the generation of sound in water, we would like the tail mass to be larger than the head mass so that the motion of the end in contact with the water will be greater than the motion of the “counter weight” provided by the tail mass. As will be demonstrated in Sect. 12.8.3, a circular piston whose circumference is less than the wavelength of the radiated sound,  $2\pi a < \lambda_{\text{fluid}} = c_{\text{water}}/f$ , has to accelerate a mass of fluid,  $m_{\text{rad}}$ , that is equivalent to the mass of fluid contained in a cylindrical volume with the same area as the piston,  $\pi a^2$ , and a height,  $h = (8/3\pi)a$ . If we let the radius of the head mass be 5.0 cm, then the *radiation mass* is  $m_{\text{rad}} = (8/3) a^3 \rho_{\text{water}} = 0.333 \text{ kg}$ .

Since the design goal is to make the head mass as light as possible, the radiation mass places a natural limit on how a natural limit on how advantageous it might be to make the head mass small. For this example, let's make the head mass (including the radiation mass of the fluid) about twice the radiation mass,  $m_h = 0.70 \text{ kg}$ . The head mass should be as stiff as possible so that it acts as a piston and does not flex. That combination of lightness and stiffness can be improved by making the head mass “ribbed” to increase rigidity and reduce its moving mass. Such a “ribbed piston” is shown in Fig. 4.9. We will let the tail mass be five times the head mass,  $m_t = 5m_h = 3.5 \text{ kg}$ .

The spring's stiffness will again be provided by a stack of piezoelectric ceramic rings that are pre-compressed by the tensioning rod. Let the diameter of the tension rod be  $D_{\text{rod}} = 6.0 \text{ mm}$  and choose the outer and inner radii of the piezoelectric rings to be  $a_{\text{out}} = 2.0 \text{ cm}$  and  $a_{\text{in}} = 1.5 \text{ cm}$ . The length of the stack will be  $L = 15.0 \text{ cm}$ . Using the previous values of Young's modulus and mass

**Fig. 4.9** The “ribbed piston” shown here was designed by Dr. R. W. M. Smith and Eric Mitchell, in 2013, for a different application [11]. They fabricated the piston from a high-performance plastic. The ribs increase stiffness to resist flexure without requiring an excessive amount of material, hence reducing the piston's moving mass



density for steel and PZT, the stiffnesses and masses are as follows:  $K_{rod} = 3.67 \times 10^7$  N/m,  $K_{PZT} = 1.83 \times 10^8$  N/m and  $K_{total} = 2.20 \times 10^8$  N/m;  $m_{rod} = 32.7$  gm and  $m_{PZT} = 0.618$  kg, so  $m_s = 0.651$  kg.

Since the two masses are not equal, we will need to properly apportion the moving mass,  $m_s$ , and  $K_{total}$  of the PZT stack and steel rod about the vibration node. We will use the equality of the frequencies on either side of the node, as we did in Sect. 3.6.2, to determine the location of the node and yield the antisymmetric normal mode frequency. If we let the node be a distance,  $b$ , from the attachment point of the head mass,  $m_h$ , then the separation between the attachment point of the tail mass,  $m_t$ , and the node must be  $L - b$ .

We have used the fact that the stiffness-length product is a constant before (see Sect. 2.2.2), although now we see it also as a direct consequence of our definition of Young's modulus in Eq. (4.1):  $KL = FL/\Delta l = ES$ . That allows us to write the stiffness of the spring between the node and the head mass as  $K_h = (K_{total}L)/b$  and the stiffness of the spring between the tail mass and the node as  $K_t = (K_{total}L)/(L-b)$ . Since  $m_t = 5m_h$ , we expect  $5(L-b) \cong b$ . If we also scale the moving mass of the spring, then the equality of the normal mode frequencies can be solved to provide the value of  $b$ .

$$\omega_h^2 = \left(\frac{K_{total}L}{b}\right) \frac{1}{m_h + \frac{bm_s}{3L}} = \left(\frac{K_{total}L}{L-b}\right) \frac{1}{m_t + \frac{(L-b)m_s}{3L}} = \omega_t^2 \quad (4.21)$$

Solving Eq. (4.21) will provide the  $b/L$  ratio.

$$\frac{b}{L} = \frac{m_t + \frac{m_s}{3}}{m_t + m_h + \frac{2m_s}{3}} \quad (4.22)$$

For the values used in this example,  $b/L = 0.802$ . (This would also tell us where we would want to support this projector so that none of its vibrations are communicated through the support structure.) Plugging  $b/L$  back into Eq. (4.21) gives  $f_h = f_t = 2.82$  kHz. If the speed of sound in water is  $c_{water} = 1500$  m/s, then  $2\pi a = 31.4$  cm and  $\lambda_{fluid} = c/f_h = 53.2$  cm  $> 2\pi a$ , so the radiation mass assumption was valid. This result is close to what would have been the normal mode frequency,  $f_a = \sqrt{K_{total}/\mu}/2\pi = 3.1$  kHz, using the reduced mass  $\mu = (m_1m_2)/(m_1 + m_2) = 0.583$  kg and assuming that the spring (the piezoelectric stack and tension rod) was massless.

These three examples of the direct use of solids as springs have been restricted to solid samples with a small aspect ratio, which is  $l \lesssim w \cong h$ , for the accelerometers, and to forces on the spring being applied longitudinally by the motor mechanism (i.e., the piezoelectric stack) and inertial effects in the *Tonpilz* case. It is rare to see long thin rods or bars being used as linear springs because the forces necessary to bend such a sample are smaller than the forces that would produce an equivalent longitudinal compression. This restriction will be quantified in the next sub-section. Also, long thin bars that are subject to compression can spontaneously buckle (i.e., collapse catastrophically) if the force exceeds a threshold value as discussed in Sect. 4.3.4.

### 4.3.2 Flexure Springs

Cantilevered beams are used as springs in applications that range from automotive suspensions to micromachined silicon sensors (like the beam from the atomic force microscope shown in Fig. 2.36). If you hold a meter stick with both hands at eye level,<sup>10</sup> with the numbers facing upward or downward, it

<sup>10</sup> You will also want to employ some protective eyewear.

is possible to apply torques to the two ends, as shown in Fig. 4.10, that will bend the meter stick into a smooth curve that corresponds (approximately) to the arc of a circle. If the numbered surface of the meter stick is facing toward you, then it will be very difficult to bend the meter stick vertically. Given enough torque, it might squirm (rotate into the previous orientation) or possibly fracture, although it does bend easily and reversibly if it is held flat (number side up or down). The radius of curvature,  $R$ , as expressed in Eq. (4.33), will be infinite before the meter stick is bent. As the bending increases, the radius will become shorter. In Fig. 4.10,  $R \cong 2.5 L$ , where  $L$  is the length of the meter stick.

What is happening to the material when the stick is bent and what is providing the restoring force that returns the stick to its straight condition after the torques are removed? When the stick is curved, as shown in Fig. 4.10, the material near the top of the stick is placed in tension and the material near the bottom of the stick is placed in compression. Since the stresses change sign going from the top of the stick to the bottom, there must be some surface near the middle that is unstressed. That surface is called the *neutral plane*. Figure 4.11 (left) shows a small segment of the bent beam (meter stick). The dashed line corresponds to the position of that neutral plane.



**Fig. 4.10** A beam (meter stick) is bent into an approximate arc of a circle by the application of opposite torques to the ends. Before bending, the radius of the arc is infinite. As more torque is applied, the bending increases and the beam's radius of curvature,  $R$ , moves in from infinity. For the bend shown here, the radius of curvature is about two and a half times the unbent length:  $R \cong 2.5 L$

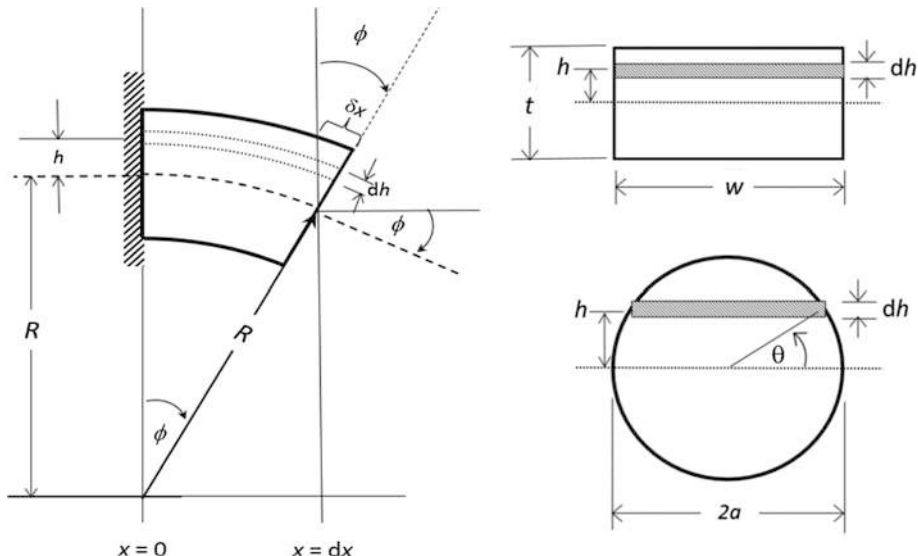


**Fig. 4.11** (Left) Diagram of a small segment of a bent beam. The dashed line represents the neutral surface. Filaments above that surface experience tension that is proportional to the distance,  $h$ , from the neutral surface. Those filaments below the neutral surface are in compression, again in proportion to their distance below the neutral surface. (Right) The geometry used to calculate the radius of gyration for a beam with a rectangular or circular cross-section

If there are no additional tensile or compressive forces applied to the beam, just the applied torque, then below the neutral plane, the compressive strain is proportional to the distance,  $h$ , below the neutral plane. Above the neutral plane, the tensile strain is also proportional to the distance,  $h$ , above the neutral plane.

$$\frac{\Delta l}{l} = \frac{h}{R} \quad (4.23)$$

To work out the forces so they can be summed (integrated) to calculate the bending moment (i.e., the restoring torque), we will consider a differential segment of a rectangular beam that is  $w$  wide,  $t$  thick, and rigidly clamped at  $x = 0$ , as shown schematically in Fig. 4.11 (left). When  $h = +(t/2)$ , the uppermost surface of the element is stretched from its equilibrium length by an amount,  $\Delta l = +\delta x$ , and the lowermost surface at  $h = -(t/2)$  is compressed by  $\Delta l = -\delta x$ .

By our definition of Young's modulus in Eq. (4.1), the stress (force per unit area) is also proportional to the distance from the neutral plane. Letting  $dS = w dh$ , the force,  $\delta F$ , produced by the filament,  $dh$ , thick and  $w$  wide, a distance,  $h$ , above the neutral plane, is related to the strain by Young's modulus,  $E$ .

$$\frac{dF}{dS} = E \frac{\delta x}{dx} \quad (4.24)$$

The strain,  $\delta x/dx$ , can be calculated using Garrett's First Law of Geometry (as stated in Sect. 1.1).

$$\frac{\delta x}{dx} = \frac{h \tan \phi}{dx} \cong h \frac{\phi}{dx} \Rightarrow \frac{dF}{dS} = E \frac{h \phi}{dx} \quad (4.25)$$

In Fig. 4.11 (left), the forces cancel but their *bending moment* about the neutral plane,  $\mathfrak{M}$ , is non-zero. That moment can be calculated by integration of the force times the distance from the neutral plane.

$$\mathfrak{M} = \int h dF = \frac{E \phi}{dx} \int h^2 dS \equiv \frac{ES \phi \kappa^2}{dx} \quad \text{where} \quad \kappa^2 = \frac{\int h^2 dS}{S} \quad (4.26)$$

The square of radius of gyration,  $\kappa^2$ , will depend upon the shape of the beam.  $\kappa^2$  is calculated below for the two cases shown in Fig. 4.11 (right).

$$\begin{aligned} \kappa_{bar}^2 &= \frac{w \int_{-t/2}^{t/2} h^2 dy}{wt} = \frac{t^2}{12} \\ \kappa_{rod}^2 &= \frac{4 \int_0^{\pi/2} (a^2 \sin^2 \theta) (a \cos^2 \theta) a d\theta}{\pi a^2} = \frac{a^2}{4} \end{aligned} \quad (4.27)$$

The stiffness of a beam in flexure depends not only upon the material but also its distribution with respect to the neutral axis. The effects of this material distribution are quantified by the square of the *radius of gyration*,  $\kappa^2$ . That is why steel used in construction frequently has a cross-section that is in the shape of an "I" or "H" to place more material farther from the neutral plane. This strategy will be limited because too much material separated from the neutral plane by too little "webbing" will allow the shape to become distorted, or twisted, when loaded, like trying to bend the meter stick against the tall dimension (the numbers facing you, instead of the edge facing you) in our first bending example.

**TABLE A.1 Properties of sections**

NOTATION.  $A$  = area (length $^2$ );  $y$  = distance to extreme fiber (length);  $I$  = moment of inertia (length $^4$ );  $r$  = radius of gyration (length);  $Z$  = plastic section modulus (length $^3$ ); SF = shape factor. See Sec. 8.15 for applications of  $Z$  and SF

Form of section	Area and distances from centroid to extremities	Moments and products of inertia and radii of gyration about central axes	Plastic section moduli, shape factors, and locations of plastic neutral axes
1. Square	$A = a^2$ $y_c = x_c = \frac{a}{2}$ $y'_c = 0.707a \cos\left(\frac{\pi}{4} - z\right)$	$I_x = I_y = I_c = \frac{1}{12}a^4$ $r_x = r_y = r'_c = 0.2887a$	$Z_x = Z_y = 0.25a^3$ $SF_x = SF_y = 1.5$
2. Rectangle	$A = bd$ $y_c = \frac{d}{2}$ $x_c = \frac{b}{2}$	$I_x = \frac{1}{3}bd^3$ $I_y = \frac{1}{3}b^3d$ $I_x > I_y \quad \text{if } d > b$ $r_x = 0.288\sqrt{bd}$ $r_y = 0.288\sqrt{b^3}$	$Z_x = 0.25bd^2$ $Z_y = 0.25d^3b$ $SF_x = SF_y = 1.5$
3. Hollow rectangle	$A = bd - b_1d_1$ $y_c = \frac{d}{2}$ $x_c = \frac{b}{2}$	$I_x = \frac{bd^3 - b_1d_1^3}{12}$ $I_y = \frac{db^3 - d_1b_1^3}{12}$ $r_x = \left(\frac{I_x}{A}\right)^{1/2}$ $r_y = \left(\frac{I_y}{A}\right)^{1/2}$	$Z_x = \frac{bd^2 - b_1d_1^2}{4}$ $SF_x = \frac{Z_x d}{2I_x}$ $Z_y = \frac{db^2 - d_1b_1^2}{4}$ $SF_y = \frac{Z_y b}{2I_y}$

**Fig. 4.12** A portion of the tabulation from the “Properties of Sections” taken from the extremely useful book, *Roark’s Formulas for Stress and Strain*. Only the first three of 29 cases are shown here. The radii of gyration for the shapes shown in the left column are provided in the middle column

Due to the critical importance of the moment of inertia<sup>11</sup> and the radius of gyration for structural engineering, there are numerous handbooks that provide the results for these integrations over nearly any imaginable cross-section. My favorite compilation for such results, as well as for the stresses on pressure vessels, bending of beams and plates, vibration of structures, etc., is *Roark’s Formulas for Stress and Strain* [12]. A portion of one page from Appendix A.1, “Properties of Sections,” taken from that book, is shown in Fig. 4.12.

For small deflections, application of Garrett’s First Law of Geometry suggests that the angle,  $\phi$ , is the same as the negative of the difference in the slope of the neutral plane at  $x = 0$  and at  $x = dx$ , which can be estimated using the first two terms in a Taylor series.

$$\phi = - \left[ \left( \frac{\partial y}{\partial x} \right)_{x+dx} - \left( \frac{\partial y}{\partial x} \right)_x \right] = - \left( \frac{\partial^2 y}{\partial x^2} \right) dx \quad (4.28)$$

In Fig. 4.11 (left),  $(\partial y/\partial x)_x = 0$ , but Eq. (4.28) would be correct even if that were not the case. Substitution of Eq. (4.28) for  $\phi$  back into Eq. (4.26) provides the relation between the bending moment,  $\mathfrak{M}$ , and the curvature of the differential element that will be useful for the calculation of the flexural vibration of beams in Sect. 5.3.

<sup>11</sup> The moment of inertia  $I = \int \rho y^2 dA$  is related to the square of the radius-of-gyration since the radius-of-gyration is equivalent to  $I$  for a material of unit mass density, if divided by cross-sectional area  $S$ . The square of the radius-of-gyration is also equivalent to the second moment of area.

$$\mathfrak{M} = -ESk^2 \frac{\partial^2 y}{\partial x^2} \quad (4.29)$$

The work done to bend the differential element in Fig. 4.11 (left) can be calculated in terms of the angle of the bend, again by use of Garrett's First Law of Geometry,  $\phi = dx/R$ . The bending moment,  $\mathfrak{M}$ , in Eq. (4.26) can be expressed in terms of that angle.

$$\mathfrak{M} = \frac{ESk^2}{dx} \phi \quad (4.30)$$

The amount of work,  $dW$ , required to bend that differential element from its equilibrium condition (straight) into an arc of angle,  $\phi$ , will be the integral of the moment.

$$dW = \int_0^\phi \mathfrak{M}(\phi') d\phi' = \frac{1}{2} \frac{ESk^2}{dx} \phi^2 \quad (4.31)$$

Substituting the expression for  $\phi$ , derived in Eq. (4.28), into Eq. (4.31) provides an expression for the change in potential energy that is done by the work of bending the differential element that is in a convenient form for integration along bars.

$$d(PE) = -dW = \frac{ESk^2}{2} \left( \frac{\partial^2 y}{\partial x^2} \right)^2 dx \quad (4.32)$$

Let's now apply Eq. (4.26) to the cantilevered beam that was drawn by Galileo and shown in Fig. 2.27. That (wooden) beam is built into a wall that constrains the slope of the beam to be zero as it leaves the wall. We can let  $y(x)$  be the transverse deflection of the beam from equilibrium as a function of distance,  $x$ , from the wall. The vertical component of the force,  $F_v$ , which causes the deflection, will be the weight of the mass,  $M$ , attached at the beam's end  $x = L$ , with  $F_v = Mg$ . Equation (4.33) provides the reciprocal of the radius of curvature of the beam,  $R^{-1}$ , at any location,  $x$ .

$$\frac{1}{R} = \frac{\frac{d^2 y}{dx^2}}{\left[ 1 + \left( \frac{dy}{dx} \right)^2 \right]^{2/3}} \cong \frac{d^2 y}{dx^2} \quad \text{if} \quad \left( \frac{dy}{dx} \right)^2 \ll 1 \quad (4.33)$$

Since only small deflections are being considered, the approximate expression for the radius of curvature can substituted into Eq. (4.26).

$$\mathfrak{M}(x) = Mg(L - x) = -\frac{ESk_{beam}^2}{R} = -\frac{E(wt)t^2}{12} \frac{d^2 y}{dx^2} \quad (4.34)$$

This provides an ordinary differential equation for the deflection,  $y(x)$ .

$$\frac{d^2 y(x)}{dx^2} = -\frac{12Mg}{Ewt^3} (L - x) \cong \frac{1}{R} = \frac{1}{h} \frac{\Delta l}{l} \quad (4.35)$$

The right-hand side of Eq. (4.35) is just a polynomial; hence, its integration (twice) from the wall at  $x = 0$  to the end at  $x = L$  is easy to perform.

$$y(x) = -\frac{6Mg}{Ewt^3} \left( Lx^2 - \frac{x^3}{3} \right) \quad (4.36)$$

The leading minus sign shows that the deflection is downward for the addition of a positive mass. It is worth noticing that this solution satisfies the boundary conditions that the wall imposes on the beam:

$y(0) = 0$  and  $(dy/dx)_x = 0 = 0$ . The deflection of the beam's end is cubic in its ratio of length to thickness. The beam's effective stiffness,  $K_{beam}$ , is thus also cubic in the ratio of thickness to length.

$$y(L) = -\frac{4Mg}{Ew} \frac{L^3}{t^3} \quad \text{and} \quad K_{beam} = \left| \frac{Mg}{y(L)} \right| = \frac{Ew}{4} \left( \frac{t}{L} \right)^3 \quad (4.37)$$

### 4.3.3 Triangularly Tapered Cantilever Spring\*

The expression for the deflection of a cantilevered beam of constant cross-sectional thickness,  $t$ , and constant width,  $w$ , was calculated, resulting in Eq. (4.37). In spring design, one of the most important constraints is the tensile strength of the spring material, particularly when a spring is subjected to cyclic strain that fully reverses every half-cycle [6]. For a rectangular beam, Eq. (4.35) demonstrates that the magnitude of the surface stress at  $y = \pm(t/2)$  is greatest at  $x = 0$  and goes to zero at the tip,  $x = L$ . That makes for a rather inefficient use of the material, since it would be preferable for all of the material to be at roughly the same state of stress, if possible, so that all parts of the beam make an equal contribution to its stiffness.

At the design limit of the spring's deflection, the stresses at all points on the surface should be at the material's stress limit (within some safety factor [6]) if the material's stiffness is being used efficiently. If you have ever used a fishing rod, you have seen this strategy in action. As shown in Fig. 4.13, the tapered fishing rod is bent into a circular arc (hence, constant radius of curvature) by the load (presumably, produced by a recalcitrant fish) applied to the tip of the rod.

It is clear from Eq. (4.35) that a beam with a linear taper (variable width),  $w(x) = (w(0)/L)(L - x)$ , would cancel the same linear dependence in the moment term and provide a constant radius of curvature.<sup>12</sup>

**Fig. 4.13** Photograph of Prof. Richard Packard, UC Berkeley Physics Department, on his boat, the *Puffin*, in Alaska, showing that the tapered rod that is his fishing pole being bent into a nearly a circular arc when loaded (by a large halibut) at its tip



<sup>12</sup> In principle, the width could be kept constant and the thickness could be tapered so  $t(x) = [t(0)/L^{1/3}](L - x)^{1/3}$ . Since spring steel is available in constant thickness sheets, it is frequently more convenient to provide a linear taper of the width.

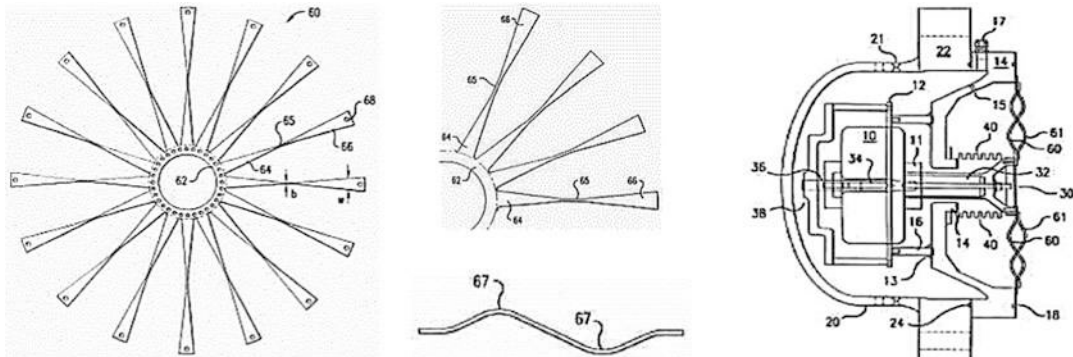
$$\frac{1}{R} \cong \frac{d^2y}{dx^2} = \frac{12Mg}{Et^3} \frac{L(L-x)}{w(0)(L-x)} = \frac{12MgL}{Ew(0)t^3} \quad (4.38)$$

Since the radius of curvature is constant, the double integration of Eq. (4.38) produces a new deflection curve,  $y(x)$ , and a new stiffness,  $K_{triangle}$ , for a beam with a linear taper.

$$y(x) = \frac{6MgLx^2}{Ew(0)t^3} \quad \text{and} \quad K_{triangle} = \frac{Mg}{z(L)} = \frac{Ew(0)}{6} \left(\frac{t}{L}\right)^3 \quad (4.39)$$

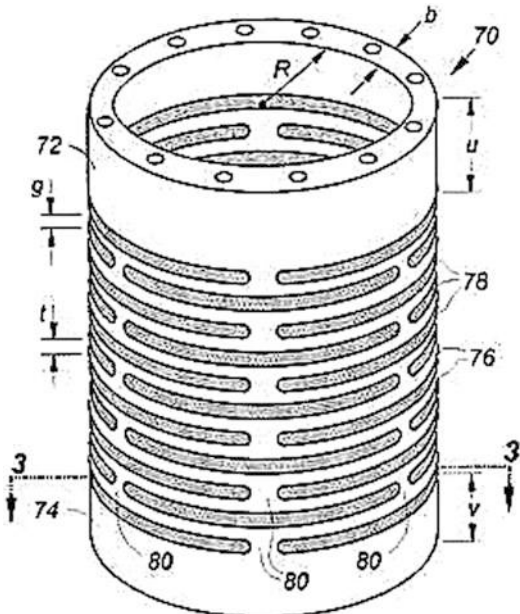
It is instructive to compare the stiffness of a tapered cantilever in Eq. (4.39) to the stiffness of a beam of constant width in Eq. (4.37). The stiffness of the constant width beam is larger by 6:4, so the tapered beam would need an initial width that is 50% larger to provide the same stiffness. Since the area of a triangle is half the base times the height, the triangular beam of the same stiffness and equal length uses 25% less material. Comparison of Eqs. (4.35) and (4.38) shows that the maximum stress is 50% lower for the triangular beam, again for the same stiffness. The triangular-shaped cantilever is clearly a more efficient use of the spring material.

Figure 4.14 shows an example of high-performance spring design that joins two triangular cantilevers. It was used to augment the stiffness of a 2 kW moving-magnet linear motor raising the natural frequency from about 20 Hz to the desired operating frequency near 60 Hz [13]. That spring was also the critical component in a test fixture (linear dynamometer) used to evaluate the performance of smaller moving-magnet linear motors [14]. Each spring in Fig. 4.14 consists of 16 leaves. Each leaf was composed of two triangular cantilever beams that are joined tip-to-tip. Because the spring in Fig. 4.14 was designed to accommodate linear displacements of  $\pm 1.0$  cm, with an overall diameter of about a half-meter, the beams were also bent into an S-shape in an orthogonal plane to relieve the longitudinal stress that would be produced by the need to lengthen each leaf as it went to its extreme



**Fig. 4.14** (Left) High-performance flexure spring that uses 16 beams made of pairs of triangular cantilevers that are joined tip-to-tip. The central ring is attached to a piston and the outer edges are clamped to the motor housing. (Center) The beams are also curved to relieve longitudinal stresses (i.e., tension) that would have caused failure due to the lengthening of the beams as they moved to their extreme transverse displacements. (Right) Two such springs (60 and 61) are shown installed on a motor housing (18) that contains a moving-magnet electrodynamic linear motor (10). (Unlike the moving-coil electrodynamic loudspeaker in Fig. 2.12, the voice coil is wound around a laminated steel core, like the cores of electrical transformers, and is stationary. The piston is attached to an armature that supports several magnets that move due to the oscillatory magnetic forces produced by the alternating currents through the stationary coils. Such moving-magnet linear motors can be far more efficient than the moving-coil version (see Table 10.4), but at the price of reduced bandwidth. Since the coils are stationary, the electrical leads are not subject to fatigue failure which is an important failure mode for moving-coil loudspeakers. Each spring's central hub is attached to a piston (30) and a flexible metal bellows (40). That bellows [17] provide a dynamic gas seal between the resonant load (not shown, but located to the right of the motor) and the back volume that contains the motor mechanism's coils and magnets)

**Fig. 4.15** A spring can be made from a cylinder that has been cut to provide a stack of cantilevers that are  $t$  thick,  $b$  wide, and spaced from each other by separation,  $g$ . The force is applied by each cantilever spring to the center of the spring below it through the “posts” (80). If the spaces (78 and 76) are filled with an elastomer, then the spring also becomes a flexure seal, similar to bellows [16]



transverse displacement (i.e., the change in hypotenuse of a right triangle with the displacement as its height and the unstrained spring’s length as its base).

That spring was machined from a flat sheet of 17-7 PH stainless steel. That alloy is as ductile as lead in its annealed state. Due to precipitation hardening (PH) during heat treatment [15], it becomes stiff, strong, and nearly lossless. The molds used create the S-bends, shown in Fig. 4.14 (center), and hold the steel sheet during heat treatment, were designed and fabricated by Dr. R. W. M. Smith.

Another method for producing flexure springs capable of large displacement is to make cuts into a hollow cylinder that stacks cantilevers on top of each other [16]. Such an arrangement is shown in Fig. 4.15.

#### 4.3.4 Buckling

There are two reasons that long thin bars or rods are not used as springs in compression. One reason becomes obvious if we compare the change in length,  $\Delta L$ , of a rod due to the application of a compressive force,  $F$ , on one end of area,  $\pi a^2$ , to the transverse deflection,  $z(L)$ , due to the same force applied perpendicular to the length,  $L$ , of the rod as diagrammed schematically in Fig. 4.16. According to our definition of Young’s modulus in Eq. (4.1),  $\Delta L = (FL)/(\pi a^2 E)$ . We can find the displacement of a cantilevered rod subject to a force of the same magnitude, but applied at right angles to the end, by substituting  $\kappa_{rod}^2 = a^2/4$  into Eq. (4.34) to produce an expression for the transverse deflection,  $z(L)$ , of a rod with circular cross-section and radius,  $a$ .

$$z(L) = \frac{8FL^3}{3Ea^4} \quad (4.40)$$

The ratio of the compressive displacement,  $\Delta L$ , to the transverse displacement,  $z(L)$ , depends only upon the *slenderness ratio*,  $L/a$ .

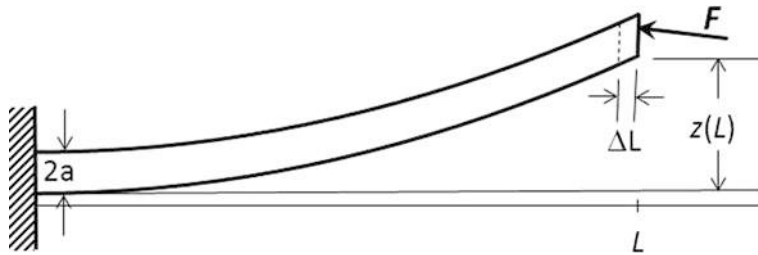
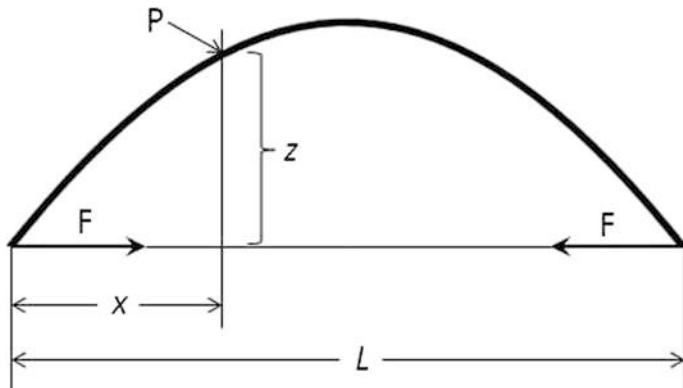


**Fig. 4.16** A bar of circular cross-section with diameter,  $2a$ , and length,  $L$ , is subject to a compressive force,  $F$ , which is not exactly aligned with its undeformed direction. The force produces both a compression,  $\Delta L$ , and a transverse displacement,  $z(L)$

**Fig. 4.17** Coordinate system for a buckled beam. The perpendicular lever arm for the force,  $F$ , about point,  $P$ , is  $z(x)$



$$\frac{z(L)}{\Delta L} = \left(\frac{8\pi}{3}\right) \left(\frac{L}{a}\right)^2 \cong 8 \left(\frac{L}{a}\right)^2 = \cot \theta \cong \frac{1}{\theta} \quad (4.41)$$

For a rod that has a diameter of 1.0 cm and is 50 cm long,  $(L/a) = 100$ . This corresponds to  $\theta = 12.5 \mu\text{rad} = 0.0007$  degrees. That result implies that if the angle the force,  $F$ , makes with the axis of the rod is greater than  $\theta$ , the transverse deflection will exceed the longitudinal compression. It would be nearly impossible to arrange the force applied to the end of a slender rod to produce only compression and no flexure.

An even bigger problem with slender rods or beams is that they will buckle if the force is greater than some threshold value,  $F_E$ , known as the *Euler force*. With a sufficiently large force, a slender structure (beam or column) will bend and then collapse, rather than compress. We can use the diagram in Fig. 4.17 to calculate that buckling force threshold. If we let the deflection of the rod from its straight (unloaded) condition be  $z(x)$ , then the bending moment that the applied force,  $F$ , creates on a piece of the rod located at point,  $P$ , is  $M(x) = F z(x)$ . That moment can be equated to the bending moment of the beam given in Eq. (4.26).

$$M(x) = Fz(x) = -\frac{ES\kappa^2}{R} = -ES\kappa^2 \left(\frac{d^2z}{dx^2}\right) \quad (4.42)$$

This produces an ordinary second-order differential equation that is now rather familiar.

$$\left(\frac{d^2z}{dx^2}\right) + \left(\frac{F}{ESk^2}\right)z = 0 \quad (4.43)$$

The solution is a sine curve.

$$z(x) = C \sin \frac{\pi x}{L} \Rightarrow \left(\frac{d^2z}{dx^2}\right) = -\left(\frac{\pi}{L}\right)^2 z(x) \quad (4.44)$$

Substituting this result back into Eq. (4.43) provides the critical force,  $F_E$ , that will result in the buckling of the beam if exceeded.

$$F_E = ESk^2 \left(\frac{\pi}{L}\right)^2 \quad (4.45)$$

This result is independent of  $z(x)$ . Once the beam starts to bend, upon application of force,  $F > F_E$ , the reaction force,  $F_E$ , is constant, so the curvature increases until the beam collapses catastrophically.

This result for  $F_E$  pertains to the situation diagrammed in Fig. 4.17, where both ends of the beam were allowed to have a non-zero slope (called a “hinged” boundary condition). If one end of the beam is clamped, so that  $(dz/dx)|_{x=L} = 0$ , then we see that by treating the clamped beam as being half as long as the beam that is hinged at both ends, we achieve the required result for the critical force that buckles the clamped-hinged beam,  $F_{cantilever} = 4F_E$ . As expected, by constraining one end of the beam to remain straight, the threshold for buckling is increased substantially.

This result is even more important for the stability of columns that support multistory buildings or rockets that need to trade off rigidity for launch weight. However, buckling is also a second important consideration for spring design that cautions against the use of slender beams as longitudinal springs.

### 4.3.5 Torsional Springs

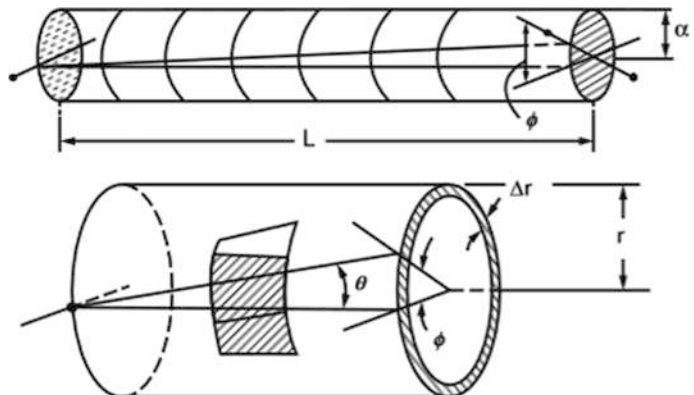
As with flexure springs, torsional stiffnesses are applied in a range of sizes from the shafts that connect propellers to gas turbines in naval warships to thin wires used to make sensitive measurements, like the determination of Newton’s gravitational constant,  $G$ , that measured a force of only  $1.7 \times 10^{-7}$  N. Using masses supported by a thin wire torsional spring, at the end of the eighteenth century, Cavendish was able to make the first determination of  $G$  [18]. Quartz fibers no thicker than human hairs have been used to provide the linear restoring torque for mirrored galvanometers (see Fig. 2.6) that have sensitivities limited only by their own temperature, as discussed in Sect. 2.4.4. It is now our goal to relate torsional stiffness to the material’s shear modulus and to its geometry.

Figure 4.18 shows a rod of length,  $L$ , and circular cross-section, with radius,  $a$ , that is clamped at  $x=0$ . It is being twisted at  $x=L$  by a torque that produces rotation by an angle,  $\phi$ . We can consider the rod to be composed of many concentric thin cylindrical shells of thickness,  $\Delta r$ , and then determine the overall stiffness by integrating from some inner radius,  $a_{in} < a$ , to the outer radius,  $a_{out} = a$ . For a solid rod, we can let  $a_{in} = 0$ . If we focus our attention on a small patch on the thin cylindrical shell with mean radius,  $r$ , and thickness  $\Delta r$ , then we see in Fig. 4.18 that the patch has been sheared by an angle  $\theta$ , when the end is twisted by an angle  $\phi$ .

$$\theta = \frac{r\phi}{L} \quad (4.46)$$

The shear stress is related to the distortion angle,  $\theta$ , by the shear modulus of the material, as expressed in Eq. (4.17).

**Fig. 4.18** (Above) Torque is applied to a rod of circular cross-section and length,  $L$ , that is rigidly fixed at  $x = 0$ . This produces a rotation of the end at  $x = L$  by an angle,  $\phi$ . (Below) A thin ring of material of thickness,  $\Delta r$ , a distance,  $r$ , from the axis of the rod has a patch of material that has been sheared by an angle,  $\theta$ . The small patch has a height,  $\Delta l$



$$\sigma_{yx} = \frac{\Delta F}{\Delta r \Delta l} = G\theta = G \frac{r\phi}{L} \quad (4.47)$$

The force,  $\Delta F$ , produces a torque,  $\Delta N$ , in conjunction with the “lever arm,”  $r$ .

$$\Delta N = r\Delta F = rG(\Delta l \Delta r)\theta = G(\Delta l \Delta r)r^2\phi/L \quad (4.48)$$

If we integrate  $\Delta N$  for the patch around the entire circumference of the cylindrical shell, the sum of the  $\Delta l$ ’s becomes  $2\pi r$  and the total torque becomes  $dN(r) = rG(2\pi r)\Delta r$  for the thin shell.

$$|N(r)| = \left| \vec{F} \times \vec{r} \right| = r\sigma_{xy}2\pi r\Delta r = 2\pi Gr^3\Delta r \frac{\phi}{L} \quad (4.49)$$

Integrating over  $\Delta r$  from an inner radius,  $a_{in}$ , to the outer radius,  $a$ , provides the torsional stiffness,  $K_{tube}$ , of the entire hollow tube of length,  $L$ .

$$N = \pi G(a^4 - a_{in}^4) \frac{\phi}{2L} \Rightarrow K_{tube} = \frac{N}{\phi} = \frac{\pi G(a^4 - a_{in}^4)}{2L} \quad (4.50)$$

For a solid rod of circular cross-section,  $K_{rod} = \pi Ga^4/2 L$ .

### 4.3.6 Coil Springs

When the word “spring” is mentioned, the most common image that word conjures is a helical coil spring. A coil spring is another efficient design that transforms extensions and compressions into shear stresses in the “wire” that is wound into a helix. Although our definition of shear stress in Eq. (4.17) “can be applied to slightly curved bars without significant error” [12], the wire of helical springs is very strongly curved, and the influence of that curvature must be included in the derivation of a relationship between the helical coil spring’s stiffness and its geometry [19].

The necessary calculations have been published in a book by Wahl [20]. A few of his results that are based on the spring geometry sketched in Fig. 4.19 are reproduced here. The stiffnesses of helical coil springs made with wire of circular, square, and rectangular cross-sections are provided in Eqs. (4.51), (4.52), and (4.53) with their parameters as defined in the caption of Fig. 4.19.

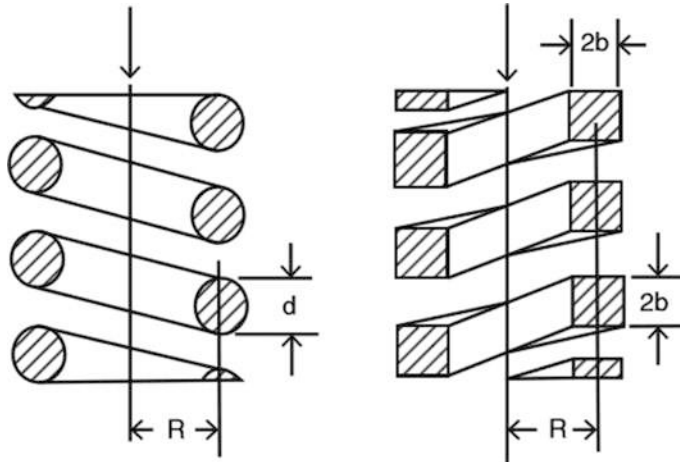


**Fig. 4.19** Geometry of helical coil springs, using circular or rectangular wire, is shown at the right. Their linear stiffness is related to their geometry and to the shear modulus,  $G$ , of the spring's material.  $R$  is the mean radius of the coil. The pitch,  $P$ , not labeled in the diagram, is the distance between the centers of adjacent coils at that radius, and the pitch angle is given by  $\alpha = \tan^{-1}(P/R)$ . The total length of the spring will be  $L = nP$ , where  $n$  is the number of coils [12].

$$K_{\text{round}} = G \frac{d^4}{64nR^3} \left[ 1 - \frac{3}{64} \left( \frac{d}{R} \right)^2 + \frac{3+\nu}{2(1+\nu)} (\tan \alpha)^2 \right]^{-1} \quad (4.51)$$

$$K_{\text{square}} = 0.3586 G \frac{b^4}{nR^3} \quad \text{if} \quad \frac{R}{b} > 3 \quad (4.52)$$

$$K_{\text{rectangle}} = G \frac{8b^4}{3\pi n R^3} \left\{ \frac{a}{b} - 0.627 \left[ \tanh \left( \frac{\pi b}{2a} \right) + 0.004 \right] \right\} \quad \text{where } a > b \quad (4.53)$$

Although helical coil springs are efficient in their use of material, they do couple torques, as well as the intended axial restoring forces, to their attached loads. A rather amusing demonstration of that coupling is provided by the Wilberforce pendulum [21], shown schematically in Fig. 4.20. For the round wire case, the axial (Hooke's law) stiffness is given by Eq. (4.51). For large ( $R/d$ ),  $K_{\text{round}} \cong Gd^4/64nR^3$ . The torsional stiffness can be expressed in terms of the longitudinal stiffness [22].

$$K_{\text{torsional}} = K_{\text{round}} R^2 (1 + \nu \cos^2 \alpha) \quad (4.54)$$

The twisting torque produced by the spring is related to its extension, so the longitudinal and torsional vibrations are coupled. This coupling is produced by a non-zero value of Poisson's ratio,  $\nu \neq 0$ . The coupled oscillator equations (see Sect. 2.7) for this case were written down by Sommerfeld [23].

$$\begin{aligned} \ddot{y} + \omega_v^2 y + (K_{\text{round}} R/m)(\nu \sin \alpha \cos \alpha) \theta &= 0 \\ \ddot{\theta} + \omega_t^2 \theta + (K_{\text{torsional}} R/I)(\nu \sin \alpha \cos \alpha) y &= 0 \end{aligned} \quad (4.55)$$

The values of  $\omega_t$  and  $\omega_v$  in the caption for Fig. 4.20 are close to those provided by Sommerfeld.

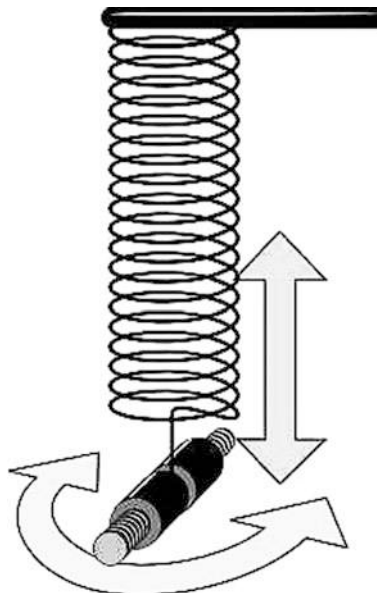


**Fig. 4.20** The Wilberforce pendulum is a helical coil spring that supports a mass,  $m$ , which has a moment of inertia,  $I$ . If the extensions and twisting were uncoupled, then the normal mode frequency for vertical vibrations would be  $\omega_v \cong (K_{round}/m)^{1/2}$ . The torsional normal mode would have a frequency of  $\omega_t \cong (K_{torsional}/I)^{1/2}$ . Since vertical displacements cause the spring to twist and twisting causes vertical motion, the two modes are coupled. If  $\omega_t \cong \omega_v$ , and the spring is initially displaced vertically, it will start vibrating up and down but will slowly begin twisting until all of the oscillatory motion becomes angular. After the vertical displacements cease, the angular oscillations will drive the vertical motion that will increase until the angular motion decays to zero and the cycle is repeated

$$\omega_v^2 = \left( \frac{K_{round}}{m} \right) (1 + \nu \cos^2 \alpha) \quad \text{and} \quad \omega_t^2 = \left( \frac{R^2 K_{round}}{I} \right) (1 + \nu \cos^2 \alpha) \quad (4.56)$$

If those frequencies are set equal to each other, the moment of inertia for the mass,  $m$ , must be  $I = m\kappa^2$ , where  $\kappa = R(1 + \nu)^{1/2}$  be the radius of gyration for the mass [24]. In principle, the measurement of  $I$  and  $m$  provides a means for determining the Poisson's ratio of the spring's material. Experimental measurements using this technique [22] have produced a reasonable value for  $\nu_{steel} \cong 0.23$ .

In addition to the twisting caused by the compression and expansion of a helical coil spring, the spring will also tilt. In some applications, neither of these "side effects" (no pun intended) are problematic, but if a helical coil spring is used to supplement the stiffness of a linear motor, the twisting or tilting can cause the magnets to touch the laminated steel around which the coil is wound, causing failure by rubbing in loudspeakers.

Such twisting and tilting can be mitigated by designing two concentric coil springs that are each double helices (like a DNA molecule). Such a coil spring pair is shown in Fig. 4.21 (left). With two concentric coil springs, it is possible to select their dimensions such that the twist produced by the outer spring is cancelled by the inner spring if their coils have opposite "handedness." Since each individual coil is composed of two helices that start at positions that are  $180^\circ$  apart, their symmetry also cancels the tilting.

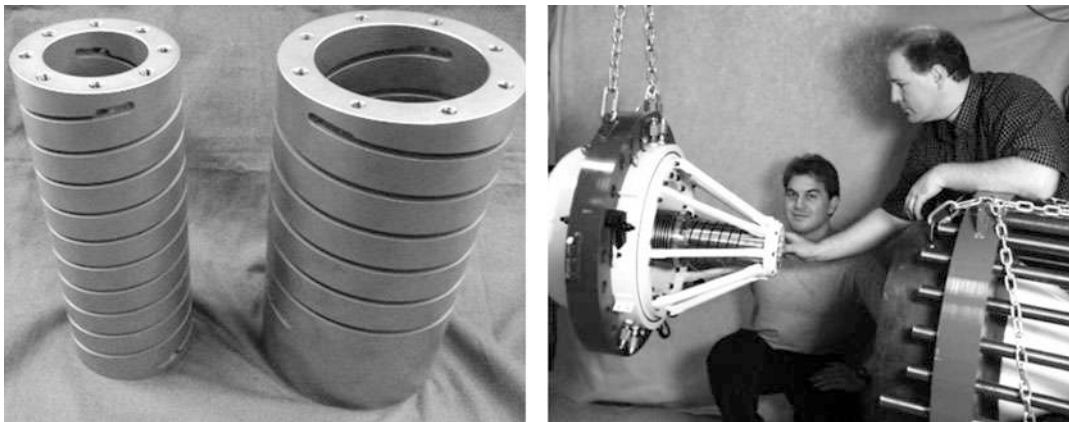


**Fig. 4.21** (Left) Photograph of two coil springs that are each a double-start helical coil. The two starting points for the helices are visible at the tops of both springs. The double helix design keeps the springs from tilting when displaced. The helices of the larger and smaller coils have opposite “handedness;” one coil advances to the right and the other advances to the left. They have been designed so that the twisting torques produced by equal compressions are equal and opposite. These springs were machined from a solid tube of maraging steel [15]. (Right) The larger diameter spring is visible in this photo of an assembled sound source which incorporates a 10 kW linear motor that is contained within the hemi-elliptical cap at the rear. A flexible metal bellow that provides a dynamic gas seal around the piston is (partially) visible between the spring and the housing. One end of the double-Helmholtz resonator [25] is also visible at the right of the photo. A cross-sectional diagram of the entire resonator is shown in Fig. 8.26. John Heake, then a graduate student, and Dr. R. W. M. Smith, the spring and bellows’ designer, are also in this photograph

#### 4.4 Viscoelasticity

The expressions for the generalization of Hooke’s law that involve the various moduli introduced in this chapter all share a common assumption: the strain produced by the stress (and vice versa) occurs instantaneously. We examined a similar assumption in Sect. 2.2.2, which used similitude (see Sect. 1.7) to calculate a “characteristic speed,”  $c \propto L\sqrt{K/m}$ , for the various parts along a helical spring of length,  $L$ , to influence each other. That perspective explained the introduction of a “quasi-static approximation,” justifying the use of a static spring stiffness,  $K$ , in the dynamical equation (i.e., Newton’s Second Law) for analysis of a simple, mass-spring harmonic oscillator (at sufficiently low frequencies). The quasi-static approximation also provides a basis for adding one-third of the spring’s mass to the “lumped” mass attached to the spring, derived in Eq. (2.27), since the displacement of each coil was assumed to be proportional to the distance from its fixed end, as illustrated for the static case by the Gerber scale in Fig. 2.2.

We now need to revisit that quasi-static assumption to understand the behavior of springs made from rubberlike elastomeric materials.<sup>13</sup> For such materials, their stiffnesses are frequency dependent, as is their internal energy dissipation [26]. Thus far, we have assumed the elastic moduli were frequency-independent and lossless. In this section, a simple model will be developed that can describe the viscoelastic behavior of rubberlike materials. The model is based on a single exponential relaxation time,  $\tau_R$ . The same model can be applied to many other physical systems such as the attenuation of sound in humid air (see Sect. 14.5.1) or seawater (see Sect. 14.5.2), to name just two. That *single*

<sup>13</sup> The terms elastomeric and rubberlike will be used interchangeably in this chapter. While all rubbers are elastomers, not all elastomers are rubbers. The distinction is codified in the American Society for Testing and Materials (ASTM) Standard D 1566, which is based on the length of time required for a deformed sample to return to its shape after removal of the deforming force, as well as the extent of that recovery [26].

*relaxation time model* leads to a complex stiffness,  $\mathbf{K}(\omega) = \mathbf{K}'(\omega) + j\mathbf{K}''(\omega)$ , where the frequency-dependent real part,  $\mathbf{K}'(\omega)$ , quantifies the stiffness and the frequency-dependent imaginary part,  $\mathbf{K}''(\omega)$ , quantifies the dissipation. It will also be shown that the two components of the complex stiffness, or equivalently the complex elastic modulus, are not independent and that their relationship is an entirely general feature of the causality inherent in any *linear response theory*.

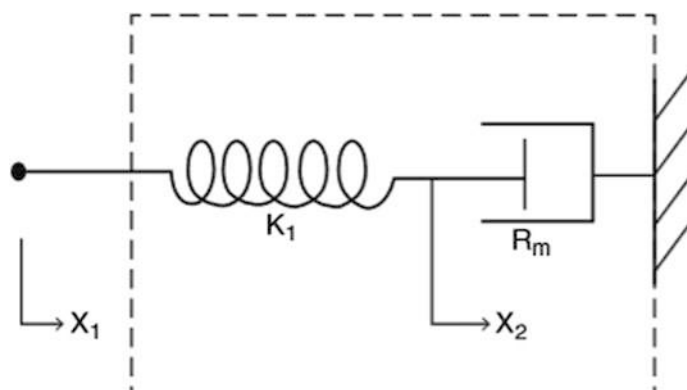
As long as the “cause” precedes the “effect,” the real and imaginary components of any *generalized susceptibility* [27], like a complex elastic modulus, the index of refraction of transparent optical materials, the dielectric susceptibility of electrical insulators [28], the speed and attenuation of sound [29], the gain and phase in electrical filter and amplifier circuits [30], the relationships between the real part (radiation resistance) and imaginary part (radiation reactance or effective hydrodynamic mass) of the radiation impedance [31], and even the absorption of sound by porous media in superfluid helium [32], etc., all obey the *Kramers-Kronig relations* (see Sect. 4.4.4) that were discovered in studies of the propagation and attenuation of X-rays during the first quarter of the twentieth century [33].<sup>14</sup>

#### 4.4.1 The Maxwell (Relaxation Time) Model

We start the development of our model describing the response of viscoelastic materials by considering the behavior of a spring that is placed in series (mechanically) with a dashpot. We have already devoted a considerable amount of effort to describing the effects of a spring and dashpot that were placed in parallel, as shown in Fig. 2.6, when we examined the damped harmonic oscillator in Sect. 2.4. Figure 4.22 shows the spring and dashpot in series inside a “black box” that allows us access only to the end of the spring that is not attached to the dashpot. The displacement of the exposed end of the spring from its equilibrium position will be designated  $x_1$ .

The other end of the spring is attached to a dashpot that is inside the black box. The displacement of that junction from its equilibrium position will be designated  $x_2$ . We let the other end of the dashpot be fixed. Since we do not have physical access to  $x_2$ , it will act as a “hidden variable” that we can use for calculation of the response of  $x_1$  to forces applied at  $x_1$ , the only location in which we have the ability to access from the outside of the black box.

**Fig. 4.22** A spring and dashpot are placed inside a “black box” (inside the dashed lines) that provides us with access only to one end of the spring whose displacement from equilibrium will be labeled  $x_1$ . Inside the box, attached to the other end of the spring, is a dashpot. The displacement of the junction between the “hidden” end of the spring and the dashpot is designated  $x_2$



<sup>14</sup> In mathematics and signal processing the Kramers-Kronig relations are known as [Sokhotski-Plemelj theorem](#) or the [Hilbert transform](#)

Before producing a mathematical analysis of our “black box,” it pays to think about the behavior of  $x_1$  in the high- and low-frequency limits. As before, similitude (see Sect. 1.7) will be able to guide our determination of the frequency,  $\omega_R$ , that separates the regimes of high- and low-frequency behavior. There is only one combination of stiffness,  $K_1$  [N/m = kg/s<sup>2</sup>], and mechanical resistance,  $R_m$  [N·s/m = kg/s], that has the units of frequency (or its inverse, time). Although we are unable to determine any numerical pre-factor, similitude guarantees that  $\omega_R \propto (K_1/R_m)$ . If  $x_1$  is driven at frequencies well above  $\omega_R$ , then  $x_2 \ll x_1$ , because the dashpot (producing a force proportional to the velocity) will not move easily at high frequencies. At high frequencies,  $x_1$  will seem to obey Hooke’s law with  $F(x_1) \cong -K_1 x_1$ .

At frequencies well below  $\omega_R$ , it will be much easier to compress the dashpot than the spring. From outside the black box,  $x_1$  will appear to be connected directly to the dashpot at sufficiently low frequencies,  $\omega \ll \omega_R$ . In that case,  $x_1 \cong |x_2|$ , so  $F(\dot{x}_1) \cong -R_m \dot{x}_1$ .

The behavior of  $x_1$  for all frequencies can be calculated by writing an equation for the force applied at  $x_1$ ,  $F(x_1)$ . Although the displacements,  $x_1$  and  $x_2$ , may not be equal, the force through the series combination must be continuous. All of the force must end up being applied to the rigid boundary at the end of the dashpot that is not connected to the spring.

$$\mathbf{F}(x_1) = -K_1(\mathbf{x}_1 - \mathbf{x}_2) = -R_m \dot{\mathbf{x}}_2 = -j\omega R_m \mathbf{x}_2 \quad (4.57)$$

The right-hand version of Eq. (4.57) assumes that the applied force at  $x_1$  is time-harmonic at a single frequency,  $\mathbf{F}(x_1) = F_1 e^{j\omega t}$ . Equation (4.57) can be solved for the ratio of the two displacements.

$$\frac{\mathbf{x}_2}{\mathbf{x}_1} = \frac{1}{1 - j\omega\tau_R} = \frac{1 + j\omega\tau_R}{1 + (\omega\tau_R)^2} \quad (4.58)$$

A *relaxation time*,  $\tau_R = R_m/K_1$ , has been introduced. It is the reciprocal of the relaxation frequency,  $\omega_R = \tau_R^{-1}$ , calculated previously from similitude. That displacement ratio behaves as we expected in the high- and low-frequency limits, now expressed as  $\omega\tau_R \gg 1$  and  $\omega\tau_R \ll 1$ , respectively.

$$\lim_{\omega\tau_R \rightarrow 0} \left[ \frac{\mathbf{x}_2}{\mathbf{x}_1} \right] = 1 \quad \text{and} \quad \lim_{\omega\tau_R \rightarrow \infty} \left[ \frac{\mathbf{x}_2}{\mathbf{x}_1} \right] = \frac{j}{\omega\tau_R} = 0 \quad (4.59)$$

Equation (4.58) can be used to substitute  $x_2$  into the expression for the force, given in Eq. (4.57), that is applied to the spring at  $\mathbf{x}_1$ .

$$\mathbf{F}(x_1) = -K_1(\mathbf{x}_1 - \mathbf{x}_2) = -K_1 \mathbf{x}_1 \left( 1 - \frac{1 + j\omega\tau_R}{1 + (\omega\tau_R)^2} \right) = \frac{-K_1 \mathbf{x}_1 \omega\tau_R}{1 + (\omega\tau_R)^2} (\omega\tau_R - j) \quad (4.60)$$

If we make the analogy to Hooke’s law,  $F = -Kx$ , then Eq. (4.60) suggests that the equivalent spring constant of the spring-dashpot combination is a frequency-dependent complex number,  $\mathbf{K}_1(\omega)$ .

$$\mathbf{K}_1(\omega) = \mathbf{K}_1'(\omega) + j\mathbf{K}_1''(\omega) = \frac{K_1(\omega\tau_R)^2}{1 + (\omega\tau_R)^2} \left[ 1 - \frac{j}{(\omega\tau_R)} \right] \quad (4.61)$$

In the high-frequency limit,  $\omega\tau_R \gg 1$ , the black box looks just like a spring with  $F(x_1) = -K_1 x_1$ . In the opposite frequency limit,  $x_1$  appears to be attached to a dashpot, once we replace  $\tau_R$  by  $(R_m/K_1)$  in Eq. (4.62).

$$\lim_{\omega\tau_R \rightarrow 0} [\mathbf{F}(\mathbf{x}_1)] = \lim_{\omega\tau_R \rightarrow 0} \left[ -(\mathbf{K}_1 \mathbf{x}_1) \frac{\omega\tau_R}{1 + (\omega\tau_R)^2} (\omega\tau_R + j) \right] = -j\omega R_m \mathbf{x}_1 \quad (4.62)$$

When a force is applied to  $x_1$ , only the dashpot can dissipate power. Using Eq. (1.73), the time-averaged power dissipation,  $\langle \Pi(t) \rangle_t$ , is derived from the product of two complex quantities.

$$\begin{aligned}\langle \Pi(t) \rangle_t &= \frac{1}{2} \Re e[\mathbf{F}^* \dot{\mathbf{x}}_2] = \frac{1}{2} \Re e \left[ \widehat{\mathbf{F}}_1 e^{-j\omega t} j\omega \widehat{\mathbf{x}}_2 e^{j\omega t} \right] = \frac{1}{2} \Re e \left[ \widehat{\mathbf{F}}_1 \widehat{\mathbf{x}}_1 \frac{j\omega - \omega^2 \tau_R}{1 + (\omega \tau_R)^2} \right] \\ &= \frac{-\omega |\widehat{\mathbf{x}}_1| |\widehat{\mathbf{F}}_1|}{2} \left( \frac{\omega \tau_R}{1 + (\omega \tau_R)^2} \right) = \frac{-|\dot{\mathbf{x}}_1| |\widehat{\mathbf{F}}_1|}{2} \left( \frac{\omega \tau_R}{1 + (\omega \tau_R)^2} \right)\end{aligned}\quad (4.63)$$

The power is a negative number because it is being dissipated. By taking the derivative of the last expression with respect to  $(\omega \tau_R)$ , we see that the maximum dissipation occurs at  $(\omega \tau_R) = 1$ .<sup>15</sup>

Equation (4.60) for the force and Eq. (4.63) for the dissipation exhibit the expected behavior in the high- and low-frequency limits. Now that we have explicit expressions for their complete frequency dependence, their behavior can be plotted. To make such plots “universal,” it is useful to scale (i.e., nondimensionalize) the stiffness and the dissipation. Since we know the high-frequency stiffness,  $K_\infty = K_1$ , we can plot the negative of the real part of Eq. (4.60) divided by  $K_\infty$  as a function of  $\omega \tau_R$ . The time-averaged power dissipation can be plotted as the energy dissipated per cycle,  $\langle \Pi \rangle, T = \langle \Pi \rangle / f$ , where  $f = 2\pi \langle \Pi \rangle / \omega$ , divided by the potential energy stored in the spring in the high-frequency limit,  $(PE)_\infty = (\frac{1}{2}) |\widehat{\mathbf{F}}_1| |\widehat{\mathbf{x}}_1|$ , again as a function of  $\omega \tau_R$ .

$$\frac{|\mathbf{K}(\omega \tau_R)|}{K_\infty} = \frac{(\omega \tau_R)^2}{1 + (\omega \tau_R)^2} \quad \text{and} \quad \frac{\langle \Pi \rangle_t}{\left( \frac{|\widehat{\mathbf{F}}_1| |\widehat{\mathbf{x}}_1|}{2} \right) f} = \pi \frac{(\omega \tau_R)}{1 + (\omega \tau_R)^2} \quad (4.64)$$

These universal curves are plotted in Fig. 4.23. The peak in the normalized dissipation has a value of  $\pi/2$  and occurs at  $(\omega \tau_R) = 1$ .

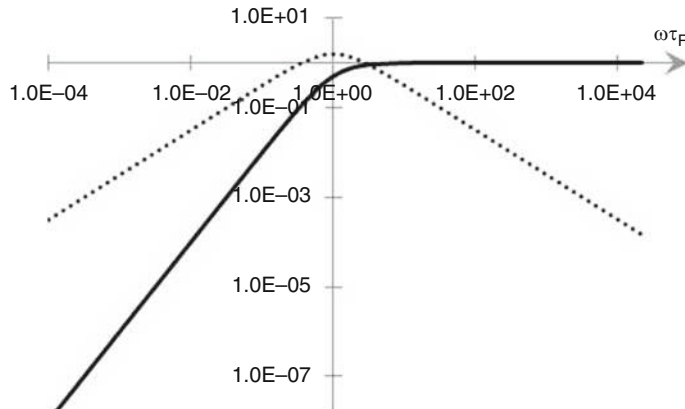


**Fig. 4.23** Logarithmic plot of the scaled stiffness,  $K(\omega \tau_R)/K_\infty$  (solid line), and the scaled dissipation per cycle (dotted line) for the Maxwell model from Eq. (4.64). The maximum scaled (i.e., nondimensionalized) dissipation per cycle is equal to  $\pi/2$  and occurs when  $\omega \tau_R = 1$ . The scaled stiffness drops to zero at  $\omega \tau_R = 0$

<sup>15</sup> For an expression like that in Eq. (4.63), it is actually easier to solve for the minimum of the inverse than to solve for the maximum:

$$\frac{d}{dx} \left( \frac{1+x^2}{x} \right) = \frac{d}{dx} \left( \frac{1}{x} + x \right) = 0$$

This series combination of a stiffness and dashpot is sometimes called the *Maxwell model* and can be used to describe materials that “creep.” It is a good description of Silly Putty® (a toy made from a silicone polymer that will bounce like a rubber ball but will flow over times on the order of several minutes or hours), solutions of corn starch and water, and very viscous fluids, like warm roofing tar. All of those materials will flow slowly over longer time scales but behave elastically over times that are short compared to the relaxation time,  $t \ll \tau_R$ .

#### 4.4.2 Standard Linear Model (SLM) of Viscoelasticity

The Maxwell model is not a good representation of a rubber spring; the rubber will exhibit non-zero stiffness even when  $\omega \cong 0$ . If that were not true, the use of rubber in springs as vibration isolators would be impossible since they must support the static load as well as isolate vibrations. The stiffness of a rubber spring increases with increasing frequency from  $K_o$  at  $\omega = 0$  to some limiting high-frequency value  $K_\infty$ . We can incorporate the stiffness,  $K_o$ , at zero frequency into the Maxwell model by placing a spring with stiffness,  $K_o$ , in parallel with our Maxwellian spring-dashpot combination. That combination is known as the *standard linear model* (SLM) for viscoelastic materials and is shown schematically in Fig. 4.24, again inside a “black box.”

The results of Sect. 4.4.1 can be applied to the SLM to calculate the apparent stiffness and the dissipation per cycle. This time we will calculate the input mechanical impedance presented to the attachment point at  $x_1$  by adding the Maxwellian combination in parallel to the spring with stiffness,  $K_o$ .

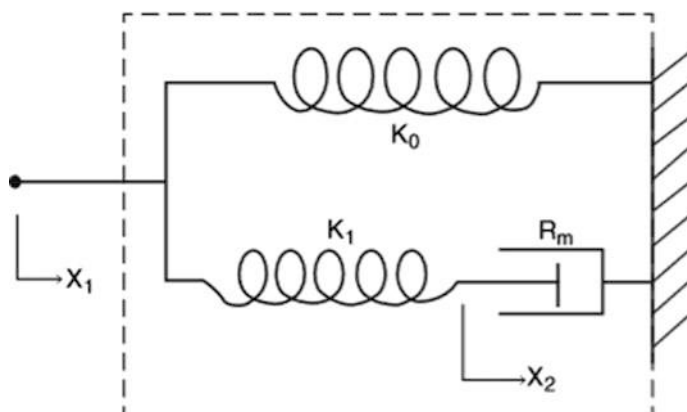
$$\mathbf{Z}_{\text{mech}} = \frac{\mathbf{F}}{\mathbf{v}_1} = \frac{\mathbf{F}}{\dot{\mathbf{x}}_1} = \frac{\mathbf{F}}{j\omega \mathbf{x}_1} = -\frac{K_o}{j\omega} + \tau_R K_1 \left( \frac{1 + j(\omega\tau_R)}{1 + (\omega\tau_R)^2} \right) \quad (4.65)$$

As the frequency approaches zero, the first term dominates. At high frequencies, when the dashpot is immobilized, the stiffnesses of the two springs add in parallel (mechanically).

$$\lim_{\omega\tau_R \rightarrow \infty} [\mathbf{Z}_{\text{mech}}] = -\frac{K_o}{j\omega} + \frac{j\tau_R K_o}{(\omega\tau_R)} = -\frac{(K_o + K_1)}{j\omega} \quad (4.66)$$

The stiffness as a function of frequency transitions smoothly from the low-frequency limit,  $K_o$ , to the high-frequency limit,  $K_\infty = K_o + K_1$ .

**Fig. 4.24** A spring of stiffness,  $K_o$ , is placed in parallel with the series spring-dashpot of the Maxwell model in Fig. 4.22 to produce the standard linear model (SLM) of a viscoelastic material. The springs and dashpot are again shown inside the “black box,” indicated by the dashed lines, to emphasize that only the terminal designated  $x_1$  is accessible and that  $x_2$  is a “hidden” variable



$$K(\omega\tau_R) = K_o + \frac{K_1(\omega\tau_R)^2}{1 + (\omega\tau_R)^2} \quad (4.67)$$

The power dissipated in the dashpot will again be due entirely to  $v_2 = j\omega x_2$ . Since the force  $F_I = -j\omega x_2 R_m$ , the time-averaged power dissipation can be expressed in terms of  $x_I$  using Eq. (4.58).

$$\langle \Pi \rangle_t = \frac{1}{2} \Re e \left[ -\omega^2 \frac{R_m}{2} \mathbf{x}_2^* \mathbf{x}_2 \right] = -R_m \frac{\omega^2 |\mathbf{x}_2|^2}{2} \left( \frac{1}{1 + (\omega\tau_R)^2} \right) \quad (4.68)$$

At high frequencies, this time-averaged power dissipation approaches a constant, so the energy dissipated per cycle is proportional to  $\omega^{-1}$ . The total maximum potential energy stored in both springs,  $E_{stored}$ , is just the sum of the individual stored potential energies.

$$E_{stored} = \frac{1}{2} K_o x_1^2 + \frac{1}{2} K_1 (x_1 - x_2)^2 = \frac{x_1^2}{2} \left[ K_o + K_1 \frac{(\omega\tau_R)^2}{1 + (\omega\tau_R)^2} \right] \quad (4.69)$$

As before, we can form the dimensionless ratio of the magnitude of the time-averaged power,  $\langle \Pi(t) \rangle_t$ , dissipated per cycle, divided by the energy stored in the springs.

$$\begin{aligned} \frac{2\pi \langle \Pi \rangle_t}{\omega E_{stored}} &= 2\pi \frac{K_1(\omega\tau_R)}{K_o [1 + (\omega\tau_R)^2] + K_1(\omega\tau_R)^2} \\ &= 2\pi \frac{(K_\infty - K_o)(\omega\tau_R)}{K_o [1 + (\omega\tau_R)^2] + (K_\infty - K_o)(\omega\tau_R)^2} \end{aligned} \quad (4.70)$$

This result is rather interesting. The magnitude of the normalized dissipation depends only upon the limiting values of the stiffness and not on  $R_m$ , except through the relaxation time,  $\tau_R = R_m/K_1$ , that determines the frequency at which the dissipation reaches its maximum value. The relaxation time,  $\tau_R$ , does not influence the magnitude of the dissipation maximum. The point,  $(\omega\tau_R)_{max}$ , where the dissipation reaches its peak value, and the value of the dissipation at that peak, can be determined from Eq. (4.70). They also depend only upon the limiting values of stiffness. This is not a coincidence; it is an inevitable consequence of linear response theory and causality, as will be demonstrated in Sect. 4.4.4.

$$(\omega\tau_R)_{max} = \sqrt{\frac{K_o}{K_\infty}} \quad \text{and} \quad \left( \frac{2\pi \langle \Pi \rangle_t}{\omega E_{stored}} \right)_{max} = 2\pi \frac{K''}{K'} = \frac{\pi K_1}{\sqrt{K_o^2 + K_o K_1}} = \frac{\pi(K_\infty - K_o)}{\sqrt{K_o K_\infty}} \quad (4.71)$$

A plot of the stiffness and normalized dissipation, as a function of  $\omega\tau_R$ , are provided in Fig. 4.25 for the case where  $2K_o = K_1$ , so  $(\omega\tau_R)_{max} = \sqrt{K_o/K_\infty} = 1/\sqrt{3} \cong 0.577$ .

### 4.4.3 Complex Stiffnesses and Moduli\*

The expressions derived in the first portion of this chapter for the moduli that relate stress and strain assumed that the material's response was instantaneous. The Maxwell model and the standard linear model for viscoelastic behavior both include a “relaxation time,”  $\tau_R$ . Thus far, we have focused only on the response of these spring and damper systems to time-harmonic excitation forces, but if we applied a

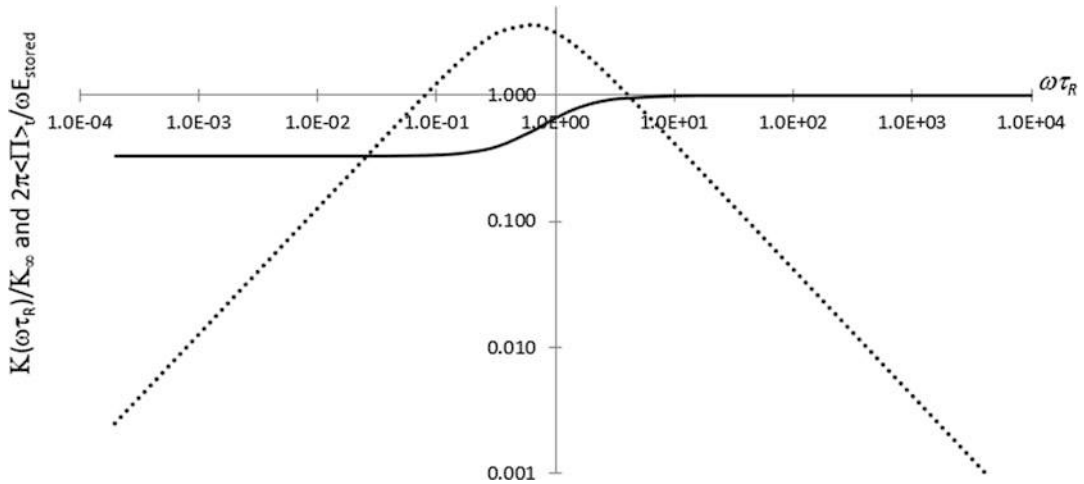


**Fig. 4.25** A logarithmic plot of the stiffness ratio,  $K(\omega\tau_R)/K_\infty$ , shown as the *solid line*, and the normalized dissipation (power dissipated per cycle divided by the energy stored), shown as the *dotted line*, as a function of the product of angular frequency,  $\omega$ , and relaxation time,  $\tau_R$ , for the standard linear model with  $K_1/K_\infty = 2$ , so  $(\omega\tau_R)_{max} = 1/\sqrt{3} = 0.577$

step force at time  $t = 0$ , then the response at times  $t > 0$  would change over times on the order of  $\tau_R$ . A more general linear response equation can be written that incorporates the possibilities of time-dependent behavior.

$$\left( a_o + a_1 \frac{d}{dt} + a_2 \frac{d^2}{dt^2} + \cdots + a_n \frac{d^n}{dt^n} \right) \boldsymbol{\sigma} = \left( b_o + b_1 \frac{d}{dt} + b_2 \frac{d^2}{dt^2} + \cdots + b_n \frac{d^n}{dt^n} \right) \boldsymbol{\epsilon} \quad (4.72)$$

Introducing a real constant,  $\chi$ , with the dimensions of inverse length [ $m^{-1}$ ], and a generic complex modulus,  $\Xi$  [Pa], we can identify the constant terms in (4.72) with various combinations of springs and dashpots. For a single spring of stiffness  $K_\infty$ ,  $\sigma = (\chi\Xi)\epsilon$ , so  $a_o$  and  $b_o$  are non-zero, but all other  $a_n = b_n = 0$  for  $n \geq 1$ . A single dashpot, with mechanical resistance,  $R_m$ , can also be cast into the form of Eq. (4.72).

$$\boldsymbol{\sigma} = \chi R_m \left( \frac{d}{dt} \right) \boldsymbol{\epsilon}$$

For this dashpot,  $a_o \neq 0$  and  $b_1 \neq 0$ , but  $b_o = 0$ , as do all other  $a_n = 0$ , with  $n \geq 1$  and  $b_n = 0$  for  $n \geq 2$ .

The response of the SLM can also be written in the form of Eq. (4.72).

$$\left[ K_1 + R_m \frac{d}{dt} \right] \boldsymbol{\sigma} = \chi \left[ K_\infty K_1 + (K_o + K_1) R_m \frac{d}{dt} \right] \boldsymbol{\epsilon}$$

For the response of the SLM, characterized by the mechanical impedance expressed in Eq. (4.65),  $a_o$ ,  $b_o$ ,  $a_1$ , and  $b_1$  are non-zero, but all other  $a_n = b_n = 0$  for  $n \geq 2$ . The coefficients of the stress and the strain in this form of Hooke's law are now linear operators (see Sect. 1.3) instead of just constants, as they were in Eqs. (4.1), (4.8), (4.14), and (4.17).

Returning to our solution for the input mechanical impedance of the SLM configuration in Eq. (4.65), we can write the stiffness as a complex quantity,  $\mathbf{K} = \mathbf{K}' + j\mathbf{K}''$ , where  $\mathbf{K}' = \Re[\mathbf{K}]$  and  $\mathbf{K}'' = \Im[\mathbf{K}]$ , as we did previously for the Maxwell model in Eq. (4.61).

$$\mathbf{K} = \mathbf{K}' + j\mathbf{K}'' = \mathbf{K}_o + \frac{\mathbf{K}_1(\omega\tau_R)}{1 + (\omega\tau_R)^2} [(\omega\tau_R) - j] \quad (4.73)$$

Taking the ratio of the negative of the imaginary part of this complex stiffness to the real part of the complex stiffness, it should become clear why I chose to scale the dissipation in the way shown in Eq. (4.70).

$$-\frac{\Im m[\mathbf{K}]}{\Re e[\mathbf{K}]} = \frac{\mathbf{K}_1(\omega\tau_R)}{\mathbf{K}_o[1 + (\omega\tau_R)^2] + \mathbf{K}_1(\omega\tau_R)^2} \quad (4.74)$$

Remembering that  $\mathbf{K}_\infty - \mathbf{K}_o = \mathbf{K}_1$ , Eq. (4.74) differs from Eq. (4.70) by a factor of  $2\pi$ . This is due to the definition of the dissipation per cycle that was used in Eq. (4.70) rather than the dissipation per radian cycle time,  $\omega^{-1}$ , that is the reciprocal of the radian frequency.

If we assume time-harmonic solutions to the operator form of Hooke's law in Eq. (4.72), the time-dependent stress-strain relation can be expressed in terms of the complex stress,  $\boldsymbol{\sigma}$ , and the complex strain,  $\boldsymbol{\epsilon}$ .

$$(a_o + a_1(j\omega) + a_2(j\omega)^2 + \cdots + a_n(j\omega)^n) \boldsymbol{\sigma} = (b_o + b_1(j\omega) + b_2(j\omega)^2 + \cdots + b_n(j\omega)^n) \boldsymbol{\epsilon} \quad (4.75)$$

The complex ratio of stress to strain can then be written as a complex elastic modulus.

$$\frac{\boldsymbol{\sigma}}{\boldsymbol{\epsilon}} \equiv \Xi = \frac{[b'(\omega) + b''(\omega)]}{[a'(\omega) + a''(\omega)]} = |\Xi|(1 + j\delta) \quad \text{where} \quad \delta = \frac{\Im m[\Xi]}{\Re e[\Xi]} \quad (4.76)$$

The fact that the ratio of two complex numbers is also a complex number allows us to introduce the *loss factor* or *damping factor*,  $\delta$ , so that the generic complex modulus,  $\Xi$ , can be represented by its magnitude,  $|\Xi|$ . In this form, the strain lags the stress by a phase angle,  $\theta = \tan^{-1} \delta$ , or by a time delay,  $\tau = \delta / \omega$ .

#### 4.4.4 Kramers-Kronig Relations

*"A few examples may promote the comprehension of a law, whose extreme generality is not unlikely to convey an impression of vagueness."* J. W. Strutt (Lord Rayleigh) [34]

The Kramers-Kronig (K-K) relations are very different from any equations provided thus far, since the K-K relationships are not "local"; the value of the real part of the response function is related to the imaginary part of the response function integrated over all frequencies,  $0 \leq \omega < \infty$ , and vice versa. If we express our generic response function as  $\Xi(\omega) = \Xi'(\omega) + j\Xi''(\omega)$ , then the following integrals relate their real and imaginary parts.<sup>16</sup>

$$\Xi'(\omega) = \frac{2}{\pi} \int_0^\infty \frac{\omega' \Xi''(\omega')}{\omega'^2 - \omega^2} d\omega' \quad (4.77)$$

<sup>16</sup>The fact that these integrals are a consequence of linear response theory and causality can be proven by the use of complex integration of functions that are "analytic in the upper half-plane" and the Cauchy residue theorem.

$$\Xi''(\omega) = \frac{-2\omega}{\pi} \int_0^\infty \frac{\Xi'(\omega')}{\omega'^2 - \omega^2} d\omega' \quad (4.78)$$

In these expressions, the integration is carried out over the dummy variable,  $\omega'$ , so that either the real or the imaginary parts of the response function at any single frequency,  $\omega$ , will be dependent upon the behavior of the other part over all frequencies, in principle, from DC ( $\omega = 0$ ) to daylight ( $\omega = \infty$ ); hence, the relations are “nonlocal.” Although the determination of one part at any frequency depends upon the other part’s behavior over a range of frequencies, the critical realization is that the two parts are not independent.

To develop confidence in their applicability, we will employ the Kramers-Kronig relations to express the real and imaginary components of the complex stiffness,  $\mathbf{K}(\omega) = \mathbf{K}'(\omega) + j\mathbf{K}''(\omega)$ , in Eq. (4.73) that were obtained from our single relaxation time model for Hooke’s law,  $\mathbf{F}_1(\omega) = -\mathbf{K}(\omega)\mathbf{x}_1(\omega)$ . Before calculating the relationship between real and imaginary components, based on the Kramers-Kronig relations, it is helpful to remember that we have an expression for the instantaneous response of the system,  $K_\infty$ . The integration of the real part of the stiffness, using Eq. (4.78), to determine the imaginary part of the stiffness, is simplified if we subtract this constant from the real part of the stiffness and change the integration variable to  $x = \ln(\omega'/\omega)$  [35].

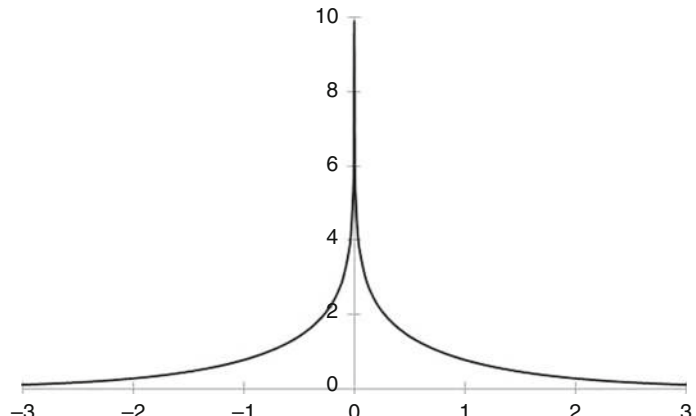
$$K''(\omega) = -\frac{2}{\pi} \int_{-\infty}^{\infty} \frac{K'(x) - K_\infty}{e^x - e^{-x}} dx = -\frac{1}{\pi} \int_{-\infty}^{\infty} \frac{K'(x) - K_\infty}{\sinh x} dx \quad (4.79)$$

Integration by parts (see Sect. 1.1.2) converts Eq. (4.79) into an expression that involves the derivative of the real part of the stiffness.

$$K''(\omega) = -\frac{1}{\pi} \int_{-\infty}^{\infty} \frac{dK'(x)}{dx} \ln \coth\left(\frac{|x|}{2}\right) dx \quad (4.80)$$

This form is particularly convenient for our single relaxation time model for two reasons: First, the derivative with respect to frequency of the real part of the stiffness, taken from Eq. (4.67), is non-zero only over a small range of frequencies near  $\omega\tau_R \approx 1$ , or  $x = 0$ . This is also evident from inspection of the solid line in Fig. 4.25; the slope is only non-zero near  $\omega\tau_R \approx 1$ . Second, the natural logarithm of the hyperbolic cotangent is also sharply peaked around  $x = 0$ , as shown in Fig. 4.26.

**Fig. 4.26** The natural logarithm of the hyperbolic cotangent of  $|x|/2$  is plotted on the vertical axis for  $-3 \leq x \leq 3$ . That function appears inside the integral in Eq. (4.80). Because it is singular at  $x = 0$ , it emphasizes the value of  $dk'/dx$  at  $x = 0$ , corresponding to  $\omega\tau_R \approx 1$



Since the  $\ln(\coth|x|/2)$  has a singularity at  $x = 0$ , it heavily weights values of the derivative near  $x = 0$ ; therefore any function,  $G(x)$ , that is multiplied by  $\ln \coth|x/2|$  can be taken outside the integral and evaluated at  $x = 0$ .

$$K''(\omega) = -\frac{1}{\pi} \int_{-\infty}^{\infty} G(x) \ln \coth\left(\frac{|x|}{2}\right) dx \quad (4.81)$$

It is then useful to expand  $G(x)$  in a Taylor series about  $x = 0$ , recognizing that  $\ln(\coth|x/2|)$  is symmetric about  $x = 0$ , so only even-order terms in the Taylor series will produce non-zero results upon integration from  $x = -\infty$  to  $x = +\infty$ .

$$G(x) \cong G(0) + \left(\frac{d^2G(x)}{dx^2}\right)_{x=0} \frac{x^2}{2!} + \left(\frac{d^4G(x)}{dx^4}\right)_{x=0} \frac{x^4}{4!} \dots \quad (4.82)$$

This transforms Eq. (4.81) into an infinite series.

$$K''(\omega) = -\frac{2}{\pi} \sum_{n=0}^{\infty} \frac{1}{(2n)!} \frac{d^{2n}G(0)}{dx^{2n}} \int_{-\infty}^{\infty} x^{2n} \ln \coth\left(\frac{|x|}{2}\right) dx \quad (4.83)$$

The integration over the sharply peaked function  $\ln(\coth|x/2|)$  converts this integral to an algebraic result since  $(0)^{2n+1} = 0$  for all  $n$ .

$$\begin{aligned} K''(\omega) &= -\frac{4}{\pi} \left( \frac{\pi^2}{8} G(0) + \frac{\pi^4}{96} \frac{d^2G(0)}{dx^2} + \dots \right) \\ &= -\frac{\pi}{2} \left( \frac{dK'(x)}{dx} \right)_{x=0} - \frac{\pi^3}{24} \left( \frac{d^3K'(x)}{dx^3} \right)_{x=0} - \dots \end{aligned} \quad (4.84)$$

At this point, all that remains is the variable transformation back to  $\omega$  from  $x$  and to evaluate the slope of the real part of the stiffness at  $x = 0$ .

$$\left( \frac{dK'}{dx} \right)_{x=0} = \frac{dK'(\omega)}{d\omega} \left( \frac{d\omega}{dx} \right)_{x=0} = \omega \left( \frac{dK'(\omega)}{d\omega} \right)_{x=0} \quad (4.85)$$

Letting  $\omega\tau_R = z$ , the slope can be calculated from Eq. (4.73) using  $d(u/v) = (v du - u dv)/v^2$  (see Sect. 1.1.2).

$$\frac{dK'(\omega)}{d\omega} = \tau_R K_1 \frac{d}{dz} \left[ \frac{z^2}{1+z^2} \right] = \tau_R K_1 \left( \frac{2z}{(1+z^2)^2} \right) \quad (4.86)$$

At  $z = \omega\tau_R = 1$ , or  $x = 0$ ,  $dK'/d\omega = \tau_R K_1/2$ . Substituting back into Eq. (4.84) provides the imaginary part of the stiffness from the slope of the real part of the stiffness.

$$K''(\omega) = -\frac{\pi}{2} \left( \frac{dK'(x)}{dx} \right)_{x=0} = -\frac{\pi\omega}{2} \left( \frac{dK'(\omega)}{d\omega} \right)_{x=0} = -\frac{\pi\omega}{2} \frac{\tau_R K_1}{2} \quad (4.87)$$

This can be compared with Eq. (4.74) by taking the negative of the ratio of  $K''(\omega)$  to  $K'(\omega)$ .

$$-\left( \frac{K''(\omega)}{K'(\omega)} \right)_{\omega\tau_R=1} = \frac{\pi}{4} \frac{K_1}{2K_o + K_1} = \frac{\pi}{8} \frac{(K_\infty - K_o)}{\left( \frac{(K_\infty + K_o)}{2} \right)} \cong 0.4 \frac{(K_\infty - K_o)}{\left( \frac{(K_\infty + K_o)}{2} \right)} \quad (4.88)$$

Again, we see that the normalized attenuation at  $\omega\tau_R = 1$  depends only upon the limiting stiffnesses,  $K_\infty$  and  $K_o$ , through their difference ( $K_\infty - K_o$ ) and their average  $(K_\infty + K_o)/2$ . Comparison to the exact results for the maximum in the normalized dissipation in Eq. (4.71) shows that the proper “average” is the geometric mean of  $K_\infty$  and  $K_o$  rather than half their sum, since the maximum does not occur exactly at  $\omega\tau_R = 1$ .

$$-\left(\frac{K''(\omega)}{K'(\omega)}\right)_{\max} = \left(\frac{\langle\Pi\rangle_t}{\omega E_{stored}}\right)_{\max} = \frac{1}{2} \frac{K_1}{\sqrt{K_o^2 + K_o K_1}} = \frac{1}{2} \frac{(K_\infty - K_o)}{\sqrt{K_o K_\infty}} \quad (4.89)$$

The peak in the  $K''(\omega)$  occurs at the maximum in the slope of  $K'(\omega)$  as shown Fig. 4.25. We can find the maximum slope from Eq. (4.86):  $(dK'/d\omega)_{\max} \cong 0.65 \text{ N-s/m}$ , and it occurs at  $(\omega\tau_R)_{\max} = 0.577$ . Substituting all of these back into Eq. (4.84) and retaining only the first term in the Taylor series, the value of  $K''(\omega)$  is equal to the exact result in Eq. (4.73) to within 2%.

$$\begin{aligned} [K''(\omega)]_{\max} &= -\frac{\pi}{2} \left( \frac{dK'(x)}{dx} \right)_{\max} = -\frac{\pi\omega}{2} \left( \frac{dK'(\omega)}{d\omega} \right)_{\max} \\ &\cong -\frac{0.65\tau_R\pi\omega}{2} K_1 \cong 1.02(\omega\tau_R)K_1 \end{aligned} \quad (4.90)$$

## 4.5 Rubber Springs

Rubberlike materials are used to make springs for vibration isolation. There is an extraordinary variety of commercial vibration mounts that use rubber and provide fixtures (threaded studs, mounting flanges, brackets, etc.) to isolate loads from vibrating foundations and vice versa. There are several reasons why rubber is so popular in such isolators. One of the most important reasons is that rubber can tolerate strains in excess of 100% (it can change its dimensions by a factor of two) while neither failing (fracture or tear) nor exhibiting significant inelasticity. Rubber also simultaneously provides both damping and stiffness (and does not “drip” like the viscous liquid in our idealized dashpots). As will be demonstrated in this section, damping is essential to control the behavior of the isolator if there is an excitation at the natural frequency determined by the mass of the load and the stiffness of the isolator(s).

When a machine is mounted on an isolator, the natural frequency of the isolator should be well below the operating frequency of the isolated machine. Of course, machines are started and stopped, and therefore during start-up, the frequency changes from zero to the operating frequency, so they must pass through the isolator’s resonance frequency. Clearly, the isolator will have to provide sufficient damping so that the vibrations are limited as the machine passes through the isolator’s natural frequency.

Another attractive feature of rubber is that chemists are very skilled at formulating rubberlike compounds in ways that can tailor its properties to produce the desired combination of damping and stiffness,<sup>17</sup> as well as make those rubberlike materials resistant to various environmental irritants (solvents, ozone) and mechanical degradation (tear and abrasion resistance).

In this section, we will combine our understanding of the simple harmonic oscillator and of viscoelasticity to provide a framework for understanding the vast literature addressing the applications of vibration isolators using rubberlike materials. A few calculations for a single degree-of-freedom

<sup>17</sup> Carbon black (soot) is a common material that is mixed with rubber to increase its stiffness and strength. The shear modulus of natural rubber (latex) can increase by an order of magnitude if it is mixed with carbon black.

vibration isolator will demonstrate the utility of the internal damping provided by rubberlike materials to the control of vibrations of an isolator that is excited by a frequency component that coincides with the isolator's natural frequency,  $\omega_o$ . Extensions of this approach to multistage isolators, Lanchester dampers, dynamic absorbers, etc., are provided in handbooks on shock and vibration control [36] and in Snowdon's textbook [39].

### 4.5.1 Effective Modulus

In the earliest sections of this chapter, the various (lossless) moduli used to describe the response of isotropic elastic solids were defined and related to each other (see Table 4.1). Rubberlike materials have values of Poisson's ratio that are very close to one-half,  $\nu_{rubber} \cong \frac{1}{2}$ , corresponding to the volume-preserving behavior of liquids derived in Eq. (4.3). In the limit that  $\nu_{rubber}$  approaches one-half, it can be shown that the effects of the bulk modulus,  $B$ , of rubber dominate the effects of the shear modulus,  $G$ , in the determination of the modulus of unilateral compression,  $D$ . Young's modulus,  $E$ , will be approximately three times the shear modulus for rubberlike materials.

$$\lim_{\nu \rightarrow \frac{1}{2}} \left[ \frac{B}{G} \right] = \lim_{\nu \rightarrow \frac{1}{2}} \left[ \frac{2(1+\nu)}{3(1-2\nu)} \right] = \infty \quad (4.91)$$

Since  $G$  can be neglected in comparison to  $B$  if  $\nu_{rubber} \cong \frac{1}{2}$ , the modulus of unilateral compression,  $D$  (aka, dilatational modulus), is nearly equal to  $B$ . The modulus of unilateral compression determines the longitudinal wave speed,  $c_{long} = (D/\rho)^{\frac{1}{2}}$ .

$$\lim_{\nu \rightarrow \frac{1}{2}} [D] = \lim_{\nu \rightarrow \frac{1}{2}} \left[ B + \left( \frac{4G}{3} \right) \right] = B \quad (4.92)$$

As shown in Eq. (4.91),  $B \gg G$ , so in this limit, Young's modulus,  $E$ , is three times the shear modulus,  $G$ .

$$\lim_{\nu \rightarrow \frac{1}{2}} [E] = \lim_{\nu \rightarrow \frac{1}{2}} \left[ \frac{9BG}{(3B+G)} \right] = 3G \quad (4.93)$$

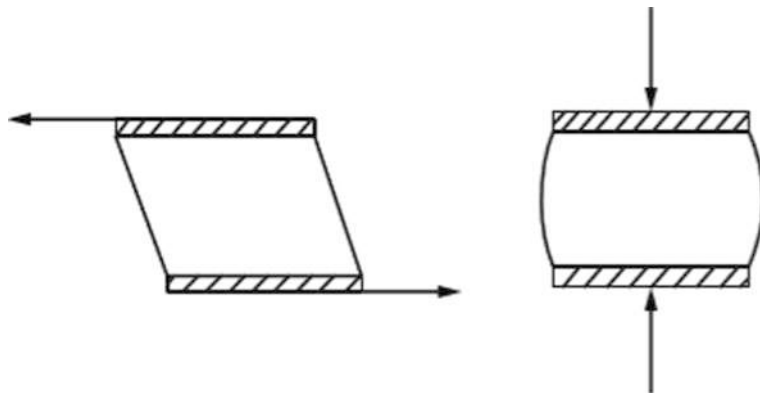
In many vibration isolation applications, rubber springs are adhesively bonded to metal plates, so the actual constraints that led to the calculation of the moduli in Table 4.1 do not always reflect their use in practice. If a rubber sample is placed in pure shear, as shown in Fig. 4.27 (left), then the shear stress and shear strain are simply related by the shear modulus,  $G$ , as shown in Eq. (4.17). If the same combination of plates bonded to rubber is subjected to compressive stresses, as shown in Fig. 4.27 (right), then the strains are less than predicted by Young's modulus,  $E$ , but more than predicted by the modulus of unilateral compression,  $D$ , for the same stress.

Empirical relations have been developed that accommodate these constraints on the boundary between the rubber and the mounting plates commonly used for rubber vibration isolators. Such rubber springs have aspect ratios that are close to unity and produce an effective (apparent) modulus,  $E_a > E$ .

$$E_a = (1 + \beta S^2)E = 3(1 + \beta S^2)G \quad (4.94)$$

In Eq. (4.94),  $S$  is called a dimensionless *shape factor* that is defined as the ratio of the area of one loaded face, such as the plate in Fig. 4.27 (right), to the total area of the unloaded faces. The values of  $\beta$  have been calculated analytically and measured experimentally. It is found that for samples that are

**Fig. 4.27** A rubberlike sample is adhesively bonded to two metal plates. (Left) The sample is subjected to shear stress. (Right) The sample is subjected to compressive stress



circular, square, or modestly rectangular (width and length are not too dissimilar), then  $\beta \cong 2$ . For the cylindrical sample of radius,  $a$ , shown schematically in Fig. 4.27 (right),  $S = (\pi a^2)/(2\pi ah) = a/2 h$ , so  $E_a \cong 3[1 + 2(a/2 h)^2] G$ . If  $h = 2a$ , producing a cylinder of unity aspect ratio, then  $E_a \cong 3.4G$ .

#### 4.5.2 Rubber-to-Glass Transition (Type I and Type II Rubbers)

The standard linear model (SLM) for viscoelasticity was predicated on the existence of a single relaxation time,  $\tau_R = R_m/K_1$ . At frequencies well below  $\omega\tau_R = 1$ , the dynamic stiffness,  $K'$ , is constant, and the normalized dissipation increases linearly with frequency but is always small:  $K''/K' \ll 1$ . This behavior is apparent in Fig. 4.25, where the normalized dissipation is plotted as  $2\pi\omega E_{\text{stored}}/\langle \Pi(t) \rangle_t = 2\pi(K''/K')$  [26]. For a rubberlike material, this behavior corresponds to a frequency-independent *dynamic shear modulus*,  $G$ , and a small dissipation factor,  $\delta \ll 1$ . For rubbers, this is designated Type I (low damping) behavior, typical of natural rubber (latex) and neoprene rubber.

At frequencies near  $\omega\tau_R \cong 1$ , the dynamic stiffness,  $K'$ , is increasing with frequency (linearly in the SLM), and the normalized dissipation is nearly constant with  $K''/K' \cong 1$ . For a rubberlike material, this behavior corresponds to a frequency-dependent dynamic shear modulus,  $G(\omega)$ , and a nearly constant (frequency independent) dissipation factor,  $\delta \cong 1$ . For rubbers, that is Type II (high damping) behavior. Synthetic rubberlike materials like Thiokol RD, plasticized polyvinyl butyl resin (PVB), plasticized polyvinyl acetate (PVA), and filled (with carbon black) butyl rubber (like auto tire tubes) are examples of rubbers exhibiting Type II behavior.

The relaxation time,  $\tau_R$ , clearly plays an important role in the behavior of rubberlike materials that are well-represented by the SLM, since it scales the excitation frequency. The relaxation time can be strongly temperature dependent. Figure 4.28, taken from Capps [26], shows Type I behavior in the “Rubbery Region” and Type II behavior in the “Glass-Rubber Transition,” where Capps uses *storage modulus* for the real part of the elastic modulus and *loss factor* or *loss tangent* for the dimensionless imaginary part.

The variation in the dynamic Young's modulus and normalized damping, represented by the ratio of the real and imaginary parts of Young's modulus, is sketched by Nolle [37] as a function of both temperature and frequency for nitrile (buna-N) rubber in Fig. 4.29. Those sketches provide a graphical representation of the mutual effects of frequency and temperature on the dynamic modulus and normalized loss.

This relationship between temperature and frequency for viscoelastic materials can be viewed as reflecting the mobility of the material's molecular arrangements at the microscopic level [26]. At a

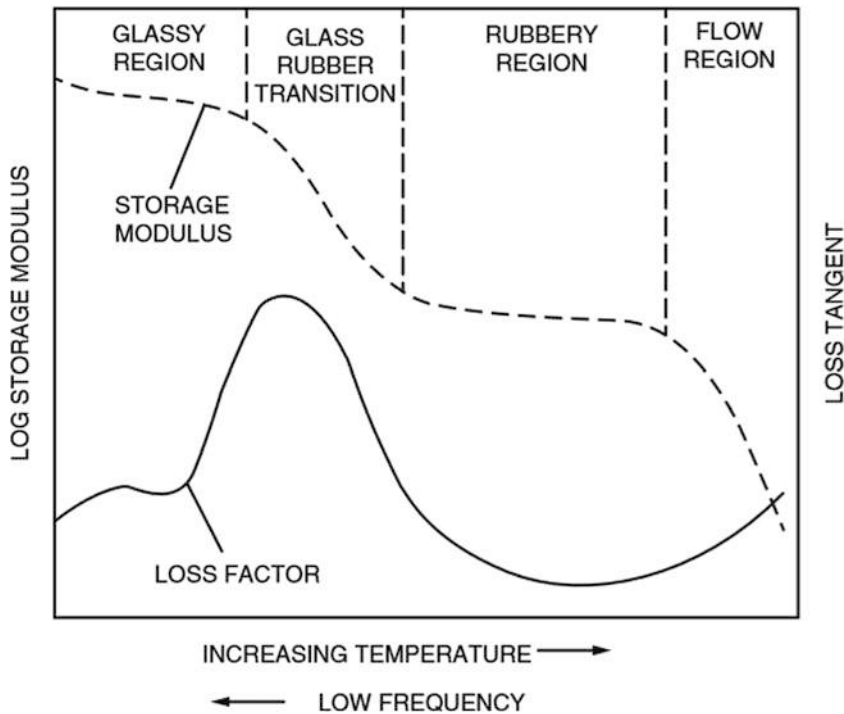


**Fig. 4.28** The behavior of rubberlike materials is a strong function of both frequency and temperature. This figure is taken from Capps [26]. At the highest frequencies and/or the lowest temperatures, rubbers are “glassy” with higher dynamic moduli and low loss. At higher temperatures and/or lower frequencies, rubberlike materials have low damping and lower moduli (Type I). In the transition region, where  $\omega\tau_R \approx 1$ , the moduli change with frequency and the damping (loss factor) reaches its peak (Type II). At sufficiently high temperatures and/or low frequencies, rubberlike materials can creep or flow. See Fig. 1.16 for creep of an elastomeric loudspeaker surround

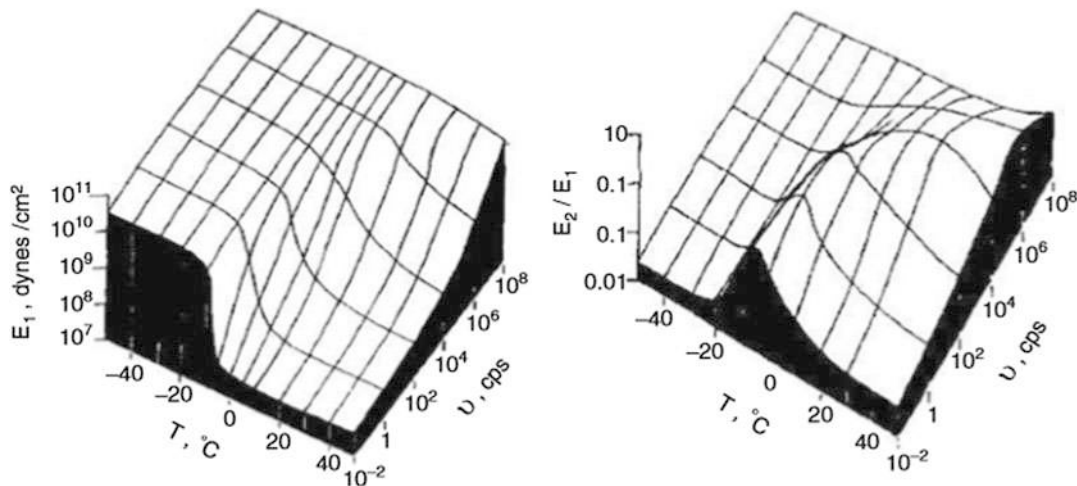


**Fig. 4.29** (Left) A sketch based on experimental measurements of the dynamic Young's modulus,  $E_1$ , for a carbon-filled buna-N rubber (compound B-5) as a function of both temperature and frequency displayed in cgs units. (Right) A sketch of the ratio of dynamic loss modulus,  $E_2$ , to dynamic Young's modulus,  $E_1$ , for the same material over frequency and temperature [37]

constant excitation frequency, the internal molecular arrangement changes to a more mobile configuration as the temperature increases and the material becomes more compliant. Conversely, a reduction in temperature causes a reduction in molecular mobility,<sup>18</sup> so the material stiffens.

If the temperature is held constant and the excitation frequency is varied, a related but inverse phenomenon can be postulated. For low frequencies, the period of the excitation is long enough that the molecules have time to coil and uncoil, resulting in rubberlike behavior (like when the rubber is warm). At high frequencies, the molecules do not have sufficient time to relax and the material is stiff (like when the rubber is cold).

For viscoelastic materials, there is a correspondence between the frequency and temperature that can be combined using the time-temperature superposition by the application of the Williams-Landel-Ferry equation [38]. Utilization of this method for producing “master curves” that plot scaled temperature and frequency on a single axis will be postponed until Chap. 5 when the measurement of complex modulus using the resonances of thin bars will be presented.

### 4.5.3 Transmissibility of Rubberlike Vibration Isolators

We can now combine our understanding of simple harmonic oscillators and viscoelastic materials to calculate the transmissibility of rubberlike vibration isolators. As before, we start with a differential equation for a single degree-of-freedom mass and spring, but this time, we will allow the spring’s stiffness to be complex, reflecting both its elasticity and its internal damping. As we proceed, we will have in mind a displacement-driven system (see Sect. 2.5.6) with a foundation that vibrates harmonically at a single frequency with an amplitude,  $x_1(t) = x_1 \cos(\omega t)$ , and we will calculate the displacement of the mass from its equilibrium position,  $\mathbf{x}_2(t) = \hat{\mathbf{x}}_2 e^{j\omega t}$ , where  $\mathbf{x}_2$  is considered to be a complex number to reflect the possibility that the phases of  $\mathbf{x}_1$  and  $\mathbf{x}_2$  will be different, as well as their amplitudes. By letting the amplitude,  $x_1$ , be a real scalar, we are setting that displacement as the phase reference for  $\hat{\mathbf{x}}_2$ .

$$m \frac{d^2 \mathbf{x}_2}{dt^2} = -\omega^2 m \mathbf{x}_2 = \gamma \Xi(\omega) (x_1 - \hat{\mathbf{x}}_2) e^{j\omega t} \quad (4.95)$$

The generic, frequency-dependent (complex) elastic modulus,  $\Xi(\omega) = |\Xi(\omega)|(1 + j\delta)$ , has been introduced along with a scalar geometrical factor,  $\gamma$ , that has the dimensions of length, to convert the modulus into a stiffness (see Sect. 4.4.3). For a shear isolator, like that shown in Fig. 4.27 (left),  $\gamma = A/h$ , where  $A$  is the area of the plate and  $h$  is the thickness of the rubber, and  $|\Xi| = G$ . For the compressional spring, shown in Fig. 4.27 (right),  $\gamma = (3A/h)(1 + \beta S^2)$ , again with  $|\Xi| = G$ .

The complex ratio of  $\mathbf{x}_2/x_1$  follows directly from Eq. (4.95).

$$\frac{\mathbf{x}_2}{x_1} = \frac{\gamma \Xi(\omega)}{(\gamma \Xi(\omega) - \omega^2 m)} = \frac{1 + j\delta(\omega)}{[1 - (\omega^2 m / \gamma |\Xi(\omega)|) + j\delta(\omega)]} \quad (4.96)$$

The square of the normal mode frequency,  $\omega_o$ , for the undriven harmonic oscillator will be given by the usual expression, although we must take care to evaluate the frequency-dependent modulus,  $\Xi(\omega)$ , at the normal mode frequency. At that frequency, the generic modulus will be designated  $\Xi_o = |\Xi(\omega_o)|$ .

<sup>18</sup> Said another way, the molecular mobility is “frozen out.”

$$\omega_o^2 = \frac{\gamma \Xi_o}{m} \quad (4.97)$$

With that definition, the complex ratio of  $\mathbf{x}_2/x_1$  can be expressed in terms of a frequency ratio,  $\Omega = \omega/\omega_o$ .

$$\frac{\mathbf{x}_2}{x_1} = \frac{(1 + j\delta(\omega))}{\left[1 - \Omega^2 \left(\frac{|\Xi_o|}{|\Xi(\omega)|}\right)^2 + j\delta(\omega)\right]} \quad (4.98)$$

For subsequent analyses, it will be convenient to define a transmissibility,  $T$ , as the magnitude of the complex ratio,  $|\mathbf{x}_2/x_1|$ , and a phase angle,  $\theta$ .

$$T \equiv \left| \frac{\mathbf{x}_2}{x_1} \right| = \frac{(1 + \delta^2(\omega))^{1/2}}{\sqrt{\left[1 - \Omega^2 \left(\frac{|\Xi_o|}{|\Xi(\omega)|}\right)^2\right]^2 + \delta^2(\omega)}} \quad (4.99)$$

$$\theta = \tan^{-1} \left( \frac{I}{R} \right) = \tan^{-1} \left\{ \frac{-\delta(\omega) \Omega^2 \left( \frac{|\Xi_o|}{|\Xi(\omega)|} \right)}{\left[1 - \Omega^2 \left( \frac{|\Xi_o|}{|\Xi(\omega)|} \right)^2\right] + \delta^2(\omega)} \right\}$$

with  $R + jI = (1 + j\delta(\omega)) \left[1 - \Omega^2 \left( \frac{|\Xi_o|}{|\Xi(\omega)|} \right)^2 - j\delta(\omega)\right]$

These expressions can now be applied to Type I and Type II rubberlike materials and to the SLM for viscoelastic materials characterized by a single relaxation time,  $\tau_R$ .

Type I rubberlike materials exhibit behavior similar to a viscoelastic material driven at frequencies that make  $\omega\tau_R \ll 1$ , resulting in a shear modulus that is frequency independent. Although viscoelastic materials in that frequency regime have normalized damping that increases linearly with frequency, the damping is always small. For Type I rubberlike materials, the dissipation factor will typically range from  $0.02 \leq \delta_I \leq 0.20$  and is usually considered to be frequency independent. Under those assumptions, Eq. (4.99) can be written for this typical Type I transmissibility,  $T_I$ , with the phase angle,  $\theta_I$ .

$$T_I = \sqrt{\frac{1 + \delta_I^2}{\left[(1 - \Omega^2)^2 + \delta_I^2\right]}} \quad \text{and} \quad \theta_I = \tan^{-1} \left[ \frac{-\delta \Omega^2}{1 - \Omega^2 + \delta_I^2} \right] \quad (4.100)$$

In the limit of high frequencies,  $\Omega \gg 1$ , such a Type I isolator will have transmissibility that decreases as the square of the frequency.

$$\lim_{\Omega \rightarrow \infty} [T_I] = \frac{1}{\Omega^2} \quad (4.101)$$

This inverse quadratic frequency dependence is often specified as  $-40$  dB/decade or  $-12$  dB/octave. At resonance, the transmissibility,  $T_I(\omega_o)$ , depends only upon the damping.

$$T_I(\omega_o) = \frac{\sqrt{1 + \delta_I^2}}{\delta_I} \cong \frac{1 + \frac{\delta_I}{2}}{\delta_I} \cong \frac{1}{\delta_I} \quad \text{for} \quad \delta_I \ll 1 \quad (4.102)$$

Figure 4.30 shows a plot of Eq. (4.100) for  $\delta_I = 0.02$  and  $\delta_I = 0.20$ .

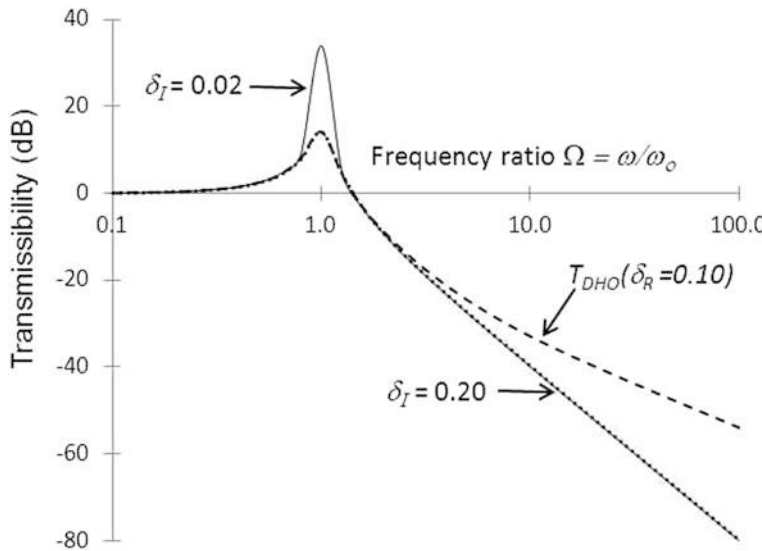


**Fig. 4.30** Transmissibility for a Type I rubberlike single degree-of-freedom mass-spring system with  $\delta = 0.02$  (solid line) and  $\delta = 0.20$  (dotted line) plotted as a function of frequency ratio,  $\Omega$ . For comparison, the dashed line represents a damped, displacement-driven, harmonic oscillator (DHO) with its damping adjusted to match the peak at  $\omega_o$  for the  $\delta = 0.20$  Type I case. At frequencies well above all this isolator's natural frequency,  $\omega_o$ , both Type I isolators have transmissibilities that decrease with the square of the frequency ( $-40$  dB/decade), but  $T_{DHO}$  only falls off at  $-20$  dB/decade

For comparison, the transmissibility,  $T_{DHO}$ , of a mass supported by a mechanically parallel spring and dashpot combination (i.e., damped harmonic oscillator) is also shown in Fig. 4.30 as the dashed line with the mechanical resistance of the dashpot,  $R_m$ , chosen to match the Type I transmissibility for  $\delta_I = 0.20$ , at  $\omega_o$ . To express Eq. (2.92) for the displacement-driven damped harmonic oscillator in the form of Eq. (4.100), the damping factor,  $\delta_I$ , will be replaced by the damped harmonic oscillator's damping ratio,  $\delta_R = \tau/\tau_{crit} = R_m\omega_o/2K$ . The exponential decay time for critical damping (see Sect. 2.4.3) is  $\tau_{crit} = \omega_o^{-1}$ .

$$T_{DHO} = \sqrt{\frac{1 + (2\Omega\delta_R)^2}{(1 - \Omega^2)^2 + (2\Omega\delta_R)^2}} \quad (4.103)$$

$$\theta_{DHO} = \tan^{-1} \left[ \frac{-(2\Omega\delta_R)\Omega^2}{1 - \Omega^2 + (2\Omega\delta_R)^2} \right]$$

The value of  $\delta_R = 0.10$  was chosen to match the peak in the transmissibility at  $\omega_o$  in Fig. 4.30 for  $\delta_I = 0.20$ .

Although the damped harmonic oscillator is frequently used as a model for typical vibration isolators, Fig. 4.30 illustrates that it is not truly representative of an isolator that uses a Type I rubberlike material as the spring. In our assumptions for the behavior of a Type I material (frequency-independent damping and stiffness), the damping factor was a constant. Inspection of Eq. (4.103) shows that the equivalent damping factor,  $2\Omega\delta_R$ , for the damped harmonic oscillator increases linearly with frequency. This behavior of a damped harmonic oscillator (DHO) accounts for

the inverse linear decrease ( $-20$  dB/decade) in  $T_{DRO}$  at frequencies well above  $\omega_o$ , rather than the inverse quadratic frequency dependence ( $-40$  dB/decade) for the Type I curves.<sup>19</sup>

Type II rubberlike materials exhibit behavior that is similar to a viscoelastic material described by the standard linear model of Sect. 4.4.2 around frequencies close to the relaxation frequency,  $\omega\tau_R \approx 1$ . In that frequency range, the stiffness is an approximately linear function of frequency. As is evident from Fig. 4.25, viscoelastic materials in that frequency range have normalized damping factors that are nearly frequency-independent and large,  $\delta_H \gtrsim 0.5$ , if  $K_0 \neq K_\infty$ . Under those assumptions, Eq. (4.99) can be written for this typical Type II transmissibility,  $T_H$ , with the phase angle,  $\theta_H$ .

$$T_H = \sqrt{\frac{1 + \delta_H^2}{[(1 - \Omega)^2 + \delta_H^2]}} \quad \text{and} \quad \theta_H = \tan^{-1} \left[ \frac{-\delta_H \Omega}{1 - \Omega + \delta_H^2} \right] \quad (4.104)$$

Figure 4.31 shows a plot of Eq. (4.104) for  $\delta_H = 0.50$  and  $\delta_H = 1.0$ . For comparison, the transmissibility of the damped harmonic oscillator,  $T_{DHO}$ , is also shown as the dashed line with the mechanical resistance of the dashpot,  $R_m$ , chosen to match the Type II transmissibility for  $\delta_H = 0.50$  at  $\omega_o$ .

The difference in the shape of  $T_{DHO}$  in Fig. 4.31 from that of the two  $T_H$  curves is related to the fact that the stiffness of the damped harmonic oscillator is constant, whereas the stiffness of the Type II isolator is assumed to increase linearly with frequency. It is that changing stiffness that broadens the peak transmissibilities around  $T_H > 0$  dB.

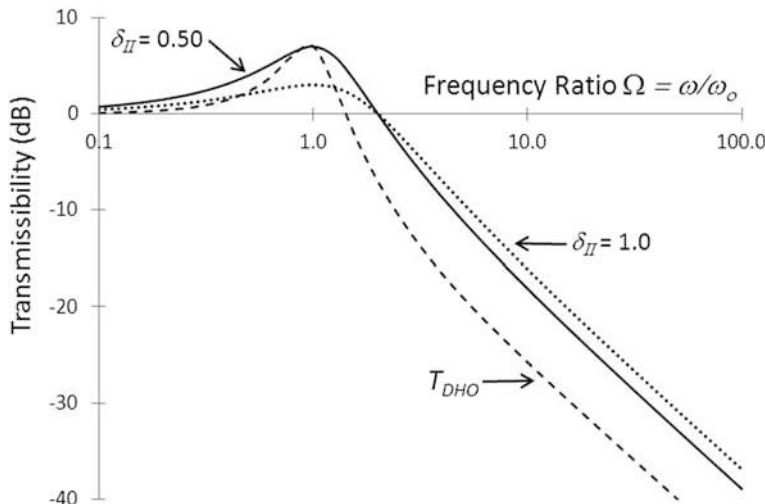


**Fig. 4.31** Transmissibility for a Type II rubberlike mass-spring system with  $\delta_H = 0.5$  (solid line) and  $\delta_H = 1.0$  (dotted line) is plotted against the frequency ratio,  $\Omega$ . For comparison, the dashed line represents a damped, displacement-driven, harmonic oscillator with its damping adjusted to match the peak at  $\omega_o$  for the Type II case,  $\delta_H = 0.50$ . At frequencies well above the isolator's natural frequency, both Type II isolators and the damped harmonic oscillator have transmissibilities that decrease linearly with increasing frequency (i.e.,  $-20$  dB/decade)

<sup>19</sup> Recall from Sect. 2.5.2 that decibel is defined in terms of a power or energy ratio (see Eq. 2.69). Since transmissibility,  $T$ , is a ratio of linear quantities, as defined in Eq. (2.96), it can be expressed as a decibel only when squared:  $\text{dB} = 10 \log_{10} T^2 = 20 \log_{10} T$ .

The transmissibility of an isolator, based on a complex stiffness which behaves according to the SLM viscoelastic model, can also be calculated. The two important considerations are the tuning of the transition frequency given in Eq. (4.71) as  $\omega_{\max} = \tau_R^{-1} \sqrt{K_o/K_\infty}$ , to the isolator's natural frequency (based on the low-frequency limiting stiffness,  $K_o$ ),  $\omega_o \equiv (K_o/m)^{1/2}$ . The difference between the zero-frequency stiffness,  $K_o$ , and the infinite-frequency stiffness,  $K_\infty$ , determines the maximum damping factor, as shown in Eq. (4.89). Following Snowdon [39], the transmissibility is parameterized by the tuning ratio,  $\aleph \equiv \omega_{\max}/\omega_o$ , and the stiffness ratio,  $\alpha \equiv K_\infty/K_o$ , which determines the maximum value of the damping factor,  $\delta_{\max}$ .

$$\delta_{\max} = \frac{\alpha - 1}{2\sqrt{\alpha}} = \frac{1}{2} \frac{K_\infty - K_o}{\sqrt{K_\infty K_o}} \quad \text{or} \quad \alpha \equiv \frac{K_\infty}{K_o} = 1 + 2\delta_{\max} \sqrt{1 + \delta_{\max}^2} + 2\delta_{\max}^2 \quad (4.105)$$

Substitution into the general transmissibility equation of Eq. (4.99) yields the transmissibility for an SLM viscoelastic isolator that includes the exact frequency dependencies of both damping and stiffness for such a single relaxation time model.

$$T_{SLM} = \sqrt{\frac{(\Omega^2 + \aleph^2)^2 + (2\aleph\Omega\delta_{\max})^2}{[(\Omega^2 + \aleph^2) - \Omega^2(\Omega^2 + \alpha\aleph^2)\left(\frac{1+\aleph^2}{1+\alpha\aleph^2}\right)]^2 + (2\aleph\Omega\delta_{\max})^2}} \quad (4.106)$$

The behavior of the SLM viscoelastic transmissibility,  $T_{SLM}$ , is shown in two graphs presented as Fig. 4.32. First, the transmissibility is calculated for three different ratios of the limiting stiffnesses:  $\alpha = K_\infty/K_o = 1.5, 3.0$ , and  $6.0$ , corresponding to  $\delta_{\max} = 0.20, 0.58$ , and  $1.02$ , respectively. For all three cases, the high-frequency behavior shows an inverse quadratic dependence on frequency in the transmissibility corresponding to  $-40$  dB/decade.

Shown for comparison in Fig. 4.32 as the dash-dotted line is also the transmissibility of a damped harmonic oscillator with a damping ratio,  $\delta_R = 0.29$ , that matches the peak transmissibility of the viscoelastic isolator with  $\delta_{\max} = 0.58$ . As shown in Fig. 4.32, the transmissibility of the viscoelastic

**Fig. 4.32** The transmissibility,  $T_{SLM}$ , of a single degree-of-freedom isolator based on the SLM viscoelastic model is calculated for three different ratios of the limiting stiffnesses:  $\alpha = K_\infty/K_o = 1.5$  (solid),  $3.0$  (dotted), and  $6.0$  (dashed), corresponding to  $\delta_{\max} = 0.20$  (solid),  $0.58$  (dotted), and  $1.02$  (dashed). All three cases have  $\omega_o = \omega_t = \tau_R^{-1}$ , so the tuning parameter,  $\aleph = 1.0$ . For comparison, the transmissibility,  $T_{DHO}$ , of a damped harmonic oscillator with  $\delta_R = 0.29$  is shown (dash-dotted) which matches the peak transmissibility of the  $\delta_{\max} = 0.58$  case.

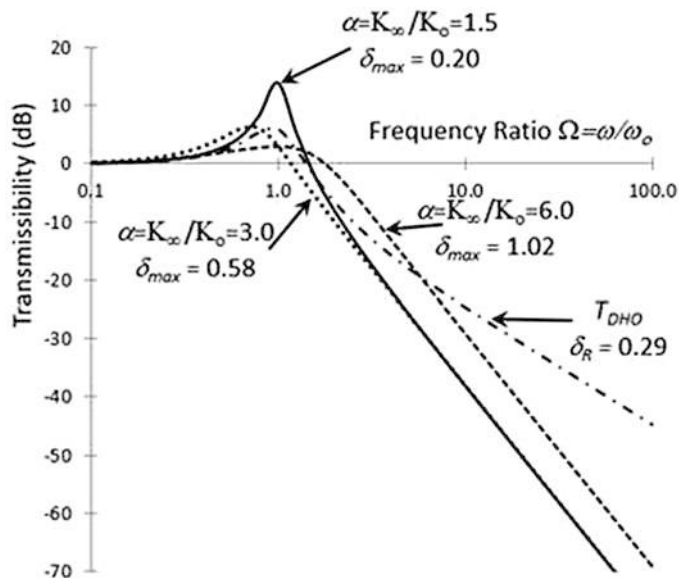
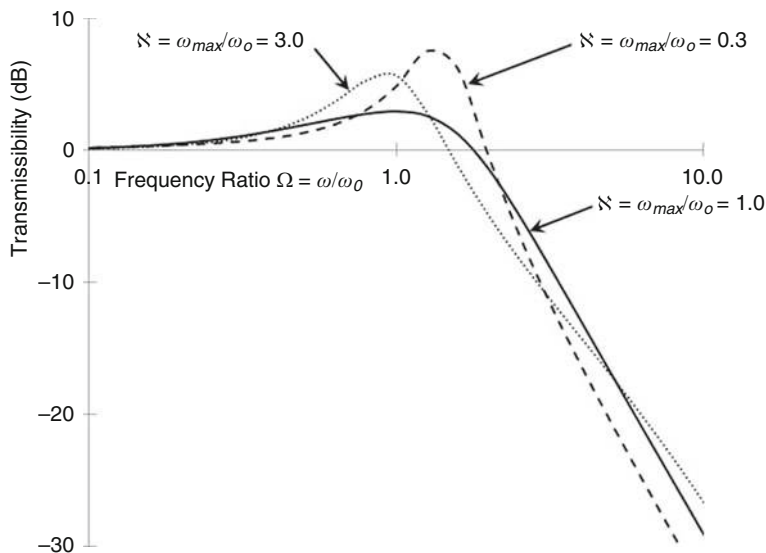


**Fig. 4.33** The effects of “tuning” the transition frequency are illustrated for the SLM viscoelastic isolator. The solid line represents  $\aleph \equiv \omega_{max}/\omega_o = 1.0$  with  $\alpha = K_\infty/K_o = 6.0$ , corresponding to  $\delta_{max} = 1.02$ , for all curves. The other two curves represent a “flat” detuning (peak transmissibility at a lower frequency) with  $\aleph = 3.0$  (dotted) and a “sharp” detuning with  $\aleph = 0.3$  (dashed)



rubber isolator falls off more rapidly with frequency than the damped simple harmonic oscillator since the rubber stiffness is constant at  $\Omega \gg 1$  and the damping is decreasing with frequency, whereas the damped harmonic oscillator’s damping is increasing with frequency although  $\delta_R$  is constant.

The viscoelastic transition frequency,  $\omega_t = \tau_R^{-1}$ , is a strong function of temperature for most viscoelastic materials. This needs to be considered in isolator design since the temperature dependence of  $\omega_t$  will shift the “tuning” parameter,  $\aleph \equiv \omega_{max}/\omega_o$ . In Fig. 4.33, all three transmissibility curves have  $\alpha = K_\infty/K_o = 6.0$  corresponding to  $\delta_{max} = 1.02$ . They differ in the tuning of the harmonic oscillator natural frequency,  $\omega_o$ , to the peak in the dissipation at  $\omega_{max}$ . The solid line in Fig. 4.33 and the solid line in Fig. 4.32 represent  $\aleph \equiv \omega_{max}/\omega_o = 1$ . The other two curves in Fig. 4.33 represent a “flat” detuning (peak transmissibility at a lower frequency) with  $\aleph = 3.0$  (dotted line) and a “sharp” detuning with  $\aleph = 0.3$  (dashed line). The tuning, which will be a function of temperature, affects both the maximum damping and the transmissibility at high frequencies.

## 4.6 Anisotropic (Crystalline) Elasticity\*

There are many materials that are not isotropic, both naturally occurring and synthetic. Wood is a composite material that exhibits different elastic behavior depending on whether forces are applied along the grain or across it. The same is true for many composite materials, whether they are carbon fiber composites or resin-soaked fiberglass. Natural crystals can have very complicated anisotropy (see Table 4.2). When a material has its own internal preferred “coordinate system,” whether it is defined by crystalline axes or the orientation of a fibrous matrix, it is possible that stresses in one direction lead to strains in other directions. This was also true of isotropic materials as illustrated by the transverse displacements caused by longitudinal stress that were transferred by a non-zero Poisson’s ratio.

**Table 4.2** The number of independent stiffness matrix elements, or combinations of matrix elements and angles, required to completely specify the elastic response of crystals varies with the symmetry of the crystals

Crystal class	Symmetry group	Independent elements and angles	Minimum elements
Triclinic	C <sub>1</sub> , C <sub>i</sub>	21	18
Monoclinic	C <sub>s</sub> , C <sub>2</sub> , C <sub>2h</sub>	13	12
Orthorhombic	C <sub>2v</sub> , D <sub>2</sub> , D <sub>2h</sub>	9	9
Tetragonal	C <sub>4</sub> , S <sub>4</sub> , C <sub>4h</sub>	7	6
Tetragonal	C <sub>4v</sub> , D <sub>2d</sub> , D <sub>4</sub> , D <sub>4h</sub>	6	6
Rhombohedral	C <sub>3</sub> , S <sub>6</sub>	7	6
Rhombohedral	C <sub>3</sub> , D <sub>3</sub> , D <sub>3d</sub>	6	6
Hexagonal	C <sub>6</sub>	5	5
Cubic		3	3

The most general form of Hooke's law that incorporates all known anisotropic effects can be expressed as a square *stiffness matrix* that relates stresses and strains.

$$\begin{pmatrix} \sigma_{xx} \\ \sigma_{yy} \\ \sigma_{zz} \\ \sigma_{xy} \\ \sigma_{yz} \\ \sigma_{zx} \end{pmatrix} = \begin{pmatrix} \sigma_{11} \\ \sigma_{22} \\ \sigma_{33} \\ \sigma_{23} \\ \sigma_{31} \\ \sigma_{12} \end{pmatrix} \equiv \begin{pmatrix} \sigma_1 \\ \sigma_2 \\ \sigma_3 \\ \sigma_4 \\ \sigma_5 \\ \sigma_6 \end{pmatrix} = \begin{pmatrix} s_{11} & s_{12} & s_{13} & s_{14} & s_{15} & s_{16} \\ s_{21} & s_{22} & s_{23} & s_{24} & s_{25} & s_{26} \\ s_{31} & s_{32} & s_{33} & s_{34} & s_{35} & s_{36} \\ s_{41} & s_{42} & s_{43} & s_{44} & s_{45} & s_{46} \\ s_{51} & s_{52} & s_{53} & s_{54} & s_{55} & s_{56} \\ s_{61} & s_{62} & s_{63} & s_{64} & s_{65} & s_{66} \end{pmatrix} \begin{pmatrix} \epsilon_1 \\ \epsilon_2 \\ \epsilon_3 \\ \epsilon_4 \\ \epsilon_5 \\ \epsilon_6 \end{pmatrix} \quad (4.107)$$

The stresses can be resolved into forces applied along a coordinate axis direction ( $x$ ,  $y$ , or  $z$ ), normal to the surface of the sample, to produce the longitudinal (compressive) stresses  $\sigma_{xx}$ ,  $\sigma_{yy}$ , or  $\sigma_{zz}$ . Shearing forces can also be applied along a coordinate axis, but orthogonal to the surface normal directions producing the shear stresses,  $\sigma_{xy}$ ,  $\sigma_{yz}$ , or  $\sigma_{zx}$ .

To simplify the matrix representation, the coordinate axes can be specified by integer indices:  $i = 1$  for  $x$ ,  $i = 2$  for  $y$ , and  $i = 3$  for  $z$ . Further simplification in the nomenclature can be achieved if the shear stresses are encoded as  $i = 4$  for  $yz$ ,  $i = 5$  for  $xz$ , and  $i = 6$  for  $xy$ . This simplified indexing scheme, known as *Voigt notation*, has been applied to the strains,  $\epsilon_i$ , as well in Eq. (4.107).

The six components of stress,  $\sigma_i$ , and the six components of strain,  $\epsilon_i$ , are related by the stiffness matrix shown in Eq. (4.107). In principle, that square matrix contains 36 independent elements. Due to the symmetry of the stresses and strains ( $\sigma_{xy} = \sigma_{yx}$ , etc.), the matrix is symmetric, with stiffness elements,  $s_{ij} = s_{ji}$ , so there are only 21 potentially independent elements.

The actual number of elements required to completely specify the elastic response of a crystal depends upon the symmetry of the crystal lattice. We already know that an isotropic solid requires only two independent elements. A cubic crystal requires three. The triclinic crystal requires all 21, although that number can be reduced by suitable choice of coordinate axes. For a triclinic crystal, the non-zero moduli are reduced to 18 by alignment of the coordinate axes with the principle directions of the crystal lattice. Table 4.2 summarizes the number of matrix elements required for complete specification of all crystal groups.

Figure 4.34 provides examples of the stiffness matrix for crystalline solids with cubic and hexagonal symmetry.

These individual matrix elements can be related to the moduli of isotropic solids where there must only be two independent matrix elements,  $s_{11}$  and  $s_{44}$ .

$$\begin{pmatrix} s_{11} & s_{12} & s_{12} & 0 & 0 & 0 \\ s_{12} & s_{11} & s_{12} & 0 & 0 & 0 \\ s_{12} & s_{12} & s_{11} & 0 & 0 & 0 \\ 0 & 0 & 0 & s_{44} & 0 & 0 \\ 0 & 0 & 0 & 0 & s_{44} & 0 \\ 0 & 0 & 0 & 0 & 0 & s_{44} \end{pmatrix} \quad \begin{pmatrix} s_{11} & s_{12} & s_{13} & 0 & 0 & 0 \\ s_{12} & s_{11} & s_{13} & 0 & 0 & 0 \\ s_{13} & s_{13} & s_{33} & 0 & 0 & 0 \\ 0 & 0 & 0 & s_{44} & 0 & 0 \\ 0 & 0 & 0 & 0 & s_{44} & 0 \\ 0 & 0 & 0 & 0 & 0 & s_{66} \end{pmatrix}$$

**Fig. 4.34** Stiffness matrices for a cubic crystal (left) contain three independent stiffnesses:  $s_{11}$ ,  $s_{12}$ , and  $s_{44}$ . The stiffness matrix for a hexagonal crystal (right) has five independent stiffnesses:  $s_{11}$ ,  $s_{33}$ ,  $s_{44}$ ,  $s_{66} = (s_{11} - s_{12})/2$ ,  $s_{12}$ , and  $s_{13}$

$$\begin{aligned} G &= s_{44} \quad \text{and} \quad E = \frac{s_{44}(3s_{11} - 4s_{44})}{s_{11} - s_{44}} \\ B &= s_{11} - \frac{4}{3}s_{44} \quad \text{and} \quad \nu = \frac{s_{11} - 2s_{44}}{2(s_{11} - s_{44})} \end{aligned} \quad (4.108)$$

Polycrystalline materials behave as though they are isotropic. Unfortunately, there is no way to calculate the moduli for a polycrystalline material based on the single-crystal moduli unless the single crystals are nearly isotropic [40]. Ledbetter has compared several techniques for averaging the monocrystalline moduli under some simplifying assumptions (e.g., small grain-to-specimen sizes, very thin grain boundaries, random grain orientations, etc.) [41].

Other physical constants (e.g., thermal expansion coefficients, dielectric constants) that describe anisotropic crystalline substances can also have different values along different directions. Piezoelectric constants are necessarily anisotropic since the absence of an inversion symmetry plane is a prerequisite for the piezoelectric behavior of crystalline materials [42].

## 4.7 There Is More to Stiffness Than Just "K"

Many of the introductory textbooks on sound and vibration are content to define a spring constant, K, and then proceed with calculation of the consequences of this symbolic “source” of a linear restoring force. Obviously, I think that choice is shortsighted. Springs are carefully engineered products with elaborate rules for design that allow spring performance to best exploit material properties and survive the rigors of millions, if not billions, of fully reversing stress cycles, often close to the elastic limits.<sup>20</sup> Only a few strategies have been introduced here, but they were intended to expose the philosophical choices and physical limitations that constrain the extent to which one can select a value for K.

The use of elastomeric materials for springs, particularly for application to vibration isolators, introduces the behavior of real materials that combine both stiffness and damping. It also provided us with exposure to the single relaxation time model which is ubiquitous in the description of the responses of linear systems. Such systems range from light waves in dielectric materials to the sound speed and attenuation in systems where the relaxation time might be determined by the collision of molecules, the absorption and desorption of vapors in equilibrium with their liquids, or the chemical

<sup>20</sup> An automotive valve spring in an engine that operates at 2000 rpm will be stressed 240 million times during the operational lifetime of 2000 h. A typical home refrigerator/freezer may last 15 years. (In America, refrigerators are replaced more often as an interior decorating choice than due to product failure.) If a refrigerator uses a spring that vibrates at 60 Hz, then the number of fully reversing stress cycles accumulated in 15 years of service would be 28 billion cycles if the compressor operated continuously.

equilibrium of ionic species dissolved in seawater. These are only a few examples of systems that this model describes so elegantly.

We will exploit this relaxation time model again in our study of sound in fluids, but it seems much simpler for me to understand and visualize, let alone calculate the consequences of a relaxation mechanism, when the model is applied to springs and a dashpot. That analysis also led us to the rather remarkable fact that the real and imaginary components of the linear response function (the complex stiffness) are not independent; specification of the limiting values of stiffness dictates the maximum value of the dissipation, in addition to the frequency dependencies of that dissipation.

Finally, this chapter has attempted to demystify definitions of elastic moduli and their interrelationships. As will be demonstrated in the next chapter, that knowledge provides a firm foundation for the understanding of wave propagation in solids in general as well as the modes of vibration of thin bars and plates. That understanding will then be inverted to exploit the measurement of the normal mode frequencies of bars and other structures to accurately determine the elastic moduli of materials.

### Talk Like an Acoustician

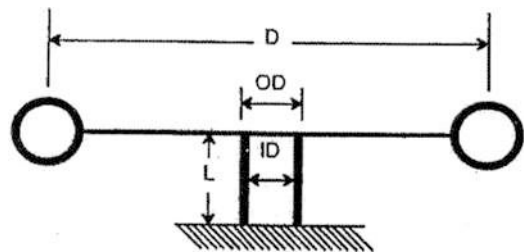
Strain	Bending moment
Stress	Radius of gyration
Young's modulus	Slenderness ratio
Poisson's ratio	Euler force
Bulk modulus	Single relaxation time model
Volumetric strain	Linear response theory
Modulus of unilateral compression	Kramers-Kronig relations
Dilatational modulus	Generalized susceptibility
Shear modulus	Relaxation time
Auxetic materials	Maxwell model
Accelerometer	Standard linear viscoelasticity model
Test mass	Dynamic modulus
Seismic mass	Storage modulus
Proof mass	Loss modulus
Ferroelectric ceramic	Loss factor or damping factor
<i>Tonpilz</i> transducers	Shape factor
Reduced mass	Stiffness matrix
Radiation mass	Voigt notation
Neutral plane	

### Exercises

1. ***Tonpilz* via Rayleigh.** The normal mode frequency for the *Tonpilz* example was based on a nodal position that made both halves of the assembly oscillate at the same frequency. Use Rayleigh's method (see Sect. 3.4.1) to calculate the same normal mode frequency by imposing a linear "trial function" and minimizing the frequency with respect to the distance from the head mass to the nodal location,  $b$  (see Fig. 4.8).
2. **Effective mass correction for a vibrating cantilevered beam.** The effective moving mass of a vibrating cantilever beam can be calculated if the displacement curve,  $z(x)$ , is known. For a beam of thickness,  $t$ , and length,  $L$ , that is made from a material with mass density,  $\rho$ , and Young's modulus,  $E$ , calculate the ratio of the moving mass to the total mass,  $m_s$ , for the two cases below:
  - (a) *Uniform beam.* A uniform beam of thickness  $t$  and width  $w$ .
  - (b) *Triangular cantilever.* A triangular cantilever of uniform thickness with the same stiffness as the beam in part (a) above.

3. **Torsionally resonant toroidal standing wave oscillator.** Instead of creating high-amplitude standing waves in a straight tube with a loudspeaker at one end and a rigid boundary at the other (see Sect. 10.7.5), it is possible to generate standing waves within a gas inside a torus that contains one rigid boundary within if the toroid oscillates about its axis at a frequency that makes one half-wavelength of the sound in the gas within the toroid equal to the circumference of the toroid [43]. Using Fig. 4.35 for this exercise, let the diameter of the torus be  $D = 0.50\text{ m}$  and the inside diameter of the gas-filled toroidal waveguide be  $10\text{ cm}$  and the wall thickness be  $1.5\text{ mm}$ . The solid plate that is welded to the torus and to the torsion tube is also  $1.5\text{ mm}$  thick. The torsion tube has a wall thickness of  $2.5\text{ mm}$  with an ID =  $8.0\text{ cm}$  and length of  $L = 12.0\text{ cm}$ .
- Frequency.* Determine the resonance frequency of this torsional oscillator if all of the components are made from steel with a density,  $\rho_{\text{steel}} = 7700\text{ kg/m}^3$ , and a shear modulus,  $G_{\text{steel}} = 140\text{ GPa}$ .
  - Fatigue failure.* What is the peak angular displacement  $\theta_I$  of the torus if the fatigue strength of the steel is  $G_{\max} = 30\text{ MPa}$ ?

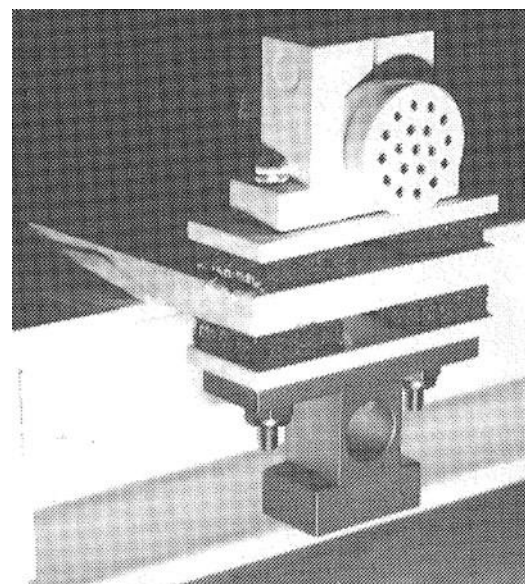
**Fig. 4.35** Cross-sectional diagram of a torsional oscillator consisting of a torus supported by a hollow cylindrical tube acting as a torsional spring



4. **Torsional stiffness of a rectangular ribbon.** Most galvanometers use a thin metallic ribbon as the torsional stiffness element that provides the restoring force for the current-carrying coil and pointer. Calculate the torsional stiffness for a thin ribbon of thickness,  $t$ ; width,  $w$ , with  $w \gg t$ ; and length,  $L$ , by assuming that torsion of the ribbon changes its rectangular cross-section into a parallelogram.
- Torsional stiffness.* Show that the expression below provides the torsional stiffness,  $K_{\text{ribbon}}$ .
- $$K_{\text{ribbon}} = G \frac{wh^3}{3L}$$
- Torsional resonance frequency.* A mirrored galvanometer consists of a mirror and a current-sensing coil (see Fig. 2.7). The coil is suspended in a magnetic field produced by a permanent magnet structure by a ribbon of beryllium (Be) that is  $100\text{ }\mu\text{m}$  thick,  $2.0\text{ mm}$  wide, and  $15\text{ cm}$  long. The shear modulus of beryllium is  $G_{\text{Be}} = 132\text{ GPa}$ . The moment of inertia of the mirror and coil is  $I_{\text{mirror}} = 3 \times 10^{-8}\text{ kg}\cdot\text{m}^2$ . What is the natural frequency of torsional vibration?
  - Noise.* Using the Equipartition Theorem as discussed in Sect. 2.4.4, determine the root-means-squared angular displacement,  $\theta_{\text{rms}} = \sqrt{\langle \theta^2 \rangle}$ , of the mirror and coil at room temperature,  $T = 20\text{ }^\circ\text{C} = 293\text{ K}$ .
5. **Cantilever springs.** Consider a thin steel beam is  $20.0\text{ cm}$  long,  $2.0\text{ cm}$  wide, and  $2.0\text{ mm}$  thick. Let Young's modulus of the steel be  $E_{\text{Steel}} = 195\text{ GPa}$ . Assume that one end of the beam is rigidly clamped at  $x = 0$ , so  $(\partial y/\partial x)_x = 0 = 0$ , and a load of  $1.0\text{ kg}$  is applied to the end at  $x = L = 20.0\text{ cm}$ .
- Uniform beam stiffness.* By how much will the end of the beam be deflected from its equilibrium (straight) shape by the  $M = 1.0\text{ kg}$  load if  $g = 9.8\text{ m/s}^2$ ?

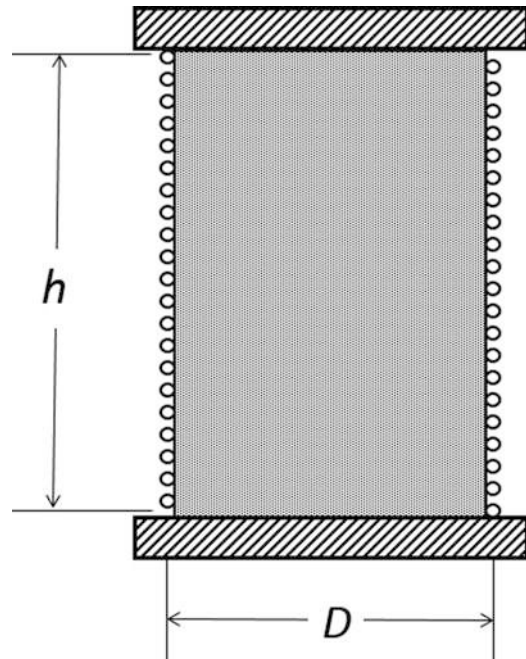
- (b) *Maximum stress and strain for the uniform beam.* At what value of  $x$  is the stress in the beam largest? At what value of  $h$ , the distance from the beam's neutral axis, is the stress largest at that value of  $x$ ? What is the maximum strain and stress that is experienced by the loaded uniform beam?
- (c) *Triangular cantilever.* What is the deflection of a similar cantilever spring, using the same amount of steel, which is also 20.0 cm long and is clamped at  $x = 0$ , but which has a base of  $w = 4.0$  cm and the mass,  $M = 1.0$  kg, is applied at the vertex of the triangle located at  $x = 20.0$  cm?
- (d) *Maximum stress and strain for the triangular beam.* At what value of  $x$  is the stress on the beam largest? At what value of  $h$ , the distance from the beam's neutral axis, is the stress largest at that value of  $x$ ? What is the maximum strain and stress that is experienced by the loaded triangular beam?
6. **Compression of a column.** An aluminum rod has a length of 10.0 cm and a diameter of 5.0 mm. Assume Young's modulus for aluminum is  $E_{Al} = 71$  GPa.
- Compression.* By how much will the beam be shortened if it is clamped at the bottom and a 5.0 kg mass is placed on the top?
  - Buckling.* How much mass would be required to cause such a beam buckle?
7. **Microphone vibration isolator.** Figure 4.36 shows a piezoelectric microphone (Endevco Model 2510) on a (symmetrical) vibration mount that supports the microphone and its clamping fixture, attached to an aluminum base ( $5 \times 1.5 \times 0.4$  cm) on two silicone rubber pads ( $1.5 \times 1.5 \times 0.5$  cm). The rubber has a shear modulus of  $G = 350$  kPa. The mass of the microphone and its mounting plate is 60 gm.
- Effective Young's modulus.* Using the dimensions of a single rubber pad in Fig. 4.36 and assuming  $\beta = 2.0$ , calculate the effective Young's modulus,  $E_a$ , for compression.
  - Compressional stiffness.* Using the value of  $E_a$ , and the dimension of a single rubber pad in Fig. 4.36, calculate the compressional stiffness for a single pad.
  - Natural frequency.* Ignoring the counterweight below the mounting bracket that attaches to the Space Shuttle's frame, calculate the microphone's natural frequency of vibration for up and down motion.

**Fig. 4.36** Photograph of a vibration isolator mounted in the cargo bay of a Space Shuttle [44]



- (d) *Shear vibration.* The microphone can also undergo shear vibration. Calculate the shear stiffness provided by the two rubber pads and use that result to calculate the natural frequency for side-to-side vibration.
8. **Strain transformer.** The cylindrical elastomeric mandrel shown in Fig. 4.37 is wrapped by a glass optical fiber and is capped at each end by rigid plates. The fiber is 80  $\mu\text{m}$  in diameter and Young's modulus of the glass is  $E = 62 \text{ GPa}$ . Poisson's ratio for the elastomer is  $\nu = \frac{1}{2}$ , so the rubber mandrel transforms compression of the mandrel into the lengthening of the optical fiber. The diameter of the cylinder is  $D = 3.98 \text{ cm}$ , and the height is  $h = 1.92 \text{ cm}$ . The mandrel is wrapped with  $N = 85$  turns of optical fiber.
- Glass stiffness-length product.* Based on Young's modulus of glass and the diameter of the optical fiber, what is the stiffness-length product,  $K_{\text{glass}}L$ , of the fiber?
  - Glass stiffness.* Based on the diameter of the mandrel and the number of turns of optical fiber, what is the stiffness of the total length of fiber,  $K_{\text{fiber}}$ ?
  - Potential energy.* The volume of the mandrel is  $V = \pi D^2 h / 4$ . Keeping in mind that the elastomer is volume-conserving, since  $\nu = \frac{1}{2}$ , write the change in potential energy of the glass fiber for a change in the mandrel height,  $\delta h$ .
  - Mandrel stiffness.* Assuming that all of the compressional stiffness of the mandrel is due to the stretching of the glass fiber during compression, use your expression for the potential energy in part (c) to determine the effective stiffness of the mandrel.
  - Moving mass.* The mass density of the elastomer is  $\rho_{2CN} = 1020 \text{ kg/m}^3$ . If the displacement of the mandrel is linear with distance from the fixed end (like the Gerber scale of Fig. 2.2), what is the effective moving mass of the mandrel?
  - Natural frequency.* If one end of the mandrel is fixed and a proof mass,  $m_{\text{test}} = 100 \text{ gm}$ , is placed on the other end, what is the natural frequency of vibration,  $f_o$ , if the contribution of the mandrel's moving mass is included?

**Fig. 4.37** Optical fiber strain transformer [45]



## References

1. L. D. Landau and E. M. Lifshitz, *Theory of Elasticity*, 2nd English edition (Pergamon, 1975). See pg. 17; ISBN 0 08 006465 5
2. G.G. Marquez, *One Hundred Years of Solitude* (Harper Collins, New York, 2003); ISBN 0-19-515544-4
3. E.H. Love, *A Treatise on the Mathematical Theory of Elasticity*, 4th edn. (Dover reprint, 1944); ISBN 0-486-60172-9
4. R.S. Lakes, Foam structures with a negative Poisson's ratio. *Science* **235**(4792), 1038–1040 (1987)
5. S. R. Lampman (ed.), *ASM Handbook, Vol. 19 – Fatigue and Fracture* (ASM International, Metals Park, 1996); ISBN 0-87170-385-8
6. J.E. Shigley, C.R. Mischke, *Mechanical Engineering Design*, 5th edn. (McGraw-Hill, Boston, 1989); ISBN 0-07-056899-5
7. O.B. Wilson, *Introduction to Theory and Design of Sonar Transducers* (Peninsula, Los Altos, 1988)
8. S. L. Ehrlich and A. F. Medeiros, Wide band transducer, U. S. Patent No. 3,860,901 (January 14, 1975)
9. D. Boucher, Process to increase the power of the low frequency electro acoustic transducers and corresponding transducers, US Patent No. 5,070486 (December 3, 1991)
10. L.D. Landau, E.M. Lifshitz, *Mechanics* (Pergamon, Oxford, 1960). See §24
11. M.E. Poese, R.M. Keolian, R.W.M. Smith, E. Mitchell, S.L. Garrett, Performance estimates for a helium-based thermoacoustic Stirling chiller. *Int. J. Low Carbon Technol.* **8**, 79–84 (2013)
12. W.C. Young, R.G. Budynas, *Roark's Formulas for Stress and Strain*, 7th edn. (McGraw-Hill, New York, 2002); ISBN 0-07-072542-X
13. S. L. Garrett, R. M. Keolian and R. W. M. Smith, High-efficiency moving magnet loudspeaker," U. S. Patent No. 6,307,287 (October 23, 2001)
14. J. Liu, S. Garrett, Characterization of a small moving-magnet electrodynamic linear motor for use in a thermoacoustic refrigerator. *J. Acoust. Soc. Am.* **118**(4), 2289–2295 (2005)
15. H.E. Boyer, T.L. Gall, *Metals Handbook: Desk Edition* (American Society for Metals, Metals Park, 1985); ISBN 0-81170-188-X
16. S. L. Garrett, Cylindrical spring with integral gas seal, US Patent No. 6,755,027 (June 29, 2004)
17. EJMA, *Standards of the Expansion Joint Manufacturers Association*, 10th edn. (EJMA, Tarrytown, 2017)
18. H. Cavendish, Experiments to determine the Density of the Earth. *Philos. Trans. R. Soc. Lond. Part II* **88**, 469–526 (1798)
19. C.J. Ancker Jr., J.N. Goodier, Pitch and curvature correction for Helical Springs. *ASME J. Appl. Mech.* **25**(4), 471–483 (1958)
20. M. Wahl, *Mechanical Springs*, 2nd edn. (McGraw-Hill, New York, 1963)
21. L.R. Wilberforce, On the vibrations of a loaded spiral spring. *Philos. Mag.* **38**, 386–392 (1896)
22. R.E. Berg, T.S. Marshall, Wilberforce oscillations and normal modes. *Am. J. Phys.* **56**(1), 32–38 (1991)
23. A. Sommerfeld, *Mechanics of Deformable Bodies: Lectures on Theoretical Physics*, vol II (Academic, New York, 1950), pp. 308–314
24. N. Feather, *Vibration and Waves* (Penguin, London, 1964), pp. 59–67
25. J. Wilhelm, K.A. Gillis, J.B. Mehl, M.R. Moldover, An improved Greenspan acoustic viscometer. *Int. J. Thermophys.* **21**, 983–999 (2000)
26. R. N. Capps, Elastomeric Materials for Acoustical Applications (Naval Research Laboratory, Underwater Sound Reference Detachment, 15 September 1989)
27. L.D. Landau, E.M. Lifshitz, *Statistical Physics*, 2nd edn. (Addison-Wesley, Reading, 1969), pp. 384–391, See §125; ISBN 0-201-04167-7
28. L.D. Landau, E.M. Lifshitz, *Electrodynamics of Continuous Media* (Pergamon, London, 1960); ISBN 0-08-09105-9. §62
29. B. Bhatia, *Ultrasonic Absorption: An Introduction to the Theory of Sound Absorption and Dispersion in Gases, Liquids, and Solids* (Oxford, 1967). Reprinted (Dover, 1985); ISBN 0-486-64917-2
30. H. Bode, Relations between attenuation and phase in feedback amplifier design. *Bell Syst. Tech. J.* **19**, 421 (1940)
31. V. Mangulis, Kramers-Kronig or dispersion relations in acoustics. *J. Acoust. Soc. Am.* **36**, 211–212 (1964).; Relation between the radiation impedance, pressure in the far field, and baffle impedance, *J. Acoust. Soc. Am.* **36**, 212–213 (1964)
32. S. Garrett, S. Adams, S. Puterman, I. Rudnick, Resonant nonlinear mode conversion in He II. *Phys. Rev. Lett.* **41**(6), 413–416 (1978)
33. R. Kronig, H.A. Kramers, Absorption and dispersion in X-rays spectra. *Z. Phys.* **48**, 174 (1928)
34. J. W. Strutt (Lord Rayleigh), *The Theory of Sound*, vol I, 2nd edn. (Macmillan, London, 1894), p. 153; Reprinted (Dover, 1945); ISBN 486-60292-3
35. M. O'Donnell, E.T. Jaynes, J.G. Miller, Kramers-Kronig relationships between ultrasonic attenuation and phase velocity. *J. Acoust. Soc. Am.* **69**(3), 696–701 (1981)

36. C.M. Harris, A.G. Piersol, *Harris' Shock and Vibration Handbook*, 5th edn. (McGraw-Hill, New York, 2002); ISBN 0-07-137081-1
37. W. Nolle, Dynamical mechanical properties of rubberlike materials. *J. Polym. Sci.* **5**(1), 1–54 (1950)
38. J.D. Ferry, *Viscoelastic Properties of Polymers*, 3rd edn. (Wiley, New York, 1980.; ISBN: 978-0-471-04894-7
39. J.C. Snowdon, *Vibration and Shock in Damped Mechanical Systems* (Wiley, New York, 1968)
40. L. D. Landau and E. M. Lifshitz, Theory of Elasticity, 2nd English edition (Pergamon, 1975). §10, see pp. 41–42- ISBN 0 08 006465 5
41. H. Ledbetter, Chapter 11: Monocrystal-polycrystal elastic-constant models, in *Handbook of Elastic Properties of Solids, Liquids, and Gases: Vol. III – Elastic Properties of Solids: Biological and Organic Materials, Earth and Marine Sciences*, ed. by M. Levy, H. Bass, R. Stern, (Academic, 2000). ISBN 0-12-445763-0
42. W.G. Cady, *Piezoelectricity* (McGraw-Hill, New York/London, 1946)
43. S. L. Garrett, Torsionally resonant toroidal thermoacoustic refrigerator,” U.S. Patent No. 5,953,921 (September 21, 1999)
44. C. D. Stehle, Vibration isolation of a microphone, U.S. Defense Technical Report No. AD A 161 018 (October 1985)
45. D.L. Gardner, T. Hofler, S.R. Baker, R.K. Yarber, S.L. Garrett, A fiber-optic interferometric seismometer. *J. Lightwave Technol.* **5**(7), 953–960 (1987)

**Open Access** This chapter is licensed under the terms of the Creative Commons Attribution 4.0 International License (<http://creativecommons.org/licenses/by/4.0/>), which permits use, sharing, adaptation, distribution and reproduction in any medium or format, as long as you give appropriate credit to the original author(s) and the source, provide a link to the Creative Commons license and indicate if changes were made.

The images or other third party material in this chapter are included in the chapter's Creative Commons license, unless indicated otherwise in a credit line to the material. If material is not included in the chapter's Creative Commons license and your intended use is not permitted by statutory regulation or exceeds the permitted use, you will need to obtain permission directly from the copyright holder.





# Modes of Bars

5

## Contents

<b>5.1</b>	<b>Longitudinal Waves in Thin Bars .....</b>	236
5.1.1	Longitudinal Waves in Bulk Solids .....	240
5.1.2	The Quartz Crystal Microbalance .....	240
5.1.3	Bodine's "Sonic Hammer" .....	242
<b>5.2</b>	<b>Torsional Waves in Thin Bars .....</b>	245
<b>5.3</b>	<b>Flexural Waves in Thin Bars .....</b>	246
5.3.1	Dispersion .....	247
5.3.2	Flexural Wave Functions .....	249
5.3.3	Flexural Standing Wave Frequencies .....	250
5.3.4	Flexural Standing Wave Mode Shapes .....	252
5.3.5	Rayleigh Waves* .....	256
<b>5.4</b>	<b>Resonant Determination of Elastic Moduli .....</b>	256
5.4.1	Mode-Selective Electrodynamic Excitation and Detection .....	258
5.4.2	Bar Sample Size and Preparation .....	259
5.4.3	Measured Resonance Spectra .....	260
5.4.4	Effective Length Correction for Transducer Mass .....	263
5.4.5	Modes of a Viscoelastic Bar .....	267
5.4.6	Resonant Ultrasound Spectroscopy* .....	270
<b>5.5</b>	<b>Vibrations of a Stiff String* .....</b>	274
<b>5.6</b>	<b>Harmonic Analysis .....</b>	277
	<b>References .....</b>	280

The perspectives and techniques that have been developed in the previous chapters will now be applied to calculation of wave propagation in solids. Their application to longitudinal and shear waves will be both familiar and simple. What you will find to be even more satisfying is the success of those same techniques for finding solutions for waves in a system that does not obey the wave equation and whose solutions are not functions of  $x \pm ct$ .

This chapter is focused mainly on waves in bars that are “thin,” meaning that the square root of their cross-sectional area is much less than their length,  $\sqrt{S} \ll L$ . The frequencies of the normal modes of such thin bars will be used to determine the bars’ elastic constants to high precision. The results for thin bars will also lead to the understanding of waves in samples with dimensions much greater than the

wavelength of the sound. Examples of short wavelength propagation in “bulk” samples range from ultrasonic waves in crystals and for biomedical diagnosis and therapy to seismic waves that penetrate our Earth and the Sun.

Before initiating these next investigations, it may be worthwhile to review the sequence of steps we have taken thus far to calculate the behavior of harmonic oscillators and waves on strings:

- Determine the relationship that governs forces and displacements in our system of interest (e.g., Hooke’s law, the equation of state, or the “constitutive equation”).
- Examine the behavior of a differential element and determine the net forces (or net torques) acting on that element.
- Assume a sufficiently small displacement from equilibrium (i.e., “linear” behavior) and apply a Taylor series expansion to evaluate the net forces (or net torques) acting on the differential element.
- Use Newton’s Second Law of Motion to calculate the acceleration of the differential element.
- Ignore any contributions to the equation relating accelerations to restoring forces that involve second-order quantities, such as products of two or more first-order deviations from equilibrium, like displacements or velocities, since such quadratic products are small compared to the linear contributions.
- Obtain a wave propagation speed.
- Apply the “machinery” to extract solutions under specific circumstances (e.g., harmonic analysis, superposition, boundary conditions, initial conditions, Fourier’s theorem, mechanical impedance at steady state).

---

## 5.1 Longitudinal Waves in Thin Bars

There are three independent types of waves that can be excited in thin bars of solid materials at frequencies that are sufficiently low that the wavelengths of these waves are much greater than the cross-sectional dimensions (i.e.,  $\lambda \gg S^{1/2}$ ): (i) longitudinal waves of compression and expansion, (ii) torsional waves that produce twisting, and (iii) flexural waves that cause the bar to bend. Having examined the elastic moduli for isotropic solids, it should be clear that for longitudinal waves in thin bars, it is Young’s modulus that quantifies the relationship between the longitudinal stresses and strains for a solid whose sides are unconstrained. Thus, the edges are free to “bulge” when compressed and to “neck down” when expanded. Assuming a bar of rectangular cross-section, as shown in Fig. 5.1, then  $(\Delta w/w) = (\Delta h/h) = -\nu(\Delta\xi/dx)$ .

The longitudinal strain,  $\varepsilon_{xx}$ , will be the ratio of the change in the length of the differential element from its original undisturbed length,  $dx$ , to its expanded length,  $\xi(x + dx) - \xi(x)$ , divided by its original length,  $dx$ . As before, a Taylor series expansion about  $\xi(x)$  will be used to simplify the expression for the longitudinal strain.

$$\varepsilon_{xx} = \frac{\xi(x + dx) - \xi(x)}{dx} \cong \frac{\left(\frac{\partial \xi}{\partial x}\right) dx}{dx} = \left(\frac{\partial \xi}{\partial x}\right) \quad (5.1)$$

Using Eq. (4.1), longitudinal stress,  $\sigma_{xx}$ , will be related to that longitudinal strain,  $\varepsilon_{xx}$ , by Young’s modulus,  $E$ , for the bar’s material, allowing  $S_x(x)$  to be the cross-sectional area of the bar as a function of position along the bar.

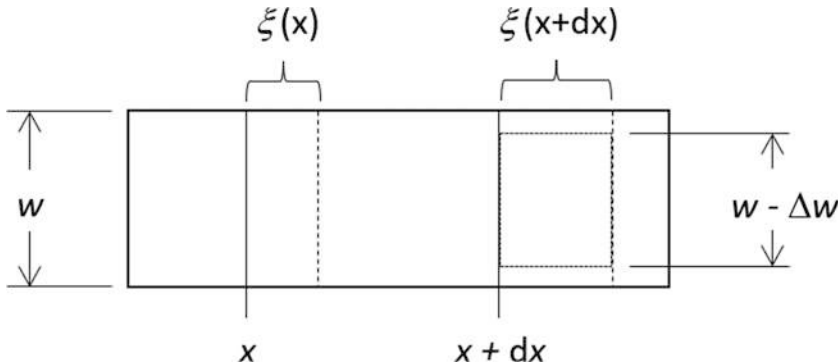


**Fig. 5.1** Coordinate system for the displacement from equilibrium,  $\xi(x)$ , caused by a longitudinal wave passing through a thin bar. At the moment shown, the differential element of the bar has expanded, so its width (and height, not shown) will decrease in accordance with Poisson's ratio

$$\sigma_{xx} = \frac{F_x(x)}{S_x(x)} = -E(x) \frac{\partial \xi(x)}{\partial x} \Rightarrow F_x = -ES_x \frac{\partial \xi}{\partial x} \quad (5.2)$$

In the right-hand version, we have assumed that neither  $E$  nor  $S_x$  is a function of position, although the dependence of  $S_x$  on strain,  $\epsilon_{xx}$ , if  $\nu \neq 0$ , will be given in Eq. (5.4).

To determine the net longitudinal force,  $dF_x$ , acting on the differential element of length,  $dx$ , we expand Eq. (5.2) in a Taylor series about  $F_x(x)$  and assume that Young's modulus is a constant.

$$dF_x = F_x(x) - F_x(x + dx) \cong \frac{\partial F_x(x)}{\partial x} dx = E \frac{\partial}{\partial x} \left( S_x \frac{\partial \xi}{\partial x} \right) dx \quad (5.3)$$

If the cross-sectional area of the bar is also a constant, it too can be taken outside of the derivative. Having introduced Poisson's ratio in Eq. (4.2), we know that the cross-sectional area will not remain constant. Again, assume a bar of rectangular cross-section, so  $S = wh$ , and then use logarithmic differentiation to calculate the relative change in cross-section.

$$\frac{\delta S_x}{S_x} = \frac{\delta w}{w} + \frac{\delta h}{h} = -2\nu \epsilon_{xx} = -2\nu \frac{d\xi}{dx} \quad (5.4)$$

Substitution of Eq. (5.4) into Eq. (5.3) provides an expression for the net longitudinal force,  $dF_x$ , acting on the differential element.

$$dF_x = E \frac{\partial}{\partial x} \left[ S_x \left( 1 - 2\nu \frac{\partial \xi}{\partial x} \right) \frac{\partial \xi}{\partial x} \right] dx \cong ES_x \frac{\partial^2 \xi}{\partial x^2} dx \quad (5.5)$$

Expanding the term in square brackets, we see that the correction to the cross-sectional area, due to Poisson's ratio, is second order in the strain, thus can be neglected in a first-order (linear) analysis. Since we are making a linear approximation, the strains are assumed to be small,  $\partial \xi / \partial x = \epsilon_{xx} \ll 1$ , so we can ignore the Poisson term because it is proportional to  $\epsilon_{xx}^2 \ll \epsilon_{xx}$ .

The net longitudinal force,  $dF_x$ , is equal to the acceleration of the mass of the differential element,  $\rho S_x dx$ , where  $\rho$  is the mass density [ $\text{kg}/\text{m}^3$ ] of the bar's material at  $x$ .

$$\rho S_x dx \frac{\partial^2 \xi}{\partial t^2} = E S_x \frac{\partial^2 \xi}{\partial x^2} dx \Rightarrow \frac{\partial^2 \xi}{\partial t^2} - \frac{E}{\rho} \frac{\partial^2 \xi}{\partial x^2} = 0 \quad (5.6)$$

We know that the solution to this wave equation will be the same superposition of a left- and right-going traveling wave as appeared in Eq. (3.18).

$$\xi(x, t) = A e^{j(\omega t - kx)} + B e^{j(\omega t + kx)} \quad (5.7)$$

Equation (5.6) is a wave equation that reveals a propagation speed (phase speed) for longitudinal waves in thin bars,  $c_B$ .

$$c_B = \frac{\omega}{k} = f\lambda = \sqrt{\frac{E}{\rho}} \quad (5.8)$$

This speed of longitudinal wave propagation depends upon the ratio of the material's modulus to its mass density. It should also be noted that neither the cross-sectional area of the bar,  $S_x$ , nor the shape of that cross-section influences  $c_B$ , as long as the wavelength,  $\lambda$ , is much greater than the width, height, or diameter of the bar:  $\lambda = c_B/f \ll \sqrt{S_x}$ . Denser and softer metals, like lead, will have slower propagation speeds, while stiffer, less dense metals, like beryllium, will have faster speeds. For pure lead,  $c_B \cong 1200$  m/s and for beryllium,  $c_B \cong 12,870$  m/s.

Using our prior experience with standing waves on strings of finite length (see Sect. 3.3.1), the process of imposing ideal boundary conditions should be familiar. Experimentally, the easiest boundary condition to apply to a thin bar of length,  $L$ , to be excited in its longitudinal mode, is that the displacements of both ends are unconstrained or “free.” If there are no forces on the end at  $x = 0$  or the end at  $x = L$ , then Eq. (5.2) can be used to express these “free” boundary conditions.

$$F_x = -E S_x \left( \frac{\partial \xi}{\partial x} \right)_{x=0} = -E S_x \left( \frac{\partial \xi}{\partial x} \right)_{x=L} = 0 \quad (5.9)$$

The derivative of Eq. (5.7) with respect to  $x$  is simplified by our choice of exponential functions of space and time.

$$F_x(x, t) = -E S_x \left( \frac{\partial \xi}{\partial x} \right) = -jk E S_x [B e^{j(\omega t + kx)} - A e^{j(\omega t - kx)}] \quad (5.10)$$

The force at  $x = 0$  can be evaluated by setting Eq. (5.10) to zero. This boundary condition can be satisfied by the superposition of traveling waves in Eq. (5.7) if  $A = B$ .

$$\begin{aligned} \xi(x, t) &= \Re e \left[ B \left( e^{j(\omega t + kx)} + e^{j(\omega t - kx)} \right) \right] \\ &= \Re e \left[ B e^{j\omega t} (e^{jkx} + e^{-jkx}) \right] = \Re e \left[ \hat{C} e^{j\omega t} \cos kx \right] \end{aligned} \quad (5.11)$$

In Eq. (5.11), we have used the fact that  $2\cos x = (e^{jkx} + e^{-jkx})$  and have absorbed  $2B$  into the new complex amplitude constant (phasor),  $\hat{C}$ , that will not be determined until the initial conditions have been specified.

As was done before for strings, setting  $F_x(L, t)$  to zero quantizes the values of the wavenumber that satisfy both boundary conditions simultaneously.

$$F_x(L, t) = -ES_x \left( \frac{\partial \xi}{\partial x} \right)_{x=L} = ES_x k_n C_n \sin(k_n L) e^{j\omega_n t} = 0 \quad (5.12)$$

This results in the same set of normal mode frequencies as the case for the fixed-fixed string in Eq. (3.20). These correspond to integer multiples of half-wavelengths between the ends of the bar.

$$\begin{aligned} \xi_n(x, t) &= \Re e \left[ \hat{\mathbf{C}}_n \cos(k_n x) e^{j\omega_n t} \right] \\ \text{with } k_n &= \frac{n\pi}{L} \Rightarrow f_n = n \frac{c_B}{2L}; \quad n = 1, 2, 3, \dots \end{aligned} \quad (5.13)$$

Once again, there is a harmonic series of normal mode frequencies. Of course, in this case, there are displacement and velocity anti-nodes at both ends of the bar instead of velocity nodes at the ends, as was the case for the fixed-fixed string. For our standing wave solutions in Eq. (5.13), the displacement is proportional to  $\cos(k_n x)$ , but for the standing wave on a fixed-fixed string,  $y_n(x) \propto \sin(k_n x)$ , as shown in Eq. (3.21).

The fundamental free-free longitudinal mode of a very large aluminum bar, 3 m in length, with a mass of 2300 kg, was used in an attempt to detect gravitational waves.<sup>1</sup> [1] Using Young's modulus and the mass density of aluminum at room temperature, the speed of longitudinal waves  $c_L = 5510$  m/s, making  $f_L \cong 860$  Hz. In operation, the bar was cooled below 4.2 K to permit the use of a superconducting quantum interferometer (SQUID) that measured the motion of a simple harmonic oscillator, tuned to  $f_L$ . The SQUID was attached to one end of the bar through a simple harmonic oscillator attached to one "free" end to amplify its motion by the  $Q$  of the harmonic oscillator. That raised the resonance frequency to 904 Hz, due to the increase in Young's modulus with decreasing temperature. The quality factor of the cryogenically cooled, freely suspended bar was enormous:  $Q \cong 10^9$  [2].

Although harder to achieve in practice, an ideal fixed-fixed bar, with  $\xi(0) = \xi(L) = 0$ , would also have integer multiple half-wavelengths between the ends of the bar, resulting in a harmonic series of normal mode frequencies. The displacement functions,  $\xi_n(x, t)$ , have the same functional form as the fixed-fixed string given in Eq. (3.12).

Like the solutions for the fixed-free string in Eqs. (3.23) and (3.24), a clamped-free bar that executes longitudinal vibrations will exhibit the same series of only odd-harmonic standing wave modes, corresponding to odd integer multiples of a quarter wavelengths between the fixed end at  $x = 0$  and the free end at  $x = L$ , where  $(\partial \xi / \partial x)_L = 0$ .

$$\begin{aligned} \frac{\partial \xi(L, t)}{\partial x} &= k_n \hat{\mathbf{C}}_n \cos(k_n L) e^{j\omega_n t} = 0 \\ \cos k_n L &= 0 \Rightarrow k_n L = \left( \frac{2n-1}{2} \right) \pi \quad \Rightarrow \quad \omega_n = \left( \frac{2n-1}{2} \right) \frac{\pi c_B}{L} \\ \Rightarrow \lambda_n &= \frac{4L}{2n-1} \quad \text{or} \quad L = (2n-1) \frac{\lambda_n}{4} \quad \text{for } n = 1, 2, 3, \dots \end{aligned} \quad (5.14)$$

<sup>1</sup> Such gravitational wave detectors are called "Weber bars" in honor of the first attempt to use a longitudinally resonant bar to detect gravitational waves that was made by J. Weber. Weber claimed to detect gravitational waves in an article entitled "Gravitational-Wave-Detector Events," Phys. Rev. Lett. **20**, 1307–1308 (1968), although his claim could not be substantiated.

### 5.1.1 Longitudinal Waves in Bulk Solids

As the ratio of the wavelength of the sound to the transverse dimensions of the bar becomes smaller, the compressive stresses associated with the longitudinal wave cannot be (partially) relieved by the bulge of the bar induced through Poisson's ratio. When the transverse dimensions of the sample substantially exceed the wavelength of the longitudinal wave, the modulus that provides the restoring force in Eq. (5.2) is no longer Young's modulus,  $E$ , but becomes the modulus of unilateral compression (also known as the dilatational modulus),  $D > E$  (see Fig. 4.4). The propagation speed for a longitudinal wave in "bulk material,"  $c_L$ , is higher than the bar speed.

$$c_L = \frac{\omega}{k} = \sqrt{\frac{D}{\rho}} > c_B \quad (5.15)$$

Expressing  $D$  in terms of  $E$  and  $\nu$  (see Table 4.1) allows the ratio of the bulk longitudinal wave speed,  $c_L$ , to the thin bar speed,  $c_B$ , to be expressed in terms of Poisson's ratio.

$$\frac{c_L}{c_B} = \frac{\sqrt{D/\rho}}{\sqrt{E/\rho}} = \sqrt{\frac{(1-\nu)}{(1+\nu)(1-2\nu)}} \quad (5.16)$$

Poisson's ratio for most common metals is about  $\nu \cong 1/3$ , so the sound speed ratio in metals is  $c_L/c_B \cong (3/2)^{1/2} \cong 1.2$ , about a 20% higher speed for longitudinal waves in bulk materials, where transverse stresses cannot be relieved, in part, by "bulge."

### 5.1.2 The Quartz Crystal Microbalance

The quartz crystal microbalance (QCM) is used to "weigh" very thin films, such as those deposited on microelectronic circuits by vacuum evaporation of metals (frequently gold). This is accomplished by monitoring the change in the resonance frequency of the vibrating piezoelectric sample. As will be shown in this section, the deposition of thin films that have thicknesses that are on the order of a single atomic layer can be detected by monitoring the resonance frequency shift.

In exact analogy with the mass-loaded string (see Sect. 3.6), a bar or plate with a mass "attached" to the free face will require that the bar or plate provide the force necessary to accelerate the mass load adsorbed or plated onto the free face that is moving with longitudinal displacement,  $\xi(L)e^{j\omega t}$ .

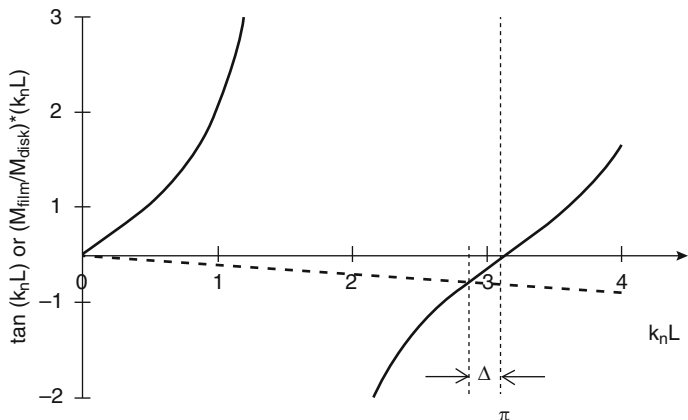
$$F_x(L, t) = M \left( \frac{\partial^2 \xi}{\partial t^2} \right)_{x=L} = -DS_x \left( \frac{\partial \xi}{\partial x} \right)_{x=L} \quad (5.17)$$

In Eq. (5.17), the modulus of unilateral compression,  $D$ , is used to relate stress and strain because we will assume that the quartz plate (usually a disk) has a diameter,  $2a$ , that may be one hundred times the plate's thickness,  $t = L$ . Since the wavelength for the fundamental vibrational mode of a free-free plate is  $\lambda = 2t$ , and  $t \ll a$ , it is clear that the use of Young's modulus in this case would be incorrect. We will treat the "rear" of the disk as being suspended in a vacuum, hence free at  $x = 0$ .

$$\xi(x, t) = \Re e \left[ \hat{\mathbf{C}} \cos(kx) e^{j\omega t} \right] \quad (5.18)$$

The face at  $x = L$  will be mass-loaded by the deposition of a thin film with mass,  $M_{film}$ , so that Eq. (5.18) can be substituted into Eq. (5.17) to determine the quantization condition on  $k_n$ .

**Fig. 5.2** Graph of the transcendental Eq. (5.20) over a small region near the origin with  $M_{film}/M_{disk} = 0.10$  is shown as the dashed line. The tangent function, shown as the solid line, has a slope = 1.0 near  $(k_n L) = 0$  or  $(k_n L) = \pi$ , so the first intersection of the dashed line and the tangent occurs at a value of  $(k_n L)$  that is slightly less than  $\pi$  by a small amount,  $\Delta$



$$-\omega^2 M_{film} C_n \cos(k_n L) e^{j\omega_n t} = DS_x k_n C_n \sin(k_n L) e^{j\omega_n t} \quad (5.19)$$

Using the fact that  $c_L^2 = \omega^2/k^2 = D/\rho$ , Eq. (5.19) can be written in a form similar to the quantization condition for the wavenumbers,  $k_n$ , of a fixed, mass-loaded string that was given in Eq. (3.68).

$$\tan(k_n L) = \frac{-\omega^2 M_{film}}{DS_x k_n} = -\frac{k_n^2 M_{film} D}{k_n DS_x \rho} \frac{L}{L} = -\frac{M_{film}}{M_{disk}}(k_n L) \quad (5.20)$$

This transcendental equation is plotted in Fig. 5.2 with  $M_{film}/M_{disk} \ll 1$ .

For a very small mass loading,  $M_{film}/M_{disk} \ll 1$ , the first intersection of  $\tan(k_n L)$  and the straight line,  $(-M_{film}/M_{disk})(k_n L)$ , occurs at a value of  $k_n L$  that is slightly less than  $\pi$  by an amount  $\Delta$ , as shown in Fig. 5.2. We expect this decrease in the wavenumber (hence, resonant frequency), since the mass-loaded frequency should be lower than the normal mode frequency for its free-free value,  $(k_1 L) = \pi$ . Since the slope of  $\tan x$  at the zero-crossings is unity,  $\Delta \cong \pi(M_{film}/M_{disk}) \Rightarrow \delta k_1 \cong -(\pi/L)(M_{film}/M_{disk})$ . Using this approximation (which, of course, becomes progressively better as the thickness of the film decreases), the relative shift in the wavenumber of the fundamental mode is  $\delta k_1/k_1$ , where  $k_1 \cong (\pi/L)$ . The relative frequency shift,  $\delta f_1/f_1$ , can be related to the film thickness, if the mass densities of the disk,  $\rho_{disk}$ , and the deposited film material,  $\rho_{film}$ , are known.

$$\frac{\delta f_1}{f_1} = \frac{\delta k_1}{k_1} = -\frac{\pi}{L} \frac{M_{film}}{M_{disk}} \left(\frac{L}{\pi}\right) = -\left(\frac{\rho_{film}}{\rho_{disk}}\right) \frac{t_{film}}{L} \quad (5.21)$$

This result is rather easy to interpret. This frequency shift is equivalent to the frequency change that would result if the disk was made longer by the thickness,  $\delta L$ , of the adsorbed film, if the adsorbed film had the same density as the density of the disk:  $\delta L = (\rho_{film}/\rho_{disk}) t_{film}$ , so  $-\delta f_1/f_1 = \delta L/L$ .

A simple example will illustrate the sensitivity of this method. We start by calculating the thickness of a monolayer of gold atoms. The atomic weight of gold is  $M_{Au} = 197$  a.m.u. = 197 gm/mole, and its mass density is  $\rho_{Au} = 19.3$  gm/cm<sup>3</sup>. The cube root of the number of gold atoms  $(N_{Au})^{1/3}$  in a volume  $V$  of a golden cube that is 1 cm along each edge will yield the spacing between layers of gold atoms, where Avogadro's number is  $N_A \equiv 6.02214076 \times 10^{23}$  particles/mole.

$$\sqrt[3]{N_{Au}} = \left(\frac{\rho_{Au} V}{M_{Au}} N_A\right)^{1/3} = 3.89 \times 10^7 / \text{cm} \quad (5.22)$$

With  $3.89 \times 10^7$  layers per centimeter, the average thickness of a single gold monolayer is  $t_{Au} = 2.57 \times 10^{-10}$  m = 2.57 Å.<sup>2</sup>

Assume that a disk of piezoelectric quartz is used that is  $L = t = 0.50$  mm thick and is vibrating in its fundamental free-free mode in a vacuum. The frequency of that mode is  $f_1 = c_L/2 L$ , where  $c_L = 5750$  m/s for quartz, so  $f_1 = 5.75$  MHz. Equation (5.21) can be used to calculate the decrease in the frequency of the fundamental mode,  $-\delta f_1$ , due to adsorption of a single monolayer of gold.

$$\delta f_1 = f_1 \left( \frac{\rho_{Au}}{\rho_{quartz}} \right) \left( \frac{t_{Au}}{L_{quartz}} \right) = -5.75\text{MHz} \left( \frac{19.3}{2.65} \right) \left( \frac{2.57 \times 10^{-10}}{5 \times 10^{-4}} \right) = -21.5\text{Hz} \quad (5.23)$$

A frequency shift of 21.5 Hz is easy to detect. For this example,  $-\delta f_1/f_1 = 3.74 \times 10^{-6}$ , or 3.74 parts per million (ppm) for addition of a single atomic layer of gold.

One common example is the control of metal deposition on integrated circuit “chips.” Gold is often “evaporated” in a vacuum system to deposit conduction paths between circuit elements and pin pads used to connect the integrated circuit to a printed circuit board. Monitoring the change in frequency of a quartz microbalance is an accurate way to determine when the desired thickness has been achieved.

### 5.1.3 Bodine’s “Sonic Hammer”

At this point in the analysis, we would normally address the response of the driven system. Since the analogies between longitudinal vibrations in a thin bar and the transverse vibrations of a string are seen to be exact, we will focus on an interesting application instead. At the opposite extreme in size from the use of longitudinal resonance to weigh thin films with better than microgram precision, we will now focus on a method of driving pilings weighing several metric tons by exciting a standing wave resonance in “thin” bars. Shown below in Fig. 5.3 (left) is a construction site where a piling is to be driven into the ground by excitation of the longitudinal standing wave resonance of the pile.

An ordinary pile driver raises and releases a mass to drive (i.e., hammer) the pile into the ground, effectively launching a longitudinal pulse that travels down the pile until it reaches the end that is in contact with the earth and where the pulse reflection transmits a force that promotes penetration of the pile. Such “drop hammers” used for pilings of the size shown in Fig. 5.3 (right) will require masses in the range of several metric tons, typically 1500–4000 kg, dropped from heights of 2 to 3 m above the piling. Each impact releases between 30 kJ and 120 kJ per blow. Assuming about one blow every 2 s, using an average of 60 kJ/blow, deposits an average power of  $30\text{ kJ} \cong 40\text{ hp}$  to the pile.<sup>3</sup>

A “sonic hammer,” exciting the pile at its longitudinal resonance frequency, stores vibrational (or strain) energy in the pile and only has to replace the energy delivered to the earth to maintain steady-state operation at constant vibratory amplitude. The maximum stored potential energy ( $PE$ )<sub>max</sub> can be calculated in the usual way for a bar of cross-sectional area,  $S_x$ ; length,  $L$ ; and volume,  $V = S_x L$ , using Eq. (1.22) or Eq. (2.14). The maximum vibrational strain amplitude is  $\varepsilon_{xx}$  and  $\xi = \varepsilon_{xx} dx$  is defined in Eq. (5.1).

---

<sup>2</sup>This is a slight underestimate because the crystalline structure of gold is face-center cubic. The accepted atomic diameter for gold is 2.88 Å.

<sup>3</sup>One horsepower [hp] is defined as 745.7 W.



**Fig. 5.3** (Left) Job site during preparation to drive a pile using resonant excitation provided by two engines from a Sherman tank. The engines provided counterrotation of eccentric masses (see Fig. 5.4) that drove the pile at its longitudinal standing wave resonance frequency. (Right) A 140 kW (200 HP) resonant driver, mounted on a 60 cm diameter steel pile, that uses a high-speed hydraulic valve to drive the pile at resonance. (Photographs courtesy of Matthew Janes)

$$(PE)_{\max} = - \int_0^L F_x d\xi = S_x \int_0^L E e_{xx}^2 dx = S_x E \int_0^L e_{xx}^2 \cos^2\left(\frac{n\pi x}{L}\right) dx = \frac{E e_{xx}^2}{2} V \quad (5.24)$$

This analysis will be applied to a steel pipe with wall thickness of 22 mm and outside diameter of 30.0 cm, that is, 17.8 m long, with a mass of 2668 kg [3]. With resonant excitation, the pipe penetrated over 9 m in 14 min. A drop hammer could sink the first few meters of pipe with 60 blows/m, but at greater depths, 150–200 blows/m were required. For 9 m penetration, over 1000 blows were required taking over 40 min.

More importantly, for construction in dense urban locales, the ground vibrations due to the use of a drop hammer exceed the limit that can cause damage to existing structures nearby. In a similar experiment, ground vibrations from a drop hammer measured 10 m from the pile showed ground accelerations of  $1.75 \text{ m/s}^2$ , while the resonant drive produced accelerations of  $0.25\text{--}0.30 \text{ m/s}^2$  at the same measurement distance [3].

At the job site, construction workers can measure the amplitude of vibration near a velocity antinode by taking a chalk stick and drawing a line along the pile's circumference. Since the surface of the pile is vibrating up and down, this draws a sinusoid and provides a visual representation of the peak-to-peak vibrational displacement,  $2\xi_o$ . For this type of installation,  $2\xi_o \cong 6 \text{ cm}$ , and the resonance frequency is roughly 100 Hz. The maximum fully reversing strain,  $\epsilon_{xx} \cong 0.03/17.8 = 1.7 \times 10^{-3}$ , is well below the elastic limit of steel. The total volume of steel in the pipe is  $V = 0.37 \text{ m}^3$ . Using  $E_{\text{steel}} = 195 \text{ GPa}$ , the total stored potential energy given by Eq. (5.24) is  $(PE)_{\max} \cong 100 \text{ kJ}$ , fairly close to the energy in a single hammer drop, except this energy is available continuously.

The rate at which this energy is delivered to the ground depends upon the quality factor of the resonance, usually dominated by the losses at the entry cavity. In this demonstration, the average

power delivered to the pipe  $\langle \Pi \rangle_t \cong 50 \text{ kW}$ .<sup>4</sup> Using Eq. (2.70), the average quality factor for the pipe's longitudinal vibration can be calculated.

$$Q = \frac{2\pi f E_{stored}}{\langle \Pi \rangle_t} \cong 1300 \quad (5.25)$$

In addition to the reduction in surrounding vibrations for the pile driving application, this resonant vibrational strategy has other applications. In particular, since the resonant method does far less damage to the surrounding material, it is a good way to take geological core samples. It is particularly well-suited to ice core sampling, since very little damage is done to the ice and it takes less time to cut the core (which is important in Arctic weather conditions). This technique has also been used for tunneling in the construction of the Bay Area Rapid Transit (BART) subway system around San Francisco, Oakland, and Berkeley in California. A similar approach has also been developed for rock crushing [5], although that device used resonant excitation of the chute to shake the crushing balls against the material, not longitudinal waves in bars.

There have been problems with these longitudinally resonant pile drivers. The early drivers were prone to failure due to the enormous cyclic loading of the bearings and gears shown in Fig. 5.4. In some cases, crane operators were responsible for the failure because they could not believe that the piles would sink so quickly and did not lower the drive mechanism quickly enough for the ground to absorb the vibrational energy. The reduced cutting load caused the  $Q$  of the pile to become so large that the increased vibrational amplitude damaged the drivers. Hydraulic actuators have largely removed that difficulty. Since the resonance frequency changes continuously as the pile or pipe enters the ground, a control system can be employed to keep the system "tuned" to the longitudinal bar resonance as its length changes and as it encounters differing soils.

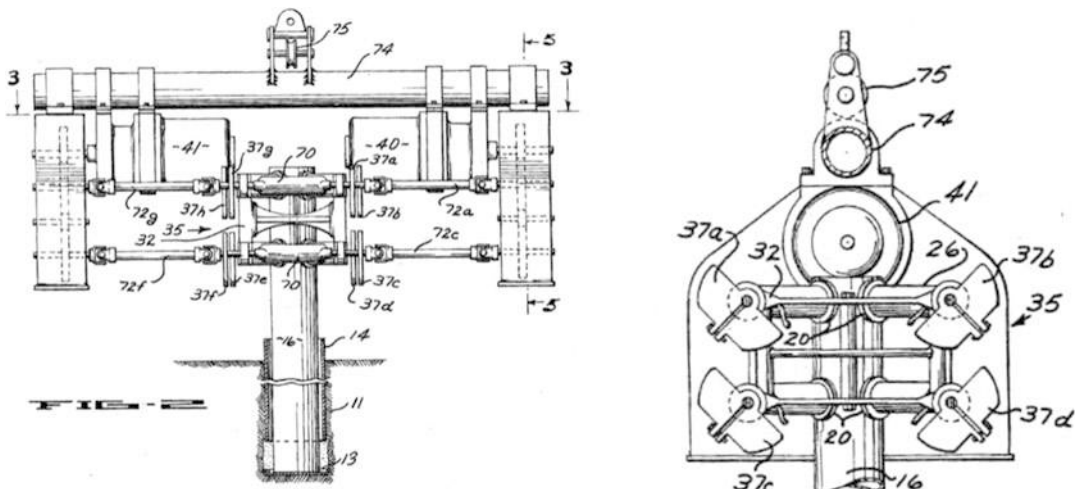


**Fig. 5.4** (Left) Mechanical driving system attached to the top of the piling for resonant excitation of longitudinal standing waves in a construction. Motors (40 and 41) drive shafts (72), through gearboxes that are connected to the eccentrically mounted masses (37) to provide the longitudinal excitation to the top of the piling (16). (Right) View showing the rotating eccentric masses (37) [4]

<sup>4</sup> Using hydraulic fluid at 17 MPa, with an average flow rate of  $U = 4.5 \text{ l/s} = 4.5 \times 10^{-3} \text{ m}^3/\text{s}$ , the hydraulic power  $\langle \Pi \rangle_t = (\Delta p) U \cong 76 \text{ kW}$ .

## 5.2 Torsional Waves in Thin Bars

The same procedure that has been used for the longitudinal waves can be applied used to calculate the speed of torsional wave propagation in thin bars or tubes of circular cross-section and to calculate the speed of shear waves in bulk solids. Since we have already calculated the torque required to twist a circular rod or tube of length,  $L$ , by an angle,  $\phi$ , in Eq. (4.50), that result can be applied to a differential length,  $dx$ , of a solid rod of radius,  $a$ . The difference in the twist at  $x$  and at  $x + dx$  is  $d\phi$ , so  $\phi/L$  becomes  $\partial\phi/\partial x$ .

$$N(x) = G \frac{\pi a^4}{2} \frac{\partial \phi}{\partial x} \quad (5.26)$$

The difference in the torque between the ends of the differential element is then approximated by a Taylor series.

$$dN(x) = N(x + dx) - N(x) = \left( \frac{\partial N}{\partial x} \right) dx = G \frac{\pi a^4}{2} \left( \frac{\partial^2 \phi}{\partial x^2} \right) dx \quad (5.27)$$

For a circular rod with constant mass density,  $\rho$ , the mass of the differential element is just  $dm = \rho \rho a^2 dx$ . The *polar moment of inertia*,  $I_{disk}$ , of a circular disk is  $ma^2/2$ , so for the differential element,  $I_{disk} = (\pi/2)\rho a^4 dx$ .

Newton's Second Law guarantees that the net torque is equal to the moment of inertia times the angular acceleration.

$$dN(x) = G \frac{\pi a^4}{2} \left( \frac{\partial^2 \phi}{\partial x^2} \right) dx = dI_{disk} \left( \frac{\partial^2 \phi}{\partial t^2} \right) dx = \frac{\pi}{2} \rho a^4 \left( \frac{\partial^2 \phi}{\partial t^2} \right) dx \quad (5.28)$$

This result can be rearranged to yield a torsional wave equation for a rod of circular cross-section that introduces the shear wave speed,  $c_s$ .

$$\frac{\partial^2 \phi}{\partial x^2} - \frac{\rho}{G} \frac{\partial^2 \phi}{\partial t^2} = 0 \Rightarrow c_s = \sqrt{\frac{G}{\rho}} \quad (5.29)$$

For a circular bar of radius,  $a$ , the propagation speed,  $c_s$ , for torsional waves does not depend upon the radius of the bar. In fact, since the volume is unchanged by shear deformation, it does not even require that the radius,  $a$ , be much less than  $\lambda$ , as was the case for longitudinal waves. Since there is no volume change, there is no "bulge" regardless of the ratio of the sample size to the wavelength. Bulk shear waves also propagate at  $c_s$ .

The torsional wave speed in a thin bar does depend on the shape of the bar's cross-section. We can generalize the torque equation that was written in Eq. (5.26) to shapes that are not circularly symmetric by introducing a *torsional rigidity*,  $J$ , which will depend upon the bar's cross-sectional shape [6].

$$N(x) = J \frac{\partial \phi}{\partial x} \quad (5.30)$$

Values for  $J/G$  are provided in the second column of Table 5.1, so for our circular bar example,  $J_{disk} = \pi Ga^4/2$ , as expressed in Eq. (5.26). Similarly, the polar moment of inertia,  $I$ , can be evaluated for the corresponding cross-sectional shape as provided in the third column of Table 5.1. Both  $J$  and  $I$  can be substituted into the wave equation to produce a torsional wave speed,  $c_{ss}$ , that is dependent upon the cross-sectional shape of a thin bar with transverse dimensions that are much less than the length [7].

**Table 5.1** Both the torsional rigidity,  $J$ , and the moment of inertia,  $I$ , of a rod depend upon the shape of its cross-section

Cross-section	$NL/G \equiv J/G$	$I$	Torsional speed
<b>Circular</b> Radius = $a$	$\frac{\pi a^4}{2}$	$\frac{\pi a^4}{2}$	$c_S$
<b>Ring</b> Outer = $a_{out}$ Inner = $a_{in}$	$\frac{\pi(a_{out}^4 - a_{in}^4)}{2}$	$\frac{\pi(a_{out}^4 - a_{in}^4)}{2}$	$c_S$
<b>Elliptical</b> Semi-major = $a$ Semi-minor = $b$	$\frac{\pi a^3 b^3}{a^2 + b^2}$	$\frac{\pi}{4} ab(a^2 + b^2)$	$\frac{2ab}{a^2 + b^2} c_S$
<b>Square</b> Edge = $w$	$9w^4/64$	$w^4/6$	$\sqrt{\frac{27}{32}} c_S \cong 0.92 c_S$
<b>Rectangular</b> Thickness = $t$ Width = $w$	$\frac{wt^3}{16} \left[ \frac{16}{3} - 3.36 \frac{t}{w} \left( 1 - \frac{t^4}{12w^4} \right) \right]$	$\frac{tw(t^2 + w^2)}{12}$	$\frac{2t}{w} c_S$ if $t \ll w$
<b>Equilateral triangle</b> Edge = $a$	$\frac{a^4 \sqrt{3}}{80}$	$\frac{\sqrt{5}a^4}{80}$	$\sqrt[4]{\frac{3}{5}} c_S \cong 0.88 c_S$

$$\frac{\partial^2 \phi}{\partial x^2} - \frac{J}{\rho I} \frac{\partial^2 \phi}{\partial t^2} = 0 \quad \Rightarrow \quad c_{SS} = \sqrt{\frac{J}{\rho I}} \quad (5.31)$$

Table 5.1 summarizes the speed of torsional waves on bars of various cross-sectional shapes by taking the ratio of the torsional stiffness-length product that relates static torque,  $N$ , to the shear modulus,  $G$ , and dividing by the polar moment of inertia,  $I$ . These factors for a rod and a hollow tube were calculated in Sect. 4.3.5 and given in Eq. (4.45). The other stiffness-length products were taken from Table 20 in Roark [8].

The torsional stiffness-length product (or ratio of torsional rigidity to shear modulus) is provided by the ratio of the torque,  $N$ , divided by the shear modulus,  $G$ . The ratio of torsional stiffness-length product to the moment of inertia,  $I$ , provides the constant multiplying the shear wave speed,  $c_S$ , for each bar cross-sectional shape.

### 5.3 Flexural Waves in Thin Bars

The last of the three independent vibrational modes of thin bars mentioned in the introduction is the flexural or bending modes. We will again follow the same procedure to determine their behavior, but that path will take us to a description that is fundamentally different from the results we have derived for transverse waves on strings or the longitudinal and torsional waves in thin bars. As was done for the case of transverse waves, we seek an expression for the vertical force,  $F_y(x)$ , on a differential element that can be related to its inertia via Newton's Second Law. We start from the expression for the bending moment,  $\mathfrak{M}$ , in the limit of small displacements, which is related to the curvature in Eq. (4.29).

$$\mathfrak{M} = -ESk^2 \frac{\partial^2 y}{\partial x^2} \quad (5.32)$$

The square of the radius of gyration,  $k^2$ , is defined in Eq. (4.29).

Using the fact that the moment is the torque produced by an applied force times its perpendicular distance from the reference point, we can calculate the vertical force that creates the moment in Eq. (5.32). It can be calculated by placing the reference location at  $x = 0$ . In that way, the vertical force applied at  $x = 0$  has no moment. The torque due to the shear force at  $x + dx$  will be the product of  $F_y(x + dx)$  and its “lever arm,”  $dx$ .

$$F_v(x + dx)dx = \mathfrak{M}(x + dx) - \mathfrak{M}(x) \quad (5.33)$$

By our choice of  $x = 0$  as the reference location,  $\mathfrak{M}(x) = 0$ . A Taylor series can then be exploited to express the moment of the vertical force,  $F_v(x + dx)dx$ , that will counteract the moment.

$$F_v(x + dx)dx = \frac{\partial \mathfrak{M}}{\partial x} dx = -ES_x\kappa^2 \frac{\partial^3 y}{\partial x^3} dx \quad (5.34)$$

This expression for the vertical component of the force plays the same role as Eq. (3.2) that relates the slope of the string to the vertical force on a string element, or Eq. (5.2) that relates the stress in the bar to the longitudinal force on the bar element. Of course, Eqs. (3.2) and (5.2) related these forces to a first derivative with respect to position of the displacement from equilibrium, while Eq. (5.34) relates the vertical force to the third derivative of the displacement.

We determine the net vertical force acting on our differential element in the usual way.

$$dF_v = F_v(x + dx) - F_v(x) = \frac{\partial F_v}{\partial x} dx = -ES_x\kappa^2 \frac{\partial^4 y}{\partial x^4} dx \quad (5.35)$$

This result is also known as the Euler-Bernoulli beam equation after Leonhard Euler and Daniel Bernoulli who first derived this result in the 1750s [9]. The combination of Young's modulus for the beam multiplied by the area and the radius of gyration is known as the *flexural rigidity*,  $ES_x\kappa^2$ , since it is a measure of the moment of the force necessary to deform the bar.

The mass of the differential element is  $\rho S_x dx$ , so Newton's Second Law produces the differential equation describing the bar's dynamic response to flexure.

$$\rho S_x dx \frac{\partial^2 y}{\partial t^2} = -ES_x\kappa^2 \frac{\partial^4 y}{\partial x^4} dx \Rightarrow \frac{\partial^2 y}{\partial t^2} + \kappa^2 c_B^2 \frac{\partial^4 y}{\partial x^4} = 0 \quad (5.36)$$

The right-hand expression makes use of the propagation speed of longitudinal waves in thin bars,  $c_B^2 = E/\rho$ , after cancellation of the common factors  $dx$  and  $S_x$ .<sup>5</sup>

### 5.3.1 Dispersion

Equation (5.36) is a linear, fourth-order, homogeneous, partial differential equation that is clearly **not** the wave equation. Its solutions will not be just any functions of the argument  $x \pm ct$ , where  $c$  is a constant (independent of frequency or wavelength) representing the propagation speed for all waves. Fortunately, Eq. (5.36) contains only even-order partial derivatives, so substitution of a complex exponential will provide a relation between frequency and wavenumber that is a real number.<sup>6</sup> This relationship can be demonstrated by substitution of our usual rightward-going traveling wave solution,  $y(x, t) = \Re e^{[\hat{\mathbf{C}} e^{j(\omega t - kx)}]}$ , into Eq. (5.36) to solve the time-independent Helmholtz equation.

<sup>5</sup>This equation is only approximately correct since the moment is also opposed by the rotary inertia of the bar. The approximation is very good when  $\lambda \gg a$ , which is our current focus. The complete equation for the dynamics, which includes rotary inertia and shear, is derived in several references, for example, D. Ross, *The Mechanics of Underwater Noise* (Pergamon, 1976); ISBN 0-08-021182-8.

<sup>6</sup>As will be shown in Chap. 9 on dissipative hydrodynamics, this is not the case for equations that contain both odd- and even-order derivatives. The Navier-Stokes equation, describing viscous dissipation; the Fourier heat diffusion equation, describing thermal conduction losses; and the Schrodinger equation of quantum mechanics all contain both odd- and even-order derivatives that require complex numbers to relate frequency and wavenumber.

$$-\omega^2 y + \kappa^2 c_B^2 k^4 y = 0 \Rightarrow k = \pm \sqrt{\frac{\omega}{\kappa c_B}} \quad (5.37)$$

The most useful equation in acoustics is the relationship between frequency and wavelength:  $f\lambda = \omega/k = c$ . Up to this point,  $c$  has been treated as a constant in all systems, irrespective of frequency or wavelength. This is not the case for solutions to Eq. (5.36). We can solve Eq. (5.37) for the ratio of frequency to wavenumber.

$$\frac{\omega^2}{k^2} = \kappa^2 c_B^2 k^2 \Rightarrow \frac{\omega}{k} = \pm (\kappa c_B) k = \pm 2\pi \frac{\kappa c_B}{\lambda} \quad (5.38)$$

The propagation speed for harmonic flexural waves of frequency,  $\omega$ , is inversely proportional to the wavelength of the disturbance.

In all our previous solutions to the dynamical response for systems described by the wave equation,  $\omega/k$  is equal to a constant,  $c$ , that is identified as the speed of propagation for all wavelike disturbances, whether they are pulses or harmonic waves, of either the traveling or standing variety, independent of their frequency or wavelength. Equation (5.38) demonstrates that the ratio of frequency to wavenumber is no longer a constant that is independent of frequency for flexural waves on bars.

$$c_{ph} \equiv \frac{\omega}{k} = \pm \sqrt{\kappa \omega c_B} \quad (5.39)$$

Because there is no longer a single speed of propagation for all disturbances, we have defined the *phase speed*,  $c_{ph} \equiv \omega/k$ . This is the speed of propagation of wave fronts of any disturbance that is a *pure tone*, having a single frequency,  $\omega$ , and a single wavelength,  $\lambda$ , thus containing only one Fourier component. A wavelike disturbance that contains more than one Fourier component will not retain its shape as it propagates under the influence of Eq. (5.36), which is still a linear equation. Since the different frequency components of such a disturbance will travel with different speeds, Eq. (5.39) implies that the higher-frequency components will get ahead of the lower-frequency components, so the waveform produced by their superposition will change over time and distance.

The dependence of propagation speed on frequency or wavelength is known as *dispersion*. Dispersion of light waves was demonstrated experimentally by Newton [10] who used a glass prism to separate white light into its different constituent wavelengths. The angle of refraction of light passing through a transparent medium depends upon the ratio of the propagation speeds, in Newton's case, between air and glass. For glass, that propagation speed depends upon the wavelength of the light. In effect, the prism provided a Fourier analysis (64 years before the birth of Fourier) of the different frequency components (different colors) that superimpose to create white light.<sup>7</sup> The genius of Isaac Newton was displayed by his use of a second prism to recombine the different colors to produce white light, thus demonstrating that the colors were not an experimental artifact.

Capillary waves on the surface of water have the same dispersion relation as flexural waves on thin bars [11],  $c_{ph} = (2\pi\sigma/\rho\lambda)^{1/2}$ , where  $\sigma$  is the surface tension of water.<sup>8</sup> Like flexural waves on thin bars,

<sup>7</sup> The laws of electromagnetism, known as Maxwell's equations, which govern the propagation of light, are also linear differential equations.

<sup>8</sup> The full dispersion relation for surface waves on fluids produces the dispersion relation (below) that also includes the force of gravity  $g$ , which dominates the restoring force at long wavelengths, as well as surface tension (capillarity). When the wavelengths are long compared to the depth,  $h$ , so  $kh \ll 1$ ,  $\tanh(kh)$  is proportional to  $kh$  and the speed is again dispersionless. On water, capillarity (surface tension,  $\sigma$ ) dominates gravity for wavelengths less than about one-half centimeter.

$$c_{ph}^2 = \frac{\omega^2}{k^2} = \left( \frac{g}{k} + \frac{\sigma}{\rho} k \right) \tanh(kh)$$



**Fig. 5.5** This photograph of a water drop's splash clearly illustrates the dispersion of waves that have a phase velocity,  $c_{ph}$ , that is inversely related to the wavelength. The components of the disturbance with the shortest wavelengths have moved ahead of the longer-wavelength components. The dispersion for surface waves on water with wavelengths less than about 5 mm is dominated by surface tension.<sup>9</sup>

shorter wavelengths (i.e., higher frequencies) propagate faster than longer wavelengths. This is visible in Fig. 5.5, where a drop of water launches cylindrically diverging surface waves with the short wavelengths moving away from the source faster than the longer-wavelength components produced by the splash.<sup>9</sup>

### 5.3.2 Flexural Wave Functions

Capitalizing on our success with the substitution of a complex traveling waveform,  $y(x, t) = \Re[\hat{\mathbf{C}} e^{j(\omega t - kx)}]$ , into Eq. (5.36) to produce the dispersion relations of Eqs. (5.37), (5.38), and (5.39), we will now seek a complete solution to Eq. (5.36) by the method known as *separation of variables*. By setting  $y(x, t) = Y(x) T(t)$ , the spatial dependence of the solution depends only upon  $Y(x)$ , and the temporal behavior depends only upon  $T(t)$ . Since Eq. (5.36) is a linear equation, we can still construct more complicated waveforms by the superposition of harmonic waves, so we will let  $T(t) = e^{j\omega t}$ . Substitution of  $T(t)$  into Eq. (5.36) converts it from a partial differential equation to an ordinary (forth-order) differential equation for  $Y(x)$ .

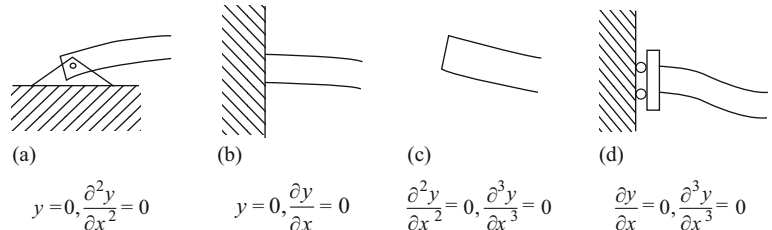
$$\frac{d^4 Y}{dx^4} = \frac{\omega^2}{\kappa^2 c_B^2} Y = \frac{\omega^4}{c_{ph}^4} Y \quad (5.40)$$

Letting  $Y(x) = Y e^{kx}$ , a simple quartic expression is generated for the wavenumber  $k$ :  $k^4 = (\omega/c_{ph})^4$ . By taking the fourth root (see Sect. 1.5.2), we generate four solutions for  $k = \pm\omega/c_{ph}$  and  $\pm j\omega/c_{ph}$ . Those four solutions are superimposed in Eq. (5.41).

$$y(x, t) = [C_1 e^{(\omega x/c_{ph})} + C_2 e^{-(\omega x/c_{ph})} + C_3 e^{j(\omega x/c_{ph})} + C_4 e^{-j(\omega x/c_{ph})}] e^{j\omega t} \quad (5.41)$$

<sup>9</sup>For ripple-tank demonstrations, the depth of the water is about 5 mm. At that depth, the restoring forces of gravity and surface tension balance to produce a frequency-independent surface wave velocity,  $c \cong 23$  cm/s. [See M. J. Lighthill, *Waves in Fluids* (Cambridge, 1978); ISBN 0 521 21689 3. Sec. 1.8 (Ripple-tank simulations)]

**Fig. 5.6** Schematic representation of four possible boundary conditions for flexure of a bar: (a) hinged, (b), clamped, (c) free, and (d) guided or sliding. From Han et al. [12]



This result confirms our first solution, a right-going traveling wave, that was used to produce Eq. (5.37), corresponding to  $C_1 = C_2 = C_3 = 0$  and  $C_4 \neq 0$ . Linearity allows us to combine these exponential solutions to produce a solution that can be expressed as four independent trigonometric functions with real constants.

$$A = (C_1 + C_2)/2, \quad B = (C_1 - C_2)/2, \quad C = (C_3 + C_4)/2, \quad D = (C_3 - C_4)/2j. \quad (5.42)$$

$$y(x, t) = \left[ A \cosh \left( \frac{\omega x}{c_{ph}} \right) + B \sinh \left( \frac{\omega x}{c_{ph}} \right) + C \cos \left( \frac{\omega x}{c_{ph}} \right) + D \sin \left( \frac{\omega x}{c_{ph}} \right) \right] \cos(\omega t + \phi)$$

Since these are solutions to a fourth-order differential equation, four boundary conditions must be specified to determine the four amplitude coefficients. The four most common “perfect” boundary conditions are clamped, free, hinged, and guided. They are summarized in Fig. 5.6.

If the bar is clamped, then the end cannot move in the vertical direction, so  $y = 0$ . The clamped end of the bar must also approach that boundary with zero slope, so  $(\partial y / \partial x) = 0$ . If the bar is free, then the boundary can exert no moments (torques), so from Eq. (5.32),  $(\partial^2 y / \partial x^2) = 0$ . The free boundary cannot provide any vertical forces, so from Eq. (5.34),  $(\partial^3 y / \partial x^3) = 0$ .

A hinged boundary (or knife-edged clamp) will also make  $y = 0$ . Due to the hinge, the boundary can exert no torques, so  $(\partial^2 y / \partial x^2) = 0$ . Of course, the hinge applies vertical forces to keep  $y = 0$ , so  $(\partial^3 y / \partial x^3) \neq 0$ . A guided or sliding boundary allows the beam to move in the vertical direction (i.e.,  $y \neq 0$ ) but constrains both the slope and the vertical force to be zero.

### 5.3.3 Flexural Standing Wave Frequencies

In Sect. 4.3.2, we calculated the deflection curve for a horizontal cantilevered beam that was clamped at  $x = 0$  ( $y = 0$  and  $\partial y / \partial x = 0$ ) and was loaded by a vertical force (e.g., a weight) at  $x = L$  (see Galileo’s illustration in Fig. 2.27). We will start this section by calculating the normal modes of oscillation for a cantilevered beam that is clamped at  $x = 0$  and is free at  $x = L$ . Using the trigonometric form of the general solution in Eq. (5.42) and applying the boundary condition at  $y(0) = 0$ ,  $\sinh(x)$  and  $\sin(x)$  are automatically zero, but  $\cos(x)$  and  $\cosh(x)$  are both equal to 1, so  $A = -C$ . For the slope to vanish at  $x = 0$ ,  $B = -D$ , since  $d(\sinh(x))/dx = \cosh(x)$  and  $d(\sin(x))/dx = \cos(x)$ . Suppressing the time dependence temporarily (no pun intended), the wave function for the cantilever beam can be written with only two arbitrary constants when it is clamped at  $x = 0$ .

$$y(x) = A \left[ \cosh \left( \frac{\omega x}{c_{ph}} \right) - \cos \left( \frac{\omega x}{c_{ph}} \right) \right] + B \left[ \sinh \left( \frac{\omega x}{c_{ph}} \right) - \sin \left( \frac{\omega x}{c_{ph}} \right) \right] \quad (5.43)$$

Evaluation of the second and third derivatives of Eq. (5.43) at  $x = L$  will provide the quantization of the allowable modal (normal mode) frequencies,  $\omega_n$ , and wavenumbers,  $k_n$ .

$$\begin{aligned} A \left[ \cosh \left( \frac{\omega_n L}{c_{ph}} \right) + \cos \left( \frac{\omega_n L}{c_{ph}} \right) \right] + B \left[ \sinh \left( \frac{\omega_n L}{c_{ph}} \right) + \sin \left( \frac{\omega_n L}{c_{ph}} \right) \right] &= 0 \\ A \left[ \sinh \left( \frac{\omega_n L}{c_{ph}} \right) - \sin \left( \frac{\omega_n L}{c_{ph}} \right) \right] + B \left[ \cosh \left( \frac{\omega_n L}{c_{ph}} \right) + \cos \left( \frac{\omega_n L}{c_{ph}} \right) \right] &= 0 \end{aligned} \quad (5.44)$$

Both of the equations in Eq. (5.44) can be used to solve for  $B$  in terms of  $A$ .

$$B = A \frac{\sin \left( \frac{\omega_n L}{c_{ph}} \right) - \sinh \left( \frac{\omega_n L}{c_{ph}} \right)}{\cos \left( \frac{\omega_n L}{c_{ph}} \right) + \cosh \left( \frac{\omega_n L}{c_{ph}} \right)} = -A \frac{\cos \left( \frac{\omega_n L}{c_{ph}} \right) + \cosh \left( \frac{\omega_n L}{c_{ph}} \right)}{\sin \left( \frac{\omega_n L}{c_{ph}} \right) + \sinh \left( \frac{\omega_n L}{c_{ph}} \right)} \quad (5.45)$$

After cancellation of the common factor of  $A$ , cross-multiplication of the left and right fractions in Eq. (5.45) produces a single equation that quantizes the normal mode frequencies,  $\omega_n$ .

$$\sinh^2 \left( \frac{\omega_n L}{c_{ph}} \right) - \sin^2 \left( \frac{\omega_n L}{c_{ph}} \right) = \left[ \cosh \left( \frac{\omega_n L}{c_{ph}} \right) + \cos \left( \frac{\omega_n L}{c_{ph}} \right) \right]^2 \quad (5.46)$$

Application of the trigonometric identities  $\cos^2(\theta) + \sin^2(\theta) = 1$  and  $\cosh^2(\theta) - \sinh^2(\theta) = 1$  produces a workable transcendental equation that can be solved for the normal mode frequencies.

$$\cosh \left( \frac{\omega_n L}{c_{ph}} \right) \cos \left( \frac{\omega_n L}{c_{ph}} \right) = -1 \quad (5.47)$$

The solution of Eq. (5.47) is inconvenient because the hyperbolic cosine will diverge exponentially. The use of the following half-angle formulas can afford further simplification.

$$\tan^2 \left( \frac{\theta}{2} \right) = \frac{1 - \cos \theta}{1 + \cos \theta} \quad \text{and} \quad \tanh^2 \left( \frac{\theta}{2} \right) = \frac{\cosh \theta - 1}{\cosh \theta + 1} \quad (5.48)$$

Since the limits of the hyperbolic tangent for large arguments are  $\pm 1$ , the following forms are both easier to graph and avoid the exponential divergence of the hyperbolic cosine.

$$\coth^2 \left( \frac{\omega_n L}{2c_{ph}} \right) = \tan^2 \left( \frac{\omega_n L}{2c_{ph}} \right) \quad \text{or} \quad \cot \left( \frac{\omega_n L}{2c_{ph}} \right) = \pm \tanh \left( \frac{\omega_n L}{2c_{ph}} \right) \quad (5.49)$$

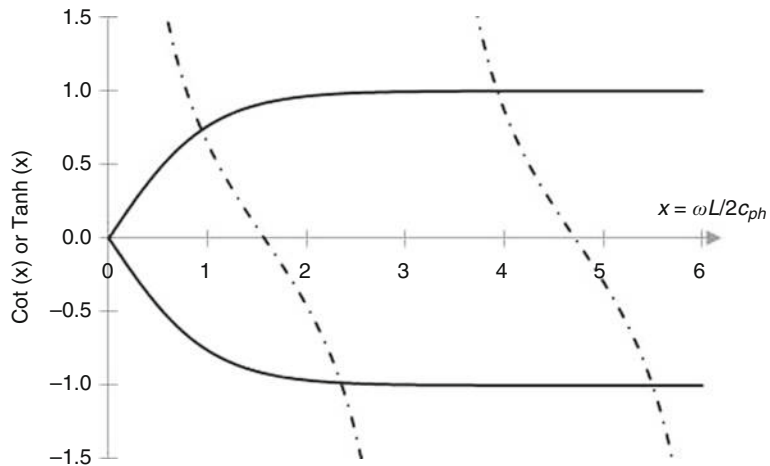
Figure 5.7 is a plot of the two functions on the right-hand side of Eq. (5.49) vs. their argument  $x = \omega L / 2c_{ph}$ . For arguments of  $x > 4$ , the value of  $\pm \tanh(x) \cong \pm 1$ .  $\text{Cot}^{-1}(x) = \pm 1$  for  $x = (2n - 1)(\pi/4)$ , so for  $n \geq 3$ ,  $\omega L / 2c_{ph} = (2n - 1)(\pi/4)$ . An equation solver can be used to calculate the lowest two solutions to Eq. (5.49) that are  $x_1 \cong 1.1937(\pi/4)$  and  $x_2 \cong 2.9884(\pi/4)$ .

Combining the solutions to Eq. (5.49) with the square of the phase speed in Eq. (5.39), the flexural normal mode frequencies,  $f_n$ , of the clamped-free bar can be written as a function of the geometry of the bar ( $L$  and  $\kappa$ ), Young's modulus, and the mass density of the beam's material,  $c_B = (E/\rho)^{1/2}$ .

$$f_n = \frac{\omega_n}{2\pi} = \frac{\pi}{8} \frac{c_B \kappa}{L^2} (1.1937^2, 2.9884^2, 5.0005^2, 7^2, 9^2, \dots) \quad (5.50)$$

It is worthwhile to point out the significant differences in this expression from those for the normal mode frequencies of the vibrating string and other systems that obey wave equations of the form of

**Fig. 5.7** The two terms on the right-hand side of Eq. (5.49) are plotted as a function of  $x = \omega L/2c_{ph}$ . The hyperbolic tangents are shown as solid lines and the dash-dot line is the cotangent. Their intersections define the normal mode frequencies,  $\omega_n$ , for a clamped-free (cantilevered) beam



Eq. (5.6) or Eq. (5.29). Even with “ideal” boundary conditions, the normal mode frequencies of the flexing bar are not harmonically related. Also, for flexural modes, frequency is inversely proportional to the length of the bar squared. The frequencies also depend explicitly on the cross-sectional shape of the bar through the radius of gyration,  $\kappa$ , as defined in Eq. (4.26). Measurement of the modal frequencies and damping has been used to determine Young’s modulus of small samples [13]. However, at least two independent modes have to be measured to determine both independent moduli for an isotropic solid [14].

### 5.3.4 Flexural Standing Wave Mode Shapes

The displacement amplitudes of the bar undergoing flexural vibrations in one of its normal modes can be determined by substituting the quantized wavenumber,  $k_n = \omega_n/c_{ph}$ , corresponding to the frequencies,  $f_n$ , of Eq. (5.50), into the mode shapes of Eq. (5.43).

$$y(x) = A_n [\cosh(k_n x) - \cos(k_n x)] + B_n [\sinh(k_n x) - \sin(k_n x)] \quad (5.51)$$

Following Eq. (5.45),  $B_n$  can be expressed in terms of  $A_n$ .

$$-B_n = A_n \frac{\cosh(k_n L) + \cos(k_n L)}{\sinh(k_n L) + \sin(k_n L)} = A_n \frac{\sinh(k_n L) - \sin(k_n L)}{\cosh(k_n L) + \cos(k_n L)} \quad (5.52)$$

Since the amplitude is arbitrary until the initial conditions are specified, we can choose to normalize the amplitudes by requiring that the integral over the length of the bar of the squared amplitude be  $(L/2)$ , just as it would be if the amplitude functions were just the sine and cosine functions used for standing wave solutions to the wave equation.

$$\int_0^L y^2(x) dx = \frac{L}{2} \quad (5.53)$$

Substitution of  $k_n L$  into Eq. (5.52) with all  $A_n = 1/\sqrt{2}$  makes  $B_1 = -0.518$ ,  $B_2 = -0.721$ , and all subsequent  $B_n = -1/\sqrt{2}$  for  $n \geq 3$ .

The mode shapes for  $1 \leq n \leq 4$  are shown in Fig. 5.8 and are compared to the solutions for the longitudinal modes of a fixed-free bar having the same wavelength. The ratio of the modal frequencies,

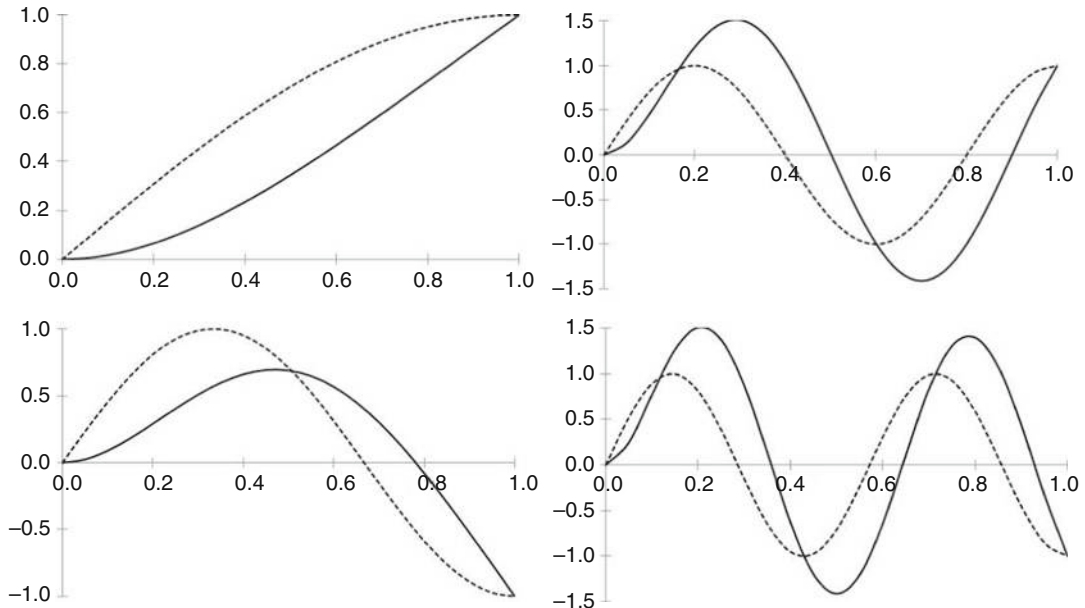


**Fig. 5.8** The mode shapes for flexural vibration of clamped-free bars (*solid line*) are compared to the longitudinal mode shapes of a fixed-free bar having the same wavelength (*dashed line*) for the four lowest modes, normalized to match the displacements of both modes at  $x = L$ . Frequency ratios and the location of the zero-crossings are provided in Table 5.2

**Table 5.2** Clamped-free (cantilevered) beam modal frequency ratios,  $f_n/f_1$ ; normalized wavelengths,  $\lambda_n/L$ ; and normalized location of standing wave displacement nodes as measured from the clamped end

Mode	$f_n/f_1$	$\lambda_n/L$	First node/L	Second node/L	Third node/L
1	1.0000	3.3508			
2	6.2669	1.3385	0.7806		
3	17.5475	0.7999	0.5017	0.8998	
4	34.3863	0.5714	0.3584	0.6428	0.9286

$f_n$ , to the fundamental mode frequency,  $f_1$ , is provided in Table 5.2, along with the normalized wavelengths,  $\lambda_n/L$ , and the normalized location of the displacement nodes as measured from the clamped end.

A bar with clamped boundaries on both ends can be solved in the same way, starting with Eq. (5.43), which satisfies the boundary conditions at  $x = 0$ . Using the same procedure to fit the clamped conditions at  $x = L$ , the wavenumbers are again quantized by a transcendental equation that is plotted in Fig. 5.9.

$$\cosh(k_n L) \cos(k_n L) = 1 \quad \text{or} \quad \tan\left(\frac{k_n L}{2}\right) = \pm \tanh\left(\frac{k_n L}{2}\right) \quad (5.54)$$

The resulting values of  $k_n L$  for the normal solutions of Eq. (5.54) can be combined with the phase speed in Eq. (5.39) to yield the flexural normal mode frequencies,  $f_n$ , of the clamped-clamped bar as a function of the geometry of the bar ( $L$  and  $\kappa$ ) and the properties of the bar's material,  $c_B = (E/\rho)^{1/2}$ .

**Fig. 5.9** The two terms on the right-hand side of Eq. (5.54) are plotted as a function of  $x = kL/2 = \omega_n L / 2c_{ph}$ . The hyperbolic tangents are shown as solid lines and the dashed lines are the tangent. Their intersections provide the normal mode frequencies,  $\omega_n$ , for a clamped-clamped or free-free bar

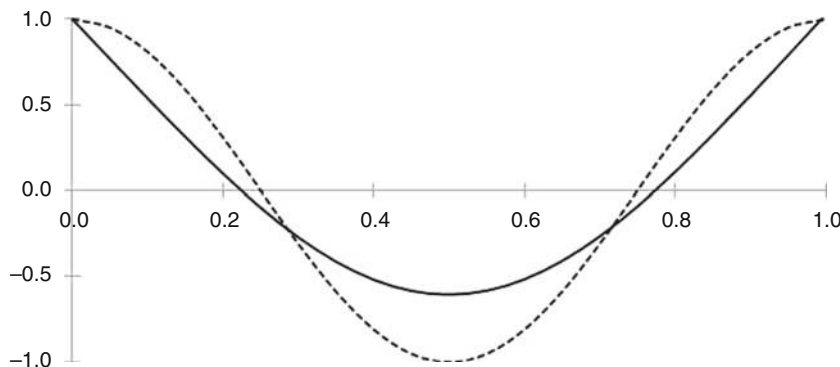
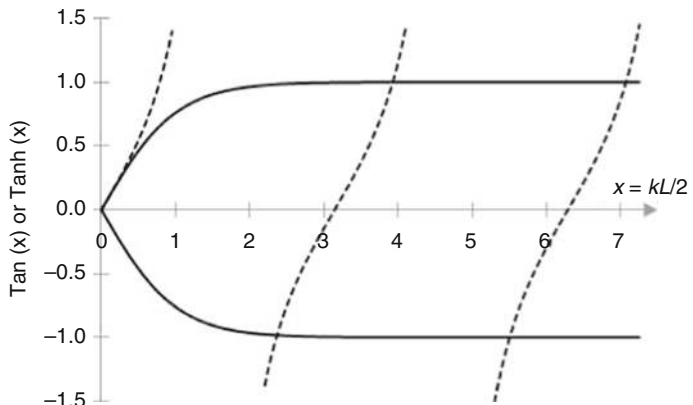


**Fig. 5.10** The flexural mode shape for a free-free bar (solid line) is compared to the longitudinal mode shapes of a free-free bar (dashed line) for the fundamental vibrational mode. Normalized to match the displacements of the flexural mode at  $x = 0$  and  $x = L$

$$f_n = \frac{\omega_n}{2\pi} = \frac{\pi}{8} \frac{c_B \kappa}{L^2} (3.01124^2, 4.99951^2, 7.00002^2, 9^2, 11^2, \dots) \quad (5.55)$$

The normal mode shapes are obtained, as before, by determining the  $B_n$ 's, again assuming  $A_n = 1/\sqrt{2}$ .

$$B_n = A_n \frac{\sin(k_n L) + \sinh(k_n L)}{\cos(k_n L) - \cosh(k_n L)} = -A_n \frac{\cos(k_n L) - \cosh(k_n L)}{\sin(k_n L) - \sinh(k_n L)} \quad (5.56)$$

Substitution of  $k_n L$  into Eq. (5.52) with all  $A_n = 1/\sqrt{2}$  makes  $B_1 = -0.6947$ , and all subsequent  $B_n = -1/\sqrt{2}$  for  $n \geq 2$ .

The flexural mode shapes for a free-free bar can be obtained by double differentiation with respect to  $x$  of the clamped-clamped mode shapes, resulting in the rather surprising fact that the normal mode frequencies for both free-free and clamped-clamped bars in flexure are identical.

The fundamental mode shape for the  $n = 1$  free-free bar is shown in Fig. 5.10. Again, it is compared to the solutions for the fundamental longitudinal free-free mode of a thin bar having the same length. The ratio of the modal frequencies,  $f_n$ , to the fundamental mode frequency,  $f_1$ , is provided in Table 5.3.

**Table 5.3** Clamped-clamped or free-free bar modal frequency ratios,  $f_n/f_1$ , and normalized wavelengths,  $\lambda_n/L$ . The remaining columns to the right of  $\lambda_n/L$  are the normalized location of standing wave displacement nodes for the free-free case

Mode	$f_n/f_1$	$\lambda_n/L$	First node/L	Second node/L	Third/L	Fourth/L	Fifth/L
1	1.0000	1.3284	0.2244	0.7734			
2	2.75654	0.8001	0.132	0.500	0.868		
3	5.40392	0.5714	0.094	0.356	0.644	0.906	
4	8.93295	0.4444	0.073	0.277	0.500	0.723	0.927

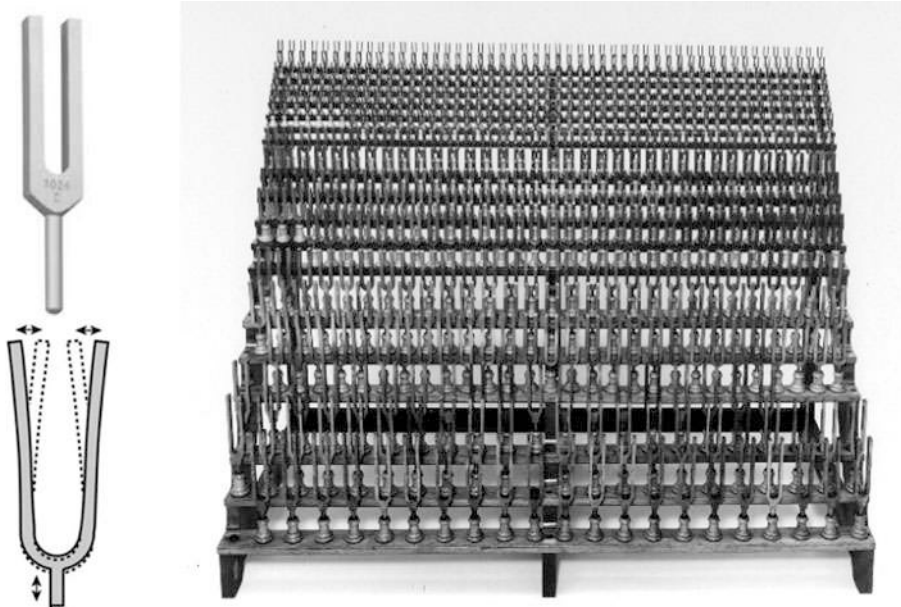


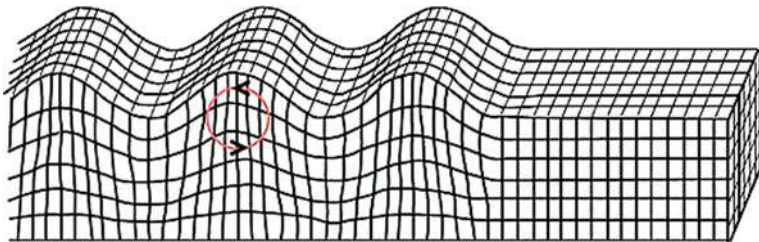
**Fig. 5.11** (Left) Traditional tuning forks are shown above with its fundamental mode of vibration shown below. (Right) This “tonometer” contains 670 tuning forks ranging from 16 Hz to 4096 Hz (eight octaves) and was built by the Prussian physicist K. Rudolph Koenig (1832–1901). It was displayed at the London Exhibition, in 1852, where it was awarded the gold medal for scientific instruments and was transported to the Philadelphia Exposition where it appeared in 1876. (Photo courtesy of the Smithsonian National Museum of American History)

The free-free flexural modes of bars are the percussive tone generators in the glockenspiel and many children’s toy instruments (e.g., Pixiphone).<sup>10</sup> By supporting the resonant bars at the nodal locations for the fundamental mode (see Table 5.3), the higher overtones will be present when the bar is struck, providing those instruments with a characteristically dramatic attack, which decays quickly, leaving the fundamental mode to linger.

A very common configuration for a free-free bar vibrating in its flexural mode is the tuning fork, shown in Fig. 5.11 (left) along with the “tonometer” that was commonly used to check the pitch of musical instruments. You may use an electronic instrument to tune your guitar or musical instrument, but the frequency standard inside the electronic device is likely to be a tiny quartz tuning fork. In fact, if

<sup>10</sup> The glockenspiel has bars of uniform cross-section, so the ratio of their overtones to the fundamental is given in Table 5.3. The underside of the bars in a xylophone is thinned near their center to make their overtones the ratio of integers:  $f_2/f_1 = 3$  and  $f_3/f_1 = 6$ .

**Fig. 5.12** Distortion of the free surface of a solid due to the propagation of a Rayleigh wave. Arrows indicate the motion of the material due to the wave



you own a “smartphone,” it probably has a tuning fork with tines that are about 2 mm long that is used as a gyroscope (angular rate sensor). The same is true for games, automotive anti-skid and navigation sensors, remote-controlled aircraft (drones), digital cameras, etc.

When the tines of a tuning fork are oscillating, as shown in Fig. 5.11, and the entire fork is rotated with some angular velocity,  $\vec{\Omega}$ , then the Coriolis force [15] can be expressed as  $\vec{F} = 2M(\vec{v} \times \vec{\Omega})$ , where  $M$  is the effective moving mass of the vibrating tines and  $\vec{v}$  is the velocity of the tines. This force will cause the tines to develop a component of their motion in a plane that is orthogonal (due to the cross-product) to the original plane of vibration. This out-of-plane motion is then sensed to determine the rate of rotation [16].

### 5.3.5 Rayleigh Waves\*

In principle, the phase speed in Eq. (5.39) could exceed the speed of light for large enough values of frequency,  $\omega$ . At such frequencies, the assumption that the transverse dimensions of the bar are much smaller than the wavelength ( $S^{1/2} \ll \lambda$ ) would be violated. As the frequency increases, these flexural waves do not bend the entire bar but become localized deformations at the surface. Such waves are known as Rayleigh waves [17], and their associated deformations are diagrammed in Fig. 5.12. A derivation of their propagation speed would take us too far from our development of waves on bars and is available elsewhere [7]. The speed of Rayleigh waves is about 10% slower than the shear wave speed,  $c_s$ , and is nondispersive.

The Rayleigh wave solutions are not contained in Eq. (5.36) because that equation does not include the contributions of rotary inertia and shear that become important at higher frequencies [18].

---

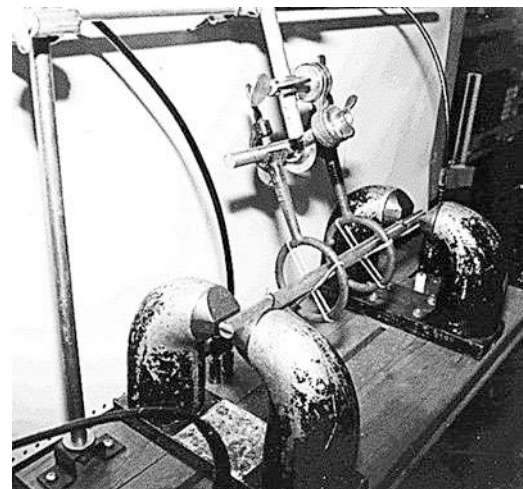
## 5.4 Resonant Determination of Elastic Moduli

*“One of the most precise ways of measuring the elastic constants of a substance is by measuring the density of the material and the speeds of two kinds of waves.”* R. P. Feynman. [14]

Having derived the normal mode frequencies for longitudinal, torsional, and flexural vibrations of a thin bar, this section will describe a simple and inexpensive apparatus that can selectively excite and detect these modes. In addition to the pedagogical value of such an apparatus, it is also an excellent way to determine the elastic moduli of materials that are not ferromagnetic [19]. Sample data will be presented and analyzed for a composite of high tensile strength epoxy [20] with 20% glass fibers (by weight) to determine its Young’s and shear moduli. In Sect. 5.4.5, the technique will be used to illustrate the viscoelastic behavior of an elastomer.

The (intentionally crude) apparatus, shown in Fig. 5.13, suspends the ends of the bar sample in between the pole pieces of two strong horseshoe magnets. Both ends of the bar are free and have coils

**Fig. 5.13** Photograph of an apparatus for selective excitation and detection of longitudinal, torsional, and flexural resonance of a thin bar. The bar is supported by crossed rubber bands attached to ring stands that suspend the bar with its ends in the gap between “horseshoe” magnets. The sample in the photo is about 25 cm long and 1.2 cm in diameter



of wire glued to their free ends that are used as the electrodynamic transducers for all three modes. In this apparatus, the gap between the magnets' pole pieces is 2.0 cm and the magnitude of the magnetic induction,  $|\vec{B}|$ , at the center of the gap between the pole pieces is about 2.0 kilogauss = 0.20 tesla.

The transducers are just two coils (about ten turns each) of ordinary insulated solid copper magnet wire that were wound around the handle of a screwdriver.<sup>11</sup> #28 gauge copper wire (376 micron diameter) has a current-carrying capacity of about 300 mA, which is more than adequate for the driven coil.<sup>12</sup> It is convenient to leave about 50 cm of wire at both ends of each coil that can be used to attach the coil to the drive amplifier or the measurement system (e.g., low-noise pre-amplifier,<sup>13</sup> oscilloscope, spectrum analyzer, or typically, all three).

Before attaching the coils, the bar should be weighed and its physical dimensions determined as accurately as possible. Those measurements will be used to determine the mass density of the sample. After weighing, the coils can be attached to the ends of the sample using any appropriate adhesive. Care must be taken to be sure that the plane defined by both coils is aligned, since the magnets' fields are usually both in the same direction. For most samples, a simple glue, like that used to assemble model airplanes (e.g., Duco™ cement), or even clear nail polish,<sup>14</sup> is entirely adequate since the forces the drive coil will be modest, typically less than 20 mN. After the coils have been glued to the sample, the assembly should be weighed again so that an effective length correction can be added to the physical length of the sample to correct for the mass of the coils and their adhesive added to the ends of the bar (see Sect. 5.4.4).

<sup>11</sup> A screwdriver handle makes an ideal mandrel since the handle has grooves to improve grip that provide spaces to weave the last turn in and out of the grooves to hold the coil together when it is slipped off the screwdriver's handle.

<sup>12</sup> Almost no current flows through the detection coil, so it could be much smaller gauge wire, but it is often convenient to make both coils from the same wire.

<sup>13</sup> If a low-noise voltage pre-amplifier is available (e.g., PAR 113, Ithaco 1201, or SRS 560), they usually also provide some adjustable low-pass filtering capabilities that can remove low-frequency seismic vibrations if the apparatus is on a table that is not rigid.

<sup>14</sup> Clear nail polish has lower viscosity, making attachment of the coils easier since capillarity will draw the polish into the coil and concentrate where the coil contacts the bar.

### 5.4.1 Mode-Selective Electrodynamic Excitation and Detection

The torsional mode can be excited preferentially by orienting both coils horizontally with the pole pieces also horizontally, as shown in Fig. 5.14 (top right). This technique was first used by Barone and Giacomini [21] to study the modes of bars having variable cross-section and then by Leonard [22] who measured the attenuation of torsional modes to disprove the existence of the “Fitzgerald effect.” [23, 24]<sup>15</sup> The short portion of the coil, which crosses the end of the bar along a diameter, should stick out slightly beyond the pole pieces. When the alternating electrical current,  $I(t) = i_1 \cos(\omega t)$ , flows in one direction through the drive coil, a Lorenz force,  $|\vec{F}(t)| = (B\ell)I(t)$ , will be downward on one side of the coil and upward on the other, where  $\ell$  is the total length of wire in the coil subjected to the magnetic field on one side of the bar. When the current changes direction, so will the forces. This twisting moment will selectively excite the torsional modes of the bar.

The other coil, on the opposite end of the bar, is in the same orientation with respect to its magnet and will generate a voltage (*emf*) that is proportional to the time rate of change of the magnetic flux,  $\Phi$ ,

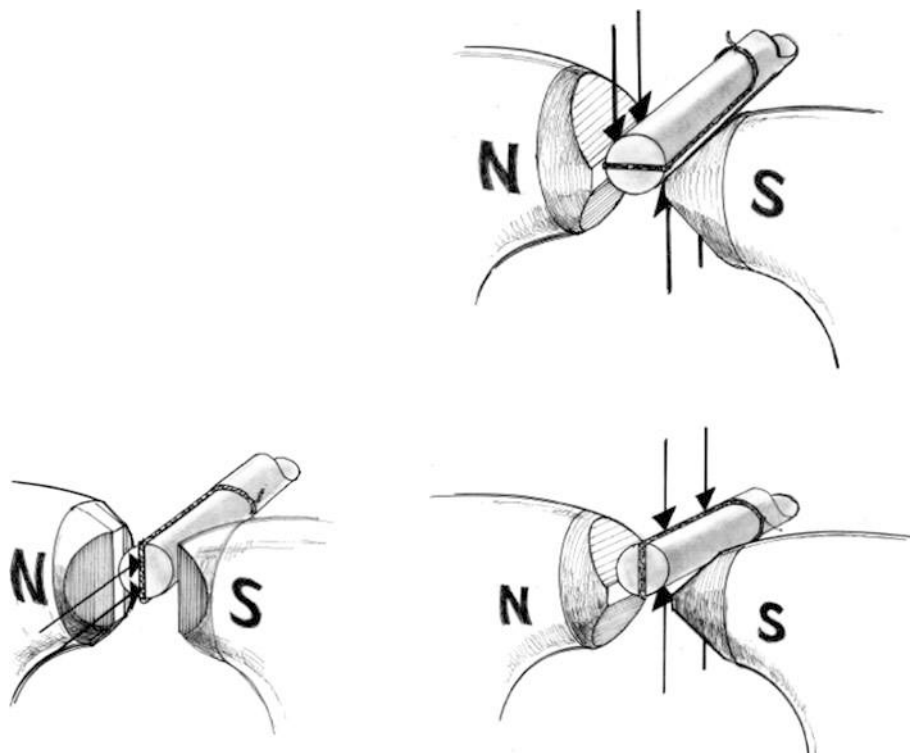


**Fig. 5.14** Arrangements of the electrodynamic transducer coils in the magnet gap for excitation and detection of the torsional (top right), flexural (bottom right), and longitudinal (bottom left) modes of a thin bar. The arrows show the strength and direction of the forces produced by the current flowing through the coils that are functioning as the drive transducers

<sup>15</sup> Fitzgerald had thought he discovered a new attenuation mechanism, but Leonard showed that Fitzgerald’s “effect” was absent, and Fitzgerald had just measured an artifact of the attachment of piezoelectric transducers to his sample.

through the receiver coil. The flux,  $\Phi$ , is the product of the projection of the surface area of the coil,  $A_{\perp} = A \cos \phi$ , times the magnitude of the magnetic induction,  $|\vec{B}|$ , times the number of turns or wire,  $N$ . Here  $A$  is the area within the coil, and  $\phi$  is the angle between a vector normal to the plane of the coil and the magnetic field lines.

$$emf = -\frac{d\Phi}{dt} = -N|\vec{B}| \frac{dA_{\perp}}{dt} = -N|\vec{B}|A \frac{d(\cos \phi)}{dt} \quad (5.57)$$

With the coil oriented as shown in Fig. 5.14 (top right),  $\phi \cong 90^\circ$ , so  $A_{\perp} \cong 0$ , and  $\Phi \cong 0$ . When a torsional wave is excited, the end of the bar will experience a time-harmonic twisting, so  $\phi(t) = \Re e[\phi_1 e^{j\omega t}]$ , generating a voltage ( $emf$ ) given by Faraday's law in Eq. (5.57). With  $\phi \cong 90^\circ$ , the sensitivity of the transducer to the twisting will be its greatest. The  $emf$  will be generated at the same frequency,  $\omega$ , as the twisting that is caused by the torsional resonance and will also be proportional to the amplitude,  $\phi_1$ .

Flexural resonances can be excited and detected by simply rotating the bar (with its attached coils) by  $90^\circ$  from the torsional mode orientation and raising (or lowering) the bar by one bar radius. This places one portion of each coil in the strongest part of the magnetic field and lifts the other part of the coil to a region of weaker magnetic field, as shown in Fig. 5.14 (bottom right). Now the vertical forces on each long section of the coil will be in opposite directions. Because of the stronger magnetic field is applied to the lower portion of the coil (as shown), there will be a net vertical force that will create a harmonic bending of the bar and excite the flexural modes of vibration.

In this orientation, the coil on the opposite end of the bar will be “dipping” in and out of the stronger regions of magnetic field. In this case  $\phi \cong 0^\circ$ , so  $A_{\perp} \cong A$ , but the magnitude of the magnetic induction,  $|\vec{B}|$ , will be changing with time,  $B(t) = B_o + \Re e[B_1 e^{j\omega t}]$ , as the receiver coil moves toward and away from the strongest regions of magnetic field. Now Eq. (5.57) will produce an  $emf = NA(dB/dt)$  that will be at the same frequency as the flexural vibrations and proportional to their amplitudes.

Finally, the longitudinal modes can be selectively excited and detected by reorienting the pole pieces to make the gap vertical, as shown in Fig. 5.14 (bottom left). This concentrates the magnetic field in the vertical direction. The end of the coil that is along the diameter at the end of the bar is placed in the strongest portion of that magnetic field. In this orientation, the driven end of the coil will be putting oscillatory longitudinal forces on the end of the bar thus exciting the longitudinal modes. Since the length of that portion of the coil is considerably shorter than the portions of the coil along the perimeter of the sample, the longitudinal modes will not be excited as strongly as the torsional and flexural modes for the same electrical current amplitude,  $i_1$ , flowing through the driving coil. Detection of the longitudinal mode is the same as the flexural mode. The magnetic flux,  $\Phi(t)$ , is modulated by the coil's motion, being pushed into and out of the strongest portions of the magnetic field by the motion of the end,  $\xi(t) = [\hat{\xi} e^{j\omega t}]$ .

#### 5.4.2 Bar Sample Size and Preparation

Sample data acquired by this method are displayed in Fig. 5.16 for the epoxy-glass composite described at the beginning of Sect. 5.4. The bar was fabricated by mixing the epoxy and then adding glass fibers to the mix. The mixture was then poured into a hollow plastic tube that had been coated on the inside with a mold release agent to facilitate removal of the sample after the epoxy had cured. The sample was pushed out of the tube and the ends were cut straight using a band saw.

Before the transducer coils were attached, the bar was weighed,  $M = 55.723 \pm 0.001$  g, and the bar's dimensions were measured. The length  $L = 33.60 \pm 0.02$  cm, but the cross-section was found to

be slightly elliptical with major and minor diameters ranging from  $d_{max} = 13.17 \pm 0.02$  mm to  $d_{min} = 12.77 \pm 0.20$  mm, yielding an average diameter of  $d = 12.97 \pm 0.20$  mm. These physical measurements produced an average mass density,  $\rho = 1256 \pm 4$  kg/m<sup>3</sup>. It is not unusual to have this degree of ellipticity in a sample which was cast in a plastic tube. The cross-section of glass tubes is more circular, but also more dangerous to fabricate, since the sample can seldom be removed without breaking the glass.

The transducer coils were attached as described previously using Duco™ cement. With a bar that has an elliptical cross-section, it is preferable to orient the coils along either the major or minor diameter so that the polarization of the flexural mode is known. For this sample, the major and minor diameters differed by about 3% corresponding to a 6% difference in the free-free flexural mode frequencies caused by the difference in the  $\kappa^2$  value that appears in Eq. (5.55).

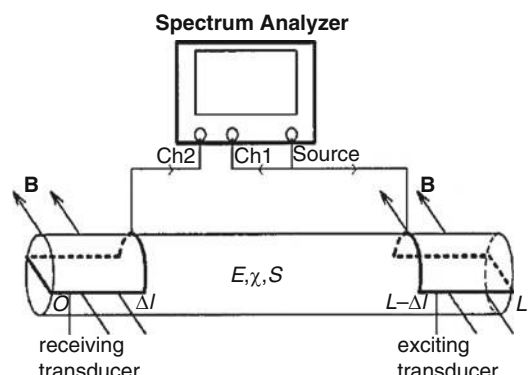
After attachment of the coils, the bar was weighed again and found to be  $1.5 \pm 0.1$  g heavier. It is difficult to be sure exactly how much the motion of the wires that connect the coil to the instrumentation contribute to the measurement, but in this case, the accuracy is not degraded significantly since the uncertainty in the effective length of the bar (see Sect. 5.4.4) is only about ½%.

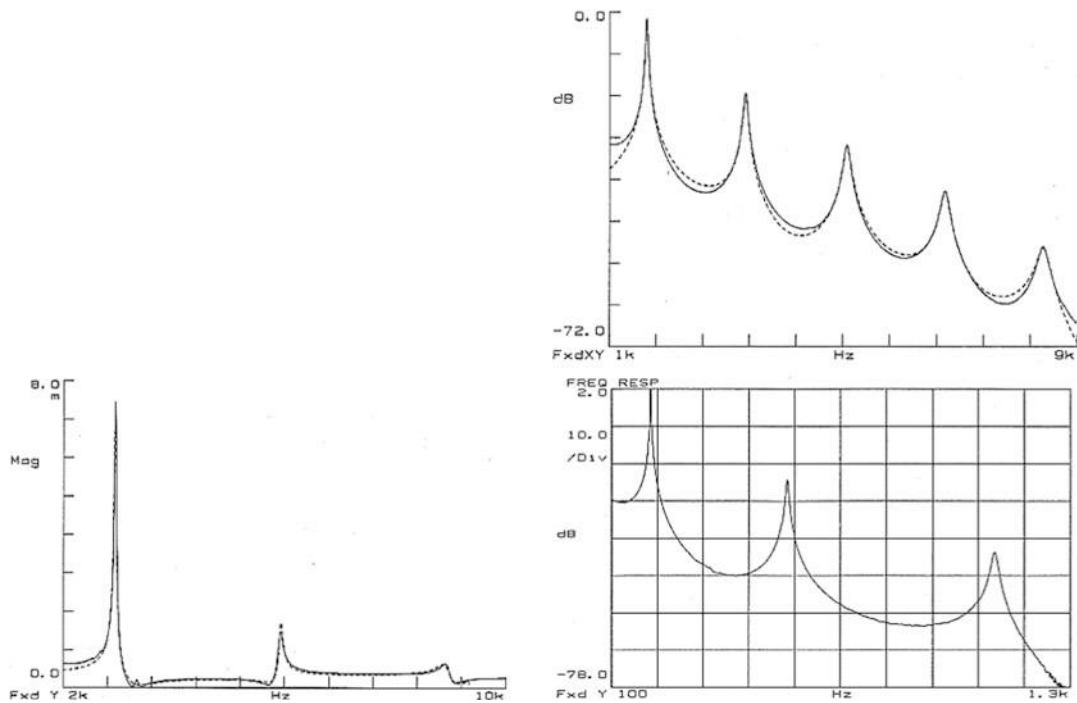
### 5.4.3 Measured Resonance Spectra

Figure 5.16 displays three resonance spectra that were acquired using a dynamic signal analyzer to measure the bar's response only in a narrow band around the frequency at which it was being driven. The setup is diagrammed schematically for the torsional mode in Fig. 5.14 (top right). The analyzer also had an internal curve-fitting program, so the measured spectral response is shown as the solid line and the curve-fit to that response is shown as the dashed line (Fig. 5.16).

The five lowest-frequency torsional modes are shown in Fig. 5.16 (upper right). They appear to be harmonically related, with uniform spacing between the resonances. That appearance is confirmed by the resonance frequencies listed in Table 5.4. It is also worthwhile to note that the *dynamic range* (the ratio of the largest measured signal to the smallest) of that measurement is about 70 dB, corresponding to an amplitude ratio in excess of 3000:1. At the minima in the spectrum (i.e., at frequencies between the resonances), the curve-fit dashed line alternates between being larger and smaller than the measurements. That is because the coils also act as an electrical transformer coupling the oscillating magnetic flux in the drive coil (weakly) into the receiver coil. This could be eliminated by orienting the planes of the two coils to be mutually perpendicular and rotating one set of magnets by 90° or by placing a magnetic shield (iron is good,  $\mu$ -metal is better) around the middle of the bar without

**Fig. 5.15** Schematic representation of the connection of the dual-channel spectrum analyzer that measured the transfer function between the drive signals, monitored in Channel 1, and the bar's resonance responses monitored in Channel 2. As shown, the apparatus was set up to measure the torsional modes of the bar [25]





**Fig. 5.16** Resonance spectra for the lowest-frequency torsional (upper right), flexural (lower right), and longitudinal (lower left) resonances. The solid lines are the measured spectra, and the dashed lines were pole-zero fits to those measured spectra

**Table 5.4** Summary of the measured normal mode frequencies of the thin bar sample of an isotropic glass-epoxy composite. The error is the standard deviation of the average of the normalized frequencies,  $f_n/f_1$ , for each mode

Mode number [n]	Frequency [Hz]	Normalized frequency [ $f_n/f_1$ ]	Average uncertainty [Hz (%)]
<b>Torsional</b>			
1	1644	1644	
2	3341	1670	
3	5080	1693	
4	6750	1688	
5	8446	1689	
Average		1677	$\pm 20$ ( $\pm 1.2\%$ )
<b>Flexural</b>			
$(3.01124)^2$	203.1	22.40	
$(4.99951)^2$	560.4	22.42	
$(7.00002)^2$	1104	22.53	
Average		22.45	$\pm 0.07$ ( $\pm 0.2\%$ )
<b>Longitudinal</b>			
1	2941	2941	
2	5936	2968	
3	8896	2965	
Average		2958	$\pm 15$ ( $\pm 0.4\%$ )

touching the bar. Those methods of eliminating the *electromagnetic cross talk* between the drive and receiver coils were not implemented because the signal-to-noise ratio was more than adequate to accurately determine the peak frequencies that were not measurably influenced by the electromagnetic cross talk.

Table 5.4 lists the measured resonance frequencies of the five lowest-frequency torsional modes. Since the modes are expected to be related harmonically, the table also forms the ratio between the frequencies,  $f_n$ , of the  $n^{\text{th}}$  mode, to the fundamental frequency,  $f_1$ . For harmonic modes of a free-free bar, that ratio should be a constant. The ratio of the standard deviation of the five modal frequencies to their average is  $\pm 1.2\%$ . Since this is in the range of our relative uncertainty of the mass density ( $\pm 0.3\%$ ), and the ellipticity ( $\pm 3\%$ ), there was no motivation to improve or to understand the source of that small anharmonicity.

The three lowest-frequency flexural modes of the bar are shown in the spectrum in Fig. 5.16 (lower right). It is obvious from inspection of that spectrum that those modes are not harmonically related. The frequency difference between the first and second modes is smaller than the difference between the second and third, as would be expected from Eq. (5.55). It is also possible to see a small amount of noise in the spectrum that appears in the “spectral tail” above 1.2 kHz. The dynamic range of that spectrum is 80 dB, corresponding to an amplitude ratio of 10,000:1. The frequencies of those modes are listed in Table 5.4, as is their normalized frequency,  $f_n/f_1$ , which has a relative uncertainty of  $\pm 0.2\%$ .

Since the shear modulus can be related to the torsional mode frequencies and Young’s modulus related to the flexural mode frequencies, we have enough information to determine the complete elastic response of our sample that is assumed to be isotropic.<sup>16</sup> Since the longitudinal modes were also measured, they can be used to estimate the accuracy of the method for the determination of Young’s modulus.

The spectrum displaying those longitudinal modes is shown in Fig. 5.16 (lower left). As mentioned, the amplitudes of the longitudinal modes are smaller than of the other two modes because the transduction is less efficient. The small bump to the right of the largest longitudinal mode is a weak excitation of the second torsional mode at 3341 Hz. Since the side portions of the coils are so much longer than the short section of coil at the end, it is possible to excite a small amount of torsional vibration even though the magnets and coils are arranged to couple preferentially to the longitudinal mode. The third resonance at nearly 9 kHz hardly looks like a resonance at all, again due to phase cancellation between the superposition of the acoustical resonance signal and the electromagnetic cross talk signal. Despite those limitations, the relative uncertainty of the normalized longitudinal mode resonance frequencies in Table 5.4 is only  $\pm 0.4\%$ , which is consistent with the precision of the measurements of the frequencies of the other two modes.

The epoxy-glass composite used in this example was chosen because it does not have a particularly large quality factor,  $Q$ , making measurement of its modal frequencies a bit more challenging. Wooden bars will produce similar results. If this same apparatus is used to measure the resonances of metal bars (e.g., aluminum or brass) or ceramics (e.g., alumina) or glass, the  $Q$  will be significantly larger, as will be the signal-to-noise ratio. Consequently, the results for the moduli will be even more precise.

---

<sup>16</sup> Although this sample is a composite, the glass fibers in the epoxy matrix are short (about 800 microns long) and randomly oriented. The sample behaves isotropically upon length scales that are on the order of the diameter and the resonance wavelengths.

### 5.4.4 Effective Length Correction for Transducer Mass

If any addition to a bar be made at the end, the period of vibration is prolonged. J. W. Strutt (Lord Rayleigh). [26]

Before calculating the moduli from the experimental data, we can eliminate one source of systematic error. Because the coils and their adhesives add mass to the end of the bar, we can calculate an effective length correction to account for this, just as was done for the quartz crystal microbalance in Sect. 5.1.2, except this time we will use Rayleigh's method instead of an approximation to the transcendental equation diagrammed in Fig. 5.2. Such effective length corrections were calculated by Rayleigh in *Theory of Sound* for the free-free longitudinal case in Vol. I, §155. The free-free flexural case is covered in Vol. I, §186. Rayleigh did not do the calculation for mass loading of the free-free torsional modes [26].

The mass of the transducers is concentrated very close to the free ends of the bar, and the length of the coils is much shorter than the length of the bar, so we can assume that all of the mass of the coil is concentrated at the end, at least for the lower-frequency modes, where the wavelength of the resonance exceeds the length of the bar or is a substantial fraction of the bar's length. We will ignore the stiffness added by the coils since they are attached close to the stress-free ends.<sup>17</sup> The coils only affect the bar's mass, so we can apply Rayleigh's method (see Sect. 3.2.2) and only concern ourselves with the changes in the kinetic energy,  $\delta(KE)$ , that cause changes in frequency,  $\delta\omega = 2\pi\delta f$ , due to the mass loading of the coils. Since  $\omega^2 \propto (PE/KE)$ , the torsional and longitudinal modal frequencies are inversely proportional to the length of the bar, and it is possible to express the length correction,  $\delta L$ , in terms of the change in kinetic energy,  $\delta(KE)$ .

$$\frac{\delta f}{f} = \frac{\delta\omega}{\omega} = -\frac{\delta L}{L} = -\frac{1}{2} \left( \frac{\delta KE}{KE} \right). \quad (5.58)$$

The effective length,  $L_{eff}$ , of the bar that compensates for the mass loading of the coils is related to the original length,  $L$ :  $L_{eff} = L + \delta L$ . If the mass of the bar prior to the attachment of the coils is  $M$  and the mass added by the coils is  $2 m$ , then after the coils are attached,  $M_{tot} = M + 2 m \equiv M + \Delta M$ , where  $(\Delta M)g$  is the change in the weight of the bar after the transducer coils are attached.

The calculation for the effective length of the bar, in the lowest-frequency longitudinal mode, is simplified if the symmetry of that mode is exploited. Since the center of the bar is a node, the entire left-half of the bar can be replaced by a rigid (fixed) end at  $x = 0$ . The fundamental longitudinal resonance can be treated as the fundamental resonance of a fixed-free bar of length,  $L' = L/2$ . The displacements,  $\xi(x, t)$ , of the fixed-free half-bar can be written in terms of the maximum displacement amplitude,  $\xi_1$ , of the free end, with  $\omega/k = c_B$  and  $k_1$  given by Eq. (5.14).

$$\xi(x, t) = \xi_1 \sin \left( \pi \frac{x}{2L} \right) \sin(\omega t) \quad (5.59)$$

The kinetic energy of the half-bar undergoing longitudinal oscillations,  $(KE_1^L/2)$ , without the added mass, can be determined by integration along the length of the half-bar,  $L' = L/2$ , where the half-mass of the half-bar is  $M' = M/2$ .

---

<sup>17</sup>The stiffness contributions of the transducer coils have been calculated by Guo and Brown [25].

$$\frac{KE_1^L}{2} = \frac{\rho S \omega^2 \xi_1^2}{2} \int_0^{L'} \sin^2\left(\pi \frac{x}{2L}\right) dx = \frac{1}{4} M' \omega^2 \xi_1^2 \quad (5.60)$$

The one coil of mass,  $m$ , at the end of the bar, will move with the velocity of the end of the bar,  $\omega \xi_o \sin \omega t$ , and will have a maximum kinetic energy,  $KE_{coil} = (m/2)\omega^2 x_1^2$ . The relative shift in the kinetic energy of the half-bar will be  $\delta(KE)/(KE) = KE_{coil}/(KE_o^L/2) = 2m/M'$ .

$$\left(\frac{\delta L}{L}\right)_L = -\frac{\delta f}{f} = \frac{1}{2} \frac{KE_{coil}}{(KE_o^L/2)} = \frac{m}{M'} = \frac{2m}{M} = \frac{\Delta M}{M} \Rightarrow L_{eff}^L = L \left(1 + \frac{\Delta M}{M}\right) \quad (5.61)$$

The same style of argument can be applied to the torsional case, except that the location of the added mass with respect to the axis of the bar is important because it is the moment of inertia,  $I$ , of the coil that will load the bar's torsional oscillations. For this case, the kinetic energy is due to rotation, so that  $KE_{coil} = (\frac{1}{2})I_{coil}(\omega \theta_1)^2$ , where  $\theta_1$  is the maximum angular displacement at the end of the bar in the fundamental mode. The moment of inertia of a disk of mass,  $\delta m$ , and diameter,  $d$ , is  $I = (1/8)(\delta m)d^2$ , so the kinetic energy of torsional oscillations,  $(KE_I^T/2)$ , of the half-bar is again given by integration over the half-length of the bar,  $L'$ .

$$\frac{KE_1^T}{2} = \frac{\rho S \omega^2 \theta_1^2}{2} \frac{d^2}{8} \int \sin^2\left(\pi \frac{x}{2L}\right) dx = \frac{M' \omega^2 \theta_1^2 d^2}{32} \quad (5.62)$$

For an ellipse,  $d^2 = d_{max} d_{min}$ .

Since the single coil mass,  $m$ , is primarily located at the bar's radius, its moment of inertia is  $I_{coil} = (\frac{1}{4})md^2$ <sup>18</sup>, and the change in the kinetic energy of rotation caused by the addition of one coil to the end of the half-bar is  $KE_{coil}^T = (1/8)m(d\omega\theta_1)^2$ .

$$\left(\frac{\delta L}{L}\right)_T = -\frac{\delta f}{f} = \frac{1}{2} \frac{KE_{coil}}{(KE_o^T/2)} = \frac{2m}{M'} = \frac{4m}{M} = \frac{2\Delta M}{M} \Rightarrow L_{eff}^T = L \left(1 + \frac{2\Delta M}{M}\right) \quad (5.63)$$

The mass of the coils have twice the effect on the frequency of the torsional modes, hence producing twice the effective length correction,  $L_{eff}^T$ , as that required for the longitudinal modes,  $L_{eff}^L$ , in Eq. (5.61).

The exact solution for the fundamental flexural mode of a free-free bar is again given by the superposition of four trigonometric functions with  $k_1 L = 4.73$ ,  $A_I = 0.5$ , and  $B_I = -0.982A_I$ .

$$y(x, t) = A_1 [\cosh(k_1 x) + \cos(k_1 x)] + B_1 [\sinh(k_1 x) + \sin(k_1 x)] \sin(\omega_1 t) \quad (5.64)$$

The kinetic energy of the bar without coils, vibrating in its flexural mode,  $KE_1^F$ , is related to the integral of its transverse velocity,  $(\partial y / \partial t)$ , over its length.

$$KE_1^F = \frac{\rho S}{2} \int_0^L \left(\frac{\partial y}{\partial t}\right)^2 dx \quad (5.65)$$

Rather than solving that integral for the kinetic energy of the unloaded bar in its fundamental mode using Eq. (5.64), we can create a second-order polynomial function,  $y_{poly}(x, t)$ , to approximate the

<sup>18</sup> Since the coil is actually on the surface of the bar, its diameter is slightly larger than  $d$ . We will neglect this difference by arguing that the part of the coil that crosses the bar's end has a lower moment of inertia. It would be a small correction to an already small correction (so works the rationalizations in the mind of an experimentalist).

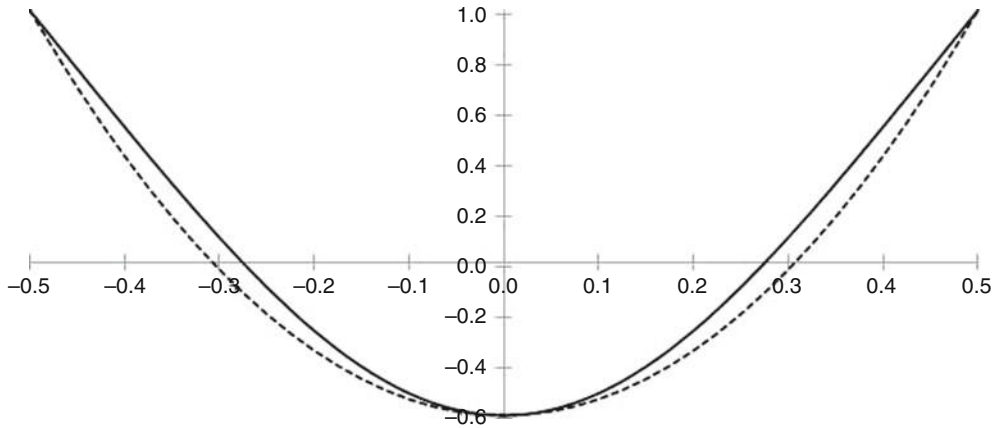


**Fig. 5.17** Comparison of the exact solution for a free-free bar vibrating in its fundamental flexural mode (*solid line*) to the second-order polynomial approximation (*dashed line*) that is matched to the maximum  $y(0) = -0.608$  at  $x = 0$  and the at the free ends where  $y(\pm L/2) = 1$

actual displacements that will be easier to integrate. To exploit the symmetry of the fundamental mode shape, we can place the origin of the coordinate system at the center of the bar.

$$y_{poly}(x, t) = Ax^2 + C \quad (5.66)$$

At the center of the bar, located at  $x = 0$ , the slope,  $(\partial y_{poly}/\partial x)_0 = 0$ . At the ends of the bar,  $x = \pm L/2$ ,  $(\partial^2 y_{poly}/\partial x^2)_{\pm L/2} = A/2 \neq 0$ , so the second-order polynomial approximation does not meet the requirement that there be no torques applied to the free end. Since  $(\partial^3 y_{poly}/\partial x^3)_{\pm L/2} = 0$ , the second-order polynomial approximation does satisfy the boundary condition that requires that there also be no vertical forces.

The displacement of the polynomial approximation can be fit to Eq. (5.64) at  $x = 0$  by making  $C = -0.608$  and fit to the two ends, where  $y(\pm L/2) = 1$ , by making  $A = 4(1 - C) = 6.432$ . Figure 5.17 shows both the exact solution of Eq. (5.64) and the second-order polynomial approximation of Eq. (5.66). The kinetic energy of the unloaded bar can be integrated over  $-L/2 \leq x \leq L/2$ , remembering that the vertical motion of the free ends has unit amplitude.

$$KE_o^F \cong \frac{\rho LS\omega^2}{2} \int_{-L/2}^{L/2} y_{poly}^2(x) dx = \left[ \frac{A^2 x^5}{5} + \frac{2ACx^3}{3} + C^2 x \right]_{-L/2}^{L/2} = \frac{0.235 M \omega^2}{2} \quad (5.67)$$

Rayleigh's method will always overestimate the energy, and the  $|y_{poly}(x)| > |y(x)|$  everywhere, as can be seen in Fig. 5.17, so I will let  $(0.235)^{-1} = 4.26 \cong 4$ . The kinetic energy of each coil of mass,  $m$ , at both ends, also with vertical motion of unit amplitude, is  $KE_{coils} = (\frac{1}{2})(2m)\omega^2 y_{poly}^2$ . From Eq. (5.55), we see that the frequency is inversely related to the square of the length of the bar.

$$\frac{\delta L}{L} = -\frac{1}{2} \frac{\delta f}{f} = -\frac{1}{2} \left( -\frac{1}{2} \frac{KE_{coils}}{KE_o^F} \right) = \frac{1}{4} \left( \frac{4\Delta M}{M} \right) = \frac{\Delta M}{M} \Rightarrow L_{eff}^F = L \left( 1 + \frac{\Delta M}{M} \right) \quad (5.68)$$

This is in agreement with Rayleigh's result for the flexural mode: "If the load be at the end, its effect is the same as lengthening of the bar in the ratio  $M:M+dM$ ." [26]

With the effective lengths removing the systematic error that would be introduced by the mass loading of the transducer coils on the ends of the bar, the moduli can be calculated. The mass ratio is

$\Delta M/M = (1.5 \text{ grams}/55.723 \text{ grams}) = 2.7 \times 10^{-2}$ . For the longitudinal and flexural modes,  $L_{\text{eff}}^L = L_{\text{eff}}^F \equiv L_{\text{eff}} = 34.50 \text{ cm}$ . Young's moduli calculated from both methods are determined by Eqs. (5.13) and (5.55).

$$E_L = 4\rho L_{\text{eff}}^2 \left( \frac{f_n^L}{n} \right)^2 \quad \text{and} \quad E_F = \left( \frac{32}{\pi} \right)^2 \frac{\rho L_{\text{eff}}^4}{d^2} \left( \frac{f_n^F}{n^2} \right)^2 \quad (5.69)$$

Before evaluating  $E_L$  and  $E_F$ , it will be useful to propagate the relative errors (see Sect. 1.8.4) to obtain an estimate of the accuracy of the results using log differentiation (see Sect. 1.1.3). It is clear that errors in  $\rho$ ,  $L_{\text{eff}}$ , and  $f_n/n$  are all statistically independent, so the errors are combined in a Pythagorean sum.

$$\frac{\delta E_L}{E_L} = \left[ \left( \frac{\delta \rho}{\rho} \right)^2 + \left( 2 \frac{\delta L_{\text{eff}}}{L_{\text{eff}}} \right)^2 + \left( 2 \frac{\delta (f_n^L/n)}{(f_n^L/n)} \right)^2 \right]^{1/2} \quad (5.70)$$

Defining the random error as being one standard deviation,  $\delta \rho / \rho = \pm 0.32\%$ ,  $\delta(L_{\text{eff}})/|L_{\text{eff}}| = \pm 0.06\%$ , and  $\delta(f_n/n)/|f_n/n| = \pm 0.5\%$ . This results in a relative overall uncertainty of  $\delta E_L / E_L = \pm 1.1\%$ . Equation (5.69) can then be evaluated:  $E_L = 5.23 \pm 0.06 \text{ GPa}$ .

The same procedures can be applied to the calculation of  $E_F$  and its relative uncertainty.

$$\frac{\delta E_F}{E_F} = \left[ \left( \frac{\delta \rho}{\rho} \right)^2 + \left( 4 \frac{\delta L_{\text{eff}}}{L_{\text{eff}}} \right)^2 + \left( -2 \frac{\delta d}{d} \right)^2 + \left( 2 \frac{\delta (f_n^F/n^2)}{(f_n^F/n^2)} \right)^2 \right]^{1/2} \quad (5.71)$$

Fortunately, the relative uncertainty in effective length is the smallest of the four pieces because it is also the most heavily weighted in Eq. (5.71). The difficulty is the assignment of  $\delta d/d$  to account for the ellipticity of the sample's cross-section. I will estimate it to be half the difference in the major and minor diameters over their average,  $\delta d/d = \pm (d_{\max} - d_{\min})/(d_{\max} + d_{\min}) = \pm 1.54\%$ . This makes  $\delta E_F / E_F = \pm 3.2\%$ , so from Eq. (5.69),  $E_F = 5.53 \pm 0.18 \text{ GPa}$ .

Although the lower limit of  $E_F \geq 5.35 \text{ GPa}$  almost overlaps the upper limit of  $E_L \leq 5.29 \text{ GPa}$ , their discrepancy is slightly outside our estimate of experimental error. This is probably due to the fact that we represented the elliptical cross-section as a circle with an average diameter  $d = (d_{\max} + d_{\min})/2$ . The entire discrepancy could possibly be removed if the polarization of the flexural vibrations were rotated by about  $30^\circ$  toward the  $d_{\min}$  orientation. Under the circumstances, if I needed a value of Young's modulus and could not repeat the experiment, I'd use the error-weighted average of the two values and append the larger of the two uncertainties:  $E = 5.31 \pm 0.18 \text{ GPa}$ .

To evaluate the shear modulus from the measured torsional mode frequencies, we use Eq. (5.63) to write  $L_{\text{eff}}^T = 35.4 \text{ cm}$ .

$$G = 4\rho \left( L_{\text{eff}}^T \right)^2 \left( \frac{f_n^T}{n} \right)^2 \quad (5.72)$$

Since this is the same relationship as for the longitudinal standing wave modes, the error propagation is again given by Eq. (5.70), now with  $\delta(f_n/n)/(f_n/n) = \pm 0.6\%$  resulting in  $\delta G/G = \pm 2.4\%$ , so from Eq. (5.72),  $G = 1.77 \pm 0.04 \text{ GPa}$ . Since  $E \cong 3G$ , Poisson's ratio is very close to one-half (see Eq. 4.93).

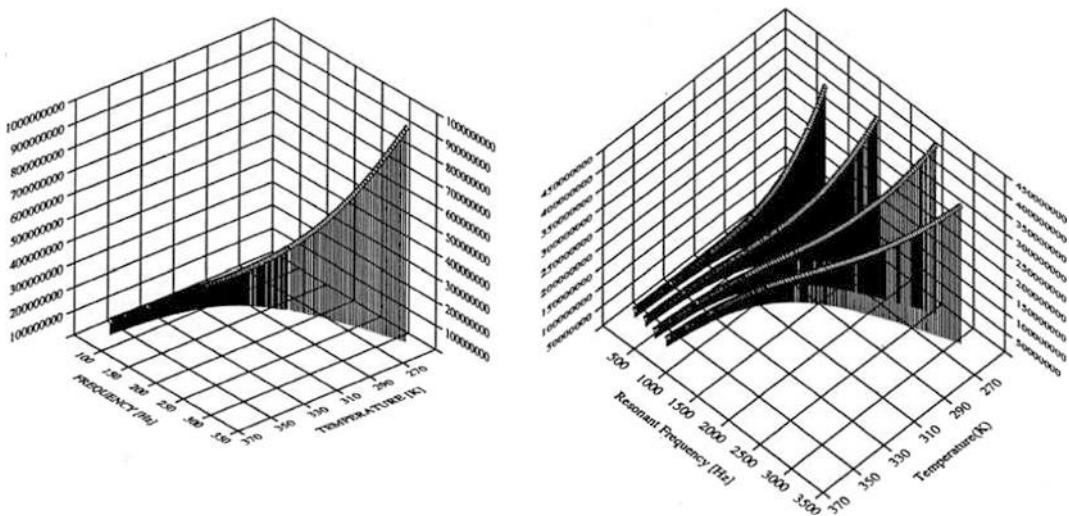


**Fig. 5.18** The results of the automated measurement of the lowest-frequency flexural mode (*left*) and the four lowest-frequency shear modes (*right*) of an elastomeric bar made of PR 1592 [27], an encapsulant used for hydrophones, over a temperature range from 260 K ( $-13^{\circ}\text{C}$ ) to 360 K ( $87^{\circ}\text{C}$ ). This temperature range includes the material's glass transition temperature. Each point in the temperature-frequency plane represents one measured resonant mode with the height above the point being the elastic modulus corresponding to that temperature and frequency [28]. The viscoelastic behavior is obvious due to the low modulus values at low frequency and high temperature and the high modulus at high frequencies and low temperatures

#### 5.4.5 Modes of a Viscoelastic Bar

The previous example demonstrated the simplicity and accuracy of extracting elastic moduli from resonance frequencies of thin bars. Often, it is necessary to determine how those elastic constants vary with some environmental parameter like temperature. Data for a bar sample cast from a viscoelastic elastomer is presented in Fig. 5.18.

The measurements of the resonance frequencies were automated by use of a phase-locked loop frequency tracking system (see Sect. 2.5.3) shown in the block diagram of Fig. 5.19. The sample, with its support structure and the magnets (like Fig. 5.13, but with fine wires providing sample support, replacing the rubber bands) was placed in an environmental control chamber to vary the sample's temperature. The bar is driven by a voltage-controlled oscillator (VCO) that produces a sinusoidal voltage that is amplified and applied to the drive coil. The signal from the receive coil is then passed through a pre-amplifier that has a high-pass filter to remove low-frequency noise and vibration. Of course, all of the electronics instruments are outside the environmental chamber.

The frequency of the VCO is controlled to keep the bar vibrating at one of its free-free normal mode frequencies by controlling the relative phase between the drive voltage and the received signal voltage. The force on the driven coil,  $F(t) = (B\ell)I(t)$ , is in phase with the current or voltage, since the coil's electrical impedance is primarily resistive. The output of an electrodynamic transducer is governed by Faraday's law, as expressed in Eq. (5.57), so the receive coil's velocity (linear or angular) and the force should be in-phase at resonance; hence, those two voltages should be in-phase.<sup>19</sup>

<sup>19</sup> Unlike the example in Sect. 2.5.3, which controlled a single degree-of-freedom simple harmonic oscillator, the bar has standing wave modes, so the phase relation between force and velocity will alternate by  $180^{\circ}$  between adjacent modes.

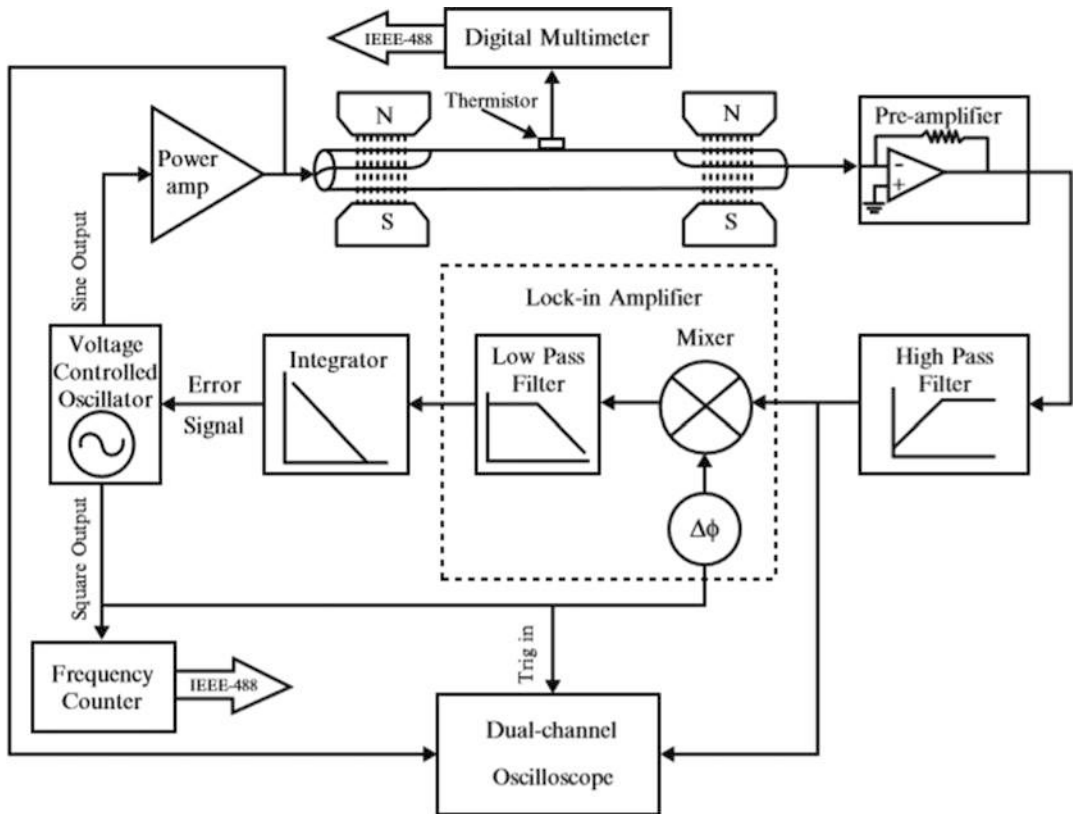


**Fig. 5.19** Block diagram of the instrumentation and electronics [19] used to automatically track the resonance frequencies and amplitudes for a vibrating bar to produce results like those shown in Fig. 5.18

A two-phase lock-in amplifier [29] was used in this application. The algorithm could be based on a simple pair of analog multiplier chips, such as the analog Devices AD633, or it could be accomplished entirely in software. One phase will generate the error signal that is integrated and fed back to the input of the VCO. Integration of the error signal allows the integrator to “store” the required voltage to tune the VCO to the resonance frequency, since the error signal voltage will be zero when the frequency-tracking system is locked onto the resonance frequency.

The other (quadrature) output signal from the lock-in will be proportional to the amplitude, since the relative phases of the two lock-in outputs will differ by  $90^\circ$ . With the feedback network forcing the output of the frequency control channel to zero, the entire signal will appear at the *quadrature* output from the other lock-in channel. Because of the low-pass filters on the outputs of the mixers (i.e., multipliers), the effective equivalent noise bandwidth ( $\Delta f$ )<sub>EQNB</sub> (see Sect. 2.5.2), even for a single-stage low-pass (RC) filter, with a roll-off of  $-6$  dB/octave, will have  $(\Delta f)_{EQNB} = (\pi/2)(\Delta f)_{-3dB}$  (see Fig. 2.8). As more stages are added, the coefficient decreases from  $\pi/2$  to 1. For a two-stage filter (i.e.,  $-12$  dB/octave), the  $(\Delta f)_{EQNB} = 1.22(\Delta f)_{-3dB}$ . For measurements that are slow, due to long thermal equilibration times, the time constant,  $\tau_{-3dB}$ , of the low-pass filter can be set to 10 s, so  $(\Delta f)_{-3dB}$  is  $(2\pi\tau_{-3dB})^{-1} = 16$  mHz making  $(\Delta f)_{EQNB} = 25$  mHz, even for a single-stage low-pass filter.

Inspection of the data in Fig. 5.18 shows the “cleanliness” that can be achieved with this resonance frequency tracking strategy. There are some challenges in setting up the system so that the gains of the amplifiers and their associated phase shifts (an inevitable consequence of the Kramers-Kronig relations), as well as the phase shifts caused by the low-pass filters and integrator, do not lead to positive feedback and oscillatory behavior in the control system. For a laboratory system, it is easy to

adjust the amplifier gains and the filter time constants since these are just knobs or rotary switches on the front panel of the lock-in amplifier. For a production system, it is useful to do a careful gain-phase analysis for all the components [30].

If we hold the current that is applied to the driven coil constant, so that its amplitude is independent of frequency, then the driving force (or torque) will remain constant. In that case, the magnitude of the response measured by the receiver transducer will be proportional to the quality factor,  $Q$ , at resonance and inversely proportional to the internal dissipation of the material. Such amplitude data was collected and recorded simultaneously with the modal frequencies of Fig. 5.18.

The data shown in Fig. 5.18 combines both the modulus and the damping from the resonance frequency and amplitude measurements made on the PR 1592 [27] elastomeric bar sample. The frequency data for a torsional mode was converted to the shear modulus, as was done for the epoxy-glass composite sample using Eq. (5.72). Similarly, the amplitude data was converted to loss tangent. Since the data was acquired over a range of temperatures that included the glass transition temperature,  $T_{glass}$ , the effective range of frequencies for this measurement is over ten orders of magnitude, although the actual frequencies only varied by about a factor of four, as seen in Fig. 5.18.

The horizontal axis in Fig. 5.20 is labeled *reduced frequency*, not frequency. As seen in our analysis of viscoelastic materials in Sect. 4.4, the influence of frequency on the response of a viscoelastic material only shows up in the equations as a product with the relaxation time,  $\tau_R$ . The behavior depends upon  $\omega\tau_R$  rather than on  $\omega$  directly. The reason that the range of reduced frequencies is so enormous in Fig. 5.20 is that viscoelastic relaxation time,  $\tau_R$ , is a very strong function of temperature.

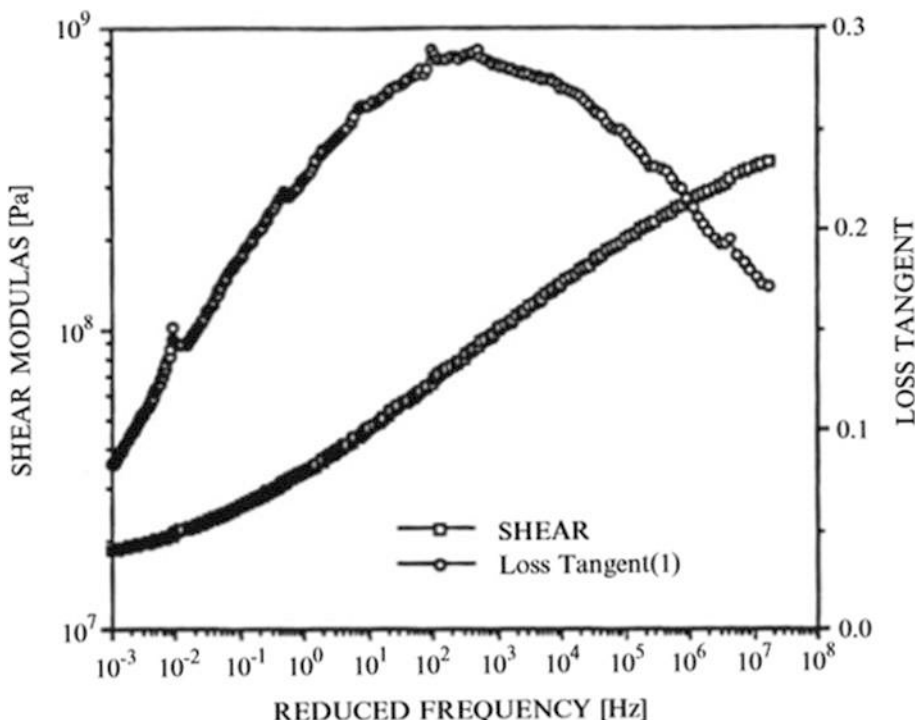


**Fig. 5.20** Master curve for the magnitude of the complex shear modulus and the associated loss tangent plotted vs. the reduced frequency. This plot combines both frequency and temperature variations using the Williams-Landel-Ferry transformation of Eq. (5.73) to produce over ten decades span in reduced frequency. This plot clearly illustrates the single relaxation time behavior introduced in Sect. 4.4. The reference temperature for this graph is 10 °C. At that temperature, the actual frequencies and reduced frequencies are identical

As shown in Fig. 4.28, most of the changes in both modulus and loss occur in the regions that are close to the glass transition temperature, being the temperature where  $\omega\tau_R \cong 1$ . This dependence on both frequency and temperature can be converted to a single parameter that is proportional to  $\omega\tau_R$  rather than to either  $\omega$  or  $\tau_R(T)$ , which is what was done to produce the reduced frequency that is plotted on the horizontal axis of Fig. 5.20. Such a curve is called the *master curve*, since it can provide the complex modulus at any frequency, if the temperature is known, or the effect a change in temperature will make on the complex modulus at a fixed frequency.

It is obvious from inspection of the plots of moduli in Fig. 5.18 that the measured moduli are much smaller at low frequencies and high temperatures, while the moduli are greatest at high frequencies and low temperatures. There are several algorithms that can be used to convert a frequency measurement made at a temperature,  $T$ , to reduced frequency, so it can be plotted with other frequency measurements made at other temperatures. The Williams-Landel-Ferry (WLF) equation [31] was used to produce the graph in Fig. 5.20 by creating a frequency shift factor,  $\alpha_T$ , so that data acquired at a frequency,  $f$ , and at a temperature,  $T$ , are plotted on the reduced frequency axis at a reduced frequency,  $f' = \alpha_T f$ .

$$\ln \alpha_T = \frac{-C_1(T - T_{glass})}{C_2 + (T - T_{glass})} \quad (5.73)$$

The constants  $C_1$ ,  $C_2$ , and  $T_{glass}$  are different for different polymers, but, as the form of Eq. (5.73) suggests, the dependence of  $\tau_R(T)$  is nearly an exponential function of the difference between the measured temperature,  $T$ , and  $T_{glass}$ .

#### 5.4.6 Resonant Ultrasound Spectroscopy\*

*“So, apparently due to a mathematical fortuity that may have occurred during a lapse in Murphy’s vigilance, the displacement vectors,  $u_i$ , which are solutions to the elastic wave equation with free boundary conditions on  $S$ , are just those points in function space at which  $L$  is stationary.” W. M. Visscher [32]*

The measurement of the elastic moduli of a long thin bar, as described in the previous sections, was simplified because the longitudinal, torsional, and flexural modes of such a bar were distinct. Furthermore, the modes could be excited and detected selectively by the orientation of the electrodynamic transducers with respect to the magnetic field. If a sample is not available in the shape of a long thin bar, it is still possible to determine the elastic moduli from measured resonance frequencies, but the extraction of the moduli from the resonance spectrum is much more difficult and computationally intensive.

In the early 1990s, a technique was developed that allows the normal mode frequencies of an object of arbitrary shape, and possibly anisotropic elasticity, to be accurately approximated if the object is freely suspended (hence, the quote that started this section regarding the “lapse in Murphy’s vigilance”). More importantly, measurement of the resonance frequencies of such normal modes of vibration can be inverted to extract the elastic moduli of the sample. This technique has become known as *resonant ultrasound spectroscopy* (RUS) [33].

Figure 5.21 shows an apparatus that can excite and detect the resonances of a very small solid rectangular parallelepiped sample (in this case). The normal modes of oscillation for such a rectangular sample are represented in Fig. 5.22. As we have done before, the “trick” is to use polynomial functions that are products of powers of the three Cartesian coordinates, where  $\lambda = \ell, m$ , and  $n$  is a set of three nonnegative integers.

$$\Phi_{\ell,m,n} = x^\ell y^m z^n \equiv \Phi_\lambda \quad (5.74)$$

These functions are then used to express the displacements,  $u_i$ , along the three Cartesian directions.

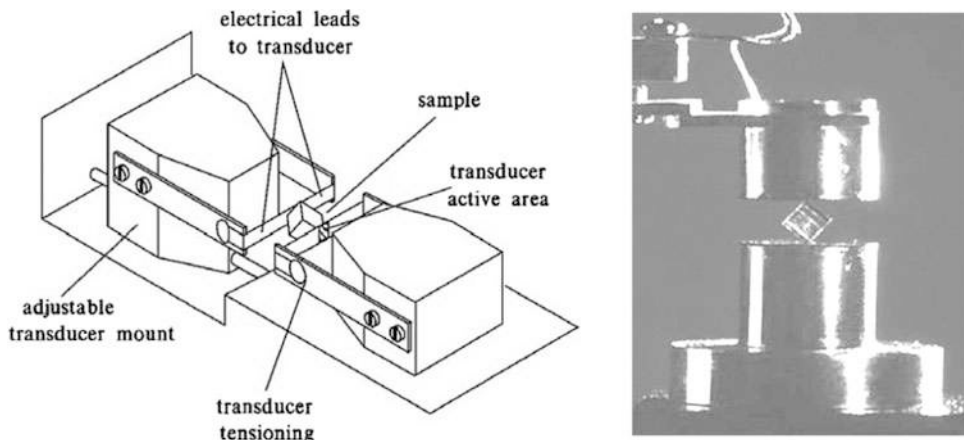


**Fig. 5.21** (Left) Schematic diagram of an apparatus that is capable of holding a very small and fragile solid sample between two piezoelectric polymer film (PVDF) transducers, 0.50 mm wide, that only touch the sample at the corners and can excite and detect the sample's normal modes of vibration [33, 34]. (Right) Photograph of a room temperature RUS apparatus that excites the sample using ordinary piezoelectric transducers

$$u_i = \sum_{\lambda \in \Omega} a_{i\lambda} \Phi_\lambda \quad (5.75)$$

The number of such functions must be sufficient for the number of modes to be determined, so that the energy can be minimized through the proper choice of the  $a_{i\lambda}$  using standard matrix methods. This polynomial approach will work regardless of the shape of the sample, as long as the motions of its boundaries are not constrained. The paper by Visscher et al. provides a rather entertaining description of the variety of such shapes: “including spheres, hemispheres, spheroids, ellipsoids, cylinders, eggs, shells, bells, sandwiches<sup>20</sup>, parallelepipeds, cones, pyramids, prisms, tetrahedra, octahedra, and potatoes.” [32]

The execution of these matrix operations was originally rather time-consuming or required a supercomputer. The examples shown in the paper by Visscher et al., in 1991, required a Cray-1 computer. Only 20 years later, the necessary calculations can be executed on a laptop computer. The results can be inverted to provide values of the elastic constants and their uncertainties, based on the measured resonance frequencies.

RUS has been extraordinarily successful in measuring the elastic properties of very small samples. Spoor and Maynard were able to measure the elastic moduli of a sample of quasicrystalline AlCuLi that had a mass of only 70 micrograms [34]. This is necessary because it is frequently difficult to grow large crystalline samples of exotic materials like quasicrystals or high-temperature superconductors. The simplicity and compactness of the apparatus also make RUS well-suited to measurements of the temperature dependences of elastic moduli and/or measurement on samples that are potentially dangerous.

My favorite examples are the studies on the solid phases of plutonium done by Albert Migliori and his colleagues at Los Alamos National Laboratory.<sup>21</sup> Plutonium exhibits four different solid phases over a relatively small range of temperatures. Shown in Fig. 5.23 are measurements of the bulk and

<sup>20</sup> Visscher was incorrect about “sandwiches.” Polynomials cannot fit a sharp interface, so the results are too inaccurate for RUS. For a sharp interface, finite elements are required.

<sup>21</sup> Large samples of plutonium self-heat by radioactive decay (or worse!).

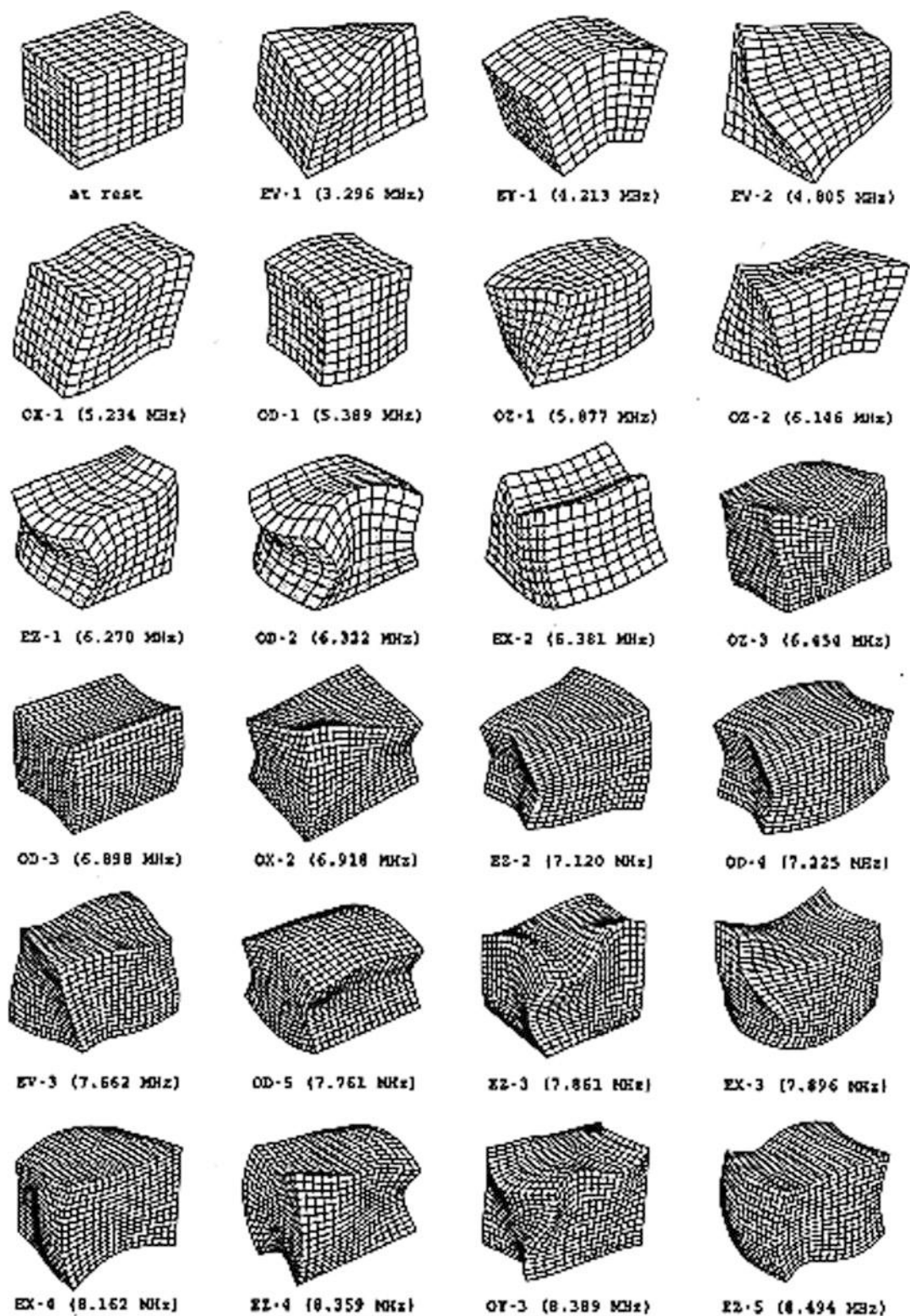


**Fig. 5.22** Normal mode vibrational patterns for a rectangular parallelepiped showing that longitudinal, flexural, and torsional motions are combined in several of the modes [36]. By fitting the polynomial mode shapes, it is possible to isolate the individual elastic moduli, even for materials with anisotropic elastic properties, as discussed in Sect. 4.6, to high accuracy

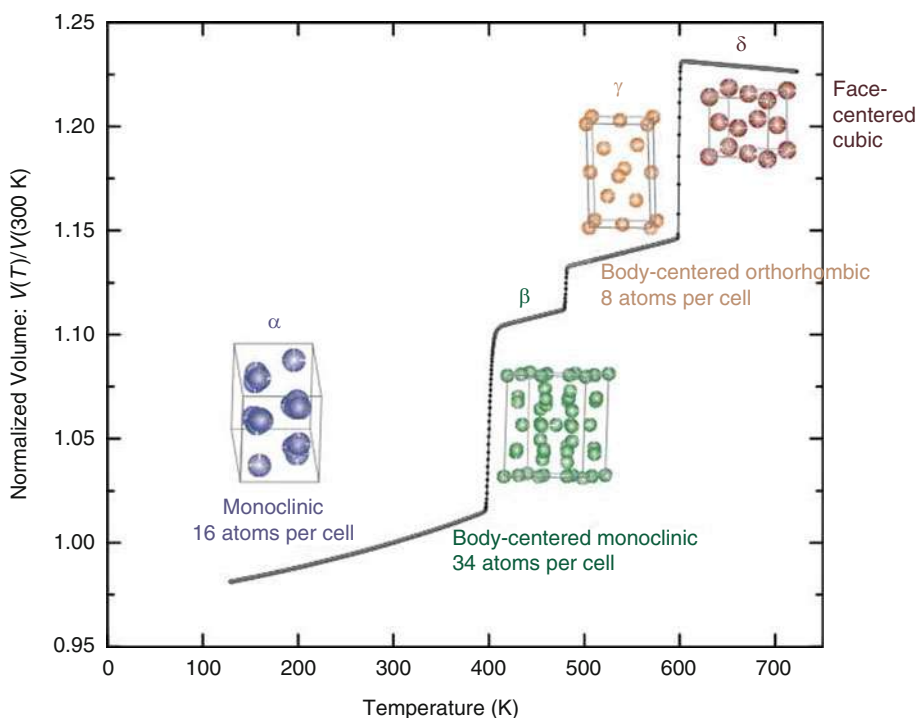
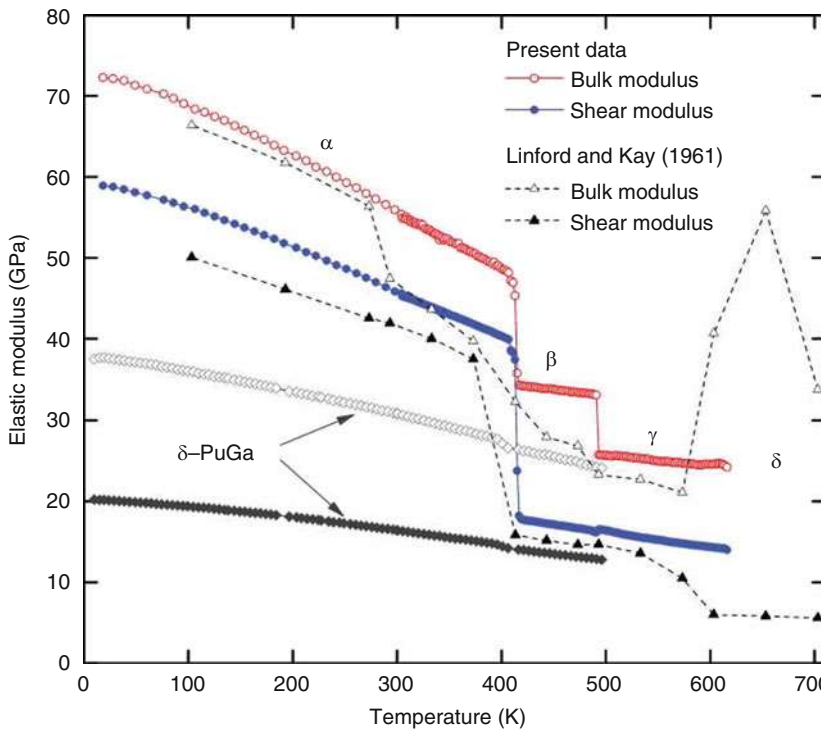


**Fig. 5.23** (Above) Shear and bulk moduli of plutonium clearly showing the transitions between the various solid phases. (Below) Plutonium's density transitions for four solid phases including diagrams of the atomic arrangements for those phases [35]

shear moduli of pure Pu from 18 K to 616 K using RUS [35]. As with other resonant determinations of elastic moduli, acoustic measurements provide extraordinary data density and unmatched precision.

## 5.5 Vibrations of a Stiff String\*

All of the calculations made in Chap. 3, which developed our understanding of the dynamics of wave motion on strings, assumed that the string was “limp,” meaning that only tension provided the restoring force—the string itself had no flexural rigidity ( $E = 0$ , so  $ESk^2 = 0$ ). Anyone who has replaced the strings on a guitar and poked the end of a finger with the stiff string knows differently; guitar strings have sufficient rigidity to penetrate the skin (painfully). Now that we have analyzed the flexure of bars, where the only restoring force is the rigidity of the bar, we are in a position to calculate the effects that rigidity adds to the behavior of strings that are also under tension.

We have already done all of the necessary work. The vertical acceleration of a differential element of a stiff string will just be the sum of the vertical forces as calculated previously in Eq. (3.3) for the tension and in Eq. (5.36) for the flexural rigidity.

$$\rho S \frac{\partial^2 y}{\partial t^2} = T \frac{\partial^2 y}{\partial x^2} - ES k^2 \frac{\partial^4 y}{\partial x^4} \Rightarrow \frac{\partial^2 y}{\partial t^2} - c_{st}^2 \frac{\partial^2 y}{\partial x^2} + c_B^2 k^2 \frac{\partial^4 y}{\partial x^4} = 0 \quad (5.76)$$

Recall that the linear mass density of a string is  $\rho_L = \rho S$ . The speed of transverse waves on a limp string will be designated  $c_{st} = (T/\rho_L)^{1/2}$ , to distinguish it from the speed of longitudinal waves in thin bars,  $c_B = (E/\rho)^{1/2}$ .

As in Sect. 5.3.1, the assumption of a rightward-going traveling wave solution of the form  $y(x, t) = \Re e[\hat{C} e^{j(\omega t - kx)}]$  will lead to an equation that yields the dispersion relation that combines tension and stiffness.

$$c_B^2 k^2 - c_{st}^2 k^2 - \omega^2 = 0 \quad (5.77)$$

The solution of this characteristic equation is just that for a quadratic equation in  $k^2$ .

$$k^2 = \frac{c_{st}^2 \pm \sqrt{c_{st}^4 + 4c_B^2 k^2 \omega^2}}{2c_B^2 k^2} = \frac{c_{st}^2}{2c_B^2 k^2} \left[ 1 \pm \sqrt{1 + \frac{4\omega^2 c_B^2 k^2}{c_{st}^4}} \right] \quad (5.78)$$

We know that the phase speed,  $c_{ph}$ , for a flexural wave depends upon the sharpness of the bend. As derived in Eq. (5.38),  $c_{ph} = (2\pi c_B k)/\lambda$  and  $c_{st}$  is independent of wavelength. We expect that in the limit of very low frequencies, hence, very long wavelengths, the tension should be the dominant restoring force. A binomial expansion can be used for  $(4\omega^2 c_B^2 k^2/c_{st}^4) \ll 1$  to illustrate this limit.

$$\lim_{\omega^2 \rightarrow 0} [k^2] = \frac{c_{st}^2}{2c_B^2 k^2} \left[ 1 \pm \left( 1 + \frac{2\omega^2 c_B^2 k^2}{c_{st}^4} \right) \right] = \frac{\omega^2}{c_{st}^2} \quad (5.79)$$

As expected, for very long wavelengths, the phase speed,  $c_{ph} = \omega/k$ , is constant and equal to the speed of transverse waves on a limp string,  $c_{st}$ .

In the opposite limit of very high frequencies and short wavelengths, we expect the phase speed,  $c_{ph}$ , that is characteristic of flexure waves on rigid bars that are not under tension.

$$\lim_{\omega^2 \rightarrow \infty} [k^2] = \frac{\omega}{c_B \kappa} \Rightarrow c_{ph} \equiv \frac{\omega}{k} = c_B \kappa k = \sqrt{c_B \kappa \omega} \quad (5.80)$$

This result is identical to Eqs. (5.38) and (5.39).

The solutions to Eq. (5.76) can be found by again using separation of variables, as we did in Sect. 5.3.2, with  $y(x, t) = Y(x)T(t) = Ye^{kx}Te^{j\omega t}$ . This substitution converts Eq. (5.76) from a partial differential equation to an ordinary differential equation.

$$\frac{d^4 Y}{dx^4} - \frac{c_{st}^2}{c_B^2 \kappa^2} \frac{d^2 Y}{dx^2} - \frac{\omega^2}{c_B^2 \kappa^2} = 0 \Rightarrow k^4 - \left( \frac{c_{st}^2}{c_B^2 \kappa^2} \right) k^2 - \frac{\omega^2}{c_B^2 \kappa^2} = 0 \quad (5.81)$$

The definition of two new constants,  $2\beta^2$  and  $\gamma^4$ , simplifies the application of the quadratic formula to Eq. (5.81).

$$k^4 - 2\beta^2 k^2 - \gamma^4 = 0, \quad \text{where } 2\beta^2 \equiv \frac{c_{st}^2}{c_B^2 \kappa^2} \text{ and } \gamma^4 \equiv \frac{\omega^2}{c_B^2 \kappa^2} \quad (5.82)$$

As before, taking the fourth root of  $k^4$  will generate four values of wavenumber, although in this case, we need to use the quadratic formula to find  $k^2$ .

$$k_{\pm}^2 = \frac{2\beta^2 \pm \sqrt{4\beta^4 + 4\gamma^4}}{2} = \beta^2 \pm \beta^2 \sqrt{1 + \frac{\gamma^4}{\beta^4}}$$

so

$$k_+^2 = \beta^2 \left[ 1 + \sqrt{1 + \frac{\gamma^4}{\beta^4}} \right] \quad \text{and} \quad k_-^2 = \beta^2 \left[ 1 - \sqrt{1 + \frac{\gamma^4}{\beta^4}} \right] \quad (5.83)$$

Since  $(\gamma/\beta)^4 = 4c_{ph}^4/c_{st}^4 > 0$ , the square roots of  $k_+^2$  will be real numbers, and the square roots of  $k_-^2$  will be purely imaginary numbers. Substitution of these results back into  $Y(x)$  produces four exponentials that are similar to those in Eq. (5.41), but with the hyperbolic trigonometric functions having  $k_+ x$  in their argument and the circular trigonometric functions using  $k_- x$ .

$$Y(x) = C_1 e^{k_+ x} + C_2 e^{-k_+ x} + C_3 e^{jk_- x} + C_4 e^{-jk_- x} \quad \text{or}$$

$$Y(x) = A \cosh(k_+ x) + B \sinh(k_+ x) + C \cos(k_- x) + D \sin(k_- x) \quad (5.84)$$

At this point, we could proceed by fitting boundary conditions, generating transcendental equations that quantize the allowable values of  $k_n$  for normal mode vibrations, and calculating the resonance frequencies,  $\omega_n$ , of those modes. Having done this once before for the flexural modes of bars (and having found it to be tedious!), we will not go down that route here again. Those readers who are nostalgic for such algebraic gymnastics are referred to Morse [37], although his final result is incorrect.<sup>22</sup>

Since our goal is to determine the change in the modal frequencies and resulting anharmonicity of the overtones for a fixed-fixed string due to its flexural rigidity,<sup>23</sup> we can assume that tension is the

<sup>22</sup> Morse's solution for the frequency in his result for his  $\nu_n$ , equal to our  $f_n$ , includes a mode-independent constant term. He is not able to produce the  $n^2$  dependence without adding another term to his Taylor series expansion, and his result is obviously incompatible with Young's observations [38].

<sup>23</sup> Piano technicians compensate for this anharmonicity. Anharmonicity is present in different amounts in all of the ranges of the instrument but is especially prevalent in the bass and high treble registers. The result is that octaves are tuned slightly wider than the harmonic 2:1 ratio. The exact amount that octaves are "stretched" by a piano tuner, by tuning the octave to a match half the frequency of the second overtone instead of the first, varies from piano to piano and even from register to register within a single piano—depending on the exact anharmonicity of the strings involved. With small pianos, the anharmonicity is so significant that they are stretched by matching the triple-octave.

dominant restoring force (since tension is what is adjusted to tune the stiff string's pitch). Additionally, the transverse displacement function,  $y(x, t)$ , of the string is not significantly affected by the string's flexural rigidity.

By now, the previous statements should suggest to the serious reader the application of Rayleigh's method, using the mode shapes,  $y_n(x, t)$ , for a fixed-fixed string in Eq. (3.21), repeated here, as the trial functions.

$$y_n(x, t) = \Re e \left[ C_n e^{j\omega_n t} \sin \left( n \frac{\pi x}{L} \right) \right]; \quad n = 1, 2, 3, \dots \quad (5.85)$$

We have already demonstrated that Rayleigh's method provides the exact solution for the modal frequencies,  $\omega_n$ , of limp fixed-fixed string in Eq. (3.32) by taking the square root of the ratio of the stability coefficient to the inertia coefficient. Since the addition of flexural rigidity does not change the linear mass density,  $\rho_L$ , of the string, the addition of flexural rigidity to the tension as a restoring force means that the relative change in frequency,  $\delta f_n/f_n$ , will be determined by the relative change in the stability coefficient (the potential energy) alone.

$$\frac{\delta f_n}{f_n} = \frac{1}{2} \frac{\delta (PE)_n}{(PE^T)_n} = \frac{1}{2} \frac{(PE^F)_n}{(PE^T)_n} \quad (5.86)$$

The expression for the potential energy due to flexure of a differential element of length,  $dx$ , given by  $d(PE^F)$ , that is bent by an angle,  $\phi$ , is provided in Eq. (4.32). This expression can be integrated over the length,  $L$ , of the string using the fixed-fixed mode shapes of Eq. (5.85).

$$\begin{aligned} (PE^F)_n &= \frac{ES\kappa^2}{2} \int_0^L \left( \frac{\partial^2 y_n}{\partial x^2} \right)^2 dx = \frac{ES\kappa^2}{2} \left( \frac{n\pi}{L} \right)^4 C_n^2 \int_0^L \sin^2 \left( \frac{n\pi x}{L} \right) dx \\ &\Rightarrow (PE^F)_n = n^4 \pi^4 C_n^2 \frac{ES\kappa^2}{4L^3} \end{aligned} \quad (5.87)$$

The maximum potential energy,  $(PE^T)_n$ , in mode  $n$  for the limp string was provided in Eq. (3.31) and reproduced here.

$$(PE)_n = \frac{\pi^2 TL}{\lambda_n^2} C_n^2 = \frac{n^2 \pi^2 T}{4L} C_n^2 \quad (5.88)$$

The relative frequency shift,  $\delta f_n/f_n$ , for any mode number,  $n$ , is given by substitution of Eqs. (5.87) and (5.88) into Eq. (5.86).

$$\frac{\delta f_n}{f_n} = \frac{1}{2} \frac{(PE^F)_n}{(PE^T)_n} = \frac{(\pi n)^2}{2} \frac{ES}{T} \left( \frac{\kappa}{L} \right)^2 = \frac{(\pi n)^2}{2L^2} \frac{c_B^2 \kappa^2}{c_{st}^2} \quad (5.89)$$

This solution reproduces the result of Young who claimed that the measurements were "entirely compatible with the relationship given" [38]. The effects of the string's stiffness grow with the square of the mode number,  $n$ . The dimensionless ratios,  $ES/T$  and  $(\kappa/L)^2$ , scale the importance of the flexural rigidity and the tension as restoring forces.

We can now do an example to estimate the anharmonicity for a piano string based on Eq. (5.89). The *speaking length*,<sup>24</sup>  $L$ , of the piano string, corresponding to "middle-C," with a frequency of

<sup>24</sup>The "speaking length" of a piano string is the distance between the bridge, located on the sound board near the hitching pin, and the *capo d'astro*, near the tuning pin. It is the speaking length that determines the distance between the fixed-fixed boundaries.

$f = 261.6$  Hz, is 63 cm. Strings are typically made from high-carbon steel (e.g., ASTM A228) with a Young's modulus of  $E = 210$  GPa and mass density of  $\rho = 7850$  kg/m<sup>3</sup>. The string is tensioned to about  $T = 780$  N. Assuming the tension dominates the flexural rigidity, the speed of transverse vibrations is  $c_{st} = \sqrt{fL} = 2\sqrt{fL} = 332$  m/s. The linear mass density of the string can be related to the tension and  $c_{st}$ :  $\rho_L = T/c_{st}^2 = 7.07 \times 10^{-3}$  kg/m. Using the mass density of steel,  $\rho_{steel}$ , the diameter of the wire is also determined,  $d = (4\rho_L/\pi\rho_{steel})^{1/2} = 1.07$  mm; hence,  $\kappa^2 = a^2/4 = d^2/16 = 7.17 \times 10^{-8}$  m<sup>2</sup>.

Young's dimensionless anharmonicity coefficient [38],  $b$ , can be expressed in terms of  $d$  using Eq. (5.89).

$$b = \frac{\pi^3}{128} \frac{E}{T} \left( \frac{d^2}{L} \right)^2 \quad (5.90)$$

Substituting the nominal values calculated for the middle-C string of a piano,  $b = 2.15 \times 10^{-4}$ , with  $\delta f_n/f_1 = n^2 b$ . The first overtone,  $n = 2$ , at the octave above middle-C is therefore sharp by 861 ppm, or about 1.5 cents.<sup>25</sup> In Table 3.2, we saw that the  $n = 5$  and  $n = 7$  harmonics did not correspond exactly to a just-temperament interval, with  $n = 5$  falling between  $E^\#$  and  $F^\flat$  and  $n = 7$  falling between  $A^\#$  and  $B^\flat$  for a scale based on middle-C. Those harmonics will be up-shifted by  $5.375 \times 10^{-3}$  (9.3 cents) and 1.011% (17.5 cents), respectively.

This example set an effective lower limit on the anharmonicity of stiff piano strings, since the anharmonicity is greatest in the upper and lower registers of the piano, farthest from middle-C.

## 5.6 Harmonic Analysis

In this chapter, we used our understanding of elasticity from the previous chapter to describe the propagation of waves in solids and used our understanding of the modal frequencies of those standing waves in solids to evaluate the elastic moduli introduced in the previous chapter—a fair exchange. More importantly, we saw in this chapter the power of harmonic analysis (i.e., the assumption of time harmonic solutions) as augmented by a more formalized version of the approach known as separation of variables. That perspective not only was useful for solutions to the wave equations but also to the solution of higher-order partial differential equations. Imposition of boundary conditions again resulted in the quantization of normal mode frequencies in the flexural cases, though requiring four boundary conditions, rather than two required for systems that obeyed the wave equation.

We are now fully equipped to take our techniques for analyzing zero-dimensional harmonic oscillators and one-dimensional systems (strings and bars) and extend them to two-dimensional membranes and plates.

### Talk Like an Acoustician

Flexural rigidity	Dynamic range
Polar moment of inertia	Electromagnetic cross talk
Torsional rigidity	Quadrature output
Phase speed	Reduced frequency
Dispersion	Master curve
Pure tone	Resonant ultrasound spectroscopy
Separation of variables	Speaking length (for piano strings)

<sup>25</sup> Recall from Sect. 3.3.3 that one cent is one one-hundredth of an equal-temperament semitone (in the logarithmic sense), or a frequency ratio of  $2^{1/1200} = 1.000578$ .

## Exercises

- Longitudinal vibration of a fixed-mass loaded bar.** The longitudinal vibrational normal modes of a thin bar with fixed-fixed and free-free boundary conditions were calculated in Sect. 5.1. In this exercise, you will calculate the longitudinal modes of a bar of length,  $L$ , and cross-sectional area,  $S_x$ , that is fixed at  $x = 0$  and has a mass,  $M$ , attached at  $x = L$ .
  - Normal mode frequencies.* If the added mass,  $M$ , has twice the mass of the bar,  $m_B = (M/2)$ , calculate the first three normal mode frequencies in terms of  $c_B$  and  $L$ .
  - Hooke's law limit.* Approximate the frequency of the gravest mode (i.e., the  $f_o$  mode corresponding nearly to a mass-spring oscillator) by assuming that the mass,  $M$ , is restored by a stiffness,  $K = ES_x/L$ . Also report these results in terms of  $c_B$  and  $L$ .
  - Effective mass approximation.* Use a Taylor series expansion [similar to the technique that produced Eq. (3.71)] to determine  $f_o$  by adding the effective mass of the bar to the mass,  $M$ , at  $x = L$ .
- Elastic moduli.** A sample of syntactic foam<sup>26</sup> is cast into a solid rod of circular cross-section with a length of 14.96 cm and a diameter of 1.55 cm. Its mass is 17.1 gm. The fundamental torsional and longitudinal resonances of the free-free vibrations of the rod were measured to be 4192 Hz and 6952 Hz, respectively. Determine the shear modulus, Young's modulus, and Poisson's ratio of this syntactic foam sample.
- M'bira.** Also known as an African thumb piano, the m'bira, shown in Fig. 5.24, is an indigenous musical instrument of the Shona. The most common tuning is called Nyamaropa. It is similar to the western Mixolydian mode that is produced by playing a sequence of eight notes (no sharps or flats) starting and ending with "G" in an equally tempered scale (see Sect. 3.3.3). Assuming that the width and thickness of the reeds are constant, and the vibrational frequencies are that of a clamped-free bar vibrating in its fundamental fixed-free mode, produce a table for the lengths of each reed, starting with  $G_4 = 392$  Hz and ending with  $G_5 = 784$  Hz, if the reed for  $G_5$  is 5.0 cm long.

**Fig. 5.24** African thumb piano



<sup>26</sup> Syntactic foam was developed in the 1960s to provide buoyancy for instruments deployed in the deep ocean. They are composite materials fabricated by filling a castable epoxy with hollow glass microspheres. Those microspheres (sometimes also called microballoons) are very rigid, so the foam is not crushed when subjected to large hydrostatic pressures.

**Table 5.5** If you don't have easy access to the necessary items, you can use the frequencies listed at the right taken for a ruler with thickness,  $t = 0.79$  mm, and width,  $w = 24.0$  mm. Based on the length,  $L = 32.4$  cm, and the mass,  $M = 47.2$  gm, the mass density of the ruler's material is  $\rho = 7680$  kg/m<sup>3</sup>

Length [m]	Frequency [Hz]
0.29	7.09
0.28	7.51
0.25	9.53
0.22	12.31
OJO	14.96
0.18	18.13
0.16	22.97
0.14	29.98
0.12	40.67

4. **Modulus of a 12" ruler.** Try to determine the elastic modulus of a steel machinist's ruler by clamping it to your desk and measuring the frequency of vibration when you "twang" the ruler. (Machinists call that ruler a "scale.") Since the length of a ruler is already accurately marked, it will be easy to determine the vibrating length, although ensuring that the end attached to your desk is "clamped" may be more difficult. A C-clamp will probably provide an adequate restraint. The thickness of your ruler can be determined with a micrometer or Vernier calipers. Measuring the frequency of vibration may be more challenging, although many "smartphones" have an FFT frequency analyzer "app" available. Measure the vibration frequencies,  $f_n$ , as a function of the free length,  $L_n$ , of the ruler and use Eq. (5.50) to measure Young's modulus of your ruler. This technique has been used to determine Young's modulus of metallic glasses [13].
- (a) *Bar speed.* Based on your data or the data in Table 5.5, think about how the data should be plotted and/or averaged to determine the bar speed,  $c_B = [E/\rho]^{1/2}$ , and its uncertainty if  $| \delta t | = 0.6\%$ , corresponding to  $\pm 1\sigma$ . Report your result and its relative uncertainty, providing any graphical output used to determine your result.
  - (b) *Young's modulus.* Use the ruler's mass density to determine the ruler's Young's modulus and its relative uncertainty. If you use the data in Table 5.5, you can let the relative uncertainty corresponding to  $\pm 1\sigma$  in the reported mass density to be  $| \delta \rho / \rho | = 1.0\%$ .
5. **Complex modulus measurement.** In Chap. 2, Problem 21 provided the amplitude and frequency at 22 points for the third torsional mode of a cylindrical rod, with a diameter of about  $1/2" = 12.7$  mm, made from Eastman Tritan® Copolyester TX1001. The effective length of the rod for torsional vibration that included the mass loading due to the coils is  $L_{eff} = 31.94$  cm. The density of the rod is  $\rho = 1.18$  gm/cm<sup>3</sup>.
- (a) *Normal mode frequency.*<sup>27</sup> The measured frequencies and amplitudes are provided in Table 2.2. Determine the resonance frequency,  $f_3$ , by choosing the largest measured amplitude and the two other amplitudes adjacent to the largest value. Fit those three frequency-amplitude pairs to a second-order polynomial, and use the resulting coefficients to make a quadratic interpolation to determine the best value for  $f_3$ . Plug  $f_3$  back into that polynomial to determine the maximum amplitude of that third mode,  $A_3(1)_{max}$ .

<sup>27</sup>If you have solved Prob. 21 in Chap. 2 by doing a least-squares fit of the data to the Rayleigh line shape of Eq. (2.63), you may use those results for  $f_3$ ,  $A_3(1)$ , and  $Q_3$  in parts (a) and (c) of this problem. Of course, if you just love to analyze high-quality resonance data (some of us do!), then do it both ways and compare your results. After that, make your friends and colleagues call you a "spectroscopist."

- (b) *Shear modulus.* Based on  $L_{eff}$ ,  $\rho$ , and  $f_3/n$ , determine the “real” part of the bar’s shear modulus at  $f_3$ .
- (c) *Quality factor.* Determine the two “down 3 dB” frequencies,  $f_+$  and  $f_-$ , by finding those frequencies which correspond to an amplitude of  $A_3(1)_{max}/\sqrt{2}$ . Since none of the measured amplitudes exactly equal that -3 dB amplitude, choose the two measurements that straddle  $A_3(1)_{max}/\sqrt{2}$  and fit a straight line between them to find  $f_-$  by linear interpolation. Do the same to find  $f_+$ . Use those two -3 dB frequencies to calculate the quality factor,  $Q_3$ , for that  $n = 3$  torsional mode using Eq. (B.3).
- (d) *Loss modulus.* Use Eq. (B.9) and your value for the elastic modulus you calculated in part (b) and  $Q_3$  to determine the “imaginary” part of the complex shear modulus.

## References

1. E. Mauceli et al., The Allegro gravitational wave detector: Data acquisition and analysis. *Phys. Rev. D* **54**(2), 1264–1275 (1996)
2. M. McHugh et al., Calibration of the ALLEGRO resonant detector. *Classical Quantum Gravity* **22**(18), S965–S973 (2005)
3. M. Janes, Sonic Pile Driving: The History and the Resurrection of Vibration Free Pile Driving. <http://www.resonancetechnology.ca/res%20driver%20history%20090112.pdf>. A very impressive video comparing the resonant and drop hammer techniques is also available from that site: <http://www.resonancetechnology.ca/gallery%20video%201.php>
4. G. Bodine, Jr., Sonic method and apparatus for driving casings through earthen formations. U.S. Patent No. 3,375,884 (April 2, 1968)
5. G. Bodine, Jr., Sonic method and apparatus for grinding rock material and the like to powder. U.S. Patent No. 3,429,512 (February 25, 1969)
6. S.P. Timoshenko, J.N. Goodier, *Theory of Elasticity*, 3rd edn. (McGraw-Hill, New York, 1970). See Chapter 11; ISBN 978-1-4020-7745-6
7. L.D. Landau, E.M. Lifshitz, *Elasticity*, 2nd edn. (Pergamon, New York, 1970).; See §18 and §25. ISBN 0 08 006465 5
8. W.C. Young, R.G. Budynas, *Roark's Formulas for Stress and Strain*, 7th edn. (McGraw-Hill, New York, 2002); ISBN 0-07-072542-X
9. S.P. Timoshenko, *History of Strength of Materials* (McGraw-Hill, New York, 1953); ISBN 0-486-61187-6
10. Newton, Opticks or a Treatise on the Reflexions, Refractions, Inflections and Colours of Light, Also Two Treatises of the Species and Magnitude of Curvilinear Figures, 1st ed. (Smith & Walford, 1704). 4th ed., with forward by A. Einstein and preface by I. B. Cohen (Dover, 1979); ISBN 978-0-486-60205-9
11. D. Heckerman, S. Garrett, G. Williams, P. Weidman, Surface tension restoring forces on gravity waves in a narrow channel. *Phys. Fluids* **22**, 2270–2276 (1979)
12. S.M. Han, H. Benaroya, T. Wei, Dynamics of transversely vibrating beams using four engineering theories. *J. Sound Vib.* **225**(5), 935–988 (1999)
13. M.B. Barmatz, H.J. Learn, H.S. Chen, A method for the determination of Young’s modulus and internal friction in metallic glasses. *Rev. Sci. Instrum.* **79**(6), 885–886 (1971)
14. R.P. Feynman, R.B. Leighton, M. Sands, *The Feynman Lectures on Physics*, vol II (Addison-Wesley, Reading, 1963), pp. 38–38
15. L.D. Landau, E.M. Lifshitz, *Mechanics* (Pergamon, Oxford, 1960). §39
16. N. Yazdi, F. Ayazi, K. Najafi, Micromachined inertial sensors. *Proc. IEEE* **86**(8), 1640–1659 (1998)
17. W. Strutt (Lord Rayleigh), On waves propagated along the plane surface of an elastic solid. *Proc. London Math. Soc.* **S1-17**, 4–11 (1885)
18. F. Graff, *Wave Motion in Elastic Solids* (Clarendon, Oxford, 1975). Reprinted by Dover, 1991; ISBN 0-486-66745-6
19. S.L. Garrett, Resonant acoustic determination of elastic moduli. *J. Acoust. Soc. Am.* **88**(1), 210–221 (1990)
20. E-Cast F-28 with Hardener 215, United Resins Corp., 1305 E. St. Gertrude Place, Unit B., Unit B, Santa Ana, CA 92705
21. A. Barone, A. Giacomini, Experiments on some electrodynamic ultrasonic vibrators. *Acustica* **4**, 182–184 (1954)
22. R.W. Leonard, Attenuation of torsional waves in Teflon. *J. Acoust. Soc. Am.* **40**(1), 160–162 (1966)

23. E.R. Fitzgerald, Simple method for observing audio frequency resonances and sound beams in crystals. *J. Acoust. Soc. Am.* **36**(11), 2086–2089 (1964)
24. R.W. Leonard, Comments on the existence of the Fitzgerald effect. *J. Acoust. Soc. Am.* **38**(4), 673–674 (1965)
25. Q.S. Guo, D.A. Brown, Determination of the dynamic elastic moduli and internal friction using thin resonant bars. *J. Acoust. Soc. Am.* **108**(1), 167–174 (2000)
26. J. W. Strutt (Lord Rayleigh), *Theory of Sound*, 2nd edn. (Macmillan, London, 1894).; Reprinted by Dover, 1948, Vol. I, Ch. VII and Ch. VIII
27. Product Research & Chemicals, Corp., 5454 San Fernando Road, Glendale, CA 91203
28. H. Tan, Resonant acoustic determination of complex elastic moduli (Unclassified), Master's Thesis in Engineering Acoustics, U. S. Naval Postgraduate School, Monterey, CA (March, 1991); DTIC Report No. AD A245 058
29. P. Horowitz, W. Hill, *The Art of Electronics*, 2nd edn. (Cambridge University Press, Cambridge, 1989). §15.15; ISBN 0-521-37095-7
30. R.E. Best, *Phase-locked Loops: Design, Simulation, and Applications*, 6th edn. (McGraw-Hill, New York, 2007); ISBN 978-0-07-149375-8
31. J.D. Ferry, *Viscoelastic Properties of Polymers*, 3rd edn. (Wiley, New York, 1980); ISBN: 978-0-471-04894-7
32. W.M. Visscher, A. Migliori, T.M. Bell, R.A. Reinert, On the normal modes of free vibration of inhomogeneous and anisotropic elastic objects. *J. Acoust. Soc. Am.* **90**(4 Pt. 1), 2154–2162 (1991)
33. V.M. Keppens, J.D. Maynard, A. Migliori, Listening to materials: From auto safety to reducing the nuclear arsenal. *Acoust. Today* **6**(2), 6–13 (2010)
34. P.S. Spoer, J.D. Maynard, A.R. Kortan, Elastic isotropy and anisotropy in quasicrystalline and cubic AlCuLi. *Phys. Rev. Lett.* **75**(19), 3462–3465 (1995)
35. Y. Suzuki, V.R. Fanelli, J.B. Betts, F.J. Freibert, C.H. Mielke, J.N. Mitchell, M. Ramos, T.A. Saleh, A. Migliori, Temperature dependence of elastic moduli of polycrystalline  $\beta$  plutonium. *Phys. Rev. B* **84**, 064105 (2011)
36. P. S. Spoer, Elastic Properties of Novel Materials using PVDF Film and Resonant Ultrasound Spectroscopy, Ph. D. thesis in Acoustics, Penn State, December, 1996
37. P.M. Morse, *Vibration and Sound* (Acoustical Society of America, New York, 1976), pp. 166–170, §16. ISBN 0-88318-287-4
38. R.W. Young, Inharmonicity of plane wire piano strings. *J. Acoust. Soc. Am.* **24**(3), 267–273 (1952)

**Open Access** This chapter is licensed under the terms of the Creative Commons Attribution 4.0 International License (<http://creativecommons.org/licenses/by/4.0/>), which permits use, sharing, adaptation, distribution and reproduction in any medium or format, as long as you give appropriate credit to the original author(s) and the source, provide a link to the Creative Commons license and indicate if changes were made.

The images or other third party material in this chapter are included in the chapter's Creative Commons license, unless indicated otherwise in a credit line to the material. If material is not included in the chapter's Creative Commons license and your intended use is not permitted by statutory regulation or exceeds the permitted use, you will need to obtain permission directly from the copyright holder.





# Membranes, Plates, and Microphones

6

## Contents

6.1	<b>Rectangular Membranes</b>	284
6.1.1	Modes of a Rectangular Membrane	286
6.1.2	Modal Degeneracy	288
6.1.3	Density of Modes	291
6.2	<b>Circular Membranes</b>	294
6.2.1	Series Solution to the Circular Wave Equation	295
6.2.2	Modal Frequencies and Density for a Circular Membrane	299
6.2.3	Mode Similarities Illustrating Adiabatic Invariance	300
6.2.4	Normal Modes of Wedges and Annular Membranes*	302
6.2.5	Effective Piston Area for a Vibrating Membrane	304
6.2.6	Normal Mode Frequencies of Tympani	306
6.2.7	Pressure-Driven Circular Membranes	308
6.3	<b>Response of a Condenser Microphone</b>	310
6.3.1	Optimal Backplate Radius	313
6.3.2	Limits on Polarizing Voltages and Electrostatic Forces	315
6.3.3	Electret Condenser Microphone	317
6.4	<b>Vibrations of Thin Plates</b>	321
6.4.1	Normal Modes of a Clamped Circular Plate	322
6.5	<b>Flatland</b>	324
	<b>References</b>	329

This is the final chapter in Part I of this textbook that addresses vibration. In this chapter, we will apply the techniques developed thus far to two-dimensional vibrating surfaces. In Part II, we begin our investigations into waves in fluids. This final vibration chapter is then appropriately transitional, since most waves that are produced in fluids result from the vibrations of two-dimensional surfaces. All acoustical stringed musical instruments<sup>1</sup> include some mechanism to transfer the vibration of the string to a two-dimensional surface, whether that is the sounding board of a piano, autoharp, or dulcimer; the

<sup>1</sup> Electrical stringed instruments have a “pickup” (transducer) that converts the string’s vibrations into an electrical signal. In performance, those electrical signals are amplified and applied to a loudspeaker which is a vibrating two-dimensional surface. For recorded music, those signals may be recorded electronically and the vibrations postponed until the recording is played back, again with the use of a two-dimensional vibrating surface.

body of a guitar, mandolin, or some member of the violin family; or the drumhead of a banjo or *erhu*. Strings are very inefficient in their ability to couple their vibrations to the surrounding fluid medium; two-dimensional surfaces are quite a good deal more efficient. Of course, drums of all kinds make sound due to the vibration of a membrane. Obviously, loudspeakers create sound in the air by the vibrations of a two-dimensional piston – there are no electrodynamic loudspeakers (see Sect. 2.5.5) that have only voice coils with no cone and/or dome attached.

In this chapter, we will first focus on vibrations of membranes and then consider vibrations of plates. The distinction between a membrane and a plate is analogous to the difference between a limp string and a rigid bar in one dimension. The restoring forces on membranes are due to the tension in the membrane, while the restoring forces for plates are due to the flexural rigidity of the plate.<sup>2</sup>

The transition to two dimensions also introduces some other features that did not show up in our analysis of one-dimensional vibrating systems. Instead of applying boundary conditions at one or two points, they will have to be applied along a line or a curve. In this way, incorporation of the boundary condition is linked inexorably to the choice of coordinate systems used to describe the resultant modal shape functions. The vibration of a circular membrane could be described in a Cartesian coordinate system, since radial and azimuthal variations in the vertical displacements could be represented by an infinite superposition of plane waves, but it is much easier if we choose a polar coordinate system to describe vibrations of a circular membrane or plate.

When we applied a force to a string, the string was deformed into a triangular shape. When a membrane is excited by a point force, its displacement is infinite since a point force will represent infinite pressure.<sup>3</sup> Our analysis will avoid this divergence by concentrating on oscillating fluid pressures rather than forces to drive the motion of membranes and the diaphragms of microphones.

It was also true for strings, or torsional and longitudinal waves in bars, that the number of modes within a given frequency interval,  $\Delta f$ , was fairly constant or exactly constant for ideal fixed-fixed or free-free boundary conditions:  $f_{n+1} - f_n = f_1$ . The number of modes within a frequency interval,  $\Delta f$ , was simply  $\Delta f/f_1$  if  $\Delta f \gg f_1$ . Under all circumstances,  $f_{n+1} \neq f_n$  for strings or bars. For two-dimensional vibrators, two indices are required to uniquely specify the frequency of a normal mode,  $f_{m,n}$ , with the number of modes in a given frequency interval increasing in proportion to the center frequency of that interval, even though the interval represents a fixed frequency span. It is also possible that modes with different mode numbers might correspond to the same frequency of vibration, a situation that is designated as “modal degeneracy.”

## 6.1 Rectangular Membranes

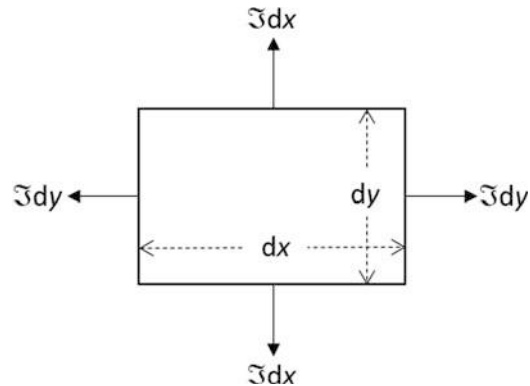
Despite the differences between one- and two-dimensional vibrating systems just mentioned, there is nothing new that we will need to employ that we have not already used in our investigations of strings to develop an equation for the transverse vibrations of a membrane or to find two-dimensional solutions to that resulting equation. In many ways, a membrane can be thought of as the layer produced

---

<sup>2</sup> The flexural rigidity of a plate is defined differently from the flexural rigidity of a bar because it is much more difficult to bend a plate along one axis if it has already been bent along another perpendicular axis. (Try this with a sheet of paper – easy to make the first bend but more difficult to make the second bend along an orthogonal axis.)

<sup>3</sup> Since the area of a point is zero, any force divided by zero area produces an infinite pressure. Similarly, we can think of the membrane’s surface tension. When a membrane is poked by a blunt end, the force magnitude is the surface tension times the circumference of the blunt end. The point force has zero circumference, so there is no balance force and infinite displacement will result.

**Fig. 6.1** Forces on a differential area element  $dA = dx dy$  of a membrane as expressed in a Cartesian coordinate system



by placing an infinite number of strings side by side, although the perspective we are about to cultivate will be far more useful.

As with the string, we will begin by calculating the net vertical force,  $dF_z$ , on a differential element of a membrane with differential area,  $dA = dx dy$ , under assumptions that are analogous to those used for strings. We will assume the membrane is sufficiently thin that the membrane's material will provide no flexural rigidity—a limp membrane. We will also assume that the membrane is uniform and that it has a surface mass density (mass per unit area),  $\rho_s$ , that is independent of position on the membrane's surface and that  $\rho_s = \rho t$ , where  $\rho$  is the mass density of the membrane's material and  $t$  is the membrane's constant thickness. We will also assume linear behavior and neglect the changes in the membrane's tension due to its transverse displacements in the same way we ignored changes in the string's length that could affect its tension, as described in Eq. (3.28). As before, we will assume sufficiently small displacements that the last statement is approximately true.

Figure 6.1 shows a differential element of a membrane, located in the  $x$ - $y$  plane, which is acted upon by tensile forces produced by a tension per unit length,  $\mathfrak{T}$ , applied at all the edges of the membrane. The tension on a differential element will depend upon the length of its edge, in this case either  $dx$  or  $dy$ . In Fig. 6.1, the restoring forces due to the two boundaries of width,  $dx$ , located between  $y$  and  $y + dy$ , are just  $\pm \mathfrak{T} dx$  pulling in opposite directions. Similarly, the restoring forces due to the two boundaries of width  $dy$ , located between  $x$  and  $x + dx$ , are just  $\pm \mathfrak{T} dy$  pulling in opposite directions.

If that differential element of the membrane is displaced in the  $z$  direction, then  $F_{z,x}$  is the net vertical force that will cause the membrane element to be restored to its equilibrium position (and overshoot, due to its mass).

$$F_{z,x} = \mathfrak{T} dy \left[ \left( \frac{\partial z}{\partial x} \right)_{x+dx} - \left( \frac{\partial z}{\partial x} \right)_x \right] = \mathfrak{T} \frac{\partial^2 z}{\partial x^2} dx dy \quad (6.1)$$

Of course, the force provided by the other pair of tensions,  $F_{z,y}$ , will have the same form, and the acceleration of the differential element in the  $z$  direction of membrane, due to both  $F_{z,x}$  and  $F_{z,y}$ , will be determined by Newton's Second Law where  $\rho_s = \rho t$  is the surface mass density. In that case,  $t$  is the membrane's thickness, although otherwise it will indicate time, as in the equations that follow.

$$\rho_S dx dy \frac{\partial^2 z(x, y, t)}{\partial t^2} = \Im \left( \frac{\partial^2 z(x, y, t)}{\partial x^2} + \frac{\partial^2 z(x, y, t)}{\partial y^2} \right) dx dy \\ \Rightarrow \frac{\partial^2 z(x, y, t)}{\partial t^2} - c^2 \left( \frac{\partial^2 z(x, y, t)}{\partial x^2} + \frac{\partial^2 z(x, y, t)}{\partial y^2} \right) = 0 \quad (6.2)$$

The right-hand version of Eq. (6.2) introduced a transverse wave propagation speed,  $c = \sqrt{\Im/\rho_S}$ , and has the form of a wave equation, but in two dimensions.

Because we will be describing the displacement of the membrane in both Cartesian and polar coordinate systems, it is convenient to express the wave equation for membranes in terms of the *Laplacian operator*,  $\nabla^2$ .

$$\nabla^2 z(x, y, t) = \frac{1}{c^2} \frac{\partial^2 z(x, y, t)}{\partial t^2} \quad (6.3)$$

In this way, the wave equation for membranes can be expressed in either coordinate system. By comparison to Eq. (6.2), it is easy to see how the Laplacian can be expressed in Cartesian coordinates. Also shown in Eq. (6.4) is the Laplacian expressed in polar coordinates, where  $r$  is the distance of a point from the origin of the coordinate system and  $\theta$  is the angle that point makes with respect to the positive horizontal axis.

$$\nabla^2 = \frac{\partial^2}{\partial x^2} + \frac{\partial^2}{\partial y^2}; \quad \nabla^2 = \frac{\partial^2}{\partial r^2} + \frac{1}{r} \frac{\partial}{\partial r} + \frac{1}{r^2} \frac{\partial^2}{\partial \theta^2} \quad (6.4)$$

The polar form will be derived in Sect. 6.2.

### 6.1.1 Modes of a Rectangular Membrane

We will start by seeking normal mode solutions with frequencies,  $\omega_{m,n}$ , for a rectangular membrane that is  $L_x$  long and  $L_y$  wide and is clamped along all four edges:  $z(0, y, t) = z(L_x, y, t) = z(x, 0, t) = z(x, L_y, t) = 0$ . Since we seek normal mode solutions that require all parts of the membrane vibrate with the same frequency,  $\omega$ , we will assume that  $z(x, y, t) = z(x, y)e^{j\omega t}$ , thus converting Eq. (6.2) from a wave equation into a time-independent *Helmholtz equation*, with  $k^2 = \omega^2/c^2$ .

$$\frac{\partial^2 z(x, y)}{\partial x^2} + \frac{\partial^2 z(x, y)}{\partial y^2} + k^2 z(x, y) = 0 \quad (6.5)$$

We will seek solutions to Eq. (6.5) by separation of variables, substituting  $z(x, y) = X(x)Y(y)$ .

$$Y \frac{d^2 X}{dx^2} + X \frac{d^2 Y}{dy^2} + k^2 XY = 0 \quad \Rightarrow \quad \frac{1}{X} \frac{d^2 X}{dx^2} + \frac{1}{Y} \frac{d^2 Y}{dy^2} = -k^2 \quad (6.6)$$

From the right-hand version of Eq. (6.6), it is clear that the left-hand term,  $(1/X)(d^2 X/dx^2)$ , depends only upon  $x$  and is independent of  $y$ . The second term,  $(1/Y)(d^2 Y/dy^2)$ , depends only upon  $y$  and is independent of  $x$ . Since  $k^2$  is a constant, it is only possible to have a solution to Eq. (6.6) for all  $x$  and  $y$  if those two terms are separately equal to constants, which we will set equal to  $-k_x^2$  and  $-k_y^2$ .

$$\frac{d^2X}{dx^2} + k_x^2 X = 0 \quad \text{and} \quad \frac{d^2Y}{dy^2} + k_y^2 Y = 0 \quad (6.7)$$

Substitution of Eq. (6.7) into Eq. (6.6) produces the *separation condition*.

$$k_x^2 + k_y^2 = k^2 = \frac{\omega^2}{c^2} \quad (6.8)$$

At this juncture, we are rather familiar with the solutions to harmonic oscillator equations like those in Eq. (6.7). By choosing sine functions for the spatial dependence of  $x$  and  $y$ , we will automatically have a solution that satisfies  $\mathbf{z}(0, y, t) = \mathbf{z}(x, 0, t) = 0$ .

$$z(x, y, t) = \Re e \left[ \hat{\mathbf{C}} \sin(k_x x + \phi_x) \sin(k_y y + \phi_y) e^{j\omega t} \right] \quad (6.9)$$

As before, imposition of the other two boundary conditions,  $z(L_x, y, t) = z(x, L_y, t) = 0$ , quantizes the allowed values of  $k_x$  and  $k_y$ .

$$k_x = \frac{m\pi}{L_x} \quad \text{and} \quad k_y = \frac{n\pi}{L_y} \quad \text{with} \quad m, n = 1, 2, 3, \dots \quad (6.10)$$

It is worthwhile to note that neither  $m = 0$  nor  $n = 0$  provides an acceptable solution since  $\sin(0) = 0$ , so the vertical displacements would be zero everywhere if either integer index were zero.

Combining the separation restriction on the sum of  $k_x^2$  and  $k_y^2$  in Eq. (6.8) with their quantization conditions in Eq. (6.10) produces an expression for the normal mode frequencies,  $f_{m,n}$ , in terms of the dimensions of the membrane,  $L_x$  and  $L_y$ , and the speed of transverse waves on the membrane,  $c = \sqrt{\mathfrak{J}/\rho_s}$ :

$$f_{m,n} = \frac{\omega_{m,n}}{2\pi} = \frac{c}{2} \sqrt{\left(\frac{m}{L_x}\right)^2 + \left(\frac{n}{L_y}\right)^2} \quad (6.11)$$

This expression for the frequencies of the normal modes of a fixed-fixed rectangular membrane in Eq. (6.11) represents a Pythagorean sum of the modes of two fixed-fixed strings of lengths,  $L_x$  and  $L_y$ .

The mode shapes can now be calculated by substituting the normal modal frequencies of Eq. (6.11) back into our separated solution,  $z(x, y) = X(x)Y(y)$ . The most important aspect of Eq. (6.9) is recognition that the mode shape is the product of the two sine functions; if the value of either function is zero for some value of the function's argument, the transverse displacement is zero for that value.

This is evident in Fig. 6.2 for all mode shapes except the (1, 1) mode which only has displacement nodes along the boundaries.<sup>4</sup> For the (2, 1) mode, there is an obvious nodal line that bisects the membrane with the displacements on either side of the nodal line being 180° out-of-phase in time. The (1, 2) mode is just like the (2, 1) mode but with the nodal line in the orthogonal direction. The (2, 2) mode has two perpendicular nodal lines with adjacent quadrants moving 180° out-of-phase; both  $X(x)$  and  $Y(y)$  go to zero along both bisectors of the membrane. The frequency of the (2, 2) modes is identical to the (1, 1) mode of a membrane that is half as long and half as wide.

---

<sup>4</sup> This is analogous to the fundamental mode of a fixed-fixed string whose mode shape has no zero crossings (see Fig. 2.28).

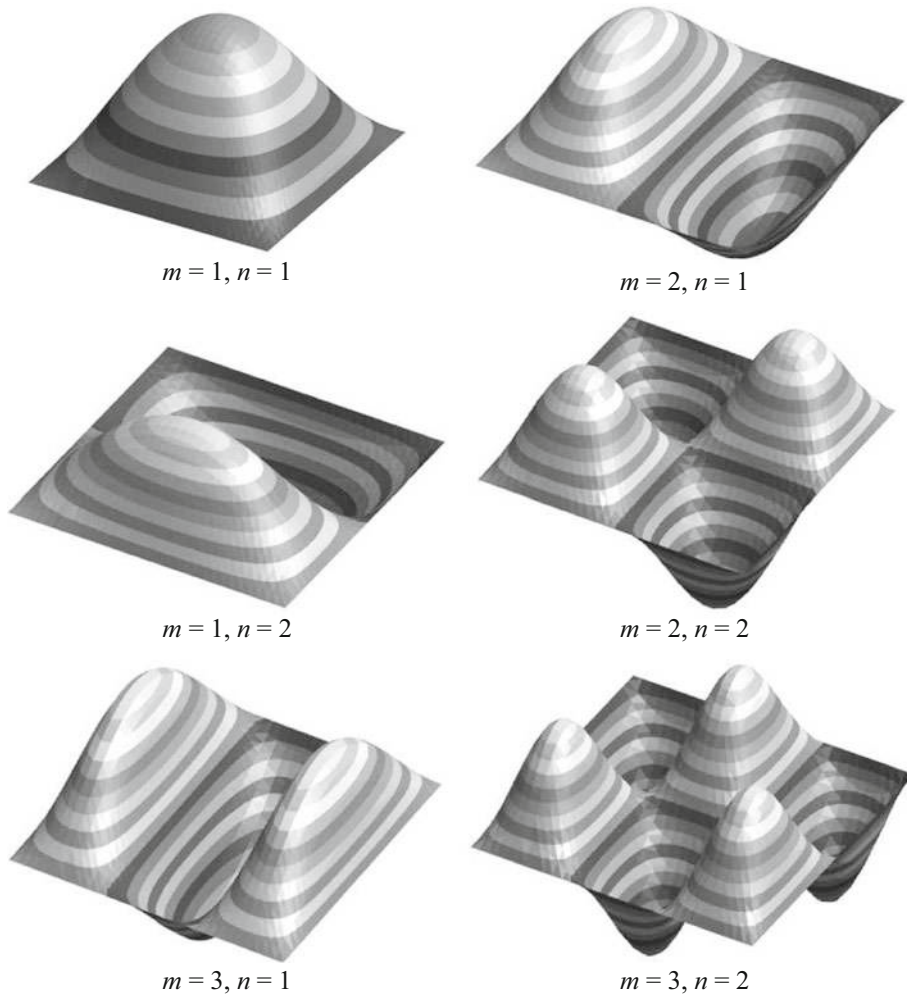


**Fig. 6.2** Greatly exaggerated mode shapes for a rectangular membrane with the grey bands indicating areas having the same transverse displacement. The left column, from top to bottom, are the  $(1, 1)$ ,  $(1, 2)$ , and  $(3, 1)$  modes. The right column, from top to bottom, are the  $(1, 2)$ ,  $(2, 2)$ , and  $(3, 2)$  modes

### 6.1.2 Modal Degeneracy<sup>5</sup>

The normalized, normal modal frequencies in Eq. (6.11) have been provided in Table 6.1 for two rectangular membranes. One example makes  $L_x = L_y\sqrt{2}$  and the other has  $L_x = (3/2)L_y$ . The normalized frequencies in Table 6.1 are the normal mode frequencies divided by the fundamental normal mode frequency,  $f_{1,1}$ . The normal mode frequencies for both cases are tabulated in order of increasing frequency from  $f_{1,1}$  to  $5f_{1,1}$ . In one case, the total number of modes is 35 and the other is 34.

The first feature that is worthy of notice is that there is no apparently systematic order by which the values of  $m$  and  $n$  progress as the frequency increases. Of course, there is order imposed by Eq. (6.11), but since  $L_x \neq L_y$ , and in both of these examples  $L_x > L_y$ , a unit increase of  $m$  causes a smaller frequency

<sup>5</sup> Not to be confused with moral degeneracy; they are entirely unrelated.

**Table 6.1** Normal mode frequencies less than or equal to  $5f_{1,1}$  for two rectangular membranes are arranged in order of increasing frequency

$L_x = \sqrt{2}L_y$						$L_x = 1.5L_y$					
$m$	$n$	$f_{m,n}/f_{1,1}$	$m$	$n$	$f_{m,n}/f_{1,1}$	$m$	$n$	$f_{m,n}/f_{1,1}$	$m$	$n$	$f_{m,n}/f_{1,1}$
1	1	1.000	5	3	3.786	1	1	1.000	3	4	3.721
2	1	1.414	6	2	3.830	2	1	1.387	6	2	3.721
1	2	1.732	4	4	4.000	1	2	1.754	5	3	3.731
3	1	1.915	1	5	4.123	3	1	1.861	7	1	3.971
2	2	2.000	7	1	4.123	2	2	2.000	4	4	4.000
3	2	2.380	2	5	4.243	3	2	2.353	6	3	4.160
4	1	2.449	6	3	4.243	4	1	2.370	1	5	4.197
1	3	2.517	7	2	4.359	1	3	2.557	7	2	4.224
2	3	2.708	5	4	4.359	2	3	2.732	2	5	4.306
4	2	2.828	3	5	4.435	4	2	2.774	5	4	4.332
5	1	3.000	8	1	4.690	5	1	2.896	3	5	4.481
3	3	3.000	4	5	4.690	3	3	3.000	8	1	4.515
1	4	3.317	7	3	4.726	5	2	3.234	7	3	4.616
5	2	3.317	6	4	4.761	4	3	3.340	6	4	4.707
4	3	3.367	8	2	4.899	1	4	3.374	4	5	4.715
2	4	3.464	1	6	4.933	6	1	3.431	8	2	4.739
6	1	3.559	5	5	5.000	2	4	3.508	5	5	5.000
3	4	3.697									

The frequencies are reported as the ratio of the modal frequency,  $f_{m,n}$ , to the frequency of the fundamental mode:  $f_{m,n}/f_{1,1}$ . (Left)  $L_x = L_y\sqrt{2}$  and (Right)  $L_x = 1.5 L_y$ . On the left, there are six modal degeneracies:  $f_{5,1} = f_{3,3} = 3.000f_{1,1}$ ,  $f_{1,4} = f_{5,2} = 3.317f_{1,1}$ ,  $f_{1,5} = f_{7,1} = 4.123f_{1,1}$ ,  $f_{2,5} = f_{6,3} = 4.243f_{1,1}$ ,  $f_{7,2} = f_{5,4} = 4.359f_{1,1}$ , and  $f_{8,1} = f_{4,5} = 4.67f_{1,1}$ . On the right, there is only a single degeneracy:  $f_{3,4} = f_{6,2} = 3.721f_{1,1}$ .

increase than a unit increase of  $n$ . If the membrane had the aspect ratio of a thin ribbon, with  $L_x = 10L_y$ , then the (17, 1) mode would have a lower frequency than the (1, 2) mode.

Another important feature of the modes in Table 6.1 is the fact that there are six pairs of modes for the  $L_x = L_y\sqrt{2}$  case that have distinctly different mode shapes yet share identical normal mode frequencies. Such modes are called *degenerate modes*. If the membrane were square, so  $L_x = L_y$ , and then all of the  $m \neq n$  modes will be double-degenerate since  $f_{m,n} = f_{n,m}$ . All modes of the square membrane having  $m = n$  are non-degenerate since there is only one mode shape corresponding to such frequencies.

Degenerate modes have special properties. Owing to the fact that they have the same frequency, they can be superimposed, and the ratio of their amplitudes and the differences in their phases can be arbitrary.<sup>6</sup> In that case, the membrane can oscillate with each point undergoing simple harmonic motion at frequency,  $f_{m,n} = f_{n,m}$ , but with an infinite variety of mode shapes. If we consider the (1, 2) and (2, 1) modes of a square membrane, and superimpose them with identical phases, but with amplitudes controlled by a sine and cosine function, then it is possible to orient the nodal line in any direction,  $\theta$ , with respect to the  $x$  axis.

$$\mathbf{z}(x, y, t) = (z_{m,n} \cos \theta + z_{n,m} \sin \theta) e^{j\omega_{m,n} t} \quad (6.12)$$

If  $\theta = +45^\circ$ , then the nodal line coincides with one diagonal of the square, and if  $\theta = -45^\circ$ , then the nodal line coincides with the other diagonal.

<sup>6</sup>Of course, since this is a linear system, any two (or more) modes can be superimposed, but since they have different frequencies, then the sum of their displacements will not be periodic unless the frequencies of the modes are commensurate (i.e., their frequencies have integer ratios).

It is also possible to have the superposition coefficients vary with time.

$$\mathbf{z}(x, y, t) = [z_{m,n} \cos(\omega_{m,n}t) \pm z_{n,m} \sin(\omega_{m,n}t)] e^{j\omega_{m,n}t} \quad (6.13)$$

For the superposition scheme in Eq. (6.13), the nodal line would rotate once per cycle, creating a traveling wave rotating in the clockwise direction for the minus sign and counterclockwise for the plus sign. Traveling waves on a membrane of finite extent are only possible through the superposition of degenerate modes. In our later treatment of fluid-filled toroidal resonators (see Sect. 13.5) and manipulation of acoustically levitated objects (see Sect. 15.6), traveling waves created by the superposition of degenerate modes will prove to be very useful.

The frequencies of degenerate modes will be split (i.e.,  $f_{m,n} \neq f_{n,m}$ ) if the symmetry of the membrane becomes broken. If the uniformity of the membrane is disturbed either by a tension that is not uniform or by the addition of a mass, making the surface mass density nonuniform, the degenerate modes will be split into two distinct modes with different frequencies. As an example of such *mode splitting*, consider a uniform square membrane with  $L_x = L_y$ , shown in Fig. 6.3, that has a small piece of putty with mass,  $M$ , stuck to its surface at  $x = L_x/4$  and  $y = L_y/2$ .

The added mass is located on a nodal line for the  $(1, 2)$  mode. If we assume that the added mass is small (i.e.,  $M \ll \rho_s L_x L_y$ ), it will not affect the frequency,  $f_{1,2}$ , in the position shown in Fig. 6.3, because it is located on a node and will remain stationary when that mode is excited. On the other hand, the added mass is located at a point of maximum transverse displacement for the  $(2, 1)$  mode. Since the mass is assumed to be small compared to the mass of the membrane, the added mass will lower the frequency,  $f_{2,1}$ , by an amount that would be easy to calculate using Rayleigh's method. Equation (6.9) can be used as the trial function to calculate the unperturbed kinetic energy,  $(KE)_{2,1}$ . The kinetic energy of the mass is just  $(M/2)v^2$ , where  $v = \dot{z}(L_x/4, L_y/2)$  is the transverse velocity of the unloaded membrane at the point  $x = L_x/4$  and  $y = L_y/2$ .

$$\frac{\delta f_{2,1}}{f_{2,1}} \cong -\frac{Mv^2}{4(KE)_{2,1}} \quad (6.14)$$

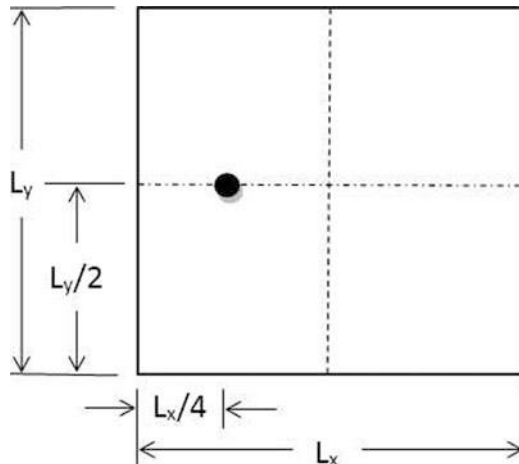


**Fig. 6.3** The symmetry of a square membrane is “broken” with a small mass (dark circle) that is bonded to the membrane at the location shown. The *dashed vertical line* is the displacement node for the  $(1, 2)$  mode, and the *dash-dotted horizontal line* is the displacement node for the  $(2, 1)$  mode. The small mass,  $M$ , is bonded to the square membrane’s surface. Without the added mass, the frequencies of those two modes are degenerate for a square membrane,  $f_{1,2} = f_{2,1}$ . The mass will split the degeneracy by lowering  $f_{1,2}$  and leaving  $f_{2,1}$  unchanged

### 6.1.3 Density of Modes

Another interesting feature of the modal frequencies in Table 6.1 is that the number of modes in any frequency range increases with increasing frequency. For example, in both the  $L_x = L_y\sqrt{2}$  and the  $L_x = (3/2)L_y$  examples, there are four modes with a relative frequency  $f_{m,n}/f_{1,1} < 2$ . For  $2 \leq f_{m,n}/f_{1,1} < 3$ , there are 6 or 7 modes; for  $3 \leq f_{m,n}/f_{1,1} < 4$ , there are 10 modes; and for  $4 \leq f_{m,n}/f_{1,1} < 5$ , there are 12 or 14 modes. For a fixed-fixed string, there would be only one mode in each frequency interval, independent of the frequency.

This increase in the *modal density* is a characteristic of a two-dimensional system, not a feature that is unique only to rectangular membranes, as will be demonstrated in Sect. 6.2.2. Figure 6.4 provides a histogram that shows the total number of modes with relative frequencies,  $f_{m,n}/f_{1,1}$ , that are less than a given normalized frequency ratio indicated on the horizontal axis. The number of modes for both examples in Table 6.1 grows at a rate that is proportional to the square of the normalized frequency.

There is a simple geometric interpretation that explains the approximately quadratic growth in the number of modes with increasing frequency. Using the quantized values of the two wavenumbers,  $k_x$  and  $k_y$ , in Eq. (6.10), it is possible to represent each mode as a point on a plane surface whose axes are  $k_x$  and  $k_y$ , as shown in Fig. 6.5.<sup>7</sup> The separation requirement in Eq. (6.8) dictates that  $k^2 = (\omega/c)^2 = k_x^2 + k_y^2$ .

At any frequency,  $k^2$  is determined by the frequency and the speed,  $c$ , of transverse waves on the membrane. The separation requirement is equivalent to specifying the radius  $k = \sqrt{k_x^2 + k_y^2}$  of a circle

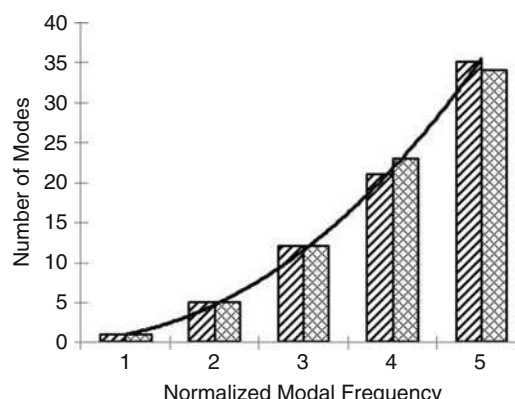
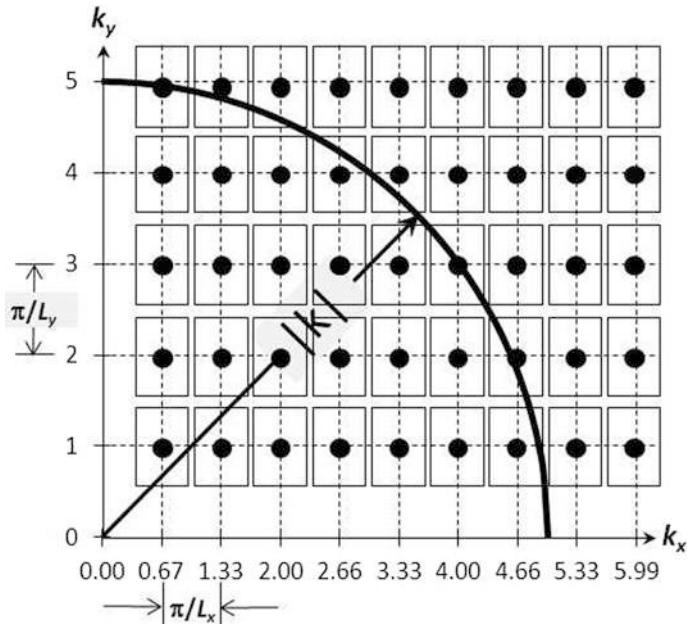


**Fig. 6.4** A histogram showing the number of modes with normalized frequencies,  $f_{m,n}/f_{1,1}$ , less than or equal to the number on the horizontal axis. The bars with diagonal lines are taken from the modes of the  $L_x = L_y\sqrt{2}$  membrane in Table 6.1 (left). The cross-hatched bars are for modes of the  $L_x = (3/2)L_y$  membrane within the same table (right). The solid line is proportional to the square of the normalized modal frequency

<sup>7</sup> This plotting strategy creates a “ $k$ -space,” also known as *reciprocal space*, although we are more familiar with a Cartesian coordinate system where the axes represent distance. In  $k$ -space, the axes have units of inverse length [ $m^{-1} \equiv \text{retem}$ ], and areas have units of [ $m^{-2}$ ]. If this bothers you, just multiply all the  $k$  values by  $(c/2\pi)$  so that the axes have units of frequency [Hz]. Of course, frequency [Hz] is the “reciprocal space” of time [s]. The  $k$ -space representation is commonly used in solid-state physics and crystallography to represent atomic lattices (the “reciprocal lattice”). The diffraction patterns created by the scattering of X-rays through a crystalline solid will project the  $k$ -space pattern on a screen. This can easily be observed by shining a laser through a fine-mesh woven screen. The resulting diffraction pattern, when projected on a screen normal to the laser beam, will generate a cross of bright dots. The farther the spacing between such dots, the finer the screen mesh, just as the circles representing the modes in Fig. 6.5 are more closely spaced in the  $k_y$  direction than the circles in the  $k_x$  direction.

**Fig. 6.5** Each black circle on this graph represents one mode of a rectangular membrane of length  $L_x$  and width  $L_y < L_x$ . The solid arc encloses one quadrant of a circle with radius  $|\vec{k}|$ . Each modal point is surrounded by a rectangle with unit reciprocal area,  $\forall_{unit} = \pi^2/L_x L_y$ . Those rectangles are shown slightly undersized to let them be distinguished from each other. Because there are no  $(m, 0)$  or  $(0, n)$  modes and no  $(0, 0)$  mode, the rectangles fill all of the space except for the two strips adjacent to the  $k_x$  and  $k_y$  axes



centered on the origin in the  $k_x - k_y$  plane, shown in Fig. 6.5. Since  $k$  is the distance from the origin of that Cartesian coordinate system to any pair of points  $(k_x, k_y)$ , any  $(k_x, k_y)$  pair inside that circle will be a mode with frequency less than or equal to  $\omega$ , and any  $(k_x, k_y)$  pair outside the circle will have a higher frequency than  $\omega$ .

We can associate a  $k$ -space rectangle of width,  $k_x = \pi/L_x$ , and height,  $k_y = \pi/L_y$ , with each point representing any single mode and designate the area of one such rectangle as the reciprocal area of a unit cell,  $\forall_{unit} = \pi^2/L_x L_y$ . Again, in  $k$ -space, this “reciprocal area,”  $\forall$ , has units of [ $\text{m}^{-2}$ ]. If we attach one unit cell to each mode by placing the center of the cell at the mode point, then we can fill all  $k$ -space with such cells except for the two strips of width,  $\pi/2L_x$  and  $\pi/2L_y$ , that are adjacent to the  $k_x$  and  $k_y$  axes.

The number of modes with frequencies less than or equal to  $\omega$  can be estimated by dividing the  $k$ -space area of one quadrant of a circle with radius,  $k$ ,  $\forall_k = (\pi/4)k^2$ , by the  $k$ -space area occupied by a single mode that we have designated  $\forall_{unit}$ . Because there are no  $(m, 0)$  or  $(0, n)$  modes and no  $(0, 0)$  mode, we should also exclude the areas of the two strips,  $\forall_{strip}$ , adjacent to the  $k_x$  and  $k_y$  axes from the area,  $\forall_k$ . To first approximation (neglecting the double counting of the area where the  $k_x$  and  $k_y$  axial strips overlap at the origin), the number of modes,  $N_{rect}(\omega)$ , with frequencies less than  $\omega$ , can be calculated by dividing those two areas.

$$N_{rect}(\omega_{m,n}) \cong \frac{\forall_k - \forall_{strip}}{\forall_{unit}} = \frac{\left(\frac{\pi}{4}\right)k_{m,n}^2 - \left(\frac{\pi}{2L_x} + \frac{\pi}{2L_y}\right)k_{m,n}}{\left(\frac{\pi}{L_x}\right)\left(\frac{\pi}{L_y}\right)} \\ = \frac{L_x L_y}{4\pi} k_{m,n}^2 - \frac{L_x + L_y}{2\pi} k_{m,n} = \frac{L_x L_y}{4\pi c^2} \omega_{m,n}^2 - \frac{L_x + L_y}{2\pi c} \omega_{m,n} \quad (6.15)$$

$$N_{rect}(f_{m,n}) \cong \frac{\pi L_x L_y}{c^2} f_{m,n}^2 - \frac{L_x + L_y}{c} f_{m,n} = \frac{\pi L_x L_y}{\lambda_{m,n}^2} - \frac{L_x + L_y}{\lambda_{m,n}}$$

At sufficiently high frequencies, so that  $k_x \gg \pi/L_x$  and  $k_y \gg \pi/L_y$ , the first term in the approximation of Eq. (6.15) becomes more accurate and demonstrates that the number of modes,  $N_{rect}(\omega)$ , below a given frequency,  $\omega$ , should increase almost like  $\omega^2$ , as was shown in Fig. 6.4 for both cases examined in Table 6.1.

We can compare the results of Eq. (6.15) to the exact mode counts in Table 6.1. There are 34 modes with normalized frequencies,  $f_{m,n}/f_{1,1} \leq 5$ , for  $L_x = 3L_y/2$  on the right-hand side of the table. For that case, Eq. (6.11) can be used to calculate the frequency of the (1, 1) mode,  $f_{1,1}$ , in terms of  $L_y$  and the speed of transverse waves,  $c$ .

$$f_{1,1} = \frac{c}{2} \sqrt{\left(\frac{4}{9}\right) \frac{1}{L_y^2} + \frac{1}{L_y^2}} = \frac{c}{L_y} \sqrt{\frac{13}{36}} \Rightarrow \frac{L_y^2}{c^2} = \frac{13}{36} \frac{1}{f_{1,1}^2} \quad (6.16)$$

These results can be substituted into Eq. (6.15) to calculate the number of modes with normalized frequencies,  $f = f_{m,n}/f_{1,1} \leq 5$ .

$$\begin{aligned} N_{rect}(f_{5,5}) &\cong \frac{3\pi L_y^2}{2c^2} f_{5,5}^2 - \frac{5L_y}{2c} f_{5,5} \Rightarrow \\ N_{rect}(f=5) &\cong \frac{3\pi}{2} \frac{13}{36} f^2 - \frac{5}{2} \sqrt{\frac{13}{36}} f = 35 \end{aligned} \quad (6.17)$$

That result is less than 3% larger than the exact result.

The approximation of Eq. (6.15) can be tested in a more rigorous way by a linearized least-squares fit (see Sect. 1.9.3) that plots the number of modes with frequencies less than or equal to  $f_{m,n}$ , divided by the frequency,  $N(f_{m,n})/f_{m,n}$ , against frequency.

$$\frac{N_{rect}(f_{m,n})}{f_{m,n}} \cong \frac{\pi L_x L_y}{c^2} f_{m,n} - \frac{L_x + L_y}{c} = mf_{m,n} + b \quad (6.18)$$

The data for  $L_x = L_y\sqrt{2}$ , taken from the left side of Table 6.1, is plotted against the normalized frequency,  $f = f_{m,n}/f_{1,1}$ , to produce the best-fit straight line in Fig. 6.6. The exact number of modes with  $f \leq 5$  is 35. Equation (6.15) gives  $N_{rect}(5) = 34.3$ , which is only a 2% difference.

The frequency difference between modes of adjacent frequencies is also decreasing with increasing frequency. The approximate number of modes,  $\Delta N$ , in a frequency interval,  $\Delta f$ , can be determined by differentiation of the expression in Eq. (6.15) for the number of modes,  $N(f_{m,n})$ , with frequencies less than  $f_{m,n}$ .

$$\begin{aligned} \frac{dN(f_{m,n})}{df_{m,n}} &= \frac{2\pi L_x L_y}{c^2} f_{m,n} - \frac{L_x + L_y}{c} \Rightarrow \\ \Delta N(f_{m,n}) &= \left( \frac{2\pi L_x L_y}{c^2} f_{m,n} - \frac{L_x + L_y}{c} \right) \Delta f \end{aligned} \quad (6.19)$$

The value of the derivative,  $dN/df_{m,n}$ , is called the *modal density*. It increases linearly with frequency in any bounded two-dimensional system. The density of modes for a one-dimensional string is a constant that is independent of frequency.

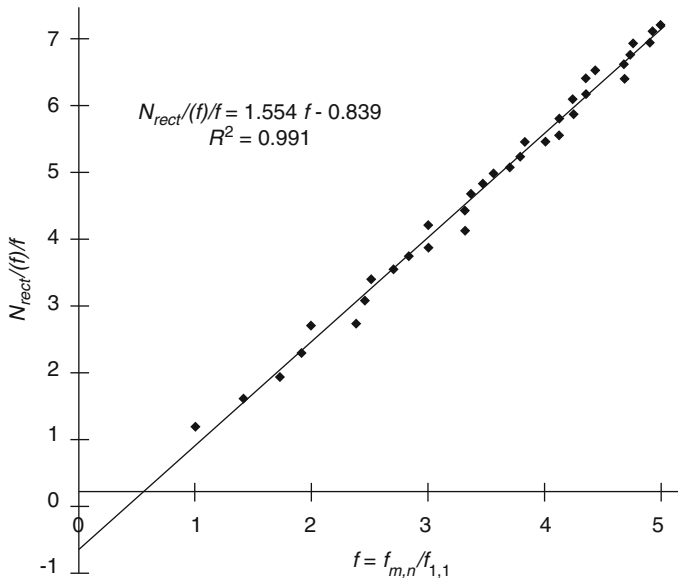


**Fig. 6.6** Plot of the number of modes with normalized frequencies,  $f = f_{m,n}/f_{1,1}$ , less than or equal to  $f$  divided by  $f$  vs.  $f$ . The best-fit straight line should be compared to the theoretical result in Eq. (6.18). Substitution of  $f = 5$  into the best-fit straight line gives  $N_{rect}(5) = 34.7$ , while the same substitution into Eq. (6.15) gives the result in Eq. (6.17):  $N_{rect}(5) = 34.3$ . The fit coefficients (i.e., slope and intercept) differ slightly from those in Eq. (6.18) because Table 6.1 data do not double-count the strip overlap

## 6.2 Circular Membranes

Rectangular membranes are rare due to the stresses at the corners that tend to rip the thin membrane material. Circular membranes are very common. Two ubiquitous examples are musical instruments (i.e., drums, banjos, and the *erhu*) and the microphones that are used to record and/or amplify their sounds. Although it is possible, in theory, to describe the transverse vibrations of a circular membrane using a Cartesian coordinate system, the specification of the fixed boundary condition for a circular membrane of radius,  $a$ , is difficult to execute when written as  $z(x^2+y^2=a^2, t)=0$  and then imposed on the wave equation in Cartesian coordinates. It is much easier to use a polar coordinate system, letting the boundary condition be expressed simply as  $z(a, \theta, t)=0$ . The price of this simplification is that we must now express the Laplacian operator in polar coordinates, as written in Eq. (6.4).

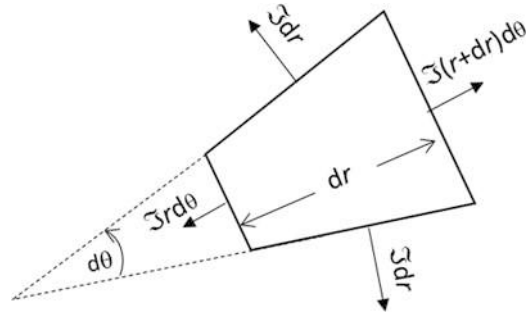
We started the derivation of the wave equation in rectangular coordinates by examination of a differential area element of the membrane,  $dA = dx dy$ , shown in Fig. 6.1, and expressed in Cartesian coordinates. We can now examine the forces acting on a differential area element,  $dA = dr (r d\theta)$ , of the membrane in polar coordinates using Fig. 6.7.

The net vertical force,  $F_{z,\theta}$ , due to tensions perpendicular to the radial direction, can be expanded in a Taylor series just as was done for the rectangular membrane element in Eq. (6.1).

$$F_{z,\theta} = \Im dr \left[ \left( \frac{1}{r} \frac{\partial z}{\partial \theta} \right)_{\theta+d\theta} - \left( \frac{1}{r} \frac{\partial z}{\partial \theta} \right)_\theta \right] = \frac{\Im}{r^2} \frac{\partial^2 z}{\partial \theta^2} r dr d\theta \quad (6.20)$$

The net force,  $F_{z,r}$ , along the radial direction receives similar treatment, again based on Fig. 6.7.

**Fig. 6.7** A differential area of membrane expressed in polar coordinates



$$F_{z,r} = \Im d\theta \left[ \left( r \frac{\partial z}{\partial r} \right)_{r+dr} - \left( r \frac{\partial z}{\partial r} \right)_r \right] = \frac{\Im}{r} \frac{\partial}{\partial r} \left( r \frac{\partial z}{\partial r} \right) r dr d\theta \quad (6.21)$$

The sum of the vertical forces can then be equated to the product of the vertical acceleration and the mass of the differential element, \$\rho\_S dA = \rho\_S (r d\theta) dr\$.

$$\frac{\partial^2 z}{\partial r^2} + \frac{1}{r} \frac{\partial z}{\partial r} + \frac{1}{r^2} \frac{\partial^2 z}{\partial \theta^2} = \nabla^2 z = \frac{1}{c^2} \frac{\partial^2 z}{\partial t^2} \quad (6.22)$$

Again, \$c^2 = \Im/\rho\_S\$ and the Laplacian, \$\nabla^2\$, are just that provided previously without justification in Eq. (6.4).

### 6.2.1 Series Solution to the Circular Wave Equation

We can separate Eq. (6.22) to convert it from a second-order partial differential equation into two ordinary differential equations while imposing harmonic time dependence: \$\mathbf{z}(r, \theta, t) = R(r)\Theta(\theta)e^{j\omega t}\$.

$$\Theta \frac{d^2 R}{dr^2} + \frac{\Theta}{r} \frac{dR}{dr} + \frac{R}{r^2} \frac{d^2 \Theta}{d\theta^2} + k^2 R \Theta = 0 \quad (6.23)$$

Multiplication by \$r^2/R\Theta\$ produces two independent ordinary differential equations coupled by \$k^2\$.

$$\frac{r^2}{R} \left( \frac{d^2 R}{dr^2} + \frac{1}{r} \frac{dR}{dr} \right) + k^2 r^2 = -\frac{1}{\Theta} \frac{d^2 \Theta}{d\theta^2} \quad (6.24)$$

Since the left-hand terms in Eq. (6.24) depend only upon \$r\$ and the right-hand term depends only on \$\theta\$, they must each separately be equal to a constant since the variations of \$r\$ and \$\theta\$ are independent of each other.

The angular dependence is easy to calculate, since it is just the solution to a simple harmonic oscillator equation.

$$\frac{d^2 \Theta}{d\theta^2} + m^2 \Theta = 0 \quad (6.25)$$

The two solutions to this differential equation will be written with curly brackets to remind us that those two solutions guarantee that every solution with \$m \neq 0\$ will be double-degenerate.

$$\Theta_m(\theta) = \begin{cases} \cos(m\theta) \\ \sin(m\theta) \end{cases} \quad (6.26)$$

Of course, any superposition of those two solutions is also a solution, since Eq. (6.24) is a linear differential equation.

For the solutions,  $\Theta_m(\theta)$ , to have physical significance, they must yield the same result if the azimuthal coordinate,  $\theta$ , is increased or decreased by integer multiples of  $2\pi$ , since that would bring us back to the same physical location on the membrane.

$$\Theta_m(\theta) = \Theta_m(\theta \pm 2n\pi) \quad \text{with } n = 0, 1, 2, 3, \dots \quad (6.27)$$

That restriction is known as a *periodic boundary condition*, and it is only satisfied if  $m$  is an integer or is zero.

The equation for the radial dependence of the transverse displacement can be generated by substitution of Eq. (6.25) into Eq. (6.24).

$$\frac{d^2R}{dr^2} + \frac{1}{r} \frac{dR}{dr} + \left( k^2 - \frac{m^2}{r^2} \right) R = 0 \quad (6.28)$$

It is important to recognize that this equation for the radial variation in the transverse vibrations of the membrane is unique for every choice of  $m$  made to satisfy the azimuthal variation given by Eq. (6.26) for  $\Theta_m(\theta)$ . Equation (6.28) actually represents an infinite number of second-order differential equations, each having two solutions for every integer value of  $m$ .

A solution to Eq. (6.28) can be generated by assuming a polynomial form,  $R_m(r) = a_0 + a_1r + a_2r^2 + a_3r^3 \dots$ , and then equating all coefficients of like powers of  $r$  that must individually sum to zero.<sup>8</sup> This will be demonstrated for only one such solution with  $m = 1$ .

$$\begin{aligned} R_1 &= a_0 &+ a_1r &+ a_2r^2 &+ a_3r^3 \\ -\frac{R_1}{r^2} &= -\frac{a_0}{r^2} &- \frac{a_1}{r} &- a_2 &- a_3r &- a_4r^2 &+ a_5r^3 \\ +\frac{1}{r} \frac{dR_1}{dr} &= \frac{a_1}{r} &+ 2a_2 &+ 3a_3r &+ 4a_3r^2 &+ 5a_4r^3 \\ +\frac{d^2R_1}{dr^2} &= &2a_2 &+ 6a_3r &+ 12a_4r^2 &+ 20a_5r^3 \end{aligned} \quad (6.29)$$

Equating the sums of like powers to zero will allow all of the polynomial's coefficients to be expressed in terms of  $a_1$ , which can only be determined once the initial conditions have been specified.

$$\begin{aligned} a_0 &= 0, & a_2 &= -\frac{a_0}{3} = 0, & a_3 &= -\frac{a_1}{8}, & a_4 &= 0 \\ a_5 &= -\frac{a_3}{24} = \frac{a_1}{8(24)}, & a_6 &= 0, & a_7 &= \frac{a_1}{16(24)(24)}, & \text{etc.} \end{aligned} \quad (6.30)$$

Clearly,  $R_1(r)$  is an odd function of  $r$  since all  $a_{2n} = 0$  for  $n = 0, 1, 2, 3, \dots$ . Substitution back into the polynomial provides a power series solution for the radial part of the solution to Eq. (6.28) when  $m = 1$ .

---

<sup>8</sup> Mathematicians know this as the Frobenius method named after German mathematician Ferdinand Georg Frobenius (1849–1917).

$$R_1(r) = \frac{a_1}{2} \left( r - \frac{2r^3}{4^2} + \frac{3r^5}{4^2 6^2} - \frac{4r^7}{4^2 6^2 8^2} + \dots \right) \quad (6.31)$$

Although this result may appear unfamiliar, it is only because we do not usually think of trigonometric functions as power series solutions to the differential equations that generated them. In fact, as shown in Eqs. (1.5 and 1.6), both sine and cosine functions can be represented by a power series. We routinely refer to those trigonometric power series solutions by their functional names (sine and cosine), and we regularly employ algebraic relationships that allow us to determine their derivatives, integrals, magnitude, and values of their arguments for maxima and minima of those functions, multiple angle formulæ, etc.

The same is true for the power series solutions to Eq. (6.28). Those equations (one for each integer value of  $m$ ) are known as Bessel's equations, and their solutions are known as *Bessel functions* that we will abbreviate as  $J_m(k_{m,n}r)$ .<sup>9</sup> The subscript “ $m$ ” on  $J_m$  refers to the corresponding variation in the azimuthal function,  $\Theta_m(\theta)$ ; hence each radial solution is tied to the azimuthal variation through the product,  $J_m(k_{m,n}r)\Theta_m(\theta)$ , to produce the complete solution to Eq. (6.22).

$$\mathbf{z}_{m,n}(r, \theta, t) = \hat{\mathbf{C}}_{m,n} J_m(k_{m,n}r) \begin{Bmatrix} \cos(m\theta) \\ \sin(m\theta) \end{Bmatrix} e^{j\omega_{m,n}t} \quad (6.32)$$

Each solution is specified by two indices:  $m$  indicates the azimuthal variations, and  $n$  designates the successive zero-crossings of the Bessel function. For example, the  $(0, 1)$  mode will have no azimuthal variation, and the normal mode frequency,  $f_{0,1}$ , will correspond to the first zero-crossing of the  $J_0$  Bessel function. A  $(1,2)$  mode will have a single nodal diameter, although its orientation will be arbitrary, due to the superposition of the  $\cos(\theta)$  and  $\sin(\theta)$ , until something breaks the azimuthal symmetry, such as a perturbation in the membrane's mass or the position of a driving force applied over a non-zero area. It also requires that the frequency of that mode,  $f_{1,2}$ , will be determined by the second zero-crossing of the  $J_1$  Bessel function, excluding the zero at the origin.

Figure 6.8 provides a graph of the first three Bessel functions of integer order:  $m = 0$ ,  $m = 1$ , and  $m = 2$ . More complete graphs for additional values of  $m$  and other useful functions are available in Junke and Emde [1]. The Bessel functions in Fig. 6.8 look similar to cosine and sine functions, although there are obvious differences. The first difference is that the Bessel functions are only plotted for positive values of their arguments  $x \geq 0$ ; a radial location that is along the negative  $x$  axis is represented in polar coordinates as a positive  $r$  with  $\theta = 180^\circ$ .

The  $m = 0$  Bessel function,  $J_0(x)$ , looks a bit like  $\cos(x)$ . It approaches the origin with a value of one and a slope of zero. On the other hand, the envelope of the amplitudes of the oscillations in  $J_0(x)$  has progressively smaller values. There is also a similarity between  $J_1(x)$  and  $\sin(x)$ . The amplitudes of both are zero at the origin, and their initial slopes near the origin are both linear, although  $[d\sin(x)/dx]_{x=0} = 1$  and  $[dJ_1(x)/dx]_{x=0} = \frac{1}{2}$ . Again, like  $J_0(x)$ , the amplitude envelope of  $J_1(x)$  also is decreasing with increasing argument. The similarity of  $J_2(x)$  and  $\sin(x)$  is like that of  $J_1(x)$  except the

<sup>9</sup>German astronomer F. W. Bessel (1784–1846) first achieved fame by computing the orbit of Halley's comet. In addition to many other accomplishments in connection with his studies of planetary motion, he is credited with deriving the differential equation bearing his name and carrying out the first systematic study of the general properties of its solutions (now called *Bessel functions*) in his famous 1824 memoir.

Nonetheless, Bessel functions were first discovered in 1732 by D. Bernoulli (1700–1782), who provided a series solution for the oscillatory displacements of a heavy hanging chain (see Sect. 3.4.3). Euler (1707–1783) later developed a series similar to that of Bernoulli, which was also a Bessel function, and Bessel's equation appeared in a 1764 article by Euler dealing with the vibrations of the circular drumhead. Fourier (1768–1836) also used Bessel functions in his classical treatise on heat in 1822, but it was Bessel who first recognized and documented their special properties.

**Fig. 6.8** Bessel functions  $J_0(x)$ ,  $J_1(x)$ , and  $J_2(x)$  are plotted for  $0 \leq x \leq 15$ .  $J_0(x)$  resembles  $\cos(x)$ , except that the amplitude decreases with  $x$ .  $J_1(x)$  resembles  $\sin(x)$  with an initially linear slope for  $x < 1$  but again with decreasing amplitude.  $J_2(x)$  also resembles  $\sin(x)$  with decreasing amplitude but with an initially quadratic slope for  $x < 1$

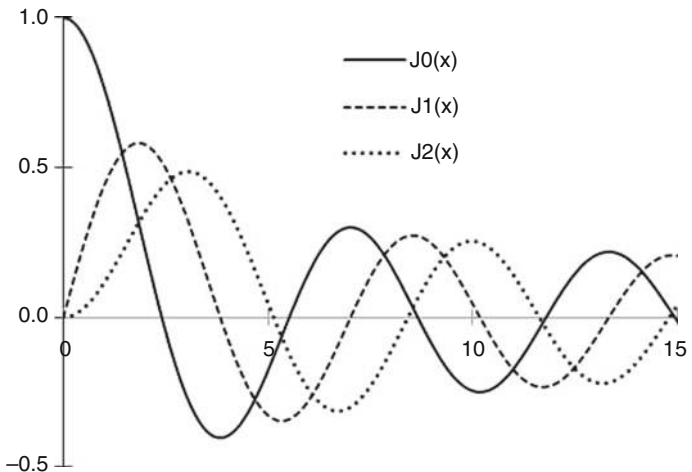
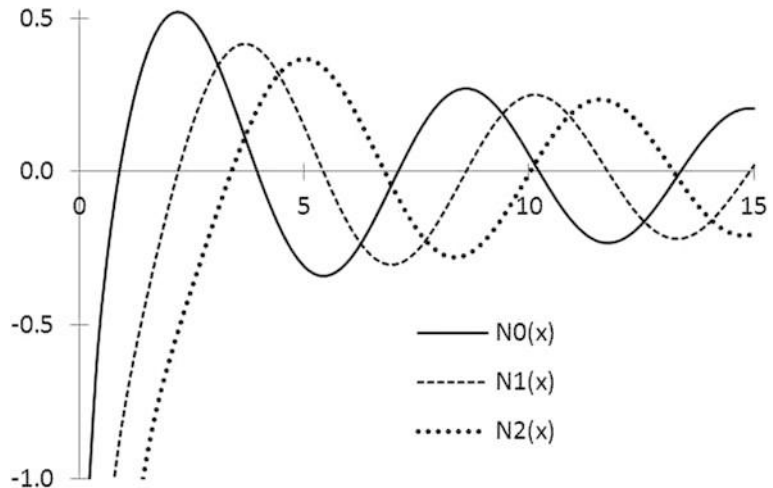


**Fig. 6.9** Neumann functions  $N_0(x)$ ,  $N_1(x)$ , and  $N_2(x)$ , are plotted for  $0 \leq x \leq 15$ . All Neumann functions diverge to  $-\infty$  in the limit that  $x$  goes to zero



initial slope,  $[dJ_2(x)/dx]_{x=0} \propto x^2$ . In fact, the initial slopes of all subsequent  $J_m(x)$  are proportional to  $x$  raised to the  $m$ :  $[dJ_m(x)/dx]_{x=0} \propto x^m$ . Many useful properties of Bessel functions are provided in Appendix C and in standard mathematical reference books [2].

Bessel's equations are all second-order differential equations, a different equation for each integer value of  $m$  in Eq. (6.28). As such, there must be two independent solutions for each value of  $m$ . The second infinite set of solutions, for various values of  $m$ , is known as the *Neumann functions*,  $N_m(x)$ . The first three Neumann functions, for  $m = 0$ ,  $m = 1$ , and  $m = 2$ , are plotted in Fig. 6.9. All Neumann functions go to negative infinity as  $x$  approaches zero:  $N_m(0) = -\infty$ , although they do so with different functional forms (e.g., logarithmically or with an inverse power function of their argument). We therefore reject the Neumann solutions for our description of the transverse vibrations of circular membranes since the displacement at the membrane's center is never infinite.

As presented in Sect. 6.2.3, the Neumann functions,  $N_m(x)$ , are required to match the second boundary condition for an annular membrane with outer radius,  $a_{out}$ , and inner radius,  $a_{in}$ . For an annulus,  $a_{in} > 0$ , so the divergent portion of the Neumann functions do not occur in the region where the membrane exists.

## 6.2.2 Modal Frequencies and Density for a Circular Membrane

The values of  $k_{m,n}$  are quantized by the imposition of the radial boundary condition  $z_{m,n}(a, \theta, t) = 0$  at  $r = a$ . This boundary condition will be satisfied by locating the arguments,  $x_n = k_{m,n}a$ , of  $J_m(x_n)$  that are the zero-crossing for  $J_m(x_n)$ . We do this without much thought for sine and cosine functions since their zero-crossings at  $x_n$  are periodic. This is not true for Bessel functions, as their zero-crossings do not have equal spacing, although the spacing becomes more equal as  $x$  increases. The values at which a Bessel function is zero is commonly designated  $j_{m,n}$ , so  $J_m(j_{m,n}) = 0$ . Appendix C includes a table of  $j_{m,n}$  zero-crossings. A more complete compilation is provided in Table 9.5 of Abramowitz and Stegun [2].

The normal mode frequencies,  $\omega_{m,n}$ , are related to the speed of transverse waves,  $c$ , and the radius,  $a$ , of the membrane through the wavenumber,  $k_{m,n}$ .

$$k_{m,n}a = \frac{\omega_{m,n}a}{c} = \frac{2\pi f_{m,n}a}{c} = j_{m,n} \quad \Rightarrow \quad f_{m,n} = \frac{j_{m,n}c}{2\pi a} \quad (6.33)$$

The mode shapes corresponding to these normal mode frequencies for a few low-order modes are sketched in Fig. 6.10 along with the corresponding values of  $j_{m,n} = k_{m,n}a$  and the ratio of the modal frequency,  $f_{m,n}$ , to the frequency of the lowest pure radial mode,  $f_{0,1} \cong (2.40483/2\pi)(c/a) = 0.38274(c/a)$ .

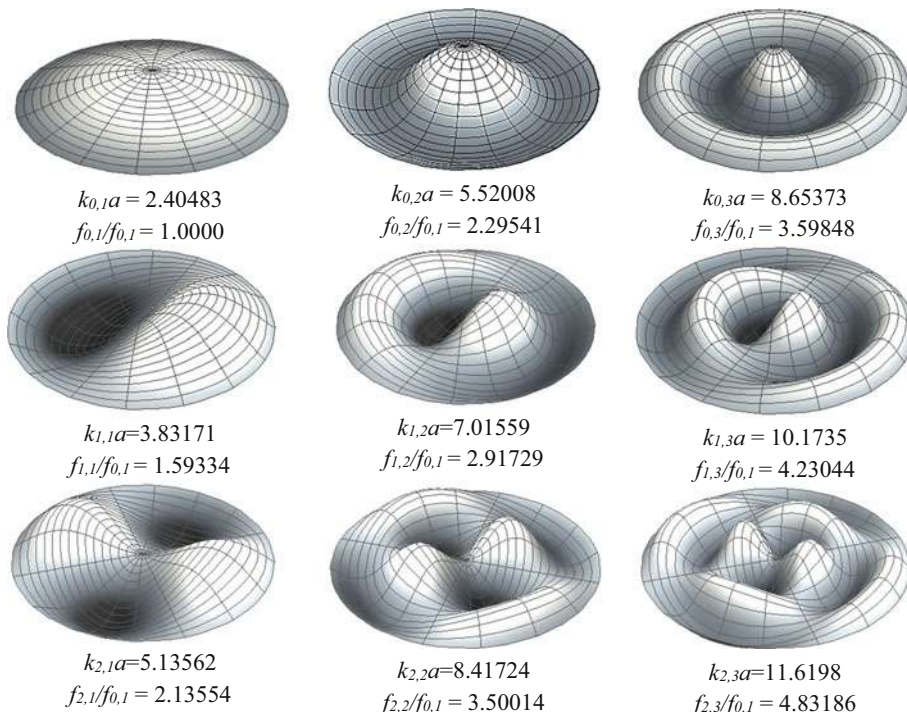


**Fig. 6.10** Greatly exaggerated mode shapes for a circular membrane with radius,  $a$ . The top row contains the first “pure radial”  $J_0$  modes:  $(0, 1)$ ,  $(0, 2)$ , and  $(0, 3)$ . The middle row shows the first three  $J_1$  modes, each with a single nodal diameter:  $(1, 1)$ ,  $(1, 2)$ , and  $(3, 1)$ . The bottom row has the first three  $J_2$  modes with two perpendicular nodal diameters:  $(2, 1)$ ,  $(2, 2)$ , and  $(2, 3)$ . Beneath each mode shape is their corresponding value of  $j_{m,n} = k_{m,n}a$  and the ratio of the mode frequency,  $f_{m,n}$ , to the fundamental radial mode,  $f_{0,1}$ . [Mode illustrations courtesy of Daniel Russell]

**Table 6.2** Normal mode frequencies less than or equal to 5.131  $f_{0,1}$  for a circular membrane are arranged in order of increasing frequency

#	$m,n$	$j_{m,n}$	$f_{m,n}/f_{0,1}$	#	$m,n$	$j_{m,n}$	$f_{m,n}/f_{0,1}$
1	0,1	2.40482	1.00000	18	3,2	9.76102	4.05893
2	1,1	3.83171	1.59334	19	6,1	9.93611	4.13174
3	1,1	3.83171	1.59334	20	6,1	9.93611	4.13174
4	2,1	5.13562	2.13555	21	1,3	10.1735	4.23044
5	2,1	5.13562	2.13555	22	1,3	10.1735	4.23044
6	0,2	5.52007	2.29541	23	4,2	11.0647	4.60104
7	3,1	6.38016	2.65307	24	4,2	11.0647	4.60104
8	3,1	6.38016	2.65307	25	7,1	11.0864	4.61005
9	1,2	7.01559	2.91730	26	7,1	11.0864	4.61005
10	1,2	7.01559	2.91730	27	2,3	11.6198	4.83188
11	4,1	7.58834	3.15546	28	2,3	11.6198	4.83188
12	4,1	7.58834	3.15546	29	0,4	11.7915	4.90328
13	2,2	8.41724	3.50015	30	8,1	12.2251	5.08357
14	0,3	8.65372	3.59848	31	8,1	12.2251	5.08357
15	5,1	8.77148	3.64745	32	5,2	12.3386	5.13077
16	5,1	8.77148	3.64745	33	5,2	12.3386	5.13077
17	3,2	9.76102	4.05893				

The frequencies are reported as the ratio of the modal frequency,  $f_{m,n}$ , to the frequency of the fundamental “pure radial” mode:  $f_{m,n}/f_{0,1}$ . Because the orientation of the nodal diameters for the  $m \neq 0$  modes is arbitrary, all  $(m, n)$  modes with  $m \neq 0$  are double-degenerate; thus they appear twice in this table

The lowest-frequency modes are listed in order of increasing frequency in Table 6.2 for  $f_{m,n}/f_{0,1} < 5.131$ . As seen with the rectangular membranes of Table 6.1, the number of modes within a fixed frequency interval,  $\Delta f$ , increases with increasing frequency. Rather than attempt to derive the number of modes,  $N_{circ}(f_{m,n})$ , with frequencies less than  $f_{m,n}$  for a circular membrane, as we did in Sect. 6.1.3, we can attempt to mimic the geometrical factors in Eq. (6.15) by substituting for membrane’s area,  $L_x L_y = \pi a^2$ , and half the membrane’s perimeter,  $L_x + L_y = \pi a$ .

$$N_{circ}(f_{m,n}) \cong \left( \frac{\pi a f_{m,n}}{c} \right)^2 - \frac{\pi a f_{m,n}}{c} \quad (6.34)$$

This can be expressed in terms of the normalized frequency ratio,  $f = f_{m,n}/f_{0,1}$ , since Eq. (6.33) gives  $(a/c) = (j_{0,1}/2\pi)(f_{m,n}/f_{0,1})$ .

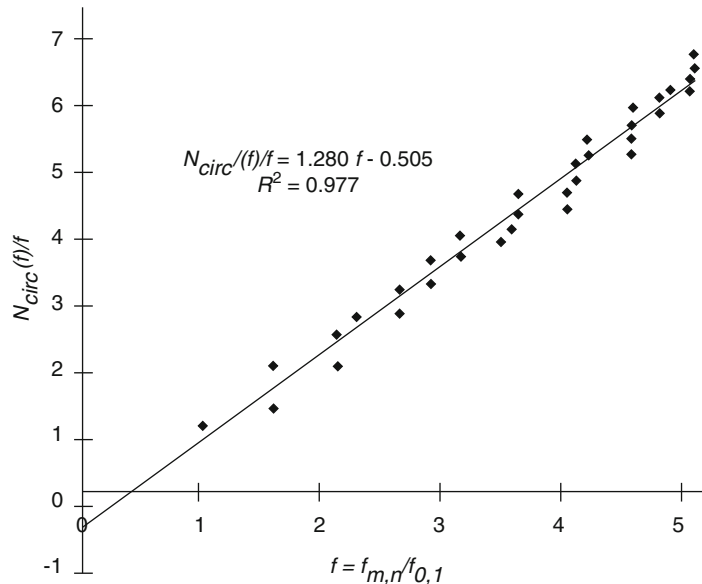
$$N_{circ}(f) \cong \frac{j_{0,1}^2}{4} \left( \frac{f_{m,n}}{f_{0,1}} \right)^2 - \frac{j_{0,1}}{2} \frac{f_{m,n}}{f_{0,1}} \cong 1.446 \left( \frac{f_{m,n}}{f_{0,1}} \right)^2 - 1.202 \frac{f_{m,n}}{f_{0,1}} \quad (6.35)$$

$N_{circ}(f = 5.131) = 32$ . This is in reasonable agreement with the 33 modes in Table 6.2 below that frequency ratio. A plot of  $N_{circ}(f)/f$  vs.  $f$ , similar to that in Fig. 6.6, is provided in Fig. 6.11 for the data in Table 6.2.

### 6.2.3 Mode Similarities Illustrating Adiabatic Invariance

We arrived at the results for the normal mode frequencies of rectangular and circular membranes by slightly different routes; in one case, we used solutions that were combinations of sine functions, and for the other case, we used combinations of trigonometric functions with integer-order Bessel

**Fig. 6.11** Plot of the number of modes with normalized frequencies,  $f = f_{m,n}/f_{0,1}$ , less than or equal to  $f$  divided by  $f$  vs.  $f$ . The best-fit straight line should be compared to the theoretical result in Eq. (6.35). Substitution of  $f = 5.131$  into the best-fit straight line gives  $N_{circ}(5.131) = 31.1$ , while the same substitution into Eq. (6.35) gives  $N_{circ}(5.131) = 32$ . The fit coefficients (slope and intercept) differ slightly from those in Eq. (6.35) because the Table 6.2 data do not double-count the strip overlap in Fig. 6.5



functions. The caption for Fig. 6.8 comments on the similarity of the integer-order Bessel functions and sine and cosine functions. Comparisons between Figs. 6.2 and 6.10 show similarities in the distribution of nodal lines that are characteristic of individual modes.

In Sect. 2.3.4, the concept of adiabatic invariance was used to demonstrate that frequency shifts,  $\delta f$ , were related to changes in the energy,  $\delta E$ , due to work being done on or work done by a vibrating system. The ratio of the frequency of a mode and the energy in that mode was a conserved quantity,  $E/f = \text{constant}$ , if the mode shape did not “hop” to another mode shape during the change [3]. We can use adiabatic invariance to examine our results for square and circular membranes by recognizing that the work done by making a deformation of the boundary could be nearly zero if the area remains unchanged.

The work we do on the mode by pushing the boundary inward and the work done by the mode when we let the vibration push the boundary outward should be nearly equal if the areas of the two membranes are equal. If we conserve that area of the square, with  $L_x = L_y$ , then the radius of the circle will be  $a = L_x/\sqrt{\pi}$ . The net work performed by pushing and pulling during that transformation, if the deformation is sufficiently slow that no additional modes are excited, will be nearly zero.

That assumption is applied to four modes with similar mode shapes in Table 6.3. The agreement between the two modal frequencies of similar mode shape is quantified by taking the difference in the modal frequencies and dividing by their average,  $\Delta f/\bar{f}$ . For the three modes with similar nodal line structures and symmetries, the agreement is always better than  $\pm 3\%$ . The agreement between the two modes that have an equal number of in- and out-of-phase segments is only about  $\pm 7\%$  since the  $f_{4,3}$  mode of the square does not share the same symmetry as the nearly equivalent circular  $f_{2,3}$  mode.

This comparison should be instructive in three ways: (i) Similar mode shapes lead to similar normal mode frequencies, even if the derivations of those frequencies are quite distinct. (ii) The agreement between the frequencies should give us confidence that both calculations were correct. (iii) Most importantly, application of adiabatic invariance can provide a tool to analyze modes of membranes (and as we will see in later chapters, also standing sound waves in three-dimensional enclosures and waveguides) that do not have boundaries that allow exact solution by the technique known as separation of variables.

**Table 6.3** The square membranes and the circular membranes have equal areas, so the radius of the circle is  $a = L_x/\sqrt{\pi}$ 

Square	Adiabatic transformation	Circle	$\Delta f/f$
$f_{1,1} = \frac{c}{\sqrt{2}L_x}$ $f_{1,1} = 0.707 \frac{c}{L_x}$		$f_{0,1} = \frac{j_{0,1}c}{2\sqrt{\pi}L_x}$ $f_{0,1} = 0.678 \frac{c}{L_x}$	-4.2%
$f_{1,2} = \frac{c\sqrt{5}}{2L_x}$ $f_{1,2} = 1.118 \frac{c}{L_x}$		$f_{1,1} = \frac{j_{1,1}c}{2\sqrt{\pi}L_x}$ $f_{1,1} = 1.081 \frac{c}{L_x}$	-3.4%
$f_{2,2} = \frac{c\sqrt{2}}{L_x}$ $f_{2,2} = 1.414 \frac{c}{L_x}$		$f_{2,1} = \frac{j_{2,1}c}{2\sqrt{\pi}L_x}$ $f_{2,1} = 1.449 \frac{c}{L_x}$	+2.4%
$f_{4,3} = \frac{5c}{2L_x}$ $f_{4,3} = 2.500 \frac{c}{L_x}$		$f_{2,3} = \frac{j_{2,3}c}{2\sqrt{\pi}L_x}$ $f_{2,3} = 2.870 \frac{c}{L_x}$	+13.8%

Adiabatic invariance suggests that the frequencies of the modes should be equal if the mode shapes are not too distorted by the transformation and the membrane's area is unchanged. Although the  $f_{4,3}$  for the square and  $f_{2,3}$  for the circle both have 12 regions vibrating in- and out-of-phase, the two membrane do not share the same symmetry

In the twenty-first century, modes of objects that do not lend themselves to analysis by separation of variables are usually treated by numerical techniques such as finite element or boundary element simulations. Although those numerical techniques are very useful and powerful, they can also produce results that are either incorrect or hard to interpret. It is always a good idea to approximate a non-separable geometry by one for which analytical results can be obtained, as we did with rectangular and circular membranes, so that mode shapes and normal mode frequencies can be compared to the numerical results. As we have demonstrated, that approach can produce results with accuracies down to the few percent level while, more importantly, providing a classification system for the modes of the non-separable geometry.

#### 6.2.4 Normal Modes of Wedges and Annular Membranes\*

The fact that a fixed boundary and a nodal line, or a nodal circle, has exactly the same influence on the solutions to the modal structure of a two-dimensional membrane means that it is possible to calculate exact, or near exact, normal mode frequencies for shapes that are not separable in any available coordinate system. This will be illustrated by an approximate calculation of the modal frequencies of a membrane that has a boundary fixed by an equilateral triangle.

To approximate an equilateral triangle, we can consider one-sixth of hexagonal membrane and then adiabatically transform the hexagon into a circular membrane vibrating in an  $m = 3$  mode, as shown in Fig. 6.12. To preserve the areas of the two figures,  $a^2 = (3\sqrt{3}/2\pi) b^2$  or  $a = b \sqrt[4]{27/4\pi^2} = 0.909b$ .

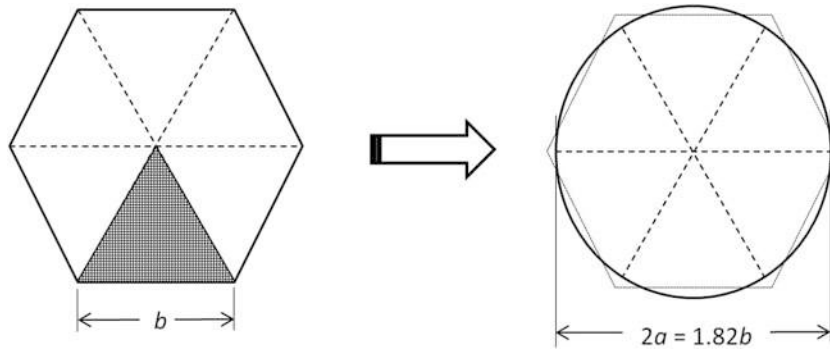


**Fig. 6.12** The normal mode frequencies of the equilateral triangular membrane, shown at the left as one-sixth of a regular hexagon, can be approximated by the  $m = 3$  normal mode frequencies of the circular membrane shown at the right. The two figures have equal areas. Higher-frequency modes of the triangular membrane can be approximated from the  $m = 3i$  modes, where  $i = 1, 2, 3, \dots$ . All  $m = 3i$  modes have nodal diameters that coincide with two of the fixed boundaries of the equilateral triangle.

**Table 6.4** Approximate normal mode frequencies of the equilateral triangular membrane, in order of increasing frequency, approximated by imposing adiabatic invariance and treating the triangle as a  $60^\circ$  wedge of a circular membrane of area equal to the hexagon in Fig. 6.12. To maintain the triangular boundary condition, only  $m = 3i$  modes can be used where  $i = 1, 2, 3, \dots$

$m$	$n$	$j_{m,n}$	$f_{m,n}/f_{3,1}$
3	1	6.380	1.000
3	2	9.761	1.530
6	1	9.936	1.557
3	3	13.015	2.040
9	1	13.354	2.093
6	2	13.589	2.130
3	4	16.223	2.543
12	1	16.698	2.617
6	3	17.004	2.665
9	2	17.241	2.702

Based on Eq. (6.33), the lowest-frequency normal mode would correspond to the  $j_{3,1}$  zero-crossing of the  $J_3$  Bessel function.

$$f_{3,1} \cong \frac{j_{3,1} c}{2\pi a} = \frac{6.38}{1.82\pi} \left( \frac{c}{b} \right) = 1.12 \left( \frac{c}{b} \right) \quad (6.36)$$

As mentioned in Sect. 6.2.1, the solution for the normal modes of an annular membrane requires superposition of the Bessel and the Neumann functions to match the fixed boundary conditions at the outer and inner radii:  $z(a_{out}, \theta, t) = z(a_{in}, \theta, t) = 0$ . Again, sometimes an approximate solution can be found if the ratio of the radii is nearly equal to the ratio of two zero-crossings of the same Bessel function. If  $a_{out}/a_{in}$  has the same ratio of two zero-crossings of some Bessel function, then the nodal circles for those modes can be considered to coincide with the inner and outer radii of the annular membrane.

If we consider an annular membrane with  $a_{out} = 12.0$  cm and  $a_{in} = 10.0$  cm, corresponding to an annulus that is 2.0 cm wide, then  $a_{out}/a_{in} = 1.20$ . The average of the three adjacent zero-crossings for the three modal combinations in Eq. (6.37) has a ratio of  $1.202 \pm 0.012$ .

$$\frac{j_{0,6}}{j_{0,5}} = 1.210; \quad \frac{j_{1,6}}{j_{1,5}} = 1.191; \quad \frac{j_{2,5}}{j_{2,4}} = 1.214 \quad (6.37)$$

To a rather good approximation, there would be three modes that satisfy the inner and outer boundary conditions.

$$\begin{aligned} f_{2,5} &= \frac{j_{2,5}}{2\pi} \left( \frac{c}{a_{out}} \right) = \frac{17.96}{2\pi} \left( \frac{c}{a_{out}} \right) = 2.858 \left( \frac{c}{a_{out}} \right) \\ f_{0,6} &= \frac{j_{0,6}}{2\pi} \left( \frac{c}{a_{out}} \right) = \frac{18.071}{2\pi} \left( \frac{c}{a_{out}} \right) = 2.876 \left( \frac{c}{a_{out}} \right) \\ f_{1,6} &= \frac{j_{1,6}}{2\pi} \left( \frac{c}{a_{out}} \right) = \frac{19.616}{2\pi} \left( \frac{c}{a_{out}} \right) = 3.122 \left( \frac{c}{a_{out}} \right) \end{aligned} \quad (6.38)$$

The mode corresponding to  $j_{0,6}$  for a circular membrane would have no nodal radii, the mode corresponding to  $j_{1,6}$  would have two nodal radii separated by  $180^\circ$ , and the  $j_{2,5}$  mode would have four nodal radii separated by  $90^\circ$ . Although this is neither a complete nor an exact solution, it is sufficient to provide a good indication of what normal mode frequencies should be observed for this particular annular membrane.

### 6.2.5 Effective Piston Area for a Vibrating Membrane

In Sect. 12.8, we will see that the energy radiated by a vibrating rigid circular piston of radius,  $a$ , which is in contact with a fluid, depends only upon the product of the piston's normal velocity and its area, if the circumference of the piston is less than the wavelength of the sound in the fluid:  $2\pi a/\lambda_{fluid} = k_{fluid} a \lesssim 1$ . The restriction that  $k_{fluid} a \lesssim 1$  is called the *compactness criterion*. Under such circumstances, it will be convenient to define a *volume velocity*, with units [ $\text{m}^3/\text{s}$ ]:  $U(t) = \Re e[\hat{\mathbf{U}} e^{j\omega t}] = \Re e[A_{piston} \hat{\mathbf{x}}(t)] = \Re e[A_{piston} \omega \hat{\mathbf{x}} e^{j\omega t}]$ . In fact, it is only the volume velocity that matters in such cases; the shape of the piston or the fact that different parts of the piston are moving with different amplitudes is irrelevant for a compact sound source,<sup>10</sup> as long as all parts of the radiating surface are moving at a single frequency,  $\omega$ .

Since the amplitude of the normal mode vibrations of a membrane depends upon position on its surface, it is convenient to define an effective piston area,  $A_{eff}$ . For a rectangular diaphragm with fixed boundary conditions along the rim, it is easy to integrate over the surface, since there is no membrane motion at the limits of integration.

$$A_{eff} = \iint_S \sin \left( \frac{m\pi x}{L_x} \right) \sin \left( \frac{n\pi y}{L_y} \right) dx dy = \frac{L_x L_y}{2} \quad \text{if } m = n = 1 \quad (6.39)$$

The effective piston area is only non-zero when both  $m$  and  $n$  are odd integers. If either  $m$  or  $n$  are even, one half of the diaphragm's area will be moving out-of-phase with the other half and will therefore produce no net volume velocity.

---

<sup>10</sup> There will be sound, of far smaller amplitude, radiated even if the net volume velocity is zero because the positively and negatively phased portions of the diaphragm's motion are offset from each other. This results in higher-order radiation process (e.g., dipole, quadrupole, etc.) that is far less efficient radiators and is discussed in Sect. 12.4.

This effective area can be used to calculate an average (effective) displacement amplitude,  $\langle z \rangle_{eff}$ , corresponding to the motion of a rigid surface with the same surface area as the diaphragm. This effective displacement would produce the same volume velocity as the actual surface that has a unit maximum displacement amplitude,  $z_{max} = 1$ .

$$\frac{\langle z \rangle_{eff}}{z_{max}} = \frac{A_{eff}}{A} = \frac{\frac{1}{2}L_x L_y}{L_x L_y} = \frac{1}{2} \quad \text{if } m = n = 1 \quad (6.40)$$

We can repeat these calculations for a circular membrane. Since the effective area will again be zero for any mode where  $m \neq 0$ , due to the exact cancellation of in-phase and out-of-phase motion across nodal diameters, the integral need only be performed for the purely radial (azimuthally constant)  $J_0(k_{0,n}r)$  modes.

$$A_{eff} = \iint_S J_o(k_{0,n}r) dS = \int_0^a J_o(k_{0,n}r) 2\pi r dr \quad (6.41)$$

That integral can be evaluated by use of one of the relations for Bessel functions of the first kind provided in Appendix C.

$$\int x J_0(x) dx = x J_1(x) \quad (6.42)$$

Letting  $x = k_{0,n}r$ ,  $r = x/k_{0,n}$ , and  $dr = dx/k_{0,n}$ , Eq. (6.42) can be used to solve Eq. (6.41).

$$A_{eff} = \frac{1}{k_{0,n}^2} \int_0^{ak_{0,n}} J_0(x) 2\pi x dx = 2\pi \frac{ak_{0,n}}{k_{0,n}^2} J_1(k_{0,n}a) = 2\pi a^2 \frac{J_1(k_{0,n}a)}{k_{0,n}a} \quad (6.43)$$

For the fundamental radial mode,  $k_{0,1}a \cong 2.4048$ . The value of  $J_1(2.4048) = 0.51915$  could have been evaluated from the series expansion in Eq. (C.5), interpolated from tables like those in Abramowitz and Stegun [2], or provided from most mathematical or spreadsheet software packages, which is how I produced the result.

$$\frac{\langle z \rangle_{eff}}{z_{max}} = \frac{A_{eff}}{\pi a^2} = 2 \frac{J_1(k_{0,1}a)}{k_{0,1}a} \cong \frac{2 \cdot 0.51915}{2.4048} = 0.432 \quad (6.44)$$

Table 6.5 provides the effective piston areas for the first four radial modes. Any mode with  $m > 0$  will have no net piston area.<sup>10</sup> As expected, the effective areas become successively smaller for the higher-order radial modes because of the cancellation produced by adjacent regions bordered by the nodal circles that move out-of-phase with each other.

**Table 6.5** Effective piston area for the four lowest-frequency purely radial normal modes of a circular membrane based on Eq. (6.43)

Mode	$k_{0,n}a$	$J_1(k_{0,n}a)$	$A_{eff}/\pi a^2$
0,1	2.40482	0.519149	0.43176
0,2	5.52008	-0.34026	-0.12328
0,3	8.65373	0.271446	0.06274
0,4	11.79153	-0.23246	-0.03943

Negative values indicate that the net volume velocity is opposite to the velocity of the membrane's center

## 6.2.6 Normal Mode Frequencies of Tympani

If a diaphragm is stretched over a gas-filled, sealed volume,  $V_o$ , as it is for a kettledrum (tympani) or a condenser microphone (see Sect. 6.3), then the stiffness of the gas behind the diaphragm provides an additional restoring force. This is similar to the effect that inclusion of the flexural rigidity of a string, calculated in Sect. 5.5, had on the normal mode frequencies of a string that was previously assumed to be limp.

If we assume that the compressions and expansions of the gas trapped behind the diaphragm occur adiabatically,<sup>11</sup> so that  $pV^\gamma = \text{constant}$ , with *polytropic coefficient* for an ideal gas,  $\gamma = c_p/c_V$ , then the excess pressure,  $\delta p$ , behind the diaphragm will be related to the change in volume,  $\delta V = A_{\text{eff}} z_{\text{max}}$ , caused by the diaphragm's displacement. Logarithmic differentiation of the Adiabatic Gas Law (see Sect. 1.1.3) relates the changes in volume to the changes in pressure.

$$pV^\gamma = \text{constant} \Rightarrow \ln p + \gamma \ln V = \ln(\text{constant}) \Rightarrow \frac{\delta p}{p_m} = -\gamma \frac{\delta V}{V_o} \quad (6.45)$$

When the diaphragm is in its equilibrium position, the mean pressure,  $p_m$ , will be the same on both sides of the diaphragm.

If the speed of transverse waves on the diaphragm,  $c = \sqrt{\mathfrak{J}/\rho_s}$ , is much less than the speed of sound in the gas,  $c_{\text{gas}}$ , then all of the gas trapped in the volume behind the diaphragm will respond to the net displacement of the diaphragm (or the volume velocity) produced by the diaphragm's displacement, as calculated in Sect. 6.2.5.

As we saw for our analysis of the stiff string in Sect. 5.5, it was possible to incorporate two restoring forces into a single equation of motion. In this case, we need to calculate the vertical force on a differential surface element of the membrane,  $dA = r dr d\theta$ , that will just be the product of the excess pressure and the area:  $dF_v = \delta p dA$ . Adding this contribution, due to *gas stiffness*, to the vertical restoring force provided by the tension in Eqs. (6.20) and (6.21), a new version of Newton's Second Law can be written that incorporates the restoring force provided by excess pressure. The equation is simplified by the fact that only the  $m = 0$  modes need to be evaluated; derivatives with respect to angle can therefore be ignored.

$$\frac{\mathfrak{J}}{r} \frac{\partial}{\partial r} \left( r \frac{\partial z}{\partial r} \right) r dr d\theta + (\delta p) r dr d\theta = \rho_s (r dr d\theta) \frac{\partial^2 z}{\partial t^2} \quad (6.46)$$

After cancelling common factor and letting  $\mathbf{z}(r, t) = R(r)\mathbf{T}(t) = R(r)e^{j\omega t}$ , we are left with an *inhomogeneous ordinary differential equation*.

$$\frac{1}{r} \frac{d}{dr} \left( r \frac{dR(r)}{dr} \right) + k^2 R(r) = -\frac{(\delta p)}{\mathfrak{J}} \quad (6.47)$$

Since the speed of sound in the gas is assumed to be much greater than the speed of transverse wave on the diaphragm, the excess gas pressure,  $\delta p$ , produced by the compression of the gas trapped behind the membrane in a sealed volume,  $V_o$ , provides the additional restoring force that depends only upon the equivalent "piston" displacement of the diaphragm. Following the same approach used in Sect. 6.2.5 and expressing the pressure using the Adiabatic Gas Law in Eqs. (6.45), (6.47) can be rewritten entirely in terms of the radial displacement function,  $z(r) = R(r)$ .

<sup>11</sup> The assumption that the compressions and expansions of the gas trapped behind the diaphragm obey the Adiabatic Gas Law will be placed on a firmer theoretical basis in Chap. 9 when the subject of thermal conduction and adiabatic temperature changes (see Sect. 1.1.3) will be related to acoustical pressure oscillations.

$$\frac{1}{r} \frac{d}{dr} \left( r \frac{dR(r)}{dr} \right) + k^2 R(r) = \frac{\gamma p_m}{\Im V_o} \int_0^a R(r) 2\pi r dr \quad (6.48)$$

If Eqs. (6.47) and (6.48) had been an ordinary homogeneous differential equations, we would recognize that  $z(r) = R(r) = J_0(k_{0,n} r)$  is one solution, along with  $R(r) = N_0(k_{0,n} r)$ . The Neumann functions are rejected here for the same reasons they were rejected in Sect. 6.2.1. Because these equations are inhomogeneous, their solutions will require that we add a *particular solution* to the homogeneous solution. Since we still require that  $z(a, t) = 0$ , the following solution will automatically satisfy that boundary condition for any value of  $k_{0,n}^{gas}$ , while the amplitude constants,  $C_0$ , can later be determined by the initial conditions (see Sect. 6.2.7).

$$z(r) = C_{0,n} [J_0(k_{0,n}^{gas} r) - J_0(k_{0,n}^{gas} a)] \quad (6.49)$$

The superscript added to the wavenumber,  $k_{0,n}^{gas}$ , will distinguish it from the normal mode wavenumbers of Eq. (6.33) that correspond to solutions that incorporate only tension as the restoring force.

The integral that results from substitution of the solution in Eq. (6.49) into the right-hand side of Eq. (6.48) can be simplified by use of Eq. (6.42).

$$\begin{aligned} \frac{2\pi\gamma p_m C_{0,n}}{\Im V_o} \int_0^a z(r) r dr &= \frac{2\pi\gamma p_m C_{0,n}}{\Im V_o} \left[ \frac{r J_1(k_{0,n}^{gas} r)}{k_{0,n}^{gas}} - \frac{r^2}{2} J_0(k_{0,n}^{gas} a) \right]_0^a \\ &= \frac{\pi a^2 \gamma p_m C_{0,n}}{\Im V_o} \left[ \frac{2 J_1(k_{0,n}^{gas} a)}{k_{0,n}^{gas} a} - J_0(k_{0,n}^{gas} a) \right] \end{aligned} \quad (6.50)$$

The recurrence relation between Bessel functions of successive orders in Eq. (C.18) can be used to express the difference of the two Bessel functions in Eq. (6.50) in terms of a single Bessel function.

$$J_{m+1}(x) = \frac{2m}{x} J_m(x) - J_{m-1}(x) \quad \Rightarrow \quad \frac{2 J_1(k_{0,n}^{gas} a)}{k_{0,n}^{gas} a} - J_0(k_{0,n}^{gas} a) = J_2(k_{0,n}^{gas} a) \quad (6.51)$$

Substitution of Eq. (6.49) into the left-hand side of Eq. (6.48) is simple since  $J_0(k_{0,n} r)$  is the solution to the homogeneous equation and  $-J_0(k_{0,n} a)$  is just a constant.

$$\begin{aligned} -k^2 J_0(k_{0,n} a) &= \frac{\pi a^2 \gamma p_m}{\Im V_o} J_2(k_{0,n}^{gas} a) \quad \Rightarrow \quad J_0(k_{0,n}^{gas} a) = -\aleph \frac{J_2(k_{0,n}^{gas} a)}{(k_{0,n}^{gas} a)^2} \\ \aleph &= \frac{\pi a^4 \gamma p_m}{\Im V_o} \end{aligned} \quad (6.52)$$

The constant,  $\aleph$ , provides a dimensionless measure of the relative importance of the gas stiffness behind the membrane and the membrane's tension per unit length that incorporates the radius of the membrane,  $a$ , and the volume of trapped gas behind the membrane,  $V_o$ . If the membrane is large and limp or if  $V_o$  is small, then  $\aleph \gg 1$ , and the gas's stiffness will dominate the membrane's restoring force. If the tension per unit length,  $\Im$ , is large and/or the back volume,  $V_o$ , is large, then  $\aleph \ll 1$ , and the tension dominates the restoring force. For that case, the solutions to Eq. (6.52) are close to those calculated in Eq. (6.33).

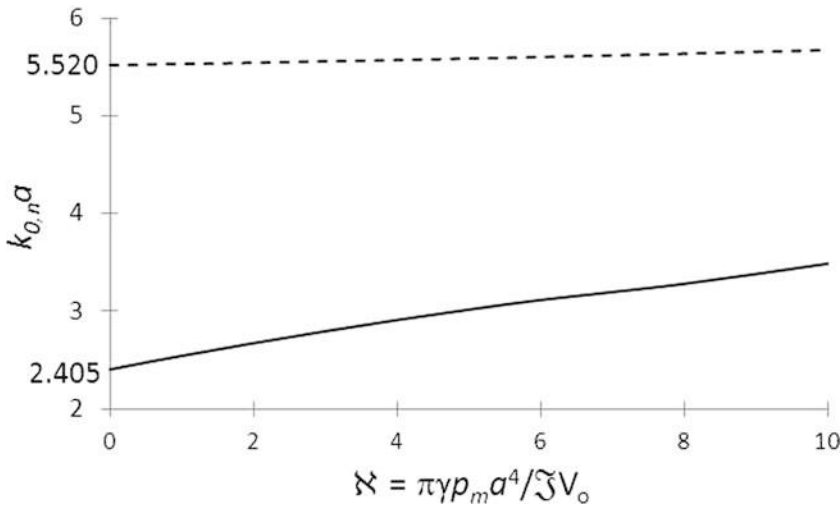


**Fig. 6.13** Increase in the wavenumber  $k_{0,1}^{gas} a$  (solid line) and  $k_{0,2}^{gas} a$  (dashed line) due to additional stiffness provided by gas at mean pressure,  $p_m$ , with polytropic coefficient,  $\gamma = c_p/c_V$ , trapped in a volume,  $V_o$ , behind a diaphragm of radius,  $a$ , and tension per unit length,  $\mathfrak{N}$ . For  $\mathfrak{N} = 0$ , the values of  $k_{0,n}^{gas} a$  are the same as those in Eq. (6.33) and Table 6.2

$$\lim_{\mathfrak{N} \rightarrow 0} [k_{0,n}^{gas} a] = k_{0,n}^{gas} a + \frac{2\mathfrak{N}}{(k_{0,n}^{gas} a)^3} \quad (6.53)$$

As we demonstrated in Sect. 6.2.5 and in Table 6.5, the effective piston area becomes smaller as  $n$  becomes larger. For that reason, the gas stiffness has a much larger effect on the  $n = 1$  normal mode vibrational frequency than on the  $n > 1$  modes. Figure 6.13 plots  $k_{0,n}^{gas} a$  for  $n = 1$  and  $n = 2$  vs. increasing values of  $\mathfrak{N}$ , from 0 to 10. In general, Eq. (6.52) provides a transcendental equation that must be solved for  $x = k_{0,n}^{gas} a$  to determine the normal mode frequencies of the membrane when both tension and gas stiffness provide the restoring forces.

$$J_0(x) = -\mathfrak{N} \frac{J_2(x)}{x^2} \quad (6.54)$$

### 6.2.7 Pressure-Driven Circular Membranes

As mentioned in the introduction of this chapter, a point force applied to a two-dimensional membrane results in an infinite displacement at the point where the force is applied since the pressure at that point is infinite.<sup>3</sup> A much more interesting and useful way to displace a membrane is to apply a pressure that is different on either of the membrane's surfaces. If we again restrict our analysis to time-harmonic excess acoustic pressures,  $\delta p(t) = \Re[\hat{\mathbf{p}}e^{i\omega t}]$ , applied to one surface of the membrane by a fluid, and if we again assume that  $c_{fluid} \gg c = \sqrt{\mathfrak{N}/\rho_s}$ , so the compactness criterion is satisfied,  $2\pi a/\lambda_{fluid} = k_{fluid} a \lesssim 1$ , then the excess pressure on the membrane can be considered to be uniform over its entire surface.

With a spatially uniform driving pressure, only the  $m = 0$  modes of the membrane will be excited, so Eq. (6.47) will describe the membrane's displacement. The particular solution to this

inhomogeneous ordinary differential equation will be similar to Eq. (6.49) but with a constant term added to the homogeneous solution that is related to the amplitude,  $|\hat{\mathbf{p}}|$ , of the time-harmonic driving pressure differential.

$$z(r) = C_{0,n} J_0(kr) - \frac{|\hat{\mathbf{p}}|}{k^2 \mathfrak{J}} \quad (6.55)$$

Note that the wavenumber in the previous equation is not subscripted because we want to evaluate the driven membrane's displacement at all frequencies, not just the discrete normal mode frequencies. The driving pressure provides the initial condition that will determine the value of the amplitude coefficient,  $C_{0,n}$ , that must also be chosen to satisfy the boundary condition,  $z(a) = 0$ .

$$C_{0,n} = \frac{|\hat{\mathbf{p}}|}{k^2 \mathfrak{J}} \frac{1}{J_0(ka)} \quad (6.56)$$

Substitution of Eq. (6.56) into Eq. (6.55) provides an expression for the driven membrane's displacement as a function of the radial distance,  $r$ , from its center.

$$z(r, t) = \Re e \left\{ \frac{\hat{\mathbf{p}} e^{j\omega t}}{k^2 \mathfrak{J}} \left[ \frac{J_0(kr) - J_0(ka)}{J_0(ka)} \right] \right\} \quad (6.57)$$

Since we have not included damping in Eq. (6.47), the amplitude of the membrane's motion will be infinite for driving frequencies corresponding to  $ka = j_{0,n}$ , since  $J_0(j_{0,n}) = 0$ .

At low frequencies, where  $kr \ll 1$ , expansion of Eq. (6.57), using only the first two terms of the power series expansion for  $J_0(x)$  in Eq. (C.4), shows that the transverse displacement of the membrane, subject to a uniform time-harmonic excess pressure, has a parabolic dependence upon the distance from the membrane's center at  $r = 0$ .

$$\lim_{kr \rightarrow 0} \left\{ z(r) = \frac{|\hat{\mathbf{p}}|}{k^2 \mathfrak{J}} \left[ \frac{J_0(kr) - J_0(ka)}{J_0(ka)} \right] \right\} = \frac{|\hat{\mathbf{p}}|}{4 \mathfrak{J}} (a^2 - r^2) = \frac{|\hat{\mathbf{p}}| a^2}{4 \mathfrak{J}} \left( 1 - \frac{r^2}{a^2} \right) \quad (6.58)$$

The fact that the membrane's displacement is independent of frequency, at sufficiently low frequencies, suggests that a small circular membrane could provide a means of measuring acoustic pressure.

The membrane's effective piston displacement,  $\langle z \rangle_{eff}$ , can be calculated by integration of  $\mathbf{z}(r, t)$ , given by Eq. (6.57), over the membrane's surface area, as was done in Sect. 6.2.5 for a circular membrane vibrating in one of its purely radial normal modes.

$$\langle z(t) \rangle_{eff} = \frac{\Re e [\hat{\mathbf{p}} e^{j\omega t}]}{k^2 \mathfrak{J} J_0(ka)} \frac{1}{\pi a^2} \int_0^a [J_0(kr) - J_0(ka)] 2\pi r dr \quad (6.59)$$

The integral is identical to the one solved in Eq. (6.50) and must produce the same result.

$$\langle z(t) \rangle_{eff} = \frac{\Re e [\hat{\mathbf{p}} e^{j\omega t}] a^2}{\mathfrak{J} (ka)^2} \frac{J_2(ka)}{J_0(ka)} \quad (6.60)$$

Using the series expansions for  $J_0(x)$  in Eq. (C.4) and for  $J_2(x)$  in Eq. (C.6), the effective transverse displacement can be written for  $ka < 1$ .

$$J_0(x) \cong 1 - \frac{x^2}{4} \quad \text{and} \quad J_2 \cong \frac{x^2}{8} \left( 1 - \frac{x^2}{12} \right) \quad \text{for } x < 1 \quad (6.61)$$

Application of the binomial expansion in Eq. (1.9) produces an expression for that ratio of the two Bessel functions in Eq. (6.60).

$$\frac{J_2(ka)}{J_0(ka)} \cong \frac{\left(\frac{(ka)^2}{8}\right)\left(1 - \frac{(ka)^2}{12}\right)}{1 - \frac{(ka)^2}{4}} \cong \left(\frac{(ka)^2}{8}\right)\left(1 - \frac{(ka)^2}{12}\right)\left(1 + \frac{(ka)^2}{4}\right) \quad (6.62)$$

Keeping only terms up to second order in  $ka$  produces a useful expression for the effective diaphragm displacement caused by application of a time-harmonic uniform excess pressure.

$$\langle z(t) \rangle_{\text{eff}} = \Re e[\hat{\mathbf{p}} e^{j\omega t}] \frac{a^2}{8\Im} \left[ 1 + \frac{(ka)^2}{6} \right] \quad \text{for } ka < 1 \quad (6.63)$$

This result extends the approximation made to produce the parabolic displacement of Eq. (6.58) to higher frequencies and shows that at low frequencies  $\langle z \rangle_{\text{eff}} = (\frac{1}{2})z(0)$ . The dependence upon  $(ka)^2$  indicates that average displacement increases as the first purely radial resonance frequency, at  $ka = 2.405$ , is approached, as expected. Since the membrane is still being driven within its stiffness-controlled frequency regime (see Sect. 2.5.1), resonance behavior can still be ignored even if the damping is small.

### 6.3 Response of a Condenser Microphone

The invention of the *condenser microphone* by Wente, in 1917 [4], marks the beginning of the electroacoustic era that took us from tuning forks, Helmholtz resonators [5], sensitive flames [6], and the Rayleigh disk (see Sect. 15.4.3) to the sophisticated electronic data acquisition and analysis tools that serve us so well today. Wente's microphone created an acoustic pressure sensing system that facilitated quantitative characterization of acoustical disturbances in air using electronic instrumentation.

Wente realized that the nearly frequency-independent displacement of a stretched diaphragm in response to pressure, expressed in Eqs. (6.58) and (6.63), could be sensed if the diaphragm formed one plate of a parallel-plate electrical capacitor with the other plate being provided by a fixed electrode (the backplate in Fig. 6.14).

Figure 6.14 provides a cut-away view of a modern condenser microphone and typical parameter values for such a one-inch condenser microphone. Based on the values in the table on the right-hand side of Fig. 6.14, the speed of transverse waves on the membrane,  $c = \sqrt{\Im/\rho_s} = 219$  m/s  $< c_{\text{air}} = 343$  m/s. The frequency of the first radial normal mode of the membrane is  $f_{0,1} = 2.4048c/2\pi a = 9.43$  kHz, if the additional stiffness of the air in the back chamber is neglected.<sup>12</sup> Based on Eq. (6.52) and the values in Fig. 6.14,  $\kappa = 1.933$ , raising  $k_{0,1} a$  from 2.4048 to  $k_{0,1}^{\text{gas}} a =$

<sup>12</sup>The measured resonance frequency in vacuum was 9.44 kHz [7].

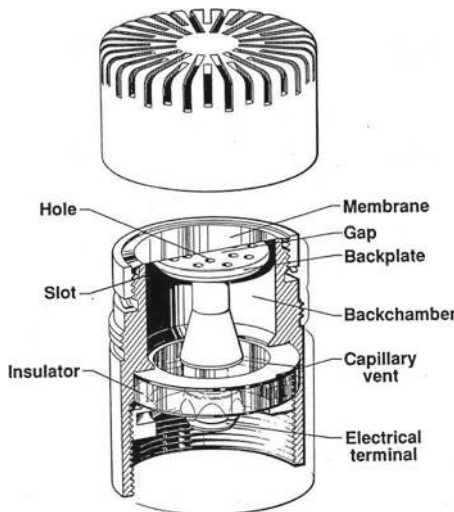


**Fig. 6.14** (Left) Cut-away view of a modern condenser microphone with its screw-on protective grid displaced upward to make the membrane visible. [Courtesy of Brüel & Kjær Instruments.] (Right) Parameter values for a typical “1-inch” condenser microphone based on a B&K Type 4126, S/N: 256903 [7, 8].

2.6651, thus increasing the gas-stiffened normal mode frequency by about 10.8% to  $f_{0,1}^{\text{gas}} = 10.45$  kHz.<sup>13</sup> Use of the approximation in Eq. (6.53) produces a slightly larger value of  $k_{0,1}^{\text{gas}} a = 2.683$ , although the difference would be indistinguishable in Fig. 6.13.

The electrical capacitance,  $C$ , of such a parallel-plate capacitor depends upon equilibrium gap,  $h_o$ , between the membrane of radius,  $a$ , and the backplate of radius,  $b$ . Since  $a \gtrsim b$  and  $h_o \ll b$  and the gap is filled with air, the capacitance of such a condenser microphone capsule can be expressed in terms of the permittivity of free space,  $\epsilon_o = 8.854 \text{ pF/m}$ .<sup>14</sup>

$$C(t) = \epsilon_o \frac{\pi b^2}{\langle g(t) \rangle} \quad (6.64)$$

Based on the values of the physical specifications in Fig. 6.14 (right), the equilibrium (unpolarized) capacitance of the microphone,  $C_o = \epsilon_o \pi b^2 / h_o = 45.9 \text{ pF}$ .

Since the displacement of the microphone’s membrane is a function of the radial distance from the center, as expressed in Eq. (6.57) or approximated at low frequencies in Eq. (6.58), it is necessary to integrate that displacement over the backplate surface area,  $\pi b^2$ , to calculate the time-dependent effective gap spacing,  $\langle g(t) \rangle = h_o + \langle h(t) \rangle$ , driven by the acoustical pressure variations. The effective gap spacing,  $\langle g(t) \rangle$ , will be the sum of the equilibrium gap spacing,  $h_o$ , and the time-harmonic, area-

<sup>13</sup> That result assumes  $\gamma = 7/5$ , but in the small space between the diaphragm and the backplate, the compressions and expansions of the gas are nearly isothermal, corresponding to  $\gamma = 1$ , rather than adiabatic. For the current discussion, this distinction is not significant.

<sup>14</sup> The dielectric constant of air at atmospheric pressure is sufficiently close to that of a vacuum that the difference can usually be ignored and the free-space value of the permittivity can be used to calculate the capacitance. If the space between the membrane and the backplate is filled with an insulating material, then the capacitance of Eq. (6.65) must be increased by the relative dielectric constant of the material, such as the Teflon used for electret microphones in Sect. 6.3.3.

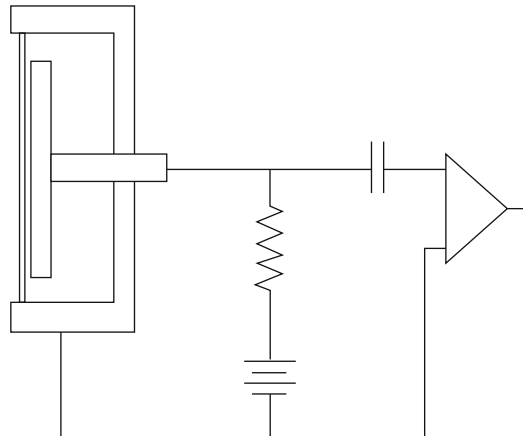


**Fig. 6.15** Schematic diagram of an electrical circuit that provides a polarizing voltage,  $V_{bias}$  (battery symbol), to the condenser microphone's backplate through an electrical resistor with very large resistance. That DC voltage,  $V_{bias}$ , is blocked by a large-value capacitor acting as a high-pass filter to allow only the time-varying voltage,  $V(t)$ , produced by the changing capacitance of the condenser microphone, to reach the pre-amplifier, while blocking  $V_{bias}$  from the input to the first-stage pre-amplifier that is usually located in close proximity to the condenser microphone, typically in the microphone's handle. (Figure courtesy of J. D. Maynard)

averaged variation in the gap,  $\langle h(t) \rangle = \Re e[\hat{\mathbf{h}}e^{j\omega t}]$ , produced by the forcing pressure differential,  $\delta p(t) = \Re e[\hat{\mathbf{p}}e^{j\omega t}]$ , if the static pressure of the air trapped back chamber that remains close to  $p_m$ .<sup>15</sup>

Logarithmic differentiation (see Sect. 1.1.3) of Eq. (6.64) relates the area-averaged variation in the gap to the variation in the capacitance of the membrane and backplate.

$$\frac{\delta C(t)}{C_o} = -\frac{\delta \langle g(t) \rangle}{h_o} = -\frac{\Re e[\hat{\mathbf{h}}e^{j\omega t}]}{h_o} \quad (6.65)$$

In ordinary operation, an electronic circuit has to be added to convert the changes in capacitance to changes in voltage (or current) that can be amplified, detected, displayed, and recorded by one or more electronic instrument (e.g., oscilloscope, dynamic signal analyzer, digital multimeter, sound level meter, etc.).

This production of a time-dependent voltage,<sup>16</sup>  $V(t) = \Re e[\hat{\mathbf{V}}e^{j\omega t}]$ , which can be sensed electronically, is typically accomplished by providing the condenser microphone with a *polarizing voltage*,  $V_{bias}$ , through an electrical resistor,  $R_{el}$ , having a high electrical resistance. A circuit for providing the DC-bias voltage is shown schematically in Fig. 6.15. The exponential time constant,  $\tau = R_{el} C_o$ , for charge to move on or off the microphone would be about one-half second if  $R_{el} = 10 \text{ G}\Omega$ . For frequencies at the lower end of the audio spectrum, defined by the traditional limits of human hearing

<sup>15</sup> The capillary vent shown in Fig. 6.14 is designed so that it will let the mean pressure equilibrate over longer times while blocking oscillatory flow of air at the lowest operational design frequency of a particular microphone.

<sup>16</sup> Note that  $\hat{\mathbf{V}}$  should be considered to be a complex number (phasor) since there can be a phase difference between  $\delta p(t)$  and  $V(t)$ .

( $20 \text{ Hz} < f < 20 \text{ kHz}$ ), the charge,  $Q_o$ , stored in the capacitor formed by the membrane and backplate is effectively constant.<sup>17</sup> If  $V_{bias} = 200 \text{ V}_{dc}$ , then  $Q_o = C_0 V_{bias} \cong 10 \text{ nanocoulombs (10 nC)}$ .<sup>18</sup>

### 6.3.1 Optimal Backplate Radius

With a constant charge,  $Q_o$ , on the condenser microphone, we can again invoke logarithmic differentiation to relate changes in capacitance,  $\delta C$ , to changes in the voltage,  $V(t)$ , that would appear across the terminals of the pre-amplifier stage in Fig. 6.15, which we assume has an infinite input electrical impedance.

$$Q_o = CV \quad \Rightarrow \quad \frac{\delta V}{V_{bias}} = \frac{V(t)}{V_{bias}} = -\frac{\delta C}{C_o} = \frac{\langle h(t) \rangle}{h_o} \quad (6.66)$$

The final term on the right-hand side of Eq. (6.66) incorporates the result of Eq. (6.65).

Before continuing to calculate an open-circuit sensitivity,  $\mathbf{M}_{oc} = \widehat{\mathbf{V}}/\widehat{\mathbf{p}}$ , for the microphone capsule based on Eq. (6.66), it will be instructive to think about our choice of a backplate area,  $\pi b^2$ , for a given diaphragm area,  $\pi a^2$ . Since the motion of the membrane is greatest at its center and the sensitivity is proportional to  $\delta C/C_o$ , making  $b$  as small as possible would provide the largest value of  $\delta C/C_o$  by making  $\langle h(t) \rangle/h_o$  have its largest value, thus making  $V(t)$  as large as possible. It would also make the electrical output impedance,  $|Z_{el}| = (\omega C_o)^{-1}$  very high, suggesting that the voltage,  $V(t)$ , that is produced will supply a very tiny electrical current.

For optimum performance and minimum electronic noise [9], the electrical power output should be maximized, not just the voltage. The electrical power is proportional to the product of current and voltage. The time-averaged electrical power,  $\langle \Pi_{el} \rangle_t$ , delivered to a load by a capacitor is related to the electrostatic energy,  $(PE)_{el}$ , stored in a capacitor that is charging and discharging at a frequency,  $\omega$ , with a voltage,  $V(t) = \Re e[\widehat{\mathbf{V}} e^{j\omega t}]$ , across its terminals.

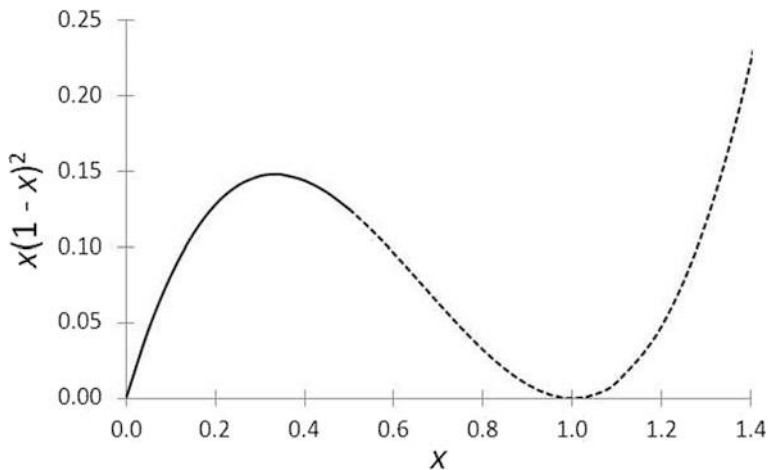
$$\langle \Pi_{el} \rangle_t = \left| \frac{d(PE)_{el}}{dt} \right| = \omega C_o \frac{|\widehat{\mathbf{V}}|^2}{2} \quad (6.67)$$

To calculate  $\widehat{\mathbf{V}}$  from Eq. (6.66), the area-averaged, pressure-driven displacement,  $\langle h(t) \rangle$ , has to be determined by integration of the membrane's displacement over the backplate area,  $\pi b^2$ . Since we seek a result for the low-frequency sensitivity, the membrane's displacement as a function of radius,  $z(r)$ , can be represented by Eq. (6.58).

<sup>17</sup> To use a condenser microphone to detect infrasonic pressures, a high-frequency “carrier” is used rather than a DC-bias voltage because the output impedance of a capacitance goes to infinity as the frequency approaches zero. Another way to detect the diaphragm’s displacement down to DC is to resonate the microphone’s capacitance,  $C$ , with an inductance,  $L$ , and use the changes in resonance frequency,  $\omega_o = (LC)^{-1/2}$ , of the electrical tank circuit, to determine the diaphragm displacement. Another way to extend the response down to DC is to make the microphone be one arm of a capacitive Wheatstone bridge circuit that uses a high-frequency AC-bias voltage [20]. Of course, careful attention must also be paid to the pressure equilibration through the capillary vent to ensure that frequency response of the microphone itself will not be reduced by air leakage through the capillary at very low frequencies.

<sup>18</sup> The SI abbreviation for coulomb is [C]. For temperature in degrees Celsius, it is [°C] to distinguish it from electrical charge.

**Fig. 6.16** Graph of Eq. (6.80) showing the local maximum at  $x = \frac{1}{3}$  with the maximum value at that point equal to  $\frac{4}{27}$ . The values of  $x \geq 0.5$  that are not physically realizable are plotted with the dashed line



$$\langle h(t) \rangle = \Re e \left[ \frac{\hat{\mathbf{p}} e^{j\omega t}}{4\pi \Im} \right] \frac{a^2}{b^2} \int_0^b \left( 1 - \frac{r^2}{a^2} \right) 2\pi r dr = \frac{a^2}{4\Im} \left( 1 - \frac{b^2}{2a^2} \right) \Re e [\hat{\mathbf{p}} e^{j\omega t}] \quad (6.68)$$

This result is reasonable. For a given pressure differential across the membrane, a larger membrane will have a larger average deflection, and a lower tension per unit length will also lead to larger average deflection. Both increases in sensitivity (with increasing area or decreasing tension) come at the cost of a lower fundamental resonance frequency, hence, a more limited useful frequency bandwidth. Substituting this result into Eq. (6.66) produces the time-dependent variation in output voltage caused by the acoustic pressure.

$$V(t) = V_{bias} \frac{\langle h(t) \rangle}{h_o} \cong V_{bias} \frac{a^2}{4h_o \Im} \left( 1 - \frac{b^2}{2a^2} \right) \Re e [\hat{\mathbf{p}} e^{j\omega t}] \quad (6.69)$$

The signal voltage,  $V(t)$ , increases as  $b^2$  decreases, as postulated earlier, but the capacitance,  $C_o$ , increases as  $b^2$  increases.

$$C_o = \epsilon_o \frac{\pi b^2}{h_o} = \epsilon_o \frac{\pi a^2}{h_o} \left( \frac{b^2}{a^2} \right) \quad (6.70)$$

Letting  $x^2 = b^2/a^2$ , Eqs. (6.69) and (6.70) can be substituted into Eq. (6.67) to calculate the time-averaged electrical power,  $\langle \Pi_{el} \rangle_t$ , produced by the pressure-driven microphone in terms of  $x$ .

$$\langle \Pi_{el} \rangle_t = \Lambda x^2 \left( 1 - \frac{x^2}{2} \right)^2; \quad \Lambda = \frac{\epsilon_o \pi \omega a^6}{2h_o^3} \left( \frac{V_{bias} |\hat{\mathbf{p}}|}{4\Im} \right)^2 \quad (6.71)$$

The optimum ratio for  $b/a = x_{opt}$  can be found by differentiation of Eq. (6.71) with respect to  $x$ .

$$\frac{d \langle \Pi_{el}(x) \rangle_t}{dx} = \Lambda \left( \frac{3x^5}{2} - 4x^3 + 2x \right) = 0 \quad \Rightarrow \quad x_{opt}^2 = \frac{4 \pm 2}{3} \quad (6.72)$$

Since  $b/a \leq 1$ , the optimum backplate-to-membrane radius ratio is  $(b/a)_{opt} = \sqrt{2/3} = 0.8165$ . The radius ratio for the 1-inch microphone in Fig. 6.13 is slightly smaller:  $b/a = 0.744$ .

To determine the theoretically maximum sensitivity of a condenser microphone, the pre-amplifier in Fig. 6.16 will be assumed to have infinite electrical input impedance, so that the full pressure-driven

voltage produced by the microphone will appear across the pre-amplifier's input terminals. To remind ourselves of this approximation, the microphone's sensitivity will be designated the *open-circuit microphone sensitivity*,  $\mathbf{M}_{oc}$ .

$$|\mathbf{M}_{oc}| \equiv \left| \frac{\widehat{\mathbf{V}}}{\widehat{\mathbf{p}}} \right| = V_{bias} \frac{\langle h(t) \rangle}{h_o} = V_{bias} \frac{a^2 \left( 1 - \frac{b}{2a^2} \right)}{4h_o \mathfrak{J}}$$

$$(|\mathbf{M}_{oc}|)_{max} = \frac{a^2}{6h_o \mathfrak{J}} V_{bias}$$
(6.73)

At sufficiently low frequencies, the voltage and pressure will be in-phase, so  $M_{oc}$  is usually represented by a real number. In reality,  $\mathbf{M}_{oc}$  must be a complex number to incorporate phase differences between pressure and output voltage. Using the parameters in the table on the right in Fig. 6.14 and applying the typical bias voltage for condenser microphones,  $V_{bias} = 200$  V<sub>DC</sub>, the optimal open-circuit sensitivity of that microphone would be  $(M_{oc})_{max} = 46.3$  mV/Pa or  $-26.7$  dB *re*: 1.0 V/Pa.

### 6.3.2 Limits on Polarizing Voltages and Electrostatic Forces

As shown in Eq. (6.73), the open-circuit sensitivity of a condenser microphone is directly proportional to the polarization voltage,  $V_{bias}$ . In principle, it appears that the larger the value of  $V_{bias}$ , the better. This section will address two limitations on the possible value for  $V_{bias}$ . The first is "arcing," which occurs if the voltage is large enough to cause a spark to jump from the diaphragm to the backplate. The second is electrostatic collapse. Since the electrostatic force between the diaphragm and the backplate increases with decreasing separation, the application of the bias voltage causes the electrostatic force to bring the diaphragm closer to the backplate. As the separation decreases, the electrostatic attractive force increases. At some point, the gap becomes small enough that the elastic restoring force due to the tension in the diaphragm is insufficient to counteract the electrostatic force that is increasing quadratically with decreasing gap.

It is worthwhile to reflect momentarily on the fact that a 200 V<sub>DC</sub> voltage difference across a 20-micron gap corresponds to an electric field strength of  $10 \times 10^6$  V/m = 10 MV/m. The accepted value for the electric field strength necessary to cause *dielectric breakdown* (i.e., sparking) in air, at atmospheric pressure, is about 3 MV/m = 3 V/ $\mu$ m [10].

The reason that a condenser microphone can exceed the breakdown threshold by a factor of three is that sparking relies on an avalanche process where one electron is accelerated to an energy that is sufficient to ionize another atom prior to its final collision (in this case with the microphone's backplate or diaphragm). For nitrogen, the ionization energy is about 15 eV, and the distance between collisions is the order of one mean free path.<sup>19</sup> For gaps on the order of 10 microns and above, the gap dependence of the breakdown voltage,  $V_{BD}$ , is given by an empirical relation known as Paschen's law [11].

$$V_{BD} = \frac{ap_m g}{\ln(p_m g) + b}$$
(6.74)

In Eq. (6.74),  $p_m$  is in atmospheres (1 atm  $\equiv$  101,325 Pa), and the gap,  $g$ , is in meters, with  $a = 4.36 \times 10^7$  V/(atm-m) and  $b = 12.8$  [12]. At atmospheric pressure, Eq. (6.74) yields  $V_{BD}/$

<sup>19</sup>The mean free path of an atom in air at atmospheric pressure is about 100 nanometers (see Sect. 9.5.1). The mean free path of electrons in air is about 500 nanometers.

$m = 3.4 \text{ MV/m}$  over 1 m, and at 20 microns,  $V_{bias} = 440 \text{ V}_{\text{DC}}$ . The suppression of breakdown in very small devices has generated renewed contemporary interest due to the development of microelectromechanical systems (MEMS) [13].

The voltage difference between the membrane and the backplate will produce an electrostatic attraction. Since the gap between the backplate and membrane is so small, it is prudent to calculate the static displacement of the membrane due to this electrostatic attraction. The *electrostatic potential energy*,  $(PE)_{el}$ , stored in a parallel-plate capacitor, depends upon the product of the square of the voltage difference and the capacitance,  $C_o$ .

$$(PE)_{el} = \frac{C_o V_{bias}^2}{2} = \frac{\epsilon_o \pi b^2}{2 h_o} V_{bias}^2 \quad (6.75)$$

Since the polarization voltage,  $V_{bias}$ , is held constant, the electrostatic force,  $F_{el}$ , is just the negative of the derivative of the potential energy (see Sect. 1.2.1) with respect to the gap height,  $h_o$ .

$$F_{el} = -\left(\frac{\partial(PE)_{el}}{\partial h_o}\right)_{V_{bias}} = \frac{\epsilon_o \pi b^2}{2 h_o^2} V_{bias}^2 = \frac{C_o V_{bias}^2}{2 h_o} \quad (6.76)$$

If we ignore the fact that the electrostatic force acts over the area of the backplate and not the entire membrane, thus assuming that  $b \cong a$ , then the electrostatic pressure,  $P_{el}$ , can be approximated well enough to determine the displacement of the membrane's center due to the polarization voltage.

$$P_{el}|_{b=a} \cong \frac{\epsilon_o}{2 h_o^2} V_{bias}^2 \quad (6.77)$$

The deflection of the membrane's center,  $z(0)$ , using the microphone parameters in Fig. 6.14 and  $V_{bias} = 200 \text{ V}_{\text{DC}}$ , is determined using Eq. (6.58).

$$z(0)|_{b=a} = \frac{P_{el} a^2}{4 \mathfrak{I}} = \frac{\epsilon_o}{8} \frac{a^2}{h_o^2} \frac{V_{bias}^2}{\mathfrak{I}} = 2.8 \times 10^{-6} \text{ m} = 2.8 \text{ microns} \quad (6.78)$$

The electrostatic force reduces the minimum gap by about 11%. The error in the electrostatic deflection introduced by assuming that  $a = b$  is negligible for our purposes [14].

$$\frac{z(0)|_{b < a}}{z(0)|_{b=a}} = \frac{b^2}{a^2} \left[ 1 + 2 \ln \left( \frac{a}{b} \right) \right] \quad (6.79)$$

For the microphone parameters in Fig. 6.4, this corresponds to a reduction in the displacement below that calculated in Eq. (6.78) resulting in an electrostatic deflection of 2.46 microns.

There is another intrinsic limit on the polarization voltage that is a result of this electrostatic deflection of the membrane. As  $V_{bias}$  increases, Eq. (6.77) shows that the electrostatic pressure increases.<sup>20</sup> The restoring force provided by the diaphragm increases linearly with reduction in gap,  $h$ , but the electrostatic attraction increases inversely as the gap squared,  $h^{-2}$ . There will be some critical

---

<sup>20</sup>The electrostatic pressure is used as a means to make absolute calibrations of condenser microphones using a grid placed above the diaphragm called an “electrostatic actuator.” Because the gap between such a grid and the microphone’s diaphragm must be small to produce significant sinusoidal electrostatic pressures, uncertainty in that gap is the most significant source of uncertainty in such calibrations. For further discussion, see H. Miura, “Laboratory Calibration Methods at Electrotechnical Laboratory, Japan,” in *AIP Handbook of Condenser Microphones: Theory, Calibration and Measurements*, G. S. K. Wong and T. F. W. Embleton, Editors (Am. Inst. Phys., 1995); ISBN 1-56396-284-5. See §8.7, “Electrostatic Actuator Measurements.”

value of the polarization voltage,  $(V_{bias})_{Crit}$  that, when exceeded, will cause a catastrophic collapse of the membrane.

The critical value of the polarization voltage can be calculated by substitution of  $P_{el}$ , from Eq. (6.77), into the expression for the membrane's average (effective) static ( $\omega = 0 \Rightarrow ka = 0$ ) deflection,  $\langle z \rangle_{eff}$ , given in Eq. (6.63), that will provide the reduction in the gap due to the polarization voltage. When we allow the gap,  $h$ , to be reduced by that average deflection, so the polarization-dependent gap,  $h(V_{bias}) = h_o - \langle z \rangle_{eff}$ , then we obtain an expression that includes the effective deflection on both sides of the equation.

$$\frac{\langle z \rangle_{eff}}{h_o} \cong \frac{\epsilon_o}{16} \frac{V_{bias}^2}{\Im} \frac{b^2}{h_o^3} \frac{1}{\left(1 - \frac{\langle z \rangle_{eff}}{h_o}\right)^2} \Rightarrow x(1-x)^2 = \frac{\epsilon_o}{16} \frac{V_{bias}^2}{\Im} \frac{b^2}{h_o^3} \quad (6.80)$$

In the right-hand version of Eq. (6.80), we have let  $x = \langle z \rangle_{eff}/h_o < \frac{1}{2}$ . That limit on  $x$  is based on the fact that the average deflection is half the maximum deflection at the center.

Figure 6.16 is a plot of  $x(1-x)^2$  vs.  $x$ . Differentiation of that function shows that there is a local maximum at  $x = \frac{1}{3}$ . At that point, the function has a value of  $\frac{4}{27} \cong 0.148$ . If the dimensionless quantity on the right-hand side of Eq. (6.80) exceeds  $\frac{4}{27}$ , then no solution is possible. This result provides the maximum magnitude of the polarization voltage  $(V_{bias})_{Crit}$ .

$$(V_{bias})_{Crit} = |V_{bias}|_{max} = \sqrt{\frac{64}{27} \frac{\Im h_o^3}{\epsilon_o b^2}} \quad (6.81)$$

For the 1-inch microphone parameters in Fig. 6.13,  $(V_{bias})_{Crit} \cong 450$  V<sub>DC</sub>. Coincidentally, the polarization voltage limits imposed by both dielectric breakdown of the air and electrostatic collapse are nearly the same.

### 6.3.3 Electret Condenser Microphone

The large polarizing voltage required for operation of the condenser microphone, described in the previous section, is readily available in a laboratory or recording studio that has dedicated microphone power supplies capable of providing stable polarizing voltages in the range of 48–200 V<sub>DC</sub>. For portable battery-operated electronics, like telephones or small tape/digital recorders, the required high voltages are not easy to produce. Fortunately, in addition to the nonstick properties of Teflon® that make it a popular coating for cooking utensils, Teflon also has the ability to trap electrical charges [15].<sup>21</sup>

Charge can be deposited in Teflon by exposure of an aluminized Teflon film to break down electrical fields [16], by ion implantation using electron beams [17] or by rubbing an alcohol-soaked cotton swab over the Teflon if there is a voltage difference as small as 300 V<sub>DC</sub> between the moist swab and the conducting surface of the Teflon film [18, 19].

---

<sup>21</sup>This property is not unique to Teflon. Other polymers, like Mylar®, also exhibit the ability to trap electrical charges. Teflon is the most common electret material for microphones because it has the highest volume electrical resistivity, which is on the order of  $10^{18}$  Ω cm.

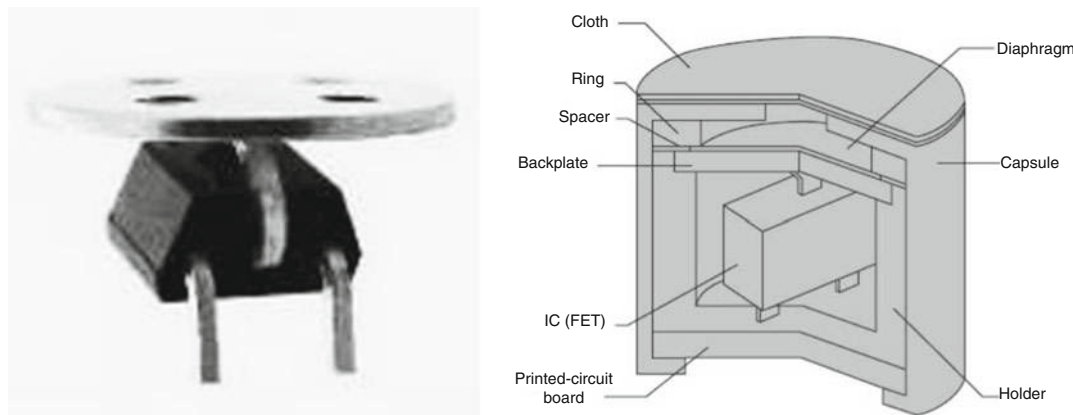


**Fig. 6.17** An electret condenser microphone can be designed so that a field-effect transistor (FET) can be included in a package that is less than a centimeter in diameter and a few millimeters in height. (*Left*) The microphone backplate can be attached directly to the gate electrode of the FET, and the source and drain terminals of the FET can be exposed. (*Right*) The aluminized Teflon membrane (diaphragm), with the aluminized surface facing away from the backplate, is typically mounted to a thin spacer (washer), and the package is usually covered by a thin sheet of porous fabric that keeps dust and other particulates off of the membrane. The membrane will be attracted to the backplate by the electrostatic forces of Eq. (6.76). [Drawing courtesy of Hosiden Corp]

There are two strategies for using charge trapped in Teflon to provide the polarizing voltage for a condenser microphone. For laboratory-quality microphones, the Teflon is bonded to the backplate, a configuration known as a “back electret.” The other option is to use a thin Teflon film (usually between 6 and 12 microns thick) as both the membrane and the electret.

The cost of an *electret microphone* can be made very low (on the order of pennies each), and the packaging can include a field-effect transistor (FET) [20]. The FET will convert the output electrical impedance  $(j\omega C_o)^{-1}$  of the microphone’s capacitance of only a few picofarads to about  $1 \text{ k}\Omega$ . Such a package can be just as small as a TO-92 transistor case. As shown in Fig. 6.17, the gate electrode of the FET can be attached directly to the microphone backplate, and the source and drain electrodes are available for transmission of the microphone signal through modest lengths of cable.

This approach has led to the sale of such microphones for use in telephones, tape recorders, hearing aids, etc., at around two billion units per year [21]. By 2010, the annual sales of electret condenser microphones had decreased, while the sale of microelectromechanical systems (MEMS) has increased to 1.1 billion units in 2013 (see Problem 15). With improvements in the MEMS devices, that trend will most likely continue.

Although the trapped charge will escape as the temperature increases, Teflon electret microphones have been used down to temperatures approaching absolute zero [22].<sup>22</sup> Electret transducers are very easy to assemble in a laboratory because the charged membrane will be held in place by the electrostatic attraction, given in Eq. (6.76), between the membrane and the conductive backplate. The sensitivity of such an electret microphone depends primarily upon the ambient air pressure and the equivalent polarization voltage,  $V_{bias} = Q_o/C_o$ , produced by the trapped charge,  $Q_o$ .

The microphone can be modeled as two capacitors that are placed in series electrically. One capacitor is formed by the conductive (usually aluminized) coating and the Teflon film. If the thickness

<sup>22</sup>The thermal activation of the trapped charge is used to stabilize the electret microphone’s sensitivity. Typically, the temperature of the assembled unit will be raised to about  $60^\circ\text{C}$  so that the charge, and hence the sensitivity, will be stable for use at temperatures less than  $60^\circ\text{C}$ .

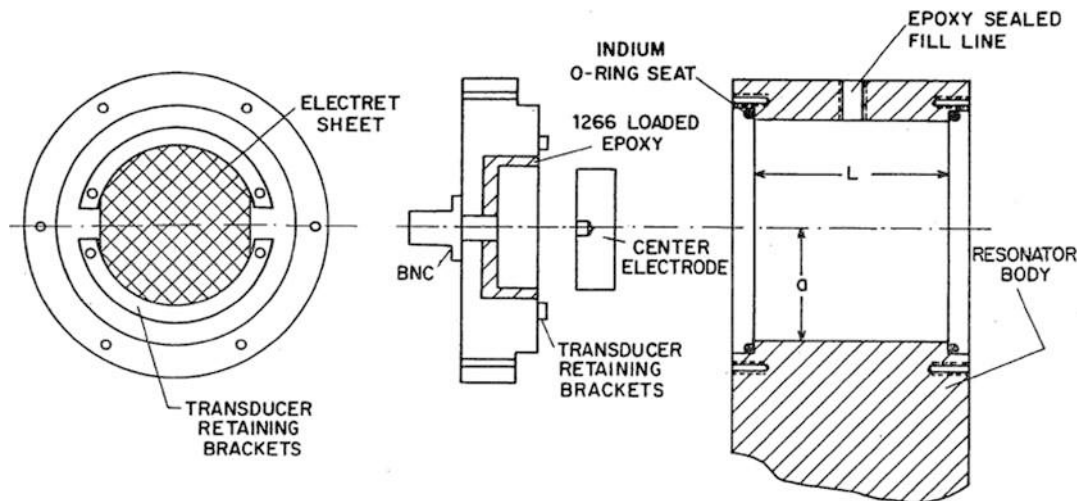


**Fig. 6.18** Cylindrical resonator of length,  $L$ , and diameter,  $2a$ , with rigid endcaps formed by electret transducers that consist of an insulated “center electrode” covered by an electrically charged, thin, aluminized Teflon® film that can either excite or detect acoustic resonances within the resonator [25].

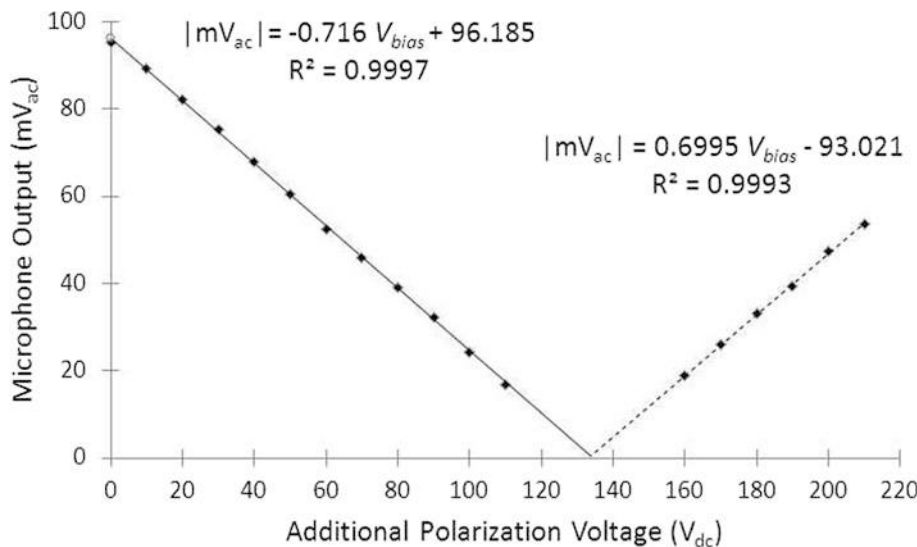


**Fig. 6.19** Change in an electret microphone output voltage vs. additional applied polarization voltage,  $V_{bias}$ . The applied polarization is opposing the polarization provided by the trapped charge. Straight-line fits to the descending (solid) and ascending (dashed) data extrapolate to  $V_{bias} = 133.7 \pm 0.7$  V<sub>DC</sub>. The data near zero microphone output have lower signal-to-noise ratios and are not plotted

of the Teflon is  $t$ , then the Teflon’s capacitance per unit area,  $C_{Teflon}/A$ , is a constant, since the thickness is not a function of the acoustic pressure on the conducting surface of the film:  $C_{Teflon}/A = \epsilon_{Teflon}\epsilon_0/t$ . The relative dielectric constant is  $\epsilon_{Teflon} = 2.1$ . For ½-mil thick ( $t = 12.7$  micron) Teflon film,  $C_{Teflon}/A \cong 150$  pF/cm<sup>2</sup>. The other series capacitor is formed by the bottom surface of the Teflon film and the backplate that are separated by a thin film of air. That average air gap,  $h_{Air}$ , will be very thin due to the

electrostatic attraction making,  $h_{Air} \ll t$ .<sup>23</sup> For that reason, the net capacitance per unit area is just that of the Teflon film. Since the Teflon® film is far less compressible than the air trapped between the Teflon and the backplate, the sound impinging on the microphone will vary the average thickness of the air gap and will produce a voltage,  $V(t) = \Re e[\hat{\mathbf{V}}e^{j\omega t}]$ , that is proportional to the equivalent polarization voltage,  $V_{bias} = Q_o/C_o$ , produced by the trapped charge,  $Q_o$ , and the time-varying thickness of the air gap, expressed in Eq. (6.66).

It is actually quite simple to accurately measure the equivalent polarization voltage,  $V_{bias}$ , using a *vibrating reed electrometer* technique [23, 24]. The data provided in Fig. 6.19 was obtained by driving a cylindrical resonator with two electret transducers on either end, similar to that shown in Fig. 6.18 [25], at its fundamental resonance and connecting the receiving electret to a circuit like that in Fig. 6.15, which has a variable polarization supply voltage. Keeping the amplitude of the acoustical resonance constant, the amplitude of the received signal can be plotted against the additional externally applied polarization voltage. Data for one such electret microphone is shown in Fig. 6.19.

The reverse bias provided by the additional polarization voltage decreased the microphone's output until the reverse bias voltage equaled the effective electret polarization voltage. When the reverse bias exceeded the effective electret polarization voltage, the microphone signal returned. The stored charge can be estimated by extrapolation of the two straight lines in Fig. 6.19 to zero microphone output. Based on that extrapolation,  $V_{bias} = 133.7 \pm 0.7 \text{ V}_{DC}$ , so  $Q_o = C_o V_{bias} = 2.7 \times 10^{-7} \text{ coulombs}$ . The capacitance of that electret microphone was about 2000 pF, corresponding to a backplate diameter of 4.25 cm.

Calculation of the electret microphone's sensitivity depends upon a relationship between the air gap thickness,  $h_{Air}(t) = h_o + \Re e[\hat{\mathbf{h}}e^{j\omega t}]$ , and the excess pressure,  $\delta p(t)$ , on its surface. We can use the Adiabatic Gas Law in Eq. (6.45), but since the equilibrium thickness of that air layer,  $h_o$ , is so small, the gas compresses isothermally rather than adiabatically, as it did in our tympani example in Sect. 6.2.6. This isothermal behavior can be represented in Eq. (6.45) by setting  $\gamma = 1$ .<sup>24</sup> It is also worthwhile to remember that the stiffness of the gas trapped between the film and the backplate provides the restoring force, since there is no tension applied to the membrane. That means that the membrane will move uniformly, like a piston, and no effective area need be calculated.

Following Eq. (6.66), the electret microphone's open-circuit sensitivity,  $M_{oc}$ , can be expressed in terms of the mean gas pressure,  $p_m$ .

$$\frac{V(t)}{V_{bias}} = \frac{\delta h_{Air}(t)}{h_o} \Rightarrow |\mathbf{M}_{oc}| = \frac{V(t)}{\delta p(t)} = \frac{|\hat{\mathbf{V}}|}{|\hat{\mathbf{p}}|} = \frac{Q_o}{p_m C_o} = \frac{V_{bias}}{p_m} \quad (6.82)$$

The effective polarization voltage for a Teflon electret mic is typically about 100 V<sub>DC</sub>, and the  $p_m \cong 100 \text{ kPa}$ , so for the electret microphone,  $|\mathbf{M}_{oc}| \cong 1.0 \text{ mV/Pa}$ .

<sup>23</sup> When I construct an electret transducer, I usually sandblast the backplate's surface to create microscopic bumps that ensure a compressible trapped air cushion. At the microscopic level, this produces a “mountain range” with the Teflon film resting on the peaks.

<sup>24</sup> As will be demonstrated in Sect. 9.3.2, the temperature of the air trapped between the Teflon film and the microphone's backplate will be held constant by the larger heat capacity of the film and backplate since the thickness of the gas layer is much smaller than the thermal penetration depth,  $\delta_\kappa$  (see Sect. 9.3.1). In air at 10 kHz,  $\delta_\kappa \cong 27 \text{ microns}$  and grows larger as the frequency decreases. Since  $2\delta_\kappa \gg h_o$ , the air cannot change its temperature adiabatically as calculated in Eq. (1.19).

## 6.4 Vibrations of Thin Plates

The vibration of thin plates has the same relationship to the vibration of membranes as the flexural vibration of bars has to the transverse vibrations of a limp string. However, the plate vibration is complicated by Poisson's ratio,  $\nu$ , in a way that was not a problem with bars because when a bar is bent, the bar's cross-section could "bulge." For a plate, the bulge is constrained by the adjacent plate material. As with the bar, the bending of a plate compresses material above the neutral plane and stretches the material below. The sideways spreading caused when  $\nu \neq 0$  will create a tendency for the plate to curl downward in a direction perpendicular to the upward bend, and vice versa. The derivation of Eq. (6.83) is treated in books devoted to the theory of elasticity [26].

$$\nabla^4 z + \frac{12(1-\nu^2)}{Et^2} \rho \frac{\partial^2 z}{\partial t^2} = 0 \quad (6.83)$$

In this equation of motion,  $t$  in the  $Et^2$  product in the denominator of Eq. (6.83) is the thickness of the plate and  $E$  is the Young's modulus of the plate's material. Of course, the "t" in the vertical acceleration,  $(\partial^2 z / \partial t^2)$ , represents time, not thickness. As before,  $\nu$  is Poisson's ratio. The similarity of Eq. (6.83) to that for the flexural vibrations of a bar in Eq. (5.31) suggests that waves in plates will also be dispersive (see Sect. 5.3.1). The differential bi-harmonic operator,  $\nabla^4$ , is difficult to separate in most coordinate systems, but in polar coordinates, it is easy enough to justify the analysis of the vibration of thin circular and annular disks.

As before, we assume time-harmonic vibration at frequency,  $\omega$ , so  $z(r, \theta, t) = \Re e[z(r, \theta)e^{j\omega t}]$ . We can also factor the resulting operator, as we did for the wave equation in Eq. (3.6), and reintroduce the square of longitudinal wave speed in bars,  $c_B^2 = E/\rho$ .

$$(\nabla^2 - \gamma^2)(\nabla^2 + \gamma^2)z(r, \theta) = 0 \quad \text{where} \quad \gamma^4 = \frac{12\omega^2(1-\nu^2)}{t^2 c_B^2} \quad (6.84)$$

This equation is satisfied when either  $(\nabla^2 z + \gamma^2 z) = 0$  or  $(\nabla^2 z - \gamma^2 z) = 0$ .

Since we are expressing both  $\nabla^2$  and  $z$  in polar coordinates, we can separate  $z(r, \theta) = R(r)\Theta(\theta)$ , as we did for the circular membrane in Eq. (6.32), to provide a solution for  $(\nabla^2 z - \gamma^2 z) = 0$ .

$$z(r, \theta) = C_{m,n} J_m(\gamma r) \begin{cases} \cos(m\theta) \\ \sin(m\theta) \end{cases} \quad (6.85)$$

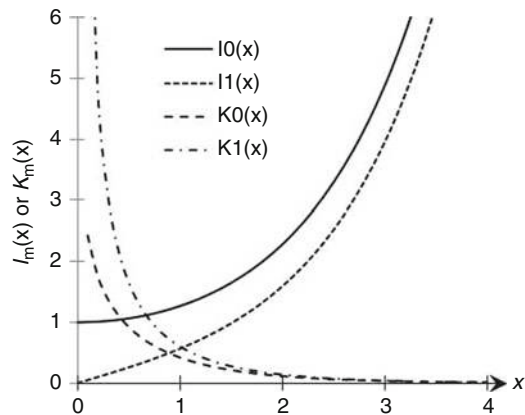
Our disk has no hole in the center, so we can reject the Neumann functions and again impose periodic boundary conditions to force  $m$  to assume only integer values, including zero.

To solve  $(\nabla^2 z + \gamma^2 z) = 0$  and thus obtain the other two solutions to our fourth-order differential equation, we can simply use Eq. (6.84) but substitute  $\gamma = j\gamma$  to impose the requisite sign change. This introduces the *modified Bessel functions*,  $I_m(r)$  and  $K_m(r)$ , that are the equivalent of the hyperbolic trigonometric functions,  $\sinh(x)$  and  $\cosh(x)$ , that provided the third and fourth solutions required to solve the fourth-order differential equation that described the flexural modes of bars.<sup>25</sup> Those hyperbolic solutions were generated when Eq. (5.36) required both real and imaginary values for the wavenumbers.

---

<sup>25</sup> We can choose to consider the modified Bessel functions to be the hyperbolic Bessel functions in the same way that  $\sinh(x)$  and  $\cosh(x)$  are the hyperbolic trigonometric functions.

**Fig. 6.20** Modified Bessel functions of the first kind,  $I_m(x)$ , are the radial solutions to  $(\nabla^2 - \gamma^2) I_m(x) = 0$  and the second kind,  $K_m(x)$ , that are solutions to  $(\nabla^2 + \gamma^2) K_m(x) = 0$ . Unlike the Bessel functions in Fig. 6.8 or the Neumann functions in Fig. 6.9, the values of the modified Bessel functions are not oscillatory functions of their arguments



The modified Bessel functions are related to the Bessel functions with purely imaginary arguments:  $I_m(x) = j^{-m} J_m(jx)$ . Bessel functions with imaginary arguments are the solution to a Bessel equation like Eq. (6.28), but with different signs [2].

$$\frac{d^2R}{dr^2} + \frac{1}{r} \frac{dR}{dr} - \left( k^2 + \frac{m^2}{r^2} \right) R = 0 \quad (6.86)$$

Unlike ordinary Bessel functions, the modified Bessel functions are not oscillatory but are monotonically increasing or decreasing functions of their arguments. This is also true of the hyperbolic trigonometric functions. Graphs of  $I_0(x)$ ,  $I_1(x)$ ,  $K_0(x)$ , and  $K_1(x)$  are provided in Fig. 6.20.

The second set of solutions to Eq. (6.86) is represented as  $K_m(x)$ , and their values, like those of the Neumann functions, are infinite at the origin. For a solid disk, the  $K_m(x)$  solutions will be rejected, but they will be required for calculation of the displacement and normal mode frequencies of annular disks [27]. The properties of the  $I_m(x)$  are similar to those of  $J_m(x)$  in Appendix C. Some of those most useful properties are reproduced below:

$$\begin{aligned} I_{m-1}(x) - I_{m+1}(x) &= \frac{2m}{x} I_m(x) \\ \frac{d}{dx} I_m(x) &= \frac{1}{2} [I_{m-1}(x) + I_{m+1}(x)] \quad \text{and} \quad \frac{d}{dx} I_0(x) = I_1(x) \\ \int x I_0(x) dx &= x I_1(x) \quad \text{and} \quad \int I_1(x) dx = I_0(x) \end{aligned} \quad (6.87)$$

It is worthwhile to notice that although these are similar to the Bessel function relations, they are not identical. The sign of the terms in the recurrence relation and most of the derivative and integral relations are reversed when applied to the modified Bessel functions.

#### 6.4.1 Normal Modes of a Clamped Circular Plate

The general solution to Eq. (6.84) for a thin disk will be the superposition of the Bessel and the modified Bessel solutions.

**Table 6.6** Quantized values of  $\gamma_{m,n} a$  that determine the normal mode frequencies of a thin disk,  $t \ll a$ , that is clamped at its outer radius,  $r = a$ . For larger values of  $n$ ,  $\gamma_{m,n} a \cong \pi[(m/2) + n]$

$m$	$n = 1$	$n = 2$	$n = 3$	$n = 4$
0	3.19622	6.30644	9.43949	12.57713
1	4.61090	7.79927	10.95806	14.10862
2	5.90568	9.19688	12.41188	15.57949
3	7.14353	10.53667	13.66009	17.00529
4	8.34662	11.83672	15.14987	18.39595

$$\mathbf{z}(r, \theta, t) = [AJ_m(\gamma r) + BI_m(\gamma r)] \begin{Bmatrix} \cos(m\theta) \\ \sin(m\theta) \end{Bmatrix} e^{j\omega t} \quad (6.88)$$

For a disk that is clamped at  $r = a$ ,  $z(a) = 0$  and  $[dz/dr]_r = a = 0$ . Imposition of the first boundary condition sets the ratio of contributions of the  $J_m(\gamma r)$  and  $I_m(\gamma r)$  solutions.

$$\frac{B}{A} = -\frac{J_m(\gamma a)}{I_m(\gamma a)} \quad (6.89)$$

This ratio remains finite because  $I_m(x) > 0$  for all  $x > 0$ .

The restriction on the slope at  $r = a$  will quantize the values of  $\gamma$ .

$$I_m(\gamma_{m,n} a) \left[ \frac{d}{dr} J_m(\gamma_{m,n} r) \right]_a - J_m(\gamma_{m,n} a) \left[ \frac{d}{dr} I_m(\gamma_{m,n} r) \right]_a = 0 \quad (6.90)$$

That equation can be transformed by use of the relationships in Appendix C for the Bessel functions and for the modified Bessel functions in Eq. (6.87). The result for the radially symmetric,  $m = 0$ , modes is particularly simple.

$$\begin{aligned} \frac{J_0(\gamma_{0,n} a)}{J_1(\gamma_{0,n} a)} &= -\frac{I_0(\gamma_{0,n} a)}{I_1(\gamma_{0,n} a)} \quad \text{for } m = 0 \\ \frac{J_m(\gamma_{m,n} a)}{I_m(\gamma_{m,n} a)} &= \frac{J_{m-1}(\gamma_{m,n} a) - J_{m+1}(\gamma_{m,n} a)}{I_{m-1}(\gamma_{m,n} a) + I_{m+1}(\gamma_{m,n} a)} \quad \text{for } m \geq 1 \end{aligned} \quad (6.91)$$

Solutions to Eq. (6.91) for small values of  $m$  and  $n$  are provided in Table 6.6 to five-digit accuracy, following the recommendation of Gabrielson [27].

$$f_{m,n} = \frac{(\gamma_{m,n} a)^2}{2\pi a^2 \sqrt{12(1 - \nu^2)}} c_B t \quad (6.92)$$

The normal mode frequencies for other values of  $m$  and  $n$  and for plates of other shapes (e.g., rectangular plates) are available in the excellent compendium by Leissa [28].

The complete solution for the transverse displacements of a thin disk vibrating in one of its normal modes can be written based on Eq. (6.88) using Eq. (6.89).

$$\mathbf{z}_{m,n}(r, \theta, t) = C_{m,n} \left[ J_m(\gamma_{m,n} r) - \frac{J_m(\gamma_{m,n} a)}{I_m(\gamma_{m,n} a)} I_m(\gamma_{m,n} r) \right] \begin{Bmatrix} \cos(m\theta) \\ \sin(m\theta) \end{Bmatrix} e^{j\omega_{m,n} t} \quad (6.93)$$

Following our previous focus on the fundamental (0, 1) normal mode, due to its dominance for coupling to a surrounding fluid medium, the effective piston area,  $A_{eff}$ , can be calculated by integration of Eq. (6.93) over the disk's surface.

$$A_{eff} = \int_0^a \left[ J_0(\gamma_{0,1}r) - \frac{J_0(\gamma_{0,1}a)}{I_0(\gamma_{0,1}a)} I_0(\gamma_{0,1}r) \right] 2\pi r dr \quad (6.94)$$

Again, letting  $x = \gamma_{0,n} r$ ,  $r = x/\gamma_{0,n}$ , and  $dr = dx/\gamma_{0,n}$ , the integration is simplified by use of Eqs. (6.87) and (6.42).

$$\frac{A_{eff}}{\pi a^2} = \frac{2}{(\gamma_{0,1}a)} \left[ J_1(\gamma_{0,1}a) - \frac{J_0(\gamma_{0,1}a)}{I_0(\gamma_{0,1}a)} I_1(\gamma_{0,1}a) \right] = 0.3289 \quad (6.95)$$

For the (0, 1) mode,  $\gamma_{0,1}a = 3.19622$ ,  $J_1(\gamma_{0,1}a) = 0.262861$ ,  $J_0(\gamma_{0,1}a)/I_0(\gamma_{0,1}a) = -0.05571$ , and  $I_m(\gamma_{0,1}a) = 4.71815$ , making  $A_{eff}/\pi a^2 = 0.3289$ . This is less than the result for a circular membrane because the disk must approach the boundary at  $r = a$ , with zero slope as well as zero displacement. The equivalent displacement that would produce the same volume velocity for a rigid piston of area,  $\pi a^2$ , can be expressed in terms of the maximum displacement at the disk's center,  $z_{max}$ . The displacement of the disk's center, using Eq. (6.93), for the (0, 1) mode is  $z(0) = 1.05571 C_{0,1}$ .

$$\frac{\langle z \rangle_{eff}}{z_{max}} = \frac{1}{1.0557} \frac{A_{eff}}{\pi a^2} = 0.312 \quad (6.96)$$

## 6.5 Flatland

This chapter has provided a glimpse into the similarities and differences between one-dimensional and two-dimensional vibrating systems. A two-dimensional membrane or plate requires two integer indices to specify each normal mode of vibration. The number of such modes within a fixed frequency interval increases as the center frequency of that interval increases, even though the width of the interval remains constant. As with a string, a membrane with negligible flexural rigidity that is placed under tension was described by a second-order differential equation, but a rigid bar or a plate, with displacements that were restored by stiffness, obeyed a fourth-order differential equation.

The string and membrane were also driven in different ways. The string was driven by the application of a force or a displacement at a point. The membrane was driven by the application of a uniform pressure difference across its surface. Solutions for the pressure-driven membrane facilitated the analysis of the condenser microphone. The effect of gas stiffness in providing an additional restoring force to that of the membrane's tension was incorporated by assuming that the gas trapped behind the membrane was compressing and expanding adiabatically or isothermally, depending upon the proximity of solid surfaces. A much more systematic analysis of the ideal gas laws will be presented in the next chapter.

### Talk Like an Acoustician

Laplacian operator	Gas stiffness
Helmholtz equation	Polytropic coefficient
Separation condition	Inhomogeneous differential equation
Degenerate modes	Particular solution
Mode splitting	Condenser microphone
Modal density	Permittivity of free space
Periodic boundary condition	Polarizing voltage
Bessel functions	Electrostatic potential energy
Neumann functions	Paschen's law
<i>k</i> -space	Open-circuit microphone sensitivity

**Fig. 6.21** Nobel Prize-winning physicist Richard P. Feynman, playing his favorite alto Solomongo [31]



Reciprocal space  
Compactness criterion  
Volume velocity

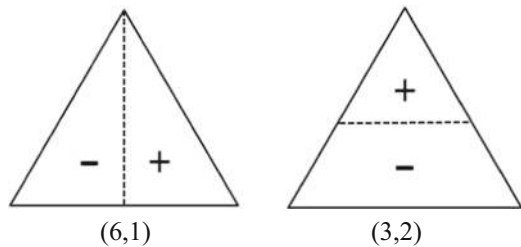
Electret microphone  
Vibrating reed electrometer  
Modified Bessel functions

## Exercises

1. **Mass-loaded square membrane.** A square membrane with  $L_x = L_y = 30.0$  cm has a mass of 10.0 gm and its fundamental normal mode frequency,  $f_{1,1} = 100.0$  Hz.
    - (a) *Tension per unit length.* What is the tension per unit length to which the membrane was stretched?
    - (b) *Split degeneracy.* If a mass,  $M = 1.0$  gm, is placed as shown in Fig. 6.3, what are the frequencies of the  $f_{1,2}$  and the  $f_{2,1}$  modes.
  2. **Modes of the baritone Solomongo.** Biblical legend has it that King Solomon, while walking through his kingdom, came across two young boys who were arguing over a drum that both wanted to play and neither wanted to share. Buoyed by his recent success in the resolution of a dispute between two women claiming to be the mother of one baby, the wise king told the boys that he would split the drum and each could keep half. The boys responded: “לְכִי הַזְדִיָּן,”<sup>26</sup> They then laughed uncontrollably. Dismayed by the boys’ response, the wise king instructed one of his guards to cut the boys’ drum in half. After a respectable interval, the boys attached planks to the half-drum bodies to close them and carefully smoothed the junction between the half-drum and the sealing plank to remove any rough edges that could rip the membrane. They then stretched a goat skin membrane over the half-drums.
- Such percussion instruments are now known as Solomongos (rhymes with bongos) and have become popular worldwide because they allow the hands to be positioned in the same way as one

<sup>26</sup>Loosely translated, the boys said, “Your royal highness, please leave us in peace and as you depart perform a miracle that would otherwise be anatomically impossible.”

**Fig. 6.22** Two sample mode shapes for the equilateral triangular membrane



would play a keyboard instrument as shown in Fig. 6.21. The baritone, with membrane diameter,  $D = 60$  cm, is particularly popular, since it can radiate intricate rhythmic patterns generated by tapping of finger tips but when struck with the palm of the hand produces heart-throbbing bass that is radiated from the half-drum's opening at the bottom.

- (a) *Fundamental mode frequency.* If the thickness of the goat skin is 1.2 mm and the average mass density of the skin is  $1200 \text{ kg/m}^3$ , what is the frequency of the fundamental mode if the total tension applied by the tuning straps is 500 N?
- (b) *Modal frequencies.* What are the mode numbers and frequencies of the next five lowest-frequency modes using mode numbering of a full circular membrane?
- (c) *Effective piston area.* Express the equivalent piston area,  $\langle A \rangle$ , for a Solomongo vibrating in its fundamental mode in terms of the maximum transverse displacement of the membrane,  $z_{\max}$ . At what radial distance from the center of the Solomongo's straight edge does the maximum displacement occur?
3. **Mode number approximation.** Determine the number of modes with normalized frequencies,  $f_m/nf_{1,1} \leq 5$ , predicted by Eq. (6.15) for the rectangular membrane with  $L_x = 3L_y/2$ . Compare your result with the exact result in Table 6.1,  $N(f_{5,5}) = 34$ , by calculating the percent difference between two determinations.
4. **Density of modes.** A rigidly clamped rectangular membrane is 10.0 cm wide and 14.1 cm long, with a transverse wave speed of 50 cm/s.
  - (a) How many modes could be excited by a band-limited noise source which has a frequency range of  $70 < f < 80$  Hz?
  - (b) How many modes could be excited by a band-limited noise source which has a frequency range of  $145 < f < 155$  Hz?
5. **Relative radii of nodal circles.** Calculate the relative radii,  $r/a$ , for the nodal circles for the six modes which have nodal circles in Fig. 6.10. The modes in the middle column will have one nodal circle in addition to the node that exists at  $r/a = 1$ . The modes in the right-hand column will have two nodal circles.
6. **Triangular membrane mode shapes.** Using diagrams like those in Fig. 6.22, sketch the approximate mode shapes for the ten lowest-frequency modes given in Table 6.4 for the membrane that is an equilateral triangle.
7. **Number of modes for a triangular membrane.** Equation (6.15) approximated the number of modes below a given frequency  $N_{rect}(f_{m,n})$  based on the area and half the perimeter of the rectangular membrane. Using the area and the half-perimeter of a circular membrane, that expression was modified to estimate the number of modes of a circular membrane,  $N_{circ}(f_{m,n})$ , in Eq. (6.34). Both expressions were successful in predicting the number of modes to within a few percent. Modify Eq. (6.15) to accommodate the area and half-perimeter of the equilateral triangle, and compare the predictions of this approximation to the ten lowest-frequency normal modes for the equilateral triangle provided in Table 6.4.

- 8. Kinetic energy of vibration.** Show that the maximum kinetic energy of a circular membrane of radius,  $a$ , oscillating in its fundamental (0, 1) mode at frequency,  $f_{0,1}$ , is correctly expressed in terms of the maximum displacement of its center,  $z_{\max}$  and  $\rho_S$ , in Eq. (6.97).

$$(KE)_{\max} = 0.135 \pi a^2 \rho_S (2\pi f_{0,1} z_{\max})^2 \quad (6.97)$$

- 9. Modes of a latex diaphragm.** A rigidly clamped 20.0-cm-diameter latex sheet is  $0.010'' = 254$  micron thick. When vibrating in its fundamental mode,  $f_{0,1} = 50.0$  Hz.
- Mass.* If the density of latex is  $\rho = 960$  kg/m<sup>3</sup>, what is the mass of the membrane?
  - Tension.* What is the membrane's tension per unit length?
  - Unperturbed modal frequencies.* What are the frequencies and mode numbers of the next five normal modes?
  - Small mass perturbation.* If a small piece of putty with mass,  $M = 0.20$  gm, is stuck to the center of the membrane, by how much is each of the frequencies of the fundamental and the next five modes changed? Report your results for parts (c) and (d) in a table with the mode numbers, unperturbed frequencies, and perturbed frequencies.
  - Large lumped-mass loading.* If the putty of part (d) above is removed and two magnetic disks, each with a mass of 10.0 gm and a diameter of 4.0 cm, are attached to the top and bottom of the membrane, what will be the frequency of the lowest-frequency normal mode?
- 10. Pressure-driven rectangular membrane.** Calculate the area-averaged displacement of a rectangular membrane driven by a time-harmonic excess pressure acoustic,  $\delta p(t) = \Re e[\tilde{p}e^{j\omega t}]$ , in a fluid that is applied to one surface of the membrane, assuming that  $c_{\text{fluid}} \gg c = (\Im/\rho_S)^{1/2}$  and  $\omega \ll 2\pi f_{1,1}$ .
- 11. Kettledrum.** The circular membrane of a tympani has a diameter of 50.0 cm and a total mass of 31.4 gm and is stretched to a tension per unit length of  $\Im = 10,000$  N/m.
- Transverse wave speed.* What is the speed of transverse waves on the membrane, ignoring the gaseous restoring force?
  - Fundamental frequency.* Determine the fundamental frequency,  $f_{0,1}$ , for the membrane if the volume of the kettle were infinite (i.e., calculate the frequency assuming there is no gas stiffness).
  - Kettle volume.* If the kettle volume,  $V_o$ , raises the frequency by a factor of 1.27, what is the volume of the kettle? How does this volume compare to the volume of a hemisphere with a diameter that is the same as the membrane?
- 12. Condenser microphone lumped-element model.** Using the low-frequency parabolic approximation for the deflection of the microphone's membrane, subject to a uniform pressure difference, given in Eq. (6.58), the transverse deflection can be expressed in terms of the maximum deflection,  $z_{\max} = z(0) = a^2(\delta p)/4\Im$ .

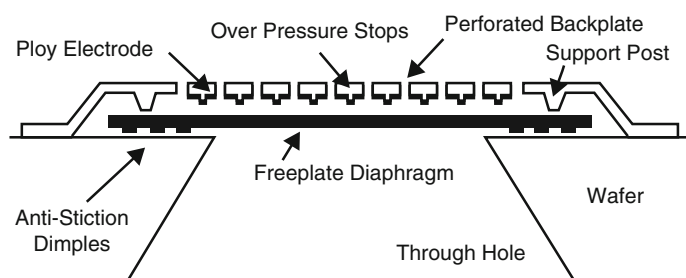
$$z(r) = z(0) \left( 1 - \frac{r^2}{a^2} \right) \quad \text{for } 0 \leq r \leq a \quad (6.98)$$

- Effective area.* Calculate the effective piston area,  $A_{\text{eff}}$ , of the membrane, and express your result as a fraction of the membrane's area,  $\pi a^2$ .
- Effective mass.* Determine the effective moving mass,  $m_{\text{eff}}$ , of the membrane by calculating the membrane's kinetic energy. Compare the effective mass to the membrane's physical mass.
- Effective stiffness.* The potential energy,  $PE$ , stored in the microphone's membrane can be calculated by integrating the work done by the force produced by the excess pressure times

the membrane's displacement over the membrane's area,  $dW = (\delta p \cdot 2\pi r dr) dz$ . Show that  $K_{eff} = 2\pi \Im$  by setting  $PE = \frac{1}{2}[K_{eff} z(0)^2]$ .

- (d) *Fundamental mode frequency.* Using the effective mass and the effective stiffness, calculate the lumped-element approximation to the frequency of the lowest-frequency normal mode,  $\omega_{0,1} = \sqrt{K_{eff}/m_{eff}}$ , and then compare your result to the exact result using the Bessel function result of Eq. (6.33).
  - (e) *Damping.* Determine the mechanical resistance,  $R_m$ , necessary to make the membrane's quality factor  $Q = 2$  using the lumped-element model.
  - (f) *Resonance response.* What is the response relative to the low-frequency value for the microphone at  $f_{1,0}$  with  $Q = 2$ ?
  - (g) *Bandwidth.* Determine the frequency below  $f_{1,0}$  at which the microphone's response exceeds the low-frequency value by 1.0 dB. Report your answer in terms of  $f_{1,0}$ .
  - (h) *High-frequency extended response.* Determine the frequency relative to  $f_{1,0}$  at which the microphone's response is  $-1.0$  dB relative to the low-frequency value above  $f_{1,0}$ . Report your answer in terms of  $f_{1,0}$ .
13. **Condenser microphone with a stretched stainless-steel diaphragm.** The 0.2% yield strength of stainless-steel alloy 316 at room temperatures is 290 MPa, and its mass density is  $\rho = 7990 \text{ kg/m}^3$ . A condenser microphone diaphragm made from that alloy has a diameter of 3.0 cm and is 0.001" (25 microns) thick.
- (a) *Maximum tension/length.* Calculate the tension per unit length that would stretch the stainless to its 0.2% yield limit.
  - (b) *Transverse wave speed.* Calculate the transverse wave speed of the diaphragm when stretched to its 0.2% limit.
  - (c) *Fundamental frequency.* Calculate the fundamental normal mode frequency  $f_{0,1}$  for that diaphragm.
  - (d) *Open-circuit sensitivity.* If a backplate of optimum radius is placed 25 microns from the diaphragm and is polarized by  $V_{bias} = 200 \text{ V}_{dc}$ , what will be the low-frequency (i.e.,  $ka < 1$ ) sensitivity of this microphone? Report your result in both  $\text{V/Pa}$  and in dB re: 1 V/Pa.
14. **Altec-Lansing Model 21C microphone.** This condenser microphone used a  $\frac{1}{2}"$  diameter,  $50 \mu\text{m}$  thick glass plate (fused silica,  $\text{SiO}_2$ ) as the diaphragm, instead of a stretched membrane. The glass plate has a sputtered gold coating to make it electrically conductive. If the Young's modulus of glass is 73.1 GPa and its shear modulus is 31.2 GPa, what is the lowest resonance frequency of the plate if it is clamped at its boundary?
15. **MEMS microphone.** Knowles Acoustics marketed the first commercial microelectromechanical systems (MEMS) silicon diaphragm miniature surface-mount SiSonic® microphone, shown schematically in Fig. 6.23, in 2003 [29].

**Fig. 6.23** Schematic cross-sectional diagram of a MEMS microphone [30]



The diaphragm is  $t = 1.0 \mu\text{m}$  thick, has an effective diameter of  $500 \mu\text{m}$ , and is made of polycrystalline silicon (polysilicon) with  $E = 169 \text{ GPa}$  and  $\nu = 0.22$  [30].

- (a) *Fundamental mode frequency.* Calculate the frequency,  $f_{0,1}$ , of the lowest purely radial normal mode, assuming that the boundary is clamped.
- (b) *Diaphragm thickness.* Based on the density of polysilicon,  $\rho_{Si} = 2.33 \text{ gm/cm}^3$ , and the atomic mass of silicon,  $M_{Si} = 28.08 \text{ a.m.u.}$ , express  $t$  in terms of the number of atoms.

## References

1. E. Jahnke, F. Emde, *Tables of Functions with Formulae and Curves*, 4th edn. (Dover, New York, 1945)
2. M. Abramowitz, I.A. Stegun, *Handbook of Mathematical Functions with Formulas, Graphs and Mathematical Tables*, Nat'l. Bur. Standards – Applied Mathematics Series #55 (U.S. Department of Commerce, National Bureau of Standards, Washington, DC, 1964)
3. M. Greenspan, Simple derivation of the Boltzmann-Ehrenfest adiabatic principle. *J. Acoust. Soc. Am.* **27**(1), 34–35 (1955)
4. E.C. Wente, A condenser transmitter as a uniformly sensitive instrument for the absolute measurement of sound intensity. *Phys. Rev.* **10**, 39–63 (1917)
5. H.L.F. Helmholtz, *On the Sensation of Tone as a Physiological Basis for the Theory of Music* (Longmans & Co, London, 1885). See Ch. III – Analysis of musical tones by sympathetic resonance. Reprinted Dover, 1954; ISBN 0-486-60753-4
6. J. Tyndall, *Sound*, 7th edn. (Longmans, Green, and Co, London, 1898), pp. 236–282, see Lecture VI – Singing Flames
7. J. Zuckerwar, Theoretical response of condenser microphones. *J. Acoust. Soc. Am.* **64**(5), 1278–1285 (1978)
8. J. Zuckerwar, Principles of operation of condenser microphones, in *AIP Handbook of Condenser Microphones*, ed. by G. S. K. Wong, T. F. W. Embleton, (American Institute of Physics, New York, 1995). See Chapter 3: ISBN 1-56396-284-5
9. H.W. Baerwald, The absolute noise level of microphones. *J. Acoust. Soc. Am.* **12**(1), 131–139 (1940)
10. J.D. Combine, *Gaseous Conductors: Theory and Engineering Application* (McGraw-Hill, New York, 1941), reprinted (Dover, 1958)
11. F. Paschen, Ueber die zum Funkenübergang in Luft, Wasserstoff und Kohlensäure bei verschiedenen Drucken erforderliche Potentialdifferenz (On the potential difference required for spark initiation in air, hydrogen, and carbon dioxide at different pressures). *Ann. Phys.* **273**(5), 69–75 (1889)
12. T.W. Dakin, D. Berg, Theory of gas breakdown, in *Progress in Dielectrics*, ed. by J. B. Berks, J. Hart, vol. 4, (Wiley, New York, 1962), pp. 152–198
13. R.S. Dhariwal, J.-M. Torres, M.P.Y. Desmulliez, Electric field breakdown at micrometre separations in air and nitrogen at atmospheric pressure. *IEE Proc. Sci. Meas. Technol.* **147**(5), 261–265 (2000)
14. M.S. Hawley, F.F. Romanow, J.E. Warren, The Western electric 640AA capacitance microphone: Its history and theory of operation, in *AIP Handbook of Condenser Microphones*, ed. by G. S. K. Wong, T. F. W. Embleton, (American Institute of Physics, New York, 1995). See Chapter 2; ISBN 1-56396-284-5
15. G.M. Sessler, J.E. West, D.A. Berkley, G. Morgenstern, Determination of spatial distribution of charges in thin dielectrics. *Phys. Rev. Lett.* **38**(7), 368–371 (1977)
16. G.M. Sessler, J.E. West, Production of high quasi permanent charge densities on polymer foils by application of breakdown fields. *J. Appl. Phys.* **43**(3), 922–926 (1972)
17. G.M. Sessler, J.E. West, Electret transducers: A review. *J. Acoust. Soc. Am.* **53**(6), 1589–1600 (1973)
18. P.W. Chudleigh, Mechanism of charge transfer to a polymer surface by conducting liquid contact. *J. Appl. Phys.* **47** (10), 4475–4483 (1976)
19. G.M. Sessler, Physical principles of electrets, in *Electrets*, ed. by G. M. Sessler, (Springer, New York, 1987); See §2.2.4 (Charging with liquid contact). ISBN 978-3-540-17335-9
20. P. Horowitz, W. Hill, *The Art of Electronics*, 2nd edn. (Cambridge University Press, New York, 1989). See Chapter 3
21. G.W. Elko, K.P. Harney, A history of consumer microphones: The electret condenser microphone meets the micro-electro-mechanical systems. *Acoust. Today* **5**(2), 4–13 (2009)
22. S.L. Garrett, S. Adams, S. Putterman, I. Rudnick, Resonant nonlinear mode conversion in He II. *Phys. Rev. Lett.* **41** (6), 413–416 (1978)
23. H. Palevsky, R.K. Swank, R. Grenchik, Design of dynamic condenser electrometers. *Rev. Sci. Instrum.* **18**(5), 298–314 (1947)

24. G. Rietveld, H.E. van den Brom, Vibration reed electrometer for accurate measurement of electrical currents below 10 pA. *IEEE Trans. Instrum. Meas.* **56**(2), 559–563 (2007)
25. E. Polturak, S.L. Garrett, S.G. Lipson, Precision acoustic gas analyzer for binary gas mixtures. *Rev. Sci. Instrum.* **57** (11), 2837–2841 (1986)
26. L.D. Landau, E.M. Lifshitz, *Elasticity* (Pergamon, 1970). See §12; ISBN 0 08 006465 5
27. T.B. Gabrielson, Frequency constants for transverse vibration of annular disks. *J. Acoust. Soc. Am.* **105**(6), 3311–3317 (1999)
28. W. Leissa, *Vibration of Plates*, NASA Report SP-160 (U.S. Government Printing Office, Washington, DC, 1969). reprinted by the Acoustical Society of America, 1993; ISBN 1-56396-294-2
29. P. Loeppert and S. B. Lee SiSonic™ – The first commercialized MEMS microphone. Solid-State Sensors, Actuators, and Microsystems Workshop, Hilton Head, June 4–8, 2006
30. W.N. Sharpe Jr., B. Yuan, R. Vaidyanathan, R.L. Edwards, Measurement of Young's modulus, Poisson's ratio, and tensile strength of polysilicon, in *Proceedings of the 10th International Workshop on Microelectromechanical Systems*, (Nagoya, Japan, 1997), pp. 424–429
31. R.P. Feynman, R.B. Leighton, M. Sands, Introduction, in *The Feynman Lectures on Physics*, vol. I, (Addison-Wesley, Reading, 1963)

**Open Access** This chapter is licensed under the terms of the Creative Commons Attribution 4.0 International License (<http://creativecommons.org/licenses/by/4.0/>), which permits use, sharing, adaptation, distribution and reproduction in any medium or format, as long as you give appropriate credit to the original author(s) and the source, provide a link to the Creative Commons license and indicate if changes were made.

The images or other third party material in this chapter are included in the chapter's Creative Commons license, unless indicated otherwise in a credit line to the material. If material is not included in the chapter's Creative Commons license and your intended use is not permitted by statutory regulation or exceeds the permitted use, you will need to obtain permission directly from the copyright holder.



---

**Part II**

**Waves in Fluids**



# Ideal Gas Laws

7

## Contents

7.1	<b>Two Ways of Knowing—Phenomenology and Microscopics</b> .....	334
7.1.1	Microscopic Models .....	336
7.1.2	Phenomenological Models .....	338
7.1.3	Adiabatic Equation of State for an Ideal Gas .....	341
7.1.4	Adiabatic Temperature Change .....	342
7.2	<b>Specific Heats of Ideal Gases</b> .....	343
7.2.1	Monatomic (Noble) Gases .....	344
7.2.2	Polyatomic Gases .....	344
7.3	<b>The Fundamental Equations of Hydrodynamics</b> .....	347
7.3.1	The Continuity Equation .....	348
7.3.2	The Navier-Stokes (Euler) Equation .....	349
7.3.3	The Entropy Equation .....	351
7.3.4	Closure with the Equation of State .....	352
7.4	<b>Flashback</b> .....	352
	<b>References</b> .....	356

In Part II, our description of fluid behavior differs from our description of the dynamics of masses and springs, strings, bars, and two-dimensional vibrating surfaces. In Part I, it was reasonable to identify the coordinates of a specific point on such a vibrating system and write an equation for the time evolution of that point based on Newton's Second Law of Motion and some description of the appropriate elastic restoring force. With fluids, it is rare that we identify a "specific point" in the fluid and try to track the motion of that parcel of fluid. [1] With fluidic systems (gases, liquids, and plasmas), we generally adopt a different perspective, since it is inconvenient (and frequently impossible) to identify a specific "fluid particle" and track its flow under the influences of various forces and the constraints of boundaries.

Instead, we choose to identify a differential volume,  $dV = dx dy dz$ , specified in coordinates ( $x$ ,  $y$ , and  $z$ ) that are fixed in our laboratory frame of reference, while calculating the changes in the properties of the fluid within that differential volume (e.g., pressure, density, temperature, enthalpy, fluid velocity, mixture concentration, void fraction, dielectric polarization) as we keep track of the amount of fluid that enters or leaves that (fixed in space) differential volume. The fact that we no longer choose to identify individual fluid parcels requires the introduction of a mass conservation equation (also

known as the continuity equation), in addition to our dynamical equation (Newton's Second Law) and our constitutive equation (Hooke's Law or some other equation of state).

When writing those three equations of fluid dynamics, which are expressed in coordinates specified in the laboratory frame of reference (rather than tracking a specific parcel of fluid), such equations are called Eulerian, after the great Swiss scientist and mathematician, Leonard Euler (1707–1783). In the case of sound waves in fluids, this is consistent with the way we would ordinarily make acoustic measurements in a fluid. Typically, a microphone or hydrophone or thermocouple or anemometer would be placed in a fixed position so we would like be able to interpret the pressures, velocities, and temperatures measured at that fixed location as the fluid moves to and fro.

There are special circumstances that allow the experimentalist to track a specific parcel of fluid by injecting a dye in a liquid or seeding a gas with small particles (e.g., smoke [1]) that move with the fluid. In such cases, that perspective is called Lagrangian, after Joseph-Louis Lagrange (1736–1813).<sup>1</sup> With only very rare exception, our development and application of the hydrodynamic equations will take the Eulerian perspective.

The goal of Part II is to provide the tools to make predictions for fluid (liquid or gaseous) systems supporting wave-like disturbances that make such fluids depart from their state of static equilibrium. In this textbook, our focus will be on relatively small disturbances from equilibrium. For sound waves in air at atmospheric pressure, which are capable of creating permanent damage to your hearing with less than 15 min of exposure per day in a work environment [2], that acoustic pressure level (115 dB<sub>SPL</sub>) corresponds to a peak excess pressure of only 16 Pa ( $1 \text{ Pa} = 1 \text{ N/m}^2$ ). Since “standard” atmospheric pressure is 101,325 Pa [3], that potentially hazardous sound level corresponds to a relative deviation from equilibrium that is less than 160 parts per million (ppm) or 0.016%.

---

## 7.1 Two Ways of Knowing—Phenomenology and Microscopics

*“If, in some cataclysm, all of the scientific knowledge were to be destroyed, and only one sentence passed on to the next generations of creatures, what statement would contain the most information in the fewest words? I believe it is the atomic hypothesis; that all things are made of atoms.”*

R. P. Feynman (1918–1988) [4]

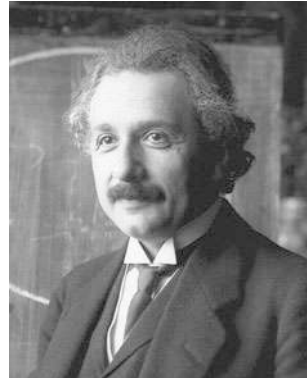


---

<sup>1</sup> Lagrange, who was of French/Italian descent (born Giuseppe Lodovico Lagrangia), was one of Euler's doctoral students. Euler recommended that Lagrange succeed him as the Director of Mathematics at the Prussian Academy of Sciences in Berlin.

*“Thermodynamics is the true testing ground of physical theory because its results are model independent. It is the only physical theory of universal content which I am convinced will never be overthrown, within the framework of applicability of its basic concepts.”*

A. Einstein (1879–1955)



Scientists and engineers have a very rigorous definition of what constitutes “knowing.” Fundamentally, scientific knowledge relies on testable hypotheses that can be verified (or falsified) experimentally and that have successfully withstood many such tests. If we say that we understand any given process or phenomenon, we mean that we can express that understanding using mathematics and we can make a quantitative calculation based on those mathematical expressions that will predict the outcome of a particular process or a specific situation, even if that device never existed or the process has never before been observed. Furthermore, our “understanding” permits us to estimate the uncertainty limits of those predictions (see Sect. 1.8). When that new process is executed, or that new device is created, the measured outcome or performance will have the predicted value within the predicted limits, if we have “understanding.”

As mentioned in the Preface, the mathematical understanding must be supplemented by a “clear and intuitively satisfying narrative.” When we have that, along with the predictive mathematics, we can usually intuit qualitative predictions before we make quantitative predictions; the qualitative and quantitative understandings provide a check on each other.

*“It is always easier to do a calculation if you already know the result.”* I. Rudnick

Scientists have two fundamentally different ways of understanding natural phenomena on the scale sizes of human interest. These scales typically range from the “microscale,” characterized by devices that have dimensions that are on the order of microns ( $1 \text{ micron} = 1 \mu\text{m} = 10^{-6} \text{ m}$ ), to the “macroscale,” such as the Earth’s oceans and atmosphere, that have characteristic length scales in the thousands of kilometers ( $10^6 \text{ m}$ ). Although these concepts also apply on galactic scales, we usually call those people who are interested in galactic-scale phenomena cosmologists, astronomers, or astrophysicists,<sup>2</sup> not acousticians.

---

<sup>2</sup> Acoustics is particularly important to cosmologists. For the first 300,000 years after the “Big Bang,” all matter was ionized and therefore opaque to electromagnetic radiation. The only “channel” for wave propagation was acoustical. The residual cosmic background radiation is still evident with the “lumpiness” in the distribution of matter observed in the universe today that came from the time when those sound waves were “frozen” into the distribution of neutral matter: <http://www.astro.ucla.edu/~wright/CMB-DT.html>.

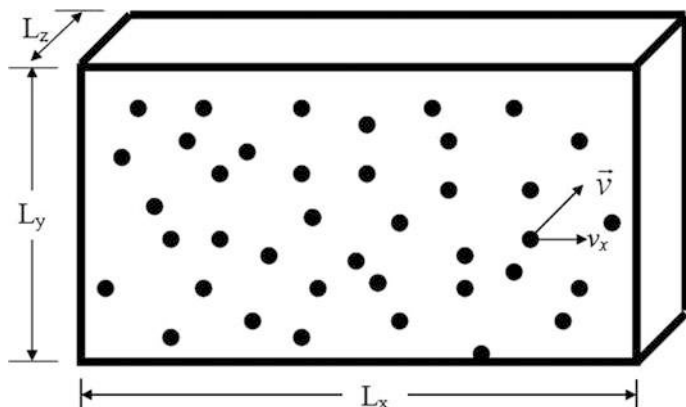
### 7.1.1 Microscopic Models

One type of this rigorous “understanding” is expressed in the first quotation that started this section: “All matter is composed of atoms.” We derive our understanding from that atomic perspective by combining the properties of those atoms with our knowledge of the interaction between those atoms. By averaging those interactions over large numbers of atoms, using the techniques of statistical mechanics,<sup>3</sup> we can produce expressions for the behavior of bulk matter summarized by mathematical statements like the *Ideal Gas Law*, to relate stresses (pressure changes) to strains (density changes) as we did with the moduli of elasticity that characterized the elastic behavior of solids in Chap. 4. In this chapter, the kinetic theory of gases and the Equipartition Theorem (see Sect. 2.4.4) will be applied to the equation of state and to ball-and-stick models of molecules to provide some intuition about the acoustical properties and behaviors of gases.

The simplest application of this approach is the use of the *kinetic theory of gases* to derive the Ideal Gas Law. We start by considering a rectangular container with rigid walls that define a closed volume,  $V = L_x L_y L_z$ , containing  $N$  atoms of a *monatomic gas* (e.g., helium or argon), as shown schematically in Fig. 7.1. We can regard those atoms as *point particles*, lacking an internal structure (unlike a molecule), each with mass,  $m$ , that can collide elastically<sup>4</sup> with each other and scatter off of the rigid walls of the container.

If we focus our attention on a single atom that is moving with vector velocity,  $\vec{v}$ , we can calculate the momentum change for the  $x$  component of momentum,  $\Delta P_x = 2mv_x$ , when that atom collides with the wall perpendicular to the  $x$  axis and rebounds. Using Newton’s Second Law of Motion, we know that the normal force on the wall,  $F_x$ , is proportional to the time rate of change of momentum. To calculate that rate, we need to know how many times that atom collides with the right wall per unit time. Since the projection of the atom’s speed in the  $x$  direction is  $v_x$ , it will collide with the right wall every  $2L_x/v_x$  seconds. The pressure exerted by that atom on that wall,  $p_x$ , is the ratio of that force,  $F_x$ , to the area of that wall,  $A_x = L_y L_z$ .

**Fig. 7.1** Schematic representation of a gas of “point particles” confined to a volume,  $V = L_x L_y L_z$ . The velocity,  $\vec{v}$ , of one particle is indicated by the vector which has a projection in the  $x$  direction of  $v_x$



<sup>3</sup> The principles and methods of statistical mechanics are treated clearly and systematically at the advanced undergraduate level in the textbook by Fred Reif, *Fundamentals of Statistical and Thermal Physics* (McGraw-Hill, 1965); ISBN 07-051800-9.

<sup>4</sup> In an elastic collision, no energy is dissipated.

$$p_x = \frac{F_x}{A_x} = \frac{1}{L_y L_z} \frac{\Delta P_x}{\Delta t} = \frac{1}{L_y L_z} \frac{2mv_x^2}{(2L_x/v_x)} = \frac{mv_x^2}{V} \quad (7.1)$$

If we recognize  $mv_x^2$  as being twice the kinetic energy of that point particle associated with the  $x$ -direction degree of freedom of that particle's motion, then we can use the *Equipartition Theorem* (see Sect. 2.4.4) to relate the particle's average kinetic energy to the temperature of the gas in thermal equilibrium. The Equipartition Theorem states that *on the average each available<sup>5</sup> quadratic degree of freedom* has an equal share of the system's energy and that share is equal to one-half of Boltzmann's constant,  $k_B \equiv 1.380649 \times 10^{-23}$  J/K =  $8.61733 \times 10^{-5}$  eV/K [5], times the absolute (kelvin) temperature,  $T$ , per degree of freedom.

For the atoms of a monatomic (noble) gas, which we have just treated as “point particles” in our calculation of the pressure on one wall of a three-dimensional box, each atom has three degrees of freedom; it can move right and left in the  $x$  direction, up and down in the  $y$  direction, and in and out of the page in the  $z$  direction. Motion in each of the three orthogonal directions corresponds to three independent degrees of freedom. The average kinetic energy associated with each degree of freedom is “quadratic” in the sense that the kinetic energy depends upon the square of the velocity in each equivalent direction.

$$\frac{1}{2}m\langle v_x^2 \rangle = \frac{1}{2}m\langle v_y^2 \rangle = \frac{1}{2}m\langle v_z^2 \rangle = \frac{1}{2}k_B T \quad (7.2)$$

The brackets indicate an average of the squared velocities where the average is taken over the entire  $N$  particles within the volume.

In the laboratory, we measure the average pressure on the wall, but the “box” typically contains enormous numbers of atoms. We usually express the number of atoms or molecules in a more convenient form by introducing the number of atoms or molecules whose mass in grams is equal to the isotopic average of the atomic or molecular mass,  $M$ . The units of  $M$  are grams/mole or kilograms/mole. Using those definitions,  $M = mN_A$ . That number of atoms or molecules is known as *Avogadro's number*,  $N_A \equiv 6.02214076 \times 10^{23}/\text{mole}$ . [5].

If the number of atoms in our box of volume,  $V$ , is  $N$ , then we can express that number as a fraction of Avogadro's number:  $n = N/N_A$ . Using Eq. (7.2) to substitute for  $m\langle v_x^2 \rangle$  in Eq. (7.1), we can express the pressure on the wall times the volume of the box in a form that is known as the Ideal Gas Law.

$$pV = Nm\langle v_x^2 \rangle = \frac{Nm}{3}\langle v^2 \rangle = \frac{2N}{3}\frac{1}{2}m\langle v^2 \rangle = \frac{2N}{3}\frac{3}{2}k_B T = nRT \quad (7.3)$$

$\mathfrak{R} \equiv k_B N_A \equiv 8.314462 \text{ J/mole-K}$  is the *universal gas constant*.<sup>6</sup>

The form of the Ideal Gas Law in Eq. (7.3), derived from the microscopic perspective, is expressed in that equation in terms of *extensive variables*. To maintain the pressure when we double the volume, we need to double the amount of gas. We may choose to express the Ideal Gas Law in terms of

<sup>5</sup> Whether or not a particular degree of freedom is “available” will be a consequence of quantum mechanics. Such quantum restrictions will be addressed specifically in Sect. 7.2.2.

<sup>6</sup> In a major redefinition of the International System of Units (SI, see Sect. 1.6), on 20 May 2019, the fundamental physical constants were assigned exact values, and other units, like the kilogram, were defined in terms of those physical constants. The universal gas constant was determined by acoustics experiments [L. Pitre, et al., Metrologia **54**, 856–873 (2017)]. If we use the definition of standard conditions of temperature ( $T = 0^\circ\text{C} = 273.15 \text{ K}$ ) and pressure ( $P = 1 \text{ atm} = 101.325 \text{ kPa}$ ), then the volume of 1 mole of an ideal gas, under those conditions, is given by Eq. (7.3) as  $22.414 \text{ liters} = 22.414 \times 10^{-3} \text{ m}^3$ .

*intensive variables* that do not depend upon the size of the system: in this case, the volume of the container. We do this by introducing the mass density of the gas,  $\rho = mN/V$ , where  $mN$  is the mass of the gas distributed uniformly within the volume,  $V$ .

$$p = \frac{n\mathfrak{R}T}{V} = \frac{mN\mathfrak{R}T}{mN_A V} = \rho \frac{\mathfrak{R}T}{M} \quad (7.4)$$

Again,  $M = mN_A$ , is the atomic or molecular mass of 1 mole of the ideal gas's constituents. In changing from  $P_x$  to  $p$ , I have also invoked *Pascal's law*, which states that in a static fluid, pressure is isotropic. The pressure on the wall normal to the  $x$  axis is the same as on all other walls. As stated by Blaise Pascal, in 1648: "In a body of equally dense fluid at rest, the pressure is the same for all points in the fluid so long as those points are at the same depth below the fluid's surface."<sup>7</sup>

Equation (7.4) is also commonly called the *isothermal* (constant temperature) *equation of state* for an ideal gas. It is an expression for  $p$  in terms of  $\rho$ :  $p = p(\rho, T)$ , for an ideal gas at a constant absolute temperature,  $T$ . We will return to the microscopic view again as we explore the heat content of a fluid and investigate the consequences of treating polyatomic (molecular) gases instead of noble (monoatomic) gases that will be represented as "point particles."

## 7.1.2 Phenomenological Models

"*Thermodynamics is a funny subject. The first time you go through it, you don't understand it at all. The second time you go through it, you think you understand it, except for one or two small points. The third time you go through it, you know you don't understand it, but by that time you are so used to it, it doesn't bother you anymore.*" (Arnold Sommerfeld [6])

A second approach to "knowing" is the phenomenological approach. We just completed a simple application of the microscopic (kinetic theory) perspective that was combined with the statistical mechanics (Equipartition) perspective to produce the Ideal Gas Law. Now we will take an approach that is not concerned about the particles that make up our fluid or their interactions. Instead, we start by asking how many *macroscopic variables* (e.g., pressure, temperature, fluid flow velocity, mixture concentration, void fraction, porosity, tortuosity, electrical charge density, electromagnetic field, gravitational field) are required to provide a complete description of our "system." We then have to write down the *conservation laws* (e.g., conservation of mass, conservation of charge, conservation of momentum) that "close" the system by invoking a number of conservation laws that equal the number of macroscopic variables.<sup>8</sup>

In this textbook, we will focus primarily on simple single-component fluids that are *homogeneous* (at equilibrium, their properties do not vary with position) and *isotropic* (at equilibrium, their properties do not vary with direction, for instance, the sound speed in all directions has the same value). There will be some useful and interesting cases where we will intentionally violate those assumptions. For example, we will study the sound speed in gas mixtures (like methane in air) and in

---

<sup>7</sup> We will deal with the part of Pascal's law that addresses "points are at the same depth below the fluid's surface" in Sect. 8.3.

<sup>8</sup> If the number of variables exceeds the number of conservation laws, the system is "underdetermined." If the number of conservation laws exceeds the number of variables, then the system is "overdetermined."

bubbly fluids (hence, inhomogeneous fluids). We will also explore the Doppler shift in a fluid with a steady flow that makes the sound speed along the direction of flow different from the sound speed against the flow or perpendicular to the flow direction (hence, anisotropic).<sup>9</sup>

For a single-component fluid at rest, only two variables are required to specify the state of the fluid.<sup>9</sup> One variable will be mechanical, such as pressure,  $p$ , or density,  $\rho$ . The other variable will be thermal, such as thermodynamic (absolute) temperature,  $T$ , or *entropy*,  $S$ . We all have experience that gives us an intuitive understanding of  $p$ ,  $\rho$ , and  $T$ , but  $S$  can cause some discomfort because we do not have direct sensory experience with entropy. For our purposes, entropy is related to the heat content of our fluid. When the entropy of a closed system with spatially uniform temperature,  $T$ , is increased by an infinitesimal amount;  $dS$ , by means of the addition of an infinitesimal amount of heat; and  $dQ$ , to the system from its surroundings, these three quantities can be related.

$$dS = \frac{dQ}{T} \quad (7.5)$$

In acoustics, it is fairly common to consider systems where the heat that can enter or leave the system is negligibly small.<sup>10</sup> Such systems are called *adiabatic* from the Greek: *a*, not; *dia*, through; and *bainen*, to go. Our adiabatic assumption leads to our first conservation equation.

$$(dS)_{\text{adiabatic}} = 0 \quad (7.6)$$

A more general treatment allows for the production of entropy by irreversible processes (e.g., heat conduction or viscous dissipation). In those cases, Eq. (7.5) and Eq. (7.6) become generalized to provide the *Second Law of Thermodynamics*, which says that the total entropy of any closed system can only increase with time.

$$\dot{S} = \frac{dS}{dt} \geq 0 \quad (7.7)$$

To complete our description of this simple two-variable system, we need one more conservation law that is known as the *First Law of Thermodynamics*: energy can be converted from one type to another or moved from one place to another, but it cannot be created or destroyed.

$$dU = dQ - dW \quad (7.8)$$

The variable,  $dU$ , is the change of internal energy of the fluid. As before,  $dQ$  is the small amount of *heat added* to the system, and  $dW$  is the small amount of work *done by* the system. These sign conventions for  $dW$  and  $dQ$  reflect the historical emphasis on engines, not refrigerators, during the period when thermodynamics was being developed.

Since we will be restricting our attention to single-component fluids that are neither electrically charged nor magnetic, the only way we can do work on the fluid is mechanically, which is analogous to the work done by moving a particle against a force as expressed in Eq. (1.22) and Eq. (2.14).

---

<sup>9</sup> How do we know that two variables are enough? The best answer is that when we assume that two are enough, we get results that are consistent with experiment. Although I've heard arguments that the number of variables can be connected with "spontaneously broken symmetries," I do not understand (or necessarily believe) such arguments. Knowing the number of variables, *a priori*, is not necessary for a phenomenological theory. You can guess the number of variables, write the corresponding conservation laws, and then see if your theory explains your existing measurements and predicts some new behaviors that are testable..

<sup>10</sup> We'll calculate how small the heat leakage will be later in Sect. 9.3 when we address thermal conduction.

$$dW = p \, dV \quad (7.9)$$

In this application, we can make the First Law of Thermodynamics more intuitive by considering a cylinder that is fitted with an idealized gas-tight frictionless piston.<sup>11</sup>

Using our definition of infinitesimal changes in entropy from Eq. (7.5) and of infinitesimal amounts of work in Eq. (7.9), we can rewrite the First Law of Thermodynamics in a form that will be useful for our calculation of the properties of an ideal gas.

$$dQ = T \, dS = dU + p \, dV \quad (7.10)$$

If we keep the piston's position fixed ( $dV = 0$ ) and we add some thermal energy (heat),  $dQ$ , then the internal energy must increase by an amount  $dU = dQ$ , resulting in an increase in the temperature of the gas contained in the cylinder. If instead, we hold the pressure of the gas in the cylinder constant by letting the piston move while  $dQ$  is added to the gas, then the piston will have to move outward, increasing the volume of the cylinder by  $dV$  and doing an amount of work,  $dW = p \, dV$ .

We are now in a position to determine how much heat is required to increase the temperature of an ideal gas by 1 degree kelvin if we combine our phenomenological result in Eq. (7.10) with the Ideal Gas Law in Eq. (7.3), derived from microscopic considerations. To simplify the mathematics, let us assume that our cylinder contains 1 mole of ideal gas ( $V_o = 22.414$  liters at STP). We define the change in internal energy of the ideal gas per degree kelvin, when the volume is fixed, as the *heat capacity at constant volume*,  $C_V$ , also known as the *isochoric heat capacity*.

$$C_V \equiv \left( \frac{\partial U}{\partial T} \right)_V = \left( \frac{\partial Q}{\partial T} \right)_V = T \left( \frac{\partial S}{\partial T} \right)_V \quad (7.11)$$

Here we have to indicate that we are taking the derivative at constant volume,  $V$ , not at constant pressure,  $p$ .

Based on our representation of the idealized cylinder and piston in Fig. 7.2, it is clear that if we keep the pressure inside the cylinder constant, then when heat is added, the piston will have to move. Compared with a constant volume process, more heat will be required to cause the same change in temperature, since we are extracting work from the system as well as raising its temperature, hence, its internal energy.

Using the product rule for differentiation (see Sect. 1.1.2), we can calculate the differential form of the Ideal Gas Law in Eq. (7.3) for 1 mole of gas ( $n = 1$  mole).

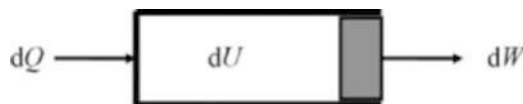


**Fig. 7.2** An idealized frictionless piston sealing a cylinder containing a gas. The internal energy of the gas is increased by an amount,  $dU$ , when an amount of heat,  $dQ$ , is added or  $dU$  is decreased by an amount.  $dW = p \, dV$ , if work is extracted

<sup>11</sup> Although the “frictionless gas-tight piston” in a cylinder is convenient for pedagogical purposes, such frictionless gas pistons are approximated quite well by Airpot® Precision Air Dashpots. These have a very circular glass cylinder that is fitted to a graphite piston. Airpot Corp., Norwalk, CT 06852; [www.airpot.com](http://www.airpot.com).

$$d(pV) = p \, dV + V \, dp = \mathfrak{R} \, dT \quad (7.12)$$

Using the definition of isochoric heat capacity in Eq. (7.11) to express the differential heat input,  $dQ$ , in terms of  $dT$  and substituting  $p \, dV$  from Eq. (7.12) into the First Law as expressed in Eq. (7.10), we can write the First Law in a way that will let us calculate the heat capacity if the addition of heat leads to both a temperature change,  $dT$ , and the production of work,  $dW$ , done by a volume change,  $dV$ , against a constant pressure,  $p$ .

$$dQ = C_V \, dT + \mathfrak{R} \, dT - V \, dp = (C_V + \mathfrak{R})dT - V \, dp \quad (7.13)$$

By holding pressure constant ( $dp = 0$ ), we can use Eq. (7.13) to express the *heat capacity of an ideal gas at constant pressure*,  $C_P$ , also called the *isobaric heat capacity*, in terms of the isochoric heat capacity,  $C_V$ , and the universal gas constant,  $\mathfrak{R}$ .

$$C_P = \left( \frac{\partial Q}{\partial T} \right)_p = T \left( \frac{\partial S}{\partial T} \right)_p = C_V + \mathfrak{R} \quad (7.14)$$

The fact that  $C_P - C_V = \mathfrak{R}$  for 1 mole of gas is a general result for any ideal gas. It was derived by combining the (phenomenological) First Law of Thermodynamics with the (microscopic) Ideal Gas Law. However, Eq. (7.14) does not tell us how to calculate the value of  $C_V$ . To calculate  $C_V$ , we will have to return to our microscopic picture and to the Equipartition Theorem. Before doing so, it is convenient to use our phenomenological result to produce the equation of state for an ideal gas under adiabatic rather than isothermal conditions.

### 7.1.3 Adiabatic Equation of State for an Ideal Gas

We have defined a constant volume (isochoric) heat capacity,  $C_V$ , and a constant pressure (isobaric) heat capacity,  $C_P$ , for 1 mole of an ideal gas. We have also been able to relate the difference of those two heat capacities for 1 mole of any ideal gas:  $C_P - C_V = \mathfrak{R}$ . Of course, we could also define a generic heat capacity,  $C$ , that would allow both pressure and volume to vary simultaneously and in arbitrary proportions. Adiabatic and isothermal processes are idealized limits (like fixed and free boundary conditions for a string). There are entire ranges of processes that are intermediate.

The generic heat capacity,  $C$ , can be written in two ways. Using Eqs. (7.10) and (7.11), a generic heat capacity is related to volume changes.

$$dQ = C \, dT = C_V \, dT + p \, dV \quad (7.15)$$

Using Eqs. (7.13) and (7.14), a generic heat capacity,  $C$ , can also be written in terms of pressure changes.

$$dQ = C \, dT = C_P \, dT - V \, dp \quad (7.16)$$

Rearranging terms and dividing Eqs. (7.16) by (7.15) produces an equation for the ratio of the relative pressure change to the relative volume change.

$$-\frac{V}{p} \frac{dp}{dV} = \frac{C_P - C}{C_V - C} \equiv \gamma' \quad (7.17)$$

The dimensionless constant,  $\gamma'$ , has been introduced to make the result of the integration of Eq. (7.17) more compact.

$$\int \frac{dp}{p} = -\gamma' \int \frac{dV}{V} \Rightarrow \ln p + \gamma' \ln V = K \Rightarrow pV^{\gamma'} = \text{const.} \quad (7.18)$$

In this result,  $K$  is just the integration constant, and the value of  $\gamma'$  will depend upon the process by which the pressure and volume are changed.

If we have an isothermal process, then  $C = C_{iso} = \infty$  in Eq. (7.15) or (7.16), because any amount of heat input,  $dQ$ , cannot cause the temperature to change. In that limit, substitution of  $C_{iso} = \infty$  into Eq. (7.17) requires that  $\gamma' = 1$ , and we recover the result of the isothermal equation of state in Eq. (7.3), where  $pV = \text{constant} = \mathfrak{R}T$  for a single mole of gas at constant (absolute) temperature,  $T$ .

For an adiabatic process,  $dS = 0$ , as claimed in Eq. (7.6). Since  $dT \neq 0$ , we must require that  $C = C_{adiabat} = 0$ , so when it is substituted into Eq. (7.15) or (7.16),  $dQ = 0$ . Plugging  $C_{adiabat} = 0$  into Eq. (7.17) makes  $\gamma' = C_p/C_v$ , therefore, the adiabatic equation of state for an ideal gas, also known as the *Adiabatic Gas Law*, takes its familiar form.

$$pV^{(C_p/C_v)} \equiv pV^\gamma = p_oV_o^\gamma = \text{constant} \quad (7.19)$$

The constant is determined when Eq. (7.19) is evaluated at some reference pressure,  $p_o$ , and reference volume,  $V_o$ . In the above expression, we have defined the ratio of the heat capacity at constant pressure to the heat capacity at constant volume to be  $\gamma \equiv C_p/C_v$ . The ratio,  $\gamma$ , is usually called the *specific heat ratio* or the *polytropic coefficient* because in a polytropic process, the heat capacities are taken to be independent of temperature. If we prefer to consider a unit mass of gas, then  $\rho = m/V \propto 1/V$ , so the adiabatic equation of state can be written in terms of the gas density.

$$p\rho^{-\gamma} = p_o\rho_o^{-\gamma} = \text{constant} \quad (7.20)$$

Note that the constants in Eqs. (7.19) and (7.20) not only have different numerical values but also have different units.

### 7.1.4 Adiabatic Temperature Change

Of course, in an isothermal process, changes in pressure or density do not change the temperature of an ideal gas. For an adiabatic process, those pressure or density changes require that the temperature of the gas also change. We can calculate that temperature change,  $dT$ , by substitution of the Ideal Gas Law of Eq. (7.3) into the adiabatic equation of state in Eq. (7.19).

$$pV^\gamma = (n\mathfrak{R}T)^\gamma p^{1-\gamma} \Rightarrow T^\gamma p^{1-\gamma} = T_o^\gamma p_o^{\gamma-1} = \frac{p_o V_o^\gamma}{(n\mathfrak{R})^\gamma} = \text{constant} \quad (7.21)$$

In Eq. (7.21), the constant is different from the constants in Eq. (7.19) or Eq. (7.20) because Eq. (7.21) has absorbed  $(n\mathfrak{R})^\gamma$  into that constant. The above expression can be differentiated by ordinary means to derive an expression for  $dT$  in terms of  $dp$ , but I would like to use the technique of *logarithmic differentiation*<sup>12</sup> to produce the same result because it is particularly convenient when dealing with power law expressions such as Eq. (7.21).

---

<sup>12</sup>This same calculation for the adiabatic temperature change in an ideal gas was done as an example of logarithmic differentiation in Sect. 1.1.3.

We start by recalling the indefinite integral of  $dx/x$ :

$$\int \frac{dx}{x} = \ln x + C \quad (7.22)$$

Here,  $C$  is some constant of integration, *not* a heat capacity. By the Fundamental Theorem of Calculus (i.e., differentiation and integration are inverse processes), when we differentiate Eq. (7.22), we obtain an expression for the differential,  $dx$ . We can take the natural logarithm of the second form of Eq. (7.21).

$$\gamma \ln T + (1 - \gamma) \ln p = \ln (\text{constant}) \quad (7.23)$$

Differentiating Eq. (7.23) using the technique of Eq. (7.22) yields an expression for the relative change in absolute temperature,  $dT/T$ , and relative change in pressure,  $dp/p$ .

$$\gamma \frac{dT}{T} = (\gamma - 1) \frac{dp}{p} \quad (7.24)$$

Since Eq. (7.24) was derived from the adiabatic equation of state in Eq. (7.19), we can rearrange terms to provide a useful expression for the change in temperature,  $dT$ , due to a change in pressure,  $dp$ , under adiabatic conditions.

$$\left( \frac{\partial T}{\partial p} \right)_S = \frac{(\gamma - 1)}{\gamma} \frac{T}{p} \quad (7.25)$$

Notice that when  $\gamma = 1$ , as it does for an isothermal process,  $(\partial T/\partial p)_S = 0$ , consistent with the meaning of “isothermal.”

As we will demonstrate later in this textbook, the propagation of sound in an ideal gas is very nearly an adiabatic process. If we reconsider the loud sound wave used as an example at the beginning of this chapter (115 dB<sub>SPL</sub>), the magnitude of the peak pressure associated with that wave was  $dp \equiv p_I = 16$  Pa. For air,  $\gamma_{\text{air}} \approx 1.403$ . If we assume the ambient temperature is 15 °C ≈ 288 K, then the magnitude of the peak excess temperature amplitude due to a 115 dB<sub>SPL</sub> sound wave,  $dT \equiv |T_I| = 0.013$  K = 0.013 °C.<sup>13</sup>

## 7.2 Specific Heats of Ideal Gases

At this point, we have derived an expression for the difference between the constant pressure (isobaric) heat capacity per mole of an ideal gas,  $C_P$ , and the constant volume (isochoric) heat capacity per mole of an ideal gas,  $C_V$ . Our thermodynamic analysis showed that  $C_P - C_V = \mathfrak{R}$ , but we do not yet have an expression for either heat capacity and cannot therefore evaluate  $\gamma$  for the adiabatic equation of state in Eq. (7.19) or for the expression in Eq. (7.25) that relates temperature changes to adiabatic pressure changes. To calculate  $C_V$  for an ideal gas, we must return to our microscopic model and to the Equipartition Theorem of Eq. (7.2).

<sup>13</sup> Note that “degrees kelvin” can be abbreviated [K] without a degree sign but “degrees Celsius” requires the degree sign, [°C]. This distinguishes it from the abbreviation for Coulomb, [C] = [A•s], the SI unit of electrical charge.

### 7.2.1 Monatomic (Noble) Gases

Our picture of noble gas atoms as “point particles” bouncing off each other and off rigid walls, but otherwise flying freely between collisions, implied that their only energy was kinetic. If we use the Equipartition Theorem, we can calculate the total average kinetic energy per particle by summing the average kinetic energy in all three degrees of freedom.

$$\frac{1}{2}m\langle v^2 \rangle = \frac{1}{2}m\left[\langle v_x^2 \rangle + \langle v_y^2 \rangle + \langle v_z^2 \rangle\right] = \frac{3}{2}k_B T \quad (7.26)$$

If we sum over a mole of particles, then we can calculate the internal (thermal) energy of 1 mole of this gas.

$$U = \frac{3}{2}N_A k_B T = \frac{3}{2}\mathfrak{R}T \quad (7.27)$$

From our definition of the isochoric heat capacity in Eq. (7.11), the heat capacity of 1 mole of a monatomic (noble) gas can be expressed in terms of the universal gas constant,  $\mathfrak{R} \equiv k_B N_A \equiv 8.314462 \text{ J/mole-K}$ .

$$C_V = \left(\frac{\partial U}{\partial T}\right)_V = \frac{3}{2}\mathfrak{R} \quad (7.28)$$

For noble (monatomic) ideal gases, the heat capacity at constant volume,  $C_V = 1.5\mathfrak{R} \cong 12.472 \text{ J/mole-K}$ . From Eq. (7.14), the isobaric heat capacity,  $C_P = 2.5\mathfrak{R} \cong 20.786 \text{ J/mole-K}$ . Therefore, we can now calculate the ratio of specific heats for noble gases:  $\gamma = C_P / C_V = 5/3$ . At sufficiently low pressures, this result is so precise that it was used to determine the universal gas constant by measuring sound speed in helium. [7]

In most cases, an intensive quantity, called the specific heat, is used to specify the heat capacity of a material, since the intensive quantity is independent of the size of the system. The most common specific heat is the heat capacity per unit mass.<sup>14</sup> Using the convention of lowercase variables for intensive quantities (the most notable exception being the temperature,  $T$ ),  $c_V = 1.5 \mathfrak{R}/M$  and  $c_P = 2.5 \mathfrak{R}/M$ , where  $M$  is the atomic mass. For example, helium has an atomic mass of  $M_{He} = 4.0026 \text{ gm/mole}$ , so for helium at constant pressure,  $c_P \cong 5.193 \text{ J/gm-K} = 5193 \text{ J/kg-K}$ .

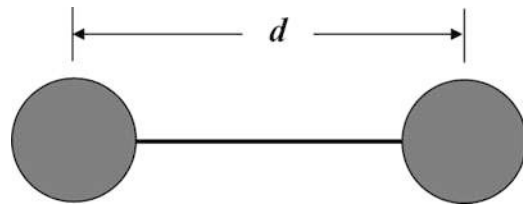
### 7.2.2 Polyatomic Gases

If instead of a noble (monatomic) gas, we have a gas that is composed of stable (i.e., not chemically reacting) *polyatomic molecules* like  $\text{N}_2$ ,  $\text{O}_2$ ,  $\text{HCl}$ ,  $\text{H}_2\text{O}$ ,  $\text{CO}_2$ ,  $\text{CH}_4$ , etc., then we need to return to the Equipartition Theorem and calculate the number of “quadratic” degrees of freedom that are entitled to their “fair share” of the average thermal energy:  $(1/2) k_B T$  per degree of freedom. Let’s start with a simple symmetric diatomic molecule, like  $\text{N}_2$  or  $\text{O}_2$ , shown schematically by the ball-and-stick model in Fig. 7.3.

In addition to the kinetic energy of the motion of the center of mass of the molecule that would contribute three “translational” degrees of freedom, as expressed in Eq. (7.26), this diatomic molecule

<sup>14</sup> In English units, the heat capacity is expressed in calories/gram where  $1.0 \text{ cal} = 4.184 \text{ J}$ . The nominal heat capacity of liquid water is  $1.0 \text{ cal/gram}$  because the calorie was originally defined as the amount of heat necessary to raise 1 gram of pure water from  $19.5$  to  $20.5^\circ\text{C}$ .

**Fig. 7.3** Schematic representation of a diatomic molecule consisting of two identical atoms separated by an average distance  $d$



can rotate about its center of mass around two perpendicular axes (the third axis, along the line connecting the centers doesn't count for point masses) and could also vibrate along the line joining the two masses. Rotational kinetic energy,  $(\frac{1}{2}) I \omega^2$ , and the kinetic and potential energies of vibration,  $KE = (\frac{1}{2}) \mu v^2$  and  $PE = (\frac{1}{2}) K x^2$ , are also “quadratic” degrees of freedom (see Sect. 2.4.4), where  $I$  is the moment of inertia for the pair of atoms about their center of mass,  $\omega$  is the angular frequency of rotation,  $K$  is the effective spring constant for simple harmonic oscillation along the line connecting the two point masses (e.g., see Ch. 2, Prob. 13), and  $\mu$  is the (effective) reduced mass of the pair (e.g., see Eq. 2.147) whose time-dependent separation is  $d + x(t)$ .

If we sum up the quadratic degrees of freedom, we get three “translational,” plus two “rotational,” plus two “vibrational” (i.e., one kinetic and one potential), for a total of seven “quadratic” degrees of freedom. If that were the case, then  $C_V = (7/2)\mathcal{R}$  and  $C_P = (9/2)\mathcal{R}$  for a diatomic gas. That is not the case for nitrogen at room temperature! The reason that result is incorrect can be traced to quantum mechanics. Remember, we are back to the “microscopic” model, and the world of atoms and molecules is governed by the laws of quantum mechanics, not classical mechanics.

In this case, it is useful to appreciate at least one specific instance where *Planck's constant*,  $h \equiv 6.62607015 \times 10^{-34} \text{ J-s} = 4.13566770 \times 10^{-15} \text{ eV-s}$ , enters acoustics. In quantum mechanical systems, the spacing between energy levels is discrete, not continuous. We rarely see a direct manifestation of quantum effects in our daily life because Planck's quantum of action,  $h$ , is so small we can easily impart any amount of action (the product of the energy times the amount of time it is being applied) we choose to a macroscopic system. However, on the atomic scale, if there is insufficient energy to change the state of an atom or molecule by one quantized energy level, then no energy can be exchanged.<sup>15</sup>

How does all of this relate to the specific heat of a diatomic molecule? The energy levels for rotation,  $E_R(j)$ , and vibration,  $E_V(n)$ , are quantized with  $j$  and  $n$  being positive integers.

$$E_V = (n + \frac{1}{2})\hbar\nu \quad \text{and} \quad E_R = \frac{j(j+1)}{2} \frac{\hbar^2}{I} \quad (7.29)$$

$I$  is the moment of inertia of the molecule and  $\nu$  is the frequency of vibration.

Let's start by calculating the quantum of vibration,  $\hbar\nu$ , for  $\text{N}_2$  as an example, then compare that energy to the average available kinetic energy per degree of freedom near room temperature ( $T = 290 \text{ K} \cong 17^\circ\text{C}$ ):  $(\frac{1}{2}) k_B T = 2 \times 10^{-21} \text{ J} = 0.0125 \text{ eV}$  per degree of freedom. (Electron volts tend to be a more convenient measure of the energy of individual atoms and molecules.)

<sup>15</sup> As of 20 May 2019, the value of Planck's constant has been assigned this “exact” value by SI System of Units. This definition led to the specification of the kilogram in terms of  $h$ , the speed of light,  $c \equiv 299,792,458 \text{ m/s}$ , and the length of the second based on the hyperfine transition frequency of cesium-133,  $\Delta\nu_{Cs} \equiv 9,192,531,770 \text{ Hz}$ . From those definitions, the kilogram is no longer based on the mass of a platinum-iridium cylinder near Paris [D. Newell, “A more fundamental International System of Units,” Physics Today **67**(7), 35–41 (2014)].

<sup>16</sup> This is quite fortunate for us, otherwise matter would not exist—electrons that orbit nuclei would radiate continuously and would spiral into their own nuclei.

For  $\text{N}_2$ , the vibrational frequency, measured by optical spectroscopy, is  $\nu(\text{N}_2) = 8.2082 \times 10^{13} \text{ Hz} = 82,082 \text{ GHz}$ . Such high frequencies are usually expressed by the corresponding wavelength of light,  $\lambda_{EM} = c/f$ , where  $c \equiv 299,792,458 \text{ m/s}$ , which is the speed of light in a vacuum. In this case,  $\lambda_{EM} = 3.65 \text{ microns}$ : a wavelength in the infrared portion of the electromagnetic spectrum. When multiplied by Planck's constant,  $E_V(\text{N}_2) = h\nu = 0.3395 \text{ eV}$ . This corresponds to a vibrational temperature  $T_V = E_V/k_B \cong 3940 \text{ K}$ . The probability of a molecule having sufficient energy to excite a vibrational mode is proportional to the *Boltzmann factor*,  $P(E)$ .<sup>17</sup>

$$P(E) = e^{-E/k_B T} \quad (7.30)$$

For our example using the vibrational frequency of  $\text{N}_2$ , the probability of colliding with a molecule having sufficient kinetic energy to excite a vibrational mode, based on Eq. (7.30), is  $P(E_V) = 1.25 \times 10^{-6} = 1.25 \text{ ppm}$  at room temperature, about once chance in a million. For that reason, the vibrational degree of freedom does not contribute to the heat capacity of  $\text{N}_2$  at room temperatures.

For nitrogen, the rotational temperature,  $T_R = E_R/k_B = 2.86 \text{ K}$ , so by Eq. (7.30), the probability that an average room temperature atom will have sufficient energy to excite a rotational mode by an off-axis collision is nearly unity:  $P(E_R) = 0.99$ . Only two rotational degrees of freedom exist for the diatomic molecule, since rotation about the axis joining the point particles does not correspond to actual rotation for the spherically symmetric end masses (since nearly all the mass is concentrated at the nucleus and rotations about that axis are indistinguishable).<sup>18</sup>

That leaves five accessible “quadratic” degrees of freedom for nitrogen near room temperature: three translational and two rotational. The specific heats for diatomic gases are therefore  $c_V = (5/2)\mathfrak{R}$  and  $c_p = (7/2)\mathfrak{R}$ , so  $\gamma = 7/5 = 1.400$ . The results for real diatomic gases are in quite good agreement with that model. For oxygen at  $15^\circ\text{C}$ ,  $\gamma = 1.401$ ; nitrogen at  $15^\circ\text{C}$ ,  $\gamma = 1.404$ ; and air at  $0^\circ\text{C}$ ,  $\gamma = 1.403$ . Of course, dry air is a mixture of about 78.1%  $\text{N}_2$ , 20.9%  $\text{O}_2$  and 0.934% Ar, and about 415 ppm of  $\text{CO}_2$  (and rising!<sup>19</sup>), so we expect the value of  $\gamma_{\text{air}}$  to be a little larger than 7/5 due to argon's contribution, which is monatomic and has  $\gamma_{\text{Ar}} = 5/3$ .

The graph in Fig. 7.4 demonstrates the effect of temperature on specific heat of  $\text{H}_2$ . The rotational temperature of the hydrogen molecule,  $T_R = 85.6 \text{ K}$ , and the vibrational temperature,  $T_V \cong 6100 \text{ K}$ . Below  $T_R$ , the molecule behaves as a monatomic gas and  $C_V = (3/2)\mathfrak{R}$ . Between 250 and 500 K, the two rotational degrees of freedom can participate and  $C_V = (5/2)\mathfrak{R}$ . Above 500 K, the two vibrational degrees of freedom are also becoming participatory. After dissociation, the number of the “particles” in the gas (now a plasma?) has doubled, so the heat capacity should be  $2(3/2)\mathfrak{R}$  since there are 2 moles of monatomic hydrogen.<sup>20</sup>

<sup>17</sup> To be quantum mechanically correct, we should use the *Planck distribution*:

$P_{\text{Planck}}(E) = [e^{E/k_B T} - 1]^{-1}$ . Expansion of the exponential using a Taylor series makes it easy to see that for sufficiently high temperatures,  $E \ll k_B T$ , the Planck distribution reduces to the Boltzmann factor.

<sup>18</sup> Another way to appreciate the fact that rotation about the axis joining the two atoms is negligible is to remember that the moment of inertia is proportional to the mass times the square of the length of the “lever arm.” For the two “dumbbell” rotational degrees of freedom, that lever arm is about half the atomic separation,  $d$ . For  $\text{N}_2$ ,  $d \cong 1.0976 \times 10^{-10} \text{ m} \cong 1.1 \text{ \AA}$ . The diameter of the nitrogen nucleus is about 1 femtometer =  $1 \times 10^{-15} \text{ m} = 10^{-5} \text{ \AA}$  (also called a Fermi), so the moment of inertia about the common axis is about  $10^{10}$  times smaller than the moment of inertia for the “dumbbell” rotation.

<sup>19</sup> A. Gore, *An Inconvenient Truth* (Rodale Press, 2006); ISBN 1594865671

<sup>20</sup> The temperature dependence of the specific heat of hydrogen was measured nearly half a century before the “photoelectric effect” and the “ultraviolet catastrophe” were understood through the introduction of quantum mechanics and Planck's constant. With the benefit of hindsight, one can consider how the development of physics might have been altered if investigators had understood this macroscopic clue to the quantum character of the microscopic world.

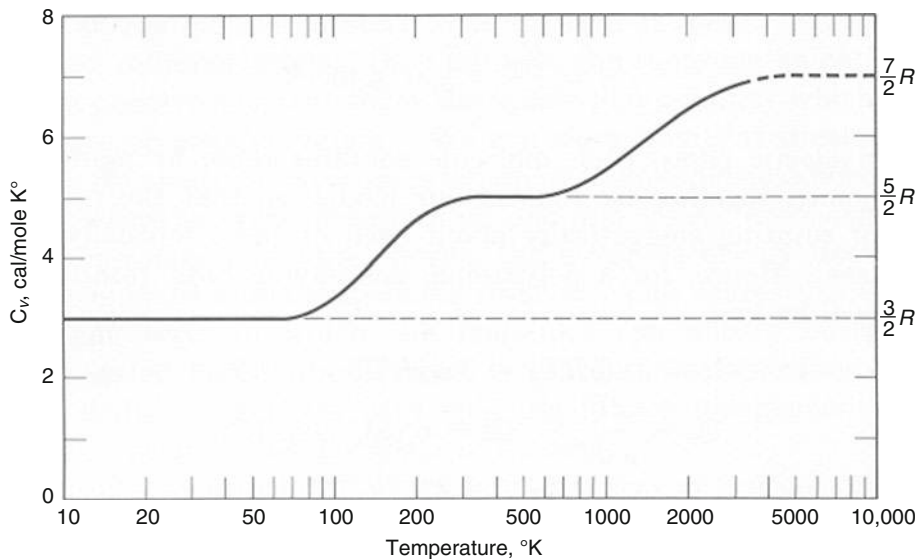


**Fig. 7.4** Variation in the molar heat capacity at constant volume for  $\text{H}_2$  gas vs. temperature. [8]

We can continue to apply this simple view for more complex molecules. For molecular gases like  $\text{H}_2\text{O}$  and  $\text{H}_2\text{S}$ , there are three rotational degrees of freedom in addition to the three degrees of freedom associated with the motion of the molecule's center of mass; hence we expect  $C_V = 3R$  and  $C_P = 4R$ , making  $\gamma = 4/3 = 1.33$ . This is quite close for steam at  $100^\circ\text{C}$  ( $\gamma = 1.324$ ) and for  $\text{H}_2\text{S}$  at  $15^\circ\text{C}$  ( $\gamma = 1.32$ ). The situation for  $\text{CO}_2$  at  $15^\circ\text{C}$  ( $\gamma = 1.304$ ) is a bit more complicated. Based on this analysis, we expect the more complex molecular gases to have still smaller values of  $\gamma$ . In any case, the polytropic coefficient for any ideal gas is bounded:  $1 < \gamma \leq 5/3$ .

As we will see later in Chap. 14, when we investigate attenuation mechanisms in air and sea water, the heat capacity is not only temperature-dependent, but it is also time-dependent. For example, consider a loudspeaker in contact with air. The impact of the speaker cone on the air molecules transfers only translational kinetic energy. The molecules then have to make several collisions (about five, on average) to distribute the additional energy equitably between translational and rotational modes, as dictated by the Equipartition Theorem, which is a statement about equilibrium. It takes a non-zero amount of time to re-establish that equilibrium and the “relaxation time” (see Sect. 4.4.1) for that process,  $\tau_R$ , can introduce phase shifts and hence dissipation. These relaxation effects are usually lumped into a term known as the “bulk viscosity.”<sup>21</sup>

### 7.3 The Fundamental Equations of Hydrodynamics

“An acoustician is merely a timid hydrodynamicist.” (A. Larraza)

<sup>21</sup> The “bulk viscosity” or “second viscosity” is a correction for the fact that there is a sixth “relaxing” variable in a system of phenomenological equations based on only five variables (see Sect. 14.5). The introduction of this “relaxation time,”  $\tau_R$ , which is responsible for the delayed equilibration between internal degrees of freedom, is reflected in a time-dependent specific heat, introduced in a rigorous manner in L. D. Landau and E. M. Lifshitz, *Fluid Mechanics* (Pergamon, 1959), §78, entitled “Second Viscosity.”

The previous discussion has introduced the concept of microscopic and phenomenological models by calculating some acoustically useful properties of ideal gases. Equilibrium thermodynamics was our first example of a phenomenological theory. Two variables were required to describe the static, single-component, homogeneous, isotropic, electromagnetically inert fluid. Two conservation laws (entropy and energy) were used to “close” that system.

For acoustics, static equilibrium is an unacceptable restriction; sound waves make fluids move! To produce a phenomenological theory that will incorporate acoustical effects, we need to introduce another three variables; the three components of the velocity vector.

$$\vec{v} = v_x \hat{e}_x + v_y \hat{e}_y + v_z \hat{e}_z \quad (7.31)$$

As before,  $v_x$  is the  $x$  component of velocity, and  $\hat{e}_x$  has been introduced as the unit vector in the  $x$  direction.

To close this chapter, I will list the conservation equations that close the five-variable system describing the hydrodynamic behavior of a single-component, electrically neutral, nonmagnetic, homogeneous, isotropic fluid. The goal of the next two chapters is to provide an understanding of these equations at a level that will empower you to apply them to acoustical problems and be able to modify them when necessary for more complicated situations. A good reference for such hydrodynamic equations is *Fluid Mechanics*, by Landau and Lifshitz. [9].

### 7.3.1 The Continuity Equation

In the introduction to this chapter, I pointed out that our Eulerian perspective for expression of the equations governing fluids was based on a preference for expressing fluid properties (i.e., pressure, density, temperature, entropy, and fluid velocity) in a fixed frame of reference defined by the laboratory and not on the fluid parcels themselves; the fluid moves in and out of our differential Eulerian volumes,  $dV = dx \ dy \ dz$ . In Part I of this textbook, all of the “particles” had equilibrium positions, and we could apply an equation of state (like Hooke’s law) and Newton’s Second Law of Motion to derive the vibrations of masses on springs, strings, bars, membranes, and plates.

Since the fluid particles are not tied to the laboratory coordinate system, we need another equation, in addition to the equation of state and dynamic equation, to keep track of the fluid in our chosen Eulerian perspective. That third equation ensures *conservation of mass* and is also known as the *continuity equation*. It can be written in vector form.

$$\frac{\partial \rho}{\partial t} + \nabla \cdot (\rho \vec{v}) = 0 \quad (7.32)$$

Equation (7.32) has the form of a “conservation equation.” It is the sum of the time derivative of a density,  $\rho$  (in this case the mass density with units of  $\text{kg/m}^3$ ), plus the divergence of a flux. The flux is the mass flux,  $\vec{J} = \rho \vec{v} = J_x \hat{e}_x + J_y \hat{e}_y + J_z \hat{e}_z$ , that represents the amount of mass that flows through a unit area in unit time. The divergence operator converts a vector, such as the mass flux in Eq. (7.32), to a scalar. It can be written in the coordinate system that is appropriate for the description of the problem of interest. The simplest version of the divergence operator ( $\nabla \cdot$ ) can be written in Cartesian coordinates.

$$(\nabla \cdot) \vec{J} = \frac{\partial}{\partial x} J_x + \frac{\partial}{\partial y} J_y + \frac{\partial}{\partial z} J_z \quad (7.33)$$

The divergence operator has the units of  $(\text{length})^{-1}$  in any coordinate system, so the expression for conservation of mass in Eq. (7.32) is dimensionally homogeneous, as it must be. If there were sources or sinks within the fluid, or if there was a time-dependent (i.e., moving) boundary, then the right-hand side of Eq. (7.32) would no longer be zero. When radiation of sound from vibrating objects is considered in Chap. 12, loudspeakers or other sound sources would provide such “source terms.”

### 7.3.2 The Navier-Stokes (Euler) Equation

Newton’s Second Law of Motion,  $m\ddot{\mathbf{x}} = \mathbf{F}_{\text{net}}$ , takes a different form when expressed in Eulerian coordinates, requiring a redefinition of the acceleration of a “fluid parcel” that is within a differential volume that is fixed in the laboratory coordinate system,  $dV = dx \ dy \ dz$ . It must include both the acceleration of the fluid within the parcel,  $\partial \vec{v} / \partial t$ , as well as the acceleration of the fluid that enters and leaves the parcel by convection,  $(\vec{v} \cdot \vec{\nabla}) \vec{v}$ .

$$\rho \left[ \frac{\partial \vec{v}}{\partial t} + (\vec{v} \cdot \vec{\nabla}) \vec{v} \right] = -\vec{\nabla} p + \mu \nabla^2 \vec{v} + \rho \vec{g} \quad (7.34)$$

This version (known as the *Navier-Stokes equation*) assumes that the *shear viscosity*,  $\mu$ , is not a function of either velocity or position and that the acceleration due to gravity,  $\vec{g}$ , is not a function of position or time.

The Laplacian operator,  $\nabla^2$ , is a scalar operator that can be expressed most simply in Cartesian coordinates.

$$\nabla^2 = \frac{\partial^2}{\partial x^2} + \frac{\partial^2}{\partial y^2} + \frac{\partial^2}{\partial z^2} \quad (7.35)$$

When it is applied to a vector, it generates another vector.

$$\nabla^2 \vec{v} = \hat{e}_x \frac{\partial^2 v_x}{\partial x^2} + \hat{e}_y \frac{\partial^2 v_y}{\partial y^2} + \hat{e}_z \frac{\partial^2 v_z}{\partial z^2} \quad (7.36)$$

The gradient operator,  $\vec{\nabla}$ , is a vector operator that can also be expressed in Cartesian coordinates.

$$\vec{\nabla} = \hat{e}_x \frac{\partial}{\partial x} + \hat{e}_y \frac{\partial}{\partial y} + \hat{e}_z \frac{\partial}{\partial z} \quad (7.37)$$

When  $\vec{\nabla}$  operates on a scalar, like  $p$ , it creates a vector.

$$\vec{\nabla} p = \hat{e}_x \frac{\partial p}{\partial x} + \hat{e}_y \frac{\partial p}{\partial y} + \hat{e}_z \frac{\partial p}{\partial z} \quad (7.38)$$

When  $\vec{\nabla}$  operates on a vector, like  $\vec{v}$ , it creates a 3 x 3 tensor. [10]

$$\vec{\nabla} \vec{v} = \begin{vmatrix} \hat{e}_x \frac{\partial v_x}{\partial x} & \hat{e}_y \frac{\partial v_x}{\partial y} & \hat{e}_z \frac{\partial v_x}{\partial z} \\ \hat{e}_x \frac{\partial v_y}{\partial x} & \hat{e}_y \frac{\partial v_y}{\partial y} & \hat{e}_z \frac{\partial v_y}{\partial z} \\ \hat{e}_x \frac{\partial v_z}{\partial x} & \hat{e}_y \frac{\partial v_z}{\partial y} & \hat{e}_z \frac{\partial v_z}{\partial z} \end{vmatrix} \quad (7.39)$$

The dot product of the velocity vector,  $\vec{v}$ , and the tensor,  $\vec{\nabla} \vec{v}$ , produces a vector.

$$(\vec{v} \cdot \vec{\nabla}) \vec{v} = \hat{e}_x v_x \frac{\partial v_x}{\partial x} + \hat{e}_y v_y \frac{\partial v_y}{\partial y} + \hat{e}_z v_z \frac{\partial v_z}{\partial z} \quad (7.40)$$

Equation (7.34) is a vector equation, so it is actually three separate equations for the three components of velocity. In Cartesian coordinates, those components would be  $v_x$ ,  $v_y$ , and  $v_z$ . In cylindrical coordinates, they are  $v_r$ ,  $v_\theta$ , and  $v_z$ . In spherical coordinates, they are  $v_r$ ,  $v_\theta$ , and  $v_\phi$ . To demonstrate that Eq. (7.34) is not as intimidating as the vector operations above might suggest, the following is the  $x$  component of that equation.

$$\rho \left[ \frac{\partial v_x}{\partial t} + v_x \frac{\partial v_x}{\partial x} \right] = - \frac{\partial p}{\partial x} + \mu \left[ \frac{\partial^2 v_x}{\partial x^2} + \frac{\partial^2 v_x}{\partial y^2} + \frac{\partial^2 v_x}{\partial z^2} \right] + \rho g_x \quad (7.41)$$

The last term on the right-hand side uses  $g_x$  to indicate the  $x$  component of the gravitational acceleration.

The fluid density times the quantity in square brackets is the one-dimensional definition of the time rate of change of the momentum in an Eulerian coordinate system, as will be justified in the next chapter. It states that the mass density times the fluid acceleration plus the flow of momentum is equal to the net force on a “fluid element.” In this case, the forces included in Eq. (7.34) and its  $x$  component in Eq. (7.41) are those due to pressure gradients,  $\vec{\nabla} p$ ; shear stresses,  $\mu \nabla^2 \vec{v}$ ; and the acceleration due to gravity,  $\rho \vec{g}$ . The quantity,  $\mu$ , is known as the shear viscosity and it has MKS units of [Pa-s]. In the form shown in Eq. (7.34), Newton’s Second Law of Motion is known as the *Navier-Stokes Equation*.<sup>22</sup> If the only forcing term is the pressure gradient, the equation is known as the *Euler Equation*.

$$\rho \left[ \frac{\partial \vec{v}}{\partial t} + (\vec{v} \cdot \vec{\nabla}) \vec{v} \right] = - \vec{\nabla} p \quad (7.42)$$

Later in this textbook, other terms will be added to the right-hand side of Eq. (7.34), such as flow resistance for porous materials like those used in acoustical ceiling tiles, or “bulk viscosity” to account for relaxation time effects.<sup>21</sup> On the other hand, we will usually ignore terms like  $\rho \vec{g}$  where such terms might have a negligible influence.<sup>23</sup>

As will be demonstrated in Sect. 10.5, energy conservation is contained within the combination of the continuity Eq. (7.32) and the Euler Eq. (7.42).

<sup>22</sup> The version of the Navier-Stokes equation in Eq. (7.34) does not include the “bulk viscosity” mentioned in footnote 21. It will be added later since it has significant impact in the attenuation of sound as discussed in Sect. 14.5.

<sup>23</sup> The  $\rho \vec{g}$  term will be important for waves on the free surface of water (e.g., tsunamis, surf) or for acoustic oscillations of planetary atmospheres that are generated by seismic events, volcanic explosions, meteors, etc.

### 7.3.3 The Entropy Equation

Entropy production was already mentioned in Eq. (7.7). An equation for entropy production can also be written in Eulerian coordinates.

$$\rho T \left[ \frac{\partial s}{\partial t} + (\vec{v} \cdot \vec{\nabla}) s \right] = \vec{\nabla} \cdot \kappa \vec{\nabla} T + (\vec{\sigma} \cdot \vec{\nabla}) \cdot \vec{v} \quad (7.43)$$

Again, the term in square brackets indicates that the (scalar) entropy per unit mass,  $s$ , can change within the Eulerian “fluid parcel” with respect to time,  $\partial s / \partial t$ , and can change if entropy is transported (convected) into or out of the parcel,  $(\vec{v} \cdot \vec{\nabla}) s$ . It is also worthwhile to recognize that Eq. (7.43) is a scalar (not vector) equation. The gradient operator,  $\vec{\nabla}$ , converts  $s$  into a vector.

$$\vec{\nabla} s = \hat{e}_x \frac{\partial s}{\partial x} + \hat{e}_y \frac{\partial s}{\partial y} + \hat{e}_z \frac{\partial s}{\partial z} \quad (7.44)$$

The dot product with  $\vec{v}$  then reduces this term back to a scalar.

$$\vec{v} \cdot \vec{\nabla} s = v_x \frac{\partial s}{\partial x} + v_y \frac{\partial s}{\partial y} + v_z \frac{\partial s}{\partial z} \quad (7.45)$$

This is a bit more complicated than the version of entropy conservation we used for our discussion of ideal gases, expressed in Eq. (7.6), because it allows for two sources of entropy generation: the first,  $\nabla \cdot \kappa \vec{\nabla} T$ , allows entropy (heat) transport by thermal conduction, where  $\kappa$  [W/m-K] is the fluid’s *thermal conductivity*. The second allows entropy to be generated by viscous effects defined by a nine-component viscous stress tensor,  $\vec{\sigma}$ . The rate of specific entropy generation,  $\dot{s}_{gen}$ , is provided by Swift. [11]

$$\dot{s}_{gen} = \frac{\kappa |\vec{\nabla} T|^2}{\rho T^2} + \frac{1}{\rho T} (\vec{\sigma} \cdot \vec{\nabla}) \cdot \vec{v} > 0 \quad (7.46)$$

Equation (7.49) shows that  $\vec{\sigma}$  is proportional to velocity so the last term in Eq. (7.46) is proportional to  $|\vec{v}|^2$  and is always positive, as is the term involving  $|\vec{\nabla} T|^2$ , so  $\dot{s}_{gen} > 0$ , as required by the Second Law of Thermodynamics.

As in the case illustrated by Eq. (7.44), a vector is created by taking the gradient of the (scalar) temperature.

$$\vec{\nabla} T = \hat{e}_x \frac{\partial T}{\partial x} + \hat{e}_y \frac{\partial T}{\partial y} + \hat{e}_z \frac{\partial T}{\partial z} \quad (7.47)$$

The dot product of the gradient operator,  $\vec{\nabla}$ , and  $\kappa \vec{\nabla} T$  again produces a scalar.

$$\vec{\nabla} \cdot \kappa \vec{\nabla} T = \frac{\partial}{\partial x} \left( \kappa \frac{\partial T}{\partial x} \right) + \frac{\partial}{\partial y} \left( \kappa \frac{\partial T}{\partial y} \right) + \frac{\partial}{\partial z} \left( \kappa \frac{\partial T}{\partial z} \right) \quad (7.48)$$

Of course, if  $\kappa$  is not a function of position, it can be taken outside the derivatives.

The last term in Eq. (7.43) accounts for the entropy generated by dissipation in viscous flow that is expressed by the *viscous stress tensor*,  $\vec{\sigma}$ . Neglecting “bulk viscosity,”<sup>21,22</sup> this nine-component tensor can also be expressed in Cartesian coordinates, where we have assumed that the shear viscosity is neither a function of position or velocity.

$$\vec{\sigma} = \mu \begin{vmatrix} -\hat{e}_x \left( \frac{4}{3} \frac{\partial v_x}{\partial x} - \frac{2}{3} \frac{\partial v_y}{\partial y} - \frac{2}{3} \frac{\partial v_z}{\partial z} \right) & \hat{e}_y \left( \frac{\partial v_x}{\partial y} + \frac{\partial v_y}{\partial x} \right) & \hat{e}_z \left( \frac{\partial v_x}{\partial z} + \frac{\partial v_z}{\partial x} \right) \\ \hat{e}_x \left( \frac{\partial v_y}{\partial x} + \frac{\partial v_x}{\partial y} \right) & -\hat{e}_y \left( \frac{4}{3} \frac{\partial v_y}{\partial y} - \frac{2}{3} \frac{\partial v_x}{\partial x} - \frac{2}{3} \frac{\partial v_z}{\partial z} \right) & \hat{e}_z \left( \frac{\partial v_y}{\partial z} + \frac{\partial v_z}{\partial y} \right) \\ \hat{e}_x \left( \frac{\partial v_z}{\partial x} + \frac{\partial v_x}{\partial z} \right) & \hat{e}_y \left( \frac{\partial v_z}{\partial y} + \frac{\partial v_y}{\partial z} \right) & -\hat{e}_z \left( \frac{4}{3} \frac{\partial v_z}{\partial z} - \frac{2}{3} \frac{\partial v_x}{\partial x} - \frac{2}{3} \frac{\partial v_y}{\partial y} \right) \end{vmatrix} \quad (7.49)$$

The dot product of the stress tensor with the gradient operator creates a vector, and the dot product of that vector with the velocity is again a scalar.

### 7.3.4 Closure with the Equation of State

We now have five hydrodynamic equations but now have gone from five variables to seven because we introduced density,  $\rho$ , as a variable in the Navier-Stokes equation written in Eq. (7.34), and specific entropy (per unit mass),  $s$ , that was introduced by the entropy equation written in Eq. (7.43). This underdetermined problem can be “closed” by introducing two equations of state. The first relates mass density,  $\rho$ , to pressure,  $p$ , and absolute temperature,  $T$ .

$$\rho = \rho(p, T) \quad (7.50)$$

We have already introduced an equation of state for an ideal gas that undergoes processes that are either isothermal in Eq. (7.4) or adiabatic in Eq. (7.20). We can do the same for any fluid, although the equations of state can become rather complicated.

Since we allowed for entropy generation in Eq. (7.46), we also need to be able to relate entropy and temperature.

$$s = s(p, T) \quad (7.51)$$

One possible relationship between entropy and temperature was established previously with the introduction of the isochoric heat capacity in Eq. (7.11), so  $ds = c_V T \, dT$ , and the isobaric heat capacity in Eq. (7.14), so  $ds = c_P T \, dT$ . In effect, we bring ourselves back to the assumption of five variables by recognizing that  $\rho$  and  $s$  are not independent variables but will be unique functions of  $p$  and  $T$  for any substance through which sound propagates.

It is important to recognize the difference between the three conservation equations and the equations of state. The form of the conservation laws are fluid independent, as long as the fluids obey our initial assumptions (e.g., single-component, electrically neutral and insulating, nonmagnetic, homogeneous and isotropic). The equations of state may differ for different fluids even though those fluids obey our initial assumptions.

Now armed with the Eulerian equations of hydrodynamics and the Ideal Gas Laws, we are ready to start exploring acoustics in fluid media. We will initiate this exploration in the next chapter by applying those equations to the simplest cases.

---

### 7.4 Flashback

In this chapter, two complementary descriptions of matter were introduced: microscopic and phenomenological. The microscopic (statistical mechanical) description led us to the Ideal Gas Law, and the

macroscopic (thermodynamic) description made it possible for us to relate the isobaric (constant pressure) and isochoric (constant volume) specific heats of an ideal gas.

To determine values for the specific heats, and their ratio (the polytropic coefficient), it was necessary to return to the microscopic viewpoint and consider the internal degrees of freedom of the particles. The “availability” of those internal degrees of freedom to influence the acoustical and thermodynamic properties of the ideal gas turned out to require the introduction of some elementary concepts from quantum mechanics.

The final topic in this chapter was the introduction of the equations of hydrodynamics and the equations of state. The generality of those equations makes them difficult to comprehend, although their algebraic structure suggested that they formed a “closed description” for a single-component, homogeneous, isotropic fluid, since the system provided five conservation laws for five phenomenological variables: a mechanical property of the fluid,  $p$  (or  $\rho$ ), a thermal property of the fluid,  $T$  (or  $s$ ), and three components of the fluid’s velocity, expressed in Cartesian coordinates as  $v_x$ ,  $v_y$ , and  $v_z$ . In the next chapter, their form will be examined, and they will be applied to hydrostatics and simple acoustical components that are small compared to the wavelength of sound.

### Talk Like an Acoustician

Ideal Gas Law	Heat capacity at constant volume
Kinetic theory of gases	Isochoric heat capacity
Inert gas	Heat capacity at constant pressure
Point particles	Isobaric heat capacity
Equipartition Theorem	Adiabatic gas law
Quadratic degree of freedom	Adiabatic equation of state
Boltzmann’s constant	Specific heat ratio
Avogadro’s number	Logarithmic differentiation
Universal Gas Constant	Monoatomic (noble) gas
Extensive variables	Polyatomic molecules
Intensive variables	Planck’s constant
Pascal’s law	Boltzmann factor
Isothermal equation of state	Planck distribution
Macroscopic variables	Conservation of mass
Conservation laws	Continuity equation
Homogeneous fluid	Navier-Stokes equation
Isotropic fluid	Euler equation
Entropy	Shear viscosity
Adiabatic	Thermal conductivity
Second Law of Thermodynamics	Viscous stress tensor
First Law of Thermodynamics	

### Exercises

1. **A billion of ‘em.** One mole ideal gas (e.g., air) at conditions of standard temperature (273.15 K) and pressure (101,325 Pa) occupies a volume of 22.414 liters/mole. The wavelength of sound,  $\lambda$ , is given by the ratio of the speed of sound,  $c$ , to the frequency,  $f$ :  $\lambda = c/f$ . Avogadro’s number,  $N_A \equiv 6.02214076 \times 10^{23} \text{ mol}^{-1}$ .

The speed of sound in air under the same conditions of temperature and pressure is  $c = 331.65 \text{ m/sec}$ . If we insist that a cubic Eulerian parcel of air contains an average of a billion gas particles, what is the highest frequency of sound in air that would correspond to the wavelength of sound being ten times longer than an edge of the Eulerian parcel?

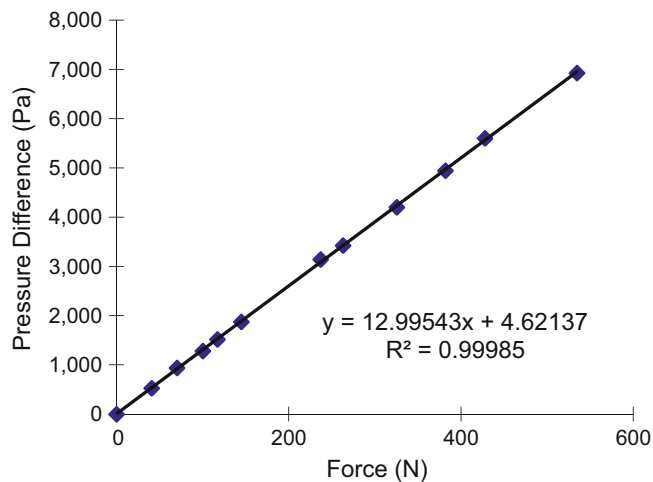
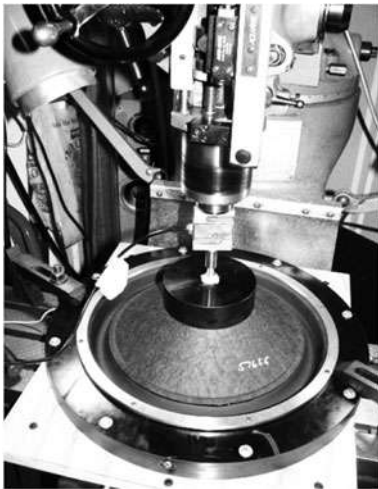


**Fig. 7.5** (Left) Photograph of an apparatus that can determine the force on a loudspeaker cone and surround (see Fig. 2.17) due to a pressure difference across the cone. (Right) Graph of the pressure difference vs. measured force on the cone



**Fig. 7.6** (Left) This simple harmonic oscillator is made from an Airport™ Precision Air Dashpot,<sup>11</sup> consisting of a glass cylinder and a tight-fitting graphite piston of diameter  $44.33 \pm 0.03$  mm that acts as a gas spring with stiffness,  $K_{\text{gas}}$ . The graphite piston and brass cylinder provide a total piston mass,  $m = 184.41$  gm. The bottom end of the glass cylinder is sealed to an aluminum platform with vacuum grease. (Right) An Endevco piezoresistive pressure sensor is threaded into the platform and is protruding through the platform. The microphone's electrical output is connected to a digital storage oscilloscope to allow accurate measurement of the natural period of the freely decaying oscillations that are similar to the trace shown in Fig. 1.18. The small (white) PVC tube with a rubber O-ring on top is placed over the microphone as protection against any possible collision between the microphone and the graphite piston

Repeat part (a), but for pure liquid water, assume its molar mass is  $M_{\text{water}} = 18.015$  gm/mole and its sound speed is  $c = 1481$  m/sec at  $20^\circ\text{C}$ .

2. **Ideal Gas Law.** The density of air at STP is  $\rho_{\text{air}} = 1.2923$  kg/m<sup>3</sup>. What would have to be the pressure of helium gas ( $M_{He} = 4.0026 \times 10^{-3}$  kg/mol) to have the same density at standard temperature?

3. **Loudspeaker cone equivalent piston area.** Shown in Fig. 7.5 (Left) is a photograph of a 15" (nominal) loudspeaker cone connected to a load cell (force gauge) and a supply of pressurized gas. Within the cone-clamping fixture at the bottom of the photo is a pressure gauge. The graph in Fig. 7.5 (Right) shows the pressure difference across the cone vs. the force the cone applied through the load cell. The straight line is a fit to the 12 data points. Based on the graph, determine the effective area of the cone. Report your result in square centimeters ( $\text{cm}^2$ ). Based on the square of the correlation coefficient for that fit ( $R^2 = 0.99985$ ), estimate the uncertainty of your determination of the loudspeaker's effective area.
4. **Rüchardt's method.** [12] A simple harmonic oscillator that combines a gas spring and a (nearly) frictionless piston (Airpot<sup>®</sup>) is shown in Fig. 7.6. The glass cylinder that contains the piston is sealed to a platform that contains a microphone that can measure and record the oscillating pressure within the cylinder if the piston is displaced from its equilibrium position and allowed to execute simple harmonic motion with frequency,  $\omega_o = 2\pi f_o = (\mathbf{K}_{\text{gas}} / m)^{1/2}$ .

The spring constant,  $\mathbf{K}_{\text{gas}}$ , of a “gas spring” comprised of a cylinder of uniform cross-sectional area,  $A$ , and volume,  $V = Ah$ , depends upon the mean pressure,  $p_m$ , of the gas contained within the cylinder.

$$\mathbf{K}_{\text{gas}} = \frac{\gamma p_m}{V} A^2 = \rho_m c^2 \frac{A^2}{V} \quad (7.52)$$

$A$ ,  $V = Ah$ , and  $p_m$  can be measured accurately. The value of  $\omega_o$  can be determined from the period of oscillation,  $T$ .

I used a ruler and a marker pen to place marks separated by 1.0 cm along the glass cylinder. The microphone and the PVC protector excluded some of the volume within the cylinder. I assumed the compressible volume was determined by the measured height of the piston plus some “fudge” length,  $h_o$ , that would take care of any excluded volumes and any offset in my marking of the cylinder’s length. The value of the polytropic coefficient of air,  $\gamma_{\text{air}}$ , could then be determined by a least-squares fit

**Table 7.1** Oscillation periods,  $T_i$ , in milliseconds, for various equilibrium heights,  $h_i$ , of the bottom of the graphite piston measured using the apparatus shown in Fig. 7.6

Heights ( $h_i$ ) (m)	Periods ( $T_i$ ) (milliseconds)
0.15	70.480
0.13	65.400
0.19	79.725
0.18	77.600
0.15	70.567
0.14	68.143
0.13	65.680
0.11	60.467
0.10	57.880
0.08	50.450
0.19	79.800
0.18	77.867
0.17	75.267
0.16	73.200
0.15	70.850
0.14	68.467

of the square of the measured periods,  $T_i^2$ , plotted against the equilibrium heights of the piston,  $h_i$  (see Sect. 1.9.3), based on the marks on the cylinder.

$$\left[ \frac{p_m A}{4\pi^2 m} \right] T_i^2 = \frac{1}{\gamma_{\text{air}}} (h_i + h_o) \quad (7.53)$$

The polytropic coefficient would therefore be equal to the reciprocal of the slope,  $\gamma_{\text{air}} = (\text{slope})^{-1}$ , and the “height offset,”  $h_o$ , would be the ratio of the intercept to the slope,  $h_o = (\text{intercept})/(\text{slope})$ .

The data in Table 7.1 was acquired at an atmospheric pressure of 97.3 kPa. (Is that the mean pressure,  $p_m$ , within the volume?) Using your favorite plotting package, determine  $\gamma_{\text{air}}$  and the relative uncertainty in slope of the best-fit line (see Sect. 1.9.2).

The accepted value for the polytropic coefficient of dry air is  $\gamma_{\text{air}} = 1.403$ . What is the relative difference between your experimental value of  $\gamma_{\text{air}}$  and the accepted value? If that relative difference is larger than the relative uncertainty in the slope, suggest at least one source of systematic error that could be responsible for that discrepancy.

## References

1. A. Swaminathan, S.L. Garrett, M.E. Poese, R.W.M. Smith, Dynamic stabilization of the Rayleigh-Bénard instability by acceleration modulation. *J. Acoust. Soc. Am.* **144**(4), 2334–2343 (2018)
2. U. S. Department of Labor, Occupational Safety & Health Administration, Standards – 29 CFR, Standard No. 1910.95(b)(1), Table G-16 – Permissible Noise Exposure
3. U. S. Standard Atmosphere, 1976 (National Oceanic and Atmospheric Administration, Report S/T 76-1562 (1976))
4. R.P. Feynman, R.B. Leighton, M. Sands, *The Feynman Lectures on Physics*, vol I (Addison-Wesley, Reading, 1963)
5. P.J. Mohr, D.B. Newell, B.N. Taylor, E. Tiesinga, Data and analysis for the CODATA 2017 special fundamental constants adjustment. *Metrologia* **55**, 125–146 (2017)
6. S.W. Angrist, L.G. Helper, G. Loren, *Order and Chaos – Laws of Energy and Entropy* (Basic Books, New York, 1967), pg. 215
7. L. Pitre, F. Sparasci, L. Risegari, C. Guianvarc'h, C. Martin, M.E. Himbert, M.D. Plimmer, A. Allard, B. Marty, P.A. Giuliano Albo, B. Gao, M.R. Moldover, J.B. Mehl, New measurement of the Boltzmann constant  $k$  by acoustic thermometry of helium-4 gas. *Metrologia* **54**, 856–873 (2017)
8. R. Resnick, D. Halliday, *Physics-Part I* (Wiley, New York, 1966)
9. L.D. Landau, E.M. Lifshitz, *Fluid Mechanics*, 2nd edn. (Butterworth Heinemann, Oxford, 1987); ISBN 0-7506-2767-0
10. D.A. Danielson, *Vectors and Tensors in Engineering and Physics* (Addison-Wesley, Redwood City, 1992); ISBN 0-201-52426-0
11. G.W. Swift, *Thermoacoustics: A Unifying Perspective for Some Engines and Refrigerators*, 2nd edn. (ASA Press/ Springer, Cham, 2017), See Sect. 2.2.4; ISBN 978-3-319-66932
12. E. Rüchardt, Eine einfache methode zur bestimmung von  $C_p/C_v$ . *Phys. Z.* **30**, 58–59 (1929)

**Open Access** This chapter is licensed under the terms of the Creative Commons Attribution 4.0 International License (<http://creativecommons.org/licenses/by/4.0/>), which permits use, sharing, adaptation, distribution and reproduction in any medium or format, as long as you give appropriate credit to the original author(s) and the source, provide a link to the Creative Commons license and indicate if changes were made.

The images or other third party material in this chapter are included in the chapter's Creative Commons license, unless indicated otherwise in a credit line to the material. If material is not included in the chapter's Creative Commons license and your intended use is not permitted by statutory regulation or exceeds the permitted use, you will need to obtain permission directly from the copyright holder.





# Nondissipative Lumped Elements

8

## Contents

8.1	<b>Oscillations About Equilibrium</b>	359
8.2	<b>Acoustical Compliance and the Continuity Equation</b>	361
8.2.1	The Continuity Equation	361
8.2.2	Linearized Continuity Equation	363
8.2.3	Acoustical Compliance	366
8.2.4	The Gas Spring	366
8.3	<b>Hydrostatic Pressure</b>	367
8.4	<b>Inertance and the Linearized Euler Equation</b>	369
8.4.1	The Venturi Tube	369
8.4.2	The Linearized Euler Equation	370
8.4.3	Acoustical Inertance	372
8.4.4	Acoustical Mass	373
8.5	<b>The Helmholtz Resonance Frequency</b>	373
8.5.1	Helmholtz Resonator Network Analysis	377
8.5.2	A 500-mL Boiling Flask	378
8.6	<b>DELTAECC Software</b>	381
8.6.1	Download DELTAECC	382
8.6.2	Getting Started with DELTAECC (Thermophysical Properties)	382
8.6.3	Creating planewave.out	384
8.6.4	Running planewave.out	388
8.6.5	Finding the Resonance Frequencies of planewave.out	389
8.6.6	State Variable Plots (*.sp)	391
8.6.7	Modifying planewave.out to Create Flask500.out	392
8.6.8	Interpreting the *.out File	392
8.6.9	The RPN Segment	394
8.6.10	Power Flow and Dissipation in the 500 mL Boiling Flask	396
8.6.11	An “Effective Length” Correction	396
8.6.12	Incremental Plotting and the *.ip File	397
8.6.13	So Much More Utility in DELTAECC	401
8.7	<b>Coupled Helmholtz Resonators</b>	402
8.8	<b>The Bass-Reflex Loudspeaker Enclosure</b>	405
8.8.1	Beranek’s Box Driven by a Constant Volume Velocity	406
8.8.2	Loudspeaker-Driven Bass-Reflex Enclosure*	409
8.9	<b>Lumped Elements</b>	412
	<b>References</b>	418

The goal of this chapter is to start applying the laws of hydrodynamics that were provided in Eqs. (7.32) and (7.42) to problems of interest in acoustics. By applying these laws to some simple acoustical networks, we can begin to develop our understanding of their meaning and their broad utility. We start by ignoring dissipation<sup>1</sup> and by choosing acoustical elements that are *small compared to the wavelength of sound*. In this nondissipative *lumped-element* approximation, the continuity equation (7.32) leads us to the definition of an *acoustical compliance*,  $C$ , that plays the same role as a capacitor in alternating current (AC) electrical circuit theory or a spring in the theory of mechanical vibrations.

Under those same approximations, the Euler equation (7.42) leads to the definition of an *acoustical inertance*,  $L$ , which is equivalent to an inductor in the electrical analogy, or a mass in the theory of mechanical vibrations. If a capacitor and inductor (or spring and mass) are combined, an electrically (mechanically) resonant (tuned) circuit is created. In acoustics, the combination of an acoustical inertance and acoustical compliance is called a *Helmholtz resonator*. If you have ever blown over the neck of a beverage bottle and produced a tone, you have excited a Helmholtz resonator. If you haven't, now's the time! (Fig. 8.1)

The other important electrical circuit element, not mentioned above, is the electrical resistor,  $R_{dc}$ . In an electrical circuit, the capacitor can store electrostatic potential energy,  $E_C = (\frac{1}{2}) CV^2$ , and the inductor can store magnetic potential energy,  $E_L = (\frac{1}{2}) LI^2$ , but neither of those idealized circuit elements can dissipate energy; that is the role of the resistor,  $\langle \Pi_{el} \rangle_t = (\frac{1}{2})R_{dc}I^2$ . Our acoustical elements, the inertance and compliance, are also idealized and do not dissipate energy because neither the Euler equation (7.42) nor the continuity equation (7.32) contains terms that are dissipative.

We will introduce dissipation from the viscous flow losses in the inertance that arise from the  $\mu \nabla^2 \vec{v}$  term in the Navier-Stokes equation (7.34). The dissipation introduced by the compliance arises from the fact that the pressure oscillations of the gas contained within the compliance produce temperature



**Fig. 8.1** Five Helmholtz resonators. The gas in each bottle's neck provides the inertance (mass), and the gas in each bottle's volume provides the compliance (1/stiffness). Such a lumped-element model provides a simple method to calculate the resonance frequency,  $\omega_o$ . The calculation of the resonance quality factor,  $Q$ , requires addition of thermoviscous boundary layer losses and radiation. A more detailed model that incorporates the conical transitions between the neck and volume can be created using the DELTAEC software to provide more accurate results

<sup>1</sup> We can “ignore” dissipation by setting the shear viscosity equal to zero,  $\mu = 0$ , in the Navier-Stokes equation (7.34) and both  $\mu$  and the thermal conductivity to zero,  $\kappa = 0$ , in the entropy equation (7.43).

changes in the gas (7.25). Since the solid walls of the compliance (volume) have a much larger heat capacity than the gas within, they remain nearly isothermal. The gas far from the walls is adiabatic, so there will be irreversible entropy generation,  $\dot{s}_{gen} > 0$ , as shown in Eq. (7.46), produced by the  $\vec{\nabla} \cdot \kappa \vec{\nabla} T$  term in the entropy equation (7.43) due to the heat flowing back and forth between the gas and the walls of the container. The thermal and viscous dissipation will provide our acoustically resistive lumped elements, playing a role analogous to the electrical resistance,  $R_{dc}$ , or the mechanical resistance,  $R_m$ . The origin of their dissipative behavior and the resulting consequences will be examined in the Chap. 9.

## 8.1 Oscillations About Equilibrium

Thus far, we have used *harmonic analysis* extensively in Part I. It is the acoustician's most powerful analytical tool. For vibrating systems, whether discrete masses and springs or distributed continua, like strings, bars, membranes, and plates, the equilibrium condition usually corresponded to the relevant coordinate being set equal to zero (e.g., the equilibrium position of a mass at  $x_o = 0$  or the displacement of the undisturbed string,  $y(x, t) = 0$ ). Acousticians express the temporal and spatial response of oscillating fluid parameters (i.e., pressure, density, velocity, temperature, and entropy) as the sum of a mean (equilibrium) value and a harmonic deviation (i.e., sinusoidally varying in space and/or time) of that parameter away from its mean value. In that way, acousticians can effortlessly convert sets of coupled differential and integral equations into a much simpler set of coupled algebraic equations.

Let us take as our first example the pressure of a fluid in which there is an acoustic disturbance from equilibrium that varies both in three-dimensional space,  $\vec{x}$ , and in time,  $t$ .

$$p(\vec{x}, t) = p_m(\vec{x}) + p_1(\vec{x}, t) \quad (8.1)$$

The mean pressure,  $p_m(\vec{x})$ , is a constant in time but may vary slowly over space.<sup>2</sup> Most commonly in acoustics, the variation in  $p_m(\vec{x})$  in space might be due to changes in depth for ocean acoustics or due to changes in altitude for propagation of sound in the atmosphere. We will examine both those possibilities later, but in most instances,  $p_m(\vec{x})$  will be assumed constant in both space and time.

The deviation from the equilibrium pressure in Eq. (8.1) is represented as  $p_1(x, t)$ . The meaning of the subscript  $m$  is obvious from its specification as the "mean" value. The subscript "1" on  $p_1$  indicates that it is the first-order (linear) deviation from equilibrium. This linear deviation from equilibrium is sometimes called the *instantaneous value*, because it is constantly changing, typically with sinusoidal time dependence. The subscripting choice is insignificant as long as you do not have to consider nonlinear effects. The velocity amplitude,  $v_1$ , is a linear deviation from equilibrium, so the kinetic energy density,  $(KE_2)/V = (\frac{1}{2})\rho_m v_1^2$ , is quadratic, where now the subscript "2" indicates that the kinetic energy density is a second-order quantity in its deviation from equilibrium. If there is no mean flow, there are no first-order terms in the kinetic energy.

All of the relevant acoustic variables in our single-component fluid can be expanded in the same way as we expanded the pressure in Eq. (8.1). The *acoustic approximation* assumes that the deviation from equilibrium is much smaller than the equilibrium value:  $|p_1| \ll p_m$ . That was certainly true for the case of the loud (115 dB<sub>SPL</sub>) sound wave used as an example at the start of Chap. 7, where  $|p_1|/p_m = 1.6 \times 10^{-4}$  (160 ppm). Just as we did for the pressure, all of the other acoustic variables can be expanded in a similar way:

<sup>2</sup> In this case, "slowly" means the relative change in mean pressure,  $\delta p_m/p_m \ll 1$ , for distances on the order of the wavelength of sound.

$$\rho(\vec{x}, t) = \rho_m(\vec{x}) + \rho_1(\vec{x}, t) \quad (8.2)$$

$$T(\vec{x}, t) = T_m(\vec{x}) + T_1(\vec{x}, t) \quad (8.3)$$

$$s(\vec{x}, t) = s_m(\vec{x}) + s_1(\vec{x}, t) \quad (8.4)$$

As before, the acoustic approximation requires that  $|\rho_1| \ll \rho_m$ ,  $|T_1| \ll T_m$  and  $|s_1| \ll s_m$ . In fact, for an adiabatic process,  $s_1 \equiv 0$ .

The velocity is treated in a slightly different way. For most of the cases of interest to us,  $\vec{v}_m = 0$ . Instead, for the first-order particle velocity,  $\vec{v}_1$ , the acoustic approximation requires that it be small compared to the sound speed<sup>3</sup>,  $c$ .

$$M_{ac} = \frac{|\vec{v}_1|}{c} \ll 1 \quad (8.5)$$

$M_{ac}$  is a dimensionless variable called the *acoustic Mach number*. When individual components of the velocity are needed, we will write  $\vec{v}_1 = u\hat{e}_x + v\hat{e}_y + w\hat{e}_z$ , as will be done in Eq. (8.10).

In most cases, an acoustician is concerned with the first-order deviation of a parameter from its equilibrium value. Furthermore, this first-order deviation is assumed to be a sinusoidal function of space and time. The assumption of harmonic behavior is not as restrictive as it may seem. *Fourier's theorem* (see Sect. 1.4) guarantees that any continuous, periodic (though possibly non-sinusoidal) function can be represented as a sum of sinusoidal functions if the system exhibits linear behavior.

These definitions allow the acoustically induced deviations from equilibrium to be expressed as complex exponentials that provide a particularly convenient functional form for integration or differentiation, as we saw in Part I. For example, we can express the deviation of the pressure from its equilibrium value for a wave traveling to the left or to the right as we did for waves on strings in Chap. 3.

$$p_1(\vec{x}, t) = \Re e \left[ \hat{\mathbf{p}} e^{j(\omega t \mp \vec{k} \cdot \vec{x})} \right] \quad (8.6)$$

As before, the minus sign (−) in the exponential corresponds to propagation in the  $+\vec{x}$  direction, and the plus sign (+) corresponds to propagation in the  $-\vec{x}$  direction. The complex pressure amplitude,  $\hat{\mathbf{p}}$ , is a phasor that combines both amplitude and phase. By using complex notation, differentiation with respect to time corresponds to a simple multiplication of  $p_1(x, t)$  by  $+j\omega$ . Differentiation with respect to position corresponds to a simple multiplication of  $p_1(x, t)$  by  $\pm jk$ , with the choice of sign depending on whether the wave is moving in the  $+x$  direction ( $-jk$ ) or in the  $-x$  direction ( $+jk$ ).

For the one-dimensional standing wave, like those first treated on strings in Sect. 3.3.1, the spatial dependence can be characterized by a trigonometric function and the time dependence by a complex exponential. The form below assumes that the standing wave has a pressure anti-node located at  $x = 0$ .

$$p_1(\vec{x}, t) = \Re e [\hat{\mathbf{p}} e^{j\omega t}] \cos(kx) \quad (8.7)$$

---

<sup>3</sup>The choice of  $c$  to represent the speed of sound (or the speed of light) evolved from the word “celerity” meaning rapidity of motion or action.

With this discussion and the assumed behavior of first-order deviations from equilibrium shown in Eqs. (8.6) and (8.7), the restriction of “small compared to a wavelength,” where  $\lambda = 2\pi/k = c/f$ , should be clear for both standing and traveling waves. We are now prepared to derive expressions for acoustical compliance and acoustical inertance from the hydrodynamic equations.

## 8.2 Acoustical Compliance and the Continuity Equation

Acoustics is a branch of fluid dynamics. Our initial approach will be to study the motion of a fluid particle in response to the forces applied to it by adjacent fluid particles. Before we can start that study, we need to decide on our frame of reference. In fact, that choice has already been made by the form in which we chose to express the equations of hydrodynamics in Eqs. (7.32), (7.34), and (7.43). Implicit in the form of those equations was the decision to choose a *laboratory frame of reference* also known as an *Eulerian coordinate system*.

In the study of fluids, there are two choices. One is the choice typically made in classical mechanics, where we write equations that describe the time evolution of each particle’s coordinates in space and time. Since our system is typically composed of Avogadro’s number of particles, we define a *fluid particle* (or *fluid parcel*) as a volume of fluid that contains enough atoms or molecules (billions) so that the fluid in the volume can be treated as a continuous medium, yet small enough so that all acoustic variables are nearly constant throughout that small volume. In effect, we are imaging that we could color those billion atoms or molecules that constitute our “particle” red and then follow the time evolution of that red spot. That choice is designated the *Lagrangian description*.

A Lagrangian description might be convenient if you are using “tracer particles” (e.g., smoke in air) and have a laser Doppler vibrometer that follows the motion of those tracer particles optically. For most laboratory measurements, it is simpler to assume that your sensors (e.g., microphone, hydrophone, thermocouple, hot-wire anemometer, etc.) are at a fixed location (in the laboratory frame of reference) and the fluid is moving past the sensor. We will be using that Eulerian description almost exclusively in this textbook.

The simplification provided by the Eulerian frame of reference, which is useful when we interpret the signals from our sensors, comes at the cost of having to redefine “acceleration.” The acceleration must include both the “local” time rate of change of a variable within our fluid parcel at the location of interest, plus the change in the variable caused by transport (convection) of the value of that variable into and out of our location of interest from some neighboring position. The term in square brackets below and in Eqs. (7.34), (7.42), and (7.43) is called (total) *convective derivative*.

$$\frac{D}{Dt} \equiv \left[ \frac{\partial}{\partial t} + (\vec{v} \cdot \vec{\nabla}) \right] \quad (8.8)$$

The convective component of the acceleration in Eulerian coordinates that arises from applying the convective derivative to the fluid velocity,  $\vec{v}(\vec{x}, t)$ , will be explained in Sect. 8.4.1, where the Euler equation is exploited to derive the acoustical inertance.

### 8.2.1 The Continuity Equation

What happens to a fluid parcel when exposed to a temporally and spatially varying pressure, a sound wave, for example? Two things happen: (i) the mass of the fluid within the parcel changes (the density of the fluid changes), and (ii) the velocity of the fluid within the parcel changes. The continuity

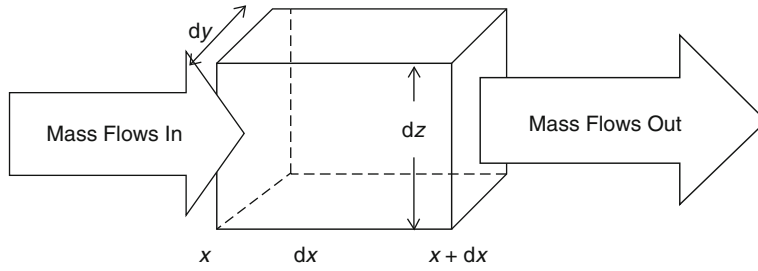


**Fig. 8.2** A Eulerian fluid element in a right-handed Cartesian coordinate system located at  $\vec{x} = \hat{x}\hat{e}_x + \hat{y}\hat{e}_y + \hat{z}\hat{e}_z$ , containing a differential volume,  $dV = (dx)(dy)(dz)$ . The fluid within  $dV$  includes so many atoms or molecules (billions of them!) that it can be considered “smooth” (rather than corpuscular), but the differential volume is sufficiently small that its state can be characterized by unique values of all acoustic variables  $p(\vec{x}, t)$ ,  $\rho(\vec{x}, t)$ ,  $\vec{v}_1(\vec{x}, t)$ ,  $T(\vec{x}, t)$ , and  $s(\vec{x}, t)$  at its location

equation, which is also known as the conservation of mass equation, expresses that density change in terms of the variation in mass flux,  $\rho\vec{v}$ , as a function of position.

$$\frac{\partial \rho}{\partial t} + \nabla \cdot (\rho\vec{v}) = 0 \quad (8.9)$$

We can examine the consequence of those changes by examining the *Eulerian volume* shown in Fig. 8.2. The rate of mass flowing into the volume from the left is mass flux,  $(\rho\vec{v})$ , times the differential area,  $dA = dy dx$ , evaluated at the left side of the differential volume. The rate of mass flow out of the volume on the right side is the same product evaluated at the right side. The rate of increase of mass inside the volume,  $\partial m / \partial t = \dot{m}$ , is the difference in the mass flow rate in and the mass flow rate out. The fact that Eq. (8.9) is a homogeneous equation guarantees that there are no sources or sinks of mass within the differential Eulerian volume,  $dV$ .

The form of the continuity equation can be justified by first considering this one-dimensional flow, diagrammed in Fig. 8.2, with the mass flow restricted to occurring only the  $x$  direction. To simplify our mathematical expressions (by elimination of subscripts), we will let the Cartesian components of the vector velocity be  $u$ ,  $v$ , and  $w$ , so that  $\vec{v} = u\hat{e}_x + v\hat{e}_y + w\hat{e}_z$ . If the flow is only in the  $x$  direction, then  $v = w = 0$ . We will also let  $u$  be only a function of  $x$ :  $u = u(x)$ .

The net change of mass,  $dm$ , during a time interval,  $dt$ , within the differential volume,  $dV$ , due to a fluid with mass density,  $\rho$ , moving with a velocity,  $u$ , in the  $x$  direction, can be written as the difference between the  $x$  component of the mass flux at  $x$ ,  $(\rho u)_x$ , times the differential area,  $dA = dy dz$ , times the time interval,  $dt$ , minus the mass that flows out from the same area located at  $x + dx$ .

$$dm = (\rho u)_x dy dz dt - (\rho u)_{x+dx} dy dz dt \quad (8.10)$$

Expanding  $(\rho u)_{x+dx}$  in a Taylor series about  $x$  and retaining only the first (linear) term in the series provide an expression for  $(\rho u)_{x+dx}$  in terms of  $(\rho u)_x$  and the partial derivative of  $(\rho u)$  with respect to  $x$ , evaluated at  $x$ .

$$\begin{aligned} (\rho u)_{x+dx} &= (\rho u)_x + \left( \frac{\partial(\rho u)}{\partial x} \right)_x dx \\ \Rightarrow (\rho u)_x - (\rho u)_{x+dx} &= - \left( \frac{\partial(\rho u)}{\partial x} \right)_x dx \end{aligned} \quad (8.11)$$

This allows us to determine the time rate of change of the mass,  $\dot{m} = \partial m / \partial t$ , and hence, the change in fluid density,  $\rho$ , within that differential Eulerian volume,  $dV$ .

$$\dot{m} = \frac{dm}{dt} = \frac{\partial \rho}{\partial t} dx dy dz = - \left( \frac{\partial(\rho u)}{\partial x} \right)_x dx dy dz \Rightarrow \frac{\partial \rho}{\partial t} + \frac{\partial(\rho u)}{\partial x} = 0 \quad (8.12)$$

The right-hand version of Eq. (8.12) is the continuity equation in one dimension, since we have assumed that there is flow only in the  $x$  direction. Expanding to three dimensions, we recover the full equation of continuity that was first introduced in Eq. (7.32) without justification.

$$\frac{\partial \rho}{\partial t} + \nabla \cdot (\rho \vec{v}) = 0 \quad (8.13)$$

In the above derivation,  $u$ ,  $v$ , and  $w$  were used as the  $x$ ,  $y$ , and  $z$  components of the velocity vector so that we did not end up with double subscripts (e.g.,  $(\rho v_x)_x$ ). Elsewhere,  $\vec{v}$  has been used as the velocity vector with Cartesian components  $v_x$ ,  $v_y$ , and  $v_z$ . The coexistence of these two velocity component designations (as well as their equivalents in cylindrical or spherical coordinates) should not cause any confusion.

### 8.2.2 Linearized Continuity Equation

Starting with the simplest case, we now consider the small length of pipe shown schematically in Fig. 8.3, filled with a compressible fluid at pressure,  $p$ . By “small,” we mean that  $\Delta x \ll \lambda$  and  $A^{1/2} \ll \lambda$ ; both the diameter and the length of the element are much less than the wavelength of sound at the frequencies of interest.

Since we (as acousticians) are “timid hydrodynamicists,” and since Fig. 8.3 represents one-dimensional flow along the  $x$  axis, we will “linearize” the continuity equation in Eq. (8.12) before we apply it to the lumped-element representation (acoustical compliance) of the small section of tube in Fig. 8.3. We substitute the expansion of the fluid mass density about equilibrium from Eq. (8.2) into the one-dimensional version of the continuity equation (8.12), and we will linearize the resulting expression by discarding any second-order terms that include products of two first-order deviations from equilibrium. Subsequently, we will demonstrate (quantitatively) that the elimination of the quadratic term is justified if  $u \ll c$ .

$$\frac{\partial(\rho_m + \rho_1)}{\partial t} + \frac{\partial}{\partial x} [(\rho_m + \rho_1)u] = 0 \quad (8.14)$$

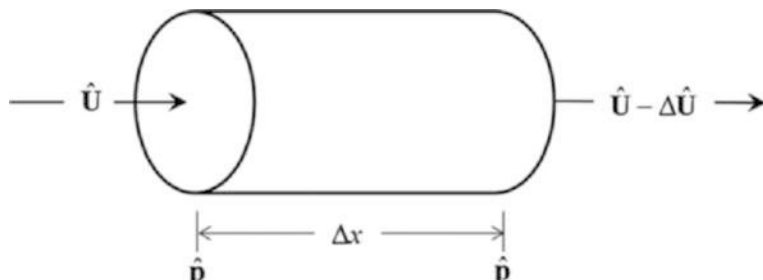


**Fig. 8.3** A short section of pipe with length,  $\Delta x \ll \lambda$ , and cross-sectional area,  $A = (\pi/4) d^2$ , with  $d \ll \lambda$ . Fluid enters the pipe at the left with a volume velocity,  $\hat{U} = \hat{u}A$ , that is reduced upon exiting at the right to  $\hat{U} - \Delta \hat{U}$ , due to the compression of the fluid within the pipe. The walls of the pipe are assumed rigid and isothermal. It is important to remember that  $\hat{U}$  is the complex amplitude of a variable that has a harmonic time dependence:  $U_1(t) = \Re e[\hat{U} e^{j\omega t}]$

Recognizing that  $\rho_m$  is a constant, so  $(\partial \rho_m / \partial t) = 0$ , the square bracket in Eq. (8.14) can be expanded.

$$\frac{\partial \rho_1}{\partial t} + \frac{\partial}{\partial x} [\rho_m u + \rho_1 u] = 0 \quad (8.15)$$

The constant coefficient,  $\rho_m$ , can be taken outside the spatial derivative.

$$\frac{\partial \rho_1}{\partial t} + \rho_m \frac{\partial u}{\partial x} + \frac{\partial (\rho_1 u)}{\partial x} = 0 \quad (8.16)$$

At this point, we recognize that the  $(\rho_1 u)$  term is a quadratic (second-order) combination of two first-order deviations from the equilibrium state. For that reason, this term can be eliminated from Eq. (8.16) to produce the linearized one-dimensional version of the continuity equation.

$$\frac{\partial \rho_1}{\partial t} + \rho_m \frac{\partial u}{\partial x} = 0 \quad (8.17)$$

We can determine the limits on the validity of excluding the  $(\rho_1 u)$  term by using harmonic analysis to convert the differential equation (8.17) into an algebraic equation by assuming that  $\rho_1$  and  $u$  are represented by a right-going traveling wave with  $c = \omega/k$ .

$$j\omega \hat{\mathbf{p}} - \rho_m jk \hat{\mathbf{u}} = 0 \quad \Rightarrow \quad \frac{\hat{\mathbf{p}}}{\rho_m} = \frac{\hat{\mathbf{u}}}{c} \quad \Rightarrow \quad \frac{|\hat{\mathbf{u}}|}{c} \equiv M_{ac} \ll 1 \quad (8.18)$$

We can take the ratio of the term we discarded in Eq. (8.16) to the term we kept to produce Eq. (8.17), again assuming a right-going traveling wave.

$$\frac{\frac{\partial(\rho_1 u)}{\partial x}}{\rho_m \frac{\partial u}{\partial x}} = \frac{-jk \hat{\mathbf{p}} \hat{\mathbf{u}}}{-\rho_m jk \hat{\mathbf{u}}} = \frac{\hat{\mathbf{p}}}{\rho_m} \quad \Rightarrow \quad \frac{|\hat{\mathbf{p}}|}{\rho_m} = M_{ac} \ll 1 \quad (8.19)$$

As long as we are in the low-amplitude acoustic limit ( $M_{ac} \ll 1$ ), then the quadratic term in Eq. (8.16) is negligible compared to the two terms which survived in our linearized continuity equation (8.17).

Before continuing to examine the consequences of the linearized continuity equation, it is worthwhile to make a temporary digression and reflect on what effects we might have been eliminating by rejecting the second-order  $(\rho_1 u)$  term in Eq. (8.16).

The time average of any harmonic first-order acoustic variable over an integer number of periods,  $nT$ , will be identically zero. That is not true for the time average,  $\langle \rho_1 u \rangle_t$ , of that quadratic term.

$$\langle \rho_m u \rangle_t = \frac{\rho_m}{T} \int_0^T u dt = 0 \quad \text{but} \quad \langle (\rho_m + \rho_1) u \rangle_t = \frac{1}{T} \int_0^T (\rho_m + \rho_1) u dt \neq 0 \quad (8.20)$$

Both  $\rho_1$  and  $u$  vary sinusoidally with time, so their product will be proportional to  $\sin(\omega t) \sin(\omega t + \phi) = (\frac{1}{2})[1 + \cos(2\omega t)] \cos \phi + (\frac{1}{2}) \sin(2\omega t) \sin \phi$ . The time average of the two trigonometric terms that contain  $(2\omega t)$  in their arguments will vanish, but the time average of the constant is non-zero. This corresponds to a second-order mass flux,  $\dot{m}_2$ , that is driven by the product of the two first-order variables.

The non-zero time-averaged flow can be understood by recognizing that the density variation,  $\rho_1$ , and the acoustic flow velocity,  $u$ , are in-phase for a one-dimensional traveling wave. During the first half-cycle,  $\rho = \rho_m + \rho_1(t)$ , which is greater than the mean value,  $\rho_m$ , while  $u$  is positive, corresponding

to mass flow toward the right. That net mass flow transports a second-order mass flux of  $\dot{m}_2(\text{right})$  to the right during the first half-cycle. During the second half-cycle,  $\rho(t)$  is smaller than the mean value,  $\rho_m$ , while  $u$  is negative, transporting a mass flux,  $\dot{m}_2(\text{left})$ , to the left. Those two mass flows are not equal and result in a net flow of mass to the right:  $\dot{m}_2 = \dot{m}_2(\text{right}) - \dot{m}_2(\text{left}) > 0$  [1]. This *nonlinear effect* is known as *streaming*, and the second-order heat flux carried by this acoustically driven flow can be detrimental to the operation of heat engines and refrigerators [2].

We are not yet ready to apply our linearized continuity equation (8.17) to the small element in Fig. 8.3 because the fluid variable in that figure is  $p$ , not  $\rho$ . How do we address this problem? We invoke the equation of state that relates pressure and density:  $\rho = \rho(p, T)$ . For this application, let us assume that the fluid which fills the tube in Fig. 8.3 is an ideal gas and that the compressions and expansions of that gas occur adiabatically, so using Eq. (7.20),  $p\rho^\gamma = \text{constant}$ . The adiabatic gas law can be differentiated logarithmically (see Sect. 1.1.3) to obtain an expression that relates pressure variations,  $\delta p$ , to density variations,  $\delta\rho$ .

$$\ln p - \gamma \ln \rho = \ln [\text{constant}] \Rightarrow \frac{\delta p}{p_m} = \frac{p_1}{p_m} = \gamma \frac{\delta \rho}{\rho_m} = \gamma \frac{\rho_1}{\rho_m} \quad (8.21)$$

Since we used the adiabatic gas law to create Eq. (8.21), we can use the ratio of  $\delta p$  to  $\delta\rho$  that provides the conversion between density variations and pressure variations.

$$\frac{\delta p}{\delta \rho} = \left( \frac{\partial p}{\partial \rho} \right)_s = \frac{p_1}{\rho_1} = \frac{\gamma p_m}{\rho_m} = \frac{\gamma \mathfrak{R} T}{M} \equiv c^2 \quad (8.22)$$

The Ideal Gas Law of Eq. (7.4) has been used to convert the ratio of  $p_m/\rho_m$  to  $\mathfrak{R}T/M$ , where  $\mathfrak{R}$  is the universal gas constant,  $T$  the absolute [kelvin] temperature, and  $M$  the atomic or molecular mass [kg/mol] of the ideal gas.

As will be shown later,  $c^2$  is the square of the *adiabatic sound speed* in an ideal gas. Substituting  $\rho_1 = \rho_m (p_1/\gamma p_m)$  from Eq. (8.22) into the linearized continuity equation (8.17), we obtain a version of the one-dimensional, linearized continuity equation that is now only valid for an ideal gas under adiabatic conditions, but that contains  $p_1$  as the thermodynamic variable instead of  $\rho_1$ .

$$\left( \frac{1}{\gamma p_m} \right) \frac{\partial p_1(x, t)}{\partial t} + \frac{\partial u(x, t)}{\partial x} = 0 \quad (8.23)$$

Having defined a volume velocity,  $U_1 = uA$ , with units of [ $\text{m}^3/\text{s}$ ], that is the product of the fluid velocity,  $u$ , and the cross-sectional area of the element,  $A$ , Eq. (8.23) can be re-written in terms of the volume velocity. Since  $\Delta x \ll \lambda$ , the second term in Eq. (8.23) can be approximated as  $-\Delta U_1/A\Delta x = -\Delta U_1/V$ , where  $V$  is the volume of the lumped element represented in Fig. 8.3. Finally, converting to complex notation for a single-frequency wave,

$$\frac{j\omega}{\gamma p_m} \hat{\mathbf{p}} - \frac{\Delta \hat{\mathbf{U}}}{V} = 0 \quad (8.24)$$

In fluid dynamics, it is also common to define a mass flow rate,  $\dot{m} = \rho_m U_1$ , that has units of [ $\text{kg/s}$ ]. The concept of volume velocity is so useful in acoustics, particularly for analysis of sound sources (e.g., loudspeakers), that acousticians generally prefer  $U_1$  to  $\dot{m}$ .

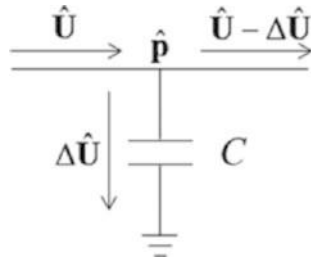


**Fig. 8.4** An equivalent circuit diagram of the lumped element shown in Fig. 8.3. The volume velocity,  $\hat{U} = \hat{u}A$ , is an alternating “current.” Part of that current,  $\Delta\hat{U}$ , enters the compliance, compressing the gas within, and the remaining current exits the compliance,  $C$ .

### 8.2.3 Acoustical Compliance

The expression for the one-dimensional, linearized, single-frequency continuity equation, as written in Eq. (8.24), will allow us to define an acoustical compliance for the short tubular element, shown in Fig. 8.3, that would be analogous to the capacitance for an electrical capacitor or the reciprocal of stiffness for a mechanical spring. By introducing the concept of a complex *acoustical impedance*,  $Z_{ac} \equiv \hat{p}/\hat{U}$ , we can make such an analogy.<sup>4</sup>

$$Z_{ac} \equiv \frac{\hat{p}}{\hat{U}} = \frac{1}{j\omega} \frac{\gamma p_m}{V} \quad (8.25)$$

Again, we recognize that  $\Delta U = U_I$ , which is the deviation of the volume velocity from its mean value, usually taken to be zero,  $U_m = 0$ .

The expression for the *capacitive reactance* of a capacitor is  $X_C = 1/(\omega C)$ . If we compare that expression to Eq. (8.25), the definition of an acoustical compliance,  $C$ , follows directly by analogy.

$$C = \frac{V}{\gamma p_m} = \frac{V}{\rho_m c^2} \quad (8.26)$$

The right-hand version simply invokes the result of Eq. (8.22), where  $c^2$  is the adiabatic sound speed in an ideal gas.

Just like the capacitive impedance, the acoustical impedance of this acoustic compliance is given as  $Z_{ac} = 1/j\omega C$ . The analogy is represented schematically using electrical component symbols in Fig. 8.4.

### 8.2.4 The Gas Spring

We can revisit the idealized cylinder from Fig. 7.2, which is closed at one end and has a leak-tight frictionless piston at the other, and then examine the concept of an acoustic compliance from another

---

<sup>4</sup> The “acoustical impedance,”  $Z_{ac} \equiv \hat{p}/\hat{U}$ , which has just been introduced is the fourth “impedance” that has appeared in this textbook. We defined the “electrical impedance,”  $Z_{el} \equiv \hat{V}/\hat{I}$ , in Sect. 2.5.5, where it was applied to an electrodynamic loudspeaker. The “mechanical impedance,”  $Z_m \equiv \hat{F}/\hat{v}$ , was introduced as the solution to the steady-state response for a damped, driven harmonic oscillator in Sect. 2.5.1. The limp string’s “characteristic impedance,”  $Z_{m,0} = \rho_L c$ , was introduced to calculate the steady-state response of a force-driven string in Sect. 3.7.

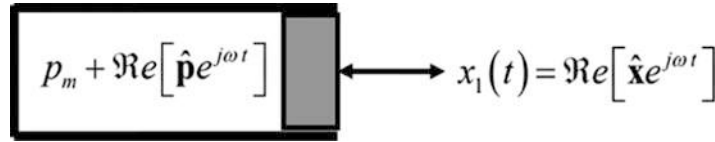


**Fig. 8.5** A schematic depiction of a piston with cross-sectional area,  $A$ , and mean length,  $L \ll \lambda$ , that contains a volume of ideal gas,  $V = AL$ , at mean pressure,  $p_m$ . The gas volume is compressed and expanded adiabatically by a leak-tight frictionless piston oscillating back and forth harmonically, covering a total distance (stroke) of  $2|\hat{x}|$  at a frequency,  $f = \omega/2\pi$

perspective by forcing the piston to undergo harmonic displacements,  $x(t) = \Re[\hat{x}e^{j\omega t}]$ , as shown in Fig. 8.5.

Logarithmic differentiation of the adiabatic equation of state for an ideal gas from Eq. (7.19) provides a relationship between the change in volume,  $dV(t) = Ax(t)$ , and the change in pressure,  $p_1(t)$ .

$$pV^\gamma = \text{constant} \quad \Rightarrow \quad \frac{p_1(t)}{p_m} = -\gamma \frac{dV(t)}{V} = -\gamma \frac{A}{V} x(t) \quad (8.27)$$

If we assume that the mean pressure,  $p_m$ , on both sides of the piston is the same, then (8.27) can be re-written in the form of Hooke's law:  $F = -Kx$ .

$$F = -K_{\text{gas}}x_1 = p_1A = -\gamma p_m \frac{A^2}{V} x_1 \quad \Rightarrow \quad K_{\text{gas}} = \frac{\gamma p_m}{V} A^2 = \rho_m c^2 \frac{A^2}{V} \quad (8.28)$$

This corresponds to a spring constant,  $K_{\text{gas}}$ , for the "gas spring" that was used<sup>5</sup> in Chap. 7, Problem 4.

Using harmonic analysis, the piston's complex (phasor) volume velocity amplitude,  $\hat{U}$ , can be related to the time derivative of its position,  $\hat{x}$ :  $\hat{U} = j\omega \hat{x}A$ . Substitution of  $x_1$  into the differential form of the Adiabatic Gas Law in Eq. (8.27) reproduces Eq. (8.24) that was used to define the acoustical compliance,  $C$ , in Eq. (8.26), if we assume that the fluid that enters the compliance due to the non-zero volume velocity,  $U$ , shown in Figs. 8.3 and 8.4, cannot leave the cylinder, or equivalently,  $U = \Delta U$ .

### 8.3 Hydrostatic Pressure

"Here come those Santa Ana winds again." Steely Dan [3]

Before we calculate the acoustic inertance of a small element using the linearized Euler equation, as we just did to calculate an acoustic compliance using the linearized continuity equation, we will make a particularly simple application of the Navier-Stokes equation (7.34) to calculate the variation of pressure with depth for a stagnant fluid in a gravitational field characterized by a gravitational acceleration,  $\vec{g}$ . Since we are assuming a stagnant fluid, all terms in (7.34) that contain velocity will vanish.

<sup>5</sup> The design of springs for acoustical systems is a very important problem in areas like loudspeaker cone suspensions and vibration isolators for machinery. For mechanical springs, a crucial design consideration is fatigue failure of the spring material. Gas springs are attractive in some applications because the gas does not "wear out." One of the most articulate engineers of acoustical systems is John Corey, the founder and owner of CFIC, Inc. and Q-Drive, in Troy, NY (now a wholly owned subsidiary of RIX Industries located in Benicia, CA.). In defense of gas springs, John likes to say, "Nobody has ever successfully measured the endurance limit of a helium atom." On the other hand, in exchange for a spring that will not suffer fatigue failure, one needs to provide a clearance (piston) seal that is not too dissipative due to gas friction or due to fluid blow-by or a flexure (diaphragm or bellows) seal that is not subject to fatigue failure.

$$\vec{\nabla} p = \rho \vec{g} \quad \text{if} \quad \vec{v} = 0 \quad (8.29)$$

Applying this to water, which we will assume is incompressible, means that the density will not be a function of depth,  $\rho \neq \rho(z)$ . If the direction of the gravitational acceleration,  $\vec{g}$ , is downward in the  $z$  direction, only the  $z$  component of  $p$  changes with depth. The integration of Eq. (8.29), to provide the pressure as a function of depth, is then straightforward.

$$\frac{dp}{dz} = \rho g \quad \Rightarrow \quad \int_0^{-z} dp = \rho g \int_0^{-z} dz \quad \Rightarrow \quad p(z) = p_o - \rho g z \quad \text{with } z \leq 0 \quad (8.30)$$

If we take our fluid to be an ocean or a lake, then the constant of integration,  $p_o$ , is just the atmospheric pressure at the surface. The hydrostatic pressure increases linearly with depth if the water is assumed to be incompressible. If we take the density of water to be  $10^3 \text{ kg/m}^3$ , then  $dp/dz \cong 10^4 \text{ Pa/m} \cong 1 \text{ bar/10 m}$ .

The same calculation can be done easily (though a bit unrealistically) for an isothermal atmosphere. In that case, the density of air will depend upon altitude. The pressure and density are related by the Ideal Gas Law (7.4), so  $\rho_m(p) = p_m(M/\mathfrak{R}T)$ . Since the height of the Earth's atmosphere is generally taken to be less than 100 km and the mean radius of the Earth is  $R_\oplus = 6378 \text{ km}$ , the variation in  $g(z)$  should be less than 0.8%. Assuming that  $g \neq g(z)$  and letting the altitude increase in the  $+z$  direction from sea level, Eq. (8.29) can also be integrated.

$$\int_0^h \frac{dp}{p} = \ln \left[ \frac{p}{p_o} \right] = \frac{gM}{\mathfrak{R}T} h \quad \Rightarrow \quad p_m(h) = p_o e^{-h/\mu} \quad (8.31)$$

The scale length,  $\mu \equiv \mathfrak{R}T/gM$ , can be evaluated under standard atmospheric conditions [4], at sea level with  $T = 288.15 \text{ K}$  ( $15^\circ\text{C}$ ), where  $g(0) = 9.8066 \text{ m/s}^2$  and  $M = 28.9644 \text{ kg/kmole}$ , resulting in a characteristic “exponential atmospheric thickness” of  $\mu = 8435 \text{ m}$ . The standard value of atmospheric pressure at sea level is  $p_o = 101,325 \text{ Pa}$  and  $\rho_o = 1.2250 \text{ kg/m}^3$  at  $15^\circ\text{C}$ . Note that the acceleration due to gravity at that altitude,  $g(\mu) = 9.7807 \text{ m/s}^2$  [4]. This deviates from its value at sea level,  $g(0)$ , by less than  $\frac{1}{4}\%$ . The pressure (and density) of an isothermal atmosphere therefore decreases exponentially with increasing altitude. Equation (8.31) can be evaluated to determine the initial decrease in atmospheric pressure from sea level with height under isothermal conditions:  $(\partial p/\partial h)_h = 0 = -p_o/\mu \cong -12 \text{ Pa/m}$ .

If instead we let the density of the atmosphere be constant, so  $p(h) = p_o - \rho_o gh$ , then Eq. (7.13) can be used to determine the adiabatic rate of change of temperature with increasing height.

$$dQ = c_p dT - dp/\rho = 0 \quad \Rightarrow \quad c_p dT = -gdz \quad \Rightarrow \quad \left( -\frac{\partial T}{\partial h} \right)_s = \frac{g}{c_p} \equiv \Gamma_d \quad (8.32)$$

$\Gamma_d$  is known as the dry (hence, the  $d$  subscript) *atmospheric lapse rate*. For dry air at  $15^\circ\text{C}$ ,  $c_p = 1005 \text{ J/kg} \cdot ^\circ\text{C}$ , so  $\Gamma_d \cong -9.8 \text{ }^\circ\text{C/km}$ . This is more realistic than the previous isothermal assumption because weather is usually transporting large parcels of air up and down, changing their pressure and temperature adiabatically. In reality, neither  $T$  nor  $p$  is independent of height in the troposphere, and the lapse rate is less than  $\Gamma_d$  because of the latent heat of water [4].

For any resident of the Los Angeles basin, the atmospheric conditions that bring hot air westward from the Mojave and Sonoran deserts that then are heated adiabatically as they descend into the basin are known as “Santa Ana winds,”<sup>6</sup> hence the quote that started this section.

<sup>6</sup>The Santa Ana winds are katabatic winds, from the Greek, meaning “to flow downhill.”

## 8.4 Inertance and the Linearized Euler Equation

Just as we did with the calculation of the compliance of a small lumped element in Sect. 8.2.3, we will begin our calculation of the inertance of a small lumped element by linearizing the relevant hydrodynamic equation. In this case, we ignore viscous and gravitational forces in Eq. (7.34) and begin with the Euler equation (7.42), reproduced below.

$$\frac{D\vec{v}}{Dt} = \frac{\partial \vec{v}}{\partial t} + (\vec{v} \cdot \vec{\nabla}) \vec{v} = -\frac{\vec{\nabla} p}{\rho} \quad (8.33)$$

### 8.4.1 The Venturi Tube

Some students find the convective contribution to the acceleration term,  $(\vec{v} \cdot \vec{\nabla}) \vec{v}$ , in the total derivative,  $D\vec{v}/Dt$ , of Eq. (8.8) and the Euler equation (8.33), to be a bit mysterious. This mystery might be cleared up if we look at a situation where  $\partial v/\partial t = 0$  everywhere in the fluid, but the fluid's acceleration is non-zero. The Venturi tube flow meter,<sup>7</sup> shown schematically in Fig. 8.6, is a simple case that will be easy to analyze [5].

If we assume the drawing in Fig. 8.6 depicts a rectangular duct of constant width but the linearly varying cross-section between  $x = 0$  and  $x = L$ , reducing the cross-sectional area by a factor of two, which is filled with an incompressible fluid,  $(\partial \rho / \partial t = 0)$ , then conservation of mass (7.32) guarantees that the velocity,  $\vec{v}$ , must increase linearly within the constriction between  $x = 0$  and  $x = L$ .

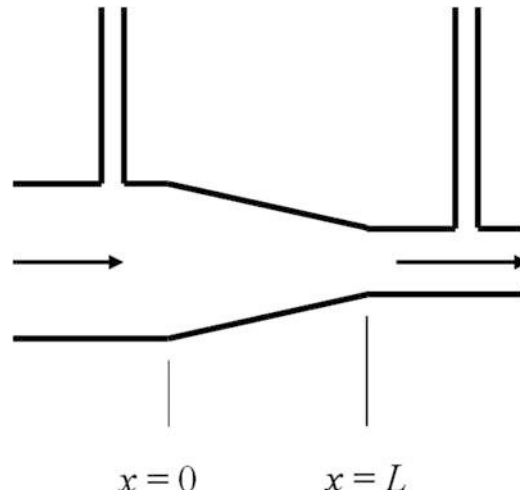


**Fig. 8.6** An incompressible fluid flowing through the Venturi must accelerate from a lower velocity at the left of the constriction to a higher velocity at the right of the constriction. Although it is obvious that the fluid must be accelerating, the time derivative of the velocity at any fixed location within the fluid is zero. The height of the fluid in the two standpipes will be different because the pressure at the left must be higher than the pressure at the right to create the fluid's acceleration required by the Euler equation (8.33) under our assumption of the fluid's incompressibility

<sup>7</sup>Named after Italian physicist Giovanni Battista Venturi (1746–1822)

$$\vec{v}(x) = v_{left} \left(1 + \frac{x}{L}\right) \hat{e}_x \quad \text{for } 0 \leq x \leq L \quad (8.34)$$

As a function of time,  $\partial \vec{v}(t)/\partial t = 0$ , but since the velocity depends upon position, the convective acceleration is non-zero.

$$\left(\vec{v} \cdot \vec{\nabla}\right) \vec{v} = v_x \frac{\partial v_x}{\partial x} \hat{e}_x + v_y \frac{\partial v_y}{\partial y} \hat{e}_y + v_z \frac{\partial v_z}{\partial z} \hat{e}_z \quad (8.35)$$

Since  $\vec{v}$  along the center line is only a function of  $x$ , only the first term on the right-hand side of Eq. (8.35) is non-zero. This convective acceleration can be related to the pressure gradient,  $\vec{\nabla} p \cong (p_{left} - p_{right})/L$ , by substitution into the Euler equation (8.33).

$$\rho \left( v_x \frac{\partial v_x}{\partial x} \right) = - \frac{\partial p}{\partial x} \quad (8.36)$$

The above version can be integrated to produce the pressure difference,  $\Delta p = p_{left} - p_{right}$ , that would lead to a height difference,  $\Delta h = \Delta p/\rho g$ , in the two standpipes shown at  $x < 0$  and  $x > L$  in Fig. 8.6.

$$-\int_{left}^{right} dp = \rho \int_{left}^{right} v_x dv_x \quad \Rightarrow \quad \Delta p = \frac{\rho}{2} \left( v_{right}^2 - v_{left}^2 \right) \quad (8.37)$$

This result is a manifestation of the Bernoulli equation that is very important in nonlinear acoustics for understanding radiation pressure [6] and acoustical levitation [8]. For our purposes here, it illustrates that there can be accelerations and pressure gradients in fluids where  $\partial \vec{v}(t)/\partial t = 0$  everywhere within the fluid.

### 8.4.2 The Linearized Euler Equation

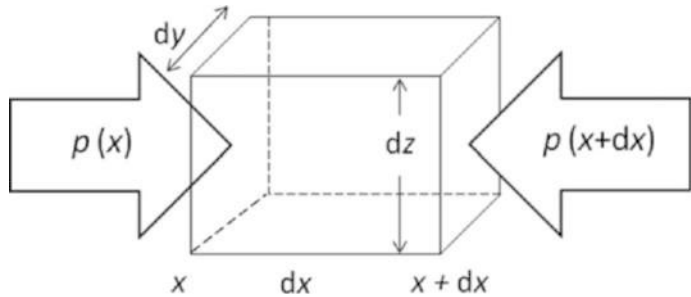
The convective term in the acceleration is manifestly second order (in the absence of steady flow) since it is proportional to the product of two first-order quantities,  $\vec{v}_1 \cdot \vec{v}_1$ . We can use the same technique of harmonic analysis as used previously in Eq. (8.19), this time to determine the conditions that justify neglect of the convective acceleration term, using sound speed,  $c = \omega/k$ .

$$\left| \frac{\left( \vec{v} \cdot \vec{\nabla} \right) \vec{v}}{\partial \vec{v}/\partial t} \right| = \left| \frac{j k \hat{\mathbf{v}}^2}{j \omega \hat{\mathbf{v}}} \right| = \frac{|\hat{\mathbf{v}}|}{c} \quad \Rightarrow \quad \frac{|\hat{\mathbf{v}}|}{c} = M_{ac} \ll 1 \quad (8.38)$$

We can neglect the second-order term in Eq. (8.33),  $\left( \vec{v} \cdot \vec{\nabla} \right) \vec{v}$ , compared to the first-order term,  $\partial \vec{v}/\partial t$ , if the velocity amplitudes are within the acoustic approximation:  $M_{ac} \ll 1$ .

As before, when we eject a particular term from the fundamental governing equations, it takes along with it many interesting phenomena. In this case, the loss of the convective acceleration term,  $\left( \vec{v} \cdot \vec{\nabla} \right) \vec{v}$ , removes our ability to understand the formation of shock waves and sonic booms. It also eliminates any non-zero time-averaged acoustic forces that are related to the Bernoulli pressure,  $\langle p_2 \rangle_t = (\rho_m/2)v^2$  [7]. These forces include radiation pressure [6], the levitation of solid objects in

**Fig. 8.7** A Eulerian volume element in a Cartesian coordinate system in the presence of a pressure gradient



intense standing wave fields,<sup>8</sup> and the manipulation of such levitated objects to cause rotations (acoustic torques) and vibrations [8].

To linearize the part of the Euler equation that remains after removal of the convective acceleration, the density can be expanded into its mean value,  $\rho_m$ , plus the first-order variation,  $\rho_1$ , as shown in Eq. (8.2).

$$\frac{\partial \vec{v}_1}{\partial t} = -\frac{\vec{\nabla} p_1}{\rho_m(1 + \rho_1/\rho_m)} \quad (8.39)$$

The acoustic approximation guarantees that  $\rho_1/\rho_m = M_{ac} \ll 1$ , so it can also be removed from Eqs. (8.33) and (8.39) to produce the linearized Euler equation that we will use to derive an expression for the lumped inertance of the small fluid element with all dimensions much less than the wavelength of sound.

$$\frac{\partial \vec{v}_1}{\partial t} = -\frac{\vec{\nabla} p_1}{\rho_m} \quad (8.40)$$

Before doing so, we can interpret Eq. (8.40) again using the Eulerian fluid particle shown in Fig. 8.7.

The force exerted on the left side of the differential volume,  $dV$ , is  $p(x)dy dz$ . The force exerted on the right side is  $p(x + dx)dy dz$ . The net force,  $F_{net}$ , is their difference.

$$F_{net} = [p(x) - p(x + dx)] dy dz \quad (8.41)$$

$p(x + dx)$  can be expanded in a Taylor series about  $x$ , as indicated by the subscript on the partial derivative.

$$p(x + dx) = p(x) + \left(\frac{\partial p}{\partial x}\right) dx \quad (8.42)$$

Using this result, the net force on the Eulerian volume element can be expressed in terms of the pressure gradient in the  $x$ -direction:  $\nabla_x p = (\partial p / \partial x)$ .

$$F_{net} = [p(x) - p(x + dx)] dy dz = -\left(\frac{\partial p}{\partial x}\right) dx dy dz = -\left(\frac{\partial p}{\partial x}\right) dV \quad (8.43)$$

<sup>8</sup> A nice acoustic levitation chamber video demonstration is available on YouTube, <http://www.youtube.com/watch?v=94KzmB2bI7s>. In a truly bizarre application, Wenjun Xie, at a university in Xi'an, China, used acoustics to levitate live insects, spiders, and fish as shown in Fig. 15.19.

Newton's Second Law of Motion states that this net force must be equal to the mass of fluid contained within  $dV$  times its acceleration. Since we have assumed a pressure gradient only in the  $x$  direction, we will again express the vector velocity in Cartesian components:

$$(\rho dV) \frac{\partial u}{\partial t} = - \left( \frac{\partial p}{\partial x} \right) dV \Rightarrow \rho \frac{\partial u}{\partial t} = - \left( \frac{\partial p}{\partial x} \right) \quad (8.44)$$

This is just the one-dimensional version of the linearized Euler equation that was derived in Eq. (8.40) from the hydrodynamic equation (8.33).

### 8.4.3 Acoustical Inertance

Consider a short pipe of constant cross-sectional area,  $A$ , filled with an incompressible fluid. For oscillations at a single frequency, we again let  $\hat{U}$  be the complex amplitude of the oscillatory volume velocity through the element as shown in Fig. 8.8. We can apply the one-dimensional linearized Euler equation (8.44) to the element, assume time-harmonic variables, and make a finite-difference approximation to the one-dimensional pressure gradient,  $\nabla_x p \cong -\Delta \Re e[\hat{p} e^{j\omega t}] / \Delta x$ .

$$j\omega \frac{\hat{U}}{A} = \frac{1}{\rho_m} \frac{\Delta \hat{p}}{\Delta x} \quad (8.45)$$

The inertance,  $L$ , can be obtained by rearranging Eq. (8.45) to take the form of an acoustical impedance,  $Z_{ac}$ , as was done previously for acoustical compliance,  $C$ , in Eq. (8.25).

$$Z_{ac} \equiv \frac{\Delta \hat{p}}{\hat{U}} = j\omega \rho_m \frac{\Delta x}{A} \quad (8.46)$$

As with our derivation of the acoustical compliance, the acoustical inertance can be identified by analogy to the *inductive reactance* of AC circuit theory:  $X_L = \omega L$ .

$$L = \frac{\rho_m \Delta x}{A} \quad (8.47)$$

Just as with the compliance,  $C$ , the inertance,  $L$ , can be represented by an electrical circuit element (inductor) as shown in Fig. 8.9.

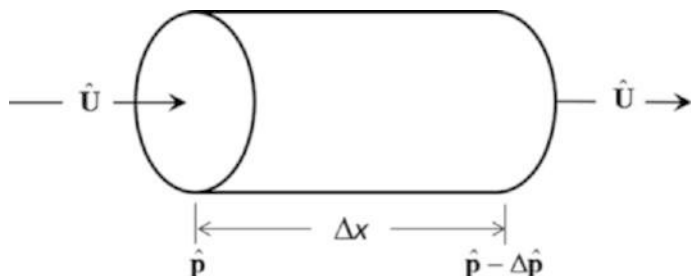


**Fig. 8.8** As in Fig. 8.3, this figure depicts a fluid element that is a short section of pipe with length,  $\Delta x \ll \lambda$ , and cross-sectional area,  $A$ , corresponding to a diameter,  $d = (4A/\pi)^{1/2} \ll \lambda$ . Fluid enters the pipe at the left with a volume velocity amplitude,  $\hat{U} = \hat{u}A$ , at a pressure amplitude,  $\hat{p}$ . Since the fluid is assumed incompressible, it also exits at the right with volume velocity amplitude,  $\hat{U}$ , but at a different pressure amplitude,  $\hat{p} - \Delta \hat{p}$ , due to the fluid's inertia

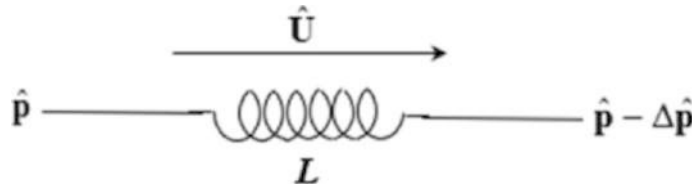


**Fig. 8.9** An equivalent circuit diagram of the lumped inertance shown in Fig. 8.8. The volume velocity amplitude,  $\hat{U} = \hat{u}A$ , is a “current” passing through the element, and the pressure difference between the ends (like a potential difference, analogous to a voltage drop across the inductor) is responsible for the acceleration of the incompressible fluid

#### 8.4.4 Acoustical Mass

As with the equivalent gas stiffness,  $K_{gas}$ , of an acoustical compliance expressed in Eq. (8.28), we can interpret our expression for acoustical inertance in Eq. (8.47) as the inertial mass of incompressible fluid, oscillating within the inertance element, due to the time-harmonic pressure gradient across it. We use Newton’s Second Law of Motion since it represents the dynamical equivalent of the fluid-mechanical Euler equation:  $F = ma$ . The mass of fluid,  $m$ , contained within the short inertance element is the incompressible fluid’s density times the volume,  $m = \rho_m (\Delta x A)$ , and its acceleration amplitude is  $\hat{a} = (j\omega \hat{U}/A)$ .

$$\begin{aligned}\hat{F} &= \Delta\hat{p}A = (\rho_m \Delta x A) \frac{j\omega \hat{U}}{A} \\ \Rightarrow \frac{\hat{p}}{\hat{U}} &= \frac{(\hat{F}/A)}{\hat{U}} \equiv j\omega L = (\rho_m \Delta x A) \frac{j\omega}{A^2} \quad \Rightarrow \quad L = \frac{\rho_m \Delta x}{A}\end{aligned}\quad (8.48)$$

At this point, it could be legitimate to complain that we were able to obtain expressions for the acoustical inertance,  $L$ , and the acoustical compliance,  $C$ , of a “lumped element” directly from Newton’s Second Law and the Adiabatic Gas Law. Why were we forced to spend so much time working through the hydrodynamic equations? Of course, the answer is that the goal of the hydrodynamic derivations of both  $L$  and  $C$  was to familiarize you with those equations, as well as to define parameters that will be useful in acoustical network analyses, since they will be applied throughout this textbook to a variety of acoustical problems.

Nondissipative, linearized lumped-element analysis was only our first and our simplest application of hydrodynamics. Their utility will now be demonstrated in the analysis of Helmholtz resonators, which are important in a variety of applications (e.g., noise control, musical acoustics, and optimization of loudspeaker enclosure performance).

---

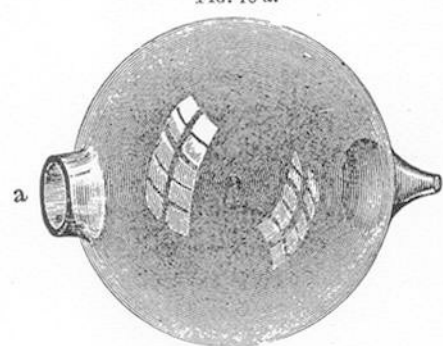
#### 8.5 The Helmholtz Resonance Frequency

Having derived expressions (in two different ways!) for the acoustical inertance and acoustical compliance of elements whose dimensions are all small compared to the wavelength of sound, we are now in a position to join those “lumped elements” together to form an *acoustical network*. To do so, we need to know the *joining conditions*. What are the quantities that are continuous at the interface between any two elements?

In this case, the answer will be simple because the variables,  $p$  and  $U$ , were chosen in our definitions of the acoustical inertance of Eq. (8.47) and the acoustical compliance of Eq. (8.26), specifically to make it easy to join the elements of differing cross-sectional areas to each other. We know that  $p$  is

Stretched membranes of this kind are very convenient for these and similar experiments on the partials of compound tones. They have the great advantage

z  
2  
3  
— — — — —  
FIG. 16 a.



b of being independent of the ear, but they are not very sensitive for the fainter simple tones. Their sensitiveness is far inferior to that of the *resonators* which I have introduced. These are hollow spheres of glass or metal, or tubes, with two openings as shewn in figs. 16 a and 16 b. One opening (a) has sharp edges, the other (b) is funnel-shaped, and adapted for insertion into the ear. This smaller end I usually coat with melted sealing wax, and when the wax has cooled down enough not to hurt the finger

on being touched, but is still soft, I press the opening into the entrance of my ear. The sealing wax thus moulds itself to the shape of the inner surface of this opening, and when I subsequently use the resonator, it fits easily and is air-tight.

**Fig. 8.10** Excerpt from *On the Sensation of Tones* (Dover, 1954), showing the (apparently glass) resonator developed by Helmholtz for frequency analysis. (a) is the neck of the resonator and (b) is a funnel-shaped tube that is intended for insertion into the ear canal

continuous across an interface, both because of Pascal's law and because the linearized Euler equation (8.40) would lead to infinite accelerations if there were non-zero pressure differences across the interfacial boundary of infinitesimal thickness.

The continuity equation requires that fluid cannot accumulate at the interface between elements (which has no volume), therefore the mass flux must also be continuous. As before, the mass flux and the volume velocity are intimately related,  $\dot{m} = \rho U$ , so an equivalent requirement is that the volume velocity also be continuous across the interface if the density is continuous, which usually implies that the temperature is the same on both sides of the interface (Fig. 8.10).

Our first application of this “lumped-element” model will be to an acoustical network that has both historical and contemporary significance: the Helmholtz resonator. It was introduced by H. L. F. Helmholtz (1821–1894) in his classic book *On the Sensations of Tone*, published in 1862, in Chapter III, titled “Analysis of Musical Tones by Sympathetic Resonance.”

If we examine Fig. 8.11, it is clear that continuity of volume velocity,  $U$ , is quite different from continuity of particle velocity,  $v$ . To conserve mass, the velocity of fluid flow in the neck of the Helmholtz resonator,  $v_{neck}$ , will be much larger than the velocities of the fluid near the neck either inside the volume,  $v_{volume}$ , of the resonator or in front of the neck. The streamlines for the flow transition will be bent [9], but if the amplitude of the oscillation is sufficiently small, the transition will be smooth.<sup>9</sup> At higher amplitudes, there could be all kinds of turbulent effects, such as vortex shedding and jetting, which will be irreversible and thus dissipative. These effects can be very important in high-amplitude resonators, but for the present linearized analyses, we are restricting our attention to

<sup>9</sup>The “smallness” criterion for the amplitude of oscillation is somewhat arbitrary, depending upon the desired accuracy of any particular calculation, but a reasonable rule of thumb is to require that the peak-to-peak displacement of the gas in the neck,  $2|\hat{\xi}|$ , is at least ten times smaller than the length of the neck:  $2|\hat{\xi}| = 2(|\hat{U}|/A)/\omega < (\Delta x_{neck}/10)$ .

**Fig. 8.11** Schematic representation of a gas-filled Helmholtz resonator consisting of a neck (inertance) of cross-sectional area,  $A$ , and length,  $\Delta x_{neck}$ , connected to volume,  $V$  (compliance), that is assumed to have perfectly rigid walls

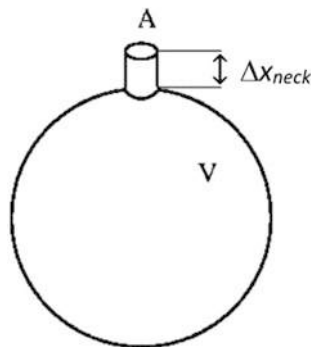


**Fig. 8.12** This very large set of 22 Helmholtz resonators is in the Garland Collection of Classic Physics Apparatus at Vanderbilt University. They were purchased to outfit the Vanderbilt physics department for the opening of the university in 1875. The tiny funnel-shaped tubes emerging from the tops of the spheres were placed in the experimentalist's ear canal; they are not the "necks" of the resonators. The necks of the resonators fit over wooden pegs in the wooden base that supports the collection

acoustical networks that oscillate by an infinitesimal amount away from their equilibrium state. At this point in our investigations, if such high-amplitude effects occur, then we would just simply decrease the excitation amplitude until they disappear.

In the days before the advent of electroacoustic transducers and amplifiers that could convert sound waves into electrical signals whose frequency content could be determined by electronic filters, spectrum analyzers, and FFT signal analyzers, acousticians could use Helmholtz resonators placed in their ears to determine the frequency of sounds. (Another option was to compare the observed tone to the frequencies of a set of tuning forks, like those shown in Fig. 5.11). Figure 8.12 shows a set of Helmholtz resonators that were used in an acoustic laboratory near the end of the nineteenth century.

As long as 12,000 years ago, Helmholtz resonators were used as musical instruments (e.g., ocarinas) in Asia and Mesoamerica [11]. Another early use of the Helmholtz resonator was as whistles, one version of such a whistle is shown in Fig. 8.13. Peruvian whistling bottles were made in pre-Columbian Peru from 500 BCE (Salinar and Gallinazo cultures along Peru's North Coast) until the Spanish conquest of the Incas (1150 AD) [12]. Today, Helmholtz resonators are used extensively as sound absorbers in architectural applications and as tuned "sound traps" in recording studios, ducts, and engine mufflers. A hollow brick that is used as a resonant absorber in rooms is shown in Fig. 8.14 [13].

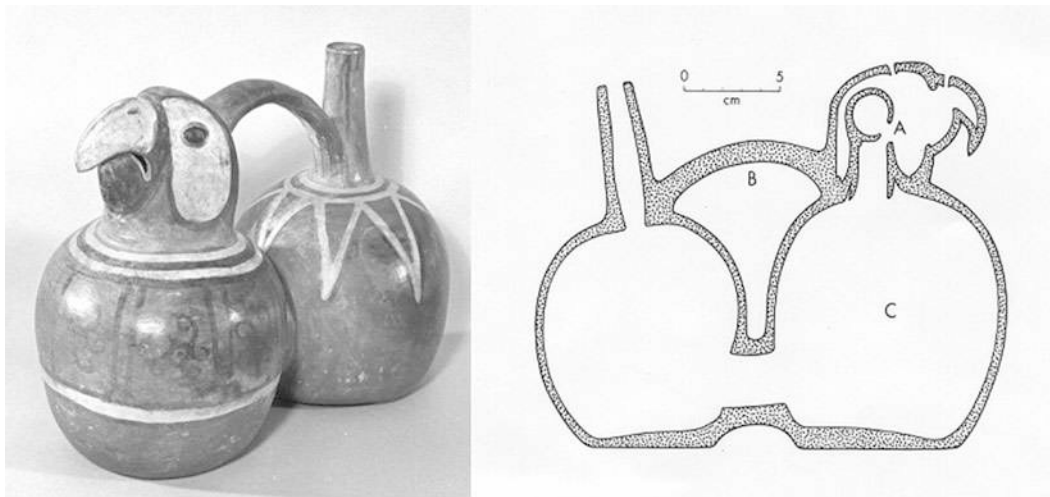


**Fig. 8.13** (Left) Photograph of a double-chambered Peruvian whistling bottle. (Right) Cross-sectional diagram of that bottle [11]. The whistle, enclosed within the bird's head, is made from the Helmholtz resonator (A). The bridge handle (B) joins the body and the neck. The function of the larger volumes (C) is still a matter of controversy after 2500 years. Some say the larger volumes were intended for the storage of fluids, and others claim the vessels were used exclusively as whistles for ceremonial purposes, possibly in conjunction with psychotropic drugs [10]

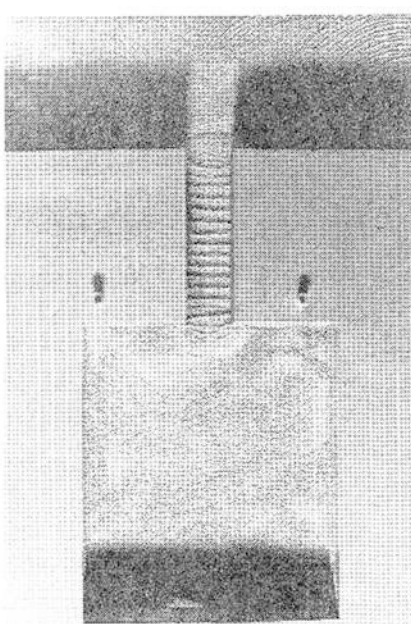


Fig. 9 Helmholtz resonance of the resonator.

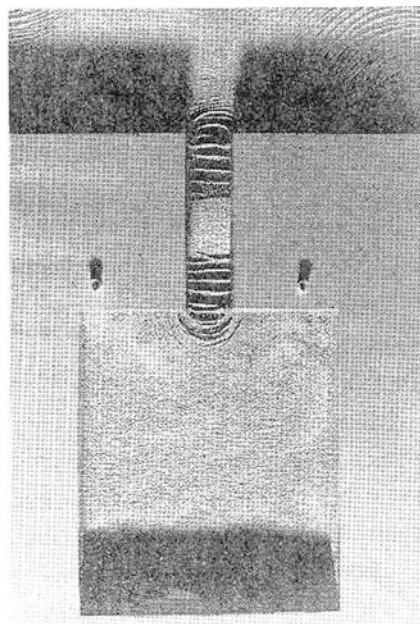


Fig. 10 Open-pipe resonance of the resonator.

**Fig. 8.14** Photographs of two hollow bricks used as low-frequency “tuned absorbers” for reverberation control in buildings. The top of each brick has been removed and replaced with a transparent cover. (Left) The brick is being driven at its Helmholtz frequency,  $f_o = 210$  Hz. The uniformly spaced striations of the cork dust indicate that the gas is oscillating within the neck with uniform velocity amplitude. (Right) The brick is driven at a frequency corresponding to the first open-open standing wave mode of the neck,  $f_1 = 1240$  Hz. The absence of striations around the center of the neck indicates that it is the location of a velocity node, while the striations near the neck's ends indicate velocity anti-nodes at those ends [13]

### 8.5.1 Helmholtz Resonator Network Analysis

We can analyze the response of our Helmholtz resonator by drawing the equivalent circuit shown schematically in Fig. 8.15. For this analysis, we will assume that the resonator is placed in an externally generated sound field with pressure amplitude,  $|\hat{\mathbf{p}}|$ , and with angular frequency,  $\omega$ , so that outside the neck of the resonator,  $p(t) = \Re e[\hat{\mathbf{p}}e^{j\omega t}]$ . Since the end of the compliance that is not joined to the neck is sealed, that pressure can only be applied to the compliance through the neck (inertance). For that reason, the “high” end of the voltage generator, representing the externally imposed pressure, is connected to the one end of the neck but is “grounded” to the closed end of the compliance (compare Fig. 8.11 with Fig. 8.15).

The volume velocity that is able to enter the compliance through the resonator’s neck represents the resonator’s response to the oscillating pressure imposed beyond the neck. Before calculating the amplitude and phase of the (complex) amplitude of the volume velocity as a function of the frequency,  $\hat{\mathbf{U}}(\omega)$ , it is useful to consider the limits of the response at frequencies well above and below the resonance frequency of the resonator,  $\omega_o$ , where the impedance of the inertance,  $Z_L = j\omega L$ , and the impedance of the compliance,  $Z_C = 1/j\omega C$ , exactly cancel each other.

From DC to frequencies less than  $\omega_o$ , the gas flows easily through the neck into the compliance, and the volume velocity amplitude,  $\hat{\mathbf{U}}$ , is controlled by the compliance, in accordance with the definition of compliance in Eq. (8.26):  $\hat{\mathbf{U}}(\omega < \omega_o) \cong j\omega C \hat{\mathbf{p}}$ . In this case, because the reactance of the inertance,  $X_L = \omega L$ , is much smaller than that of the reactance of the compliance,  $X_C = (\omega C)^{-1}$ , the amplitude of the pressure difference between the ends of the neck,  $\Delta\hat{\mathbf{p}}$  (see Figs. 8.11 and 8.15), is negligible for small  $\omega$  and  $|\hat{\mathbf{p}}| \geq |\hat{\mathbf{p}}_{cav}|$ .

At frequencies above resonance,  $\omega_o$ , the inertance of the neck controls how much gas can flow into the compliance:  $\hat{\mathbf{U}}(\omega > \omega_o) \cong \hat{\mathbf{p}}/(j\omega L)$ . At sufficiently high frequencies, the neck blocks flow into the compliance so  $|\hat{\mathbf{p}}_{cav}(\omega \gg \omega_o)| \ll |\hat{\mathbf{p}}|$ , as long as the frequency is still well below that for excitation of the first standing wave mode of the neck,  $\omega_I$ , shown on the right-hand side of Fig. 8.14, or the resonance frequencies of the volume (see Chap. 13 and particularly Sect. 13.4 if the volume is spherical).

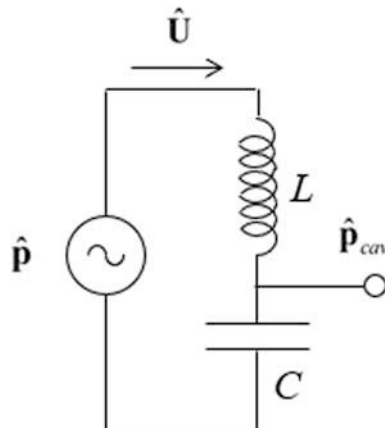


**Fig. 8.15** This is an electrical equivalent circuit diagram of the Helmholtz resonator shown in Fig. 8.11. The volume velocity amplitude,  $\hat{\mathbf{U}} = \hat{\mathbf{u}}A$ , is a “current” passing through the neck (inertance) and into the cavity (compliance). That current is driven by an oscillating pressure,  $p(t) = \Re e[\hat{\mathbf{p}}e^{j\omega t}]$ , imposed on the end of the neck that is not joined to the cavity (compliance) and is represented by a voltage generator. The voltage that appears at the junction of the inertance and compliance represents the pressure amplitude inside the compliance,  $\hat{\mathbf{p}}_{cav}$ . As long as the wavelength of sound is small compared to the characteristic dimensions of the volume,  $V^{1/3} \ll \lambda$ , then  $\hat{\mathbf{p}}_{cav}$  will be uniform within the compliance

With those frequency limits in mind, we can write down the general expression for the amplitude of the volume velocity that enters the compliance through the neck:  $\hat{\mathbf{U}}(\omega) = \hat{\mathbf{p}}/\mathbf{Z}(\omega)$ . With  $L$  and  $C$  “in series,” the total acoustical impedance,  $\mathbf{Z}(\omega)$ , is just the sum of the neck’s acoustical impedance,  $j\omega L$ , and the volume’s acoustical impedance,  $j\omega C$ .

$$\mathbf{Z}(\omega) = \mathbf{Z}_L + \mathbf{Z}_C = j\omega L + \frac{1}{j\omega C} \quad (8.49)$$

The acoustical impedance, as written in Eq. (8.25), determines the amplitude of the oscillating component of the pressure,  $\hat{\mathbf{p}}_{cav}$ , inside the compliance, based on the control of the amplitude of the volume velocity,  $\hat{\mathbf{U}}(\omega)$ , that is imposed by the acoustical impedance in Eq. (8.49).

$$\hat{\mathbf{p}}_{cav} = \frac{\hat{\mathbf{U}}}{j\omega C} = \frac{1}{j\omega C} \left[ \frac{\hat{\mathbf{p}}}{j\omega L + (j\omega C)^{-1}} \right] \quad (8.50)$$

The term within the square brackets in Eq. (8.50) incorporates the substitution  $\hat{\mathbf{U}}(\omega) = \hat{\mathbf{p}}/\mathbf{Z}(\omega)$ . When the denominator within the square brackets vanishes, the theory (in its current dissipationless form!) predicts that the pressure inside the compliance will become infinite, since  $\mathbf{Z}(\omega_o) = 0$  at the Helmholtz resonance frequency.

$$\omega_o = \frac{1}{\sqrt{LC}} = c \sqrt{\frac{A}{V\Delta x_{neck}}} \quad (8.51)$$

The divergence of  $|\hat{\mathbf{p}}_{cav}|$  as  $\omega$  approaches  $\omega_o$  will be eliminated when we add dissipation to our lumped-element model using DELTAEC in Sects. 8.6.7 and 8.6.8 and in the analyses provided in Sect. 9.4.4 that apply the thermoviscous boundary layer losses. The acoustic pressure amplitude in the compliance is “amplified” by the resonance near  $\omega_o$  and attenuated far above  $\omega_o$ .

$$\frac{\hat{\mathbf{p}}_{cav}}{\hat{\mathbf{p}}} \cong \frac{\mathbf{Z}_C}{\mathbf{Z}_C + \mathbf{Z}_L} = \frac{\omega_o^2}{\omega_o^2 - \omega^2} \quad \text{if } \omega \neq \omega_o \quad (8.52)$$

It is also important to consider the phase of  $\hat{\mathbf{p}}_{cav}/\hat{\mathbf{p}}$  at low and at high frequencies compared to  $\omega_o$ , based on the right-hand term in Eq. (8.50). At  $\omega \ll \omega_o$ , fluid easily enters the compliance, and both  $p(t)$  and  $p_{cav}(t)$  are in-phase; when the pressure outside the volume is high, the pressure inside the volume is high also. For  $\omega \gg \omega_o$ , the sign in the denominator in Eq. (8.50) becomes negative indicating that  $p(t)$  and  $p_{cav}(t)$  are 180 degrees ( $\pi$  radians) out-of-phase. That phase reversal is exploited to invert the phase of the radiation from the rear of a loudspeaker cone in a bass-reflex loudspeaker enclosure so it will add to the pressure produced by the front of the loudspeaker, as discussed in Sect. 8.7. In that case, the Helmholtz resonator is used to enhance the low-frequency output of a loudspeaker.

### 8.5.2 A 500-mL Boiling Flask

With Eq. (8.51), we are now in a position to calculate the frequency of a Helmholtz resonator and compare measured results to the theory. Substitution of the resonator dimension and sound speed, provided in the caption of Fig. 8.16, into Eq. (8.51) predicts  $f_o = \omega_o/2\pi = 245.3$  Hz. The experimentally determined frequency is  $f_{exp} = 213.8$  Hz. The measured frequency is nearly 13% lower than the calculated result. That discrepancy is far greater than expected based on our ability to accurately determine the flask’s physical dimensions or our ability to measure the resonance frequency (about  $\pm 1.5$  Hz out of 214 Hz or approximately  $\pm 0.7\%$ ).



**Fig. 8.16** Photograph of a 500 ml boiling flask and a B&K 1" microphone (Type 4144; S/N 473976) mounted on a ring stand. The resonance frequency was determined by blowing over the neck to excite the Helmholtz resonance and measuring the frequency of the microphone signal using an HP 3561A Spectrum Analyzer. The nominal volume of the flask is  $500 \times 10^{-6} \text{ m}^3$ . The diameter of the neck is  $D_{\text{neck}} = 25.0 \pm 0.1 \text{ mm}$ , so the neck's cross-sectional area is  $A = \pi(D_{\text{neck}})^2/4 = 490.9 \times 10^{-6} \text{ m}^2$ . The length of the neck, as measured from the top of the lip to the first flare into the volume, is  $\Delta x_{\text{neck}} = 49.2 \text{ mm}$ . The temperature in the laboratory during measurements tabulated in Fig. 8.17 was  $22.5^\circ\text{C}$ , corresponding to a speed of sound,  $c = 345 \text{ m/sec}$ . To the right and left of the ring stand are the graduated cylinder and the syringe used to measure the water added to the flask that varied the volume producing the data plotted in Fig. 8.17

As we will see later, this discrepancy is mostly a result of the fact that the oscillating gas flow does not stop abruptly neither at the lip of the neck nor at the neck's entrance into the spherical volume of the boiling flask.<sup>10</sup> The gradual transition of the flow from the oscillations within the neck to the stagnant gas surrounding the exterior of the resonator and inside of the volume is usually represented by a “radiation mass,” which we will calculate when we study the radiation from a baffled piston (e.g., loudspeaker) in Sect. 12.8.3 and an unbaffled piston in Sect. 12.9. That additional mass increases the inertance of the neck and is usually incorporated into Eq. (8.51) by defining an “effective length,”  $\Delta x_{\text{eff}} > \Delta x_{\text{neck}}$ , that is the sum of the physical length (in this case,  $\Delta x_{\text{neck}} = 49.2 \text{ mm}$ ) plus some constant times the radius of the neck.<sup>11</sup>

<sup>10</sup> The frequency is also lowered to a lesser degree by the fact that some of the gas in the spherical volume is being compressed and expanded isothermally in regions close to the boundary and the viscous drag of the gas adjacent to the walls of the neck increase its effective inertance. These effects will be included in the DELTAEC model in Sects. 8.6.10 and 8.6.11. The theory of these thermoviscous boundary layer effects is covered in Chap. 9 and calculated explicitly for a Helmholtz resonator in Sects. 9.4.3 and 9.4.4.

<sup>11</sup> As we will see, the standard “recommended effective length correction” improves the agreement between the measurement and the theory of Eq. (8.51), although it is not exact, since the flow transition between the neck and volume is somewhat shape-dependent as discussed by J. B. Mehl, “Greenspan acoustic viscometer: Numerical calculations of fields and duct-end effects,” *Journal of the Acoustical Society of America* **106**(1), 73–82 (1999).

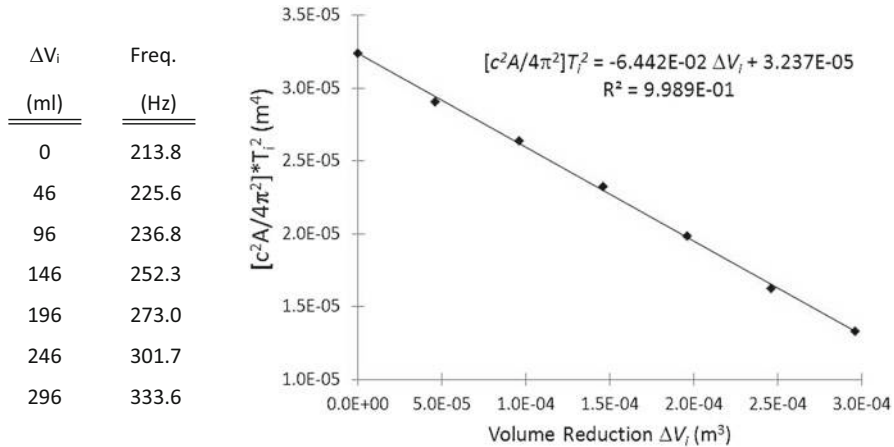


**Fig. 8.17** The data in the table at the left is plotted on the graph at the right based on the linearized least-squares expression in Eq. (8.54). The scaled period squared,  $[c^2 A / (4\pi^2)] * T_i^2$ , is plotted against the added volume of water,  $\Delta V_i$ . Based on the slope and intercept of the best-fit line (see Sect. 1.9),  $\Delta x_{eff} = 64.4 \pm 1.0$  mm, and  $V_o = 502.4$  ml

Although we are not ready to make a theoretical calculation of an effective length correction for the neck in our example, we can use Eq. (8.51), and the measured frequency, to make an experimental determination of the neck's effective length based on the measured Helmholtz resonance frequency,  $f_{exp}$ .

$$\Delta x_{eff} = \left( \frac{c}{2\pi f_{exp}} \right)^2 \frac{A}{V} \quad (8.53)$$

Substitution of the measured value for  $\Delta V = 0$  in Fig. 8.17 into Eq. (8.53) produces a value of  $\Delta x_{eff} = 64.7$  mm, corresponding to a length correction of  $\Delta x_{eff} - \Delta x_{neck} = 15.5$  mm =  $1.24a$ , where  $a = D_{neck}/2$  is the radius of the neck.

In principle, the effective length is independent of the volume of the Helmholtz resonator, as long as the flow contours representing the streamlines from the neck are not perturbed by interactions with the closed end of the volume. We can test this assumption by changing the volume,  $V$ , of the resonator. This can be accomplished by injecting measured quantities of water (assumed to be incompressible) into the boiling flask using the apparatus in Fig. 8.16. Neither the sound speed,  $c$ , the neck area,  $A$ , nor the neck length,  $\Delta x_{neck}$ , would be affected by these incremental changes in volume,  $\Delta V_i$ .

Equation (8.51) can be rearranged to allow the square of the measured period,  $T_i^2 = f_i^{-2}$ , to be plotted against the added volume of water,  $\Delta V_i$ .

$$\left[ \frac{c^2}{4\pi^2} A \right] T_i^2 = \Delta x_{eff} (V_o - \Delta V_i) \quad (8.54)$$

The slope of the best-fit line in Fig. 8.17 will determine  $\Delta x_{eff}$ . The empty volume of the resonator,  $V_o$ , will also be determined by the fit:  $V_o = -(intercept)/(slope)$ .

It is visually apparent from the quality of the least-squares straight-line fit to the data in Fig. 8.17 that Eq. (8.51) and Eq. (8.54) do an excellent job of representing the behavior of the Helmholtz resonator. The relative uncertainty in the slope can be related to the square of the correlation coefficient

for the fit,  $R^2 = 0.9989$  (see Sect. 1.9.2), producing a relative uncertainty in the effective length of  $\pm 1.5\%$ . That is a little better than what would be predicted based on a relative uncertainty in the resonant frequency measurement ( $\pm 0.7\%$ ) and an estimate of the relative uncertainty in the volume changes of about  $1 \text{ ml} \div 50 \text{ ml} = 2\%$ . It is also encouraging that the ratio of the intercept to the slope produced an effective empty volume for the resonator of 502.4 ml.

## 8.6 DELTAEC Software

To this point, we have not yet exploited the power of digital computation beyond the generic spreadsheet and curve-fitting programs provided by mass-marketed commercial software packages. Several software packages have been developed specifically to serve the acoustic community. In underwater acoustics, ray-tracing programs are very popular, as are commercial packages such as LMS Sysnoise [14] used for modeling sound in three-dimensional spaces, BassBox Pro [15] for designing loudspeaker enclosures, or X-OverPro for designing loudspeaker crossovers.

The program that has become an important tool for thermoacousticians [16] since 1985 is the *Design Environment for Low-amplitude Thermoacoustic Energy Conversion* (DETAEC). Drs. G. W. Swift and W. W. Ward developed it at Los Alamos National Laboratory for design and analysis of thermoacoustic engines, refrigerators, and gas mixture separators. It was updated in 2013 to provide an improved user interface with the help of John Clark [17]. Although it has the capability to model heat exchangers and porous media used in such thermoacoustic systems, DETAEC is also well-suited to the design and/or analysis of any quasi-one-dimensional acoustical network consisting of ducts, horns, waveguides, compliances, branches, flow impedances, and loudspeakers in a variety of fluid media bounded by a variety of solids.<sup>12</sup>

Its results have been tested extensively in laboratories worldwide, and it executes calculations very quickly. This high computational speed is accomplished by using analytical results for the transverse variation in the complex pressure and velocity fields. For example, in a CONE segment, solutions to the Webster horn equation [18] provide the pressure as a function of position even through the cross-sectional area is changing and there are non-zero radial components of the fluid's velocity.

DETAEC numerically integrates along one spatial dimension using a low-amplitude, acoustic approximation<sup>13</sup> assuming sinusoidal time dependence,  $e^{j\omega t}$ . It simultaneously integrates the continuity equation (7.32), the Navier-Stokes equation (7.34), and other equations, such as the energy equation, in a geometry specified by the user's choice of a sequence of "segments," such as ducts, compliances, transducers, heat exchangers, and thermoacoustic stacks or Stirling regenerators. DETAEC always assumes steady-state conditions and harmonic time dependence of all acoustic variables.

We will use DETAEC initially to revisit the 500 ml flask used as a Helmholtz resonator in the example of Sect. 8.5.2. Since DETAEC includes the dissipative effects that we have ignored thus far, it

<sup>12</sup> The current version of DETAEC includes the thermophysical properties of the following gases and liquids: nitrogen, dry air, humid air, carbon dioxide, hydrogen, deuterium, helium, neon, He/Ar and He/Xe gas mixtures, natural gas combustion products, liquid sodium, and sodium/potassium eutectic (NaK). Solids include an "ideal" solid with infinite heat capacity and infinite thermal conductivity, copper, nickel, stainless steel, tungsten, molybdenum, Kapton®, Mylar®, and Celcor® (a porous ceramic matrix). It also allows the user to create their own \*.tpf file to represent the temperature and pressure-varying thermophysical properties of user-specified fluids and solids.

<sup>13</sup> DETAEC also supports some nonlinear (i.e., high-amplitude) acoustical effect such as boundary layer turbulence, "minor loss," and amplitude-dependent interfacial discontinuities.

will provide some additional performance information, as well as serve as a familiarization exercise for the software.

### 8.6.1 Download DELTAEC

The latest version of DELTAEC is freely available on the web. Before downloading the software, the *DELTAEC User's Guide*, and sample DELTAEC files, it is a good idea to create a DELTAEC “folder” in your computer’s main directory. The following link would take you close to the download site:

<http://www.lanl.gov/thermoacoustics/DeltaEC.html>

The DELTAEC software installer is also available at the Springer web site for this textbook and the Springer site for Swift’s textbook *Thermoacoustics: A Unifying Perspective for Some Engines and Refrigerators*. [21].

You will have to unzip (Mac) or execute (Windows) the file. That process also installs a copy of the *DELTAEC User's Guide*. The manual is in \*.pdf format and contains searchable hyperlinked text. We will only be concerned with the first four chapters of the *Guide*, but the Reference Sections (Chaps. 8, 9, 10, 11 and 12) are very useful once you have learned the basics. The Reference Sections also contain the equations that are implemented in the software.

This textbook will employ a “two-pronged approach” to familiarize you with some of the elementary acoustical functions that are provided by DELTAEC. The primary sources of information are the first four chapters of the *User's Guide*. The first chapter provides some background on the software and how it functions. The second chapter introduces the user interface by modeling the 1992 Penn State Championship Bottle both as a Helmholtz resonator and as an open-closed standing wave resonator of variable cross-section (see Problem 6 at the end of this chapter). The plotting features of DELTAEC are covered in the third chapter, and the reverse Polish notation (RPN) segment, which lets the user perform customized calculations within a model, is covered in the fourth chapter and introduced here (briefly) toward the end of Sect. 8.6.8.

Although the *DELTAEC User's Guide* should be your primary reference for exploitation of DELTAEC software, the *Guide* will be augmented in this textbook by providing several examples in the remainder of this section and the next. These examples are directly related to acoustical networks that have already been analyzed and will apply DELTAEC to model a standing wave resonator, the 500 ml Helmholtz resonator from Sect. 8.5.1, three coupled Helmholtz resonators in Sect. 8.7, and a bass-reflex loudspeaker enclosure based on the Helmholtz resonator model in Sect. 8.8.

### 8.6.2 Getting Started with DELTAEC (Thermophysical Properties)

After installing the DELTAEC software on all of your computers, a DELTAEC icon should appear on each computer’s desktop near the lower left corner of the screen. You can open DELTAEC by double-clicking on the icon. The design of that icon is motivated by the thermal core of a traveling-wave thermoacoustic engine developed at Los Alamos National Laboratory [19].

DELTAEC usually requires the thermophysical properties of both the fluid supporting the wave and the properties of the solid that contains the fluid in each segment to execute the integrations. We can access this feature directly to have DELTAEC provide these data. When you open DELTAEC by clicking on the icon (instead of opening an existing \*.out file), you will be presented with a “window” that is blank but has pull-down menus at the top. Under the “Help” menu, you can access the *User's Guide*. Under the “Tools” menu, you can access the ThermoPhys(ical) Prop(erties) window shown in Fig. 8.18.



**Fig. 8.18** Screenshot of the DELTAEC Thermophysical Properties window. The default material parameters are for 1 bar (100,000 Pa) helium gas at 300 K and an acoustic excitation at 100.0 Hz

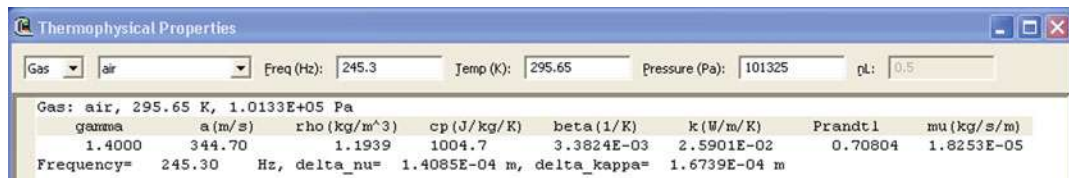


**Fig. 8.19** Screenshot of the thermophysical values for the air used in the 500 ml Helmholtz resonator of the example in Sect. 8.5.2

That window can also be opened from the keyboard by typing “t” when the computer’s attention is on the main DELTAEC window.

As our first example, we’ll use the environmental conditions under which the algebraic results for the 500 ml Helmholtz resonator (Figs. 8.16 and 8.17) were calculated to provide the equilibrium fluid parameters for the air inside that resonator. In the Thermophysical Properties window, modify the gas type to be “air” using the pull-down arrow, the frequency to be 245.3 Hz, and the pressure to be standard atmospheric pressure of 101,325 Pa. Since DELTAEC variables are specified exclusively in MKS units, the temperature must be input in absolute [kelvin] units. The data for our 500 ml example was taken at 22.5 °C, so input the absolute temperature,  $T_m = (22.5 + 273.15)$  K = 295.65 K, into the “Temp(K)” window.

With all of those values appearing in their appropriate location, use your mouse to click on “Show.” This should instantly generate the requested thermophysical properties of air under the specified conditions as shown in Fig. 8.19.

The thermophysical property file header in Fig. 8.19 includes the fluid type (air), the mean temperature ( $T_m = 295.65$  K), and the mean pressure ( $p_m = 101,325$  Pa). The second line contains the frequency-independent fluid properties and their associated units. The first four parameters in the top line are the ratio of specific heats “gamma,” sound speed “a (m/s),”<sup>14</sup> density “rho (kg/m<sup>3</sup>),” and specific heat at constant pressure “cp (J/kg/K).” These parameters should already be familiar.

The subsequent transport parameters will be discussed in Chap. 9, where the dissipative terms in Eqs. (7.34) and (7.43) are analyzed. The isobaric coefficient of thermal expansion,  $\beta_p = - (1/\rho) (\partial \rho / \partial T)_p$ , “beta (1/K),” is just the reciprocal of the absolute temperature,  $T_m$ , for an ideal gas. In our case,  $\beta_p = (1/T_m) = 0.33824 \times 10^{-2} \text{ K}^{-1}$ , agreeing with the DELTAEC output to the five decimal places displayed. Next in line are the thermal conductivity, “k (W/m/K);” the dimensionless Prandtl number (see Sect. 9.5.4), “Prandtl”; and the shear viscosity, “mu (kg/s/m).”

The bottom data line in Fig. 8.19 lists the frequency, “frequency=,” and two frequency-dependent results: the viscous boundary layer thickness, “delta\_nu=,” also known as the viscous

<sup>14</sup>The Los Alamos Thermoacoustics Group uses Rayleigh’s traditional notation for sound speed,  $a$ , instead of the more contemporary choice of  $c$  to represent sound speed. This is because  $c$  is used quite frequently in thermoacoustics to designate specific heats.

penetration depth,  $\delta_\nu$ , and the thermal boundary layer thickness, “`delta_kappa=`,” aka the thermal penetration depth,  $\delta_\kappa$ , which will be derived and discussed thoroughly in Chap. 9.

### 8.6.3 Creating planewave.out

There are several ways to create a DELTAEC model of an acoustical network. The result of such a model is a \*.out file that consists of a sequence of segments like those shown in Fig. 8.21. One can start “from scratch,” but I generally prefer to modify an existing file using the file editing commands in DELTAEC.

We will start by creating a file “from scratch” that represents a simple plane wave resonator of constant cross-section that is shown schematically in Fig. 8.22 and will result in the DELTAEC model shown in Figs. 8.20 and 8.21. Once we gain some experience with the way DELTAEC expects you to insert segments and input the parameters contained within each segment, we will modify planewave.out to create a DELTAEC model of the Helmholtz resonator example based on the 500 mL boiling flask in Sect. 8.5.2. To begin creating “planewave.out,” you should have already downloaded DELTAEC from the Los Alamos Lab’s “Thermoacoustics Home Page.”

If DELTAEC is still open (because you were working on the thermophysical example), you can go to the “File” pull-down menu tab, and click “New.” That action will produce a file with a single BEGIN segment and title the model “NewModel.” Next to “NewModel” is “Change Me” in a blue font. By double-clicking on an item in a blue font, you are able to change it. Double-click on “Change Me” and type in “Planewave Resonator.” There will also be a box that will let you add comments, but we won’t put in any comments, so just click the “OK” button.

Before going further, now would be a good time to save the file. This is done by going to the “File” drop-down menu and selecting “Save As.” Choose the directory in your computer where you would like to save this file (a convenient choice is the same folder that holds the DELTAEC program), and then title the file “planewave.out.” You will see that the “tab” at the top of the DELTAEC model will change its name from “NewModel” to “planewave.” As we add segments, it is a good idea to “Save” the file at regular intervals or before quitting.

*BEGIN Segment.* All DELTAEC models start with a BEGIN segment that specifies the “global” features of the model, like the gas or liquid type (e.g., helium, air, humid air, sodium, etc.); the mean fluid pressure,  $p_m$ ; the mean temperature of the fluid at the start of the model,  $T_m$ ; and the acoustic frequency,  $f$ . You can see these parameters when you click on the “+” sign at the left of BEGIN. This will “unpack” the segment and let you see the parameters it specifies. For very long models, being able to unpack individual segments with the “+” or “compact” with the “–” can be convenient.

In the unpacked form, you see seven parameters in blue font that we are free to modify. For this example, we’ll accept the default values for (0a) = Mean P = 100 kPa, (0b) = Freq = 100 Hz, and the beginning temperature, (0c) = TBeg = 300 K. We’ll also accept the default Gas Type as helium. We can ignore the “Optional Parameters” for now. The use of the segment number and

```

1 planewave(1) Planewave Resonator
2 0 BEGIN Planewave Resonator
12 1 SURFACE Piston Face
19 2 DUCT Resonator Body
26 3 SURFACE End Cap
33 4 HARDEND Rigid Termination

```

**Fig. 8.20** Screenshot of the file “planewave(1).out” is shown before the individual segments are expanded. At the left are the line numbers that you will notice are not consecutive. That is because several lines are suppressed and only the segment numbers and their titles are shown

```

1 1 planewave(1) Planewave Resonator
2 2 BEGIN Planewave Resonator
3   1.0000E+5 a Mean P Pa
4     100.00 b Freq Hz
5     300.00 c TBeg K
6 Gues 1000.0 d |p| Pa
7 Gues 0.0000 e Ph(p) deg
8   1.0000E-2 f |U| m^3/s
9     0.0000 g Ph(U) deg
10 Optional Parameters
11 helium Gas type
12 1 SURFACE Piston Face
13   1.0000E-2 a Area m^2      0.0000 A |p| Pa
14                               0.0000 B Ph(p) deg
15                               0.0000 C |U| m^3/s
16                               0.0000 D Ph(U) deg
17                               0.0000 E Htot W
18 ideal Solid type          0.0000 F Edot W
19 2 DUCT Resonator Body
20   Same 1a 1.0000E-2 a Area m^2 Mstr 0.0000 A |p| Pa
21     0.35449 b Perim m 2a 0.0000 B Ph(p) deg
22     5.0000 c Length m 0.0000 C |U| m^3/s
23 Master-Slave Links
24 Optional Parameters
25 ideal Solid type          0.0000 F Edot W
26 3 SURFACE End Cap
27   Same 2a 1.0000E-2 a Area m^2      0.0000 A |p| Pa
28                               0.0000 B Ph(p) deg
29                               0.0000 C |U| m^3/s
30                               0.0000 D Ph(U) deg
31                               0.0000 E Htot W
32 ideal Solid type          0.0000 F Edot W
33 4 HARDEND Rigid Termination
34 Targ 0.0000 a R(l/z)      0.0000 A |p| Pa
35 Targ 0.0000 b I(l/z)      0.0000 B Ph(p) deg
36                               0.0000 C |U| m^3/s
37                               0.0000 D Ph(U) deg
38 Possible targets          0.0000 E Htot W
39                               0.0000 F Edot W

```

**Fig. 8.21** Screenshot of the fully expanded file “planewave(1).out” before running the program. Since the file has not yet run, all of the results contained in the right-hand column are *red*. These “results,” which are designated with capital letters, contain only *red* zeros. The highlighted “Gues(ses)” on lines 0d and 0e indicate the pressure magnitude, and phase,  $|p|$  and  $\text{Ph}(p)$ , are the “guesses.” Their values are also *red* because the program has not yet modified those guesses to satisfy the “targets.” The highlighted “Targ(ets)” on line (4a) and line (4b) indicate that those values are “targets.” DELTAEC will attempt to adjust the values of the guesses to meet the targets when the program is run.

parameter in parentheses is a convenient way to identify parameters in the model. Notice again that all parameters are specified in MKS units.

Our intention will be to drive this resonator with a sinusoidally varying volume velocity. We’ll set the initial volume velocity magnitude,  $(0f) = |U| = 0.010 \text{ m}^3/\text{s}$ , by clicking on the blue **0.0000** in the  $(0f)$  position. Doing so should bring up the “Parameter Edit: Of  $|U|$ ” window. Type 0.01 into the “Value” line and then click “OK.” That should assign **1.0000E - 2**  $\text{m}^3/\text{s}$  as the value for  $(0f)$ . By

leaving ( $0 \text{ g} = \text{Ph (U)} = 0$ ), we define all other phases in the model with respect to the phase of the driving volume velocity.

Since we are specifying the volume velocity that will drive the resonator, we will rely on DELTAEC to calculate the resulting acoustic pressure magnitude,  $|\hat{p}|$ , and the phase of that pressure,  $\text{Ph } (\hat{p})$ , with respect to  $\text{Ph } (U) = 0 \text{ deg}$ . at any frequency,  $\text{Freq} = (0\text{b})$ . To impose this choice, we can double-click on **100** that is the default value in (0d) to open the “Parameter Edit: 0d  $|\hat{p}|$ ” window. Type in **1000** for the Value, check the “Set as Guess” box, and click “OK.” This brings up a Gues label to the left of (0d) to remind us that DELTAEC will be allowed to modify this value of  $|\hat{p}|$  to satisfy the model and its boundary conditions. It also puts our guess for pressure in red font to warn us that its value is not based on a solution of the model: (0d) =  $|\hat{p}| = \textcolor{red}{1000.0} \text{ Pa}$ . Since we don’t know the phase of the pressure with respect to volume velocity, we also need to make (0e) =  $\text{Ph } (\hat{p})$  a guess. Just click on the default value **0.0000** to bring up the “Parameter Edit: 0e  $\text{Ph}(\hat{p})$ ,” check the “Set as Guess” box, and click “OK.”

This indicates that the values are only “guesses” and DELTAEC’s “shooting method” has been given “permission” to change those values to satisfy constraints placed on the model by the quantities that have been designated “targets.” In this file, those “targets” will be the rigid (infinite) impedances specified in the final HARDEND segment, (4a) and (4b). That completes the BEGIN segment.

*SURFACE Segment.* Now we can specify the area of the “piston” that will produce the volume velocity we specified in (0f). Although we could just let the BEGIN segment produce that volume velocity, since the end of the resonator has some surface area, including a SURFACE segment after the BEGIN segment will mean that any dissipation on that “end cap,” acting as a piston, will be included in our model. To add this next segment, just “right click” in the model, and an “Append” option will appear with a list of possible segments listed alphabetically. You may have to use the arrow to scroll down to see SURFACE. When it appears, just click on it, and DELTAEC will add the new SURFACE segment to your model.

It is useful to name the segment, so click on “**Change Me**” that is to the right of SURFACE, type in “Piston Face,” and then click “OK.” Again, we will not include any comments. SURFACE has only one parameter and we’ll set it to (1a) =  $\text{Area} = 0.01 \text{ m}^2$ . Just click on **0.0000** to bring up the “Parameter Edit: 1a Area” window, enter a “Value” of 0.01, and then click “OK.” SURFACE is a solid, so the segment allows specification of “Solid Type.” Accept the default value of “**ideal**.” “Ideal” just means that we want DELTAEC to assume the solid has infinite heat capacity and infinite thermal conductivity, resulting in a surface that holds the gas isothermal at the gas-solid interface.<sup>15</sup> If you double-click on “**ideal**,” it will bring up the menu of other built-in solid materials (e.g., stainless steel, copper, mylar, etc.). All physical segments in DELTAEC require specification of the gas type and/or solid type.

Unlike the BEGIN segment, the SURFACE segment has a list of six “Results,” from (0A) =  $|\hat{p}|$  to (0F) =  $\dot{E}_\text{dot}$ , at the right-hand side of the segment. All of the numerical results are in red font to warn us that the model has not run and that the current values are only placeholders. After the program has run successfully, all of the results that are currently shown in red will change to green, indicating the upgrade in the model status to actual “results.”

The results will be discussed once the model is complete and has run successfully in Sect. 8.6.4. Now might be a good time to “Save” the file to include the newest segment either by using the “File”

<sup>15</sup> The ability of a solid to hold the temperature of the gas constant at the solid-gas interface is quantified by the  $\varepsilon_s$  parameter discussed in G. W. Swift, “Thermoacoustic engines,” *Journal of the Acoustical Society of America* **84**(4), 1145–1180 (1988), Eq. (59). For most solids in contact with ideal gases at “ordinary” pressures,  $\varepsilon_s \cong 0$ , although if a sound wave is propagating through a liquid metal it is impossible to specify any solid material with sufficient heat capacity and thermal conductivity to hold the liquid isothermal at the liquid-solid interface.

drop-down menu or by simply clicking on the “floppy disk” icon on the banner beneath the drop-down menus.

*DUCT Segment.* We now add the resonator, a tube of circular cross-section. “Right click” in the model to activate the “Append” option and choose DUCT. Click on “[Change Me](#)” that is to the right of DUCT, name this segment “Resonator Body,” and then click “OK.” To specify the DUCT’s cross-sectional area (2a), click on the default value to bring up the “Parameter Edit: 2a Area” window. This time we will not enter a value but instead click on the “SameAs” button. Since the only other parameter in our model with units of area is (1a), DELTAEC has guessed that (1a) might be a good choice. This is correct, so just click “OK.” That will make the area of the DUCT the same as the area of the SURFACE (piston) segment. Choosing to link those areas makes it easy to change the cross-sectional area of the entire model by just changing the cross-sectional area of the piston.

DETAEC has also chosen to make a “Master-Slave” linkage. It automatically chose the DUCT’s Perimeter (2b) to be equal to 0.35449 m. DELTAEC guessed that our DUCT was circular and made the Perimeter,  $\Pi = \sqrt{4\pi A}$ . It also placed a notice to the right of (2a) and (2b) to remind us of that link with “Mstr 2a” to indicate that the value of (2a) is controlling the value of (2b). Again, if we chose to modify the cross-sectional area of the DUCT, then that Master-Slave link would keep the DUCT’s cross-section circular. To accommodate ducts of different shape, the perimeter of the duct (2b) can be specified independently from its area (2a). You can see that choice if you double-click on Master-Slave Links to bring up the dialog box that has made the default choice: “Maintain constant perimeter as area changes.” Double-click on the Length (2c) and make the length of the DUCT be 5.00 m.

Although DELTAEC claims to work for “low-amplitude” acoustics, there are features that allow models to incorporate some nonlinear fluid dynamics to accommodate higher amplitudes. Double-click on the [Optional Parameters](#) to open a dialog box that will let you choose low-amplitude (laminar) flow or high-amplitude (turbulent) flow. Click on the “Laminar” button. For turbulent flow, you would also have to specify a surface roughness factor.

*SURFACE Segment.* Append another SURFACE segment to represent the other end of the resonator. Name that segment “End Cap,” then double-click on the Area, and make it “SameAs” (2a).

*HARDEND Segment.* The final HARDEND segment is a “logical” segment that is required to complete the file. It is one of only two possible choices, the other being SOFTEND. Use “Append” to add the final HARDEND segment and rename it as “Rigid Termination.”

In a SOFTEND segment, the real and imaginary parts of the impedance are specified by the user. If the SOFTEND is infinitely “soft,” then both the real part of the impedance,  $R$  (4a), and the imaginary part,  $I$  (4b), are zero. Of course, there are other choices that would make sense in other situations. For example, the real part of the SOFTEND impedance could be made equal to  $\rho_m c/A$  for a duct to create an anechoic termination that would make the solution a traveling wave instead of a standing wave, as discussed in Sect. 3.6.3 for a string with a resistive termination.

For an ideal HARDEND, the impedance is infinite. Since  $\infty$  is a difficult concept for a computer, HARDEND requires specification of the real and imaginary parts of the complex admittance, which is the (complex) reciprocal of the impedance. For an infinitely rigid and lossless HARDEND condition,  $\Re [1/z] = \Im [1/z] = 0.0000$ , as shown in lines (4a) and (4b) of Fig. 8.21.

We will make each of those rigid boundary conditions a “Target” that DELTAEC will attempt to satisfy. This is done by double-clicking on “[Possible Targets](#).” That will bring up a dialog box that allows us to select the first two of three possible targets. Check the box next to (4a) to make the real (i.e., dissipative) part of the admittance a target,  $R(1/z) = 0$ , and check the second box (4b) to make the imaginary (i.e., reactive) part of the admittance,  $I(1/z) = 0$ , also a target. To the left of both of those entries is “Targ.” If you double-click on zero in either (4a) or (4b), you will open the dialog box that shows that the “Set Target” box has been checked. This now designates the values

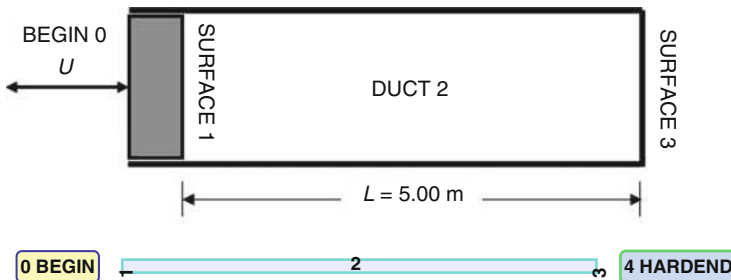


**Fig. 8.22** (Above) A schematic diagram (not to scale) of the helium-filled plane-wave resonator modeled by planewave.out. The cross-sectional areas of the two SURFACE segments and the DUCT are all  $0.010 \text{ m}^2$ . (Below) This drawing is generated by DELTAEC's “View Schematic” function available under the “Display” pull-down menu. It preserves the physical shape of this long, slender resonator. The numbers in the drawing generated by DELTAEC correspond to the segment numbers in the model displayed in Fig. 8.20 (collapsed) and Fig. 8.21 (expanded)

specified in (4a) and (4b) as “targets” that DELTAEC’s “shooting method” will try to make the results in 4G and 4H equal to those targets by modifying the values of guesses, 0d and 0e.

At this point, you should be sure to “Save” the model and then compare it to the screenshot in Fig. 8.21. If you click the “ $\square/\square$ ” icon in the banner, the entire model should collapse to just the segment titles as shown in the screenshot in Fig. 8.20. Click on that icon again and all of the segments for the entire model should “unpack.”

Figure 8.22 provides a schematic diagram of the physical resonator’s parts that are modeled in the planewave.out file shown above the “schematic” generated by DELTAEC’s “View Schematic” function available under the “Display” pull-down menu. I like to check the schematic view since it is drawn to scale. If I’ve entered a geometrical parameter incorrectly (e.g., a length in centimeters instead of meters), then the schematic view will look incorrect.

#### 8.6.4 Running planewave.out

There are two ways to run DELTAEC. One way is to just let the program integrate its way through a file starting at the BEGIN statement. If complex  $\hat{\mathbf{p}}$  and  $\hat{\mathbf{U}}$  are specified in the BEGIN segment, then DELTAEC just integrates its way through the model, matching the complex values (both magnitude and phase) of  $\hat{\mathbf{p}}$  and  $\hat{\mathbf{U}}$  at the interfaces between segments of the model. I find that I rarely use that mode because most models have constraints that are not specified in the BEGIN segment and those constraints determine the values of  $\hat{\mathbf{p}}$  and  $\hat{\mathbf{U}}$  in all of the segments, including BEGIN, as was the case with the HARDEND condition in segment (#4) that dictated the complex pressure in the BEGIN segment (#0), given the amplitude of the excitation by the assumed volume velocity of magnitude,  $|U| = 0.01 \text{ m}^3/\text{s}$ , in (0f).

Most of the time, I use the “equation solver” mode that lets DELTAEC adjust the “guesses” in an attempt to achieve the “targeted” values. The “shooting method” requires that there be an equal number of guesses and targets.<sup>16</sup> They can be viewed at any time by going to the “Display” pull-down menu and selecting “Guesses Targets.” You can also access this display from the keyboard by typing “g” while the computer’s focus is on the main DELTAEC window.

<sup>16</sup> In using DELTAEC, choosing the guesses and targets will require that the user have a reasonably good understanding of the network that is being modeled. For example, targeting the frequency while guessing the pressure would make no sense, since the sound speed of an ideal gas is pressure-independent, as demonstrated in Sect. 10.3.2.

Guesses:			Targets:			Results		
desc	addr	value	desc	addr	value	addr	value	unit
BEGIN: p	0d	1000.0	Pa	HARDE:R(1/z)	4a	0.0000	4G	0.0000
BEGIN:Ph(p)	0e	90.000	deg	HARDE:I(1/z)	4b	0.0000	4H	0.0000

Buttons at the bottom: Close, Edit, Remove, Add Guess, Add Jarg, Clear All.

**Fig. 8.23** Screenshot of the “Guesses and Targets” window shows the current choices of guesses that the solver will modify to reach the targets. The targeted values are in *blue*, but the guesses and the results are still in *red*, since the program has not yet been run. The *red* values of  $|p|$  and  $\text{Ph}(p)$  are the values that were input to the file. Since these are designated “guesses,” DELTAEC will change them in an attempt to force the real part of the admittance,  $R(1/z)$  in (4a), and the imaginary part,  $I(1/z)$  in (4b), to both simultaneously be zero

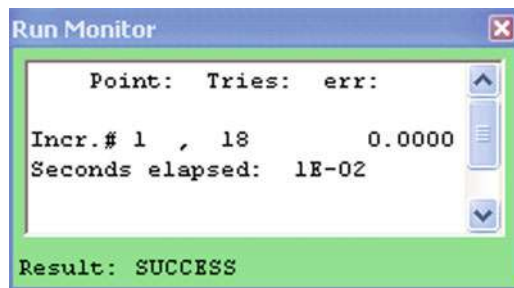


**Fig. 8.24** Screenshot of the Run Monitor window after running planewave.out once. The Run Monitor says that a successful result was achieved after 18 iterations in the span of only 10 milliseconds. The “error” = 0.0000 is a measure of how close to the targeted values the program was able to reach by adjusting the guesses. (The “error” is the length of a vector that DELTAEC creates to represent the distance between the results and the targets. The user is free to provide weights for the components of the error vector that may differ from the DELTAEC defaults)

The particular choice of targets and guesses shown in Fig. 8.23 implies that we will be asking DELTAEC to determine the response of the modeled system to a volume velocity of  $0.010 \text{ m}^3/\text{s}$  imposed on one end of the resonator at a frequency of  $100 \text{ Hz}$ .

The time has come to run planewave.out. The run starts either (i) by clicking on the *blue* run arrowhead at the top of the DELTAEC window, (ii) by going to the “Tools” pull-down menu and selecting run, or (iii) by typing “r.” DELTAEC responds by generating a “Run Monitor” window that is shown in Fig. 8.24. We can view the Guesses Targets window again and see how the guesses have changed. We see that under the specified conditions ( $U_l = 0.010 \text{ m}^3/\text{sec}$  and  $Freq. = 100 \text{ Hz}$ ), the pressure at the piston location (0d) is *3,853.2 Pa* and the phase difference between  $\hat{U}$  and  $\hat{p}$  at that location is *41.520°*.

Looking back at the expanded planewave.out file, we see that all of the results in the right-hand column and both guesses, (0d) and (0e), have changed from *red* to *green* indicating that the solver has found a self-consistent solution.

### 8.6.5 Finding the Resonance Frequencies of planewave.out

As we might imagine, there is nothing special about operation at 100 Hz. We could ask DELTAEC’s solver to find the fundamental half-wavelength,  $\lambda/2$ , resonance frequency,  $f_l$ . Before doing so, let’s run

Thermophysical Properties to get the speed of sound under the current conditions within the resonator:  $c$  (or  $a$ ) = 1019.2 m/s. Simple nondissipative acoustical theory suggests that the fundamental frequency,  $f_1 = c/2L = 101.92$  Hz, much like the fundamental frequency of the fixed-fixed string in Sect. 3.3.1. If we remove the phase of the pressure (0e) from the guess vector and instead make frequency (0b) a guess, we can have DELTAEC's solver find the resonance frequency. ***By setting the phase of the pressure (0e) to be the same as the phase of the volume velocity (0 g), the power delivered to the resonator from the piston is maximized.*** This is exactly the same result that determined the resonance of the damped, driven simple harmonic oscillator in Sect. 2.5.

We make the changes suggested above by returning to the “Guesses Targets” window or the expanded planewave.out file, clicking on the BEGIN:Ph(p) entry, then pressing the “Delete” button, and confirming the choice by pressing the “Yes” button in the “Clear Guess” window. Now we must add frequency as a guess. This is done by clicking the “Add Guess” button command and responding with 0b, the address of frequency in the BEGIN segment. We must also make the pressure be in-phase with the volume velocity by forcing 0e = 0°. This is easily accomplished by simply clicking on the value of 0e in the planewave.out file and changing its value from 43.6° to 0°.

Alternatively, the previous changes to the guesses and the reset of pressure phase (0e) to zero could have been accomplished by going directly to the expanded version of the BEGIN segment (#0) and double-clicking on 43.6°, which will bring up a “Parameter Edit: 0e Ph(p)” dialog box. Typing “0” into the value and unchecking “Set as Guess” will have the same effect as the procedure using the “Guesses Targets” window. Double-clicking on the frequency will again bring up the “Parameter Edit: 0b Freq” dialog box, and clicking on “Set as Guess” will make (0b) the second “Guess.”

Now run the program again. This time the Run Monitor tells us that DELTAEC made 10 runs in 10 msec. The frequency (0b) has changed to 100.91 Hz (just a bit lower than our estimate of 101.92 Hz, because our half-wavelength calculation ignored dissipation), and  $|p|$  has increased to 5,132.8 Pa from 3853.2 Pa, which was its value when we were near resonance at 100 Hz, but not at resonance.

To demonstrate the versatility of the DELTAEC solver, let's change the frequency back to 100 Hz, and ask DELTAEC to “tune” the length of the resonator to put the fundamental resonance exactly at 100 Hz at the specified value of the mean gas temperature. We return to the “Guesses Targets” window to “Delete” (0b) from the guess vector and make its value 100.0 Hz. This time, click on the value of the duct length (2c). When the Parameter Edit window opens, you will have the option of checking a box which says “Set as Guess.” Check the box. If you look at the “Guesses Targets” window, you will see that the DUCT: Length (2c) is now a guess.

Run the program again to now calculate the length that the DUCT segment would be required to make 100.0 Hz the resonance frequency. As expected, to lower the frequency by just under 1%, the length has grown by just under 1% to 5.0453 m.

In a lossless plane wave resonator with rigid ends and uniform cross-sectional area, the higher resonances corresponding to integer numbers of half-wavelengths fitting between the ends to produce a harmonic series of resonance frequencies,  $f_n = n f_1$ , where  $n = 1, 2, 3, \dots, \infty$ , just as we observed with the fixed-fixed string in Sect. 3.3.1. To have DELTAEC calculate a few of these overtones, remove DUCT: Length (2c) from the guesses, replace it with BEGIN: Freq (0b) as the “guess,” and then change the value of (0b) in the file to 200 Hz. If you run again, DELTAEC finds  $f_2 = 200.80$  Hz. Modify frequency (0b) again to be 300 Hz to look for  $f_3 = 302.68$  Hz. The reason the sequence of harmonics is not exactly in integer ratios is that there is dissipation and dispersion within the resonator. We will be able to understand (calculate!) these effects from the acoustic solutions of the hydrodynamic equations once dissipation has been introduced in Chap. 9 and the plane wave solutions to those equations are covered in Chap. 10.

### 8.6.6 State Variable Plots (\*.sp)

We can convince ourselves that DELTAEC has found the fundamental resonance frequency by using another valuable feature of the software. DELTAEC will display plots of the acoustic variables throughout the model by selecting “Plot SP file” from the “Display” pull-down menu. To improve the resolution of those plots, click on “Edit,” and choose “Options” from the drop-down menu. Increase the number of Runge-Kutta steps in the “Nint” box from 10 to 50 and click “OK.” Now “run” again and select “Plot SP file” from the “Display” drop-down menu. In the “header” shown in Fig. 8.25, uncheck  $\text{Im}[p]$  and check  $\text{Im}[U]$  to display the acoustic pressure and acoustic volume velocity for the  $n = 3$  mode of this plane wave resonator. As expected, there are three half-wavelengths with the volume velocity being zero at both ends and the acoustic pressure being maximum at both ends.

Figure 8.25 shows that the real component of pressure,  $\text{Re}[p]$ ; the imaginary component of the volume velocity,  $\text{Im}[U]$ ; and acoustic power flow,  $\text{Edot}$ , have been selected for plotting. Figure 8.26 shows the plots of those selected variables for both the fundamental (half-wavelength) with  $f_1 = 100$  Hz and the second mode (two half-wavelengths) with  $f_2 = 200.8$  Hz.

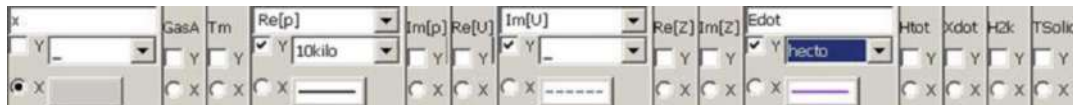


**Fig. 8.25** Screenshot of the state variable plot variable selection window that allows the user to specify which variables should be plotted, as well as the color and line type (e.g., solid, dashed). For the state variable plots shown in Fig. 8.26, I have chosen to plot the real part of the pressure,  $\text{Re}[p]$ ; the imaginary part of the volume velocity,  $\text{Im}[U]$ ; and the magnitude of the acoustic power flow,  $\text{Edot}$ , by clicking the corresponding boxes. The  $x$  axis of the graph is selected as the  $x$  position along the resonator. Since all plots share a common vertical axis, DELTAEC has plotted the pressure in units of  $10\text{kilo}$  (Pa), the volume velocity unscaled ( $\text{m}^3/\text{sec}$ ), and the power in  $\text{hecto}$  (W). Other choices could have been made with the pull-down menus, and other variables could have been plotted by checking other boxes (e.g.,  $\text{Tm}$ ,  $\text{Re}[Z]$ , etc.)

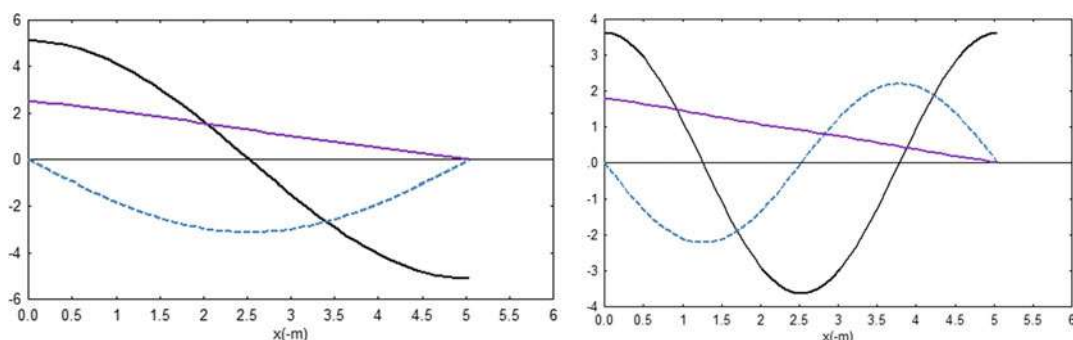


**Fig. 8.26** Screenshot of the state variable plots for the fundamental (left)  $f_1 = 100.0$  Hz and second harmonic (Right)  $f_2 = 200.8$  Hz modes of the helium-filled resonator of length 5.0453 m. Since the pressure and volume velocity in a standing wave are approximately  $90^\circ$  out-of-phase, I have plotted  $\text{Re}[p]$  (black solid line) and  $\text{Im}[U]$  (blue dashed line), as well as the power (solid purple line) vs. position along the resonator from the source ( $x = 0$ ) to the rigid end ( $x = 5.0453$  m). To allow all of my chosen variables to be clearly visible on a single plot, DELTAEC has scaled those variables. In the above plots, the pressure has been divided by 10,000 and plotted in unit of 10 kPa, the volume velocity is plotted as [ $\text{m}^3/\text{s}$ ], and the power has been divided by 100 and plotted as hectowatts

### 8.6.7 Modifying planewave.out to Create Flask500.out

We will modify planewave.out to represent the Helmholtz resonator of Sect. 8.5.2 by removing the two SURFACE segments, changing the gas from helium to air, changing the dimensions of the DUCT to represent the length and cross-sectional area of the neck of the 500 ml flask in Fig. 8.16, and placing a COMPLIANCE segment between the DUCT and the HARDEND to represent the boiling flask's 500 ml volume.

Start by clicking on the blue title above the BEGIN statement and changing it to “500 ml Boiling Flask (Helmholtz Resonator)” After changing the title, select “Save As” from the “Edit” pull-down menu, and save the file as “500mlFlask.out.”

Under the “Edit” pull-down menu, select “Kill Segment,” then select “1 SURFACE,” and watch it disappear from the file. Now that the first SURFACE is gone, DUCT becomes Segment #1. Double-click on the value of area (1a), change it to  $490.9\text{e-}6 \text{ m}^2$ , and then click “OK.” The neck cross-section is circular, so the perimeter should be  $\Pi = 2(\pi A_{duct})^{1/2} = 0.07854 \text{ m}$ . The Master-Slave link should have done that for you. We will use the physical length of the neck as our DUCT length (1c) =  $49.2\text{e-}3 \text{ m}$ . Finally, click on the title of the segment DUCT and change it to “Neck” It might be a good idea to save your changes at this point. There is a save icon near the top left of the model.

Some of the variables in the BEGIN Segment #0 also need modification. Again, by clicking on helium, air can be selected from the menu of gases. Modify Mean P (0a) to be the standard value of 101,325 Pa and the beginning temperature TBeg (0c) =  $295.65^\circ\text{K}$ . Based on the analysis in Sect. 8.5.2, the Helmholtz frequency is expected to be about 250 Hz, so modify (0b) to reflect that. In the schematic representation of Fig. 8.15, we let the flask be pressure-driven at the open end of the neck. Modify (0d) to be 1.0 Pa,<sup>17</sup> and uncheck the “Set as Guess” box. Set the magnitude of the volume velocity, |U| at (0f), as a guess, after clearing (0d) from the guess vector. Put |U| “in the correct ballpark” by modifying (0f) to be 0.001  $\text{m}^3/\text{sec}$ .

Now all that is left is to “Kill” the other SURFACE that is now in Segment #2, and then insert a COMPLIANCE ahead of HARDEND, which became Segment #2 after the last SURFACE was deleted from the file. Under the “Edit” pull-down menu, select “Insert,” use the dialog box pull-down to select COMPLIANCE, and place it before Segment #2 HARDEND.

Renaming the COMPLIANCE from “Change Me” to “500 ml sphere” would be an appropriate choice. Since the 500 ml volume is spherical, the surface area is  $A_{sphere} = 4\pi(3V/4\pi)^{2/3} = 3.0465 \times 10^{-2} \text{ m}^2$ . We should really also subtract the neck area, since that part of the sphere has no surface, so put  $2.9974\text{e-}2 \text{ m}^2$  in “2a.” The volume is 500 ml =  $5\text{e-}4 \text{ m}^3$ . The solid type can remain “ideal.”

Segment #3 can be left as HARDEND, since we do not want any gas to flow out of the end of the volume that is opposite the neck represented by the DUCT in segment #1. Before going further, it would be wise to save this file again. Look over the file to see if you have made any obvious data entry errors (e.g., volume should be 5e-4 and not 5e4), and then hit the “Run” arrow.

### 8.6.8 Interpreting the \*.out File

The results of running 500mlFlask.out are shown in Fig. 8.27. In the BEGIN segment (#0), the inputs that were “guesses” have been changed to the values that produced the best agreement with the

<sup>17</sup> Since this is a linear system, the frequency will be amplitude-independent. By choosing the pressure amplitude to be unity at the entrance to the neck (0d), the numerical value of the pressure amplitude at resonance in the Helmholtz resonator's volume will correspond to the quality factor of the resonance as expressed in Eq. C.1.

```

1 500 mlFlask 500 ml Boiling Flask (Helmholtz resonator)
2 0 BEGIN      Initial
3           1.0133E+05 a Mean P Pa
4 Gues       241.73 b Freq   Hz
5           295.65 c TBeg   K
6           1.0000 d |p|    Pa
7           0.0000 e Ph(p) deg
8 Gues       4.0777E-04 f |U|    m^3/s
9           0.0000 g Ph(U) deg
10 Optional Parameters
11 air        Gas type
12 1 DUCT      Neck
13           4.9090E-04 a Area   m^2
14           7.8540E-02 b Perim   m
15           4.9200E-02 c Length m
16 Master-Slave Links
17 Optional Parameters
18 ideal      Solid type
19 2 COMPLIANCE 500 ml sphere
20           2.9974E-02 a SurfAr m^2
21           5.0000E-04 b Volume m^3
22 Master-Slave Links
23           1.0843E-19 C |U|    m^3/s
24           179.30 D Ph(U) deg
25 ideal      Solid type
26 3 HARDEND   Final
27 Targ      0.0000 a R(1/z)
28 Targ      0.0000 b I(1/z)
29           74.355 A |p|    Pa
30           -89.898 B Ph(p) deg
31           1.0843E-19 C |U|    m^3/s
32           179.30 D Ph(U) deg

```

**Fig. 8.27** Screenshot of the output file for 500mlFlask.out. Input parameters are displayed in the left-hand INPUT column in *blue* with the results in *green*. Calculated results show up in the right-hand “OUTPUT” column, also in *green*. The source (in the BEGIN segment) delivers 203.9  $\mu\text{W}$  (1E), and only 29.9  $\mu\text{W}$  leaves the neck (1F), indicating that the neck dissipated 174  $\mu\text{W}$ . The power that left the neck was dissipated by thermal relaxation effects at the surface of the COMPLIANCE (see Sect. 9.3.2 and Fig. 9.10)

“targets.” We see that the resonance frequency, defined as the frequency where  $\hat{\mathbf{U}}$  and  $\hat{\mathbf{p}}$  were in-phase (specified by  $0e = 0$   $\text{g} = 0^\circ$ ), is 241.73 Hz. This is close to the result of  $f_o = 245.3$  Hz calculated previously using Eq. (8.51).<sup>18</sup> At resonance, the magnitude of the volume velocity (0f) that enters the neck, driven by a 1.0 Pa (peak) pressure amplitude in front of the neck, is given in (0d) as 407.8  $\text{cm}^3/\text{s}$ .

The first four results in the right-hand column of the next three segments will always be the complex pressure and volume velocity at the *exit* from the segment. At the exit of Segment #1 (where it joins the COMPLIANCE), the magnitude of the pressure is  $|p| = 74.353$  Pa. It retains that value throughout the

<sup>18</sup> The fact that the resonance frequency found by DELTAEC is lower than the calculation based on Eq. (8.51) reflects the fact that DELTAEC includes the additional inertance of the fluid in the viscous boundary layer “attached” to the surface of the resonator’s neck and the isothermal compressibility of the gas in the thermal boundary layer on the surface of the cavity. These dissipative boundary layer effects will be the focus of Chap. 9.

remaining two segments. This is a new result that we could not obtain from our nondissipative analysis of this network in Sect. 8.5.1, and it is important!

In our nondissipative analysis of Eq. (8.52), the ratio of the pressure in the cavity to that in front of the neck diverged at resonance:  $|\hat{\mathbf{p}}_{cav}/\hat{\mathbf{p}}| = \infty$ . Since DELTAEC includes the viscous dissipation caused by the drag of the oscillatory air flow within the neck, and the thermal relaxation losses due to thermal conduction between gases undergoing adiabatic temperature changes, derived in Eq. (7.25), within the volume, the pressure amplitude is now finite. In fact, the “gain” is the quality factor of the Helmholtz resonator,  $Q = |\hat{\mathbf{p}}_{cav}/\hat{\mathbf{p}}| = (2A)/(0d) \cong 74$  (or + 37.4 dB). This pressure increase over a narrow frequency band is just what Helmholtz sought by “plugging” the resonators that share his name into his own ear.

The amplitude of the gas displacement in the neck,  $\xi_1$ , can be determined by “integrating” the volume velocity divided by the product of the neck area times the angular frequency:  $|\hat{\xi}| = |\hat{\mathbf{U}}|/(2\pi f A_{neck}) = 0.547$  mm. That is about 1.1% of the total neck length, so our assumption of a 1.0 Pa excitation in (0d) was well within our assumption of linear behavior.<sup>9</sup>

### 8.6.9 The RPN Segment

One of the most powerful features of DELTAEC is its ability to perform user-defined calculations within any model using the variable values calculated by the program. Such calculations can be done automatically within the program using the RPN segment available in DELTAEC. The serious student is referred to the *DELTAECEC User’s Guide* for a detailed discussion of the RPN segment, including tables that summarize the wide variety of accessible variables, convenient variable abbreviations for thermophysical properties and state variables (e.g., frequency, mean temperature, power flows, pressure, volume velocity, etc.) included in Table 11.2 of the *User’s Manual*, and executable mathematical functions (e.g., square roots and other real and complex algebraic operations, circular and hyperbolic trigonometric functions, Bessel functions, logs, and exponentials) also included in Tables 11.3 through 11.7 of the *User’s Manual*.

To illustrate, an RPN segment has been added to 500mlFlask.out and the file saved as 500mlRPN.out. That RPN segment, shown in Fig. 8.28, automatically calculates the peak-to-peak displacement,

```

1 500mlRPN 500 ml Boiling Flask (RPN Example)
2 BEGIN Initial
12 DUCT Neck
19 COMPLIANCE 500 ml sphere
26 RPN Peak-to-Peak Gas Displacement in the Neck
27 0.0000 a G or T 1.0938 A mm
28 2 Of * 1a / w / 1000 *
29 HARDED Final

```

**Fig. 8.28** Screenshot of a modified version of 500 mlFlask.out, shown in Fig. 8.27, which now includes an RPN segment (#3) that calculates the peak-to-peak gas displacement in the neck of the 500 ml boiling flask automatically and reports the result (3A) in millimeters

$2|\hat{\xi}|$ , of the gas in the resonator's neck. To eliminate the need for parentheses, the RPN segment uses Reverse Polish Notation:<sup>19</sup> variables are “declared,” and then an operation on the variable (e.g., taking the cosine of an angle) is executed. If an operation requires two variables (e.g., multiplying one variable by another), then both variables appear before the operation.<sup>20</sup>

For example, the magnitude of the volume velocity entering the neck,  $|\hat{U}|$ , that is provided in (0f), must be divided by the cross-sectional area of the neck in (1a), to obtain the average gas velocity in the neck. That velocity then needs to be integrated, so that peak gas velocity must be divided by  $\omega$  to obtain the peak gas displacement,  $|\hat{\xi}|$ . Since the desired result is the peak-to-peak displacement,  $2|\hat{\xi}|$ , the result of the integration must be multiplied by two. In algebraic notation,  $2\xi = 2*(0f) / [w * (1a)]$ .<sup>21</sup> If the result is to be displayed in millimeters, the entire expression must be multiplied by 1000.

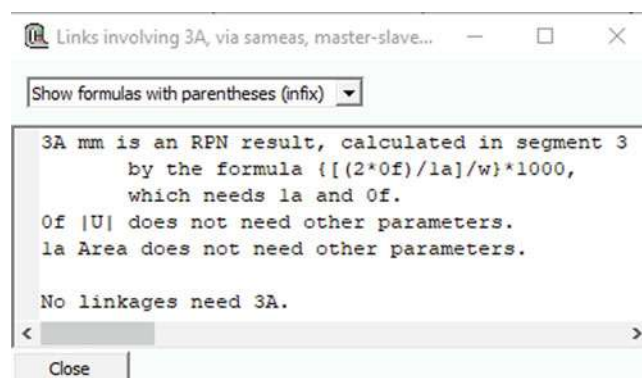
In RPN, that same calculation is written,  $2\xi = 2 (0f) * (1a) / w / 1000 *$  or  $2\xi = 2000 0f * 1a / w /$ , to provide the result in millimeters. In the first version, the number “2” and (0f) are multiplied (\*), and then (1a) divides (/) the previous result. The RPN abbreviation for  $\omega$ , which is “w,” divides (/) that result, followed by “1000” and a multiplication (\*). For that RPN segment shown in Fig. 8.28, “ChngeMe” has been replaced by “mm,” representing millimeters in the “units” column as a reminder that the result is given in (3A) as millimeters.

That RPN segment (#3) is shown along with the other “collapsed” segments of the model in Fig. 8.28. The RPN segment result (3A) is exactly twice what was calculated for  $|\hat{\xi}|$  “by hand” from the results in the \*.out file in Fig. 8.27.

<sup>19</sup> Reverse Polish notation (RPN) is a system where the “operator” follows the variable(s). The “Polish” designation is in honor of its inventor, Jan Łukasiewicz (1878–1956). That form of data entry and calculation was used in the scientific calculators made by Hewlett-Packard since the introduction the HP-35 in 1972, the first handheld scientific calculator. RPN is used in HP calculators to the present day. It is preferred by most scientists and engineers of my generation because it takes fewer key strokes and because operations are unambiguous without requiring parentheses.

<sup>20</sup> If you prefer parentheses, DELTAEC can display an RPN formula in that notation. Double-click on the RPN result, and then click “List Linkages” to show the formula using parentheses.

<sup>21</sup> DELTAEC will show an RPN result using “algebraic notation,” using parentheses if you click on the RPN result then choose “List Linkages.”



### 8.6.10 Power Flow and Dissipation in the 500 MI Boiling Flask

The magnitude of the volume velocity,  $|\hat{\mathbf{U}}|$ , that leaves the neck ( $1C = 398.06 \text{ cm}^3/\text{s}$ ) is slightly reduced from the value that entered the neck ( $1f = 407.77 \text{ cm}^3/\text{s}$ ) due to the compliance of the gas in the neck itself. It is worth noticing that in the compliance,  $\hat{\mathbf{U}}$  and  $\hat{\mathbf{p}}_{cav}$  are almost exactly  $90^\circ$  out-of-phase (1B), as they should be for a compliance described in Eq. (8.25). Of course, the volume velocity exiting the compliance is zero ( $|\hat{\mathbf{U}}| < 1.08 \times 10^{-19} \text{ m}^3/\text{s}$ ) to satisfy the HARDEND condition in Segment #3 of Fig. 8.27 and Segment #4 in Fig. 8.28.

The next two results shown in Fig. 8.27 are  $H_{tot}$  (1E) and  $E_{dot}$  (1F).  $E_{dot}$  is the acoustic (mechanical) power that exits the segment, and  $H_{tot}$  is the total power (effectively the sum of the acoustical power plus thermal power converted from acoustical power by dissipation) leaving the segment.<sup>22</sup> Following Sect. 1.5.4, the acoustic power is one-half of the product of the acoustic pressure magnitude,  $|\hat{\mathbf{p}}|$ , times the volume velocity magnitude,  $|\hat{\mathbf{U}}|$ , times the cosine of the phase angle between those quantities. Since  $\hat{\mathbf{U}}$  and  $\hat{\mathbf{p}}$  are in-phase, the input acoustical power is  $\langle \Pi_{in} \rangle_t = |\hat{\mathbf{p}}| |\hat{\mathbf{U}}| / 2 = (0d) * (0f) / 2 = 203.88 \mu\text{W}$ . Energy is conserved so the total power,  $H_{tot}$ , that moves through our resonator is fixed, hence (1E) = (2E) = (3E) =  $203.89 \mu\text{W}$ . That total power cannot exit the model, but at the end of the model has been converted entirely to heat by thermoviscous dissipative processes.

The power dissipated in the neck is the difference between the acoustic power that entered from the BEGIN segment ( $1E = 203.88 \mu\text{W}$ ) and what exited from the neck ( $1f = 29.919 \mu\text{W}$ ) and entered the COMPLIANCE. Therefore, those viscous losses in the neck dissipated  $173.96 \mu\text{W}$ , and that power was deposited on the neck as heat and/or swept away and dumped elsewhere by thermoacoustic boundary layer processes [20], which are beyond the scope of this textbook. Since the walls of the neck are “ideal” and have infinite heat capacity, the temperature of the neck did not increase. Thermoacoustic heat transport can actually cause portions of the duct to cool even in the presence of viscous heating [21].

The thermal relaxation dissipation in the compliance can be determined by subtracting  $E_{dot}$  that leaves the compliance (2F) from  $E_{dot}$  that enters (1F):  $29.919 \mu\text{W} - 5.94 \times 10^{-20} \text{ W} = 29.919 \mu\text{W}$ . That heat is deposited on the walls of the COMPLIANCE.

Apparently, for this Helmholtz resonator, 85% of the dissipation in the model is due to the viscous losses produced by the oscillatory gas motion in the neck. At this point, radiation losses from the neck of the resonator have not been calculated.<sup>23</sup>

### 8.6.11 An “Effective Length” Correction

At this point, you should be able to try a few things with DELTAEC on your own (or with the few prompts that follow). Let’s have DELTAEC adjust the length of the neck so that the resonance frequency becomes the measured value,  $f_{exp} = 213.8 \text{ Hz}$ . This can be accomplished by opening 500mlFlask.out,

<sup>22</sup> See G. W. Swift, *Thermoacoustics: A Unifying Perspective for Some Engines and Refrigerators*, 2nd edn. (Springer/Acoust. Soc. Am., 2017); ISBN 978-3-319-66932-8, Chapter 5.2, for a discussion of the difference between total power and acoustic power.

<sup>23</sup> The radiation efficiency will be calculated later in this textbook (see Sect. 12.2.1). For those who can’t wait,  $\langle \Pi_{rad} \rangle_t = (\pi \rho_m f^2 / 2c) |\hat{\mathbf{U}}|^2$ . DELTAEC could have calculated those automatically, as well, if a PISTBRANCH or OPNBRANCH segment were placed before the neck that models a flanged open end or unflanged open end.

then inserting another DUCT of zero length ahead of the existing DUCT segment representing the neck, and naming that new segment “[Effective Length Correction](#).” It would also be a good time to rename the title of the model (Line #1) as “[500 ml Boiling Flask \(Effective Length\)](#).” Use “SaveAs” in the “File” drop-down menu to save the file as “FlaskEffLength.out.”

As a convenience, DELTAEC will add a “Master-Slave Link” to the relationship between area and perimeter to keep the shape of the inserted duct circular. We do not want that link because we do not want the “effective length duct” to add any thermoviscous dissipation. To sever the link, just click on [Master-Slave Links](#) and select “none.”<sup>24</sup>

In the new file, make the new effective length DUCT’s area (1a) be “[sameas 2a](#)” by double-clicking on the value of (1a). This will bring up the “Parameter Edit” window for (1a). Click on the “SameAs” button and place “2a” in the window. The “SameAs” feature is very convenient, since various segments of a model whose dimension should be linked can be changed by changing only one variable in one segment. Set the perimeter to an arbitrarily small value, (1b) = [0.0001](#) m, since the effective length correction is not a “physical” duct that would introduce additional thermoviscous loss.<sup>25</sup> Change the value of frequency in (0b) to [213.8](#) Hz, and remove frequency (0b) from the guess vector. Let the length of the “effective length” duct (1c) be a “guess.” Just double-click on the value of (1c) and check the “Set as Guess” box when the “Parameter Edit” window opens. Figure 8.29 shows the \*.out file produced after that model has run successfully.

The resulting effective length correction, (1c) = 13.54 mm, slightly less than the value (15.5 mm) obtained when we used the expression in Eq. (8.53), which ignored dissipation. Again, less “effective length” was required to obtain the experimentally measured frequency since some of the necessary frequency reduction was provided by gas compliance and viscous dissipation in the neck and thermal-relaxation effects within the 500 ml volume. We will calculate the effective length correction in Sects. [12.8](#) and [12.9](#).

### 8.6.12 Incremental Plotting and the \*.ip File

Our initial exploration of DELTAEC’s capabilities will conclude by using the software to create a plot of the pressure magnitude and phase within the 500 ml volume as a function of frequency. DELTAEC produces two types of plots: One is the “State Plot,” introduced in Sect. 8.6.6, that allows all of the different results for an individual run to be plotted, usually as a function of position along the apparatus (e.g., real and imaginary pressure magnitude,  $E_{dot}$ , etc.). The State Plot is particularly useful for models that are complicated and contain branching and thermoacoustic elements, such as heat exchangers, that change energy flows and temperatures throughout the apparatus being modeled. They also provide essential confirmation of the normal mode shapes for standing waves in complex networks (see Fig. 8.26).

The other plot type is the “Incremental Plot.” An incremental plot lets the user to choose two variables (called the “outer” and “inner” plotting variables) that can be incremented or decremented over a range of equally spaced values. One choice might be a range of static pressures (outer plot

<sup>24</sup> As with many items in this section, DELTAEC supports a lot more capabilities that we have space to explore in an introduction. If you want to know more about Master-Slave links or any other feature, you are referred to the *User’s Guide*.

<sup>25</sup> There is also some dissipation due to the fluid shear which accompanies the divergence of the streamlines at both ends of the neck. A detailed analysis of this dissipation mechanism and the effective length correction is provided in K. A. Gillis, J. B. Mehl, and M. R. Moldover, “Theory of the Greenspan viscometer,” *Journal of the Acoustical Society of America* **114**(1), 166–173 (2003).

```

1 1 FlaskEffLength 500 ml Boiling Flask (Effective Length)
2 0 BEGIN Initial
3      1.0133E+05 a Mean P Pa
4          213.80 b Freq Hz
5          295.65 c TBeg K
6          1.0000 d |p| Pa
7          0.0000 e Ph(p) deg
8 Gues      4.1866E-04 f |U| m^3/s
9          0.0000 g Ph(U) deg
10 Optional Parameters
11 air          Gas type
12 1 DUCT      Flask Neck Effective Length Correction
13 Same 2a 4.9090E-04 a Area m^2
14          1.0000E-04 b Perim m
15 Gues      1.3539E-02 c Length m
16          5.0000E-04 d Srough
17 Master-Slave Links
18 Optional Parameters
19 ideal Solid type
20 2 DUCT      Neck
21 3 COMPLIANCE 500 ml sphere
22          2.9974E-02 a SurfAr m^2
23          5.0000E-04 b Volume m^3
24 Master-Slave Links
25          0.0000 C |U| m^3/s
26          0.0000 D Ph(U) deg
27          2.0933E-04 E Htot W
28 ideal Solid type
29 4 HARDEND Final

```

**Fig. 8.29** Screenshot of the output file for “FlaskEffLength.out.” DELTAEC has adjusted the length of an additional duct so that the frequency (0b) is the measured value,  $f_{exp} = 213.8$  Hz, taken from Fig. 8.17. Notice that the quality factor, based on the magnitude of the pressure in the COMPLIANCE,  $|p| = (1A)$ , has increased to produce  $Q = 85.8$ , which is larger than  $Q = 74.4$ , in Fig. 8.27. This increase is due to the additional stored kinetic energy produced by the velocity of the flow in the effective length correction, which introduced no additional dissipation, since the “perimeter” of that duct (1b) was set to be negligibly tiny

variable) that are used to generate plots over a specified range of frequencies (inner plot variable) for each pressure. In the following example, only one (outer) plot variable, the frequency (0b), will be incremented (or decremented) to generate a resonance response curve similar to Fig. 2.12 for the damped simple harmonic oscillator.

The magnitude (2A) and phase (2B) of the pressure inside the compliance of the 500mlFlask.out file in Fig. 8.27 will now be set up to be plotted as a function of frequency (0b). The magnitude of the pressure in front of the neck (0d) will remain constant at 1.0 Pa as the frequency is being swept below and above the resonance frequency. Since the resonance occurs around 240 Hz, the plot will be set up to go from 230 Hz to 250 Hz, placing the Helmholtz resonance frequency roughly in the middle of the plotting range.

It is a good idea to have a model that is converged at the starting point before attempting an incremental plot. Since the plot will start at 230 Hz, click on (0b) and set it to 230 Hz and be sure it is *not* designated as a “Guess.” The phase could be positive or negative or any phase value that is modulo an integer multiple of 360°, but the phase, though correct, may be inconvenient for display of the plotting results. To avoid phases that exceed +360° or are less than -360°, click on (0 g), and set it to

zero degrees. Then run the model to be sure that it converges at the starting point (230 Hz) for the plot. Seeing that the model converged and produced an initial phase between the pressure in front of the neck and the volume velocity at the neck's entrance of about 82.3°, the model is ready to begin plotting.

To set up the plot, make the magnitude (0f) and phase (0 g) of the volume velocity “guesses.” Then double-click on the 230 Hz (0b). In the “Parameter Edit” window, check the “Incr Plot” box. That choice will launch the “Incr(emental) Plot Editor” window. Since the last run of the model was at 230 Hz, DELTAEC will assume that the initial value of the frequency plotting range is 230 Hz, so that frequency will automatically appear in the “From” window. To set the plotting range between 230 Hz and 250 Hz, put 250 Hz in the “To” window, and then set the number of plotting points (#Points) to 81. By specifying 81 points, a step size of 0.25 Hz/point is automatically displayed. An “OPlt” designator will appear to the right of (0b) in the \*.out file to indicate that frequency is now an independent (outer) plotting variable. Save this new model as 500 mlFlask(Plot).out to distinguish it from previous models.

DETAEC will automatically include the guesses in the plot file and will tabulate the results in a text file that will be automatically designated 500 mlFlask(Plot).ip. In this case, those guesses are the magnitude (0f) and phase (0 g) of the volume velocity driven through the neck by the externally applied 1.0 Pa pressure. Since we want to plot the magnitude (2A) and phase (2B) of the pressure within the compliance, we click on those results, and check the “Plot(Independent)” box in the “O(uter) Par(ameter) edit” dialog box. This should produce a “P” to the left of (2A) and (2B) indicating that these results will now also be contained in the incremental plot file.

To check the plotting setup, go to the “Display” pull-down menu, and select “Incremental Plot Sum (mary).” That will produce the Incremental Plot Summary window reproduced in Fig. 8.30.

When you click on the run arrow, DELTAEC will run itself 81 times in about one-half second, ending at 250 Hz, and will have created a new incremental plot file and named it 500mlFlask(Plot).ip. You can examine the content of this plot file in a variety of ways. It can be “opened” in your favorite commercial plotting program (e.g., Excel™) or text editor (e.g., WordPad or NotePad), or it can be examined within DELTAEC using the native DELTAEC plotting software by clicking on “Display” and selecting the “Plot IP file” from the pull-down menu. Figure 8.31 shows a portion of the \*.ip file, opened with a text editor, containing the first 13 results between 230 and 233 Hz.

If you repeat the plot or if you have plotted the file previously, DELTAEC will provide the option of “overwriting” the existing \*.ip file, or you can choose to “append” this new run to the previous file (a useful option if you are spanning a large frequency range that you have broken up into shorter runs). If you want to keep the original file, DELTAEC will provide the option to “Rename” the new file.

Outer:				Inner:			Dependent:			
addr	desc	unit		addr	desc	unit	addr	desc	value	unit
0b	Freq	Hz					0f	U	8.067573810	m^3/s
Start:	230.0						0g	Ph (U)	-78.4908432	deg
End:	250.0						2A	p	14.24839938	Pa
Step:	0.25						2B	Ph (p)	-168.391958	deg
Points:	81									

**Close** **Rewind...**

**Fig. 8.30** Screenshot of the Incremental Plot Summary window shows that we have selected frequency (0b) as our independent plotting variable and that variable will range from 230 Hz to 250 Hz in 81 steps of 0.25 Hz. It will generate a plot file (\*.ip) that will contain the independent plotting variable (0b) and the dependent “guess” variables,  $|U|$  (0f) and  $\text{Ph}(U)$  (0g), as well as the pressure magnitude,  $|p|$  (2A), and phase,  $\text{Ph}(p)$  (2B), in the COMPLIANCE

BEGIN:Freq	BEGIN: U	BEGIN:Ph(U)	COMPL: p	COMPL:Ph(p)
Hz	m^3/s	deg	Pa	deg
Ob	of	0g	2A	2B
230.000	5.5251E-05	82.2980	10.5660	-7.5949
230.250	5.6461E-05	82.1270	10.7860	-7.7664
230.500	5.7723E-05	81.9480	11.0150	-7.9454
230.750	5.9040E-05	81.7610	11.2550	-8.1324
231.000	6.0417E-05	81.5660	11.5060	-8.3279
231.250	6.1857E-05	81.3610	11.7680	-8.5325
231.500	6.3364E-05	81.1470	12.0420	-8.7468
231.750	6.4945E-05	80.9220	12.3300	-8.9716
232.000	6.6603E-05	80.6860	12.6320	-9.2077
232.250	6.8345E-05	80.4380	12.9490	-9.4559
232.500	7.0177E-05	80.1770	13.2820	-9.7171
232.750	7.2107E-05	79.9020	13.6330	-9.9923
233.000	7.4141E-05	79.6110	14.0030	-10.283

**Fig. 8.31** Screenshot of the first 13 results produced by DELTAEC's incremental plotting function and placed in the \*.ip file, for the response of the 500 ml boiling flask, is shown using a simple text editor. The file also includes a “header” with the “variable” (e.g., BEGIN: Freq), its units (e.g., Hz), and its “address” in the model (e.g., Ob)

Checking the file using DELTAEC's built-in plotter is convenient, since it is a faster way to examine the plot than to export the file to another spreadsheet or mathematics software package. I always check the plotted data with DELTAEC's indigenous plotting function to make sure that I have plotted the data that I wanted over my range of interest. A DELTAEC-generated incremental plot from the example just run is shown in Fig. 8.32. That incremental plotting window lists the plot variables that can be selected for plotting by checking the desired boxes. In this example, BEGIN: Freq@0b has been selected as the *x* axis for the plot. COMPL|p|@2A and COMP: Ph(p) @2B are chosen as the *y* axis variables.

The “windows” below the variables provide a variety of options for scaling the plot. In all three cases, the variable values in Fig. 8.32 are not scaled, hence the “\_” symbol in that window. The window below the *y* axis variables allows selection of the shape, the size, and the color of the plotted points, as well as the options for a line to connect the points. The line color and style (e.g., solid, dashed, dotted, dash-dot) and line width can also be selected by the user. Under the “Options” drop-down menu, “Enable Legend” has been selected to produce the legend in the upper-right corner of the plot in Fig. 8.32. The legend identifies the plotted dependent variables as well as their units and scaling.

Since DELTAEC automatically includes thermoviscous dissipation, the 180° phase shift from below to above the resonance frequency is no longer discontinuous as predicted by the nondissipative result in Eq. (8.52). As shown in Fig. 8.32, the phase changes smoothly through resonance with the largest rate of change of phase as a function of frequency occurring at the resonance frequency. This is demonstrated in Fig. 8.33, where the phase of the plotted frequency closest to the resonance (241.75 Hz) and the phases of the two adjacent frequencies calculated in 500mlFlask(Plot).ip are fit to a straight line.

Agreement between the quality factor based on the amplitude gain and the quality factor based on the slope of the phase vs. frequency would be improved if smaller frequency increments around resonance were selected in the DELTAEC plotting file.

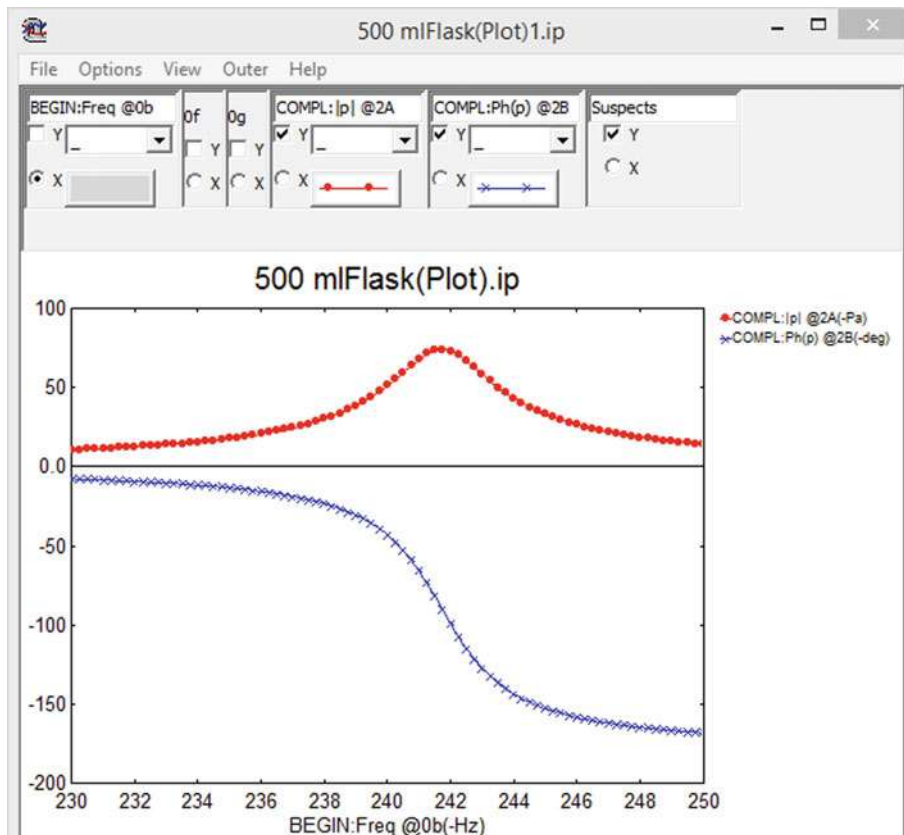


**Fig. 8.32** Screenshot of the output window generated by DELTAEC for the incremental plot file 500mlFlask(Plot).ip. The pressure magnitude (2A) (red circles) and phase (2B) (blue crosses) in the COMPLIANCE segment were selected for plotting against frequency. The label for the x axis was also generated by DELTAEC. The legend is generated automatically and shows that the units for pressure are [Pa] and for phase is [deg]

### 8.6.13 So Much More Utility in DELTAEC

DELTAEC is a very versatile and powerful (and free!) computational tool that is provided with extensive documentation. This introduction could not really demonstrate the full power of the software, but it should have provided the minimum background for its further exploitation in this textbook and in your careers as acousticians. Students are encouraged to download and print parts of *DELTAEC User's Guide*, such as the Reference Section, which describes the use of the various segments and the section on the RPN Segment (*User's Guide* Chap. 4).

The RPN segment permitted the user great flexibility in calculating quantities of interest automatically within a DELTAEC model every time it is run. It also produces potential targets (e.g., phase differences) that might be more appropriate targets for the solver to use in making the model conform more closely to the behavior of the physical apparatus.

The next two sections will use DELTAEC to analyze two more “lumped-element” networks. They were chosen because they employ inertances and compliances and because they would be rather tedious to analyze without the assistance of DELTAEC.

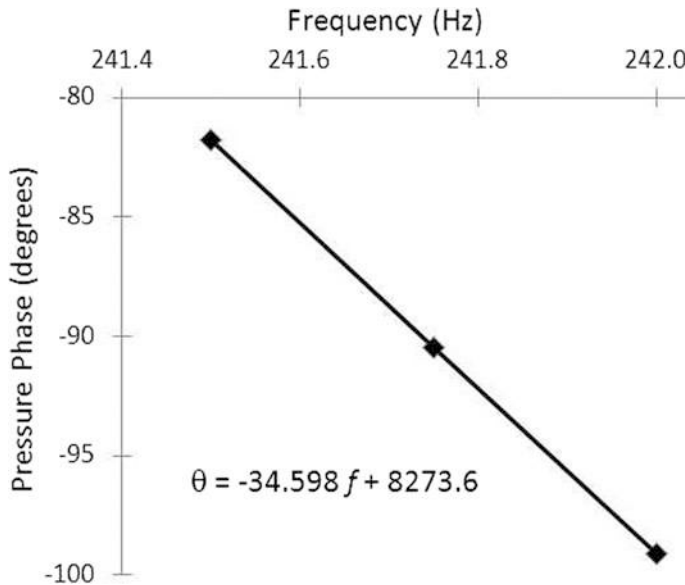


**Fig. 8.33** The rate of change of phase around the resonance frequency of the 500 ml boiling flask is fit by a straight line with the slope,  $(d\theta/df)_{f_o} = -34.6^\circ/\text{Hz}$ . That slope is related to the quality factor,  $Q$ , of the resonance. The relation from Eq. 2.76 is reproduced as  $Q = \left| \frac{\pi f_o}{360^\circ} \frac{d\phi}{df} \right|_{f_o} = \left| \frac{f_o}{114.6^\circ} \frac{d\phi}{df} \right|_{f_o}$ . The slope suggests that  $Q = 72.1$ , in reasonable agreement with  $Q = |p_{cav}/p_l| = 74.3$  calculated at resonance in Fig. 8.27, since the slope of the best-fit line is necessarily less than the slope evaluated exactly at  $f_o$ .

## 8.7 Coupled Helmholtz Resonators

The Helmholtz resonator is the fluid analogy of the mass-spring simple harmonic oscillator. The mass of the gas in the neck (see Sect. 8.4.4) is acted upon by the gas in the volume which provides a restoring force as a gas spring (see Sect. 8.2.4). After treating single degree-of-freedom harmonic oscillators in Chap. 2, we went on to analyze coupled oscillators with  $j$  masses connected to  $j+1$  springs in Sect. 2.6. We can do the same with coupled Helmholtz resonators. A simple physical example, built by Anthony Atchley, that has three necks (masses) and four volumes (gas springs) is shown in Fig. 8.34.

To obtain an approximate idea of what frequencies to expect, we can analyze a double-Helmholtz resonator that is created when one neck is connected to two identical volumes [22, 23]. That network is equivalent to a single (gas) mass restored by two mechanically parallel (gas) springs (see Sect. 2.2.1). Since two springs of equal stiffness provide a stiffness that is twice that of each individual spring, Eq. (8.51) can be modified to calculate the resonance frequency,  $\omega_{Double}$ .

$$\omega_{Double} = \frac{1}{\sqrt{LC}} = c \sqrt{\frac{2A}{\Delta x_{neck} V}} \quad (8.55)$$

Using parameter values taken from the caption below Fig. 8.34, the volume of a single compliance is  $V = 2.04 \times 10^{-5} \text{ m}^3$ . The neck has a length,  $\Delta x_{neck} = 19 \text{ mm}$ , and cross-sectional area,  $A = 4.6 \times 10^{-5} \text{ m}^2$ . If the air temperature is  $23^\circ \text{C}$ , then  $c = 345 \text{ m/s}$ , and  $f_{Double} = \omega_{Double}/2\pi = 846 \text{ Hz}$ .

With three necks and four gas springs, the triple-Helmholtz resonator has three degrees of freedom and therefore will possess three lumped-element normal mode frequencies. The DELTAEC model,

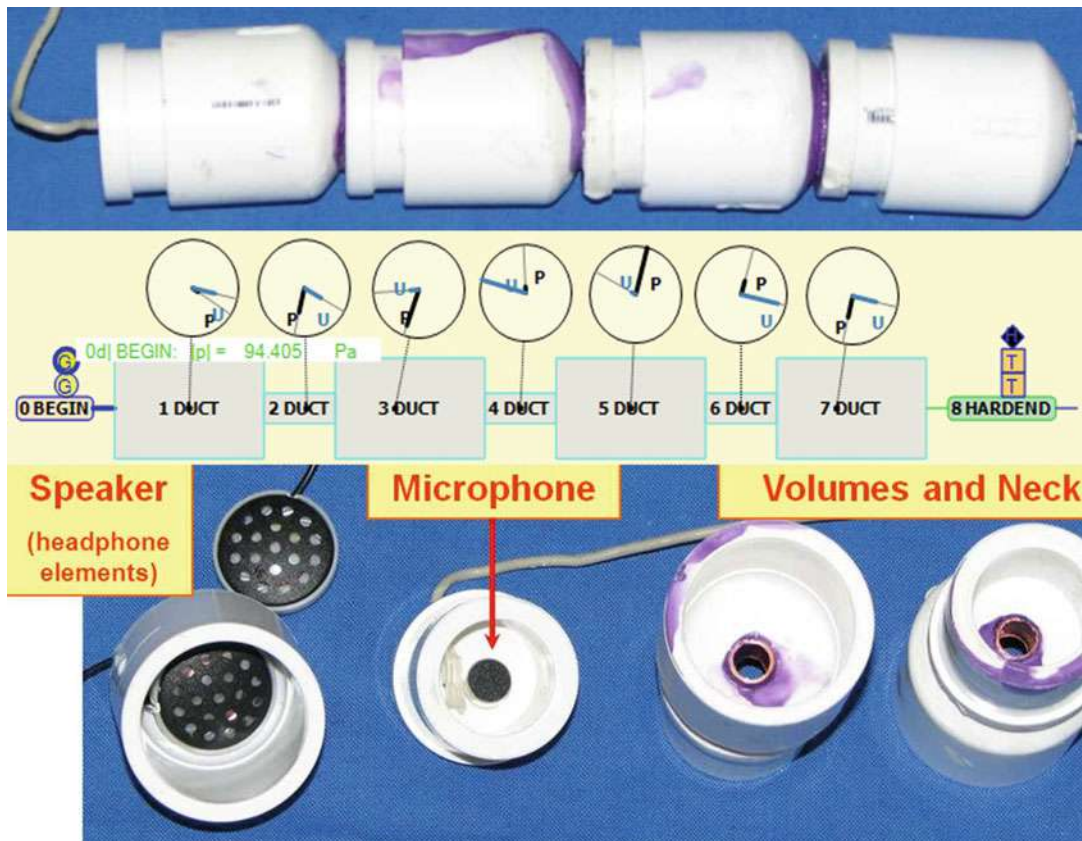


**Fig. 8.34** Coupled Helmholtz resonators made from copper tubing (necks) and PVC plumbing caps (volumes), built by Anthony Atchley. (*Top*) An assembly of three necks and four volumes that create a table-top triple-Helmholtz resonator. Each neck is 19 mm long with an inner diameter of 7.6 mm. Each volume is 4.0 cm long with an inner diameter of 25.4 mm. (*Middle*) DELTAEC’s “Schematic View” of TripleHelmholtz.out. As shown, it is possible to place a “phasor gauge” in any (or all) segment to show the relative phase of the pressure and volume velocity. To activate this feature, it is necessary to hold down the “alt” button and click your mouse on the segment of interest. In this illustration, the schematic view was produced for the third normal mode at 1010.9 Hz. In DUCT 1, acoustic pressure and volume velocity are nearly in-phase indicating that there is a large component of energy in the traveling wave near the BEGIN segment of the model. By the end of the model, the pressure and volume velocity in DUCT 5, DUCT 6, and DUCT 7 are nearly 90° out-of-phase, indicating that the energy is primarily due to the standing wave. (*Bottom*) A small loudspeaker is located at the end of the first volume, and a small microphone is located at the end of the fourth volume. The PVC volumes and necks are also disassembled for visual inspection

shown in “Schematic View” in Fig. 8.34, can be run to determine the three resonance frequencies, and three \*.sp. files (see Sect. 8.6.6) can be generated showing the gas’s volume velocity magnitudes corresponding to the three normal modes. Those normal modes are shown in Fig. 8.35, along with the analogous displacements of three discrete masses connected together by strings.

Although the second normal mode is similar to two double-Helmholtz resonators, oscillating 180° out-of-phase, with the gas in the central neck at rest, examination of the \*.sp. file for that mode, in Fig. 8.36, shows that in such a small network, with a high ratio of surface area to volume, the thermoviscous losses are significant. The previous lossless analysis of the double-Helmholtz resonator shows that in such a network, the normal mode frequency should be 846 Hz. The DELTAEC model

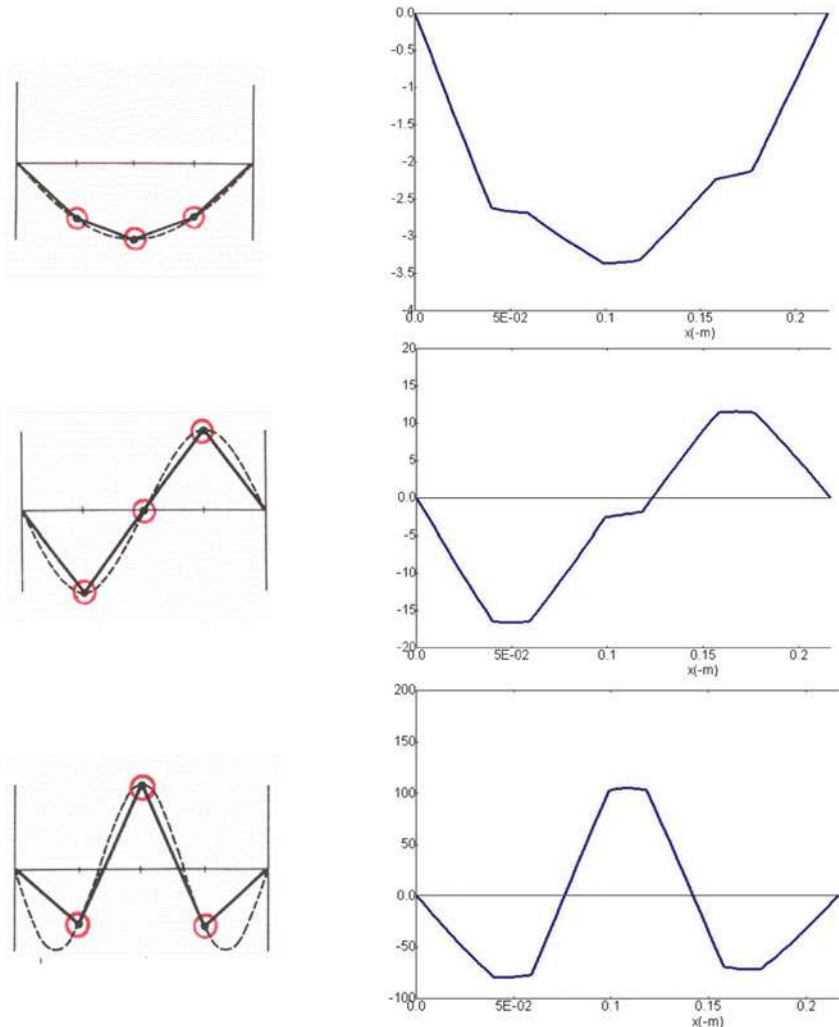


**Fig. 8.35** Mode shapes for the three normal modes of the triple-Helmholtz resonator are plotted vs. position for the network shown in Fig. 8.34. Normal mode frequencies, determined from the DELTAEC model, are 231.4 Hz for the mode at the *top*, 670.8 Hz for the mode at the *middle*, and 1010.9 Hz for the mode at the *bottom*. The *left column* represents the displacements of the modes if discrete masses (*circles*) were mounted on a string, as discussed in Sect. 2.7.7, with the *dashed lines* representing the analogous normal modes for a continuous fixed-fixed string. The *right column* represents the magnitude of the volume velocity of the gas as it moves through the triple-Helmholtz resonator as plotted by three DELTAEC \*.sp. files (see Sect. 8.6.6). For the lowest-frequency mode (231.4 Hz), all of the gas is moving in the same direction during any phase of the cycle. The highest velocity occurs in the central neck. In the second normal mode (670.8 Hz), the gas in the central neck is nearly stationary. Further detail for this mode is provided in Fig. 8.36. The highest-frequency mode has the gas motion of adjacent necks vibrating 180 degrees out-of-phase

places that normal mode resonance frequency at 671 Hz. It is clear from this state variable plot in Fig. 8.36 that the gas in the central neck is not at rest and the pressure on opposite ends of the left pair of volumes, which would be equal and opposite for the lossless case, is unequal in magnitude (28.8 Pa vs. 22.5 Pa). The same is true for the right pair of volumes (21.0 Pa vs. 18.2 Pa).

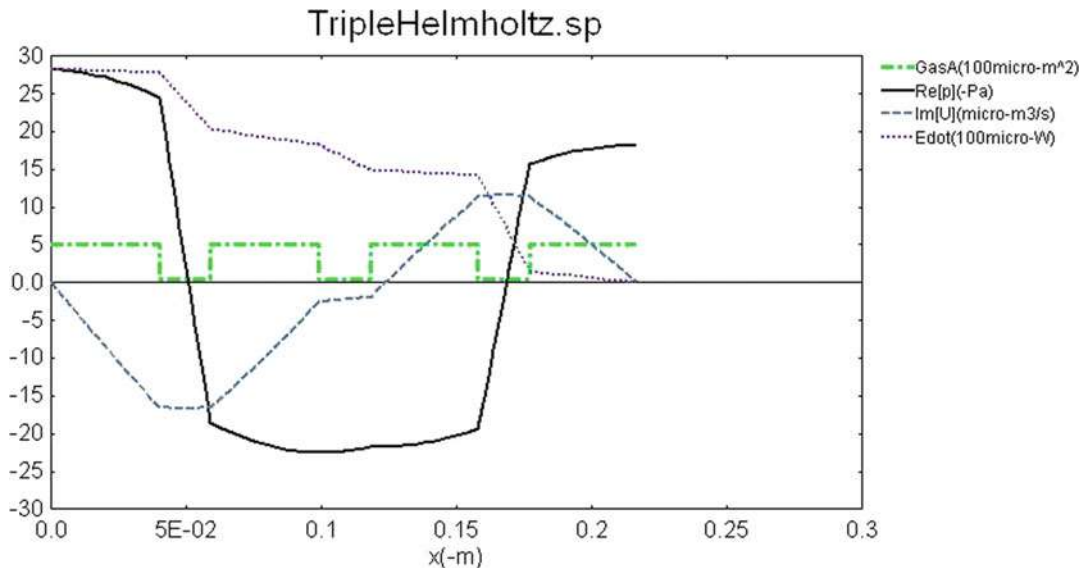


**Fig. 8.36** State variable plot for the second normal mode of the triple-Helmholtz resonator shown in Fig. 8.34, with a resonance frequency of 670.8 Hz. The green dash-dot line represents the gas-filled cross-sectional area for the model (in  $\text{cm}^2$ ). The black solid line represents the real component of the pressure (in Pa),  $\Re [p]$ . The blue dashed line represents the imaginary component of the volume velocity (in  $\text{cm}^3/\text{s}$ ),  $\Im [U]$ . The purple dotted line represents the 2.83 mW of acoustic power that flows from the loudspeaker and is entirely dissipated when it reaches the end of the fourth volume, as it must, for a system in steady-state operation. This result differs from the approximation that assumes that the mode is equivalent to two lossless double-Helmholtz resonators oscillating 180 degrees out-of-phase with a resonance frequency of 846 Hz. It is clear from this state variable plot that the gas in the central neck is not at rest and the pressure on opposite ends of the left pair of volumes, which would be equal and opposite for the lossless double-Helmholtz case, is unequal in magnitude (28.8 Pa vs. 22.5 Pa). The same is true for the right pair of volumes (21.0 Pa vs. 18.2 Pa)

## 8.8 The Bass-Reflex Loudspeaker Enclosure

As will be shown in greater detail later (see Sect. 12.5.1), a moving-coil electrodynamic loudspeaker is a very inefficient source of sound at low frequencies if it is not surrounded by a rigid enclosure. Such an enclosure allows only the front surface of the speaker's cone to radiate into the listening space and suppresses the out-of-phase volume velocity produced by the rear of the speaker that would otherwise have cancelled the volume velocity created by the front of the speaker. This strategy is illustrated on the left-hand side of Fig. 8.37. One unfortunate consequence of such strategies is that the volume velocity produced by the back of the loudspeaker, though just as large as that produced by the front, is “wasted.”

The phase reversal produced when a Helmholtz resonator is driven above its resonance frequency,  $\omega_o$ , shown in Eq. (8.52) and plotted in Fig. 8.32, can productively utilize the volume velocity produced by the back of the loudspeaker. Such a *bass-reflex loudspeaker enclosure*, shown on the right-hand side of Fig. 8.37, exploits this phase reversal by taking the volume velocity generated from the rear of the loudspeaker's cone and inverting its phase, so the motion of the gas oscillating in the port (i.e., the neck of the Helmholtz resonator) adds (nearly in-phase) to the gas being driven by the front of the loudspeaker cone. At low frequencies, the separation of the cone's center and the vent is much less than one-half wavelength, so the volume velocity exiting the port will combine (using vector algebra to incorporate the phase differences) with the volume velocity produced by the front of the speaker to

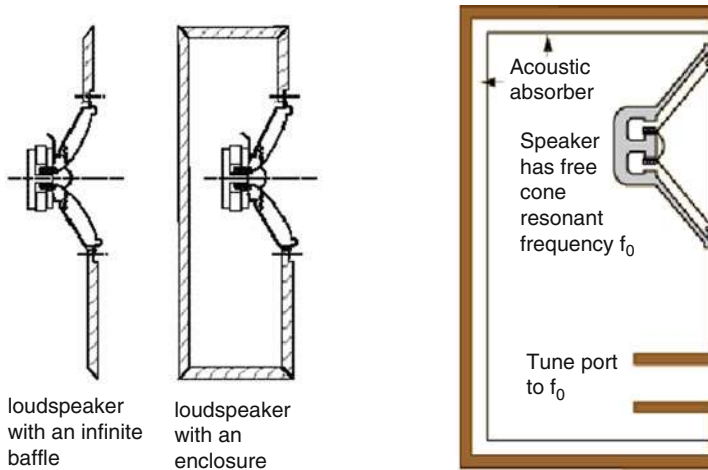


**Fig. 8.37** The two sketches at the left show a loudspeaker mounted in an infinite baffle and in a sealed enclosure. Both strategies prevent the sound radiated from the back surface of the loudspeaker cone from cancelling the sound radiated from the front. At the right, the speaker is mounted in a Helmholtz resonator, with volume,  $V$ , which is commonly called a bass-reflex enclosure or a vented box enclosure. The “vent” (or port) is shown as an inertance of length,  $L$ , and cross-sectional area,  $A$ . The “acoustic absorber” is a porous medium (e.g., fiberglass) that is intended to attenuate standing waves within the rectangular enclosure (see Sect. 13.1.1)

produce the net volume velocity magnitude,  $|U_{net}|$ , that can exceed the volume velocity produced by the front of the loudspeaker.

There are several other technical issues that need to be considered for successful design of a bass-reflex loudspeaker enclosure that will not be addressed here. For example, the free-cone resonance of the speaker is strongly coupled to the Helmholtz resonance, and inclusion of damping material in the port can be useful in smoothing the overall response. (DETAEC will automatically incorporate those effects for us if we specify the flow resistance of the damping material in the port as shown in Segment #3 of Fig. 8.39.) Since the volume velocity through the port can be substantial at frequencies close to the (strongly coupled) Helmholtz resonance frequency, flow noise generated by turbulence in the port and jetting caused by the high-speed gas flow in the port can be annoying. That flow noise is referred to by audio component manufacturers as the “port noise complaint” [24].

### 8.8.1 Beranek's Box Driven by a Constant Volume Velocity

It will be worthwhile to pursue this application a little further because it is an example of a Helmholtz resonator that is driven in a way that is different from the external pressure drive of our first example, shown schematically in Fig. 8.15 and modeled by DETAEC in Figs. 8.27 and 8.29. A schematic diagram of a Helmholtz resonator being driven by a volume velocity source feeding the interior of the compliance is shown in Fig. 8.38. This configuration places the compliance of the volume and the inertance of the port acoustically in parallel. The volume velocity,  $|U|$ , provided by the rear of the speaker cone, goes simultaneously toward compressing the gas in the volume and driving gas through the neck (port).

To illustrate a Helmholtz resonator driven by a volume velocity source located within the compliance, a crude DETAEC model of the bass-reflex enclosure is developed to represent the example in

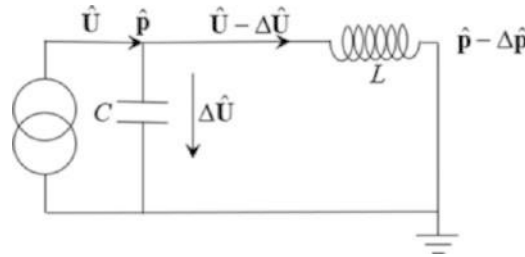


**Fig. 8.38** This equivalent circuit diagram of a Helmholtz resonator driven by a current source (*overlapped circles*) represents the volume velocity magnitude,  $|\hat{U}| = \omega A_{cone} |\hat{\xi}|$ , created by the motion of the rear of a loudspeaker's cone, having an area,  $A_{cone}$ , moving sinusoidally with peak displacement amplitude,  $|\hat{\xi}|$ . Part of that volume velocity amplitude,  $\Delta\hat{U}$ , goes into compressing the air in the enclosure of compliance,  $C$ ; the remainder,  $\hat{U} - \Delta\hat{U}$ , exits the port that has an inertance,  $L$ .

Beranek's *Acoustics* textbook [25]. It's crude because it assumes that the loudspeaker produces a constant volume velocity of  $0.040 \text{ m}^3/\text{s}$ , which is independent of frequency. In fact, the volume velocity of the loudspeaker is frequency-dependent, due to the mass, stiffness, and damping (mechanical impedance) of the loudspeaker (see Sect. 2.5.5). The frequency dependence of the complex input electrical impedance of the loudspeaker's voice coil and associated magnet structure also modifies the current, hence the resulting force, if the coil is driven by a source of constant voltage. These effects will be ignored initially to demonstrate the phase-inversion effect of the bass-reflex approach. In the next section, a real loudspeaker (JBL 2242 PHL, S/N: J033N-51645), easily modeled using DELTAEC, will be used to excite the same enclosure in a more realistic way from a "constant voltage" source.

This example will also ignore any damping material (e.g., fiberglass) that might be used to line the interior surface of the compliance. Such material is designated in Fig. 8.37 (Right) as "acoustic absorber." That material is used to suppress standing waves within the enclosure (see Sect. 13.1), which occur at frequencies much higher than those which we consider here for the bass-reflex enclosure's behavior.

Beranek's speaker example has an effective piston area,  $A_{cone} = 8.03 \times 10^{-2} \text{ m}^2$ , and his enclosure has an internal volume,  $V = 0.31 \text{ m}^3 (30'' \times 35'' \times 18'')$ . The surface area of this acoustical compliance is  $2.86 \text{ m}^2$ . (This surface area could be increased in a DELTAEC model to represent the "acoustic absorber" that is included to suppress standing waves within the enclosure that occur at frequencies that are much higher than those of interest in the analysis of the bass-reflex behavior.) Beranek's port area,  $S_p = 0.055 \text{ m}^2$ , corresponding to a port diameter of about 8 cm (3.14"). The port has a length of 0.25 m (9.8"), neglecting any end corrections. An acoustic flow resistance of  $500 \text{ Pa}\cdot\text{s}/\text{m}^3$  (see Segment #3) has been added to the port to control the behavior at resonance.<sup>26</sup> These parameter choices are reflected by the output file, BeranekBox(U-drive).out, shown in Fig. 8.39.

Care must be taken to understand the phase differences between the volume velocity of the source (set at  $0^\circ$  in BEGIN),  $\hat{U}_{drive}$ , and the volume velocity produced by the front of the loudspeaker. The front of the loudspeaker is moving in the direction opposite that of the back side that produces  $\hat{U}_{drive}$ . The net volume velocity,  $U_{net}$ , must be the vector sum of the volume velocity from the *front* of the loudspeaker plus the volume velocity of the gas moving through the port. The magnitude of the net velocity can be calculated using the Law of Cosines.

<sup>26</sup>Using these box parameters and neglecting damping, the Helmholtz frequency for the box containing air with a sound speed of  $347 \text{ m/sec}$  is  $43.6 \text{ Hz}$ , using Eq. (8.51) and adding one flanged end correction to create an effective length for the port,  $L_{eff} = 28.4 \text{ cm}$ .

```

1 □BeranekBox(U-source)-Fig. 38 Beranek's 15" Base-Reflex Enclosure
2 □ 0 BEGIN      Initial
3           1.0000E+05 a Mean P Pa
4           10.000 b Freq   Hz
5           300.00 c TBeg   K
6 Gues      -25.201 d |p|   Pa
7 Gues      209.24 e Ph(p) deg
8           4.0000E-02 f |U|   m^3/s
9           0.0000 g Ph(U) deg
10 Optional Parameters
11 air        Gas type
12 □ 1 COMPLIANCE Beranek's enclosure volume (30"x35"x18")
13 □ 2 DUCT       Bass Reflex Port
14 □ 3 IMPEDANCE Flow resistance in the port
15           500.00 a Re(Zs) Pa-s/m^3            3.8033E-13 A |p|   Pa
16           0.0000 b Im(Zs) Pa-s/m^3            -92.677 B Ph(p) deg
17 Master-Slave Links
18           4.1863E-02 C |U|   m^3/s
19           -4.3766 D Ph(U) deg
20           0.43978 E Htot   W
21           2.3611E-16 F Edot   W
22 □ 4 SOFTEND    Exit from the port
23 Targ      0.0000 a Re(z)            3.8033E-13 A |p|   Pa
24 Targ      0.0000 b Im(z)            -92.677 B Ph(p) deg
25           4.1863E-02 C |U|   m^3/s
26           -4.3766 D Ph(U) deg
27           0.43978 E Htot   W
28           2.3611E-16 F Edot   W
29 Possible targets
30           3.6757E-17 G Re(z)          W
31           -1.2388E-15 H Im(z)          W
32           300.00 I T    K
33 □ 5 RPN       Net volume velocity (A) and degrees phase difference (B)
34           0.0000 a G or T            3.6382E-03 A m^3/s
35           184.38 B Degrees
36
37 180 4D - # cos Of 2C * * 2 * Of Of * + 2C 2C * + sqrt
38
39
40
41
42
43
44
45
46
47

```

**Fig. 8.39** Screenshot of the DELTAEC model of Beranek's bass-reflex loudspeaker enclosure that is driven by a constant amplitude volume velocity source ( $0f$ ) located in the compliance that produces  $|\hat{U}_{drive}| = 4.0 \times 10^{-4} \text{ m}^3/\text{s}$ . Segment #3 places some damping material (e.g., fiberglass) in the port to control the amplitude at resonance. Segment #5 is an RPN target that calculates the phase difference between the volume velocity from the front of the loudspeaker ( $180^\circ - 1e$ ) and within the port ( $2D$ ), to calculate the net volume velocity (5A) using Eq. (8.56). Note the RPN Segment #5 calculates and displays two quantities,  $|U_{net}|$  and  $\phi$ . The graph in Fig. 8.40 is based on this file. The blue highlight of the drive frequency (0b) and the result of the vector sum (5A) and (5B) indicates that the frequency,  $|U_{net}|$ , and  $\phi$  will appear in the "Highlighted Parameters" window available under the "Display" pull-down menu

$$c^2 = a^2 + b^2 - 2ab \cos \phi \quad \Rightarrow \quad U_{net}^2 = U_{drive}^2 + U_{port}^2 - 2|U_{drive}||U_{port}| \cos \phi \quad (8.56)$$

To calculate the phase of the volume velocity through the port,  $U_{port}$ , relative to the volume velocity from the front of the loudspeaker,  $U_{speaker} = -U_{drive}$ , it is helpful to recognize that  $U_{drive}$  and  $U_{port}$  will be in-phase at frequencies well below  $\omega_o$ . Therefore, the phase difference between  $U_{speaker}$  and  $U_{port}$  at any frequency,  $\phi(f) = \phi_{drive} + 180^\circ - \phi_{port} = 180^\circ - \phi_{port}$ , since  $\phi_{drive} = 0^\circ$ , by definition in the BEGIN segment (0 g). The full calculation is executed by DELTAEC from the file BeranekBox (U-source).out, shown in Fig. 8.39. The results of those calculations are plotted in Fig. 8.40.

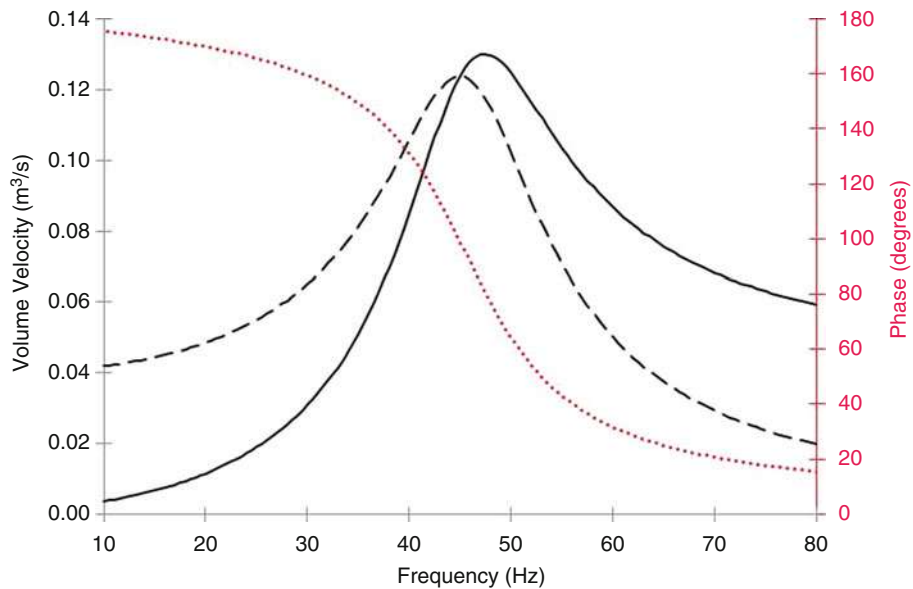


**Fig. 8.40** Plot of the response of Beranek's bass-reflex loudspeaker enclosure, driven by a constant volume velocity source,  $|\hat{\mathbf{U}}_{\text{drive}}| = 4.0 \times 10^{-4} \text{ m}^3/\text{s}$ , located in the compliance. If a loudspeaker were producing that volume velocity, its motion would be 180 degrees out-of-phase with the volume velocity source. The phase difference between the volume velocity generated by a loudspeaker and the volume velocity through the port,  $\phi(f)$ , is represented by the *dotted line* whose value should be read from the right-hand axis labeled "Phase (degrees)." The magnitude of the volume velocity through the port,  $|U_{\text{port}}|$ , is shown as the *dashed line* and is referenced to the left-hand axis labeled "Volume Velocity ( $\text{m}^3/\text{s}$ )". The magnitude of the vector sum of the port velocity and the loudspeaker velocity,  $|U_{\text{net}}|$ , is shown by the *solid line* that is also scaled by the left axis. At low frequencies, the magnitude of the net volume velocity,  $|U_{\text{net}}|$ , is less than the volume velocity of the source,  $|U_{\text{drive}}|$ , due to phase cancellation, and approaches zero as the frequency goes to zero. Note that above 32.5 Hz, the net volume velocity is larger than the volume velocity source,  $|U_{\text{drive}}|$ . For that reason, it is very rare to see small loudspeaker enclosures that do not use the bass-reflex (Helmholtz resonator) approach to enhance their low-frequency output.

The enhancement of the bass response, shown by the fact that net volume velocity exceeds the volume velocity from the front of the speaker's cone at frequencies above about 35 Hz, helps compensate for the decrease in the sensitivity of human hearing at low frequencies (see Fig. 10.5).

### 8.8.2 Loudspeaker-Driven Bass-Reflex Enclosure\*

It will be worthwhile to place a real loudspeaker in Beranek's bass-reflex loudspeaker enclosure as the last example in this chapter. Techniques for measurement of electrodynamic loudspeaker parameters were demonstrated in Sect. 2.5.5. DELTAEC provides a selection of segments that easily incorporate a loudspeaker into a DELTAEC model. The resulting combination of an electromechanical harmonic oscillator and a fluidic Helmholtz resonator presents challenges if approached algebraically. We will see that incorporation of a loudspeaker in a Helmholtz resonator within DELTAEC is no more difficult than the model of Beranek's bass-reflex enclosure that was run with a constant amplitude volume velocity source in the BEGIN statement of the model shown in Fig. 8.39. Although the use of such a DELTAEC model for optimization of the system's performance can be more complicated, just "plugging in" the appropriate DELTAEC segment to represent the loudspeaker is simple.

```

1 ⊖2nd BeranekJBL-VSpeaker(Plot) JBL 2242 in Beranek's Bass-Reflex
2 ⊕ 0 BEGIN Initial
12 ⊖ 1 VSPEAKER JBL 2242 PHL (S/N: J033N-51645)
13          0.1300 a Area m^2           34.432 A |p| Pa
14          4.8424 b R ohms            70.976 B Ph(p) deg
15          1.2500E-3 c L H           P 3.8022E-2 C |U| m^3/s
16          32.200 d BLProd T-m      158.51 D Ph(U) deg
17          0.1780 e M kg            1.8078 E Htot W
18          9410.0 f K N/m          2.8191E-2 F Edot W
19          10.000 g Rm N-s/m       1.8078 G WorkIn W
20          10.000 h |V| V           10.000 H Volts V
21
22
23          0.74724 I Amps A
24          -61.062 J Ph(V/I)deg   3.8022E-2 K |Ux| m^3/s
25          158.51 L Ph(-Ux)deg
26 ideal Solid type
27 ⊖ 2 RPN Speaker Input Impedance (Magnitude)
28          0.0000 a G or T P           13.383 A Ohms
29 1H 1I /
30 ⊖ 3 COMPLIANCE Beranek's enclosure volume (30"x35"x18")
31 ⊖ 4 DUCT Bass Reflex Port
32 ⊖ 5 IMPEDANCE Flow resistance in the port
33 ⊖ 6 SOFTEND Exit from the port
34 ⊖ 7 RPN Net volume velocity (A) and degrees phase differnce (B)
35          0.0000 a G or T P           4.8371E-2 A m^3/sec
36          P                          -10.429 B Degrees
37 -180 1D + 6D - # cos 2 * 1C * 6C * 1C 1C * + 6C 6C * + sqrt
38
39
40
41
42
43
44
45
46
47
48
49
50
51
52
53
54
55
56
57
58
59
60
61
62
63
64

```

**Fig. 8.41** Screenshot of the output file for a JBL 2242 PHL electrodynamic loudspeaker driving Beranek's bass-reflex enclosure modeled in Fig. 8.40. In this DELTAEC file, the enclosure is driven by a constant voltage source of amplitude 10.0 V<sub>pk</sub> (0h) corresponding to a root-mean-squared voltage of 7.07 V<sub>rms</sub> applied across the speaker's voice coil. An RPN segment (#2) has been added to calculate the magnitude of the driver's electrical input impedance,  $Z_{el} = V/I = (1G)/(1H)$ . All of the collapsed segments are identical to those in Fig. 8.39

In this example, the measured parameters of a JBL Model 2242 PHL (S/N: J033N-51645) will characterize the loudspeaker in the VSPEAKER segment that is included in BarenekBox-VSpeaker.out, shown in Fig. 8.41. Because modern solid-state audio amplifiers produce a nearly constant voltage replica of the audio signal (at least until the current limit is exceeded), a VSPEAKER segment is used to represent the speaker and amplifier combination. As shown in Fig. 8.41, the loudspeaker is specified entirely by the parametric inputs to Segment #1.<sup>27</sup> The user must provide the radiating area of the

<sup>27</sup>The particular choice of parameters used in the DELTAEC electrodynamic speaker specification is not unique. Within the loudspeaker design community, the Thiele-Small parameters are far more common, especially in catalog descriptions of commercial drivers (see Fig. 2.42), although the DELTAEC parameter choice is more general, since DELTAEC must accommodate a variety of gases, pressures, and temperatures.

Of course, there is a one-to-one correspondence between the parameters required by DELTAEC and the Thiele-Small parameters [A. N. Thiele, "Loudspeakers in vented boxes," J. Audio Eng. Soc. **19**, 382–392 (May 1971) and 471–483 (June 1971)]. For example, instead of specifying  $K$ ,  $m$ , and  $R_m$ , the stiffness,  $K$ , will be expressed as the equivalent volume stiffness of air,  $V_{AS}$  [m<sup>3</sup>], if the speaker's radiating area,  $S_D$  [m<sup>2</sup>], is known (see Fig. 7.5). The moving mass,  $m$ , can be extracted from the free-cone resonance frequency,  $f_s$  [Hz], and the mechanical damping,  $R_m$  [kg/s], will be related to the dimensionless mechanical quality factor,  $Q_{MS}$ .

$$K = \gamma p_m S_D^2 / V_{AS}$$

$$m = K / 4\pi^2 f_s^2$$

$$R_m = 2\pi f_s m / Q_{MS}$$

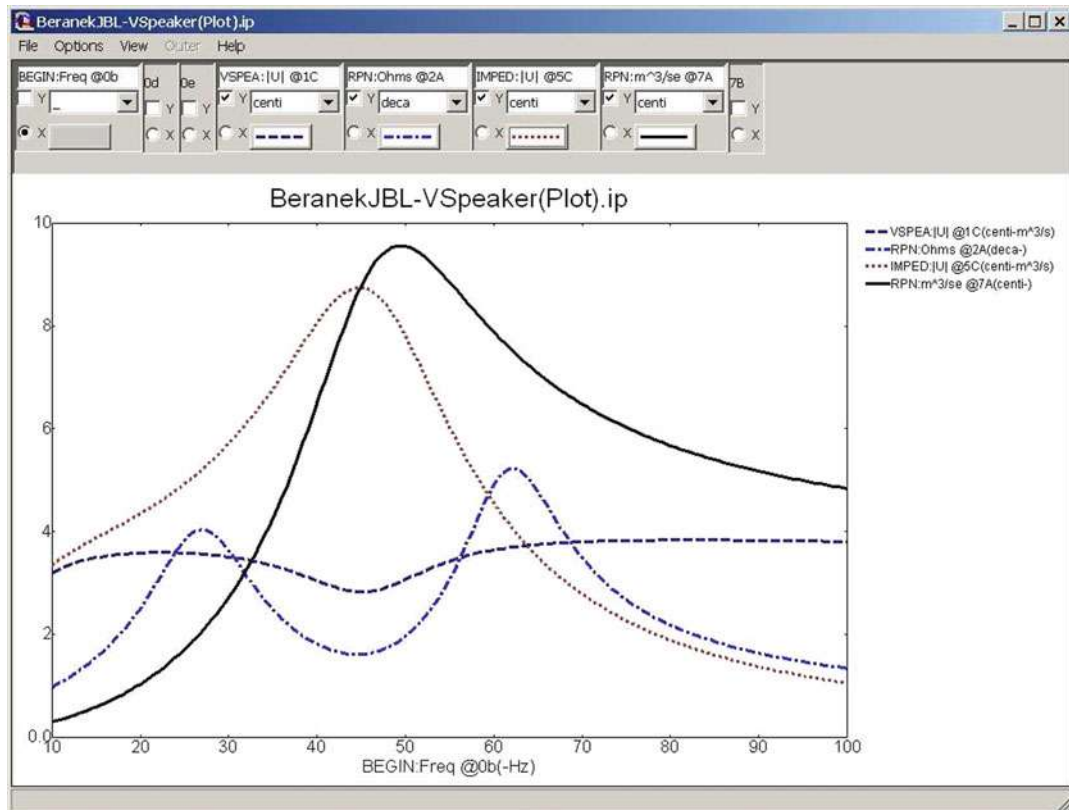


**Fig. 8.42** Screenshot of the frequency response of the JBL 2242 PHL driving Beranek's bass-reflex enclosure that is modeled in Fig. 8.41. This graph shows the magnitudes of the speaker's input electrical impedance (blue dash-dotted line), the volume velocity of the air oscillating in the port (brown dotted line), the magnitude of the volume velocity produced by the loudspeaker cone (dashed line), and the magnitude of the net volume velocity produced by the vector sum of the volume velocities,  $|U_{net}|$ , produced by the port and the loudspeaker (black solid line). At frequencies above 33 Hz, the net volume velocity (black solid line) exceeds the volume velocity from the front of the loudspeaker alone (blue dashed line), demonstrating the enhancement provided by the Helmholtz resonance as a consequence of its ability to invert phase above resonance

speaker (1a), the DC resistance of the voice coil (1b), the inductance of the voice coil (1c), and the force factor, also known as the  $B\ell$ -product (1d). The moving mass of the cone plus voice coil plus suspension surround and spider (1e) is also required, along with the suspension stiffness (1f) and the mechanical resistance (1g), as well as the amplitude of the driving voltage (1h). Of course, all of the input parameters must be provided to DELTAEC in SI units.

Figure 8.42 provides a graph that includes the speaker's input electrical impedance (2A) and the magnitude of the volume velocity produced by the front side of the speaker's cone (1C) when driven by an input voltage of 7.07 V<sub>rms</sub> applied to the voice coil that is independent of frequency. The net volume velocity,  $|U_{net}|$ , is produced by the vector sum of the speaker's cone and the gas oscillating within the enclosure's port.

The loudspeaker's mechanical (free-cone) resonance frequency,  $f_s = \sqrt{K/m}/2\pi \cong 36.6$  Hz, if it were measured in a vacuum. The Helmholtz resonance of the enclosure without the loudspeaker ( $f_o = 43.6$  Hz) can be determined from BeranekBox(U-source).out in Fig. 8.39. A first approximation to a bass-reflex loudspeaker enclosure design usually makes the Helmholtz frequency of the enclosure (with the loudspeaker immobilized) roughly equal to the speaker's free-cone resonance frequency. No attempt was made to "tune" the enclosure, possibly by modifying the port's dimensions or its damping, to

enhance the loudspeaker's performance, but it is obvious from inspection of Fig. 8.42 that above 33 Hz, the net volume velocity produced by the speaker/enclosure combination is greater than that produced by the front radiating surface of the loudspeaker only, without any (conscious) optimization effort.

The dash-dotted curve in Fig. 8.42, representing the magnitude of the input electrical impedance,  $|Z_{in}|$ , of the loudspeaker's voice coil, shows two peaks corresponding to the two normal mode frequencies of a two degree-of-freedom coupled harmonic oscillator (see Sect. 2.7). The two independent resonance frequencies of the Helmholtz resonator alone,  $f_o$ , and the free-cone resonance frequency of loudspeaker alone,  $f_s$ , differ by  $\Delta f_{independent} = |f_o - f_s| = 143.6 - 36.6| \text{ Hz} = 7.0 \text{ Hz}$ . The separation of the two peaks in the electrical impedance of the loudspeaker,  $\Delta f_{coupled} = (62 - 27) \text{ Hz} = 35 \text{ Hz}$ . This is a clear manifestation of the "level repulsion" exhibited by two strongly coupled harmonic oscillators that was discussed in Sect. 2.7.6.

The peak in the magnitude of the volume velocity through the port, which occurs at about 45 Hz, corresponds to the dip in the volume velocity provided by the front surface of the loudspeaker, demonstrating that the energy dissipated in the port produces a perceptible additional load on the loudspeaker's motor mechanism. This loading, of course, was not evident in the DELTAEC model of Fig. 8.39, which assumed a constant value for the driver's volume velocity.

## 8.9 Lumped Elements

This (rather long) chapter was intended to accomplish two major goals: First, it provided the initial application of the equations of hydrodynamics to acoustical problems of interest by linearizing the continuity equation and linearizing the Euler equation to produce the acoustical compliance and acoustical inertance of small acoustical elements. The decision to define acoustical impedance as the ratio of the acoustic pressure to volume velocity facilitated the combination of inertances and compliances, since volume velocity is continuous across the junction between lumped elements that typically can have different cross-sectional areas. Though it is true that these elements were small compared to the acoustic wavelength, at the frequencies of interest, as was demonstrated at the end of Chap. 2, combinations of many such elements provide a logical transition to wave motion in distributed systems with dimensions comparable to (or greater than) the wavelength of sound (see Fig. 10.1). Of course, the lumped elements have significant utility within their own domain of applicability.

Second, this chapter also introduced DELTAEC software that could be used to predict the behavior of network of such "lumped elements," focusing first on the combination of an inertance and a compliance to produce a Helmholtz resonator, driven by external oscillating pressure or by an internal source of volume velocity. DELTAEC provided a computational structure that could be applied to networks of lumped elements and included the effects of thermoviscous dissipation on the surfaces of those elements. Application of DELTAEC to a 500 ml boiling flask provided a "benchmark" problem that we will be able to use to test the hydrodynamic models for dissipative process that will be the subject of the next chapter.

The comparison between our nondissipative model, which produced an expression for a Helmholtz resonator's resonance frequency, and some simple (but sufficiently accurate) measurements of that frequency exposed a substantial discrepancy between theory and experiment. That discrepancy was removed by postulating an "effective length correction," since the dependence of the frequency on the volume of the resonator seemed to follow the behavior dictated by the simple nondissipative network calculation. Only "hand-waving" plausibility arguments, appealing to effects of flow adjacent to the resonator's neck, were provided as "justification." That is not science! We will need to create a legitimate theory that produces a quantitative "end correction" that can be related to the neck's radius and the specific geometrical constraints on the flow of fluid into and out of the neck in the vicinity of the neck's openings. Such a theory will be forthcoming when the radiation from circular pistons is developed in Chap. 12.

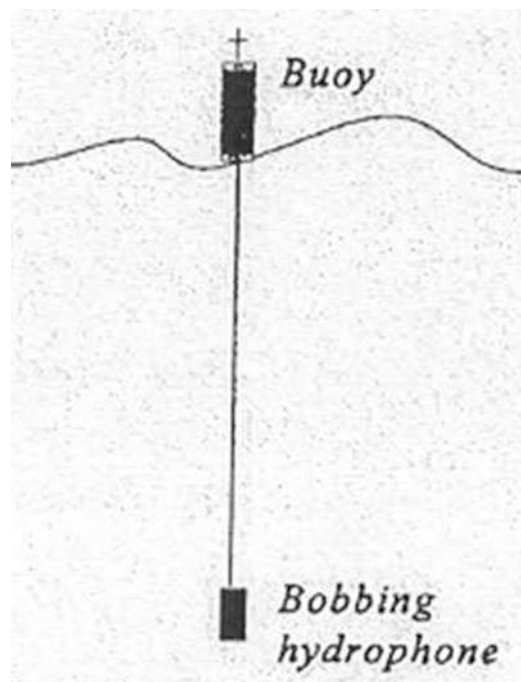
**Talk like an Acoustician**

Lumped element	Fluid particle or fluid parcel
Acoustical compliance	Lagrangian description
Acoustical inertance	Eulerian volume
Helmholtz resonator	Nonlinear effect
Harmonic analysis	Streaming
Isotropic fluid	Adiabatic sound speed
Mean value	Acoustical impedance
Instantaneous value	Capacitive reactance
Acoustic approximation	Atmospheric lapse rate
Acoustic Mach number	Inductive reactance
Fourier's theorem	Acoustical network
Laboratory frame of reference	Joining conditions
Eulerian coordinate system	Bass-reflex loudspeaker enclosure

**Exercises**

1. **Atmospheric lapse rate.** Commercial jet aircraft typically cruise at altitudes around 36,000 feet.
  - (a) *Temperature.* What would be the temperature of air at that altitude if we assume a dry adiabatic gas and a sea-level pressure of 100 kPa and sea-level temperature of 15 °C?
  - (b) *Density.* Assuming an isothermal atmosphere with a temperature that is the average of 15 °C and the temperature calculated in part (a), what would be the density and pressure of the air at cruising altitude?
2. **Bobbing Hydrophone.** Suppose a hydrophone is suspended some distance below a buoy that is floating at the surface of a body of water as shown in Fig. 8.43. If there are waves on the surface that

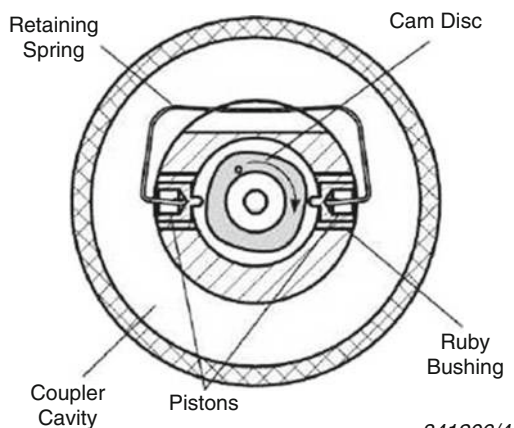
**Fig. 8.43** Hydrophone suspended from a floating buoy



cause the buoy to move in the vertical direction by an amount,  $z(t) = \Re e[\hat{\mathbf{A}} e^{j\omega t}]$ , where  $|\hat{\mathbf{A}}| = 0.20 \text{ m}$ , determine the amplitude of the pressure signal detected by the hydrophone at the same frequency,  $\omega$ , if we assume that the separation between the hydrophone and the buoy is constant and the water is incompressible.

3. **Up, up, and away.** A thin rigid spherical shell that is 1.00 m in diameter has a mass of 0.50 kg when evacuated. At “sea level” ( $h = 0$ ) on the surface of the Earth, under typical atmospheric conditions ( $T = 15.0^\circ\text{C}$ ,  $P = 101,325 \text{ Pa}$ ), such a sphere would displace 0.641 kg of air; therefore it is buoyant and would rise. If we assume conditions specified by the *1976 Standard US Atmosphere* [4], then the density of air,  $\rho(h)$ , would decay exponentially, as described in Eq. (8.31), as a function of height,  $h$ , above the Earth’s surface. The density of air at sea level is  $\rho_o = 1.225 \text{ Kg/m}^3$ . The characteristic exponential decay length,  $\mu \equiv \Re T/gM = 8435 \text{ m}$ .
  - (a) *Altitude.* What is the equilibrium height above the Earth,  $h_o$ , to which the hollow sphere will rise?
  - (b) *Väisälä-Brunt frequency.* Since the equilibrium is stable, if the sphere is displaced from its equilibrium position, its height will oscillate about equilibrium. The effective mass of the oscillating sphere will include a contribution from the motion of the surrounding air. That additional “hydrodynamic mass” is equal to one-half of the mass of air that the sphere displaces (see Sect. 12.5.1) [26]. Assuming negligible damping, what is the period of free oscillation of the sphere when it is displaced (vertically) from its equilibrium position and released if the additional “hydrodynamic mass” of the surrounding fluid is added to the mass of the sphere? The acceleration due to gravity at the equilibrium position can be taken as  $9.8 \text{ m/s}^2$ .
  - (c) *Damping.* The drag force on a sphere in a viscous fluid is given (at low Reynolds numbers) by  $F_{vis} = 6\pi\eta rv$ , where  $r$  is the radius of the sphere,  $v$  is its velocity, and  $\eta = 1.72 \times 10^{-5} \text{ N-sec/m}^2$  is the viscosity of air at the equilibrium height. Determine the decay time,  $\tau$ , for the oscillations of the sphere to decay to  $1/e$  of their initial amplitude.
  - (d) *Spherical shell strength.* The spherical shell is not really rigid. It is made of a carbon fiber composite with density,  $\rho = 1.6 \text{ gm/cm}^3$ ; Young’s modulus,  $E = 70 \text{ GPa}$ ; Poisson’s ratio,  $\nu = 0.1$ ; and ultimate compressive strength of 500 MPa. Can such a shell survive at sea level without imploding? If so, what change in radius occurs as it goes from sea-level pressure to the pressure calculated at the equilibrium height calculated in part (a)?
4. **Pistonphone microphone calibrator.** A pistonphone is a handheld instrument commonly used to calibrate microphone systems. As shown in Fig. 8.44, it is essentially a rigid-walled cavity driven at a single frequency by two horizontally opposed pistons that ride on a rotating cam so that each

**Fig. 8.44** Pistonphone microphone calibrator.  
(Drawing courtesy of Brüel and Kjær)



piston has known displacement amplitude. The dimensions of the cavity are all much smaller than the wavelength of sound at the operating frequency. For the purpose of this problem, assume the cavity is cylindrical with a height of 1.50 cm and a radius of 1.80 cm. Let the volume of the cavity be  $3.8 \text{ cm}^3$ , and ignore the space taken by the piston-cam system. Assume the mean pressure in the cavity,  $p_m = 101 \text{ kPa}$ ,  $c_{air} = 343 \text{ m/sec}$ , and that  $\gamma_{air} = 1.403$ .

- (a) *Piston volume velocity.* Treating the cavity as a lossless compliance, what must be the magnitude of the peak (not effective) volume velocity produced by the pistons for the peak sound pressure within the cavity to be  $44.8 \text{ Pa}_{\text{peak}}$  (equivalent to a sound pressure level of  $124 \text{ dB}_{\text{SPL re: } 20 \mu\text{Pa}_{\text{rms}}}$ ) when driven at 250 Hz?
  - (b) *Phase.* What is the approximate (to within  $\pm 5^\circ$ ) phase difference between the pressure in the cavity and the volume velocity of the piston?
  - (c) *Piston motion.* What is the peak-to-peak displacement of each piston if there are two pistons (as shown in Fig. 8.44) and each piston has a diameter of 3 mm, assuming that both pistons have the same displacement amplitudes?
5. **1.0 liter flask.** In Sect. 8.5.2, we used Eq. (8.54) to determine the empty resonator volume,  $V_o$ , and the effective neck length,  $\Delta x_{\text{eff}}$ , by adding known amounts of water to a flask and measuring the corresponding resonance frequency using a microphone inside the flask. [Note: The mic volume was  $6 \text{ cm}^3$ .] Now you can enjoy doing this on your own for this larger flask with the data provided in Table 8.1. The diameter of the neck is 33.85 mm and its physical length is 85 mm.
- (a) *Effective length.* Calculate  $V_o$  and  $\Delta x_{\text{eff}}$ .
  - (b) *Effective length correction.* Calculate the additional length that had to be added to the physical length to produce  $\Delta x_{\text{eff}}$ , and also express this length in terms of the radius of the neck.
  - (c) *Water compressibility.* Is the compressibility of the water in the flask negligible in comparison to the compressibility of the air? Assume the flask contains 400 mL of water for your calculations.
6. **The Penn State commemorative bottle.** The bottle shown in Fig. 8.45 can be modeled in DELTAEC with a DUCT as a neck, a CONE as the transition between the neck and the volume, and another DUCT that has the volume of the end of the bottle closed with a SURFACE segment followed by a HARDEND segment.
- (a) *Helmholtz resonance frequency.* Determine the resonance frequency of the resonator in Fig. 8.45 if the bottle is filled with air at 101,325 Pa at a temperature of 20 °C.
  - (b) *Quality factor.* Use the results of the DELTAEC model to find the  $Q$  of the Helmholtz resonance (neglecting radiation losses).
  - (c) *Standing waves.* Use your DELTAEC model to calculate the frequencies of the three lowest-frequency standing wave resonances of the bottle.
  - (d) *\*.sp plots.* Plot the cross-sectional area,  $\text{GasA}$ ; the in-phase pressure magnitude,  $\Re[p]$ ; and the out-of-phase volume velocity,  $\Im[U]$ , for the Helmholtz mode and the two lowest-frequency standing wave modes.

**Table 8.1** Resonance frequencies for the 1.0 liter flask

Injection (Hz)	Frequency (ml)
6	149.1
106	156.8
206	165.5
306	175.8
406	188.2
506	203.1

**Fig. 8.45** The neck length for this bottle is 17.8 mm and its inner radius is 8.26 mm. The volume is a cylinder that is 12.7 cm long with an inner radius of 24.4 mm. The length of the conical section that joins the neck to the volume is 10.0 cm

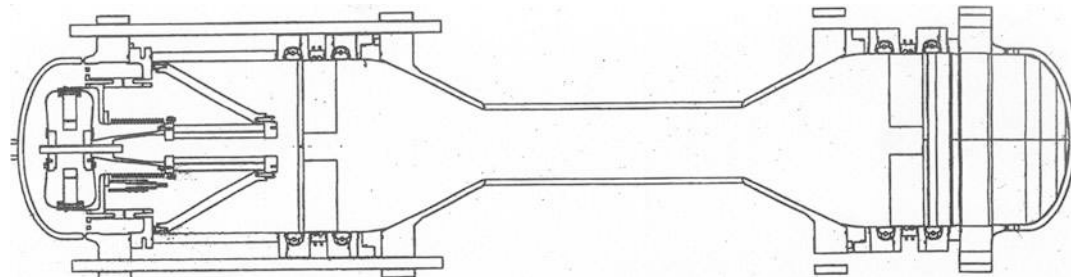


**Fig. 8.46** This double-Helmholtz resonator is about 2.0 m long and contains a moving-magnet electrodynamic loudspeaker in the left-hand volume that can produce as much as 6 kW of acoustical power at an electroacoustic efficiency,  $\eta_{ac} \cong 90\%$  [28]. The loudspeaker and part of the resonator are shown in the photograph in Fig. 4.21 (Right). The left-hand volume,  $V_{left} = 0.145 \text{ m}^3$ , and the right-hand volume,  $V_{right} = 0.125 \text{ m}^3$ . These volumes include the conical transitions. The neck that connects the two volumes is 0.711 m long and has an inner radius of 9.68 cm

7. **Double-Helmholtz resonator.** The double-Helmholtz resonator shown in Fig. 8.46 was used as a thermoacoustic refrigerator [27].

- Density.* The resonator is pressurized with 88% helium and 12% xenon at 3.0 MPa and is at a temperature of 20 °C. Calculate the mean atomic weight of the noble gas mixture,  $M_{mix} = x M_{Xe} + (1 - x) M_{He}$ , where  $x$  is the xenon concentration. Use the mean atomic weight to determine the mixture's density. [Note: You must provide your calculation, but you are welcome to check your answer using the DELTAEC ThermoPhysical Properties.]
- Resonance frequency.* As a double-Helmholtz resonator with unequal volume compliances, calculate the resonance frequency of the resonator in Fig. 8.46 that is filled with an 88/12 mixture of helium and xenon at 3.0 MPa.

- (c) *Gas velocity.* In this resonator, the pressure ratio,  $|\hat{\mathbf{p}}|/p_m$ , in the right-hand volume was 5.5%. What is the amplitude of the particle velocity of the gas in the neck? Also report that velocity amplitude in miles per hour and as a percentage of the sound speed.
- (d) *DELTAECC model.* Make a DELTAECC model of this double-Helmholtz resonator that is driven by a piston in the left-hand volume with volume velocity  $0.010 \text{ m}^3/\text{sec}$ . The surface areas of the compliances are  $A_{left} = 2.3 \text{ m}^2$  and  $A_{right} = 1.6 \text{ m}^2$ . [Note: The imposed volume velocity will not produce the full 6 kW mentioned in the caption to Fig. 8.46.]
8. **Helmholtz resonator.** In Sect. 8.5.2, the effective length correction for the neck of a Helmholtz resonator and the volume of the resonator were determined by measured variations in the resonator's volume, a procedure that you were asked to repeat in Problem 5. In this problem, you will do the same, but by substitution of differing necks with carefully measured physical lengths. Figure 8.47 shows a Helmholtz resonator that is constructed from plumbing fixtures that include 6" (nominal) Schedule-40 PVC pipe and a 6" PVC 90° elbow. One end of the resonator is closed with a  $\frac{1}{4}$ " thick PVC plate, and the base is medium-density fiberboard (MDF). The inside diameter of the pipe (1.5" nominal) used for the necks is  $D_{neck} = 40.8 \text{ mm}$ . Assume a room temperature sound speed of 343 m/s.
- (a) *Enclosure volume and effective length correction.* Using the data in Table 8.2, determine the volume of the Helmholtz resonator's compliance and the effective length correction and their relative uncertainties.



**Fig. 8.47** (Left) PVC Helmholtz resonator that includes a piston that can be removed rapidly from the neck to excite a free-decay of the Helmholtz resonance. At the bottom of the enclosure is a BNC connector that provides access to a microphone built into the enclosure volume. (Right) Several necks of different lengths can be inserted into the fixture near the MDF base of the Helmholtz resonator. Individual necks have lengths of 47.3 mm, 79.0 mm, 116.7 mm, 160.7 mm, and 213.9 mm as listed in Table 8.2. Also visible is a cap to seal the necks and the piston

**Table 8.2** The neck lengths and measured free-decay periods in milliseconds,  $T_i$ , for the five necks shown in Fig. 8.47 when they are inserted into the volume produced by the 6" PVC pipe and 90° elbow

Neck (mm)	Period (ms)
47.3	14.98
79.0	17.29
116.7	19.65
160.7	21.85
213.9	24.50

**Table 8.3** Zero-crossing-to-peak amplitude of the signal from a microphone located inside the Helmholtz resonator's compliance (volume). Each amplitude has been given a sign since the sign of the amplitude alternates each half-cycle. Since time is expressed in terms of the number of cycles, it is not necessary to know either the frequency or the period to calculate  $Q$

Cycle #	0-to-Peak (mV)
0.0	+1306
0.5	-1219
1.0	+1175
1.5	-1100
2.0	+1050
2.5	-981
3.0	+944
3.5	-881
4.0	+850
4.5	-806
5.0	+775
5.5	-731
6.0	+700
6.5	-656
7.0	+625
7.5	-588
8.0	+569
8.5	-541
9.0	+516
9.5	-491
10.0	+472
10.5	-450
11.0	+431
11.5	-406
12.0	+384
12.5	-369
13.0	+353
13.5	-338
14.0	+319
14.5	-300

- (b) *Quality factor.* Based on the peak-to-peak values of the free-decay amplitudes given in Table 8.3 for each half-cycle of vibration, determine the  $Q$  of the resonance.

---

## References

1. C. E. Bradley, Acoustic streaming field structure: The influence of the radiator, *J. Acoust. Soc. Am.* **100**(3), 1399–1408 (1996). See Fig. 2.
2. D. Gedeon, DC gas flows in Stirling and pulse-tube cryocoolers, in *Cryocoolers 9*, R. G. Ross (ed.), pp. 385–392 (Plenum Press, 1997).
3. D. Fagen and W. Becker, Babylon Sisters, *Gaucho* (MCA, 1984), Roger Nichols, engineer, Gary Katz, producer.
4. U. S. *Standard Atmosphere, 1976* (National Oceanic and Atmospheric Administration, Report S/T 76-1562, 1976).

5. R. W. Fox and A. T. MacDonald, *Introduction to Fluid Mechanics*, 4th ed. (J. Wiley & Sons, 1992). See example problem 5.5, pp. 209–211; ISBN 0-471-54852-9
6. R.T. Beyer, Radiation pressure – the history of a mislabeled tensor. *J. Acoust. Soc. Am.* **63**(4), 1025–1038 (1978)
7. L. D. Landau and E. M. Lifshitz, *Fluid Mechanics*, 2nd ed. (Butterworth-Heinemann, 1987). See §5; ISBN 0 7506 2767 0
8. M. Barmatz, Overview of Containerless Processing Technologies, in *Materials Processing in the Reduced Gravity Environment of Space*, ed. by G. E. Ridone, (New York, Elsevier, 1982), pp. 25–37
9. J.B. Mehl, Greenspan acoustic viscometer: Numerical calculation of fields and duct-end effects. *J. Acoust. Soc. Am.* **106**(1), 73–82 (1999)
10. F. Hoffman, Aw, c'mon and take a hit, *Flash*, No. 2 (1977), pp. 30–33.
11. C. C. Mann, *1491*, 2nd ed. (Vintage, 2011); ISBN 978-1-4000-3205-1.
12. S.L. Garrett, D.K. Stat, Peruvian whistling bottles. *J. Acoust. Soc. Am.* **62**(2), 449–453 (1977)
13. Mukai, et al., Experimental study on the absorption characteristics of resonance-type brick/block walls, *J. Acoust. Soc. Japan (E)* **20**(6), 433–438 (1999).
14. <http://www.lmsintl.com/SYSNOISE>.
15. <http://www.ht-audio.com/bassbox.htm>.
16. S. L. Garrett and S. Backhaus, The power of sound, *American Scientist* **88**(6), 516–525 (2000) is available at the *American Scientist Magazine* web site: <http://www.americanscientist.org/issues/feature/2000/6/the-power-of-sound>.
17. W. Ward, J. Clark, and G. Swift, *Design Environment for Low-amplitude Thermoacoustic Energy Conversion* (DETAEC), Ver. 4.6b2.7, Los Alamos National Laboratory Report N° LA-CC-16-053 (4 Dec 2017).
18. P. M. Morse, *Vibration and Sound*, 2nd ed. (McGraw-Hill, 1948), Ch. VI, §24, pp. 265–288. This classic textbook has been reprinted by the Acoustical Society of America, 1981; ISBN 0-88318-876-7.
19. S. Backhaus, G.W. Swift, A thermoacoustic Stirling heat engine. *Nature* **399**, 335–338 (1999)
20. P. Merkli, H. Thomann, Thermoacoustic effects in resonant tubes. *J. Fluid Mech.* **70**, 161–177 (1975)
21. G. W. Swift, *Thermoacoustics: A Unifying Perspective for Some Engines and Refrigerators*, 2nd ed. (Springer/Acoust. Soc. Am., 2017); ISBN 978-3-319-66932-8.
22. J. Wilhelm, K.A. Gillis, J.B. Mehl, M.R. Moldover, An improved Greenspan acoustic viscometer. *Int. J. Thermophys.* **21**, 983–997 (2000)
23. K.A. Gillis, J.B. Mehl, M.R. Moldover, Theory of the Greenspan viscometer. *J. Acoust. Soc. Am.* **114**(1), 166–173 (2003)
24. P. Roth, *Portnoy's Complaint* (Random House, 1969); ISBN 978-0394441198-6.
25. L. L. Beranek, *Acoustics* (McGraw-Hill, 1954); ISBN 07-004835-5. This classic textbook has been reprinted by the Acoustical Society of America, 1996; ISBN 0-88318-494-X.
26. S. Garrett, The effect of “Kelvin Drag” on the oscillations of a neutrally buoyant sphere. *Am. J. Phys.* **49**, 807 (1981)
27. R.A. Johnson, S.L. Garrett, R.M. Keolian, Thermoacoustic cooling for surface combatants. *Nav. Eng. J.* **112**(4), 335–345 (2000)
28. J. F. Heake, “Characterization of a 10-kilowatt Motor/Alternator for Thermoacoustic Refrigeration,” Master of Science in Acoustics, Penn State University, December 2001.

**Open Access** This chapter is licensed under the terms of the Creative Commons Attribution 4.0 International License (<http://creativecommons.org/licenses/by/4.0/>), which permits use, sharing, adaptation, distribution and reproduction in any medium or format, as long as you give appropriate credit to the original author(s) and the source, provide a link to the Creative Commons license and indicate if changes were made.

The images or other third party material in this chapter are included in the chapter's Creative Commons license, unless indicated otherwise in a credit line to the material. If material is not included in the chapter's Creative Commons license and your intended use is not permitted by statutory regulation or exceeds the permitted use, you will need to obtain permission directly from the copyright holder.





# Dissipative Hydrodynamics

9

## Contents

9.1	The Loss of Time Reversal Invariance .....	422
9.2	Ohm's Law and Electrical Resistivity .....	424
9.3	Thermal Conductivity and Newton's Law of Cooling .....	425
9.3.1	The Thermal Boundary Layer .....	427
9.3.2	Adiabatic Compression Within a Bounded Volume .....	430
9.3.3	Energy Loss in the Thermal Boundary Layer* .....	432
9.3.4	Adiabatic vs. Isothermal Propagation in an Ideal Gas .....	433
9.4	Viscosity .....	434
9.4.1	Poiseuille Flow in a Pipe of Circular Cross-Section .....	435
9.4.2	The Viscous Boundary Layer .....	436
9.4.3	Viscous Drag in the Neck of a Helmholtz Resonator .....	438
9.4.4	Quality Factors for a Helmholtz Resonator .....	440
9.5	Kinetic Theory of Thermal and Viscous Transport .....	443
9.5.1	Mean Free Path .....	443
9.5.2	Thermal Conductivity of an Ideal Gas .....	444
9.5.3	Viscosity of an Ideal Gas .....	446
9.5.4	Prandtl Number of an Ideal Gas and Binary Gas Mixtures* .....	447
9.6	Not a Total Loss .....	449
	References .....	451

In the previous chapter, the resonance frequency,  $\omega_o$ , of a Helmholtz resonator was calculated. When driven at that frequency, the predicted pressure amplitude inside the resonator's volume (compliance) became infinite. This was because the theory used to model that inertance and compliance network in Figs. 8.11 and 8.15, and in Eq. (8.50), did not include any dissipation. By introducing DELTAEC, we were able to calculate the amount of power dissipated in the neck (inertance) and volume (compliance) of a 500 ml boiling flask. In this chapter, those losses will be calculated from hydrodynamic "first principles."

Just as we used lumped acoustical elements in Chap. 8 to begin our exploration of the linearized, nondissipative forms of the hydrodynamic equations, we will again use lumped elements to introduce thermal and viscous dissipative effects, restricting our attention (temporarily) to thermoviscous effects

at solid-fluid boundaries. Later, in Chap. 14, those dissipative mechanisms will be generalized to include dissipative effects (attenuation), with the addition of molecular relaxation effects (see Sect. 4.4), which will be incorporated by the introduction of a “bulk viscosity,” to account for dissipation of sound waves propagating in spaces that are far from any boundaries.

## 9.1 The Loss of Time Reversal Invariance

There are certain phenomena that can be “played backward” in a movie or video that do not look different than when played forward. If we took a video of a wavelike pulse propagating on a string or a slinky, like the Gaussian pulses in Figs. 3.2, 3.3, and 3.4, it would be very difficult to tell whether the video was being played forward or backward. This indifference to the “arrow-of-time” is called *time reversal invariance*.

On the other hand, there are certain things that do not look right played backward. An egg dropping to the floor and cracking does not make sense played backward—a yellow slimy mess that self-organizes into an unbroken shell and then levitates. The murder at the start of *Memento* [1] shows the bullet case reentering the gun and a Polaroid™ photo fading out and then reentering its camera.

When dissipation is included in our hydrodynamic equations, time reversal invariance must be abandoned. This can be demonstrated mathematically by focusing on a traveling wave moving to the right, along the  $x$  axis, as described in Eq. (1.9), which represented complex exponential form.

$$p(x, t) = p_m + \Re e \left[ \hat{\mathbf{p}} e^{j(\omega t - kx)} \right] \quad (9.1)$$

The complex amplitude of the wave,  $\hat{\mathbf{p}}$ , can introduce an additional phase factor to compensate for some arbitrary choice of the time origin,  $t = 0$ . If we reverse the sign of the time, the phase factor changes from  $j(\omega t - kx)$  to  $-j(\omega t + kx)$ , which is the equivalent of making the wave propagate in the negative  $x$  direction. When we change the direction of time, the sign of the velocity also changes (Figs. 9.1 and 9.2).

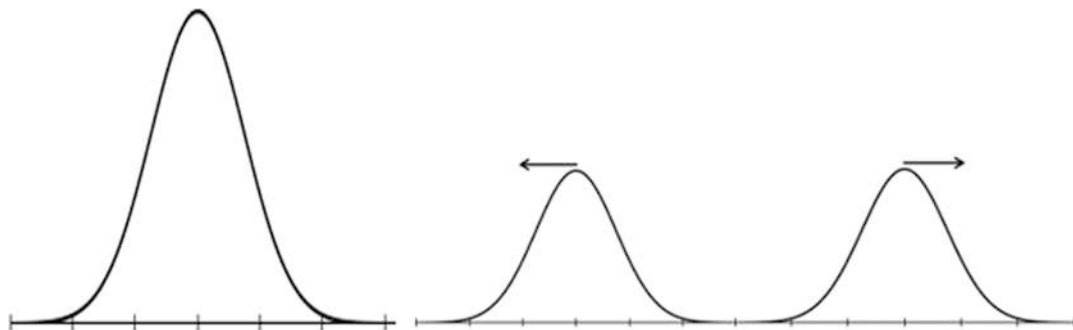


**Fig. 9.1** Sketches of pulses in a nondissipative medium showing the (transverse) pulse amplitude propagating reversibly in time along one dimension. We could assume that the pulse started at  $t = 0$ , as the single lump shown on the *left*, and then became two pulses of the same width and shape having amplitudes equal to half the original pulse height, traveling in opposite directions. We could also assume that the arrows showing the direction of motion for the two pulses at the *right* could be reversed. Then the pulses are moving toward each other; they superimpose to form the larger pulse on the *left* and then pass through each other to become the two pulses shown at the *right* with their *arrows* (as drawn) again showing the direction of their subsequent motion after they had passed through each other

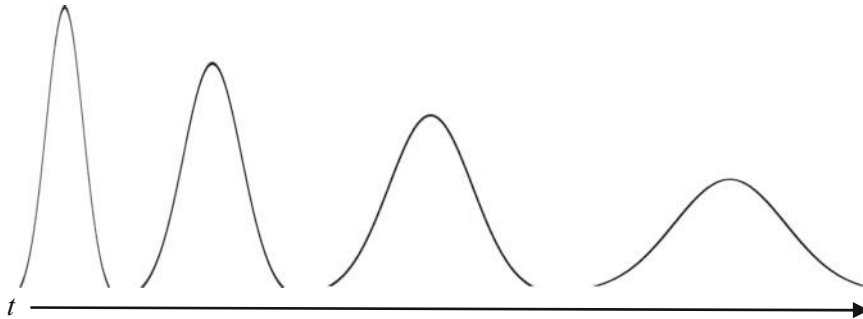


**Fig. 9.2** Unlike Fig. 9.1, the time evolution of the pulse at the left can only proceed in the direction indicated by the arrow. The progression of the pulse is determined by a diffusion equation like Eq. (9.4). If the pulse at the *left* represents an initial temperature distribution in a fluid, over time the temperature would diffuse as shown due to the thermal conductivity of the medium. If the pulse represented the injection of dye into a stagnant fluid, the diffusion of the dye would be represented by the subsequent pulse shapes. The most diffuse pulse, shown at the *right*, would never spontaneously self-focus into the more concentrated temperature or dye distribution shown at the *left*

In the continuity equation (7.32), the reversal of time changes the sign of the time derivative,  $\partial\rho/\partial t$ . The term that includes the divergence,  $\nabla \cdot (\rho \vec{v})$ , also has its sign reversed because the velocity changes sign. Both terms on both sides of the continuity equation are thus “negated” by the time reversal so the equation is unaffected; just multiply the whole equation by  $(-1)$  and we are back where we started.

This is not the case for the Navier-Stokes equation (7.34), even in its linearized form that discards the convective term,  $(\vec{v} \cdot \nabla) \vec{v}$ , and ignores gravity.

$$\rho \frac{\partial \vec{v}(\vec{x}, t)}{\partial t} = -\vec{\nabla} p(\vec{x}, t) + \mu \nabla^2 \vec{v}(\vec{x}, t) \quad (9.2)$$

Since both the velocity and the time change sign, the derivative,  $\partial \vec{v}/\partial t$ , does not change sign. On the right-hand side of Eq. (9.2), the pressure,  $p(\vec{x}, t)$ , is a thermodynamic variable and therefore a Galilean invariant; its value is a property of the medium that is not a function of the reversal of time or of uniform motion of the coordinate system.

We’d be in fine shape with both the time derivative and the gradient of the pressure, since the sign of neither changes under time reversal (i.e., the Euler equation is time reversal invariant). But the Laplacian operator,  $\nabla^2$ , that is multiplied the *shear viscosity*,  $\mu$ , operates on the velocity, which does change sign when time is reversed. The Navier-Stokes equation, as written in Eq. (9.2), is therefore not time reversal invariant. Neither is the linearized entropy equation, as written in Eq. (7.43), even if the viscous entropy generation term is neglected and we assume that the *thermal conductivity*,  $\kappa$ , is independent of position, where  $s$  is the specific entropy (per unit mass) [J/K – kg] = [m<sup>2</sup>/s<sup>2</sup> – K].

$$\rho T \frac{\partial s(\vec{x}, t)}{\partial t} = \kappa \nabla^2 T(\vec{x}, t) \quad (9.3)$$

Here again, both  $s(\vec{x}, t)$  and  $T(\vec{x}, t)$  are Galilean invariant thermodynamic properties of the fluid that do not change under time reversal. The sign of  $\partial s/\partial t$  does change since the sign of the time is reversed. Equation (9.3) can be transformed into the *Fourier Diffusion Equation* after substituting the

relation between changes in heat per unit mass,  $dq$ , and changes in entropy per unit mass,  $ds$ . We have  $dq = T ds$ , from Eq. (7.5), and the relation between the addition of heat and the change in temperature at constant pressure,  $dq = \rho c_p dT$ , for a polytropic substance, from Eq. (7.14).

$$\frac{\partial T(\vec{x}, t)}{\partial t} = \frac{\kappa}{\rho c_p} \nabla^2 T(\vec{x}, t) \quad (9.4)$$

Equations that have the form of Eq. (9.2) and Eq. (9.4) are *diffusion equations*. They produce dissipation and they violate time reversal invariance. If those irreversible effects are present, then energy will be dissipated. We can clearly see a difference if the video is played forward or backward in the presence of dissipation.

## 9.2 Ohm's Law and Electrical Resistivity

We will start our investigation of dissipative hydrodynamics with thermal conduction. To do so, we will make an analogy to dissipation in direct current (dc) electrical circuit theory, since most students who go on to careers in engineering and science learn *Ohm's law* in high school.

Our previous representation of ideal compliances and inertances were analogous to ideal capacitors and inductors; energy could be stored as compressive (elastic) potential energy in a compliance or as kinetic energy in an inertance, but it would not be dissipated, as it could in an electrical circuit where the current flows through an electrical resistance,  $R_{dc}$ . The relationship between the current flowing through the resistance,  $I$ , and the voltage difference,  $\Delta V$ , across the resistance is known as Ohm's law:  $I = \Delta V/R_{dc}$ . The electrical resistance is a (mathematically) real quantity (usually considered to be a constant that is independent of current<sup>1</sup>), so that the current and the voltage are in-phase; hence,  $\phi = 0$ .

The time-averaged electrical power,  $\langle \Pi_{el} \rangle_t$ , dissipated in the resistor is a positive-definite function of either the current or the voltage.

$$\langle \Pi_{el} \rangle_t = \frac{I \Delta V}{2} \cos \phi = \frac{I^2 R_{dc}}{2} = \frac{(\Delta V)^2}{2R_{dc}} \quad (9.5)$$

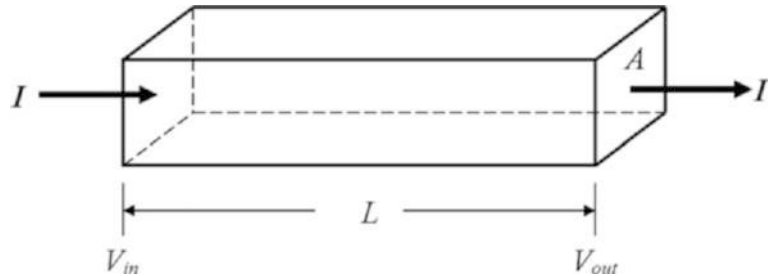
As we have done with our acoustical variables,  $\Delta V$  and  $I$  are designated by their peak values, not the root-mean-squared values that would be displayed by an ac voltmeter. The phase angle between  $I(t)$  and  $\Delta V(t)$  is  $\phi$ , but since  $I(t)$  is in-phase with  $\Delta V(t)$ ,  $\cos \phi = 1$ . It does not matter whether the current is flowing to the right or to the left; power will be dissipated in a resistor and entropy will be created by an irreversible process. This electrical power dissipation in a resistor is usually called *Joule heating*, after James Prescott Joule (1818–1889).

Considering a material, shown schematically in Fig. 9.3, having a constant electrical conductivity,  $\sigma$ , with units of  $[(\Omega - m)^{-1}]$ ,<sup>2</sup> the electrical resistance measured across its length,  $R_{dc}$ , will depend

<sup>1</sup> William Hewlett, an electrical engineering student at Stanford University, used a current-dependent resistance (a flashlight bulb) to stabilize the amplitude of an audio oscillator circuit as his master's thesis. That oscillator subsequently became the HP-200. It was the first product developed commercially by the original Silicon Valley startup: Hewlett-Packard. The first five of their "production" models were purchased by Walt Disney to produce sound effects in the animated feature film, *Fantasia*.

<sup>2</sup> Before the French-dominated *Le Système International d'Unités* was adopted, the unit of conductance was the mho (ohm spelled backward). They re-named the unit of electrical conductance the siemens [S]. These are the same folks, who, in their collective wisdom, re-named the unit of frequency from the obscure cycles-per-second (cps) to the hertz [Hz].

**Fig. 9.3** Electrical current,  $I$ , flows through a conductor with electrical conductivity,  $\sigma$ , from a higher electrical potential,  $V_{in}$ , to a lower electrical potential,  $V_{out}$ . The electrical resistance,  $R_{dc}$ , of the resistor of length,  $L$ , and cross-sectional area,  $A$ , is  $R_{dc} = L/\sigma A$



directly upon its length,  $L$ , and inversely upon its cross-sectional area,  $A$ . For that resistor, the current passing through the resistor,  $I$ , and the voltage difference,  $\Delta V$ , across the resistor are related by the direct current (dc) version of Ohm's law.

$$I = \frac{\Delta V}{R_{dc}} = \frac{\sigma A}{L} (V_{in} - V_{out}) \quad (9.6)$$

If two identical pieces of the same material, like that shown in Fig. 9.3, were put side-by-side (in parallel), their areas would add, and the resistance would be cut in half. If  $\Delta V = V_{in} - V_{out}$  remains constant, the current would double. If two pieces were placed end-to-end (in series), their lengths would add without changing their areas, and the resistance would be doubled. Again, if  $\Delta V$  remained constant, the current would be reduced by half, relative to the single sample.

### 9.3 Thermal Conductivity and Newton's Law of Cooling

*Newton's Law of Cooling* has exactly the same form as Ohm's law, as written in Eq. (9.6), where we recognize  $I$  as the rate of electrical charge flow, with units of amperes [A] or coulombs/second [C/s]. By analogy, the rate of heat flow,  $\dot{Q}$ [J/s], is linearly related to the temperature difference,  $\Delta T$ , across the length,  $L$ , of the sample. It is also proportional to the thermal conductivity of the material,  $\kappa$ , having units of [W/K-m] or [ $W/^{\circ}\text{C}\cdot\text{m}$ ].

$$\dot{Q} = \frac{\Delta T}{R_{th}} = \frac{\kappa A}{L} (T_{in} - T_{out}) = \kappa A \frac{\Delta T}{L} \quad (9.7)$$

The SI units of heat flow are watts [W] or joules/second [J/s]. As expressed in the right-hand term of Eq. (9.7), the heat flow (thermal power flow) is proportional to the temperature gradient,  $\Delta T/L$  (Fig. 9.4).

As shown in Fig. 9.5, analysis of the heat flow,  $\dot{Q}$ , through a sample like that in Fig. 9.4, but with length,  $dx$ , converts Newton's Law of Cooling in Eq. (9.7) into the Fourier Diffusion Equation (9.4). The heat flux,  $\dot{q}_{in}$ , with units of heat (energy) per unit area per unit time [ $\text{W}/\text{m}^2$ ], enters the slab at  $x$ , and  $\dot{q}_{out}$  exits at  $x + dx$ .

The thermal power,  $\dot{Q}_{net}$ , that is deposited in the slab results in an increase in the temperature of the slab with time. If we assume that the differential element of length,  $dx$ , has cross-sectional area,  $A$ , and the material has a specific heat per unit mass,  $c_p$ , that is independent of temperature, then the heat capacity of the differential element is the mass of the element,  $\rho A dx$ , times the specific heat (per unit mass). By Eq. (9.8), this net input of thermal power must result in a change in the temperature of the slab with time.

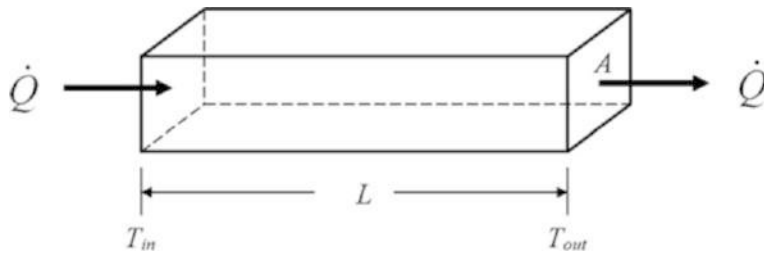


**Fig. 9.4** Heat power,  $\dot{Q}$ , flows through a thermal conductor made from a material with constant thermal conductivity,  $\kappa$ , from a higher temperature,  $T_{in}$ , to a lower temperature,  $T_{out}$ . The thermal resistance,  $R_{th}$ , of the sample of length,  $L$ , and cross-sectional area,  $A$ , is  $R_{th} = L/\kappa A$

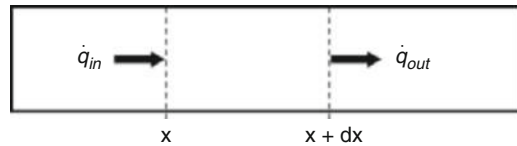


**Fig. 9.5** A different heat flux,  $\dot{q}_{in}$ , flows into a differential “slab” of thickness,  $dx$ , and area,  $A$ , than flows out,  $\dot{q}_{out}$ , at  $x + dx$ . As a result, the heat that remains within the differential element,  $\dot{Q}_{net}$ , causes the temperature of that element to change in accordance with the definition of heat capacity,  $C_p = (\partial Q/\partial T)_P$ , where we assume the sample is held at constant pressure

$$\dot{Q}_{net} = \rho c_p A dx \frac{dT}{dt} = \dot{Q}(x) - \dot{Q}(x + dx) = A[\dot{q}(x) - \dot{q}(x + dx)] \quad (9.8)$$

Since the heat flows in response to a temperature gradient, as expressed by Newton’s Law of Cooling (9.7), and Eq. (9.8) produces the net heat transport in terms of the (one-dimensional) temperature gradients,  $\partial T/\partial x$ , evaluated at  $x$  and  $x + dx$ .

$$\rho c_p A dx \frac{dT}{dt} = A \left[ -\kappa \left( \frac{\partial T}{\partial x} \right)_x + \kappa \left( \frac{\partial T}{\partial x} \right)_{x+dx} \right] \quad (9.9)$$

At this point, we are only one Taylor series expansion away from Fourier’s Diffusion Equation.

$$\begin{aligned} \left( \frac{\partial T}{\partial x} \right)_{x+dx} &\cong \left( \frac{\partial T}{\partial x} \right)_x + \frac{\partial}{\partial x} \left( \frac{\partial T}{\partial x} \right)_x dx + \dots \\ \Rightarrow \quad \left( \frac{\partial T}{\partial x} \right)_{x+dx} - \left( \frac{\partial T}{\partial x} \right)_x &\cong \left( \frac{\partial^2 T}{\partial x^2} \right)_x dx \end{aligned} \quad (9.10)$$

Since  $dx$  is a small quantity (compared to what?), we can neglect the terms containing higher powers  $(dx)^n$  of  $dx$  and combine Eq. (9.9) and Eq. (9.10), while bringing the thermal conductivity,  $\kappa$ , outside the derivative, assuming that it is spatially uniform.

$$\frac{\partial T}{\partial t} = \frac{\kappa}{\rho c_p} \frac{\partial^2 T}{\partial x^2} = \frac{\kappa}{\rho c_p} \nabla^2 T = \alpha \nabla^2 T \quad (9.11)$$

The earlier expression is identical to the Fourier Heat Diffusion Equation that we derived from our linearization of the entropy equation (7.43) under the same assumption of a constant temperatur-

independent thermal conductivity. The new constant introduced in the right-hand term of (9.11),  $\alpha = \kappa/\rho c_p$ , is the *thermal diffusivity*.<sup>3</sup> Energy and temperature units cancel in this ratio, so  $\alpha$  has units of length-squared divided by time [ $\text{m}^2/\text{s}$ ] [2].

The thermal diffusivity is useful because it is a measure of the ability of a material to conduct thermal energy relative to its ability to store thermal energy. Materials with a large  $\alpha$  will respond quickly to changes in their thermal environment, while materials with small  $\alpha$  will respond more sluggishly, taking longer to reach a new equilibrium condition if the temperature of the surroundings is changed. The thermal diffusivity of most metallic solids and gases (near room temperature) is  $\alpha \cong 10^{-5} \text{ m}^2/\text{s}$ , while for insulating solids and many liquids,  $\alpha \cong 10^{-8} \text{ to } 10^{-7} \text{ m}^2/\text{s}$ . Of course, if the fluid is in motion, the convective heat transport (e.g., “wind chill”) can dominate conductive heat transport [3].

### 9.3.1 The Thermal Boundary Layer

As acousticians, we are interested in the acoustical solutions to Eq. (9.11) that involve time-harmonic temperature deviations,  $T(t) = T_s \cos(\omega t)$ , typically at a single frequency,  $\omega$ , from some mean temperature,  $T_m$ . As claimed before, harmonic analysis is the acoustician’s most powerful mathematical tool. We will begin by applying Eq. (9.11) to a semi-infinite wall defining a plane surface at  $x = 0$  that has an oscillating temperature,  $T(0, t) = T_m + T_s \cos(\omega t)$ . By letting  $T_s$  be a scalar, we are defining the phase of the temperature response with respect to the oscillating temperature of the boundary. The wall is in contact with a fluid that has a thermal diffusivity,  $\alpha = \kappa/\rho c_p$ , as diagrammed in Fig. 9.6.

We will assume that the space-time behavior of the fluid at  $x \geq 0$  is that of a wave traveling to the right,  $T_{\text{fluid}}(x, t) = T_m + \Re e[\hat{\mathbf{T}} e^{j(\omega t - \mathbf{k}x)}]$ , and substitute this expression into the one-dimensional version of Eq. (9.11) to convert the differential equation into an algebraic equation.

$$j\omega \hat{\mathbf{T}} = -\alpha \mathbf{k}^2 \hat{\mathbf{T}} \quad (9.12)$$

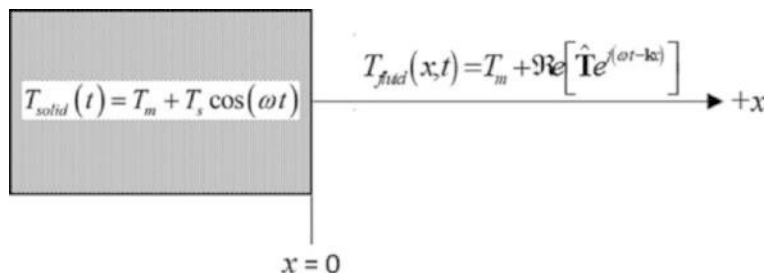


**Fig. 9.6** A semi-infinite solid with an oscillatory surface temperature,  $T_{\text{solid}}(0, t) = T_m + T_s \cos(\omega t)$ , is in contact at the plane  $x = 0$  with a fluid at the same mean temperature,  $T_m$ . Since there is only fluid at  $x \geq 0$ , we will assume a right-going wavelike space and time dependence for the oscillating component of the fluid’s temperature,  $T_{\text{fluid}}(x, t) = T_m + \Re e[\hat{\mathbf{T}} e^{j(\omega t - \mathbf{k}x)}]$

<sup>3</sup>This material parameter is also sometimes called the *thermometric conductivity* and abbreviated as  $\chi$ . For instance see, L. D. Landau and E. M. Lifshitz, *Fluid Mechanics*, 2nd ed. (Butterworth-Heinemann, 1987); ISBN 0 7506 2767 0. See §50.

Cancelling the  $\hat{\mathbf{T}}$ s and dividing both sides by  $-\alpha$ , Eq. (9.12) becomes  $\mathbf{k}^2 = -j\omega/\alpha = \omega/j\alpha$ . Taking the square root<sup>4</sup> of  $\mathbf{k}^2$  (see Sect. 1.5.2), we find that  $\mathbf{k}$  is a complex number, having real and imaginary parts of equal magnitude.

$$\mathbf{k} = \sqrt{\frac{\omega}{j\alpha}} = \frac{1-j}{\sqrt{2}} \sqrt{\frac{\omega}{\alpha}} = (1-j) \sqrt{\frac{\omega}{2\alpha}} \equiv \frac{1-j}{\delta_\kappa} \quad (9.13)$$

It is convenient to define a real scalar physical length,  $\delta_\kappa$ , based on the reciprocal wavenumber that is the (exponential) thickness of the oscillatory thermal boundary layer. The scale length of thermal diffusion,  $\delta_\kappa$ , is very important in acoustics (see “`delta_kappa`” in Fig. 8.19) and is called the *thermal penetration depth*.

$$\delta_\kappa \equiv \sqrt{\frac{2\kappa}{\rho c_p \omega}} = \sqrt{\frac{2\alpha}{\omega}} = \sqrt{\frac{\alpha}{\pi f}} \quad (9.14)$$

The complex wave number,  $\mathbf{k}$ , has equal real and imaginary parts. In electromagnetism, this similar behavior occurs when an electromagnetic wave impinges on an electrically conducting (usually metallic) solid or the surface of an ionic solution (e.g., seawater). In that case, the equivalent to Eq. (9.14) is known as the “*skin depth*” (see Sect. 9.4.2).

This behavior is different from that which occurs at the interface between two optically transparent media when the angle of incidence exceeds the critical angle<sup>5</sup> or at the interface between two acoustical media with different specific acoustical impedances (see Sect. 11.2.1). For the case of total internal reflection, the wavenumber within the excluded medium is entirely imaginary and the disturbance is known as an *evanescent wave*.

The complex wavenumber,  $\mathbf{k}$ , in Eq. (9.13) still has the units of reciprocal length [ $\text{m}^{-1}$ ]. Substitution of  $\mathbf{k}$  from (9.13) back into the assumed solution,  $T_{\text{fluid}}(x, t) = T_m + \Re e^{[\hat{\mathbf{T}} e^{j(\omega t - \mathbf{k}x)}]}$ , shown in Fig. 9.6, and application of the boundary condition at  $x = 0$ , provides an explicit expression for the spatial distribution of temperature oscillations within the fluid.

$$T_1(x, t) = \Re e^{[\hat{\mathbf{T}}_s e^{-x/\delta_\kappa} e^{j(\omega t - x/\delta_\kappa)}]} \quad \text{for } x \geq 0 \quad (9.15)$$

Expanding Eq. (9.15) in terms of real trigonometric functions, Euler’s formula in Eq. (1.53) will facilitate plotting of the real and imaginary parts of the spatial dependence of  $T_1(x)$ , shown in Fig. 9.7.

<sup>4</sup> To take the square root of  $-j = j^{-1}$ , it is sometimes useful to draw a diagram on the complex plane by expressing  $j^{-1}$  as  $-j$ , drawn vertically downward at  $-90^\circ$  from the positive real axis. The square root operation divides that angle by two, resulting in a unit vector rotated only  $-45^\circ$  away from the real axis having a projection of  $(2)^{-\frac{1}{2}}$  along the real axis and  $-(2)^{-\frac{1}{2}}$  along the imaginary axis demonstrating that one root of  $\sqrt{-j}$  is  $(1-j)/\sqrt{2}$ . Regarding  $-90^\circ$  as  $+270^\circ$ , and again dividing by two, yields the other root,  $(j-1)/\sqrt{2}$ .

<sup>5</sup> Evolution has found these waves useful for the control of light reaching the optic nerve of insects with compound eyes. Did you ever notice that it is hard to swat a fly under a wide range of lighting conditions? How can you control the light levels when your eye has a thousand lenses? One iris for each lens is clearly out of the question, since each lens has a diameter of only about 30  $\mu\text{m}$ . The mechanism employed by insects to control light levels makes each lens the entrance to an optical waveguide (called an ommatidium by the entomologists), much like an optical fiber used in telecommunications, that channels light from the lens down to the optic nerve (see Fig. 11.6). In bright light, a chemical change in the fluid surrounding the waveguides causes a precipitate to form that scatters the wave decaying (exponentially) beyond the waveguide into the fluid. Scattering of this diffusion wave reduces the light that makes it down the waveguide to the optic nerve. For further information on the physics of insect vision and some relevant graphics, see R. P. Feynman, *Lectures on Physics*, Vol. I (Addison-Wesley 1963), §36-4.

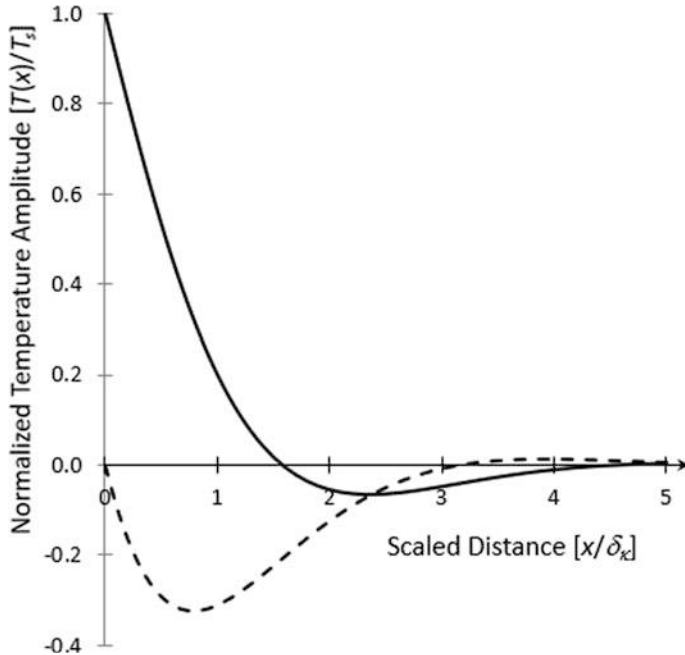


**Fig. 9.7** The real (solid) and imaginary (dashed) components of the oscillatory portion of the temperature near a wall that has an oscillating temperature at its surface. The y axis is normalized so that  $T_s = 1$ . The x axis is scaled by the thermal penetration depth,  $\delta_\kappa$ . The real part of Eq. (9.16) is in-phase with the temperature oscillations at the surface of the solid and is equal to the magnitude of those oscillations, thus satisfying the boundary condition at  $x = 0$ :  $T_{\text{fluid}}(0, t) = T_{\text{solid}}(0, t)$  at all times. At a distance of  $0.7854\delta_\kappa$  from the wall, the amplitudes of the real and imaginary parts have equal magnitude

$$T_1(x) = T_s e^{-x/\delta_\kappa} \left[ \cos\left(\frac{x}{\delta_\kappa}\right) - j \sin\left(\frac{x}{\delta_\kappa}\right) \right] \quad \text{for } x \geq 0 \quad (9.16)$$

It is clear from Fig. 9.7 that Eq. (9.15) and Eq. (9.16) satisfy the boundary condition requiring that the temperatures of the solid and the fluid, at their plane-of-contact,  $x = 0$ , are exactly equal,  $\Re[T_1(0, t)] = T_s$ , and in-phase,  $\Im[T_1(0, t)] = 0$ , at all times. If the adjacent temperatures were not equal, then the discontinuity would require Eq. (9.11) to produce infinite heat flows. The temperature disturbance in the fluid is localized quite near the wall. At distances greater than  $x = 4\delta_\kappa$ , the effects of the wall's oscillating temperature correspond to temperature oscillations in the fluid that are less than 2% of those at the interface between the wall and the fluid.

The situation encountered more commonly in acoustical systems is that the temperature of the fluid is oscillating while the wall temperature remains constant, typically due to the solid's higher thermal conductivity and heat capacity per unit volume. For example, in an ideal gas, the amplitude of adiabatic temperature oscillations,  $T_{1, \text{adiab}}$ , far from any solid boundaries, were given by Eq. (7.25):  $T_{1, \text{adiab}} = T_m[(\gamma - 1)/\gamma](|\hat{\mathbf{p}}|/p_m)$ . Typically, a solid boundary will keep an ideal gas's temperature constant on the solid-gas interface plane, which is defined as  $x = 0$  in Fig. 9.6. In that case, the boundary condition is that  $T_1(0, t) = 0$ .

$$T_1(x, t) = T_{1, \text{adiab}} \Re e^{\left[ e^{j\omega t} \left( 1 - e^{-(1+j)x/\delta_\kappa} \right) \right]} \quad \text{for } x \geq 0 \quad (9.17)$$

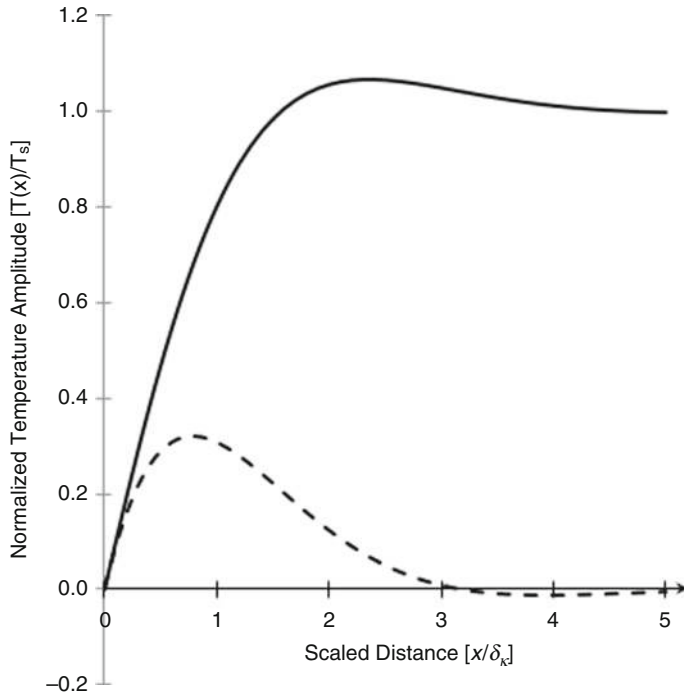


**Fig. 9.8** The real (solid line) and imaginary (dashed line) parts of the oscillatory portion of the temperature near an isothermal surface are plotted for the situation where the fluid far from the wall has a normalized oscillating temperature magnitude,  $|T_1(x/\delta_\kappa) \gg 1| = 1$ , that might be caused by adiabatic expansion and compression of an ideal gas given by Eq. (7.25). The  $x$  axis is again scaled by the thermal penetration depth,  $\delta_\kappa$ . The isothermal surface at  $x = 0$  requires that both the real and imaginary parts of Eq. (9.18) vanish at the interface:  $T_s(0, t) = 0$ . The thermal influence of the wall extends only a distance of about four thermal penetration depths into the fluid

The real and imaginary parts of that solution, provided in Eq. (9.18), are plotted in Fig. 9.8.<sup>6</sup>

$$T_1(x, t) = T_{1, \text{adiab}} \Re e \left[ e^{j\omega t} \left\{ 1 - e^{-x/\delta_\kappa} \cos \left( \frac{x}{\delta_\kappa} \right) + j \left[ e^{-x/\delta_\kappa} \sin \left( \frac{x}{\delta_\kappa} \right) \right] \right\} \right] \text{ for } x \geq 0 \quad (9.18)$$

### 9.3.2 Adiabatic Compression Within a Bounded Volume

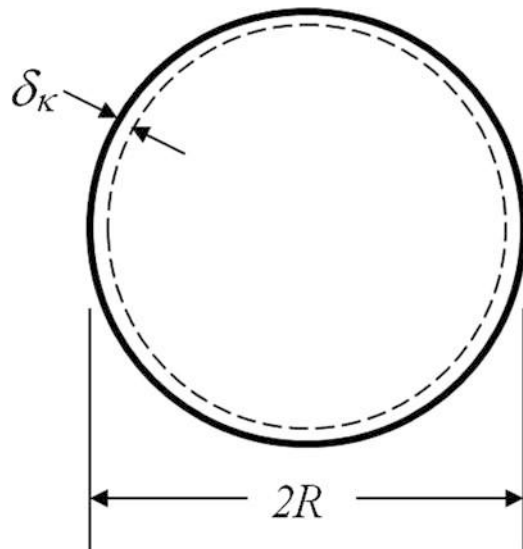
At various places in Chaps. 7 and 8, I have claimed that the acoustic compressions and expansions of an ideal gas take place adiabatically. Having produced an acoustical solution the Fourier Heat Diffusion Equation (9.11), and having defined the thermal penetration depth,  $\delta_\kappa$ , in Eq. (9.14), we

<sup>6</sup> It is difficult for most people to visualize the spatial and temporal dependence of the temperature based only on plots of the real and imaginary parts of the solution as a function of position, such as those provided in Figs. 9.7 and 9.8. An animation of the temperature variation for an ideal gas near a solid (isothermal) wall is available at the Los Alamos National Laboratory Thermoacoustics Home Page: <http://www.lanl.gov/thermoacoustics/Book/index.html>. In the second paragraph on the page at that site, you have the option to download a zipped animation file. You can “unzip” the file and then run the DOS-executable animation THERMAL.EXE. The animation starts with the pressure and velocity in a standing wave and then zooms into the solid boundary to animate the temperature in the fluid as a function of space and time. The animation goes further to calculate the work done by an imaginary piston moving with the fluid to demonstrate that power is dissipated during the transition from adiabatic compressions far from the wall to isothermal compressions at the fluid-solid boundary.

Gas: air, 295.65 K, 1.0133E+05 Pa							
gamma	a(m/s)	rho(kg/m^3)	cp(J/kg-K)	beta(1/K)	k(W/m-K)	Prandtl	mu(kg/m-s)
1.4000	344.70	1.1940	1004.7	3.3824E-03	2.5901E-02	0.70804	1.8253E-05
Frequency= 241.73 Hz, delta_nu= 1.4188E-04 m, delta_kappa= 1.6862E-04 m							

**Fig. 9.9** Screenshot of the thermophysical properties of dry air at  $T_m = 295.65 = 22.5^\circ\text{C}$  for the 500 ml boiling flask analyzed in Sect. 8.5.2 and modeled in DELTAEC in Fig. 8.27

**Fig. 9.10** Schematic representation of the spherical volume of radius,  $R$ , that forms the acoustical compliance of the Helmholtz resonator depicted in Fig. 8.16. Within a spherical shell of thickness,  $\delta_K$ , adjacent to the glass, the pressure oscillations of the gas are nearly isothermal. Throughout the remaining volume, the compressions and expansions of the gas are adiabatic



are now equipped to determine the circumstances that are necessary so that acoustic compressions and expansions occur nearly isothermally in the vicinity of solid surfaces.

Before addressing this question of adiabatic vs. isothermal in a more formal context, it might be useful to examine the effects of thermal conduction in an acoustical compliance, such as the air-filled 500 ml volume of the Helmholtz resonator, shown in the photograph of Fig. 8.16. As shown in Fig. 8.27, the resonance frequency of the empty resonator was (0b) = 241.7 Hz. Figure 9.9 shows the DELTAEC Thermophysical Property output for that case. The value of the thermal penetration depth is visible at the lower right-hand corner:  $\text{delta\_kappa} = \delta_K = 168.62 \mu\text{m}$ .

The radius of the 500 ml spherical volume,  $R = (3V/4\pi)^{1/3} = 4.92 \text{ cm}$ . At the interface between the glass and the air, the gas must remain isothermal. The exaggerated boundary layer's thickness is shown schematically by the dashed spherical surface in Fig. 9.10.

At a distance of  $2\delta_K$  from the glass, the magnitude of the temperature oscillations of the gas (9.18) is 86.5% of their value far from that boundary, based on Eq. (9.18) as determined by the magnitude of the pressure oscillations within the volume,  $p_{cav}$ , according to Eq. (7.25). We can “split the difference” and approximate the effect of the wall by considering the gas a distance,  $\delta_K$ , or less from the glass as being compressed and expanded isothermally and the gas farther than  $\delta_K$  from the wall undergoing adiabatic compressions and expansions. The “isothermal region” of the 500 ml sphere has the volume of a spherical shell,  $V_{\text{isothermal}} = 4\pi\delta_K R^2$ , with the shell radius,  $R = 4.92 \text{ cm}$ , and a thickness,  $\delta_K = 168.6 \mu\text{m}$ , for the conditions specified in Fig. 9.9. The ratio of the “isothermal” volume to the “adiabatic” volume can be calculated.

$$\frac{V_{\text{isothermal}}}{V_{\text{adiabatic}}} \cong \frac{4\pi R^2 \delta_K}{(4\pi/3)R^3} = \frac{3\delta_K}{R} \quad \text{if } R \gg \delta_K \quad (9.19)$$

For our case,  $\delta_\kappa / R = 3.43 \times 10^{-3}$ , so the volumetric ratio in Eq. (9.19) is 1.0%. This shows that use of  $\gamma$  in the expression for the compliance of the volume,  $C = V/\gamma p_m$ , in Eq. (8.26), was justified. Since  $\gamma_{air} \cong 7/5 = 1.40$ , the isothermal compliance ( $\gamma_{iso} \equiv 1$ ) is 40% larger than its adiabatic value, so we would expect the resonance frequency predicted by Eq. (8.51) to be lower by about 0.2%, due to the increased compressibility of the gas within the isothermal boundary layer.

### 9.3.3 Energy Loss in the Thermal Boundary Layer\*

Heat is transferred from the compressed (hence, hotter) gas to the solid (isothermal) substrate during one-half of the acoustic cycle and is transferred from the solid substrate back to the expanded (hence, cooler) gas during the other half of the acoustic cycle. The entropy lost during these two heat transfers is non-zero even though the amount of heat transferred is nearly identical. The reason is that the change in entropy is related to the ratio of the heat transfer,  $dQ$ , to the absolute temperature at which that heat transfer takes place,  $T$ . Since the heat transferred from the substrate to the gas occurs at a lower average temperature, approximately  $T_m - (T_1/2)$ , than the heat transfer from the gas to the substrate, taking place at approximately  $T_m + (T_1/2)$ , where  $T_1$  is the adiabatic temperature change far from the substrate's surface, derived previously in Sects. 1.1.3 and 7.1.3, there will be a net increase in the total entropy,  $(\Delta S)_{net} > 0$ , during the complete cycle.

Although an exact calculation of this acoustic energy loss per unit surface area per unit time,  $\dot{e}_{th}$ , occurring in the thermal boundary layer requires an integral over a complete cycle, that derivation is somewhat more complicated than the analogous calculation of the energy loss due to viscous shear stresses in the fluid,  $\dot{e}_{vis}$ , provided in Sect. 9.4.3. Instead of the exact calculation, we can use Newton's Law of Cooling to estimate the heat transferred per unit surface area during each half-cycle assuming a square-wave pressure change,  $\pm p_1$ , rather than a sinusoidal variation of pressure.

The heat transferred from the gas to the substrate,  $dQ_{+1/2}$ , per unit area,  $A$ , during one-half of an acoustic period,  $(2f)^{-1}$ , can be approximated, assuming  $T_1$  is constant during the transfer and  $\partial T / \partial x \cong T_1 / \delta_\kappa$ . The heat transfer from the substrate to the gas is  $dQ_{-1/2}$ .

$$\frac{dQ_{\pm 1/2}}{A} \cong \frac{\pm \kappa}{2} \frac{T_1}{f \delta_\kappa} \propto \frac{\pm \kappa}{2f \delta_\kappa} \left( \frac{|\hat{\mathbf{p}}|}{p_m} \right) \quad (9.20)$$

The entropy change,  $dS_{\pm 1/2}$ , for each half-cycle depends upon the temperature at which each heat transfer,  $dQ_{\pm 1/2}$ , takes place.

$$\frac{dS_{\pm 1/2}}{A} \cong \frac{dQ_{\pm 1/2}}{A} \left( \frac{1}{T_m \pm (T_1/2)} \right) = \frac{\pm \kappa}{2f T_m \delta_\kappa} \left( \frac{T_1}{1 \pm (T_1/2T_m)} \right) \quad (9.21)$$

The net increase in entropy,  $(\Delta S)_{net} = dS_{+1/2} - dS_{-1/2}$ , can be approximated by a binomial expansion of the factor in parentheses in Eq. (9.21), since  $T_1/2T_m \ll 1$ .

$$\frac{(\Delta S)_{net}}{A} \propto \frac{\kappa}{f \delta_\kappa} \frac{T_1}{2T_m} \left[ \left( \frac{1}{1 - (T_1/2T_m)} \right) - \left( \frac{1}{1 + (T_1/2T_m)} \right) \right] \propto \left( \frac{T_1}{T_m} \right)^2 \propto \left( \frac{|\hat{\mathbf{p}}|}{p_m} \right)^2 \quad (9.22)$$

The conversion of this net entropy increase into a net energy dissipation per cycle per unit area simply requires multiplication by  $T_m$ . It should be clear that the thermal boundary layer's acoustic energy dissipation per unit area, per unit time,  $\dot{e}_{th}$ , is both positive-definite and proportional to  $|\hat{\mathbf{p}}|^2$ . An exact calculation [4], assuming the proper time averaging over a sinusoidal modulation of the acoustic pressure, is analogous to the calculation for  $\dot{e}_{vis}$  that will result in Eq. (9.37).

$$\dot{e}_{th} = -\frac{(\gamma - 1)}{4\gamma} \frac{|\hat{\mathbf{p}}|^2}{p_m} \delta_\kappa \omega \quad (9.23)$$

As expected,  $\dot{e}_{th}$  vanishes for an isothermal process where  $\gamma = 1$ .

### 9.3.4 Adiabatic vs. Isothermal Propagation in an Ideal Gas

Having introduced the thermal penetration depth as the real (exponential) length that characterizes the thickness of oscillatory thermal boundary layer, we can use  $\delta_\kappa$  to show that sound waves in ideal gases are very nearly adiabatic. To do this, let us start with the assumption that sound propagation is adiabatic and calculate the frequency above which that assumption breaks down.

If we refer to the sinusoidal waves shown in Fig. 3.5, the crests (displacement maxima) correspond to a temperature,  $T_1$ , that is higher than  $T_m$  by the amount specified in Eq. (7.25):  $T_1 = T_m[(\gamma - 1)/\gamma](p_1/p_m)$ . Similarly, the temperature of the gas at the troughs (pressure minima) is lower than  $T_m$  by  $-T_1$ . The crests and troughs are separated in space by one-half wavelength,  $\lambda/2$ . Can heat diffuse between the warmer crests and the cooler troughs during a half-cycle? The diffusion distance is given by the thermal penetration depth. At 345 Hz,  $\lambda/2 = 0.50$  m in air. At the same frequency,  $\delta_\kappa = 141$  μm. During one half-cycle,  $T/2 = 1.45$  ms, heat cannot diffuse far enough to equalize the temperatures of the peaks and troughs of the wave.

The above argument can be made more general by setting the wavenumber,  $k = \omega/c$ , for the adiabatic sound wave equal to the wavenumber for thermal diffusion,  $\delta_\kappa^{-1}$ , and solving for the frequency,  $\omega_{crit}$ , at which those two are equal. This is also equivalent to setting the adiabatic sound speed,  $c_s = (\partial p/\partial \rho)_s = \omega/k$ , equal to the “speed of heat,”  $c_{th} = \omega\delta_\kappa$ .

$$\omega_{crit} = \frac{\rho_m c_p c^2}{2\kappa} \quad (9.24)$$

For air at 300 K and standard pressure, the critical frequency,  $\omega_{crit} = 2.72 \times 10^9$  rad/s, or  $f_{crit} = \omega_{crit}/2\pi = 432$  MHz. At that frequency, the wavelength of sound is less than one micron, so our assumption of adiabatic sound propagation is quite good for all frequencies of interest in gases.<sup>7</sup>

At  $f_{crit}$  for air, the half-wavelength of sound corresponds to only 11 times the average distance between molecules. At these frequencies, our hydrodynamical approach, which assumes that fluids can be represented as a continuum, is starting to break down and corpuscular effects start to become important.

Of course, at lower pressures, this effect occurs at lower frequencies, so our analysis has to transition from hydrodynamical to ballistic, where the individual particle collisions dominate the propagation.<sup>8</sup> It has recently been shown that ballistic propagation should be considered in the study

<sup>7</sup> In liquids,  $\omega_{crit}$  is even higher. In water,  $f_{crit} = 1210$  GHz, although this is less significant because the difference between the adiabatic and isothermal sound speeds are so small due to the smaller thermal expansion coefficient. At 4 °C, the density of water reaches its maximum value, so the thermal expansion coefficient vanishes and the isothermal and adiabatic sound speeds are equal. The existence of life on this planet probably owes much to the fact that ice is less dense than water.

<sup>8</sup> This transition from hydrodynamic to *ballistic propagation* is known as the “Knudsen limit.” In that regime, the real and imaginary components of the wavenumber become equal. Based on M. Greenspan, “Propagation of Sound in Five Monatomic Gases,” J. Acoust. Soc. Am. **28**(4), 644–648 (1956), the hydrodynamic results should not be used for frequencies above  $\omega \cong c^2/10\alpha$ . An excellent review article by Greenspan appears in *Physical Acoustics*, Vol. II A, edited by W. P. Mason and R. N. Thurston (Academic Press, 1964), pp. 1–45.

of sound propagation high in the Earth's atmosphere and in the atmospheres other planets in our solar system [5].

## 9.4 Viscosity

The irreversibility in the Navier-Stokes equation (7.34) arises from the term proportional to the shear viscosity,  $\mu \nabla^2 \vec{v}$ . The fundamental difference between a solid and a fluid (liquid or gas) is that shear deformations of a solid are restored elastically (see Sect. 4.2.3), while fluids cannot sustain a state of static shear indefinitely. Figure 9.11 depicts two parallel plates separated by a distance,  $d$ , that are in relative motion at a velocity,  $v_x$ , and contain a viscous fluid in between.

A “no-slip” boundary condition is applied to the viscous fluid at the interface between the fluid and the solid surface. The force,  $F_x$ , per unit area,  $A_y$ , of the plate, is given by the equivalent of Ohm's law for the relevant component of the shear stress,  $\tau_{xy}$ , as a function of the velocity gradient.

$$\tau_{xy} = \frac{F_x}{A_y} = \mu \frac{\partial v_x}{\partial y} \quad (9.25)$$

We can take Eq. (9.25) to be our definition of the *shear viscosity*,  $\mu$ , which has the units of [Pa-s].

This differs slightly from Ohm's law (9.6) and Newton's Law of Cooling (9.7) because the electrical potential difference (voltage) and the temperature difference are both real scalars. Velocity is a vector, so the shear stress,  $\vec{\tau}$ , is a tensor. If the shear viscosity,  $\mu$ , is not a function of the shear rate, then fluids that obey Eq. (9.25) are known as *Newtonian fluids*.<sup>9</sup>

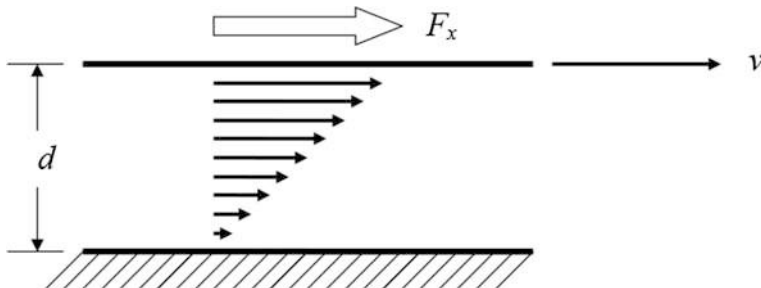


**Fig. 9.11** Two-dimensional representation of a fluid that is being sheared by the relative motion of two parallel plates. The *lower plate* is shown as stationary and the *upper plate* is moving in the  $x$  direction at a uniform speed,  $v_x$ . The outlined arrow ( $\Rightarrow$ ) represents the constant force,  $F_x$ , that is required to overcome the fluid's frictional drag. That force is applied in the  $x$  direction, on the plate with area,  $A_y$ , normal to the  $y$  axis. Due to the non-slip boundary condition at the interface between the viscous fluid and the plates, the velocity of the fluid is the same as that of the plates over the planes where the substrates and fluid are in contact

<sup>9</sup> The entire field of rheology is dedicated to the study of non-Newtonian fluids and plastic flows. Non-drip paints are thixotropic fluids; their viscosities decrease with increasing strain rate. You want a paint that has a low viscosity when it is being applied to reduce drag on the paint brush (and wrist of the painter), but a high viscosity once it is applied to a surface to keep it from dripping. Viscoelastic fluids like Silly Putty™ are also non-Newtonian fluids. A detailed discussion of viscosity and of non-Newtonian flow is provided by R. B. Bird, W. E. Steward, and E. N. Lightfoot, *Transport Phenomena* (J. Wiley & Sons, 1960); ISBN 0-471-07392-X, in Chapter 1.

The shear viscosity,  $\mu$ , is also sometimes called the *dynamic viscosity* or *absolute viscosity* to distinguish it from the *kinematic viscosity*,  $\nu \equiv \mu/\rho$ . We will see in the next sub-section that the kinematic viscosity plays the same role for viscous flow as the thermal diffusivity,  $\alpha$ , plays for heat transfer. Both  $\nu$  and  $\alpha$  are *diffusion constants* and have the SI units of [m<sup>2</sup>/s].

### 9.4.1 Poiseuille Flow in a Pipe of Circular Cross-Section

When one plate moves parallel to a stationary plate, as shown in Fig. 9.11, the velocity of the fluid varies linearly across the gap (as symbolized by the arrows of different length) and the  $y$  component of the gradient of the velocity,  $\nabla_y v_x = \partial v_x / \partial y$ , is a constant. We can calculate the velocity profile for steady-state flow (i.e.,  $\partial v_x / \partial t = 0$ ) in a tube of circular cross-section, with radius,  $a$ , by solving the Navier-Stokes equation (7.34). Due to the cylindrical symmetry of the problem, the  $x$  component of the Navier-Stokes equation for a Newtonian fluid can be expressed in cylindrical coordinates [6]:<sup>10</sup>

$$\begin{aligned} \rho \left( \frac{\partial v_x}{\partial t} + v_r \frac{\partial v_x}{\partial r} + \frac{v_\theta}{r} \frac{\partial v_x}{\partial \theta} + v_x \frac{\partial v_x}{\partial x} \right) = \\ - \frac{\partial p}{\partial x} + \mu \left[ \frac{1}{r} \frac{\partial}{\partial r} \left( r \frac{\partial v_x}{\partial r} \right) + \frac{1}{r^2} \frac{\partial^2 v_x}{\partial \theta^2} + \frac{\partial^2 v_x}{\partial x^2} \right] + \rho g_x \end{aligned} \quad (9.26)$$

Although Eq. (9.26) looks rather intimidating,<sup>11</sup> in most applications many of the terms vanish. In the case of steady-state flow in a pipe, only two terms from Eq. (9.26) survive in Eq. (9.27).

$$\frac{\mu}{r} \frac{\partial}{\partial r} \left( r \frac{\partial v_x}{\partial r} \right) = \frac{\partial p}{\partial x} = \frac{\Delta p}{L} \quad (9.27)$$

The last term on the right-hand side of Eq. (9.27) assumes that the flow is in response to a pressure difference,  $\Delta p$ , in a pipe of length,  $L$ . The equation can be integrated twice to produce an expression for the velocity as a function of radius,  $v_x(r)$ .

$$v_x(r) = \frac{\Delta p}{4\mu L} r^2 + C_1 \ln[r] + C_2 \quad (9.28)$$

$C_1$  and  $C_2$  are constants of integration. Since  $v_x(0)$  must remain finite,  $C_1 = 0$ . (For flow in the annular space between two pipes,  $C_1$  becomes useful for matching the boundary condition at the inner radius.<sup>12</sup>) The constant  $C_2$  is determined from the non-slip boundary condition that requires  $v_x(a) = 0$ .

$$v_x(r) = \frac{\Delta p}{4\mu L} (a^2 - r^2) \quad (9.29)$$

<sup>10</sup> Any book on hydrodynamics or vector calculus will provide expressions for differential vector operators in at least cylindrical and spherical coordinates. Some examples are mentioned in Refs. [2, 3, 6], at the end of in this chapter, as well as most books on engineering mathematics.

<sup>11</sup> There are two more of these for the (radial)  $r$  component and the (azimuthal)  $\theta$  component of Eq. (9.26) that are just as ugly!

<sup>12</sup> See Ref. [6], for solutions in tubes of other cross-sections, in §17, pp. 53–54 for (Problem 1) annular, (Problem 2) elliptical, and (Problem 3) triangular ducts.

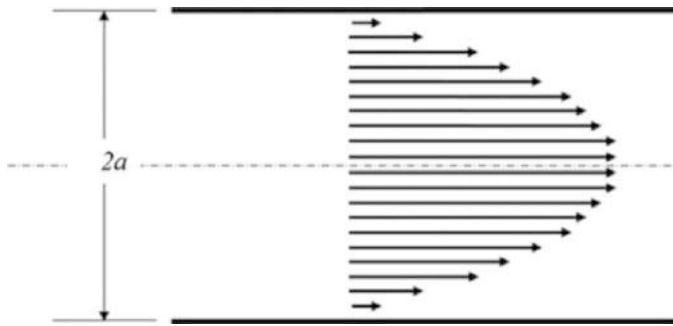


**Fig. 9.12** Schematic representation of the velocity vectors for steady flow through a pipe of cylindrical cross-section with radius,  $a$ . The velocity profile, given in Eq. (9.29), is parabolic. This flow behavior is known as “Poiseuille flow.” (Jean Léonard Marie Poiseuille (1797–1869) was a French physicist and physiologist who first published this result, in 1840, during his investigation of blood flow in narrow capillaries. The CGS unit of viscosity, the poise, was named in his honor.) When looking at this two-dimensional representation, it is important to keep its cylindrical symmetry in mind. Imagine the entire sketch rotated about the dashed centerline

The pipe’s “discharge” (i.e., mass flow,  $\dot{m}$ , or volume velocity,  $U = \dot{m}/\rho$ ) can be calculated by integrating the parabolic velocity profile of Eq. (9.29), shown in Fig. 9.12, over the pipe’s cross-sectional area.

$$\dot{m} = \rho U = 2\pi\rho \int_0^a v_x(r)r \ dr = \frac{\pi\rho a^4}{8\mu} \frac{\Delta p}{L} \quad (9.30)$$

This result, known as *Poiseuille’s formula*, is valid as long as the parabolic profile has been established<sup>13</sup> and the flow velocity in the pipe is slow enough that the flow remains laminar (like Fig. 9.12) and does not become turbulent.<sup>14</sup>

## 9.4.2 The Viscous Boundary Layer

Just as we used a surface with a time-dependent temperature in contact with a stagnant fluid to derive an expression for the thermal penetration depth,  $\delta_\kappa$ , in Eq. (9.14), we can assume transverse oscillations of a solid surface, as shown in Fig. 9.13, to derive an expression for the oscillatory viscous boundary layer.

We will assume that the space-time behavior of the fluid for  $x \geq 0$  is that of a wave traveling to the right,  $v_y(x, t) = \Re e[\hat{v}_y e^{j(\omega t - kx)}]$ . We assume that the fluid is otherwise at rest so there is no mean flow:  $\vec{v}_m = 0$ . Since the transverse motion of the wall does not compress any fluid, the pressure is constant throughout the fluid, allowing us to ignore the  $\vec{\nabla}p$  term in Eq. (9.2).

<sup>13</sup> When flow enters a smaller tube from a larger reservoir, it must travel some distance before the flow becomes “organized” into the parabolic profile shown in Figure 9.12. This distance is known as the “entrance length,”  $L$ , and is usually expressed in terms of the tube’s inner diameter,  $D$ , and the Reynolds number,  $Re$  (see the next footnote):  $L/D \cong 0.06 Re$ .

<sup>14</sup> The criterion for the transition to turbulence in smooth-walled round pipes is usually given in terms of the nondimensional Reynolds number,  $Re = \rho < v > D/\mu$ , where  $< v >$  is the flow velocity averaged over the pipe’s area,  $\pi D^2/4$ . The transition from laminar (Fig. 9.12) to turbulent flow is usually taken to occur at a Reynolds number greater than  $2200 \pm 100$  in circular pipes with a “smooth” surface finish. Further details regarding the transition to turbulence are given in most fluid dynamics textbooks, such as Refs. [2, 3, 6], and presented as a “Moody chart,” where the nondimensional drag is plotted vs. Reynolds number for various values of surface roughness.

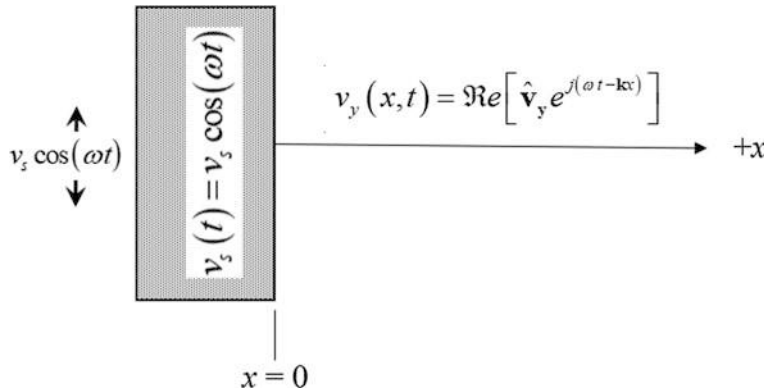


**Fig. 9.13** A semi-infinite solid surface oscillates in the  $y$  direction with a transverse oscillatory velocity,  $v_s \cos(\omega t)$ . The surface is in contact with a fluid along the  $x = 0$  plane. At that interface, the fluid moves with the same velocity as the solid due to the non-slip boundary condition at  $x = 0$ . Since there is only fluid at  $x \geq 0$ , we will assume a right-going wavelike space and time dependence for the oscillating component of the fluid velocity,  $v_y(x, t)$ , as we did for temperature oscillations in Fig. 9.6

$$\rho \frac{\partial v_y(x, t)}{\partial t} = \mu \nabla^2 v_y(x, t) \quad (9.31)$$

We can substitute the wavelike expression into the two remaining terms in this one-dimensional version of the linearized Navier-Stokes equation to again obtain the required relationship between  $\omega$  and  $\mathbf{k}$ :

$$j\omega \hat{v}_y = -\frac{\mu}{\rho} \mathbf{k}^2 \hat{v}_y = -\nu \mathbf{k}^2 \hat{v}_y \quad (9.32)$$

We have again utilized  $\nu$ , called the kinematic viscosity, which has the units of [ $\text{m}^2/\text{s}$ ], just like the thermal diffusivity,  $\alpha$ , which was introduced in Eq. (9.11). As before, we have solved Eq. (9.31) for the complex wavenumber,  $\mathbf{k}$ , and introduce a *viscous penetration depth*,  $\delta_\nu$ , to characterize the shear wave within the fluid.

$$\mathbf{k} = \sqrt{\frac{-j\omega}{\nu}} = \frac{1-j}{\sqrt{2}} \sqrt{\frac{\omega}{\nu}} = (1-j) \sqrt{\frac{\omega}{2\nu}} \equiv \frac{1-j}{\delta_\nu} \quad \Rightarrow \quad \delta_\nu = \sqrt{\frac{2\mu}{\rho\omega}} = \sqrt{\frac{2\nu}{\omega}} \quad (9.33)$$

From this point on, the results for  $v_y(x, t)$  in the viscous fluid are identical to those already presented for  $T_1(x, t)$ .<sup>15</sup> Figure 9.7 would describe the velocity field in front of the transversely oscillating boundary of Fig. 9.13 if the  $x$  axis were scaled by  $\delta_\nu$  instead of by  $\delta_\kappa$ . Similarly, if the boundary were stationary and the fluid far from the boundary were moving with an oscillatory velocity amplitude,  $v_y$ , then Fig. 9.8 would describe the motion of the fluid if the  $x$  axis were scaled by  $\delta_\nu$  instead of  $\delta_\kappa$ .<sup>16</sup>

<sup>15</sup> Mathematicians would call the Fourier Heat Diffusion equation (9.11) and the Navier-Stokes equation (9.2) “isomorphic.” The fact that  $T$  is the variable in Eq. (9.11) and  $v_y$  is the variable in Eq. (9.31) only bores most mathematicians. The forms of the solutions to both equations must be identical.

<sup>16</sup> For an animated visualization of the fluid in the oscillatory viscous boundary layer, we can again turn to the Los Alamos Thermoacoustics Home Page and run OSCWALL.EXE to see exactly the situation (rotated by 90°) that is diagrammed in Fig. 9.13. The reverse case of a stationary wall and fluid moving uniformly far from the wall is animated in VISCOUS.EXE. In that animation, a vibrating piston sets up the fundamental  $\lambda/2 = L$  standing wave in a tube and then focuses in on a portion of the resonator’s wall at the velocity anti-node near the center of the tube.

The solutions would be identical for Maxwell's equations governing the electric field,  $\vec{E}$ , due to an electromagnetic wave impinging on an electrically conducting medium.

$$\frac{\partial \vec{E}}{\partial t} = \frac{1}{\sigma\mu} \nabla^2 \vec{E} \quad (9.34)$$

In that case,  $\delta = (2/\sigma\mu\omega)^{1/2}$  is known as the electromagnetic “skin depth.” Here  $\mu$  is the magnetic permeability (not viscosity), and  $\sigma$  is the same electrical conductivity as introduced earlier in Ohm's law (9.6).

### 9.4.3 Viscous Drag in the Neck of a Helmholtz Resonator

We now return once again to the example of our 500 ml flask in Fig. 8.16 and calculate the effects of viscosity on the flow through the neck of our Helmholtz resonator. From Fig. 9.9, we see that the viscous penetration depth for that example is  $\delta_\nu = 141.9 \mu\text{m}$ . Since the radius of the neck,  $a = D_{\text{neck}}/2 = 12.5 \text{ mm}$ , the ratio,  $\delta_\nu/a = 0.0114 \ll 1$ , so the effect of the non-slip boundary condition at the stationary neck surface does not extend very far into the air that fills the neck. In that limit, we describe the motion of the fluid in the neck as *plug flow* that is diagrammed schematically in Fig. 9.14.

The relevant component of the shear stress on the surface of the neck,  $\tau_{xy}$ , is determined by Eq. (9.25). In this case, the fluid near the neck's axis is moving with speed,  $v_x$ , in the axial direction, and the fluid in contact with the neck must be stationary to satisfy the non-slip boundary condition. Since  $|k\mathbf{l}| \propto |1/\delta_\nu|$ , it is easy to evaluate the velocity gradient,  $\partial v_x / \partial y \propto v_x / \delta_\nu$ , where  $v_x$  is the peak fluid velocity in the neck far from surface of the neck and  $y$  is the radial direction normal to the surface of the neck.

$$\tau_{xy} = \frac{F_x}{A_y} = \mu \frac{\partial v_x(y, t)}{\partial y} = \mu \frac{|\hat{\mathbf{v}}_x|}{\delta_\nu} \propto \mu \frac{v_x}{\delta_\nu} \quad (9.35)$$

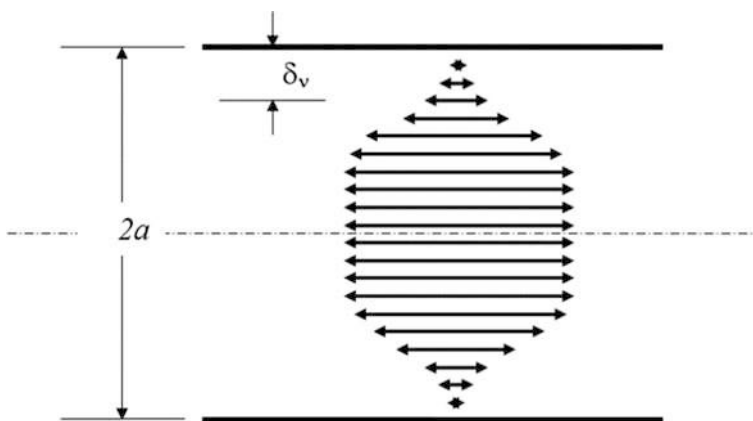


**Fig. 9.14** Schematic representation of oscillatory “plug flow” in the cylindrical neck of a Helmholtz resonator with radius,  $a \gg \delta_\nu$ . In the region far from the walls, the velocity is independent of the radial distance from the central axis of the neck. The velocity decays exponentially over a characteristic exponential distance,  $\delta_\nu$ , to zero at the walls where it must vanish to satisfy the non-slip boundary condition for a viscous fluid. When looking at this drawing, it is important to keep the cylindrical symmetry in mind. Imagine the entire sketch rotated about the dashed centerline

In this application,  $A_y$  is the surface area on the inside of the neck. The wall and the fluid are in relative motion since the wall is stationary and the fluid is oscillating. Since the physical neck length,  $L = 49.2$  mm, and the diameter,  $D_{neck} = 25.0$  mm,  $A_y = \pi D_{neck} L = 3.864 \times 10^{-3}$  m<sup>2</sup>. The time-averaged power dissipated,  $\langle \Pi_{vis} \rangle_t$ , per unit area by the viscous shear stress,  $\dot{e}_{vis} = \langle \Pi_{vis} \rangle_t / A_y$ , is one-half the time average of the product of the peak stress,  $\tau_{xy}$ , times the peak velocity,  $v_x$ , where  $T = f^{-1}$  is the period.

$$\dot{e}_{vis} = \frac{\langle \Pi_{vis} \rangle_t}{A_y} = \frac{1}{T} \int_0^T [\tau_{xy} \cdot v_x(t)] dt \propto \frac{\mu}{T} \int_0^T \frac{v_x^2(t)}{\delta_\nu} dt \quad (9.36)$$

The oscillatory flow velocity,  $v_x(r, t)$ , through the neck of the resonator is uniform (except in the thin viscous boundary layer). The sinusoidal time dependence of the velocity can be represented as  $v_x(t) = v_x \cos(\omega t)$ .

$$\dot{e}_{vis} = \frac{\langle \Pi_{vis} \rangle_t}{A_y} \propto \frac{\mu}{2} \frac{v_x^2}{\delta_\nu} = \frac{\rho_m}{4} \left| \frac{\hat{\mathbf{U}}}{A_y} \right|^2 \delta_\nu \omega \quad (9.37)$$

The far right expression for  $\dot{e}_{vis}$  is obtained by using the definition of the viscous penetration depth in Eq. (9.33) to substitute for the shear viscosity,  $\mu = (\delta_\nu^2 \rho_m \omega)/2$ , and by letting  $\langle v_x \rangle = |U_I|/A$ . As with any dissipative mechanism, like Joule heating in Eq. (9.5),  $\dot{e}_{vis}$  is positive-definite and independent of the sign (direction) of  $v_x$  or  $U$ .

Although the result for  $\dot{e}_{vis}$  in Eq. (9.37) is correct, the use of proportionalities instead of equalities was motivated by the fact that the actual expression for the viscous stress tensor is not the one provided in Eq. (9.35) but a complex phasor,  $\hat{\boldsymbol{\tau}}_{xy}$ , that lags  $\hat{\mathbf{v}}$  by 45° in time.<sup>17</sup>

$$|\hat{\boldsymbol{\tau}}_{xy}| = \frac{\sqrt{2}\mu v_x}{\delta_\nu} e^{-y/\delta_\nu} \quad (9.38)$$

By examining the DELTAEC model of the 500 ml flask shown in Fig. 8.27, we can calculate the average value of  $\langle v_x \rangle = |U_I|/A$  based on input (2a), the cross-sectional area of the neck,  $A = 4.909 \times 10^{-4}$  m<sup>2</sup>. The volume velocity entering the neck is given in Segment #0, where (0f) gives  $|U_I| = 4.0777 \times 10^{-4}$  m<sup>3</sup>/s at the open end of the neck. The volume velocity leaving the neck and entering the compliance is given in Segment #1, where result (1C) gives  $|U_I| = 3.9806 \times 10^{-4}$  m<sup>3</sup>/s for an average volume velocity  $\langle U_I \rangle = 4.0292 \times 10^{-4}$  m<sup>3</sup>/s, so  $\langle v_x \rangle = |U_I|/A = 0.8208$  m/s. Using the viscosity from Fig. 9.9,  $\mu = 1.835 \times 10^{-5}$  Pa-s, and  $\delta_\nu = 141.9$  μm, Eq. (9.37) yields an average viscous power dissipation per unit area of  $\dot{e}_{vis} = \langle \Pi_{vis} \rangle_t / A = 42.0$  mW/m<sup>2</sup>.

The surface area of the neck  $A_y = \pi D_{neck} L = 3.86 \times 10^{-3}$  m<sup>2</sup>, so the time-averaged power dissipated in the neck due to viscous drag in the oscillatory boundary layer  $\langle \Pi_{vis} \rangle_t = \dot{e}_{vis}(\pi D_{neck} L) = 167.4$  μW. This is quite close to the value in the DELTAEC model that provides for the dissipation in the neck (1E)-(1F) = 174 μW. The small discrepancy (about 3.7%) arises from the fact that we took an average of the flow velocity that was not weighted (i.e., integrated) to accommodate the  $v_x^2$  dependence of  $\dot{e}_{vis}$  in Eq. (9.37). DELTAEC is correct. Using the same results from the DELTAEC model of Fig. 8.27, to calculate the average of the squared velocity,  $\langle v_x^2 \rangle = 0.6818$  m<sup>2</sup>/s<sup>2</sup>, so  $\langle \Pi_{vis} \rangle_t = \dot{e}_{vis}(\pi D_{neck} L) = 170.2$  μW. This result is even closer to the correct DELTAEC result. We

<sup>17</sup> A more rigorous general derivation of the viscous boundary layer dissipation and of the acoustic power is provided by Swift in his textbook, *Thermoacoustics* [10]. See §4.4.2 and Chap. 5.

have avoided evaluation of any integrals, but in the process have developed a fundamental understanding of dissipation in the viscous boundary layer.

Although we have not derived the corresponding power dissipation per unit area due to thermal conduction,  $\dot{e}_{th}$ , the strategy was presented in Sect. 9.3.3 and is illustrated in the THERMAL.EXE animation.<sup>18</sup>

$$\dot{e} = \dot{e}_{vis} + \dot{e}_{th} = -\frac{\rho_m}{4} \left| \frac{\widehat{\mathbf{U}}}{A} \right|^2 \delta_\nu \omega - \frac{(\gamma - 1)}{4\gamma} \frac{|\widehat{\mathbf{p}}|^2}{p_m} \delta_\kappa \omega \quad (9.39)$$

The second term in Eq. (9.39) can be applied to the 500 ml Helmholtz resonator of Fig. 8.16 to calculate the power dissipated by the irreversible thermal conduction between the (isothermal) walls of the compliance and the gas undergoing adiabatic expansions and compressions far from the walls.

Using Fig. 8.27, the DELTAEC result (2A) = (3A) gives  $|p_{cav}| = 74.355$  Pa. Figure 9.9 provides the air's thermal conductivity,  $\kappa = 2.59 \times 10^{-2}$  W/K-m, and the thermal penetration depth,  $\delta_\kappa = 168.6$  μm, resulting in  $\dot{e}_{th} = 9.98$  mW/m<sup>2</sup>. The surface area of the spherical compliance is input (2a):  $A_{sphere} = 2.9974 \times 10^{-2}$  m<sup>2</sup>. The product gives the time-averaged power dissipated in on the surface of the spherical volume due to thermal relaxation loss in the oscillatory boundary layer  $\langle \Pi_{th} \rangle_t = \dot{e}_{th} A_{sphere} = 29.91$  μW. This is exactly the value that the DELTAEC model provides as (1F)-(2F) = 29.92 μW.

#### 9.4.4 Quality Factors for a Helmholtz Resonator

Having expressions for thermoviscous boundary layer dissipation, we can calculate the quality factor,  $Q$ , of the Helmholtz resonator shown in Fig. 8.16.  $Q$  is a dimensionless measure of the sharpness of the resonance (see Appendix B). Without dissipation,  $Q = \infty$ , as seen in Eq. (8.52). Based on the DELTAEC model in Fig. 8.28 and Eq. (C.1), the  $Q = |p_{cav}|/p_l$  result (3A)/input (0d) = 74.355.

Figure 8.32 displays the incremental plot file, \*.ip, for the same resonator providing that amplitude and phase of  $p_{cav}(f)$ . We can approximate the derivative of the phase with respect to frequency at resonance by fitting the three phases (the one closest to resonance and the two above and below it) vs. frequency for an approximate value of  $(\partial\theta/\partial f)_{f_o} \cong 34.6^\circ/\text{Hz}$ . Substitution into Eq. (B.4) gives  $Q \cong 73.6$ . Running DELTAEC over a finer frequency step size around  $f_o$  should produce a slightly greater value for the slope of the phase vs. frequency.

It will be instructive to calculate the  $Q$  for both the viscous and thermal losses individually since the final results will be simple and rather intuitively satisfying. To begin, recall the definition of  $Q$  based on the ratio of the energy stored in the system,  $E_{stored}$ , to the energy dissipated in one cycle,  $E_{dissipated/cycle} = \langle \Pi_{dis} \rangle_t T = \langle \Pi_{dis} \rangle_t / f$ . From Eq. (B.2),

$$Q = 2\pi \frac{E_{stored}}{E_{dissipated/cycle}} = \frac{\omega E_{stored}}{\langle \Pi_{dissipated} \rangle_t} \quad (9.40)$$

For our Helmholtz resonator, the quality factors for each dissipative process will be calculated individually. Since the energy dissipation is additive, the total quality factor,  $Q_{tot}$ , will be the reciprocal of the sum of the reciprocals of the quality factors for the viscous dissipation,  $Q_{vis}$ , for thermal

<sup>18</sup> A derivation of Eq. (9.39) is provided in G. W. Swift, *Thermoacoustics: A unifying perspective for some engines and refrigerators*, 2nd ed. (Acoust. Soc. Am., 2017); ISBN 978-3-319-66932-8, Chapter 5.1.

conduction,  $Q_{th}$ , and for radiation of sound,  $Q_{rad}$  (actually, an “accounting loss” as discussed in Sect. 3.7 for a string).

$$\frac{1}{Q_{tot}} = \frac{1}{Q_{vis}} + \frac{1}{Q_{th}} + \frac{1}{Q_{rad}} \quad (9.41)$$

Like any single-degree-of-freedom simple harmonic oscillator, the stored energy oscillates between its kinetic and potential forms with the sum being constant at steady state. As in Eq. (2.18), the maximum kinetic energy,  $(KE)_{max}$ , can be used to represent the value of the stored energy. For the Helmholtz resonator, the kinetic energy is determined by the velocity of the fluid in the resonator’s neck, with cross-sectional area,  $A = \pi a^2$ . Because the viscous penetration depth is much less than the radius of the neck,  $\delta_\nu \ll a$ , we will assume “plug flow,” as shown schematically in Fig. 9.14, and approximate the moving mass of the gas in the neck of our Helmholtz resonator to be all of the mass,  $m$ , of the gas within the neck, as was done in Sect. 8.4.4.

$$m = \rho_m A L_{neck} = \rho_m (\pi a^2) L_{neck} \quad (9.42)$$

Just as the thin viscous boundary layer was neglected in the calculation of the moving mass, the gas velocity,  $v_I = |U_I|/A_{neck}$ , will be assumed to be independent of the radial distance from the neck’s center line (i.e., plug flow).

$$E_{stored} = (KE)_{max} = \frac{1}{2} m v_I^2 = \frac{\rho_m A_{neck} L_{neck}}{2} \left| \frac{\hat{\mathbf{U}}}{\pi a^2} \right|^2 \quad (9.43)$$

Since our results will be compared to the DELTAEC model of the 500 ml flask in Fig. 8.27, we will neglect the kinetic energy of the gas beyond the ends of the neck that produced the effective length correction necessary to match the theoretically calculated and experimentally determined resonance frequencies.

To calculate the energy dissipated by viscous shear on the surface of the neck of the resonator having surface area,  $A_{neck} = 2\pi a L_{neck}$ , and cross-sectional area,  $\pi a^2$ , the power dissipation per unit area,  $\dot{e}_{vis}$ , given in Eq. (9.37), will be used.

$$E_{dis/cycle} = \frac{\dot{e}_{vis} A_{neck}}{f_o} = \frac{\rho_m}{4 f_o} \left| \frac{\hat{\mathbf{U}}}{\pi a^2} \right|^2 \delta_\nu \omega_o A_{neck} = \frac{\pi}{2} \left| \frac{\hat{\mathbf{U}}}{\pi a^2} \right|^2 \rho_m \delta_\nu 2\pi a L_{neck} \quad (9.44)$$

When we take the ratio of Eq. (9.43) to Eq. (9.44) to calculate  $Q$ , using Eq. (9.40), the amplitude of the oscillation squared, proportional to  $|U_I/A_{neck}|^2$ , will cancel. This must be the case, since we are considering a linear system and linearity demands that the quality factor must be amplitude independent.

$$Q_{vis} = 2\pi \frac{E_{stored}}{E_{dis/cycle}} = 2\pi \frac{(\rho_m \pi a^2 L_{neck})/2}{(\pi/2) \delta_\nu 2\pi a L_{neck}} = \frac{2\pi a^2 L_{neck}}{\delta_\nu 2\pi a L_{neck}} = \frac{a}{\delta_\nu} \quad (9.45)$$

This is a wonderfully simple and intuitively satisfying result:  $Q_{vis} = a/\delta_\nu$ . The quality factor due to viscous dissipation at the surface of the neck of a Helmholtz resonator is simply the dimensionless ratio of the neck’s radius to the viscous penetration depth in the gas.

A numerical calculation for  $Q_{vis}$  in a cylindrical duct involves the integration of the flow field using a  $J_o$  Bessel function with a complex argument,  $(j-1)r/\delta_\nu$ , to represent the velocity, resulting in an approximation that is valid to within 0.3% for  $a/\delta_\nu > 3$  [7].

$$Q_{vis} \cong \frac{a}{\delta_\nu} + \frac{\delta_\nu}{5a} - \frac{3}{4} \quad \text{for } \frac{a}{\delta_\nu} \geq 3 \quad (9.46)$$

The same approach can be used to calculate the quality factor for thermal dissipation on the surface of the Helmholtz resonator's volume (i.e., compliance). Since the amplitude of the pressure oscillations within the volume is proportional to  $p_J$ , as shown in Eq. (9.39), it will be convenient to convert  $|U_J/\pi a^2|$  in Eq. (9.43) to a pressure amplitude, since the quality factor for thermal losses,  $Q_{th}$ , must also be amplitude independent in the linear acoustics limit. From Eq. (8.25), the adiabatic compliance of a volume,  $V$ , can be used to relate pressure amplitude,  $|\hat{\mathbf{p}}|$ , to the volume velocity amplitude,  $|\hat{\mathbf{U}}|$ .

$$\hat{\mathbf{p}} = \frac{1}{j\omega} \frac{\gamma p_m}{V} \hat{\mathbf{U}} \quad \Rightarrow \quad E_{stored} = (KE)_{max} = \frac{\rho_m L_{neck}}{2A_{neck}} \frac{\omega_o^2 V^2}{\gamma^2} \frac{|\hat{\mathbf{p}}|^2}{p_m^2} \quad (9.47)$$

Substitution of  $\dot{e}_{th}$  from Eq. (9.39), times the surface area of the spherical compliance,  $S_{Vol} = 4\pi R^2$ , into Eq. (9.40) produces the expression for the thermal contribution to the quality factor,  $Q_{th}$ .

$$Q_{th} = \frac{2\pi \frac{\rho_m L_{neck}}{2A_{neck}} \frac{\omega_o^2 V^2}{\gamma^2} \frac{|\hat{\mathbf{p}}|^2}{p_m^2}}{\frac{(\gamma - 1)}{4\gamma f_o} \frac{|\hat{\mathbf{p}}|^2}{p_m} S_{Vol} \delta_\kappa \omega_o} = \left[ \omega_o^2 \frac{\rho_m}{\gamma p_m} \frac{L_{neck} V}{A_{neck}} \right] \frac{2(4\pi/3)R^3}{(\gamma - 1)\delta_\kappa 4\pi R^2} \quad (9.48)$$

The Helmholtz resonance frequency,  $\omega_o$ , is given in Eq. (8.51), and  $c^2 = \gamma p_m / \rho_m$ , so the term in Eq. (9.48) contained within the square brackets is just unity, proving again that “substitution is the most powerful technique in mathematics” (see Sect. 1.1).

$$Q_{th} = \frac{2}{3(\gamma - 1)} \frac{R}{\delta_\kappa} \quad (9.49)$$

As expected, the thermal quality factor becomes infinite (i.e., lossless) if the expansions and compressions of the gas within the entire volume of the Helmholtz resonator are isothermal,  $\gamma_{iso} = 1$ . We also see again that the quality factor is proportional to the ratio of a length characterizing the size of the spherical volume,  $R$ , and the thermal penetration depth,  $\delta_\kappa$ .

The results for  $Q_{vis}$  in Eq. (9.45) and  $Q_{th}$  in Eq. (9.49) can be used to estimate the quality factor for the 500 ml boiling flask example that was used to create the DELTAEC file in Fig. 8.27, using the penetration depths at  $f_o = 241.73$  Hz, provided in Fig. 9.9, when combined as shown in Eq. (9.41). This results in a  $Q_{vis} = 88$ , and a  $Q_{th} = 482$ , for  $Q_{tot} = 74.4$ . The DELTAEC model also gives  $Q = 74.4$ .

Although the time-averaged radiated power,  $\langle \Pi_{rad} \rangle_t$ , will not be derived until Chap. 12 (see Eq. 12.18), it was mentioned in Footnote 24 in Chap. 8.

$$\langle \Pi_{rad} \rangle_t = \pi \frac{\rho_m f_o^2}{2c} |\hat{\mathbf{U}}|^2 \quad (9.50)$$

The dependence upon  $|U_J|^2$  means that it is easy to calculate a contribution to the quality factor from the radiation “loss” using Eq. (9.43) to express the stored energy.

$$Q_{rad} = 2\pi \frac{\frac{\rho_m \pi a^2 L_{neck}}{2} \left| \frac{\hat{\mathbf{U}}}{\pi a^2} \right|^2}{\pi \frac{\rho_m f_o}{2c} |\hat{\mathbf{U}}|^2} = 2 \frac{(\lambda L_{neck})}{\pi a^2} \quad (9.51)$$

The expression on the far right in Eq. (9.51) uses  $c = \lambda f$  to express the quality factor as proportional to the ratio of two areas. For the 500 ml flask DELTAEC model in Fig. 8.27, where  $\lambda = 1.426$  m at resonance,  $Q_{rad} = 286$ . This is more than three times greater than  $Q_{vis}$ , reinforcing the earlier result from the DELTAEC model that showed that viscous loss in the neck was the dominant loss mechanism in that example.

## 9.5 Kinetic Theory of Thermal and Viscous Transport

Thus far, in this chapter, we have taken a phenomenological approach to describe the dissipation caused by thermal conduction and viscous shear. Those mechanisms have been characterized by diffusion equations that introduced two phenomenological constants: the thermal conductivity,  $\kappa$ , and the shear viscosity,  $\mu$ . Those constants are properties of the fluid that might depend upon pressure and/or temperature. By introducing a simple microscopic model for these diffusive processes, we can gain additional insight into the relationship between these constants and the microscopic properties of ideal gases.

The same microscopic model that was used in Chap. 7 to derive the Ideal Gas Law and to introduce the mean squared particle velocity and the Equipartition Theorem in Eq. (7.2) can be resurrected to calculate  $\kappa$  and  $\mu$  for an ideal gas by adding the concept of a mean free path,  $\bar{l}$ , characterizing an average distance that an atom or molecule in a gas will travel before colliding with another of its own kind.<sup>19</sup>

For the following calculations, we assume that the gas is “dilute” [8]. This means that we will assume that each particle spends a relatively large fraction of its time at distances far from other particles so that the time between collisions is much greater than the time involved in a collision. We also assume that the probability of a simultaneous collision between more than two particles can be neglected. Finally, we assume de Broglie wavelength,  $\lambda_B = h/mv$ , for the particles with momentum,  $mv$ , is much shorter than the separation between particles so quantum-mechanical effects can be ignored:  $\lambda_B \ll \bar{l}$ .

### 9.5.1 Mean Free Path

If we assume that our “point particles” have a mass,  $m$ , and an effective hard sphere diameter,  $D$ , then two identical particles in the gas will collide if their centers are separated by a distance that is less than or equal to  $D$ . We focus our attention on a single particle that is moving with a mean velocity,  $\bar{v}'$ , determined by the Equipartition Theorem, as applied in Eq. (7.26),  $\langle v^2 \rangle^{1/2} \equiv \bar{v}' = \sqrt{3k_B T/m}$ . This mean thermal velocity is designated  $\bar{v}'$  to remind us that we have assumed that all other particles are not moving. Assuming (temporarily) that all other particles are stationary, then the moving particle sweeps out a cylindrical volume,  $V_{Swept} = \pi D^2 \bar{v}' t$ , in a time,  $t$ .

The number of (stationary) particles within that swept volume depends upon the (number) density of the gas,  $n = \rho/m$ , where  $m$  is the mass of an individual particle. During the time interval,  $t$ , there will be  $W = nV_{Swept}$  stationary gas particles within that cylinder. The collision rate,  $\dot{n} = (W/t) = \pi D^2 \bar{v}' n$ . The *mean free path*,  $\bar{l}$ , is the distance the particle travels between collisions that take place, on average, every  $\bar{\tau} = \dot{n}^{-1}$  seconds.

<sup>19</sup> A more detailed and systematic discussion of these concepts is given by E. H. Kennard in his classic textbook, *Kinetic Theory of Gases with an Introduction to Statistical Mechanics* (McGraw-Hill, 1938).

Of course, all the other particles are not stationary but are moving with the same mean (thermal) velocity,  $\bar{v}'$ , so the actual velocity that we need in our expression for the mean free path is the mean relative particle velocity,  $v_{rel} \equiv \bar{v}$ . If two particles are traveling in exactly the same direction, their mean relative velocity would be zero. If they are moving directly toward each other, their mean relative velocity would be  $2\bar{v}'$ . Integration over all possible directions could determine the average relative velocity, but it is easier to utilize the “reduced mass,”  $\mu = m_1m_2/(m_1 + m_2)$ , to determine mean relative velocity. Placing the reduced mass into the Equipartition Theorem produces the mean relative velocity in the same way the reduced mass was used to determine the antisymmetric frequency of two otherwise free particles that were joined by a spring, as discussed in Sect. 4.3.1, then applied to the Tonpilz transducer.

Since the particles are assumed to be identical,  $\mu = m/2$ , so the value of the relative velocities of the particles,  $\bar{v}_{rel}$ , is given by the Equipartition Theorem.

$$\langle v_{rel}^2 \rangle^{1/2} \equiv \bar{v} = (3k_B T / \mu)^{1/2} = (6k_B T / m)^{1/2} = \bar{v}' \sqrt{2} \quad (9.52)$$

That result can be used to calculate the mean free path as introduced when we initially assumed that the other particles were stationary.

$$\bar{\ell} = \frac{\bar{v}}{\pi D^2 \bar{v}' n} = \frac{1}{\pi \sqrt{2} D^2 n} \quad (9.53)$$

It is useful to recognize that the mean free path is independent of  $\bar{v}$  or  $\bar{v}'$  and therefore independent of temperature. At higher temperatures, the particles are moving faster, but  $V_{Swept}$  is correspondingly larger.

Near room temperature, for air at atmospheric pressure, the number density can be calculated from the Ideal Gas Law or from the molar volume and Avogadro’s number:  $n = \rho/m = p_m/k_B T \cong 2.5 \times 10^{25}$  particles/m<sup>3</sup>  $\cong N_A/(22.4 \times 10^{-3} \text{ m}^3)$ . For air, a typical molecular diameter,  $D_{air} \cong 2 \times 10^{-10} \text{ m} = 2 \text{ \AA}$ , so  $\pi D^2 \cong 1.3 \times 10^{-19} \text{ m}^2$ , making  $\bar{\ell} \cong 2.2 \times 10^{-7} \text{ m} = 0.22 \text{ microns}$ . Using the same values, the time between collisions is  $\bar{\ell}/\bar{v} \cong 6 \times 10^{-10} \text{ seconds}$ , or the collision rate,  $\dot{n}$ , is  $2 \times 10^9/\text{second} = 2 \text{ GHz}$ . Each molecule of air at atmospheric pressure and room temperature experiences about two billion collisions each second.

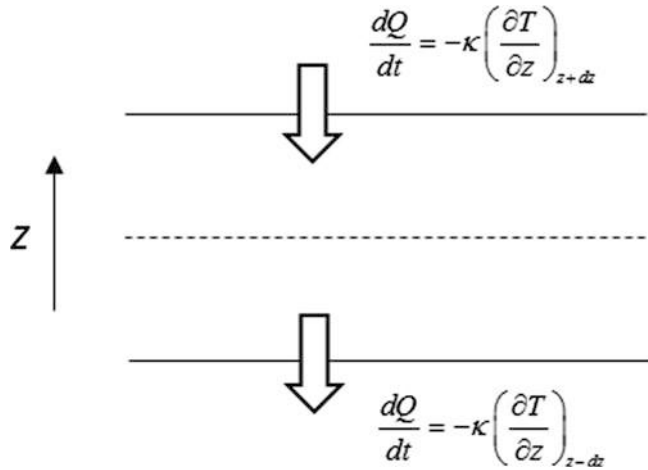
### 9.5.2 Thermal Conductivity of an Ideal Gas

With our understanding of the mean free path, we are now able to determine a value of the thermal conductivity of an ideal gas from the microscopic model. If we assume a linear temperature gradient in a gas, then the thermal energy that is transported by a gas particle will be based on the temperature that particle had at the position where it suffered its last collision. Figure 9.15 provides a suitable geometry for such a calculation by assuming that the temperature gradient,  $\partial T/\partial z \neq 0$ , exists in the  $z$  direction.

The number of particles crossing a unit area per unit time (i.e., the particle flux) in the  $z$  direction is determined by the particle density,  $n$ , and the mean particle velocity,  $\bar{v}'$ . If there are  $n$  particles per unit volume, roughly one-third of them have velocities in the  $z$  direction and half of those, or  $n/6$  particles per unit volume, have mean velocities in the  $(-z)$  direction.

Particles which cross the dashed line in Fig. 9.15 from below have, on average, experienced the last collision at a distance,  $\bar{\ell}$ , below that plane. But the mean energy per particle,  $\bar{e}$ , is a function of  $T$  and,

**Fig. 9.15** Coordinate system for the calculation of the thermal conductivity,  $\kappa$ , of an ideal gas. The heat flux, represented by the arrows, is determined by number of particles crossing the line per unit time and the temperature of the particles that was determined by the last collision they suffered before crossing the line



since  $T = T(z)$ , the mean energy is also a function of  $z$ ,  $\bar{e}(z)$ . The particles crossing from below carry with them a mean energy,  $\bar{e}(z - \bar{\ell})$ , and the ones above experienced the last collision at a distance,  $\bar{\ell}$ , above that plane,  $\bar{e}(z + \bar{\ell})$ . Each “free particle,” which has three degrees of freedom, carries an average kinetic energy of  $\bar{e} = 3k_B T/2$ , corresponding to a heat capacity of  $3k_B/2$  per particle (see Sect. 7.2.1).

$$\left(\frac{\partial Q}{\partial t}\right)_{above} = \frac{1}{6} n \bar{v}' \bar{e}(z + \bar{\ell}) = \left(\frac{n \bar{v}'}{6}\right) \left[ \frac{3k_B}{2} \left( T + \bar{\ell} \frac{\partial T}{\partial z} \right) \right] \quad (9.54)$$

Similarly, the heat flux going in the opposite direction from below,  $\dot{q}_{below}$ , is determined by the last collision that took place at a slightly lower temperature.

$$\left(\frac{\partial Q}{\partial t}\right)_{below} = \frac{1}{6} n \bar{v}' \bar{e}(z - \bar{\ell}) = \left(\frac{n \bar{v}'}{6}\right) \left[ \frac{3k_B}{2} \left( T - \bar{\ell} \frac{\partial T}{\partial z} \right) \right] \quad (9.55)$$

The net energy flux,  $\dot{q}_{net}$ , from hot to cold, is given by the difference of the fluxes calculated in Eqs. (9.54) and (9.55).

$$\left(\frac{\partial Q}{\partial t}\right)_{net} = \left(\frac{\partial Q}{\partial t}\right)_{below} - \left(\frac{\partial Q}{\partial t}\right)_{above} = -\left(\frac{n \bar{v}' \bar{\ell} k_B}{2}\right) \frac{\partial T}{\partial z} \quad (9.56)$$

As indicated in Fig. 9.15, the thermal conductivity of a gas,  $\kappa_{gas}$ , can be expressed in terms of the result in Eq. (9.56).

$$\frac{\partial Q}{\partial t} = -\kappa \frac{\partial T}{\partial z} \Rightarrow \kappa_{gas} = \frac{1}{2} n \bar{v}' \bar{\ell} k_B \quad (9.57)$$

A more rigorous kinetic theory for thermal conductivity of inert gases at low pressures was developed by Chapman in England and Enskog in Sweden. Their approach calculates the numerical pre-factor in Eq. (9.57) to be 0.37, rather than 0.5, since the particles that are not going straight up or down along the  $z$  direction experienced their last collision at a distance less than  $\bar{\ell}$  [9]. Their calculations also describe the thermal conductivity of polyatomic molecules quite accurately.

Using the Equipartition Theorem to let  $\langle v^2 \rangle^{1/2} \equiv \bar{v}' = \sqrt{3k_B T/m}$  provides a microscopic expression for the thermal conductivity of an ideal gas,  $\kappa_{gas}$ .

$$\kappa_{\text{gas}} = 0.37 \frac{n k_B \bar{v}'}{\pi \sqrt{2} D^2 n} = 0.37 \frac{k_B}{2\pi D^2} \sqrt{\frac{3k_B T}{m}} \simeq \frac{0.1}{D^2} \frac{k_B^{3/2}}{m^{1/2}} \sqrt{T} \quad (9.58)$$

Our application of a microscopic model, based on the collision of hard spheres, demonstrates that the thermal conductivity of an ideal gas is independent of the pressure or density of the gas (at least as long as the dimensions of the system are much larger than the mean free path) for most gases at pressures below 1 MPa and is inversely proportional to the square root of the particle's mass and inversely proportional to the particle's cross-sectional area.

The model also predicts that the thermal conductivity will be proportional to the square root of the absolute temperature,  $\sqrt{T}$ . For real gases, the observed temperature dependence of the thermal conductivity of ideal gases is closer to  $T^{0.7}$  [10], due to the fact that the gas particles are not "hard spheres" but interact through a molecular force field like the Lennard-Jones potential shown in Fig. 2.39.

### 9.5.3 Viscosity of an Ideal Gas

A microscopic determination of the viscosity can be obtained in exactly the same way using the momentum transported by a particle of mass,  $m$ , across a plane. We can use an approach similar to that expressed in the geometry of Fig. 9.15. As before, we assume that the density of the gas is sufficiently low that the mean free path is much greater than the particle diameter but much less than the typical dimensions of the system (e.g., the spacing between the moving plates in Fig. 9.11 or the diameter of the tube in Figs. 9.12 and 9.14).

The mean shear velocity,  $v_x$ , is again determined by the last collision the particle suffered prior to crossing the plane from above or from below, and the momentum in the  $x$  direction transported by each particle is  $mv_x$ . The particle density can be used to calculate the momentum transported per unit area, per unit time,  $P$ .

$$P_{\text{above}} = \frac{n \bar{v} m}{6} \left[ v_x + \frac{\partial v_x}{\partial z} \bar{\ell} \right] \quad \text{and} \quad P_{\text{below}} = \frac{n \bar{v} m}{6} \left[ v_x - \frac{\partial v_x}{\partial z} \bar{\ell} \right] \quad (9.59)$$

The net momentum change per unit area is the difference of the two expressions in Eq. (9.59).

$$P_{\text{above}} - P_{\text{below}} = \tau_{xz} = \frac{n \bar{v}' m \bar{\ell}}{3} \left( \frac{\partial v_x}{\partial z} \right) \quad (9.60)$$

Comparison of Eq. (9.60) to the phenomenological expression for one component of shear stress,  $\tau_{xy}$ , in Eq. (9.25), produces a microscopic expression for the shear viscosity of an ideal gas,  $\mu_{\text{gas}}$ .

$$\mu_{\text{gas}} = \frac{\bar{v}' m \bar{\ell}}{3} = \frac{\rho \bar{v}' \bar{\ell}}{3} = \frac{1}{\pi D^2} \left( \frac{m k_B T}{6} \right)^{1/2} = \frac{0.13}{D^2} k_B^{1/2} m^{1/2} T^{1/2} \quad (9.61)$$

Just like the thermal conductivity of an ideal gas, this estimate of the shear viscosity is independent of the pressure or density and proportional to the square root of the absolute temperature and to the square root of the particle mass. Like the ideal gas thermal conductivity, the actual temperature dependence of the viscosity for real gases is also closer to  $T^{0.7}$  [10].

### 9.5.4 Prandtl Number of an Ideal Gas and Binary Gas Mixtures\*

The relative importance of thermal conductivity and viscosity can be expressed in a dimensionless ratio that is known as the *Prandtl number*,  $\text{Pr} = \mu c_P/\kappa$ , where  $c_P$  is the specific heat (per unit mass) at constant pressure. This ratio is particularly important for convective heat transfer where the viscosity determines the energy dissipation from imposed flow and the thermal conductivity determines the heat transport. Liquid metals, like mercury or sodium-potassium eutectic (NaK), have a very small Prandtl number because of their low viscosity (hence, the popular designation as “quicksilver,” in the case of mercury) and high thermal conductivity, due to the efficient heat transport provided by the conduction electrons. On the other hand, viscous fluids with low thermal conductivity, like molasses, have large Prandtl numbers.

For monatomic ideal gases, the isobaric heat capacity per particle (see Sect. 7.2.1) is  $(5k_B/2)$  so the isobaric specific heat per particle is  $(5k_B/2m)$ . In combination with the ideal gas viscosity in Eq. (9.61) and thermal conductivity in Eq. (9.58), it is easy to demonstrate that the Prandtl number for ideal gases should be a constant.

$$\text{Pr}_{\text{gas}} \equiv \frac{\mu_{\text{gas}} c_P}{\kappa_{\text{gas}}} = \frac{\delta_v^2}{\delta_\kappa^2} = \frac{0.13}{0.37} \frac{5k_B}{2m} \frac{D^2}{D^2} \frac{k_B^{1/2} m^{1/2} T^{1/2}}{k_B^{3/2} T^{1/2} / m^{1/2}} \cong 0.9 \quad (9.62)$$

Measured values for the Prandtl number of monoatomic gases are not 0.9 but closer to  $2/3$ . For other polyatomic gases, the Prandtl numbers are also constant and range from about 0.7 to 0.9 [11]. This is due to the fact that it is those “hard spheres” that are responsible for both the heat and the momentum transport.

A similar result, known as the Wiedemann-Franz Law [12], shows that the ratio of the thermal conductivity,  $\kappa$ , and the electrical conductivity,  $\sigma$ , of metallic solids is a constant, independent of the particular metal, that depends only upon temperature.

$$L \equiv \frac{\kappa}{\sigma T} = \frac{\pi^2}{3} \left( \frac{k_B}{e} \right)^2 \quad (9.63)$$

$L$  is the Lorenz number and depends only upon fundamental constants (the charge on the electron,  $e$ , and Boltzmann’s constant,  $k_B$ ). Again, this is due to the fact that it is the electrons in metals that provide both heat transport and electrical conductivity.

For ideal gases, a more rigorous calculation was made by Eucken [13] that related the thermal conductivity of gases to their viscosity.

$$\kappa_{\text{gas}} = \left( c_P + \frac{5\mathfrak{R}}{4M} \right) \mu_{\text{gas}} \quad \Rightarrow \quad \text{Pr}_{\text{gas}} = \frac{c_P}{c_P + 1.25(\mathfrak{R}/M)} \quad (9.64)$$

Eucken’s formula gives the correct result for monatomic (noble) gases using the universal gas constant,  $\mathfrak{R} \equiv 8.314462 \text{ J/mol-K}$ , and is a very good approximation for most polyatomic gases.

Although the Prandtl number for ideal gases is a constant, it is possible to reduce the Prandtl number for gas mixtures. In a mixture of a light and heavy gas, the light species can dominate the heat transfer while the heavier species dominates the momentum transfer. Swift has demonstrated this by a simple calculation for inert gas mixtures based on the results from the microscopic model, using the subscripts “1” and “2” to designate two different gases.

$$\begin{aligned}
 k_B T &\propto (\frac{1}{2})m_1\bar{v}_1^2 \propto (\frac{1}{2})m_2\bar{v}_2^2 \\
 \mu_{mix} &\propto (n_1\bar{v}_1 m_1 + n_2\bar{v}_2 m_2)\bar{\ell} \propto n_1\sqrt{m_1} + n_2\sqrt{m_2} \\
 \kappa_{mix} &\propto (n_1\bar{v}_1 + n_2\bar{v}_2)c_P\bar{\ell} \propto n_1/\sqrt{m_1} + n_2/\sqrt{m_2} \\
 c_P &\propto \frac{\mathfrak{R}}{n_1 m_1 + n_2 m_2}
 \end{aligned} \tag{9.65}$$

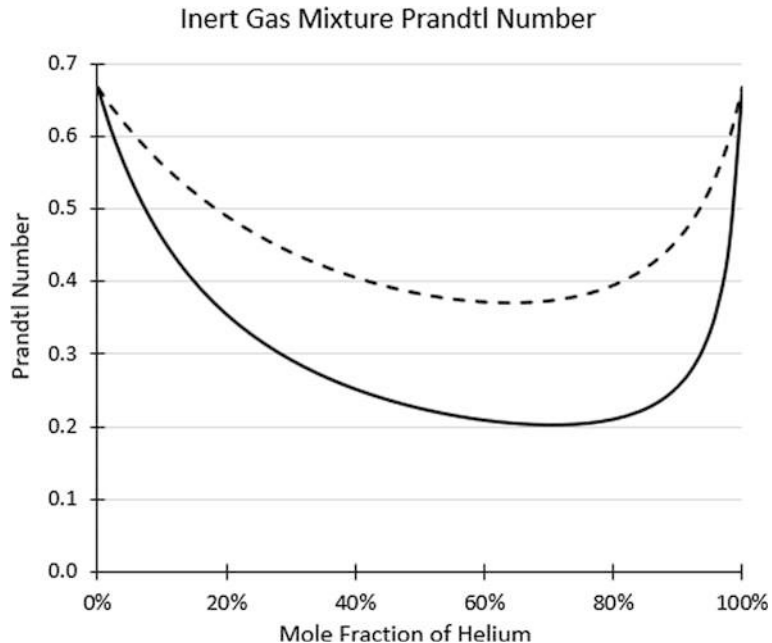
These proportions can be used to form the ratio of a mixture's Prandtl number,  $\text{Pr}_{mix}$ , to the pure gas Prandtl number,  $\text{Pr}_{gas}$ , in terms of the molar concentration of species "1,"  $x_1 = n_1/(n_1 + n_2)$ , and to the square root of their mass ratio,  $\beta = \sqrt{m_1/m_2}$ .

$$\frac{\text{Pr}_{mix}}{\text{Pr}_{gas}} = \frac{n_1\sqrt{m_1} + n_2\sqrt{m_2}}{\left(\frac{n_1}{\sqrt{m_1}} + \frac{n_2}{\sqrt{m_2}}\right)(n_1 m_1 + n_2 m_2)} = \frac{1 - (1 - \beta)x_1}{\left[1 + \left(\frac{1}{\beta} - 1\right)x_1\right]\left[1 - (1 - \beta^2)x_1\right]} \tag{9.66}$$

Figure 9.16 plots the gas mixture Prandtl number as a function of the mole fraction of helium,  $x_1$ , for helium-argon mixtures with  $\beta_{He/Ar} = 0.316$  and helium-xenon mixtures with  $\beta_{He/Xe} = 0.175$ . For pure gases (i.e.,  $x_1 = 0\%$  or  $x_1 = 100\%$ ),  $\text{Pr}_{mix} = 2/3$ , but a mixture of a light and a heavy gas can produce lower Prandtl numbers. The results in Fig. 9.16 demonstrate that the Prandtl number of a helium-argon mixture can be reduced to a minimum value of  $\text{Pr}_{He/Ar} = 0.37$  and a helium-xenon mixture can produce a minimum Prandtl number as low as  $\text{Pr}_{He/Xe} = 0.20$ . The lowest inert gas Prandtl number would be achieved with a mixture of  ${}^3\text{He}$  and radon,  $\text{Pr}_{He/Rn} = 0.14$ , although such a mixture would be highly radioactive. A more detailed kinetic theory calculation produces nearly identical results [14].

The use of gas mixtures that reduce Prandtl number have been shown to improve the performance of thermoacoustic engines and refrigerators [15], although it has also been shown that such high-amplitude sound waves can also introduce concentration gradients in mixtures [16].

**Fig. 9.16** The Prandtl number of inert gas mixtures as a function of the mole fraction of helium. The *dashed line* represents helium-argon mixtures and the *solid line* represents helium-xenon mixtures



## 9.6 Not a Total Loss

Just as we had examined the lossless equations of hydrodynamics in Chap. 8 by applying them to simple “lumped elements,” this chapter has introduced the diffusion equations that govern dissipation in fluidic acoustical systems (thermal conduction also contributes to dissipation in solids) by applying them to a Helmholtz resonator that had been modeled by DELTAEC in the previous chapter. In doing so, two new length scales were introduced: the thermal and viscous penetration depths,  $\delta_\kappa$  and  $\delta_\nu$ . Those length scales play the same critical role that wavelength and wavenumber played in the nondissipative equations. Comparison of the thermal penetration depth to the wavelength provided quantitative justification for the assumption we will exploit in the following chapter where sound waves are treated as being adiabatic oscillatory excursions away from equilibrium.

As in Chap. 7, the microscopic models and the phenomenological models of dissipative processes in ideal gases provided complementary insights into the behavior of the phenomenological constants,  $\kappa$  and  $\mu$ , with respect to changes in density and temperature, as well as supplying an intuitive picture of the processes by which heat and momentum are transported. The simple kinetic theory, based on a “hard sphere” collision assumption, introduced an additional important length scale: the mean free path,  $\bar{l}$ . When  $\bar{l} \ll \lambda$ , our continuum model of diffusive processes provides an appropriate description.

With the thermodynamic, hydrodynamic, and microscopic analyses introduced in this chapter and in Chap. 7, the fundamentals necessary to understand wave propagation in fluids, and particularly in ideal gases, will be put to use in the remainder of this textbook.

### Talk Like an Acoustician

Time reversal invariance	Ballistic propagation
Shear viscosity	Newtonian fluids
Dynamic (or absolute) viscosity	Diffusion constant
Fourier Diffusion Equation	Non-slip boundary condition
Ohm's law	Shear (or dynamic or absolute) viscosity
Joule heating	Kinematic viscosity
Newton's Law of Cooling	Poiseuille's formula
Thermal diffusivity	Oscillatory plug flow
Thermometric conductivity	Viscous penetration depth
Thermal penetration depth	Entrance length
Skin depth	Thermal velocity
Instantaneous value	Mean free path
Acoustic approximation	Prandtl number

### Exercises

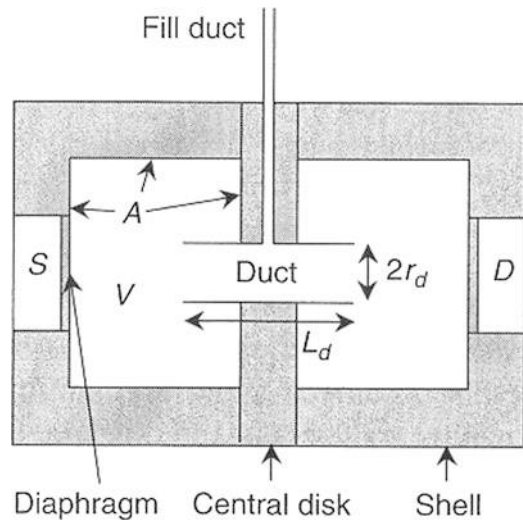
- Moon free path.** Atmospheric pressure on the moon is about  $10^{-13}$  atm. =  $10^{-8}$  Pa. Assume that the moon's atmosphere has the same chemical composition as Earth's and calculate the mean free path for molecules in our moon's atmosphere. Is the concept of pressure meaningful for such a long mean free path? Why or why not?
- Vacuum insulation.** As long as the characteristic dimensions of a gas-filled space are much greater than the mean free path of the gas particles, the thermal conductivity is independent of gas pressure. To reduce thermal conduction through a gas, the vacuum space gap,  $g$ , must be less than the mean free path,  $\bar{l}$ , of the gas molecules trapped in the vacuum insulation space.

The inverse relationship between number density,  $n$ , and mean free path,  $\bar{l}$ , illustrated in Eq. (9.53), is no longer valid when  $\bar{l}$  becomes larger than  $g$ . Beyond that point, the thermal resistance of the insulation space will increase linearly in proportion to increase of the mean free path because there are fewer gas particles to transport heat and those particles are more likely to collide with the walls than they are to collide with each other.

How low must the gas pressure in the insulation space be so that the thermal resistance of the vacuum space is ten times smaller than the thermal resistance when  $g \ll \bar{l}$  if  $g = 10$  mm, assuming that the vacuum space contains some air?

3. **Relaxation frequency for a capacitive microphone.** The volume inside a condenser microphone that is behind the diaphragm (see Fig. 6.14) must be isolated from the acoustical pressure variations which drive the motion of the microphone's diaphragm. Because the microphone diaphragm must be able to withstand slow changes in pressure encountered during transportation (e.g., shipping by air), a capillary tube is provided so that changes in ambient gas pressure,  $p_m$ , can be relieved, but acoustical pressure variations at the frequencies of interest are not allowed to influence the gas pressure within the microphone's back volume.
  - (a) *Poiseuille resistance.* Use Eq. (9.30) to write an expression for the acoustic flow resistance,  $R_{ac} = \Delta p/U$ , appropriate to steady gas flow in the Poiseuille regime.
  - (b) *Relaxation time.* Using the result from part (a), write an expression for the exponential relaxation time,  $\tau = R_{ac}C$ , where the compliance,  $C$ , given in Eq. (8.26), is determined by the microphone's back volume,  $V_{back}$ , assuming that the compressions and expansions of the gas within that volume are adiabatic. Discuss whether or not the adiabatic assumption is valid.
  - (c) *Viscous penetration depth.* For audio applications, the low-frequency cut-off is usually taken to be 20 Hz, corresponding to the nominal lower limit of human hearing [17]. Determine the viscous penetration depth at that frequency in air at 20 °C with  $p_m = 100$  kPa.
  - (d) *0.010" diameter capillary.* If the back volume of the microphone is  $V_{back} = 674$  mm<sup>3</sup> and it is connected to a capillary tube that has an inside diameter of 250 microns, and a length of 10.0 mm, determine the exponential relaxation time,  $\tau$ , for pressure equilibration and corresponding cut-off frequency,  $f_{-3dB} = (2\pi\tau)^{-1}$ .
4. **Viscous damping of an oscillating spar buoy.** The spar buoy shown in Fig. 2.33 has a diameter of 25 cm. The bottom 3.0 m of the buoy is submerged. Its vertical oscillations have a period of 3.6 seconds. The buoy's effective moving mass,  $m_o = 154$  kg.
  - (a) *Viscous penetration depth.* If the water has a density,  $\rho_{H_2O} = 1026$  kg/m<sup>3</sup>, and a shear viscosity,  $\mu_{H_2O} = 1.07 \times 10^{-3}$  Pa-s, how large is the viscous penetration depth at the buoy's natural frequency of vertical oscillations?
  - (b) *Viscously entrained mass.* What is the additional mass of water trapped in the viscous boundary layer if we assume that mass is the mass of water within one viscous penetration depth? (The circular bottom of the buoy can be ignored since it is not applying any shear stresses on the water.)
  - (c) *Viscous damping.* Determine the mechanical resistance,  $R_m$ , by calculating the viscous drag of the water on the buoy. Use your value of  $R_m$  to determine the exponential relaxation time,  $\tau = 2m_o/R_m$ , if the only source of damping is the viscous drag provided by the surrounding water.
5. **Greenspan viscometer.** Shown in Fig. 9.17 is a schematic cross-section of a cylindrically symmetric (about the “Duct” axis) double-Helmholtz resonator that has been used by the National Institute of Standards and Technology (formerly, the Bureau of Standards) to make an acoustical determination of the viscosity of gases [18]. Both volumes,  $V$ , are identical and  $A$  is the total surface area of

**Fig. 9.17** Cross-sectional schematic representation of a Greenspan viscometer [19]



each volume. “S” and “D” are PZT stacks that act as the excitation and detection transducers that are covered by a “Diaphragm” which can be considered perfectly rigid.

For this problem, assume that the viscometer is filled with neon gas at a mean pressure,  $p_m = 1.0 \text{ MPa}$ . Both compliances have the same volume,  $V = 29 \text{ cm}^3$ , and the same surface area,  $A = 55 \text{ cm}^2$ . The duct length,  $L_d = 3.1 \text{ cm}$ , and the radius of the duct,  $r_d = 2.3 \text{ mm}$ . This viscometer produced measurements of viscosity that differed from published results obtained by other methods by less than  $\pm 0.5\%$  and sound speeds that differed by less than  $\pm 0.2\%$  [18].

- Helmholtz resonance frequency.* Assuming that the neon gas is lossless, calculate the resonance frequency of this dual Helmholtz resonator using a sound speed in neon of  $c_{Ne}$  ( $20^\circ\text{C}$ ) =  $449 \text{ m/s}$ .
- Gas displacement in the duct.* If the amplitude of the acoustic pressure in either volume is  $10.0 \text{ Pa}$ , what is the peak-to-peak displacement of the gas in the duct?
- Viscous penetration depth.* Based on the resonance frequency, calculate the viscous penetration depth if the neon has a density,  $\rho_{Ne}$  ( $20^\circ\text{C}$ ) =  $8.28 \text{ kg/m}^3$ , and a viscosity,  $\mu_{Ne}$  ( $20^\circ\text{C}$ ) =  $3.13 \times 10^{-5} \text{ Pa-s}$ .
- Quality factor.* Calculate the quality factor,  $Q$ , for this Helmholtz resonance.
- Viscosity.* In the limit that  $\delta_v \ll r_d$ , express the gas viscosity,  $\mu$ , in terms of the Helmholtz resonance frequency,  $f_o$ , the gas density,  $\rho$ , and the resonance quality factor,  $Q$ .
- Thermal relaxation.* Investigate how negligible the thermal boundary layer losses are in the compliances.

## References

1. C. Nolan, *Memento*, Newmarket Productions (Columbia TriStar, 2001).
2. F. M. White, *Mass and Heat Transfer* (Addison-Wesley, 1991). See §1.3.5; ISBN 0-201-17099-X.
3. F. P. Incropera and D. P. DeWitt, *Fundamentals of Heat and Mass Transfer*, 3rd ed. (J. Wiley & Sons, 1990). See Ch. 6; ISBN 0-471-61246-4.
4. G. W. Swift, *Thermoacoustics: A unifying perspective for some engines and refrigerators*, 2nd ed. (Acoust. Soc. Am., 2017); ISBN 978-3-319-66932-8. See Eq. (5.11).

5. A.D. Hanford, L.N. Long, The absorption of sound on Mars using the direct simulation Monte Carlo. *J. Acoust. Soc. Am.* **119**, 3264 (2006)
6. L. D. Landau and E. M. Lifshitz, *Fluid Mechanics*, 2nd ed. (Butterworth-Heinemann, 1987). See §15; ISBN 0 7506 2767 0.
7. J.R. Olson, G.W. Swift, Energy dissipation in oscillating flow through straight and coiled pipes. *J. Acoust. Soc. Am.* **100**(4), 2123–2131 (1996)
8. F. Reif, *Fundamentals of Statistical and Thermal Physics* (McGraw-Hill, 1965). See §12.4.
9. S. Chapman and T. G. Cowling, *Mathematical Theory of Non-Uniform Gases*, 2nd ed. (Cambridge Univ. Press, 1951).
10. G. W. Swift, *Thermoacoustics: A unifying perspective for some engines and refrigerators*, 2nd ed. (Acoust. Soc. Am., 2017). See §2.3.2, pg. 48–49; ISBN 978-3-319-66932-8.
11. R. B. Bird, W. E. Stewart, E. N. Lightfoot, *Transport Phenomena* (Wiley & Sons, 1960). See Table 8.3–1.
12. G. Wiedemann, R. Franz, Relative conductivity of solids. *Ann. Phys. Chemie* **89**, 497–531 (1853)
13. A. Eucken, On the thermal conductivity of several gases. *Physik. Z.* **14**, 324–332 (1913)
14. F.W. Giacobbe, Estimation of Prandtl numbers in binary mixtures of helium and other noble gases. *J. Acoust. Soc. Am.* **96**(6), 3538–3580 (1994)
15. S.L. Garrett, J.A. Adeff, T.J. Hofler, Thermoacoustic refrigerator for space applications. *J. Thermophys. Heat Transf. (AIAA)* **7**(4), 595–599 (1993)
16. G.W. Swift, D.A. Geller, S.N. Backhaus, High-purity thermoacoustic isotope separation. *J. Acoust. Soc. Am.* **136**(2), 638–648 (2014)
17. N. Fletcher, Condenser microphones – a tutorial. *Acoust. Australia* **30**(3), 109–113 (2002)
18. J. Wilhelm, K.A. Gillis, J.B. Mehl, M.R. Moldover, An improved Greenspan acoustic viscometer. *Int. J. Thermophys.* **21**, 983–999 (2000)
19. M. R. Moldover, K. A. Gillis, J. J. Hurly, J. B. Mehl and J. Wilhelm, “Acoustic Measurements in Gases,” in *Experimental Methods in Physical Sciences*, Vol. 39 (Academic Press, 2001). See Chap. 10; ISBN 0-12-475986-6.

**Open Access** This chapter is licensed under the terms of the Creative Commons Attribution 4.0 International License (<http://creativecommons.org/licenses/by/4.0/>), which permits use, sharing, adaptation, distribution and reproduction in any medium or format, as long as you give appropriate credit to the original author(s) and the source, provide a link to the Creative Commons license and indicate if changes were made.

The images or other third party material in this chapter are included in the chapter's Creative Commons license, unless indicated otherwise in a credit line to the material. If material is not included in the chapter's Creative Commons license and your intended use is not permitted by statutory regulation or exceeds the permitted use, you will need to obtain permission directly from the copyright holder.





# One-Dimensional Propagation

10

## Contents

10.1	<b>The Transition from Lumped Elements to Waves in Fluids</b>	454
10.2	<b>The Wave Equation</b>	456
10.2.1	General Solutions to the Wave Equation	458
10.3	<b>The Dispersion Relation (Phase Speed)</b>	459
10.3.1	Speed of Sound in Liquids	460
10.3.2	Speed of Sound in Ideal Gases and Gas Mixtures	460
10.4	<b>Harmonic Plane Waves and Characteristic Impedance</b>	463
10.5	<b>Acoustic Energy Density and Intensity</b>	464
10.5.1	Decibel Scales	465
10.5.2	Superposition of Sound Levels (Rule for Adding Decibels)	468
10.5.3	Anthropomorphic Frequency Weighting of Sound Levels	468
10.6	<b>Standing Waves in Rigidly Terminated Tubes</b>	470
10.6.1	Quality Factor in a Standing Wave Resonator	472
10.6.2	Resonance Frequency in Closed-Open Tubes	474
10.7	<b>Driven Plane Wave Resonators</b>	474
10.7.1	Electroacoustic Transducer Sensitivities	476
10.7.2	The Principle of Reciprocity	477
10.7.3	In Situ Reciprocity Calibration	478
10.7.4	Reciprocity Calibration in Other Geometries	481
10.7.5	Resonator-Transducer Interaction	482
10.7.6	Electrodynamic Source Coupling Optimization*	488
10.8	<b>Junctions, Branches, and Filters</b>	490
10.8.1	Abrupt Discontinuities and the Acoustic Admittance	490
10.8.2	Tuned Band-Stop Filter	492
10.8.3	Stub Tuning	494
10.9	<b>Quasi-One-Dimensional Propagation (Horns)</b>	495
10.9.1	Semi-infinite Exponential Horns	495
10.9.2	Salmon Horns*	499
10.9.3	Horns of Finite Length*	500
	<b>References</b>	510

Having already invested in understanding both the equation of state in Chap. 7 and in the hydrodynamic equations in Chap. 8, only straightforward algebraic manipulations will be required to derive the wave equation, justify its solutions, calculate the speed of sound in fluids, and derive the expressions for acoustic intensity and the acoustic kinetic and potential energy densities. The “machinery” developed to describe waves on strings will be sufficient to describe one-dimensional sound propagation in fluids, even though the waves on the string were transverse and the one-dimensional waves in fluids are longitudinal.

Most treatments of one-dimensional propagation in acoustics courses start their discussion of waves in fluids at this point (possibly treating lumped-element systems later), but with our understanding of the fundamental phenomenological equations already established for lumped elements, we will be able to take a more rigorous approach that will also allow incorporation of other effects that can be combined with the dissipative effects introduced in Chap. 9, particularly for calculation of the attenuation of sound in Chap. 14. Also, having examined combinations of inertances and compliances, the transition from lumped fluid elements to waves in fluids is philosophically identical to the transition from coupled simple harmonic oscillators to waves on strings.

## 10.1 The Transition from Lumped Elements to Waves in Fluids

The equation of state, as exemplified by the adiabatic gas law of Eq. (7.20), and the linearized versions of the continuity equation combined with the adiabatic gas law in Eq. (8.23) were used to create lumped compliances in Sect. 8.2.3. The linearized version of the Euler Eq. (8.40) was used to create lumped inertances, and then both inertance and compliance were applied to fluid elements that were small compared to the wavelength of sound in Sect. 8.4.3. Those equations can now be extended to continuous fluid media in systems that are substantial fractions of a wavelength or larger.

Since the lumped-element model was linear, we are free to combine solutions. Although the neck of our Helmholtz resonator in Sect. 8.5.2 was represented entirely by its inertance (gas mass) and the spherical volume was represented entirely by its compliance (gas stiffness), in general, a single “lumped” element could simultaneously exhibit both properties by linear superposition. If there are changes in the volume velocity of the fluid entering and leaving the element,  $\Delta U$ , as well as a pressure difference,  $\Delta p$ , across an element, like those diagrammed schematically in Figs. 8.3 and 8.8, then the element would exhibit both inertance (due to  $\Delta p$ ) and compliance (due to  $\Delta U$ ).

In this chapter, we will expand our focus to include acoustical systems with characteristic dimensions comparable to, or longer than, the wavelength of sound in the fluid. These can also be modeled using lumped parameters, if we employ enough elements. For instance, a resonator with diameter that is a small fraction of the wavelength, but a length that is equal to one-half of the wavelength of sound, can be modeled as a sequence of compliances and inertances as depicted schematically in Fig. 10.1.

As demonstrated in Sect. 2.7.7, the behavior of standing waves on strings can be approximated by identical discrete masses coupled by identical lengths of a massless string under uniform tension. The fundamental mode of nine such coupled oscillators is shown in Fig. 2.30 to be a good approximation to the half-sinewave mode of a string, like that shown in Fig. 3.6. This approach has some significant utility if you are interested in studying systems with changing cross-section. As shown in Fig. 10.2, a horn of finite length, analyzed in Sect. 10.9.3, can be approximated by a series of stepped ducts of increasing cross-section.

The broadband, omnidirectional sound source shown in Fig. 10.3 was designed to radiate sound uniformly in all directions and to give reproducible and reliable results for evaluation of building acoustics with a sufficient overall sound pressure level to provide adequate signal-to-noise ratios. The

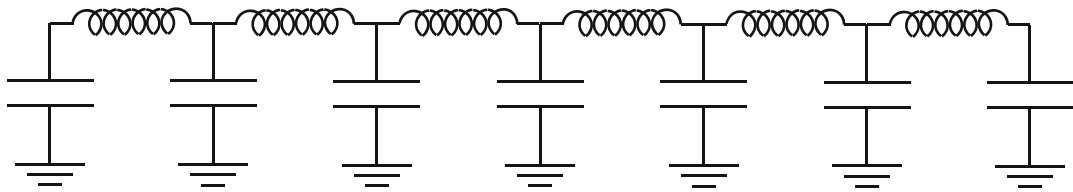
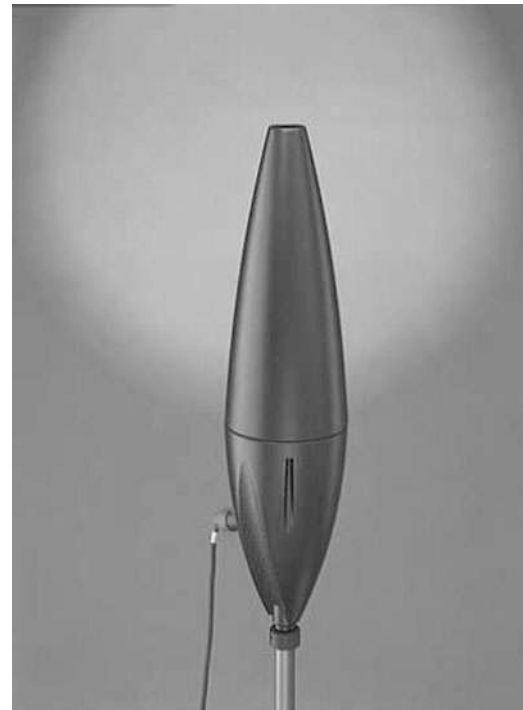


**Fig. 10.1** A half-wavelength resonator (*above*) of constant cross-sectional area with rigid ends is approximated as a series of seven lumped compliances and six lumped inertances. The elements near the ends contribute primarily compliance since the longitudinal motion of the fluid must vanish at the boundary (velocity nodes). Most of the energy stored near the ends is compressive (potential). The central elements contribute mostly inertance since the fluid velocity at the center is largest (near the velocity anti-node). Most of the energy within the central pair of inertances is kinetic. In fact, the approximation is nearly as good if the central compliance is removed from the model (but only for the fundamental half-wavelength mode!). The two pairs of elements that are intermediate between the two end elements and the central elements must provide both significant inertance and compliance



**Fig. 10.2** A stepwise approximation to a horn. The number of elements is chosen so the area change between elements is small [1]

**Fig. 10.3** The Brüel & Kjær Type 4295 sound source was “carefully engineered to radiate sound evenly in all directions” by Dr. Jean-Dominique Polack. The source was designed to conform to the standard 1/3-octave band sound level and directionality requirements by using a resonator coupled to an electrodynamic loudspeaker. Although a resonator is about as far from a “broadband” sound source as one might possibly imagine, it does satisfy the standards as written



International Organization for Standardization (ISO) has published two standards for broadband sound sources that are used for architectural acoustical evaluations in buildings [2]. The standards require uniform levels, within a frequency-dependent number of decibels (see Sect. 10.5.1) in each of twenty-one 1/3-octave frequency bands (ISO 3382). The source must also radiate sound uniformly in all directions (ISO 140).

A very clever acoustician, Jean-Dominique Polack,<sup>1</sup> realized that he could design a very simple source consisting of a single loudspeaker radiating out of a small aperture (to ensure omnidirectionality, as shown in Fig. 12.32a) that would be very compact and efficient by making a resonator and “tuning” the resonances within each 1/3-octave band (though not necessarily at the band center frequency). He did this by writing a finite element code that incorporated 28 lumped elements and then adjusted those elements to place the resonances within the 1/3-octave bands specified by ISO 3382.<sup>2</sup>

At some point, it makes sense to model the entire resonator as a continuum just as it did in our transition from coupled simple harmonic oscillators to strings. We do that by specifying a continuous function that describes the pressure and fluid velocity at each point in space and time—a wave function.

## 10.2 The Wave Equation

Our study of the fundamental equations of hydrodynamics has provided us with a set of three Eqs. (7.32), (7.34), and (7.42) that describe the motion of any homogeneous, viscous, thermally conducting, and isotropic, single-component fluid. We supplemented those hydrodynamic equations by equations of state (7.49) and (7.50) that provide relationships among the mechanical variables ( $p$  and  $\rho$ ) and thermodynamic variables ( $T$  and  $s$ ) that appear in the hydrodynamic equations.

The linearized, one-dimensional, nondissipative versions of those equations are first-order partial differential equations that define relationships among different variables. For example, the continuity equation or mass conservation Eq. (8.17) relates changes in density to the divergence of the fluid velocity or mass flux. Similarly, the linearized one-dimensional Euler Eq. (8.40) relates changes in the velocity to gradients in the pressure. An equation of state, for example, (7.19), can relate changes in pressure to changes in density.

It is possible to combine those first-order partial differential equations to create a second-order partial differential equation for a single variable. To illustrate this process, let us start with a one-dimensional version of the linearized continuity Eq. (8.17), where we let  $v_x = u = v_I$ ,

$$\frac{\partial \rho_1(x, t)}{\partial t} + \rho_m \frac{\partial v_1(x, t)}{\partial x} = 0, \quad (10.1)$$

and the linearized one-dimensional Euler equation, where again  $v_x = u = v_I$ ,

<sup>1</sup> Prof. Polack was on the faculty at the Danish Technical University (less than a 10 min drive from Lyngby to the Brüel & Kjær Headquarters in Nærum, Denmark) when he made this design. He is currently a professor at Université Pierre et Marie Curie and the Head of Doctoral School of Mechanics, Acoustics, Electronics and Robotics (SMAER, ED 391).

<sup>2</sup> The resultant resonator was conical. It can be modeled easily in DELTAEC as a single CONE element (plus an electrodynamic driver VESPEAKER at one end and an OPNBRANCH radiation condition at the other end). This is a lot easier than 28 lumped elements once you accept that a cone will solve the problem.

$$\frac{\partial v_1(x, t)}{\partial t} + \frac{1}{\rho_m} \frac{\partial p_1(x, t)}{\partial x} = 0. \quad (10.2)$$

That set of two first-order coupled differential equations contains three (potentially complex) variables:  $p_1$ ,  $v_1$ , and  $\rho_1$ . To “close” the system, we need one additional equation to eliminate either  $p_1$  or  $\rho_1$ . Closure can be achieved by invoking an equation of state. In this case, we will choose to express density in terms of pressure,  $\rho = \rho(p)$ , which can be expanded in a Taylor series to eliminate  $\rho_1$  in favor of  $p_1$  in Eq. (10.1).

$$\rho_1 = \left( \frac{\partial \rho}{\partial p} \right)_s p_1 + \left( \frac{\partial^2 \rho}{\partial p^2} \right)_s \frac{(p_1)^2}{2!} + \left( \frac{\partial^3 \rho}{\partial p^3} \right)_s \frac{(p_1)^3}{3!} \dots \quad (10.3)$$

As was demonstrated in Sect. 9.3.4, at nearly all frequencies of interest in gases or liquids, sound propagation is adiabatic. For that reason, we have taken the derivatives of the density with respect to pressure in Eq. (10.3) while holding entropy per unit mass constant, as indicated by the subscript,  $s$ , on the partial derivatives. Since we are interested in the linearized result, we retain only the first term in the Taylor series of Eq. (10.3). As we will see shortly, it is convenient to name that derivative<sup>3</sup> the reciprocal of the square of the speed of sound,  $c^{-2}$ .

$$\frac{1}{c^2} = \left( \frac{\partial \rho}{\partial p} \right)_s \quad (10.4)$$

Substituting Eq. (10.4) into Eq. (10.1), we obtain,

$$\frac{1}{c^2} \frac{\partial p_1(x, t)}{\partial t} + \rho_m \frac{\partial v_1(x, t)}{\partial x} = 0 \quad (10.5)$$

Now Eqs. (10.2) and (10.5) constitute a pair of homogeneous first-order coupled differential equations in two variables. Those equations can be combined to eliminate either  $p_1$  or  $v_1$ . Let us start by eliminating  $v_1$ . That can be accomplished by multiplying the linearized Euler Eq. (10.2) by  $\rho_m$  and taking its derivative with respect to  $x$ .<sup>4</sup>

$$\rho_m \frac{\partial^2 v_1(x, t)}{\partial x \partial t} + \frac{\partial^2 p_1(x, t)}{\partial x^2} = 0 \quad (10.6)$$

We can then take the time derivative of the linearized continuity Eq. (10.5).

$$\frac{1}{c^2} \frac{\partial^2 p_1(x, t)}{\partial t^2} + \rho_m \frac{\partial^2 v_1(x, t)}{\partial t \partial x} = 0 \quad (10.7)$$

Since the order of differentiation is irrelevant, when Eq. (10.6) is subtracted from Eq. (10.7), we are left with a second-order, homogeneous, partial differential equation in only one variable.

---

<sup>3</sup> Some say thermodynamics is the field where every partial derivative has its own name.

<sup>4</sup> We assume that  $\rho_m$  is independent of  $x$  throughout most of this book. Many thermoacoustic phenomena, including engines and refrigerators, rely on the  $x$  dependence of  $T_m$  and  $\rho_m$ , so the fundamental equations of thermoacoustics are more complicated [8].

$$\frac{\partial^2 p_1(x, t)}{\partial t^2} - c^2 \frac{\partial^2 p_1(x, t)}{\partial x^2} = 0 \quad (10.8)$$

The result in Eq. (10.8) is the well-known one-dimensional *wave equation*. It provides us with an expression that can relate the time and space dependence of  $p_1(x, t)$ . Since pressure and density deviations from equilibrium are related by the square of the sound speed, then we would obtain the same wave equation for  $\rho_1$ .

$$\frac{\partial^2 \rho_1(x, t)}{\partial t^2} - c^2 \frac{\partial^2 \rho_1(x, t)}{\partial x^2} = 0 \quad (10.9)$$

If the combination process is reversed by taking the spatial derivative of the linearized continuity Eq. (10.5), we obtain,

$$\frac{\partial^2 p_1(x, t)}{\partial x \partial t} + \rho_m c^2 \frac{\partial^2 v_1(x, t)}{\partial x^2} = 0 \quad (10.10)$$

Similarly, the linearized Euler Eq. (10.2) can be multiplied by  $\rho_m$ , and then the time derivative can be taken.

$$\rho_m \frac{\partial^2 v_1(x, t)}{\partial t^2} + \frac{\partial^2 p_1(x, t)}{\partial t \partial x} = 0 \quad (10.11)$$

Once again, ignoring the order of differentiation, subtraction of Eq. (10.10) from Eq. (10.11) produces the wave equation for the linear contribution to the  $x$  component of the acoustic particle velocity,  $v_1$ .

$$\frac{\partial^2 v_1(x, t)}{\partial t^2} - c^2 \frac{\partial^2 v_1(x, t)}{\partial x^2} = 0 \quad (10.12)$$

### 10.2.1 General Solutions to the Wave Equation

The wave equation, as written in Eq. (10.8) or Eq. (10.12), is a second-order partial differential equation. As such, it must have two linearly independent solutions:  $y_a$  and  $y_b$ . Of course, any one-dimensional, linear, wave equation will be isomorphic to the version that appeared first as the equation for propagation of transverse waves on a string in Eq. (3.4).

As was demonstrated in Sect. 3.1, it is not difficult to show that any arbitrary function having  $(ct \pm x)$  in its argument is a solution. Whether  $c$  is the speed of sound in a fluid, or the speed of transverse waves on a string,  $f(ct \pm x)$  are the solutions to Eq. (3.4) as well as Eqs. (10.8), (10.9), and (10.12). If we choose pressure as the variable that characterizes the amplitude of the sound wave, then the excess acoustic pressure due to the sound wave,  $p_1(x, t)$ , can be expressed as the superposition of the right-going and left-going waves.

$$p_1(x, t) = p_1^{right}(ct - x) + p_1^{left}(ct + x) \quad (10.13)$$

As with our solutions for waves on strings, for purposes of computational convenience and conformity with physical reality for most acoustical systems, we employ the trigonometric functions, or complex exponential functions, or combinations of those functions as our solutions of choice for single-frequency waves, as we did for traveling waves.

$$p_1(\vec{x}, t) = \Re e \left[ \hat{\mathbf{p}}_{\text{left}} e^{j(\omega t + \vec{k} \cdot \vec{x})} + \hat{\mathbf{p}}_{\text{right}} e^{j(\omega t - \vec{k} \cdot \vec{x})} \right] \quad (10.14)$$

Standing waves can be represented as the superposition of a right- and left-going traveling waves of equal amplitudes. Letting  $\hat{\mathbf{p}}_{\text{left}} = Ae^{-j(\phi_t + \phi_x)} / 2$  and  $\hat{\mathbf{p}}_{\text{right}} = Ae^{-j(\phi_t - \phi_x)} / 2$ , with  $\vec{k} \cdot \vec{x} = kx$ , and making  $\Im m[A] = \Im m[\phi_t] = \Im m[\phi_x] = 0$ , Eq. (10.14) becomes,

$$p_1(x, t) = A \cos(kx - \phi_x) \cos(\omega t - \phi_t) \quad (10.15)$$

As before, the scaling of time by angular frequency,  $\omega$ , and position by wavenumber,  $k$ , is a particularly useful choice that makes the argument of the functions dimensionless.

The same functions could just as well have been written for the linear variations in the density,  $\rho_1(x, t)$ , from its equilibrium value,  $\rho_m$ , or the variation in the particle velocity,  $v_1(x, t)$ , where we have assumed  $v_m = 0$ .

### 10.3 The Dispersion Relation (Phase Speed)

Once we have used the wave equation to demonstrate that the solutions for each variable that characterizes its linear deviation from equilibrium have wave-like space and time behavior, the wave equation does not provide any immediate additional utility. To demonstrate this fact, we can return to the coupled first-order linearized continuity Eq. (10.1) and Euler Eq. (10.2).

By using the complex notation of Eq. (10.14) with  $\hat{\mathbf{p}}_{\text{left}} = 0$  to describe a single-frequency right-going propagating wave, differentiation with respect to time corresponds to a simple multiplication of  $p_1$  by  $+j\omega$  and differentiation with respect to position corresponds to a simple multiplication of  $p_1$  by  $-jk$ . Application of this convenience (aka complex) transformation (harmonic analysis) to the linearized continuity Eq. (10.5) yields,

$$\frac{j\omega \hat{p}_{\text{right}}}{c^2} - jk\rho_m \hat{v}_{\text{right}} = 0. \quad (10.16)$$

Similarly, the linearized Euler Eq. (10.2) becomes,

$$j\omega \hat{v}_{\text{right}} - \frac{jk\hat{p}_{\text{right}}}{\rho_m} = 0. \quad (10.17)$$

This pair of linear coupled algebraic equations, (10.16) and (10.17), will only have a nontrivial solution if the determinant of their coefficients vanishes.

$$\begin{vmatrix} \frac{+j\omega}{c^2} & -jk\rho_m \\ \frac{-jk}{\rho_m} & +j\omega \end{vmatrix} = 0 \quad (10.18)$$

Evaluation of the determinant specified in Eq. (10.18) produces a relationship between  $\omega$  and  $k$  that is known as a *dispersion relation*.

$$k^2 - \frac{\omega^2}{c^2} = 0 \quad (10.19)$$

This result provides the definition of the phase speed,  $c \equiv \omega /k$ , thus justifying the concepts of wavenumber,  $k$ ; wavelength,  $\lambda$ ; frequency,  $f$ ; and period,  $T$ , that we have been using since Chap. 3:  $c = f\lambda = \omega/k$ .

### 10.3.1 Speed of Sound in Liquids

The square of the adiabatic speed of sound is expressed as the thermodynamic derivative of pressure with respect to density in Eq. (10.4). For fluids, that result is related to another thermodynamic derivative; the adiabatic bulk modulus,  $B_s$ , has the same units as pressure:

$$B_s = -V \left( \frac{\partial p}{\partial V} \right)_s = -\frac{1}{\rho} \left( \frac{\partial p}{\partial (1/\rho)} \right)_s = \rho \left( \frac{\partial p}{\partial \rho} \right)_s \quad (10.20)$$

In Sect. 4.2.1, the previous derivation for the bulk modulus in solids did not specify whether the modulus was evaluated under isothermal or adiabatic conditions since there is very little difference between those values for solids.

The adiabatic bulk modulus is the reciprocal of the adiabatic compressibility. By comparison of Eq. (10.20) to Eq. (10.4), we see that the adiabatic sound speed in a fluid can be expressed in terms of the adiabatic bulk modulus and the fluid's mass density.

$$c = \sqrt{\frac{B_s}{\rho_m}} \quad (10.21)$$

The form of Eq. (10.21) is typical of sound propagation speeds because it shows that the speed is determined by the ratio of a restoring “stiffness” to an inertial mass density.

The bulk modulus is an intensive material property. For most liquids, it is usually found in handbooks and can be a complicated function of both pressure and temperature. The expression for the speed of sound in seawater, given in Eq. (11.26), includes terms that are a function of salinity, as well as pressure [3]. Even a simple cryogenic liquid, such as liquid nitrogen ( $\text{LN}_2$ ), exhibits complicated pressure dependence of its sound speed:

$$\begin{aligned} c(\text{LN}_2) = & 854.1 + 0.8370p - 0.9072 \times 10^{-3}p^2 \\ & + 0.9697 \times 10^{-6}p^3 - 0.4904 \times 10^{-9}p^4 \end{aligned}$$

where  $c$  is in [m/s] and  $p$  is in atmospheres (1 atm  $\equiv 101,325$  Pa) [4].

### 10.3.2 Speed of Sound in Ideal Gases and Gas Mixtures

For an ideal gas, the form of the sound speed is particularly simple and universal. Logarithmic differentiation of the ideal gas adiabatic equation of state,  $p\rho^{-\gamma} = \text{constant}$ , immediately produces an expression for the speed of sound in an ideal gas, based on Eq. (10.4):

$$\frac{dp}{p_m} = \gamma \frac{d\rho}{\rho_m} \Rightarrow c = \left( \frac{\partial p}{\partial \rho} \right)_s^{1/2} = \sqrt{\frac{\gamma p_m}{\rho_m}} \quad (10.22)$$

The Ideal Gas Law (7.4) allows Eq. (10.22) to be expressed in terms of the molecular (or atomic) mass of the gas,  $M$ ; its absolute [kelvin] temperature,  $T$ ; and the universal gas constant,  $\mathfrak{R}$ :

$$c^2 = \frac{\gamma \mathfrak{R} T}{M} \quad (10.23)$$

It is worthwhile to reflect on the adiabatic sound speed for ideal gases as expressed in Eq. (10.23) for several reasons: First, it demonstrates that *the sound speed in an ideal gas is not a function of pressure*. This is not obvious from Eq. (10.22), which could (naïvely) be interpreted to imply that the sound speed increases with the square root of pressure. This is incorrect, because the ratio of pressure to density depends only upon absolute [kelvin] temperature, polytropic coefficient, and molecular weight.

Equation (10.23) also highlights the fact that the sound speed is proportional to the square root of absolute [kelvin] temperature. As of 20 May 2019, the international standard absolute temperature scale is based on sound speed measurements [5], just as the *exact* value of Boltzmann's constant,  $k_B \equiv 1.380649 \times 10^{-23} \text{ J/K}$ , and the universal gas constant,  $\mathfrak{R} \equiv k_B N_A \equiv 8.314462 \text{ J/mole-K}$ , has been tied to sound speed measurements since the mid-1980s [6].

The third reason that Eq. (10.23) is important is that it provides a means of calculating the speed of sound in gas mixtures. If we have a binary mixture of ideal gases with a concentration,  $x$ , of one species with molecular mass,  $M_1$ , and concentration,  $(1 - x)$ , of the second species with molecular mass,  $M_2$ , then the mean molecular mass of the gas mixture,  $M_{mix}$ , is simply their concentration-weighted average:

$$M_{mix} = xM_1 + (1 - x)M_2 \quad (10.24)$$

This expression can be generalized to mixtures, such as air, with more than two constituents (see Table 10.1).

Since the polytropic coefficient,  $\gamma = c_p/c_V$ , also known as the ratio of specific heats, is an intensive quantity, it is not correct to calculate  $\gamma_{mix}$  as a weighted average of the individual polytropic coefficients, although it is not too bad an approximation in some circumstances [7], since the range of  $\gamma$  is limited:  $1 < \gamma \leq 5/3$ . To calculate  $\gamma_{mix}$  correctly, the heat capacities are averaged:

$$\gamma_{mix}(x) = \frac{c_p}{c_V} = \frac{xc_{p,1} + (1 - x)c_{p,2}}{xc_{V,1} + (1 - x)c_{V,2}} \quad (10.25)$$

This result can be written in another form if the concentration weighting is applied to the reciprocals of  $(\gamma - 1)$  [8].

$$\frac{1}{\gamma_{mix} - 1} = \frac{x}{\gamma_1 - 1} + \frac{1 - x}{\gamma_2 - 1} \quad (10.26)$$

A similar approach can be used to estimate the transport coefficients in gas mixtures: thermal conductivity, viscosity, and Prandtl number, as was done in Sect. 9.5.4 [9].

Since the sound speed is independent of pressure and the temperature dependence can be easily compensated, being proportional to the square root of absolute temperature,<sup>5</sup> it is possible to build sonic gas analyzers that determine the concentration of a contaminant quickly, accurately, and inexpensively [12, 13]. The helium contamination alarm, shown schematically in Fig. 10.4, uses the variation in sound speed to detect leakage of air into a helium gas recovery system [14]. Other more sophisticated systems have been developed that allow flow-through measurement with differential processing to increase common-mode rejection of flow and environmental noise [12, 15].

---

<sup>5</sup> Analog Devices, Inc. sells a wonderful temperature sensing integrated circuit (AD 592) that sources one microampere of current for each degree of absolute temperature, making electronic temperature compensation nearly trivial.

**Table 10.1** Properties of the constituents of standard dry air at  $T_m = 0^\circ\text{C}$  [10] which produce a sound speed of 331.44 m/s [11]

Constituent	Molar mass [gm/mol]	Mole fraction	Contribution [gm/mol]	$c_p$ [kJ/kg-K]	$\gamma = c_p/c_v$
N <sub>2</sub>	28.013 4	0.780 84	21.873 983	1.0404	1.400
O <sub>2</sub>	31.998 8	0.209 476	6.702 981	0.09187	1.395
Ar	39.948	0.009 34	0.373 114	0.5216	1.667
CO <sub>2</sub>	44.009095	0.000 314	0.013 819	0.8460	1.289
Ne	20.183	1.818E-05	0.000 367	1.0299	1.667
Kr	83.80	1.14E-06	0.000 096	0.2480	1.667
CH <sub>4</sub>	16.043 03	2.0E-06	0.000 032	2.2193	1.304
He	4.002 6	5.24E-06	0.000 021	5.1931	1.667
N <sub>2</sub> O	44.012 8	2.70E-07	0.000 012	0.8721	1.27
Xe	131.30	8.7E-08	0.000 011	0.1583	1.667
CO	28.01	1.9E-07	0.000 006	1.0420	1.40
H <sub>2</sub>	2.015 94	5.0E-07	0.000 001	14.3020	1.405
H <sub>2</sub> O	18.015 34	0	0	1.8624	1.32

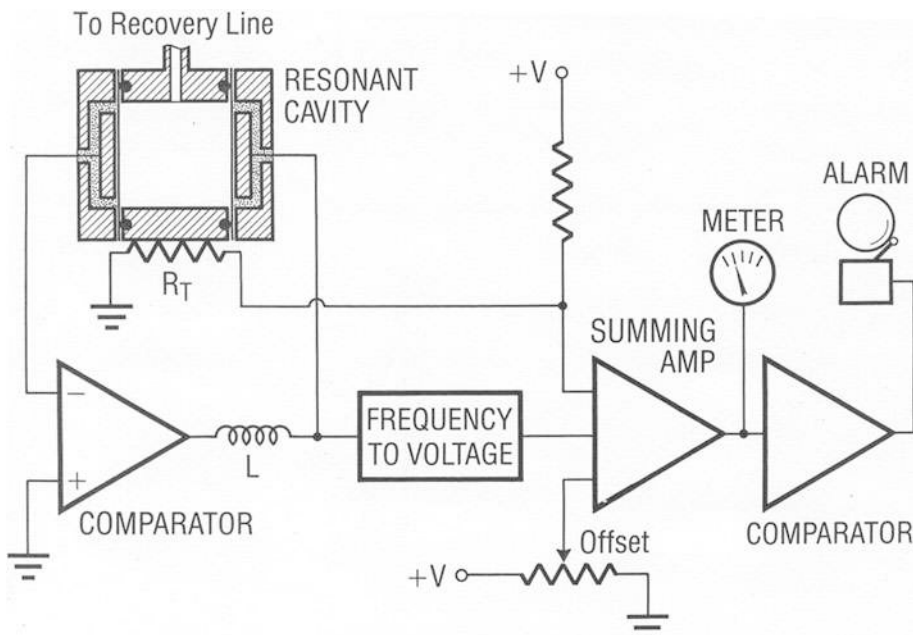


**Fig. 10.4** The cylindrical plane wave resonator in the upper left corner of this block diagram is closed at each end by electret (12  $\mu\text{m}$  thick aluminized Teflon<sup>®</sup>) transducers (see Sect. 6.3.3) [16]. One electret transducer is used as a microphone and the other as a speaker. A slot at the resonator's midplane allows the resonator to sample the helium gas flowing through the recovery line without degrading the resonator's quality factor. The system is maintained at its fundamental resonance frequency by applying the amplified microphone output to the speaker through an inductor tuned to the electret speaker's electrical capacitance. (In a public address system, this would be considered feedback squeal.) A 37 m coil of #44 copper wire ( $R_T \cong 350 \Omega$ ) is epoxied to the resonator and is used as a thermometer. A frequency-to-voltage conversion (tachometer) chip [17] produces a dc voltage proportional to the resonance frequency that is summed with the temperature-dependent voltage produced by  $R_T$  along with an offset voltage that is adjusted when pure helium gas is in the recovery line. If air enters the recovery line, the frequency decreases, and an alarm is activated and the recovery valve is closed [14]

## 10.4 Harmonic Plane Waves and Characteristic Impedance

The linearized first-order Euler Eq. (10.2) can be solved to relate the acoustic fluid (particle) velocity,  $v_1$ , to the acoustic pressure,  $p_1$ . For a harmonic, one-dimensional plane traveling wave, expressed in Eq. (10.14), the ratio of pressure to particle velocity is  $z$ , remembering that  $c = \omega/k$ .

$$z \equiv \left| \frac{p_1}{v_1} \right| = \rho_m c \quad (10.27)$$

This property of a fluid is sufficiently important to be given its own name: the *specific acoustic impedance* or the *characteristic impedance*. The units of specific acoustic impedance are Pa-s/m, also called the *rayl* (sometimes the MKS rayl to distinguish it from the cgs rayl), in honor of the third Lord Rayleigh (J. W. Strutt, 1842–1919).

Another short digression regarding the three impedances used in acoustics is beneficial at this point. We have previously encountered an impedance that we called the acoustic impedance. It was defined as the ratio of the pressure to the volume velocity at one location:  $\mathbf{Z}_{\text{ac}} = \hat{\mathbf{p}}/\hat{\mathbf{U}}$ . That impedance was particularly useful for describing systems that join elements with differing cross-sectional areas (e.g., Helmholtz resonator) to ensure the continuity of mass flow. We will also see that another version, the acoustic transfer impedance,  $\mathbf{Z}_{\text{tr}}$ , will be very useful in problems that involve acoustic radiation and transduction (see Sect. 10.7). The acoustic transfer impedance is given by the pressure at one location (the receiver) divided by the volume velocity produced at the source of sound.

In Eq. (10.27), we have just defined a specific acoustic impedance, the ratio of pressure to particle velocity, which is a property of the acoustic medium and is independent of geometry. It is especially useful in the description of plane waves, particularly when they impinge on boundaries between media with different properties, as will be addressed in detail in Chap. 11. The third impedance is the mechanical impedance,  $\mathbf{Z}_{\text{mech}} = \hat{\mathbf{F}}/\hat{\mathbf{v}}$ . The mechanical impedance is useful for determining the steady-state response of a vibro-mechanical network.

Frequently in acoustics, and particularly for problems involving transduction, these different complex impedances (as well as the electrical impedance,  $\mathbf{Z}_{\text{el}} = \hat{\mathbf{V}}/\hat{\mathbf{I}}$ ) need to be combined to couple an electromechanical system to an acoustical medium. It is easy to relate the three impedances for a system with a characteristic cross-sectional area,  $A$ .

$$\mathbf{Z}_{\text{ac}} = \frac{\hat{\mathbf{p}}}{\hat{\mathbf{U}}} = \frac{\hat{\mathbf{p}}}{A\hat{\mathbf{v}}} = \frac{\hat{\mathbf{F}}/A}{A\hat{\mathbf{v}}} = \frac{\mathbf{Z}_{\text{mech}}}{A^2} \quad \text{and} \quad |\mathbf{Z}_{\text{ac}}| = \frac{z}{A} \quad (10.28)$$

In Eq. (10.28), the pressure amplitude,  $\hat{\mathbf{p}}$ ; volume velocity amplitude,  $\hat{\mathbf{U}}$ ; and particle velocity amplitude,  $\hat{\mathbf{v}}$ , were all complex phasors to emphasize the fact that impedance is a concept that is based on linear acoustics and the assumption of a single-frequency wave-like disturbance from equilibrium.

The specific acoustic impedance,  $z = \rho_m c$ , is convenient for representing the space and time dependence of the acoustic fluid (particle) velocity,  $v_1(x, t)$ , for a traveling wave moving in the positive  $x$  direction. Below, Eq. (10.29) has  $\pm\rho_m c$  in the denominator to remind us that a wave traveling in the minus  $x$  direction would have a negative specific acoustic impedance.

$$v_1(\vec{x}, t) = \frac{p_1(\vec{x}, t)}{\pm\rho_m c} = \Re e \left[ \frac{\hat{\mathbf{p}}}{\pm\rho_m c} e^{j(\omega t \mp \vec{k} \cdot \vec{x})} \right] \quad (10.29)$$

The continuity equation can be used to relate density variations,  $\rho_1(x, t)$ , to the particle velocity,  $v_1(x, t)$ , of a plane wave with the final version restricted to a single-frequency wave.

$$\rho_1(\vec{x}, t) = \rho_m \frac{v_1(\vec{x}, t)}{c} = \frac{1}{c^2} \Re e \left[ \hat{\mathbf{p}} e^{j(\omega t + \vec{k} \cdot \vec{x})} \right] \quad (10.30)$$

The dot product that appears in the spatial dependence within the argument of the exponential functions in Eqs. (10.14) and (10.29) can be expanded into its Cartesian components for an arbitrary choice of directions with respect to the Cartesian axes.

$$p_1(\vec{x}, t) = \Re e \left[ \hat{\mathbf{p}} e^{j(\omega t - k_x x - k_y y - k_z z)} \right] \quad \text{where} \quad \left( \frac{\omega}{c} \right)^2 = k_x^2 + k_y^2 + k_z^2 \quad (10.31)$$

Normally, if a plane wave is propagating in an arbitrary direction, it is easier to re-orient the coordinate axes so that one axis is along the direction of propagation and the one-dimensional expressions will suffice. In an isotropic medium, the wave vector,  $\vec{k}$ , defines a direction that is perpendicular to the wave's planes of constant phase.

## 10.5 Acoustic Energy Density and Intensity

Since our hydrodynamic equations provide a complete description of the fluid, there should be no need to introduce any additional equations to account for the energy density of the fluid or for the acoustical energy transported by the waves. For the nondissipative case, that fact can be demonstrated by combining the continuity equation and the Euler equation in another way.

We start by writing the linearized three-dimensional vector form of the continuity Eq. (8.9), augmented by the equation of state (10.4), as expressed in the one-dimensional version in Eq. (10.5).

$$\frac{\partial \rho_1}{\partial t} + \rho_m \nabla \cdot \vec{v}_1 = \frac{1}{c^2} \frac{\partial p_1}{\partial t} + \rho_m \nabla \cdot \vec{v}_1 = 0 \quad (10.32)$$

The continuity equation can be combined with the linearized three-dimensional vector form of the Euler equation.

$$\rho_m \frac{\partial \vec{v}_1}{\partial t} + \vec{\nabla} p_1 = 0 \quad (10.33)$$

If we take the dot product of  $\vec{v}_1$  with Eq. (10.33) and multiply Eq. (10.32) by  $p_1$  and add the two equations together, we can collect terms if we notice that the product rule (see Sect. 1.1.2) produces the following identities:

$$\vec{v}_1 \cdot \frac{\partial \vec{v}_1}{\partial t} = \frac{1}{2} \frac{\partial v_1^2}{\partial t} \quad \text{and} \quad p_1 \frac{\partial p_1}{\partial t} = \frac{1}{2} \frac{\partial p_1^2}{\partial t} \quad (10.34)$$

We can also exploit the vector version of the product rule for differentiation (see Sect. 1.1.2).

$$\nabla \cdot (p_1 \vec{v}_1) = p_1 \nabla \cdot \vec{v}_1 + \vec{v}_1 \cdot \vec{\nabla} p_1 \quad (10.35)$$

The combination can be expressed as a conservation equation for acoustic energy.

$$\frac{\partial}{\partial t} \left[ \frac{1}{2} \rho_m v_1^2 + \frac{1}{2} \frac{p_1^2}{\rho_m c^2} \right] + \nabla \cdot (\vec{p}_1 \vec{v}_1) = 0 \quad (10.36)$$

As was established in Sect. 7.3.1, when the continuity Eq. (7.32) was first introduced, Eq. (10.36) has the form of a *conservation equation*: it is *the time derivative of a density plus the divergence of a flux*. It is easy to identify the  $(\frac{1}{2})\rho_m v_1^2$  term in Eq. (10.36) as the kinetic energy density of the sound wave; therefore  $(\frac{1}{2})p_1^2/\rho_m c^2$  must be the potential energy density. In this case, the corresponding flux is the *acoustic intensity*,  $I$ .

$$\vec{I} = p_1 \vec{v}_1 \quad (10.37)$$

The energy densities and the intensity are quadratic combinations of first-order acoustic variables. The two energy densities within the square brackets in Eq. (10.36) are positive-definite quantities. Why do we *not* neglect these second-order quantities when, up to this point, we have discarded all second-order quantities? In this case, this second-order quantity is the leading-order contribution. When we linearized other equations, there were linear terms that dominated second-order terms, typically by a factor of  $M_{ac}$ , for example, in Eqs. (8.18) and (8.19). For energetic variables (e.g., energy density, intensity, enthalpy flux), there are no first-order contributions in the absence of steady flow.

In the presence of dissipation, the acoustical energy is not conserved, and Eq. (10.36) would no longer be homogeneous, although it would have the same form:

$$\frac{\partial}{\partial t} E + \nabla \cdot \vec{I} = -D \quad (10.38)$$

In Eq. (10.38),  $E$  is the energy density,  $\vec{I}$  is the (vector) intensity, and  $D$  is a dissipation factor [18].

$$D = \frac{1}{c^2} \left( \frac{4}{3} \mu + \zeta \right) \left| \frac{\partial \vec{v}}{\partial t} \right|^2 + \left( \frac{\gamma - 1}{\gamma} \right) \frac{\kappa}{\rho_m^2 c_p c^4} \left| \frac{\partial p}{\partial t} \right|^2 + \mu \left| \vec{\nabla} \times \vec{v} \right|^2 \quad (10.39)$$

The (irreversible) dissipation created by the shear viscosity,  $\mu$ , and the thermal conductivity,  $\kappa$ , should be familiar from the expressions for boundary-layer losses provided in Eq. (9.34). The first term in Eq. (10.39) introduces a new “viscosity,”  $\zeta$ , which is called a “bulk viscosity” (or also called “second viscosity”). As will be discussed in Sect. 14.5, the bulk viscosity has been added to account for relaxation absorption (e.g., the fact that it takes some non-zero time for the Equipartition Theorem to distribute energy equitably between translational and rotational degrees of freedom) [19]. The second term in Eq. (10.39), proportional to the thermal conductivity,  $\kappa$ , is obviously thermal loss, since it contains  $(\gamma - 1)/\gamma$  as a coefficient and is proportional to the square of the acoustic pressure. The final term arises from (rotational) flow with non-zero curl, such as the shear produced in the viscous boundary layer that was calculated in Sect. 9.4.3.

### 10.5.1 Decibel Scales

The Bell Telephone Laboratories developed much of the “modern” (twentieth-century) science of acoustics and its implementation in engineering practice. For almost a century, Bell Telephone (renamed AT&T in 1899) enjoyed a telecommunications monopoly within the United States. This allowed the company to recoup its investment in equipment and capital improvements like buildings, poles, purchased right-of-way, etc. Eventually (1913), the US Government put a cap on Bell’s profits, limiting them to 10% after taxes. To operate under this lower margin, Bell invested “excess profits” by

spending them on research and development within two of its subsidiaries: Bell Laboratories and Western Electric. Despite this cap on profits, Bell became one of the most successful companies in the history of the world. It was the largest US corporation until a forced divestiture was imposed by the US Congress in 1984.

Most of us are more familiar with the later Nobel Prize winning research accomplishments of Bell Labs. The best-known of these is the invention of the transistor (Bardeen, Brittan, and Shockley, 1947) and the invention of the laser (Schawlow and Townes, 1948). Also credited to Bell Lab scientists are the discovery of local electronic states in solids (Anderson Localization, 1977) and the discovery of the 4 K residual cosmic black-body background radiation left over from the “Big Bang” (Penzias and Wilson, 1978), as well as acoustical engineering advances that did not receive the Nobel, such as the electret microphone (Sessler and West 1964). More recent Nobel Prizes include optical trapping (Chu 1997)<sup>6</sup> and the quantum Hall effect (Stormer 1998).

During the interval between the two world wars, many of the engineering concepts we use today evolved from research at Bell Labs that were directed toward the commercialization of a worldwide telecommunication network. The later research involved major advances in digital electronics including the “sampling theorem” of Claude Shannon (1948), the concept of digital filters introduced by R. W. Hamming (1977), and the fast Fourier transform by John Tukey (1965), along with the development of the UNIX operating system (1971). Before the advent of digital electronics, Bell Labs did the systems engineering that started with the characterization of vocalization and auditory perception (Fletcher and Munson, see Fig. 10.5) and carried through with the competition between transmission loss and amplification<sup>7</sup> required to transmit human voices around the world. The focus on the competition between amplifier gain and transmission loss led to the introduction of the decibel.

The decibel (abbreviated dB) was introduced by Bell Labs engineers to quantify the reduction in audio level over a 1-mile length of standard telephone cable. It was originally called the transmission unit, or TU, but was renamed in 1923 or 1924 in honor of the laboratory’s founder and telecommunications pioneer, A. G. Bell. Before the days of hand-held electronic calculators, it was easier to add or subtract logarithms than it was to multiply long strings of gain and loss factors.

Although there are periodic debates about whether or not to dispose of the decibel, in acoustics it is unlikely that the decibel will disappear during the span of your career [20]. One reason for the decibel’s persistence into the age of digital electronics is physiological. The dynamic range of human hearing covers about 14 orders of magnitude in intensity. In some sense, sound pressure levels expressed in decibels provide a “centigrade scale” for sound levels that nicely matches human auditory experience; 0 dB<sub>SPL</sub> is about the quietest sound a human can detect, and 100 dB<sub>SPL</sub> is about as loud a sound as we can tolerate.

By far, the most important feature of the decibel is that *the decibel is always a base-10 logarithmic measure of a ratio, never a ratio itself.*

The intensity level,  $IL$ , is expressed in decibels.

---

<sup>6</sup> In acoustics, the equivalent of “optical trapping” is acoustical levitation superstability (see Sect. 15.4.7): M. Barmatz and S. L. Garrett, “Stabilization and oscillation of an acoustically levitated object,” US Pat. No. 4,773,266 (Sept. 27, 1988).

<sup>7</sup> In my estimation, one of the most significant engineering breakthroughs of the twentieth century was the invention, by Harold S. Black (1899–1983) at Bell Labs, of the negative feedback amplifier in 1928. In Black’s own words, “Our patent application was treated in the same manner as one for a perpetual-motion machine. In a climate where more gain was better, the concept that one would throw away gain to improve stability, bandwidth, etc., was inconceivable before that time.”

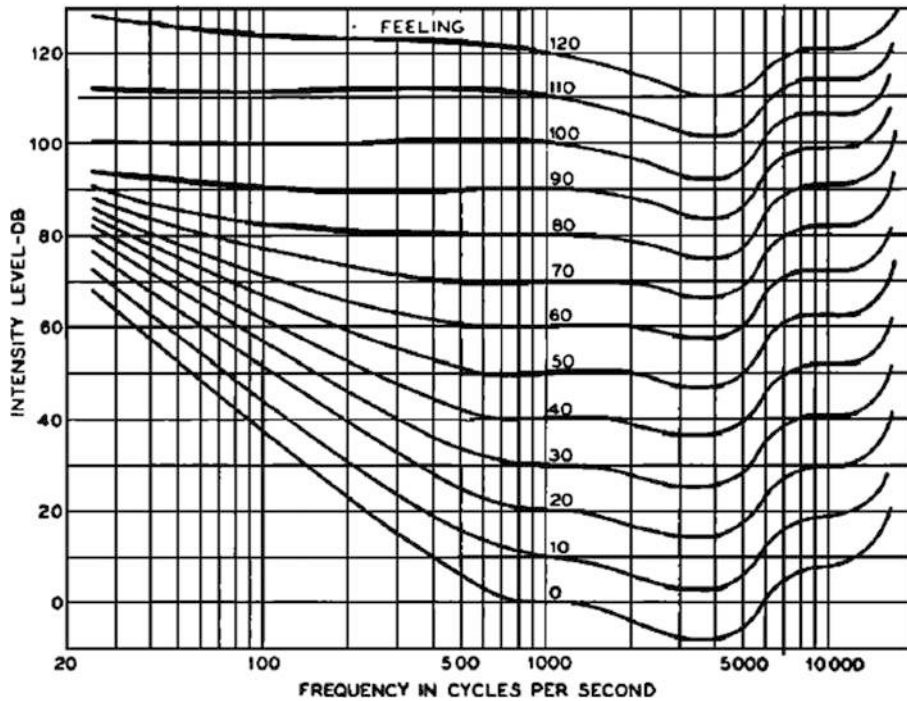


**Fig. 10.5** The equal-loudness contours, known as the Fletcher-Munson curves, are taken from [21]. The solid lines correspond to the intensity of sound in air, in dB re:  $1 \text{ pW/m}^2$ , which is required to produce a perceived loudness equal to that of a  $1.0 \text{ kHz}$  tone with the same intensity level. That “loudness level” is called the “phon.” To produce a loudness level of 60 phon, at  $1.0 \text{ kHz}$ , the sound pressure level would be  $60 \text{ dB}_{\text{SPL}}$ . The “0 dB” curve is often called the “threshold of hearing,” and the “120 dB” curve is called the “the threshold of feeling”

$$IL = 10 \log_{10} \left( \frac{I}{I_{ref}} \right) \quad (10.40)$$

The time-averaged acoustic intensity,  $I = \langle p_1 v_1 \rangle_t$ , is defined by the energy conservation Eq. (10.36). The time-averaged *reference intensity*,  $I_{ref}$ , used to define  $IL$  in Eq. (10.40), will depend upon the situation. For sound in air,  $I_{ref} \equiv 10^{-12} \text{ W/m}^2 = 1 \text{ pW/m}^2$ . Using our definition of specific acoustic impedance for plane waves in Eq. (10.27), the value of the specific acoustic impedance in dry air is  $z = \rho_m c = 413.3 \text{ Pa}\cdot\text{sec}/\text{m}$  (rayls) at  $20^\circ\text{C}$ , so  $I_{ref}$  can also be expressed in terms of the root-mean-squared pressure,  $p_{rms}$ , of sound.

$$I = \langle p_1 v_1 \rangle_{time} = \frac{1}{2} p_1 \frac{p_1}{\rho_m c} = \frac{p_{rms}^2}{\rho_m c} \quad (10.41)$$

In Eq. (10.41), we let  $p_{rms} = p_1 / \sqrt{2}$  by assuming that the pressure was varying sinusoidally in time.<sup>8</sup> If that is the case, then  $I_{ref}$  corresponds to a root-mean-squared pressure amplitude,  $p_{rms} = 20.33 \mu\text{Pa}_{rms}$ . For convenience, the *reference sound pressure* in air is defined as  $P_{ref} \equiv 20 \mu\text{Pa}_{rms}$ .

<sup>8</sup> The “true” definition of a root-mean-squared (rms) amplitude is always tied to the power associated with that amplitude. To account for non-sinusoidal waveforms, engineers introduce a dimensionless “crest factor,” CF, that is defined as the ratio of the peak value of a waveform to its rms value. For a sine waveform, CF (sine) =  $\sqrt{2}$ , for a triangular waveform, CF (triangle) =  $\sqrt{3}$ , and for a half-wave rectified sinewave, CF (half-wave rectified) = 2. Most instruments that claim to measure the “true rms” value of a parameter (e.g., voltage) will exhibit an accuracy that decreases with increasing crest factor. For measurement of Gaussian noise, instruments that tolerate  $3 < CF < 5$  are usually adequate.

The concept of sound pressure level, expressed in decibels, appeared in Chap. 7 to describe the amplitude of a dangerously loud sound: 115 dB<sub>SPL</sub>.

$$dB_{SPL} = 20 \log_{10} \left( \frac{P_{rms}}{P_{ref}} \right) \quad (10.42)$$

The fact that the base-ten logarithm in Eq. (10.42) is multiplied by 20 instead of 10, as in Eq. (10.40), reflects the definition of *the decibel as the base-10 logarithm of a power or intensity ratio, even when its value is determined by the ratio of amplitudes.*

If the decibel is used to express an amplitude-independent ratio (like the gain of an amplifier or the attenuation of a filter), then a reference level is not required, but the ratio must still be the logarithm of a power or energy ratio. For example, if the voltage gain of an amplifier is ten, then that gain can be expressed as  $20\log_{10}(10) = +20$  dB.

When a decibel refers to an absolute measurement, then it is important to include the reference along with the reported value. That can be accomplished in several ways. One is the subscript used for 115 dB<sub>SPL</sub> that implied that  $P_{ref} = 20 \mu\text{Pa}_{rms}$  for sound pressure levels (SPL). The preferred method is always to explicitly include the reference: 115 dB re: 20  $\mu\text{Pa}_{rms}$ .

There are several frequency-weighting schemes that are used to produce a dB level that reflects the (amplitude-dependent!) frequency response of human hearing that will be addressed in Sect. 10.5.3.<sup>9</sup> For example, an A-weighted sound pressure level ( $L_A$ ) can be expressed as 115 dB(A) or 115 dB<sub>A</sub>.

### 10.5.2 Superposition of Sound Levels (Rule for Adding Decibels)

As just mentioned, the decibel was introduced to turn a multiplicative string of gains and losses into an arithmetic sum. When it comes to the superposition of sound fields, the decibel must be employed with extreme care!

If we add two sound sources, each with a sound pressure level of 60 dB<sub>SPL</sub>, the result is either 63 dB<sub>SPL</sub> if the sources are *incoherent*, since their powers add, or as much as 66 dB<sub>SPL</sub> if the sources are *coherent* (having the same frequency) and in-phase, since their pressures would add. If the sources are coherent and out-of-phase, there may be no sound at all. *In no case will the sum of two 60 dB<sub>SPL</sub> sources ever result in 120 dB<sub>SPL</sub>!*

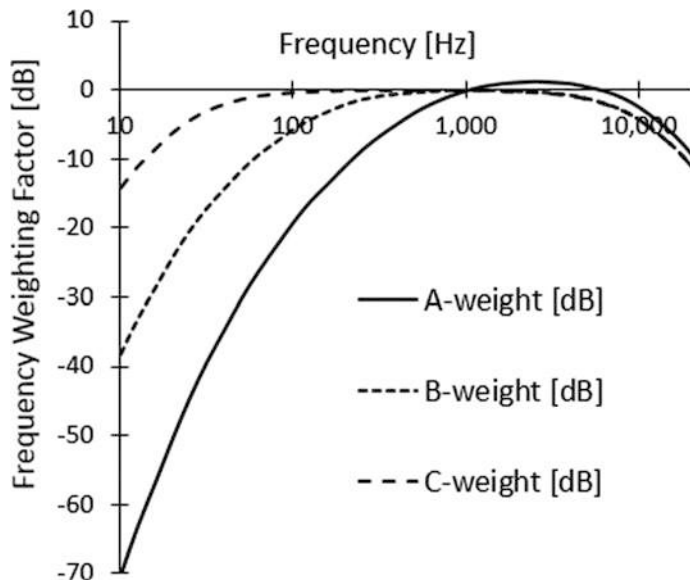
### 10.5.3 Anthropomorphic Frequency Weighting of Sound Levels

It is common to assert that healthy humans can detect sound with frequencies ranging from 20 Hz to 20 kHz, but the sensitivity of human hearing is very dependent upon both frequency and amplitude, as well as on the listener's age, health, and prior exposure to loud sounds. The frequency dependence of human hearing is represented by *equal-loudness contours* that were first measured by Fletcher and Munson at Bell Labs in 1933 [21]. Subsequent determinations were made to produce equal-loudness contours that specified the auditory acuity of different age groups [22], and consensus contours have been codified in an international standard [23]. For our present purposes, the *Fletcher-Munson curves*, shown in Fig. 10.5, provide an illustration of the amplitude dependence of the normal frequency dependence of human hearing, although more recent determinations exist [24].

---

<sup>9</sup>The weighting of A, B, C, and D (no weighting) levels are specified in several international standards, for example, the International Standards Organization (ISO) 3746:2010, and are plotted in Fig. 10.6.

**Fig. 10.6** Frequency-weighting factors for specification of sound level meter responses to simulate human loudness perception as specified in ANSI 1.4-1983. [25] The A-weighting was intended for sounds with intensities lower than  $55 \text{ dB}_{\text{SPL}}$  and the C-weighting for sounds with intensities above  $85 \text{ dB}_{\text{SPL}}$ . The B-weighting was intended for levels between the A and C limits but has been utilized very rarely



Examination of Fig. 10.5 suggests that “normal” human hearing is most sensitive at frequencies between 3 kHz and 4 kHz (near the  $\lambda/4$  resonance of the ear canal<sup>10</sup>) and that sensitivity degrades at higher and lower frequencies. The curves also demonstrate that there is less frequency dependence at higher sound levels. We are nearly 60 dB less sensitive to a tone at 40 Hz as we are to a tone of the same intensity at 1 kHz near the threshold of hearing, but our sensitivity is nearly frequency independent between 20 Hz and 1.0 kHz if the intensity of the tone is 100 dB *re*:  $20 \mu\text{Pa}_{\text{rms}}$ .

The contours (i.e., solid lines) in Fig. 10.5 are labeled with the sound pressure level of a 1.0 kHz tone. Those contours define a loudness level with the unit of “phons.” A 1.0 kHz tone with a sound pressure level of 60 dB *re*:  $20 \mu\text{Pa}_{\text{rms}}$  would be perceived as having a loudness equal to a 40 Hz tone with a sound pressure level of 80 dB *re*:  $20 \mu\text{Pa}_{\text{rms}}$ ; both would have a loudness of 60 phons.

When attempting to quantify the perceived loudness of a tone, it would be convenient to have a way to express the loudness of a tone that takes human perception into account. Early attempts to create a metric that includes that frequency dependence, shown in Fig. 10.5, introduced three frequency-weighting schemes to simulate hearing acuity at three different levels. These weighting schemes were called A-weighted for levels below  $55 \text{ dB}_{\text{SPL}}$ , B-weighted for sounds greater than  $55 \text{ dB}_{\text{SPL}}$  but less than  $85 \text{ dB}_{\text{SPL}}$ , and C-weighted sound pressure levels for sounds with intensities in excess of  $85 \text{ dB}_{\text{SPL}}$ . These filter functions were standardized for the design of sound level meters [25] and are shown in Fig. 10.6.

The frequency-weighting standard [25] also includes tolerances for the levels that must be met by a Type-0 (laboratory quality), a Type-1 (field measurement), and a Type-2 (general purpose) sound level meter, as well as three exponential integration intervals: fast ( $\tau = 125 \text{ ms}$ ), slow ( $\tau = 1.0 \text{ s}$ ), and impulse (rise time,  $\tau_{\uparrow} = 35 \text{ ms}$  and release time constant,  $\tau_{\downarrow} = 1.5 \text{ s}$ .) As a practical matter, the standard also provides an implementation of the frequency weighting using passive R-C filter networks.

Such frequency-weighted metrics are usually designated dB(A) or  $\text{dB}_A$  and dB(C) or  $\text{dB}_C$ . Over time, the use of B-weighting has fallen out of favor, and frequently A-weighting is used regardless of

<sup>10</sup> The transfer function for sound pressure at the eardrum to the sound pressure presented to the outer ear is above 14 dB of gain from 2.5 to 3.2 kHz as shown in Table 2 of the ANSI-ASA S3.4 Standard.

the intensity of the sound being measured. In some instances, particularly with measurement of airport noise [26], the difference between the dB(A) and dB(C) levels are used to quantify the presence of low-frequency signals.

The frequency-weighting scheme used for sound level meters was just the first attempt to relate physical measurements to human auditory perception. In many cases, that metric is used to predict the level of annoyance produced by unwanted sounds (noise) [27] or the reduction in speech intelligibility in the presence of background noise [28]. Many other metrics have been established to correlate annoyance to the sound amplitude, frequency, and intermittency of noise sources, but almost all involve measurement of A-weighted levels. Sounds that may not be annoying during the day or at work might produce stress and interrupt sleep if they occur during the evening or nighttime. Various metrics provide algorithms for combining levels measured as a function of time.

Several metrics, in addition to the A-weighted level, have been adopted by the US Environmental Protection Agency (EPA) for annoyance assessment. The Equivalent Sound Level,  $L_{eq}$ , is just the time averaged, A-weighted sound pressure,  $p_A$ , using  $P_{ref} = 20 \mu\text{Pa}_{\text{rms}}$ .

$$L_{eq} = 10 \log_{10} \left[ \frac{1}{T} \int_0^T \frac{p_A^2}{P_{ref}^2} dt \right] \quad (10.43)$$

The time interval,  $T$ , for calculation of this average is not specified. For the Day-Night Sound Level,  $L_{dn}$ , the calculation period is 24 h, and an additional 10 dB is added to the measured  $L_{eq}$  for hours between 10:00 pm (22h00) and 7:00 am (07h00), to calculate  $L_{dn}$ .

$$L_{dn} = 10 \log_{10} \left\{ \frac{1}{24} \left[ 15 \left( 10^{L_d/10} \right) \right] + \left[ 9 \left( 10^{[L_n+10]/10} \right) \right] \right\} \quad (10.44)$$

A further refinement, which attempts to better predict the community response to noise [26], introduces a 5 dB boost to A-weighted levels measured in the evening between 7:00 pm (19 h00) and 10:00 pm (22 h00), resulting in a sum similar to Eq. (10.44) that produces the Community Noise Equivalent Level (CNEL), also known as the Day Evening Night Sound Level,  $L_{den}$ . For a continuous sound level of 60 dB<sub>A</sub>,  $L_{eq} = 60 \text{ dB}$ ,  $L_{dn} = 64.4 \text{ dB}$ , and  $L_{den} = 66.7 \text{ dB}$ .

A detailed investigation of such annoyance metrics is beyond the scope of this textbook, but an understanding of these frequency-weighted sound levels forms the basis for understanding most other metrics.

## 10.6 Standing Waves in Rigidly Terminated Tubes

Based on our experience describing standing waves on strings with idealized boundary conditions in Sect. 3.3.1, it is easy to calculate the standing wave modal frequencies for a tube of length,  $L$ , and cross-sectional area,  $A$ , if  $(A)^{1/2} \ll \lambda$ . Under such circumstances, all of the fluid motion within the tube will be longitudinal, thus parallel to the tube's axis.<sup>11</sup> When more than one of an enclosure's dimensions is comparable to the wavelength of sound,  $\lambda$ , then the sound within such an enclosure

<sup>11</sup> When we include thermoviscous dissipation on the walls of the tube, the velocity will not be constant throughout the tube's cross-section, since the no-slip boundary condition for a viscous fluid requires that the longitudinal velocity vanish at the tube's walls. In many cases, the ratio of the viscous penetration depth,  $\delta_v$ , to the tube's radius,  $a$ , is small,  $\delta_v \ll a$ , so the flow velocity is nearly uniform throughout most of the tube's cross-section. The thermal effects near the wall increase the compressibility of the gas (see Sect. 9.3.2), so they also create a small velocity perpendicular to the wall.

can no longer be considered “one-dimensional.” Such three-dimensional enclosures will be analyzed systematically in Chap. 13.

For simplicity, this section will focus on a rigid tube that is circular in cross-section, so that  $A = \pi a^2$ , where  $a$  is the circular tube’s radius. If the tube has rigid end caps at both ends,  $x = 0$  and  $x = L$ , then the fluid cannot penetrate the ends so  $v_1(0, t) = v_1(L, t) = 0$  for all times,  $t$ . Since  $v_1(x, t)$  will obey the wave Eq. (10.12), a standing wave solution, like that for  $p_1(x, t)$  in Eq. (10.15), can be written which automatically satisfies the boundary condition at  $x = 0$ .

$$v_1(x, t) = \Re e[\hat{\mathbf{v}} \sin(kx)e^{j\omega t}] \quad (10.45)$$

Repeating our experience with the fixed-fixed string in Sect. 3.1.1, the acceptable values for the wavenumber,  $k_n$ , are quantized by imposition of the boundary condition at  $x = L$ .

$$\sin(k_n L) = 0 \Rightarrow k_n L = n\pi \quad \text{for } n = 1, 2, 3, \dots \quad (10.46)$$

The frequencies of the standing wave (normal) modes in the tube are therefore also restricted to discrete values,  $f_n = n(c/2L)$ .

$$2\pi f_n = \omega_n = k_n c = \frac{n\pi c}{L} \Rightarrow \lambda_n = \frac{2L}{n} \quad \text{or} \quad L = n\left(\frac{\lambda_n}{2}\right) \quad (10.47)$$

The physical interpretation of this result is identical to the one provided for the modes of a fixed-fixed string: the normal mode shapes correspond to placing  $n$  sinusoidal half-wavelengths within the overall length of the tube,  $L$ . Substitution of these normal mode frequencies,  $\omega_n$ , and wavenumbers,  $k_n$ , into the functional form of Eq. (10.45) provides the description of the shapes,  $\hat{\mathbf{v}}_n(x)$ , for each of the normal modes.

$$\hat{\mathbf{v}}_n(x) = C_n \sin\left(n\frac{\pi x}{L}\right); \quad n = 1, 2, 3, \dots \quad (10.48)$$

In this form,  $C_n$  is a real scalar velocity amplitude for each mode that will be determined by the amplitude of excitation for that mode. (We could let the  $C_n$  be complex if we are considering the superposition of several modes, each having its own time phase.)

Having the explicit solution of Eq. (10.48) for the space and time distribution of the longitudinal particle velocity of the fluid, the pressure distribution,  $p_1(x, t)$ , can be determined from Euler’s equation.

$$\vec{\nabla} p_1 = \frac{\partial p_1}{\partial x} = -\rho_m \frac{\partial v_1}{\partial t} \Rightarrow \frac{\partial \hat{\mathbf{p}}_n}{\partial x} = -j\rho_m \omega_n C_n \sin(k_n x) \quad (10.49)$$

Integrating both sides of Eq. (10.49) over  $x$  produces the expressions for the distribution of pressure within the rigidly terminated tube.

$$\begin{aligned} \int \frac{\partial \hat{\mathbf{p}}_n}{\partial x} dx &= \hat{\mathbf{p}}_n(x) = -j\rho_m \omega_n C_n \int \sin(k_n x) dx \\ &= \frac{j\rho_m \omega_n C_n}{k_n} \cos(k_n x) \Rightarrow \hat{\mathbf{p}}_n(x) = j(\rho_m c) C_n \cos(k_n x) \end{aligned} \quad (10.50)$$

The appearance of  $\cos(k_n x)$  in this result for  $\hat{\mathbf{p}}_n(x)$  indicates that there will be pressure maxima (anti-nodes) at both boundaries. The “ $j$ ” indicates that the acoustic pressure will be  $90^\circ$  out of phase with the velocity, so that when the pressure reaches its maximum, the velocity will everywhere be zero,

and vice versa; when the fluid's longitudinal particle velocity is the greatest, the acoustic pressure throughout the resonator will be zero.

For a tube that is open on both ends, the solutions to the wave equation produce resonance frequencies,  $f_n$ , that are identical to those for longitudinal waves in a free-free bar presented in Eq. (5.13), except it is  $p_1(0, t) = p_1(L, t) = 0$ .

$$\begin{aligned}\hat{\mathbf{v}}_n(x) &= C_n \cos(k_n x) \text{ with } k_n = \frac{n\pi}{L} \Rightarrow f_n = n \frac{c}{2L}; \quad n = 1, 2, 3, \dots \\ \hat{\mathbf{p}}_n(x) &= j(\rho_m c) C_n \sin(k_n x)\end{aligned}\quad (10.51)$$

In reality, the open-end condition is not exactly “pressure released.” Thinking back to our investigations of the natural frequency of a Helmholtz resonator in Sect. 8.5, we needed to add an “effective length” to the open end of a tube. The same will be true for standing waves in narrow tubes for which  $a \ll \lambda$ . That effective length correction will be discussed in Sects. 12.8 and 12.9. For the moment, we could use a correction that extends the length of an open tube by  $0.613a$ , as given in Eq. (12.133), if there are no other constraints on the flows in, out, or around the “open end.”

### 10.6.1 Quality Factor in a Standing Wave Resonator

Using the definitions of kinetic and potential energy density produced by the energy conservation Eq. (10.36), when the acoustic pressure is zero throughout the resonator, all of the energy will be kinetic, and when the velocity is zero everywhere, all the energy will be potential. The sum of the kinetic and potential energies at any instant will be constant. These facts can be exploited to calculate the quality factors,  $Q_n$ , for the  $n$ th plane wave mode of a resonator, based on the expression for thermoviscous boundary layer losses in Eq. (9.38).

The sum of the kinetic and potential energies,  $E_{tot}$ , at any instant will be constant:  $E_{tot} = (KE)_{max} = (PE)_{max}$ . To evaluate the  $Q$  due to viscous losses along the cylindrical surface of the resonator, it is convenient to calculate the maximum kinetic energy by integrating the maximum kinetic energy density throughout the volume of the resonator using the expression for the acoustic fluid velocity in Eq. (10.48).

$$(KE)_{max} = \frac{\rho_m C_n^2 \pi a^2}{2} \int_0^L \sin^2\left(n \frac{\pi x}{L}\right) dx = \frac{\pi a^2 L \rho_m C_n^2}{4} \quad (10.52)$$

From Eq. (9.37), the power dissipated by viscous shear at the resonator's walls, with surface area,  $S = 2\pi aL$ , will also be given by an integral of the fluid's particle velocity from Eq. (10.48).

$$\langle \Pi_{vis} \rangle_t = \frac{\rho_m \delta_\nu \omega}{4} 2\pi a C_n^2 \int_0^L \sin^2\left(n \frac{\pi x}{L}\right) dx = \frac{\rho_m \delta_\nu \omega}{4} \pi a L C_n^2 \quad (10.53)$$

The viscous contribution to the quality factor,  $Q_{vis}$ , will just be the radian frequency,  $\omega$ , times the ratio of the stored energy, given in Eq. (10.52), to the time-averaged power dissipation in Eq. (10.53), as expressed in Eq. (B.2).

$$Q_{vis} = \frac{\omega E_{Stored}}{\langle \Pi_{vis} \rangle_t} = \omega \left( \frac{\pi a^2 L \rho_m C_n^2}{4} \right) \left( \frac{\rho_m \delta_\nu \omega}{4} \pi a L C_n^2 \right)^{-1} = \frac{a}{\delta_\nu} \quad (10.54)$$

As expected for a linear system, the excitation amplitude of the modes,  $C_n$ , cancels, and we are left with a very simple expression that is identical to the result for  $Q_{vis}$  due to viscous shear in the neck of a

Helmholtz resonator, given in Eq. (9.44). Based on the definition of the viscous penetration depth,  $\delta_\nu = \sqrt{2\mu/\rho_m\omega}$ , in Eq. (9.33), the viscous quality factor will increase with the square root of the modal frequency,  $f_n = \omega_n/2\pi$ .

The calculation can be repeated for the thermal relaxation losses on the resonator's surface. Assuming the resonator is made from a material that has a much higher “accessible” heat capacity than the ideal gas which fills it, Eq. (9.23) can be used to calculate the time-averaged thermal power dissipation on the resonator's cylindrical surface,  $\langle \Pi_{th} \rangle_t$ .

$$\begin{aligned}\langle \Pi_{th} \rangle_t &= \frac{(\gamma - 1)}{4\gamma} \delta_\kappa \omega \frac{(\rho_m c)^2 C_n^2}{p_m} (2\pi a) \int_0^L \cos^2\left(n \frac{\pi x}{L}\right) dx \\ &= \frac{(\gamma - 1)}{4\gamma} \frac{(\rho_m c)^2 C_n^2}{p_m} \delta_\kappa \omega \pi a L = \frac{(\gamma - 1)}{4} \rho_m \delta_\kappa \omega C_n^2 \pi a L\end{aligned}\quad (10.55)$$

The final version in Eq. (10.55) makes use of the fact that for adiabatic sound waves in ideal gases,  $c^2 = \gamma p_m / \rho_m$ . The expression for  $E_{tot} = (KE)_{max}$  from Eq. (10.52) will serve nicely here for calculation of  $Q_{th}$ .

$$Q_{th} = \frac{\omega E_{Stored}}{\langle \Pi_{th} \rangle_t} = \omega \frac{\left( \frac{\pi a^2 L \rho_m C_n^2}{4} \right)}{\left( \frac{(\gamma - 1)}{4} \rho_m \delta_\kappa \omega C_n^2 \pi a L \right)} = \frac{1}{(\gamma - 1)} \frac{a}{\delta_\kappa} \quad (10.56)$$

Although there is no viscous shear on the resonator's rigid end caps, since the fluid's particle velocity is normal to their surfaces, there are still thermal relaxation losses since both rigid ends are always pressure anti-nodes where the fluid will experience the maximum adiabatic temperature variations. The calculation for  $Q_{ends}$  is identical to Eq. (10.54) except that the pressure does not have to be averaged along the  $x$  direction.

$$\langle \Pi_{th} \rangle_{ends} = 2 \frac{(\gamma - 1)}{4\gamma} \delta_\kappa \omega \frac{(\rho_m c)^2 C_n^2}{p_m} (\pi a^2) = \frac{(\gamma - 1)}{2} \rho_m \delta_\kappa \omega C_n^2 (\pi a^2) \quad (10.57)$$

$$Q_{ends} = \omega \left( \frac{\pi a^2 L \rho_m C_n^2}{4} \right) \left( \frac{(\gamma - 1)}{2} \rho_m \delta_\kappa \omega C_n^2 (\pi a^2) \right)^{-1} = \frac{1}{2(\gamma - 1)} \frac{L}{\delta_\kappa} \quad (10.58)$$

Since the dissipation is additive, the total quality factor,  $Q_{tot}$ , will require the parallel combination of the three individual contributions to the quality factor.

$$\frac{1}{Q_{tot}} = \frac{1}{Q_{vis}} + \frac{1}{Q_{th}} + \frac{1}{Q_{ends}} \quad (10.59)$$

In this derivation, it is assumed that the resonator's walls and end caps are made of a material that holds those surfaces strictly isothermal. The dimensionless ratio,  $\epsilon_s = \rho_s c_p \delta_\kappa / \rho_s c_s \delta_s$ , determines how close the resonator's boundaries are to enforcing isothermality at the solid-fluid interface where  $\rho_s$ ,  $c_s$ , and  $\delta_s$  are the density, specific heat, and thermal penetration depths for the solid. If  $\epsilon_s \ll 1$ , then the solid-fluid interface remains isothermal. If not, then the quality factor must include  $\epsilon_s$  [29].

$$\frac{1}{Q} = \frac{\delta_\nu}{a} + \frac{(\gamma - 1)}{(1 + \epsilon_s)} \frac{\delta_\kappa}{a} + \frac{(\gamma - 1)}{(1 + \epsilon_s)} \frac{2\delta_\kappa}{L} \quad (10.60)$$

### 10.6.2 Resonance Frequency in Closed-Open Tubes

The resonance frequencies of a closed-open tube are analogous to those of the fixed-free string of Sect. 3.3.1. Again, ignoring the need to apply an effective length correction to the open end of the tube, the expression for the standing wave solutions is identical to Eq. (3.24) and results in successive modes corresponding to an odd-integer number of quarter wavelengths equal to the length of the resonator,  $L$ , if we assume that the rigid end of the resonator is located at  $x = 0$  and the open end is at  $x = L$ .

$$\begin{aligned}\hat{\mathbf{v}}_n(x) &= C_n \sin(k_n x) \\ \hat{\mathbf{p}}_n(x) &= j(\rho_m c) C_n \cos(k_n x) \\ k_n &= \frac{(2n-1)\pi}{2L} \Rightarrow f_n = (2n-1) \frac{c}{4L}; \quad n = 1, 2, 3, \dots\end{aligned}\tag{10.61}$$

For the closed-open tube, the expression for the quality factor in Eq. (10.59) requires an additional term to account for radiation losses (see footnote 24 in Chap. 8),  $Q_{rad}$ , and thermal relaxation loss only occurs at the closed end,  $Q_{end}$ .

$$\frac{1}{Q_{tot}} = \frac{1}{Q_{vis}} + \frac{1}{Q_h} + \frac{1}{Q_{end}} + \frac{1}{Q_{rad}}\tag{10.62}$$

---

### 10.7 Driven Plane Wave Resonators

As we have done throughout this textbook, after the normal modes have been calculated, our attention has shifted to the excitation of those modes. Once again, the steady-state response will be determined by an impedance. In this case, the appropriate impedance will be the *acoustic transfer impedance*,  $\mathbf{Z}_{tr} = \hat{\mathbf{p}}_M / \hat{\mathbf{U}}_S$ . The acoustic impedance,  $\mathbf{Z}_{ac} = \hat{\mathbf{p}} / \hat{\mathbf{U}}$ , was introduced in Chap. 8 during our investigation of lumped elements and the Helmholtz resonator because pressure and volume velocity were continuous across the junctions between lumped elements, even if their cross-sectional areas were different. The acoustic transfer impedance,  $\mathbf{Z}_{tr}$ , simply relates the pressure at one location (labeled the microphone location),  $\hat{\mathbf{p}}_M$ , presumably a place where a microphone or other pressure transducer is located, to the volume velocity,  $\hat{\mathbf{U}}_S$ , produced at a different (source) location, typically where the sound is being generated.

For a plane wave resonator of constant cross-sectional area, the acoustic transfer impedance at resonance can be calculated directly from the definition of the quality factor,  $Q_n$ , of the  $n$ th mode, given in Appendix B, used earlier in Eq. (10.54) and reproduced below.

$$Q = 2\pi \frac{E_{stored}}{E_{dissipated/cycle}} = \frac{\omega E_{stored}}{\langle \Pi_{dissipated} \rangle_t}\tag{10.63}$$

At steady state, the time-averaged power dissipation must be equal to the power produced by the driver. For simplicity, we will treat the driver as a source of volume velocity, located at  $x = L$ , as shown in Fig. 10.9,  $\hat{\mathbf{U}}_S(L) = \hat{\mathbf{x}}(L)A_{pist} = \hat{\mathbf{v}}(L)A_{pist}$ , where we have assumed that the volume velocity source is a rigid piston located at  $x = L$ , having area,  $A_{pist}$ , with the longitudinal speed,  $\dot{x}(L)$ , of that piston being everywhere uniform at its surface.

As before, at resonance, the phase angle,  $\phi$ , between  $\hat{\mathbf{p}}_M$  and  $\hat{\mathbf{U}}_S$ , will be zero, so the power produced by the piston working against the acoustic pressure is simply  $\langle \Pi \rangle_t = (\frac{1}{2})|\hat{\mathbf{p}}_M||\hat{\mathbf{U}}_S|$ , remembering that

$\hat{\mathbf{p}}_M$  and  $\hat{U}_S$  are peak amplitudes and that a sinusoidal time dependence has been assumed for both variables.<sup>12</sup>

The potential energy stored in the plane wave resonator can be calculated in the same way as the stored kinetic energy was calculated in Eq. (10.52), but in this case, we integrate the potential energy density,  $(\frac{1}{2})|\hat{\mathbf{p}}(x)|^2/(\rho_m c^2)$ , based on Eq. (10.36), over the resonator's volume,  $V_{res}$ . For simplicity, we will assume a cylindrical resonator with constant radius,  $a$ , and overall length,  $L$ .

$$(PE)_{max} = \frac{\pi a^2}{2\rho_m c^2} |\hat{\mathbf{p}}_M|^2 \int_0^L \cos^2\left(n \frac{\pi x}{L}\right) dx = \frac{\pi a^2 L}{4\rho_m c^2} |\hat{\mathbf{p}}_M|^2 = \frac{V_{res}}{4\gamma p_m} |\hat{\mathbf{p}}_M|^2 \quad (10.64)$$

Substituting  $|\hat{\mathbf{p}}_M| = |\hat{\mathbf{p}}_n| = (\rho_m c) C_n$  shows that Eq. (10.64) and Eq. (10.52) are identical, illustrating the fact that all of the energy stored in a standing wave changes back and forth between kinetic energy and potential energy.

The rightmost term in Eq. (10.64) assumes the resonator, having an internal volume,  $V_{res} = \pi a^2 L$ , is filled with an ideal gas, so that  $c^2 = \gamma p_m / \rho_m$ . Substitution into Eq. (10.63) produces an expression for the acoustic impedance at the driven end of the resonator at plane wave resonance frequencies,  $f_n$ , with quality factors,  $Q_n$ ,

$$Q_n = \frac{\omega V_{res} |\hat{\mathbf{p}}_M|^2}{4\gamma p_m (\frac{1}{2}) |\hat{\mathbf{p}}_M| |\hat{U}_S|} \Rightarrow \mathbf{Z}_{tr} \equiv \frac{\hat{\mathbf{p}}_M}{\hat{U}_S} = \pm \frac{Q_n}{\pi f_n} \frac{\gamma p_m}{V_{res}} \quad (10.65)$$

The “±” in the right-hand version of Eq. (10.65) accounts for the fact that the phase difference between  $\hat{\mathbf{p}}_M$  and  $\hat{U}_S$  alternates by  $180^\circ$  between odd and even modes if the source and receiver are not located at the same end of the resonator.

For reasonably high values of  $Q_n$ , the acoustic pressure amplitudes,  $\hat{\mathbf{p}}_M$ , based on Eq. (10.50), at both ends of a plane wave resonator with rigid terminations (i.e., closed-closed) are equal:  $|\hat{\mathbf{p}}(0)| = |\hat{\mathbf{p}}(L)| = |\hat{\mathbf{p}}_M|$ . In that case, the acoustic transfer impedance and the acoustic impedance are equal:  $\mathbf{Z}_{ac} = \mathbf{Z}_{tr}$ . Equation (10.65) allows us to express the pressure at the ends of the resonator and, by Eq. (10.50), the pressure anywhere in the resonator, in terms of the volume velocity created by the source,  $\hat{U}_S(L)$ .

$$|\hat{\mathbf{p}}(0)| = |\hat{\mathbf{p}}(L)| = |\hat{\mathbf{p}}_M| = \frac{Q_n}{\pi f_n} \frac{\gamma p_m}{V_{res}} |\hat{U}_S(L)| \quad \text{for } Q_n \gg 1 \quad (10.66)$$

It is possible to measure both the resonance frequencies,  $f_n$ , predicted by Eq. (10.47), and the quality factors,  $Q_n$ , predicted by Eq. (10.59), in conjunction with Eqs. (10.54) and (10.58), if the sound source and receiver are both fairly rigid themselves. Aluminized Teflon™ electret material (typically 6–12 microns thick) placed against a rigid backplate provides an excellent approximation to the rigid end conditions that were assumed in the calculations of Sect. 10.6. Such an electret transducer pair was used for measurement of air contamination in a helium recovery line that is shown in Fig. 10.4 [14], as well as a version used to detect the isotopic ratio of  ${}^3\text{He}$  to  ${}^4\text{He}$  [7]. Both of those resonators provided an almost ideal realization of a rigidly capped cylinder that incorporates an electret transducer (see Sect. 6.3.3) that functions as a volume velocity source (electrostatic loudspeaker) on one end and as a receiver (electret microphone) on the other.

<sup>12</sup> For simplicity, we can assume that the source and microphone are both located at the same end of the resonator. If they were at opposite ends, then their relative phase would shift by  $180^\circ$  degrees in going from an odd to an even mode of the resonator.

### 10.7.1 Electroacoustic Transducer Sensitivities

We can go one step further by introducing the transducer sensitivities that will allow us to model a resonator with its electroacoustic transducers as an electrical “black box” that can be represented as the linear passive four-pole networks shown schematically in Fig. 10.7.

Following MacLean [30], we can choose the following definitions for the microphone sensitivities,  $\mathbf{M}$ , and the source strengths,  $\mathbf{S}$ , for those electroacoustic transducers. These source strength and sensitivities are expressed as complex numbers because there can be frequency-dependent phase differences between the acoustic and electrical variables.

$$\mathbf{M}_o = \left( \frac{\partial V}{\partial p} \right)_{i=0} = \frac{\text{Open circuit mic output voltage}}{\text{Pressure at the mic}} \quad (10.67)$$

$$\mathbf{M}_s = \left( \frac{\partial i}{\partial p} \right)_{V=0} = \frac{\text{Short circuit mic output current}}{\text{Pressure at the mic}} \quad (10.68)$$

$$\mathbf{S}_o = \left( \frac{\partial p}{\partial i} \right) = \frac{\text{Pressure produced at the mic}}{\text{Current supplied to the source}} \quad (10.69)$$

$$\mathbf{S}_s = \left( \frac{\partial p}{\partial V} \right) = \frac{\text{Pressure produced at the mic}}{\text{Voltage applied to the source}} \quad (10.70)$$

The subscripts “*o*” and “*s*” on those microphone sensitivities refer to the transducer terminals being left open (infinite load electrical impedance) or short-circuited (zero load electrical impedance). Using those definitions, it is possible to write the transfer function,  $\mathbf{H}(f)$ , that provides the microphone’s output voltage,  $\hat{V}_2$ , in terms of the voltage applied across the speaker,  $\hat{V}_1$ .

$$\hat{V}_2 = \mathbf{M}_o \left( S_s \hat{V}_1 \right) \Rightarrow \mathbf{H}(f) = \frac{\hat{V}_2}{\hat{V}_1} = \mathbf{M}_o \mathbf{S}_s \quad (10.71)$$

Alternatively, the electrical transfer impedance,  $\mathbf{Z}_{el}(f)$ , could be written to relate the current into the source to the microphone’s open-circuit output voltage.

$$\hat{V}_2 = \mathbf{M}_o \left( S_o \hat{i}_1 \right) \Rightarrow \mathbf{Z}_{el}(f) = \frac{\hat{V}_2}{\hat{i}_1} = \mathbf{M}_o \mathbf{S}_o \quad (10.72)$$

Either expression might be useful in the design of an electronic circuit, like the feedback circuit of Fig. 10.4 or a phase-locked-loop frequency tracker that was described in Sect. 2.5.3. Although

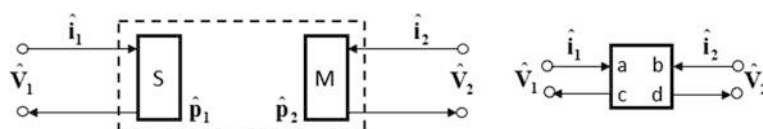


**Fig. 10.7** (Left) The dashed box indicates an acoustic network that contains an electroacoustic source,  $S$ , and a microphone,  $M$ , that are coupled together through an acoustic medium that can be characterized by an acoustic transfer impedance,  $Z_{tr}$ . Although this looks physically similar to a plane wave resonator, this schematic representation is generic and could represent any combination of a loudspeaker and a microphone that are coupled by an acoustical medium in an arbitrary geometry (see, e.g., Fig. 10.25). (Right) A generic linear, passive, four-pole electrical network that represents the transducers coupled by the acoustic medium with four matrix elements:  $a$ ,  $b$ ,  $c$ , and  $d$ , as represented in Eq. (10.73)

Eq. (10.65) provides a useful expression for a plane wave resonator's acoustic transfer impedance,  $Z_{tr}$ , one would also need to know the sensitivities of the transducers for such a design.

Fortunately, the formalism that has just been introduced, using the electroacoustic networks diagrammed schematically in Fig. 10.7, provides a technique for obtaining the electroacoustic transducer's sensitivities from purely electrical measurements, if we know the acoustic transfer impedance of the medium coupling the source and the receiver and the boundary conditions.

### 10.7.2 The Principle of Reciprocity

The *Principle of Reciprocity* was first introduced into acoustics by Lord Rayleigh, in 1873, when he derived the reciprocity relation for a system of linear equations and gave “a few examples [to] promote the comprehension of a theorem which, on account of its extreme generality, may appear vague.” [31] He cited physical examples in acoustics, optics, and electricity and then credited Helmholtz with a derivation of the result in a uniform, inviscid fluid in which may be immersed any number of rigid, fixed solids, pointing out the principle “will not be interfered with” even in the presence of damping.

The consequences of the reciprocity principle for the absolute calibration of microphones, without requiring the use of a “primary pressure standard,” were not appreciated until 1940, when MacLean [30], and independently Cook [32], showed it was possible to determine the absolute sensitivity of an electroacoustic transducer by making only electrical measurements. Since that time, the reciprocity calibration method has been universally adopted by standards organizations worldwide as the method of choice for absolute determination of the sensitivity of microphones [33] and hydrophones [34].

The reciprocity calibration technique can be applied to any electroacoustic transducer that is **reversible** (i.e., can be operated as either a speaker or as a microphone in gas or as hydrophone or projector in liquid), **linear**, and **passive**. Passivity implies that the transducer does not contain an independent internal power source, amplifier, etc.

The four-pole electrical network shown in Fig. 10.7 (right) can be represented by two coupled linear algebraic equations. To simplify the following derivation, we will treat the constants as well as the electrical currents and voltages to be real scalars,

$$\begin{aligned} V_1 &= ai_1 + bi_2 \\ V_2 &= ci_1 + di_2 \end{aligned} \tag{10.73}$$

The reciprocity principle dictates that if a stimulus is applied on the left side of the network, producing a response on the right side, then when the same stimulus is applied to the right side, the response on the left side must be identical to the response when the situation was reversed.<sup>13</sup>

Reciprocity can be illustrated using the network in Fig. 10.7 with the corresponding representation as the coupled linear Eqs. (10.73): Driving the left side, ①, with a voltage,  $V = V_1$ , while an ammeter is attached across the terminals on the network's right side, ②, creating a “short circuit” (i.e.,  $V_2 = 0$ ), the ammeter would read a current,  $i_2$ . When the situation is reversed and the ammeter shorts the left side terminals, ①, so  $V_1 = 0$ , the same voltage is impressed across the network's right-side terminals, ②, so  $V = V_2$ . Then the reciprocity principle requires that  $i_2$  produced in the first case is equal to  $i_1$  produced in the second.

<sup>13</sup> The reciprocity principle also applies in vector form. If we applied a vector force at some location, ①, on a flexible structure, and the vector displacement is measured at some other location, ②, we would observe the same vector displacement at ① if the same vector force were applied at ②.

This reciprocal behavior imposes a constraint on the coefficients (matrix elements) of Eq. (10.73), which all have the units of electrical impedance. This constraint can be demonstrated by implementing the sequence described in the previous paragraph using primed variables to indicate the “reversed” situation.

$$\begin{aligned} \text{Shorting 2 : } V_2 = 0 &= ci_1 + di_2 \Rightarrow i_1 = \frac{-d}{c}i_2 \\ \text{Shorting 1 : } V_1 = 0 &= ai_1' + bi_2' \Rightarrow i_2' = \frac{-a}{b}i_1' \end{aligned} \quad (10.74)$$

Using these conditions, it is possible to calculate the voltages that appear across the terminals of the driven side of the network.

$$\begin{aligned} \text{Driving 1 : } V &= -\frac{ad}{c}i_2 + bi_2 \Rightarrow V = \left(b - \frac{ad}{c}\right)i_2 \\ \text{Driving 2 : } V &= ci_1' - \frac{da}{b}i_1' \Rightarrow V = \left(c - \frac{ad}{b}\right)i_1' \end{aligned} \quad (10.75)$$

Since we have driven the network with  $V$  on both sides, the reciprocity principle demands that the observed short circuit currents also be equal in both cases:  $i_2 = i_1'$ . Equating the two expressions for voltage in Eq. (10.75), the reciprocity principle requires that  $b = c$ .

$$b - \frac{ad}{c} = c - \frac{ad}{b} \quad (10.76)$$

These linear equations obey the reciprocity principle if the off-diagonal terms are equal:  $b = c$  [35].

There has been a common misconception in most textbooks regarding the application of the reciprocity relations to electrodynamic transducers and others that incorporate magnetic fields (e.g., variable reluctance, magnetostrictive) [36]. This arises from the fact that the “reversibility” requirement must be applied to both the transducer and the coupling medium. For example, in the presence of steady flow, a volume velocity source at location ① will produce an acoustic pressure at location ② when that same volume velocity source was applied at location ② to produce acoustic pressure at location ① *only* if the steady flow was reversed. Since magnetic fields are the result of electrical currents (including the microscopic electrical currents in permanent magnetic materials [37]), those currents must be reversed, resulting in a sign change for the magnetic fields.

Starting in 1950 [38], this reversibility requirement was disguised by designating transducers that used magnets as “anti-reciprocal” making the off-diagonal terms have opposite signs in those cases:  $b = -c$  [39]. Hunt’s perspective has been perpetuated [40].

### 10.7.3 In Situ Reciprocity Calibration

If the first transducer in Fig. 10.7 (left) is driven, then using expressions like Eqs. (10.71) and (10.72), the voltage and current output of the second transducer can be calculated. If we reverse the roles, and drive the second transducer to calculate the voltage and current output of the first transducer, it is possible to show that the ratio of a transducer’s strength as a source to its sensitivity as a microphone is entirely determined by the acoustic transfer impedance and is independent of the particular transducer or its transduction mechanism (e.g., electrodynamic, electrostatic, or piezoelectric), as long as the transducers are linear, passive, and reciprocal [30]. Let subscript 1 indicate the first case, and let subscript 2 indicate the role reversal.

$$\frac{\mathbf{S}_{o,1}}{\mathbf{M}_{o,1}} = \frac{\mathbf{S}_{o,2}}{\mathbf{M}_{o,2}} = \frac{\mathbf{S}_{s,1}}{\mathbf{M}_{s,1}} = \frac{\mathbf{S}_{s,2}}{\mathbf{M}_{s,2}} = \mathbf{Z}_{tr} = \frac{\hat{\mathbf{p}}_1}{\hat{\mathbf{U}}_2} = \frac{\hat{\mathbf{p}}_2}{\hat{\mathbf{U}}_1} \quad (10.77)$$

Using relationships in Eq. (10.77) to eliminate  $\mathbf{M}$  in favor of  $\mathbf{S}$  or vice versa in Eq. (10.71) or Eq. (10.72), it is possible determine the sensitivities of two identical, reversible, electroacoustic transducers.

$$\hat{\mathbf{V}}_2 = \mathbf{M}_o \mathbf{S}_o \hat{\mathbf{i}}_1 = \mathbf{M}_o^2 \mathbf{Z}_{tr} \hat{\mathbf{i}}_1 = \frac{\mathbf{S}_o^2}{\mathbf{Z}_{tr}} \hat{\mathbf{i}}_1 \Rightarrow \mathbf{M}_o = \sqrt{\frac{\hat{\mathbf{V}}_2}{\hat{\mathbf{i}}_1 \mathbf{Z}_{tr}}} \text{ and } \mathbf{S}_o = \sqrt{\frac{\hat{\mathbf{V}}_2 \mathbf{Z}_{tr}}{\hat{\mathbf{i}}_1}} \quad (10.78)$$

Although we will show how this can be applied if the two transducers are not identical and if only one is reversible, it is impossible to overestimate the importance of the result of Eq. (10.78) for the progress of electroacoustics and for acoustic measurement and instrumentation in general. Equation (10.78) establishes the fact that the sensitivity of a transducer can be determined by knowing the properties of the acoustic medium (e.g.,  $\rho_m$  and  $c$ ) and its boundaries, calculating  $\mathbf{Z}_{tr}$  and then making purely electrical measurements without the necessity of a primary pressure standard.<sup>14</sup>

We now need to remove the restriction that the two reversible transducers were identical that was imposed above to quickly move from Eq. (10.77) to Eq. (10.78) and demonstrate the plausibility of an absolute transducer calibration based only on electrical measurements. This is easily accomplished by introducing a third transducer that need not be reversible but that can act as a “signal strength monitor.” In fact, only one transducer needs be reversible for the following procedure to produce absolute calibrations of all three transducers.

Once again, we will assume that we are placing all three transducers in a rigidly terminated standing wave resonator filled with an ideal gas so we can let Eq. (10.65) be used to provide the required  $\mathbf{Z}_{tr}$ . We also assume that the transducers are themselves sufficiently rigid that their presence in the resonator does not alter the sound field.<sup>15</sup>

Figure 10.8 is a schematic representation of such a resonator that has a source, S, at one end; a reversible transducer, R, at the opposite end; and an auxiliary microphone, M, also located at one end.



**Fig. 10.8** Schematic representation of a gas-filled plane wave resonator that has a reversible transducer, R, at one end and a sound source, S, at the other end. A third transducer that functions only as a microphone, M, can be located at either end of the resonator

<sup>14</sup> The primary calibration of voltage is simpler (in principle, although it requires temperatures near absolute zero for the Josephson junction) since it is possible to relate the dc voltage across a superconducting Josephson junction to the resulting oscillation frequency,  $f$ , since their ratio is determined by Planck's constant,  $h$ , and the charge on an electron,  $e$ :  $V \equiv nhf/2e$ , where  $n$  is an integer.  $2e/h = (483.5978)$  MHz/ $\mu$ V.

<sup>15</sup> This is equivalent to saying that the transducers are non-compliant in much the same way that the “constant displacement drive” for a string does not “feel” the load of the string and preserves the “fixed” boundary condition. For reciprocity calibration of transducers that behave as an ultracompliant driver (i.e., a constant force drive equivalent), see [43].

Although M and S could be reversible, it is not required for execution of the following procedure. An actual physical realization of this configuration is shown in Fig. 10.25, where both S and R are reversible but M can only function as a microphone. This procedure exploits the fact that all transducers are assumed to exhibit linear behavior and results in an absolute reciprocity calibration of R and a calibration relative to R for both S and M:

- (a) We start by driving the reversible transducer with a current,  $i_2$ , and then measuring the output voltage,  $V_m$ , of the microphone, M.
- (b) The source, S, is then driven with a current,  $i_1$ , that is sufficient to make the output of microphone, M, return to  $V_m$ . This recreates the sound field in the resonator produced when R was driven by  $i_2$  in step (a).
- (c) Having reproduced the sound field that the reversible transducer created in step (a), the reversible transducer's open-circuit output voltage,  $V_2$ , is measured.

These three measurements are now sufficient to calibrate all three transducers without requiring that any be “identical.”

Since the first (reversible) transducer is obviously identical to itself, Eq. (10.78) can be used to determine its open-circuit sensitivity as a microphone,  $\mathbf{M}_o$ , and its source strength,  $\mathbf{S}_o$ , since we know  $\mathbf{Z}_{tr}$  from Eq. (10.65). For the remainder of this sub-section, we will let the sinusoidal voltages and currents be represented their rms values.

$$|\mathbf{M}_o| = \sqrt{\frac{V_2}{i_2 |\mathbf{Z}_{tr}|}} \quad \text{and} \quad |\mathbf{S}_o| = \sqrt{\frac{V_2 |\mathbf{Z}_{tr}|}{i_2}} \quad (10.79)$$

Knowing the reversible microphone's sensitivity, the pressure at either end of the resonator is determined:  $p_I = V_2 / |\mathbf{M}_o|$ . Since that is the pressure that also appears at M, its sensitivity,  $M_{o,aux}$ , is determined by its voltage output,  $V_m$ .

$$|\mathbf{M}_{o,aux}| = |\mathbf{M}_o| \frac{V_m}{V_2} \quad (10.80)$$

Finally, the source strength of transducer S is determined, again because  $p_I$  is known when  $i_1$  was applied to S.

$$|\mathbf{S}_{o,source}| = \frac{V_2}{|\mathbf{M}_o| i_1} \quad (10.81)$$

Since the linearity of the transducers' response is required, it is not necessary to readjust the amplitude of the drive to re-create the sound field originally produced when the reversible transducer was used as the sound source. It would be equally valid to simply use the ratio of the voltage produced by the auxiliary microphone when the reversible transducer, R, was driven,  $V_{M,1}$ , in step (a) and the corresponding auxiliary microphone output voltage,  $V_{M,2}$ , when the source, S, was driven. The result for the reversible transducer's open-circuit sensitivity,  $\mathbf{M}_o$ , is given in Eq. (10.82) for calibration at a resonance frequency,  $f_n$ , with the corresponding quality factor,  $Q_n$ .

$$|\mathbf{M}_{o,1}(f_n)| = \left( \frac{\pi V_{res}}{\gamma p_m} \right)^{1/2} \left[ \frac{V_2}{i_2} \frac{V_{M,1}}{V_{M,2}} \frac{f_n}{Q_n} \right]^{1/2} \quad (10.82)$$

Historically, other authors have referred to the reciprocal of the acoustic transfer impedance as the “reciprocity factor,”  $\mathbf{J} = (\mathbf{Z}_{tr})^{-1}$ , but I see no reason to obscure the origin of this “factor” by giving it a separate designation. In fact, I contend that the reciprocity calibration method was limited to only small

“couplers” (see Fig. 10.27) or free-field geometries until Rudnick’s classic paper on reciprocity calibration in “unconventional geometries” appeared in 1978 [41].

The fact that an absolute calibration could be made in any electroacoustical system for which the acoustic transfer impedance could be calculated made it possible to perform in situ transducer calibrations in almost any apparatus and under actual conditions of use. One extreme example of the utility of this approach is demonstrated by the reciprocity calibration of electret microphones used to make an absolute determination of the sound pressures generated by resonant mode conversion in superfluid helium at temperatures within one degree of absolute zero ( $1\text{ K} = -272\text{ }^{\circ}\text{C} = -458\text{ }^{\circ}\text{F}$ ) [42]. Not only was the sensitivity of such a transducer different from the same transducer calibrated in air, but the sensitivity could change after the apparatus was brought back to room temperature and then submerged again in liquid helium.

The reciprocity method was extended to force-driven transduction by Swift and Garrett in 1987 to allow reciprocity calibration of magnetohydrodynamic sound sources [43]. Such “ultracompliant” sources and receivers are the equivalent of what we called a “constant force” driver, which were contrasted to “constant displacement” or “constant velocity” drive mechanisms that were used to excite finite or semi-infinite strings in our investigations of the driven string in Sects. 3.7 and 3.8.

### 10.7.4 Reciprocity Calibration in Other Geometries

Most reciprocity calibrations for either hydrophones [44] or microphones [45] are executed in a coupler (cavity) that is small compared to the wavelength of sound at the calibration frequencies (see Fig. 10.24), or under free-field conditions, usually within an anechoic chamber (see Fig. 12.41) [46]. As before, the only requirement for such calibrations is knowledge of the appropriate acoustic transfer impedance. Until the radiation produced by small sources that create spherically spreading pressure waves in unbounded media are discussed Chap. 12, we will not be able to calculate the acoustic transfer function for free-field conditions. The acoustic transfer impedance for that case is included here for the reader’s convenience. The distance separating the “acoustic centers”<sup>16</sup> of the source and the receiver is  $d$ .

$$\text{Free-field : } |\mathbf{Z}_{\text{tr}}| = \frac{\rho_m c}{2d\lambda} \quad (10.83)$$

Free-field reciprocity calibrations of microphones in air have been demonstrated to frequencies as high as 100 kHz in 1948 [47] and more recently up to 150 kHz [48].

For a coupler with internal volume,  $V$ , and all internal dimensions much smaller than the wavelength,  $V^{1/3} \ll \lambda$ , the acoustic transfer impedance is given by the cavity’s compliance in Eq. (8.26).

$$\text{Coupler : } \mathbf{Z}_{\text{tr}} = \frac{\rho_m c^2}{j\omega V} = \frac{\gamma p_m}{j\omega V} \quad (10.84)$$

A schematic diagram of a typical commercial coupler used for reciprocity calibration systems, like the Brüel & Kjær Type 4143, is shown in Fig. 10.24 that is provided with two coupler volumes with nominal internal volume of  $20\text{ cm}^3$  and  $3.4\text{ cm}^3$  [49]. To perform a reciprocity calibration to high frequencies, the coupler must be rather small. In that case, it is sometimes necessary to modify the cavity’s compliance to include the compliance of the transducers’ diaphragms. Alternatively, higher-

<sup>16</sup>The acoustic center of a reversible microphone or a sound source under free-field conditions is defined as the extrapolated center of the spherically diverging wave field (see Problem 4 in Chap. 12).

frequency calibrations can be made by filling the coupler with a gas such as He or H<sub>2</sub> that have significantly higher sound speeds. Also, to reach the highest levels of precision, it may be necessary to determine an effective polytropic coefficient (i.e., ratio of specific heats),  $\gamma_{eff}$ , to take into account that the gas near the coupler's and the microphone's surfaces has an isothermal compressibility as discussed in Sect. 9.3.2. Since the coupler volume tends to be minimized to allow calibration at higher frequencies, the surface-to-volume ratio can introduce a significant correction to the coupler's compliance (i.e., acoustic transfer impedance), particularly at lower frequencies where the thermal penetration depth is longer and, hence, the isothermal volume is a larger fraction of the coupler's volume.

Recently, a reciprocity calibration was made using a coupler with a volume of 1.5 m<sup>3</sup> that included two 10" sub-woofers as the reversible transducers and produced reciprocity calibrations of infrasound sensors used for monitoring compliance with the Comprehensive Nuclear-Test-Ban Treaty [50] for frequencies between 0.005 Hz  $\leq f \leq$  10 Hz [51].

For a double Helmholtz resonator, like that shown in Fig. 9.18, having equal volumes,  $V$ , on either side, joined by a duct of cross-sectional area,  $A = \pi r_d^2$ , with length,  $L_d$ , the transfer impedance depends upon the resonance frequency,  $\omega_o = c\sqrt{2A/L_dV}$ , and the quality factor,  $Q$ .

$$\text{Double Helmholtz resonator : } |\mathbf{Z}_{tr}| = \frac{\rho_m c Q}{\sqrt{8AV/L_d}} \quad (10.85)$$

A plane wave tube of cross-sectional area,  $A$ , that may include an echoic termination to guarantee unidirectional wave propagation can also be a useful geometry for reciprocity calibrations, as long as the plane wave propagation is ensured by requiring that  $A^{1/2} \ll \lambda$ .

$$\text{Planewave tube : } |Z_{tr}| = \frac{\rho_m c}{A} \quad (10.86)$$

The result for a plane wave resonator from Eq. (10.65) of volume,  $V_{res}$ , operating in its  $n$ th mode, with resonance frequency,  $f_n$ , and quality factor,  $Q_n$ , filled with an ideal gas, is repeated below.

$$\text{Planewave resonator (gas-filled) : } |\mathbf{Z}_{tr}| = \frac{Q_n}{\pi f_n} \frac{\gamma p_m}{V_{res}} \quad (10.87)$$

### 10.7.5 Resonator-Transducer Interaction

The coupling of two or more systems that possess their own individual resonance frequencies has been one focus of this textbook since coupled simple harmonic oscillators were introduced in Sect. 2.7. The topic of this section of Chap. 10 is the driven plane wave resonator, so it is natural that the coupling of an electrodynamic loudspeaker to such a resonator be examined. As introduced in Eq. (2.55) for a forced simple harmonic oscillator, we start by writing down Newton's Second Law of Motion to account for the net force, in this case being the force on the speaker's piston, which has an instantaneous velocity,  $\dot{\xi}_1(t)$ , with positive  $\xi$  toward the left in Fig. 10.9.

$$m_o \frac{d^2 \xi_1}{dt^2} + R_m \frac{d\xi_1}{dt} + K \xi_1 = f - A_{pist} p(t) \quad (10.88)$$

The speaker's moving mass,  $m_o$ ; suspension stiffness,  $K$ ; and mechanical resistance,  $R_m$ , were discussed in Sect. 2.5.5, as was the force,  $f(t) = (B\ell)I(t)$ , that the magnet and voice coil (i.e., motor mechanism) exert on the piston of area,  $A_{pist}$ . The situation is diagrammed schematically in Fig. 10.9.

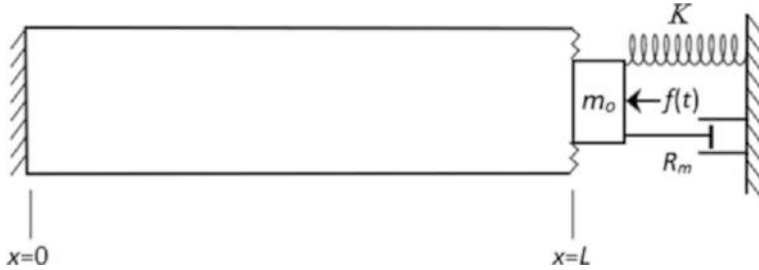


**Fig. 10.9** Schematic representation of a plane wave resonator of uniform cross-sectional area,  $A_{res}$ , that is driven by an electrodynamic loudspeaker with a piston of area,  $A_{pist}$ , located at  $x = L$ . The zig-zag lines connecting the piston to the resonator at  $x = L$  represent some flexure seal (e.g., the “surround” of the speaker shown in Fig. 2.16 right or the bellows in Fig. 4.14 and in Fig. 4.21 right). The piston’s effective area,  $A_{pist}$ , will include some contribution from the flexure seal. In general,  $A_{pist} \neq A_{res}$

In addition to Newton’s Second Law in Eq. (10.88), the fluid in the resonator that is in contact with the piston must have the same volume velocity as that of the piston,  $U_1(L) = -A_{pist}\dot{\xi}_1$ . Under steady-state conditions for a single-frequency excitation, the reaction force,  $A_{pist}\hat{\mathbf{p}}$ , on the piston produced by the acoustic pressure at its surface,  $A_{pist}\hat{\mathbf{p}}(L)$ , can be expressed in terms of the acoustical impedance presented by the resonator. By placing the rigid end of the resonator at  $x = 0$ , Eq. (10.45) can be used to express the velocity of the gas, while Euler’s equation determines the gas pressure as a function of position and time, (temporarily) neglecting any resonator dissipation.

$$\begin{aligned} \mathbf{Z}_{ac} \equiv \frac{\hat{\mathbf{p}}}{\hat{\mathbf{U}}} &= \frac{j\rho_m c \hat{\mathbf{v}} \cos(kx)}{A_{res} \hat{\mathbf{v}} \sin(kx)} = j \frac{\rho_m c}{A_{res}} \cot(kx) \\ \Rightarrow \quad \hat{\mathbf{p}}(L) &= -\mathbf{Z}_{ac}(L) A_{pist} \hat{\xi} \end{aligned} \quad (10.89)$$

If dissipation in the resonator is represented by an exponential decay constant,  $\alpha$ , so the amplitude of a traveling plane wave decays in proportion to  $e^{-\alpha x}$ , and using Eq. (B.5) the quality factor of a plane wave resonance is  $Q = (\frac{1}{2}) k/\alpha = \pi/(\alpha\lambda)$ , then the acoustic impedance has a slightly more complicated dependence upon  $(kL)$ , which reduces to Eq. (10.89) in the limit that  $(\alpha L) \ll 1$  [52].

$$\mathbf{Z}_{ac}(kL) = \frac{\rho_m c}{A_{res}} \frac{\alpha L - j \cos(kL) \sin(kL)}{\sin^2(kL) + (\alpha L)^2 \cos^2(kL)} \quad (10.90)$$

The motor mechanism (voice coil and magnet) must supply the force that displaces the piston’s mass, damping, and stiffness and must also supply the force that the piston exerts on the fluid. However, we can easily investigate the resonance frequencies analytically by neglecting all dissipation (i.e., both  $R_m$  and  $\alpha$ ) and realizing that no external force is needed to maintain an oscillation on resonance with no dissipation. (The dissipative terms will be included in the DELTAEC model of Fig. 10.11.) Then, the moving mass of the speaker is just bouncing on the sum of the two elastic forces:  $-j\omega \hat{\xi} K$  from the speaker’s suspension and  $A_{pist}\hat{\mathbf{p}}$  from the gas pressure oscillations. Since the fluid’s effect is represented by the acoustic impedance,  $Z_{tr} \equiv \hat{\mathbf{p}}/\hat{\mathbf{U}}$ , in Eq. (10.89) or (10.90), and the speaker’s components are represented by a mechanical impedance,  $\mathbf{Z}_{mech} = \hat{\mathbf{F}}/\hat{\mathbf{v}}$ , we can convert both to the mechanical domain using Eq. (10.28).

$$j\left(m_o\omega - \frac{K}{\omega}\right) = jA_{pist}^2 \frac{\rho_m c}{A_{res}} \cot(kL) \quad (10.91)$$

The plotting of this equation is simplified if the driver parameters are nondimensionalized by taking the ratio of the speaker's moving mass,  $m_o$ , to the mass of gas contained within the resonator,  $m_{gas}$ .

$$m^* = \frac{m_o}{m_{gas}} = \frac{m_o}{\rho_m A_{res} L} \Rightarrow m_o = m^* \rho_m A_{res} L \quad (10.92)$$

The speaker's stiffness can be normalized by taking its ratio with respect to the zero-frequency stiffness of the gas as given in Eq. (8.28).

$$K^* = \frac{K}{K_{gas}} = \frac{KV}{\rho_m c^2 A_{res}^2} = \frac{KA_{res}L}{\rho_m c^2 A_{res}^2} = \frac{KL}{\rho_m c^2 A_{res}} \Rightarrow K = \frac{K^* \rho_m c^2 A_{res}}{L} \quad (10.93)$$

Equation (10.91) can be re-written as a function of the speaker's nondimensionalized parameters,  $m^*$  and  $K^*$ , and  $(kL)$ , where the "k" in the parentheses is the wavenumber. The ratio of the piston area to the resonator area is  $A^* = A_{pist}/A_{res}$ .

$$\begin{aligned} m^* \frac{\omega}{c} \rho_m L A_{res} - \frac{K^* \rho_m c A_{res}}{\omega L} &= \rho_m \frac{A_{pist}^2}{A_{res}} \cot(kL) \\ m^*(kL) - \frac{K^*}{(kL)} &= (A^*)^2 \cot(kL) \end{aligned} \quad (10.94)$$

The driver-resonator interaction can be illustrated by coupling the speaker we evaluated in Chap. 2, Prob. 19, that was characterized using the techniques of Sect. 2.5.5, to a rigidly terminated cylindrical resonator. That speaker had a free-cone resonance frequency,  $f_o = 55$  Hz, and an effective piston area,  $A_{pist} = 125$  cm<sup>2</sup>. For computational simplicity, let's connect that speaker to a 1.0-meter-long, air-filled cylinder with an inside diameter,  $D = (4A_{pist}/\pi)^{1/2}$ , so  $A^* = 1$ , and terminated at the other end,  $x = 0$ , by a rigid end cap. If the air is dry and at a mean pressure,  $p_m = 101,325$  Pa, and temperature,  $T_m = 20$  °C = 293 K, the speed of sound,  $c = 343.2$  m/s. Using the results of Eq. (10.51) for such a resonator with both ends rigid,  $f_l = c/2 L = 171.6$  Hz, with the subsequent harmonic series of longitudinal standing wave modes at  $f_n = nf_l$ , if both ends were rigid.

Using those speaker parameters, while neglecting dissipation in the speaker and the resonator,  $m^* \cong 3/4$  and  $K^* \cong 3/4$ . Letting  $A^* = 1$ , the graphical solution to Eq. (10.94) is shown in Fig. 10.10, where the solid line represents  $\cot(kL)$  for the resonator and the short-dashed line represents the frequency dependence of the speaker's mechanical impedance. The lowest-frequency intersection at  $(k_o L) = 0.397\pi$  is close to the speaker's free-cone resonance. Subsequent intersections correspond fairly closely to the closed-closed resonances of the resonator,  $(k_n L) = n\pi$ , for  $n \geq 1$ .

If the rear of the loudspeaker is enclosed by a rigid hemisphere, the additional gas stiffness, approximated in Eq. (10.95), raises the speaker's nondimensionalized stiffness,  $K^* \cong 23$ . That case corresponds to the long-dashed line in Fig. 10.10. Now the speaker's resonance frequency corresponds to  $(k_o L) = 1.654\pi$ , placing it above the resonator's rigid-rigid  $n = 1$  mode, as well as the free-cone resonance, and below the  $n = 2$  mode. In both cases, the speaker's mechanical resonance "repels" the isolated resonator's harmonic standing wave modes. This *level repulsion* is also illustrated in Table 10.2.

To include dissipation in the speaker and the resonator, it is easier to model such a resonator and driver using the ISPEAKER segment in DELTAEC, as shown in Fig. 10.11. Segment #1 provides the values of the essential loudspeaker parameters in MKS units:  $A_{pist}$  (1a); voice coil resistance,  $R_{dc}$  (1b); voice coil inductance,  $L$  (1c);  $B\ell$ -product (1d); moving mass,  $m_o$  (1e); suspension stiffness,  $K$  (1f); and

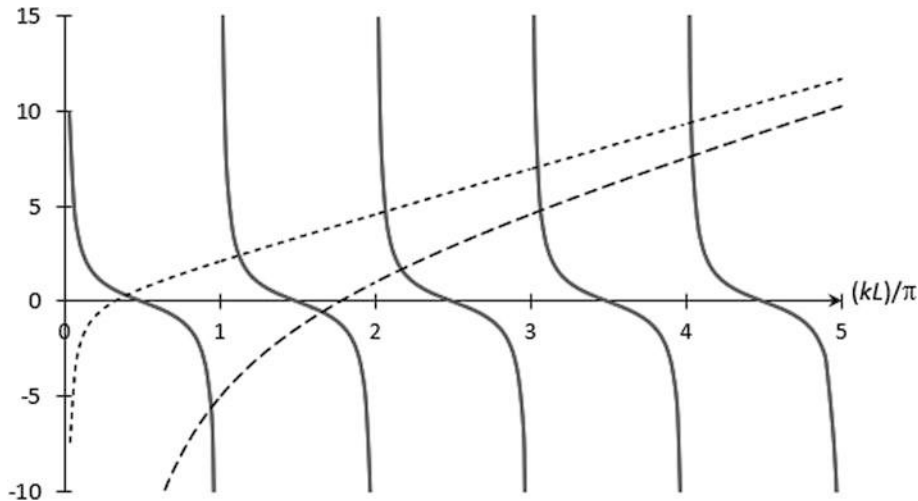


**Fig. 10.10** Graphical method of solution to the transcendental Eq. (10.94) with  $A^* = 1$ . The *solid curves* represent the right-hand side of that equation, and the *dashed curves* are the left-hand side. The values for the horizontal axis are  $(kL)/\pi$ . The short dashes represent the mechanical parameters ( $m^* \cong \frac{3}{4}$  and  $K^* \cong \frac{3}{4}$ ) of loudspeaker from Chap. 2, Prob. 19, that are included in the DELTAEC screenshot of Fig. 10.11. The *long dashes* represent the same loudspeaker but with the rear of the speaker enclosed by a hemispherical enclosure (see Fig. 10.13) that provides additional gas stiffness and makes  $K^* \cong 23$

**Table 10.2** Solutions to Eq. (10.94) for  $m^* = \frac{3}{4}$  with the speaker's mechanical resonance at 55 Hz

Mode	$K^* = \frac{3}{4}$	$f_n$	$K^* = 23$	$f_n$
	$(kL)/\pi$	[Hz]	$(kL)/\pi$	[Hz]
0	0.39718	68.2	1.65441	283.9
1	1.12399	192.9	0.94316	161.8
2	2.06602	354.5	2.16703	371.9
3	3.04457	522.4	3.06495	525.9
4	4.03358	692.2	4.04106	693.4

The left column corresponds to  $K^* = \frac{3}{4}$ , and the right column corresponds to  $K^* = 23$  and a speaker with enclosure resonance of 299 Hz. In both cases, the speaker's resonance “repels” the standing wave solutions for an ideal rigid-rigid plane wave resonator which would have  $(k_n L) = n\pi$  for  $n \geq 1$ . Frequencies are based on  $f_I = c/2L = 171.6$  Hz

mechanical resistance,  $R_m$  (1f). The choice of drive current,  $I$  (1 h), is arbitrary but reasonable. The DELTAEC model lets us plot the coupled speaker-resonator response as a function of frequency, including dissipation in both the resonator and the driver, as shown in Fig. 10.12. Several interesting features can be seen clearly.

For reference, the dashed line represents the standing wave solutions for an isolated closed-closed resonator,  $f_n = nf_I$ , based on the results of Eq. (10.51). The spectrum for the coupled systems shows an additional resonance at about 68 Hz corresponding to the mechanical resonance of the speaker as already calculated for the lossless case in Table 10.2. At that frequency, the resonator is shorter than a half-wavelength so the “load” presented by the resonator behaves as a gas stiffness,  $K_{gas}$ , that adds to the speaker’s mechanical suspension stiffness,  $K$ , raising the speaker’s resonance frequency above its free-cone value,  $f_o = 55$  Hz. The frequency of the speaker’s resonance and those of the first five standing wave modes of the resonator that are produced by the DELTAEC model are listed in Table 10.3.

```

3 ⊕ 0 BEGIN      Initial
13 ☐ 1 ISPEAKER Morel MW 142, S/N 0496
14 Loudspeaker parameters from Ch. 2, Prob. 19
15     1.2500E-02 a Area   m^2          13.829 A |p|    Pa
16           6.3000 b R      ohms         -180.0 B Ph(p) deg
17           2.6000E-04 c L      H          2.1970E-02 C |U|    m^3/s
18           7.1000 d BLProd T-m        105.30 D Ph(U) deg
19           1.1500E-02 e M      kg          4.7964 E Htot   W
20           1335.0 f K      N/m        4.0084E-02 F Edot   W
21           1.0400 g Rm     N-s/m       4.7964 G WorkIn W
22           1.0000 h |I|      A          15.281 H Volts  V
23
24
25           1.0000 I Amps   A          -51.116 J Ph(V/I) deg
26           2.1970E-02 K |Ux|   m^3/s
27 ⊕ ideal      Solid type
28 ☐ 2 RPN      Speaker Electrical Impedance
29     0.0000 a G or T   P          15.281 A Ohms
30 ⊕ 1H 1I /
31 ☐ 3 DUCT     Duct
32 ☐ 4 SURFACE   Second End
33 ☐ 5 HARDEND   Final

```

**Fig. 10.11** Screenshot of a DELTAEC model with the ISPEAKER (#1) and the RPN (#2) segments expanded. The RPN calculates the magnitude of the speaker's electrical impedance and the ISPEAKER segment provides the speaker parameters in MKS units

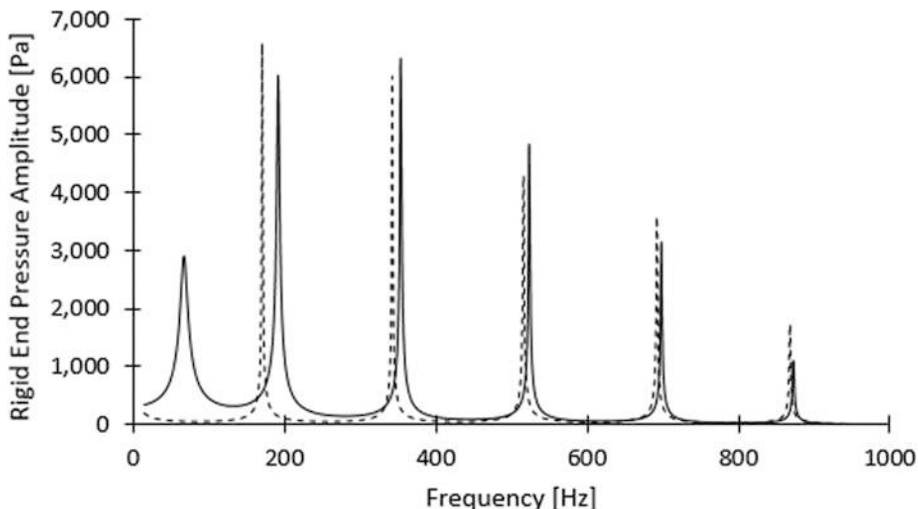


**Fig. 10.12** The *solid line* represents the frequency response of the coupled speaker-resonator system that was generated by the DELTAEC model in Fig. 10.11 with  $m^* = \frac{3}{4}$  and  $K^* = \frac{3}{4}$ . The *dashed line* is the frequency response created with rigid terminations at both ends and a boundary that excites the modes with a constant volume velocity. The *lowest-frequency peak* represents the resonance of the loudspeaker. The standing wave modes are shifted to higher frequencies due to the complex mechanical impedance of the loudspeaker

Figure 10.13 shows a DELTAEC model that uses the IESPEAKER segment to incorporate an enclosure behind the speaker that is a hemisphere with the same diameter as the piston that produced the  $K^* = 23$  case. The acoustic pressure generated by that combination is shown in Fig. 10.14, and the frequencies of the peak are included in Table 10.3.

**Table 10.3** Summary of the frequencies of the speaker's mechanical resonance ( $n = 0$ ) and the frequencies of the first five modes of the resonator,  $f_n$ , that include dissipation

Mode	Rigid	$f_o = 55$ Hz	Enclosed
0	—	68	269
1	171	192	159
2	343	354	366
3	517	524	527
4	693	699	700
5	869	874	874

The modes of the closed-closed resonator (Rigid), given by Eq. (10.51), are provided for reference. These frequencies are in excellent agreement with the results of the nondissipative calculations summarized in Table 10.2.

```

1 ⊖ Enclosed 5 in Speaker Enclosed 5 in. WM 142
2 ⊕ 0 BEGIN      Dry air at standard atmosphere and 20 deg C
12 ⊖ 1 COMPLIANCE Rear Speaker Enclosure
13   5" diameter hemisphere
14     2.5300E-02 a SurfAr m^2           1.0032E+04 A |p|    Pa
15     6.6300E-04 b Volume m^3            -90.43 B Ph(p)  deg
16 Master-Slave Links
17   7.9247E-02 C |U|    m^3/s
18   179.50 D Ph(U)  deg
19   0.0000 E Htot    W
19 ideal   Solid type
20 ⊖ 2 IESPEAKER Morel MW 142, S/N 0496
21   1.2500E-02 a Area   m^2           580.56 A |p|    Pa
22   6.3000 b R       ohms            -92.742 B Ph(p)  deg
23   2.6000E-04 c L       H           7.9247E-02 C |U|    m^3/s
24   7.1000 d BLProd T-m            179.46 D Ph(U)  deg
25   1.1500E-02 e M       kg           25.655 E Htot    W
26   1335.0 f K       N/m            0.88574 F Edot   W
27   1.0400 g Rm      N-s/m          25.655 G WorkIn W
28   1.0000 h |I|      A             51.311 H Volts   V
29   0.0000 i Ph(I)  deg            1.0000 I Amps   A
30
31 ideal   Solid type
32 ⊖ 3 RPN      Speaker Electrical Impedance
33 ⊖ 4 DUCT     Duct
43 ⊖ 5 SURFACE Second End
50 ⊖ 6 HARDEND Final

```

**Fig. 10.13** Screenshot of the DELTAEC model with the “enclosed speaker” IESPEAKER (#2) segment expanded and the “enclosure back volume” COMPLIANCE (#1) segment expanded

The enclosure's small back volume contributes significantly more gas stiffness,  $K_{gas}$ , to the speaker's suspension than the speaker's own mechanical stiffness,  $K$ . Since the enclosure's dimensions are all much smaller than the wavelength of the sound at that frequency, the expression for gas stiffness in Eq. (8.28) can be employed to approximate the enclosed speaker's resonance frequency.

$$K_{gas} = \gamma p_m \frac{A_{pist}^2}{V} = 39,400 \text{ N/m} \quad \Rightarrow \quad f_o = \frac{1}{2\pi} \sqrt{\frac{K + K_{gas}}{m_o}} = 299 \text{ Hz} \quad (10.95)$$

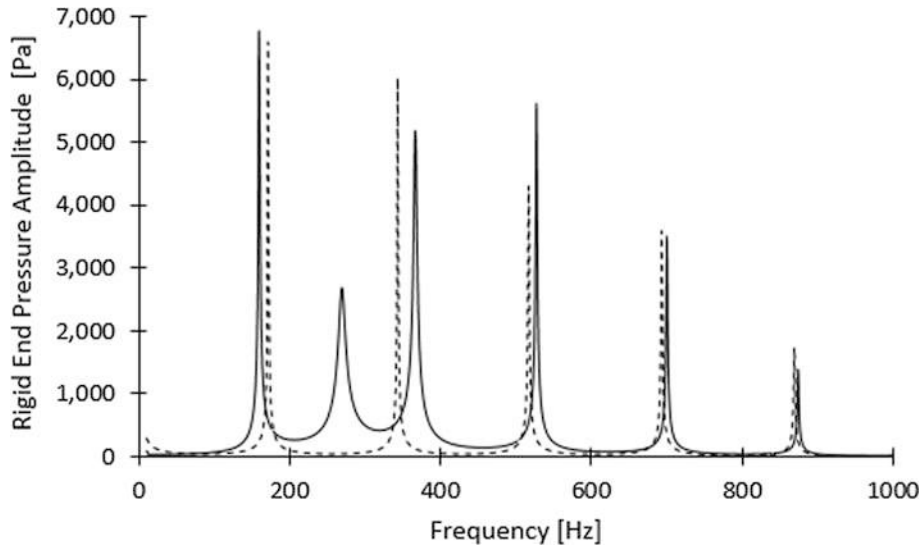


**Fig. 10.14** The *solid line* represents the frequency response of the coupled “enclosed” speaker-resonator system that was generated by the DELTAEC model in Fig. 10.13 with  $m^* = \frac{1}{4}$  and  $K^* = 23$ . The *dashed line* represents the frequency response created with a rigid termination at both ends and a boundary that provides a constant volume velocity, as it was in Fig. 10.12. The frequency peak produced by the mechanical resonance of the loudspeaker now appears between the  $n = 1$  and the  $n = 2$  standing wave resonances. The frequencies of the standing wave modes are “repelled” by the coupled loudspeaker resonance exhibiting the same “level repulsion” that appeared first when coupled harmonic oscillators were introduced in Sect. 2.7.6 and was also demonstrated in the bass-reflex loudspeaker enclosure’s response in Fig. 8.42

This value is 30 Hz higher than the result in Table 10.2 because the “load,” produced by the gas, on the front surface of the loudspeaker’s piston is not included in the calculation of Eq. (10.95).

### 10.7.6 Electrodynamic Source Coupling Optimization\*

In many applications where an electrodynamic loudspeaker is coupled with a resonator, it is advantageous to optimize the electroacoustic efficiency of the coupling. If it is assumed that the acoustical properties of the resonator have been determined by the application, then it is possible to demonstrate that the efficiency of the driver’s excitation of that resonance will depend upon the area of the driver’s piston,  $A_{pist}$ .

There are two sources of dissipation in an electrodynamic driver. One is related to the driver’s mechanical damping,  $R_m$ , that is proportional to the square of the driver’s piston velocity,  $|\hat{\mathbf{v}}_d|^2 = |\hat{\xi}|^2 = (\hat{\mathbf{U}}/A_{pist})^2$ .

$$\langle \Pi_m \rangle_t = \frac{R_m}{2} |\hat{\mathbf{v}}_d|^2 = \frac{R_m}{2} \frac{|\hat{\mathbf{U}}|^2}{A_{pist}^2} \equiv a \frac{|\hat{\mathbf{U}}|^2}{A_{pist}^2} \quad (10.96)$$

The other loss mechanism is due to the time-averaged electrical dissipation (i.e., Joule heating),  $\langle \Pi_{dc} \rangle_t$ , produced by the driving current’s passage through the driver’s voice coil,  $\hat{\mathbf{I}}$ , that has an electrical

resistance,  $R_{dc}$ . The force,  $\hat{\mathbf{F}}$ , that the driver must produce is related to the product of the acoustic pressure on the driver's face,  $\hat{\mathbf{p}}$ , and the piston's area,  $A_{pist}$ .

$$\hat{\mathbf{F}}(\hat{\mathbf{I}}) = \hat{\mathbf{p}}A_{pist} = (B\ell)\hat{\mathbf{I}} \Rightarrow \hat{\mathbf{I}} = \frac{\hat{\mathbf{p}}A_{pist}}{(B\ell)} \quad (10.97)$$

At resonance, the pressure on the face of the piston,  $\hat{\mathbf{p}}$ , and the volume velocity that the piston produces,  $\hat{\mathbf{U}}$ , will be in-phase. Furthermore, since the resonant load is specified, their ratio must be the acoustical impedance of the resonator at the piston's location:  $\mathbf{Z}_{ac} = \hat{\mathbf{p}}/\hat{\mathbf{U}}$ .

$$\langle \Pi_{dc} \rangle_t = \frac{R_{dc}}{2} |\hat{\mathbf{I}}|^2 = \frac{R_{dc}}{2} \left( \frac{\hat{\mathbf{p}}A_{pist}}{(B\ell)} \right)^2 = \frac{R_{dc}}{2} \left( \frac{\mathbf{Z}_{ac}\hat{\mathbf{U}}A_{pist}}{(B\ell)} \right)^2 \equiv bA_{pist}^2 |\hat{\mathbf{U}}|^2 \quad (10.98)$$

Inspection of Eqs. (10.96) and (10.98) reveals that those two dissipation mechanisms have a reciprocal dependence upon the square of the piston's area. As the area of the piston decreases, the piston's velocity must increase to provide the same amount of volume velocity. On the other hand, as the area of the piston increases, the force required to move the piston, hence the required current flow through the voice coil, must increase with the area of the piston.

The total time-averaged driver dissipation,  $\langle \Pi_{driver} \rangle_t$ , is the sum of Eq. (10.96) and Eq. (10.98). Since the volume velocity is common to both terms (and dictated by the power requirement of the application), the optimum piston area,  $A_{opt}$ , can be obtained by differentiating the total driver dissipation with respect to the piston's area.

$$\frac{\langle \Pi_{driver} \rangle}{|\hat{\mathbf{U}}|^2} = \frac{a}{A_{pist}^2} + bA_{pist}^2 \Rightarrow \frac{\partial \left( \frac{\langle \Pi_{driver} \rangle}{|\hat{\mathbf{U}}|^2} \right)}{\partial A_{pist}} = -\frac{2a}{A_{opt}^3} + 2bA_{opt} = 0 \quad (10.99)$$

Since both the acoustical impedance of the resonator at resonance, given by Eq. (10.65), and the mechanical resistance of the driver are real constants, they can be represented by a dimensionless constant,  $s$ , that relates the real component of the acoustical impedance times the resonator's cross-sectional area,  $A_{res}$ , to the mechanical resistance of the driver:  $A_{res}^2 |\mathbf{Z}_{ac}| = sR_m$ .

For optimum efficiency, the driver must be operated at its mechanical resonance frequency,  $\omega_o$ , making  $\mathbf{X}_m(\omega_o) = j(\omega_o m_o - K/\omega_o) = 0$ , so that none of the electrodynamic force is wasted accelerating the driver's mass,  $m_o$ , at  $\omega > \omega_o$  or deflecting the driver's suspension stiffness,  $K$ , at  $\omega < \omega_o$ . Also, by the maximum power transfer theorem, "load matching" requires that  $s = 1$ .

$$\left( \frac{A_{opt}}{A_{res}} \right)^4 = \frac{R_m(B\ell)^2}{R_{dc}Z_{ac}^2 A_{res}^4} = \frac{R_m(B\ell)^2}{R_{dc}R_m^2} = \left[ \frac{(B\ell)^2}{R_m R_{dc}} \right] \equiv \beta \quad (10.100)$$

The quantity in square brackets is a dimensionless number,  $\beta$ , known as the Wakeland number, that depends only upon the driver's parameters.

$$\frac{A_{opt}}{A_{res}} = \beta^{1/4} \cong \sqrt{\sigma} \quad (10.101)$$

In some cases, it may not be possible or practical to use this optimum piston area since there may be other constraints that limit the piston's excursion or the goal may be to deliver the maximum power to the load at some lower efficiency.

**Table 10.4** Motor parameters for various electrodynamic drivers that have been used by thermoacoustics researchers [54]

Driver	(Bℓ)	R <sub>dc</sub>	R <sub>m</sub>	σ	η <sub>max</sub>	Π <sub>electric</sub>
	[N/A]	[Ω]	[kg/s]		[%]	[W]
MW-142 [55]	7.5	5.1	1.9	2.6	44	150
JBL 2206H [56]	18.1	5.3	9.5	2.7	47	300
Altec 290-16 K [57]	21.5	10.6	2.8	4.1	61	10
STAR [58]	15.3	8.2	1.8	4.1	61	20
SETAC [59]	18	1.7	2.2	9.4	81	200
Bose LM-1 [60]	18.36	1.36	2.34	10.34	82.4	100
B-300 [61]	8.0	0.05	15	9.3	81	300
C-2 [61]	41	0.24	48	12	85	2000
C10 [61]	85	0.52	80	13	86	10,000

The first three entries are “off-the-shelf” commercial loudspeakers. The STAR and SETAC drivers are custom-designed and built moving-coil devices. The last four drivers are moving-magnet devices. The last three were designed for single-frequency transduction at high efficiency and high power by Q-Drive, located in Troy, NY

A more detailed analysis is provided by Wakeland who shows that the maximum efficiency, η<sub>max</sub>, is related to that dimensionless driver parameter, β ≡ (Bℓ)<sup>2</sup>/(R<sub>m</sub>R<sub>dc</sub>), and introduces σ = √β + 1 [53]. Wakeland’s more accurate determination of σ approaches the simpler result of Eq. (10.101) as the value of β increases. Typical values of β for high-power, high-efficiency electrodynamic drivers are usually above 5 and less than 200.

$$\eta_{\max} = \frac{\beta}{\beta + 2\sqrt{\beta + 1} + 2} = \frac{\sigma - 1}{\sigma + 1} \quad (10.102)$$

A summary of the optimum efficiencies for several electrodynamic loudspeakers is given in Table 10.4 [53]. For the MW-142 in Problem 19 of Chap. 2, β = 5.8 and η<sub>max</sub> = 44%. For a 10 kW moving-magnet electrodynamic driver, shown in Fig. 4.21, β = 175 and η<sub>max</sub> = 86%.

## 10.8 Junctions, Branches, and Filters

We now change our focus from one-dimensional plane wave resonators to one-dimensional traveling plane waves in tubes with diameters, D, that are again small compared to the wavelength, D ≈ √A ≪ λ. The behavior of such traveling waves will be examined when they impinge on a junction between tubes that have an abrupt change in cross-sectional area, A. The reflection and transmission of energy at such a junction will be determined by the discontinuity in the acoustical impedance (or acoustical admittance) on either side of such a junction that could be due to changes in mean density, ρ<sub>m</sub>, times sound speed, c, in addition to changes in cross-sectional area. The analysis will be extended to branches that join one tube to several others or to other acoustical networks (e.g., to a Helmholtz resonator). In all of these cases, we will again impose continuity of mass flow (i.e., volume velocity) across the junction and where the pressure at the junction is necessarily single-valued.

### 10.8.1 Abrupt Discontinuities and the Acoustic Admittance

By this time, continuity of mass flow suggests that the tubes should be characterized by an acoustic impedance, although as we are about to demonstrate, the reciprocal of the acoustic impedance, known

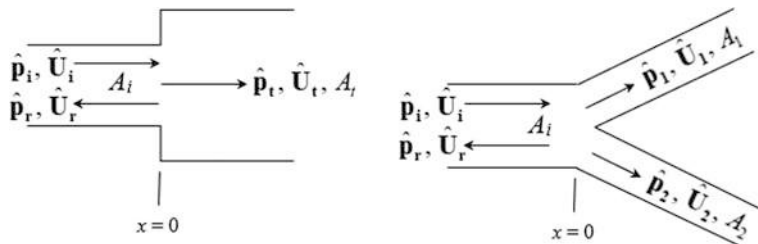


**Fig. 10.15** (Left) Single-frequency traveling wave with amplitude,  $\hat{\mathbf{p}}_i$ , is incident on a junction between tubes of different cross-sectional areas. Some energy is transmitted and some reflected. (Right) Traveling wave impinges from a single tube on a junction with two tubes, all with different cross-sectional areas

as the *acoustic admittance*,  $\mathbf{Y}_{\text{ac}}$ , will provide a more convenient characterization. For the case of the right-going wave that encounters a discontinuity in cross-sectional area, as diagrammed in Fig. 10.15 (left), the boundary conditions at  $x = 0$  can be expressed by forming the ratio of volume velocity to pressure.

$$\hat{\mathbf{p}}_i + \hat{\mathbf{p}}_r = \hat{\mathbf{p}}_t \quad \text{and} \quad \hat{\mathbf{U}}_i + \hat{\mathbf{U}}_r = \hat{\mathbf{U}}_t \quad \Rightarrow \quad \frac{\hat{\mathbf{U}}_i + \hat{\mathbf{U}}_r}{\hat{\mathbf{p}}_i + \hat{\mathbf{p}}_r} = \frac{\hat{\mathbf{U}}_t}{\hat{\mathbf{p}}_t} \quad (10.103)$$

Since all three waves are traveling waves,  $\mathbf{Y}_{\text{ac}} = \mathbf{Z}_{\text{ac}}^{-1} \equiv (\hat{\mathbf{U}}/\hat{\mathbf{p}}) = \pm A/\rho_m c$ , with the minus sign for the reflected wave because it will be traveling to the left. The continuity of volume velocity and the fact that the pressure at the junction is single-valued, shown in Eq. (10.103), can be expressed in terms of  $\mathbf{Y}_{\text{ac}}$ , which are real numbers.

$$Y_i(\hat{\mathbf{p}}_i - \hat{\mathbf{p}}_r) = Y_t \hat{\mathbf{p}}_t = Y_t(\hat{\mathbf{p}}_i + \hat{\mathbf{p}}_r) \quad \Rightarrow \quad Y_i \frac{\hat{\mathbf{p}}_i - \hat{\mathbf{p}}_r}{\hat{\mathbf{p}}_i + \hat{\mathbf{p}}_r} = Y_t \quad (10.104)$$

Equation (10.104) can be solved for the *amplitude reflection coefficient*,  $R \equiv |\hat{\mathbf{p}}_r|/|\hat{\mathbf{p}}_i|$ , and the *amplitude transmission coefficient*,  $T \equiv |\hat{\mathbf{p}}_t|/|\hat{\mathbf{p}}_i|$ .

$$R \equiv \frac{|\hat{\mathbf{p}}_r|}{|\hat{\mathbf{p}}_i|} = \frac{Y_i - Y_t}{Y_i + Y_t} \quad \text{and} \quad T \equiv \frac{|\hat{\mathbf{p}}_t|}{|\hat{\mathbf{p}}_i|} = \frac{2Y_i}{Y_i + Y_t} \quad (10.105)$$

These results seem sensible. If the properties of the tube do not change at  $x = 0$ , then  $Y_i = Y_t$ , so  $R = 0$  and  $T = 1$ ; the wave just keeps moving to the right, as it should through a uniform tube in the absence of dissipation. On the other hand, if  $A_t \ll A_i$ , and the same fluid medium fills both sections, then  $Y_i \gg Y_t$ , so the incident and reflected wave amplitudes are identical and the transmitted pressure,  $p_t$ , is doubled, though the volume flow rate moving past the junction is much smaller.

If the situation is reversed so if  $A_t \gg A_i$ , and the same fluid medium fills both sections, then  $Y_i \ll Y_t$ , so the incident and reflected waves have opposite phases since  $R \cong -1$ , and the transmitted pressure is very small,  $T \ll 1$ . This would be the case if the incident tube opened up to the atmosphere (i.e.,  $Y_t = \infty$ ). In that case, the volume flow rate would be unrestricted, but the transmitted acoustic pressure amplitude,  $|\hat{\mathbf{p}}_t|$ , would be very small since the cincident tube is effectively attached to an infinite fluid pressure reservoir.

Based on the intensities of the three waves, it is also possible to calculate a power reflection coefficient,  $R_{\Pi}$ , and power transmission coefficient,  $T_{\Pi}$ , that will be proportional to the squares of the pressures times the acoustic admittance,  $\langle \Pi \rangle_t = |\hat{\mathbf{p}}|^2 Y/2$ .

$$R_{\Pi} = \frac{|\hat{\mathbf{p}}_r|^2}{|\hat{\mathbf{p}}_i|^2} = \frac{(Y_i - Y_t)^2}{(Y_i + Y_t)^2} \quad \text{and} \quad T_{\Pi} = \frac{Y_t}{Y_i} \frac{|\hat{\mathbf{p}}_t|^2}{|\hat{\mathbf{p}}_i|^2} = \frac{4Y_i Y_t}{(Y_i + Y_t)^2} \quad (10.106)$$

Energy conservation is confirmed by the fact that  $R_{\Pi} + T_{\Pi} = 1$ ; any power that is not reflected must be transmitted. If the admittances are closely matched, so  $Y_2/Y_1 \cong 1$ , and then there is almost perfect transmission of the energy since the reflected portion is roughly  $(\frac{1}{4})(Y_2/Y_1 - 1)^2$ . This result provides justification for the stepwise approximation to a horn in Fig. 10.2, where the number of elements is chosen so the area change between adjacent elements is small so that reflections from the discontinuities can be ignored and the propagation can be considered to remain unidirectional.

Having identified the acoustic admittance as the physical quantity that determines the distribution of the incident, reflected, and transmitted energy, it is not difficult to generalize the previous results for a tube that branches into many tubes of differing acoustic admittance at the junction, such as the system diagrammed in Fig. 10.15 (right).

$$Y_i(\hat{\mathbf{p}}_i - \hat{\mathbf{p}}_r) = \left( \sum_{n=1}^N Y_n \right) \hat{\mathbf{p}}_t \quad \text{where} \quad Y_n = \frac{A_n}{\rho_n c_n}$$

$$\text{and} \quad \hat{\mathbf{p}}_t = \hat{\mathbf{p}}_i + \hat{\mathbf{p}}_r = \hat{\mathbf{p}}_1 = \hat{\mathbf{p}}_2 = \dots = \hat{\mathbf{p}}_n$$
(10.107)

The amplitude reflection and transmission coefficients are the corresponding generalizations of Eq. (10.105).

$$R = \frac{\hat{\mathbf{p}}_r}{\hat{\mathbf{p}}_i} = \frac{Y_i - \sum_{n=1}^N Y_n}{Y_i + \sum_{n=1}^N Y_n} \quad \text{and} \quad T = \frac{\hat{\mathbf{p}}_t}{\hat{\mathbf{p}}_i} = \frac{2Y_i}{Y_i + \sum_{n=1}^N Y_n} \quad (10.108)$$

The power transmission coefficients must be different for different outlet tubes. For the  $n$ th outlet tube,  $\langle \Pi_{t,n} \rangle_t = (\frac{1}{2})\Re e[\hat{\mathbf{p}}_n \hat{\mathbf{U}}_n^*] = (\frac{1}{2})Y_n |\mathbf{p}_t|^2$ . Meanwhile,  $\langle \Pi_i \rangle_t = (\frac{1}{2})Y_i |\hat{\mathbf{p}}_i|^2$ . We can use  $T = \hat{\mathbf{p}}_t/\hat{\mathbf{p}}_i$  in Eq. (10.108) to write the power transmission coefficient into the  $n$ th tube:

$$T_{\Pi,n} = \frac{\langle \Pi_n \rangle_t}{\langle \Pi_i \rangle_t} = \frac{Y_n}{Y_i} \frac{|\hat{\mathbf{p}}_n|^2}{|\hat{\mathbf{p}}_i|^2} = \frac{4Y_i Y_n}{\left( Y_i + \sum_{n=1}^N Y_n \right)^2} \quad (10.109)$$

By using Eqs. (10.108) and (10.109), one can verify that energy is conserved to exhibit the reassuring result:

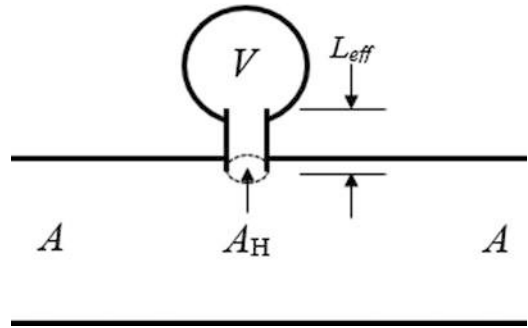
$$R_{\Pi} + \sum_{n=1}^N T_{\Pi,n} = R^2 + \sum_{n=1}^N T_{\Pi,n} = 1 \quad (10.110)$$

An interesting application of the pressures in branching systems to the human cardiovascular system, in particular the iliac bifurcation of the aorta, is discussed by Lighthill [1].

### 10.8.2 Tuned Band-Stop Filter

Based on the diagrams in Fig. 10.15, it appears that our interest is focused on the junction between semi-infinite pipes where we expect unidirectional propagation in the  $+x$  direction and an acoustic

**Fig. 10.16** Helmholtz resonator as a side branch on a duct of uniform cross-sectional area,  $A$ . The intrusion of the “neck” into the duct and into the volume represents the effective length of the neck,  $L_{eff}$ , which is greater than its physical length, as observed in Sect. 8.5.2



admittance for right-going traveling waves, as expressed in Eq. (10.86) or Eq. (10.107), so that  $Y_n = A/\rho_m c$  for all  $n \geq 1$ . There is no such restriction on  $Y_n$ . In the following application, we will use the formalism of Eq. (10.109) to calculate the transmission coefficient for sound that propagates along a duct that uses a Helmholtz resonator as a side branch to produce a *band-stop filter* that is shown schematically in Fig. 10.16.

The lumped element approach of Chap. 8 can be exploited to analyze this band-stop filter, also known as a “trap,” that can be useful for suppression of a single frequency in ducts, like those produced by a fan’s blade-passage frequency.

As calculated in Sect. 8.5.1, the series combination of an inertance and a compliance can have a vanishingly small input acoustical impedance when  $X_C$  and  $X_L$  cancel each other at the Helmholtz frequency,  $\omega_o$ . If a Helmholtz resonator is attached to a duct as a side branch, shown schematically in Fig. 10.16, all of the incident volume velocity is diverted to the branch leaving nothing to produce a transmitted pressure at the Helmholtz frequency through the duct beyond the branch to the right of the junction.

As shown in Fig. 10.16, a Helmholtz resonator that combines a compliance with internal volume,  $V$ , and a neck of cross-sectional area,  $A_H$ , with an effective length (see Sect. 8.5.2),  $L_{eff}$ , is connected to a duct of otherwise uniform cross-sectional area,  $A$ . This situation can be incorporated into Eq. (10.109) by letting  $N = 2$ , with  $Y_i = Y_1 = Y_t = R_{ac}^{-1} = A/\rho_m c$  and  $\mathbf{Y}_2 = 1/jX_H$  where  $X_H = X_L + X_C = \omega L - (1/\omega C)$  and  $\omega_o = 1/\sqrt{LC}$ .

$$X_H = \omega L - \frac{1}{\omega C} = \omega L \left( 1 - \frac{\omega_o^2}{\omega^2} \right) = \omega_o L \left( \frac{\omega}{\omega_o} - \frac{\omega_o}{\omega} \right) \quad (10.111)$$

Substitution into Eq. (10.109) provides the power transmission coefficient.

$$\begin{aligned} T_{II,1} &= \frac{4Y_i Y_1}{|Y_i + Y_1 + \mathbf{Y}_2|^2} = \frac{4Y_i^2}{\left| 2Y_i + \frac{1}{jX_H} \right|^2} \\ &= \frac{1}{1 + \frac{R}{4X_H^2}} = \frac{1}{1 + \frac{1}{\frac{4\omega_o^2 L^2}{R_{ac}^2} \left( \frac{\omega}{\omega_o} - \frac{\omega_o}{\omega} \right)^2}} \end{aligned} \quad (10.112)$$

Introduction of an exponential time constant,  $\tau_{L/R} = L/R_{ac}$ , can simplify and symmetrize the expression for the transmission coefficient.

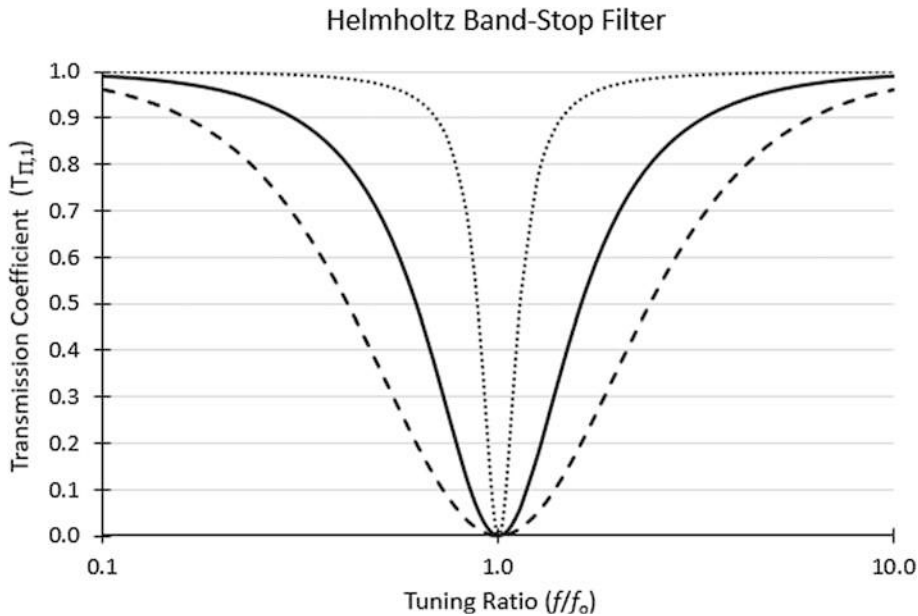


**Fig. 10.17** Power transmission coefficient,  $T_{\Pi,1}$ , for a duct with a Helmholtz resonator as a side branch. The *solid line* corresponds to  $(2\omega_o\tau_{LR}) = 1.0$ , with the *dashed line* for  $(2\omega_o\tau_{LR}) = 0.5$  and the *dotted line* for  $(2\omega_o\tau_{LR}) = 4.0$ .

$$T_{\Pi,1} = \frac{1}{1 + \frac{1}{(2\omega_o\tau_{LR})^2} \left( \frac{\omega}{\omega_o} - \frac{\omega_o}{\omega} \right)^2} = \frac{(2\omega_o\tau_{LR})^2 \left( \frac{\omega}{\omega_o} - \frac{\omega_o}{\omega} \right)^2}{(2\omega_o\tau_{LR})^2 \left( \frac{\omega}{\omega_o} - \frac{\omega_o}{\omega} \right)^2 + 1} \quad (10.113)$$

This transmission coefficient is plotted for three values of the dimensionless product of twice the Helmholtz resonance frequency times the exponential time constant,  $0.5 \leq (2\omega_o\tau_{LR}) \leq 4.0$ , in Fig. 10.17, as a function of the frequency ratio,  $f/f_o$ , on a logarithmic axis.

If the frequency is either much lower or much higher than the Helmholtz frequency, then the squared frequency ratio difference term in Eq. (10.113),  $[(\omega/\omega_o) - (\omega_o/\omega)]^2$ , dominates, and nearly all of the power is transmitted past the branch:  $T_{\Pi} \cong 1$ . If  $\omega = \omega_o$ , then the frequency term in the numerator is zero, so no power is transmitted in the limit that the dissipation in the Helmholtz resonator can be neglected.

At the Helmholtz frequency,  $\omega_o$ , the energy conservation condition in Eq. (10.110) requires that all of the power be reflected. With the admittance of the Helmholtz resonator at resonance being infinite (in the absence of dissipation), the phase-inverted reflection from the junction is what would be expected since, from the left, the situation would be indistinguishable from the case where  $A_t \gg A_i$  in Eq. (10.105).

### 10.8.3 Stub Tuning

One final *high-pass filter* application can be very useful if steady flow needs to be removed from acoustic propagation through the duct. Sirens can have very high efficiency [62], but they require steady gas flow. That steady flow can be diverted from a duct while allowing the high-amplitude

acoustic pressure wave to be transmitted through the duct if a thin membrane is placed across the duct and a vent tube that is one-quarter wavelength long is placed between the siren and the membrane.

If the membrane is sufficiently thin and flexible, the sound will pass through nearly unattenuated (see Sect. 11.1.1). If the “stub” is one-quarter wavelength long, at the siren’s frequency, then it will act as a  $1:\pm\infty$  transformer (see Sect. 3.8.1 and Fig. 3.10), so the nearly zero low-frequency acoustical impedance of the open end will present a nearly infinite acoustical impedance at the duct end for sound at the siren’s frequency; all the sound goes down the duct, and all the siren’s gas flow goes out the stub.

## 10.9 Quasi-One-Dimensional Propagation (Horns)

Thus far, this chapter has examined propagating plane waves in ducts and standing plane waves in resonators, both having constant cross-sectional areas,  $A$ , that are assumed to have linear dimensions that are much smaller than the wavelength of sound,  $\sqrt{A} \ll \lambda$ . The spatial dependence of such waves has been specified by a single coordinate. In all cases, the evolution of the waves depended only upon the  $x$  coordinate, and all of the wave’s acoustic variables (i.e., pressure, density, temperature, and particle velocity) have been uniform over planes that are perpendicular to the  $x$  axis. This geometry is responsible for the term “plane wave” that we use to designate such behavior.

In fact, the dependence on a single spatial coordinate is not unique to one-dimensional propagation. In Chap. 12, when the radiation of sound in a three-dimensional unbounded fluid medium is analyzed, spherically diverging sound waves are also characterized by a single spatial coordinate, the radial distance,  $r$ , from the omnidirectional source’s acoustic center. In the nondissipative limit, energy is conserved so that the pressure amplitude at a distance,  $r$ , is inversely proportional to that distance. The integral of the time-averaged intensity,  $\langle I \rangle_t = \langle [p^2(r, t)] \rangle_t / 2\rho_m c$ , over any spherical surface of area,  $A(r) = 4\pi r^2$ , centered on the source, remains constant.

For such spherically symmetric wave propagation, all fluid particle motion is radial. There would be no fluid motion that would cross the boundary of any cone with its apex centered at the source. For that reason, any conical horn of infinite length, with rigid surfaces, would support identical wave motion within its constant apex angle.<sup>17</sup> This argument should be reminiscent of the analysis of nodes of standing waves on pendula in Sect. 3.6.2, as well as arguments regarding membrane mode shapes that exploited nodal lines and nodal circles to calculate the behavior of those modes in Sect. 6.2.4 and Prob. 2 in Chap. 6 for membrane shapes that are not bounded by a rectangle or circle.

### 10.9.1 Semi-infinite Exponential Horns

Bolstered by such arguments, it is attractive to extend the analysis of one-dimensional propagation in a duct of uniform cross-sectional area to horns that have a monotonic change in cross-sectional area with distance,  $A(x)$ , which is a function of only the  $x$  coordinate, if we assume that the area changes slowly over distances comparable to the wavelength of the sound wave propagating through the horn.

Long before the development of electroacoustics and before an acoustical theory for horns existed, horns were recognized as an apparatus for concentrating sound energy and for improving the coupling between vibrating surfaces to the surrounding fluid medium. Several (amusing?) historical implementations are shown in Fig. 10.18. In the early days of electroacoustics, when the power

<sup>17</sup> Within the cone, the pressure amplitudes would be larger than those of a spherically spreading wave if the source’s volume velocity was the same in both cases. If the cone subtends a solid angle,  $\Omega$ , then the pressures would be enhanced by a factor of  $4\pi/\Omega$ , assuming the additional load would not reduce the source’s volume velocity.

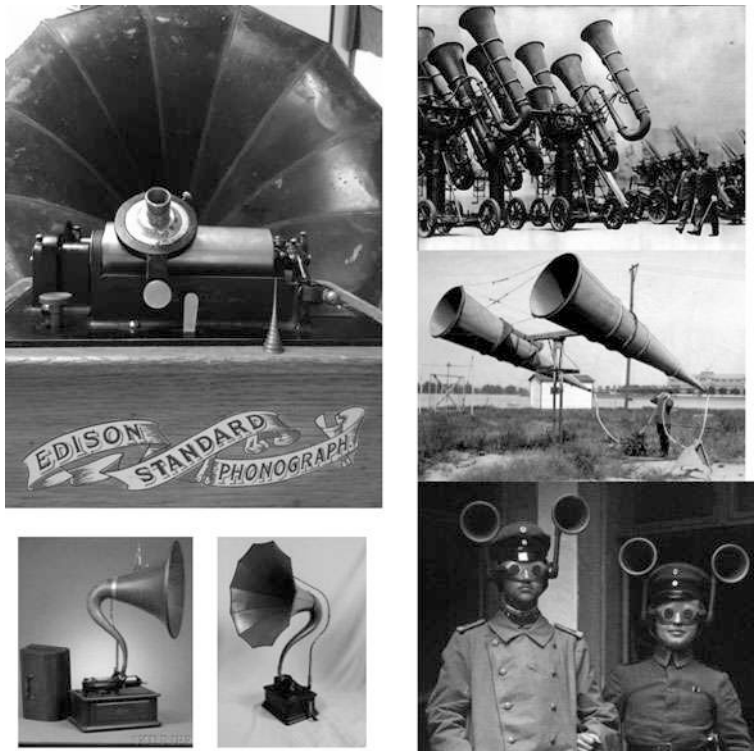


**Fig. 10.18** (Top left) Two horns from the author's personal collection. The "Triumph" straight horn, located behind the Edison Standard Phonograph, has a 24" (61 cm) diameter opening that reduces to a  $\frac{1}{2}$ " (1.3 cm) diameter at the apex for an area ratio of 2300:1. That horn is 36" (91 cm) long. Placed on that phonograph is a very small solid stepped exponential horn that is  $1\frac{1}{4}$ " (5.5 cm) long that was used by Prof. W. L. Nyborg to concentrate ultrasonic energy for streaming [63] and cellular (biological) cavitation experiments in fluids (courtesy of Prof. Richard Packard, a former Nyborg master's student). (Bottom left) Two curved Edison phonograph horns. (Top right) A horn-based aircraft detection and localization system used by the Imperial Japanese Army in 1936, known as the "Wartuba." (Center right) Another aircraft system used for stereo localization, photographed at Bolling Air Force Base, near Washington, DC, in 1921. (Bottom right) Personal listening device worn by German soldiers in 1917 that is combined with binoculars so that the aircraft can be seen as well as heard

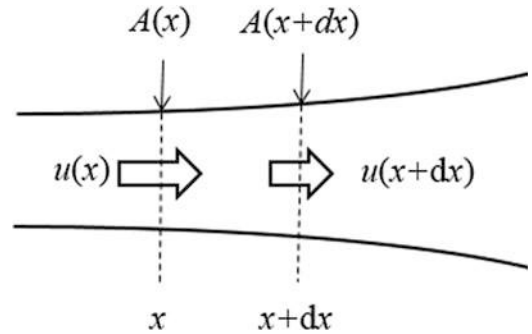
available using vacuum tube audio amplifiers was limited and motion pictures added sound tracks, horns were required to increase the efficiency of loudspeakers to ensonify the large volumes of theaters and auditoria [64].

To formulate a quasi-one-dimensional model of horns, it is necessary to modify the linearized one-dimensional continuity Eq. (10.1) that was derived in Sect. 8.2.1, based on the geometry specified in Fig. 8.2. In analogy with Eqs. (8.10)–(8.12), the change in the mass of fluid within a differential slab of volume,  $dV = A(x) dx$ , will be due to the difference in mass of fluid that enters  $A(x)$  with velocity along the  $x$  direction of  $u(x)$  and the mass that exits through an area,  $A(x + dx)$ , with velocity,  $u(x + dx)$ , as shown in Fig. 10.19.

$$\begin{aligned} \dot{m} &= (\rho_m u A)_x - (\rho_m u A)_{x+dx} = - \left( \frac{\partial(\rho_m u A)}{\partial x} \right)_x dx \\ \frac{\partial \rho_1}{\partial t} + \frac{\rho_m}{A(x)} \left( \frac{\partial(u_1 A)}{\partial x} \right) &= \frac{\partial \rho_1}{\partial t} + \frac{\rho_m u_1}{A(x)} \left( \frac{\partial A}{\partial x} \right) + \rho_m \left( \frac{\partial u_1}{\partial x} \right) = 0 \end{aligned} \quad (10.114)$$

The linearized Euler Eq. (10.2) remains unchanged. The linearized equation of state (10.4) still relates adiabatic pressure and density changes, but the square of the sound speed here will now be subscripted,

**Fig. 10.19** This geometry can be used for the derivation of a continuity equation that applies to a duct of continuously varying cross-sectional area,  $A(x)$ . To conserve volume velocity, the  $x$ -component of the fluid particle velocity,  $u(x)$ , must decrease as the cross-sectional area of the horn increases



$c_o$ , to remind us that it is the equilibrium thermodynamic sound speed,  $c_o^2 = (\partial p / \partial \rho)_s$ , as distinguished from the phase speed,  $c_{ph} = \omega / k$ , since those two speeds will not be the same, as they were for the truly one-dimensional problem in Eq. (10.19).

$$\rho_m \frac{\partial u}{\partial t} + \frac{\partial p}{\partial x} = \rho_m \frac{\partial u}{\partial t} + c_o^2 \frac{\partial \rho}{\partial x} = 0 \quad (10.115)$$

The second term in the continuity Eq. (10.114) involves the derivative,  $(1/A)(\partial A / \partial x) = \partial \ln(A) / \partial x$  (see Sect. 1.1.3), suggesting that a particularly simple solution to these coupled first-order differential equations might exist if the cross-sectional area of the horn varied as an exponential function of distance,  $x$ , along the horn's axis.

$$A(x) = A_o e^{2x/h} \quad (10.116)$$

A *flare constant*,  $h$ , has been introduced to scale the rate of change in area from its initial area,  $A_o \equiv A(0)$ . Using the same nondissipative argument for energy conservation made in the previous discussion of the conical horn, the amplitude of the acoustic pressure variation along the horn's axis must also decrease exponentially since the product,  $p^2(x)A(x)$ , must remain constant. Since the horn is semi-infinite, we need only to consider wave motion that propagates in the  $+x$  direction.

$$p_1(x, t) = \Re e \left[ \hat{\mathbf{p}}_o e^{-x/h} e^{j(\omega t - \kappa x)} \right] \text{ and } \rho_1(x, t) = \Re e \left[ \frac{\hat{\mathbf{p}}_o}{c_o^2} e^{-x/h} e^{j(\omega t - \kappa x)} \right] \quad (10.117)$$

Our symbol for the wavenumber,  $\kappa$ , is chosen to remind ourselves that it has yet to be determined. The initial acoustic pressure phasor at the throat of the horn is  $\hat{\mathbf{p}}_o$ .

Substitution of Eqs. (10.116) and (10.117) into the coupled differential Eqs. (10.114) and (10.115) allows them to be converted to coupled algebraic equations.

$$\begin{aligned} j\omega \rho_m \hat{\mathbf{u}} - c_o^2 \left( \frac{1}{h} + j\kappa \right) \hat{\mathbf{p}} &= 0 \\ \rho_m \left[ \frac{2}{h} - \frac{1}{h} - j\kappa \right] \hat{\mathbf{u}} + j\omega \hat{\mathbf{p}} &= 0 \end{aligned} \quad (10.118)$$

As before, when seeking the dispersion relation, like that in Eq. (10.19), the determinant of the coefficients of the acoustic field variables,  $\hat{\mathbf{p}}$  and  $\hat{\mathbf{u}}$ , must vanish if nontrivial solutions to Eq. (10.118) exist.

$$\begin{vmatrix} j\omega \rho_m & -\frac{c_o^2}{h}(1 + j\kappa h) \\ \frac{\rho_m}{h}(1 - j\kappa h) & j\omega \end{vmatrix} = 0 \quad (10.119)$$

We now can construct the necessary dispersion relation between wavenumber,  $\kappa$ , and frequency,  $\omega$ .

$$\omega^2 = \frac{c_o^2}{h^2} + c_o^2 \kappa^2 \Rightarrow \kappa = \pm \frac{\omega}{c_o} \sqrt{1 - \frac{c_o^2}{(\omega h)^2}} \Rightarrow c_{ph} = \frac{\omega}{\kappa} = \frac{c_o}{\sqrt{1 - \frac{c_o^2}{(\omega h)^2}}} \quad (10.120)$$

It is clear from Eq. (10.120) that the solution no longer corresponds to wave motion for frequencies below a cut-off frequency,  $\omega_{co} = 2\pi f_{co} = c_o/h$ . The phase speed,  $c_{ph}$ , can be re-written in terms of the ratio of that cut-off frequency,  $\omega_{co}$ , to the drive frequency,  $\omega$ .

$$c_{ph} \equiv \frac{\omega}{\kappa} = \frac{c_o}{\sqrt{1 - \frac{\omega_{co}^2}{\omega^2}}} = \frac{c_o}{\sqrt{1 - \frac{f_{co}^2}{f^2}}} \quad \text{with} \quad \omega_{co} = 2\pi f_{co} = \frac{c_o}{h} \quad (10.121)$$

When  $\kappa$  becomes imaginary, the acoustic pressure in Eq. (10.117) decays exponentially, and the disturbance becomes more localized at the apex (throat) of the horn as the frequency decreases below  $\omega_{co}$ . For an infinite exponential horn in air that changes its diameter by a factor of  $e = 2.72$  over 1 m (i.e.,  $h = 1.0$  m), the cut-off frequency,  $f_{co} \cong 55$  Hz.

We also neglected dissipation, so the transmitted power is independent of distance. That constant transmitted power can be calculated at the horn's apex by using Euler's Eq. (10.115) and Eq. (10.117) to calculate the gas particle velocity,  $\hat{\mathbf{u}}(0)$ , and the associated volume velocity,  $\hat{\mathbf{U}}(0) = A(0)\hat{\mathbf{u}}(0)$ .

$$\hat{\mathbf{U}}(0) = \hat{\mathbf{u}}A_o = \frac{A_o}{\rho_m c} \left[ \sqrt{1 - \left( \frac{f_{co}}{f} \right)^2} - j \left( \frac{f_{co}}{f} \right) \right] \hat{\mathbf{p}}(0) \quad \text{if } f > f_{co} \quad (10.122)$$

The transmitted power,  $\langle \Pi \rangle_t$ , depends on the time-averaged product of pressure and volume velocity (see Sect. 1.5.4).

$$\langle \Pi \rangle_t = \frac{1}{2} \Re e [\hat{\mathbf{p}}(0) \hat{\mathbf{U}}^*(0)] = \frac{\hat{\mathbf{p}}(0)}{2} \frac{A(0) \hat{\mathbf{p}}(0)}{\rho_m c_o} \sqrt{1 - \left( \frac{f_{co}}{f} \right)^2} \quad \text{for } f > f_{co} \quad (10.123)$$

Using Eq. (10.122), the magnitude of the volume velocity at the apex,  $|\hat{\mathbf{U}}(0)|$ , can be used to simplify Eq. (10.123) and compare the time-averaged power radiated down the horn to the power radiated by a simple source generating a spherically spreading wave due to a volume velocity at the surface of a spherical-pulsating source,  $\hat{\mathbf{U}}(a)$ , given in Eq. 12.24.

$$|\hat{\mathbf{U}}(0)| = \frac{\hat{\mathbf{p}}(0)A(0)}{\rho_m c_o} \left[ \left( \sqrt{1 - \frac{f_{co}^2}{f^2}} \right)^2 + \left( \frac{f_{co}^2}{f^2} \right)^2 \right]^{\frac{1}{2}} = \frac{\hat{\mathbf{p}}(0)A(0)}{\rho_m c_o} \quad (10.124)$$

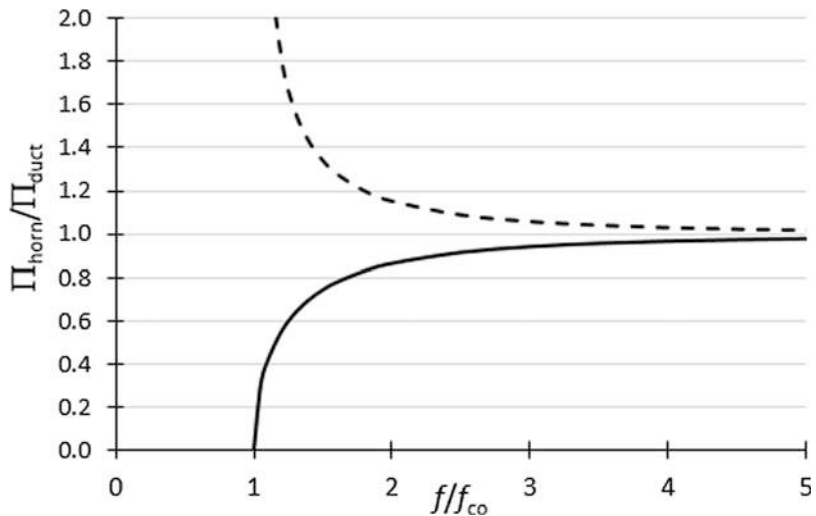
$$\langle \Pi \rangle_t = \frac{1}{2} \frac{\rho_m c_o}{A(0)} |\hat{\mathbf{U}}(0)|^2 \sqrt{1 - \frac{f_{co}^2}{f^2}} \quad (10.125)$$

For a spherical source radiating in an infinite three-dimensional fluid, the time-averaged power can be expressed in a similar form that excludes the frequency dependence in the square root and substitutes  $\lambda^2/\pi$  for the horn's cross-sectional area at its apex,  $A(0)$ .

$$\langle \Pi \rangle_t = \frac{1}{2} \frac{\rho_m c_o}{(\lambda^2/\pi)} |U(a)|^2 \quad (10.126)$$

This result shows that the horn can act as a transformer to increase the power radiated by a physically compact source of volume velocity above  $\omega_{co}$  since  $A(0) \ll \lambda^2/\pi$ . This is the reason that

**Fig. 10.20** The relative power transmission coefficient for infinitely long exponential (*solid*) and catenoidal (*dashed*) horns.  $\Pi_{\text{horn}}$  is compared to the power transmitted through a duct,  $\Pi_{\text{duct}}$ , of the same initial cross-sectional area,  $A(0) = A_{\text{pist}}$ , as a function of the ratio of the source's frequency to the cut-off frequency of the horn,  $f/f_{\text{co}}$



horns are used routinely to improve the radiation efficiency of pistons with diameters that are much smaller than the wavelength of the sound they must produce. Since the propagation is reversible, it is also the reason that the horns, like those shown in Fig. 10.22 (right), were used to concentrate sound energy and deliver it to the ear of a hearing-impaired listener with increased amplitude (i.e., the “ear trumpet”).

The power transmitted by a piston down a duct,  $\langle \Pi_{\text{duct}} \rangle_t = (\frac{1}{2})\rho_m c_o |\hat{\mathbf{U}}(0)|^2$ , with the same cross-sectional area as the piston’s effective area,  $A_{\text{pist}}$ , can be compared to the power transmitted down an infinitely long exponential horn with the same initial area,  $A_{\text{pist}} = A(0)$ . As shown in Fig. 10.23, that ratio approaches unity monotonically for frequencies above cut-off (Fig. 10.20).

These results assume that a one-dimensional description of the horn used to derive the continuity Eq. (10.114) provides a sufficiently good approximation to the acoustic behavior of the medium exhibiting the wave-like behavior within the horn. Thus far, the conditions under which such an approximation might be valid have not been addressed. The surfaces of constant phase for a geometry like that depicted in Fig. 10.22 must intersect the horn’s surface at a right angle. If the horn’s cross-sectional area changes too rapidly, then the wave fronts will not “cling” to the horn’s surface [65]. For an infinite horn, the only physical parameters that characterize its geometry are the initial area,  $A(0)$ , and its flare constant,  $h$ . For this quasi-one-dimensional analysis to be accurate,  $r_o \cong \sqrt{A(0)} \ll h$ , where  $r_o$  is the effective radius of the horn’s throat at  $x = 0$ .

### 10.9.2 Salmon Horns\*

As shown in Sect. 10.2, it is also possible to combine the first-order continuity and Euler equations with the equation of state to produce a wave equation for a horn in the quasi-one-dimensional limit that is a homogeneous second-order partial differential equation.

$$\frac{1}{A} \frac{\partial}{\partial x} \left( A \frac{\partial p(x, t)}{\partial x} \right) - \frac{1}{c_o^2} \frac{\partial^2 p(x, t)}{\partial t^2} = 0 \quad (10.127)$$

Our investigation of the exponential horn was motivated by the fact that  $(1/A)(\partial A/\partial x) = \partial \ln(A)/\partial x$  equaled a constant for the exponential change in cross-section that was assumed in Eq. (10.116).

A more general family of solutions was suggested by Salmon [66] who required that the entire dependence of Eq. (10.127) on area be a positive constant.<sup>18</sup>

$$\frac{\partial^2(p\sqrt{A})}{\partial x^2} - \left(\frac{\omega}{c_o}\right)^2(1-\beta^2)\left(p\sqrt{A}\right) = 0 \text{ where } \beta^2 = 1 - \left(\frac{\omega_{co}}{\omega}\right)^2 \quad (10.128)$$

Solutions to this time-independent Helmholtz equation are parameterized by two constants: the flare constant,  $h$ , and the constant,  $C$ , which controls the superposition of the two solutions to that second-order differential equation.

$$A(x) = A(0) \left[ \cosh\left(\frac{x}{h}\right) + C \sinh\left(\frac{x}{h}\right) \right]^2$$

and  $p_1(x, t) \propto \Re e \left[ \frac{\hat{\mathbf{p}}(0)}{\sqrt{A(x)}} e^{j(\omega t - \kappa x)} \right]$  (10.129)

As for any linear solution, the amplitude,  $\hat{\mathbf{p}}(0)$ , is arbitrary until the initial conditions at  $x = 0$  are specified. For  $C = 1$ , the exponential horn is recovered. With  $C = 0$ , the horn's shape is catenoidal. In the limit that  $h \rightarrow \infty$  and  $C = (h/x_o)$ , the horn's shape is conical with an apex angle,  $\phi = \tan^{-1}(r_o/x_o)$ , for the apex of the cone located at  $x = 0 < x_o$  and an initial area,  $A(0) = \pi r_o^2$ , assuming the cone has circular cross-sections. For  $0 < C < \sqrt{2}$ , the relative transmission coefficient,  $\Pi_{\text{horn}}/\Pi_{\text{duct}}$ , plotted in Fig. 10.23, has a maximum at  $(f/f_{\text{co}})_{\text{max}}$ . Under that condition, with  $(f/f_{\text{co}}) > (f/f_{\text{co}})_{\text{max}}$ , the relative power transmission coefficient asymptotically approaches  $\Pi_{\text{horn}}/\Pi_{\text{duct}} = 1$ .

$$\left(\frac{\Pi_{\text{horn}}}{\Pi_{\text{duct}}}\right)_{\text{max}} = \frac{1}{2C\sqrt{1-C^2}} \text{ for } 0 < C < \sqrt{2} \text{ at } \left(\frac{f}{f_{\text{co}}}\right)_{\text{max}} = \sqrt{\frac{1-C^2}{1-2C^2}} \quad (10.130)$$

For  $C = 0.5$ ,  $(\Pi_{\text{horn}}/\Pi_{\text{duct}})_{\text{max}} = 1.15$  at  $(f/f_{\text{co}})_{\text{max}} = 1.22$ , providing fairly uniform transmission above the cut-off frequency.

### 10.9.3 Horns of Finite Length\*

Our analyses of horns of infinite length (i.e., no reflected wave) have introduced several useful concepts, particularly the existence of the low-frequency cut-off,  $\omega_{co}$ , but real horns are never infinitely long. Finite-length horns fall into two general categories: (i) The horns that terminate musical instruments depend on reflection from the “bell” to define the standing wave that determines the instrument’s pitch. (ii) The horns used to couple sources to the surrounding space try to avoid resonances that reduce the uniformity of radiated sound as a function of frequency above cut-off.<sup>19</sup>

Horns of finite length will exhibit resonances at frequencies above cut-off, at least until the radiation impedance at the bell is sufficient to couple most of the energy out of the horn, thus nearly eliminating

<sup>18</sup> If  $\beta^2$  is negative, then there is a family of sinusoidal horn shapes (e.g., a globe terminated in a cusp) that describe the shape of the bell of the flute commonly associated with Indian snake charmers or the English horn, first used in the by Rossini, in 1829, in the opera, *William Tell*. [See B. N. Nagarkar and R. D. Finch, “Sinusoidal horns,” J. Acoust. Soc. Am. **50**(1) 23–31 (1971).]

<sup>19</sup> A nonuniform power transmission coefficient does not necessarily reduce the value of guided-wave enhancement of the coupling to an electrodynamic transducer, since human perception of low-frequency musical content is not particularly sensitive to such a nonuniform response. The best example of such a psycho-acoustic tolerance may be the success of the Bose Wave™ radio that employs a long serpentine duct that is driven by the rear of the forward-radiating speakers as shown in US Pat. No. 6,278,789 (Aug. 21, 2001).

the back-reflected wave from the bell. Although an exact calculation will be postponed until Sect. 12.8.3, a reasonable rule-of-thumb is that the resonances will be suppressed once the circumference of the bell exceeds the wavelength of the sound.

At reasonably high frequencies, horn-coupled loudspeakers can both be efficient and provide fairly uniform radiation over a significant range of frequencies. Above 1.0 kHz,  $\lambda < 35$  cm, so the bell of a horn that is only 10 cm in diameter will provide acceptable performance (see Problem 17). The engineering design of such horn-coupled electrodynamic loudspeakers (commonly called compression drivers) is beyond the scope of this treatment and can involve considerations of directionality, the compliance of the space between the driver's diaphragm and the start of the horn, as well as the nonlinear distortion [67, 68] that can be produced due to the very high acoustic pressures near the throat. Several textbooks with a greater focus on audio engineering provide detailed guidance [69, 70].

Resonances in horns are particularly pronounced at low frequencies. The lowest note on a double bass or an electric bass guitar is usually  $E_1 = 41.2$  Hz, based on  $A_4 = 440$  Hz. The corner horn shown in Fig. 10.21 has a catenoidal shape with a flare constant,  $h = 1.37$  m, selected to make  $f_{co} = c_o / 2\pi h = 40$  Hz. It is driven by an Axon Model 6S3 direct radiator loudspeaker. The front of that speaker radiates midrange frequencies, and the rear of the speaker drives the horn.

Also shown in Fig. 10.21 (right) is a tweeter for high frequencies with a passive cross-over network attached to the triangular top of the horn. The resonance frequencies and corresponding mode shapes were calculated using a DELTAEC model, shown in Fig. 10.22, that represent the catenoidal horn as eight CONE segments driven at constant voltage by the electrodynamic speaker with parameters listed in the VSPEAKER segment (#1). The bell of the horn is terminated with an OPNBRANCH segment (#11) that simulates radiation loading.

### Talk Like an Acoustician

Wave equation	Equal-loudness contours
Dispersion relation	Fletcher-Munson curves
Bulk modulus	Sound level meter
Adiabatic compressibility	Crest factor
Specific acoustic impedance	Acoustic transfer impedance
Characteristic impedance	Principle of reciprocity
Acoustical impedance	Reciprocity calibration
Mechanical impedance	Level repulsion
Rayl	Wakeland number
Acoustic intensity	Acoustic admittance
Reference intensity	Amplitude reflection coefficient
Reference sound pressure	Amplitude transmission coefficient
Coherent sound sources	Power transmission coefficient
Linearized Euler equation	Band-stop filter
Linearized Continuity equation	Low-pass filter
Homogeneous	High-pass filter
Isotropic	Exponential horn
Conservation equation	Catenoidal horn
	Flare constant
	Cut-off frequency

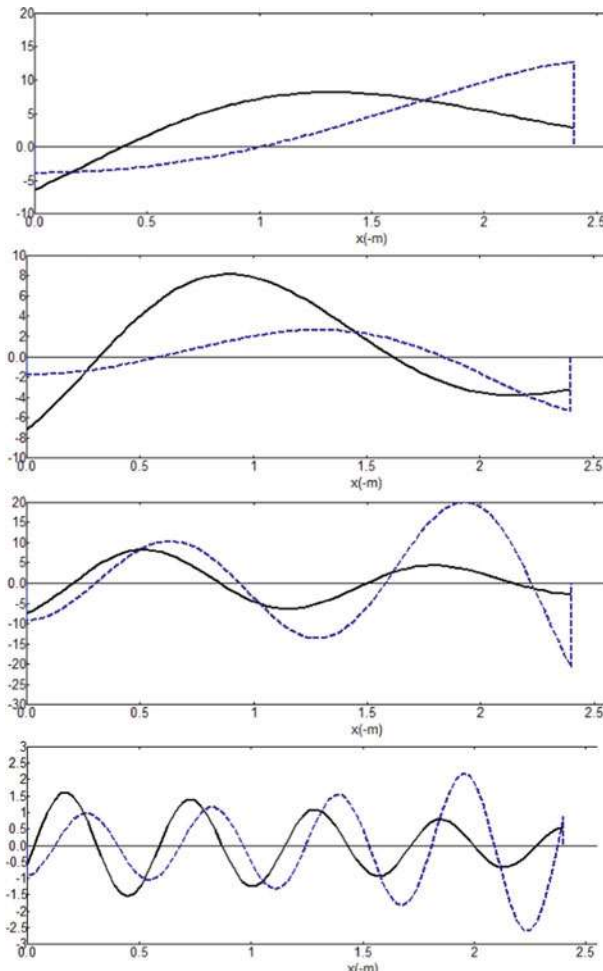


**Fig. 10.21** (Right) Corner horn (this horn design, suggested by I. Rudnick, is particularly simple because it involves cutting a single sheet of plywood with a hand-held circular saw that has its blade set at  $45^\circ$ , creating a smooth cut that will produce a leak-tight seal against the walls of a room. Even though the plywood is fairly thin ( $3/8'' \cong 9.5$  mm), it produces a rigid boundary since it is curved initially along one axis making it very stiff against bending along an orthogonal direction. The plywood is held against the walls with a single turnbuckle anchored in the corner. The place where the turnbuckle should be attached to the plywood is found by applying force to one location that pushes the plywood smoothly against the wall. A horizontal “stringer” is then screwed and glued to the plywood to accept the hook. The stringer’s position is visible in Fig. 10.21 due to the six flat-head screws that can be seen forming a line about one-sixth of the way above the bell.) created by a single sheet of plywood that is cut to produce a catenoidal change in cross-sectional area from  $173 \text{ cm}^2$  at the top to  $0.152 \text{ m}^2$  at the opening over a length of  $8' \cong 2.4 \text{ m}$ . (Left) Plots of the acoustic pressure (solid black line) that is in-phase with the volume velocity (dashed blue line) within the horn created when the speaker, at the throat, is driven with an electrical input of  $10 \text{ V}_{\text{pk}} = 7.07 \text{ V}_{\text{ac}}$ . At  $x = 0$ , the volume velocity is equal to that produced by the rear of the loudspeaker. From top to bottom:  $f_1 = 77 \text{ Hz}$ ,  $f_2 = 139 \text{ Hz}$ ,  $f_3 = 204 \text{ Hz}$ , and  $f_8 = 618 \text{ Hz}$

## Exercises

1. **Traveling wave acoustic field variables.** Express the space and time dependence, as well as the amplitudes, for the following acoustic field variables if  $p_1(x, t) = \Re e[\hat{\mathbf{p}} e^{j(\omega t - kx)}]$ .
  - (a) *Acoustic density,  $\rho_1(x, t)$*

```

1 CatenoidSpeaker(2) Student Area Catenoid
2 + 0 BEGIN Initial
12 - 1 VSPEAKER Axon 6S3
13      0.1247 a Area m^2          67.841 A |p| Pa
14      5.6300 b R ohms            145.07 B Ph(p) deg
15      2.6000E-04 c L H          1.1539E-02 C |U| m^3/s
16      5.7200 d BLProd T-m       145.07 D Ph(U) deg
17      1.2000E-02 e M kg         8.2775 E Htot W
18      1329.0 f K N/m           0.3914 F Edot W
19      1.0800 g Rm N-s/m        8.2775 G WorkIn W
20      10.000 h |V| V           10.000 H Volts V
21
22      1.6733 I Amps A          8.3511 J Ph(V/I)deg
23      1.1544E-02 K |Ux| m^3/s
24 ideal Solid type             145.07 L Ph(-Ux)deg
25 - 2 RPN Phase of Pressure and Volume Velocity at Throat
26 This is the criterion for a coupled horn-loudspeaker resonance
27 Targ 0.0000 a G or T          -1.0976E-09 A Degrees
28 1B 1D -
29 + 3 CONE First Segment
38 - 4 CONE Second
39 Same 3d 1.8200E-02 a AreaI m^2          116.66 A |p| Pa
40 Same 3e 0.6140 b PerimI m                 83.088 B Ph(p) deg
41      0.3000 c Length m                   1.1465E-02 C |U| m^3/s
42      2.0800E-02 d AreaF m^2            138.60 D Ph(U) deg
43      0.6580 e PerimF m                 8.2775 E Htot W
44 Master-Slave Links                  0.37868 F Edot W
45 Optional Parameters
46 ideal Solid type
47 + 5 CONE Three
56 + 6 CONE Four
65 + 7 CONE Five
74 + 8 CONE Six
83 + 9 CONE Seven
92 - 10 CONE Eight
93 Same 9d 0.1012 a AreaI m^2          92.985 A |p| Pa
94 Same 9e 1.4500 b PerimI m          53.844 B Ph(p) deg
95 Same 3c 0.3000 c Length m        9.2681E-03 C |U| m^3/s
96      0.1517 d AreaF m^2          19.200 D Ph(U) deg
97      1.7760 e PerimF m          8.2775 E Htot W
98 Master-Slave Links                  0.3545 F Edot W
99 Optional Parameters
100 ideal Solid type
101 + 11 OPNBRANCH Radiation Load
109 + 12 RPN Wavenumber
112 + 13 RPN Radiated Power
115 + 14 RPN Power = Press * Volume Velocity / 2
118 + 15 HARDEND OPNBRANCH is the only "exit"

```

**Fig. 10.22** Screenshot of a DELTAEC model for the corner horn shown in Fig. 10.21 (right) that calculated the resonance frequencies and produced the mode shapes in Fig. 10.21 (left). The resonance condition was imposed by the RPN target (Seg. #2) that seeks a condition where the volume velocity and pressure are in-phase at the horn's throat

- (b) *Acoustic particle velocity*,  $v_1(x, t)$   
 (c) *Kinetic energy density*, ( $KE$ )  
 (d) *Potential energy density*, ( $PE$ )  
 (e) *Time-averaged intensity*,  $\langle I \rangle_t$
2. **Standing wave acoustic field variables.** Express the space and time dependence, as well as the amplitudes, for the following acoustic field variables if  $p_1(x, t) = \Re[\hat{\mathbf{p}} \cos(kx)e^{j\omega t}]$ .
- (a) *Acoustic density*,  $\rho_1(x, t)$   
 (b) *Acoustic particle velocity*,  $v_1(x, t)$   
 (c) *Kinetic energy density*, ( $KE$ )  
 (d) *Potential energy density*, ( $PE$ )  
 (e) *Time-averaged intensity*,  $\langle I \rangle_t$
3. **Concert A4.** A sound wave in dry air at  $T_m = 20^\circ\text{C}$ , with frequency,  $f = 440$  Hz, has a sound pressure level of 76.0 dB, re:  $20 \mu\text{Pa}_{\text{rms}}$ . Determine the following characteristics of that tone.
- (a) *Time-averaged intensity*,  $\langle I \rangle_t$   
 (b) *Intensity level*, re:  $1.0 \times 10^{-12} \text{ W/m}^2$   
 (c) *Peak particle speed*,  $v_I$   
 (d) *Peak-to-peak particle displacement*,  $2x_I$   
 (e) *Peak acoustic temperature change*,  $T_I$
4. **Speed of shallow water gravity waves (surf).** The Euler and continuity equations for an incompressible fluid ( $\rho = \text{constant}$ ), with a free surface in a gravitational field, having a gravitational acceleration,  $g$ , are provided below. (For this problem, let  $g = 9.8 \text{ m/s}^2$ .) The equilibrium depth of the fluid is  $h_o$ . Consider small-amplitude traveling surface waves ( $|\hat{\mathbf{h}}| \ll h_o$ ) propagating in the  $+x$  direction:  $h(x, t) = h_o + |\hat{\mathbf{h}}| \sin(\omega t - kx)$ .

$$\frac{\partial h_1(x, t)}{\partial t} + h_o \frac{\partial v_1(x, t)}{\partial x} = 0 \quad (10.131)$$

$$\frac{\partial v_1(x, t)}{\partial t} = -\frac{1}{\rho_m} \frac{\partial}{\partial x} [\rho_m g h_1(x, t)] = -g \frac{\partial h_1(x, t)}{\partial x} \quad (10.132)$$

- (a) *Which equation is which?* One of the above equations is the linearized continuity equation for this system, and the other is the linearized Euler equation. Identify which equation represents continuity and which is Euler.
- (b) *Propagation speed.* Use Eqs. (10.131) and (10.132) to derive an expression for the propagation speed (not the horizontal particle velocity  $v_I$ ) of a small-amplitude surface wave. Does this agree with the results based on similitude that were calculated in Chap. 1, Problem 8d?
- (c) *Small-amplitude approximation.* Under what conditions is the vertical velocity of the surface,  $dh_1/dt$ , small compared to the horizontal particle speed,  $v_I$ ? What is required so that  $(dh_1/dt)/v_I \ll 1$ ?
- (d) *The Boxing Day tsunami.* On 26 December 2004, at 00:58:53 UTC, there was a magnitude 9.0 earthquake off the west coast of Northern Sumatra (3.29 N 95.94E) which launched a tsunami (tidal wave). Seven hours later, the wave reached the shores of Somalia (2.03 N 45.35E), a distance of approximately 5600 km across the Indian Ocean from the deadly quake's epicenter. Assuming that the tsunami was a "shallow water gravity wave" (which it was!), determine the average depth of the Indian Ocean along the nearly equatorial path from the epicenter to the coast of Somalia.

5. **Addition of three incoherent sound sources.** At a particular position in a shop, three machines produce individual sound pressure levels of 90, 93, and 95 dB<sub>SPL</sub>, all referenced to 20 μPa<sub>rms</sub>. Determine the total sound pressure level if all of the machines are running simultaneously. Assume each noise source is statistically independent of all of the others so that their powers (not pressures) are combined. Report your result in dB re: 20 μPa<sub>rms</sub>.
6. **dB addition.** A noise is generated by 80 pure tones of different frequencies but identical power. At locations equidistant from all sources, each individual tone has a sound pressure level of 60 dB re: 20 μPa<sub>rms</sub>. Determine the sound pressure level at that location if all 80 sources are radiating simultaneously.
7. **Underwater sound intensity reference level.** The sound pressure reference level currently used for sound in water is  $R_{ref}(H_2O) = 1.0 \mu\text{Pa}_{rms}$ . What would be the corresponding sound intensity reference level in water,  $I_{ref}(H_2O)$ ?
8. **Cavitation threshold.** The motion of the face of an underwater (SONAR) transducer toward the water causes a local compression, and when it moves away a half-cycle later, it creates local suction. If the suction pressure creates a tension in the fluid that exceeds the cavitation threshold, it “tears” a hole in the medium, producing bubbles.
  - (a) *Hydrostatic pressure.* If the transducer is located 50 m below the surface, what is the static water pressure,  $p_m$ , remembering that the pressure on the surface is one atmosphere,  $p_o = 101.3 \text{ kPa}$ .
  - (b) *Cavitation level.* What is the intensity level, re: 1 μPa<sub>rms</sub>, of a pressure wave that would create a peak negative pressure,  $|-p| = p_m$ , and cause an instantaneous rupture in the water?
9. **Climate change.** Table 10.1 shows standard dry air having a CO<sub>2</sub> mole fraction of 314 ppm. As of June 2020, the mole fraction was found to have increased to 415 ppm [71]. How much does this change the sound speed in dry air?
  - (a) *Approximate sound speed change.* Get an approximate result by ignoring the change in  $\gamma$ .
  - (b) *Polytropic coefficient.* Use  $\gamma_{air} = 1.4$  and  $\gamma_{CO2} = 1.3$ . Will the change in sound speed due to the change in  $\gamma_{mix}$  have the same sign as that due to the change in  $M_{mix}$ ?
  - (c) *Sound speed change.* Use Eq. (10.25) to calculate the change in  $\gamma$ , and use that result to obtain a more accurate result for the change in sound speed.
10. **Schlagwetter-pfeife.** The presence of methane in mines presents a significant hazard due to the possibility of underground explosions. In the late-1800s, one of the world’s most famous industrial chemists, Fritz Haber,<sup>20</sup> invented the “methane whistle” to determine the presence of hydrogen or methane in air extracted from underground mines [72]. By 1888, these methane whistles also began to appear in the United Kingdom [73]. Air was pumped from the mine out through one whistle, and fresh air was pumped through the other. Assume the whistles were identical and in good thermal contact, so both surface air and the sub-surface air passing through the whistles were at the same temperature. Determine the concentration (mole fraction) of methane (CH<sub>4</sub>) in the mine air if the air whistle had a frequency of 440 Hz and the pair of whistles produced 10 beats per second at 20 °C.
11. **Sonic hydrogen detector design.** Hydrogen gas is very flammable in air with the flammability ranging between mole fractions of 4% and 74%. With the possible future advent of hydrogen-powered vehicles, the National Transportation Safety Board has asked you to design an acoustic resonator that will use the change in frequency caused by a change in sound speed to alert occupants of a home if the concentration of hydrogen gas in their garage exceeds a mole fraction

<sup>20</sup> Fritz Haber was also one of the world’s most infamous chemists, having developed the gas that was used to murder prisoners in the Nazi death camps.

of 1.5%. For the purposes of this problem, you may take the mean molecular mass of air to be  $M_{air} = 29.0$  gm/mole and the mean molecular mass of hydrogen to be  $M_{hydrogen} = 2.0$  gm/mole. Both gases can be treated as consisting primarily of diatomic molecules, and the temperature in the garage can be taken as 10 °C.

- (a) *Frequency shift.* What is the relative change in frequency,  $\delta f/f_0$ , in percent, that would correspond to the addition of 1.5% of hydrogen to previously pure dry air, assuming that the resonator's frequency was  $f_0$  before the hydrogen was injected into the resonator?
  - (b) *Temperature effects.* How much must the temperature of the garage be increased to raise the resonator's frequency by the same amount as you calculated in part (a) if there were no hydrogen gas present in the air?
12. **Bulk modulus.** Eq. (10.20) expresses the adiabatic bulk modulus,  $B_s \equiv -V(\partial p/\partial V)_s$ , in terms of the square of the adiabatic sound speed,  $c^2 = (\partial p/\partial \rho)_s$ . Show that Eq. (10.133) is correct.

$$\frac{1}{\rho} \left( \frac{\partial p}{\partial (\nu_\rho)} \right)_s = -\rho \left( \frac{\partial p}{\partial \rho} \right)_s \quad (10.133)$$

13. **Slow waves in a water-filled pipe.** Sound speed is determined by a medium's compressibility and its inertia. In this problem, water will provide the inertia, but if the water is contained within a pipe, the distensibility of the pipe will generally produce an increased compressibility since the pipe's walls will stretch.

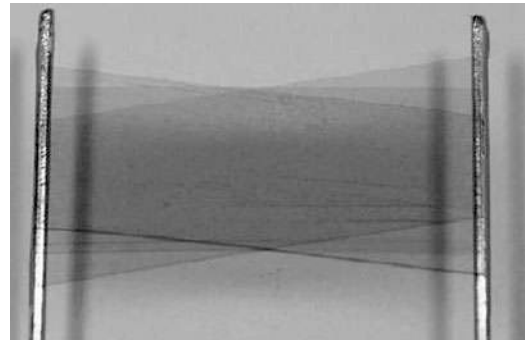
- (a) *Bulk modulus of water.* If the density of water is  $\rho_{water} = 1000$  kg/m<sup>3</sup> and the sound speed in the water is  $c_{water} = 1500$  m/s, what is the value of the bulk modulus of water?
- (b) *Effective bulk modulus of a PVC pipe.* Consider a PVC pipe with a mean radius,  $a = 8.0$  cm, and a wall thickness,  $t = 7.0$  mm. Simple elasticity theory relates the change in the pipe radius,  $\Delta r$ , to the increase of pressure,  $\Delta p$ , within the pipe.

$$\Delta r = \frac{a^2}{tE} \Delta p \quad (10.134)$$

For PVC, the Young's modulus,  $E_{PVC} = 3.40 \times 10^9$  Pa. Consider a short length of this pipe, and calculate the effective bulk modulus by calculating the change in volume,  $\Delta V$ , of the pipe due to a change in the internal pressure,  $\Delta p$ , within the pipe.

- (c) *Wave propagation speed in a water-filled PVC pipe.* If we assume that the water is incompressible (i.e., the bulk modulus of the water is infinite) in comparison to the effective bulk modulus of the PVC pipe, what is the speed of sound propagation for a pressure wave traveling in the water contained within the PVC pipe?
  - (d) *Effect of the water's compressibility.* In part (a) of this problem, you calculated the bulk modulus of water, and your result should have been substantially less than infinity. Will the water's compressibility increase or decrease the sound propagation speed you calculated in part (c)?
  - (e) *Effect of the water's compressibility.* Calculate the sound propagation speed due to the water's density and the combined bulk modulus of both the pipe and the water. [Hint: Think of the two moduli as "springs" and ask yourself if those springs add in series or parallel.]
14. **Thermophone** [74]. An array of three sheets of carbon nanotubes are stretched between two electrically conducting wires as shown in Fig. 10.23 [75]. For the purpose of this problem, we can assume that the nanotubes act as an electrical resistance and have neither heat capacity nor volume.

**Fig. 10.23** Carbon nanotube sheets that act as an electrical resistance heating element



To test this device, it will be placed in a gas-tight cylindrical cavity with a volume of 2.5 liters =  $2.5 \times 10^{-3} \text{ m}^3$ . Assume the mean pressure in the cavity  $p_m = 101 \text{ kPa}$ , the mean temperature is  $T_m = 300 \text{ K}$ , so that  $c_{air} = 347 \text{ m/s}$  and  $\gamma_{air} = 1.403$ . Under those conditions,  $\rho_{air} = 1.173 \text{ kg/m}^3$ , the specific heat of the air is  $c_p = 1005 \text{ J/kg-K}$ , the viscosity of air is  $\mu = 1.85 \times 10^{-5} \text{ Pa-sec}$ , the air's thermal expansion coefficient at constant pressure is  $\beta_p = (T_m)^{-1} = 3.33 \times 10^{-3} \text{ K}^{-1}$ , and the air's thermal conductivity is  $\kappa = 2.62 \times 10^{-2} \text{ W/m-K}$ .

- (a) *Thermal penetration depth.* An AC electrical current is passed through the carbon nanotube sheets that cause them to be heated at a frequency of 120 Hz. What is the thermal penetration depth,  $\delta_k$ , in air at that frequency?
- (b) *Gas temperature change near the sheets.* The total surface area of the three sheets, including both the back and front surfaces of the sheets,  $A_{tot} = 15 \text{ cm}^2$ . If the instantaneous total power,  $\Pi(t)$ , delivered to the sheets can be expressed as  $\Pi(t) = 2.0 \text{ W}[1 - \cos(240\pi t)]$ , and if all of that heat is deposited in a volume equal to the product of the total surface area of the sheets,  $A_{tot}$ , and the thermal penetration depth  $\delta_k$ , what is the amplitude,  $T_1$ , of the oscillating change in the temperature of the gas within that volume that is varying harmonically as  $T(t) = T_m + T_1[1 - \cos(240\pi t)]$ ?
- (c) *Thermally induced volume change.* During one-quarter of a cycle, the temperature of the gas changes by  $T_1$ , as calculated in part (b) of this problem. The coefficient of thermal expansion of an ideal gas at constant pressure,  $\beta_p$ , is provided in Eq. (10.135).

$$\beta = \frac{1}{T_m} = \frac{1}{V} \left( \frac{\partial V}{\partial T} \right)_p \quad (10.135)$$

What is the change in the volume of the gas,  $\delta V$ , caused by its heating during one-quarter cycle?

- (d) *Thermally induced pressure change.* The wavelength of sound at 120 Hz is approximately  $\lambda = c_{air}/f \cong 2.9 \text{ m}$ , which is much larger than any dimension of the sealed cylindrical enclosure  $d \cong V^{1/3} \cong 0.14 \text{ m}$ . Using the change in volume,  $\delta V$ , calculated in part (c), and the adiabatic gas law or the acoustical impedance of a small cavity provided in Eq. (8.25), determine the corresponding change in pressure,  $\delta p$ , caused by the periodic heating within the 2.5 liter, air-filled cylinder.

15. **Reciprocity calibration coupler transfer impedance.** Shown in Fig. 10.24 is a schematic representation of an apparatus, taken from [45], that is used to calibrate a condenser microphone by the reciprocity method. That method requires that the acoustic transfer impedance of the cavity (shown as the “Closed Air Volume”) is known.

**Fig. 10.24** A small cavity is created in the space between two reversible condenser microphones

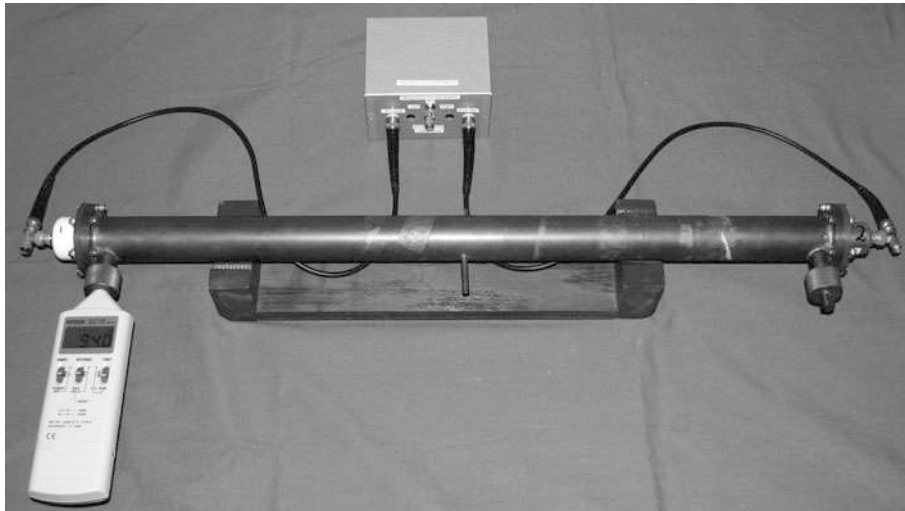
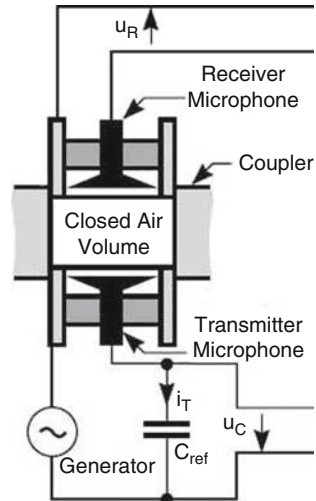


**Fig. 10.25** A standing wave resonator used for reciprocity calibration is capped at each end with the small, reversible, electrodynamic transducers shown in Fig. 10.26. Two  $\frac{1}{2}$  inch (1.27 cm) compression fittings are located very close to the ends of the resonator. An Extech™ Model 407736, Type-2 sound level meter is placed in one fitting, and the other is plugged with a solid rod. The small tube at the center allows gases other than air to be used as the calibration medium. At the top of the photo is a custom switch box that allows the swept-sine signal produced by a dynamic signal analyzer to be routed to either reversible transducer #1 or #2 after it has been passed through a precision 1.000 ohm current-sensing resistor

Assuming that the two microphones can be treated as rigid caps and that all dimensions of the “Closed Air Volume” are much smaller than the acoustic wavelength, write an expression for the acoustic transfer impedance  $Z_{tr} = \hat{\mathbf{p}}_R / \hat{U}_T$ , where  $\hat{\mathbf{p}}_R$  is the complex pressure amplitude at the “Receiver Microphone,”  $\hat{U}_T$  is the volume velocity produced by the “Transmitter Microphone,” and the volume of the “Closed Air Volume” is  $V$ .

16. **Reciprocity calibration in a plane wave resonator.** The apparatus shown in Fig. 10.25 is used to produce a reciprocity calibration of the two reversible electroacoustic transducers shown in

**Fig. 10.26** The two small reversible electrodynamic transducers that are used for the reciprocity calibration. The US penny is shown as a size comparison. Each reversible transducer is mounted on a plate that matches the flanges at the ends of the waveguide. The free-cone resonance frequency of the larger transducer is about 2.8 kHz, and that of the smaller one is about 1.7 kHz. Each transducer is mounted on a flange that attaches to the end of the resonator shown in Fig. 10.25

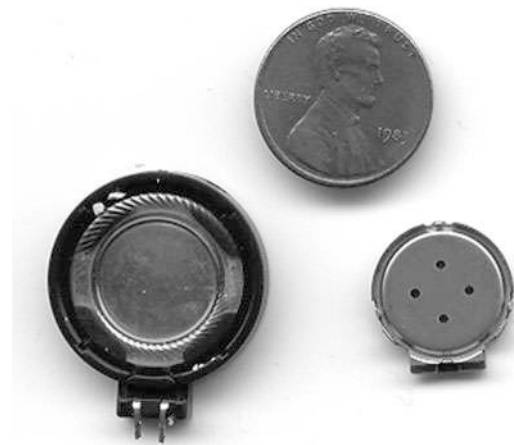


**Table 10.5** Summary of measured results for the reciprocity calibration of the two transducers shown in Fig. 10.26 produced using the resonator shown in Fig. 10.25

Driving transducer #1					
$f_2$ [Hz]	$Q_{2,1}$	$i_1$ [mA <sub>ac</sub> ]	$V_2$ [ $\mu$ V <sub>ac</sub> ]	Level [dB <sub>C</sub> ]	$V_{m,1}$ [mV <sub>ac</sub> ]
485.83	71.2	3.62	292.4	111.8	81.48
Driving transducer #2					
$f_2$ [Hz]	$Q_{2,2}$	$i_2$ [mA <sub>ac</sub> ]	$V_1$ [ $\mu$ V <sub>ac</sub> ]	Level [dB <sub>C</sub> ]	$V_{m,2}$ [mV <sub>ac</sub> ]
485.83	70.9	9.647	781.3	102.3	27.02

Fig. 10.29. The resonator tube has an inside diameter of 34.37 mm, and its length is 70.12 cm. Assume the calibration procedure took place in dry air at 20 °C and at a mean pressure,  $p_m = 98$  kPa.

The data presented in Table 10.4 were produced at the resonance frequency of the second plane wave resonance,  $f_2$ , by first driving Transducer #1 with current,  $i_1$ , and measuring Transducer #2's open voltage,  $V_2$ , along with the C-weighted output of the sound level meter,  $V_{m,1}$ , while also measuring  $Q_{2,1}$ . The second data set in that table was obtained when Transducer #2 was driven. Using the dimensions of the resonator, the thermophysical properties of the air and the data in Table 10.5 make the following calculations:

- Acoustic transfer impedance.* Calculate the value of the acoustic transfer impedance for the second standing wave mode of the resonator.
  - Transducer #1 open-circuit microphone sensitivity.* Using the appropriate measurements from Table 10.5, calculate the open-circuit sensitivity,  $M_1$ , of Transducer #1 and the sensitivity of the sound level meter by comparison to  $M_1$ .
  - Transducer #2 open-circuit microphone sensitivity.* Using the appropriate measurements from Table 10.5, calculate the open-circuit sensitivity,  $M_2$ , of Transducer #2 and the sensitivity of the sound level meter by comparison to  $M_2$ . What is the relative difference in the sensitivity of the sound level meter based on the two independent reciprocity calibrations?
17. **Tweeter horn.** A commercial horn with a 1" (2.5 cm) diameter throat is 10" (25 cm) long and opens to a bell with a diameter of 4" (10 cm).

- (a) *Flare constant.* If the horn has a cross-sectional area that grows exponentially, determine the flare constant,  $h$ .
- (b) *Cut-off frequency.* If the horn were infinitely long, what would be its cut-off frequency?

## References

1. M.J. Lighthill, *Waves in Fluids* (Cambridge University Press, 1978). See §2.6; ISBN 0 521 29233 6 (paperback)
2. <http://www.iso.org/iso/en/ISOOnline.frontpage>
3. V.A. Del Grosso, New equation for the speed of sound in natural waters (with comparisons to other equations). *J. Acoust. Soc. Am.* **56**(4), 1084–1091 (1974)
4. A.J. Zuckerwar, D.S. Mazel, *Sound Speed Measurements in Liquid Oxygen-Liquid Nitrogen Mixtures*, NASA Technical Paper 2464 (NASA Langley Research Center, Hampton, 1985)
5. M.R. Moldover, R.M. Gavioso, J.B. Mehl, L. Pitre, M. de Podesta, J.T. Zhang, Acoustic gas thermometry. *Metrologia* **51**, R1–R19 (2014)
6. M.R. Moldover et al., Measurement of the universal gas constant  $\mathfrak{R}$  using a spherical acoustic resonator. *J. Res. Natl. Bur. Stand.* **93**, 85–144 (1988)
7. E. Polturak, S.L. Garrett, S.G. Lipson, Precision acoustic gas analyzer for binary mixtures. *Rev. Sci. Inst.* **57**(11), 2837–2841 (1986)
8. G.W. Swift, *Thermoacoustics: A Unifying Perspective for Some Engines and Refrigerators*, 2nd edn. (ASA Press/Springer, 2017). See Eq. (2.74), pg. 50; ISBN 978-3-319-66932-8
9. F.W. Giacobbe, Estimation of Prandtl numbers in binary mixtures of helium and other noble gases. *J. Acoust. Soc. Am.* **96**(6), 3568–3680 (1994)
10. G.S.K. Wong, Speed of sound in standard air. *J. Acoust. Soc. Am.* **79**(5), 1359–1366 (1986)
11. M. Greenspan, Comments on ‘Speed of sound in standard air’. *J. Acoust. Soc. Am.* **82**(1), 370–372 (1987)
12. Stanford Research Systems Model BGA244, Binary Gas Analyzer, [www.thinkSRS.com](http://www.thinkSRS.com)
13. S. Garrett, Sonic gas analyzer for hydrogen and methane. *Proc. Acoustics 08*, Paris, 29 June–4 July, 2008, pp. 2767–2772
14. S.L. Garrett, G.W. Swift, R.E. Packard, Helium gas purity monitor for recovery systems. *Physica* **107B**, 601–602 (1981)
15. M.V. Golden, R.M. Keolian, S.L. Garrett, Sonic gas analyzers, in *Proc. 16<sup>th</sup> Int. Congress on Acoustics and 135<sup>th</sup> Meeting Acoust. Soc. Am.*, vol. III, (Seattle, WA, 20–26 June 1998), pp. 1705–1706
16. G.M. Sessler, J.E. West, Electret transducers: A review. *J. Acoust. Soc. Am.* **53**(6), 1589–1600 (1973)
17. National Semiconductor Model LM2907
18. J.N. Tjøtta, S. Tjøtta, Nonlinear equations of acoustics, in *Frontiers of Nonlinear Acoustics: Proc. 12<sup>th</sup> International Symposium on Nonlinear Acoustics*, ed. by M. F. Hamilton, D. T. Blackstock, (Elsevier Scientific Publishers, Ltd, London, 1990)
19. L.D. Landau, E.M. Lifshitz, *Fluid Mechanics*, 2nd edn. (Butterworth-Heinemann, 1987). §81; ISBN 0 7506 2767 0
20. F.M.F. Chapman, Decibels, SI units, and standards. *J. Acoust. Soc. Am.* **108**(2), 480 (2000)
21. H. Fletcher, W.A. Munson, Loudness, its definition, measurement, and calculation. *J. Acoust. Soc. Am.* **5**(2), 82–108 (1933)
22. D.W. Robinson, R.S. Dadson, A re-determination of the equal-loudness relations for pure tones. *Br J. Appl. Phys.* **7**, 166–188 (1956)
23. ISO 226, *Acoustics – Normal Equal-Loudness Contours* (International Standards Organization, Geneva, 2003)
24. B.R. Glasberg, B.C.J. Moore, Prediction of absolute thresholds and equal loudness contours using a modified loudness model. *J. Acoust. Soc. Am.* **120**(2), 585–588 (2006)
25. *American National Standard for Sound Level Meters*, ANSI-ASA S1.4-1983, most recently reaffirmed by the American National Standards Institute (ANSI), 21 Mar 2006
26. S. Fidell, A review of US aircraft noise regulatory policy. *Acoustics Today* **11**(4), 26–34 (2015)
27. P.D. Schomer, Criteria for assessment of noise annoyance. *Noise Control Eng. J.* **53**(4), 132–144 (2005)
28. *American National Standard Method for the Calculation of the Speech Intelligibility Index*, ANSI-ASA S3.5-1997
29. G.W. Swift, Thermoacoustic engines. *J. Acoust. Soc. Am.* **84**(4), 1145–1180 (1988). See Eq. (59)
30. W.R. MacLean, Absolute measurement of sound without a primary standard. *J. Acoust. Soc. Am.* **12**(1), 140–146 (1940)
31. J. W. Strutt (Lord Rayleigh), *Proc. London Math. Soc.* **4**, 357 (1983); *Scientific Papers*, Vol. I, (Dover, 1964), pp. 140. Note: The *Scientific Papers* are available from the Acoustical Society of America in a fully-searchable version on CD-ROM

32. R.K. Cook, Absolute pressure calibrations of microphones. *J. Res. Natl. Bur. Stand.* **25**, 489 (1940) and *J. Acoust. Soc. Am.* **12**(1), 415–420 (1941)
33. G.S.K. Wong, T. F. W. Embleton (eds.), *AIP Handbook of Condenser Microphones* (Am. Inst. Phys., 1995). Chapters 8–12; ISBN 1-56396-284-5
34. R.J. Bobber, *Underwater Electroacoustic Measurements* (Naval Research Laboratory, Underwater Sound Reference Division (U.S. Govt. Printing Office), 1970). See §2.3
35. L.L. Foldy, H. Primakoff, A general theory of passive linear electroacoustic transducers and the electroacoustic reciprocity theorem. *I. J. Acoust. Soc. Am.* **17**(2), 109–120 (1945). Also H. Primakoff and L. L. Foldy “A general theory of passive linear electroacoustic transducers and the electroacoustic reciprocity theorem. II,” *J. Acoust. Soc. Am.* **19**(1), 50–58 (1947)
36. R.M. Keolian, personal communication
37. R.P. Feynman, R.B. Leighton, M. Sands, *The Feynman Lectures on Physics*, vol II (Addison-Wesley, 1964). See §37–1
38. F.V. Hunt, Symmetry in the equations for electromechanical coupling. *J. Acoust. Soc. Am.* **22**(5), 672 (1950)
39. F.V. Hunt, *Electroacoustics: The Analysis of Transduction and Its Historical Background* (Harvard, 1954). See “Symmetry and Equivalent Circuits” and “The Burdens of Antisymmetry,” pp. 105–116
40. L.E. Kinsler, A.R. Frey, A.B. Coppens, J.V. Sanders, *Fundamentals of Acoustics*, 4th edn. (Wiley, 2000). See Ch. 14.4(b), “Antireciprocal Transducers”; ISBN 0-471-84789-5
41. I. Rudnick, Unconventional reciprocity calibration of transducers. *J. Acoust. Soc. Am.* **63**(3), 1923–1925 (1978)
42. S.L. Garrett, S. Adams, S. Putterman, I. Rudnick, Resonant nonlinear mode conversion in He II. *Phys. Rev. Lett.* **41**(6), 413–416 (1978)
43. G.W. Swift, S.L. Garrett, Resonance reciprocity calibration of an ultracompliant transducer. *J. Acoust. Soc. Am.* **81**(5), 1619–1623 (1987)
44. R.J. Bobber, *Underwater Electroacoustic Measurements* (Naval Research Laboratory, Underwater Sound Reference Division (U.S. Govt. Printing Office), 1970)
45. G.S.K. Wong, Primary pressure calibration by reciprocity, in *AIP Handbook of Condenser Microphones*, ed. by G. S. K. Wong, T. F. W. Embleton, (1995). Am. Inst. Phys.; ISBN 1-56396-284-5
46. V. Nedzelintsky, Primary method for calibrating free-field response, in *AIP Handbook of Condenser Microphones*, ed. by G.S.K. Wong, T.F.W. Embleton, (1995). Am. Inst. Phys.; ISBN 1-56396-284-5
47. I. Rudnick, M.N. Stein, Reciprocity free field calibration of microphones to 100 Kc in air. *J. Acoust. Soc. Am.* **20**(6), 818–825 (1948)
48. S. Barrera-Figueroa, Free-field reciprocity calibration of measurement microphones at frequencies to 150 kHz. *J. Acoust. Soc. Am.* **144**(4), 2572–2583 (2018)
49. E. Frederiksen, J.I. Christensen, Pressure reciprocity calibration – instrumentation, results, and uncertainty. *Brüel & Kjær Tech. Rev.* **1**, 5–26 (1998)
50. H.E. Bass, J. Bhattacharyya, M.A. Garcés, M. Hedlin, J.V. Olsen, R.L. Woodward, Infrasound. *Acoustics Today* **2**(1), 9–19 (2006)
51. T.B. Gabrielson, Reciprocity calibration for infrasound sensors. *J. Acoust. Soc. Am.* **141**(5), 3568 (2017)
52. L.E. Kinsler, A.R. Frey, A.B. Coppens, J.V. Sanders, *Fundamentals of Acoustics*, 4th edn. (Wiley, 2000). See Eq. (10.5.4); ISBN 0-471-84789-5
53. R.S. Wakeland, Use of electrodynamic drivers in thermoacoustic refrigerators. *J. Acoust. Soc. Am.* **107**(2), 827–832 (2000)
54. M.A.G. Timmer, K. de Blok, T.H. van der Meer, Review on the conversion of thermoacoustic power into electricity. *J. Acoust. Soc. Am.* **143**(2), 841–857 (2018)
55. Morel Acoustics USA, Inc., Brookline, MA
56. W.C. Ward, Cost-effective electrodynamic drivers with improved efficiency for thermoacoustic refrigerators. *J. Acoust. Soc. Am.* **100**(4), 2847 (1996)
57. M. Fitzpatrick, Electrodynamic driver for the Space Thermoacoustic Refrigerator (STAR), M.S. thesis, Physics Department, Naval Postgraduate School, Monterey, CA, 1988; DTIC report no. ADA 192337, p. 80
58. S.L. Garrett, J.A. Adeff, T.J. Hofler, Thermoacoustic refrigerator for space applications. *AIAA J. Thermophys. Heat Transf.* **7**(4), 595–599 (1993)
59. S.L. Garrett, High power thermoacoustic refrigerator. US Pat. No. 5,647,216 (15 July 1997)
60. J. Liu, S. Garrett, Characterization of a small moving-magnet electrodynamic linear motor for use in a thermoacoustic refrigerator. *J. Acoust. Soc. Am.* **118**(4), 2289–2295 (2005)
61. G.A. Yarr, J.C. Corey, Linear electrodynamic machine. US Pat. No. 5,389,844 (14 Feb. 1995)
62. C.H. Allen, I. Rudnick, A powerful high frequency siren. *J. Acoust. Soc. Am.* **19**(5), 857–865 (1947)
63. W.L. Nyborg, Acoustic streaming, in *Physical Acoustics*, ed. by W. P. Mason, vol. IIB, (Academic, 1964)
64. J.K. Hilliard, Historical review of horns used for audience-type sound reproduction. *J. Acoust. Soc. Am.* **59**(1), 1–8 (1976)

65. P.M. Morse, *Vibration and Sound*, 2nd edn. (McGraw-Hill, 1948). Reprinted by the Acoust. Soc. Am., 1995. See Fig. 58; ISBN 0-88318-876-7
66. V. Salmon, Generalized plane wave horn theory. *J. Acoust. Soc. Am.* **17**(3), 199–211 (1946). and “A new family of horns,” *J. Acoust. Soc. Am.* **17**(3), 212–218 (1946)
67. I. Rudnick, On the attenuation of high amplitude waves of stable saw-tooth form propagating in horns. *J. Acoust. Soc. Am.* **30**(4), 339–342 (1948)
68. P. Bèquin, C.L. Morfey, Weak nonlinear propagation of sound in a finite exponential horn. *J. Acoust. Soc. Am.* **109**(6), 2649–2659 (2001)
69. L.L. Beranek, *Acoustics*. *Acoust. Soc. Am.* (1996). Chapter 9; ISBN 0-88318-494-X
70. M. Kleiner, *Electroacoustics* (Taylor & Francis, 2013). Chapter 19; ISBN 978-1-4398-3618-70
71. <https://www.co2.earth/daily-co2>
72. H. Witschi, Profiles in toxicology, Fritz Haber: 1868–1934. *Toxicol. Sci.* **55**, 1–2 (2000)
73. P.W. Mullen, *Modern Gas Analysis* (Interscience, 1955)
74. L.L. Beranek, *Acoustic Measurements* (Wiley, 1949), pp. 161–171
75. A.E. Aliev et al., Underwater sound generation using carbon nanotube projectors. *Nano Letters (Am. Chem. Soc.)* **10**, 2374–2380 (2010)

**Open Access** This chapter is licensed under the terms of the Creative Commons Attribution 4.0 International License (<http://creativecommons.org/licenses/by/4.0/>), which permits use, sharing, adaptation, distribution and reproduction in any medium or format, as long as you give appropriate credit to the original author(s) and the source, provide a link to the Creative Commons license and indicate if changes were made.

The images or other third party material in this chapter are included in the chapter's Creative Commons license, unless indicated otherwise in a credit line to the material. If material is not included in the chapter's Creative Commons license and your intended use is not permitted by statutory regulation or exceeds the permitted use, you will need to obtain permission directly from the copyright holder.





# Reflection, Transmission, and Refraction 11

## Contents

11.1	<b>Normal Incidence</b> .....	514
11.2	<b>Three Media</b> .....	518
11.2.1	A Limp Diaphragm Separating Two Gases .....	520
11.2.2	An Impedance Matching Antireflective Layer .....	520
11.2.3	The “Mass Law” for Sound Transmission Through Walls .....	520
11.2.4	Duct Constriction/Expansion Low-Pass Filters .....	521
11.3	<b>Snell’s Law and Fermat’s Principle</b> .....	523
11.3.1	Total Internal Reflection .....	526
11.3.2	The Rayleigh Reflection Coefficient .....	528
11.4	<b>Constant Sound Speed Gradients</b> .....	529
11.4.1	Constant Gradient’s Equivalence to Solid Body Rotation .....	531
11.4.2	Sound Channels .....	534
11.4.3	Propagation Delay* .....	536
11.4.4	Under Ice Propagation .....	537
11.4.5	Sound Focusing .....	538
	<b>References</b> .....	541

In Chap. 10, we transitioned from a lumped-element perspective to a formalism which treated fluids as continuous media that include the effects of both compressibility and inertia throughout. We described disturbances from equilibrium using a wave equation and focused attention on planewaves that could be described as propagating along one spatial dimension. In this chapter, we will examine the behavior of such one-dimensional waves propagating through media that are not homogeneous. We start with an examination of the behavior of planewaves impinging on a planar interface between two fluid media with different properties and then extend that analysis to multiple interfaces and to waves that impinge on the interface from an angle that is not perpendicular to that surface. This exploration concludes with consideration of wave propagation through a medium whose properties change slowly and continuously through space.

What does “slowly” mean in the previous sentence? To answer that question, we will break down the general problem of propagation through an inhomogeneous medium into two limiting cases. As before, such limiting cases suggest appropriate (usually simple) analytical approaches that will develop useful intuition for understanding cases that may be intermediate between the simpler limits. In this

chapter, the interesting limits depend on the scale of the medium's inhomogeneity relative to the wavelength of the sound that impinges on it (from afar, since we consider only planewaves). If a wave encounters a deviate region with a size that is on the order of its own wavelength or smaller, and that region has a different density, a different compressibility, or both, then we treat the inhomogeneous region as a “scatterer.” Those cases will be examined in Chap. 12 when the problem of radiation in three dimensions is analyzed and the scattering body will be driven by the impinging sound wave causing the ensonified region to behave as a radiating “source.” That “scattered” sound field will be superimposed on the incident sound field.

In this chapter, we will consider the opposite limit, where the size of the boundary that separates regions with different acoustical properties is much larger than the wavelength of the sound. In fact, many cases to be examined here will assume that the extent of the boundary is infinite. In those cases, the problem is treated as one where the wave incident on such an interface will be both reflected back into the medium from which it originated and be transmitted into the second medium on the other side of the interface.

For the case where the interface is not discontinuous, what we will mean by requiring that the medium's properties (e.g., sound speed and density) “are varying slowly” will again be related to the rate at which the property changes in space relative to the wavelength of the sound. For example, if we specify the change in sound speed with position,  $dc/dz \equiv g$ , then  $g$  will have the units m/s per m, which is equivalent to a frequency. The wave also has a characteristic frequency,  $f = c/\lambda$ , that is the ratio of the sound speed to the wavelength. If  $g \ll f$ , then any significant change in sound speed will occur over a very large number of wavelengths.

## 11.1 Normal Incidence

All of us are familiar with echoes, whether produced by a handclap reflected from a large building; a loud “hello” shouted from a precipice and reflected from a bluff, as diagrammed in Fig. 11.1; or a “flutter echo” produced by some impulsive sound source reverberating between long parallel walls. In those cases, a sound wave in air impinges on a rigid solid surface. The air's particle velocity that accompanies the pressure wave (via the Euler equation) cannot penetrate the solid. To satisfy this rigid boundary condition, we can imagine a sound wave of equal amplitude, but propagating in the opposite direction, coming from within the solid toward the interface, just as was done when examining the reflection of a pulse propagating along a string in Sect. 3.2. As justified in Sect. 12.4.1, the superposition of the two waves cancels the velocity at the interface, satisfying the condition that the interface is impenetrable to the gas, while doubling the acoustic pressure amplitude on that surface.

To compare how a real wave reflects in the “rigid boundary” case (and to determine how “rigidly” the boundary behaves), let's say the magnitude of the incident planewave,  $|\hat{\mathbf{p}}_i|$ , approaching the boundary is 94 dB<sub>SPL</sub>  $\Rightarrow |\hat{\mathbf{p}}_i| = \sqrt{2}$  Pa = 1.0 P<sub>ams</sub>. Again, we focus on a single-frequency wave and indicate the incident wave's amplitude and phase by the complex phasor,  $\hat{\mathbf{p}}_i$ . The time-averaged intensity of a 94 dB<sub>SPL</sub> planewave in air is  $\langle I_{air} \rangle_t = |\hat{\mathbf{p}}_i|^2 / (2\rho c)_{air} = 10^{(94/10)} \times 10^{-12} \text{ W/m}^2 \cong 2.5 \text{ mW/m}^2$ . (If this is not instantaneously obvious, you need to review Sect. 10.5.1.)

Let's also say the wave was reflected from a concrete wall. Since the pressure amplitude at the wall is double that of the sound wave far from the wall, and that the pressure is continuous across the interface, we can calculate the intensity of the sound that entered the wall. The density of concrete is about 2600 kg/m<sup>3</sup> and the speed of compressional waves in concrete is about 3100 m/s, so  $(\rho c)_{concrete} = 8.06 \text{ MPa-s/m}$ . Since the pressure at the wall is twice that of the wave in air,  $|\hat{\mathbf{p}}_t| =$

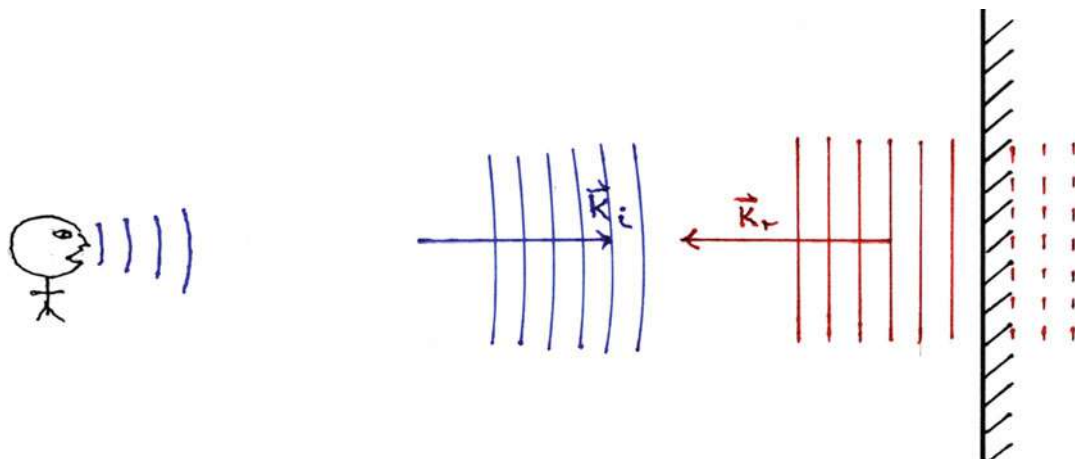


**Fig. 11.1** The sound produced by this person is nearly a planewave (wave fronts shown in blue), characterized by the wavenumber,  $\vec{k}_i$ , when it is reflected by a large flat rigid surface. The duration of the sound pulse is sufficiently short that the reflected wave, characterized by  $\vec{k}_r$ , and the incident wave only interact near the surface. To satisfy the condition that no fluid can enter or leave the solid interface, we imagine another planewave of equal amplitude traveling back (with wave fronts shown in red) toward the source. Where the incident and reflected wave superimpose at the rigid surface, the pressure is doubled, but the slope of the pressure,  $(dp/dx)_x = 0$ , evaluated at the interface, is zero. By Euler's equation, the total acoustic particle velocity normal to the surface vanishes, as required

$2|\hat{\mathbf{p}}_i| = 2\sqrt{2}$  Pa, the time-averaged intensity of the sound penetrating the concrete is  $\langle I_{concrete} \rangle_t = |\hat{\mathbf{p}}_t|^2/(2pc)_{concrete} = 0.5 \mu\text{W/m}^2$ , less than 0.02% of the intensity of the sound in air.

The equations developed in this chapter can be used to show that the amplitude of a wave in air that is reflected from a concrete wall is nearly the same as the incident wave, but not quite. Our assumption that the echo had the same amplitude as the incident sound wave was just as solid as the concrete.

We can also compare the particle velocity of the sound in air with that of the compressional wave within the concrete. In dry air, a 94 dB<sub>SPL</sub> sound wave would have a particle velocity amplitude of  $|\hat{\mathbf{v}}_i| = |\hat{\mathbf{p}}_i|/(\rho c)_{air} = 3.3$  mm/s. In the concrete, the pressure of the transmitted wave is twice that in air (far from the wall), but  $|\hat{\mathbf{v}}_t| = 2|\hat{\mathbf{p}}_i|/(\rho c)_{concrete} = 0.35$   $\mu\text{m/s}$ . Again, we see that our assumption of a rigid and immobile boundary was good to about one part in ten thousand (0.01%). We can check our intensity results using Eq. (10.36), since we also know  $\langle I \rangle_t = |\hat{\mathbf{p}}_t||\hat{\mathbf{v}}_t|/2$ , since  $\hat{\mathbf{p}}_t$  and  $\hat{\mathbf{v}}_t$  are in-phase for our assumed traveling wave. In dry air at one atmosphere,  $p_m = 101,325$  Pa, and letting  $T_m = 7^\circ\text{C}$ ,  $(\rho c)_{air} = 423$  Pa-s/m. This gives  $\langle I_{air} \rangle_t = 2.4$  mW/m<sup>2</sup> and in the concrete  $\langle I_{concrete} \rangle_t = 0.5 \mu\text{W/m}^2$ , in good agreement with the earlier calculation, as must be the case.

Using Eq. (9.38), the power dissipated per unit area due to the thermal relaxation losses at the interface can be calculated and compared to the incident intensity, since the concrete wall will behave as an isothermal boundary.<sup>1</sup> Since this loss mechanism is frequency dependent, let's do the calculation for  $f = 1$  kHz. From the DELTAEC Thermophysical Properties of air at 300 K and 1 bar =  $10^5$  Pa,

<sup>1</sup> To determine if the concrete wall forces the air that it contacts to behave isothermally, we can calculate the heat capacity per unit area that is contained within a layer of the material that is one thermal penetration depth thick,  $\rho c_p \delta_\kappa$ . Using the thermophysical properties available in DELTAEC,  $(\rho c_p \delta_\kappa)_{air} = 0.10 \text{ J/m}^2 \cdot ^\circ\text{C}$ . Approximate values for concrete are  $\rho = 2600 \text{ kg/m}^3$ ,  $c_p = 880 \text{ J/kg} \cdot ^\circ\text{C}$ , and  $\kappa = 0.29 \text{ W/m} \cdot ^\circ\text{C}$ , so at 1 kHz,  $\delta_\kappa = 6.35 \mu\text{m}$  and  $(\rho c_p \delta_\kappa)_{Concrete} = 14.5 \text{ J/m}^2 \cdot ^\circ\text{C} \gg (\rho c_p \delta_\kappa)_{air} = 0.10 \text{ J/m}^2 \cdot ^\circ\text{C}$ . For a more detailed discussion, see Eq. (59) for  $\varepsilon_s$  in G. W. Swift, "Thermoacoustic engines," J. Acoust. Soc. Am. **84**(4), 1145–1180 (1988).

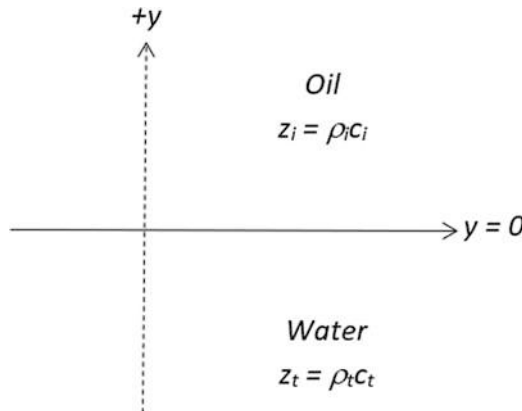


**Fig. 11.2** Coordinate system for two fluids that can be thought of as oil floating on water. The dashed line is normal to the plane interface between the two fluids at  $y = 0$ . In this diagram, it is assumed that the sound originates from the oil which has a specific acoustic impedance of  $z_i = \rho_i c_i$ . A wave will be transmitted across the interface into a second medium (water) with a specific acoustic impedance  $z_t = \rho_t c_t$ .

$\delta_k = 84.6 \mu\text{m}$ , corresponding to a thermal absorption of  $0.76 \mu\text{W/m}^2$ . This is a minuscule loss (0.03%), although thermal relaxation at the interface is responsible for a slightly larger decrease in the reflected amplitude, at this frequency, than the intensity of the sound that enters the concrete. Why do we not need to calculate the viscous boundary layer dissipation?

Now that we have the behavior of a common reflection situation “under our belts,” we can start our formal investigation of reflection and transmission of planewaves impinging normally on an interface between any two dissimilar media. For these calculations, keep in mind a very simple case of two immiscible liquids in a uniform gravitational field. Let’s assume that we have a sea of oil floating on a sea of water, as shown in Fig. 11.2, with the “up” direction being  $+y$  and  $y = 0$  at the interface between the two liquids. The mass density of the oil,  $\rho_{oil}$ , is less than the density of water. To simplify the specification of variables on either side of the interface, we will designate parameters of the wave and of the medium above the interface ( $y > 0$ ) with the subscript,  $i$  (incident), and those below the interface ( $y < 0$ ) with the subscript,  $t$  (transmitted).

Let’s imagine that a single-frequency plane sound wave originates far above the interface and is propagating in the  $-y$  direction. That wave excites the interface with a pressure amplitude,  $|\hat{\mathbf{p}}_i|$ . We can express the pressure amplitude as a function of  $y$  and  $t$  above the interface

$$p_i(y, t) = \Re e \left[ \hat{\mathbf{p}}_i e^{j(\omega t + k_i y)} \right] \quad \text{for } y > 0. \quad (11.1)$$

That incident plane pressure wave also has an associated fluid particle velocity,  $\hat{\mathbf{v}}_i$ , that is related to the pressure by the Euler equation.

$$v_i(y, t) = \Re e \left[ \frac{\hat{\mathbf{p}}_i}{\rho_i c_i} e^{j(\omega t + k_i y)} \right] = \Re e \left[ \frac{\hat{\mathbf{p}}_i}{z_i} e^{j(\omega t + k_i y)} \right] \quad \text{for } y > 0 \quad (11.2)$$

In the right-hand term of Eq. (11.2),  $z_i$  is the specific acoustic impedance of the oil. Using our generic expression, Eq. (10.21), for the sound speed,  $c$ , in a fluid with an adiabatic bulk modulus,  $B_s$ ,  $c \equiv \sqrt{B_s/\rho}$ , we see that the specific acoustic impedance is a combination of the fluid’s density and compressibility,  $z = \rho c = \sqrt{\rho B_s}$ .

As for the echo case, there will be a wave that is reflected at the interface that will travel in a direction opposite to that of the incident wave.

$$p_r(y, t) = \Re e \left[ \hat{\mathbf{p}}_r e^{j(\omega t - k_r y)} \right] \quad \text{for } y > 0 \quad (11.3)$$

The presence of the incident wave will excite motion in that interface which will also generate a wave propagating into the water as well as the wave that is reflected back into the oil. To demonstrate the necessity for the simultaneous existence of the incident, reflected, and transmitted waves, we need to consider the properties of the interface between the two media.

Since we will treat these media and the waves they contain as a linear system, we can guarantee that the reflected and transmitted waves both have the same frequency as the incident wave:  $\omega = \omega_i = \omega_r = \omega_t$ . As we have seen for the simple harmonic oscillator, at steady state, the forced linear system can only respond at the forcing frequency. It is the incident wave that is forcing the motion of the interface. Since the frequencies of all of the waves must be the same, and the sound speeds in the two media might differ, the wavelength of the sound in the water will be different than that in the oil:  $\lambda_t = c_t f = 2\pi/k_t$ .

$$p_t(y, t) = \Re e \left[ \hat{\mathbf{p}}_t e^{j(\omega t + k_t y)} \right] \quad \text{for } y < 0 \quad (11.4)$$

Our second requirement at the interface is that the two fluids always remain in contact. There are cases where the amplitude of the incident wave is sufficiently large to produce a vapor cavity at the interface, but we will limit our attention here to wave amplitudes that are insufficient to create such *cavitation effects* [1]. In most practical cases, the boundaries do not separate, so the normal velocities of the two fluids must match at the interface for all times.

$$v_i(0, t) + v_r(0, t) = v_t(0, t) \quad (11.5)$$

Our final requirement is dictated by the fact that the interface,  $y = 0$ , is only a mathematical construct—it has no mass. Since that interface is massless, Newton's Second Law of Motion would guarantee that any pressure difference across the interface would produce a non-zero force that would create infinite fluid accelerations. To guarantee that does not happen, we require that the pressure be continuous across that interface for all time.

$$p_i(0, t) + p_r(0, t) = p_t(0, t) \quad (11.6)$$

Those three conditions are sufficient to completely determine the behavior of the waves at the interface when we recognize that  $v_t(y, t)$  is related to  $p_t(y, t)$  by the specific acoustic impedance of the water,  $z_t$ . Taking the ratio of Eq. (11.6) to Eq. (11.5), the amplitude ratio of the reflected and transmitted waves to the amplitude of the incident wave can be calculated.

$$\frac{p_i(0, t) + p_r(0, t)}{v_i(0, t) + v_r(0, t)} = \frac{p_t(0, t)}{v_t(0, t)} = z_t \quad (11.7)$$

Recognizing that the incident and reflected waves are both in the oil, but are traveling in opposite directions, the magnitude of the specific acoustic impedance,  $|z_t|$ , is the same for both waves, but their signs are opposite. This leads to the further simplification of Eq. (11.7).

$$\frac{p_i(0, t) + p_r(0, t)}{p_i(0, t) - p_r(0, t)} = -z_t \quad (11.8)$$

Again, because we are limiting ourselves to linear acoustics, it is only the ratios of the amplitudes that have any significance. If we double the amplitude of the incident wave, the amplitudes of the reflected and transmitted waves must also double. It is therefore reasonable to define a *pressure reflection coefficient*,  $R \equiv \hat{\mathbf{p}}_r/\hat{\mathbf{p}}_i$ , as we did in Eq. (10.105). With that definition and a little algebraic manipulation, Eq. (11.8) can be re-written in a compact form to represent the magnitude of the pressure reflection coefficient,  $R$ .

$$R \equiv \frac{\hat{\mathbf{p}}_r}{\hat{\mathbf{p}}_i} = \frac{z_t - z_i}{z_t + z_i} = \frac{(z_t/z_i) - 1}{(z_t/z_i) + 1} \quad (11.9)$$

This result makes sense and is reminiscent of Eq. (10.105). If the two media have the same specific acoustic impedances, there is no reflection. Plugging in the specific acoustic impedances for air and concrete produces the same result as we obtained for the “echo” example that began this treatment and produced nearly perfect reflection:  $R = 0.9999$ .

In the case of oil over water, as shown in Fig. 11.2, then  $z_i < z_t$  so  $R$  is positive and the phase of the reflected wave will be the same as the incident wave, although their amplitudes will differ, similar to the in-phase pulse reflection in Fig. 3.4. If the situation were reversed so that the incident wave originated in the water, then  $z_i > z_t$  so  $R$  is negative and the phase of the reflected wave will be inverted, as shown for the pulses in Fig. 3.3.

Defining the *pressure transmission coefficient* in a similar way,  $T \equiv \hat{\mathbf{p}}_t/\hat{\mathbf{p}}_i$ , the pressure continuity boundary condition of Eq. (11.6) can now be written as  $1 + R = T$ .

$$T \equiv \frac{\hat{\mathbf{p}}_t}{\hat{\mathbf{p}}_i} = \frac{2z_t}{z_t + z_i} = \frac{2(z_t/z_i)}{(z_t/z_i) + 1} \quad (11.10)$$

The factor of two is reassuring, since we expected pressure doubling at the interface in the echo example where  $z_t \gg z_i$ , and we saw the same factor of two in Eq. (10.105).

For oil above water, we can use  $\rho_{oil} = 950 \text{ kg/m}^3$ ,  $c_{oil} = 1540 \text{ m/s}$ ,  $z_{oil} = (\rho c)_{oil} = 1.463 \times 10^6 \text{ Pa-s/m}$ , and  $\rho_{water} = 998 \text{ kg/m}^3$ ,  $c_{water} = 1481 \text{ m/s}$ , and  $z_{water} = (\rho c)_{water} = 1.478 \times 10^6 \text{ Pa-s/m}$ . The specific acoustic impedance of these two liquids is very close, so for a planewave originating in the oil,  $R = 0.005$  and  $T = 1.005$ . If the planewave originated in the water,  $R = -0.005$  and  $T = 0.995$ . The fact that  $R$  is negative for sound traveling from water into oil indicates that the wave reflected back into the water from the interface is reflected with a  $180^\circ$  phase shift with respect to the incident wave.

If Fig. 11.2 represented air over water, as on a lake, then the impedance contrast would be similar to the echo example, if we assume dry air at one atmosphere,  $p_m = 101,325 \text{ Pa}$ , and  $T_m = 20^\circ\text{C}$ , then  $(\rho c)_{air} = 413 \text{ Pa-s/m}$ . If the wave originated in the air, the results would be similar to the echo example. If the wave originated in the water,  $R = -0.9994$ , so again the reflection is almost perfect, but the reflected wave is  $180^\circ$  out-of-phase with incident wave. The pressure transmission coefficient is  $T = 0.00056$ , so we call that interface, in such a situation (i.e., the wave originating in the medium of higher specific acoustic impedance), a *pressure release boundary*.

## 11.2 Three Media

If we had two gases in contact, then we would need a membrane to keep them from diffusing into each other. Similarly, we might be interested in the transmission of sound between two living spaces separated by a wall. There is no reason why we could not extend the same style of argument just employed with one interface between two media. We would need five waves instead of three since the

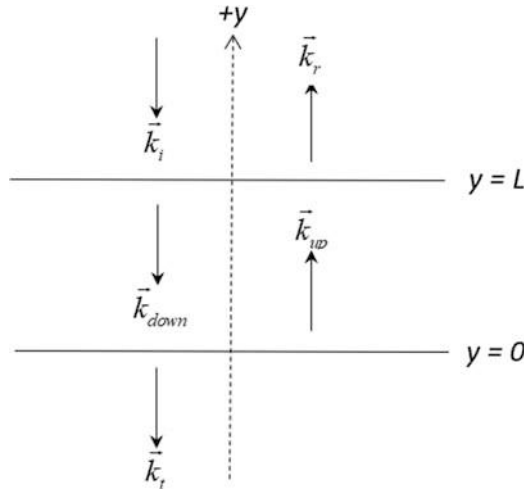


**Fig. 11.3** For a planewave that propagates through three media, bounded by two parallel interfaces, two additional waves need to be included for propagation through the central region. In this diagram, two waves are “trapped” inside the central medium, between  $y = 0$  and  $y = L$ , that has a specific acoustic impedance of  $z_c = \rho_c c_c$ . The wavevector of the incident planewave,  $\vec{k}_i$ , and the reflected wavevector,  $\vec{k}_r$ , are both in the upper medium with  $z_i = \rho_i c_i$ . The transmitted wave represented by the wavevector,  $\vec{k}_t$ , is in the lower medium, with specific acoustic impedance  $z_t = \rho_t c_t$ . All wave vectors are colinear and normal to both interfaces

central region, with specific acoustic impedance,  $z_c$ , can support both waves moving up and moving down, as shown in Fig. 11.3.

$$p_{up}(y, t) = \Re e \left[ \hat{\mathbf{p}}_{up} e^{j(\omega t - k_c y)} \right] \quad \text{and} \quad p_{down}(y, t) = \Re e \left[ \hat{\mathbf{p}}_{down} e^{j(\omega t + k_c y)} \right] \quad (11.11)$$

Again, linearity guarantees that these two new waves also have a frequency  $\omega = \omega_{up} = \omega_{down}$ , so their wavelengths and wavenumbers depend upon the speed of sound in the central medium:  $\lambda_c = c_c/f = 2\pi/|\vec{k}_c|$ . We would need to impose the continuity of normal particle velocity (11.5) and the continuity of pressure (11.6) on two planes,  $y = 0$  and  $y = L$ , if the central medium has thickness,  $L$ . We are again only interested in the amplitude ratios (i.e., specification of the incident amplitude,  $\hat{\mathbf{p}}_i$ , is still arbitrary) and can calculate the complex pressure reflection coefficient,  $\mathbf{R}$ .

$$\mathbf{R} = \frac{(1 - z_t/z_i) \cos(k_c L) + j(z_c/z_t - z_t/z_c) \sin(k_c L)}{(1 + z_t/z_i) \cos(k_c L) + j(z_c/z_t + z_t/z_c) \sin(k_c L)} \quad (11.12)$$

The power transmission coefficient will be a scalar, as it was in Eq. (10.109), and will be related to the reflection coefficient through energy conservation, as it was in Eq. (10.110).

$$T_{\Pi} = \frac{4}{2 + (z_t/z_i + z_i/z_t) \cos^2(k_c L) + \left( z_c^2/z_t z_i + z_t z_c/z_c^2 \right) \sin^2(k_c L)} \quad (11.13)$$

In many cases, the incident and transmitted media are the same,  $z_i = z_t$ , simplifying the power transmission coefficient.

$$T_{\Pi} = \left[ 1 + (\frac{1}{4}) (z_c/z_i - z_i/z_c)^2 \sin^2(k_c L) \right]^{-1} \quad \text{if} \quad z_i = z_t \quad (11.14)$$

### 11.2.1 A Limp Diaphragm Separating Two Gases

If we apply Eq. (11.12) to the case of two different gases separated by a membrane with  $z_c \gg z_i$  and  $z_c \gg z_t$ , which is so thin (i.e.,  $L \ll \lambda_c$ ) that  $(z_t/z_i) \sin(k_c L) \ll 1$  and  $\cos(k_c L) \cong 1$ , then the pressure amplitude reflection coefficient is the same as (11.9), so  $R \cong (z_t - z_i)/(z_t + z_i)$ , making the diaphragm effectively transparent and the pressure reflection coefficient dependent only upon the relative specific acoustic impedances of the gases.

Let us consider a limp latex diaphragm, having a thickness of  $0.006'' = 150 \mu\text{m}$ , separating air from molecular hydrogen,  $\text{H}_2$ . At 1.0 kHz, with  $c_{\text{latex}} \cong 1000 \text{ m/s}$ ,  $(k_c L) = \omega L/c_{\text{latex}} \cong 0.001$ . Using  $(\rho c)_{\text{latex}} \cong 50 \text{ kPa}\cdot\text{s/m}$ ,  $(z_c/z_i) \sin(k_c L) \cong 0.1 \ll 1$ , the simplified reflection coefficient of Eq. (11.9) will provide a decent approximation.

For ideal gases,  $(\rho c)_{\text{gas}} = \sqrt{\gamma p_m \rho_m}$ . Since the diaphragm is assumed to be limp, the pressures of the gases on either side must be identical (otherwise the limp membrane would bulge and then burst), so  $(z_t/z_i)_{\text{gas}} = \sqrt{M_t/M_i}$ , where  $M$  is the molecular mass of each gas. For air and hydrogen, the ratio of specific acoustic impedances is about  $\sqrt{15}$ , or its reciprocal, if the planewave originates on the air side, making  $R = \pm 0.59$ , with the sign dependent upon whether the planewave originates on the air side (+) or the  $\text{H}_2$  side (-).

### 11.2.2 An Impedance Matching Antireflective Layer

An important special case covered by Eq. (11.12) occurs when the thickness of the intermediate layer is one-quarter of a wavelength to create a perfectly transmitting condition that repeats for integer multiples of half-wavelengths being added to the original quarter wavelength, resulting in an odd-integer multiple of one-quarter of the wavelength of sound,  $L = (2n - 1)\lambda_c/4$ ;  $n = 1, 2, 3, \dots$ ; hence,  $(k_c L) = (n - \frac{1}{2})\pi$ . In that case,  $\cos(k_c L) \cong 0$  and  $\sin(k_c L) = 1$ . In addition, if  $z_c = \sqrt{z_i z_t}$ , then  $\mathbf{R} = 0$  for frequencies near  $f = (n - \frac{1}{2})c_c/2L$ , and the intermediate medium is known as a *quarter-wavelength impedance matching layer*.

In high-quality optics, like camera lenses, this effect is used to make antireflective coatings that optimize the transmission of light through the lens. Since this effect is wavelength-dependent, those optical coatings look magenta when they are optimized for transmission of green light ( $520 \text{ nm} \lesssim \lambda_{\text{green}} \lesssim 570 \text{ nm}$ ), since red ( $620 \text{ nm} \lesssim \lambda_{\text{red}} \lesssim 740 \text{ nm}$ ) and blue ( $450 \text{ nm} \lesssim \lambda_{\text{blue}} \lesssim 495 \text{ nm}$ ) will have non-zero optical reflection coefficients.

Impedance matching layers are very useful for ultrasonic transducers used in medical imaging to optimize the transmission from the transducer material (typically a piezoelectric ceramic) to flesh and to maximize the return signal's excitation of the transducer during detection.

### 11.2.3 The "Mass Law" for Sound Transmission Through Walls

If we consider a solid wall separating two rooms, both containing air, then  $z_c \gg z_i = z_t$ . In that case, the power transmission coefficient of Eq. (11.14) is further simplified.

$$T_{\Pi} \cong \left[ \frac{2z_i}{z_c \sin(k_c L)} \right]^2 \quad \text{if } z_c \gg z_i = z_t \quad (11.15)$$

For reasonably small wall thicknesses,  $L \ll \lambda_c = c_c/f$ ,  $\sin(k_c L) \cong k_c L$ , so the reduction of sound intensity transmission through the wall depends upon the surface mass density of the wall,  $\rho_s = \rho_c L$ .

$$T_{\Pi} \cong \left( \frac{2}{k_c L} \frac{z_i}{z_c} \right)^2 \cong \left[ \frac{z_i}{\pi f(\rho_c L)} \right]^2 \quad \text{if } k_c L \ll 1 \quad (11.16)$$

For this reason, in architectural acoustics, this result is known as the “mass law” and is particularly important for multi-occupant dwellings (e.g., apartment buildings) because the transmission of sound depends inversely on the square of both the surface mass density of the wall and of the frequency of the sound.<sup>2</sup> [2] This inverse-square dependence upon frequency explains why the bass from a neighbor’s stereo in an adjoining apartment is more annoying than conversation.

#### 11.2.4 Duct Constriction/Expansion Low-Pass Filters

We can exploit Eq. (11.14) for the power transmission coefficient to analyze the one-dimensional propagation through a duct that has an expansion chamber or constriction as shown in Fig. 11.4. Following the analysis in Sect. 10.8, and recognizing that such a system has the same sound speed and fluid density throughout, we can copy the five-wave procedure used in Sect. 11.2, but require the continuity of volume velocity, instead of particle velocity, to produce the analog of Eq. (11.14) where  $A$  replaces  $z_i = z_t$  and  $A_c$  replaces  $z_c$  [3].

$$T_{\Pi} = \frac{1}{1 + \frac{[(A_c/A) - (A/A_c)]^2}{4} \sin^2(kL)} \quad (11.17)$$

It is worthwhile to notice that this coefficient for the power transmission is symmetric with respect to the area ratio,  $A_c/A$ , and its reciprocal,  $A/A_c$ . That means that the result does not depend upon whether the area change is produced by an expansion chamber,  $A_c/A > 1$ , shown in Fig. 11.4 (left), or by a constriction,  $A/A_c > 1$ , shown in Fig. 11.4 (right).

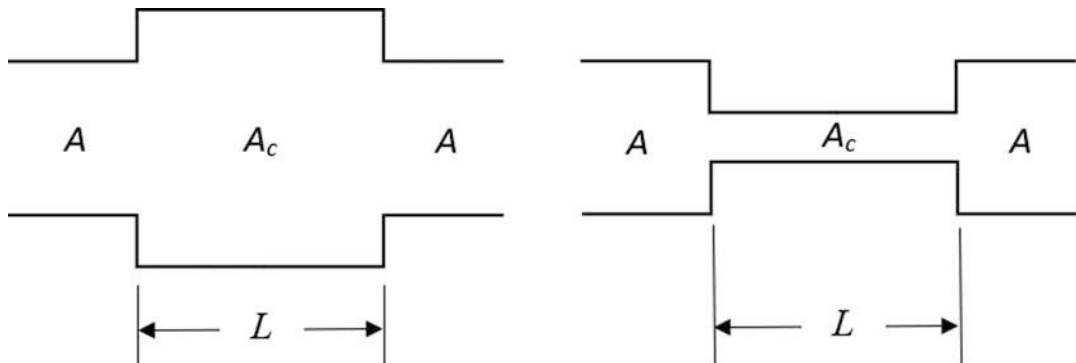


**Fig. 11.4** (Left) A compliance with volume,  $V = A_c L$ , is placed in a tube of otherwise uniform cross-sectional area,  $A$ , to create a low-pass filter. (Right) A constriction with cross-sectional area,  $A_c < A$ , is placed in a tube of otherwise uniform cross-sectional area,  $A$ , to produce a low-pass filter

<sup>2</sup> It is important to remember that this “mass law” is a low-frequency result, as indicated in Eq. (11.16). At higher frequencies, other effects can become significant.

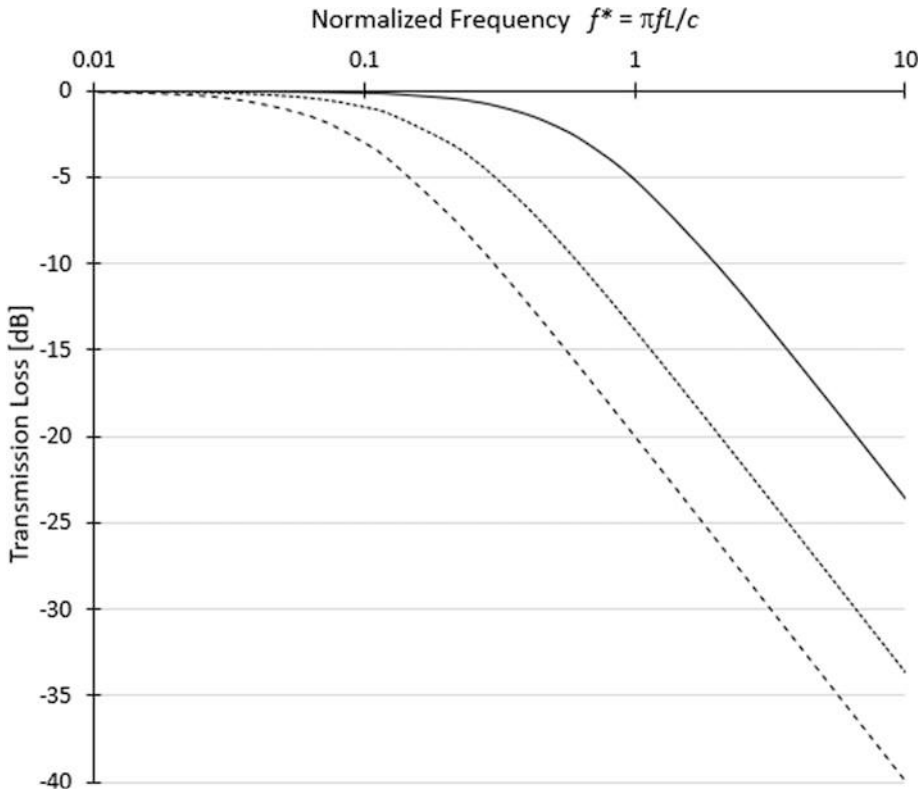


**Fig. 11.5** The expansion/constriction duct transmission loss,  $T_{\Pi}$ , for small  $kL$ , in dB =  $10 \log_{10} T_{\Pi}$  for area ratios of  $A_c/A = 2$  or  $0.5$  (solid line),  $A_c/A = 5$  or  $0.2$  (dotted line), and  $A_c/A = 10$  or  $0.1$  (dashed line) plotted against a normalized frequency,  $f^*$ , that is scaled by the length of the expansion or constriction,  $L$ , and the sound speed,  $c$ :  $f^* = \pi f L/c$ , which is also  $f^* = \pi L/\lambda = kL/2$

If we start by examining the limit where  $L \ll \lambda$  or  $kL \ll 1$ , we see that either the expansion chamber or the constriction acts as a low-pass filter as shown in Fig. 11.5 for  $A_c/A = 2$ ,  $A_c/A = 5$ , and  $A_c/A = 10$ .

$$T_{\Pi} = \left\{ 1 + \frac{\pi^2 L^2}{c^2} \left[ \left( \frac{A_c}{A} \right) - \left( \frac{A}{A_c} \right) \right]^2 f^2 \right\}^{-1} \quad \text{for } kL \ll 1 \quad (11.18)$$

As expected from Eq. (11.18), the transmission for  $kL < 1$  is reduced by 20 dB/decade, in accordance with the  $f^{-2}$  frequency dependence. It is clear from Fig. 11.5 that the frequency at which the transmission is reduced by 3 dB is dependent upon the area ratio. For  $A_c/A = 2$  or  $0.5$ ,  $f^{*-3\text{dB}} = 0.665$ ; for  $A_c/A = 5$  or  $0.2$ ,  $f^{*-3\text{dB}} = 0.208$ ; and for  $A_c/A = 10$  or  $0.1$ ,  $f^{*-3\text{dB}} = 0.101$ .

As frequency increases, the requirement that  $kL < 1$  will be violated. In Fig. 11.5, that means that  $f^* \leq 1/2$ . This restriction indicates that the frequency bandwidth of the expansion/constriction strategy is rather limited as a low-pass filter. From Eq. (11.17), we see that the transmission coefficient becomes one (i.e., 0 dB, no attenuation), when  $kL = \pi$  or  $f^* = \pi/2$ , and returns to one for all successive  $kL = n\pi$  as shown in Fig. 11.6. The maximum transmission loss,  $(T_{\Pi})_{\max}$ , occurs when  $L$  is equal to an odd multiple of quarter wavelength,  $(2n - 1)\lambda/4$ , making  $f = (2n - 1)c/4L$ .

$$(T_{\Pi})_{\max} \cong -10 \log_{10} \left[ \left( \frac{1}{4} \right) \left( \frac{A_c}{A} + \frac{A}{A_c} \right)^2 \right] \quad (11.19)$$

For  $A_c/A = 5$  or  $0.2$ ,  $(T_{\Pi})_{\max} = -8.3$  dB; and for  $A_c/A = 10$  or  $0.1$ ,  $(T_{\Pi})_{\max} = -14.1$  dB.

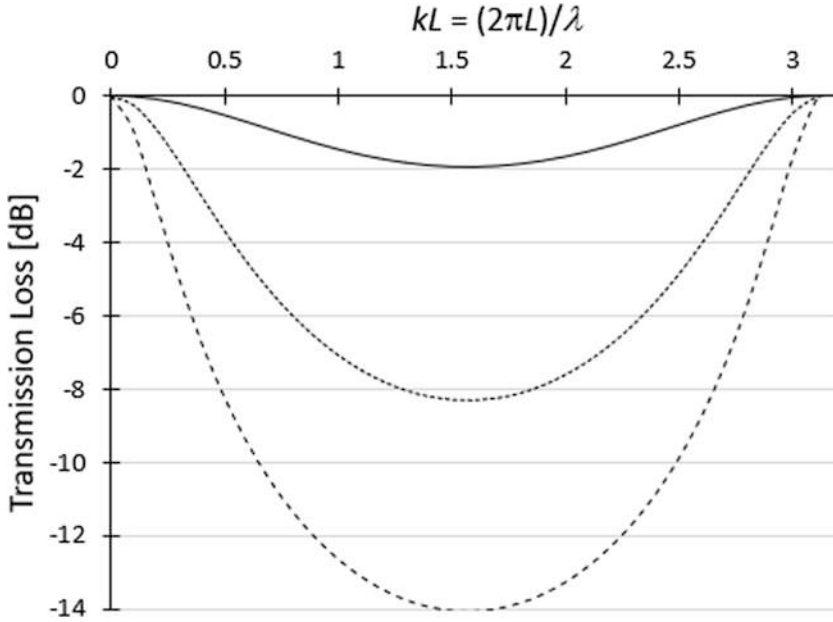


**Fig. 11.6** The expansion/constriction duct transmission loss,  $T_{\Pi}$ , in dB =  $10\log_{10}T_{\Pi}$ . Shown are area ratios of  $A_c/A = 2$  or 0.5 (solid line),  $A_c/A = 5$  or 0.2 (dotted line), and  $A_c/A = 10$  or 0.1 (dashed line) plotted against a normalized frequency,  $0 \leq kL = (2\pi L/\lambda) \leq \pi$ . This behavior repeats for integer multiples of  $\pi$  with no loss for  $kL = 0$  or  $\pi$  and maximum loss for  $kL = \pi/2$

As will be shown in Sect. 13.5.4, for frequencies above  $f_{l,i} = 0.578 c/a$ , where  $a = \sqrt{A/\pi}$  is the radius of the circular duct, the planewave nature of propagation in the duct can no longer be guaranteed. That further limits the utility of such a strategy. Despite these limitations, elaborate combinations of expansion chambers and constrictions are used to attenuate sound in automotive exhaust mufflers using techniques that go well beyond those discussed here [4].

### 11.3 Snell's Law and Fermat's Principle

The previous results for planewaves normally incident on an interface between two media can be extended to planewaves that impinge on the interface from some arbitrary angle,  $\theta_i$ , with respect to the normal direction that characterized the surface. The incident wavevector will now have two components,  $\vec{k}_i = k_y \hat{e}_y + k_x \hat{e}_x$ , where  $\hat{e}_y$  and  $\hat{e}_x$  are unit vectors in the  $+y$  and  $+x$  directions.

$$\begin{aligned} p_i(x, y, t) &= \Re e \left[ \hat{\mathbf{p}}_i \exp j \left( \omega t + |\vec{k}_i| y \cos \theta_i - |\vec{k}_i| x \sin \theta_i \right) \right] \\ p_r(x, y, t) &= \Re e \left[ \hat{\mathbf{p}}_r \exp j \left( \omega t - |\vec{k}_i| y \cos \theta_r - |\vec{k}_i| x \sin \theta_r \right) \right] \\ p_t(x, y, t) &= \Re e \left[ \hat{\mathbf{p}}_t \exp j \left( \omega t + |\vec{k}_t| y \cos \theta_i - |\vec{k}_t| x \sin \theta_t \right) \right] \end{aligned} \quad (11.20)$$

We can make a simple geometrical argument regarding the directions of the reflected and transmitted planewaves by adopting a perspective that was introduced by the Dutch physicist, Christiaan

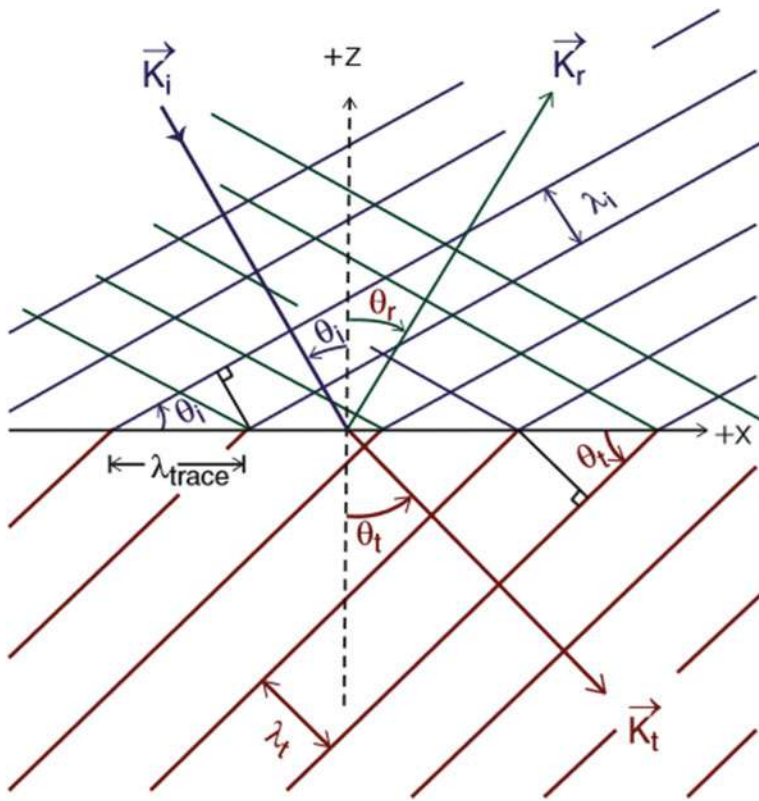


**Fig. 11.7** Diagram showing an incident wave with wavevector,  $\vec{k}_i$ , intersecting a plane interface at an angle,  $\theta_i$ , relative to the normal to the interface. Wave fronts of equal phase are shown perpendicular to the wavevector spaced by one wavelength of the incident sound,  $\lambda_i$ . That incident wave excites a reflected wave (green) and a transmitted wave (red). Successive maxima of pressure along the interface are separated by the “trace wavelength,”  $\lambda_{trace}$ , that is common to all three waves. Based on the wavelengths in this figure, the sound speed in the lower medium,  $c_t$ , is greater than the sound speed in the upper medium,  $c_i < c_t$ . When the incident angle equals the critical angle,  $\theta_i = \theta_{crit}$ , then the direction of  $\vec{k}_t$  is along the interface (i.e.,  $\theta_t = 90^\circ$ ), and we have total internal reflection for all  $\theta_i \geq \theta_{crit}$ , so no energy is transmitted

Huygens, in 1678,<sup>3</sup> that makes a simple argument which matches boundary conditions at the interface. Figure 11.7 shows the incident wavevector,  $\vec{k}_i$ , with lines normal to  $\vec{k}_i$ , indicating the planes of constant pressure phase. We will imagine those lines represent the pressure maxima of the waves propagating toward the interface. Those wave fronts impinge on the interface, and we will consider each intersection of those incident wave fronts and the interface to be a source of pressure maxima for both the reflected and transmitted planewaves.

The spacing between those maxima along the interface, which we will call the *trace wavelength*,  $\lambda_{trace}$ , is easy to calculate from trigonometry and Garrett’s First Law of Geometry<sup>4</sup>:  $\sin \theta_i = \lambda_i / \lambda_{trace}$ . For normally incident planewaves, the trace velocity  $c_{trace} = f\lambda_{trace} = \infty$ , since the wave fronts of equal phase intersect the interface so that the phase of the pressure on the interface is the same at all locations at every instant. Since  $\lambda_{trace}$  is the same for both the reflected and transmitted waves, the sound speeds

<sup>3</sup> C. Huygens, *Traité de la Lumière* (completed in 1678, published in Leyden in 1690).

<sup>4</sup> “Angles that look alike are alike.”

in the two media will determine the angle that the reflected planewave,  $\theta_r$ , and the angle transmitted planewave,  $\theta_t$ , make with the direction of the normal to the interface.<sup>5</sup>

$$\lambda_{trace} = \frac{\lambda_i}{\sin \theta_i} = \frac{\lambda_r}{\sin \theta_r} = \frac{\lambda_t}{\sin \theta_t} \quad (11.21)$$

The sound speed,  $c_i$ , is the same for both the incident and reflected planewaves, so  $\theta_r = \theta_i$ ; the angle of incidence equals the angle of reflection. This case is called *specular reflection*. If the interface has a surface roughness that is characterized by random assortments of “bumps” that are all much smaller in height and extent than the wavelength of sound, the reflection will be *diffuse*.

Again, in a linear system, the frequency,  $\omega$ , with which the incident planewave drives the interface, must also be the frequency of the driven reflected and transmitted planewaves. Since  $\lambda = c/f$ , we can invert Eq. (11.21) to produce a result known as *Snell's law*.<sup>6</sup>

$$\frac{\sin \theta_i}{c_i} = \frac{\sin \theta_r}{c_i} = \frac{\sin \theta_t}{c_t} \quad (11.22)$$

Before moving on to calculation of the pressure reflection and transmission coefficients, it worth noticing that Snell's law could have been derived by insisting that propagation time from one location in the upper medium to some other location in the lower medium is minimized by the same condition on the angles that is expressed in Eq. (11.22). This approach utilizes *Fermat's principle* (1622)<sup>7</sup>: “The actual path between two points taken by a [wave] is the one that is traversed in the least time.”

For the actual path to be an extremum of the total transit time, a neighboring path must take the same time; their time difference being at most second order in the deviation of the alternate path from the path of least time. Figure 11.8 provides a diagram of the path of least time (ACB) and a nearby path (AXB).

In the upper medium of Fig. 11.5, the perpendicular XE makes CE the reduction in distance traveled by the nearby path AX. The time savings by traveling via AC is therefore  $t_i = CE/c_i$ . Similarly, in the lower medium, the perpendicular CF makes XF the additional distance traveled by the nearby path XB. The excess time in the lower medium is therefore  $t_t = XF/c_t$ . Since  $\angle EXC = \theta_i$  and  $\angle FCX = \theta_t$ , we can express the two transit times for the nearby path in terms of the common length XC using simple trigonometry.

$$t_i = \frac{EC}{c_i} = \frac{XC \sin \theta_i}{c_i} = t_t = \frac{XF}{c_t} = \frac{XC \sin \theta_t}{c_t} \quad (11.23)$$

Equation (11.23) also yields Snell's law after dividing through by XC.

---

<sup>5</sup> Since the trace wavelength is constant, its reciprocal, the trace wavenumber,  $2\pi/\lambda_{trace}$ , is also constant. In the underwater acoustic propagation community, this is commonly called “conservation of the horizontal wavenumber” [12]. Since I associate the term “conservation” with quantities that obey equations like (10.35), I prefer to consider the horizontal wavenumber to be an invariant, like the trace wavelength.

<sup>6</sup> Snell's law is known as Descartes' law in France. Willebrord Snellius (1580–1626) was not the first to produce that result. The law was first accurately described by the Persian scientist, Ibn Sahl, in Baghdad, where in 984, he used the law to derive lens shapes that focus light with no geometric aberrations as described in the manuscript *On Burning Mirrors and Lenses*.

<sup>7</sup> The principle of least time was actually first applied to reflections from a mirror much earlier, by Hero of Alexandria, around 60 CE. Since the reflected light propagates at the same speed as the incident light, this is equivalent to the path that is also the shortest geometrical distance.

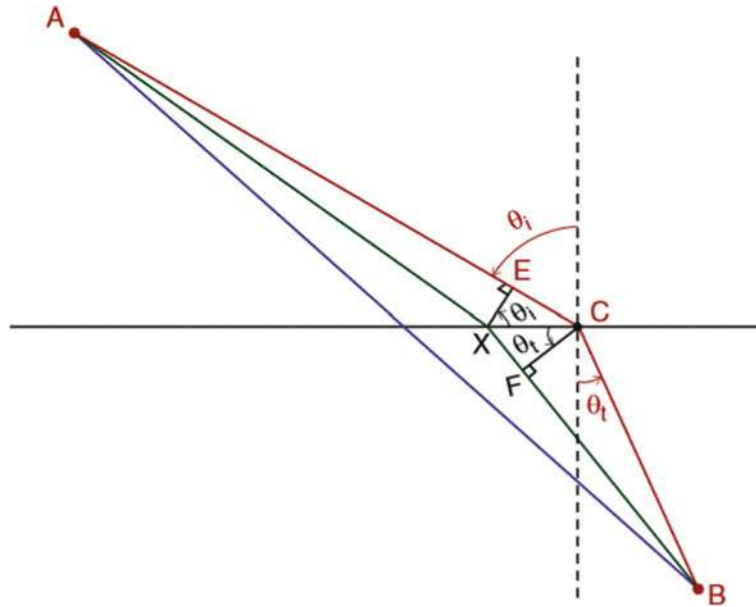


**Fig. 11.8** Three paths from point A in the upper medium to point B in the lower medium. In this diagram, it is assumed that the propagation speed of the wave in the lower medium,  $c_t$ , is slower than the propagation speed in the upper medium,  $c_i > c_t$ . The path AB (blue) is the shortest distance, and the path ACB (red) takes the least time. The angles  $\theta_i$  and  $\theta_t$  can be determined by calculating the additional travel time beyond that required for ACB when going along the path through AXB (green) and setting that excess equal to zero [5]

### 11.3.1 Total Internal Reflection

In passing from a faster medium into a slower medium,  $c_i > c_t$ , the angle that the transmitted wavevector makes with respect to the normal at the interface,  $\theta_t$ , is smaller than the incident angle,  $\theta_i$ , also measured from the normal. If the incident medium has a slower sound speed than the transmission medium,  $c_i < c_t$ , then it is possible that the angle of transmission,  $\theta_t$ , dictated by Snell's law, could become a complex number. In that case, we can define a *critical angle*,  $\theta_{crit}$ , where  $\theta_t = 90^\circ$  (i.e., the transmitted wave travels along the interface but not into the second medium).

$$\sin \theta_{crit} = \frac{c_i}{c_t}; \quad \text{if } c_i < c_t \quad (11.24)$$

This is a consequence of the fact that the minimum trace velocity,  $c_{trace} = f\lambda_{trace}$ , shown in Fig. 11.7, in the lower medium, is limited to  $c_t$ , which equals  $c_{trace}$  when  $\theta_t = 90^\circ$ . Using the fact that  $\cos^2 \theta + \sin^2 \theta = 1$ , the angle of transmission can be expressed in terms of the angle of incidence and the sound speed ratio.

$$\cos \theta_t = \sqrt{1 - \sin^2 \theta_t} = \sqrt{1 - (c_t/c_i)^2 \sin^2 \theta_i} = -j\sqrt{(c_t/c_i)^2 \sin^2 \theta_i - 1} \quad (11.25)$$

If  $c_t > c_i$ , the first term under the square root becomes imaginary, which is expressed explicitly in the final term at the right of Eq. (11.25).

Substitution of Eq. (11.25) into the expression for the transmitted pressure in Eq. (11.20) produces an exponential decay of the sound with increasing distance away from the interface, for incident angles that exceed the critical angle, producing an inverse characteristic depth,  $(1/\delta)$ .

$$k_z = \frac{1}{\delta} = \left| \vec{k}_t \right| \sqrt{(c_t/c_i)^2 \sin^2 \theta_i - 1} \quad (11.26)$$

$$p_t(x, z, t) = \Re e \left[ \hat{\mathbf{p}}_t e^{+(y/\delta)} e^{j[\omega t - |\vec{k}_t| x \sin \theta_i]} \right]; \quad \text{for } y \leq 0 \quad (11.27)$$

This solution is a wave that is localized just below the interface. For angles of incidence,  $\theta_i < \theta_{crit}$ , the transmitted wave fills the half-space of the lower medium, as shown in the lower half of Fig. 11.7. When  $\theta_i = \theta_{crit}$ , all of that outgoing energy collapses to the surface in a layer with exponential thickness,  $\delta$ . The thickness of that layer decreases monotonically as  $\theta_i$  increases beyond  $\theta_{crit}$ .

If we apply the Euler equation to Eq. (11.27) to determine the velocity,  $v_t$ , normal to the surface, we find  $\hat{\mathbf{v}}_t = j \hat{\mathbf{p}}_t (\omega \rho \delta)$ , so the pressure and particle velocity are  $90^\circ$  out-of-phase. The intensity leaving the interface is zero since there is no in-phase component of pressure and velocity. That does not mean that the layer contains no energy, just that none of the energy is propagating. If there were some scattering centers (i.e., defects, voids, inclusions of material with some compressibility, and/or density contrast), the energy trapped in that layer could be reradiated (i.e., scattered; see Sect. 12.6) and escape.

The concept of *total internal reflection* was first recognized in optics. One application of total internal reflection that I find particularly inspiring occurs in the compound eyes of insects and other arthropods. With thousands of lenses, the use of an equal number of irises, like those in avian and mammalian eyes, is not particularly efficient. In the arthropod's compound eye, each lens is connected to the optic nerve by a transparent tube that contains the light by total internal reflection, due to the difference between the index of refraction (i.e., the optical equivalent of our specific acoustic impedance) between the tube and the surrounding fluid. The way that insects control the amount of light that reaches the optic nerve is by a chemical reaction in the fluid that surrounds the tube. Under bright lighting, the fluid will produce a precipitate with small particles that scatters light out of the trapped layer, thereby reducing the amount of light reaching the optic nerve. The physical structure of the compound insect eye is shown in Fig. 11.9.

Proof of this system's efficacy is the fly's ability to avoid getting swatted outdoors in broad daylight and indoors in a darkened room. (We should now pause briefly out of respect for Darwin and the power

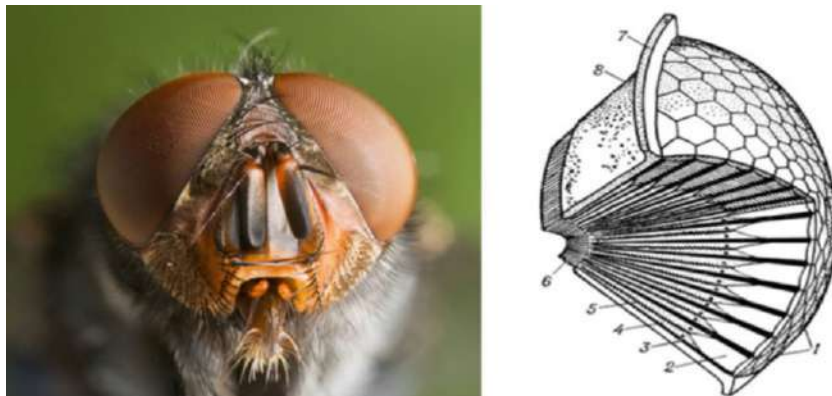


**Fig. 11.9** (Left) The compound eyes of the blue bottle fly. (Right) Each of the “tubes” is optical fibers, called an *ommatidium*. They guide light from the lens to the optic nerve endings (4 and 5) using total internal reflection to regulate the transmission of the light. Ant eyes have about six *ommatidia* and dragonfly eyes have as many as 25,000. This anatomical drawing of a compound eye shows the corneal lens (1) and the crystalline cone (2) which combine to form the dioptric apparatus. At the base is the light-sensitive rhabdom (5 and 6). The space between the tubes (3) contains the pigment cells that will form a precipitate that scatters some of the optical energy out of the trapped layer at the interface if the light is too bright, effectively reducing the field of view (known in optics as the “numerical aperture” of the lens). (Photo and diagram taken from Wikipedia)

of natural selection.) I would be most interested in finding a similar system for controlling the sound amplitude that reaches the auditory nerve in any animal, although the ability to focus sound seems ubiquitous in marine mammals, as shown for the Cuvier's beaked whale in Fig. 11.18.

### 11.3.2 The Rayleigh Reflection Coefficient

Although we have calculated the angles of reflection and transmission for planewaves of sound impinging on a planar interface from an arbitrary direction, we have yet to calculate the amplitude reflection coefficient in terms of the specific acoustic impedances, as we did for the case of normal incidence at the interface between two media in Eq. (11.9). To produce the equivalent of Eq. (11.9) for oblique incidence (i.e.,  $\theta_i \neq 0^\circ$ ), we need to generalize the velocity boundary condition of Eq. (11.5), since it is only the normal component of the velocity that needs to be continuous across the boundary to avoid cavitation at the interface.<sup>8</sup>

$$|\hat{\mathbf{v}}_i| \cos \theta_i + |\hat{\mathbf{v}}_r| \cos \theta_r = |\hat{\mathbf{v}}_t| \cos \theta_t \quad (11.28)$$

Pressure continuity, expressed in Eq. (11.6), is unchanged since pressure is a scalar quantity.

Forming the ratio of those boundary conditions, as we did in Eq. (11.7), leads to the desired result for the ratio of the reflected pressure to the incident pressure  $R \equiv \hat{\mathbf{p}}_r / \hat{\mathbf{p}}_i$ .

$$R \equiv \frac{\hat{\mathbf{p}}_r}{\hat{\mathbf{p}}_i} = \frac{\frac{z_t}{\cos \theta_t} - \frac{z_i}{\cos \theta_i}}{\frac{z_t}{\cos \theta_t} + \frac{z_i}{\cos \theta_i}} \quad (11.29)$$

Once again, we are confronted with an expression for the reflection coefficient that can vanish, providing perfect transmission, if the numerator of Eq. (11.29) is zero.

$$\frac{\cos \theta_t}{\cos \theta_i} = \frac{z_t}{z_i} \quad (11.30)$$

Using Snell's law to eliminate  $\theta_t$ , this angle, called the *angle of intromission*,  $\theta_{intro}$ , can be expressed in terms of both the impedance and sound speed or mass density ratios.

$$\sin^2(\theta_{intro}) = \frac{(z_t/z_i)^2 - 1}{(z_t/z_i)^2 - (c_t/c_i)^2} = \frac{1 - (z_i/z_t)^2}{1 - (\rho_1/\rho_2)^2} \quad (11.31)$$

Not every combination of media will have an angle of intromission that depends upon both sound speed and density ratios. For  $\theta_{intro}$  to be real, both the numerator and denominator of Eq. (11.31) must have the same sign.

There are four combinations of impedance and sound speed ratios:

- (i) **No  $\theta_{crit}$  and no  $\theta_{intro}$**  If both  $z_t/z_i < 1$  and  $c_t/c_i < 1$ , there is no critical angle, so  $0 < R < -1$  for all  $\theta_i$ . For this case,  $\theta_i > \theta_t$ , so  $(\cos \theta_t / \cos \theta_i) > 1$  and  $z_t/z_i < 1$ , so there can be no angle of intromission.

---

<sup>8</sup>If we were treating the interface between two viscous liquids or between a viscous liquid and a solid surface, then we would need to impose a “no-slip” boundary condition on the transverse components of particle velocity. This is particularly important for the fluid-solid boundary since the viscous stress on the interface can couple to shear waves into the solid and vice versa. The coupling of shear waves in the solid to viscous waves in liquids has been used to measure fluid density and viscosity.

- (ii) **Real  $\theta_{crit}$  but no  $\theta_{intro}$**  If both  $z_r/z_i > 1$  and  $c_r/c_i > z_r/z_i$ , then there will be a critical angle above which there will be total internal reflection so  $R = 1$  if  $\theta_i > \theta_{crit}$ . Since  $c_r/c_i > z_r/z_i$ , the numerator of Eq. (11.31) will be positive, but the denominator will be negative, so there can be no  $\theta_{intro}$ .
- (iii) **Real  $\theta_{intro}$  but no  $\theta_{crit}$**  If  $z_r/z_i > 1$  and  $c_r/c_i < 1$ , then there will be no critical angle, so  $0 \leq R < 1$  for all  $\theta_i$ . Since  $c_r/c_i < z_r/z_i$ , both the numerator and the denominator of Eq. (11.31) will be positive, so there will be an angle of intromission,  $\theta_i = \theta_{intro} < 90^\circ$ .
- (iv) **Real  $\theta_{intro}$  and real  $\theta_{crit}$**  If  $c_r/c_i > 1$  and  $z_r/z_i < 1$ , then there will be both a critical angle,  $\theta_{crit} < 90^\circ$ , above which there will be total internal reflection so  $R = 1$  if  $\theta_i > \theta_{crit}$ , and both the numerator and the denominator of Eq. (11.31) will be negative, so there will be an angle of intromission  $\theta_i = \theta_{intro} < \theta_{crit} < 90^\circ$ .

Total transmission at the angle of intromission has been observed in high-porosity marine sediments, like silty clays, which exhibit a sound speed through its bulk which is lower than that of the interstitial fluid within its pores. When high-porosity sediment is at the water/sediment interface, there can be total transmission of sound into the seafloor. Measurements of the angle of intromission in coastal regions around Italy indicate that the properties of the high-porosity sediments are surprisingly uniform over large areas [6].

## 11.4 Constant Sound Speed Gradients

To this point in our discussion of the refraction of sound, we have only considered plane boundaries that separate media with a discontinuity in their sound speed, density, and/or specific acoustic impedance. There are many situations of interest where the *refraction* (or bending) of a planewave of sound can create interesting and significant effects resulting from a gradual change in the acoustical properties of the medium. These effects are easily calculable in the limit that such sound speed changes are a linear function of position when those changes occur over a distance that extends over very many acoustic wavelengths.

Figure 11.10 shows two examples of sound refraction in air that supports a temperature gradient that depends upon the time of day. As expressed by the quadratic dependence of sound speed on the mean temperature of an ideal gas in Eq. (10.23), the change in sound speed,  $\Delta c$ , with height,  $z$ , above the ground is related to the changes in the absolute temperature,  $T$ .

$$\frac{dc}{dz} = \left( \frac{dc}{dT} \right) \left( \frac{dT}{dz} \right) = \frac{c}{2T} \left( \frac{dT}{dz} \right) \quad (11.32)$$

Similar refractive effects occur in the ocean where the speed of sound in seawater is a complicated function of temperature, salinity, and depth (pressure).

$$c = 1493.0 + 3(t - 10) - 0.006(t - 10)^2 - 0.04(t - 18)^2 + 1.2(S - 35) - 0.01(t - 18)(S - 35) + D/61 \quad (11.33)$$

In Eq. (11.33), the sound speed,  $c$  in m/s, is a function of the temperature,  $t$ , in degrees Celsius. The salinity,  $S$ , is measured in grams of salt per kilogram of water, and  $D$  is the depth below the surface measured in meters [8]. That formula is valid within  $\pm 0.2$  m/s for  $-2^\circ\text{C} \leq t \leq +24.5^\circ\text{C}$ ,  $0.030 \leq S \leq 0.042$ , and  $0 \leq D \leq 1000$  m.

Figure 11.11 shows the sound speed variation with depth that was measured over 9 years in the ocean 15 miles (24 km) south-east of Bermuda. Although significant sound speed variation over the 9 years is apparent within roughly 2 km of the surface, it is possible to represent the change in sound speed with depth using a *piecewise-linear approximation*.

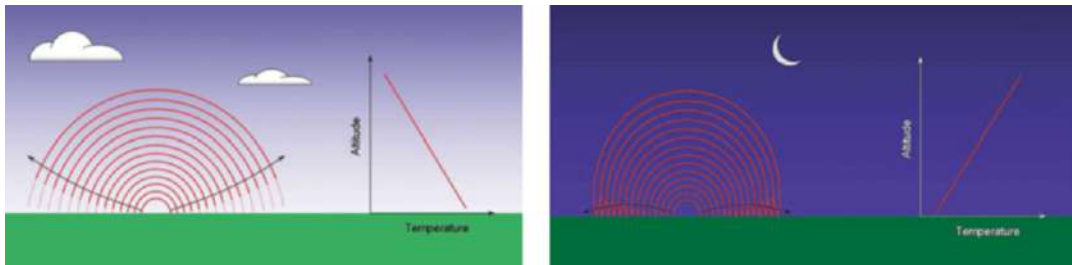


**Fig. 11.10** (Left) During the day, the temperature of the atmosphere generally decreases with altitude above the ground causing sound waves to refract upward since the speed of sound is proportional to  $\sqrt{T}$ . (Right) The opposite conditions can occur at night when the temperature of the air in contact with the ground is colder than the air above it (a “temperature inversion”). This causes sound to be refracted downward. If there is wind, it can also cause the sound speed to vary with height above the ground. (Figures courtesy of T. B. Gabrielson [7])

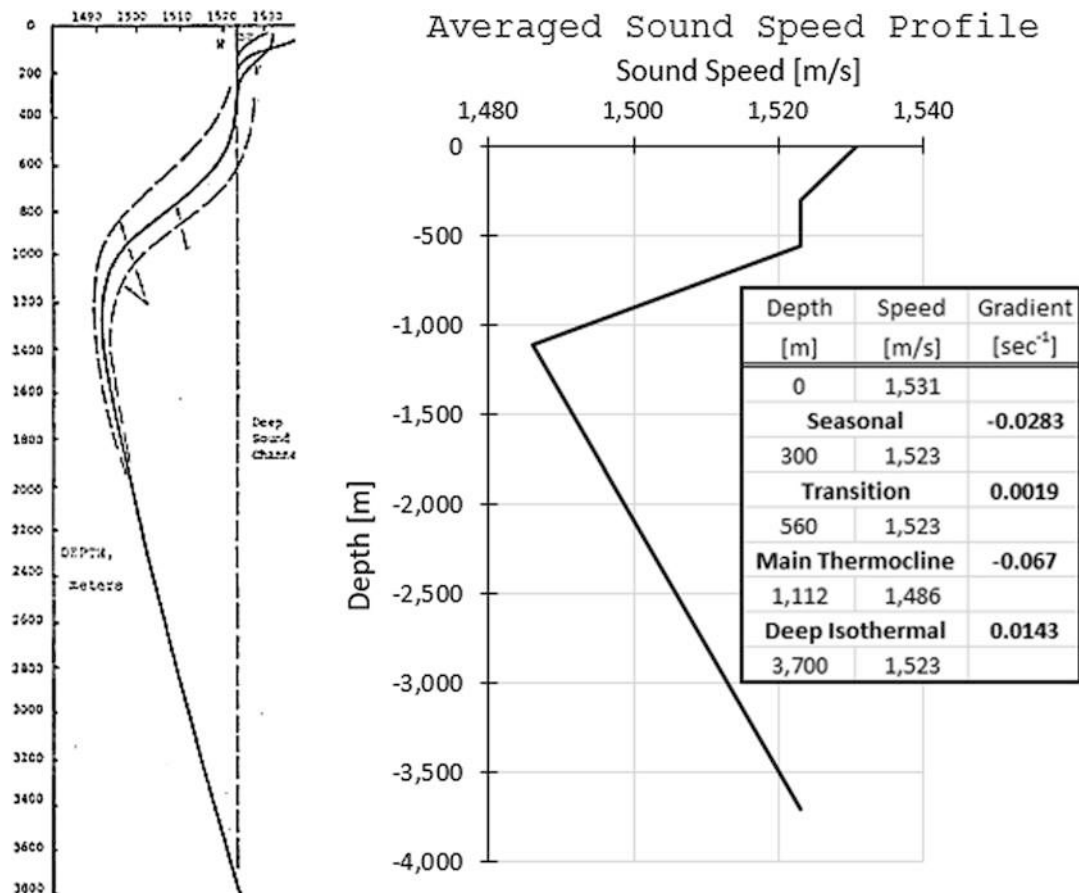


**Fig. 11.11** (Left) These deep-ocean sound speed profiles were taken every 2 weeks over a 9-year period at a location 24 km SE of Bermuda. [9] The solid curve is the average and the dashed curves show the extremes. This typical deep-sea profile may be divided into a number of layers having different properties. At the top, the diurnal layer shows day-night variability and responds to weather changes. Below it, down to the depth of about 300 m, lays the seasonal thermocline that is above the main thermocline, which exhibits the strongest sound speed gradient. Below the thermocline, beneath 1200 m, the deep isothermal layer has a constant temperature of +4 °C. There, the sound speed’s increase with depth is dominated by the increasing pressure. (Right) The measured sound speed profile is replaced by a piecewise-linear approximation that provides a constant sound speed gradient for each layer, as indicated by the embedded table. At a depth of approximately 3700 m, the sound speed is the same as it is at a depth of approximately 560 m. Between those two depths, sound can be trapped in the “deep sound channel” in the same way that light is trapped in an optical fiber, except the core of an optical fiber that is about 10  $\mu\text{m}$  and the sound channel that is about 1 km, a height ratio of about  $10^8$

### 11.4.1 Constant Gradient's Equivalence to Solid Body Rotation

The goal in this sub-section is to develop a simple formalism that will permit calculation of the path of planewaves in a medium with a sound speed that is a linear function of height or depth. Furthermore, we would like to be able to track the trajectory of the sound (i.e., follow the direction of the wavevector) through regions of changing sound speed gradient, a process known as *ray tracing*. To do this, we must first recognize that the propagation of sound through a region of constant sound speed gradient is isomorphic to the solid body rotation of a disk, since the tangential velocity,  $\vec{v}_{\tan}$ , of any point on the rotating disk is proportional to its (linear) distance,  $|\vec{r}|$ , from the axis of rotation.

$$\vec{v}_{\tan} = \vec{r} \times \vec{\omega} \quad (11.34)$$

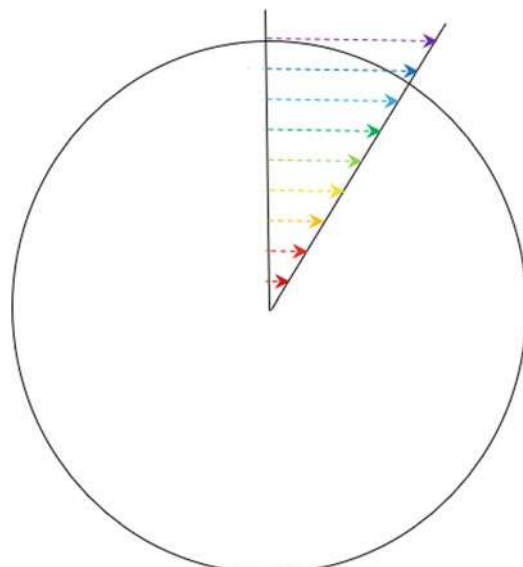
Since this equation refers to a rotating disk, the use of the cross-product might seem to be pedantic excess, but it is intended to remind you of your study of solid body rotational dynamics during your freshman physics course.

If we limit ourselves to linear changes in sound speed with height or depth, then the sound speed gradient is a constant:  $dc/dz \equiv g$ . In analogy with a rotating disk of radius,  $R$ , as diagrammed in Fig. 11.12, we can equate sound speed,  $c$ , with the tangential velocity of a point on the rim of the disk,  $\vec{v}_{\text{rim}}$ , and integrate our above definition; it is easy to see that  $g$  plays the same role as  $\omega$  (and has the same units) in Eq. (11.34).

$$\int_0^{v_{\text{rim}}} dc = g \int_0^R dz \Rightarrow R = \frac{|\vec{v}_{\text{rim}}|}{g} \quad (11.35)$$

I like to think of the refraction (bending) of the sound wave's trajectory in a constant sound speed gradient by picturing the advance of the planewave fronts as represented schematically in Fig. 11.13.

**Fig. 11.12** Shown at the right is a disk that is rotating. The dashed, colored arrows indicate the tangential velocity that increases linearly with distance from the axis of rotation. Such a velocity distribution in space is identical to the assumed constant sound speed gradient that will control the refraction of sound waves



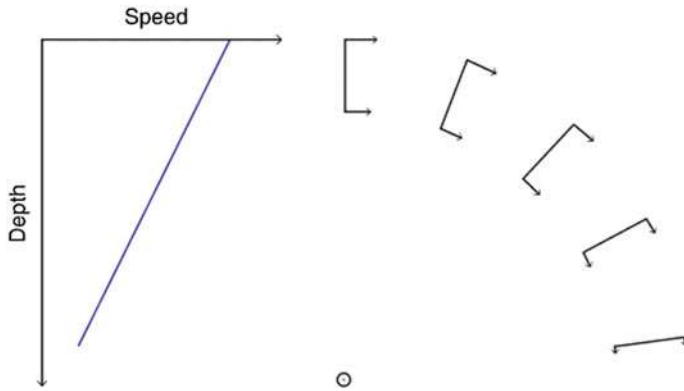


**Fig. 11.13** A conceptual sketch of planewave fronts moving through a medium with the velocity gradient shown at the left. The arrows at the top of the wave fronts are always longer than the arrows at the bottom. This turns the wave front downward until the wave front is nearly horizontal. Once horizontal, both ends of the wave front will move with the same speed, and the wave will continue downward without changing direction

To introduce this “disk rotation” approach to analysis of the propagation of planewaves through a medium with constant speed gradients, let’s consider the measurement of road noise during the day, when the temperature of the air is decreasing with increasing altitude, as shown in Fig. 11.10 (left).

Assume that you are asked to determine the sound pressure level created by traffic on a highway at a proposed housing location that is 150 m from the highway. By measuring the average temperature at a height of 0.5 m and at 5 m, you determine that the sound speed at 0.5 m is 342.8 m/s and at 5.0 m is 341.3 m/s. How high must your microphone be above the ground, at a distance of 150 m from the source, to ensure that you intercept sound that leaves the highway in an initially horizontal direction?

To begin, let’s calculate the sound speed gradient,  $dc/dz = g \cong \Delta c/\Delta z = (2.8-1.3 \text{ m/s})/4.5 \text{ m} = 0.333 \text{ s}^{-1}$ . Since the sound speed decreases with height, we know that the wave will be refracted upward, as shown in Fig. 11.10 (left). We’ll assume that the noise is generated at the intersection of the tire and the road at  $z = 0$ , where  $c_o = 343.0 \text{ m/s}$  (extrapolating down to the surface from the lowest measurement at 0.5 m above the ground).

We now need to calculate the radius,  $|R|$ , of this limiting ray’s circular path.

$$|R| = \frac{c_o}{g} = 1029 \text{ m} \quad (11.36)$$

A simple trigonometry identity can be used to determine the height,  $h = 11.0 \text{ m}$ , above the ground that a microphone must be placed to receive the sound radiated by the tires. For me, drawing a sketch, like in Fig. 11.14, is always crucial.

$$\begin{aligned} \sin \theta &= \frac{150}{1029} = 0.146 \quad \Rightarrow \quad \theta = 0.146 \text{ rad} = 8.38^\circ \\ h &= |R| - |R| \cos \theta = |R|(1 - \cos \theta) \cong |R| \frac{\theta^2}{2} = 11.0 \text{ m} \end{aligned} \quad (11.37)$$

The final expression above made use of the small-angle expansion of cosine in Eq. (1.6).

Although the refractive process was not understood until the twentieth century [7], reports of the existence of an acoustic “shadow zone” appeared much earlier. Below is the account of R. G. H. Kean as he watched the Battle of Gaines’s Mill during the American Civil War [10]:

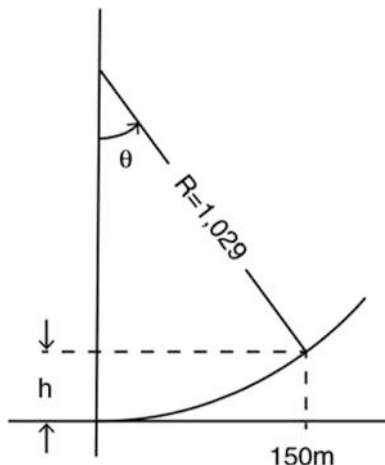


**Fig. 11.14** Sketch (not to scale) of the ray path of the sound generated by the tire noise on a road surface. The observation point is 150 m from the sound source. Between the ground and the circular arc is a “shadow zone” that is created by the upward refraction of the sound produced by the sound speed gradient,  $dc/dz = 0.333 \text{ s}^{-1}$ , which was used to calculate the radius,  $|R| = 1029 \text{ m}$ , applying Eq. (11.36). A microphone must be placed at least a distance,  $h$ , above the ground to intercept the tire noise. At the surface ( $h = 0$ ), the sound speed is  $c_o = 343.0 \text{ m/s}$ . At  $h = 11.0 \text{ m}$  above the surface, the sound speed is  $339.3 \text{ m/s}$

I distinctly saw the musket-fire of both lines . . . I saw batteries of artillery on both sides come into action and fire rapidly. Yet looking for near two hours, from about 5 to 7 P.M. on a midsummer afternoon, at a battle in which at least 50,000 men were actually engaged, and doubtless at least 100 pieces of field-artillery . . . *not a single sound of the battle* was audible to General Randolph and myself . . . [However, the] cannonade of that very battle was distinctly heard at Amhurst Court-house, 100 miles west of Richmond, as I have been most credibly informed.

The process of refraction in a sound speed gradient, as illustrated in a particularly simple form in Fig. 11.14, is entirely reversible. If we were to say that we had a sound source directed  $8.4^\circ$  below the horizontal direction, located 11.0 m above the ground, then we could just as easily say that it would intersect the ground 150 m away, based on Fig. 11.14 and the results of Eq. (11.37).

Since much of the interest in the propagation of sound in a sound speed gradient (linear or otherwise) tends to concern sound waves that are nearly grazing the horizontal axis, the *grazing angle* is more commonly used in Snell’s law than the angle measured with respect to the normal to the surface, which was our previous choice for discussion of reflection and transmission from a plane surface of discontinuity. If we now use the grazing angle, then we can rewrite Eq. (11.22) by letting  $\theta$  be the angle below the horizontal and  $c_o$  be the sound speed at a location where the sound waves are propagating horizontally (i.e.,  $\cos 0^\circ = 1$ ).

$$\frac{c}{\cos \theta} = c_o \quad (11.38)$$

Let’s apply the above version of Snell’s law to the example in Fig. 11.14. That ray is horizontal at  $h = 0$ , where  $c_o = 343.0 \text{ m/s}$ . Assuming, as before, a constant sound speed gradient, at the “source height” of 11.0 m,  $c = 339.3 \text{ m/s}$ . Plugging directly into Eq. (11.38),  $\cos \theta = c/c_o$ , so  $\theta = 0.147$  radians =  $8.4^\circ$ . Of course, we could have used Eq. (11.37) to calculate the sound speed 11.0 m above the surface, since we already knew that  $\theta = 8.4^\circ$ .

### 11.4.2 Sound Channels

We will now apply this formalism to a particularly interesting case that occurs in a sound speed profile like the one shown in Fig. 11.11, describing the deep ocean off of Bermuda, which we have approximated by a series of contiguous line segments with constant (but different) sound speed gradients. There is a sound speed minimum of  $c_{min} = 1486$  m/s, at a depth of 1112 m, between the main thermocline and the deep isothermal layer. As evident from Fig. 11.13, in such a constant gradient (i.e., linear sound speed profile), the sound will “go to the slow,” and therefore, we expect that some sound will become trapped around that sound speed minimum in a *sound channel*.

In this sub-section, we will trace several rays from a submerged source to develop an understanding of the channel’s propagation characteristics. Assume that there is a sound source at a depth of 800 m, where the sound speed (by interpolation) is 1507 m/s. We start by calculating the upward angle from the source that will result in a horizontal ray at the top of the upper gradient,  $z = 560$  m, where the sound speed is  $c_{max} = 1523$  m/s. By Snell’s law, as expressed in terms of the grazing angles in Eq. (11.38),  $\theta_1 = \cos^{-1}(1507/1523) = 0.145$ ; hence,  $\theta_1 = 8.31^\circ$ . The radius of the circular path of the ray,  $|R_1| = c_o/g = (1523 \text{ m/s} \div 0.067 \text{ s}^{-1}) = 22.73 \text{ km}$ . Based on the diagram in Fig. 11.15, the sound ray intersects the top of the channel at a horizontal distance that is  $r_1 = |R_1| \sin \theta_1 = 3.3 \text{ km}$  from the source.

From the top of the channel ( $z = 560$  m), the ray will return to the channel axis along the same circular path and will intersect the axis ( $z = 1112$  m) at  $\theta_2 = \cos^{-1}(1486/1523)$ , so  $\theta_2 = 0.221 \text{ rad} = 12.66^\circ$ . The horizontal distance,  $r_2 - r_1 = |R_1| \sin \theta_2 = 5.0 \text{ km}$ .

The ray enters the deep isothermal layer where  $|R_2| = (1486 \text{ m/s} \div 0.0143 \text{ s}^{-1}) = 103.9 \text{ km}$ . (The center of that circle is only a geometrical “construction point,” so the fact that it is located above the stratosphere should not be a cause for our concern.) Since we have defined the bottom of the channel as the location where the sound speed in the deep isothermal layer equals the sound speed at the top of the

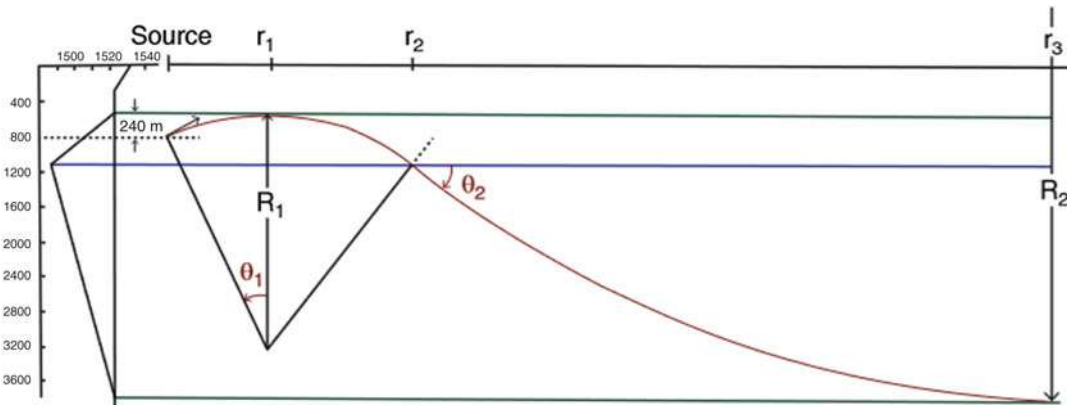


**Fig. 11.15** The diagram of the sound speed vs. depth at the left is based on the piecewise-linear approximation of Fig. 11.11. There is a sound speed minimum at a depth of  $z = 1112$  m that is the axis of a sound channel shown by the horizontal blue line. The velocity maxima are shown by the horizontal green lines at depths of 560 m and 3700 m, corresponding to  $c_{max} = 1523$  m/s. The ray paths, ranges, depths, and especially the ray path radii,  $|R_1|$  and  $|R_2|$ , are not drawn to scale. The limiting ray paths for a sound source located at a depth of 800 m, and horizontal distance,  $r = 0$ , are shown in red, launched at an angle of  $\theta_1 = 8.31^\circ$  above the horizontal. The turning point for the ray in the upper layer occurs at a horizontal distance from the source of  $r_1$ , while the turning point for the ray in the lower layer occurs at a horizontal distance from the source of  $r_3$ . The ray crosses the channel axis at  $r_2$  and enters the lower layer at an angle  $\theta_2$  below the horizontal.

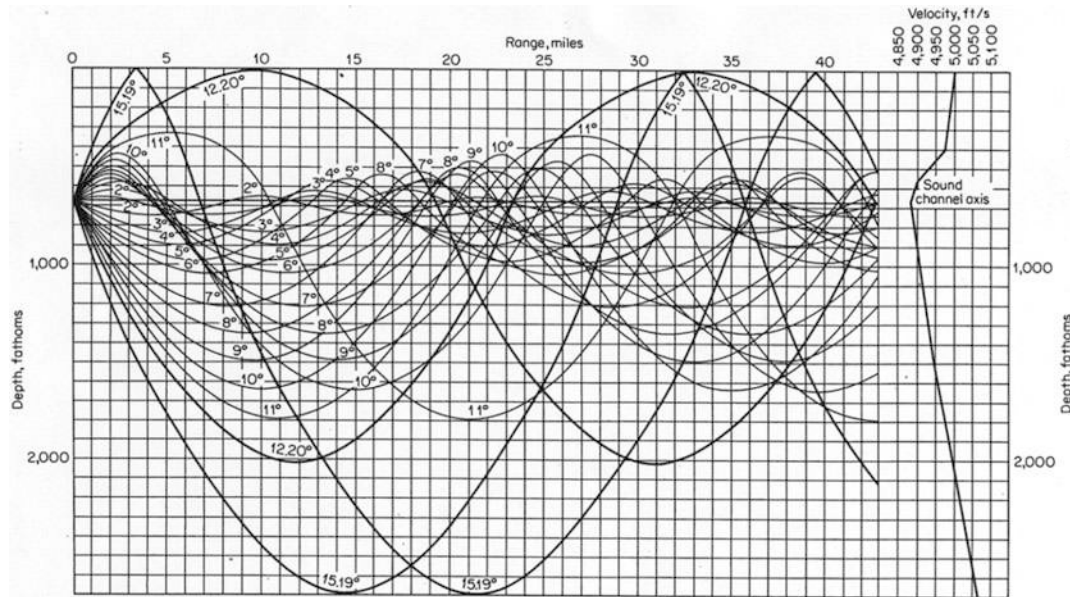


**Fig. 11.16** Ray diagram for transmission paths in the deep sound channel for a source located on the channel axis. Depth is in fathoms (1 fathom = 6 feet = 1.829 m), range is in miles (1 mi = 1.609 km), and sound speed is in feet/second (1 fps = 30.48 cm/s), as a function of depth is provided at the right side of the graph. For angles  $\theta > \theta_{max} = 12.2^\circ$ , waves escaping the channel are reflected from the air-water interface [11]

main thermocline,  $c_{max} = 1523$  m/s, Snell's law will guarantee that it will reach that depth with a ray that is again horizontal, after traveling a horizontal distance,  $r_3 - r_2 = |R_2| \sin \theta_2 = 22.8$  km. From that point at horizontal distance from the source,  $r_3$ , the path should repeat indefinitely with the cycle distance from the top of the channel back to the top of the channel being  $2(r_3 - r_1) = 55.6$  km.

To calculate the angular width of the sound radiated by our source located at  $z = 800$  m below the surface, which will be trapped in the channel, we need to follow a ray that leaves the source at an angle below horizontal,  $\theta_{-1}$ , that will also take it to the depth ( $z = 3700$  m) where the sound speed is again  $c_{max}$ . That initially downward-directed ray will also have to cross the sound channel axis at  $\theta_2 = 12.66^\circ$  if it is to become horizontal at  $z = 3700$  m. Again, Snell's law guarantees that  $(1507 \text{ m/s} \div \cos \theta_{-1}) = (1486 \text{ m/s} \div \cos \theta_2) = 1523 \text{ m/s}$ , so  $|\theta_{-1}| = |\theta_2| = 8.31^\circ$ . That result is easy to visualize since we can imagine a “virtual source” that is located  $2r_1$  away from the original source, where the ray makes an angle of  $-8.31^\circ$  with respect to the horizontal. Any ray that leaves the source within  $\pm 8.31^\circ$  will be trapped in the sound channel created by the two sound speed gradients.

Again, Snell's law makes it easy to see that an initially horizontal ray leaving our source at a depth of  $z = 800$  m will go up and down in the channel from a depth of  $z = 800$  m to a depth of  $z = 2581$  m, where the sound speed will again be 1507 m/s and the rays will again be horizontal. Figure 11.16 diagrams ray paths from a more complicated sound channel for a source located on the channel axis [11].

The results illustrated in the previous example can be generalized by defining a maximum angle  $\pm\theta_{max}$  (above or below the horizontal) that will result in the trapping of a wave launched at the channel axis, in terms of the minimum sound speed at the axis,  $c_{min}$ , and the maximum sound speed,  $c_{max}$ , at the bottom and top of the channel.

$$\cos \theta_{\max} = \frac{c_{\min}}{c_{\max}} \quad (11.39)$$

Expanding  $\cos \theta_{\max}$  for small angles and defining  $\Delta c = c_{\max} - c_{\min}$ , Eq. (11.39) can be approximated as  $\theta_{\max} \cong \sqrt{2Dc/c_{\max}}$ . When the source is above or below the height or depth of the channel by a distance,  $z_o$ , in a layer  $D$  thick, Snell's law, and the requirement that a trapped ray at the channel boundary is horizontal, provides the range of trapping angles,  $\theta_{\pm 1} = \pm \theta_{\max} \sqrt{z_o/D}$ , when the source is not located on the sound channel's axis. Along the channel axis,  $z_o = D$ . At the extremes,  $z_o = 0$ , only the horizontal ray is trapped. The long-range transmission ability of the deep sound channel was used during World War II to rescue aviators that crashed at sea.<sup>9</sup> A downed pilot would drop a small explosive charge that was rigged to detonate near the depth of the sound channel axis. If the sound were detected with two or more hydrophones, also located at the axis depth, the reception times could be used to localize the search by triangulation. Successful rescues were made this way using hydrophones connected to shore stations that were thousands of miles from the aircraft impacts. More recently, the same ability to make localizations at sea has been used for missile-impact location [12], and measurement of the time delays has been used to measure the mean temperature of the deep ocean [13].

### 11.4.3 Propagation Delay\*

It is interesting to calculate the difference in the propagation times for sound traveling along different paths to reach the same horizontal distance from the source. Although the path along the axis is the shortest, it is also going through the medium with the minimum sound speed. The longer (curved) paths travel through water that has a faster sound speed. Does the shorter path beat the faster path?

Let's first consider the ray that is generated on the sound channel axis and travels along a circular path to the top of the channel. The initial angle of such a ray above the horizontal is  $\theta_{\max} \cong \sqrt{2Dc/c_{\max}}$ , as already shown. The transit time,  $T_{upper}$ , for that ray can be calculated if we integrate from  $\theta = 0^\circ$  to  $\theta = \theta_{\max}$ , where the sound speed depends upon angle,  $c(\theta) = c_{\max} \cos \theta$ .

$$T_{upper} = \int_0^{\theta_{\max}} \frac{|R|d\theta}{c(\theta)} = \int_0^{\theta_{\max}} \frac{|R|d\theta}{c_{\max} \cos \theta} = \frac{|R|}{c_{\max}} \int_0^{\theta_{\max}} \frac{d\theta}{\cos \theta} \quad (11.40)$$

There is an analytical solution for the above definite integral, but simply writing the answer provides no useful physical insight.

$$\int_0^{\theta_{\max}} \frac{d\theta}{\cos \theta} = \int_0^{\theta_{\max}} \sec \theta \, d\theta = \ln [\csc \theta - \cot \theta]_0^{\theta_{\max}} \quad (11.41)$$

In these problems, the angles are generally small, so the series expansion of the sine and cosine functions and the binomial expansion can both be employed to simplify the integration and its interpretation.

$$\int_0^{\theta_{\max}} \frac{d\theta}{\cos \theta} \cong \int_0^{\theta_{\max}} \frac{d\theta}{(1 - \frac{\theta}{2})} \cong \int_0^{\theta_{\max}} \left(1 + \frac{\theta^2}{2}\right) d\theta = \theta_{\max} + \frac{\theta_{\max}^3}{6} \quad (11.42)$$

The transit time for the axial ray,  $T_{axial}$ , that goes the same horizontal distance,  $r = |R| \sin \theta_{\max}$ , is just  $T_{axial} = r/c_{\min}$ . Since  $c_{\min} = c_{\max} \cos \theta_{\max}$ , the same approach can be used.

<sup>9</sup> In this context, the channel was known as the *SOFAR channel*, which stood for *sound fixing and ranging*.

$$T_{axial} = \frac{|R| \sin \theta_{max}}{c_{max} \cos \theta_{max}} \approx \frac{|R|}{c_{max}} \frac{\left(\theta_{max} - \frac{\theta_{max}^3}{6}\right)}{\left(1 - \frac{\theta_{max}^2}{2}\right)} \approx \frac{|R|}{c_{max}} \left(\theta_{max} - \frac{\theta_{max}^3}{6}\right) \left(1 + \frac{\theta_{max}^2}{2}\right) \quad (11.43)$$

We have to be vigilant at this point to be sure we are evaluating Eq. (11.43) to the same level of approximation as we had in Eq. (11.42), which is correct to third order in  $\theta_{max}$ . The product of the two binomials includes a term that is linear in  $\theta_{max}$  as well as two terms that are third order.

$$T_{axial} = \frac{|R|}{c_{max}} \left(\theta_{max} - \frac{\theta_{max}^3}{6} + \frac{\theta_{max}^3}{2}\right) = \frac{|R|}{c_{max}} \left(\theta_{max} + \frac{\theta_{max}^3}{3}\right) \quad (11.44)$$

These calculations demonstrate that the (longer) curved path is traversed in less time than the shorter (axial) path. We can use Eq. (11.44) with Eqs. (11.40) and (11.42) to approximate the travel time difference,  $\Delta T$ .

$$\Delta T = T_{axial} - T_{upper} \approx \frac{|R|}{c_{max}} \left[ \left(\theta_{max} + \frac{\theta_{max}^3}{3}\right) - \left(\theta_{max} + \frac{\theta_{max}^3}{6}\right) \right] = \frac{|R|}{c_{max}} \frac{\theta_{max}^3}{6} \quad (11.45)$$

#### 11.4.4 Under Ice Propagation

Sound propagation under Arctic ice provides an interesting variation on the sound channel, since sound can be reflected specularly (i.e.,  $\theta_r = \theta_i$ ) from the ice sheet and the speed of sound under the ice increases monotonically with depth. The lack of solar heating at the surface causes the main thermocline, shown in Fig. 11.11, to be absent under Arctic ice. Typical ray paths under Arctic ice are shown in Fig. 11.17.

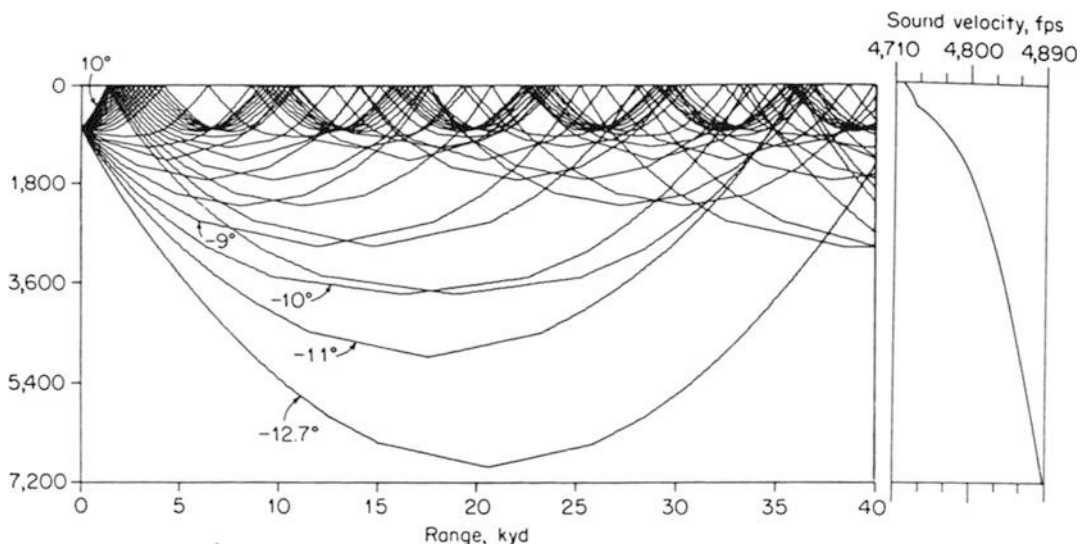


**Fig. 11.17** Typical sound speed profile (right) and ray paths (left) under Arctic ice. Depth is in fathoms (1 fathom = 6 feet = 1.829 m), range is in kiloyards (1 kyd = 0.9144 km), and sound speed is in feet/second (1 fps = 30.48 cm/s) [14]

### 11.4.5 Sound Focusing

A final illustration of these refractive processes in constant sound speed gradients, at a much different scale than the global sound propagation in the deep sound channel, comes from the evolution of marine mammals. The Cuvier's beaked whale (*Ziphius cavirostris*) is a member of the Ziphiidae family of toothed whales. It relies on echolocation, but in an aqueous environment, the excessive hydrodynamic drag and turbulence noise that would be produced by external "ears" (i.e., pinna), like those found on land mammals, is unacceptable. In this whale, the "ear" is located internally behind the jaw (in green), as shown in Fig. 11.18.

Figure 11.19 demonstrates that this region acts like a lens. Parallel rays that enter the "channel" are focused to a single point (see Fig. 11.20). As we have done many times now, we can represent the distribution of sound speeds in the whale's mandible using a piecewise-linear approximation. In this

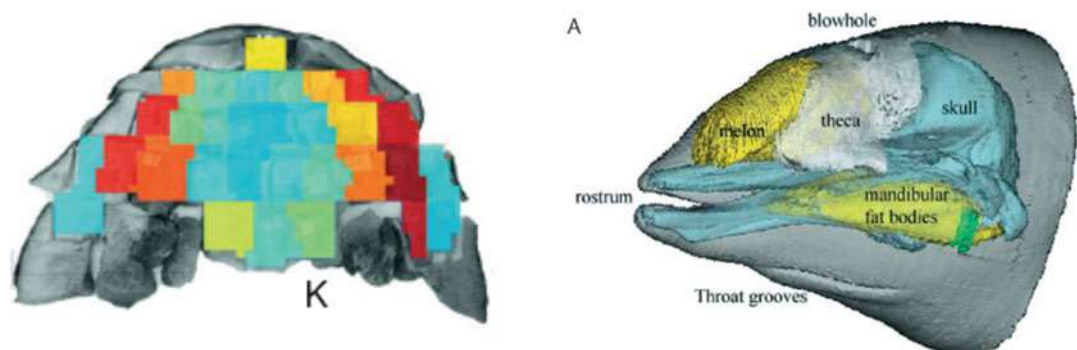


**Fig. 11.18** The sound-sensing organ of the Cuvier's beaked whale is shown by the small green area in the drawing of the whale's head at the right. At the left is a tomographic slice through the mandibular fat body which acts as a sound channel (i.e., lens) to focus sounds from the water to the whale's sound-sensing organ. The sound speed of the mandibular fat body (in yellow at the right) shows the sound speed as a function of location (red corresponding to 1700 m/s and light blue corresponding to 1300 m/s). Diagrams from Sodervilla, et al. [15]

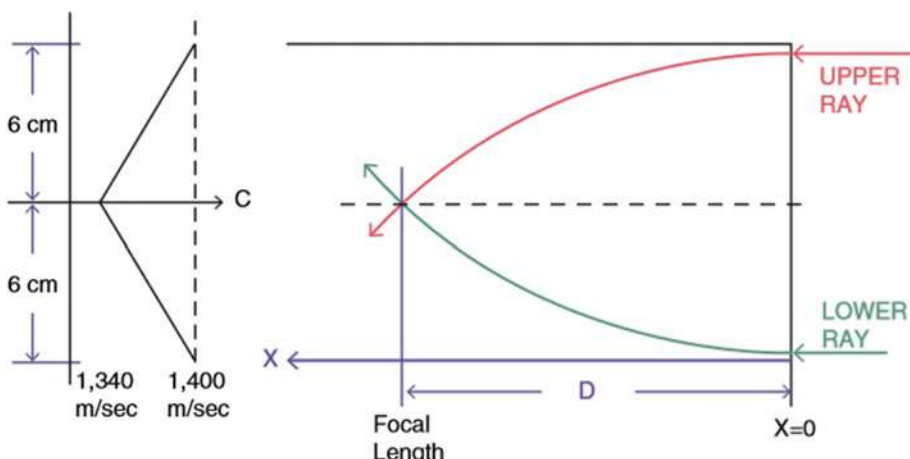


**Fig. 11.19** A simplified approximation to the sound channel (i.e., lens) created by the mandibular fat body that assumes that the sound speed gradient is constant, with its minimum value (1340 m/s) along the axis, and its maximum value (1400 m/s) at the upper and lower extremes, 6.0 cm above and below the sound channel axis

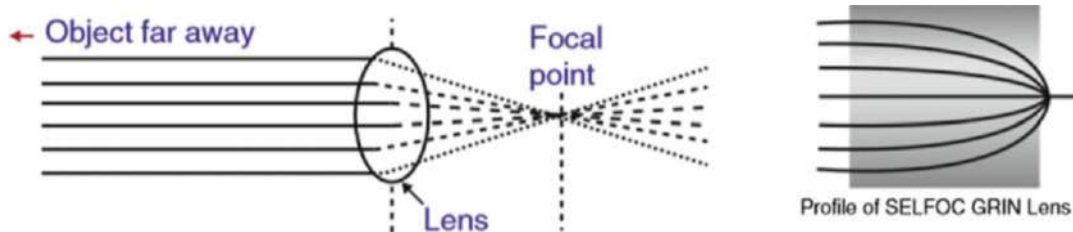


**Fig. 11.20** (Left) Ray paths for an ordinary lens. (Right) Ray paths for a graded-index (GRIN) lens. In both cases, parallel rays enter the lens and are focused to a single point

case, the sound speed gradient  $g = 60 \text{ m/s} \div 0.06 \text{ m} = 1000 \text{ s}^{-1}$ ; hence,  $|R| = c_o/g = 1.4 \text{ m}$ . Using Snell's law,  $\cos \theta_{max} = 0.957$ ; hence,  $\theta_{max} = 16.8^\circ$ . This makes the “focal length” of the whale’s acoustic lens,  $d_{focal} = |R| \sin \theta_{max} = 40.5 \text{ cm}$ , just about the extent of the mandibular fat bodies.

The strategy of using a propagation speed profile to act as a lens is very popular in fiber-optic telecommunication systems and fiber-optic sensors. As shown in Fig. 11.20, this application is intended to capture light from an LED or solid-state laser and focus that light into the core of single-mode optical fibers that typically have waveguide (core) diameters on the order of 10 microns or less. In sensor applications [16–18], it usually is used to spread the light from an optical fiber over the surface of some sensing element after which a second GRIN lens injects the modulated light back into the optical fiber.

The graded-index lens was patented by Nippon Sheet Glass in 1968 and given the trademark SELFOC®. According to the accepted evolutionary timeline [19], marine mammals had produced the acoustical equivalent of GRIN lenses for at least 32 million years before the NSG patent was issued.

#### Talk Like an Acoustician

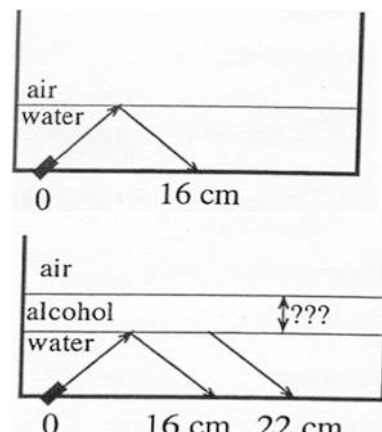
Cavitation effects	Fermat’s principle
Pressure reflection coefficient	Critical angle
Pressure transmission coefficient	Total internal reflection
Pressure release boundary	Angle of intromission
Impedance matching layer	Refraction
Antireflective coating	Piecewise-linear approximation
Trace wavelength	Ray tracing
Specific acoustic impedance	Grazing angle
Specular reflection	Sound channel
Diffuse reflection	SOFAR channel
Snell’s law	

#### Exercises

1. **Air-water interface.** A 1.0 kHz planewave in water with pressure amplitude,  $|\hat{\mathbf{p}}| = 100 \text{ Pa}$ , is normally incident on the air-water interface (i.e., the propagation direction is at a right angle to the air-water surface; hence,  $\theta_i = 0^\circ$ ). You may assume the speed of sound in water is 1500 m/s and the speed of sound in air is 343 m/s. The density of water can be taken as  $1000 \text{ kg/m}^3$  and of air to be  $1.19 \text{ kg/m}^3$ .
  - (a) *Transmitted amplitude.* What is the amplitude of the pressure that is transmitted into the air?
  - (b) *Trace velocity.* What is the “trace velocity” of the waves along the interface?

- (c) *Intensities.* What is the intensity of the incident wave in the water and the transmitted wave in air?
- (d) *Transmission loss.* Express the reduction in the intensity of the wave when it crosses the interface from the water into the air in decibels.
- (e) *Oblique incidence.* If the angle of incidence is increased to  $45^\circ$ , what is the amplitude of the pressure transmitted into the air?
- (f) *Trace velocity.* What is the “trace velocity” of the waves along the interface?
- (g) *Transmitted pressure.* If the planewave originates in that air and makes an angle of  $45^\circ$  to the normal, what is the magnitude of the acoustic pressure of the sound in the water?
2. **Matching layer.** What is the density and sound speed required for a 1.0-cm-thick layer of material that produces complete transmission of sound from water into steel if the frequency of the sound wave is 20 kHz? Let  $\rho_{\text{water}} = 1000 \text{ kg/m}^3$  and  $c_{\text{water}} = 1500 \text{ m/s}$ ,  $\rho_{Fe} = 7700 \text{ kg/m}^3$ , and  $c_{Fe} = 6100 \text{ m/s}$ .
3. **Alcohol on water.** An acoustics experiment is performed in an aquarium partially filled with water ( $c = 1500 \text{ m/s}$  and  $\rho_m = 1000 \text{ kg/m}^3$ ). At the bottom of the aquarium, an ultrasonic transducer shoots a narrow beam of sound up to the surface of the water at an angle of  $45^\circ$ , and the sound beam reflects back down to the bottom of the aquarium where it hits a distance along the bottom that is 16.0 cm from the transducer. This situation is diagrammed in the upper portion of Fig. 11.21. You may assume the bottom of the aquarium is perfectly absorbing, so the beam does not bounce back up again and that the problem is entirely two dimensional.
- After making the required measurement, the experimenter comes back from lunch and finds that a layer of ethyl alcohol ( $c = 1150 \text{ m/s}$  and  $\rho_m = 790 \text{ kg/m}^3$ ) has carefully been poured on top of the water in the aquarium. (Good grief!) Now a second beam of sound comes down and hits the bottom at a distance of 22.0 cm from the ultrasonic transducer, as diagrammed in the lower portion of Fig. 11.21. How thick is the layer of alcohol on top of the water, assuming that the two liquids do not mix?
4. **Oblique incidence at a water-sediment boundary.** A sinusoidal planewave with effective pressure  $p_{rms} = 100 \text{ Pa}$  is incident at  $45^\circ$  on a silt bottom with  $\rho_{silt} = 2000 \text{ kg/m}^3$  and  $c_{silt} = 2000 \text{ m/s}$ .
- Angle of refraction.* What angle does the planewave make with respect to the normal once it enters the silt bottom?
  - Transmitted pressure.* What is the effective pressure of the wave in the silt bottom?
  - Angle of intromission.* At what angle does the planewave have to approach the silt from the water so that there is 100% transmission into the silt and no wave reflected back into the water?

**Fig. 11.21** (Above) The sound beam of an ultrasonic transducer bounces off the free surface of a water-filled aquarium. (Below) the beam is displaced after a layer of alcohol is added to the surface



5. **Critical ray and skip distance in a “mixed layer.”** The sound speed at the water’s surface is 1490 m/s and increases linearly to  $c_o = 1491.5$  m/s with depth to the bottom of the mixed layer at  $D = 100$  m. Below that depth, there is a constant negative sound speed gradient  $g_2 = -0.045 \text{ s}^{-1}$ . For an underwater sound source (projector) at a depth,  $z_s = 60.0$  m, determine the critical (grazing) angle,  $\theta_o$ , for the limiting ray that remains trapped in the mixed layer and the “skip distance,”  $r_s$ , between the successive locations where the critical ray intersects the surface.
6. **Arctic refraction.** The water in the Arctic is nearly isothermal. Sound speed increases with depth because of the pressure effect. Assume the surface temperature is  $0^\circ\text{C}$ , the salinity is 35 ppt, and the sound speed, in meters/second, as a function of depth, is given by the Eq. (11.46), where  $z$  is the depth below the surface expressed in meters [20].

$$c(z) = 1449 + 0.016z \quad (11.46)$$

The turning depth of the ray is 2.0 km where the sound speed is  $c(2 \text{ km}) = 1481 \text{ m/s}$ .

- (a) *Initial grazing angle.* What is the initial angle that ray makes with the water-ice interface? Report the angle which the ray makes with the water’s surface, not the angle with respect to the normal to the surface.
- (b) *Return to the surface.* What is the distance along the surface at which the ray returns to the ice-water interface?

## References

1. E.A. Neppiras, Acoustic cavitation. *Phys. Rep.* **61**(3), 159–251 (1980)
2. V.O. Knudsen, C.M. Harris, *Acoustical Design in Architecture* (Acoustical Society of America, 1978). See Rigid Partitions, pp. 208–210; ISBN 0-88318-267-X.
3. R.B. Lindsay, *Mechanical Radiation* (McGraw-Hill, 1960). See §9.6
4. T.F.W. Embleton, Mufflers, in *Noise and Vibration Control*, ed. by L. L. Beranek, (McGraw-Hill, 1971), p. 379
5. R.P. Feynman, R.B. Leighton, M. Sands, *The Feynman Lectures on Physics*, vol I (Addison-Wesley, 1965). Chapter 26–3
6. C.W. Holland, Geoacoustic inversion for fine-grained sediments. *J. Acoust. Soc. Am.* **111**(4), 1560–1564 (2002)
7. T.B. Gabrielson, Refraction of sound in the atmosphere. *Acoustics Today* **2**(2), 7–17 (2006)
8. C.C. Leroy, Simple equations for accurate and more realistic calculation of the speed of sound in sea water. *J. Acoust. Soc. Am.* **46**(1)(Pt. 2), 216–226 (1969)
9. L. M. Jones & W. A. VonWinkle, *Sound Velocity Profiles in an Area South of Bermuda*, Underwater Sound Laboratory Report No. 632 (1965)
10. C.D. Ross, *Civil War Acoustic Shadows* (White Mane Books, Shippensburg, 2001). “Outdoor sound propagation in the US Civil War,” *Appl. Acoustics* **59**, 137–147 (2000)
11. M. Ewing, J.L. Worzel, Long-range sound transmission, in *Propagation of Sound in the Ocean*, vol. 3, Geo. Soc. Am. Memo. **27**, (1948)
12. H.H. Baker, Missile impact localization system. *Bell Telephone Lab. Res.* **39**, 195 (1961). A similar on-line discussion is available at <https://insidegnss.com/on-target-offshore-scoring-of-precision-guided-munitions/>
13. K.G. Sabra, B. Cornuelle, W.A. Kuperman, Sensing deep-ocean temperatures. *Phys. Today* **69**(2), 32–38 (2016)
14. R. J. Urick, *Sound Propagation in the Sea* (Defense Advanced Research Projects Agency Report 1979). Reprinted as *Principles of Underwater Sound* (McGraw-Hill, 1975); ISBN 0-07-066086-7
15. M.S. Soldervilla et al., Cuvier’s beaked whale (*Ziphius cavirostris*) head tissue physical properties and CT imaging. *J. Exp. Biol.* **208**, 2319–2332 (2005)
16. S.L. Garrett, M.R. Brininstool, J.T. Newmaster, T. Hofler, Fiber optic angular orientation sensor using digital serial encoding. US Pat. No. 5,042,157 (Aug. 27, 1991)

17. A. Migliori, G.W. Swift, S.L. Garrett, Remotely readable fiber optic compass. US Pat. No. 4,577,414 (Mar. 25, 1986)
18. M.R. Brininstool, J.T. Newmaster, S.L. Garrett, Fiber-optic remote angular position sensor including a polarization track. US Pat. No. 5,073,711 (Dec. 17, 1991)
19. A. Berta, J.L. Sumich, *Marine Mammals: Evolutionary Biology* (Academic, 1999); ISBN 0-12-093225-3.
20. C.S. Clay, H. Medwin, *Acoustical Oceanography* (Wiley-Interscience, 1977), pp. 90–91; ISBN 0-471-16041-5.

**Open Access** This chapter is licensed under the terms of the Creative Commons Attribution 4.0 International License (<http://creativecommons.org/licenses/by/4.0/>), which permits use, sharing, adaptation, distribution and reproduction in any medium or format, as long as you give appropriate credit to the original author(s) and the source, provide a link to the Creative Commons license and indicate if changes were made.

The images or other third party material in this chapter are included in the chapter's Creative Commons license, unless indicated otherwise in a credit line to the material. If material is not included in the chapter's Creative Commons license and your intended use is not permitted by statutory regulation or exceeds the permitted use, you will need to obtain permission directly from the copyright holder.





# Radiation and Scattering

12

## Contents

12.1	<b>Sound Radiation and the “Causality Sphere”</b> .....	546
12.2	<b>Spherically Diverging Sound Waves</b> .....	548
12.2.1	Compact Monopole Radiation Impedance .....	550
12.2.2	Compact Monopole Acoustic Transfer Impedance .....	553
12.2.3	General Multipole Expansion* .....	554
12.3	<b>Bubble Resonance</b> .....	555
12.3.1	Damping of Bubble Oscillations .....	557
12.4	<b>Two In-Phase Monopoles</b> .....	560
12.4.1	The Method of Images .....	564
12.5	<b>Two Out-Of-Phase Compact Sources (Dipoles)</b> .....	567
12.5.1	Dipole Radiation .....	571
12.5.2	Cardioid (Unidirectional) Radiation Pattern .....	574
12.5.3	Pressure Gradient Microphones .....	575
12.5.4	The DIFAR Directional Sonobuoy .....	578
12.6	<b>Translational Oscillations of an Incompressible Sphere</b> .....	578
12.6.1	Scattering from a Compact Density Contrast .....	580
12.6.2	Scattering from a Compact Compressibility Contrast .....	583
12.6.3	Scattering from a Single Bubble or a Swim Bladder .....	584
12.6.4	Multiple Scattering in the “Effective Medium” Approximation .....	586
12.7	<b>N-Element Discrete Line Array</b> .....	588
12.7.1	Beam Steering and Shading .....	591
12.7.2	Continuous Line Array .....	593
12.8	<b>Baffled Piston</b> .....	595
12.8.1	Rayleigh Resolution Criterion .....	599
12.8.2	Directionality and Directivity .....	599
12.8.3	Radiation Impedance of a Baffled Circular Piston .....	602
12.8.4	Radiation Impedance of a Baffled Rectangular Piston* .....	604
12.8.5	On-Axis Near-Field Pressure from a Circular Baffled Piston* .....	604
12.9	<b>Radiation Impedance of an Unbaffled Piston</b> .....	607
12.10	<b>Linear Superposition</b> .....	610
	<b>References</b> .....	618

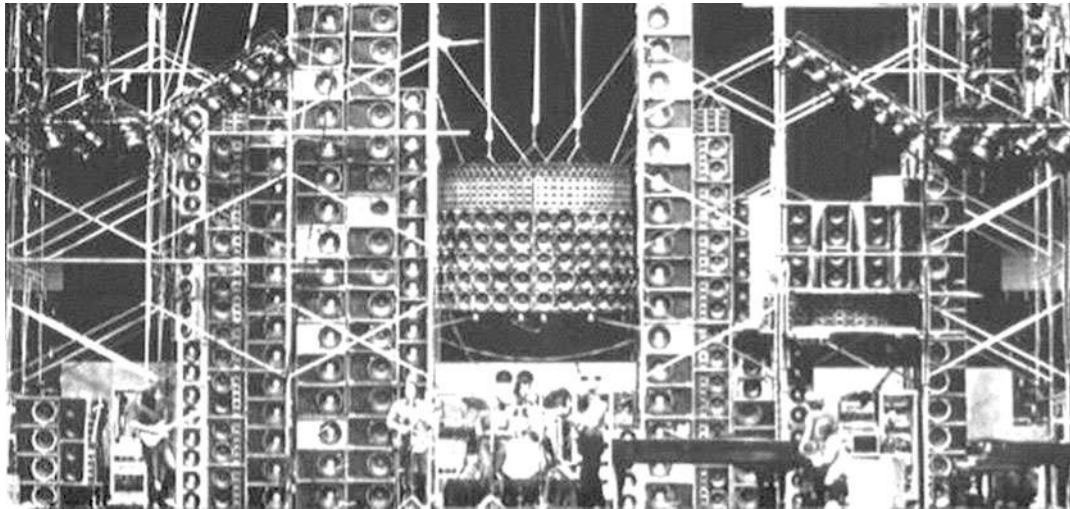


**Fig. 12.1** Photograph of the sound reinforcement system used by the Grateful Dead [1]. Nearly the entire stage is occupied with discrete vertical line arrays of loudspeakers to radiate the full-frequency spectrum of their music toward the audience with minimal leakage toward the ceiling where there would be excessive reverberation that would degrade the intelligibility

At this point, we have made a rather extensive investigation into the sounds that excite Helmholtz resonators as well as the departures from equilibrium that propagate as plane waves through uniform or inhomogeneous media. We have not, as yet, dealt with how those sounds are actually produced in fluids. Our experience tells us that sound can be generated by vibrating objects (e.g., loudspeaker cones, stringed musical instruments, drums, bells), by modulated or unstable flows (e.g., jet engine exhaust, whistles, fog horns, speech), by electrical discharges in the atmosphere (i.e., thunder), or by optical absorption (e.g., modulated laser beams). In this chapter, we will develop the perspective and tools that will be used for the calculation of the radiation efficiency of various sources and combinations of sources, like the sound reinforcement system shown in Fig. 12.1.

Only sound sources that behave in accordance with linear acoustics will be examined (until Chap. 15). We will find that the entire problem of both radiation and of scattering from small discrete objects can be reduced to understanding the properties of a compact source of sound that is small compared to the wavelength of the sound it is radiating.

*“Superposition is the compensation we receive for enduring the limitations of linearity.”* Blair Kinsman [2]

We will then combine many of these radiation units, called *monopoles*, in various ways, including the option of having different units in different locations with different relative phases. Through superposition, this will permit construction of other convenient radiators that range from transversely vibrating incompressible objects (represented by two closely spaced monopoles that are radiating  $180^\circ$  out-of-phase) to arrays of discrete radiators (e.g., line arrays of various sizes like those shown in Fig. 12.1). Integration over infinitesimal monopole sound sources will allow modeling of extended vibrating objects (i.e., continuous, rather than discrete) such as loudspeaker cones, lightning bolts, and laser beams.

For convenience, our initial vision of a *compact source* will be assumed to be a pulsating sphere with radius,  $a \ll \lambda$ . That pulsating sphere produces a sinusoidally varying volume velocity,  $U_1(a, t) = \Re e[\hat{U}(a)e^{j\omega t}]$ . To generate such a volume velocity, we will let the radius of that sphere,

**Fig. 12.2** The loudspeaker enclosure at the right has an irregular shape and provides a total enclosed volume,  $V$ . To be treated as a “compact source,” we require  $V^{1/3} \ll \lambda = c/f = 2\pi c/\omega$ . The loudspeaker cone, visible at the top of the enclosure, has an effective piston area,  $A_{pist}$



$r$ , oscillates harmonically with a single frequency,  $\omega = 2\pi f$ . Those radial oscillations can be represented as  $r(t) = \Re e[a + \hat{\xi}e^{j\omega t}]$ ; hence  $|U_1(a, t)| = 4\pi a^2 \omega |\hat{\xi}|$ , where we have made the assumption that  $a \gg |\hat{\xi}|$ , so that the surface that applies force to the surrounding fluid can be treated as a spherical shell.

As will be demonstrated, an ordinary loudspeaker enclosure, like the one shown in Fig. 12.2, can be treated as a “compact source,” or monopole, if its characteristic physical dimensions are small compared to the wavelength of sound produced. If the loudspeaker enclosures were approximated by a rectangular parallelepiped with volume,  $V$ , then “compactness” would require that  $V^{1/3} \ll \lambda$ .

The oscillatory motion of the loudspeaker cone will be the source of the oscillatory volume velocity in the surrounding fluid. If the cone’s effective piston area is  $A_{pist}$ , located at  $x = 0$ , and its linear position as a function of time is  $x_1(0, t) = \Re e[\hat{\mathbf{x}}e^{j\omega t}]$ , then  $|\hat{\mathbf{U}}(0, t)| = \omega |\hat{\mathbf{x}}| A_{pist} \cos(\omega t + \phi)$ .

As long as the compactness criterion is satisfied, it is theoretically impossible to remotely determine the physical shape of a compact source—if the radiation from a source is that of a monopole, then it is only the source’s volume velocity,  $U_1(a, t)$ , that is related to the sound pressure,  $p_1(R, t)$ , detected at distances,  $R \gg a$ , beyond the maximum physical extent of the source.<sup>1</sup>

Within the constraint of compactness, it does not matter if  $|\hat{\mathbf{U}}(a)| = 4\pi a^2 \omega |\hat{\xi}|$  or  $|\hat{\mathbf{U}}(0)| = A_{pist} \omega |\hat{\mathbf{x}}|$ , the sound radiated into the far field will be identical. Given that realization, then for a compact source, dimensional analysis guarantees that the solution of the steady-state radiation problem reduces to calculation of the acoustic transfer impedance,  $\mathbf{Z}_{tr} = \hat{\mathbf{p}}(R)/\hat{\mathbf{U}}(a)$ , with units that are the same as those for the acoustic impedances we have studied in our investigation of lumped elements:  $|\mathbf{Z}_{tr}| \propto \rho_m c/A$ ,

<sup>1</sup> The inability to remotely determine the shape of a sound source that is smaller than the wavelength of the sound it is radiating is known in both acoustics and in optics as the *Rayleigh resolution criterion*. See Sect. 12.8.1.

where  $\rho_m$  is the mean density of the medium,  $c$  is its sound speed, and  $A$  is a constant with the dimensions of area [ $\text{m}^2$ ]. The transfer impedances for several systems were provided in Sect. 10.7.4 since they were required to make reciprocity calibrations of electroacoustic transducers.

## 12.1 Sound Radiation and the “Causality Sphere”

Light travels at the speed of light; sound travels at the speed of sound. Although those statements seem simplistic, if not tautological, they have calculable consequences that are significant. If a disturbance has a duration,  $\Delta t$ , then those speeds guarantee that the consequences of that event can initially only have influence within a distance,  $d = c\Delta t$ , from the source of that disturbance. The term *causality sphere* was introduced in Einstein’s Theory of General Relativity as the boundary in spacetime beyond which events cannot affect an outside observer. Although most commonly associated with cosmological issues and black holes, the concept is directly relevant to every form of energy that can only move through space with a finite propagation speed.

Before attempting a direct calculation of the acoustic pressure radiated by a compact source that is pulsating in an unbounded fluid medium, it will be instructive to make a simple estimate of the acoustic transfer impedance between an oscillating source of fluid located at the origin of some coordinate system and the pressure at some remote location, a distance,  $R$ , from the origin, using only the adiabatic gas law derived in Sect. 7.1.3:  $pV^\gamma = \text{constant}$ . Before making such a calculation for a source of sound radiating spherically in three dimensions, it will be reassuring to use the same procedure to reproduce a result that we have derived earlier by other means.

If we consider a close-fitting piston at the end of an infinite tube of uniform cross-section,<sup>2</sup> so that both the tube and the piston have a cross-sectional area,  $A$ , then that piston can launch a sound wave down the tube. If the piston produces a volume velocity,  $U(0, t) = \Re e[\widehat{\mathbf{U}}(0)e^{j\omega t}]$ , then the acoustic transfer impedance,  $\mathbf{Z}_{\text{tr}}$ , of such a tube, provided in Eq. (10.85) or in Eq. (10.106), can be used to calculate the steady-state acoustic pressure of the traveling wave produced by the piston’s oscillations.

$$\widehat{\mathbf{p}} = \mathbf{Z}_{\text{tr}} \widehat{\mathbf{U}}(0) = \frac{\rho_m c}{A} \widehat{\mathbf{U}}(0) \quad \text{and} \quad p_1(x, t) = \Re e[\widehat{\mathbf{p}} e^{j(\omega t - kx)}] \quad (12.1)$$

This result describes a plane wave that propagates down the tube with magnitude,  $|\widehat{\mathbf{p}}|$ , while assuming that thermoviscous dissipation on the tube walls is negligible.

Let’s now calculate this same result in another way. If we consider an interval during which the piston moves between its extreme positions, the piston will sweep out a volume in one-half of a period,  $\delta V = |\widehat{\mathbf{U}}(0)| (T/2) = |\widehat{\mathbf{U}}(0)| / 2f$ , where  $T = f^{-1} = 2\pi/\omega$  is the period of the piston’s oscillations. In that time, the piston can “influence” a volume of the fluid within the tube,  $V = (A\lambda/2) = (AcT/2)$ , since the sound could travel a distance equal to one-half wavelength. Substitution of  $\delta V$  and  $V$  into the adiabatic gas law produces a corresponding  $\delta p$ .

<sup>2</sup> Making the tube infinitely long is just a computational convenience. Any tube long enough that any reflections from the end of the tube return to the region of interest long after the interval of interest would suffice. Alternatively, a tube that had an anechoic termination (e.g., absorbing wedge) or had a matching resistive termination,  $R_{ac} = \rho_m c/A$ , would also behave as though it were infinitely long.

$$pV' = \text{const.} \Rightarrow \frac{\delta p}{p_m} = -\gamma \frac{\delta V}{V} \Rightarrow \delta p = p_1 = -\gamma p_m \frac{\delta V}{V}$$

$$|\hat{\mathbf{p}}| = \left| -\gamma p_m \frac{T}{2} \frac{\hat{\mathbf{U}}(0)}{Ac(T/2)} \right| = \frac{\gamma p_m |\hat{\mathbf{U}}(0)|}{Ac} = \frac{\rho_m c^2}{Ac} |\hat{\mathbf{U}}(0)| = \frac{\rho_m c}{A} |\hat{\mathbf{U}}(0)| \quad (12.2)$$

The result for  $|\hat{\mathbf{p}}|$  is identical to the previous result from Eq. (12.1).

The situation diagrammed in Fig. 12.3 assumes that there is a compact sphere of radius,  $a$ , at the origin of a coordinate system,  $R = 0$ . The radius of that sphere oscillates sinusoidally with a radial displacement magnitude,  $|\xi|$ . The surface area of that sphere is  $4\pi a^2$ , so if  $|\xi| \ll a$ , then when the sphere goes from its equilibrium value,  $a$ , to its maximum radius,  $a + |\xi|$ , it will sweep out a volume change,  $\delta V = 4\pi a^2 |\xi|$ . The time it takes to sweep that volume change is one-quarter of the acoustic period,  $T/4 = (4f)^{-1}$ .

Since the speed of sound is  $c$ , any “disturbance” created by the source during that quarter period can only influence the fluid out to a distance,  $R_{\lambda/4} = c(T/4)$  from the source. Let’s assume we are making a video that starts when the spherical source goes through its equilibrium radius,  $r = a$ , then continues

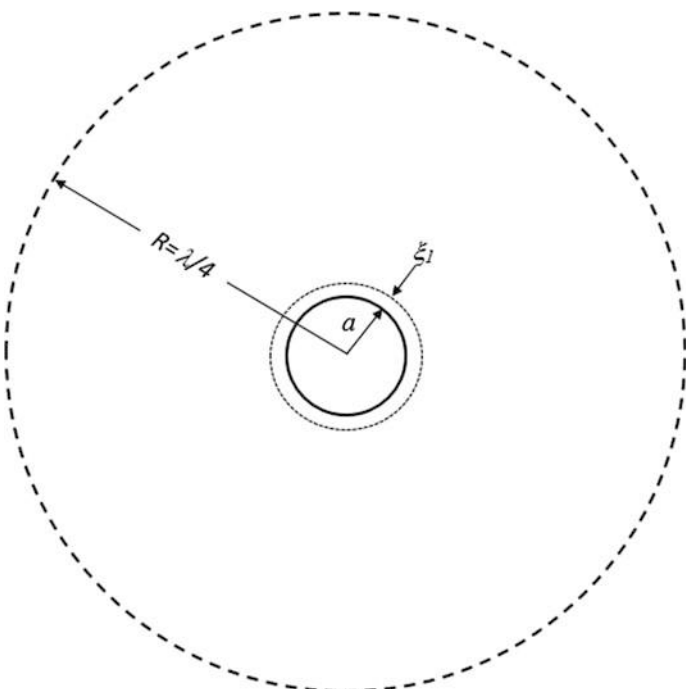


**Fig. 12.3** The “Sphere of Causality.” This diagram represents two concentric spheres. The inner sphere has a radius,  $a$ . That radius oscillates sinusoidally at a frequency,  $f = \omega/2\pi$ , with an amplitude,  $|\xi|$ . The radius of the inner sphere goes from its equilibrium value,  $r = a$ , to its maximum displacement,  $r = a + |\xi|$ , in one-quarter of an acoustic period:  $T/4 = (4f)^{-1}$ . During that time, the effects of that displacement of fluid volume,  $\delta V = 4\pi a^2 |\xi|$ , can only propagate a distance of one-quarter wavelength from the origin,  $R_{\lambda/4} = \lambda/4 = c/4f$ . That distance is the radius of the causality sphere since information carried by sound can only propagate at the speed of sound,  $c$ . The volume enclosed by that “causality sphere,” indicated by the dashed circle in two dimensions, is  $V_{\lambda/4} = (\pi/48)\lambda^3$

expanding for one-quarter of an acoustic period,  $T/4$ . During that time interval, the source changes its volume by  $\delta V = U_1(a)/\omega$ , since the radius is changing sinusoidally with time, pushing fluid out ahead of it. Once again, as in Eq. (12.2), logarithmic differentiation of the adiabatic gas law will relate the average pressure change,  $\langle p_1(R) \rangle_s$ , within the causality sphere of volume,  $V_{\lambda/4} = (4\pi/3)R^3 = (\pi/48)\lambda^3$ , to  $\delta V$ .

$$\frac{\langle p_1 \rangle_s}{p_m} = \gamma \frac{\delta V}{V_{\lambda/4}} \Rightarrow \langle p_1 \rangle_s = \gamma p_m \frac{|\hat{\mathbf{U}}(a)|}{\omega V_{\lambda/4}} = \rho_m c^2 \frac{|\hat{\mathbf{U}}(a)|}{\omega V_{\lambda/4}} \quad (12.3)$$

The final version at the right of Eq. (12.3) again uses the fact that the square of the sound speed in an ideal gas is given by  $c^2 = \gamma p_m / \rho_m$ . We can solve for the average acoustic transfer impedance  $\langle \mathbf{Z}_{\text{tr}} \rangle_s = \langle p_1(R) / U_1(a) \rangle_s$  between the volume velocity at the surface of the source,  $U_1(a)$ , and the average pressure,  $\langle p_1(R) \rangle_s$ , at an observation point just inside the causality sphere at  $R = \lambda/4$ .

$$\langle \mathbf{Z}_{\text{tr}} \rangle_s = \frac{\langle p_1(R) \rangle_s}{U_1(a)} = \frac{6}{\pi^2} \frac{\rho_m c}{R \lambda} \simeq 0.61 \frac{\rho_m c}{R \lambda} \quad (12.4)$$

As we will see when we solve the exact hydrodynamic equations, this approximate result is close to the exact result, which produces a numerical pre-factor for Eq. (12.4) that is 0.50 instead of 0.61.

This result is only approximate since the actual acoustic pressure within the “causality sphere” is a function of the distance from the source. We would have obtained a different result for the numerical pre-factor in Eq. (12.4) had we let the “event” last one-half period so that the source went from its minimum radius,  $a - |\hat{\xi}|$ , to its maximum radius,  $a + |\hat{\xi}|$ . That change in volume,  $\delta V$ , would be doubled, but the volume of the “causality sphere” would have increased by a factor of eight. Under that scenario, the numerical pre-factor in Eq. (12.4) would have decreased from 0.61 to 0.15.

This variability is due to the fact that the pressure within the causality sphere is not uniform. We expect wavelike motion, not simple hydrostatic compression, as assumed by the use of the adiabatic gas law in Eq. (12.2) to produce  $\delta p$ . This was not an issue in the causality calculation for the duct where  $p_1$  was uniform throughout for a traveling wave in one dimension, since the “average” and the amplitude were identical. For the three-dimensional case, acoustic pressure amplitude is a function of distance from the source.

The purpose of such a crude calculation was to demonstrate that the earlier concepts introduced to produce an equation of state, describe sound in lumped-element networks, or for one-dimensional propagation are just as relevant to understanding the process of sound radiation. In the next section, the exact result will be derived when the wave equation is solved exactly for a spherically symmetric wave expanding in three dimensions.

## 12.2 Spherically Diverging Sound Waves

The exact result for the acoustic transfer impedance,  $\mathbf{Z}_{\text{tr}}$ , which provides the acoustic pressure at every remote location,  $p_1(R)$ , in terms of the volume velocity created at the source,  $U_1(a)$ , can be obtained if we solve the wave equation in spherical coordinates. The Euler equation, also expressed in spherical coordinates, can be used to match the radial velocity of the fluid to the radial velocity of the compact spherical source,  $\hat{\mathbf{v}}_r(a)$ , remembering that the representation of the volume velocity of the source as a pulsating sphere is only a mathematical convenience. The result will be applicable to any compact source, independent of its shape.

When the wave equation was derived in Cartesian coordinates in Sect. 10.2, the result was generalized by expressing the wave equation in vector form by introducing the Laplacian operator,  $\nabla^2 = \partial^2/\partial x^2 + \partial^2/\partial y^2 + \partial^2/\partial z^2$ . For the compact source in an unbounded medium, a spherical coordinate system would be appropriate (and convenient) since all directions are equivalent; we expect no variation in the sound field with either polar angle,  $90^\circ \geq \theta \geq -90^\circ$ , or azimuthal angle  $0^\circ \leq \varphi < 360^\circ$ . In spherical coordinates, the Laplacian can be written in terms of  $r$ ,  $\theta$ , and  $\varphi$  [3].

$$\nabla^2 = \frac{1}{r^2} \left[ \frac{\partial}{\partial r} \left( r^2 \frac{\partial}{\partial r} \right) \right] + \frac{1}{r^2 \sin \theta} \frac{\partial}{\partial \theta} \left( \sin \theta \frac{\partial}{\partial \theta} \right) + \frac{1}{r^2 \sin^2 \theta} \frac{\partial^2}{\partial \varphi^2} \quad (12.5)$$

Since the space surrounding our source is assumed to be isotropic, hence spherically symmetric,  $p_1(R)$  does not depend upon  $\theta$  or  $\varphi$ , so derivatives with respect to those variables must vanish. Equation (12.5) can be substituted into the linearized wave equation.

$$\nabla^2 p = \frac{1}{r^2} \left[ \frac{\partial}{\partial r} \left( r^2 \frac{\partial p}{\partial r} \right) \right] = \frac{1}{c^2} \frac{\partial^2 p}{\partial t^2} \quad (12.6)$$

The “product rule” for differentiation can be used to demonstrate that Eq. (12.6) is equivalent to Eq. (12.7).

$$\frac{\partial^2 (rp)}{\partial r^2} = \frac{1}{c^2} \frac{\partial^2 (rp)}{\partial t^2} \quad (12.7)$$

This is just a new single parameter (i.e., quasi-one-dimensional) wave equation that describes the space and time evolution of the product of radial distance from the origin and the acoustic pressure at that distance,  $(rp)$ ; hence the solution to Eq. (12.7) is  $(pr) = \Re e \left[ \hat{\mathbf{C}} e^{j(\omega t \mp kr)} \right]$ , where  $\hat{\mathbf{C}}$  is a constant (phasor) that may be complex to account for any required phase shift and an arbitrary designation of the time we chose to make  $t = 0$ . We will specify that complex (phasor) amplitude,  $\hat{\mathbf{C}}$ , by matching this solution to the volume velocity of the source at its surface,  $r = a$ . The two solutions to Eq. (12.7) correspond to outgoing ( $\omega t - kr$ ) or incoming ( $\omega t + kr$ ) spherical waves, also referred to as divergent and convergent waves, respectively. Since we are considering radiation *from* a sound source in a homogeneous, isotropic, unbounded medium (i.e., no reflections), we will now focus only on the outgoing solution.

$$p_1(r, t) = \Re e \left[ \frac{\hat{\mathbf{C}}}{r} e^{j(\omega t - kr)} \right] \quad (12.8)$$

The magnitude of the acoustic pressure decreases with distance from the source. As will be demonstrated in the derivation of Eq. (12.18), the total radiated power,  $\Pi_{rad}$ , is independent of distance from the source’s acoustic center (i.e., the origin of our spherical coordinate system) if dissipation is ignored.

To match the velocity of the fluid to the velocity of the source at its surface,  $r = a$ , Eq. (12.8) can be substituted into the linearized Euler equation.

$$\rho_m \frac{\partial \vec{v}}{\partial t} = -\vec{\nabla} p \quad (12.9)$$

The gradient operator,  $\vec{\nabla}$ , can also be expressed in spherical coordinates [3].

$$\vec{\nabla} p(r, \theta, \varphi) = \frac{\partial p(r, \theta, \varphi)}{\partial r} \hat{r} + \frac{1}{r} \frac{\partial p(r, \theta, \varphi)}{\partial \theta} \hat{\theta} + \frac{1}{r \sin \theta} \frac{\partial p(r, \theta, \varphi)}{\partial \varphi} \hat{\varphi} \quad (12.10)$$

Again, for our spherically symmetric case,  $p_1(r, t)$  is independent of  $\theta$  and  $\varphi$ , so only the first term on the right-hand side of Eq. (12.10) is required to calculate the radial component of the wave velocity,  $v_r(r, t)$ . The application of the product rule generates two terms.

$$\begin{aligned} \rho_m \frac{\partial v_r}{\partial t} &= -\frac{\partial}{\partial r} \left[ \frac{\hat{\mathbf{C}}}{r} e^{j(\omega t - kr)} \right] \\ &= \frac{\hat{\mathbf{C}}}{r^2} e^{j(\omega t - kr)} + jk \frac{\hat{\mathbf{C}}}{r} e^{j(\omega t - kr)} = \frac{\hat{\mathbf{C}}}{r} e^{j(\omega t - kr)} \left[ \frac{1}{r} + jk \right] \end{aligned} \quad (12.11)$$

Since we have assumed single-frequency harmonic time dependence, the time derivative in Eq. (12.11) can be replaced by  $j\omega$  while recalling that  $c = \omega/k$ .

$$v_r(r, t) = \Re e \left[ \frac{p_1(r, t)}{j\omega \rho_m} \left( \frac{1}{r} + jk \right) \right] = \Re e \left[ \frac{p_1(r, t)}{\rho_m c} \left( 1 + \frac{1}{jkr} \right) \right] \quad (12.12)$$

### 12.2.1 Compact Monopole Radiation Impedance

Equation (12.12) can be rewritten to provide the specific acoustic impedance,  $\mathbf{z}_{sp} = \hat{\mathbf{p}}/\hat{\mathbf{v}}_r$ , for propagation of outgoing (diverging) spherical waves. As with plane waves, the sign of the specific acoustic impedance is reversed for incoming (convergent) spherical waves.

$$\mathbf{z}_{sp} \equiv \frac{\hat{\mathbf{p}}}{\hat{\mathbf{v}}_r} = \frac{\rho_m c}{1 + (1/jkr)} = \rho_m c \frac{(kr)^2}{1 + (kr)^2} + j\rho_m c \frac{kr}{1 + (kr)^2} = \rho_m c \cos \phi e^{j\phi} \quad (12.13)$$

All three versions of Eq. (12.13) are useful, although in different contexts. The rightmost version suggests a geometric interpretation based on Fig. 12.4.

For very large values of  $kr$ , the curvature of the spherical wave fronts is slight, and the wave fronts (locally) are approximately planar. For  $kr = 2\pi r/\lambda \gg 1$ ,  $\mathbf{z}_{sp} = \hat{\mathbf{p}}/\hat{\mathbf{v}}_r \cong \rho_m c$ , for the propagation of outgoing (diverging) spherical waves, as shown by the solid line in Figs. 12.5 and 12.6 that approaches that constant value as  $ka$  increases. The specific acoustic impedance becomes a real number, and the acoustic pressure,  $\hat{\mathbf{p}}$ , and the radial component of the fluid's acoustic particle velocity,  $\hat{\mathbf{v}}_r$ , are very nearly in-phase,  $\phi \cong 0^\circ$ .

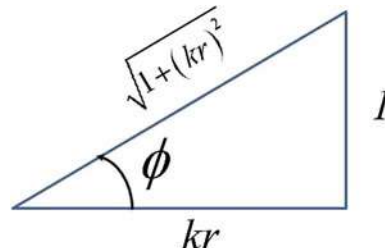


**Fig. 12.4** Geometric interpretation of Eq. (12.13) representing the phase,  $\phi$ , of the (complex) specific acoustic impedance,  $\mathbf{z}_{sp}$ , for an outgoing spherical wave. The phase angle,  $\phi$ , between the acoustic pressure,  $\hat{\mathbf{p}}$ , and the radial component of the acoustic particle velocity,  $\hat{\mathbf{v}}_r$ , is  $\phi = \cot^{-1}(kr)$

**Fig. 12.5** The complex radiation impedance of a monopolar sound source,  $z_{sp}$ , divided by the fluid medium's characteristic impedance,  $\rho_m c$ , from Eq. (12.13). The solid line is the real part of the radiation impedance, and the dashed line is the imaginary part. For small  $ka$ , the slope of the imaginary part is initially proportional to frequency, indicating mass-like behavior of the fluid at the monopole's surface

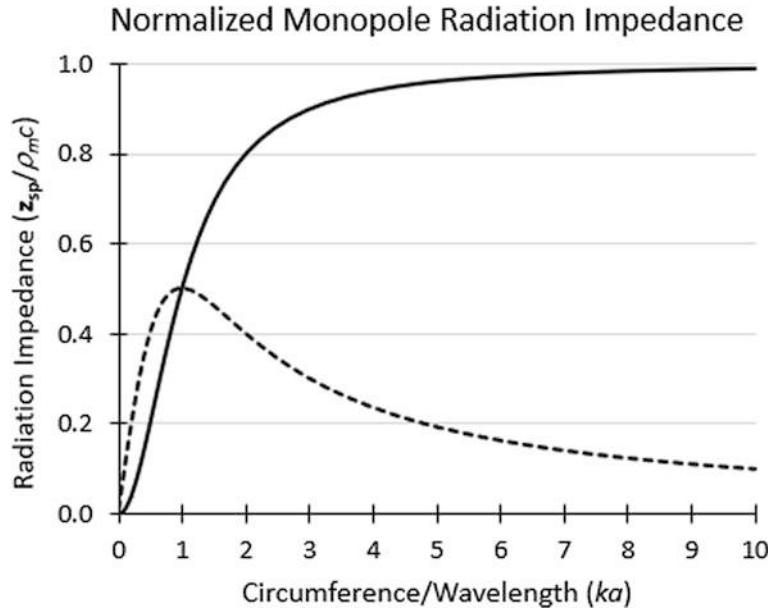
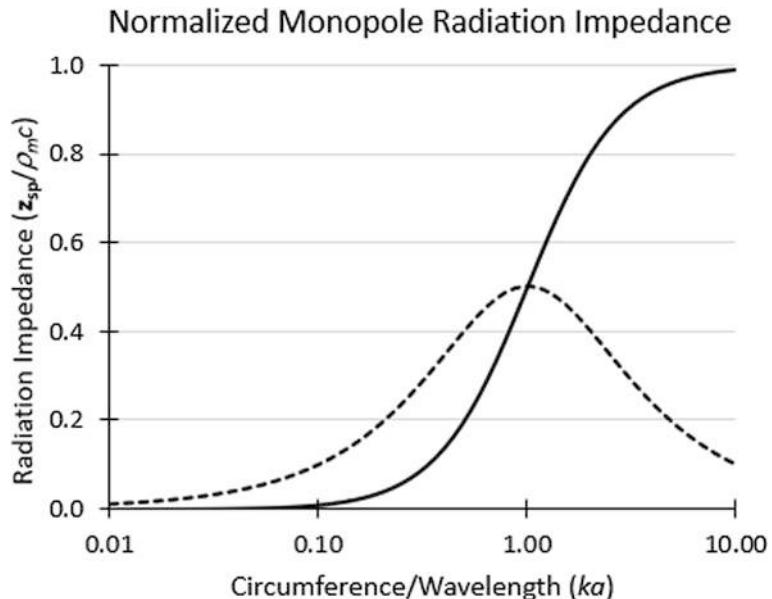


**Fig. 12.6** The complex radiation impedance of a monopolar sound source,  $z_{sp}$ , divided by the fluid medium's characteristic impedance,  $\rho_m c$ , from Eq. (12.13), except that the horizontal axis is now logarithmic. The solid line is the real part of the radiation impedance, and the dashed line is the imaginary part. Plotted this way, the similarity to Fig. 4.25 and Fig. 5.20, for the real and imaginary elastic modulus of a viscoelastic solid, and Fig. 14.3 or Fig. 14.4, for the sound speed and attenuation in  $F_2$ , is apparent



It is instructive to reproduce Fig. 12.5, but with a logarithmic  $ka$  axis as shown in Fig. 12.6. The similarity between the shape of the real and imaginary portions of the radiation impedance and the real and imaginary parts of the elastic modulus in Fig. 4.25 and Fig. 5.20, or the sound speed and attenuation in fluorine gas in Fig. 14.4, is not coincidental. It is a consequence of any linear response theory that is constrained by causality, as specified in the Kramers-Kronig relations of Eqs. (4.77) and (4.78), discussed in Sect. 4.4.4. Just as in those examples, the real and imaginary parts of the radiation impedance are not independent [4].

In the opposite limit, at  $ka = 2\pi a/\lambda \ll 1$ ,<sup>3</sup> on the surface of the radially pulsating source, the specific acoustic impedance is almost purely imaginary, as shown by the dashed line in Figs. 12.5 and 12.6.

$$\lim_{ka \rightarrow 0} [\mathbf{z}_{\text{sp}}(a)] \cong j\rho_m c k a = j\omega \rho_m a \quad (12.14)$$

Recalling our experience with the simple harmonic oscillator, Eq. (12.14) suggests that the fluid surrounding the source is behaving like an *effective mass*. The magnitude of the force,  $|\hat{\mathbf{F}}(a)|$ , acting on the pulsating sphere can be obtained by integrating the pressure,  $\hat{\mathbf{p}}(a)$ , over the surface of the sphere to produce the mechanical reactance,  $x_{\text{rad}}(a) = \Im[\mathbf{Z}_{\text{mech}}(a)]$ , that the pulsating sphere “feels” at its surface.

$$\begin{aligned} \Im[\mathbf{Z}_{\text{mech}}] &= \Im \left[ \frac{\hat{\mathbf{F}}(a)}{\hat{\mathbf{v}}_r(a)} \right] = 4\pi a^2 (\rho_m \omega a) \\ &= \omega \rho_m (4\pi a^3) = 3\omega \rho_m \left( \frac{4\pi}{3} a^3 \right) \quad \text{for } ka \ll 1 \end{aligned} \quad (12.15)$$

The volume of the spherical source is  $V = (4\pi/3)a^3$ , so the effective (inertial) *hydrodynamic mass* of the fluid surrounding the spherical source is equal to three times the mass of the fluid displaced by the source radiating sound in the small  $ka$  limit.

This is critical for the design of sound sources that operate in dense fluids (i.e., liquids rather than gases) since the source has to provide sufficient power to accelerate and decelerate the surrounding fluid as it pulsates. We generally represent this load as a *radiation reactance*,  $x_{\text{rad}}$ . As will be discussed shortly, in Sect. 12.3, for a spherical gas bubble in a liquid, this effective mass is the dominant source of inertia for simple harmonic bubble oscillations.

Although the largest component of the specific acoustic impedance at the surface of the sphere is imaginary (i.e., mass reactance), the real (i.e., resistive) component must be non-zero, because radiation of sound is the mechanism by which energy from the source is propagated into the surrounding fluid. The second version of  $\mathbf{z}_{\text{sp}}$  in Eq. (12.13) is useful here since it provides the real and imaginary contributions individually.

$$\Re \left\{ \lim_{ka \rightarrow 0} [\mathbf{z}_{\text{sp}}(a)] \right\} \equiv r_{\text{rad}} \cong \rho_m c (ka)^2 \quad (12.16)$$

It is worthwhile pointing out that real impedances are commonly associated with dissipative processes that convert acoustical or vibrational energy to heat. In the case of radiation, power is removed from the source, but our calculations have been lossless (i.e., we have been using the Euler equation, not the Navier-Stokes equation). The real component of the radiation impedance is an “accounting loss” rather than an irreversible increase in entropy. For radiation, the energy propagates away; it is not absorbed, it is expelled.

The total, time-averaged radiated acoustic power,  $\langle \Pi_{\text{rad}} \rangle_t$ , is the rate at which the source does “ $p*dV$ ” work on the surrounding fluid for the in-phase components of the acoustic pressure,  $\hat{\mathbf{p}}(a)$ , and the (radial) acoustic particle velocity,  $\hat{\mathbf{v}}_r(a)$ , at the source’s surface.

---

<sup>3</sup> A convenient way to express the compactness criterion,  $ka \ll 1$ , for a compact spherical source is to say that the equatorial circumference of the source,  $2\pi a$ , is much less than the wavelength:  $2\pi a \ll \lambda$ .

$$\begin{aligned}\langle \Pi_{rad} \rangle_t &= \frac{1}{T} \int_0^T \widehat{\mathbf{F}}(a) \cdot \widehat{\mathbf{v}}_r(a) dt dS = \frac{1}{T} \int_0^T |\widehat{\mathbf{p}}(a)| \left| \frac{dV(a)}{dt} \right| \cos \phi dt \\ &= \frac{1}{T} \int_0^T |\widehat{\mathbf{p}}(a)| |\widehat{\mathbf{U}}(a)| \cos \phi dt\end{aligned}\quad (12.17)$$

The component of  $\widehat{\mathbf{p}}(a)$  that is in-phase with  $\widehat{\mathbf{v}}_r(a)$  can be expressed in terms of the radiation resistance,  $r_{rad}$ , which is the real part of the specific acoustic impedance,  $\mathbf{z}_{sp}(a)$ , on the surface of the sphere. Since  $\Re[\widehat{\mathbf{p}}(a)] = r_{rad}|\widehat{\mathbf{v}}_r(a)|$  and  $|\widehat{\mathbf{U}}(a)| = 4\pi a^2 |\widehat{\mathbf{v}}_r(a)|$ , we can express Eq. (12.17) in terms of  $r_{rad}$  and  $\widehat{\mathbf{v}}_r(a)$ .

Using the expression for  $r_{rad}$  in Eq. (12.16) and expressing  $\widehat{\mathbf{v}}_r(a)$  in terms of the magnitude of the source strength,  $|\widehat{\mathbf{U}}(a)|$ , provide a compact expression for the time-averaged power,  $\langle \Pi_{rad} \rangle_t$ , radiated from the source based on the real component of the specific acoustic impedance at the source's surface,  $\Re[\mathbf{z}_{sp}(a)] \equiv r_{rad}$ .

$$\langle \Pi_{rad} \rangle_t = \frac{\pi}{2} \frac{\rho_m c}{\lambda^2} |\widehat{\mathbf{U}}(a)|^2 = \frac{\pi}{2} \frac{\rho_m}{c} f^2 |\widehat{\mathbf{U}}(a)|^2 \quad (12.18)$$

The right-hand version of this result demonstrates why it is more difficult to radiate low frequencies. Either the velocity of the surface needs to be increased, which frequently causes distortion, or the loudspeaker's area must be increased, assuming that  $(ka)^2 \ll 1$ . This is why the enclosures for reproduction of bass utilize loudspeakers of large diameter to provide adequate source strength,  $|\widehat{\mathbf{U}}(a)|$ , as suggested in Fig. 12.1.

### 12.2.2 Compact Monopole Acoustic Transfer Impedance

To determine the amplitude constant,  $\widehat{\mathbf{C}}$ , in Eq. (12.8), we can consider our pulsating sphere of mean radius,  $a$ , and radial velocity,  $\widehat{\mathbf{v}}_r(a) = j\omega \widehat{\xi}$ , and evaluate Eq. (12.12) at  $r = a$ .

$$v_r(a, t) = \Re[e^{j\omega t}] = \Re\left[\frac{\widehat{\mathbf{C}}}{a\rho_m c} e^{j(\omega t - ka)} \left(1 + \frac{1}{jka}\right)\right] \quad (12.19)$$

The compactness requirement guarantees that  $ka \ll 1$ , so  $e^{-jka} \cong 1$  and  $[1 + (1/jka)] \cong (1/jka)$ . Substituting these *near-field* limits into Eq. (12.19), along with the fact that  $|\widehat{\mathbf{U}}(a)| = 4\pi a^2 |\widehat{\mathbf{v}}_r(a)|$ , uniquely determines the complex (phasor) pressure amplitude constant,  $\widehat{\mathbf{C}}$ .

$$\widehat{\mathbf{C}} = \omega \rho_m c \widehat{\xi} k a^2 = \frac{\rho_m c k}{4\pi} |\widehat{\mathbf{U}}(a)| \quad (12.20)$$

Substitution of  $\widehat{\mathbf{C}}$  back into Eq. (12.8) provides the exact solution for the acoustic pressure,  $p_1(r, t)$ , in terms of the magnitude of the source's volume velocity,  $|\widehat{\mathbf{U}}(a)|$ , and the wavelength of sound,  $\lambda = (2\pi/k)$ .

$$p_1(r, t) = \frac{\rho_m c k}{4\pi r} |\widehat{\mathbf{U}}(a)| \Re[e^{j(\omega t - kr)}] = \frac{\rho_m c}{2r\lambda} |\widehat{\mathbf{U}}(a)| \Re[e^{j(\omega t - kr)}] \quad (12.21)$$

The exact solution for the acoustic transfer impedance,  $\mathbf{Z}_{\text{tr}}$ , can be calculated from Eq. (12.21), providing the solution to this steady-state radiation problem.

$$|\mathbf{Z}_{\text{tr}}| \equiv \left| \frac{\widehat{\mathbf{p}}(R)}{\widehat{\mathbf{U}}(a)} \right| = \frac{\rho_m c}{2R\lambda} = 0.50 \frac{\rho_m c}{R\lambda} \quad (12.22)$$

This result compares closely to the “causality sphere” approximation of Eq. (12.4) that was based on the adiabatic gas law but ignored the wavelike variation in pressure with position that is expressed exactly in Eq. (12.8).

The acoustic transfer impedance will now let us express the acoustic pressure,  $\widehat{\mathbf{p}}(R)$ , at some remote point in the far field ( $kR \gg 1$ ), a distance,  $R$ , from the sound source’s acoustic center,  $R = 0$ . This compact sound source of source strength,  $|U_1(a)|$ , radiates sound with a wavelength,  $\lambda = c/f = 2\pi c/\omega$ . At that location in the far field, we can assume that  $\widehat{\mathbf{p}}(R)$  is in-phase with  $\widehat{\mathbf{v}}_r(R)$ , based on Eq. (12.13), and that their ratio is given by the progressive plane wave value of the characteristic impedance  $\mathbf{z}_{\text{sp}}(R) = \rho_m c$ . This simplifies the calculation of the far-field time-averaged intensity of the sound,  $\langle \vec{I}(R) \rangle_t$ , using Eq. (10.36).

$$\begin{aligned} \langle \vec{I}(R) \rangle_t &= (\tfrac{1}{2}) \Re e [\widehat{\mathbf{p}}(R) \widehat{\mathbf{v}}_r^*(R)] = \frac{|\widehat{\mathbf{p}}(R)|^2}{2\rho_m c} \\ &= \frac{1}{2\rho_m c} \left( \frac{\rho_m c}{2R\lambda} |\widehat{\mathbf{U}}(a)| \right)^2 = \frac{\rho_m c}{8R^2\lambda^2} |\widehat{\mathbf{U}}(a)|^2 \end{aligned} \quad (12.23)$$

The time-averaged acoustic intensity is inversely proportional to the square of the distance from the sound source, but the time-averaged total radiated power,  $\langle \Pi_{\text{rad}} \rangle_t$ , is independent of distance, since all forms of dissipation have been neglected.

$$\langle \Pi_{\text{rad}} \rangle_t = 4\pi R^2 \langle I(R) \rangle_t = \frac{\pi}{2} \frac{\rho_m c}{\lambda^2} |\widehat{\mathbf{U}}(a)|^2 \quad (12.24)$$

Of course, in the absence of any dissipation in the surrounding fluid, this is the same radiated power we calculated “locally” by using the radiation resistance “felt” by the source,  $r_{\text{rad}}(a)$ , on its surface (i.e., in the near field), expressed in Eq. (12.18).

### 12.2.3 General Multipole Expansion\*

Since the monopole is such a significant concept for our understanding of radiation and scattering, it is worthwhile to review the assumptions and processes that led to the results of Eqs. (12.13), (12.15), (12.18), (12.19), (12.21), (12.22), and (12.23). Fundamentally, the three-dimensional problem of Eq. (12.5) was transformed to the quasi-one-dimensional problem of Eq. (12.6) based on a claim of spherical symmetry (i.e., isotropy) and the assertion that the shape of the pulsating source of volume velocity was irrelevant (and unknowable based on the far-field radiation pattern),<sup>1</sup> so that only the source strength,  $|\widehat{\mathbf{U}}(a)|$ , was significant for determination of the radiated sound field.

That assertion of source-shape independence was not proven, since it would be necessary to solve the full three-dimensional problem, then determine under what circumstances the higher-order multipolar contributions are negligible. The solution to the full three-dimensional problem, using the Laplacian of Eq. (12.5) in the wave equation, is a product of spherical Bessel functions,  $j_n(kr)$ , and the associated Legendre polynomials,  $P_l^m(\cos \theta)$ .

$$p(r, \theta, \vartheta; t) = \Re e \left[ \sum \widehat{\mathbf{C}}_{n,m,l} e^{j\omega t} j_n(kr) \sqrt{\frac{2l+1}{2\pi} \frac{(l-m)!}{(l+m)!}} P_l^m(\cos \theta) \begin{Bmatrix} \cos(m\varphi) \\ \sin(m\varphi) \end{Bmatrix} \right] \quad (12.25)$$

The constants,  $\widehat{\mathbf{C}}_{n,m,l}$ , are determined in the same way as we determined  $\widehat{\mathbf{C}}$  in Eq. (12.8); by matching the velocity components of the wave (using Euler's equation) to the velocity distribution on the surface of the source. The complete set of functions provided in the infinite summation of Eq. (12.25) can be fit to a source of any shape where the various parts of the surface are moving in any direction and with any relative phase, although the result is still restricted to a single frequency [5]. Our solution of Eq. (12.8) corresponds to the spherically symmetric  $n = 0$  spherical Bessel function,  $j_0(kr) = \sin(kr)/(kr)$ , which forces  $m = l = 0$ , so that there is no angular dependence.<sup>4</sup>

Our analysis, based on a compact spherical source, produced results that are applicable to sound sources that have no resemblance to a sphere, for example, a circular piston executing simple harmonic oscillations mounted in an enclosure that is a rectangular parallelepiped or the body of a dog (e.g., Fig. 12.2). The results obtained only depend upon specification of the source strength,  $|\widehat{\mathbf{U}}(a)|$ , and our ability to enclose the source within a spherical shell having a circumference much less than the wavelength (i.e.,  $ka \ll 1$ ) that is pulsating with a complex radial oscillation amplitude,  $\hat{\xi}$ , making the source strength magnitude,  $|\widehat{\mathbf{U}}(a)| = 4\pi a^2 \omega |\hat{\xi}|$ .

After using hydrodynamic mass to calculate the resonance frequency of a bubble in the next section, we will continue to avoid dealing with the complete mathematical solution of Eq. (12.25) by using the principle of superposition to sum the acoustic fields of simple monopole sources. This will facilitate calculation of the behavior of more complex sources that lack spherical symmetry and produce a significant angular dependence of their radiated sound fields.

## 12.3 Bubble Resonance

Having calculated the hydrodynamic mass associated with the radial oscillations of a compact spherical source in Eq. (12.15), this concept can be applied to an interesting and important lumped-element fluidic resonator for which the hydrodynamic mass makes the entire inertial contribution. A gas bubble in a liquid will have an equilibrium radius,  $a$ , that is determined by the competition between the surface tension that will cause the bubble to collapse and the gas pressure inside the bubble that will resist the external force of the liquid pressure and of the surface tension.

The static pressure difference,  $p_{in} - p_{out}$ , across a curved interface is given by *Laplace's formula* that can be expressed in terms of the principle radii of curvature and the surface tension,  $\alpha$  [6].

$$p_{in} - p_{out} = \alpha \left( \frac{1}{R_1} + \frac{1}{R_2} \right) \quad (12.26)$$

For a spherical bubble,  $R_1 = R_2 = a$ , where  $a$  is the radius of the bubble, so the pressure difference caused by the surface tension is  $2\alpha/a$ . If the gas inside the bubble is the vapor of the surrounding liquid, then there will be a minimum bubble radius,  $R_{min}$ , determined when the vapor pressure and Laplace

<sup>4</sup> Solutions to the full three-dimensional wave equation are available in most textbooks on advanced engineering mathematics or mathematical physics. This version was taken from E. Butkov, *Mathematical Physics* (Addison-Wesley, 1968).

pressures are equal. In the case where  $a < R_{min}$ , the bubble is unstable and will collapse by squeezing the vapor back into the liquid state.

For a “clean” air-water interface at 20 °C, the surface tension,  $\alpha = 72.5 \times 10^{-3}$  N/m, and  $P_{vap} = 2.3$  kPa, so  $R_{min} = 0.063$  mm = 63 µm. As we will see, our interests are concentrated on larger bubbles, many of which may contain a non-condensable gas (e.g., air) that stabilizes the bubbles against collapse.

The gas pressure,  $p_{in}$ , within a stable bubble surrounded by water, is usually determined by the depth of the bubble below the water’s surface. Since  $p_{in} = p_o + \rho_m g z$ , where  $p_o$  is atmospheric pressure,  $g$  is the acceleration due to gravity,  $\rho_m$  is the mass density of the water (not the gas!), and  $z$  is the distance below the free surface, as discussed in Sect. 8.3. If the mean radius of the bubble,  $a$ , is displaced from equilibrium by an amount,  $|\hat{\xi}|$ , while maintaining its spherical shape, the excess force,  $\delta F(\hat{\xi})$ , that the pressure applies to the bubble’s surface can be determined from the adiabatic gas law, if we assume that  $a > \delta_\kappa$ , so the compressions and expansions are nearly adiabatic, again using Eq. (12.2).

$$\delta p_{in} = -\gamma p_{in} \frac{\delta V}{V} = -\gamma p_{in} \frac{4\pi a^2 |\hat{\xi}|}{\left(\frac{4\pi}{3}\right)a^3} = -3\gamma p_{in} \frac{|\hat{\xi}|}{a} \quad (12.27)$$

Integrated over the surface area of the bubble, this excess pressure,  $\delta p_{in} = |\hat{\mathbf{p}}|$ , produces an excess force,  $\delta F(\hat{\xi})$ , which is proportional to the amplitude of the oscillatory change in radius,  $\hat{\xi}$ , and motivates an expression that is equivalent to Hooke’s law:

$$\delta F = (4\pi a^2) \delta p_{in} = -12\pi a \gamma p_{in} |\hat{\xi}| \quad \Rightarrow \quad K_{eff} = 12\pi a \gamma p_{in} \quad (12.28)$$

The minus signs in Eqs. (12.27) and (12.28) arise because the pressure increases when  $|\hat{\xi}|$  decreases. By analogy with Hooke’s law, the effective stiffness constant,  $K_{eff}$ , is just the magnitude of the coefficient of such displacements,  $\hat{\xi}$ .

The only inertial mass of any significance is the hydrodynamic mass,  $m_{eff}$ , of the fluid that must accelerate in and out radially as the bubble’s radius changes. This hydrodynamic mass can be calculated using Eq. (12.15).

$$m_{eff} = 3\rho_m V = 4\pi a^3 \rho_m \quad (12.29)$$

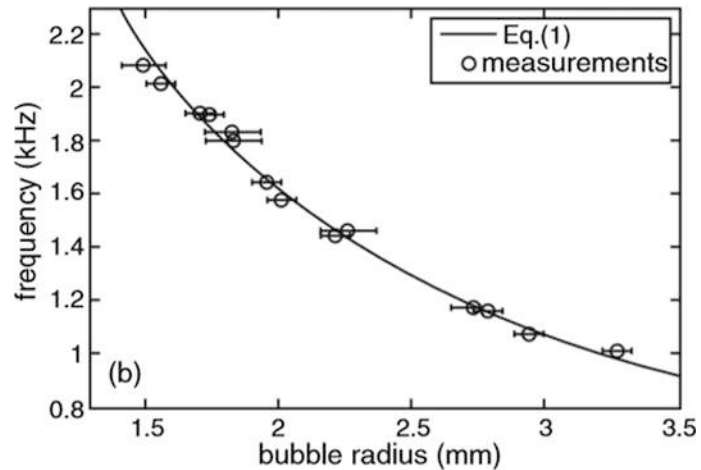
That effective mass can be combined with the effective gas stiffness of Eq. (12.28) to create a simple harmonic oscillator with a resonance frequency,  $f_o = \omega_o/2\pi$ .

$$\omega_o = \sqrt{\frac{K_{eff}}{m_{eff}}} = \frac{1}{a} \sqrt{\frac{3\gamma p_{in}}{\rho_m}} \quad (12.30)$$

Here, it is important to remind ourselves that  $p_{in}$  is the gas pressure but  $\rho_m$  is the density of the surrounding water. If the restoring force due to surface tension is included, Eq. (12.30) can be modified to incorporate that additional restoring force (stiffness) [7].

$$\omega_o = \frac{1}{a\sqrt{\rho_m}} \sqrt{3\gamma p_{in} - \frac{2\alpha}{a}} \quad (12.31)$$

**Fig. 12.7** Resonance frequencies of millimeter-sized bubbles whose resonance frequency was measured acoustically in a desktop aquarium [9]. At a frequency of 1.5 kHz,  $\delta_k = 68 \mu\text{m} \ll a$ , placing these measurements well within the adiabatic limit (see Fig. 12.9). The solid line represents the full theory of Commander and Prosperetti [10], which is very nearly the same as the Minnaert theory from Eq. (12.30) in this limit



Although the addition of the surface tension appears to decrease the resonance frequency in Eq. (12.31), the surface tension increases the frequency since  $p_{in}$  also would now include the Laplace pressure of Eq. (12.26). In applying either Eq. (12.30) or Eq. (12.31) to evaluate  $\omega_o$ , it is important to remember that  $p_{in}$  is the pressure of the gas inside the bubble, with  $\gamma$  being determined by the gas, but  $\rho_m$  is the density of the surrounding fluid since it is the dominant source of inertance (i.e., kinetic energy storage).

Equations (12.30) and (12.31) were first derived by Minnaert in 1933 [7]. Although his frequency was calculated under adiabatic conditions for spherical bubbles, Strasberg has shown that even for spheroidal bubbles with a ratio of major-to-minor axes of a factor of two, the oscillation frequency differs from the Minnaert result by only 2%<sup>5</sup> [8]. Figure 12.7 shows some recent table-top laboratory measurements of bubble resonance frequencies vs. bubble radius which agree with Eq. (12.30) to within experimental error [9].

### 12.3.1 Damping of Bubble Oscillations

The damping of the bubble resonances is a consequence of losses due to radiation and due to boundary layer thermal relaxation at the air-water interface (as it was for the spherical compliance of a Helmholtz resonator calculated in Sect. 9.4.4). The reciprocal of the quality factor that characterizes each of these dissipative effects can then be summed, as in Eq. (9.40) or Eqs. (10.58) and (10.61), to determine  $Q_{total}$  in the adiabatic limit where  $a \gg \delta_k$ .

$$\frac{1}{Q_{total}} = \frac{1}{Q_{th}} + \frac{1}{Q_{rad}} \quad (12.32)$$

Using Eq. (9.38), the time-averaged power dissipation per unit area due to thermal relaxation,  $\dot{e}_{th}$ , is quadratic in the amplitude of the oscillating pressure within the bubble,  $|\hat{p}|^2$ , and the total, time-averaged power dissipation,  $\langle \Pi_{th} \rangle_t$ , will be  $\dot{e}_{th}$  times the surface area of the bubble.

<sup>5</sup>This insensitivity of resonance frequency to shape is a consequence of adiabatic invariance as demonstrated in the discussion of enclosures that cannot be modeled by separable coordinate systems, in Sect. 13.3.5.

$$\dot{e}_{th} = \frac{\gamma - 1}{4\gamma} \frac{|\hat{\mathbf{p}}|^2}{p_m} \omega \delta_\kappa \quad \Rightarrow \quad \langle \Pi_{th} \rangle_t = 4\pi a^2 \dot{e}_{th} = \frac{\gamma - 1}{\gamma} \pi a^2 \omega \delta_\kappa \frac{|\hat{\mathbf{p}}|^2}{p_m} \quad (12.33)$$

The total energy stored in the bubble oscillation is equal to the maximum potential energy density,  $(P.E./Vol.)_{max}$ , times the volume of the bubble,  $(4\pi/3)a^3$ . The potential energy density was calculated in Eq. (10.35).

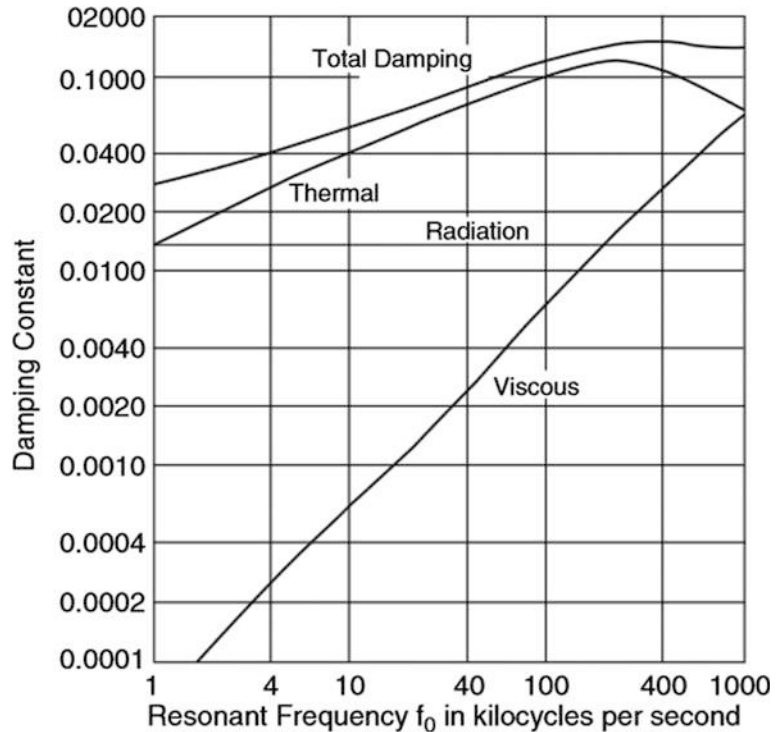
$$\left(\frac{P.E.}{V}\right)_{max} = \frac{1}{2} \frac{|\hat{\mathbf{p}}|^2}{\rho_m c^2} = \frac{1}{2} \frac{|\hat{\mathbf{p}}|^2}{\gamma p_{in}} \quad \Rightarrow \quad E_{stored} = \frac{2\pi a^3}{3} \frac{|\hat{\mathbf{p}}|^2}{\gamma p_{in}} \quad (12.34)$$

The quality factor due to thermal relaxation losses on at the spherical gas-water interface can be expressed using Eq. (B.2).

$$Q_{th} = \frac{\omega E_{stored}}{\langle \Pi_{th} \rangle_t} = \frac{2}{3(\gamma - 1)} \frac{a}{\delta_\kappa} \quad \text{for } a > \delta_\kappa \quad (12.35)$$

Note that this result is identical to the result for  $Q_{th}$  calculated for thermal relaxation loss on the surface of the spherical volume with radius,  $R$ , of a Helmholtz resonator in Eq. (9.48). From Eq. (9.14),  $\delta_\kappa = \sqrt{2\kappa/\rho_m c_P \omega}$ , so  $\delta_\kappa$  is proportional to  $\omega^{-1/2}$ . From Eq. (12.30),  $a$  is proportional to  $\omega^{-1}$ , so the thermal quality factor,  $Q_{th}$ , is proportional to  $\omega^{-1/2}$ . In the adiabatic limit, the thermal damping, which is proportional to the reciprocal of the  $Q_{th}$ , increases with the square root of frequency, as shown in Fig. 12.8.

**Fig. 12.8** The damping constant for an air-filled bubble in water that is shown on the vertical axis is the reciprocal of the quality factors of Eqs. (12.35) and (12.37). The observed peak in the thermal damping and in the total damping occurs where the behavior of the gas inside the bubble is transitioning between adiabatic at lower frequencies to isothermal at higher frequencies. This is shown explicitly in Fig. 12.9. The viscous damping, unimportant below 500 kHz, is due to shear stresses at the air-water interface [11].



The time-averaged power lost to acoustic radiation is given by Eqs. (12.18) and (12.24). The bubble's source strength,  $|\hat{\mathbf{U}}(a)|$ , is related to the internal gas pressure oscillation amplitude,  $|\hat{\mathbf{p}}|$ , by the adiabatic gas law in the form that appears in Eq. (12.2).

$$|\hat{\mathbf{p}}| = (\gamma p_{in}) \frac{\delta V}{V} = (\gamma p_{in}) \frac{|\hat{\mathbf{U}}(a)|}{\omega V} \Rightarrow |\hat{\mathbf{U}}(a)| = \frac{\omega V}{\gamma p_{in}} |\hat{\mathbf{p}}| \quad (12.36)$$

Substitution of Eq. (12.36) into the expression for quality factor used in Eq. (12.35) determines the quality factor due to the power radiated by the bubble,  $Q_{rad}$ . This reduces to another even simpler form after various substitutions.

$$Q_{rad} = \frac{\omega E_{stored}}{\Pi_{rad}} = c_{H_2O} \sqrt{\frac{3\rho_{H_2O}}{\gamma p_{in}}} \quad (12.37)$$

The radiation quality factor,  $Q_{rad}$ , as well as its reciprocal, corresponding to the radiative loss, is frequency independent, so by Eq. (12.30), it is also independent of the resonant bubble's radius. This behavior is illustrated in Fig. 12.8, taken from Devin [11].

The peak in the dissipation due to thermal relaxation on the air-water interface visible in Fig. 12.8 corresponds to the behavior of the gas changing over from adiabatic for larger bubbles at lower resonance frequencies to isothermal for smaller bubbles at higher frequencies. Such behavior is characteristic of a single relaxation time process like that shown in Fig. 4.25. This adiabatic-to-isothermal transition is shown explicitly in Fig. 12.9, also from Devin [11], which plots the thermal damping and the gas stiffness as a function of the ratio of the bubble's diameter,  $2a$ , to the thermal penetration depth,  $\delta_k$ .

To develop some appreciation for these results, consider an air-filled bubble with a diameter of 1.0 mm ( $a = 5 \times 10^{-4}$  m) that is located 10 meters below the surface of the water, so that  $p_{in} = 1.0$  MPa. Since  $3\gamma p_{in} \cong 4.2$  MPa  $\gg 2\alpha/a = 290$  Pa, Eq. (12.30) can be used to calculate the Minnaert frequency,

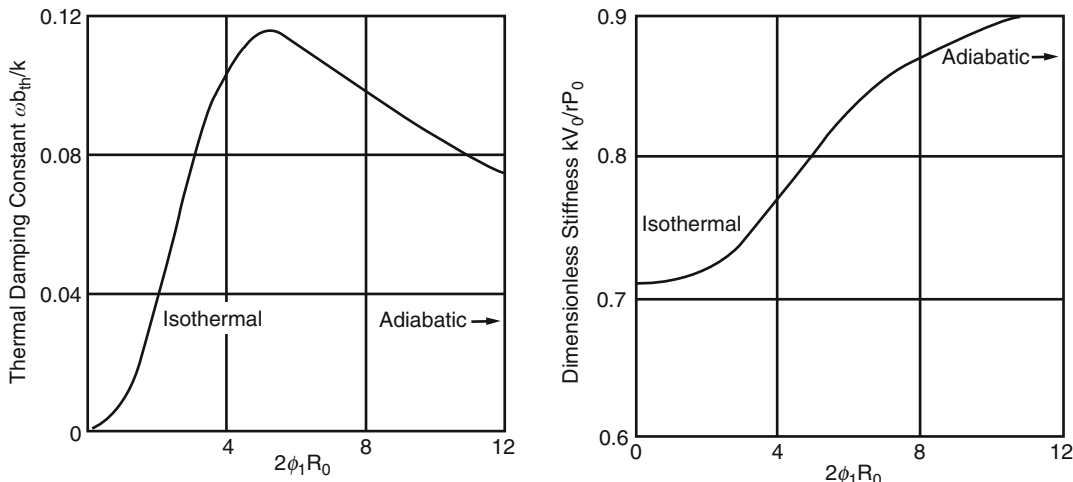


**Fig. 12.9** (Left) The thermal damping factor is plotted as a function of the ratio of bubble diameter,  $2a$ , to the thermal penetration depth,  $\delta_k$ :  $2\phi_1 = 2/\delta_k$ , or  $2\phi_1 R_o = 2a/\delta_k$ . The damping has its peak at about  $a \cong (\delta_k/2)$ . (Right) The transition of the stiffness of the gas within the bubble from adiabatic behavior for large bubbles to isothermal for small bubbles is also plotted in terms of  $2\phi_1 R_o = 2a/\delta_k$  [11]

$f_o = \omega_o/2\pi = 20.6$  kHz. At that frequency, the thermal penetration depth in air,  $\delta_\kappa$ , is 5.9 microns. Using Eq. (12.35),  $Q_{th} = 144$ , and using Eq. (12.37),  $Q_{rad} = 70$ , making  $Q_{total} = 47$ .

## 12.4 Two In-Phase Monopoles

Armed with our understanding of the radiation from a compact source (monopole) in an unbounded homogeneous isotropic fluid medium, we can begin our investigation of more complex radiators, like the line arrays filling the stage in Fig. 12.1 and the piston source (woofer) of Fig. 12.2. We will start by consideration of just two monopole sources that are oscillating in-phase,<sup>6</sup> with equal amplitudes, at some frequency,  $f = \omega/2\pi$ , which have their acoustic centers separated by a distance,  $d$ , as shown in Fig. 12.10.

To calculate the radiated sound field of that pair of in-phase sources (sometime called a *bipole*), we will use the principle of superposition to combine the pressures produced by the two monopoles that are treated individually. There is an interesting philosophical point implicit in that approach, since the behavior of the individual monopoles was predicated on their radiation pattern being spherically symmetric. Clearly that symmetry has been broken for the case of two compact sources radiating simultaneously. The reason that we can use the superposition of spherically symmetric sources to produce a non-spherically symmetric radiation pattern is (again) the fact that we are restricting ourselves to “linear acoustics.”

We are assuming that the radiation from one source does not change either the properties of the medium or the radiation behavior of the other source. There are cases where this assumption is violated, sometimes with disastrous consequences [12]. The understanding of the inter-element interactions in high-amplitude SONAR array applications became important in the late 1950s when

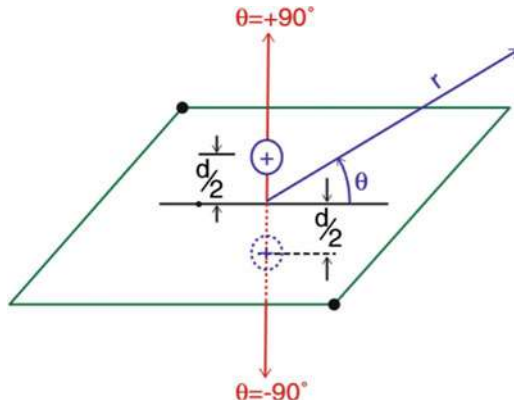


**Fig. 12.10** Two compact (monopole) sound sources separated by a distance,  $d$ , that are radiating in-phase (as indicated by their “+” signs). The line through their centers (red) defines a unique direction. The plane (green) is the perpendicular bisector of the line joining the centers of the two sources. The vector,  $\vec{r}$  (blue), is the distance from the intersection of the line and plane to an observation point that makes an angle,  $\theta$ , with that symmetry plane. Due to the rotational symmetry about the line, the radiated sound field is independent of the azimuthal angle,  $\varphi$ .

<sup>6</sup> It is probably worthwhile mentioning that a requirement for the existence of a constant phase relationship between two oscillators is that they must be oscillating at the same frequency. If they were oscillating at different frequencies, their relative phases would be changing linearly with time.

high-powered search SONAR arrays were developed using the then newly available lead-zirconate-titanate piezoelectric ceramic materials [13, 14].

We will restrict ourselves to the case where superposition is valid and add the pressure fields of the two monopole sources. Before calculating the pressure field by this method, we can examine a few simple cases. If the separation of the two sources is much closer than a wavelength,  $d \ll \lambda$ , then we have essentially doubled the source strength, and our expression for the acoustic transfer impedance of a monopole in Eq. (12.22) tells us that we have doubled the acoustic pressure and quadrupled the radiated acoustic power, based on Eq. (12.18) or Eq. (12.24).

If the separation of the two sources is exactly one-half wavelength,  $d = \lambda/2$ , then when the sound produced by the first source reaches the location of the second source, the two sources will be radiating  $180^\circ$  out-of-phase. Along the direction of the line joining the two sources, known by those who specialize in array design as the *end-fire direction* ( $\theta = \pm 90^\circ$ ), the radiated pressure will be zero if the strengths of the two individual monopole sources are identical. Along the equatorial plane ( $\theta = 0^\circ$ ), shown in Fig. 12.10, the distance to either source is identical so the pressure on that plane is doubled. Those who specialize in array design call the direction defined by that plane as the *broadside direction*.

To calculate the sound field of the dipole produced at any observation point a distance,  $|\vec{r}|$ , from the midpoint of the line joining the sources at an angle,  $\theta$ , above the equatorial plane, as shown in Figs. 12.10 and 12.11, we can simply sum the spherically symmetric radiation produced by the individual sources, given by Eq. (12.21), paying particular attention to their relative phases in the far field.

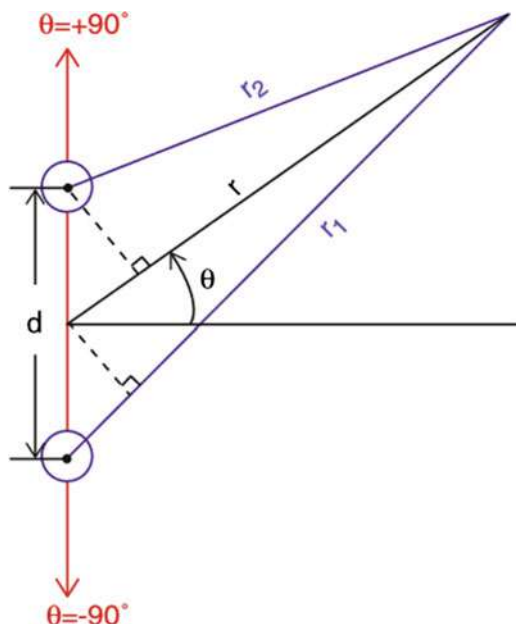


**Fig. 12.11** Coordinate system for superposition of the two in-phase compact sources separated by a distance,  $d$ . The distance from the center of the two sources to the observation point is indicated by  $\vec{r}$ , which makes an angle,  $\theta$ , with the plane that is the perpendicular bisector of the line joining the two sources. The distance from the upper source is  $r_2$ , and the distance from the lower source is  $r_1$ . The dashed perpendicular lines show the difference in path lengths between the two sources and the vector  $\vec{r}$ . In this diagram, the upper sources are closer than  $r$  by a distance,  $\Delta r_2 \cong (d/2) \sin \theta$ . The lower source is farther by a distance,  $\Delta r_1 \cong (d/2) \sin \theta$

$$p(|\vec{r}|, \theta; t) = \Re e \left[ \frac{|\hat{\mathbf{C}}_1|}{|\vec{r}_1|} e^{j(\omega t - k_1 |\vec{r}_1| + \phi)} + \frac{|\hat{\mathbf{C}}_2|}{|\vec{r}_2|} e^{j(\omega t - k_2 |\vec{r}_2| - \phi_2)} \right] \quad (12.38)$$

For the dipole, we can let  $\phi_1 = \phi_2 = 0$ , since the sources are in-phase and let  $k_1 = k_2 = k = \omega/c$ , since the only way they can maintain a fixed phase relation is if they have the same frequency,  $\omega_1 = \omega_2 = \omega$ . We are assuming the source strengths are identical, having included their relative phases explicitly allowing their amplitudes to be represented by a scalar,  $C = |\hat{\mathbf{C}}_1| = |\hat{\mathbf{C}}_2| = \rho_m c k |\hat{\mathbf{U}}(a)| / 4\pi$ , according to Eq. (12.20).

The two distances between the observation point and the individual sources can be expressed in terms of the path length differences,  $\Delta r$ , that are indicated in Fig. 12.10 by the lines to the dashed perpendiculars to  $\vec{r}$ .

The sum expressed in Eq. (12.38) can be re-written to incorporate the dipole assumptions and the geometry of Fig. 12.10.

$$p(|\vec{r}|, \theta; t) = \Re e \left\{ \left[ \frac{e^{-jk\Delta r_1}}{(1 + \Delta r_1/|\vec{r}|)} + \frac{e^{+jk\Delta r_2}}{(1 - \Delta r_2/|\vec{r}|)} \right] \frac{C}{|\vec{r}|} e^{j(\omega t - k|\vec{r}|)} \right\} \quad (12.39)$$

The factor at the far right of Eq. (12.39) has the form of an ordinary diverging spherical wave. The terms in square brackets require an interpretation that will become most transparent if we consider an observation point that is far from the two sources, in terms of their separation,  $|\vec{r}| \gg d$ . In that case,  $\Delta r_1 \cong \Delta r_2 \ll |\vec{r}|$ .

In the far field,  $|\vec{r}| \gg d$ , we can neglect the small differences created by  $\Delta r$  in the denominators of the terms in the square brackets of Eq. (12.39), since those involve the ratio,  $\Delta r/|\vec{r}| \ll 1$ . Since  $\Delta r$  appears within the arguments of exponentials, we will interpret their effects by expressing the path length differences applying simple trigonometry in Fig. 12.11 and Garrett's First Law of Geometry.

$$\Delta r_1 \cong \Delta r_2 \cong \frac{d}{2} \sin \theta \quad (12.40)$$

Substitution of this far-field (i.e.,  $|\vec{r}| \gg d$ ) result into Eq. (12.39) produces a pressure distribution,  $p(r, \theta, t)$ , with a directional component involving the angle,  $\theta$ . Given a source strength, the amplitude depends only upon the separation of the sources,  $d$ , and the wavelength of the radiated sound,  $\lambda = 2\pi/k$ .

$$\begin{aligned} p(|\vec{r}|, \theta; t) &\cong \Re e \left\{ [e^{-jk\Delta r_1} + e^{+jk\Delta r_2}] \frac{C}{|\vec{r}|} e^{j(\omega t - k|\vec{r}|)} \right\} \\ &= \Re e \left\{ [e^{-jk\frac{d}{2}\sin\theta} + e^{jk\frac{d}{2}\sin\theta}] \frac{C}{|\vec{r}|} e^{j(\omega t - k|\vec{r}|)} \right\} \end{aligned} \quad (12.41)$$

The trigonometric identity,  $\cos \theta = (\frac{1}{2})(e^{j\theta} + e^{-j\theta})$ , allows expression of the final result in terms of a product of the axial pressure along the equatorial plane,  $\theta = 0^\circ$ ,  $p_{ax}(|\vec{r}|) = p(|\vec{r}|, \theta = 0^\circ)$ , and a *directionality factor*,  $H(\theta)$ .

$$p(|\vec{r}|, \theta; t) = p_{ax}(|\vec{r}|; t)H(\theta) = \Re e \left\{ \frac{2Ce^{j(\omega t - k|\vec{r}|)}}{|\vec{r}|} \right\} \left[ \cos \left( \frac{kd}{2} \sin \theta \right) \right] \quad (12.42)$$

First, let's check that  $p_{ax}(|\vec{r}|)H(\theta)$  in Eq. (12.42) produces the intuitive results with which this investigation was initiated.

$$H(\theta) = \cos \left( \frac{kd}{2} \sin \theta \right) \quad (12.43)$$

If  $d \ll \lambda$  and  $\phi = 0^\circ$ , then  $kd/2 = \pi d/\lambda \ll 1$ ; hence  $H(\theta) \cong \cos 0^\circ = 1$  for all  $\theta$ , demonstrating that the combination of two sources behaves as a single source with twice the source strength, since  $p_{ax}(|\vec{r}|) = 2C/|\vec{r}|$ . If  $d = \lambda/2$ , then  $kd/2 = \pi/2$ , so when  $\sin \theta = \pm 1$ ,  $H(\theta) = \cos (\pm \pi/2) = 0$ ; hence, we observe no sound radiated along the direction of the line joining the centers of the two monopole sources ( $\theta = \pm 90^\circ$ ), again, as expected.

With some confidence in Eqs. (12.42) and (12.43), we can now explore arrangements of the two sources that produce sound fields that may not be as intuitively obvious. From Eq. (12.43), it is easy to see that  $H(\theta) = 1$  anytime that  $(kd/2) \sin \theta_n = n\pi$ , where  $n = 0, 1, 2, \dots$ . There will be  $n$  directions,  $\theta_n$ , where the sound radiated by the dipole will be maximum when  $\sin \theta_n = 2n\pi/kd = n\lambda/d$  with  $n \leq d/\lambda$ . Similarly,  $H(\theta) = 0$  if  $(kd/2) \sin \theta = (2m+1)\pi/2$ , where  $m = 0, 1, 2, \dots$ . There will be  $m$  directions,  $\theta_m$ , where the sound radiated by the dipole will be zero when  $\sin \theta_m = (2m+1)\pi/kd = (2m+1)\lambda/2d$ , with  $(2m+1) \leq 2d/\lambda$ .

Figure 12.12 shows the resulting beam pattern in two and three dimensions for  $d/\lambda = 3/2$ , or  $kd = 3\pi$ . There will be two nodal directions:  $m = 0$ , so  $\sin \theta_{m=0} = 1/3$  and  $\theta_{m=0} = 19.5^\circ$ , and  $m = 1$ , so  $\sin \theta_{m=1} = 3/3$  and  $\theta_{m=1} = 90^\circ$ . Note that if  $m = 2$ ,  $(2m+1)\pi/kd = 5\pi/3\pi > 1$ . There will also be

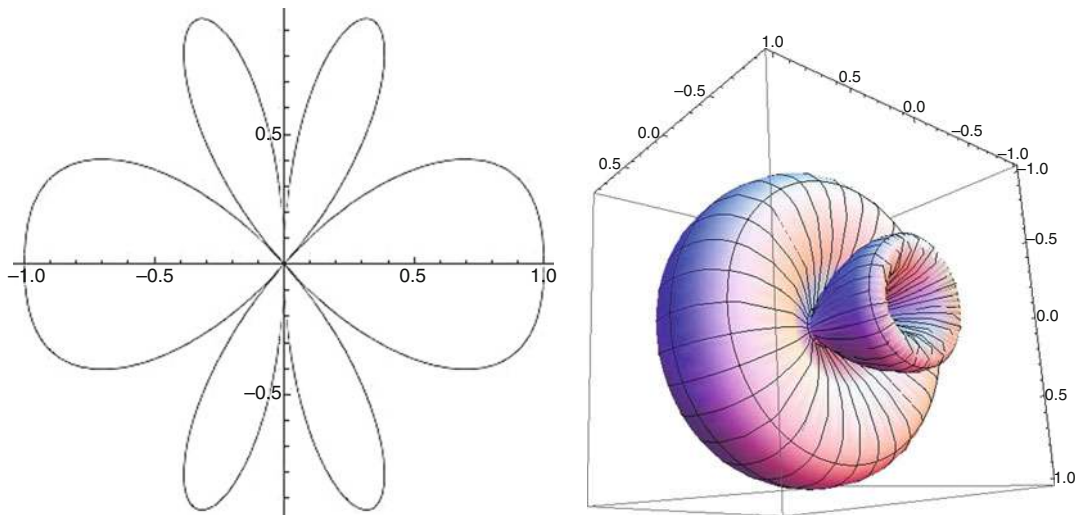


**Fig. 12.12** Two representations of the directionality factor,  $H(\theta)$ , of the sound field radiated by a pair of in-phase compact simple sources of equal amplitude that are separated by  $d = 3\lambda/2$ , corresponding to  $kd = 3\pi$ . (Left) The two-dimensional representation of  $H(\theta)$  provided in Eq. (12.43) that exploits the rotational symmetry about the axis joining the two sources to illustrate the essential structure of the directionality for that two-element array. (Right) The body of revolution formed by  $H(\theta)$  is three-dimensional surface. This figure is rotated from the orientation at the left to provide a better view of the node that occurs along the polar directions. [Directionality plots courtesy of Randall Ali]

two maximal (i.e., anti-nodal) directions. With  $n = 0$ ,  $\sin \theta_{n=0} = 0$ , so  $\theta_{n=0} = 0^\circ$ . With  $n = 1$ ,  $\sin \theta_{n=1} = 2/3$ , so  $\theta_{n=1} = 41.8^\circ$ .

Recall that the axial symmetry guarantees that these directional nodes (i.e., zero pressure directions for sources of identical source strength) and anti-nodes (i.e., directions of maximum sound pressure) define cones in three dimensions, as shown in Fig. 12.12 (right).

### 12.4.1 The Method of Images

A more important feature of  $H(\theta)$ , as given in Eq. (12.43) for the dipole configurations shown in Figs. 12.10 and 12.11, is that along the equatorial plane ( $\theta = 0^\circ$ ),  $H(\theta)$  always exhibits a local maximum:  $dH(0)/d\theta = 0$ . Based on the Euler equation, expressed in spherical coordinates in Eqs. (12.9) and (12.10),<sup>7</sup> the particle velocity  $v_\theta(\theta = 0^\circ)$ , that is everywhere normal to the equatorial plane ( $\theta = 0^\circ$ ), must vanish. Since no fluid passes through that plane, the radiation field of the dipole would be unchanged if the equatorial plane was replaced by an infinite rigid boundary. This fact provides a rigorous motivation for incorporation of boundaries by the “method of images” that allows us to place “phantom” sources outside the fluid volume of interest to satisfy a boundary condition; in this case, the division of an infinite space into a semi-infinite “half-space” through the introduction of a rigid, impenetrable boundary. This result demonstrates that if a single monopole were placed a distance,  $d/2$ , in front of a rigid, impenetrable surface, the fact that the component of the fluid’s acoustical particle velocity that is normal to that surface vanishes allows us to satisfy that boundary condition as long as we remain aware that the half-space behind the boundary is not a legitimate domain for the solution.

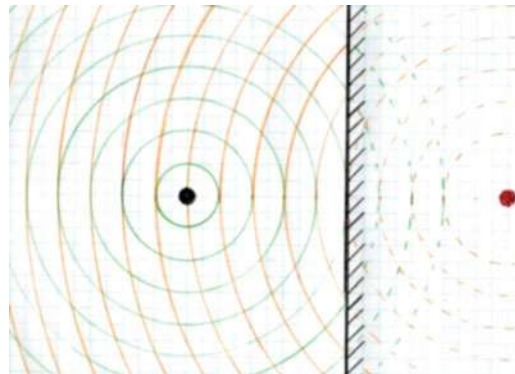
To initiate the discussion of the reflection of plane waves in Chap. 11, we considered the case of an echo bouncing off a large rigid surface depicted in Fig. 11.1. There, to satisfy the boundary condition, we *postulated* a counter-propagating wave to cancel the fluid particle velocity created by the incoming wave. Now we have shown explicitly that such a wave could be created by an “image source” that would also satisfy the boundary condition. In addition, the method of images has provided a solution that is not restricted to plane waves, although it contains the plane wave solution in the limit that  $d/2 \gg \lambda$ . The image solution also reinforces the fact that the acoustic pressure on the boundary is twice that which would have been produced by the same source radiating into an infinite (rather than semi-infinite) medium.

Figure 12.13 is a two-dimensional projection of an example where a spherical source of sound is located a distance of five wavelengths from a rigid reflector. An image source, an equal distance behind the reflector, is oscillating in-phase with the source to guarantee that the normal particle velocity at the rigid reflector will be zero. The resultant sound field within the fluid provides the classic “two-slit” interference pattern that was discovered by Thomas Young in 1803 for light waves [15]. Figure 12.13 is Young’s original diagram that shows the same result as shown for a single light source in front of a rigid boundary. Young first discovered interference effects when he heard the “beats” produced by two sound sources radiating with slightly different frequencies.

Why did we not observe these interference effects when we investigated the reflection and refraction of plane waves in Chap. 11? The answer is simple: we did not look! In Chap. 11, we assumed that the plane waves consisted of pulses that were of sufficiently short duration that they interfered at the boundary but did not overlap far from the boundary, as shown in Fig. 11.1. The current

---

<sup>7</sup>Note that the definition of the polar component of the velocity  $v_\theta$ , given in Eqs. (8.7) and (8.8), is  $v_\theta = (j\omega r\rho_m)^{-1}(\partial p/\partial\theta)$  so  $v_\theta$  would diverge at  $r = 0$ . This is not a problem because  $r$  has its minimum value at  $r = a$ .



**Fig. 12.13** The compact spherical source at the left (black) is placed a distance of five wavelengths,  $d/2 = 5\lambda$ , from a rigid boundary indicated by the hatched black line. The condition that the normal components of velocity at the boundary vanish is satisfied by placing an image source (red), oscillating in-phase with the real source (black), at the same distance behind the boundary. In this figure, the two sources are separated by ten wavelengths so  $kd = 2\pi d/\lambda = 20\pi$ . We visualize the resulting sound field with green circles, representing pressure maxima, separated by one wavelength, emanating from the real source and orange circles emanating from the image source. Behind the boundary, the circles are shown as dashed since there is no actual sound in that region. Within the fluid, any place where green and orange circles touch, the pressure will be doubled. Midway between those intersections, there will always be silence

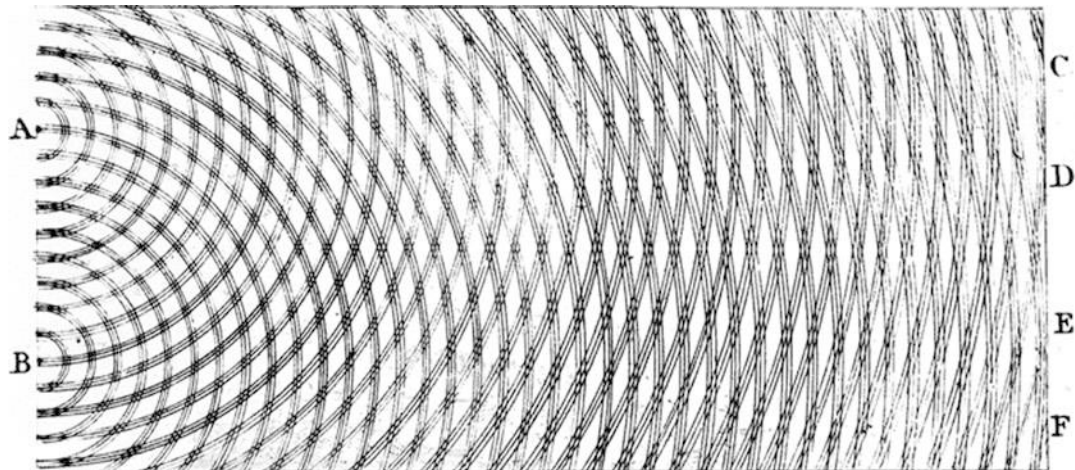


**Fig. 12.14** Diagram representing the superposition of two in-phase light sources located at points *A* and *B*, separated by nine wavelengths, from the original paper by Thomas Young [15]. Amplitude doubling is apparent along the line starting at the left from the midpoint between *A* and *B* to the right of the diagram between *D* and *E*. This result is known as the “Young’s double-slit experiment” and was central to the debate about the wavelike vs. the corpuscular nature of light [16].

treatment of a spherical source of sound adjacent to a rigid impenetrable boundary assumed continuous waves. If we return to Fig. 11.1, we see the incident plane wave fronts (blue) and the reflected plane wave fronts (green) produce pressure doubling where they intersect and silence half-way between.

The method of images has allowed us to solve the rather challenging problem of the sound field of a spherically radiating sound source in the proximity of a rigid boundary for an arbitrary separation between the source and the boundary. If we examine the opposite limit from that shown in Fig. 12.13 (or Fig. 12.14 for light) and consider a source that is much closer to the boundary than the wavelength of the sound it is radiating,  $d/2 \ll \lambda$  or  $kd \ll 1$ , then we see that the source produces everywhere twice

the pressure it would have if the boundary were not present. This case is commonly referred to as a *baffled source*, the “baffle” being the rigid boundary.

Since the acoustic pressure and the associated acoustic particle velocity are both doubled, the intensity of the sound is increased by a factor of four, although the radiated power is only doubled, since we can now only integrate the radiated intensity over a hemisphere. How is it possible that the same source can produce twice the acoustic pressure and radiate twice the acoustic power just by placing it very near a rigid boundary?

The answer is built into our assumptions regarding the behavior of the source. Throughout this discussion of radiation, we have assumed that the volume velocity of the source is independent of the load that it “feels” from the surrounding fluid, that is, we have assumed a “constant current” source.<sup>8</sup> The presence of the boundary doubled the pressure at the source (and elsewhere), so the specific acoustic impedance of the fluid at the source’s surface, as expressed in Eq. (12.13),  $z_{sp}(a) = \hat{p}(a)/\hat{v}_r(a)$ , is doubled. It is possible that this increase in radiative resistance (though not hydrodynamic mass which depends upon the equilibrium fluid mass density) could reduce the volume velocity of a real source.

We can play the same trick again if we want to calculate the sound pressure radiated by a compact source of constant source strength that is located in a corner, as shown schematically in Fig. 12.15. If again we assume that  $d/2 \ll \lambda$  or  $kd \ll 1$ , then we see that the source produces everywhere four times the pressure it would have if the boundaries were not present, again assuming the real source provides a constant volume velocity.<sup>9</sup> The intensity is now 16 times as large as that radiated by the same source in

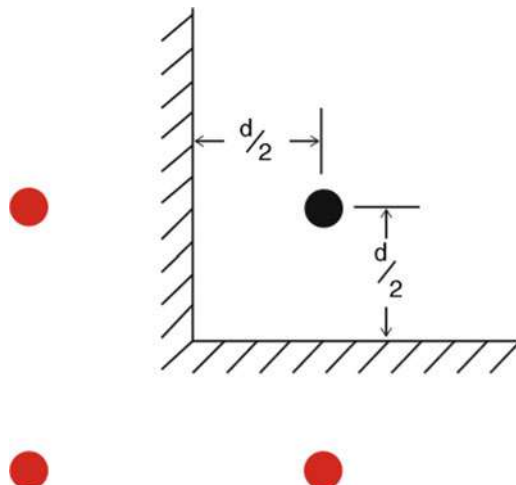


**Fig. 12.15** Schematic representation of a compact spherical source located near the intersection of two rigid impenetrable plane surfaces indicated by the hatched black lines. In this case the source (black) creates three image sources (red). The upper left and bottom right image sources cannot create the zero normal acoustic particle velocity on the two orthogonal rigid surfaces without the third image source at the bottom left to provide a symmetrical quartet that ensures the orthogonal cancellation

<sup>8</sup> For discussion of “constant force” acoustic sources (e.g., magnetohydrodynamic transducers), see G. W. Swift and S. L. Garrett, “Resonance reciprocity calibration of an ultracompliant transducer,” J. Acoust. Soc. Am. **81**(5), 1619–1623 (1987).

<sup>9</sup> This is the reason that the user’s manual for the Bose “SoundLink Mini” recommends that those small speakers be placed near a wall or in a corner to enhance their bass response.

the absence of the two orthogonal boundary planes, but the radiated power is only 4 times as large since the intensity is now integrated only over one quadrant of a sphere.

This approach can be repeated to create a sound field for a source near the intersection of three rigid, orthogonal, impenetrable planes by reflecting the arrangement in Fig. 12.15 about the third orthogonal plane, creating a total of eight sources (i.e., seven image sources). This results in 8 times the pressure, 64 times the intensity, and 8 times the radiated power (by integration over the octet of a sphere).

Needless to say, the effects of rigid impenetrable walls are very important for sound reinforcement applications in rooms, both for enhancement of bass response when  $kd < 1^9$  and for variation in the sound field amplitude with position for higher frequencies when  $kd > 1$ . The interference effects diagrammed in Figs. 12.13 and 12.14 produce significant variability in the acoustic intensity for different frequencies in different locations. Such variation is highly undesirable in a critical listening environment such as a recording studio (and its control booth) or a concert venue. We will revisit this problem from a different perspective (i.e., “normal modes”) when we analyze the sound in three-dimensional enclosures and waveguides in Chap. 13 of this textbook.

As we could see by going from one perfectly reflecting plane to two and then to three orthogonal reflecting planes, the application of the method of images can start to become complicated. If fact, if we considered only two parallel planes with a single source located in between, an infinite number of image sources would be required, since each image source would generate another behind the opposite boundary and so on ad infinitum [17]. The method has been applied successfully to more complex problems, like sound in a wedge-shaped region [18], similar to a gently sloping beach, or curved surfaces [19], and is popular for solving boundary-value problems in other fields, such as electrostatics (i.e., image charges) near conducting or dielectric interfaces and in magnetostatics due to image current loops [20].

## 12.5 Two Out-Of-Phase Compact Sources (Dipoles)

We can repeat the previous analysis for two out-of-phase monopoles, separated by a distance,  $d$ , using the same analytical approaches that produced our bipole results in Eq. (12.42). This out-of-phase combination of two compact monopoles is known as a *dipole*. The results for the dipole will be useful, important, and dramatically different, since the out-of-phase superposition leads to cancellation of the radiated acoustic pressure in the limit that the separation of the two out-of-phase sources becomes very small compared to the wavelength of sound,  $kd \ll 1$ .

If we designate the upper source in Fig. 12.11 as having a phase  $\phi_2 = 180^\circ = \pi$  radians with  $\phi_1 = 0^\circ$ , but retain our other assumptions,  $k_1 = k_2 = k = \omega/c$ ,  $\omega_1 = \omega_2 = \omega$ , and let  $\hat{\mathbf{C}}_1 = -\hat{\mathbf{C}}_2$  and  $C = |\hat{\mathbf{C}}_1| = \rho_m c k |\hat{\mathbf{U}}(a)| / 4\pi$ , then we can proceed by changing the sign of one term within the square brackets in Eq. (12.39).

$$p(|\vec{r}|, \theta; t) = \Re e \left\{ \left[ \frac{e^{-jk\Delta r_1}}{(1 + \Delta r_1/|\vec{r}|)} - \frac{e^{+jk\Delta r_2}}{(1 - \Delta r_2/|\vec{r}|)} \right] \frac{C}{|\vec{r}|} e^{j(\omega t - k|\vec{r}|)} \right\} \quad (12.44)$$

Using the trigonometric relation of Eq. (12.40) to again represent the path length differences, the far-field pressure of the dipole can be expressed in analogy with the bipole result of Eq. (12.41).

$$p(|\vec{r}|, \theta; t) \cong \Re e \left\{ \left[ e^{-jk\frac{d}{2}\sin\theta} - e^{jk\frac{d}{2}\sin\theta} \right] \frac{C}{|\vec{r}|} e^{j(\omega t - k|\vec{r}|)} \right\} \quad (12.45)$$

The trigonometric identity  $\sin\theta = (2j)^{-1}(e^{j\theta} - e^{-j\theta})$  allows the final result to be expressed in terms of a product of the maximum pressure along the axial direction  $\theta = 90^\circ$ ,  $p_{ax}(|\vec{r}|) = p(|\vec{r}|, 90^\circ)$ , and a directionality factor,  $H_{dipole}(\theta)$ .

$$\begin{aligned} p(|\vec{r}|, \theta) &= p_{ax}(|\vec{r}|)H_{dipole}(\theta) = \Re e \left\{ -j \frac{2C}{|\vec{r}|} e^{-jkr} \left[ \sin \left( \frac{kd}{2} \sin \theta \right) \right] \right\} \\ &= \Re e \left\{ -j \frac{\rho_m c k}{2\pi |\vec{r}|} e^{-jkr} |\hat{\mathbf{U}}(a)| \left[ \sin \left( \frac{kd}{2} \sin \theta \right) \right] \right\} \\ &= \Re e \left\{ -j \frac{\rho_m c}{|\vec{r}| \lambda} e^{-jkr} |\hat{\mathbf{U}}(a)| H_{dipole}(\theta) \right\} \end{aligned} \quad (12.46)$$

Comparison of the final expression in Eq. (12.46) to the expression for the pressure produced by a monopole in Eq. (12.21) shows that  $p_{ax}(|\vec{r}|)$  is twice the pressure produced by a single monopole. This is as expected. If the two anti-phase sources are separated by odd-integer multiples of the half-wavelength,  $d = (2n + 1)\lambda/2$ , then the pressure along the line joining their centers will be twice that of a single monopole with source strength,  $|\hat{\mathbf{U}}(a)|$ . Unlike the dipole, the directionality factor,  $H_{dipole}(\theta)$ , suppresses acoustic pressure along the equatorial plane,  $\theta = 0^\circ$  for  $kd \ll 1$ . The dipolar radiation patterns are shown in Fig. 12.16 for  $kd \ll 1$  and in Fig. 12.16 for  $kd = 3\pi$ .

If  $d \ll \lambda$ , then  $kd/2 = \pi d/\lambda \ll 1$ ; hence we can use the small-angle Taylor series approximation of  $\sin x \approx x$  to express  $H_{dipole}(\theta) \approx (kd/2) \sin \theta$ , which has a maximum value of  $(kd/2)$  at  $\theta = 90^\circ$  and at  $\theta = 0^\circ$  is zero. This is what we would expect; the path lengths to both sources are always equal for any observation point on the equatorial plane, and the anti-phased sources will always sum to zero pressure along that direction. In the small  $kd$  limit, the maximum pressure is always smaller than that of a monopole of equal source strength by a factor of  $(kd)$ .

$$\hat{\mathbf{p}}_{dipole}/\hat{\mathbf{p}}_{monopole} \propto kd \quad \text{for } kd \ll 1 \quad (12.47)$$

A compact dipole source is always a less efficient radiator than a monopole of equivalent source strength (i.e., volume velocity).

It is worthwhile pointing out that the reduction in radiated pressure, symbolized by Eq. (12.46), is the reason that all loudspeakers intended for radiation of low-frequency sound are placed in some kind of enclosure so that the source strength due to the oscillations of the speaker's diaphragm that are produced by the back surface of the speaker cone does not cancel the volume velocity generated by the cone's front surface.<sup>10</sup>

Just as we used the dipole to produce the sound field of a source at an arbitrary distance from a rigid boundary, the dipole produces a "pressure release surface" along the entire equatorial plane. This is a convenient way to satisfy the boundary condition for a source submerged below the air-water interface. If we imagine the situation depicted in Fig. 12.13, but let the black and red simple sources be  $180^\circ$  out-of-phase, then the plane bisecting the line connecting the two sources will support oscillatory fluid flow perpendicular to the plane but no oscillatory pressure. The cancellation of the acoustic pressure along that plane is clearly seen in Fig. 12.12 if the green circles radiating from the black source

<sup>10</sup> There are schemes, such as the bass-reflex enclosure, analyzed in Sect. 8.8, that use an acoustical network, like a Helmholtz resonator or transmission line, to allow the back-side volume velocity to add to that from the front side in a way that they are more nearly in-phase over the frequencies of interest.

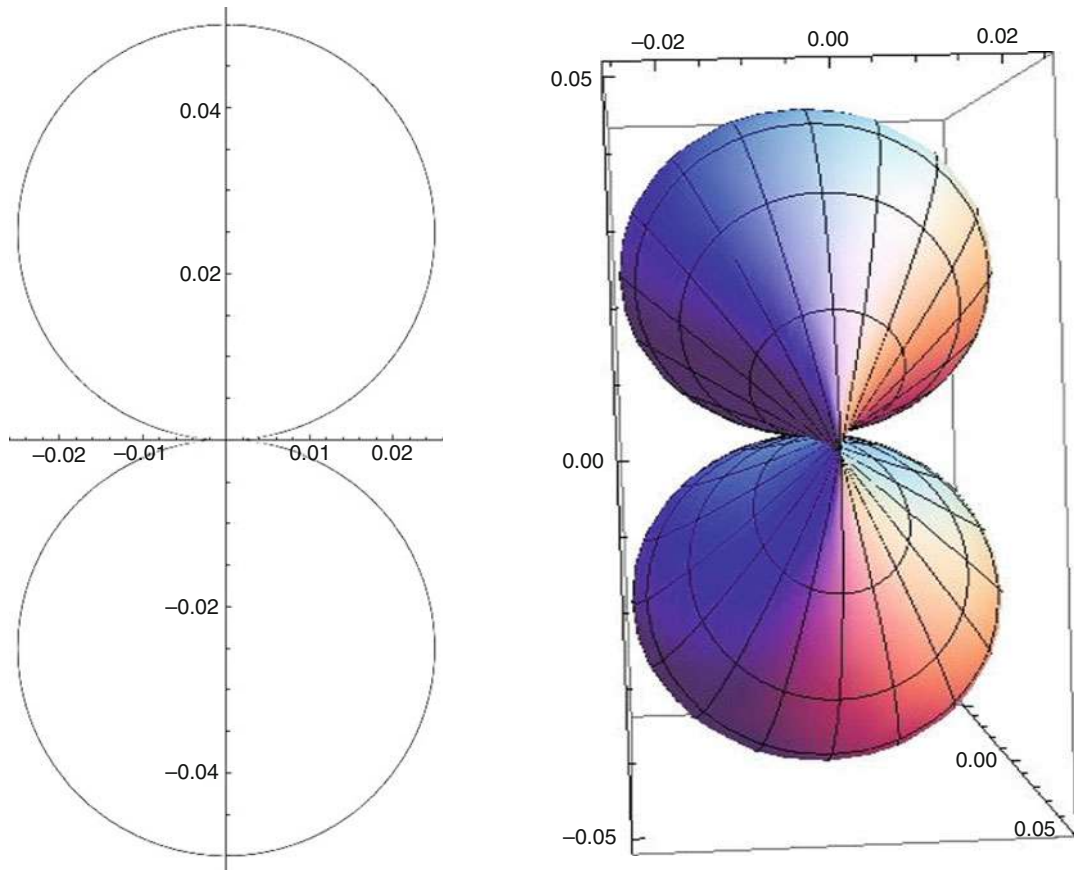


**Fig. 12.16** Dipole directional pattern,  $H(\theta)$ , for two compact spherical sources separated by a distance,  $d$ , that is significantly less than one wavelength of sound:  $kd \ll 1$ . (Left) The radiation is bi-directional as shown by this two-dimensional plot. It is important to recognize that the directionality function in Eq. (12.46) dictates that the two lobes are out-of-phase with respect to each other. (Right) Body of revolution formed by  $H(\theta)$  is a three-dimensional representation of the dipole's directivity, viewed along the equatorial plane, to show the null. [Directionality plots courtesy of Randall Ali]

represent pressure maxima and the orange circles radiating from the red source represent pressure minima. Where those circles intersect the pressure sums to zero.

If the separation of the two anti-phase sources is greater than a half-wavelength (i.e.,  $kd \geq \pi$ ), then the dipole will generate a directional pattern with multiple nodal surfaces (again, those surfaces are cones in three dimensions) and multiple maxima, as shown in Fig. 12.17. This is just what we saw for the bipole in that limit, shown in Fig. 12.11, which also set  $kd = 3\pi$ .

From Eq. (12.46), it is easy to see that  $H_{dipole}(\theta) = 0$  anytime that  $(kd/2) \sin \theta_m = m\pi$ , where  $m = 0, 1, 2, \dots$ . There will be  $m$  directions,  $\theta_m$ , where the sound radiated by the dipole will be zero when  $\sin \theta_m = 2m\pi/kd = m\lambda/d$  where  $m \leq d/\lambda$ . Similarly,  $H_{dipole}(\theta) = 1$  if  $(kd/2) \sin \theta_n = (2n + 1)\pi/2$  where  $n = 0, 1, 2, \dots$ . There will be  $n$  directions,  $\theta_n$ , where the sound radiated by the dipole will be maximum when  $\sin \theta_n = (2n + 1)\pi/kd = (2n + 1)\lambda/2d$  where  $(2n + 1) \leq 2d/\lambda$ .

Figure 12.18 shows the beam pattern for  $d/\lambda = 2$ , or  $kd = 4\pi$ . There will be three nodal directions,  $m = 0$ , so  $\sin \theta_{m=0} = 0^\circ$  and  $\sin \theta_{m=1} = 1/2$  so  $\theta_{m=1} = 30^\circ$  and  $\sin \theta_{m=2} = 2/2$  and  $\theta_{m=2} = 90^\circ$ . Note that if  $m = 3$ ,  $(2m + 1)\pi/kd = 7\pi/4\pi > 1$ . There will be two maximal directions. With  $n = 0$ ,  $\sin \theta_{n=0} = 1/4$ , so  $\theta_{n=0} = 14.5^\circ$ . With  $n = 1$ ,  $\sin \theta_{n=1} = 3/4$ , so  $\theta_{n=1} = 48.6^\circ$ .

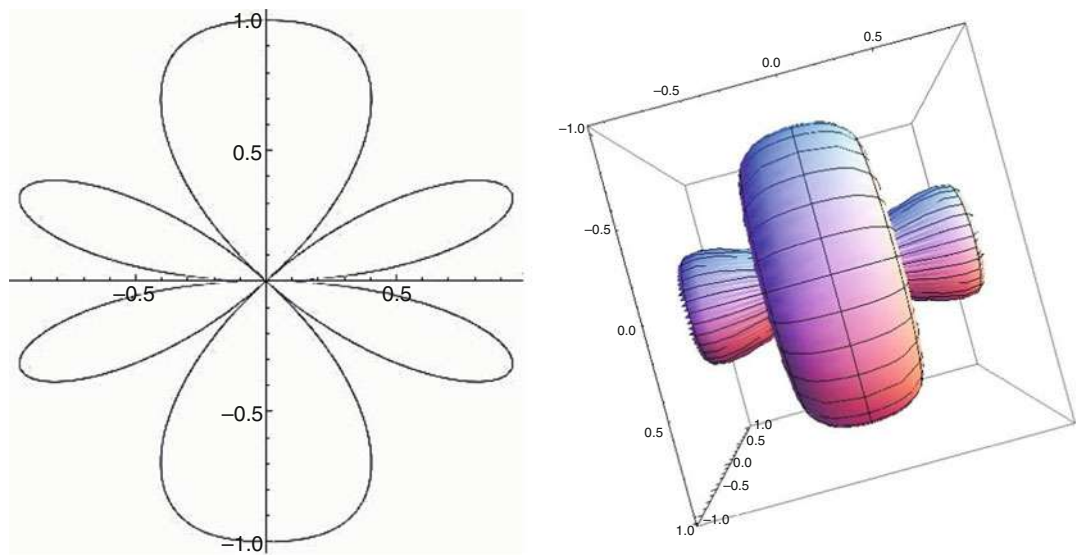


**Fig. 12.17** Two representations of the directionality,  $H(\theta)$ , produced by the sound field radiated by a pair of compact simple sources of equal amplitude which are  $180^\circ$  out-of-phase (i.e., a dipole) that are separated by  $3\lambda/2$ , corresponding to  $kd = 3\pi$ . (Left) The two-dimensional representation of  $H_{dipole}(\theta)$ , provided in Eq. (12.46), that exploits the rotational symmetry about the axis joining the two sources to provide the essential structure of the directionality for that two-element array. (Right) The body of revolution formed by  $H(\theta)$  is three-dimensional. This figure is tilted slightly from the orientation at the left to provide a better view of the anti-node that occurs along the polar directions. Comparison of this figure to Fig. 12.12 shows that they are identical, differing only in the reversal of the nodes and anti-nodes along polar and equatorial directions. [Directionality plots courtesy of Randall Ali]

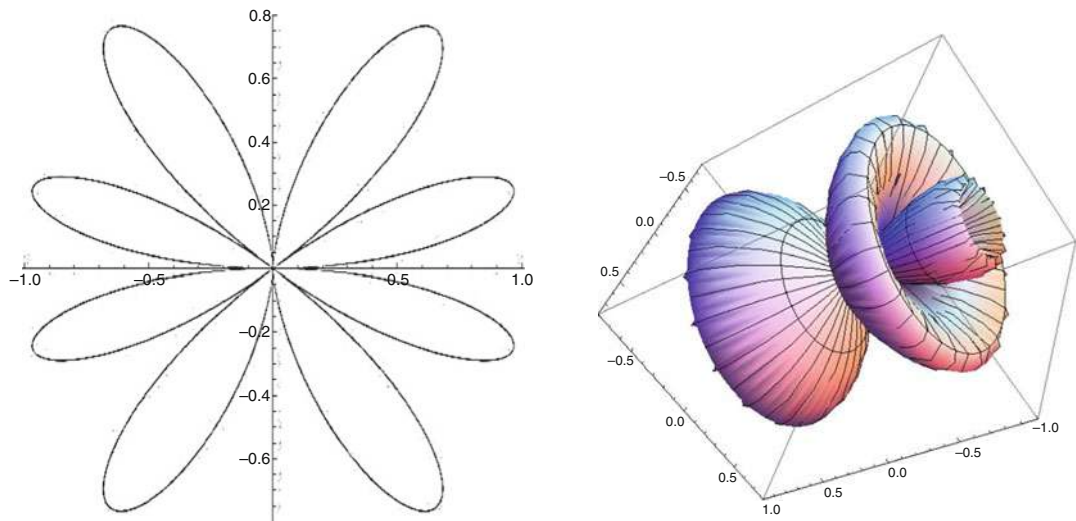


**Fig. 12.18** Two representations of the directionality,  $H(\theta)$ , for the sound field radiated by a pair of compact simple sources of equal amplitude which are  $180^\circ$  out-of-phase (i.e., a dipole) that are separated by  $2\lambda$  corresponding to  $kd = 4\pi$ . (Left) A two-dimensional representation that shows the nodal directions are  $\theta_{null} = 0^\circ, 30^\circ$ , and  $90^\circ$ . The maxima occur for  $\theta_{max} = 14.5^\circ$  and  $48.6^\circ$ . (Right) Body of revolution formed by  $H(\theta)$  is a three-dimensional representation of the directionality of the sound field that is rotated to show both the nodal surface that is the equatorial plane ( $\theta_{null} = 0^\circ$ ) and the two conical lobes above and below the equatorial plane. [Directionality plots courtesy of Randall Ali]

### 12.5.1 Dipole Radiation

The compact monopole and the compact dipole play a central role in our understanding of both the radiation and the scattering of sound by objects placed in an otherwise uniform medium. In Chap. 10, the speed of sound was interpreted as being determined by the complementary (and independent) influences of the compressibility and the inertia of the medium. If an object that is much smaller than the wavelength of sound has a compressibility that differs from the surrounding medium, then the incident sound's pressure will cause that object to compress more or compress less than the surrounding medium. If we think of a bubble in a fluid, then the incident sound will cause the bubble to be compressed and expanded more than the surrounding fluid. That forced oscillatory change in the bubble's volume is equivalent to the generation of a volume velocity that will be the source of a spherically spreading sound wave producing an acoustic pressure described in Eq. (12.21) and radiating sound power to the far field as described in Eqs. (12.18) and (12.24), within an otherwise unbounded medium.

Since we still chose to limit our attention to amplitudes that are small enough that linear superposition holds, the scattered wave and the original disturbance that excited the bubble's oscillations will interfere. In case of a bubble, if the frequency of excitation produced by an incident sound wave is close to the Minnaert frequency of Eq. (12.30), the scattered pressure can even exceed the incident pressure.<sup>11</sup> If the scattering object is less compressible than the surrounding medium, then the less compressible object can be represented as producing a volume velocity that is out-of-phase with the incident pressure wave as a means of satisfying the boundary conditions at the surface of that less compressible object.

The characteristic of the medium that is complementary to the compressibility for determining sound speed is the medium's mass density. If a compact object has the same density as the surrounding medium, then the object will experience the same acoustic velocity as that induced in the surrounding medium by the incident sound wave. If the compact object is denser than the surrounding medium, then the object's velocity will be less than that created by the incident sound wave in the surrounding medium and will thus produce relative motion between the object and the medium. For an object that is less dense, a bubble, for example, then its induced motion will be greater than the surrounding fluid's motion, again producing relative motion between the object and the surrounding medium but with opposite sign. In both cases, the relative motion will produce dipole radiation.

This previous discussion was intended to motivate the need to produce a description of dipole radiation that is as complete and detailed as the description of monopole radiation provided in Sect. 12.2. The solution of most other problems in radiation and scattering can be expressed in terms of the superposition of compact monopoles and compact dipoles. For monopoles, the compactness criterion was expressed in terms of the equivalent radius,  $a$ , of the monopole, and the wavenumber,  $k = 2\pi/\lambda$ , such that  $ka \ll 1$ .<sup>3</sup> For a dipole, the compactness criterion is expressed in terms of the separation,  $d$ , as depicted in Figs. 12.10 and 12.11, of the two out-of-phase sources of volume velocity,  $kd \ll 1$ .

As before, our expression for the pressure radiated by a dipole, in Eq. (12.46), can be used to produce the corresponding fluid velocity using the Euler equation.

---

<sup>11</sup> A similar effect can be observed by bringing a Helmholtz resonator close to an unbaffled loudspeaker driven at a frequency close to the resonator's natural frequency. When the resonator is close to the speaker, the sound level increases.

$$\begin{aligned} p(|\vec{r}|, \theta) &= \Re e \left\{ -j \frac{\rho_m c}{\lambda |\vec{r}|} \left| \hat{\mathbf{U}}(a) \right| k d \sin \theta \right\} \\ &= \Re e \left\{ -jk^2 \frac{\rho_m c}{4\pi |\vec{r}|} \left| \vec{d} \hat{\mathbf{U}}(a) \right| \cos \theta_p \right\} \quad \text{if } kd \ll 1 \end{aligned} \quad (12.48)$$

In this expression, the magnitude of the product of the source strength and the separation of the two out-of-phase monopoles has been combined,  $|\vec{d} \hat{\mathbf{U}}(a)|$ . That combination is known as the *dipole strength* and is sometimes given a different symbol.

I like to leave the dipole strength in the format of Eq. (12.48) to remind myself that there is now a unique direction,  $\vec{d}$ , associated with the dipole strength. It is also important to remember that  $|\hat{\mathbf{U}}(a)|$  is the volume velocity of one of those two monopoles, just as it was throughout the derivation that resulted in Eq. (12.46).

The appearance of the unique direction,  $\vec{d}$ , breaks the spherical symmetry exploited to derive the monopole radiation, although azimuthal symmetry is still preserved (i.e., rotation about the  $\vec{d}$ -axis has no physical significance). Since Eqs. (12.46) and (12.48) depend upon the angle,  $\theta$ , measured with respect to the elevation above the plane, which is the perpendicular bisector of the  $\vec{d}$ , as shown in Figs. 12.10 and 12.11, the right-hand version of Eq. (12.48) introduces the polar angle,  $\theta_p$ , that is measured from line joining the two out-of-phase monopoles. The amplitude of the particle velocity will also have a polar component,  $\hat{\mathbf{v}}_\theta$ , as well as a radial component,  $\hat{\mathbf{v}}_r$ . This is dictated by the expression for the pressure gradient in spherical coordinates that was provided in Eq. (12.10).

To capture both the near- and far-field behavior, the pressure produced by the compact dipole can be expanded in a Taylor series by taking the gradient of the monopole pressure and multiplying that gradient by the separation,  $\vec{d}$ .

$$p_{dipole}(|\vec{r}|, \theta, t) = \Re e \left\{ -k^2 \frac{\rho_m c |\vec{d} \hat{\mathbf{U}}(a)|}{4\pi |\vec{r}|} \cos \theta_p \left( 1 + \frac{j}{k |\vec{r}|} \right) e^{j(\omega t - k |\vec{r}|)} \right\} \quad (12.49)$$

In the far field, for  $kr \gg 1$ , Eq. (12.49) reduces to Eq. (12.48). As with the monopole, the dipole pressure field varies inversely with distance,  $|\vec{r}|$ , from the dipole. Use of the Euler equation and the expression for the pressure gradient in Eq. (12.10) provides expressions for the radial and polar components of the particle velocity produced by dipole radiation.

$$\hat{\mathbf{v}}_r = -k^2 \frac{|\vec{d} \hat{\mathbf{U}}(a)|}{4\pi |\vec{r}|} \cos \theta_p \left( 1 + \frac{2j}{k |\vec{r}|} - \frac{2}{(k |\vec{r}|)^2} \right) e^{j(\omega t - k |\vec{r}|)} \quad (12.50)$$

$$\hat{\mathbf{v}}_\theta = -jk \frac{|\vec{d} \hat{\mathbf{U}}(a)|}{4\pi |\vec{r}|^2} \sin \theta_p \left( 1 + \frac{j}{k |\vec{r}|} \right) e^{j(\omega t - k |\vec{r}|)} \quad (12.51)$$

The existence of a polar component to the velocity field should not be surprising. If we think of the dipole as one monopole expelling fluid during one-half of the acoustic cycle that is ingested by the other monopole, followed by a role reversal during the next half-cycle, there has to be a component of the fluid's velocity, at least close to the two out-of-phase monopoles, that has a polar contribution, in

addition to the radial contribution. The fluid must shuttle back and forth, as illustrated by the streamlines in Fig. 12.22.

The radial component of the time-averaged radiated intensity is proportional to the in-phase product of pressure and particle velocity.

$$\langle I_r \rangle_t = \rho_m c \left( \frac{k^2 |\vec{d}\hat{\mathbf{U}}(a)|}{4\pi |\vec{r}|} \right)^2 \cos^2 \theta_p \quad \text{for } ka \ll 1 \quad (12.52)$$

There are no components of the intensity vector,  $\vec{I}$ , in either the polar or azimuthal directions:  $I_{\theta_p} = I_{\phi} = 0$ . The total radiated power,  $\langle \Pi_{\text{dipole}} \rangle_t$ , is just the integral of Eq. (12.52) over all directions, but  $\langle I_r \rangle_t \propto r^{-2}$ , so the radiated power will be independent of distance, as it was for monopoles, since dissipation is still being neglected.

$$\langle \Pi_{\text{dipole}} \rangle_t = 2\pi r^2 \int_0^\pi \langle I_r \rangle_t \sin \theta_p \, d\theta_p = \rho_m c \frac{4\pi^2}{3\lambda^4} |\vec{d}\hat{\mathbf{U}}(a)|^2 = \frac{\rho_m \omega^4}{12\pi c^3} |\vec{d}\hat{\mathbf{U}}(a)|^2 \quad (12.53)$$

This result has made use of the following definite integral:

$$\int_0^\pi \cos^2 \theta_p \sin \theta_p \, d\theta_p = \frac{2}{3} \quad (12.54)$$

The pressure and velocity can be used to calculate the compact dipole's mechanical impedance,  $\mathbf{Z}_{\text{dipole}}$ , of the compact dipole,  $r = a$ .

$$\mathbf{Z}_{\text{dipole}}(a) = \frac{\rho_m c (\pi a^2)}{3} (ka)^4 + \frac{j\omega}{2} \left( \rho_m \frac{4\pi a^3}{3} \right) \left[ 1 + \frac{(ka)^2}{2} \right] \quad (12.55)$$

As with the monopole result in Eq. (12.16), the dipole's radiation resistance is the real part of Eq. (12.55). For the compact monopole, the radiation resistance is proportional to  $(ka)^2$ , while for the compact dipole, it is proportional to  $(ka)^4$ . Higher-order combinations have radiation resistances that are proportional to even higher powers of  $(ka)$ . For a quadrupole,  $r_{\text{rad}} \propto (ka)^6$ , as addressed in Problem 10 and in Eq. (12.136).

Again, as in the case of the monopole's mechanical impedance in Eq. (12.15), the imaginary contribution is reminiscent of the mass reactance. In the dipole case, the effective mass,  $m_{\text{eff}}$ , is one-half the mass of the fluid that is displaced in the limit that  $(ka) \ll 1$ . When applied to two out-of-phase monopoles, this additional mass has to be accelerated and decelerated. As will be seen in Sect. 12.6, this is also the hydrodynamic mass that must be added to a rigid sphere executing oscillatory motion in a fluid, as it was in Chap. 8, Problem 3 [21].

In general, the hydrodynamic mass is proportional to the “order,”  $m$ , of the monopoles that are combined to create the compact source [22].

$$\frac{m_{\text{eff}}}{\rho_m \left( \frac{4\pi a^3}{3} \right)} = \frac{3}{[(m+1) \cdot 1 \cdot 3 \cdot 5 \cdot \dots \cdot (2m+1)]} \quad (12.56)$$

For a monopole,  $m = 0$  so the ratio is 3, as calculated in Eq. (12.15). For the dipole,  $m = 1$ , so the ratio is  $\frac{1}{2}$ , as calculated in Eq. (12.55). For a quadrupole,  $m = 2$  so that ratio would be  $\frac{1}{15}$ .

### 12.5.2 Cardioid (Unidirectional) Radiation Pattern

The assumption behind our calculation of radiation from a compact spherical source was that its radiation pattern was omnidirectional. Our solution for the dipole source resulted in patterns that were bi-directional for two identical anti-phased sources that were separated by less than one-half wavelength, as shown in Fig. 12.16. In some applications, we seek a source (or receiver) that is unidirectional [23]. One way to achieve this goal is by combining a compact ( $ka \ll 1$ ) omnidirectional (spherical) source and a compact ( $kd \ll 1$ ) dipole.

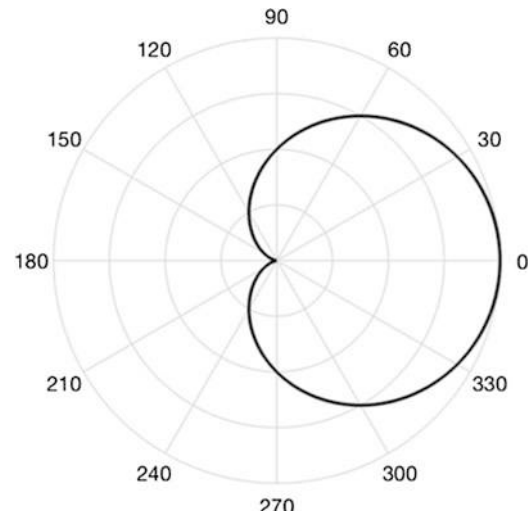
The fact that the two lobes of the compact dipole's directional pattern are  $180^\circ$  out-of-phase with each other means that when a dipole is added to an omnidirectional source, their fields will add in one direction but will subtract in the opposite direction. If the far-field pressure amplitude of the omnidirectional source and the dipole are equal, then the sound field in one direction will be twice that of the omnidirectional source operating in isolation, but in the opposite direction, the omnidirectional source and the dipole will exactly cancel, and no sound will be radiated along that direction.

Such a superposition of a dipole and an omnidirectional source produces a *cardioid directivity* pattern, shown in Fig. 12.19, which appears to be heart-shaped in its two-dimensional representation. Although our definition of angle,  $\theta$ , was based on elevation above the plane normal to the line connecting the source pair, as shown in Figs. 12.10 and 12.11, a more common choice is the polar angle measured from the line joining the two sources. To avoid confusion, the polar angle will be subscripted,  $\theta_p$ , in this section as it was when it was introduced in the previous section.

$$H_{dipole}(\theta_p) = \cos \theta_p \quad \text{if } kd \ll 1 \quad (12.57)$$

Equation (12.47) demonstrates that the ratio of the far-field radiated sound pressure from a dipole source to that from an omnidirectional compact spherical sound source is frequency dependent. Since the spacing,  $d$ , between the sources that produce the dipole is usually fixed, it is necessary to provide a frequency-dependent attenuation to the omnidirectional source if the cardioid pattern is to be maintained over a range of frequencies. This can be accomplished by high-pass filtering the signal that drives the omnidirectional source. The sum will produce a constant directional pattern as long as  $kd < 1$ , although the amplitude of the signal will grow linearly with frequency from low frequencies up

**Fig. 12.19** The superposition of an omnidirectional source and a compact dipole produces the cardioid directional pattern shown in a two-dimensional representation. The pattern is called a cardioid because it resembles a heart-shaped ♥ pattern. The amplitude is twice that of the omnidirectional source for  $\theta_p = 90^\circ$  and is zero for  $\theta_p = -90^\circ$ .  
[Directionality plot courtesy of Randall Ali]



to the frequency where  $kd \cong 1$ . If the amplitude of the dipole and monopole contributions are equal, their sum produces a cardioid directional function,  $H_{\text{cardioid}}(\theta_p)$ .

$$H_{\text{cardioid}}(\theta_p) = 1 + \cos \theta_p \quad (12.58)$$

### 12.5.3 Pressure Gradient Microphones

It is more common to produce a cardioid pattern for microphones than for sound sources. One obvious method would be to use two closely spaced omnidirectional microphone cartridges. The sum of their signals would provide an omnidirectional output that could be high-pass filtered (electronically), while their difference would provide the dipole signal that could be combined with the filtered “omni” signal to produce a properly frequency-weighted sum.

More clever systems can exploit acoustical networks that allow the sound pressure to access both sides of a single diaphragm. This approach was patented by Benjamin Bauer [24] and was the basis of the Shure Model 55S “Unidyne®” microphone, shown in Fig. 2.20 (right). That iconic microphone celebrated the 75th anniversary of its initial production in 2014 [25].

Bauer’s approach is shown schematically in Fig. 2.19 (*left*). In that diagram, the front of the diaphragm is exposed directly to the sound pressure,  $\hat{\mathbf{p}}_{\text{front}}$ . The rear of the diaphragm is facing a volume (compliance) that is exposed to the same sound wave, though at a slightly different position, through a flow resistance, frequently provided by fabric, a mesh screen, or a combination of both. Figure 12.20 is a simplification of the microphone in Fig. 2.19 (*left*) that eliminates the transduction mechanism and shows only the diaphragm (without its suspension) and a rear-access port filled with a porous medium acting as a flow resistance,  $R_{\text{flow}}$ , providing access to the volume (compliance),  $V$ , where the internal pressure within that volume,  $\hat{\mathbf{p}}_{\text{back}}$ , applies a force to the rear of the diaphragm.

In Fig. 12.20, the microphone is shown in two different orientations with respect to a propagating plane wave that is assumed to be approaching from the left. Before determining the values of  $R_{\text{flow}}$  and  $V$  that would produce a cardioid directional pattern from the resulting motion of a single diaphragm, it will be useful to consider the case where  $R_{\text{flow}} = 0$ , so that the pressure at the port is applied directly to the rear of the diaphragm.

If  $R_{\text{flow}} = 0$ , then the lower orientation ( $\theta_p = \pm 90^\circ$ ), shown in Fig. 12.20, will have  $\hat{\mathbf{p}}_{\text{front}} = \hat{\mathbf{p}}_{\text{back}} = \hat{\mathbf{p}}_{\text{rear}}$  so that there will be no net force on the diaphragm of area,  $A_{\text{pist}}$ . For the upper orientation ( $\theta_p = 0^\circ$ ), the sound that reaches the port must propagate an additional effective distance,  $\Delta\ell$ , before reaching the port.<sup>12</sup> The net force,  $\hat{\mathbf{F}}_{\text{net}}$ , caused by the pressure difference across the diaphragm, will depend upon the area of the diaphragm,  $A_{\text{pist}}$ , and the pressure gradient in the direction of propagation,  $\partial p / \partial x$ , produced by the plane wave as well as the orientation of the normal to the microphone’s diaphragm with respect to the wave’s direction of propagation,  $\theta_p$ .

Since it is assumed that the presence of the microphone does not distort the sound field of the incoming plane wave, the pressure at the port,  $\hat{\mathbf{p}}_{\text{rear}}$ , can be expressed in terms of the pressure on the diaphragm,  $\hat{\mathbf{p}}_{\text{front}}$ . The pressure of a traveling plane wave can be expressed as a complex exponential, as in Eq. (10.14), to simplify calculation of the gradient.

<sup>12</sup> Although it is clear that the “effective distance,”  $\Delta\ell$ , will depend upon the diameter of the enclosure, calculation of the pressure distribution and phase shift between the sound impinging on the diaphragm and the sound reaching the port is complicated, even for a spherical enclosure, requiring expansion of the sound field into a superposition of Legendre polynomials. See Ref [4], §VII.27.

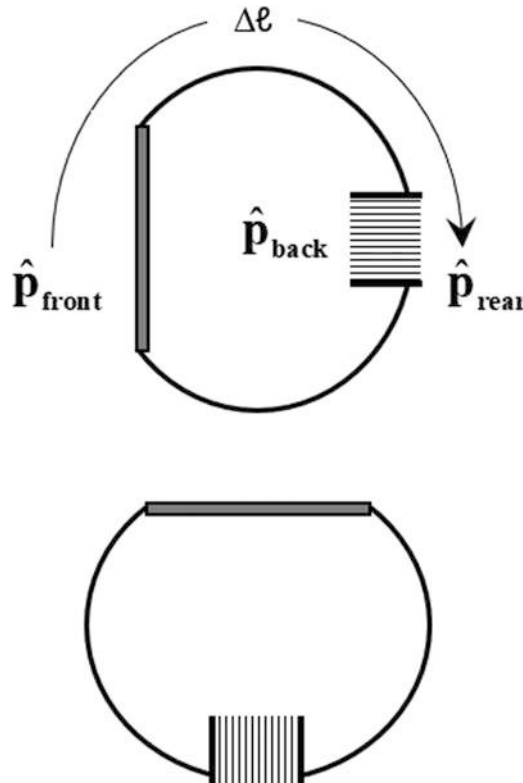


**Fig. 12.20** Schematic representation of two microphone enclosures that omits any transduction mechanism, like the electrodynamic scheme shown in Fig. 2.19 (left). Sound pressure impinging on either the upper or lower enclosure applies a force directly on the “front” of the diaphragm (grey rectangle). Sound can also cause air flow through the flow resistance at the rear of the enclosure (parallel lines) that will create pressure within the volume (compliance) and thus apply a force to the rear of the diaphragm. Assume that a plane wave is traveling to the right and that the presence of enclosures does not perturb that wave. (*Upper*) In the orientation shown ( $\theta_p = 0^\circ$ ), the sound must travel an additional distance,  $\Delta\ell$ , before it reaches the port containing the resistance. (*Lower*) In this orientation ( $\theta_p = \pm 90^\circ$ ), the wave excites both the diaphragm and the resistance port at the same time (i.e., in-phase) so that  $\Delta\ell = 0$

$$\hat{p}_{\text{rear}} = \hat{p}_{\text{front}} + \frac{\partial(\hat{p}_{\text{front}} e^{-jkx})}{\partial x} \Delta\ell = \hat{p}_{\text{front}} [1 - jk(\Delta\ell) \cos \theta_p] \quad (12.59)$$

The net force across the diaphragm is proportional to the pressure difference, since  $R_{\text{flow}}$  has been temporarily set to zero and access to the rear of the diaphragm is unimpeded.

$$\hat{\mathbf{F}}_{\text{net}} = A_{\text{pist}} (\hat{p}_{\text{front}} - \hat{p}_{\text{rear}}) = jk \hat{p}_{\text{front}} A_{\text{pist}} (\Delta\ell) \cos \theta_p \quad (12.60)$$

Since  $k = \omega/c$ , and  $j\omega\hat{v}$  is proportional to the pressure gradient through the Euler equation, these pressure gradient microphones are also called velocity microphones.

For the case where  $R_{\text{flow}} = 0$ , the diaphragm in an enclosure like those shown in Fig. 12.20 will have a bi-directional sensitivity pattern like that for a compact dipole, as shown in Fig. 12.16, if the diaphragm’s motion is converted to some electrical signal by an appropriate transduction mechanism.

A popular implementation of such a *pressure gradient microphone* in studio recording applications [23] is the *ribbon microphone* [26]. In that case, the “diaphragm” is a very thin corrugated metal strip placed in a magnetic field. The acoustically induced pressure difference on either side of the “ribbon” causes it to vibrate and generate an electrical voltage that is proportional to its velocity [27].

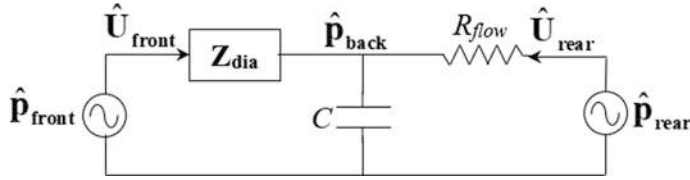


**Fig. 12.21** Equivalent circuit representation of the pressure gradient microphone in Fig. 12.20. The diaphragm will respond to the pressure difference,  $\Delta\hat{p} = \hat{p}_{\text{front}} - \hat{p}_{\text{back}}$ . The relationship between  $\hat{p}_{\text{front}}$  and  $\hat{p}_{\text{rear}}$  is provided in Eq. (12.59)

If  $R_{\text{flow}} \neq 0$ , then the combination of  $R_{\text{flow}}$  and the compliance of the microphone's enclosure volume,  $V$ , can be characterized by a time constant,  $\tau_{RC}$ , that produces a low-pass filter between the acoustical pressure felt by the back of the diaphragm,  $\hat{p}_{\text{back}}$ , and the acoustical pressure at the entrance to the port,  $\hat{p}_{\text{rear}}$ , as expressed in Eq. (12.59).

$$\tau_{RC} = R_{\text{flow}}C = \frac{R_{\text{flow}}V}{\gamma p_m} \quad (12.61)$$

The net force on the diaphragm of the pressure gradient microphone, shown in Fig. 12.20, can be determined by using the equivalent circuit of Fig. 12.21. The acoustical impedance of the diaphragm,  $Z_{\text{dia}}$ , represents the stiffness, moving mass, and mechanical damping of the microphone's diaphragm. The compliance of the volume is  $C$ , and the flow resistance of the rear port is  $R_{\text{flow}}$ .

$$\begin{aligned} \hat{p}_{\text{front}} &= \hat{U}_{\text{front}} \left( Z_{\text{dia}} + \frac{1}{j\omega C} \right) - \frac{\hat{U}_{\text{back}}}{j\omega C} \\ \hat{p}_{\text{rear}} &= \frac{\hat{U}_{\text{front}}}{j\omega C} - \hat{U}_{\text{front}} R_{\text{flow}} \left( 1 + \frac{1}{j\omega R_{\text{flow}} C} \right) \end{aligned} \quad (12.62)$$

The pressure difference,  $\Delta\hat{p}$ , across the diaphragm, can be found by combining Eq. (12.59) with Eq. (12.62).

$$\frac{\Delta\hat{p}}{\hat{p}_{\text{front}}} = \frac{Z_{\text{dia}} R_{\text{flow}} \left[ 1 + \frac{(\Delta\ell)}{c\tau_{RC}} \cos\theta_p \right]}{Z_{\text{dia}} R_{\text{flow}} - j \left[ \frac{R_{\text{flow}} + Z_{\text{dia}}}{\omega C} \right]} = D \left( 1 + B \cos\theta_p \right) \quad (12.63)$$

Two constants have been introduced for the right-hand version of Eq. (12.63).  $B = \tau_{\Delta\ell}/\tau_{RC}$  is the ratio of the front-to-back propagation delay,  $\tau_{\Delta\ell} = (\Delta\ell)/c$ , and the filter's time constant,  $\tau_{RC}$ .  $D$  involves the physical properties of the diaphragm and its suspension, the enclosure's volume, and the flow resistance of the port.

$$B = \frac{(\Delta\ell)}{cR_{\text{flow}}C} = \frac{\tau_{\Delta\ell}}{\tau_{RC}} \quad \text{and} \quad D = \frac{Z_{\text{dia}}}{Z_{\text{dia}} + \left[ \frac{R_{\text{flow}} + Z_{\text{dia}}}{j\omega\tau_{RC}} \right]} \quad (12.64)$$

By making the propagation delay equal to the filter time constant,  $B = 1$ , the cardioid directionality pattern of Fig. 12.19 is produced. If  $R_{\text{flow}} = \infty$ , so that the port is blocked,  $B = 0$  and the pattern is omnidirectional (i.e., monopolar). In the first case, where  $R_{\text{flow}} = 0$ ,  $\tau_{RC} = 0$ , so  $B = \infty$  and the dipole directionality of Fig. 12.16 is obtained.

### 12.5.4 The DIFAR Directional Sonobuoy

The ability to produce a directional sensor that was demonstrated in Sect. 12.5.1 and a commercially viable implementation that produces unidirectional (cardioid) sensitivity in air was described in Sect. 12.5.3. In underwater acoustic applications, it is often advantageous to have a hydrophone system that can determine the direction of a submerged sound source. In principle, if two such systems were deployed, then the location of the source could be determined by triangulation.

The most widely used such directional hydrophone system is the US Navy's AN/SSQ-53 DIFAR sonobuoy. During the Cold War, submarine surveillance aircraft used to eject these sonobuoys, when flying close to the ocean surface, to locate submarines. This practice was so widespread that there are sections of the ocean floor at strategically significant geographical locations (known to sailors as "choke points") that are literally covered with such sonobuoys that would be programmed to sink after a pre-determined interval after deployment, usually ranging for 30 min to 8 h. Today, such directional sonobuoys are still manufactured by a number of vendors, and smaller numbers of such sonobuoys are now used for studying marine mammals, as well as for military purposes.

The Directional Frequency Analysis and Recording (DIFAR) sonobuoy combines two orthogonal dipole sensors, usually called the N–S and the E–W dipole, with an omnidirectional hydrophone. In addition, the DIFAR system would also have an electronic magnetic compass [28] to determine the free-floating directional hydrophone's orientation and a radio-frequency transmitter that could send the hydrophone and compass information over a user-selectable choice of 96 different channels that would broadcast over a range of radio frequencies between 136.0 MHz and 173.5 MHz. Before ejection, a unique channel would be chosen for each DIFAR to allow multiple hydrophones to operate simultaneously in adjacent areas without interference.

Just as before, the N–S dipole could be summed with the omnidirectional hydrophone to produce a northward listening cardioid, or the N–S dipole could be subtracted from the omnidirectional hydrophone to produce a southward listening cardioid. A similar east–west directionality could be synthesized, all with reference to the orientation established by the internal magnetic compass. By comparing the magnitude of the received signals in each direction, the direction to the source could be determined. The use of frequency-selective signal processing could simultaneously determine the direction to different sources if their radiated sound signature had unique frequency content.

A more efficient method that uses only three dipole sensors, with axes that are separated by  $120^\circ$ , to obtain the desired directional information and avoid the possibility that a source could be oriented along a detection node has been described and demonstrated [29]. The function relies upon the trigonometric sum of the signals being a constant [30].

$$\sum_{k=0}^N \cos^2\left(\phi + \frac{2\pi k}{N}\right) = \frac{N}{2} \quad (12.65)$$

This is the generalization of the better-known trigonometric identity,  $\cos^2\phi + \sin^2\phi = 1$ .

---

## 12.6 Translational Oscillations of an Incompressible Sphere

As we have shown, sound sources that displace fluid by changing their volume periodically in time will behave as simple (compact) spherically symmetric radiators if  $ka \ll 1$ . On the other hand, two such sources in close proximity with oscillations that are  $180^\circ$  out-of-phase will produce a dipolar radiation field. As expressed in Eq. (12.58), the radiation efficiency of the compact dipole ( $kd \ll 1$ ) is less than

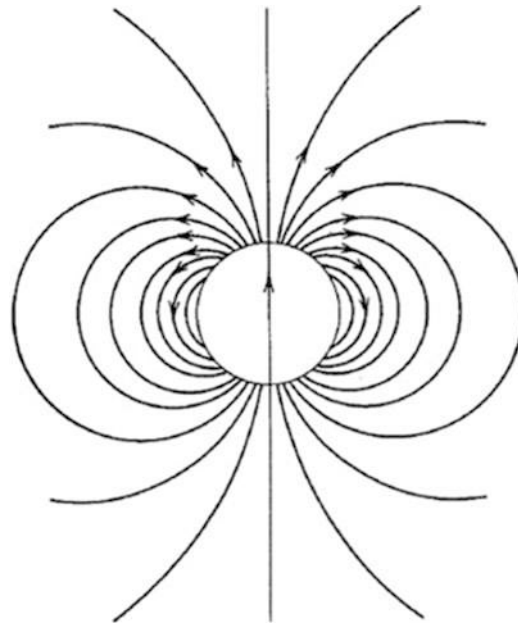


**Fig. 12.22** The translational oscillatory excursions of solid objects produce fluid flow that is identical to that of two out-of-phase simple (monopole) sources, if the dimensions of the objects are small compared to the wavelength of sound at the frequency of the oscillations. The flow pattern for an incompressible sphere, shown here by the fluid's streamlines, is the same as that produced by a dipole. As the sphere moves upward, it displaces fluid that is then collected below the sphere. Since the sphere is assumed to be incompressible, the amount of fluid pushed away by the upward motion must be the same as that pulled in behind the sphere [31]

the monopole (simple source) having the same source strength. In effect, the fluid volume ejected by one of the dipole's pair of sources is ingested by the other during one-half of the cycle, and their roles reverse during the following half-cycle, so there is no net production of volume velocity. It is only the phase difference produced by the displacement of their centers which results in non-zero radiated sound pressure. This dipole behavior can therefore be produced by a rigid object of constant volume that simple oscillates (translationally) back and forth and consequently produces no net periodic change in fluid volume.

A loudspeaker that is not placed in an enclosure behaves as a rigid disk that is oscillating back and forth. The amount of fluid that is displaced in one direction by the motion of one side of disk (i.e., speaker cone) is the same as the fluid that is pulled in the opposite direction by the other side of the disk. There is no net periodic change in fluid volume. Similarly, the incompressible sphere that experiences oscillatory translational motion, as shown by the streamlines in Fig. 12.22, pushes fluid ahead while it sucks the same amount of fluid from behind.

The equivalence of the sound radiated by a rigid sphere undergoing translational oscillations to a dipole can be established again by expressing the velocity of the sphere's surface in Hankel functions and Legendre polynomials [31]. If the center of the sphere has a time-dependent velocity,  $u(t) = \Re[e[\hat{\mathbf{u}}_0 e^{j\omega t}]$ , and  $ka \ll 1$ , then its equivalent dipole strength,  $\left| \vec{d} \hat{\mathbf{U}}(a) \right|_{sphere}$ , can be expressed by equating the time-averaged power,  $\langle \Pi_{rad} \rangle_t$ , calculated in Eq. (12.53), with the same result for the oscillating compact rigid sphere of volume,  $V_{sphere} = 4\pi a^3/3$  [32].

$$\left| \vec{d}\hat{\mathbf{U}}(a) \right|_{sphere} = \frac{3|\hat{\mathbf{u}}_0|}{2\sqrt{2}} V_{sphere} \cong 1.06 |\hat{\mathbf{u}}_0| V_{sphere} \quad (12.66)$$

I like to interpret this equivalence by considering a cylinder of radius,  $a$ , having the same volume of the sphere of that radius, making the height,  $h$ , of such a cylinder equal to  $4a/3$ . In that picture, the volume velocity,  $|\hat{\mathbf{U}}(a)|$ , generated by the disk that forms one end of the cylinder, with area,  $A_{pist} = \pi a^2$ , is simply  $|U(a)| = A_{pist} |\hat{\mathbf{u}}_0|$ . If the separation of the ends is set equal to  $|\vec{d}| = h = 4a/3$ , then the source strength of the “equivalent” cylinder is the same as that of the sphere to within 6% (0.5 dB):  $\left| \vec{d}\hat{\mathbf{U}}(a) \right|_{sphere} = 1.06 \left| \vec{d}\hat{\mathbf{U}}(a) \right|_{cylinder}$ .

### 12.6.1 Scattering from a Compact Density Contrast

Having expressed the dipole strength of an incompressible sphere executing translational oscillations in Eq. (12.66), the scattering produced by such a compact inhomogeneity, due to its presence in a sound field, can be calculated by determining the relative motion of the fluid and the center of the sphere.<sup>13</sup> If we assume a plane wave, then the free-field complex pressure amplitude at the sphere’s location in the absence of the rigid sphere would be  $\hat{\mathbf{p}}_{ff}$ . The complex amplitude of the net translational force,  $\hat{\mathbf{F}}$ , will be the integral of that pressure over the surface of the sphere in the direction determined by the gradient of the pressure where  $\hat{n} = \vec{k}/|\vec{k}|$  is the unit vector in the same direction as the plane wave’s propagation and  $\hat{\mathbf{v}} = \hat{\mathbf{p}}_{ff}/\rho_m c$  is the free-field fluid particle velocity amplitude [33].

$$\begin{aligned} \hat{\mathbf{F}} &= \oint_S \hat{\mathbf{p}}_{ff} d\vec{S} \cdot \hat{n} = j\omega \rho_m V_{sphere} \hat{\mathbf{v}} \left( 3 \frac{\sin(ka) - ka \cos(ka)}{(ka)^3} \right) \\ \hat{\mathbf{F}} &= j\omega \rho_m V_{sphere} \hat{\mathbf{v}} (1 - \beta) \quad \text{where } \beta \cong \frac{(ka)^2}{10} - \frac{(ka)^4}{280} + \dots \end{aligned} \quad (12.67)$$

For a compact source,  $ka \ll 1$ , so  $\beta$  can usually be neglected.

The complex velocity amplitude of the sphere,  $\hat{\mathbf{u}}_0$ , that appears in Eq. (12.66), is determined by the one-dimensional linearized Euler equation.

$$-\frac{\partial (\hat{\mathbf{p}}_{ff} e^{j(\omega t - k|\vec{r}|)})}{\partial |\vec{r}|} = \rho_m \frac{\partial (\hat{\mathbf{v}} e^{j(\omega t - k|\vec{r}|)})}{\partial t} = j\omega \rho_m \hat{\mathbf{u}}_0 e^{j(\omega t - k|\vec{r}|)} \quad (12.68)$$

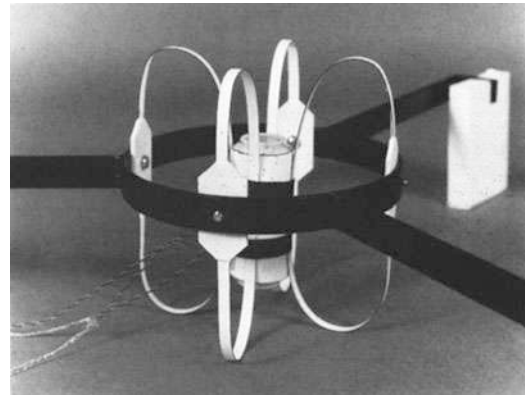
The net force can then be approximated by the product of the free-field pressure gradient and the volume of the rigid sphere.

$$\hat{\mathbf{F}} \cong - \left( \frac{\partial (\hat{\mathbf{p}}_{ff} e^{j(\omega t - k|\vec{r}|)})}{\partial |\vec{r}|} \right) V_{sphere} = j\omega \rho_m \hat{\mathbf{u}}_0 V_{sphere} e^{j(\omega t - k|\vec{r}|)} \quad \text{if } \beta = 0 \quad (12.69)$$

If there are no other external forces on the sphere’s surface (possibly produced by the some elastic suspension system like that shown in Fig. 12.23) and no other contributions to fluid flow (possibly

<sup>13</sup> In this treatment, the fluid is assumed to be inviscid so that there are no shear forces involved in the scattering process.

**Fig. 12.23** Neutrally buoyant fluid particle velocity sensor and its suspension system. The four white plastic loops provide the elastic suspension system for the neutrally buoyant geophone (see Sect. 2.6 and Figs. 2.22 and 2.23) at the center which is 8 cm long and 3.5 cm in diameter [33]



produced by the sphere being subjected to a steady current), then it is possible to determine the ratio of the sphere's velocity amplitude,  $\hat{\mathbf{u}}_0$ , to the free-field fluid particle velocity,  $\hat{\mathbf{v}}$ , in the absence of the sphere [34].

$$\left| \frac{\hat{\mathbf{u}}_0}{\hat{\mathbf{v}}} \right| = \frac{3\rho_m}{\rho_m + 2\rho_s} \quad \text{where } \rho_s = \frac{m_{sphere}}{V_{sphere}} \quad (12.70)$$

This result demonstrates that the velocity of a spherical volume which has a non-zero *density contrast* with the surrounding fluid will move at a velocity that is not the same as the surrounding fluid.

This result is plausible in the limit of a neutrally buoyant sphere that has the same effective density as the surrounding fluid,  $\rho_s = \rho_m$ , since such an inhomogeneity must move with the fluid. Also, an immobile rigid sphere that is somehow constrained would have an infinite effective density,  $\rho_s = \infty$ , thus producing  $|\hat{\mathbf{u}}_0| = 0$ , based on Eq. (12.70), as implied by its assumed immobility.

The more interesting consequence of Eq. (12.70) is that an object that is less dense than the surrounding medium (e.g., a bubble) “moves ahead” of the fluid (see Problem 14). For a very low effective density object, like a gas bubble in a liquid,  $\rho_s \ll \rho_m$ ,  $\hat{\mathbf{u}}_0 = -3\hat{\mathbf{v}}$ . In the case of scattering of sound by a bubble, this increase in translational velocity is not nearly as important as the fact that such a compressible object will radiate as a monopole when driven by  $\hat{\mathbf{p}}_{ff}$ . For the case of a fish with a gas-filled swim bladder, the tripling of the bladder’s velocity makes it a much more sensitive detector of the acoustically induced motion of the surrounding fluid motion (see Problem 5).

Since a neutrally buoyant object with  $\rho_s = \rho_m$  moves with the surrounding fluid, it is possible to make a dipole sensor by instrumenting the object with some inertial vibration sensor, like an accelerometer or a geophone (see Sect. 2.6). One advantage of such a dipole sensor over the subtraction of two monopole (omnidirectional) sensors is that there is no requirement that the two omnidirectional sensors have exactly the same sensitivity and frequency response to guarantee that resulting minimum in the directional pattern has zero sensitivity. A laboratory version of such a velocity sensor that incorporates a geophone as the motion sensor is shown in Fig. 12.23. A high-sensitivity, low-noise, two-axis fiber-optic interferometric accelerometer [35] in a neutrally buoyant case could also serve as a two-axis velocity sensor [36].

Having an expression that relates the translational velocity of a solid object driven by an externally imposed sound field to the velocity of the surrounding fluid makes it possible to use Eq. (12.49) to calculate the relative velocity amplitude,  $\hat{\mathbf{v}}_{rel}$ , of the rigid sphere with respect to the fluid’s velocity,  $\hat{\mathbf{v}} = \hat{\mathbf{p}}_{ff}/(\rho_m c)$ .

$$\hat{\mathbf{v}}_{\text{rel}} = \hat{\mathbf{u}}_0 - \hat{\mathbf{v}} = \frac{2(\rho_m - \rho_s)}{(\rho_m + 2\rho_s)} \hat{\mathbf{v}} = \frac{2(\rho_m - \rho_s)}{(\rho_m + 2\rho_s)} \frac{\hat{\mathbf{p}}_{\text{ff}}}{\rho_m c} \quad (12.71)$$

For the infinitely dense sphere (i.e., fixed and rigid),  $\hat{\mathbf{v}}_{\text{rel}} = -\hat{\mathbf{v}}$ ; the relative velocity is the negative of the fluid's velocity. The equivalent dipole scattering strength,  $\left| \vec{d}\hat{\mathbf{U}}(a) \right|_{\text{sphere}}$ , is given by Eq. (12.66) in terms of the relative velocities of the sphere and the fluid.

$$\left| \vec{d}\hat{\mathbf{U}}(a) \right|_{\text{sphere}} = \frac{3V_{\text{sphere}}}{\sqrt{2}} \frac{(\rho_m - \rho_s)}{(\rho_m + 2\rho_s)} \frac{\hat{\mathbf{p}}_{\text{ff}}}{\rho_m c} \quad (12.72)$$

Substitution into the expression for the dipole's far-field pressure in Eq. (12.48) provides the scattered acoustic pressure,  $p_{\text{scat}}(|\vec{r}|, \theta_d)$ , in terms of the incident acoustic pressure,  $\hat{\mathbf{p}}_{\text{ff}}$ .

$$\begin{aligned} p_{\text{scat}}(|\vec{r}|, \theta_p) &= \Re e \left\{ -jk^2 \hat{\mathbf{p}}_{\text{ff}} e^{j(\omega t - k|\vec{r}|)} \frac{3V_{\text{sphere}}}{4\pi\sqrt{2}} \frac{1}{|\vec{r}|} \left( \frac{\rho_m - \rho_s}{\rho_m + 2\rho_s} \right) \cos \theta_p \right\} \\ &= \Re e \left\{ \frac{-j(ka)^2}{\sqrt{2}} \hat{\mathbf{p}}_{\text{ff}} e^{j(\omega t - k|\vec{r}|)} \left( \frac{a}{|\vec{r}|} \right) \left( \frac{\rho_m - \rho_s}{\rho_m + 2\rho_s} \right) \cos \theta_p \right\} \end{aligned} \quad (12.73)$$

The second expression assumes that the scattering volume is spherical. Although this treatment ignores the viscous forces on the rigid sphere, it can be shown, using the results of Sect. 9.4, that such forces are usually negligible in the limit that  $ka \ll 1$  [33].

The far-field intensity is proportional to the square of the acoustic pressure, as given by Eq. (10.40), so the ratio of the time-averaged scattered intensity,  $\langle I_{\text{scat}} \rangle_t$ , to the free-field time-averaged incident intensity,  $\langle I_{\text{ff}} \rangle_t$ , is proportional to  $(ka)^4$ .

$$\left| \frac{\langle I_{\text{scat}} \rangle_t}{\langle I_{\text{ff}} \rangle_t} \right| = \left( \frac{p(|\vec{r}|, \theta_p)}{|\hat{\mathbf{p}}_{\text{ff}}|} \right)^2 = \frac{(ka)^4}{2} \left( \frac{a}{|\vec{r}|} \right)^2 \left( \frac{\rho_m - \rho_s}{\rho_m + 2\rho_s} \right)^2 \cos^2 \theta_p \quad (12.74)$$

The dependence of the scattered intensity has the same  $\omega^4$  frequency dependence as the scattering of light, known as *Rayleigh scattering*, which accounts for the blue color of the sky [37, 38]. In the case of light scattering from molecules, the cause is different: the electromagnetic wave induces a fluctuating dipole moment and that oscillating dipole radiates the scattered electromagnetic wave.

For the description of a scattering object's ability to produce scattered energy, it is convenient to express the ratio of the scattered power to the incident intensity in terms of a *differential scattering cross section*,  $d\sigma/d\Omega$ , with units of [ $\text{m}^2/\text{steradian}$ ]. It is the ratio of the time-averaged power scattered into a given solid angle element,  $d\Omega = \sin \theta d\theta d\varphi$ , to the mean energy flux density of the incident wave (i.e., the intensity). The integral of  $d\sigma/d\Omega$  over all solid angle is the *total scattering cross section*,  $\sigma$ . Again, using the definite integral of Eq. (12.54), the total scattering cross-section for the rigid sphere of effective density,  $\rho_s$ , can be calculated.

$$\sigma = (\pi a^2)(ka)^4 \frac{28}{9} \left( \frac{\rho_m - \rho_s}{\rho_m + 2\rho_s} \right)^2 \quad \text{for } ka \ll 1 \quad (12.75)$$

In the above form, it is clear that an incompressible (i.e., rigid) spherical region with a density that is different from the surrounding medium scatters far less power than the incident plane wave intensity times the contrast region's physical cross-sectional area,  $\pi a^2$ . The density contrast factor is also limited to

a small range:  $1 \geq [(\rho_m - \rho_s)/(\rho_m + 2\rho_s)]^2 \geq 0$ . If the sphere is immobilized (i.e.,  $\rho_s = \infty$ ), then  $\sigma = (7/9)(\pi a^2)(ka)^4$ . A similar result for a thin disk of radius,  $a_{disk}$ , is  $\sigma_{disk} = (16/27)(\pi a_{disk}^2)(ka_{disk})^4$  [39].

### 12.6.2 Scattering from a Compact Compressibility Contrast

The same strategy can be employed to determine the scattered pressure field due to a plane wave that impinges on a compact region that has a different compressibility than the surrounding medium. The adiabatic compressibility,  $K_s$ , of the surrounding medium is the reciprocal of its adiabatic bulk modulus,  $B_s$ , so by Eq. (10.21),  $K_s = B_s^{-1} = (\rho_m c^2)^{-1}$ . Again, for a compact scatterer, the shape of the scattering body is irrelevant.<sup>5</sup> For convenience, the compact *compressibility contrast* region will be treated as a sphere with volume,  $V_{sphere} = 4\pi a^3/3$ .

The radius of the sphere,  $a$ , will be modulated by the amplitude of the incident pressure wave,  $\hat{\mathbf{p}}_{ff}$ , that is assumed to arise due to a traveling plane wave. The volume change of that scatterer is related to the bulk modulus of the fluid in that compact region by Eq. (10.20).

$$\delta V = 3V_{sphere} \frac{\delta a}{a} = 3V_{sphere} \frac{|\hat{\xi}|}{a} = -V_{sphere} \frac{|\hat{\mathbf{p}}_{ff}|}{B_s} = -V_{sphere} \frac{|\hat{\mathbf{p}}_{ff}|}{\rho_s c_s^2} \quad (12.76)$$

In this case,  $\rho_s$  is the density of the fluid in the compact scattering region, and  $c_s^2$  is the square of the sound speed of that contrasting fluid.

Just as the relative velocity of the fluid and the sphere in Eq. (12.71) was used to calculate the dipole strength in Eq. (12.72), the induced volume change,  $\delta V$ , in Eq. (12.76), must be compared to the change in the equilibrium volume of a region with equal volume if the medium were uniformly compressible. That difference between the volume change in the region with the compressibility contrast and the volume change that would have occurred can be used to calculate the amplitude of the equivalent scattering volume velocity,  $\hat{\mathbf{U}}_{scat}(a)$ .

$$\hat{\mathbf{U}}_{scat}(a) = -\omega \hat{\mathbf{p}}_{ff} \frac{V_{sphere}}{\rho_s c_s^2} \left( 1 - \frac{\rho_s c_s^2}{\rho_m c^2} \right) \quad (12.77)$$

If the compressibility of the scattering region is the same as that of the surrounding fluid, then  $|\hat{\mathbf{U}}_{scat}(a)| = 0$ , as it must, so that there is no scattered wave if there is no inhomogeneity. If the scattering region is much more compressible than the surrounding fluid (e.g., a gas-filled bubble in water), then the more compressible medium dominates the induced volume velocity; hence  $|\hat{\mathbf{U}}_{scat}(a)| = \omega \delta V$ , where  $\delta V$  is given by Eq. (12.76).

A particularly interesting case is the incompressible sphere, where  $\rho_s c_s^2 \gg \rho_m c^2$ . For a steel sphere,  $\rho_s c_s^2 \cong 290$  GPa, and for water,  $\rho_s c_{H_2O}^2 \cong 2.25$  GPa. For air under standard conditions,  $\rho_m c^2 = \gamma p_m \cong 142$  kPa. In that case,  $\hat{\mathbf{U}}_{scat}(a)$  is determined by the compressibility of the medium (not the sphere),  $\rho_m c^2$ , thus producing a scattered wave that satisfies the rigid boundary condition at the sphere,  $\delta V = 0$  and  $\delta a = |\hat{\xi}| = 0$ , when combined with the incident wave.

The source strength in Eq. (12.77) will produce isotropic spherical acoustic pressure waves,  $p(|\vec{r}|)$ , with an amplitude determined by Eq. (12.21), where the contrasting compressible region is again represented by a sphere of volume,  $V_{sphere} = 4\pi a^3/3$ .

$$\frac{p(|\vec{r}|)}{|\hat{\mathbf{p}}_{ff}|} = \frac{(ka)^2}{3} \left( \frac{a}{|\vec{r}|} \right) \left( \frac{\rho_m c^2}{\rho_s c_s^2} - 1 \right) \quad (12.78)$$

The far-field intensity is proportional to the square of the acoustic pressure, as given by Eq. (10.40), so the ratio of the time-averaged scattered intensity,  $\langle I_{scat} \rangle_t$ , to the time-averaged free-field incident intensity,  $\langle I_{ff} \rangle_t$ , is proportional to  $(ka)^4$ , as it was for the rigid sphere in Eq. (12.74). Integration over all solid angle to obtain the total scattering cross-section is simplified, since this scattered sound field is isotropic.

$$\sigma = \frac{4}{9} (\pi a^2) (ka)^4 \left( \frac{\rho_m c^2}{\rho_s c_s^2} - 1 \right)^2 \quad \text{for } ka \ll 1 \quad (12.79)$$

Again, the total scattering cross-section,  $\sigma$ , will be smaller than the geometrical cross-section,  $\pi a^2$ , by a factor of  $(ka)^4$ , as it was in Eq. (12.75), except the density contrast factor,  $\left[ (\rho_m c^2 / \rho_s c_s^2) - 1 \right]^2$ , can be very large. For air trapped near the water surface,  $\left[ (\rho_{H_2O} c_{H_2O}^2 / \rho_{air} c_{air}^2) - 1 \right]^2 = 2.5 \times 10^8$ . Under such circumstances, the total scattering cross-section can be much larger than the physical cross section. For the case of a bubble being driven at frequencies near its Minnaert frequency, it can be even larger.

### 12.6.3 Scattering from a Single Bubble or a Swim Bladder

The results of the previous section are correct as long as the sound field driving the compressions and expansions of the compressibility contrast region occur at frequencies below the Minnaert frequency in Eq. (12.30). Although that frequency was calculated in Sect. 12.3, as it applied to a stable spherical gas-filled bubble in a liquid, the result is generally applicable to any compressible region regardless of the shape, as long as that region is compact [8].

Any periodic change in volume of that region requires that the surrounding fluid be accelerated. The acceleration of the surrounding fluid is conveniently represented by an effective (hydrodynamic) mass, calculated in Eq. (12.15), that is equal to three times the mass of the fluid displaced by the compressible region's volume. The competition between the compressibility of the contrast region and the inertia of the surrounding fluid will drive quasi-one-dimensional harmonic oscillations with the variation in the radius of the bubble,  $\xi_1(t) = \Re e[\hat{\xi} e^{j(\omega t)}] = \Re e[\hat{\xi} e^{j(\omega t + \Theta)}]$ , where the phase,  $\Theta$ , has been included explicitly to emphasize the fact that the response of the bubble's radius to the varying pressure produced by the incident wave will not necessarily be in-phase with the acoustic pressure that is driving the bubble, as would be the case for any driven simple harmonic oscillator (see Sect. 2.5.1).

Recall that if the forcing function is applied at a frequency,  $\omega$ , below the natural frequency,  $\omega_o$ , which would be the Minnaert frequency of Eq. (12.30) or Eq. (12.31), then the driven system is stiffness-controlled. In the case of the bubble, this means that the bubble's radius,  $a + \xi_1(t)$ , will decrease when the acoustic pressure due to the incident sound wave increases. With  $\omega < \omega_o$ , the inertia of the surrounding fluid is not important in determining the bubble's response, and the expression for the resultant volume velocity,  $\hat{\mathbf{U}}_{scat}(a)$ , given in Eq. (12.77), will provide an accurate representation of the spherically symmetric scattered sound field when substituted into the monopolar transfer impedance of Eq. (12.22).

If the incident wave has a frequency that is larger than the Minnaert frequency, the bubble's behavior is mass controlled and therefore dominated by the inertia of the surrounding fluid. In this

limit, there are two interesting differences. The first is that above resonance, the phase will shift by nearly  $180^\circ$ . This fact was exploited to extend the low-frequency performance of a bass-reflex loudspeaker enclosure in Sect. 8.8. The radius of the bubble will grow when the acoustic pressure of the incident wave is positive. Also, as the frequency increases above  $\omega_o$ , the radial velocity of the bubble's surface will decrease.

If the incident sound field is oscillating at a frequency very close the bubble's natural frequency,  $\omega \approx \omega_o$ , then the bubble's motion will be resistance-controlled so that the amplitude of the bubble's radial velocity will be determined by its quality factor, calculated in Sect. 12.3.1.

Treating the bubble as a quasi-one-dimensional simple harmonic oscillator, the force is determined by the free-field pressure amplitude of the incident wave,  $\hat{\mathbf{p}}_{\text{ff}}$ , times the mean surface area of the bubble,  $4\pi a^2$ , assuming that  $ka \ll 1$ , so that  $\hat{\mathbf{p}}_{\text{ff}}$  is uniform over the bubble's surface. The bubble's radial velocity,  $\dot{\xi}_1(t) = \Re e[j\omega \hat{\xi} e^{j\omega t}]$ , in response to the pressure's driving force, is given by the mechanical impedance in Eq. (2.62).

$$\left| \hat{\mathbf{U}}_{\text{scat}}(a) \right| = 4\pi a^2 \dot{\xi}_1 = (4\pi a^2)^2 \frac{|\hat{\mathbf{p}}_{\text{ff}}|}{|\mathbf{Z}_{\text{mech}}|} = \frac{12\pi a}{\rho_m \omega_o} \frac{|\hat{\mathbf{p}}_{\text{ff}}|}{\left[ \left( \frac{\omega}{\omega_o} - \frac{\omega_o}{\omega} \right)^2 + \frac{1}{Q^2} \right]^{1/2}} \quad (12.80)$$

The acoustic transfer impedance of Eq. (12.22),  $\mathbf{Z}_{\text{tr}}$ , relates the isotropically scattered pressure,  $p(r)$ , to the complex incident acoustic pressure amplitude,  $\hat{\mathbf{p}}_{\text{ff}}$ .

$$p(|\vec{r}|) = \mathbf{Z}_{\text{tr}} |\hat{\mathbf{U}}_{\text{scat}}(a)| \Rightarrow \frac{p(|\vec{r}|)}{|\hat{\mathbf{p}}_{\text{ff}}|} = 3 \left( \frac{a}{|\vec{r}|} \right) \left( \frac{\omega}{\omega_o} \right) \left[ \left( \frac{\omega}{\omega_o} - \frac{\omega_o}{\omega} \right)^2 + \frac{1}{Q^2} \right]^{-1/2} \quad (12.81)$$

In the limit of low frequencies,  $\omega < \omega_o$ , Eq. (12.81) recovers the  $(ka)^2$  dependence of the radiated pressure from Eq. (12.78).

$$\lim_{\omega \rightarrow 0} \left[ \frac{p(|\vec{r}|)}{|\hat{\mathbf{p}}_{\text{ff}}|} \right] = 3 \left( \frac{a}{|\vec{r}|} \right) \left( \frac{\omega}{\omega_o} \right)^2 \propto (ka)^2 \quad (12.82)$$

At frequencies above the Minnaert frequency, the radiated pressure is independent of the driving frequency.

As before, the scattered pressure in Eq. (12.81) can be used to calculate the total scattering cross-section for a resonant bubble as a function of the driving frequency [40].

$$\sigma = \frac{(4\pi a^2)(\omega/\omega_o)^2}{\left[ \left( \frac{\omega}{\omega_o} - \frac{\omega_o}{\omega} \right)^2 + \frac{1}{Q^2} \right]} \quad (12.83)$$

Using the 1.0 mm diameter air-filled bubble at a depth of 10 m, which was the example at the end of Sect. 12.3.1, we can evaluate Eq. (12.83) at  $f_o = 20.6$  kHz with  $Q_{\text{total}} = 47$ . With  $c_{H_2O} = 1500$  m/s,  $(ka) = 0.043 \ll 1$ . Figure 12.24 plots the ratio of the total scattering cross-section to the bubble's geometric cross-section,  $4\pi a^2$ , as a function of frequency. At resonance, the bubble's scattering cross-section is  $Q^2 = 2210$  times larger than its geometrical cross-section. Resonant scattering from bubbles or other gas-filled density contrast regions, like fish swim bladders, shown in Fig. 12.23, can be significant.

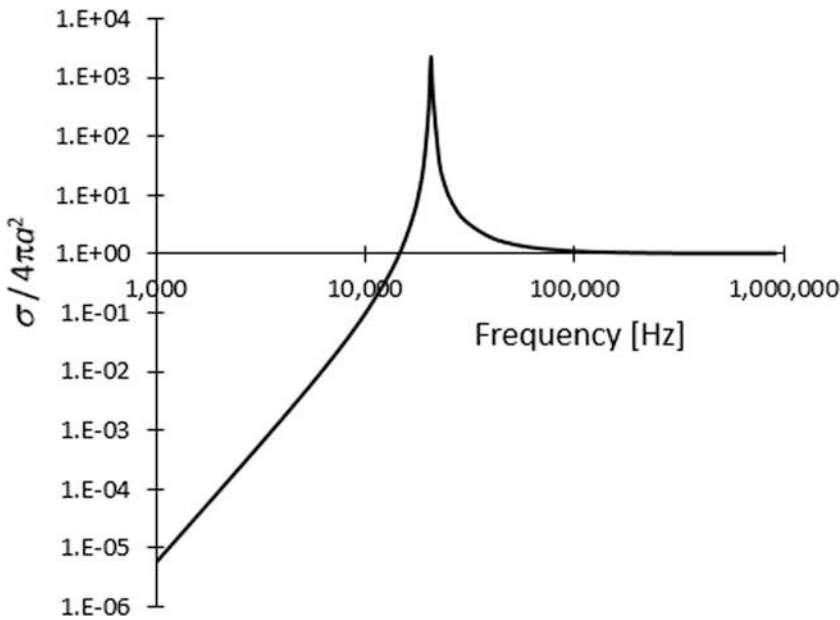


**Fig. 12.24** Ratio of the scattering cross-section,  $\sigma$ , for a 1 millimeter diameter air-filled bubble, 10 m below the surface, to the bubble's geometric cross-sectional area,  $4\pi a^2$ . That bubble's Minnaert frequency is  $f_o = 20.6$  kHz and its quality factor is  $Q_{total} = 47$

#### 12.6.4 Multiple Scattering in the “Effective Medium” Approximation

Multiple scattering of sound from a large number of small objects can require rather complicated computations. Like many topics addressed in this textbook, there are limiting cases that can be solved quite easily and which are both important and illustrate an approach with more general utility. If the scatterers are identical and if they are spaced in a regular lattice, then those regularly spaced identical inhomogeneities will behave as a diffraction grating, and there will be specific directions that will experience large scattered wave amplitudes at certain frequencies. The formalism that can address that case for a regular one-dimensional array of identical scattering object will be the focus of Sect. 12.7.

Another interesting and important case is that of a medium that has a dispersion of scattering particles that are positioned randomly and have a variety of different sizes. Such a medium might be a “bubble cloud” if the scatters were gas bubbles of different sizes in a fluid medium or a fog consisting of liquid droplets dispersed within a gaseous medium. For both the bubble cloud and the fog, if the  $(k\bar{a}) \ll 1$ , for the effective average scatterer radius,  $\bar{a}$ , and if there is a high number density of compact scattering regions, then an approach known as the *mean field approximation* can create a useful representation of multiple scattering.

In the long wavelength limit at frequencies much lower than the lowest bubble resonance frequency of the largest bubble, a bubble cloud will have an effective density that is close to that of the liquid, but its compressibility will be dramatically larger than the liquid, even if the gaseous fraction is small. This can result in a sound speed within the bubble cloud that is slower than the speed of sound in either the surrounding liquid or the gas that fills the bubbles. In a fog, the sound speed will be close to that of the speed in the pure gas since the presence of fluid droplets produces only a small increase in both the mean bulk modulus and the mean density.

Such a mean field approximation can be developed by considering the volume fraction of each component.<sup>14</sup> For a bubble cloud, the minority species is the gas phase that occupies a volume fraction,  $x$ . The liquid phase occupies the remaining volume,  $(1 - x)$ . The effective density of the mixture can be approximated by the mass density weighted fraction of the individual components' mass densities.

$$\rho_{mean} = x\rho_{gas} + (1 - x)\rho_{liquid} \quad (12.84)$$

The mean field bulk modulus,  $B_{mean}$ , can be calculated by remembering that the stiffness of two springs that are placed in series is the parallel combination of their individual stiffnesses (see Sect. 2.2.1).

$$B_{mean} = \left[ \left( \frac{x}{B_{gas}} \right) + \left( \frac{1 - x}{B_{liquid}} \right) \right]^{-1} \quad (12.85)$$

Using the definition of the sound speed in Eq. (10.21), Eqs. (12.84) and (12.85) can be combined to produce an effective sound speed,  $c_{eff}$ , for the mixture.

$$\frac{1}{c_{eff}^2} = \frac{\rho_{mean}}{B_{mean}} = \left[ x\rho_{gas} + (1 - x)\rho_{liquid} \right] \left[ \left( \frac{x}{B_{gas}} \right) + \left( \frac{1 - x}{B_{liquid}} \right) \right]^{-1} \quad (12.86)$$

Figure 12.25 is a plot of that effective sound speed for a bubble cloud with air at atmospheric pressure ( $\rho_{gas} = 1.21 \text{ kg/m}^3$ ,  $B_{gas} = 142 \text{ kPa}$ ) and water ( $\rho_{liquid} = 1000 \text{ kg/m}^3$ ,  $B_{liquid} = 2.25 \text{ GPa}$ ). As required, the effective sound speed is equal to the speed of sound in pure water,  $c_{H_2O} = 1500 \text{ m/s}$ , if there are no bubbles ( $x = 0$ ), and the speed of sound in air,  $c_{Air} = 344 \text{ m/s}$ , when there is no water ( $x = 1$ ). There is also a substantial range of gas volume fractions (sometime called *void fractions*)

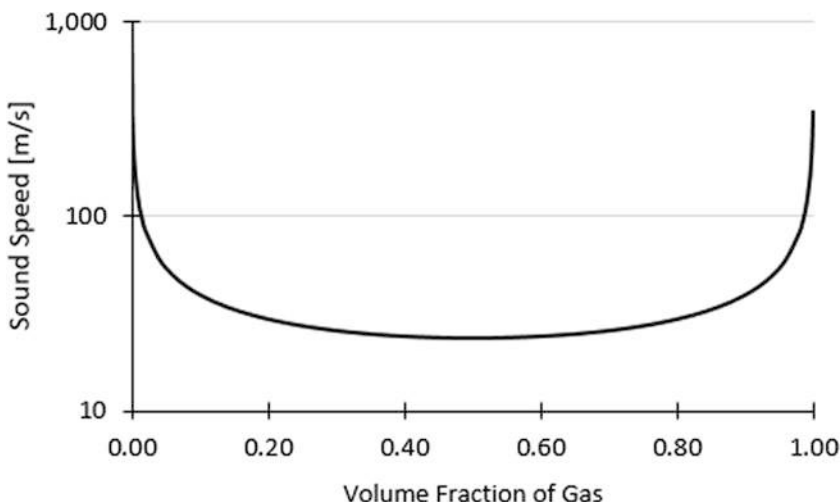


**Fig. 12.25** Effective sound speed in a bubble cloud as a function of gas volume fraction if the dispersion of bubbles with various radii contains air near atmospheric pressure and the surrounding liquid is water. It is assumed that all the bubbles are small enough that  $(k\bar{a}) \ll 1$ , and the frequencies of interest are all well below the lowest bubble resonance frequency. At zero void fraction, the speed is just that in pure water

<sup>14</sup>In this simplified treatment, it is assumed that the gas in the bubbles is not condensable so that the evaporation and condensation of the liquid's vapor can be ignored. A more complete theory that incorporates evaporation and condensation for both bubbles and for fogs is given in Ref. [3], §64, Problems 1 (bubbles) and 2 (fog).

where the sound speed is much less than the sound speed in air. For  $0.01 < x < 0.99$ ,  $c_{\text{eff}} < 100$  m/s and for  $0.06 < x < 0.94$ ,  $c_{\text{eff}} < 50$  m/s, with a broad minimum effective sound speed of 24 m/s around  $x = 0.50$  [41]<sup>15</sup>

The very low value of  $c_{\text{eff}}$  for a bubbly liquid can be observed if cocoa powder is placed in a mug that is then filled with hot water. The air trapped in the powder will form bubbles that will rise and coalesce over the span of less than a minute. If the mug is tapped with a spoon, the frequency of the sound will change with time, rising in pitch as the bubbles move to the surface. In some cases, the frequency change can be more than three octaves. This rise in pitch is commonly known as “the hot chocolate effect” [42].

The same effect can also be observed when a glass is filled with hot tap water, particularly if the tap is partially throttled. The water will be cloudy due to the formation of small bubbles that will coalesce and rise causing the pitch of the quarter wavelength standing wave resonance (assuming the bottom is rigid and the top is a pressure-released surface) that is excited in the bubbly liquid to increase in frequency.

The sound speed reduction due to the introduction of bubbles in a solvent has developed into a technique for the analysis of transient dissolution processes for chemical compounds that is known as Broadband Acoustic Resonance Dissolution Spectroscopy (BARDS) [43]. Various extensions of this approach have been developed to study other effects like wettability of pharmaceutical powders [44].

The effect on sound speed is not nearly as dramatic for a fog of small liquid droplets suspended in a gaseous medium. For small droplet concentrations, the stiffness of the gas is increased slightly because the relatively incompressible liquid droplets exclude some of the more compressible gas volume. That effect is overwhelmed by the increase in the medium’s effective mass density, although at typical droplet volume fractions, the reduction in the effective sound speed is small.

## 12.7 N-Element Discrete Line Array

The same procedure we applied to the superposition of two compact sources of equal source strength and frequency in Sect. 12.4 can be applied to any number,  $N$ , of such sources that are separated by a uniform distance,  $d$ , between adjacent sources along a line. Figure 12.26 provides a coordinate system where we measure the angle,  $\theta$ , above the plane normal to the line joining the sources, with  $|\vec{r}|$  as distance from the central source to the observation point. As before, there will be no azimuthal dependence to sound field due to the rotational symmetry about the axis joining the sources.

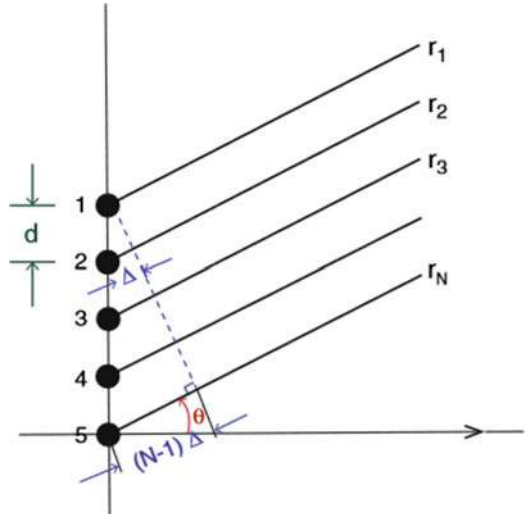
As before, we can sum the contribution of each simple source at the observation point a distance,  $r_n$ , from the  $n$ th element, where  $n = 0, 1, 2, \dots, (N - 1)$ .

$$p(r, t) = \Re e \left[ \sum_{n=0}^{N-1} \frac{\hat{\mathbf{C}}_n}{r_n} e^{j(\omega t - kr_n + \phi_n)} \right] \quad (12.87)$$

Each straight-line path from each source to the observation point has a different length. In the far-field approximation ( $kr \gg 1$ ), these path length differences,  $\Delta r_n$ , have little effect on the relative pressure amplitude radiated to the observation point but can produce a significant difference in the summation through their associated phase differences. Using the geometry of Fig. 12.26, the dashed blue line is drawn perpendicular to each propagation path providing the difference in the propagation distance that

<sup>15</sup>This result is known as “Wood’s equation.” In the first edition of A. B. Wood, *A Textbook of Sound* (MacMillan, New York, 1930), Wood quotes Mallock’s result from [40], but in the second edition, there is no mention of Mallock.

**Fig. 12.26** Coordinate system for the superposition of  $N = 5$  compact sources that are separated from each other by a uniform distance,  $d$ . The resultant sound field will be symmetric about the line joining the sources so that there will be no azimuthal variation. The dashed black lines illustrate the path length differences between the observation point a distance,  $r_1$ , from the top source and the individual paths



is proportional to the  $n$ -index of each source and to the inter-element separation,  $d$ , between adjacent sources.

$$\Delta r_n = nd \sin \theta \equiv n\Delta \quad (12.88)$$

Considering sources of equal amplitude,  $\hat{\mathbf{C}}_n = C$ , that are all oscillating in-phase,  $\phi_n = \phi = 0^\circ$ , then both  $C_n$  and  $r_n \approx r$  can be brought out in front of the summation of Eq. (12.87).

$$p(|\vec{r}|, \theta, t) = \frac{C}{|\vec{r}|} \Re \left[ e^{j(\omega t - k|\vec{r}|)} \sum_{n=0}^{N-1} e^{-j(nk\Delta)} \right] \quad (12.89)$$

The summation has been transformed to a geometric series that can be evaluated by standard techniques [45].

$$\sum_{k=1}^n aq^{k-1} = \frac{a(1 - q^n)}{1 - q}; \quad q \neq 1 \quad (12.90)$$

Application of Eq. (12.90) to Eq. (12.89) results in the geometric series where  $q \equiv e^{-jk\Delta}$ .

$$\sum_{n=0}^{N-1} q^n = \frac{1 - e^{-jkN\Delta}}{1 - e^{-jk\Delta}} = \left[ \frac{\sin(kN\Delta/2)}{\sin(k\Delta/2)} \right] \quad (12.91)$$

We are left with the desired directionality,  $H(\theta)$ , with an axial pressure that is  $N$  times the amplitude of each individual source [46].

$$H(\theta) = \left| \frac{\sin(N \frac{kd}{2} \sin \theta)}{N \sin(\frac{kd}{2} \sin \theta)} \right| \quad (12.92)$$

To appreciate the discrete line array's directionality,  $H(\theta)$ , it is useful to plot both the numerator and denominator of Eq. (12.92) separately. Figure 12.27 provides such a graph, as well as the absolute value of the ratio, for the case where  $kd = 8$  (so  $d = 8\lambda/2\pi = 1.273\lambda$ ) and  $N = 5$ , with all sources radiating in phase ( $\phi_n = 0^\circ$ ).

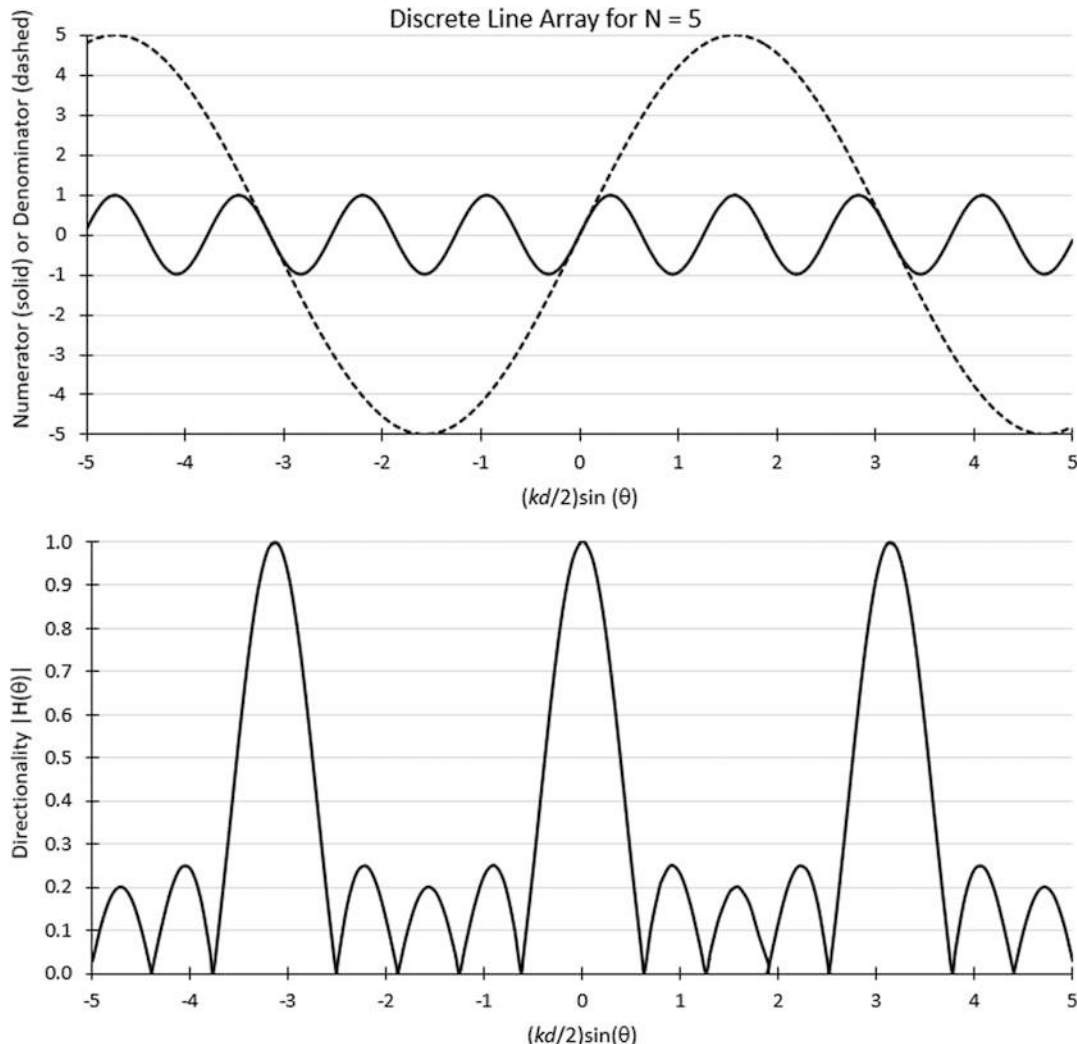


**Fig. 12.27** (Above) Plot of the numerator and denominator of Eq. (12.92) for  $kd = 8$  (so  $d = 8\lambda/2\pi = 1.273\lambda$ ) and  $N = 5$  vs.  $(kd/2)\sin\theta$ . (Below) Absolute value of the numerator divided by the denominator. A polar plot is provided in Fig. 12.28

At the origin ( $\sin\theta = 0$ ), the value of the ratio is unity, as can be shown if you expand both sine functions in a power series and keep only the leading (first-order) terms. The directionality has local maxima when there is a path length difference of one wavelength between adjacent sources. For that case, the denominator vanishes at  $(kd/2)\sin\theta = n\pi$ ;  $n = 0, 1, 2, \dots$ . Since  $N$  is an integer, the numerator also goes to zero.

When the total length of the array,  $L = (N - 1)d$ , is much less than a wavelength, the array behaves like an omnidirectional simple source with a source strength that is  $N$ -times greater than the individual (identical) elements. As the separation increases, the radiated pressure in the polar direction ( $\theta = 90^\circ$ ) decreases until  $d = \lambda/2$ , which produces a minimum at  $\theta = 90^\circ$  if  $N$  is an even number, while the angular width of the major lobe becomes narrower with increasing  $N$ .

The directional pattern of Eq. (12.92) has nulls in directions determined by  $(Nkd/2)\sin\theta = m\pi$ , where  $m = 0, 1, 2, \dots, Nd/\lambda$ . For the central beam ( $\theta = 0^\circ$ ), the nulls occur at  $\sin\theta = \pm\lambda/Nd$ . For large

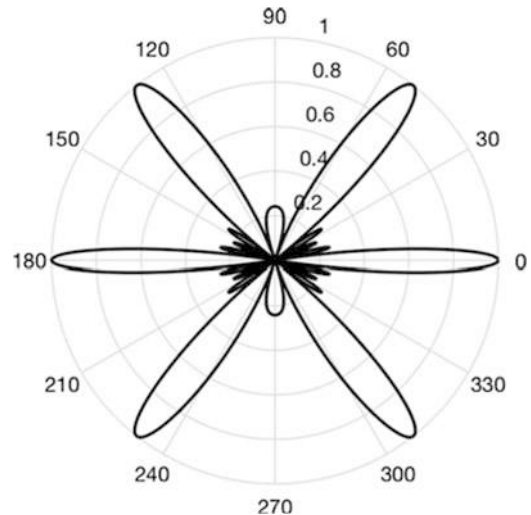
values of  $N$ , the full width<sup>16</sup> of the central maximum is  $2\theta = 2\lambda/Nd \cong 2\lambda/L$ . The beam pattern becomes more “focused” as the length of the array increases. This fact is responsible for the tall line arrays that are visible on stage in Fig. 12.1.

### 12.7.1 Beam Steering and Shading

A discrete line array can produce a narrow beam. Since the previous analysis sets the relative phases of all of the monopole sources to zero, the main lobe was always aligned with the plane that is the perpendicular bisector of the line, as seen in Fig. 12.28. There are applications where the main-lobe directionality of a line array of sources or sensors would be more useful if the main lobe could be steered toward other orientations. This can be accomplished introducing progressive times delays,  $\tau_n$ , to each element in the line array such that  $\tau_n = (n - 1)\tau_1$ , for  $n = 2, 3, 4, \dots$ . Those delays would produce phase shifts,  $\phi_n = (n - 1)\phi_1 = (n - 1)\omega\tau_1$ , that can be included in the exponential factor for each term in the summation of Eq. (12.87). Such delays would be equivalent to increasing or decreasing the path length differences,  $\Delta r_n$ , that were calculated in Eq. (12.88).

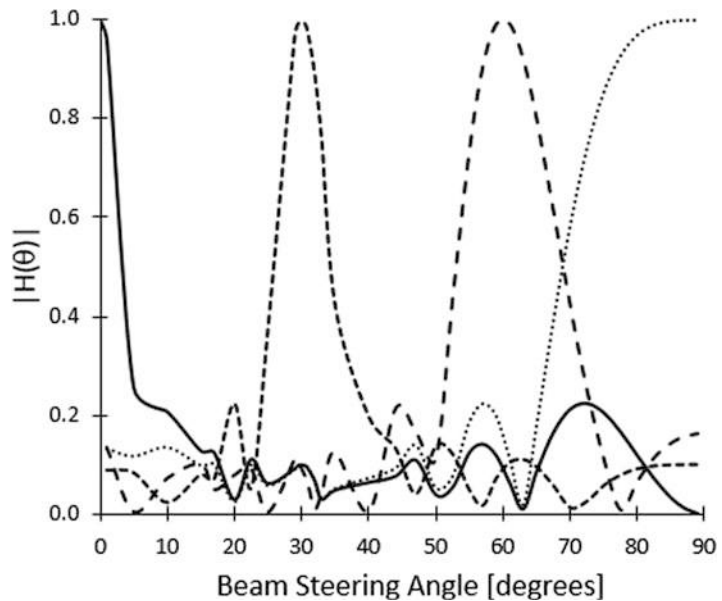
Referring to Fig. 12.26, if the signal sent to the  $n = 2$  element was delayed by the travel time from  $n = 2$  to  $n = 1$ ,  $\tau_2 = d/c$ , then the signal from  $n = 2$  would be in-phase with the signal from  $n = 1$  when it arrived at element 1 and those two signals would add constructively in the direction along their common axis. Similarly, if the  $n = 3$  element was delayed by twice that amount,  $\tau_3 = 2\tau_2$ , the signal from  $n = 3$  would add in-phase to both the delayed  $n = 2$  signal and the  $n = 1$  signal, and their superposition would make the amplitude of the signal be three times as large in the direction along their common axis. Such an arrangement is called an *end-fire array* since the strongest signal radiates from the end of the array along the direction of array’s axis.

**Fig. 12.28** Two-dimensional polar plot of the directionality of a five-element ( $N = 5$ ) discrete array of in-phase sources that are separated by  $d = 8/k$  (so  $d = 8\lambda/2\pi = 1.273 \lambda$ ). It is important to remember that the three-dimensional radiation pattern has azimuthal symmetry so that the actual radiation pattern is obtained if this two-dimensional plot is rotated about the polar ( $90^\circ - 270^\circ$ ) axis



<sup>16</sup> Definitions of “beam width” vary. Above we have defined the width as the angular separation of adjacent nulls. Other common designations of broadside beam width are angular separation of the beam pattern that are  $-3$  dB,  $-6$  dB,  $-10$  dB or  $-20$  dB from the maximum at  $\theta = 0^\circ$ .

**Fig. 12.29** Directionality of an  $N = 10$  element line array that is 8.1 wavelengths long. The solid line represents broadside directivity ( $\theta_\tau = 0^\circ$ ) and produces a -3 dB full width,  $\Delta\theta_{-3\text{dB}} = 2.8^\circ$ . The dotted line represents end-fire directivity ( $\theta_\tau = 90^\circ$ ) and produces a -3 dB full width,  $\Delta\theta_{-3\text{dB}} = 36.2^\circ$ . Also shown are two intermediate cases with  $\theta_\tau = 30^\circ$  (shorter dashed line) having  $\Delta\theta_{-3\text{dB}} = 6.6^\circ$  and  $\theta_\tau = 60^\circ$  (longer dashed line) having  $\Delta\theta_{-3\text{dB}} = 11.5^\circ$



In general, the direction of the main lobe,  $\theta_\tau$ , will be determined by the delay time,  $\tau_1$ , between each radiating element (monopole).

$$\sin \theta_\tau = c\tau_1/d \quad (12.93)$$

If there is no time delay,  $\tau_1 = 0$ , then the axis of the main lobe is on the plane that is the perpendicular bisector of the line joining the  $N$ -elements of the array and  $\theta_\tau = 0^\circ$ . If  $\tau_1 = \pm d/c$ , as in the initial discussion, then  $\theta_\tau = \pm 90^\circ$ , producing the end-fire condition. Introduction of the non-zero phase delays,  $\phi_n$ , in Eq. (12.87), produces the expected modification to the zero delay directionality result in Eq. (12.92).

$$H(\theta) = \frac{\left| \sin \left[ N \frac{kd}{2} (\sin \theta - \sin \theta_\tau) \right] \right|}{N \sin \left[ \frac{kd}{2} (\sin \theta - \sin \theta_\tau) \right]} \quad (12.94)$$

As shown in Fig. 12.29, an undesirable consequence of the beam steering is the broadening of the main lobe as the steering angle increases from broadside ( $\theta_\tau = 0^\circ$ ) to end-fire ( $\theta_\tau = 90^\circ$ ).

The use of modern digital electronics makes the insertion of the individual element time delays both simple and accurate. Long ago, in the era of vacuum tube analog electronics, a low-frequency end-fire array was constructed to produce a directional sound reinforcement system for the Hollywood Bowl in Los Angeles, CA. The Bowl is an outdoor venue with a band shell over the stage area. Since low-frequency sound travels great distances (see Chap. 14), there were complaints from homeowners in the surrounding neighborhood of Griffith Park who were bothered by those sounds.

To produce a directional low-frequency array that would concentrate the reinforcement in the direction of the audience and limit the spreading to the surrounding communities, an analog delay system was constructed that consisted of one loudspeaker at one end of a long tube. The other end of the tube was terminated by an anechoic wedge absorber to eliminate reflections. All along the length of that tube, microphones were inserted, and their delayed signals were amplified to drive individual bass enclosures at the microphone locations. The propagation delay of the sound in the tube was exactly that required to satisfy the end-fire condition,  $\theta_\tau = 90^\circ$ .

As a final comment regarding the practical implementation of line arrays, it is worthwhile to remember that the directionality of a line array is scaled by the ratio of the array's overall length,  $L$ , to the wavelength of the radiated sound,  $\lambda$ . For sound reinforcement systems that are used to enhance musical performances, the range of wavelengths is very large. For that reason, in Fig. 12.1, it is easy to see that the longest arrays are for projection of bass, and the shortest arrays were for treble, with intermediate-length arrays dedicated to the mid-frequencies. Such large sound reinforcement systems are not economically justified for smaller venues.

One common approach to keep the directivity of a line array fairly constant over a significant frequency range is to provide passive cross-over circuits that apply the lowest frequency material to all the speakers in the line array but to provide progressive attenuation to the outer elements for higher frequencies in an attempt to keep the effective length of the array more constant with respect to the wavelength of the radiated sound.

The adjustment of the individual amplitude coefficients,  $C_n$ , that appear in Eq. (12.87) in a discrete line array, produces a *shaded array*. Various shading strategies are also adopted to suppress side lobes, although they always reduce the directivity of the main lobe since they make the effective overall length of the array less than its physical length. Of course, that was the objective of the shading scheme to increase the frequency range of a single array while trying to maintain a more constant directivity. For large numbers of individual elements in an array, combination of delays and shading allow adaptive steering of both beams and nulls. This can be very useful when trying to find quiet targets in environments cluttered by discrete noise sources.

### 12.7.2 Continuous Line Array

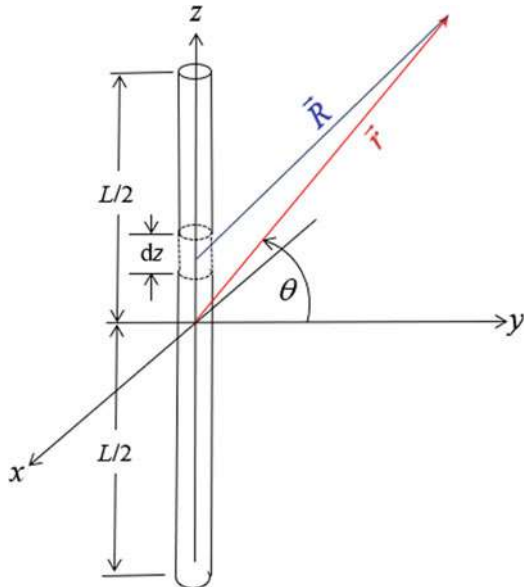
There are line sources that can be considered a continuous distribution of source strength. One example is the ionization path of lightning, and another is the tire noise that is radiated continuously from the surface of a highway. Instead of considering the superposition of discrete sources, as we did in the previous section, in this section we will assume that there is a continuous distribution of volume velocity along a straight line of total length,  $L$ , as diagrammed in Fig. 12.30, where we have assumed that the source is aligned with the  $z$  axis and is centered at the  $x$ - $y$  plane.

If each differential element of volume velocity,  $d|\hat{\mathbf{U}}(a)| = 2\pi a |\hat{\mathbf{v}}_r(a)| dz$ , where  $\hat{\mathbf{v}}_r(a)$  is the radial velocity of the cylindrical line source at its surface, is treated as a differential source of acoustic pressure,  $dp_1(|\vec{R}|)$ , then the total pressure is given by the integral from  $-L/2$  to  $+L/2$  over all the differential source strength elements. That integral can be evaluated by using the expression for the pressure radiated by a simple source in Eq. (12.21).

$$\begin{aligned} p_1(|\vec{R}|, \theta, t) &= \Re e \left[ \int_{-L/2}^{L/2} dp_1 = \frac{j\rho_m c k}{4\pi} \int_{-L/2}^{L/2} \frac{e^{j(\omega t - k|\vec{R}|)}}{|\vec{R}|} d\hat{\mathbf{U}}(a) \right] \\ &= \Re e \left[ \frac{j\rho_m c k a \hat{\mathbf{v}}_r(a)}{2} \int_{-L/2}^{L/2} \frac{e^{j(\omega t - k|\vec{R}|)}}{|\vec{R}|} dz \right] \end{aligned} \quad (12.95)$$

In the far-field limit,  $|\vec{r}| \gg L$ , the numerator of the term within the integral of Eq. (12.95) can be approximated by  $|\vec{R}| \cong |\vec{r}| \sin \theta$ .

**Fig. 12.30** A schematic representation of a continuous line source of length,  $L$ , is assumed to produce a volume velocity amplitude of  $|\hat{\mathbf{U}}(a)|$  by a harmonic change in its radius,  $a$ , that is uniform along its full length. Each differential element of volume velocity along the length of the cylindrical line source of length,  $dz$ , produces a differential source strength,  $d|\hat{\mathbf{U}}(a)| = 2\pi a |\hat{\mathbf{v}}_r(a)| dz$ , where  $\hat{\mathbf{v}}_r(a)$  is the amplitude of the radial velocity of the cylindrical line source at its surface



$$p_1(|\vec{r}|, \theta, t) \cong \Re e \left[ j \frac{\rho_m c k a \hat{\mathbf{v}}_r(a)}{2} \frac{e^{j(\omega t - k|\vec{r}|)}}{|\vec{r}|} \int_{-L/2}^{L/2} e^{jkz \sin \theta} dz \right] \quad (12.96)$$

The integral can be evaluated since its argument is an exponential.

$$\int_{-L/2}^{L/2} e^{jkz \sin \theta} dz = \frac{e^{jkz \sin \theta}}{jk \sin \theta} \Big|_{-L/2}^{L/2} = \frac{e^{jk \frac{L}{2} \sin \theta} - e^{-jk \frac{L}{2} \sin \theta}}{jk \sin \theta} = \frac{2 \sin \left( \frac{kL}{2} \sin \theta \right)}{k \sin \theta} \quad (12.97)$$

Expression of this result can be simplified by use of the “sinc” function:  $\text{sinc}(x) \equiv (\sin x)/x$ , which is plotted in Fig. 12.31.<sup>17</sup>

$$H(\theta) = \left| \text{sinc} \left( \frac{kL}{2} \sin \theta \right) \right| \quad (12.98)$$

The far-field acoustic pressure along the equatorial plane is related to the total source strength,  $|\hat{\mathbf{U}}(a)| = 2\pi a |\hat{\mathbf{v}}_r| L$ .

$$p_{ax}(|\vec{r}|) = \frac{\rho_m c |\hat{\mathbf{v}}_r| k La}{2 |\vec{r}|} = \frac{\rho_m c}{2 |\vec{r}| \lambda} |\hat{\mathbf{U}}(a)| \quad (12.99)$$

Once again, we see that the amplitude of the axial pressure field,  $p_{ax}$ , is given by our earlier expression for the monopolar acoustic transfer impedance,  $Z_{tr}$ , of Eq. (12.22).

<sup>17</sup> The sinc function is also known as a zeroth-order spherical Bessel function of the first kind:  $j_0(z) = (\sin z)/z$ . For example, see M. Abramowitz and I. A. Stegun, *Handbook of Mathematical Functions with Formulas, Graphs, and Mathematical Tables*, National Bureau of Standards, Applied Mathematics Series #55, pg. 438.

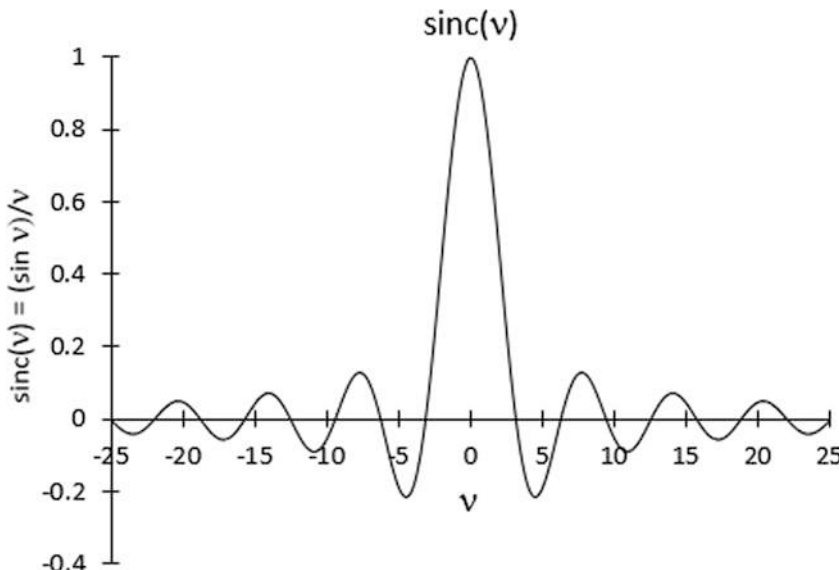


**Fig. 12.31** Plot of  $\text{sinc}(\nu) = \sin(\nu)/\nu$  over the interval  $-25 \leq \nu \leq +25$ . For application to a continuous line source of length  $L$ , where  $\nu = (kL/2) \sin \theta$

## 12.8 Baffled Piston

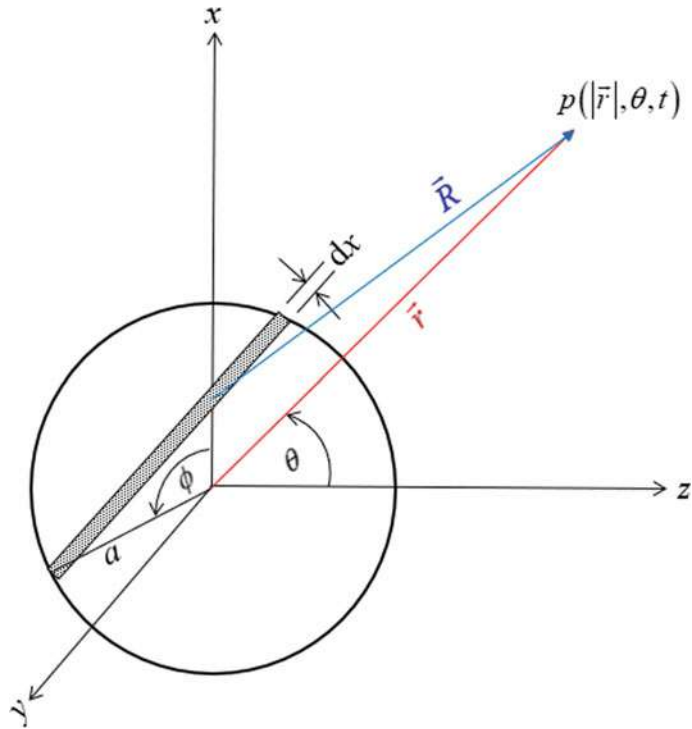
The most ubiquitous man-made electroacoustic source of sound is the baffled piston.<sup>18</sup> As will be demonstrated in this section, the radiation from a circular piston of radius,  $a$ , has a frequency dependence which will produce a uniform sound power that is fairly constant over a broad range of frequencies if the source of volume velocity (e.g., created by an electrodynamic loudspeaker) is operating in its mass-controlled region. The radiated sound is also reasonably omnidirectional if the circumference of the piston is less than the radiated wavelength (i.e.,  $2\pi a \lesssim \lambda$  or  $ka \lesssim 1$ ).

As with the analysis of the continuous line array in Sect. 12.7, each differential surface element of a baffled piston can be treated as a differential pressure source to be summed by integration over the surface of the piston to produce the total radiation field produced by that piston. As demonstrated in the case of a simple source in the proximity of a rigid boundary, the differential source element on the surface of the baffled piston produces twice the far-field pressure of an equivalent source radiating omnidirectionally in an unbounded medium. If it is assumed that the amplitude and phase of the normal surface velocity of the piston,  $|\hat{v}_\perp| \equiv v_\perp$ , is uniform over the entire piston,<sup>19</sup> then the differential element of volume velocity that corresponds to a differential element of the piston's area,  $dS$ , can be written as  $d|\hat{\mathbf{U}}| = v_\perp dS$ .

<sup>18</sup> The moving-coil electrodynamic loudspeaker was invented by two Danish engineers, Peter Laurits Jensen and Edwin S. Pridham, in 1915.

<sup>19</sup> Since no piston is infinitely rigid, there will be some frequency above which the piston will no longer have a uniform perpendicular velocity,  $v_\perp$ , over the entire surface of the piston. Loudspeaker designers refer to this behavior as "cone breakup." In some clever designs that have the loudspeaker's "dust cap" bonded directly to the voice coil former (i.e., the hollow cylinder around which the coil is wound), the breakup of the cone at radii greater than the dust cap's radius is used to make the oscillation of the dust cap the primary sound source, since the cone breakup results in waves propagating along the cone which produces no net (integrated) volume velocity. For radiation from flexing disks, see M. Greenspan, "Piston radiator: Some extensions to the theory," J. Acoust. Soc. Am. **65**(3), 608–621 (1979).

**Fig. 12.32** Geometry used for calculation of the far-field pressure,  $p(|\vec{r}|, \theta, t)$ , produced by the vibration of a rigid piston of radius,  $a$ , that is oscillating with a velocity,  $|\hat{\mathbf{v}}_\perp|$ , in an infinite baffle represented by the  $x$ - $y$  plane



As shown in Fig. 12.32, the differential element of piston area is chosen to be a strip of height,  $dx$ , and width,  $2a \sin(\phi)$ , so  $dS = 2a \sin(\phi) dx$ . The pressure radiated to the far field ( $kr \gg 1$ ) by that differential strip is related to the differential volume velocity,  $d|\hat{\mathbf{U}}(\phi)|$ , that strip imparts to the adjacent fluid medium.

$$p(|\vec{R}|, \theta, t) = \Re e \left[ j \frac{\rho_m c k v_\perp}{2\pi} \int_S \frac{e^{j(\omega t - k|\vec{R}|)}}{|\vec{R}|} dS \right] \quad (12.100)$$

To evaluate this integral, an expression for the vector,  $\vec{R}$ , that connects a point on the surface of the piston to an observation point,  $p(|\vec{r}|, \theta, t)$ , in the far field is required.

$$\vec{R} = (|\vec{r}| \sin \theta - x) \hat{e}_x + |\vec{r}| \cos \theta \hat{e}_y = (|\vec{r}| \sin \theta - a \cos \phi) \hat{e}_x + |\vec{r}| \cos \theta \hat{e}_y \quad (12.101)$$

$\hat{e}_x$  is the unit vector in the  $x$  direction and  $\hat{e}_y$  is the unit vector in the  $y$  direction. The magnitude of  $|\vec{R}|$  in the far field can be expressed as the Pythagorean sum.

$$\begin{aligned} |\vec{R}| &= |\vec{r}| \sqrt{\left( \sin \theta - \frac{a}{|\vec{r}|} \cos \phi \right)^2 + \cos^2 \theta} \\ &= |\vec{r}| \sqrt{1 - \frac{2a}{|\vec{r}|} \sin \theta \cos \phi - \left( \frac{a}{|\vec{r}|} \right)^2 \cos^2 \phi} \end{aligned} \quad (12.102)$$

In the far field, that distance can be approximated by the binomial expansion which is valid for  $a/r \ll 1$ .

$$\left| \vec{R} \right| \cong \left| \vec{r} \right| \left[ 1 - \left( \frac{a}{\left| \vec{r} \right|} \right) \sin \theta \cos \phi \right] = \left| \vec{r} \right| - a \sin \theta \cos \phi \quad (12.103)$$

As usual, in the far field, we will ignore the effects of the variation in  $\left| \vec{r} \right|$  for the amplitude of the spherical spreading but include it for the superposition of phases. Combining Eq. (12.103) with the expression for the differential element of area,  $dS = 2a \sin(\phi) dx$ , Eq. (12.100) can be re-written as an integral over  $dx$ .

$$p\left(\left| \vec{r} \right|, \theta, t\right) = \Re e \left[ j \frac{\rho_m c k a v_{\perp}}{\pi} \frac{e^{j(\omega t - k \left| \vec{r} \right|)}}{\left| \vec{r} \right|} \int_{-a}^a e^{jka - \sin \theta \cos \phi} \sin \phi d\phi \right] \quad (12.104)$$

The integral can be re-cast into a “standard form” by substituting the integration variable,  $dx = a \sin(\phi) d\phi$ , and changing the corresponding limits of integration.

$$p\left(\left| \vec{r} \right|, \theta, t\right) = \Re e \left[ j \frac{\rho_m c k a^2 v_{\perp}}{\pi} \frac{e^{j(\omega t - k \left| \vec{r} \right|)}}{\left| \vec{r} \right|} \int_0^{\pi} e^{jka - \sin \theta \cos \phi} \sin^2 \phi d\phi \right] \quad (12.105)$$

The complex exponential in the argument of the integral can be expressed as the sum of trigonometric functions:  $e^{jx} = \cos(x) + j \sin(x)$ . That integration over the imaginary component vanishes by symmetry leaving an integral definition of the  $J_1$  Bessel function of the first kind [47]. The first three of these Bessel and Neumann functions were plotted in Figs. 6.8 and 6.9.

$$J_{\nu}(z) = \frac{(z/2)^{\nu}}{\pi^{1/2} \Gamma(\nu + 1/2)} \int_0^{\pi} \cos(z \cos \phi) \sin^{2\nu} \phi d\phi \quad (12.106)$$

The Gamma function,  $\Gamma(\nu + 1/2)$ , is a generalization of the factorial for non-integers,  $z! = \Gamma(z + 1)$ . It can be evaluated by use of Euler’s integral.

$$\Gamma(z) = \int_0^{\infty} t^{z-1} e^{-t} dt \quad (12.107)$$

For  $\nu = 1$  and  $z = 1.5, 2$   $\Gamma(1.5) = \sqrt{\pi}$ . Equations (12.106) and (12.107) produce an integral expression for  $J_1(z)$ .

$$J_1(z) = \frac{z}{\pi} \int_0^{\pi} \cos(z \cos \phi) \sin^2 \phi d\phi \quad (12.108)$$

Comparing Eq. (12.108) with Eq. (12.105), the magnitude of the far-field pressure of a baffled oscillating rigid piston can be expressed as the product of an axial pressure,  $p_{ax}\left(\left| \vec{r} \right|\right)$ , and the directionality,  $H(\theta)$ , in terms of the piston’s volume velocity,  $\left| \hat{\mathbf{U}} \right| = A_{pist} v_{\perp}$ .

$$\begin{aligned} p\left(\left| \vec{r} \right|, \theta\right) &= p_{ax}\left(\left| \vec{r} \right|\right) H(\theta) = \frac{\rho_m c k a^2 v_{\perp}}{2 \left| \vec{r} \right|} \left[ \frac{2 J_1(ka \sin \theta)}{ka \sin \theta} \right] \\ &= \frac{\rho_m c}{\left| \vec{r} \right| \lambda} \left| \hat{\mathbf{U}} \right| \left| \frac{2 J_1(v)}{v} \right| \quad \text{for } \nu = (ka) \sin \theta \end{aligned} \quad (12.109)$$

The final expression demonstrates again that the monopole’s acoustic transfer impedance,  $\mathbf{Z}_{tr}$ , provides the magnitude of the axial (maximum) far-field pressure in terms of the volume velocity of the

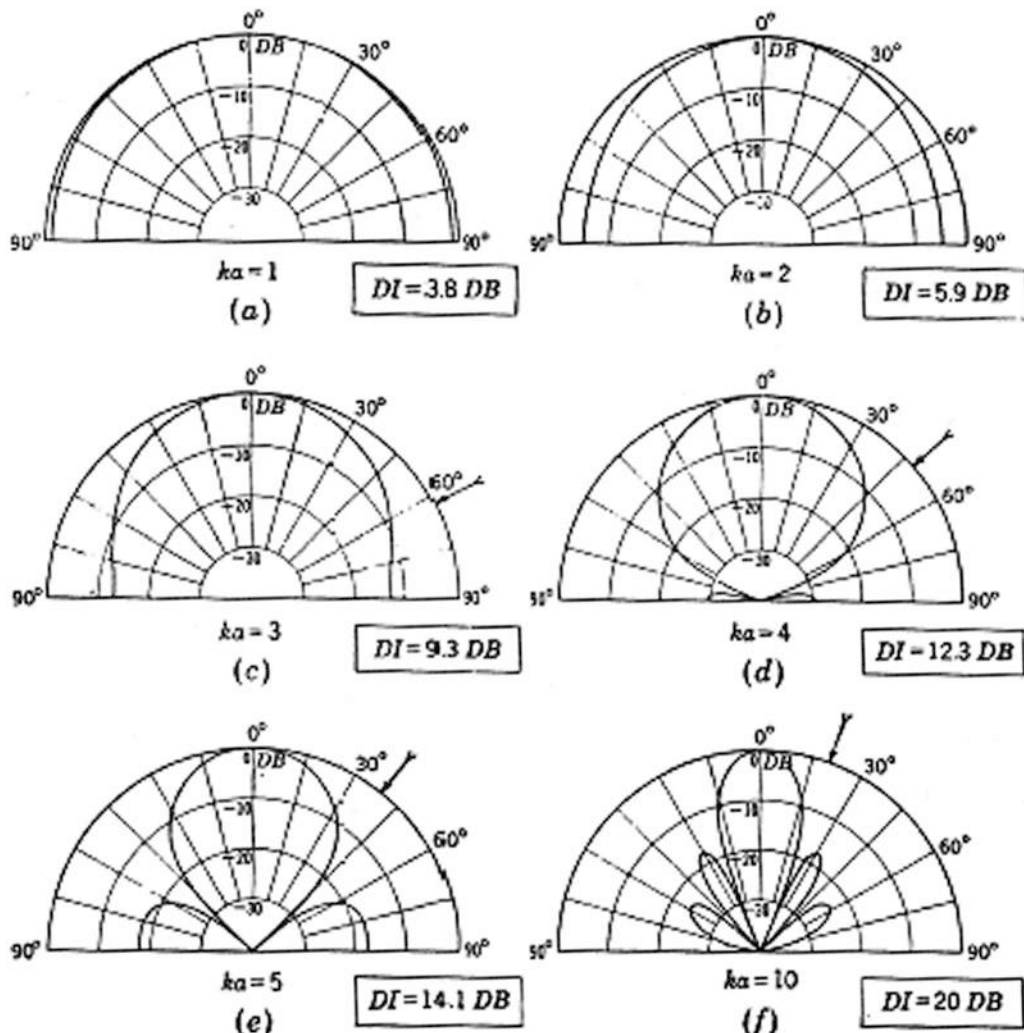


**Fig. 12.33** Beam patterns for a baffled, rigid, circular piston as a function of  $ka = 2\pi a/\lambda$  from  $ka = 1$  (nearly omnidirectional) to  $ka = 10$ . The relative strength of the first side lobe,  $31^\circ$  from the polar axis, for  $ka = 10$ , is  $-17.6$  dB. The angle that the first nodal cone makes with the polar axis for  $ka = 10$  is  $\theta_1 = 22.5^\circ$ . The directivity,  $D$ , is the reciprocal of  $H^2(\theta)$  integrated over all solid angles (see Sect. 12.8.2). The directivity index,  $(DI)$ , is  $10 \log_{10}(D)$ . The arrows in (c) through (f) show one direction of  $DI = 0$  [49]

source, although the expression is twice that of Eq. (12.22) since the source is baffled and therefore radiates into a *semi-infinite half-space*. Several directional patterns,  $|H(\theta)| = 2 J_1(v)/v$ , for various values of  $1 \leq (ka) \leq 10$ , where  $v = ka \sin\theta$ , are plotted in Fig. 12.33.

The relative amplitudes of the lobes are determined by the values of the maxima of  $|H(\theta)| = 2 J_1(v)/v$ . Fortunately, the derivative of  $J_1(v)/v$  is related to  $J_2(v)$  [48].

$$\begin{aligned} \left( \frac{1}{z} \frac{d}{dz} \right)^k \{ z^{-\nu} J_\nu(z) \} &= (-1)^k z^{-\nu-k} J_{\nu+k}(z); \quad k = 0, 1, 2 \dots \\ \Rightarrow \quad \frac{d}{dz} \left( \frac{J_1(z)}{z} \right) &= -\frac{J_2(z)}{z} \end{aligned} \quad (12.110)$$

The first *minor lobe* (i.e.,  $\theta \neq 0^\circ$ ) will occur for values of  $J_2(j_{2,n}) = 0$ . This extremum occurs at  $j_{2,1} = 5.13562$ , where  $2J_1(j_{2,1})/j_{2,1} \cong 0.132$ . That first minor lobe will occur in the direction where  $ka \sin \theta = j_{2,1} = 5.13562$ . Since the Taylor series expansion of  $J_1(z)$  about the origin is  $J_1(z) = z/2 + z^3/16 - \dots$ , the value of  $2J_1(0)/0 = z/z = 1$ . Therefore, the ratio of the amplitude of the main lobe to the amplitude of the first minor lobe is  $20 \log_{10}(0.132) = -17.6$  dB.

For a baffled rigid piston operating at a frequency such that  $ka = 10$  as shown in Fig. 12.33(f), the first side lobe will be directed along  $\theta_{n=1} = \sin^{-1}(5.136/ka) = 31^\circ$ , and the first null will occur at  $\theta_{m=1} = \sin^{-1}(3.83/ka) = 22.5^\circ$ . The second null visible in Fig. 12.33(f) for the case of  $ka = 10$  occurs at  $\theta_{m=2} = \sin^{-1}(7.016/ka) = 44.6^\circ$ . Since  $j_{1,3} = 10.17347$ , the apparent null at  $90^\circ$  in Fig. 12.32(f) for the  $ka = 10$  example is not exactly zero. The second side lobe for  $ka = 10$  occurs at  $j_{2,2} = 8.417$  so  $\theta_{n=2} = \sin^{-1}(8.417/ka) = 57.3^\circ$ .

### 12.8.1 Rayleigh Resolution Criterion

To reiterate the results of the previous section, the peaks and nulls of the directionality can be determined in the same way as was done for the discrete line array and continuous line source, except that the values of the arguments,  $j_{1,m}$ , of the  $J_1(j_{1,m})$  Bessel function corresponding to the nulls and extrema are not simply integer multiples of  $\pi$  or  $\pi/2$ . The nulls occur for directions,  $\theta_m$ , where  $ka \sin \theta_m = j_{1,m}$ . Values of  $j_{1,m}$  are available in mathematical tables [50], and some for small values of  $n$  and  $m$  are provided in Appendix C. The first null occurs for  $j_{1,1} = 3.83171$ . Subsequent zero crossings occur at  $j_{1,2} = 7.01559$ ,  $j_{1,3} = 10.17347$ ,  $j_{1,4} = 13.32369$ , etc.

$$\sin \theta_1 = \frac{3.83}{ka} = \frac{3.83}{2\pi} \left( \frac{\lambda}{a} \right) = 0.61 \left( \frac{\lambda}{a} \right) = 1.22 \left( \frac{\lambda}{D} \right) \quad (12.111)$$

The result at the far-right expression in Eq. (12.111) is known in optics as the *Rayleigh resolution criterion*. It is used as the minimum observable diffraction-limited angular separation between two objects viewed through an aperture of diameter  $D = 2a$ .<sup>20</sup> We can consider two sound sources located in the far field that are separated by some angle,  $\theta$ , with one source located at  $+θ/2$  and the other at  $-θ/2$ . If the “piston” is the baffled diaphragm of a microphone, then the argument of the  $|H(\theta)|$  is determined by  $v = ka \sin \theta$ , when substituted into Eq. (12.109). The ability to resolve two sources of equal amplitudes that are separated by some angle,  $\theta$ , is illustrated in Fig. 12.34.

### 12.8.2 Directionality and Directivity

It is possible to quantify the directivity of an extended source by comparing the axial pressure at some distance,  $r$ , in the far field, with a simple source that radiates the same time-averaged power omnidirectionally. That ratio is called the directivity,  $D$ .

<sup>20</sup>In Rayleigh’s own words, “This rule is convenient on account of its simplicity and it is sufficiently accurate in view of the necessary uncertainty as to what exactly is meant by resolution.” J. W. Strutt (Lord Rayleigh), “Investigations in optics, with special reference to the spectroscope,” Phil. Mag. **8**(49), 261–274 (1879). See §1. Resolving, or Separating, Power of Optical Instruments; also *Collected Works* (Dover, New York, 1963), Vol. I, pp. 415–418.

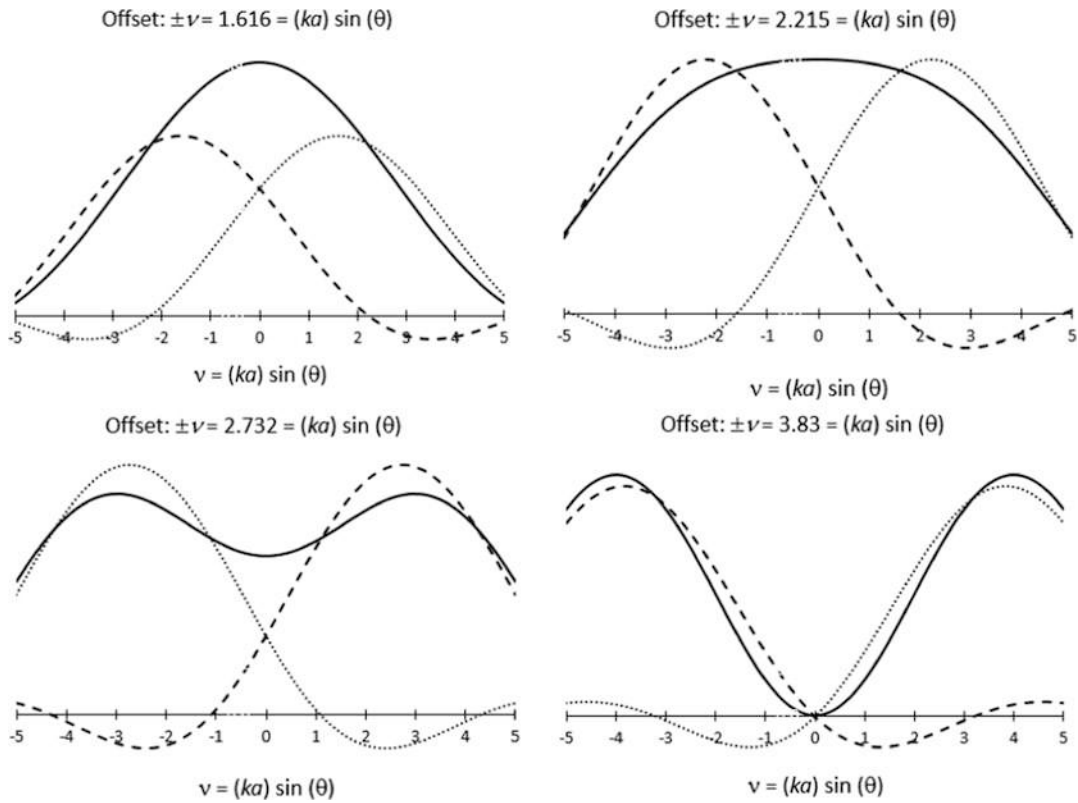


**Fig. 12.34** Illustration of the “Rayleigh resolution criterion” showing the image of two sources that have different angular separation. The dotted and dashed lines represent the received amplitude of individual signals located at  $\pm\theta = \sin^{-1}(\nu/ka)$  as function of  $\nu = (ka) \sin \theta$ . The solid line is the sum of their signals. (Above) These two peaks are not resolved. For  $\nu = 1.616$ , the two peaks cross at their  $-3$  dB points, and for  $\nu = 2.215$ , the two peaks cross at their  $-6$  dB points. Those appear as a single object although the apparent angular width has been increased over the width of the individual sources. (Below) These two peaks are resolved. For  $\nu = 2.732$ , the two peaks cross at their  $-10$  dB points, and for  $\nu = 3.83$ , the two peaks cross where both have zero amplitude

$$D = \frac{\langle I_{ax}(r) \rangle_t}{\langle I_{omni}(r) \rangle_t} = \frac{|\hat{\mathbf{p}}_{ax}(r)|^2}{|\hat{\mathbf{p}}_{omni}(r)|^2} \quad (12.112)$$

The total power radiated by the directional source requires the integration of the  $H^2(\theta)$  over all *solid angle*,  $d\Omega$ .

$$d\Omega \equiv \frac{dS}{r^2} \quad (12.113)$$

This is similar to the two-dimensional definition of angle as the arc length divided by the radius which, though dimensionless, is given the unit “radian.” Solid angle is also dimensionless and its unit is the *steradian*. If Eq. (12.113) is integrated over the entire surface of a sphere of any radius, the solid angle has its maximum value of  $4\pi$  steradians.

The total time-averaged power,  $\langle \Pi \rangle_t$ , radiated by a sound source can be obtained by integrating the square of the far-field pressure over all solid angle.

$$\langle \Pi \rangle_t = \frac{1}{2\rho_m c} \int_{4\pi} p_1^2(r, \theta, \phi) r^2 d\Omega = \frac{r^2 |\mathbf{p}_{ax}(r)|^2}{2\rho_m c} \int_{4\pi} H^2(\theta, \phi) d\Omega \quad (12.114)$$

For a compact omnidirectional source,  $H_{omni}(\theta) = 1$ , so that the total time-averaged radiated power,  $\langle \Pi_{omni} \rangle_t = 4\pi r^2 |\hat{\mathbf{p}}_{omni}|^2 / 2\rho_m c$ . The ratio of the on-axis time-averaged intensity,  $\langle I_{ax}(r) \rangle_t$ , as expressed in Eq. (12.112), to the on-axis time-averaged intensity of a monopole with equivalent source strength,  $\langle I_{omni}(r) \rangle_t$ , produces an expression that relates the square of the directionality,  $H^2(\theta)$ , to the *directivity*,  $D$ .

$$D = \frac{|\hat{\mathbf{p}}_{ax}(r)|^2}{|\hat{\mathbf{p}}_{omni}(r)|^2} = \frac{4\pi}{\int_{4\pi} H^2(\theta, \phi) d\Omega} \quad (12.115)$$

This integral can be evaluated for a continuous line source of directionality,  $|H(\theta)|$ , given by Eq. (12.98), if the integration variable is changed from  $d\Omega$  to  $dv = (\frac{1}{2})kL \cos(\theta)d\theta$ .

$$D_{line} = \frac{(kL/2)}{\int_0^{kL/2} \left( \frac{\sin v}{v} \right)^2 dv} \quad (12.116)$$

If the line array is very long (i.e.,  $kL \gg 1$ ), then the limit of integration can be taken to infinity since  $v^2$  in the denominator of the integral will limit the result since  $|\sin v| \leq 1$ . The definite integral is available in standard integral tables [51].

$$\int_0^\infty \frac{\sin^2 ax}{x^2} dx = \frac{a\pi}{2} \quad (12.117)$$

For long line arrays, substitution of Eq. (12.117) into Eq. (12.116) produces an approximate directivity for a long line array.

$$\lim_{kL \rightarrow \infty} D_{line} = \frac{kL}{\pi} = \frac{2L}{\lambda} \quad (12.118)$$

For a rigid circular piston in a baffle, substitution of  $|H(\theta)|$  from Eq. (12.109) into Eq. (12.115) produces an integral that is similar to Eq. (12.116).

$$D_{piston} = \frac{4\pi}{\int_0^{\pi/2} \left[ \frac{2J_1(ka \sin \theta)}{ka \sin \theta} \right]^2 2\pi \sin \theta d\theta} = \frac{(ka)^2}{1 - \frac{J_1(2ka)}{ka}} \quad (12.119)$$

The low-frequency directionality of the baffled piston can be obtained from the series expansion of  $J_1(x) = (x/2) + (x^3/16) + \dots$

$$\lim_{ka \rightarrow 0} [D_{piston}] = 2 \quad (12.120)$$

This result for a baffled piston in the low-frequency limit is reasonable because we have assumed that the baffle restricts radiation only into a semi-infinite half-space. Because of the oscillatory behavior of  $J_1(2ka)$  and the fact that  $|J_1(x)| < 0.582$ , the high-frequency limit of the piston's directivity can be calculated directly from Eq. (12.119).

$$\lim_{ka \rightarrow \infty} [D_{piston}] = (ka)^2 \quad (12.121)$$

For many applications, it is useful to express the directivity as a *directivity index*, DI, that is often also referred to as the *array gain*.

$$DI = 10 \log_{10} D \quad (12.122)$$

The polar plots of piston directionality in Fig. 12.33 also include the directivity index reported in decibels.

### 12.8.3 Radiation Impedance of a Baffled Circular Piston

At the surface of the baffled rigid piston, the fluid exerts a force that has components that are both in-phase with the piston's velocity (manifested as a mechanical radiation resistance) and that are in-phase with the piston's acceleration (manifested as hydrodynamic mass loading). It was fairly easy to derive the hydrodynamic mass for a compact spherical source resulting in Eq. (12.15) and the radiation resistance in Eq. (12.16), and somewhat more difficult to do the same for a dipole to obtain the results in Eq. (12.55). The equivalent calculations for a baffled rigid piston are more complicated, since Bessel functions are required, [52], but result in an expression for the resistive component that is proportional to a function,  $R_1(2ka)$ , and for the reactive component that is proportional to another function,  $X_1(2ka)$ . The mechanical impedance,  $\mathbf{Z}_{\text{mech}}$ , is evaluated at the surface of the oscillating piston.

$$\mathbf{Z}_{\text{mech}} \equiv \frac{\hat{\mathbf{F}}}{\hat{\mathbf{v}}_{\perp}} = \rho_m c \pi a^2 [R_1 + jX_1] \quad (12.123)$$

The resistive coefficient of the mechanical reactance,  $R_1$ , is related to the  $J_1$  Bessel function.

$$\begin{aligned} R_1(2ka) &= 1 - \frac{2J_1(2ka)}{2ka} \quad \text{for all values of } (2ka) \\ &\cong \frac{(2ka)^2}{2 \cdot 4} - \frac{(2ka)^4}{2 \cdot 4^2 \cdot 6} + \frac{(2ka)^6}{2 \cdot 4^2 \cdot 6^2 \cdot 8} \dots \quad \text{for } (2ka) < 2 \end{aligned} \quad (12.124)$$

For small values of  $2ka$ ,  $R_1(2ka \ll 1) = (ka)^2/2$ . At high frequencies,  $R_1(ka \gg 1)$  approaches one, as shown by the solid line in Fig. 12.34, so the piston radiates plane waves, as expected.

The quadratic dependence of the radiation resistance on frequency,  $R_1 \propto \omega^2$ , for small values of  $2ka$ , is responsible for the large frequency bandwidth of direct-radiating loudspeakers. Electrodynamic speakers are typically operated at frequencies above their natural (free-cone) resonance frequency and are therefore operated in their mass-controlled regime. As such, their acceleration is constant, but the velocity of their speaker cone,  $v_{\perp}$ , is decreasing linearly with frequency:  $|\hat{\mathbf{v}}_{\perp}| \propto \omega^{-1}$ . Since the time-averaged radiated power is proportional to the square of that velocity,  $\langle \Pi_{\text{rad}} \rangle = (\frac{1}{2})(\rho_m c \pi a^2) R_1 |\hat{\mathbf{v}}_{\perp}|^2$ ,  $\langle \Pi_{\text{rad}} \rangle_t$  is frequency independent, as long as the piston remains rigid at those frequencies and  $2ka \leq 1$ .

The reactive function can be expressed as an integral that is related to the first-order Struve function,  $H_1(2ka)$  [53].

$$\begin{aligned} X_1(2ka) &= \frac{2H_1(2ka)}{(2ka)} = \frac{4}{\pi} \int_0^{\pi/2} \sin(2ka \cos \alpha) \sin^2 \alpha \, d\alpha \\ &\cong \frac{2}{\pi} - J_0(2ka) + \left( \frac{16}{\pi} - 5 \right) \frac{\sin(2ka)}{2ka} + \left( 12 - \frac{36}{\pi} \right) \frac{1 - \cos(2ka)}{(2ka)^2} \\ &\cong \frac{4}{\pi} \left[ \frac{2ka}{3} - \frac{(2ka)^3}{3^2 \cdot 5} + \frac{(2ka)^5}{3^2 \cdot 5^2 \cdot 7} - \dots \right] \quad \text{for } (2ka) < 2 \end{aligned} \quad (12.125)$$

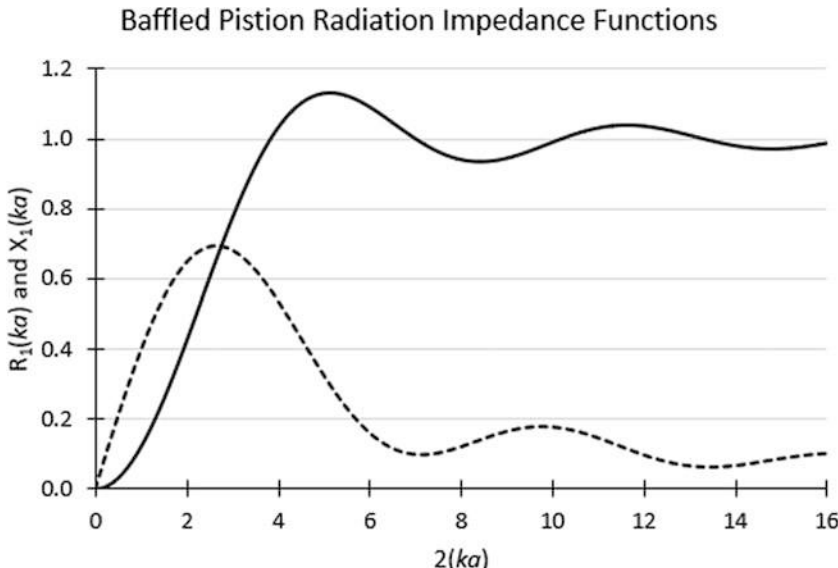


**Fig. 12.35** Functional dependence of the real (resistive) mechanical reactance,  $R_1(2ka)$ , as a solid line, and imaginary (reactive),  $X_1(2ka)$ , as a dotted line, plotted as a function of  $2(ka)$ , for a rigid, baffled piston. For small values of  $2(ka)$ , the initial slope of  $R_1(2ka)$  is proportional to  $(2ka)^2$ , and the initial slope of  $X_1(2ka)$  is proportional to  $2(ka)$

The middle version is valid to within about  $\pm 1\%$  for all values of  $(2 ka)$  [54]. The frequency variation of both components of the baffled piston's radiation impedance functions,  $R_1$  and  $X_1$ , is plotted in Fig. 12.35.

For small values of  $2 ka$ ,  $X_1(2ka \ll 1) = 8(ka)/3\pi$ . As before, we expect the reactive part of the mechanical radiation impedance,  $\rho_m c \pi a^2 X_1$ , to represent the baffled piston's (near-field) hydrodynamic mass loading. From Eqs. (12.123) and (12.125), the force corresponding to this mass reactance can be written in terms of the fluid density times a cylindrical volume of fluid that has the same area as the piston,  $\pi a^2$ , and a height,  $\ell_{\text{Baffled}} = (8a/3\pi) \cong 0.85 a$ , if we let  $\omega = ck$ . As shown below, for the baffled piston,  $m_{\text{eff}} = \rho_m (8/3)a^3$  when  $(2ka) < 1$ .

$$\begin{aligned} \lim_{2ka \rightarrow 0} [\mathbf{F}_{\text{Reactive}}] &= j\Im \mathbf{m}[\mathbf{Z}_{\text{mech}} v_{\perp}] = j\rho_m c \pi a^2 \frac{8}{3\pi} (ka) \\ &= j\omega \left( \rho_m \pi a^2 \cdot \frac{8a}{3\pi} \right) = j\omega m_{\text{eff}} = j\omega \rho_m \left( \frac{8}{3} a^3 \right) \end{aligned} \quad (12.126)$$

That hydrodynamic mass was added to the head mass of the Tonpilz transducer in Sect. 4.3.1. We postulated an effective mass correction (without proof!), in Sect. 8.5.2, when we added an empirical “effective length” correction,  $L_{\text{eff}} = L + 1.24a$  from Eq. (8.53), to the physical length,  $L$ , of the neck of our 500 mL Helmholtz resonators.

According to the results of Eq. (12.126),  $0.85a$  of the empirical correction,  $1.24a$ , was due to the effective mass of the fluid that leaves the neck and enters the compliance (volume) if that junction can be modeled as a “baffled piston.” That leaves  $0.39a$  that would be the effective mass for the fluid in the other end of the neck.

That total correction was about 15% smaller in Sect. 8.6.11 where we used DELTAEC to produce the necessary neck length correction because DELTAEC included the frequency reduction due to thermoviscous effects in the neck and the compliance:  $L_{\text{eff}} = L + 1.08 a$ .

It is a good idea to compare the results for the radiation impedance of the baffled piston plotted in Fig. 12.35 with those of the simple spherical source (monopole) that were plotted in Figs. 12.5 and 12.6. Both exhibit an initially quadratic increase in the real part and an initially linear increase in the imaginary part. Both have the imaginary part decreasing toward zero, and both have the real part approaching one for large  $ka$ .

Because the spherical source can only produce radial fluid velocities, there is no “wavnness” in either  $R_1$  or  $X_1$  at higher values of  $ka$  in Figs. 12.5 and 12.6. For the baffled piston, at larger values of  $ka$ , pressure created by the motion of one portion of the piston can interfere with other parts, thus producing the oscillations of  $R_1$  of  $X_1$  seen in Fig. 12.35.

### 12.8.4 Radiation Impedance of a Baffled Rectangular Piston\*

A similar derivation for the radiation impedance of a rigid baffled rectangular piston can be made by integrating the differential element of volume velocity that corresponds to a differential element of the piston’s area,  $dS$ , written as  $d|\hat{\mathbf{U}}| = v_\perp dS$ , using the geometry of Fig. 12.32, but for a region of width,  $w$ , and height,  $h$ . If  $w$  and  $h$  are not too different, the radiation resistance and reactance can be written for such a rectangular piston [55].

$$R_1 + jX_1 = \begin{cases} \frac{k^2}{16} (w^2 + h^2) + j \frac{8k}{9\pi} \frac{w^2 + wh + h^2}{w + h} & \text{for } kw \ll 1 \text{ and } kh \ll 1 \\ 1 + j \frac{8}{\pi k(w + h)} & \text{for } kw \gg 1 \text{ and } kh \gg 1 \end{cases} \quad (12.127)$$

As with the baffled circular piston, for large  $kw$  and  $kh$ , the radiation resistance is just that for plane waves, as it was in Eq. (12.124) for the circular piston. Also, if we consider a square piston with  $w = h$ , then in the small  $kh$  limit, in analogy with Eq. (12.123),  $m_{eff} = \rho_m(4h/3\pi)A_{pist}$  for the square piston which is almost equal to  $m_{eff} = \rho_m(8a/3\pi)A_{pist}$  for the circular piston since equal values of  $A_{pist}$  would make  $h = a\sqrt{\pi} \cong 1.77a$  for the square piston.

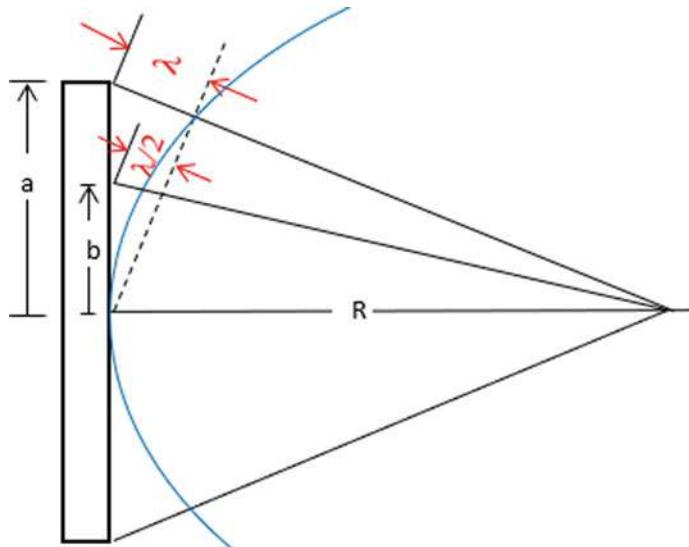
### 12.8.5 On-Axis Near-Field Pressure from a Circular Baffled Piston\*

This exploration of radiation from a baffled, rigid piston will conclude with an examination of the boundary between the near and far fields. Based on the earlier investigations of extended sources with dimensions that are larger than the wavelength of sound, we expect interference effects. These are also observed with piston sources when the frequency of sound corresponds to  $ka > 2\pi$ .

We can estimate the distance along the axis of the piston where the transition is observed from near-field (interference) to the far-field (spherical spreading) behavior. In the far field, a smooth monotonic decrease in the acoustic pressure amplitude is expected that varies inversely with distance from the surface of the piston according to  $p_{ax}(r)$  in Eq. (12.109).

Figure 12.36 provides a diagram of a piston with the arc of a circle centered at a point a distance,  $R$ , from the surface of the piston. If we have chosen  $R$  such that the distance from the edge of the piston to the point at  $R$  is  $R + \lambda$ , then we can think of the piston as being separated into a central disk where the path length differences,  $\Delta$ , are less than or equal to  $\lambda/2$  and an outer ring with  $\lambda/2 \leq \Delta \leq \lambda$ . The radius of the inner disk can be set to  $b = a/\sqrt{2}$ . If the surface areas of the ring,  $A_{ring} = \pi(a^2 - b^2)$ , and the disk,  $A_{disk} = \pi b^2$ , are roughly equal (they are exactly equal if  $b = a/\sqrt{2}$ ), then the pressure generated at  $R$  due

**Fig. 12.36** A simple geometric construction that can be used to estimate the distance from the surface of a piston where we expect the last destructive interference to occur on the axis of the piston. The rigid, baffled piston has a radius,  $a$ , that is significant when compared to the wavelengths of sound radiated by the piston. The inner radius,  $b$ , is chosen so that the areas of the inner disk and outer ring are equal. The radius of the orange arc is  $R$



to the volume velocity created by the inner disk will cancel the pressure generated at  $R$  due to the volume velocity created by the outer ring.

From the geometry of Fig. 12.36, the value of  $R$  beyond which there can be no further interference,  $R_{min}$ , can be calculated using the right triangle of height  $a$ , base  $R$ , and hypotenuse,  $R + \lambda$ .

$$(R + \lambda)^2 = R^2 + a^2 \quad (12.128)$$

Expansion of the binomial and cancellation of  $R^2$ , common to both sides, produces the required value of  $R_{min}$ .

$$\frac{2R_{min}}{\lambda} = \frac{a^2}{\lambda^2} - 1 \quad \Rightarrow \quad R_{min} = \frac{a^2}{2\lambda} - \frac{\lambda}{2} \quad (12.129)$$

Destructive interference along the axis can only occur for pistons with  $ka = 2\pi a/\lambda > 2\pi$ . The distance,  $R_{min}$ , which determines the farthest axial null is  $r_1 \cong a^2/2\lambda = a(ka)/4\pi$ . Examination of Fig. 12.36 shows that this approximation becomes more accurate as  $ka$  increases in accordance with Eq. (12.129).

As we move away from the piston, past  $R$ , we initially expect the axial pressure amplitude to increase then eventually decrease due to the  $1/r$  behavior of  $p_{ax}(r)$  in the far field, as described in Eq. (12.109). A more detailed calculation gives the location,  $r_1$ , of the peak in the axial response beyond  $R$  [56].

$$r_1 = \frac{a^2}{\lambda} - \frac{\lambda}{4} \quad \Rightarrow \quad \frac{r_1}{a} = \frac{(ka)}{2\pi} - \frac{\pi}{2(ka)} \quad (12.130)$$

Figure 12.37 provides plots of the axial pressure,  $p_{ax}(r)$ , for three values of  $2\pi \leq ka \leq 8\pi$ , and the caption provides the corresponding values for  $r_1$ . Depending upon the accuracy required for prediction of the far-field behavior, it is generally a good policy to make the start of the far field twice  $r_1$ , although some choose to define  $r_1$  as the start of the far field. Figure 12.37 provides the same representation for

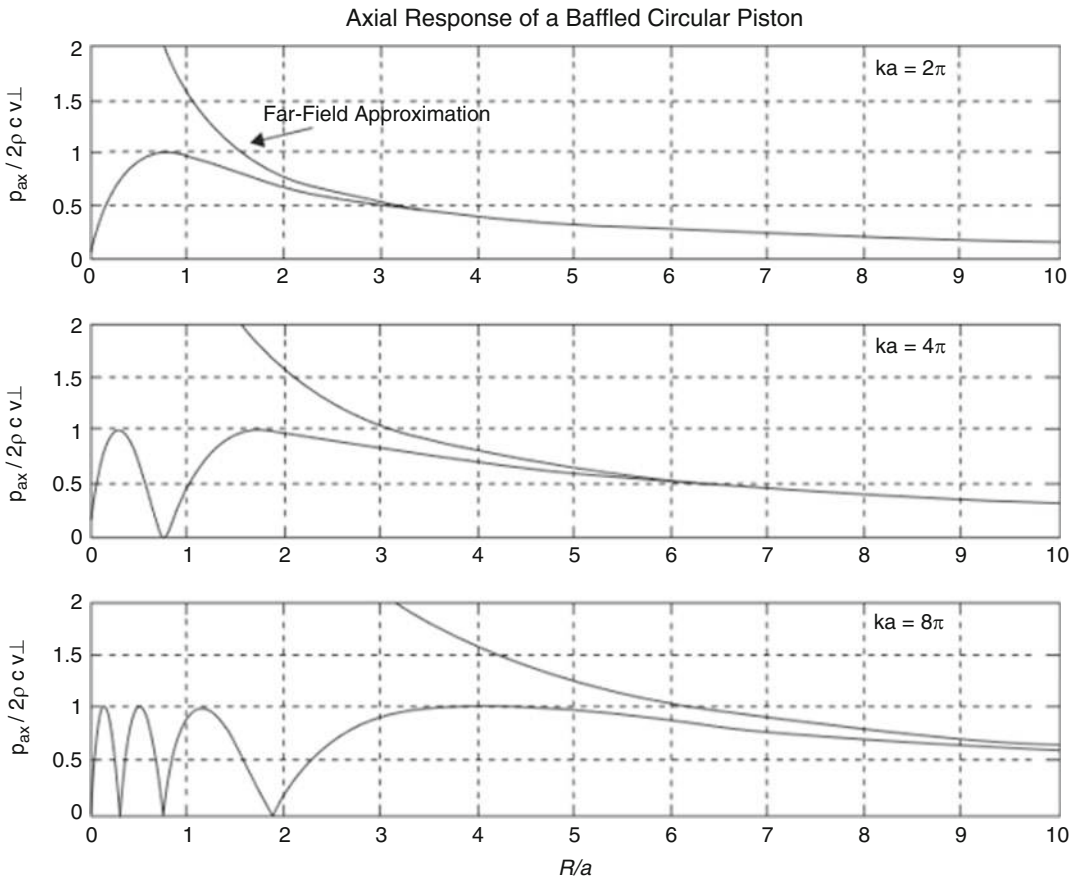


**Fig. 12.37** On-axis pressure for three rigid, baffled pistons with  $2\pi \leq ka \leq 8\pi$ . As the radius of the piston,  $a$ , becomes larger than the wavelength of sound,  $\lambda = 2\pi/k$ , there are more opportunities for constructive and destructive interference from various parts of the piston to modulate the sound pressure amplitude along the axis at distances smaller than  $R \cong a^2/\lambda$ . According to Eq. (12.129), for  $ka = 2\pi$ ,  $r_1 = 3a/4$ , for  $ka = 4\pi$ ,  $r_1 = 7a/4$ , and for  $ka = 8\pi$ ,  $r_1 = 15a/4$ . The smooth line shows the far-field pressure that varies inversely with distance,  $r$ , from the piston. [Graphs courtesy of A. A. Atchley]

the variation in axial pressure in the near field but uses a logarithmic representation of the  $x$  axis so that the rapid oscillations of the axial pressure near the piston for large  $ka$  can be resolved. In both figures, the number of maxima in the near field axial interference pattern is roughly equal to the number of wavelengths required to span one piston radius.

A good approximation of the peak pressure amplitude from the surface of the piston out to the far field which removes the interference effects is provided below and is shown in Fig. 12.38 as the dotted line labeled “MM” [57].

$$|p_{ax}(r)| = \frac{p_{ax}(0)}{\sqrt{1 + (r/a)^2}} \quad (12.131)$$

The dotted line labeled “M” in Fig. 12.37 is represented by a similar expression [58].

$$|p_{ax}(r)| = \frac{2p_{ax}(0)}{\sqrt{1 + (2r/a)^2}} \quad (12.132)$$

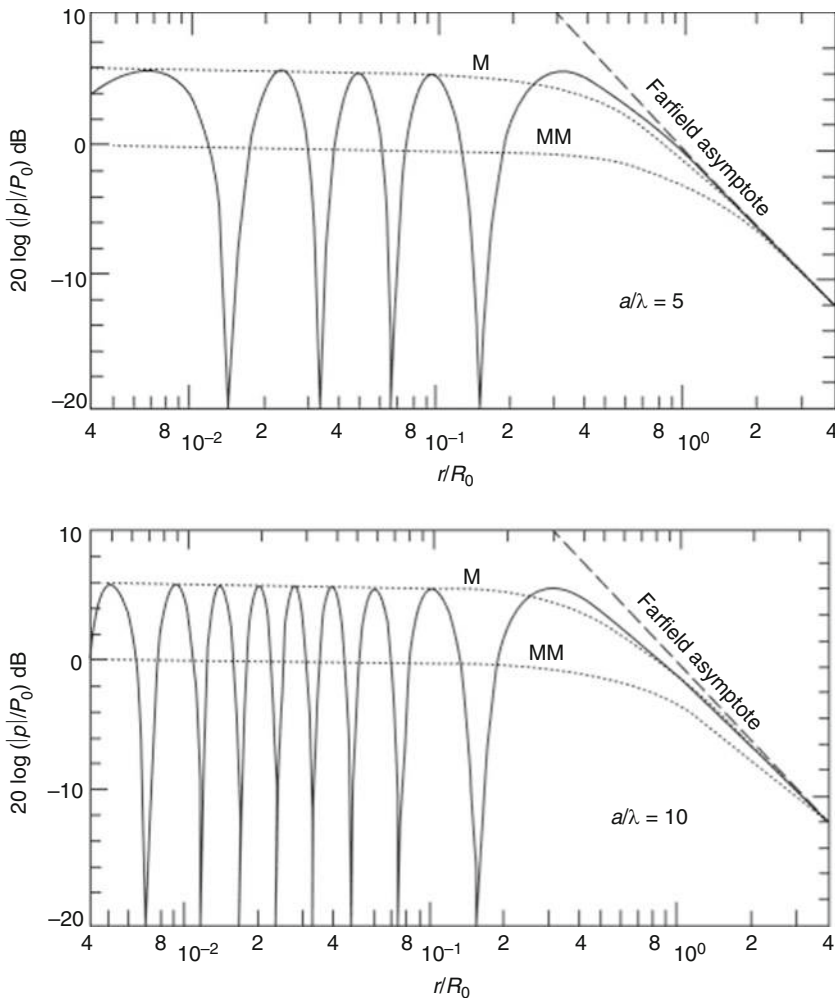


**Fig. 12.38** Plot of the log of the amplitude of the on-axis pressure from a rigid, baffled piston vs. the log of the distance from the surface of the piston scaled by the radius of the piston,  $R_o = a$ . In this figure, the distance is plotted on a logarithmic axis to make the spacing of the interference pattern appears roughly constant. In this log-log representation, the far-field asymptote is the straight (dashed) line with slope  $-1$ . The upper plot is for  $ka = 10\pi$  ( $a/\lambda = 5$ ), and the lower plot is for  $ka = 20\pi$  ( $a/\lambda = 10$ ). The dotted lines, “M” and “MM,” are useful for approximation of the near-field pressure amplitudes [59]

These approximations have been useful in the design of nonlinear underwater sound sources (see Sect. 15.3.3), where a significant amount of nonlinear mixing takes place in the near field.

## 12.9 Radiation Impedance of an Unbaffled Piston

The “effective mass” added to the surface of a circular baffled piston due to the fluid loading was calculated exactly in Sect. 12.8.3 and produced a hydrodynamic load that was equivalent to the mass of fluid contained in a cylindrical volume that had the same area as the piston,  $\pi a^2$ , and a height of  $\ell_{Baffle} = (8a/3\pi) \cong 0.85 a$ , if  $ka \ll 1$ . That correction was not enough to account for the experimental result in Sect. 8.5.2 that required  $\ell_{Flask} = 1.24 a$ , as expected, because there was additional kinetic

energy due to the entrained flow at both ends of the Helmholtz resonator's neck. The end of the neck that enters the compliance should have a flow field that is similar to that of the baffled piston but the other end is unbaffled; the entrained gas that oscillates at that open end can have a component that moves "backward" without the constraint imposed by the baffle.

It turns out that the exact solution for the radiation impedance of an unbaffled circular piston is considerably more difficult than the solution for the baffled piston, and an exact result for radiation from the end of a tube of infinite length with thin, rigid walls was not obtained until 1948 [60].<sup>21</sup>

$$\lim_{ka \rightarrow 0} \left[ \frac{h}{a} \right] = \frac{1}{\pi} \int_0^\infty \frac{1}{x^2} \ln \frac{1}{2I_1(x)K_1(x)} dx = 0.6133 \quad (12.133)$$

$$\Rightarrow \ell_{L\&S} = 0.6133a \quad \text{if } ka \ll 1$$

$I_1(x)$  and  $K_1(x)$  are the modified Bessel functions (of complex argument) that were plotted in Fig. 6.20. The variation in  $\ell/a$  as a function of  $(ka)$  for the unbaffled piston is plotted in Fig. 12.40. Until then, the unbaffled end correction was based on experimental measurements on closed-open pipes, as illustrated schematically in Fig. 12.39. Rayleigh found  $\ell/a \cong 0.6$  using organ pipes with and without a flange [61].<sup>22</sup>

Rather than attempt an exact derivation of the result in Eq. (12.133) for the unbaffled piston, it will be easier to argue that the radiation from the unbaffled piston, at small values of  $ka$ , should be similar to the radiation from the spherical source (i.e., a compact monopole), analyzed in Sect. 12.2.1, since the body of the closed-open resonator in Fig. 12.39 does not exclude much volume from the infinite space surrounding the piston.

Since it is the volume velocity produced by the unbaffled piston that determines the sound radiation, we can ask what should be the radius,  $b$ , of the "equivalent" spherical source to provide the same radiating area as the piston of radius,  $a$ :  $A_{pist} = \pi a^2 = A_{sphere} = 4\pi b^2$ . This equivalence requires that  $b = a/2$  resulting in an equivalent hydrodynamic mass,  $m_{eff}$ , for the monopole equivalent.

$$m_{eff} = 3\rho_m V_{sphere} = 3\rho_m (4\pi/3)(a/2)^3 = (\frac{1}{2})a(\pi a^2) = (a/2)A_{pist} \quad (12.134)$$

By that argument, for an unbaffled piston, the effective length correction is  $\ell_{Unbaffled} \cong 0.5a$ . That result is 18% less than the exact result in Eq. (12.133), and both results are less than  $\ell_{Baffled} = 0.85a$  for the baffled circular piston.



**Fig. 12.39** Schematic representation of a closed-open pipe. Motion of the fluid oscillating at the open is represented by the piston shown as the dotted rectangle that produces a sinusoidal volume velocity,  $\hat{U}e^{j\omega t}$

<sup>21</sup> The solution was sufficiently difficult that one of the authors was the theoretical physicist, Julian Schwinger (1918–1994), who shared the 1965 Nobel Prize in Physics for quantum electrodynamics with Sin-Itiro Tomonaga and Richard Feynman. The other, Harold Levine, continued his career as a mathematics professor at Stanford University, specializing in integral equations.

<sup>22</sup> Rayleigh also reports a "careful experimental determination" made by Blaikley [Phil. Mag. 7, 339, (1879)] that used a brass tube of 5.3 cm diameter that had one end submerged in water to produce the adjustable distance for the closed end and five tuning forks for frequencies between 254 Hz and 707 Hz. The length of the tube above the water was adjusted to be co-resonant with the forks and resulted in an experimental effective length at the open end of  $\ell = (0.576 \pm 0.014) a$ .

**Fig. 12.40** Plot of the end correction for radiation from an unbaffled pipe in terms of the pipe's radius:  $\ell/a$  for  $0 \geq ka < 4$  from Levine and Schwinger [60]

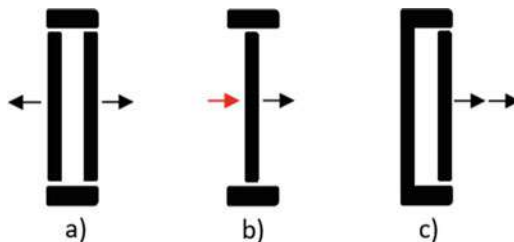
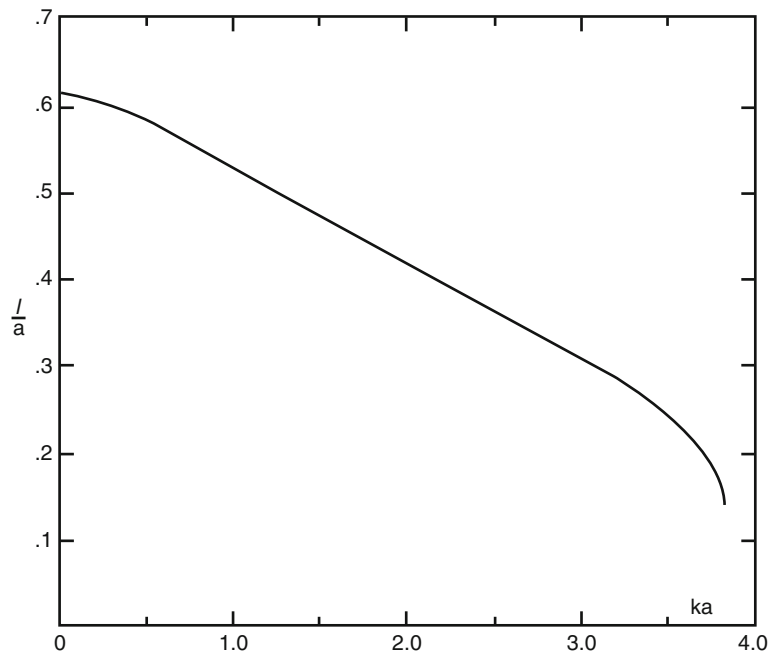


**Fig. 12.41** The flow field from an unbaffled piston is constructed from the superposition of two anti-phase baffled pistons in (a) plus the field of a rigid disk oscillating along its axis in (b) to produce the required flow in (c), since disk's oscillations cancel the rearward piston and doubles the forward piston's flow. (Figure courtesy of D. A. Brown)

Before leaving this topic, it is worthwhile mentioning the calculation of the unflanged end correction made by Lev Gutin a decade before the publication of the Levine and Schwinger result. Gutin used the superposition two oppositely phased baffled pistons plus the translational oscillations of a rigid disk to produce the flow field of an unbaffled piston as shown schematically in Fig. 12.41 [62].

Gutin's calculation resulted in an effective length correction in the small  $ka$  limit of  $\ell_{Gutin} = 0.636 a$ . This is only 3.7% larger than today's accepted value of  $\ell_L \& s = 0.6133 a$ .

Bringing this back to the measured effective length for the 500 ml boiling flask used to study the frequency of a Helmholtz resonator in Sect. 8.5.2, we see that simply adding a baffled correction to one end of the resonator's neck and an unbaffled correction to the other end produces a “theoretical” correction of  $\ell = [(8/3\pi) + 0.6133]a \cong 1.462a$ . That is greater than the measured value of  $\ell = 1.24a$ , even in the absence of the resonance frequency reduction due to the inclusion of thermoviscous losses in the DELTAEC model of Fig. 8.27, which resulted in a correction of only  $\ell_{DeltaEC} = 1.07 a$ . Those frequency measurements in Fig. 8.17 were clearly within the small  $ka$  limit:  $ka \cong 0.05 \ll 1$ .

In conclusion, it is fair to say that the kinetic energy of the gas oscillations at the end of a duct that is either baffled or unbaffled requires the addition of some hydrodynamic mass to account for the flow at the exits of such ducts. It is also fair to say that the effective length correction required to incorporate the entrained flow is sensitive to the actual circumstances that influence those entrained flows. James Mehl studied the duct end correction using a boundary-integral equation and examined the effects of the rounding of duct edges and the effects of finite chamber size and provides an extensive list of references to articles that have studied such *end corrections* [63].

---

## 12.10 Linear Superposition

Chapter 12 is the longest chapter in this textbook. Although its title is “Radiation and Scattering,” it could easily have been entitled “Multiple Applications of Linear Superposition.” It started by examining the sound radiated by a “compact” source of oscillatory volume velocity in an approximate model that demonstrated that the periodic insertion and removal of fluid could only affect the acoustic pressure variations within a “causality sphere” whose volume was limited by the speed of sound. Going beyond that perspective, it was possible to obtain an exact solution for the spherically symmetric waves produced such a sound source by solving the wave equation in an infinite, homogeneous, and isotropic three-dimensional fluid medium and assuming that the volume velocity was produced by a sphere whose radius underwent a harmonic variation as a function of time.

The solution for a compact monopole source also permitted the calculation of the complex radiation impedance at the source’s surface. We used the imaginary component of that radiation impedance to demonstrate that it was necessary for the source to overcome the inertia of the surrounding fluid. Quantifying that fluid inertia facilitated the calculation of the simple harmonic oscillations of a gas bubble in a liquid. The real component of that radiation impedance was used to calculate the time-averaged acoustical power that such a simple monopole source would radiate.

Armed with the behavior of a compact monopole, we used linear superposition to examine the behavior of various collections of such monopoles, both discrete (e.g., to examine sources near reflecting surfaces and linear arrays) and continuous (e.g., to integrate the effects of infinitesimal sources over the surface area of a pulsating tube or the surface of an oscillating piston).

The most significant superposition was that of two sources that were separated by a small fraction of a wavelength,  $kd \ll 1$ , and were  $180^\circ$  out-of-phase, thus producing a “compact dipole.” That significance was due to the fact that the flow produced by such a dipole was equivalent to the flow produced when a rigid sphere (or other solid object) makes translational oscillatory excursions through an otherwise stagnant fluid.

The compact monopole and the compact dipole provided a basis for the calculation of sound that is scattered by inhomogeneities in a fluid that are small compared to the wavelengths of the sound scattered by such inhomogeneities. Sound waves in fluids are a consequence of the competition between the fluid’s compressibility and mass density. Monopoles let us calculate the sound scattered from compressibility contrasts, and dipoles did the same for scattering from density contrasts.

As was the case so many times in this textbook, very simple systems examined in limits that permitted calculation of their acoustical behavior have provided models that can guide our intuition and create a vocabulary for the understanding of a much greater range of systems. A stage with hundreds of loudspeakers in dozens of clusters, as shown in Fig. 12.1, can make perfect sense from the right perspective.

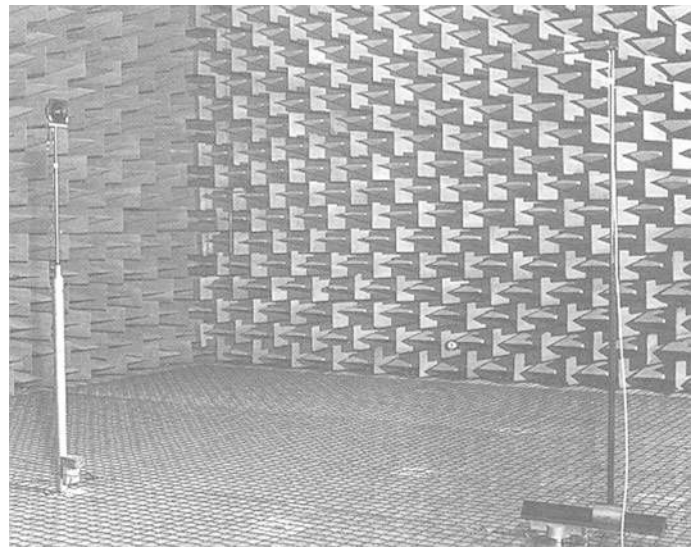
### Talk Like an Acoustician

Causality sphere	
Monopole	Directivity index
Compact source	Dipole
Compactness criterion	Dipole strength
Rayleigh resolution criterion	Pressure gradient microphone
Acoustic transfer impedance	Ribbon microphone
Specific acoustic impedance	Cardioid directionality
Characteristic impedance	Semi-infinite half-space
Radiation reactance	Minor lobe
Radiation resistance	Solid angle
Effective mass	Steradian
Hydrodynamic mass	Density contrast
End correction	Compressibility contrast
Laplace's formula	Differential scattering cross section
Source strength	Total scattering cross section
Far field	Rayleigh scattering
Near field	Mean field approximation
Bipole	Void fraction
End-fire direction	Array gain
Broadside direction	Beam steering
Directionality factor	End-fire array
Baffled source	Shaded array
Directivity	End corrections

### Exercises

- Big sphere at high frequency.** A pulsating sphere operates at a frequency such that  $ka \gg 1$  with a radius,  $r(t) = \Re e^{[\hat{\xi} e^{j\omega t}]}$ , so the amplitude of the radial velocity at the surface of the sphere is  $|\hat{v}_r| = \omega |\hat{\xi}|$  and  $|\hat{\xi}| \ll a$ . Calculate (a) the radiated pressure amplitude, (b) particle velocity amplitude, and (c) the time-averaged intensity as a function of the distance from the center of the sphere, along with (d) the total time-averaged radiated power.
- Spherical (monopole) source in air.** A compact source in air radiates 10 mW of time-averaged acoustical power at 400 Hz in air at 20 °C with  $p_m = 100$  kPa. At a distance of 0.5 m from the center of the source, calculate (a) the radiated time-averaged intensity, (b) the amplitude of the acoustic pressure, (c) the amplitude of the particle speed and its phase relative to the acoustic pressure, and (d) the peak-to-peak particle displacement of the air.
- Radiation from a point source.** A spherical point source is radiating sinusoidally in air; the resultant radiation propagates through free space. The acoustic power of this source is 1000 W at 1000 Hz.
  - Amplitude.** Calculate the time-averaged intensity, the sound pressure amplitude, and the acoustic particle velocity at 1.0 and 10.0 meters from the center of the source.
  - Phase.** Calculate the phase angle (in degrees) between the sound pressure and particle velocity at distances of 0.5, 1.0, and 10.0 meters from the source.
- Spherical spreading.** You are assigned to check the quality of a new anechoic room that has been built by your employer. You decide to test the room by making a measurement of the pressure detected by a microphone as a function of the separation between the microphone and the sound

**Fig. 12.42** Sound source (loudspeaker) and microphone located in an anechoic chamber



source that is an ordinary loudspeaker in a room as shown in Fig. 12.42. You do not have a priori knowledge of the distances between the *acoustic centers* of the microphone and speaker and the points on those two transducers between which you are measuring their physical separation,  $d$ .

To compensate for this uncertainty, you define the effective acoustic separation,  $d_{ac} = d + a$ , to be the measured physical separation,  $d$ , plus some (possibly frequency-dependent) length,  $a$ , that may be positive or negative.

If the room is truly anechoic, then the decrease in microphone output voltage,  $V(d)$ , as a function of source-receiver physical separation,  $d + a$ , should exhibit spherical spreading, indicated by Eq. (12.135), where  $B$  is a constant and  $a$  is an adjustable parameter that accounts for the fact that the measured distance and the distance between the acoustic centers of the source and receiver might be different from their physical separation,  $d$ .

$$V(d) = \frac{B}{d+a} \quad (12.135)$$

Transform this equation so that the data can be plotted in a way that represents the spherical spreading as a straight line vs. the measured (physical) separation,  $d$ , between the source and microphone, to produce a value of  $a$  that can be determined from the slope of the line, its intercept, or both the slope and the intercept. Write an expression for  $a$  in terms of the slope and/or intercept of your transformed equation.

5. **Swim bladder resonance.** Many fish species use an air-filled sac, known as a “swim bladder,” to control their buoyancy. Fish also use “constrictor muscles,” shown schematically in Fig. 12.43, to excite motion of that organ to generate sound, usually consisting of a train of repetitive pulses that are typically in the frequency range of 100 Hz to 1.0 kHz, and also to receive sounds, since Eq. (12.77) demonstrates that the air-filled bladder will compress much more than the surrounding water in response to an impinging sound wave [64].

If such a fish is swimming at a depth of 5 m below the water’s surface, what would have to be the volume of the swim bladder,  $V_{swim}$ , so that it would be resonant at 500 Hz? To simplify the calculation, it is reasonable to assume that the mass density of fish flesh is roughly equivalent to that

**Fig. 12.43** Swim bladder anatomy

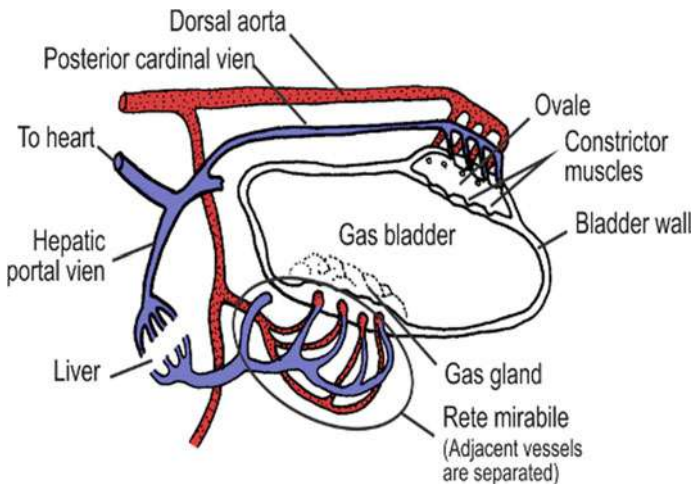
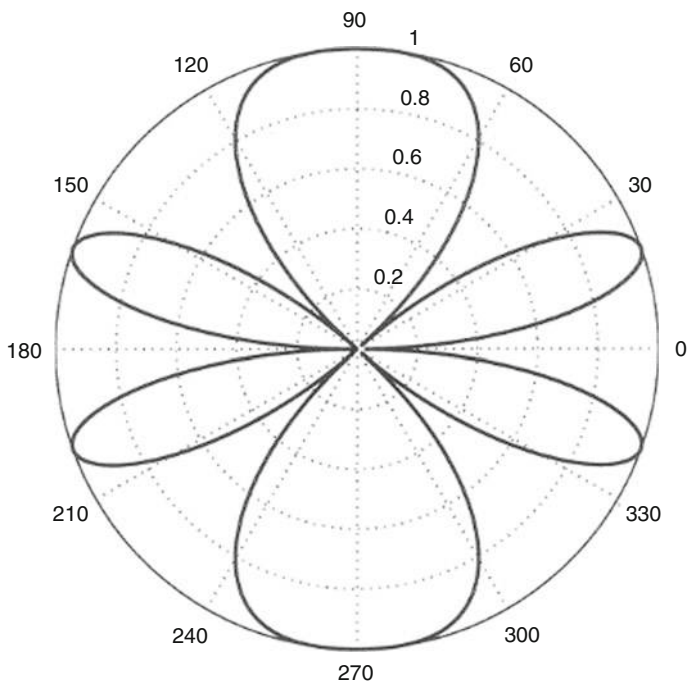


**Fig. 12.44** Directional pattern for two sound sources of equal amplitude separated by a distance,  $d$ , between their centers



of the surrounding water, so the hydrodynamic mass loading would be approximately the same as assumed for a bubble in Eq. (12.29). Although the swim bladder is not spherical, its equivalent radius,  $a_{eff} = (3V_{swim}/4\pi)^{1/3}$ , still makes  $(ka_{eff}) \ll 1$ , so its approximately prolate spheroidal shape will not create a substantial difference between the resonance frequency of the bladder and an equivalent spherical volume [8].

6. **Train in the tunnel.** A train traveling at 60 mph enters a long tunnel with the same cross-sectional area and frontal shape as the train. Assume both gas leakage around the train and friction between the train and tunnel walls are negligible. Estimate the amplitude of the pressure wave created in the tunnel. [Hint: One approach might be to think about the speed of the wave front and the speed of the train (piston), then apply that trusty adiabatic gas law.]

- 7. Far-field radiation pattern.** The far-field radiation pattern, shown in Fig. 12.44, was created by two simple (compact) sound sources of equal source strength separated by a distance,  $d$ . The two sources are aligned along the vertical axis (the  $90^\circ - 270^\circ$  axis) of the figure and radiate with equal amplitude.
- Bipole or Dipole.* What is the phase difference between the two sources in degrees?
  - Separation.* What is the value of  $kd$  for this pair of sources?
- 8. Four-element line array.** The far-field radiation pattern shown in Fig. 12.45 was created by four simple (compact) sound sources that are oscillating in-phase and are separated by a distance,  $d$ , along a straight line. The total length of the array is  $L = 3d$ . What is the value of  $d$ , expressed in terms of the wavelength of sound that is being radiated?
- 9. Continuous line source.** One quadrant of the far-field directional radiation pattern produced by a uniform line source is shown in Fig. 12.46. The uniform line array is oriented along the  $90^\circ - 270^\circ$  axis. Nodal cones are shown making angles with the vertical axis (i.e.,  $\theta_p = 0^\circ$ ) of approximately  $15^\circ$ ,  $32^\circ$ , and  $52^\circ$ .

**Fig. 12.45** Directional pattern for a four-element line array

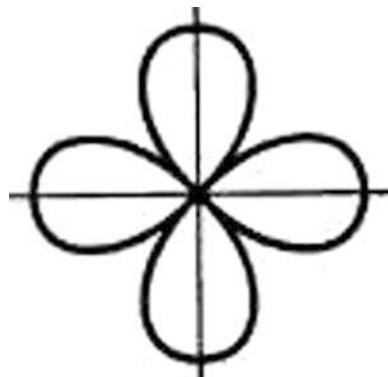


**Fig. 12.46** Directional pattern of a continuous line array

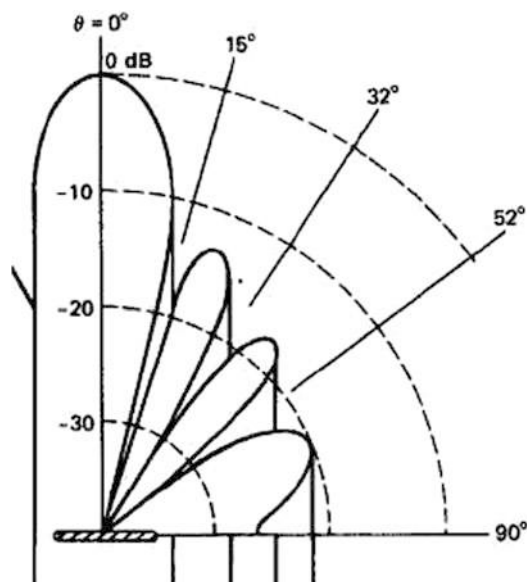
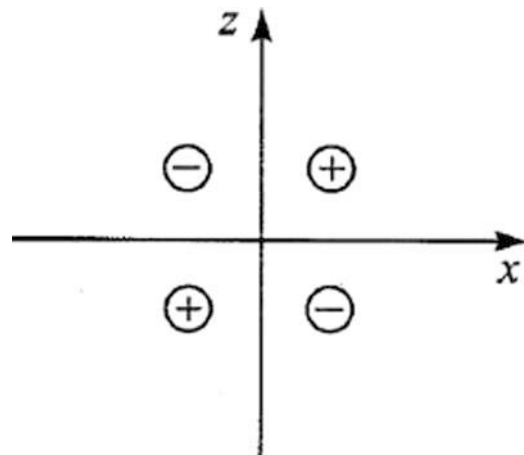


**Fig. 12.47** Quadratic quadrupole



Determine the dimensionless length of the line array,  $2\pi L/\lambda = kL$ , where  $L$  is the physical length of the array and  $\lambda$  is the wavelength of the sound radiated by the uniform line source.

10. **Quadratic quadrupole radiation impedance.**<sup>23</sup> A quadratic quadrupole is a compact collection of four simple sources. As shown in Fig. 12.47, one pair are in-phase ( $\phi = 0^\circ$ ) as indicated by the  $\oplus$  symbol, and the other pair have  $\phi = 180^\circ$  out-of-phase with the first pair as indicated by the  $\ominus$  symbol. The radius of each simple source is  $a$ . The radiation impedance for such a quadrupole is given in Eq. (12.136) for  $ka < 1$ .

$$\mathbf{Z}_{\text{quad}} = \rho_m c \frac{4\pi a^2 (ka)^6}{1215} - j\omega \rho_m \frac{4\pi a^3}{45} \left[ 1 + \frac{(ka)^2}{9} + \frac{4(ka)^4}{81} + \dots \right] \quad (12.136)$$

- (a) *Impedances.* There are three types of impedances that are commonly used in acoustics. Is the impedance in Eq. (12.136) a characteristic, mechanical, or acoustical impedance?
- (b) *Effective radiation mass.* In the limit of sources whose circumference is significantly smaller than one wavelength (i.e.,  $2\pi a \ll \lambda$ ), express the “effective mass” of that collection of four oscillating simple sources in terms of mass of the fluid displaced by one spherical source with radius,  $a$ .
11. **Long line array.** A line array of simple sources is designed so that  $kL = 50$ .
- Major lobes.* How many maxima does it produce for  $0^\circ \leq \theta \leq 90^\circ$ ?
  - Nodal lines.* How many nodal lines (in the two-dimensional representation) are there within the same angular interval?
  - Beam width.* Find the full angular beam width,  $\Delta\theta$ , of the lobe centered at  $\theta = 0^\circ$  if the full beam width is defined as the angle between the nodal directions that limit the central lobe.
  - Other beam width definitions.* What is the angular width of the beam if that beam width corresponds to a ratio of the main lobe amplitude to the down 3 dB, 6 dB, 10 dB, and 20 dB full angular widths:  $\Delta\theta_{-3\text{dB}}$ ,  $\Delta\theta_{-6\text{dB}}$ ,  $\Delta\theta_{-10\text{dB}}$ , and  $\Delta\theta_{-20\text{dB}}$ .

<sup>23</sup> There are also “linear quadrupoles” that consist of a double-strength source at the center and two sources with phase opposite to the central source, all arranged in a straight line:

$\ominus \quad \oplus\oplus \quad \ominus.$

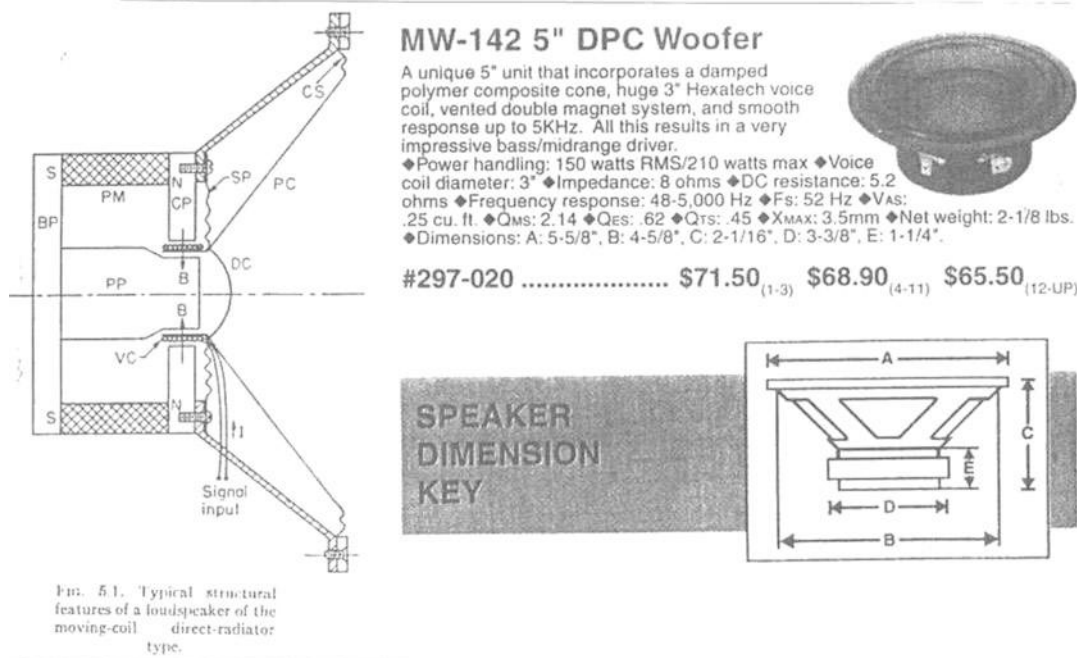


Fig. 5.1. Typical structural features of a loudspeaker of the moving-coil direct-radiator type.

**Fig. 12.48** (Left) Cross-section of a conventional moving-coil direct radiator type loudspeaker showing the suspension (CS), the spider (SP), speaker cone (PC), dust cap (DC), and voice coil (VC). The radial magnetic field (B) is produced by the permanent magnetic material (PM) with north (N) and south (S) magnetic polarity, the central pole piece (PP), the backplate (BP), and the front pole piece (CP). Figure from Hunt [65]. (Right) Catalog listing a 5" Morel model MW-142 loudspeaker

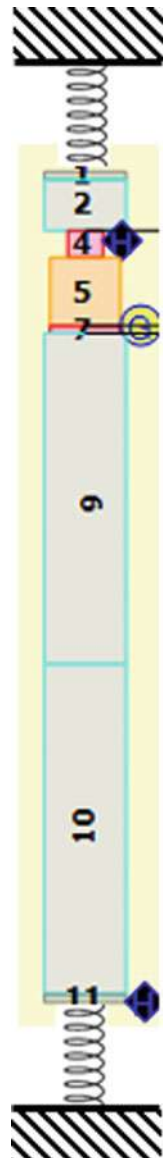
- (e) *Lobe amplitude ratio.* What is the ratio of the amplitude of the peak of the first side lobe to the peak of the central lobe? Report that ratio in dB.
12. **Piston angular null.** A baffled circular piston of radius,  $a$ , radiates sound at frequency,  $\omega$ . What is the smallest angle,  $\theta_1$ , with respect to the piston's axis, at which the radiated sound pressure is zero. Express your answer in terms of the wavenumber,  $k = \omega/c$ , and the radius of the piston.
13. **"Flat" frequency range for an electrodynamic loudspeaker.** The speaker shown in Fig. 12.48 (rsight) has a moving mass  $m_o = 11.8$  g, a suspension stiffness,  $K = 1440$  N/m, a mechanical resistance,  $R_m = 1.9$  kg/s, and a force factor,  $(B\ell) = 7.1$  N/A. The effective diameter of the piston is  $2a = 11.0$  cm. Assume it is mounted in an infinite baffle like that shown in Fig. 8.37.
- (a) *Free-cone resonance.* Calculate the free-cone resonance frequency,  $f_o$ , of this speaker.
- (b) *Forced motion.* Assume the speaker is mounted in an infinite baffle and it is driven by a sinusoidal current,  $I(t) = 1.41 \cos(\omega t)$  amperes. The force on the piston produced by this current flowing through the speaker's voice coil is  $F(t) = (B\ell)I(t)$ . Plot the magnitude and phase (with respect to the driving current) of the volume velocity,  $\hat{U}(f)$ , created by the piston from 10 Hz to 3500 Hz. Use logarithmic axes for both frequency and volume velocity but plot phase angle on a linear scale, preferably on the same graph. You may neglect any

fluid loading of the piston (e.g., effective hydrodynamic mass) in all parts of these calculations.

- (c) *Effective air mass.* What is the hydrodynamic mass of the air that is being accelerated by the front face of the piston for  $ka < 1$  if  $p_m = 100 \text{ kPa}$  and  $c = 20^\circ\text{C}$ .<sup>24</sup> Compare this result to the speaker's moving mass,  $m_o$ .
  - (d) *Radiated power.* The (mechanical) radiation resistance,  $\rho_m c \pi a^2 R_1(2ka)$ , can be used to convert the volume velocity calculated in part (b) to the time-averaged radiated power,  $\langle \Pi_{rad} \rangle_t = (\frac{1}{2}) \Re e[\mathbf{Z}_{\text{mech}}] \left| \widehat{\mathbf{U}} / A_{\text{pist}} \right|^2$ . Plot the radiated power in dB *re*: 1 watt vs. the log of frequency from 10 Hz to 3500 Hz.
  - (e) *"Flat" region of the speaker's far-field radiation.* Over what range of frequencies is the speaker's time-averaged radiated power constant to within  $\pm 2 \text{ dB}$ ? Provide the limiting frequencies,  $f_{\min}$  and  $f_{\max}$ , as well as the  $\pm 2 \text{ dB}$  frequency bandwidth,  $\Delta f_{\pm 2\text{dB}} = f_{\max} - f_{\min}$ .
14. **Party balloon.** A young child is in the back seat of an automobile that is initially at rest with all of the windows closed. In the hand of the child's outstretched arm is a string that is attached to a helium-filled balloon. If the car accelerates forward, does the balloon get closer to the child or to the driver? Is your answer consistent with Eq. (12.71) and with the Equivalence Principle of Einstein's Theory of General Relativity?
15. **Thermoacoustic sound source suspension and dipole radiation.** The device shown in Fig. 12.49 represents the DELTAEC model (segments numbered 1 through 11) of a nuclear-powered thermoacoustic engine (resonator) [66]. It is only free to move in the vertical direction as it is suspended between two identical springs, each with stiffness, K. The resonator is a rigid body with a total mass of 0.35 kg. Heat produced by nuclear fission of enriched  $^{235}\text{U}$  maintains a standing acoustic wave within the resonator that causes the gas mixture (80% helium, 20% argon), at a mean pressure of  $p_m = 2.0 \text{ MPa}$ , to oscillate back and forth within the resonator. The gas resonance occurs at the fundamental, half-wavelength, frequency,  $f_1 = 1588 \text{ Hz}$ .
- (a) *Resonator length.* If the mean temperature of the gas mixture in the resonator is  $30^\circ\text{C}$ , what is the length of the resonator?
  - (b) *Force.* The oscillatory motion of the gas causes a reaction force on the ends of the resonator. (Think of the gas in the resonator bouncing back and forth between the resonator end caps of segments #1 and #11.) If the moving gas has an effective mass,  $m = 6 \times 10^{-4} \text{ kg}$ , according to the DELTAEC model, the effective (peak) velocity of that effective mass is 16 m/s. What is the magnitude of the peak force that the oscillatory gas applies to the resonator?
  - (c) *Static deflection.* If the total mass of the resonator is 0.35 kg, what is the stiffness of one of the two identical springs, K, so that the resonator's weight in a gravitational field of acceleration,  $g = 9.8 \text{ m/s}^2$ , causes the resonator to drop by only 1.0 mm?
  - (d) *Suspension resonance frequency.* Using the stiffness calculated above in part (c), what is the natural frequency of the mass-spring system (ignoring the gas motion), remembering that both springs contribute to the restoring force?
  - (e) *Resonator displacement.* Using the force calculated in part (a), what is the resonator's peak-to-peak oscillatory displacement?
  - (f) *Radiated dipole power.* Using the displacement calculated in part (e) and the resonator's length calculated in part (a), what is the acoustic power radiated by the oscillatory

<sup>24</sup>With the loudspeaker mounted in an infinite baffle, there would also be an equal hydrodynamic mass due to the sound radiated into the space on the other side of the baffle. With the same speaker mounted in a sealed box, the rear of the cone would feel the stiffness of the gas within the box. For this problem, we will ignore that rear radiation.

**Fig. 12.49** Schematic representation of an elastically suspended thermoacoustic resonator



displacement of the cylindrical resonator if each of the resonator's end caps has an area,  $A_{end} = 2.8 \text{ cm}^2$ , and the surrounding fluid is water?

## References

1. R. Weir, J. Garcia, D. Healy, R. Wickersham, Large room acoustics versus music. *J. Acoust. Soc. Am.* **58**, S1 (1975)
2. B. Kinsman, *Wind Waves: Their Generation and Propagation on the Ocean Surface* (Prentice-Hall, Englewood Cliffs, 1965)
3. L.D. Landau, E.M. Lifshitz, *Fluid Mechanics*, 2nd edn. (Butterworth-Heinemann, Boston, 1987). See §15; ISBN:0-7506-2767-0. ISBN:0-7506-2767-0

4. V. Mangulis, Relation between the radiation impedance, pressure in the far field, and baffle impedance. *J. Acoust. Soc. Am.* **36**, 212–213 (1964)
5. P.M. Morse, *Vibration and Sound*, 2nd edn. (McGraw-Hill, New York, 1948). See §27. Reprinted by the Acoust. Soc. Am., 1995; ISBN:0-88318-876-7
6. L.D. Landau, E.M. Lifshitz, *Fluid Mechanics*, 2nd edn. (Butterworth-Heinemann, Boston, 1987). §61; ISBN:0-7506-2767-0
7. M. Minnaert, Musical air bubbles and the sounds of running water. *Philos. Mag.* **16**, 235–248 (1933)
8. M. Strasberg, The pulsation frequency of nonspherical gas bubbles in liquids. *J. Acoust. Soc. Am.* **25**(3), 536–537 (1953)
9. T.F. Argo IV, P.S. Wilson, V. Palan, Measurement of the resonance frequency of single bubbles using a laser Doppler vibrometer. *J. Acoust. Soc. Am.* **123**(6), EL212–EL125 (2008)
10. K.W. Commander, A. Prosperetti, Linear pressure waves in bubbly liquids: comparison between theory and experiments. *J. Acoust. Soc. Am.* **85**(2), 732–746 (1989)
11. C. Devin Jr., Survey of thermal, radiation, and viscous damping of pulsating air bubbles in water. *J. Acoust. Soc. Am.* **31**(12), 1654–1667 (1959)
12. O.B. Wilson, *An Introduction to the Theory and Design of Sonar Transducers* (Peninsula, Los Altos, 1989). ISBN:978-0932146229
13. R.L. Prichard, Mutual acoustic impedance between radiators in an infinite rigid plane. *J. Acoust. Soc. Am.* **32**(6), 730–737 (1960)
14. S. Hanish, *A Treatise on Acoustic Radiation, Vol. IV – Mutual Radiation Impedance and Other Special Topics* (Naval Research Lab, Washington, DC, 1987)
15. T. Young, The Bakerian Lecture [1803]: experiments and calculations relative to physical optics. *Phil. Trans. R. Soc. London* **94**, 1–16 (1804)
16. A. Howie, J.E. Ffowcs-Williams, Preface. *Phil. Trans. R. Soc. London* **A360**, 805–806 (2002)
17. J. Cui, M.F. Hamilton, P.S. Wilson, E.A. Zabolotskaya, Bubble pulsations between parallel plates. *J. Acoust. Soc. Am.* **119**(4), 2067–2072 (2006)
18. A.D. Pierce, *Acoustics: An Introduction to Its Physical Principles and Applications* (McGraw-Hill, New York, 1981), pp. 482–486; ISBN:0-07-049961-6. Also reprinted by the Acoustical Society of America, 3rd ed. 2019; ISBN 978-3-030-11214-1
19. W.R. Smythe, *Static and Dynamic Electricity* (McGraw-Hill, London, 1939). §5.08
20. J.D. Jackson, *Classical Electrodynamics* (Wiley, New York, 1962). See Prob. 5.8
21. L.D. Landau, E.M. Lifshitz, *Fluid Mechanics*, 2nd edn. (Butterworth-Heinemann, Boston, 1987). §11; ISBN:0-7506-2767-0
22. P.M. Morse, K.U. Ingard, *Theoretical Acoustics* (McGraw-Hill, New York, 1968). §7.1
23. A.U. Case, The vocal microphone: technology and practice. *Phys. Today* **69**(3), 74–75 (2016)
24. B. Baumzweiger, Microphone apparatus, US Patent No. 2,184,247, 19 Dec 1939
25. M.S. Pettersen, 75<sup>th</sup> anniversary of the Shure Unidyne® microphone. *J. Acoust. Soc. Am.* **136**(4), 2129 (2014)
26. W.L. Dooley, Ribbon microphones. *J. Acoust. Soc. Am.* **136**(4), 2130 (2014)
27. L.L. Beranek, *Acoustics* (Acoustical Society of America, New York, 1996). See Part XVI, §6.7; ISBN:0-88318-494-X
28. T.B. Gabrielson, *Theory of operation for the DIFAR flux-gate compass*. Naval Air Development Center Technical Memorandum 3031-86-02, April 1986
29. D.A. Brown, Bearing measurements using a compact wideband sensor by forming three dipoles. *J. Acoust. Soc. Am.* **134**(5), 4052 (2013). Also see D.A. Brown, B. Aronov, C.L. Bachand, Acoustic transducers for underwater navigation and communication. U.S. Patent No. 8,638,640, 28 Jan 2014. Fig. 10A
30. R.M. Keolian, S.L. Garrett, C.B. Cameron, Demodulators for optical fiber interferometers with [3 X 3] outputs. U.S. Patent No. 5,313,266, 17 May 1994. See Fig. 17
31. S. Tempkin, *Elements of Acoustics* (Wiley, New York, 1981). See §5.5; ISBN:0-471-05990-0
32. L.D. Landau, E.M. Lifshitz, *Fluid Mechanics*, 2nd edn. (Butterworth-Heinemann, Boston, 1987). §74, see Problem 1; ISBN:0-7506-2767-0
33. T.B. Gabrielson, D.L. Gardner, S.L. Garrett, A simple neutrally-buoyant sensor for direct measurement of particle velocity and intensity in water. *J. Acoust. Soc. Am.* **97**(4), 2227–2237 (1995)
34. L.D. Landau, E.M. Lifshitz, *Fluid Mechanics*, 2nd edn. (Butterworth-Heinemann, Boston, 1987). For an alternative derivation see §11, Problem 1; ISBN:0-7506-2767-0
35. S.L. Garrett, D.L. Gardner, Multiple axis fiber optic interferometric seismic sensor. U.S. Patent No. 4,893,930, 16 Jan 1990
36. D.L. Gardner, S.L. Garrett, A fiber optic interferometric seismic sensor with hydrophone applications. U.S. Navy J. Underw. Acoust. JUA(USN) **38**(1), 1–21 (1988)
37. J.W. Strutt (Lord Rayleigh), On the light from the sky, its polarization and colour. *Philos. Mag.* **XLI**, 107–120 and 274–279 (1871); *Scientific Papers*, Vol. I (Dover, 1964) §8

38. J.W. Strutt (Lord Rayleigh), On the scattering of light from small particles. *Philos. Mag.* **XLI**, 447–454 (1871); *Scientific Papers*, Vol. I (Dover, 1964) §9
39. H. Lamb, *The Dynamical Theory of Sound*, 2nd edn. (Arnold, London, 1925). §79. Reprinted by Dover, 1960
40. T.G. Leighton, *The Acoustic Bubble* (Cambridge University Press, Cambridge, 1994). ISBN:0-12441-920-8. See §4.1.2
41. A. Mallock, The damping of sound in frothy liquids. *Proc. R. Soc. A* **84**(572), 391–395 (1910)
42. F.S. Crawford, The hot chocolate effect. *Am. J. Phys.* **50**(5), 398–404 (1982)
43. D. Fitzpatrick, J. Kruse, B. Vos, O. Foley, D. Gleeson, E. O’Gorman, R. O’Keefe, Principles and Application of Broadband Acoustic Resonance Dissolution Spectroscopy (BARDs): a sound approach for the analysis of compounds. *Anal. Chem.* **84**, 2202–2210 (2012)
44. R.V.G. Peddapati, M. Rizwan Ahmed, C.A. Blackshields, M.J. Sousa-Gallagher, S. McSweeney, J. Kruse, A.M. Crean, D. Fitzpatrick, Broadband Acoustic Resonance Dissolution Spectroscopy (BARDs): a novel approach to investigate the wettability of pharmaceutical power blends. *Mol. Pharm.* **15**, 31–39 (2018)
45. I.S. Gradshteyn, I.M. Ryzhik, *Tables of Integrals, Series, and Products*, 4th edn. (Academic, London, 1980). See Eq. (0.112); ISBN:0-12-294760-6
46. K.U. Ingard, *Fundamentals of Waves and Oscillations* (Cambridge University Press, Cambridge, 1988). ISBN:0-521-33957-X
47. M. Abramowitz, I.A. Stegun, *Handbook of Mathematical Functions with Formulas, Graphs, and Mathematical Tables*, National Bureau of Standards, Applied Mathematics Series #55. p. 360, Eq. 9.1.20
48. M. Abramowitz, I.A. Stegun, *Handbook of Mathematical Functions with Formulas, Graphs, and Mathematical Tables*, National Bureau of Standards, Applied Mathematics Series #55. p. 360, Eq. 9.1.30
49. L.L. Beranek, *Acoustics* (Acoustical Society of America, New York, 1996). See Part X, §4.3; ISBN:0-88318-494-X
50. M. Abramowitz, I.A. Stegun, *Handbook of Mathematical Functions with Formulas, Graphs, and Mathematical Tables*, National Bureau of Standards, Applied Mathematics Series #55. p. 409, Table 9.5: Zeros and Associated values of Bessel Functions and Their Derivatives
51. I.S. Gradshteyn, I.M. Ryzhik, *Tables of Integrals, Series, and Products*, 4th edn. (Academic, London, 1980). p. 446, Eq. 3.821(9); ISBN:0-12-294760-6
52. P.M. Morse, K.U. Ingard, *Theoretical Acoustics* (McGraw-Hill, New York, 1968), pp. 383–387
53. M. Abramowitz, I.A. Stegun, *Handbook of Mathematical Functions with Formulas, Graphs, and Mathematical Tables*, National Bureau of Standards, Applied Mathematics Series #55. Chapter 12: Struve Functions and Related Functions, p. 496ff
54. R.M. Aarts, A.J.E.M. Janssen, Efficient approximation of the Struve function in the calculation of sound radiation quantities. *J. Acoust. Soc. Am.* **140**(6), 4154–4160 (2016)
55. P.M. Morse, U.K. Ingard, *Theoretical Acoustics* (McGraw-Hill, New York, 1968). See Eq. (7.4.45)
56. M. Greenspan, Piston radiator: some extensions of the theory. *J. Acoust. Soc. Am.* **65**(3), 608–621 (1979)
57. R.H. Mellen, M.B. Moffett, A model for parametric sonar radiator design. *U. S. Navy J. Underw. Acoust.* **22**, 105–116 (1972)
58. H.M. Merklinger, *High intensity effects in the non-linear acoustic parametric end-fire array*. Ph.D. thesis, University of Birmingham, 1971
59. D.T. Blackstock, *Fundamentals of Physical Acoustics* (Wiley, New York, 2000). Chapter 13, §C; ISBN:0-471-31979-1
60. H. Levine, J. Schwinger, On the radiation of sound from an unflanged circular pipe. *Phys. Rev.* **73**(4), 383–406 (1948)
61. J.W. Strutt (Lord Rayleigh), *Theory of Sound*, vol II, 2nd edn. (Macmillan, London, 1896). (Dover, 1945). §314 and App. A
62. L. Gutin, Über das Schallfeld der Kolbenstrahlern. *Tech. Phys. USSR* **4**, 404 (1937). Note that this is a German translation of an article that originally appeared in Russian
63. J.B. Mehl, Greenspan acoustic viscometer: numerical calculation of fields and duct-end effects. *J. Acoust. Soc. Am.* **106**(1), 73–82 (1999)
64. N.A.M. Schellart, A.N. Popper, Functional aspects of the evolution of the auditory system in Actinopterygian fish, in *The Evolutionary Biology of Hearing*, ed. by D. B. Webster, R. R. Fay, A. N. Popper, (Springer, New York, 1992), pp. 295–322
65. F.V. Hunt, *Electroacoustics* (Harvard University Press, Cambridge, MA, 1954). See Fig. 5.1
66. S.L. Garrett, J.A. Smith, R.W.M. Smith, B.J. Heidrich, M.D. Heibel, Fission powered in-core thermoacoustic sensor. *Appl. Phys. Lett.* **108**, 144102 (2016). Using the sound of nuclear energy. *Nucl. Technol.* **195**(3), 353–362 (2016)



# Three-Dimensional Enclosures

13

## Contents

13.1	<b>Separation of Variables in Cartesian Coordinates</b> .....	622
13.1.1	Rigid-Walled Rectangular Room .....	623
13.1.2	Mode Characterization .....	624
13.1.3	Mode Excitation .....	625
13.1.4	Density of Modes .....	626
13.2	<b>Statistical Energy Analysis</b> .....	627
13.2.1	The Sabine Equation .....	630
13.2.2	Critical Distance and the Schroeder Frequency .....	633
13.3	<b>Modes of a Cylindrical Enclosure</b> .....	635
13.3.1	Pressure Field Within a Rigid Cylinder and Normal Modes .....	635
13.3.2	Modal Density Within a Rigid Cylinder .....	641
13.3.3	Modes of a Rigid-Walled Toroidal Enclosure*	644
13.3.4	Modal Degeneracy and Mode Splitting .....	646
13.3.5	Modes in Non-separable Coordinate Geometries .....	648
13.4	<b>Radial Modes of Spherical Resonators</b> .....	651
13.4.1	Pressure-Released Spherical Resonator .....	652
13.4.2	Rigid-Walled Spherical Resonator .....	653
13.5	<b>Waveguides</b> .....	654
13.5.1	Rectangular Waveguide .....	655
13.5.2	Phase Speed and Group Speed .....	656
13.5.3	Driven Waveguide .....	658
13.5.4	Cylindrical Waveguide .....	659
13.5.5	Attenuation from Thermoviscous Boundary Losses .....	660
	<b>References</b> .....	670

In this chapter, solutions to the wave equation that satisfies the boundary conditions within three-dimensional enclosures of different shapes are derived. This treatment is very similar to the two-dimensional solutions for waves on a membrane of Chap. 6. Many of the concepts introduced in Sect. 6.1 for rectangular membranes and Sect. 6.2 for circular membranes are repeated here with only slight modifications. These concepts include separation of variables, normal modes, modal degeneracy, and density of modes, as well as adiabatic invariance and the splitting of degenerate modes by perturbations. Throughout this chapter, familiarity with the results of Chap. 6 will be

assumed. The similarities between the standing-wave solutions within enclosures of different shapes are stressed. At high enough frequencies, where the individual modes overlap significantly, statistical energy analysis will be introduced to describe the diffuse (reverberant) sound field.

The formalism developed for three-dimensional enclosures also provides the description for sound propagation in waveguides, since a waveguide can be treated as a three-dimensional enclosure where one of the dimensions is extended to infinity.

### 13.1 Separation of Variables in Cartesian Coordinates

The linearized wave equation for the acoustic pressure,  $p$ , can be written in a vector form that is independent of any particular coordinate system.

$$\nabla^2 p_1(\vec{x}, t) = \frac{1}{c^2} \frac{\partial^2 p_1(\vec{x}, t)}{\partial t^2} \quad (13.1)$$

The expression of the Laplacian operator,  $\nabla^2$ , in terms of partial derivatives, depends upon the choice of coordinate system. The simplest coordinate system is Cartesian. We will continue to assume that pressure is time-harmonic,  $p_1(x, y, z, t) = \Re e[\hat{\mathbf{p}}(x, y, z)e^{j\omega t}]$ . Since  $k = \omega/c$ , Eq. (13.1) can be written in the time-independent form known as the Helmholtz equation.

$$\nabla^2 p_1 = \frac{\partial^2 p_1}{\partial x^2} + \frac{\partial^2 p_1}{\partial y^2} + \frac{\partial^2 p_1}{\partial z^2} = -k^2 p_1 \quad (13.2)$$

The Helmholtz equation is a partial differential equation. In Cartesian coordinates, it can be separated into three ordinary differential equations by assuming that variation of the pressure in each spatial coordinate is independent of the other coordinates<sup>1</sup> [1].

$$p_1(x, y, z, t) \equiv \Re e[X(x)Y(y)Z(z)e^{j\omega t}] \quad (13.3)$$

Substitution of Eq. (13.3) into Eq. (13.2) produces an equation where the partial derivatives become ordinary derivatives. Since each function now depends only upon a single coordinate, it is no longer necessary to use partial derivatives.

$$YZ \frac{d^2 X}{dx^2} + XZ \frac{d^2 Y}{dy^2} + XY \frac{d^2 Z}{dz^2} + k^2 XYZ = 0 \quad (13.4)$$

Dividing through by  $XYZ$  makes each term independent of the others.

$$\frac{1}{X} \frac{d^2 X}{dx^2} + \frac{1}{Y} \frac{d^2 Y}{dy^2} + \frac{1}{Z} \frac{d^2 Z}{dz^2} + k^2 = 0 \quad (13.5)$$

Since each term in the separated Helmholtz equation (13.5) depends upon a different coordinate, and their sum is equal to a constant,  $-k^2$ , each term must be separately equal to a constant. This is the same as the “separation condition” imposed in the two-dimensional case in Eq. (6.8).

<sup>1</sup> The three-dimensional Helmholtz equation can be separated in 11 coordinate systems. With the exception of [confocal paraboloidal coordinates](#), all are particular cases of the [confocal ellipsoidal](#) system: [Cartesian](#), [confocal ellipsoidal](#), [confocal paraboloidal](#), [conical](#), [cylindrical](#), [elliptic cylindrical](#), [oblate spheroidal](#), [paraboloidal](#), [parabolic cylindrical](#), [prolate spheroidal](#), and [spherical](#) coordinates. <http://mathworld.wolfram.com/HelmholtzDifferentialEquation.html>

$$k^2 = \frac{\omega^2}{c^2} = k_x^2 + k_y^2 + k_z^2 \quad (13.6)$$

Each term then generates a simple harmonic oscillator equation.

$$\frac{d^2X}{dx^2} + k_x^2 X = 0 \quad (13.7)$$

By this time, we are quite familiar with the solutions to the above ordinary, second-order, homogeneous differential equation. Instead of both sine and cosine functions, in the following, only cosine functions will be chosen (for reasons that will become apparent once rigid boundary conditions are imposed), and three phase factors will be included to retain the generality of the solution.

$$p_1(x, y, z, t) = \Re[\hat{\mathbf{p}} \cos(k_x x + \phi_x) \cos(k_y y + \phi_y) \cos(k_z z + \phi_z) e^{j\omega t}] \quad (13.8)$$

To emphasize that this could be a traveling plane wave (before imposition of boundary conditions), the solution can be written as a product of complex exponentials.

$$p_1(x, y, z, t) = \Re[e^{j(\omega t + \phi)} e^{j(\mp k_x x + k_y y + k_z z)}] \quad (13.9)$$

### 13.1.1 Rigid-Walled Rectangular Room

If we consider a fluid confined in a rectangular room with rigid impenetrable walls, then we can impose the six boundary conditions on the normal component of the fluid velocity at each of the six planes that define the interior of the room. From the Euler equation, we see that this condition is equivalent to requiring that the slope of the pressure normal to the boundary vanishes.

$$\frac{\partial u_x(0)}{\partial t} = 0 = -\frac{1}{\rho_m} \left( \frac{\partial p_1}{\partial x} \right)_{x=0} \Rightarrow \left( \frac{\partial p_1}{\partial x} \right)_{x=0} = 0 \quad (13.10)$$

At the planes which pass through the origin of coordinates, we can eliminate all of the phases in Eq. (13.8),  $\phi_i$ , since the cosine terms all have zero slope at  $x = y = z = 0$ . If we introduce the lengths of the enclosure's edges as  $L_x$ ,  $L_y$ , and  $L_z$ , then the solutions (*eigenvalues*) are quantized in a way that satisfies the remaining three (zero slope) boundary conditions of Eq. (13.10) at  $x = L_x$ ,  $y = L_y$ , and  $z = L_z$ .

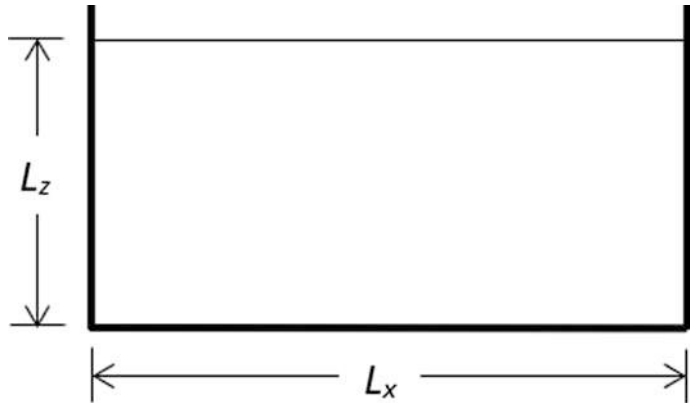
$$k_x = \frac{n_x \pi}{L_x}; \quad k_y = \frac{n_y \pi}{L_y}; \quad k_z = \frac{n_z \pi}{L_z}; \quad n = 0, 1, 2, \dots \quad (13.11)$$

The modal frequencies,  $f_{ijk}$ , are then designated by three integers:  $i = n_x$ ,  $j = n_y$ , and  $k = n_z$ .

$$f_{ijk} = \frac{\omega_{ijk}}{2\pi} = \frac{c}{2} \sqrt{\left(\frac{n_x}{L_x}\right)^2 + \left(\frac{n_y}{L_y}\right)^2 + \left(\frac{n_z}{L_z}\right)^2} \quad (13.12)$$

Each mode can then be written as the product expressed in Eq. (13.3) and repeated in Eq. (13.13), where the complex (phasor) amplitude of each mode,  $\hat{\mathbf{A}}_{ijk}$ , is dependent upon the source impedance (i.e., a volume velocity source or a pressure source or something in between), its amplitude, and the location of the source within the standing wave field.

**Fig. 13.1** Representation of a rigid-walled enclosure containing a liquid with a pressure-released free surface at the plane,  $z = L_z$



$$p_{ijk}(x, y, z, t) = \Re e \left[ \hat{A}_{ijk} \cos(k_x x) \cos(k_y y) \cos(k_z z) e^{j\omega_{ijk} t} \right] \quad (13.13)$$

Of course, there are other possible boundary conditions. The other extreme is a perfectly pressure-released boundary condition. One such example might be approximated by a fish tank or swimming pool shown schematically in Fig. 13.1, where the thickness of the boundaries is intended to emphasize the rigidity of the five planes that contain the liquid. (Note that it is very difficult to produce a container that behaves as a rigid boundary since water is very nearly incompressible.)

At the free surface of the water (i.e., the water-air interface), the normal component of the fluid velocity,  $u_z$ , is unrestricted, and the acoustic pressure amplitude,  $p_1(L_z)$ , is zero (but not the slope!). On the  $x$ - $y$  plane at  $z = 0$ , we have the original “rigid” boundary condition, so the form of the solution is the same as in the rigid enclosure case Eq. (13.13), but at  $z = L_z$ ,  $p_1(x, y, z = 0, t)$  must vanish for all times. If we impose the pressure-released boundary condition at  $z = L_z$  (the air-water interface), then the quantization condition on  $k_z$  changes to that for a closed-open pipe (see Sect. 10.6.2).

$$k_x = \frac{n_x \pi}{L_x}; \quad k_y = \frac{n_y \pi}{L_y}; \quad k_z = \frac{(2n_z - 1)\pi}{2L_z}; \quad \begin{cases} n_x, n_y = 0, 1, 2, \dots \\ n_z = 1, 2, 3, \dots \end{cases} \quad (13.14)$$

The  $n_z = 0$  solution does not exist since constant pressure in the  $z$  direction is not an option that satisfies the boundary conditions at  $z = L_z$  and  $z = 0$  simultaneously.

### 13.1.2 Mode Characterization

For the rigid-walled rectangular enclosure, the modes can be classified into three categories:

- Axial: only one mode number is non-zero.
- Tangential: only one mode number is zero.
- Oblique: no mode number is zero.

Each mode is unique and has a complex amplitude,  $\hat{A}_{ijk}$ , which is a function of how and where it is excited, although the frequencies of the individual modes may not be unique. Depending upon the excitation, some values of  $|\hat{A}_{ijk}|$  may be zero. As discussed in Sect. 6.1.2, when two or more different modes share the same frequency, they are called *degenerate modes*.

**Table 13.1** Modes of a cubical room with  $L_x = L_y = L_z$  and a rectangular room where  $L_y = L_x\sqrt{2}$  and  $L_z = L_x/\sqrt{2}$ 

Cubical room				Rectangular room			
$2L_x f_{ijk}/c$	$n_x$	$n_y$	$n_z$	$2L_x f_{ijk}/c$	$n_x$	$n_y$	$n_z$
1.000	1	0	0	0.707	0	1	0
	0	1	0	1.000	1	0	0
	0	0	1	1.225	1	1	0
1.414	1	1	0	1.414	0	0	1
	1	0	1		0	2	0
	0	1	1	1581	0	1	1
1.732	1	1	1	1.732	1	0	1
2.000	2	0	0		1	2	0
	0	2	0	1.871	1	1	1
	0	0	2	2.000	2	0	0
2.236	2	1	0		0	2	1
	1	2	0	2.121	2	1	0
	2	0	1		0	3	0
	1	0	2	2.236	1	2	1
	0	2	1	2.345	1	3	0
	0	1	2	2.449	2	0	1
2.449	2	1	1		2	2	0
	1	2	1	2.550	2	1	1
	1	1	2		0	3	1
2.828	2	2	0	2.739	1	3	1
	2	0	2	2.828	0	0	2
	0	2	2		0	4	0
3.000	3	0	0	2.915	0	1	2
	0	3	0		2	3	0
	0	0	3	3.000	1	0	2
	2	2	1		3	0	0
	2	1	2		1	4	0
	1	2	2				

If the enclosure is cubical (i.e.,  $L_x = L_y = L_z$ ), then there will be many degenerate modes. Even if the dimensions of the room are not identical, there can be “accidental degeneracies.” The normalized modal frequencies,  $(2L_x f_{ijk})/c$ , for a cubical room with  $L_x = L_y = L_z$  and for a rectangular room with  $L_y = L_x\sqrt{2}$ , and  $L_z = L_x/\sqrt{2}$ , are given in Table 13.1 [2]. For the cubical room, there are 28 distinct modes but only 8 unique normalized frequencies less than or equal to  $2L_x f_{3, 0, 0}/c = 3.00$ . For the rectangular room, there are 27 distinct modes but 17 unique normalized frequencies less than or equal to  $2L_x f_{3, 0, 0}/c = 3.00$ .

The volumes of both rooms are the same as are the total number of modes, to within a single mode. The number of degenerate modes is larger for the cubical room, but the rectangular room also has several degenerate modes, even though the ratios of the boundary lengths are irrational numbers.

### 13.1.3 Mode Excitation

As with any linear model, the amplitude coefficients of the individual modes described by Eq. (13.13),  $\hat{A}_{ijk}$ , are undetermined until the method of excitation is specified. If we assume that a mode will be excited by a volume velocity source, like a loudspeaker, and that the volume velocity produced by the

source is independent of the acoustic load (i.e., a “constant current” source), then the amplitude of a given mode will depend upon the local value of the fluid’s impedance. In any corner of a rectangular room, the pressure is a maximum for all modes, and the fluid’s particle velocity must vanish. This makes the impedance (theoretically) infinite at those eight locations so a constant volume velocity source would produce infinite acoustic pressure amplitudes. In reality, the magnitude of the impedance will depend upon the damping of the mode, as reflected in the quality factor of the mode,  $Q_{ijk}$ . We have done this calculation to relate  $|Z_{ac}|$  to  $Q_n$  for a one-dimensional resonator in Eq. (10.64).

When the loudspeaker is located in the corner of a rigid-walled room, all of the modes can be excited. Of course, which specific mode might be excited will depend upon the frequencies produced by the loudspeaker. If the same speaker were moved from the corner to an edge where two walls intersect and was half-way between the other two walls, then only one-half as many modes could be excited. For example, if the speaker were placed at  $x = L_x/2$  with  $y = 0$  and  $z = 0$ , then  $|\hat{A}_{ijk}|$  could only be non-zero if  $i$  were an odd integer, so  $p_{ijk}(L_x/2, 0, 0) \neq 0$ . If  $i$  is an even number, then the speaker is located at an acoustic pressure node, and the impedance would be zero.

If the speaker is then moved away from the edge to the center of one wall, another half of the modes could not be excited in that position; only one-quarter of the modes could be excited. Now if the speaker were lifted off of that wall and placed in the exact center of the room, another half of the modes would be excluded and only one-eighth of the modes could be excited.

Equation (13.13) describes the pressure field in a rectangular, rigid-walled enclosure. If a volume velocity source is located at a pressure node for any mode, that mode cannot be excited and  $|\hat{A}_{ijk}|$  for that mode would be zero.

### 13.1.4 Density of Modes

In a one-dimensional resonator (e.g., a rigid tube with rigid ends), the normal modes were equally spaced in frequency, and only one integer index,  $n$  (the mode number), was required to specify each modal frequency.

$$f_n = n \frac{c}{2L} \quad \Rightarrow \quad n = \frac{2f_n L}{c} \quad (13.15)$$

The *density of modes* is the number of modes within a frequency band that is  $\Delta f$  wide. For the one-dimensional case,  $dn/df$  is a constant,

$$\frac{dn}{df} = \frac{2L}{c} \quad \Rightarrow \quad \Delta n = \frac{2L}{c} \Delta f \quad (13.16)$$

We can visualize the results of Eqs. (13.15) and (13.16) by looking at the modes as points on the one-dimensional  $k_x$ -axis shown in Fig. 13.2.



**Fig. 13.2** A graphical representation of the modes in a one-dimensional closed-closed resonator. Each mode is represented as a discrete point on the (wavenumber)  $k_x$ -axis. Since the spacing between adjacent modes is uniform, the density of modes is also a constant

Constant spacing in one-dimensional  $k$ -space corresponds to a linearly increasing number of modes with increasing frequency (bandwidth) and a constant density of modes.

In higher-dimensional spaces, the density of modes is a function of frequency. For a two-dimensional system, like the rectangular membranes in Sect. 6.1 and the circular membrane in Sect. 6.2, the number of modes with frequencies below some maximum frequency,  $f_{\max}$ , increased with the square of that frequency. In that two-dimensional case, the number of modes was approximated by the  $k$ -space reciprocal area,  $\forall$ , contained within the quadrant of a circle that had a radius,  $|\vec{k}| = 2\pi f_{\max}/c$ . This geometrical construction for a two-dimensional system is illustrated in Fig. 6.5.

In three-dimensional enclosures, the density of modes is also a function of frequency. The number of modes,  $N$ , with frequency less than  $f_{\max}$ , is equal to the number of points representing individual modes contained within the volume of an octet of a  $k$ -space sphere (i.e., only positive values of  $k$ ) in *wavenumber space* or  *$k$ -space* with a radius  $k_{\max} = \omega_{\max}/c = 2\pi f_{\max}/c$ . The volume of a “unit cell” in  $k$ -space is  $\pi^3/(L_x L_y L_z)$ . In analogy with Eq. (6.15), the number of modes can be approximated by the volume of the octet of the sphere divided by the volume of the unit cell.

$$N = \frac{\text{Octet Volume}}{\text{Unit Cell}} \cong \frac{(\pi/6)k_{\max}^3}{\pi^3/(L_x L_y L_z)} = \frac{4\pi f_{\max}^3 V}{3c^3} \quad (13.17)$$

To obtain the density of modes, we differentiate Eq. (13.17) as we did in two dimensions in Eq. (6.19).

$$\frac{dN}{df} \cong \frac{4\pi f^2 V}{c^3} \quad (13.18)$$

A more accurate result can be obtained if we include points in  $k$ -space representing the axial modes (on the 12 edges of total length,  $L$ ) and points in  $k$ -space representing tangential modes (on the six planes of total area  $A$ ).

$$\frac{dN}{df} \cong \frac{4\pi f^2 V}{c^3} + \frac{\pi f A}{2c^2} + \frac{L}{8c} \quad (13.19)$$

This result should be compared with the similar two-dimensional result for a rectangular membrane in Eq. (6.19) or the circular membrane in Eq. (6.34).

To determine when our analysis should transition between the discrete modal picture we have just developed and the statistical approach we are about to introduce, we need to understand the concept of *reverberation time*.

## 13.2 Statistical Energy Analysis

We would like to know when it is reasonable to calculate the sound level in an enclosure using a modal model and when it would be more fruitful to ignore the enclosure’s modal structure and apply statistical energy analysis to determine sound levels by writing an energy balance equation to calculate the rate of change of the sound level in an enclosure.

Time-averaged acoustic power,  $\langle \Pi \rangle_t$ , enters the enclosure from a source (e.g., a loudspeaker or an orchestra) and power “leaves” by passing through the boundary (through a window?), converting to heat due to thermoviscous absorptive processes at the boundaries (see Eq. (9.38)) or at the surface of

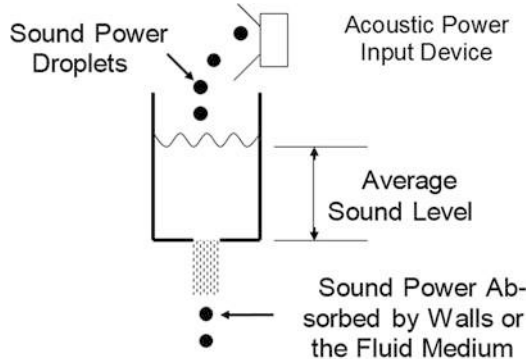


**Fig. 13.3** The steady-state sound level in an enclosure is analogous to filling a leaky bucket. Sound energy (droplets) enters the bucket representing the sound source. Fluid leaves the bucket through a leak representing absorption by the walls and the contents of the enclosure. The leakage rate is proportional to the depth of the fluid. When the amount that enters and the amount that leaves are equal, the liquid level, analogous to the sound level, achieves steady state

objects in the room (e.g., upholstered seats, people's clothing) or due to attenuation within the fluid itself (see Sects. 14.3 and 14.5.1). Figure 13.3 illustrates a "bucket" analogy that, though crude, accurately represents the energy balance approach.

The energy balance approach to calculation of the sound pressure in a diffuse sound field within an enclosure is analogous to a bucket that is filled with "sound droplets" by some source represented schematically in Fig. 13.3 by a loudspeaker. Droplets (energy) leak out of the bucket through a hole that provides some flow resistance. Steady state is achieved when the level of the fluid in the bucket (analogous to the average sound level) is sufficient to force fluid through the resistance at the same rate at which fluid is entering the bucket. If the resistance of the leak is large (representing very little absorption, thus making it difficult for the sound to leave), then the steady-state level will be high, and it will take more time to reach that level since the power of the sound source is constant (analogous to the number of droplets per second). If the resistance is small, then it is easy for the sound to leave the enclosure (by being absorbed and turned into heat and/or escaping through a door or window). The level then will reach its steady-state value that is lower and the time to reach steady state is shorter.

Instead of treating modes individually, the problem can be approached from another direction. Let's assume that the density of modes is so high, and individual modes are so closely spaced, both in frequency and in wave-vector direction, and that the acoustic energy in the room distributes itself uniformly among the available modes (as we did by invoking the Equipartition Theorem for the distribution of thermal energy when calculating heat capacities of ideal gases in Sect. 7.1.1). We have previously derived a conservation equation (10.35), for both the kinetic and potential energy density of sound waves.

$$\frac{\partial}{\partial t} \left[ \frac{1}{2} \rho_m v_1^2 + \frac{1}{2} \frac{p_1^2}{\rho_m c^2} \right] + \nabla \cdot (p_1 \vec{v}_1) = 0 \quad (13.20)$$

Since the total energy density is the sum of the instantaneous kinetic and potential energy densities, and the time-averaged value of both energy densities are equal (by the virial theorem in Sect. 2.3.1), we can choose to express the total as the maximum value of either. For this analysis, we chose the potential energy density,  $\epsilon$ , since we are normally interested in sound pressure.

$$\varepsilon = \frac{PE}{V} = \frac{p_r^2}{\rho_m c^2} \quad (13.21)$$

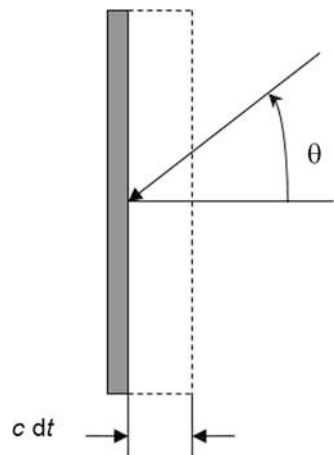
The square of the acoustic pressure,  $p_r^2$ , is the mean square pressure based on the incoherent sum of all of the pressures of all of the modes averaged over all angles. As a more operational definition, the square root,  $\sqrt{p_r^2} \equiv p_{rms}$ , provides the root-mean-squared pressure that would be measured by an omnidirectional microphone. If the sound field within the enclosure is truly a *diffuse sound field*, we can make the further claim that  $p_r^2$  is independent of location within the enclosure and incident from all angles.

Sound energy leaves the enclosure by converting to heat through absorption within the medium or by thermal or viscous interactions with the boundaries. For development of this model, it is customary to ignore the attenuation within the medium and define an absorption coefficient that designates the fraction of energy that is not reflected at the wall. The “bulk” losses for frequencies below about 5 kHz and enclosures with volumes less than  $10^6 \text{ ft}^3$  ( $30,000 \text{ m}^3$ ) will usually be insignificant compared to the surface absorption, besides, it is easy to put the bulk losses back into the equation later, as in Eq. (13.30).

Assuming that the sound that impinges on a wall does so with equal probability from all angles, the time-averaged intensity (power impinging per unit area) of the sound can be calculated by examination of an infinitesimal volume,  $dV$ , containing the energy,  $\varepsilon$  ( $dV$ ), coming toward from a wall from all directions at the speed of sound,  $c$ . The energy will reach a “patch” of the wall having an area,  $dS$ , and be partially reflected and partially absorbed during an infinitesimal time,  $dt$ , as shown in Fig. 13.4.

The area of the “patch” will depend upon the viewing angle. Energy arriving from a direction normal to the patch will see an area of  $dS$ , but sound that is nearly perpendicular to the patch will see nearly zero area. That is, the effective area of the patch,  $dS_{eff} = dS \cos \theta$ , where  $\theta$  is the angle with respect to the normal to the patch. Also, an incoming ray arriving at the patch from an angle,  $\theta$ , must be within a distance,  $c dt \sin \theta$ , to arrive in a time,  $dt$ . Combining these two orientational effects with the fact that *half of the energy is traveling away from the patch*, we can calculate the energy that impinges on our patch during a time,  $dt$ , by integrating over the arrival angle,  $\theta$ .

**Fig. 13.4** The geometry used to calculate the time-averaged incident energy flux (intensity) impinging on a differential element of area,  $dS$ , at the enclosure boundary (wall), from a diffuse sound field



$$\frac{dE}{dS} = \frac{\epsilon(cdt)}{2} \int_0^{\pi/2} \sin \theta \cos \theta d\theta = \frac{\epsilon c}{4} dt \quad (13.22)$$

This result is exactly the same as was derived in the kinetic theory calculations in Sect. 9.5.2.

How much sound gets absorbed by the walls? The amount of absorbed energy will vary depending upon the nature of the surface (e.g., rigid concrete or porous carpet). In keeping with our statistical treatment, if there are  $n$  different surface treatments, each with area,  $A_i$ , and absorption coefficient,  $\alpha_i$ , the average absorption coefficient (or effective absorptive area) for the entire enclosure,  $\langle A \rangle$ , is the properly weighted sum over all of the enclosure's surfaces.

$$\langle A \rangle = \sum_{i=1}^n \alpha_i A_i \quad (13.23)$$

These surfaces are not limited to the walls, but could include seats and their occupants, over-garments, wall treatments (e.g., drapes), etc.

We are now in a position to write the *energy balance equation*.

$$\frac{d(\epsilon V)}{dt} + \langle A \rangle \frac{c\epsilon}{4} = \langle \Pi \rangle_t \quad (13.24)$$

The solution to such a first-order differential equation is well known.

$$\epsilon(t) = \frac{p_{eff}^2}{\rho_m c^2} = \frac{4\langle \Pi \rangle_t}{c\langle A \rangle} \left( 1 - e^{-t/\tau_E} \right) \quad (13.25)$$

The exponential time,  $\tau_E = 4 V/c \langle A \rangle$ , represents the time required for the *energy* in the diffuse field to reach  $63.2\% = 1 - e^{-1}$  of its steady-state value after the source is turned on or to decay from its steady-state value,  $\epsilon (t = \infty)$ , given in Eq. (13.27), by 63.2% after the source is turned off. It is useful to remember that we have usually designated the exponential equilibration time,  $\tau$ , to represent the change in *amplitude* not *energy*. Since the energy is a quadratic function of the amplitude,  $\tau = 2\tau_E$ .

If the absorption is small, then it takes a long time for the sound pressure to reach the steady-state value corresponding to the steady-state energy density,  $\epsilon(t = \infty)$ .

$$\epsilon(t = \infty) = \frac{4\langle \Pi \rangle_t}{c\langle A \rangle} = \frac{p_r^2(t = \infty)}{\rho_m c^2} \quad (13.26)$$

Similarly, if the average absorptive area,  $\langle A \rangle$ , is small, the enclosure will take more time to respond to changes in source sound level.

### 13.2.1 The Sabine Equation

Wallace Clement Sabine (1868–1919) was a young physics professor at Harvard University when he was asked, in 1885, by Charles Eliot, then president of the university, if he could do something about the poor speech intelligibility in the lecture hall at the Fogg Art Museum on campus [3]. To determine the origin of the problem, Sabine measured the time it took for sound to decay in various rooms on campus, using only a “clapboard” to create an impulse, his hearing, and a stopwatch. On 30 October

1898, he discovered a correlation between that decay time and the volume of the rooms and their average absorptive area. The resulting relation is known as the Sabine equation.<sup>2</sup>

$$T_{60} = \tau_E \ln[10^6] = 13.82\tau_E = 13.82 \frac{4V}{c\langle A \rangle} = 0.16 \frac{V}{\langle A \rangle} \quad (13.27)$$

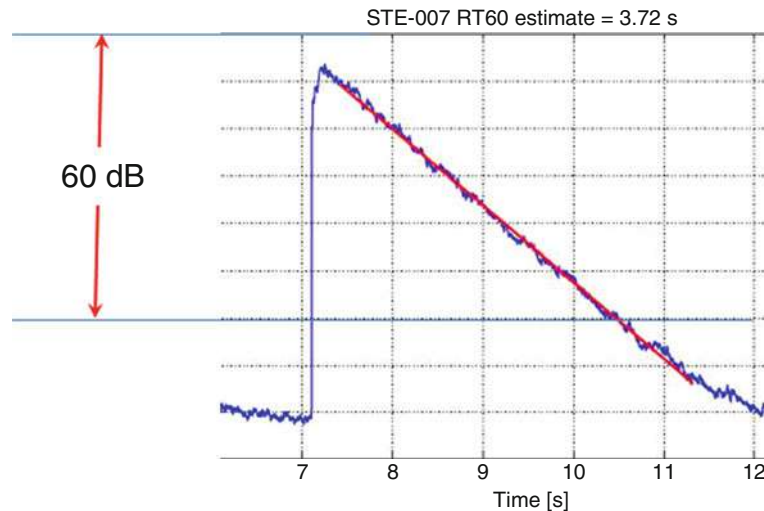
The numerical value in the rightmost term of Eq. (13.27) applies only to sound in air if both volume,  $V$ , and average absorptive area,  $\langle A \rangle$ , are measured in metric units. If the dimensions of the room are measured in English units (feet), then the numerical factor in Eq. (13.27) becomes 0.047.

The reverberation time,  $T_{60}$ , was chosen because it was approximately the time required for the decaying sound Sabine was timing to become inaudible after the initial impulse. Today,  $T_{60}$  corresponds to the time it takes for sound to decay by 60 dB (for the time-averaged acoustic intensity<sup>3</sup> to decay by a factor of one million). In terms of the exponential energy decay time,  $\tau_E$ ,  $T_{60} = \ln[10^6]\tau_E = 13.83\tau_E$ . Today's high-quality electroacoustics and digital recording and post-processing makes it possible in many circumstances to obtain very precise determinations of the reverberation time, as shown in Fig. 13.5.

Sabine's success improving the acoustics at the Fogg Auditorium led him to a commission for the design of Boston's Symphony Hall, shown in Fig. 13.6, with a maximum seating of 2625, which opened 15 October 1900. To this day, it is still considered one of the world's best concert halls [4]. Its successful opening ushered in a new era for the use of scientific methods in the design of musical performance spaces.

The technology for determining the frequency-dependent, angle-averaged sound absorption of surfaces based on measurements of their fundamental physical properties (e.g., average hydraulic pore radius, porosity, and tortuosity) is not widely understood within the architectural community, and the instrumentation for measurement of the fundamental properties (complex flow resistance and

**Fig. 13.5** Reverberation decay record for a very noisy (reverberant) dining hall at the YMCA Camp Fitch on the shore of Lake Erie, in Pennsylvania. The vertical axis displays the received dB level. The straight line (red) fit to the data is equivalent to a  $T_{60} = 3.72$  s. (Data courtesy of Matthew E. Poese)



<sup>2</sup> Tradition has it that when Sabine realized the inverse relationship between reverberation time and average absorptive area, he ran downstairs from his study, shouting to his mother, "Mother, it's a hyperbola!"

<sup>3</sup> The interval selected for the time averaging of the sound pressure level measurement,  $\tau_{ave}$ , needs to be long enough to integrate over the desired range of frequencies,  $\Delta\omega \cong \tau_{ave}^{-1}$ , yet short enough that it will not dominate the reverberant decay:  $\tau_{ave} < \tau_E$ .



**Fig. 13.6** View of Boston Symphony Hall from the back of the upper balcony facing the stage [4]. In addition to the uniformity of the reverberation times shown in Table 13.2, the rectangular hall has many “sound scatterers” of different shapes and sizes (statues, alcoves, proscenium arch, and balcony facings, along with other assorted “protuberances”) to scatter sound of different wavelengths and thus encourage a uniform angular distribution among the reflections [5]

complex compressibility) are not widely available [6]. For that reason, the standard method for measurement of absorption coefficients uses the measurement of change in reverberation time of an enclosure with and without the absorptive sample present [7, 8].

$$a_s = a_o + 0.16 \frac{V}{S_s} \left( \frac{1}{T_s} - \frac{1}{T_o} \right) \quad (13.28)$$

The average absorptivity of the empty test enclosure is  $a_o$ . The reverberation time of the empty enclosure,  $T_{60} = T_o$ . The reverberation time within the same enclosure with an area,  $S_s$ , of absorbing material is reduced to  $T_s$ .

To incorporate absorption within the medium, the Sabine equation (13.27) can be augmented with an energy attenuation coefficient,  $m$ .

$$T_{60} = \frac{0.16 V}{\langle A \rangle + 4mV} \quad (13.29)$$

The expression in Eq. (13.29) is usually deemed adequate for architectural applications. A useful correlation for the attenuation coefficient in air (in units of inverse meters), for frequencies between  $1500 \text{ Hz} \leq f \leq 10,000 \text{ Hz}$ , and relative humidity,  $20 \leq RH(\%) \leq 70$ , is given in Eq. (13.31).

$$m = 5.5 \times 10^{-4} (50/RH\%) (f/1000)^{1.7} \quad (13.30)$$

The validity of this correlation is established in Chap. 14, Problem 1, using values taken from the American National Standards Institute [9].

### 13.2.2 Critical Distance and the Schroeder Frequency

The pressure radiated by a simple source (i.e., a compact monopole) can also be expressed in terms of its time-averaged radiated power,  $\langle \Pi_{\text{rad}} \rangle_t$ , using the expression for time-averaged intensity in Eq. (12.24) and the fact that the monopole field is spherically symmetric.

$$\langle \Pi_{\text{rad}} \rangle_t = 4\pi R^2 \left| \left\langle \vec{I} \right\rangle_t \right| = 4\pi R^2 \frac{p_1^2(R)}{2\rho_m c} \Rightarrow \frac{p_1^2(R)}{2} = p_{\text{rms}}^2 = \frac{\rho_m c}{4\pi R^2} \langle \Pi_{\text{rad}} \rangle_t \quad (13.31)$$

That radiated pressure can be equated to the steady-state pressure in the diffuse sound field,  $p_r^2(t = \infty)$ , that was calculated in Eq. (13.26), to determine the *critical distance*,  $r_d$ , where the direct and diffuse sound field energies would be equal.

$$p_r^2(t = \infty) = \rho_m c \frac{4\langle \Pi_{\text{rad}} \rangle_t}{\langle A \rangle} = \frac{\rho_m c}{4\pi r_d^2} \langle \Pi_{\text{rad}} \rangle_t \Rightarrow r_d = \frac{1}{4} \sqrt{\frac{\langle A \rangle}{\pi}} \quad (13.32)$$

At distances from a source greater than  $r_d$ , the diffuse field will dominate. At distances less than  $r_d$  from the source, the direct radiation will dominate. This is particularly important when considering sound absorption in a factory situation. Adding absorption to the walls will not help reduce the noise a worker will have to tolerate if (s)he is closer to the source (e.g., a punch press, band saw, grinder) than  $r_d$ .

We have now analyzed the modes of a rectangular enclosure that is suited to the low-frequency behavior of sound in the enclosure. We have also analyzed the behavior at high frequencies, when the modes have sufficient overlap that the sound field can be treated as being both isotropic and homogeneous (i.e., diffuse). It is therefore imperative to identify a cross-over frequency between those two regimes.

Ever since the discussion of the simple harmonic oscillator in Sect. 2.5.2, the “width” of a resonance (mode) has been related to the bandwidth,  $\Delta f_{-3\text{dB}}$ , over which the power in the resonance is within 3 dB of its peak value, or, equivalently, that the pressure amplitude is within  $\sqrt{2}$  of the amplitude at resonance, as indicated in Eq. (2.68). Using our multiple definitions for the quality factor,  $Q$ , in Appendix B, our appreciation of the fact that the energy decay rate,  $\tau_E$ , is one-half the exponential amplitude decay rate,  $\tau$ , and the fact that  $T_{60} = 13.82\tau_E$  in Eq. (13.27), it is possible to express the  $-3$  dB bandwidth,  $\Delta f_{-3\text{dB}}$ , in terms of  $T_{60}$ .

$$Q = \frac{f}{\Delta f_{-3\text{dB}}} = \frac{1}{2} \omega \tau = \pi f \tau = 2\pi f \tau_E \Rightarrow \Delta f_{-3\text{dB}} = \frac{13.82}{2\pi T_{60}} \simeq \frac{2.2}{T_{60}} \quad (13.33)$$

Manfred Schroeder suggested that the cross-over frequency between modal behavior and the diffuse sound field approach should correspond with the frequency where there are three modes within a frequency bandwidth of  $\Delta f_{-3\text{dB}}$ .<sup>4</sup> Using the leading term in our approximation for the density of modes

---

<sup>4</sup> The choice of three “available” modes within the  $-3$  dB bandwidth is, of course, rather arbitrary. P. M. Morse in his textbook, *Vibration and Sound* (McGraw-Hill, 1948), provides (in Eq. 34.8) a more detailed criterion that also incorporates the spread in the frequency range radiated by the source.

$$f_{\min} = \left\{ \frac{c^3}{4\pi V + [\Delta f + (4/T_{60})]} \right\}^{1/2}$$

Based on the acceptance by the architectural acoustics community of the Schroeder frequency, apparently Eq. (13.34) is adequate for most applications.

**Table 13.2** Average measured reverberation times,  $T_{60}$ , in six consecutive one-octave bands of frequencies for the unoccupied (empty) and occupied (full) concert hall [4].

Band center (Hz)	125	250	500	1000	2000	4000
$T_{60}$ -empty (seconds)	2.13	2.29	2.40	2.63	2.66	2.38
$T_{60}$ -full (seconds)	1.95	1.85	1.85	1.85	1.65	1.30

One of the reasons the hall, shown in Fig. 13.6, is so highly rated is that the reverberation times are amazingly uniform across a broad range of frequencies

in Eq. (13.18), Schroeder's “three mode overlap” criterion can be determined in terms of the enclosure volume,  $V$ , and the reverberation time,  $T_{60}$ .

$$\frac{dN}{df} \Delta f = 3 = \frac{2.2}{T_{60}} \frac{4\pi V}{c^3} f_s^2 \quad (13.34)$$

Solving for frequency, we obtain the cross-over frequency, known as the *Schroeder frequency*,  $f_s$ , where the third expression in Eq. (13.36) assumes a sound speed  $c = 343$  m/s [10].

$$f_s = \left( \frac{c^3}{4 \ln 10} \right)^{1/2} \left( \frac{T_{60}}{V} \right)^{1/2} = c \left( \frac{6}{\langle A \rangle} \right)^{1/2} \cong 2000 \left( \frac{T_{60}}{V} \right)^{1/2} \quad (13.35)$$

For a room about the size of a typical classroom ( $10 \text{ m} \times 8 \text{ m} \times 4 \text{ m} = 320 \text{ m}^3$ ), with  $T_{60} \cong 0.4$  s, the Schroeder frequency is  $f_s \cong 70$  Hz. The lowest-frequency normal mode in such a classroom would be  $f_{1,0,0} = c/2L_x = 17$  Hz, so there are about 2 octaves of mode-dominated behavior below 70 Hz.

As shown in Table 13.2, for Boston Symphony Hall ( $V = 26,900 \text{ m}^3$ ),  $T_{60} = 1.85$  s at 500 Hz when the hall is fully occupied. This corresponds to  $f_s \cong 17$  Hz, so a diffuse sound field model can be used throughout the range of human hearing. Of course, in rooms with smaller volumes ( $< 100 \text{ m}^3$ ), the response will exhibit substantial location dependence (i.e., the behavior will be modal) for frequencies below 200 Hz [11].

It is worth noting that the Schroeder frequency and the critical distance are just two aspects of the same phenomena that measure the dominance of the diffuse field relative to the sound that is radiated directly by a source. Converting  $f_s$  to a length by dividing  $c$  by  $\lambda_s$ , their equivalence becomes clear.

$$\frac{c}{f_s} = \lambda_s \cong 3r_d \quad (13.36)$$

The primary purpose for our investigation into the properties of sound waves confined within a rectangular enclosure was to illustrate the differences between three-dimensional resonators and one-dimensional resonators. The following is a compilation of those differences:

- **Three indices** are required to specify a mode uniquely and the order of those indices is significant. For example, if an enclosure is not cubical,  $f_{1,0,2} \neq f_{2,0,1}$ .
- The relationship among resonances is **anharmonic**, even for “ideal” boundary conditions. The ratio of the frequencies of the overtones to that of the fundamental is not given by integer multiples, as it is for the modes of a one-dimensional resonator (or a guitar string).
- Different modes may be **degenerate**, having the same natural frequency but different mode shapes.
- Like other standing-wave systems, **excitation** of an individual mode by a source will depend upon the location of the source in relation to the modal shape. It will also depend upon the source's impedance (i.e., whether the source produces a volume velocity that is independent of the room impedance, or a pressure that is independent of the room impedance, or something in between those limits).

- The number of modes within a given range of frequencies,  $\Delta f$ , (or the **density of modes**) is not a constant, as it was for the one-dimensional resonator. The number of modes below a certain frequency is cubic in that frequency and the density of modes is a quadratic function of the frequency in three dimensions.
- When the modal density is large enough that the frequency spacing between successive modes is smaller than the  $-3$  dB bandwidth of the individual modes (i.e.,  $f > f_s$ ), it is possible to describe the sound field within the enclosure as “diffuse.” In that limit, it is useful to apply statistical energy analysis by assuming that the power is distributed uniformly among all available modes (as we did for the energy of individual particles in an ideal gas using the Equipartition Theorem). That analytical approach can be used to predict both the steady-state, root-mean-square pressure of the sound field in terms of the time-averaged acoustic power input to the room,  $\langle \Pi \rangle_t$ , and also predict the characteristic exponential time,  $\tau_E$ , required for the room to achieve its steady-state pressure.
- In architectural applications, when  $\tau_E$  is used to describe exponential the decay time of the sound field after the sound source is abruptly terminated, it is commonly re-defined as a “**reverberation time**,”  $T_{60} = \tau_E \ln(10^6) = 13.82 \tau_E$ , that corresponds to the time which is required for the acoustic energy to decay by a factor of one million.

---

### 13.3 Modes of a Cylindrical Enclosure

As we are about to discover, the techniques and results that were applied to the resonances of a rectangular enclosure will serve us well again as we investigate the resonances within enclosures of other shapes. Our first venture beyond the Cartesian world-view will be the analysis of a rigid-walled cylindrical resonator like the one shown in Fig. 13.7. In physical and engineering acoustics, the cylindrical resonator is more common than the rectangular enclosure that is nearly ubiquitous for loudspeaker enclosures<sup>5</sup> and in architectural analyses.

There are several reasons that cylindrical shapes are so common. For systems that are required to contain substantial internal pressures (or to protect inhabitants from external pressures, such as in submarines), the cylinder is a much more efficient shape to exploit the strength of the container’s materials. (When was the last time you saw a rectangular bottle used for storage of compressed gases or propane for bar-b-ques?) It is also useful because if the oscillatory motion of the fluid within the resonator is purely radial, there will be no viscous “scrubbing losses” on the cylindrical surface.

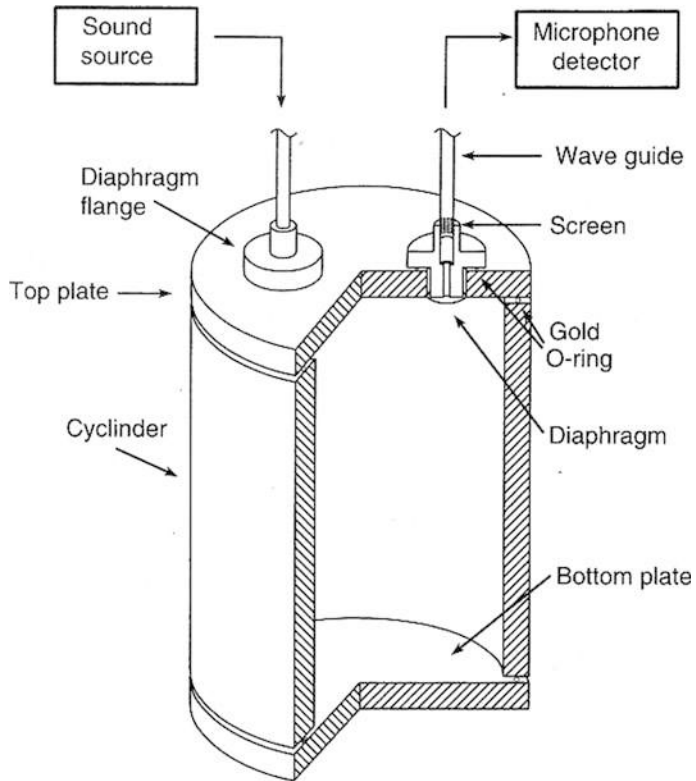
#### 13.3.1 Pressure Field Within a Rigid Cylinder and Normal Modes

As in Sect. 6.2.1, the solution to the Helmholtz equation (13.2) in cylindrical coordinates is more complicated than the solution in Cartesian coordinates because the azimuthal and radial motions of the oscillating fluid are not independent. As before, the rationale for our acceptance of this complication is that it will be much simpler to impose the boundary conditions at  $r = a$  in cylindrical coordinates. If the

---

<sup>5</sup> A notable exception are the cylindrical speaker enclosures made in ACS 097S, a First Year Seminar at Penn State. Those enclosures use PVC plumbing to provide the “pressure barrier” between the volume velocity produced by the front and rear of the loudspeaker cone described in S. L. Garrett and J. F. Heake, “Hey kid! Wanna build a loudspeaker? The first one’s free,” Audio Engineering Society Convention Paper #5882, 10–13 October 2003 or S. L. Garrett, “Two-Way Loudspeaker Enclosure Assembly and Testing as a Freshman Seminar”, *Proc. 17th Int. Cong. Sound & Vibration* (Curran Assoc., 2011); ISBN 97816617822551.

**Fig. 13.7** Cylindrical resonator made of stainless steel used at the National Bureau of Standards to measure the speed of sound at very low or very high temperatures. This versatility is facilitated by using waveguides terminated by metallic diaphragms to allow the sound source and microphone to be far from the resonator [12]



Cartesian solution were retained, the rigidity of the cylindrical surface would be imposed by requiring that the radial component of the velocity vanish and writing  $u_r(x^2 + y^2 = a^2) = 0$ . Specification of the radial component of velocity (or the gradient of the pressure relative to the normal to the cylindrical surface) would be even more challenging.

Faced with this difficulty, we abandon the Cartesian description and accept the fact that we will have to introduce functions that are not superpositions of either simple trigonometric or simple exponential functions as the price we have to pay for simplification in specification of the boundary conditions. As before, we assume single-frequency harmonic time variation and start with the linearized, time-independent Helmholtz equation, but this time we express the Laplacian operator,  $\nabla^2$ , in cylindrical coordinates.

$$\nabla^2 p_1 = \frac{\partial^2 p_1}{\partial r^2} + \frac{1}{r} \frac{\partial p_1}{\partial r} + \frac{1}{r^2} \frac{\partial^2 p_1}{\partial \theta^2} + \frac{\partial^2 p_1}{\partial z^2} = -k^2 p_1 \quad (13.37)$$

The acoustic pressure,  $p_1(r, \theta, z)$ , is then expressed using separation of variables,<sup>1</sup> as a product of functions, each of which depending only upon a single coordinate.

$$p_1(r, \theta, z, t) = \Re e[R(r)\Theta(\theta)Z(z)e^{i\omega t}] \quad (13.38)$$

Substitution of Eq. (13.38) into the Helmholtz equation (13.37) produces the equivalent of Eq. (13.4).

$$\Theta Z \frac{d^2 R}{dr^2} + \frac{\Theta Z}{r} \frac{dR}{dr} + \frac{RZ}{r^2} \frac{d^2 \Theta}{d\theta^2} + R\Theta \frac{d^2 Z}{dz^2} + k^2 R\Theta Z = 0 \quad (13.39)$$

In this case, multiplying through by  $r^2/R\Theta Z$  generates three independent, second-order, ordinary differential operators.

$$\frac{r^2}{R} \frac{d^2 R}{dr^2} + \frac{r}{R} \frac{dR}{dr} + \frac{1}{\Theta} \frac{d^2 \Theta}{d\theta^2} + \frac{r^2}{Z} \frac{d^2 Z}{dz^2} + k^2 r^2 = 0 \quad (13.40)$$

As before, the only way Eq. (13.40) can be satisfied by three independent functions is for each independent function of only one of the coordinates to be equal to a constant and that those constants sum to  $-k^2$ . The solution for  $Z(z)$  is identical with the one-dimensional resonator problem.

$$\frac{d^2 Z}{dz^2} + k_z^2 Z = 0 \quad (13.41)$$

If the ends of the cylinder are rigid, so that  $u_z(0) = u_z(L_z) = 0$ , then the values of  $k_z$  are quantized exactly as they were in the analysis of the closed-closed one-dimensional resonator in Eq. (10.45).

$$k_z = \frac{n_z \pi}{L_z}; \quad n_z = 0, 1, 2, \dots \quad (13.42)$$

Here, the fact that  $n_z = 0$  is an acceptable solution admits modes within the cylindrical enclosure that might have variations of  $p_1$  with radius,  $r$ , and/or with azimuthal angle,  $\theta$ , but which do not vary with axial height,  $z$ .

With the exception of the axial modes that have only  $z$  dependence, for a cylindrical enclosure, it is not possible to separate the modes into a form where the fluid motion has purely azimuthal motion that is independent of the radial coordinate,  $r$ . For “sloshing modes” that have  $u_\theta \neq 0$ , the magnitude of  $u_\theta$  is not independent of radius,  $r$ . The magnitude of the fluid velocity along the azimuthal direction,  $\theta$ , is greatest at the largest values of  $r$ , near the outer boundary,  $r = a$ , and must vanish near the origin,  $r = 0$ . This coordinate coupling can be appreciated from the form of the azimuthal component of the linearized Euler equation when expressed in cylindrical coordinates [13].

$$\frac{\partial u_\theta}{\partial t} = -\frac{1}{\rho_m r} \frac{\partial p_1}{\partial \theta} \quad (13.43)$$

This interdependence of the radial and azimuthal functions will become apparent when addressing the solution for the angular azimuthal function,  $\Theta(\theta)$ .

$$\frac{d^2 \Theta}{d\theta^2} + m^2 \Theta = 0 \quad (13.44)$$

Again, the solutions to this equation are simple and (by this time) well known. What is less familiar may be the quantization of  $m$  by imposition of *periodic boundary conditions* that satisfy the requirement that the solution for the pressure be single-valued. The solutions for  $\Theta(\theta)$  can be expressed as complex exponentials or sine and cosine functions or, as before in Eq. (13.8), as cosine functions that include a potentially mode-dependent phase factor,  $\varphi_{m,n}$ .

$$\Theta(\theta) = \cos(m\theta + \varphi_{m,n}) \quad (13.45)$$

At this moment, it will not be obvious why a double index was assigned to the phase factor, but it will be fully justified shortly.

Since cylindrical coordinates have been chosen to specify each unique position within the resonator, the physically realizable values of the azimuthal coordinate are limited to  $0 \leq \theta < 2\pi$ . If the value of  $\theta$  exceeds  $2\pi$ , we have gone around the resonator more than once and therefore  $\Theta(\theta) = \Theta(\theta + 2n\pi)$

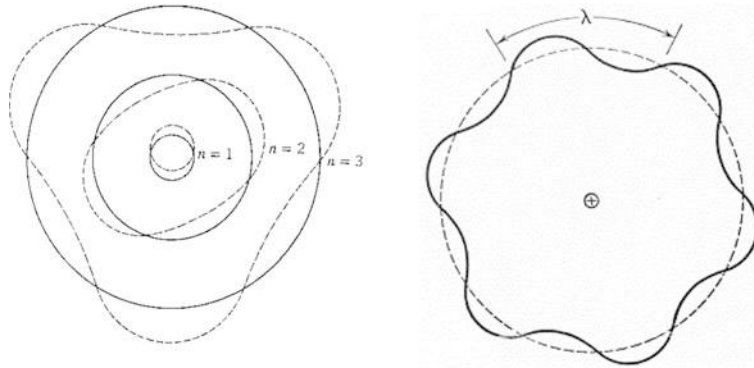


**Fig. 13.8** The imposition of a periodic boundary condition on the azimuthal modes of a cylindrical enclosure is similar to the Bohr-Sommerfeld quantization condition for electron “orbits” around a hydrogen nucleus using figures taken from two elementary textbooks on “modern physics.” At the *left*, one, two, and three wavelength disturbances (*dashed lines*) along the circumferences (*solid lines*) are shown corresponding to the  $m = 1, m = 2$  and  $m = 3$  modes [14]. At the *right* is drawn the  $m = 6$  mode where the equilibrium pressure is shown as the dashed line and six wavelengths,  $\lambda$ , are shown as a *solid line* [15]

where  $n = 0, 1, 2, \dots$ . It is easy to see from Fig. 13.8 that the only way for this “periodic boundary condition” to be satisfied is if  $m$  is also an integer:  $m = 0, 1, 2, \dots$ .

A more physical way to understand the integer quantization of the acoustic pressure for azimuthal variations is to see that in a cylindrical geometry the boundary condition on the solution requires that both the pressure and the slope of the pressure be continuous with angle where the ends of the wave join. That condition cannot be satisfied if only a half-wavelength fits within the circumference,  $2\pi a$ . As can be seen in Fig. 13.8, the continuity of pressure and the slope of pressure requires that integer numbers of wavelength fit within a circumference

With the solutions for  $\Theta(\theta)$  in hand, we are now able to address the differential equation that determines the radial function,  $R(r)$ .

$$r^2 \frac{d^2 R}{dr^2} + r \frac{dR}{dr} + (k^2 r^2 - m^2) R = 0 \quad (13.46)$$

Before finding the solutions for  $R(r)$ , the form of Eq. (13.46) is worthy of comment. Since we have determined that  $m$  is an integer, Eq. (13.46) really represents an infinite number of second-order, homogeneous, ordinary differential equations—one equation for each integer value of  $m$ . Also, this is clearly not a simple harmonic oscillator equation, even if  $m = 0$ .

As demonstrated previously in Sect. 6.2.1, Eq. (13.46) for  $R(r)$  is Bessel’s equation. Since it is a second-order differential equation, it will have two linearly independent solutions for each integer value of  $m$ , but none of those functions will be sines or cosines. They are integer-order Bessel functions of the first and second kinds, sometimes referred to as Bessel functions,  $J_m(kr)$ , and Neumann functions,  $Y_m(kr)$ . The first three of each of the functions were plotted in Figs. 6.8 and 6.9. The subscript indicates the integer value of  $m$  that appears in Bessel’s equation (13.46).

The next step in this procedure is the imposition of radial boundary conditions that will quantize the values of  $k_r$ . For a rigid cylinder, we have only the condition that the boundary be impenetrable to the fluid, so  $u_r(a) = 0$ . This requirement can be implemented by way of the linearized Euler equation [16].

$$\nabla_r R(a) = \frac{dR(a)}{dr} = \frac{d[J_m(ka)]}{dr} = -\rho_m \frac{\partial u_r(a)}{\partial t} = 0 \quad (13.47)$$

What about the Neumann solutions? Those solutions cannot satisfy the boundary condition at  $r = 0$  if we require that our solutions,  $R(r)$ , remain finite at  $r = a$  because  $Y_m(0) = -\infty$  for all values of  $m$  (see Fig. 6.9). If we were solving for the radial modes of an annulus, with outer radius,  $a$ , and inner radius,  $b \neq 0$  (see Sect. 13.3.3), then the Neumann solutions,  $Y_m(kr)$ , would have to be added to the Bessel solutions to satisfy the inner and the outer boundary conditions simultaneously.

$$\begin{aligned}\nabla_r R(b) &= \frac{dR(b)}{dr} = \frac{d[AY_m(kb) + BJ_m(kb)]}{dr} = -\rho_m \frac{\partial u_r(b)}{\partial t} = 0 \\ \nabla_r R(a) &= \frac{dR(a)}{dr} = \frac{d[AY_m(ka) + BJ_m(ka)]}{dr} = -\rho_m \frac{\partial u_r(a)}{\partial t} = 0\end{aligned}\quad (13.48)$$

Since there are multiple solutions for  $R(r)$  that are coupled to the solutions for  $\Theta(\theta)$ , the quantization of  $k_\theta$  and  $k_r$  are coupled. For each value of  $m = 0, 1, 2, \dots$ , there is a different function that describes the radial pressure amplitude variation. For each value of those  $m$  functions, there are  $n$  different values of  $kr$  where the slope of  $J_m(ka)$  vanishes, corresponding to  $d[J_m(ka)]/dr \equiv J'_m(ka) = 0$  in Eq. (13.47).

Although this boundary condition is analogous to the requirement that the slopes of the sine or cosine functions vanish for the  $Z(z)$  solutions, the extrema of the Bessel functions are not simply related to integer multiples of  $\pi$ . Fortunately, the arguments,  $\alpha_{mn} = k_{mn}a$ , corresponding to the extrema of Bessel and Neumann functions, are tabulated in many books on “special functions.” Some values taken from Abramowitz and Stegun [17] are provided in Table 13.3 as well as in Appendix C.

**Table 13.3** Values of the arguments,  $j'_{m,s} = \alpha_{mn}$ , of integer-order Bessel functions ( $0 \leq m \leq 2$ ) which make the slope of the function vanish

Bessel functions of integer order						
Zeros and associated values of Bessel functions and their derivatives						
$x$	$j'_{0,x}$	$J_0(j'_{0,x})$	$j'_{1,x}$	$J_1(j'_{1,x})$	$j'_{2,x}$	$J_2(j'_{2,x})$
1	0.00000 00000	+1.00000 00000	1.84118	+0.58187	3.05424	+0.48650
2	3.83170 59702	-0.40275 93957	5.33144	-0.34613	6.70613	-0.31353
3	7.01558 66698	+0.30011 57525	8.53632	+0.27330	9.96947	+0.25474
4	10.17346 81351	-0.24970 48771	11.70600	-0.23330	13.17037	-0.22088
5	13.32369 19363	+0.21835 94072	14.86359	+0.20701	16.34752	+0.19794
6	16.47063 00509	-0.19646 53,715	18.01553	-0.18802	19.51291	-0.18101
7	19.61585 85105	+0.18006 33753	21.16437	+0.17346	22.67158	+0.16784
8	22.76008 43806	-0.16718 46005	24.31133	-0.16184	25.82604	-0.15720
9	25.90367 20876	+0.15672 49863	27.45705	+0.15228	28.97767	+0.14836
10	29.04682 85349	-0.14801 11100	30.60192	-0.14424	32.12733	-0.14088
11	32.18967 99110	+0.14060 57982	33.74618	+0.13736	35.27554	+0.13443
12	35.33230 75501	-0.13421 12403	36.88999	-0.13137	38.42265	-0.12879
13	38.47476 62348	+0.12861 66221	40.03344	+0.12611	41.56893	+0.12381
14	41.61709 42128	-0.12366 79608	43.17663	-0.12143	44.71455	-0.11937
15	44.75931 89977	+0.11924 98120	46.31960	+0.11724	47.85964	+0.11537
16	47.90146 08872	-0.11527 36941	49.46239	-0.11345	51.00430	-0.11176
17	51.04353 51836	+0.11167 04969	52.60504	+0.11001	54.14860	+0.10846
18	54.18555 36411	-0.10838 53489	55.74757	-0.10687	57.29260	-0.10544
19	57.32752 54379	+0.10537 40554	58.89000	+0.10397	60.43635	+0.10266
20	60.46945 78453	-0.10260 05671	62.03235	-0.10131	63.57989	-0.10008

Also tabulated are the values of the Bessel function at the associate extrema,  $J_m(j'_{m,s})$  [17]

$$k_{mn} = \frac{\alpha_{mn}}{a} \quad \text{where} \quad \frac{d[J_m(\alpha_{mn})]}{dx} = 0 \quad (13.49)$$

The form of  $k_{mn}$  in Eq. (13.49) was chosen to emphasize the similarity to the quantization condition for the axial solutions in Eq. (13.42),  $k_z = n_z \pi / L_z$ , derived initially. In this case, the numerical factor,  $\alpha_{mn}$ , takes the place of  $n_z \pi$ , and the characteristic resonator dimension in this case is the radius,  $a$ , instead of the height of the cylinder,  $L_z$ .

The frequencies of the modes within a rigid-walled cylindrical waveguide can now be written in terms of the Pythagorean sum of  $k_{mn}$  and  $k_z$ , where the integer index,  $l = n_z$ .

$$f_{lmn} = \frac{c}{2} \sqrt{\left(\frac{n_z}{L_z}\right)^2 + \left(\frac{\alpha_{mn}}{\pi a}\right)^2} \quad (13.50)$$

The complete expression for the acoustic pressure,  $p_1(r, \theta, z, t)$ , for each normal-mode standing wave within the rigid-walled cylindrical enclosure is the product of the separate functions.

$$p_1(r, \theta, z, t) = \Re e \left[ \hat{A}_{lmn} \cos(k_z z) J_m(k_{mn} r) \cos(m\theta + \varphi_{lmn}) e^{j\omega_{lmn} t} \right] \quad (13.51)$$

As before, each complex (phasor) modal amplitude,  $\hat{A}_{lmn}$ , depends upon the excitation coupling. The phase factor,  $\varphi_{lmn}$ , is included to allow for the *twofold degeneracy* produced by the fact that the nodal diameters for modes with  $m \geq 1$  can have an arbitrary angular orientation with respect to the chosen coordinate axes in the absence of any features that might break the azimuthal symmetry (e.g., see Fig. 13.15).

One obvious feature that would break azimuthal symmetry would be the inclusion of a speaker (e.g., a volume velocity source) at some specific angular location,  $\theta_{drive}$ , other than on the axis of the cylinder ( $r = 0$ ). In that case,  $\varphi_{mn}$  would be chosen to lock the nodal diameters for modes with  $m \geq 1$  to the transducer's location.

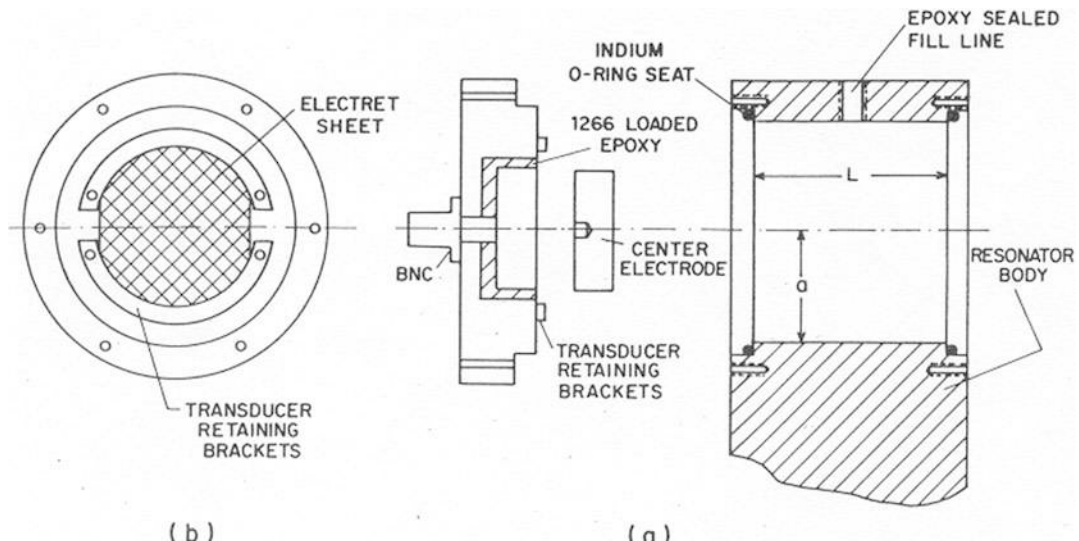


**Fig. 13.9** Cylindrical resonator of equal length and diameter,  $L = 2a = 5.00$  cm. The circular end caps are reversible electret condenser transducers (see Sect. 6.3.3) that have a slightly smaller diameter than the resonator cavity [18]

**Table 13.4** Summary of Bessel mode frequencies and location of nodal circles for the lowest-frequency  $m = 1, 2$ , and  $3$  modes, assuming  $l = 0$ .

$n_z$	$m$	$n$	$\alpha_{mn}$	$f_{lmn}$ (Hz)	Nodal circles		
					Node ( $r/a$ )	Node ( $r/a$ )	Node ( $r/a$ )
0	0	1	3.831706	24,393	0.6276		
0	0	2	7.015587	44,663	0.3428	0.7868	
0	0	3	10.17347	64,766	0.2364	0.5426	0.8506
0	1	1	1.84118	11,721	0		
0	1	2	5.33144	33,941	0	0.7187	
0	1	3	8.53632	54,344	0	0.4489	0.8219
0	2	1	3.05424	19,444	0		
0	2	2	6.70613	42,693	0	0.7658	
0	2	3	9.96947	63,468	0	0.5151	0.8443

The corresponding values of  $\alpha_{mn}$  appear in Table 13.3

The frequencies are based on a rigid-walled cylindrical resonator of radius,  $a = 2.50$  cm, and a sound speed near that of helium gas at 16 °C:  $c = 1000$  m/s. The radial and azimuthal mode shapes are sketched in Fig. 13.10. The ratios of the radius of the nodal circles to the radius of the cylinder,  $r/a$ , were determined by the values of the zero crossings of the corresponding Bessel functions.

The rigid-walled cylindrical resonator in Fig. 13.9 will be used to illustrate the application of the solution for the normal mode frequencies in Eq. (13.50). That resonator was designed to measure the isotopic ratio of  $^3\text{He}$  to  $^4\text{He}$  by measuring the speed of sound in such a gas mixture [18]. The frequencies of the axial (height) modes are as easy to calculate as they were for the closed-closed case of the one-dimensional resonator.

Since the resonator was used to measure sound speed in a helium isotopic mixture, the frequencies in Table 13.4 and Eqs. (13.53) and (13.54) assume a sound speed,  $c = 1000$  m/s, corresponding to the sound speed in pure  $^4\text{He}$  at about 289 K (16 °C).

$$f_{l,0,0} = l \left( \frac{c}{2L_z} \right) = l \cdot 10,000 \text{ Hz; } l = 0, 1, 2, \dots \quad (13.52)$$

The Bessel mode frequencies (i.e.,  $l = 0$ ) are just as easy to calculate except that we will not be able to use consecutive integers to relate the radius to the resonance frequency.

$$f_{0,m,n} = \alpha_{mn} \left( \frac{c}{2\pi a} \right) = \alpha_{mn} \cdot 6,366.2 \text{ Hz} \quad (13.53)$$

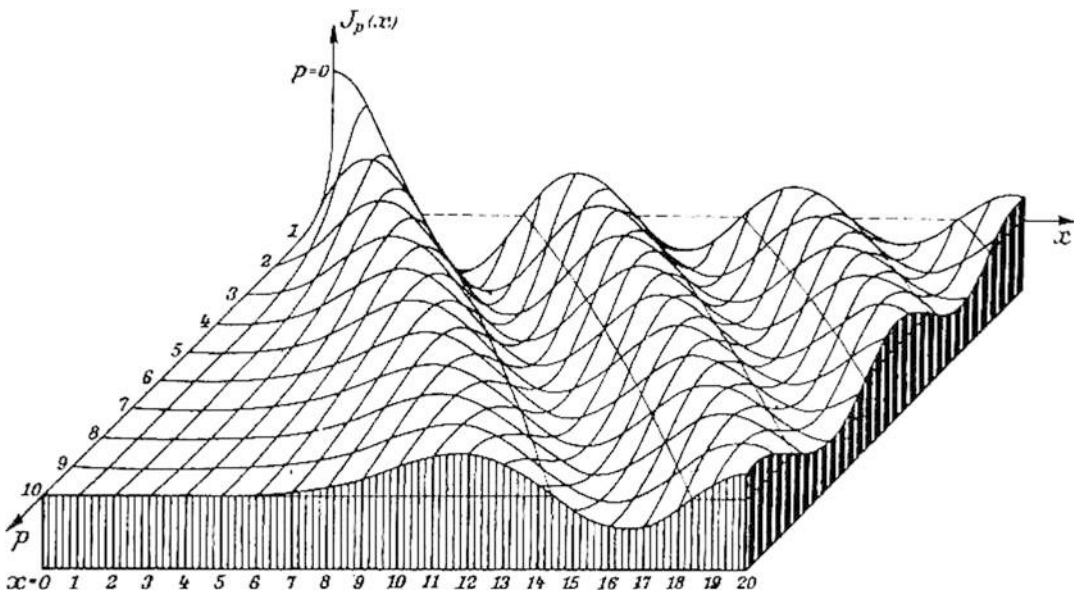
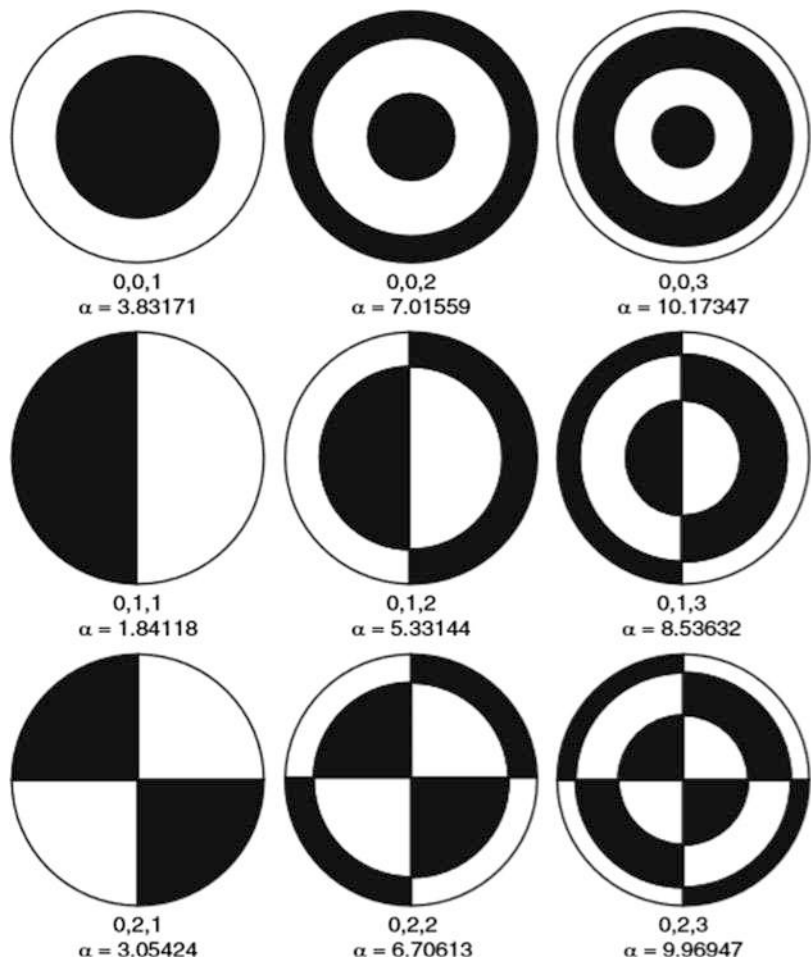
The first three resonances of the three lowest-frequency Bessel modes for this example are summarized in Table 13.4. That table also includes the ratios of the radii of the nodal circles to the radius of the cylinder,  $r/a$ , as determined by the values of the zero crossings of the corresponding Bessel functions. Two-dimensional representations of the mode shapes are provided in Fig. 13.10.

Figure 13.10 shows the nodal locations and the relative phases of the different parts of the resonator for those modes. It does not reveal anything about the relative amplitudes as a function of mode number. The tendency for the acoustic pressure to be localized nearer to  $r = a$  as the non-axial mode number increases is best illustrated in Fig. 13.11.

### 13.3.2 Modal Density Within a Rigid Cylinder

The order of the modes in Table 13.4 was determined by the mode number sequence. Inspection of Table 13.4 shows that this does not place the modes in ascending order with respect to frequency.

**Fig. 13.10** Nodal circles and nodal diameters are drawn to scale for the first three  $m = 0, 1$ , and 2 modes of a cylindrical resonator. Black regions are  $180^\circ$  out-of-phase with white regions. Under each (triplet) mode number designation is the value of  $\alpha = ka$  for that mode



**Fig. 13.11** Plots of Bessel functions of the first kind,  $J_m(x)$ , as a function both of the argument,  $x$ , and of the function index,  $p = m$ . As  $p$  increases, more of the amplitude is localized near the perimeter of the cylinder [19]

**Table 13.5** Lowest-frequency modes, rounded to integer frequencies, of the helium-filled resonator shown in Fig. 13.9

Order	$l$	$m$	$n$	$f_{lmn}$ (Hz)	Order	$l$	$m$	$n$	$f_{lmn}$ (Hz)
1	1	0	0	10,000	22	2	4	1	39,319
2	0	1	1	11,721	23	2	1	2	39,395
3	1	1	1	15,407	24	4	0	0	40,000
4	0	2	1	19,444	25	3	3	1	40,191
5	2	0	0	20,000	26	4	1	1	41,682
6	1	2	1	21,865	27	1	5	1	42,049
7	2	1	1	23,182	28	0	2	2	42,693
8	0	0	1	24,393	29	1	2	1	43,848
9	1	0	1	26,364	30	4	2	1	44,475
10	0	3	1	26,746	31	0	0	2	44,663
11	2	2	1	27,894	32	3	4	1	45,233
12	1	3	1	28,554	33	3	1	2	45,299
13	3	0	0	30,000	34	2	5	1	45,477
14	2	0	1	31,544	35	1	0	2	45,768
15	3	1	1	32,209	36	4	0	1	46,851
16	2	3	1	33,397	37	2	2	2	47,145
17	0	1	2	33,941	38	4	3	1	48,118
18	1	4	1	35,299	39	1	6	1	48,790
19	1	1	2	35,383	40	2	0	2	48,936
20	3	2	1	35,750	41	5	0	0	50,000
21	3	0	1	38,666	42	3	5	1	50,677

The modes are listed in ascending order of their frequencies up to frequencies less than or equal to 50 kHz. The number of modes with frequencies less than the first five axial mode frequencies is plotted in Fig. 13.12. This table is based on Eq. (13.54) and assumes that  $c = 1000$  m/s.

Using the previous expression for modal frequency in Eq. (13.50), and modifying it for this specific example in Fig. 13.9, the frequencies of the individual modes can be calculated and placed in order of ascending frequency, as shown in Table 13.5.

$$f_{lmn} = \frac{c}{2} \sqrt{\left(\frac{n_z}{L_z}\right)^2 + \left(\frac{\alpha_{mn}}{\pi a}\right)^2} = 500\text{Hz} \sqrt{\left(\frac{l}{0.05}\right)^2 + \left(\frac{\alpha_{mn}}{0.025\pi}\right)^2} \quad (13.54)$$

As was done for the rectangular enclosure in Eqs. (13.17) and (13.19), we can write an expression to predict the number of modes below a maximum frequency,  $f_{\max}$ .

$$N \cong \frac{4\pi f_{\max}^3 V}{3c^3} + \frac{\pi f_{\max}^2 A}{4c^2} + \frac{f_{\max} L}{8c} \quad (13.55)$$

For a cylindrical enclosure,  $V = \pi a^2 L_z$  and  $A = 2\pi a^2 + 2\pi aL_z$ , as expected, but the total effective “edge length,”  $L = 4\pi a + 4L_z$ , has a form that could not have been easily anticipated [20]. For our example, the polynomial approximation in Eq. (13.55) is plotted in Fig. 13.12, along with the cumulative mode count for the modes having frequencies less than 1 Hz above the frequency of the pure axial modes up to a maximum frequency,  $f_{\max} = f_{5,0,0} + 1 = 50,001$  Hz.

From the excellent agreement illustrated in Fig. 13.12 between the modal frequencies in Table 13.5 and the  $k$ -space volume polynomial approximation of Eq. (13.55), it is clear that the approximation is quite good for a resonator of modest aspect ratio (i.e.,  $L_z \cong 2a$ ), even when the mode indices are fairly low.

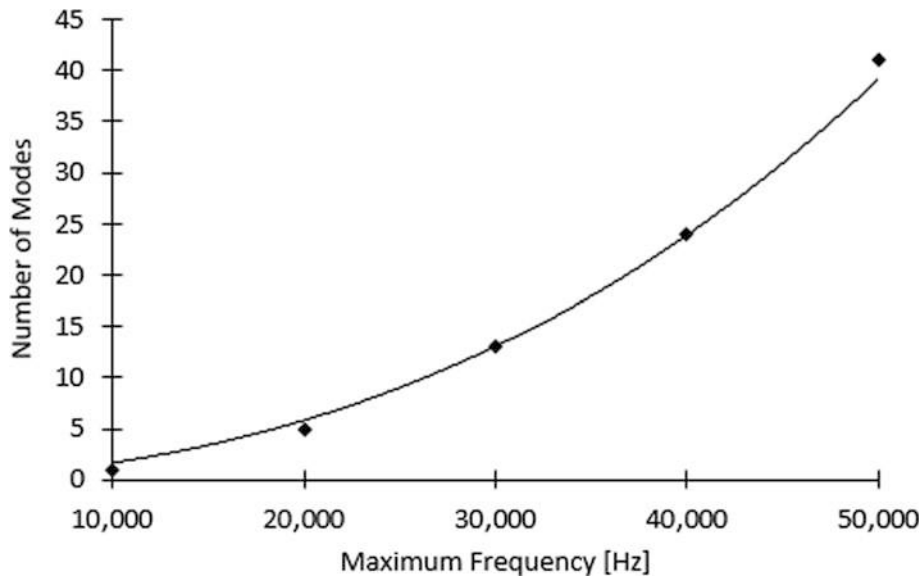


**Fig. 13.12** Plot of the number of modes with frequencies less than the value on the  $x$  axis for the sample resonator shown in Fig. 13.9. The diamonds represent the number of modes listed in Table 13.5. The line is the polynomial approximation in Eq. (13.55)

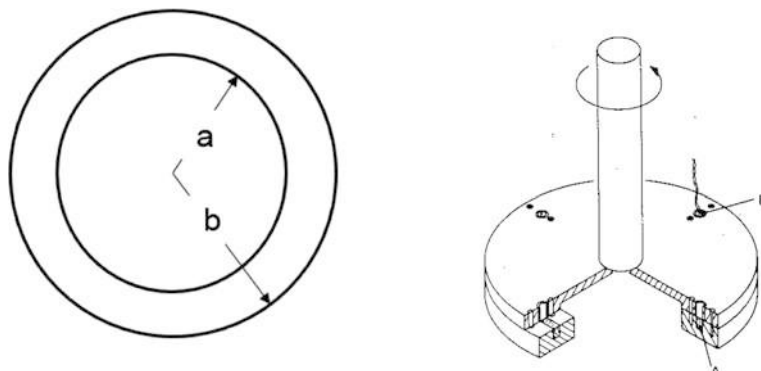


**Fig. 13.13** (Left) Plan view of an annular (toroidal) resonator with inner radius,  $a$ , and outer radius,  $b \equiv (1 + \delta) a$ . The resonator's radial cross-section is rectangular. The height of the resonator is  $L_z$ , as before, and its width is  $b - a$ . (Right) Cut-away view of a toroidal resonator mounted on a shaft for rotation [21]. The dotted material, labeled "A" in the toroid, represents the annular duct of rectangular cross-section that contains the fluid. A transducer on the "roof" of the resonator is indicated as "B" with lead wires attached

### 13.3.3 Modes of a Rigid-Walled Toroidal Enclosure\*

We ignored the Neumann solutions for the cylindrical enclosure because they became infinite at  $r = 0$ . For a toroidal resonator, like the one shown in Fig. 13.13 (Right), we need the Neumann solutions to simultaneously match the inner and outer radial boundary conditions. Since there is no fluid on the axis of the torus,  $r = 0$ , the fact that  $N_m(0)$  diverges does not present any difficulty.

The general solution for the pressure can be expressed in polar coordinates as before with the azimuthal component expressed as a trigonometric function.

$$p_1(r, \theta) = [AJ_m(k_{mn}r) + BN_m(k_{mn}r)] \cos(m\theta + \varphi_{m,n}) \quad (13.56)$$

From the Euler equation [16], the impenetrability of the walls requires that the radial pressure gradient must vanish. This boundary condition leads to pair of equations.

$$\begin{aligned} \left(\frac{\partial p}{\partial r}\right)_{r=a} &= 0 \Rightarrow [AJ'_m(k_{mn}a) + BN'_m(k_{mn}a)] = 0 \\ \left(\frac{\partial p}{\partial r}\right)_{r=b} &= 0 \Rightarrow [AJ'_m(k_{mn}b) + BN'_m(k_{mn}b)] = 0 \end{aligned} \quad (13.57)$$

In Eq. (13.57), the prime symbol indicates differentiation of the functions with respect to the radius. Setting the determinate of the coefficients to zero leads to a transcendental equation that can be solved for the natural frequencies.

$$J'_m(k_{mn}a) \cdot N'_m(k_{mn}b) - J'_m(k_{mn}b) \cdot N'_m(k_{mn}a) = 0 \quad (13.58)$$

Needless to say, the general solution is messy [22].

If we restrict our attention to the case where the difference between the outer and inner radii,  $(b - a)$ , is small compared to their average,  $(b + a)/2$ , then there will be many azimuthal modes ( $m > 0$ ) with frequencies that are lower than the first radial or height modes. Assuming also that  $L_z \ll a$ , the first height mode will occur at approximately  $f_{1,0,0} = c/2L_z$ , and the first radial mode will occur at approximately  $f_{0,0,1} = c/2(b-a)$ .

The lowest-frequency azimuthal mode,  $f_{0,1,0}$ , will correspond to one complete wavelength fitting within the effective circumference of the toroid as already shown schematically in Fig. 13.8. The fact that the first mode corresponds to one full wavelength arises again from the requirement that the azimuthal boundary condition is periodic and the function describing the amplitude of the acoustic pressure,  $p_1(r, \theta, z, t)$ , is single-valued. The ends of the wave must match in both pressure amplitude and slope. (No “kinky” solutions are acceptable, although not on moral grounds.)

Subsequent azimuthal modes will be integer multiples of the fundamental azimuthal mode as long as  $f_{0,m,0}$  is less than  $f_{0,0,1}$  or  $f_{1,0,0}$ .

$$f_{0,m,0} = m \left( \frac{c}{2\pi a_{eff}} \right) \quad (13.59)$$

The obvious choices for  $a_{eff}$  would be some arithmetic or geometric average of the inner and outer radii. To first order in  $\delta \equiv (b-a)/a$ , the average  $(a + b)/2$ , the geometric mean,  $(ab)^{1/2}$ , and the Pythagorean average,  $\sqrt{(a^2 + b^2)/2}$ , all give  $a_{eff} \cong b(1-\delta/2)$ . Maynard has calculated the result that is correct to second order in  $\delta$  [23].

$$a_{eff} = a \sqrt{1 + \delta + (\delta^2/6)} \quad (13.60)$$

The measured frequency response of a toroidal resonator is shown in the photograph of a spectrum analyzer’s screen in Fig. 13.14. For this example, there are 24 equally spaced azimuthal modes with frequencies provided by Eq. (13.59). Those modes are excited and detected by capacitive electret transducers located on the “roof” of the resonator as shown in Fig. 13.13 (Right). Their amplitude initially grows with increasing frequency as the half-wavelength of the modes approach the diameter of the transducers. The amplitude decreases as the wavelength continues to decrease for successively higher-frequency azimuthal modes, since some portions of the transducer’s diaphragm are being driven out-of-phase with other portions.

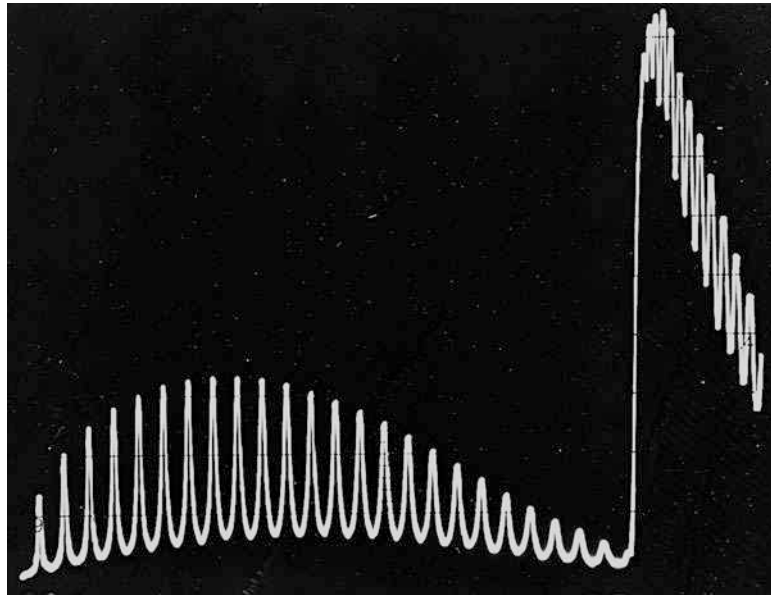


**Fig. 13.14** Amplitude vs. frequency as measured by a Hewlett-Packard Model 3580A Spectrum Analyzer for a toroidal resonator that has  $la - bl \ll (a + b)/2$ . The modes are excited and detected by transducers mounted on the “roof” of a resonator similar to the resonator depicted in Fig. 13.13 (Right). Above the 24<sup>th</sup> azimuthal mode, the amplitude of the signal jumps as the first height mode is excited. The amplitude jump is due to the fact that the transducers on the roof couple preferentially to height modes

Above the 24<sup>th</sup> azimuthal mode, the amplitude of the signal jumps as the first height mode at frequency,  $f_{1,0,0} = (c/2L_z)$ , is excited. The first height mode is followed by a succession of mixed modes with frequencies,  $f_{1,m,0}$ . Eleven such mixed modes are visible in Fig. 13.14 ( $f_{1,1,0}$  through  $f_{1,11,0}$ ) before the frequency limit of the spectrum analyzer display at 50 kHz is exceeded.

### 13.3.4 Modal Degeneracy and Mode Splitting

As demonstrated in the analysis of a rectangular room, the degeneracy of modes is related to the symmetry of the enclosure. In Table 13.1, the cubical room had a larger fraction of degenerate modes than the rectangular room. In a cylindrical enclosure, the rotational symmetry makes each azimuthal ( $m \geq 1$ ) mode twofold degenerate. Since we can consider standing waves to be the superposition of traveling waves (see Sect. 3.3.1), the degeneracy of azimuthal modes in a cylindrical enclosure can be viewed from the standing wave perspective or from the traveling wave perspective. For example, when viewed as a standing wave, the nodal diameter of the  $m = 1$  mode can be vertical or horizontal (as shown in Fig. 13.15) or have any angular orientation with respect to the coordinate axes (as a superposition of the horizontal and vertical components). This is an example of its twofold degeneracy.

That degeneracy can be “split” if there is some additional feature within the resonator that breaks the azimuthal symmetry. For example, if an incompressible obstacle were placed in the resonator along the circular boundary, as shown in Fig. 13.15, then the mode with the (pressure) nodal diameter passing through the obstacle will have a lower frequency than the mode with the orthogonal nodal diameter.

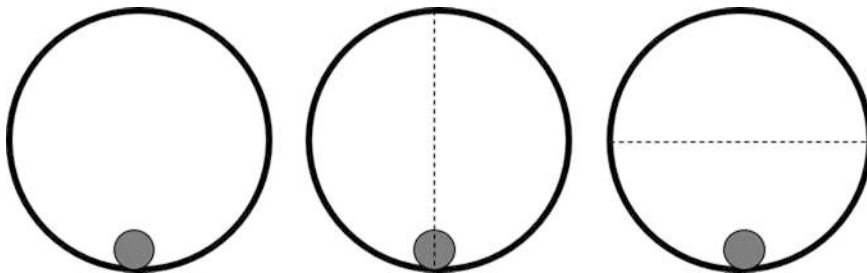


**Fig. 13.15** (Left) A cylindrical resonator is drawn with a rigid, incompressible object, shown as a gray circle, located adjacent to the cylindrical boundary. If the 0,1,1 mode is excited, then the resonance frequency of the mode will depend upon the orientation of the nodal diameter (shown as a *dashed line*) with respect to that obstacle. (Center) Since the acoustic pressure along the node is zero, the frequency of the mode that has a nodal line that intersects the obstacle will be lower than the degenerate mode (in the absence of the obstacle). (Right) The mode that has the nodal line that is farthest away from the incompressible obstacle will have a frequency that is higher than the degenerate modes

In the case where the obstacle is located on the (pressure) nodal line, there are no acoustic pressure oscillations, and the fact that the obstacle is incompressible does not change the potential energy of the mode. On the other hand, the nodal line is the location where the azimuthal component of the pressure gradient,  $\nabla_\theta p_1$ , is greatest and therefore where the azimuthal component of the velocity,  $u_\theta$ , is greatest. Since the obstacle is rigid, the fluid must accelerate to pass around the obstacle so the square of the local fluid velocity is positive-definite and must increase, therefore increasing the kinetic energy of the fluid. By Rayleigh's method (see Sect. 3.3.2), this increase in kinetic energy will reduce the resonance frequency for that mode since the potential energy is unchanged.

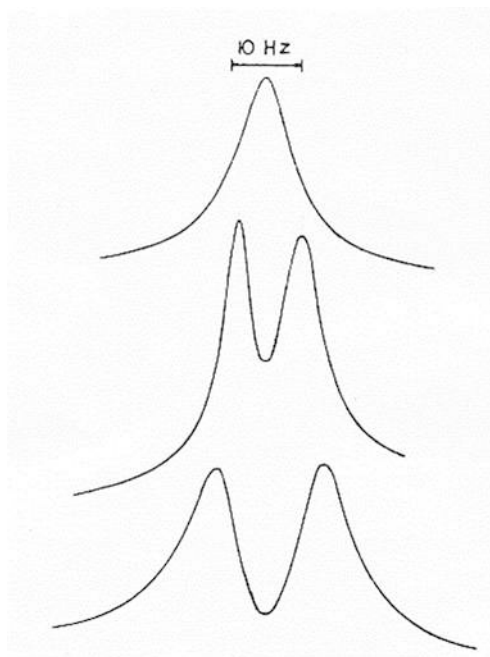
An alternative understanding that leads to the same result (a reduction in modal resonance frequency) is to assume that the perimeter (hence, the azimuthal acoustic path-length) of the cylinder has increased due to the obstacle. Since the frequency of the azimuthal mode depends upon the circumference (which is more obvious if we consider the azimuthal solutions corresponding to integer wavelengths fitting into an effective circumference,  $2\pi a_{eff}$ , for a toroidal enclosure), again, the modal frequency is reduced.

When the nodal line is farthest from the obstacle, the acoustic pressure oscillations,  $p_1$ , are the largest at the location of the obstacle. Since the fluid has become less compressible in that region, the potential energy must increase, as must the resonance frequency. Alternatively, we can imagine that the obstacle could morph into a wedge of the same volume as that of the obstacle. This would reduce the effective circumference and also result in an increase in the resonance frequency of the mode above the degenerate frequency value in the absence of the obstacle.

Just as the modal degeneracy can be lifted by consideration of a standing wave interpretation, it is also possible to split the degeneracy from the traveling wave viewpoint. Since the standing wave can be constructed from two counter-propagating traveling waves, we can split the degeneracy in the azimuthal modes by allowing the fluid within the cylindrical or toroidal enclosure to be rotating in either the clockwise or counter-clockwise directions.

If the fluid is rotating in the clockwise direction, then the speed of sound for the clockwise propagating wave will be increased, and the speed of the counter-clockwise wave will be decreased. Again, picturing the azimuthal modes as consisting of integer numbers of wavelengths fitting within an effective circumference,  $2\pi a_{eff}$ , the clockwise mode will have a higher frequency than the unperturbed mode, and the counter-clockwise mode will have a lower frequency. Experimental results for the “Doppler” splitting of an azimuthal mode due to fluid rotation are shown in Figs. 13.16 and Fig. 13.25 [21].

**Fig. 13.16** The amplitude of a degenerate azimuthal resonance of a cylindrical resonator (top) is shown plotted vs. frequency. As the fluid begins to rotate, the mode “splits” into two distinct resonances whose frequency difference increases with increasing rotational velocity. Since the frequency difference between the two amplitude peaks can be measured with great accuracy [24], it is possible to use the splitting of the resonance to accurately determine the fluid’s rotational velocity



### 13.3.5 Modes in Non-separable Coordinate Geometries

Not all enclosures will have shapes that conform to the 11 coordinate systems in which the Helmholtz equation is separable [1]. Although there is a proliferating variety numerical software package that can solve the Helmholtz equation in arbitrary geometries by finite-element or boundary-element methods, such programs do not (yet) provide any useful classification system for the resulting normal mode shapes and frequencies. Also, if the solution is important, it is essential that an alternative analytical approximation technique be available to check the accuracy of the numerical answers,<sup>6</sup> especially if the modal analysis is being made as part of the design process and a physical model of the system does not yet exist to allow the numerical results can be tested experimentally.

The principle of *adiabatic invariance* was introduced first in Sect. 2.3.4, where it was applied to a simple harmonic oscillator, then again for two-dimensional systems in Sect. 6.2.3, to address the problem of non-separable geometries that described the boundaries of membranes. Adiabatic invariance was then employed to approximate the frequencies and mode shapes of wedge-shaped membranes in Sect. 6.2.4. The same approach will now be applied to a non-separable three-dimensional enclosure. In this case, the enclosure is the cargo bay of the Space Shuttle, shown in plan view and in cross-section in Fig. 13.17.

The cross-section of the Space Shuttle cargo bay is similar to a rigid-rigid cylinder, like those shown in Figs. 13.1 and 13.9, except that the cross-section is not circular but is a hemi-ellipse that is joined to a truncated portion of an irregular octagon. As with the application of adiabatic invariance to the two-dimensional membranes, we will exploit the fact that the ratio of the energy of a mode,  $E_{lmn}$ , to its normal mode frequency,  $f_{lmn}$ , remains constant if the constraints on the system (i.e., the boundary

<sup>6</sup>“A computer can provide the wrong answer with seven-digit accuracy thousands of times each second.”

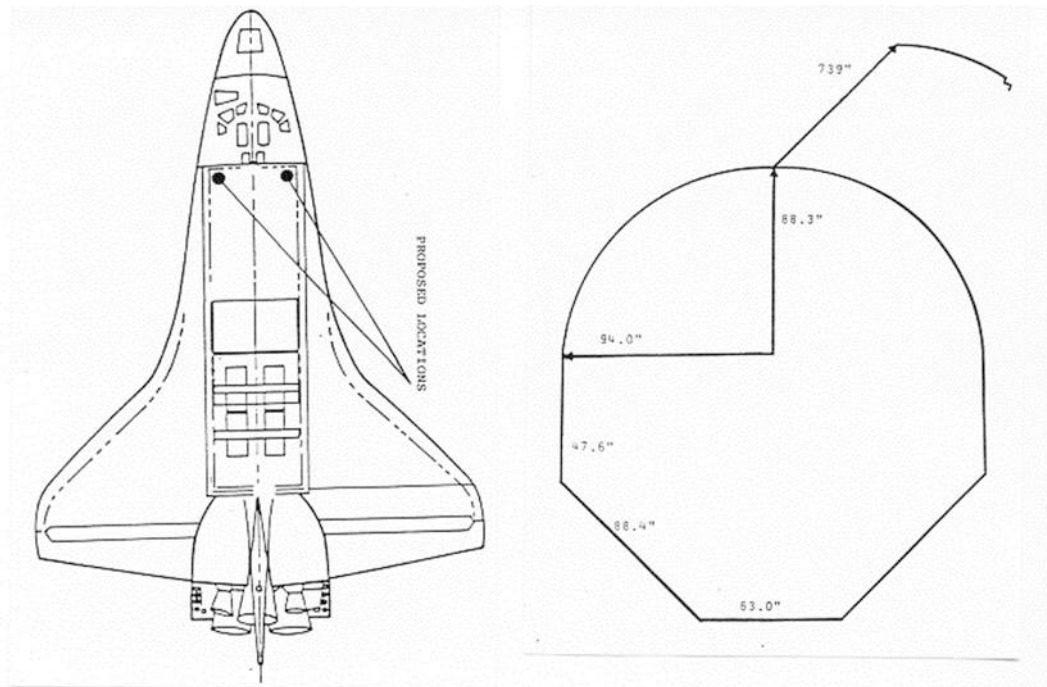


**Fig. 13.17** (Left) Plan view of the Space Shuttle and (Right) cross-section of the Shuttle's cargo bay. The cargo bay's cross-section is a hemi-ellipse, which provides the cargo bay's doors, above a truncated portion of an irregular octagon. The hemi-ellipse has a semi-major axis of  $94'' = 2.39$  m and a semi-minor axis of  $88.3'' = 2.24$  m. The bottom of the octagonal section is  $53'' = 1.35$  m, with the slanted side lengths of  $88.4'' = 2.25$  m and vertical side lengths of  $47.6'' = 1.21$  m

conditions) are deformed slowly when compared to the period of oscillation. Said differently, the “adiabatic” portion of the principle requires that the deformation of the boundaries occurs over a time that is many times greater than the period of oscillation,  $T_{lmn} = f_{lmn}^{-1}$  [25].

$$\left( \frac{E_{lmn}}{f_{lmn}} \right)_{\text{Adiabatic}} = (\text{constant})_{lmn} \quad (13.61)$$

As will be demonstrated in Sect. 15.4.4, the sound within an enclosure exerts a non-zero, time-averaged radiation pressure on the boundaries that is proportional to the square of the sound amplitude, expressed as either acoustic pressure or acoustic velocity. The energy of the system will be changed if the boundaries move in a way that increases or decreases the energy of the mode by doing “pdV work” against that radiation pressure. If that magnitude of the radiation pressure is fairly uniform at the boundaries, and if the deformation results in no net change in the enclosure’s volume, Eq. (13.61) requires that the modal frequency will remain constant.

If the length of the cargo bay remains constant, then the frequencies of the acoustic modes of the cargo bay,  $f_{lmn}$ , will be the same as those of a cylindrical resonator of length,  $L_z$ , and radius,  $a$ , if the cargo bay’s cross-sectional area is set equal to  $\pi a^2$ . This approach was tested experimentally using a scale model of the cargo bay, made from a transparent plastic, shown in Fig. 13.18.

The normal mode frequencies corresponding to each mode were determined by exciting the cavity at a corner using a compression driver that was connected to a flexible tube, visible at the bottom right in Fig. 13.18. Those measured frequencies are provided in Table 13.6. A small probe microphone that

**Fig. 13.18** Photograph of a two-dimensional transparent plastic model of the Space Shuttle's cargo bay, shown Fig. 13.17. The grid lines drawn on the top of the model helped locate the microphone used to plot the equal acoustic pressure contours presented in Fig. 13.19.

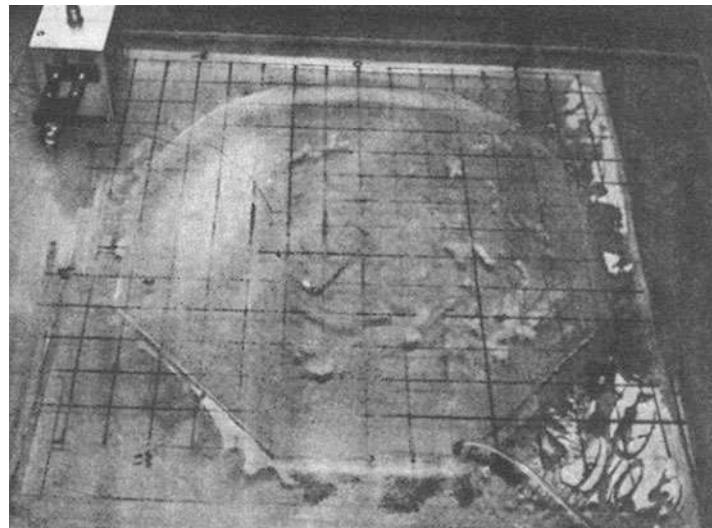


**Table 13.6** The measured frequencies of the normal modes of the space shuttle cargo bay model are identified with the corresponding mode numbers for a cylindrical enclosure

Mode	Freq. (Hz)	Ratio $f_{0,m,n}/f_{0,1,1}$	Cylinder $f_{0,m,n}/f_{0,1,1}$	$\Delta\%$
0,1,1	41.1	1.000	1.000	0
0,2,1	67.4	1.635	1.658	-1.4
0,0,1	85.3	2.076	2.082	-0.3
0,3,1	94.0	2.287	2.283	+0.2
0,4,1	114.5	2.782	2.891	-3.8

The percentage difference between the measured frequency ratios and the frequency ratios for a cylindrical enclosure,  $\Delta\%$ , has an average of  $-1.3\% \pm 1.8\%$

penetrated the base of the model was then used to trace the pressure nodes by sliding the enclosure along the base. The lines where the acoustic pressure had half the maximum value (measured at the perimeter) were also traced. Both the nodal lines (solid) and half-amplitude lines (dashed) are shown for the four lowest-frequency purely “azimuthal modes” in Fig. 13.19.

It is worth examining the nodal lines in Fig. 13.19 and comparing those nodal lines to the nodal diameters for the corresponding azimuthal modes of cylindrical enclosures that are shown in Fig. 13.10. Because the height of the model cavity,  $L_z$ , is very short,  $L_z \ll a$ , the lowest-frequency “height mode” occurs at a frequency well above any of the purely azimuthal modes in Fig. 13.19:  $f_{1,0,0} = c/2L_z \gg f_{0,m,0}$ . The similarity between the cylindrical nodal diameters and model’s nodal lines provides confirmation that the mode number identification used for the modes of the cargo bay, based on a cylindrical mode classification system, is justified and also provides a convenient nomenclature that can be used to identify the individual modes.

The accuracy of normal mode frequency predictions are established in Table 13.6 by forming the ratio of the measured mode frequencies,  $f_{0,m,n}$ , to the lowest-frequency measured mode,  $f_{0,1,0}$ . That ratio is compared to the same ratio for the cylindrical enclosure’s modes that are determined by Eq. (13.50).

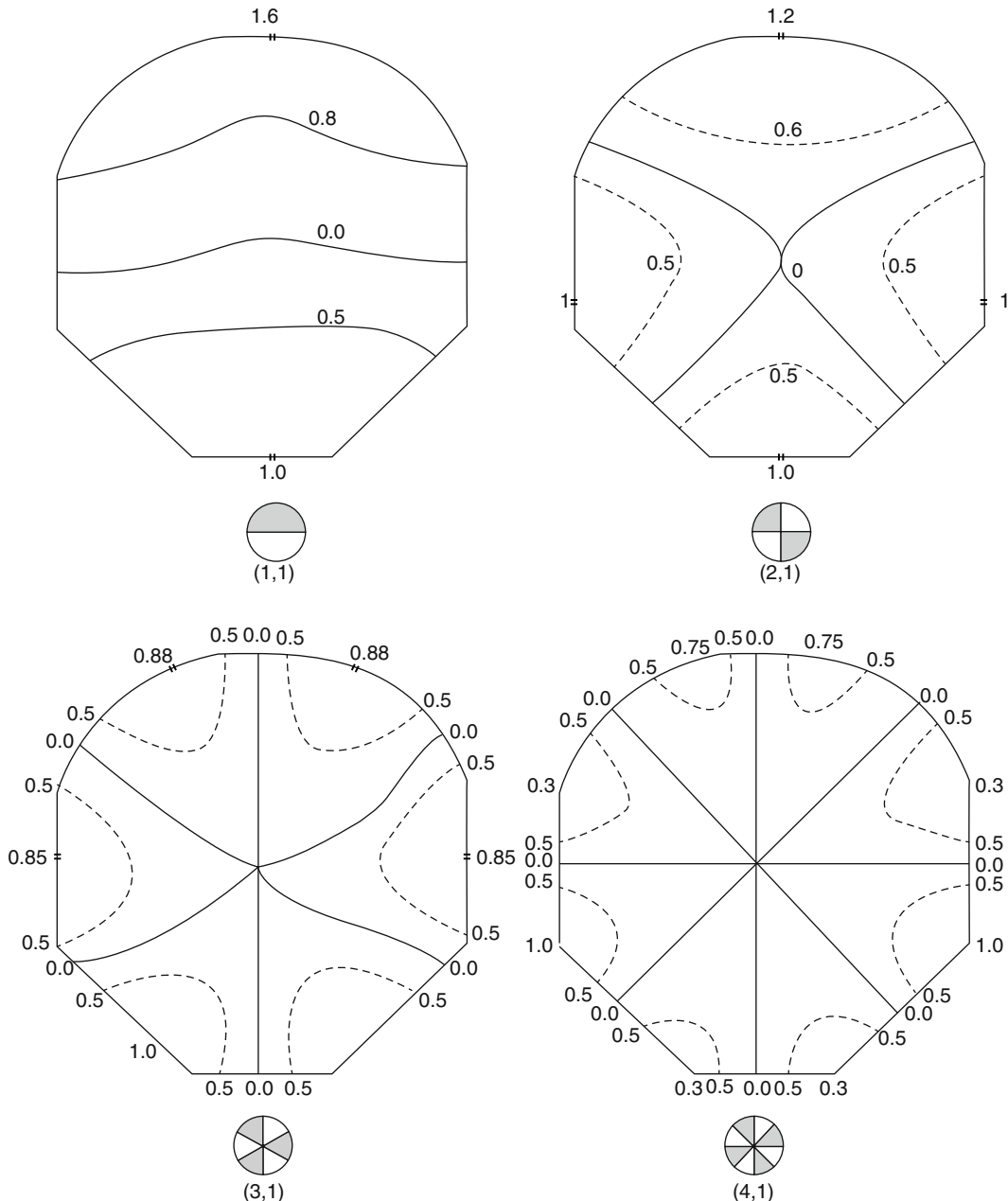


**Fig. 13.19** Measured acoustic pressure contours for the lowest-frequency azimuthal modes ( $0,m,0$ ) using the plastic quasi-two-dimensional mock-up in Fig. 13.18 of the Space Shuttle's cargo bay. The lines shown in the contour maps are pressure nodal lines or half-amplitude lines. Below each contour map is the corresponding pressure distribution for a rigid-walled cylindrical resonator similar to those provided in Fig. 13.10

## 13.4 Radial Modes of Spherical Resonators

Spherical enclosures have played an important role in high-precision acoustical measurements because they can achieve high quality factors since there is no fluid shearing at the boundary for the radial modes of a spherical resonator; therefore, there are no viscous losses associated with those modes. In

Chap. 12, only the outgoing solution for three-dimensional spherical spreading in Eq. (12.8) was investigated because that chapter's focus was on radiation and scattering in an unbounded medium. In a spherical resonator, there is a boundary that reflects the outgoing spherical wave and produces a converging spherically symmetric wave that produces radial standing-wave modes when superimposed on the outgoing wave, just as the addition of a right- and left-going plane waves created standing waves in Eqs. (3.18) and (3.19).

The proper superposition of the diverging and converging spherical waves must eliminate the infinite pressure that occurs at the origin,  $r = 0$ . This divergence did not create any difficulty for the radiation calculations in Chap. 12 because it was assumed that the radius,  $a$ , of the volume velocity source was non-zero. To eliminate that unphysical infinity, the superposition of the outgoing and converging spherical waves will be formed from their difference.

$$\begin{aligned} p_1(r, t) &= \Re \left[ \frac{\hat{C}}{r} e^{j(\omega t - kr)} - \frac{\hat{C}}{r} e^{j(\omega t + kr)} \right] = \Re \left[ \frac{-\hat{C} e^{j\omega t}}{r} (e^{jkr} - e^{-jkr}) \right] \\ &= \Re \left[ \frac{2j\hat{C} e^{j\omega t}}{r} \sin(kr) \right] = \frac{C'}{r} \sin(kr) \cos(\omega t + \varphi) \end{aligned} \quad (13.62)$$

At the origin, for  $r = 0$ , Eq. (13.62) produces  $p_1(0, t) = kC' \cos(\omega t + \varphi)$  when the small ( $kr$ ) expansion of  $\sin(kr)$  is used to evaluate the radial acoustic pressure at  $r = 0$ . In the final expression, all of the constants have been coalesced into a scalar amplitude,  $C'$ , to emphasize the similarity with other standing-wave solutions like Eq. (10.44).

### 13.4.1 Pressure-Released Spherical Resonator

If the spherical boundary is pressure-released and located at a radial distance,  $a$ , from the center of the sphere, then the radial modes are harmonic.

$$p_1(a) = 0 = \frac{C'}{a} \sin(k_{0,0,n}^{\text{release}} a) \quad \Rightarrow \quad k_{0,0,n}^{\text{release}} = \frac{n\pi}{a}; \quad n = 1, 2, 3, \dots \quad (13.63)$$

This is easy to implement for a water-filled thin-walled glass sphere. Since water is nearly incompressible, the thin glass wall of the spherical vessel moves with the water. If additional precision is required, the effective radius of such a spherical resonator can be increased by an amount determined by the mass density of the thin glass in exactly the same way the thin gold layer created a density-weighted increase in the effective length of a resonant bar for the analysis of the quartz micro-balance in Sect. 5.1.2.

Wilson and Leonard used a commercial round-bottom Pyrex™ boiling flask as a pressure-released spherical resonator to contain the water so that very small sound absorption could be measured in a laboratory over the range of frequencies between 50 kHz and 500 kHz [26]. The sphere was suspended from a support using three 250-μm-diameter steel wires so that any loss due to sound transmission through the supports was minimized. The sphere was placed in a vacuum chamber with the air pressure reduced to less than 1.0 mmHg (133 Pa) to minimize radiation losses. In addition to the absence of any viscous dissipation, the thermal relaxation losses at the boundary were also negligible because the thermal expansion coefficient of water is so close to zero at room temperatures<sup>7</sup> and the boundary was

<sup>7</sup> The expansion coefficient vanishes at 4 °C where the density of water is a maximum. If ice were not less dense than water, you would not be reading this footnote, since when water froze in the winter, it would sink to the bottom of the lake and more ice would form at the surface and sink. The fact that ice floats insulates the water below. Since all animals evolved from a watery origin, it is possible that there might be no animal life as we know it on this planet if ice were denser than water.

pressure-released. A similar pressure-released spherical resonator would correspond to a gas-filled spherical balloon in a vacuum, like the Echo satellites, which were placed in low Earth orbit near the beginning of the US space program in August 1960 (see Problem 11 and Fig. 13.34) [27]. Such a pressure-released boundary condition for a spherical resonator has also been shown to be an accurate representation of the modes of the liquid (aqueous humor) in the mammalian eyeball [28].

### 13.4.2 Rigid-Walled Spherical Resonator

If the boundary of the spherical resonator is rigid and impenetrable, then the Euler equation can be used to relate the standing-wave pressure,  $p_1(r)$ , in Eq. (13.62), to the radial velocity of the fluid at the boundary,  $u_r(a)$ .

$$\nabla_r p_1(a) \propto \frac{dp_1(a)}{dr} = C' \left[ \frac{k_{0,0,n}^{\text{rigid}} \cos(kr)}{r} - \frac{\sin(k_{0,0,n}^{\text{rigid}} r)}{r^2} \right]_{r=a} \propto -\rho_m \frac{\partial u_r(a)}{\partial t} = 0 \quad (13.64)$$

$$\frac{(k_{0,0,n}^{\text{rigid}} a) \cos(k_{0,0,n}^{\text{rigid}} r)}{a} = \frac{\sin(k_{0,0,n}^{\text{rigid}} a)}{a^2} \Rightarrow \tan(k_{0,0,n}^{\text{rigid}} a) = (k_{0,0,n}^{\text{rigid}} a)$$

The values of  $k_{0,0,n}^{\text{rigid}}$  are thus quantified by a simple transcendental equation whose solutions will be familiar from earlier investigations of a mass-loaded string in Sect. 3.6. The values of  $(ka)$  that satisfy Eq. (13.64) are provided in Table 13.7.

The frequencies of radial modes of a gas-filled spherical resonator were used by scientists at the US National Bureau of Standards, in Gaithersburg, MD, to produce the most accurate value of Boltzmann's constant,  $k_B$ , and the universal gas constant,  $\mathfrak{R}$  [29]. The Bureau's acoustical determination of these fundamental constants constituted a reduction in their uncertainty by a factor of 5 over previous determinations and subsequently was made less than 1 ppm by using microwave resonance frequencies and the speed of light (known to 1 ppb) to determine the sphere's volume<sup>8</sup> [30]. A cross-sectional diagram of the resonator and its surrounding pressure vessel is provided in Fig. 13.20.

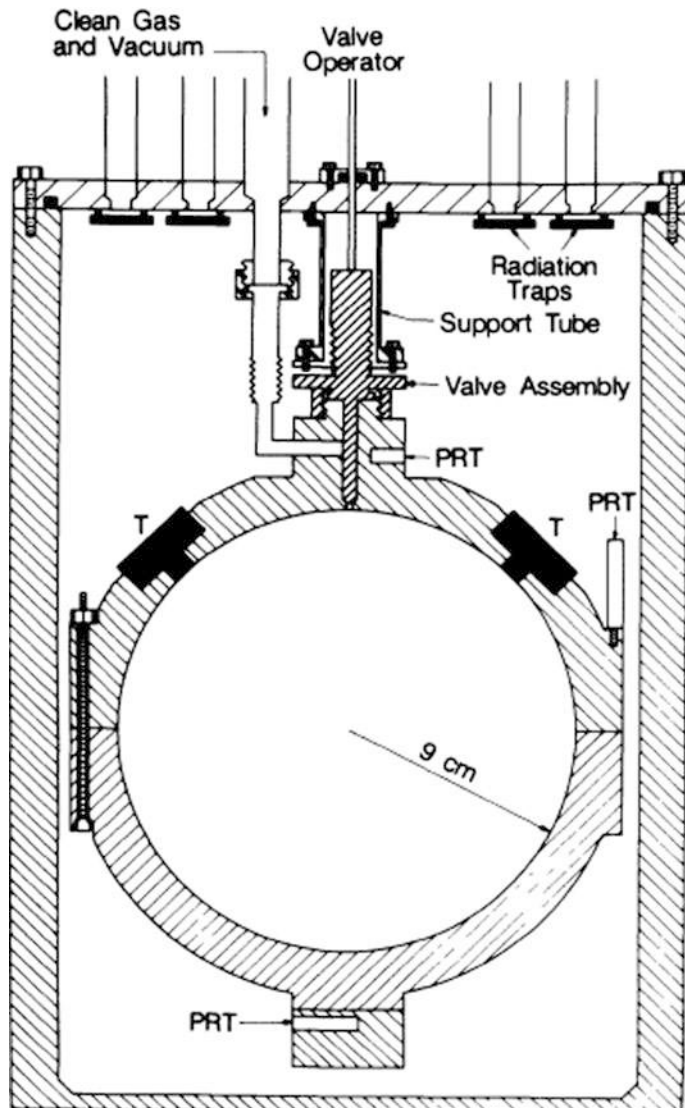
For large values of  $n$ ,  $(k_{0,0,n}^{\text{rigid}} a) \cong (n + \frac{1}{2})\pi$

**Table 13.7** Solutions for the radial mode frequencies,  $f_{0,0,n}^{\text{rigid}} = (k_{0,0,n}^{\text{rigid}} a)c/(2\pi a)$ , for a rigid, impenetrable spherical resonator based on Eq. (13.64)

Radial mode	$(k_{0,0,n}^{\text{rigid}} a)$	$(k_{0,0,n}^{\text{rigid}} a)/\pi$
1	4.49341	1.430
2	7.72525	2.459
3	10.90412	3.471
4	14.06619	4.477
5	17.22076	5.482
6	20.37130	6.484
7	23.51945	7.486

<sup>8</sup>Boltzmann's constant,  $k_B$ , and the universal gas constant,  $\mathfrak{R}$ , are the second least precisely known physical constants after Newton's Universal Gravitational Constant,  $G$ . As of 20 May 2019, the value of  $k_B$  and  $\mathfrak{R}$  are taken as being exact (see Appendix A).

**Fig. 13.20** Cross-sectional diagram of the spherical resonator and pressure vessel that were used by the US National Bureau of Standards (now known as the National Institute for Standards and Technology) to determine the universal gas constant, [29]. The transducer assemblies are indicated as “T,” and the locations of the platinum resistance thermometers are indicated by “PRT.” The pressure vessel was immersed in a stirred liquid bath (not shown) which maintained the temperature of the apparatus and the gas within the sphere at a constant temperature



### 13.5 Waveguides

The conceptual and mathematical apparatus that has just been developed to understand the sound field in three-dimensional rectangular or cylindrical enclosures can easily be extended to describe sound propagation in a waveguide. Waveguides can be man-made or can occur naturally.<sup>9</sup> They are important because sound waves that are contained within a waveguide do not suffer the  $1/r$  decrease in sound

<sup>9</sup> The National Weather Service in Tallahassee, FL, felt obligated to issue a weather statement on 9 March 2011 in response to “strange sounds being reported in their area explaining that the unusual sound that was observed was ‘caused by thunder from a distant lightning strokes . . . bouncing off a very stable layer above the ground. This is called ducting . . . and can allow sound to travel unusually long distances.’”

pressure amplitude that accompanies three-dimensional spherical spreading. Such waveguides have utility in the transmission of sound from the source to a receiver. One early waveguide is the stethoscope invented in 1816 by the Parisian physician, René Laennec [31]. Waveguides (called speaking tubes) were also used on sailing ships, at least as early as the 1780, to communicate orders from the ship's captain to sailors, and they were still in use on naval warships during World War II.

### 13.5.1 Rectangular Waveguide

Consider the waveguide of rectangular cross-section shown in Fig. 13.21. Application of the wavenumber quantization conditions for a rectangular enclosure in Eq. (13.11) will apply, but now  $L_z = \infty$ .

As a consequence,  $k_z$  is no longer restricted to only discrete values, but becomes a continuous variable. The separation condition of Eq. (13.6) will now determine  $k_z$  as a function of the frequency,  $\omega$ , at which the waveguide is being excited.

$$k_z^2 = \left(\frac{\omega}{c}\right)^2 - k_x^2 - k_y^2 \text{ where } k_x = \frac{\ell\pi}{L_x} \text{ and } k_y = \frac{m\pi}{L_y}; \quad \ell, m = 0, 1, 2, 3, \dots \quad (13.65)$$

The corresponding sound field can be written as in Eq. (13.13) except that the option for boundary conditions that are not all rigid and impenetrable will be retained by the choice of either sine or cosine functional dependence (or their superposition) in the  $x$  and  $y$  directions, as indicated by the curly brackets.

$$p_{\ell m}(x, y, z; t) = \Re e \left[ \hat{\mathbf{A}}_{\ell m} \begin{Bmatrix} \sin(k_x x) \\ \cos(k_x x) \end{Bmatrix} \begin{Bmatrix} \sin(k_y y) \\ \cos(k_y y) \end{Bmatrix} e^{j(\omega t - k_z z)} \right] \quad (13.66)$$

Notice that the complex amplitude pre-factor (phasor),  $\hat{\mathbf{A}}_{\ell m}$ , has only two indices since the  $z$  wavenumber,  $k_z$ , is not quantized.

The quantized wavenumbers that satisfy the transverse boundary conditions for a waveguide of rectangular cross-section can be combined into a single wavenumber with two subscripted indices, where  $k_x$  and  $k_y$  are specified in Eq. (13.65), for a rigid-walled rectangular waveguide.

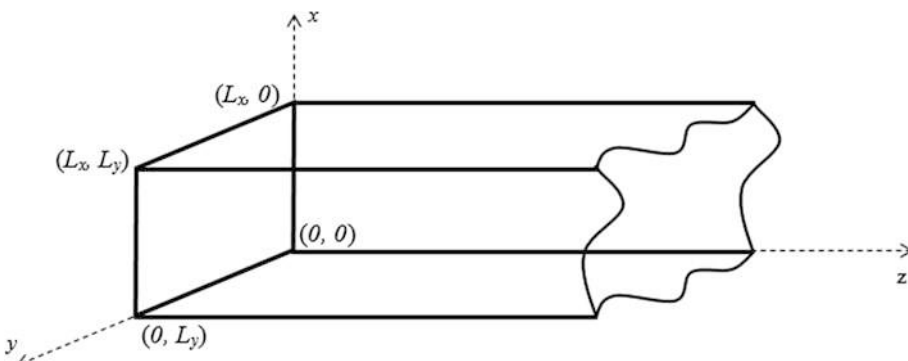


**Fig. 13.21** Waveguide of rectangular cross-section that extends to infinity in the  $z$  direction

$$k_{\ell m}^2 \equiv k_x^2 + k_y^2 \Rightarrow k_z = \pm \sqrt{\left(\frac{\omega}{c}\right)^2 - k_{\ell m}^2} = \pm \left(\frac{\omega}{c}\right) \sqrt{1 - \left(\frac{\omega_{\ell m}}{\omega}\right)^2} \quad (13.67)$$

This wavenumber consolidation makes it possible to generalize the following results to rigid-walled waveguides of circular cross-section later in Sect. 13.5.4, by letting  $k_{\ell m} = \alpha_{mn} / a$ , where  $\alpha_{mn}$  is quantized by Eq. (13.49).

The consequences for  $k_z$  that arise from Eq. (13.67) are significant. For the plane wave mode, when the wave fronts within the guide are normal to the  $z$  direction and there is no variation in the pressure or particle velocity in the transverse plane (i.e.,  $k_x = k_y = 0$ ), then  $\Im m[k_z] = 0$ , and  $k_z = \omega / c$ .<sup>10</sup> On the other hand, if  $k_{\ell m} > \omega / c$ , then the real part of the wavenumber will vanish,  $\Re e[k_z] = 0$ . Substitution of a purely imaginary value of  $k_z$  into the pressure field within the waveguide, as specified in Eq. (13.66), creates a pressure field that decays exponentially with distance beyond the source of such a disturbance within the waveguide. The characteristic exponential decay distance,  $\delta = \Im m[k_z^{-1}]$ , for frequencies well below cut-off for a particular higher-order mode,  $\omega \ll \omega_{\ell m}$ , will be determined by the height or width or combination of the height and width of the waveguide, depending upon the mode.

$$\lim_{\omega \rightarrow 0} [\delta] = \frac{j}{k_{\ell m}} = j \frac{L_x}{\ell \pi} \text{ or } j \frac{L_y}{m \pi} \text{ or } j \sqrt{\left(\frac{L_x}{\ell \pi}\right)^2 + \left(\frac{L_y}{m \pi}\right)^2} \text{ if } \omega < \omega_{\ell m} \quad (13.68)$$

The frequency at which a non-plane wave mode with  $k_x \neq 0$  or  $k_y \neq 0$  or both  $k_x$  and  $k_y$  being non-zero is known as the *cut-off frequency*,  $\omega_{co} = 2\pi f_{co}$ , for that mode. Such exponentially decaying behavior was demonstrated for sound propagation in exponential horns in Sect. 10.9.1 for frequencies below the cut-off determined by the horn's flare constant. Each waveguide mode will have its unique cut-off frequencies determined by  $k_{\ell m}$ :  $2\pi f_{co} = \omega_{co} = ck_{\ell m}$ .

### 13.5.2 Phase Speed and Group Speed

The phase speed for propagation down the waveguide is  $c_{ph} = \omega / k_z$ . Below cut-off for any of the higher-order modes of the waveguide,  $\omega < \omega_{co} = c k_{\ell m}$ , only plane waves will propagate down the guide. In that case,  $k_z = \omega / c$ , so  $c_{ph} = c$ , as was the case for plane waves propagating in an unbounded medium with a constant thermodynamic sound speed,  $c$ . At frequencies that are high enough that one or more non-plane modes can be excited,  $\omega > \omega_{\ell m}$ , the phase speed becomes a function of frequency.

$$c_{ph} = \frac{\omega}{k_z} = \frac{c}{\sqrt{1 - \left(\frac{\omega_{co}}{\omega}\right)^2}} \quad (13.69)$$

This phase speed is plotted in Fig. 13.22 for the plane wave (0,0) mode and the next two highest-frequency non-plane modes, (1,0) and (2,0), where it has been assumed that  $L_x \gg L_y$  so  $\omega_{2,0} < \omega_{0,1}$ .

It is useful to make a geometrical interpretation of the variation of the phase speed in a waveguide with the frequency of the sound,  $\omega$ , that is propagating within. Just as the boundary conditions were satisfied in a rigidly terminated resonator by the superposition of two counter-propagating traveling waves, it is possible to extend that same model to a waveguide if we let the two traveling plane waves propagate in different directions.

<sup>10</sup>There will necessarily be some variation in the plane wave's velocity in the  $z$  direction within the very thin thermoviscous boundary layer specified in Eqs. (9.14) and (9.33). The attenuation and dispersion created by these boundary layer effects will be calculated in Sect. 13.5.5.

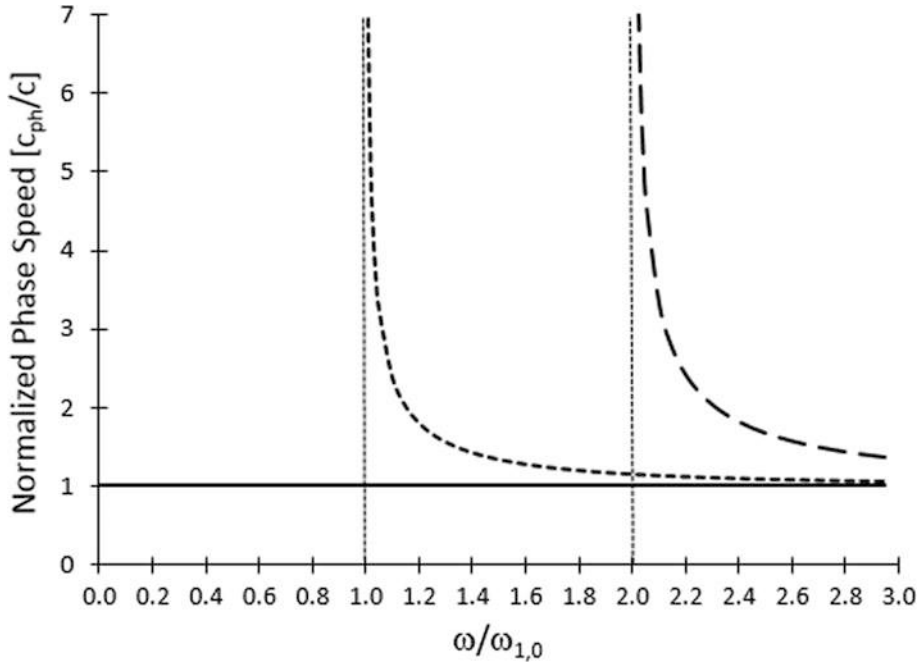


**Fig. 13.22** Phase speed,  $c_{ph}$ , relative to the thermodynamic sound speed,  $c = \sqrt{(\partial p / \partial \rho)_s}$ , as a function of frequency,  $\omega$ , relative to the cut-off frequency,  $\omega_{1,0}$ , of the first non-planar mode. The phase speed of the plane wave mode (0,0) is the solid line. The short-dashed line is the relative phase speed of the (0,1) mode, and the long-dashed line is the relative phase speed of the (2,0) mode. In this figure, it is assumed that  $L_x \gg L_y$  so  $\omega_{2,0} < \omega_{0,1}$ .

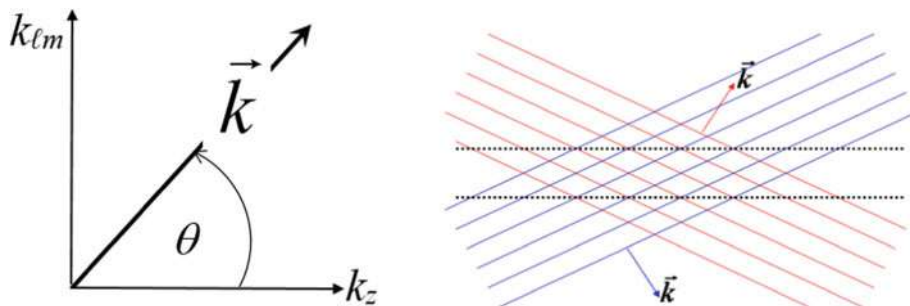


**Fig. 13.23** (Left) The wavevector (bold arrow),  $\vec{k}$ , that characterizes the direction of the plane wave is projected on to the  $z$  axis to produce  $k_z$  and on to the  $y$  axis to produce the cut-off wavenumber,  $k_{\ell m}$ . In accordance with the separation equation (13.65), the Pythagorean sum of  $k_x$  and  $k_{\ell m}$  is length of  $|\vec{k}|$ . (Right) The top and bottom boundaries of the waveguide are shown as horizontal dotted lines. The wave fronts of the two traveling plane waves always overlap at both boundaries indicating that those rigid surfaces correspond to the locations of the acoustic pressure amplitude maxima.

In Fig. 13.23 (Right), there are two plane waves indicated by equally spaced wave fronts and two wavevectors,  $\vec{k}$ , that are perpendicular to their respective wave fronts. For one set of wave fronts, the angle that  $\vec{k}$  makes with the  $z$  axis is  $\theta$ . For the other set of wave fronts, the angle that  $\vec{k}$  makes with the  $z$  axis is  $-\theta$ . Using the diagram in Fig. 13.23 (Left) that projects  $\vec{k}$  onto  $k_z$  and  $k_{\ell m}$ , the angle,  $\theta$ , that  $\vec{k}$

makes with the  $z$  axis can easily be written, and the phase speed,  $c_{ph}$ , can be expressed in terms of that angle, as well.

$$\cos \theta = \frac{k_z}{|\vec{k}|} \Rightarrow c_{ph} = \frac{\omega}{k_z} = \frac{\omega}{|\vec{k}| \cos \theta} = \frac{c}{\cos \theta} \quad (13.70)$$

The top and bottom of the waveguide are represented by the horizontal dotted lines in Fig. 13.23 (Right). Inspection of that figure reveals that both sets of wave fronts, moving in different directions determined by their respective wavevectors,  $\vec{k}$ , always intersect at the waveguide boundaries, making that intersection a pressure maximum, as it must be if the boundary is rigid and impenetrable.

With this geometric interpretation in mind, the following picture emerges for the relationship between phase speed; the wave's frequency,  $\omega$ ; and the cut-off frequency,  $\omega_{\ell m}$ . For a plane wave mode with frequency,  $\omega < \omega_{\ell m}$ , that wavevector,  $\vec{k}$ , is aligned with the  $z$  axis and  $\theta = 0^\circ$ , so  $c_{ph} = c$ . If a higher-order waveguide mode is excited, so  $\omega > \omega_{\ell m}$ , then at cut-off, the wavevector,  $\vec{k}$ , is parallel to  $k_{\ell m}$  and  $k_z = 0$ . In that case, there is a simple standing wave created by the superposition of the two plane waves traveling in opposite directions and  $\theta = 90^\circ$ . The wave fronts are parallel to the waveguide boundaries, so the phase is identical at all times everywhere along the waveguide, assuming the sound field within the waveguide has reached steady state. For the phase to (instantaneously) be the same over any non-zero distance, the phase speed must be infinite. This infinite phase speed at the cut-off frequency is apparent from Fig. 13.22, since the curves representing the phase speed of the non-plane wave modes are asymptotic to the vertical lines that extend from each mode's cut-off frequency.

At cut-off, the two traveling waves are moving up and down (i.e.,  $\theta = 90^\circ$ ) in Fig. 13.23 (Right); they are making no progress whatsoever in the  $z$  direction. If the sound energy is to travel down the waveguide in the  $z$  direction,  $\theta < 90^\circ$ . For example, if  $\tan \theta = 10$  (so  $\theta = 84.3^\circ$ ), then the plane waves move forward along the  $z$  axis by one-tenth as far as the wave fronts have moved going up and down between the waveguide's rigid boundaries during the same time interval. The speed at which the sound energy moves forward along the  $+z$  axis, down the waveguide, is the group speed,  $c_{gr}$ . Figure 13.23 (Left) can be used to express the group speed in terms of the angle,  $\theta$ , that the wavevector,  $\vec{k}$ , makes with the  $z$  axis.

$$c_{gr} = c \cos \theta = c \sqrt{1 - \left(\frac{\omega_{\ell m}}{\omega}\right)^2} \Rightarrow c_{gr} c_{ph} = c^2 \quad (13.71)$$

### 13.5.3 Driven Waveguide

As with any linear system, the complex (phasor) amplitude coefficient,  $\hat{A}_{lm}$ , of the sound field within the waveguide, as expressed in Eq. (13.66), depends upon the amplitude of the excitation and the geometrical distribution of the sources that create the excitation. A two-dimensional Fourier decomposition can be used to calculate the values of  $\hat{A}_{lm}$ , just as the harmonic content of a plucked string was calculated in terms of the string's normal modes in Sect. 3.5. Rather than make such a calculation, it will be instructive to exam the excitation of a waveguide by two rectangular pistons placed in the end of a waveguide of square cross-section, illustrated in Fig. 13.24.

For a rigid-walled rectangular waveguide, like those shown in Figs. 13.21 and 13.24, the excitation of a mode will depend upon the projection of the piston's volume velocity complex amplitude distribution,  $\hat{U}(x, y)$ , upon the basis functions defined by the wavenumbers in Eq. (13.65) that satisfy

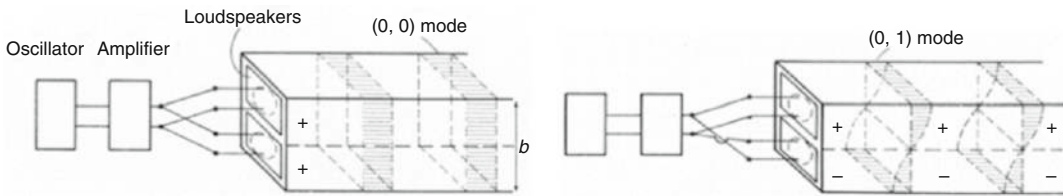


**Fig. 13.24** (Left) A waveguide of square cross-section is driven by two identical rectangular pistons located that the end of the waveguide,  $z = 0$ . If both pistons are driven in-phase, then only the plane wave mode  $(0,0)$  can be excited. (Right) If the two rectangular pistons are driven  $180^\circ$  out-of-phase, so the net volume velocity is zero, then no plane wave is generated. If the drive frequency,  $\omega$ , is greater than the cut-off frequency,  $\omega_{0,1} = \pi c/b$ , then the  $(0,1)$  mode will be excited [32]

the boundary conditions. Since those cosine functions are all orthogonal (for the rigid waveguide, but not necessarily for the functions that satisfy more general boundary conditions), a piston with a uniform distribution of volume velocity,  $|\widehat{\mathbf{U}}(x,y)| = \text{constant}$ , can only excite the plane wave  $(0,0)$  mode at any frequency. That sound will propagate down the waveguide in the  $+z$  direction with  $c_{ph} = c_{gr} = c$ . This plane wave excitation is illustrated in Fig. 13.24 (Left).

If the piston's volume velocity distribution has a non-zero projection onto the basis functions that satisfy the waveguide's boundary conditions in the  $x$  and  $y$  directions, then those modes will be excited, as long as the excitation frequency,  $\omega$ , equals or exceeds that mode's cut-off frequency,  $\omega \geq \omega_{\ell m}$ .

In Fig. 13.24 (Right), the upper piston moves forward while the lower piston moves backward. The net volume velocity is zero so there will be no coupling to the plane wave mode. If the frequency of vibration of those two transducer segments,  $\omega$ , is less than the cut-off frequency for the  $(0,1)$  mode,  $\omega < \omega_{0,1} = \pi c/b$ , where  $b = L_y$ , then the fluid being pushed forward and pulled back by the two transducer segments will just “slosh” between those segments, and all of the fluid's motion will be confined to a distance of about  $z \leq L_z = b$ , as would be expected for an exponentially decaying mode that decays with a distance,  $\delta$ , given by Eq. (13.68).

If the drive frequency of the two out-of-phase transducers in Fig. 13.24 (Right) is higher than the cut-off frequency for the  $(0,1)$  mode,  $\omega > \omega_{0,1} = \pi c/b$ , then the transducers will excite the  $(0,1)$  mode that will propagate down the waveguide in the  $+z$  direction with the phase and group speeds determined by Eqs. (13.69) and (13.71).

### 13.5.4 Cylindrical Waveguide

With the exception of rectangular ducts used for space heating and air conditioning inside buildings, most acoustical waveguides have a circular cross-section. From the acoustical perspective, waveguides of circular cross-section are preferred because cylindrical tubes deform much less than rectangular tubes of equal wall thickness when subjected to a static or dynamic (acoustic) pressure difference between the fluid inside and the medium surrounding the waveguide. They also have the minimum perimeter for any cross-sectional area, so boundary layer thermoviscous dissipation is minimized (see Sect. 13.5.5). Because we chose to specify the transverse composite wavenumber for the rectangular waveguide as  $k_{\ell m}$ , all of the results for cut-off frequency,  $\omega_{mn}$ ; phase speed,  $c_{ph}$ ; and group speed,  $c_{gr}$ , will be identical to the rectangular case if  $k_{\ell m} = \alpha_{mn}/a$  for the cylindrical waveguide, where  $\alpha_{mn}$  is quantized by Eq. (13.49).

$$\begin{aligned} f_{co} &= \frac{\omega_{co}}{2\pi} = \frac{\omega_{mn}}{2\pi} = c \frac{k_{mn}}{2\pi} = c \frac{\alpha_{mn}}{2\pi a} \\ c_{ph} &= \frac{\omega}{k_z} = \frac{c}{\sqrt{1 - \left(\frac{\omega_{co}}{\omega}\right)^2}} \quad \text{and} \quad c_{gr} = \frac{c^2}{c_{ph}} \end{aligned} \quad (13.72)$$

Of course, in Eq. (13.72),  $m$  is the azimuthal mode number and the order of the Bessel function associated with that mode, and  $n$  indicates the number of nodal circles, as diagrammed in Fig. 13.10.

The excitation of a specific mode will depend upon the projection of the transducer's volume velocity distribution on the transverse basis functions,  $J_m(k_{mn}r)$  and  $\cos(m\theta + \varphi_{mn})$ , described in Eq. (13.51). For a rigid-walled cylindrical waveguide with radius,  $a$ , Eq. (13.72) and Table 13.3 place the cut-off frequency of the lowest-frequency non-plane wave mode at  $f_{1,1} = \alpha_{1,1}(c/2\pi a) \cong 1.8412(c/2\pi a) = 0.293 c/a$ . The transverse pressure distribution of the (1,1) mode is shown in Fig. 13.10.

If the transducer produces a uniform volume velocity and is centered on the waveguide's axis, then the symmetry of such an excitation will not couple to the (1,1) mode because the (1,1) mode, as well as any other azimuthal mode,  $m \geq 1$ , presents a pressure that is equally positive and negative about any diameter. In that case, the lowest-frequency purely radial mode would be the lowest-frequency non-plane wave mode that could be excited at frequency,  $f_{0,1} > \alpha_{0,1}(c/2\pi a) \cong 3.8317(c/2\pi a) \cong 0.61 (c/a)$ . That mode also has regions where the pressure at the perimeter is out-of-phase with the pressure at the center. Table 13.4 indicates that the pressure at  $r \geq 0.6276a$  will be out-of-phase with the pressure in the central region.

To calculate the net pressure, the radial pressure variation given by the Bessel function,  $J_o(k_{0,1}r)$ , must be integrated over the waveguide's circular cross-section, as was done previously for circular membranes in Sect. 6.2.5, to obtain the effective piston area,  $A_{eff}$ .

$$A_{eff} = \iint_S J_o(k_{0,1}r) dS = \int_0^a J_o(k_{0,1}r) 2\pi r dr \quad (13.73)$$

Using the identity in Eq. (C.27), the integral in Eq. (13.73) can be evaluated.

$$A_{eff} = \frac{1}{k_{0,1}^2} \int_0^{k_{0,1}a} J_0(x) 2\pi x dx = 2\pi \frac{k_{0,1}a}{k_{0,1}^2} J_1(k_{0,1}a) = 2\pi a^2 \frac{J_1(\alpha_{0,1})}{\alpha_{0,1}} = 0 \quad (13.74)$$

A uniform piston with the same cross-sectional area as the waveguide will not excite the first radial mode. If the goal was to preferentially excite the first radial mode, the piston's volume velocity would be non-zero for  $r < 0.6276a$  and zero for  $0.6276a < r \leq a$ . Ideally, an annulus that would extend to the perimeter,  $r = a$ , and have an inner radius,  $b = 0.6276a$ , that produces a volume velocity that was equal and 180° out-of-phase with the central disk would provide optimal coupling to the (0,1) mode. On the other hand, a full area transducer, like that shown in Fig. 13.13, would excite the longitudinal modes strongly while suppressing both the azimuthal modes and the first radial mode.

### 13.5.5 Attenuation from Thermoviscous Boundary Losses

The calculation of the attenuation of a plane wave propagating down a waveguide is straightforward using the expression for *thermoviscous losses* provided in Eq. (9.38). That equation can be re-written by using the Euler relation for plane waves from Eq. (10.26),  $\hat{\mathbf{v}} = \hat{\mathbf{p}}/(\rho_m c)$ , and assuming that the fluid within the waveguide is an ideal gas,  $\gamma p_m = \rho_m c^2$ . For simplicity, a cylindrical resonator is assumed, so

the perimeter of the waveguide is  $2\pi a$  and its cross-sectional area is  $\pi a^2$ . For a rectangular waveguide, the corresponding geometrical factors would be  $2(L_x + L_y)$  and  $L_x L_y$ .

$$2\pi a \dot{e}_{tv} = \frac{\dot{E}}{L} = \frac{\langle \Pi \rangle_t}{L} = - \left( \delta_\nu + \frac{\gamma-1}{\gamma} \delta_\kappa \right) \frac{2\pi a \omega |\hat{\mathbf{p}}|^2}{4\gamma p_m} \quad (13.75)$$

That time-averaged power dissipation per unit length,  $\langle \Pi \rangle_t / L$ , on the surface of the waveguide, can be compared to the acoustic energy stored per unit length by expressing the total energy density as the maximum potential energy density, provided in Eq. (10.35), multiplied by the waveguide's cross-sectional area (i.e., volume per unit length,  $L$ ).

$$\frac{E_{stored}}{L} = \pi a^2 (PE)_{max} = \frac{\pi a^2 |\hat{\mathbf{p}}|^2}{2\rho_m c^2} = \frac{\pi a^2 |\hat{\mathbf{p}}|^2}{2\gamma p_m} \quad (13.76)$$

The ratio of Eqs. (13.75) and (13.76) is a constant for any frequency,  $\omega$ , as long as the waveguide is excited in only its plane wave mode.

$$\frac{\dot{E}}{E} = - \frac{\left( \delta_\nu + \frac{\gamma-1}{\gamma} \delta_\kappa \right)}{a} \omega \equiv \frac{-1}{\tau_{tv}} \quad (13.77)$$

This form is rather satisfying. The pre-factor is simply the ratio of a “blended” boundary layer thickness, taking both the viscous and thermal dissipation into account, to the radius of the circular waveguide. Of course, since the waveguide is a linear system, the acoustic amplitude,  $|\hat{\mathbf{p}}|$ , has cancelled out of that ratio. Since both  $\delta_\nu$  and  $\delta_\kappa$  are proportional to  $\omega^{-\frac{1}{2}}$ ,  $\dot{E}/E \propto \sqrt{\omega}$ .

When the rate of change of any variable is proportional to its value, then the variable will either decay or grow exponentially. Since this ratio is negative in Eq. (13.77), the sound amplitude will decay exponentially as the sound propagates down the waveguide. The corresponding thermoviscous exponential decay time,  $\tau_{tv}$ , is just the reciprocal of  $\dot{E}/E$ . The distance of travel and the travel time are simply related by the sound speed,  $c$ , so the spatial attenuation coefficient,  $\alpha_{tv} = (c\tau_{tv})^{-1}$ .

$$\alpha_{tv} = \frac{1}{c\tau_{tv}} = - \frac{\left( \delta_\nu + \frac{\gamma-1}{\gamma} \delta_\kappa \right)}{a} \frac{\omega}{c} \propto \sqrt{\omega} \quad (13.78)$$

The resulting attenuation of the plane wave as a function of distance can be expressed in terms of the product of the plane wave solution of Eq. (13.66) and a decaying exponential factor.

$$p_{0,0,k}(x, y, z, t) = \Re e \left[ \hat{\mathbf{A}}_{0,0} e^{-\alpha_{tv} z} e^{j(\omega t - k_z z)} \right] \quad (13.79)$$

The thermoviscous boundary layer attenuation for higher-order waveguide modes can be related to the plane wave attenuation by invoking the geometrical perspective developed with the aid of Fig. 13.23. That perspective treats the higher-order waveguide modes as a combination of two traveling waves with wavevectors which make an angle,  $\pm\theta$ , with the  $z$  axis of the waveguide. From that perspective, the higher-order modes travel a distance that is  $(\cos \theta)^{-1}$  longer than the plane wave mode. That perspective produced a simple expression for group speed and can also determine the attenuation constant for non-plane wave modes,  $\alpha = \alpha_{tv}/\cos \theta$ .

The effect of the thermoviscous boundary layers also introduces some dispersion. Within the thermal boundary layer,  $\delta_\kappa$ , the compressibility of the gas transitions from its adiabatic value far

from the walls to an isothermal compressibility at the wall. Also, within the viscous boundary layer thickness, the effective density of the gas is increasing toward infinity since the no-slip boundary condition at the wall makes the gas immobile. This small increase in compressibility and simultaneous increase in the effective density both conspire to reduce the sound speed. Since both boundary layer thicknesses are usually small compared to the waveguide's radius, the resulting dispersion is generally negligible in waveguides of large cross-section.

### Talk Like an Acoustician

Eigenvalues	Energy balance equation
Axial mode	Critical distance
Tangential mode	Schroeder frequency
Oblique mode	Periodic boundary conditions
Degenerate modes	Twofold degeneracy
Density of modes	Adiabatic invariance
Wavenumber space	Cut-off frequency
$k$ -space	Thermoviscous losses
Diffuse sound field	

### Exercises

For these problems, unless otherwise specified, assume the sound speed in air is 345 m/s, in water is 1500 m/s, and in liquid is  ${}^4\text{He}$  at 1.20 K and saturated vapor pressure is 237.4 m/s.

1. **The Golden Temple.** A rectangular room is  $L_y = 20$  m wide,  $L_x = 32.36$  m deep, and  $L_z = 12.36$  m high. Those dimensions are in the “golden ratio.”
  - (a) *Modes.* Calculate the frequencies of the 27 lowest-frequency modes of the room. Tabulate the modes in ascending order of frequency (lowest to highest), indicating the mode numbers corresponding to each frequency.
  - (b) *Modal excitation and detection.* Assume the modes are excited by a volume velocity source located in a corner of the room. Indicate which of the 27 lowest-frequency modes listed above would be detected by a microphone placed exactly in the center of the room (i.e.,  $x = L_x/2$ ,  $y = L_y/2$ , and  $z = L_z/2$ ).

Unless otherwise indicated, you may assume that the walls of the temple are made of wood-paneling (1/2" thick backed by a 3" deep air space). On each of the two long walls, are five pairs of glass windows (windowpanes, one above the other) that are 3.0 m wide and 4.85 m tall (a total of 20 windows). The window pairs on each wall are separated by five 2.0-m-wide fiberglass panels (total of 10 panels) that are 2" thick and mounted off of the wall by a 1" airspace that reaches from the floor to the ceiling to help reduce reverberation time. The ceiling is covered entirely with acoustical plaster. The floor has thick carpet laid directly over a concrete base. There are 192 upholstered (cloth covered) seats.

Table 13.8 can be used to determine the sound absorption coefficients of the temple's surfaces and its contents for this problem, but the reader is cautioned to use a more comprehensive and authoritative sources for design of actual venues. The most comprehensive compilation of such data for use in reverberation time calculations that I have found is provided by Cyril Harris in *Noise Control in Buildings: A Practical Guide for Architects and Engineers* [33].

**Table 13.8** Representative average Sabine absorptivity for various surfaces

Octave-band center frequency (Hz) →	125	250	500	1000	2000
Material	Absorptivity				
½" wood paneled walls w/3" air space	0.30	0.25	0.20	0.17	0.15
Windowpane glass	0.35	0.25	0.18	0.12	0.07
2" thick fiberglass w/1" air space	0.35	0.65	0.80	0.90	0.85
Acoustical plaster	0.07	0.17	0.40	0.55	0.65
Thick carpet	0.02	0.06	0.14	0.35	0.60
Upholstered (cloth covered) seats/seat	0.20	0.35	0.55	0.65	0.60

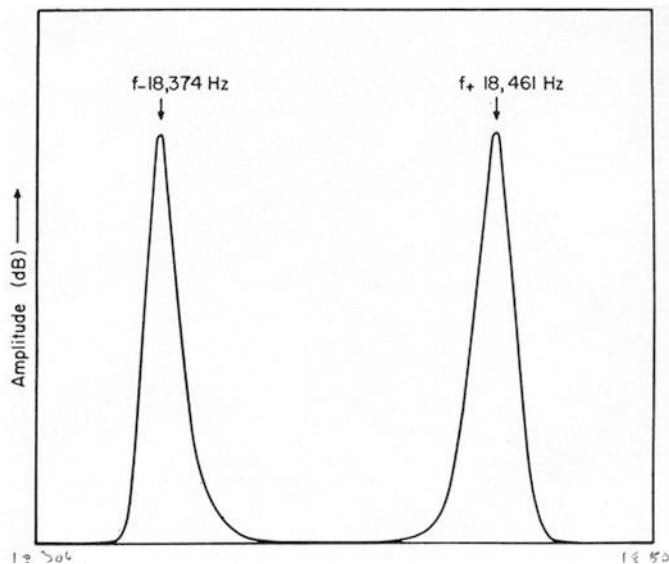
- (c) *Schroeder frequency.* Calculate the room's Schroeder frequency,  $f_S$ , based on the average absorption,  $\langle A \rangle$ , at 125 Hz. Using the approximate analytical expression for number of modes of the room, estimate the number of modes in the room with frequencies less than  $f_S$ .
- (d) *Reverberation time.* Calculate reverberation times at 125 Hz, 500 Hz, and 2 kHz using the Sabine Equation.
- (e) *The Eyring and Norris reverberation time.* An alternative to the Sabine equation was proposed by Carl Eyring, at Bell Labs, which is more accurate for more absorptive ("dead") rooms and reduces to the Sabine's result in "live" rooms where the total surface area of the room is  $S$  and  $\langle A \rangle / S \ll 1$  [34].

$$T_{60} = \frac{0.161 V}{-S \ln [1 - (\langle A \rangle / S)]} \quad (13.80)$$

The use of the numerical pre-factor assumes that  $S$ ,  $\langle A \rangle$ , and  $V$  are all expressed in metric units. Recalculate the reverberation times from part (d) using the Eyring-Norris expression.

- (f) *Critical distance.* Calculate the distance,  $r_d$ , that a listener must be from a person speaking (assume 500 Hz), without electronic sound reinforcement, at the front of the room, so that the listener receives equal amounts of direct and diffuse sound pressure.
- (g) *Steady-state diffuse sound pressure level.* If a solo violinist produces a  $B_4$  note (at approximately 494 Hz) that radiates 2.0 mW of acoustic power into the room, what is the approximate sound pressure level (in dB re: 20  $\mu\text{Pa}_{\text{rms}}$ ) observed in the diffuse sound field?
- (h) *Bulk absorption.* Using the approximate expression for bulk absorption in Eq. (13.30), calculate the importance of  $4 \text{ mV}/\langle A \rangle$  relative to surface absorption at 125 Hz, 500 Hz, and 2 kHz, if the relative humidity is 50%.
2. **Hot tub modes.** Calculate the ten lowest-frequency modes of a rigid-walled circular swimming pool that is 5.0 m in diameter and is filled with water to a depth of 2.0 m. The surface above the water is pressure-released by the water-air interface.
3. **Toroidal resonator.** Shown in Fig. 13.25 is the spectrum (amplitude vs. frequency) of a rigid-walled toroidal resonator with inner,  $a$ , and outer,  $b$ , radii such that  $|a - b| \ll (a + b)/2$  and  $|a - b| < L_z$ . The modes of the resonator are excited and detected using a speaker and microphone mounted on the "roof" of the toroid. There are 25 azimuthal modes with frequencies less than the first height mode.
- (a) *Effective radius.* If  $L_z = 1.00 \text{ cm}$ , what is the mean radius,  $a_{\text{eff}}$ , of the toroid if the fluid in the toroid is liquid helium with a sound speed (non-rotating) of  $c_l = 237.4 \text{ m/sec}$  and the split degenerate modes in Fig. 13.25 correspond to  $m = 24$ ?
- (b) *Doppler mode splitting.* Shown in Fig. 13.25 is a degenerate pair of azimuthal modes that have been split into two distinct modes by uniform rotation of the fluid within the toroid with an

**Fig. 13.25** Degenerate modes of a toroidal resonator that are split due to steady flow in the torus



Frequency (Hz)	Detectable by $M_{\text{middle}}$ ?	Detectable by $M_{\text{center}}$ ?
430	NO	YES
860		
1290		
1720		
2010		
2056		
2150		

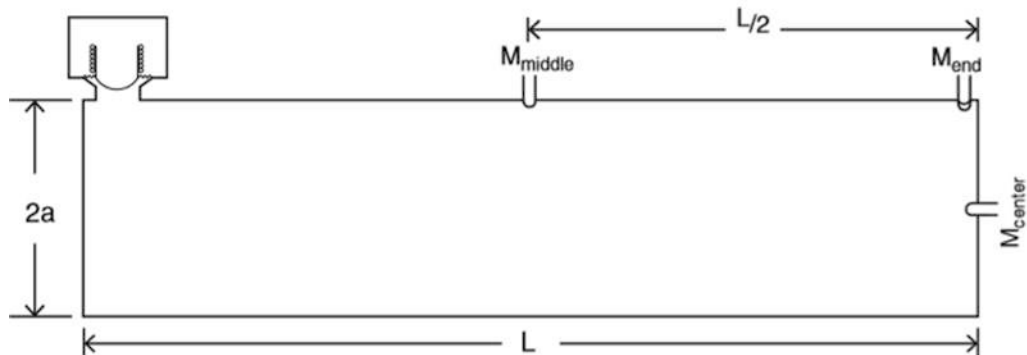


**Fig. 13.26** Cross-sectional diagram of a cylindrical resonator that is  $L$  long and has a diameter,  $D = 2a$ . It is driven by an electrodynamic loudspeaker at the left end of the tube and three microphones are located as shown

azimuthal velocity,  $v_\theta$ , in the clockwise direction. Based on the frequencies of the split modes,  $f_+ = 18,461$  Hz and  $f_- = 18,374$  Hz, what is the fluid's speed of rotation?

4. **Cylindrical resonator.** A rigid-walled cylindrical resonator with diameter,  $D = 2a$ , and length,  $L$ , is shown in Fig. 13.26 in cross-section. It is driven by the small electrodynamic loudspeaker

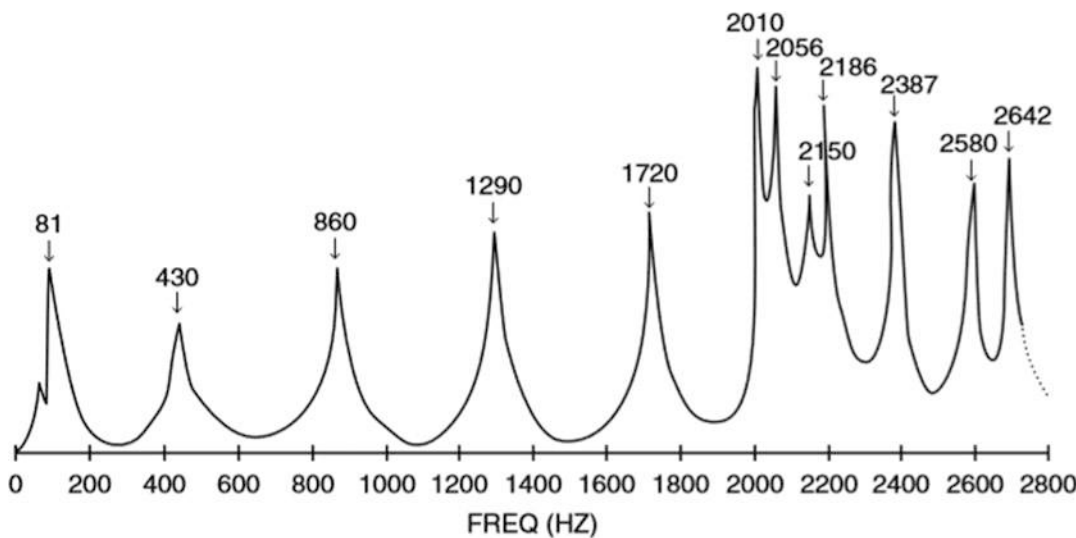


**Fig. 13.27** Sketch of the frequency response of the cylindrical resonator shown in Fig. 13.26. The frequency of each resonance is indicated by the arrow, ↓, and is labeled by its frequency in hertz. The signal being displayed was acquired by  $M_{end}$ , located at the intersection of the tube and the end cap opposite the loudspeaker

adjacent to one end at the intersection of one end cap and the cylindrical wall. The resonator contains three microphones:  $M_{end}$  is located on the cylindrical wall at the rigid end opposite the speaker,  $M_{middle}$  is also on the cylindrical wall but at the middle of the resonator, and  $M_{center}$  is at the center of the rigid end cap on the end of the resonator that is opposite the speaker.

Sketched in Fig. 13.27 is the resonance spectrum produced by driving by the loudspeaker and detecting the sound pressure using  $M_{end}$ . The frequency of each peak in the spectrum is labeled.

- Sound speed.* If  $L = 40$  cm, what is the speed of sound of the gas contained within the resonator?
- Resonator radius.* What is the radius,  $a$  (in centimeters), of the resonator?
- Resonance detectability.* Complete the table below by indicating which of the resonance peaks would be observable at the middle microphone  $M_{middle}$  and at the microphone at the center of the rigid end  $M_{center}$  by placing a YES in the space if the microphone detects the mode and a NO in the space if the microphone does not detect the mode.

- Pressure-released rectangular waveguide.** The data for phase speed,  $c_{ph}$  vs. frequency, provided in Table 13.9, was obtained for a rectangular, water-filled waveguide, with an anechoic termination, that has a free surface (the air-water interface) and boundaries lined with highly compressible closed-cell foam making all of the boundaries pressure-released. The acoustic pressure in the waveguide was determined by inserting a small hydrophone below the free surface. The hydrophone's location was determined ( $\pm 0.5$  mm) from a scale attached to the top of the waveguide over distance up to 3 m from the source. The phase speed was determined with an oscilloscope in the  $x$ - $y$  (Lissajous) mode, and the distance was recorded to determine the wavelength in the  $z$  direction by measuring the distance between successive changes in phase of  $360^\circ$  at precisely known frequencies. Photographs of the waveguide and the anechoic termination are provided in Fig. 13.28.

The phase speed can be expressed in terms of two parameters, the thermodynamic speed of sound in the medium,  $c_o$ , and the cut-off frequency,  $f_{co}$ . Transform Eqs. (1.117) or (13.69) so the data in Table 13.9 can be plotted as a straight line and use a best-fit straight line to extract the values for  $c_o$  and  $f_{co}$  and their estimated statistical uncertainties.

**Table 13.9** Phase speed in a pressure-released waveguide

Frequency (Hz)	$C_{\text{phase}}$ (m/s)
16,000	1952
15,000	2064
14,000	2218
13,500	2330
12,500	2700
12,000	2986
11,500	3496
11,250	3890
11,000	4536
10,750	5870



**Fig. 13.28** Waveguide and anechoic termination. (*Left*) The waveguide is filled with water to a depth of about 17 cm. The three walls of the waveguide are lined with Styrofoam™ to provide a pressure-released surfaces. Note the millimeter scale attached to the top-right edge of the guide. (*Right*) The anechoic termination, not visible at the left, is shown. It is designed to provide a gently sloping beach of sound absorptive rubber “pyramids”

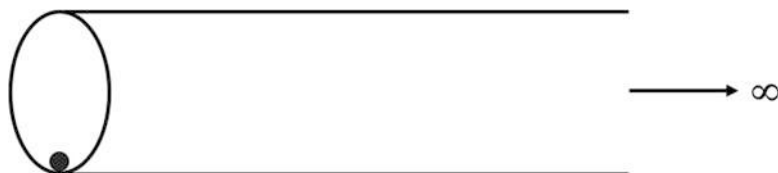


**Fig. 13.29** Cylindrical waveguide with a source that is indicated by the *solid black circle* is located at an intersection of a rigid end cap and the cylindrical waveguide wall

6. **Cylindrical waveguide.** An air-filled ( $c = 345$  m/sec) semi-infinite rigid tube of circular cross-section (radius,  $a = 2$  cm) is driven at the closed end by a compact source located inside the (closed) end-plane at an intersection of the plane and the tube ( $z = 0$ ), shown schematically in Fig. 13.29 as the black circle.

- (a) *Number of modes.* If the source is driven sinusoidally at a frequency,  $f = 12.0$  kHz, how many propagating modes will be excited and what will be their phase speeds?

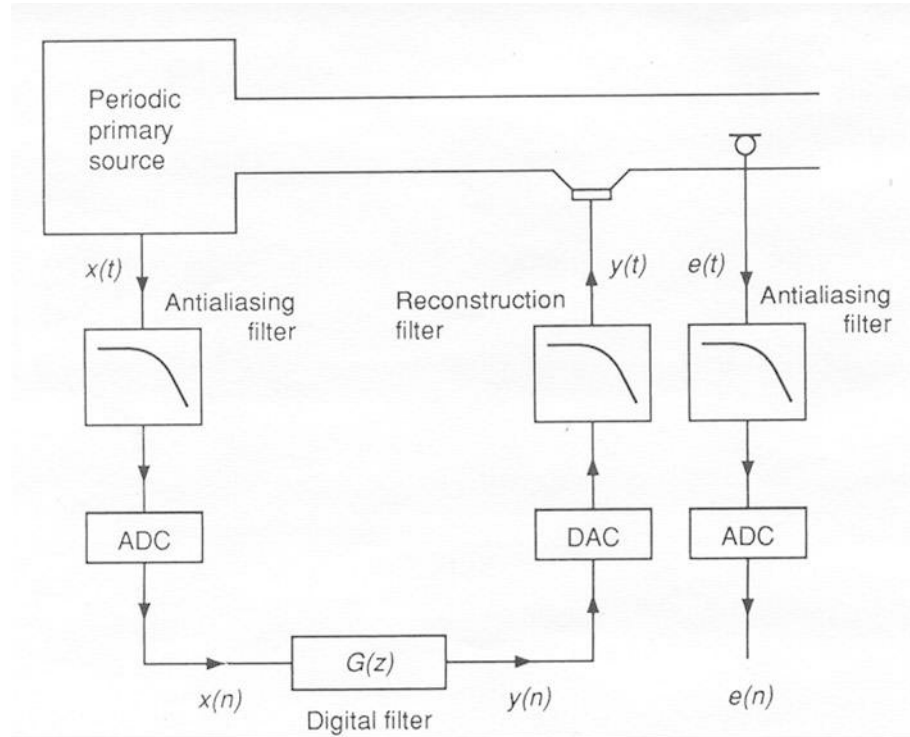
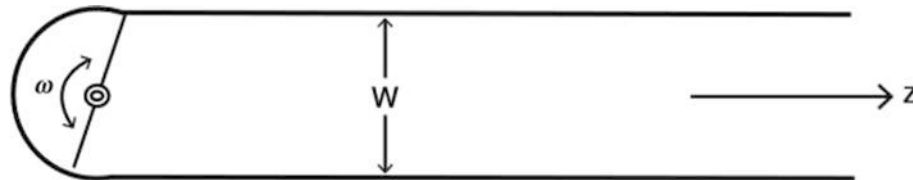


**Fig. 13.30** Block diagram of an active noise cancellation system. The duct which contains the loudspeaker and the microphone has a square cross-section that is 1.0 ft  $\times$  1.0 ft

- (b) *Excitation of modes.* If the source is moved to the center of the end cap, which of the above modes will no longer be excited?
- 7. **Group speed.** A 20-m-long piece of 6" (nominal) Schedule 40 PVC pipe (inner radius,  $a = 5.11$  cm) [35] contains air ( $c = 345$  m/s) at atmospheric pressure and is closed at both ends by rigid terminations. A 20.0-millisecond-long tone burst containing 100 cycles of a 5 kHz tone is launched from one of the rigid ends at the intersection of the end and the pipe wall. (See the diagram for Problem 6 in Fig. 13.29.) The pulse propagates to the other end where it is reflected and arrives back at the first end. What is maximum difference in arrival times of the pulse that has been “dispersed” by the fact that the group speed is different for acoustic energy that travels in the different modes? [*Hint:* The first arrival will be the leading edge of the pulse that made the round trip at the thermodynamic sound speed  $c_o$ :  $t_{first} = (40\text{ m})/(345\text{ m/s}) = 116\text{ ms}$ .]
- 8. **Active noise cancellation in an air conditioning duct.** Shown in Fig. 13.30 is the block diagram for an active noise control system that injects sound with a loudspeaker that is intended to cancel the sound produced by the “periodic primary source,” for example, a fan that is part of the ventilation system [36]. If the rigid-walled duct has a square cross-section with inside dimension of 1.0 ft  $\times$  1.0 ft., what is the highest-frequency component of the noise that can be cancelled if the control algorithm can only process plane wave fronts traveling at the thermodynamic sound speed in air ( $c = 345$  m/s)?
- 9. **Paddle-driven rectangular waveguide.** Shown below is the top view of a rigid-walled waveguide that is being driven by a rigid paddle that oscillates sinusoidally at radian frequency,  $\omega = 1400$  rad/s, about a fixed axis with an amplitude,  $\theta_o = 0.20$  radians, so that  $\theta(t) = 0.20 \sin(\omega t)$ .

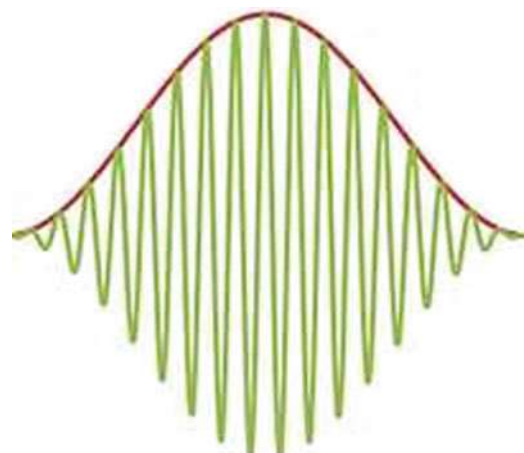
The width of the waveguide,  $W = 40$  cm, and the height of the waveguide is much less than its width,  $H \ll W$ . The waveguide extends to infinity in the  $z$  direction and is filled with sulfur hexafluoride gas ( $\text{SF}_6$ ) which has a sound speed  $c = 151$  m/s at room temperature (Fig. 13.31).

- Phase Speed.* What is the phase speed,  $c_{ph}$ , of the only mode which the paddle is capable of exciting that can propagate down the waveguide in the  $z$  direction?
  - Group Speed.* If the paddle creates a pulse with 17 cycles at the same frequency,  $\omega = 1400$  rad/s, by increasing the amplitude of its motion from 0 radians to 0.2 radians and back to 0 radians with the sine-squared amplitude envelope shown in Fig. 13.32, how long does it take for the center of the envelope to travel 100 meters down the waveguide?
10. **Modes in a non-separable nuclear reactor coolant pool.** Shown in Fig. 13.33 is the plan view of a nuclear research reactor cooling pool [37]. It is filled with light (ordinary) water to a depth of 24 ft. = 7.32 m. Other dimensions are included in the caption of Fig. 13.33.
- Transformed dimensions.* What is the equivalent length of the pool, if it is transformed into a uniform rectangular shape that is 4.27 m wide and the depth remains 7.32 m?
  - Lowest-frequency modes.* Assuming that the surface of the pool is pressure-released and all the other five boundaries are rigid and impenetrable, determine the 20 lowest-frequency modes and their corresponding mode numbers. Present your results in tabular form.
  - Schroeder frequency and critical distance.* The reverberation time measured at 1.6 kHz was  $T_{60} = 0.17$  s. What are the values of the Schroeder frequency,  $f_S$ , and the critical distance,  $r_d$ ?
  - Number of modes below  $f_S$ .* Determine the approximate number of modes at frequencies below  $f_S$ .



**Fig. 13.31** This waveguide is excited by the rotational oscillations of the paddle vibrating at angular frequency,  $\omega$

**Fig. 13.32** Pulse train generated by the oscillating paddle in Fig. 13.31



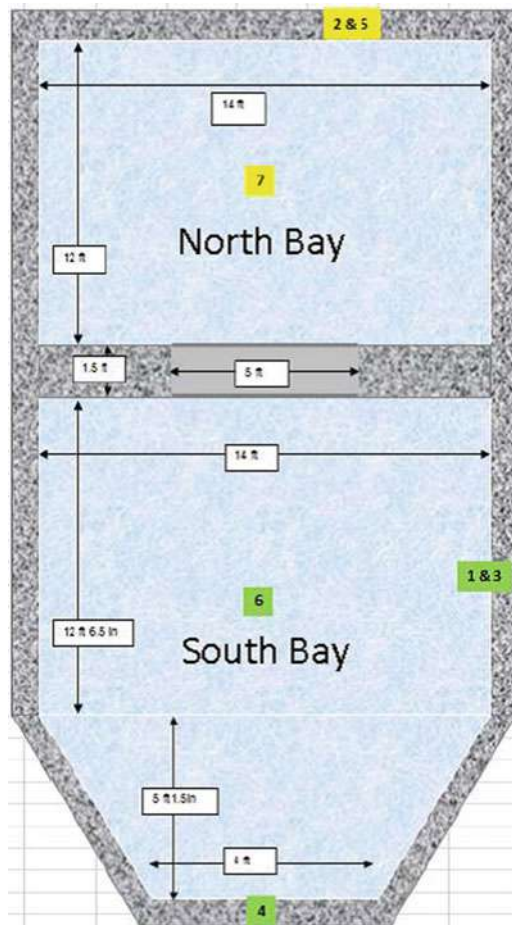


**Fig. 13.33** Plan view of the two coupled pools in the Breazeale Nuclear Reactor. The depth of the water in both bays is 7.32 m (24'). The “floor” of the South Bay is an irregular hemi-hexagon. The reactor’s core is usually located at about the center of that hexagonal portion. For modal calculations, assume that the pool is acoustically equivalent to a rectangular pool with the same planar area. The narrowest portion of the South Bay is 1.22 m wide, and the 14-ft.-wide rectangular portion extends 3.82 m behind the dividing wall. That wall is 46 cm thick and has a 1.52-m-wide gap. Under that adiabatic transformation, the “equivalent” reactor pool should be 4.27 m (14') wide. Your transformation should preserve the volume of the water contained in both bays. The hemi-hexagonal South Bay has a volume,  $V_{reactor} = 151 \text{ m}^3 \cong 40,000 \text{ gallons}$ . The North Bay has a volume,  $V_{storage} = 114 \text{ m}^3 \cong 30,000 \text{ gallons}$ . Your modal analysis will designate the vertical direction as the  $z$  axis, the width as the  $x$  axis (horizontal in this figure), and the length as the  $y$  axis (vertical in this figure)

- (e) *Density of modes.* What is the density of modes having frequencies below  $f_S$ ?
11. **Echo satellite.** A gas-filled balloon was launched into low Earth orbit on 12 Aug 1960 to act as a reflector of radio waves used for communications. The balloon, shown symbolically on the postage stamp in Fig. 13.34, had a diameter of 30.5 m, and the balloon’s material was 12.7-micron-thick metalized PET (Mylar™) film [27]. The Echo I satellite re-entered the Earth’s atmosphere and burnt up on 24 May 1968.
- Radial modes.* The fundamental frequency of radial mode of the gas inside the balloon was  $f_{0,0,1}^{\text{release}} = 3.6 \text{ Hz}$ . What were the frequencies of the next three higher-frequency radial modes?
  - Gas sound speed.* What was the speed of sound of the gas contained within the balloon?

**Fig. 13.34** US postage stamp commemorating the Echo Program



**Fig. 13.35** Nine-segment transducer that excites a waveguide with the same cross-sectional area

+	-	+
-	+	-
+	-	+

12. **Modes of a rigid-walled spherical resonator.** Determine the three lowest-frequency radial resonance frequencies for the spherical resonator used by the US National Bureau of Standards, shown in Fig. 13.20, to determine the universal gas constant,  $\mathfrak{R} \equiv 8.314462 \text{ J mol}^{-1} \text{ K}^{-1}$ , if the sphere was filled with argon at  $T = 273.16 \text{ K}$  and standard atmospheric pressure,  $p_m = 101,325 \text{ Pa}$ . The radius of the sphere is  $a = 9.000 \text{ cm}$ .
13. **Effective radius of the Space Shuttle cargo bay model in Fig. 13.18.** Assuming the plastic model of the cargo bay contains air, what is the value of the cargo bay model's effective radius,  $a$ , and its uncertainty, based on the frequencies provided in Table 13.6?
14. **Waveguide mode excitation.** An air-filled waveguide is excited at  $z = 0$  with a transducer that is diagrammed in Fig. 13.35. The waveguide and transducer both have  $L_x = 15 \text{ cm}$  and  $L_y = 12 \text{ cm}$ . The phasing of the nine independent transducer segments is indicated by the + and - signs.
  - (a) *Plane wave mode.* Will the plane wave mode of the waveguide be excited if the amplitude of all sections are the same?
  - (b) *Lowest-frequency non-plane wave modes.* What are the mode numbers and cut-off frequencies of the three lowest-frequency non-plane wave modes that will be excited by this transducer?
  - (c) *Impulse excitation.* If all of the transducer's segments are excited by a single pulse of very short duration, and the indicated phasing is maintained (e.g., the central segment moves forward and the ones above and below it move backward), which mode will be detected first by a microphone placed a great distance,  $z \gg L_x$  and  $z \gg L_y$ , from the transducer?

## References

1. L.P. Eisenhart, Separable systems in Euclidean 3-space. Phys. Rev. **45**(6), 427–428 (1934)

2. P.M. Morse, *Vibration and Sound*, 2nd edn (McGraw-Hill, New York, 1948), p. 396. Reprinted (ASA, 1981). ISBN 0-88318-876-7
3. B.F.G. Katz, E.A. Wetherill, The fall and rise of the Fogg art Museum lecture hall: A forensic study. *Acoust. Today* **3** (3), 10–16 (2007)
4. L. L. Beranek, *Concert and Opera Halls: How they Sound* (Acoustical Society of America, New York, 1996); ISBN 1-56396-530-5
5. L.L. Beranek, Concert hall acoustics: Recent findings. *J. Acoust. Soc. Am.* **139**(4), 1548–1556 (2016)
6. J. Liu, S. Garrett, Relationship between Nusselt number and the thermoviscous (Rott) functions. *J. Acoust. Soc. Am.* **119**(3), 1457–1462 (2006). See for discussion of complex compressibility
7. *Sound Absorption and Sound Absorption Coefficients by the Reverberation Room Method*, ASTM C423 (American Society for Testing and Materials, Philadelphia, PA 19103)
8. *Measurement of Sound Absorption in a Reverberation Room*, ISO 354 (International Organization for Standardization, CH-1211 Geneva 20, Switzerland)
9. R.J. Peppin, A. Scharine, *Methods for Calculation of the Absorption of Sound in the Atmosphere* (American National Standard, ANSI/ASA S1.26-2014). See §5.2.1
10. M.R. Schroeder, The ‘Schroeder frequency’ revisited. *J. Acoust. Soc. Am.* **99**(5), 3240–3241 (1996)
11. M. Kleiner, J. Tichy, *Acoustics of Small Rooms* (Taylor & Francis, Boca Raton, 2014); ISBN 978-0-203-86924-6 (eBook-PDF)
12. K.A. Gillis, M.R. Moldover, A.R.H. Goodwin, Accurate acoustic measurements in gases under difficult conditions. *Rev. Sci. Inst.* **62**, 2213–2217 (1991)
13. L.D. Landau, E.M. Lifshitz, *Fluid Mechanics*, 2nd edn. (Butterworth-Heinemann, Oxford, 1987). ISBN 0 7506 2767 0. §15
14. R. Eisberg, R. Resnick, *Quantum Physics of Atoms, Molecules, Solids, Nuclei, and Particles* (Wiley, New York, 1974); ISBN 0-471-23464-8
15. R.T. Weidner, R.L. Sells, *Elementary Modern Physics* (Allyn and Bacon, Boston, 1960)
16. L.D. Landau, E.M. Lifshitz, *Fluid Mechanics*, 2nd edn (Butterworth-Heinemann, Oxford, 1987). See Eq (15.18); ISBN 0 7506 2767 0
17. M. Abramowitz, I. Stegun, *Handbook of Mathematical Functions with Formulas, Graphs, and Mathematical Tables* (National Bureau of Standards, Applied Mathematics Series #55, 1964)
18. E. Polturak, S.L. Garrett, S.G. Lipson, Precision acoustic gas analyzer for binary gas mixtures. *Rev. Sci. Inst.* **57**(11), 2837–2841 (1986)
19. E. Jahnke, F. Emde, *Tables of Functions with Formulae and Curves*, 4th edn (Dover, New York, 1945)
20. P.M. Morse, *Vibration and Sound*, 2nd edn (McGraw-Hill, 1948). Reprinted by the Acoust. Soc. Am., 1995. See §32; ISBN 0-88318-876-7
21. I. Rudnick, Physical Acoustics at UCLA in the Study of Superfluid Helium, in Proc. E. Fermi Summer School, Varenna, Italy, 1974
22. P.M. Morse, K.U. Ingard, *Theoretical Acoustics* (McGraw-Hill, 1968), Problem 19, pp. 603–604
23. J.D. Maynard, *Topics in Acoustics*, Class Notes (The Pennsylvania State University (2006)
24. D.C. Swanson, Precision spectral peak frequency measurement using a window leakage ratio function. *Mech. Systems and Sig. Process* **54–55**, 1–15 (2015)
25. M. Greenspan, Simple derivation of the Boltzmann-Ehrenfest adiabatic principle. *J. Acoust. Soc. Am.* **27**(1), 34–35 (1955)
26. O.B. Wilson, R.W. Leonard, Measurements of sound absorption in aqueous salt solutions using a resonance method. *J. Acoust. Soc. Am.* **26**(2), 223–226 (1954)
27. H.M. Jones, I.I. Shapiro, P.E. Zadunaisky, Solar radiation effects, gas leakage rates, and air densities inferred from the orbit of Echo I, in *Proceedings 2nd International Space Science Symposium*, ed. by H.C. Van De Hulst, C. De Jager, A.F. Moore, Florence, April 10–14, 1961 (North Holland, 1961)
28. P.-J. Shih, Y.-R. Guo, Resonance frequency of fluid-filled and prestressed spherical shell – A model of the human eyeball. *J. Acoust. Soc. Am.* **139**(4), 1784–1792 (2016)
29. M.R. Moldover, J.P.M. Trusler, T.J. Edwards, J.B. Mehl, R.S. Davis, Measurement of the universal gas constant  $\mathfrak{R}$  using a spherical acoustic resonator. *Phys. Rev. Lett.* **60**(4), 249–252 (1988) and M.R. Moldover, et al, *J. Res. Natl. Bur. Stand.* **93**, 85–144 (1988)
30. L. Pitre, F. Sparasci, L. Risegari, C. Guianvarc'h, C. Martin, M.E. Himbert, M.D. Plimmer, A. Allard, B. Marty, P.A. Giuliano Albo, B. Gao, M.R. Moldover, J.B. Mehl, New measurement of the Boltzmann constant  $k$  by acoustic thermometry of helium-4 gas. *Metrologia* **54**, 856–873 (2017)
31. B.G. Schreger, Laennec’s new system of diagnosis. *Q. J. Foreign Med. Surg.* **2**, 51–68 (1820)
32. K.U. Ingard, *Fundamentals of Waves and Oscillations* (Cambridge, 1988); ISBN 0 521 33957 X
33. C. M. Harris, *Noise Control in Buildings: A Practical Guide for Architects and Engineers* (McGraw-Hill, 1994); ISBN 0-07-028887-8

34. C.F. Eyring, Reverberation time in ‘dead’ rooms. *J. Acoust. Soc. Am.* **1**(1), 217–241 (1930)
35. E.A. Avallone, T. Baumeister II (eds), *Marks’ Standard Handbook for Mechanical Engineers*, 10th edn (McGraw-Hill, 1996). See Table 8.7.31, pp. 8–193; ISBN 0-07-004997-1
36. P.A. Nelson, S.J. Elliot, *Active Control of Sound* (Academic Press, 1993) ISBN 0-12-515426-7
37. S.L. Garrett, J.A. Smith, R.W.M. Smith, B.J. Heidrich, M.D. Heibel, Using the sound of nuclear energy. *Nuc. Technol.* **195**(3), 353–362 (2016)

**Open Access** This chapter is licensed under the terms of the Creative Commons Attribution 4.0 International License (<http://creativecommons.org/licenses/by/4.0/>), which permits use, sharing, adaptation, distribution and reproduction in any medium or format, as long as you give appropriate credit to the original author(s) and the source, provide a link to the Creative Commons license and indicate if changes were made.

The images or other third party material in this chapter are included in the chapter's Creative Commons license, unless indicated otherwise in a credit line to the material. If material is not included in the chapter's Creative Commons license and your intended use is not permitted by statutory regulation or exceeds the permitted use, you will need to obtain permission directly from the copyright holder.





# Attenuation of Sound

14

## Contents

14.1	An Almost Correct Expression for Viscous Attenuation .....	674
14.2	Bulk Thermoviscous Attenuation in Fluids .....	677
14.3	Classical Thermoviscous Attenuation .....	681
14.4	The Time-Dependent Equation of State .....	682
14.5	Attenuation due to Internal Relaxation Times .....	684
14.5.1	Relaxation Attenuation in Gases and Gas Mixtures .....	687
14.5.2	Relaxation Attenuation in Fresh and Salt Water .....	688
14.6	Transmission Loss .....	692
14.6.1	Short and Very Short Wavelengths .....	692
14.6.2	Very Long Wavelengths .....	693
14.7	Quantum Mechanical Manifestations in Classical Mechanics .....	693
	References .....	697

There are four mechanisms that cause sound energy to be absorbed and sound waves to be attenuated as they propagate in a single-component, homogeneous fluid:

- Viscous (shear) effects in bulk fluids
- Thermal conduction in bulk fluids
- Molecular absorption in bulk fluids
- Thermoviscous boundary layer losses

The decrease in the amplitude of acoustical disturbances or in the amplitude of vibrational motion (due to dissipative mechanisms) has been a topic of interest throughout this textbook. In this chapter, we will capitalize on our investment in such analyses to develop an understanding of the attenuation of sound waves in fluids that are not influenced by proximity to solid surfaces. Such dissipation mechanisms are particularly important at very high frequencies and short distances or very low frequencies over geological distances.

The parallel addition of a mechanical resistance element to the stiffness and mass of a simple harmonic oscillator led to an exponential decay in the amplitude of vibration with time in Sect. 2.4. The

(mechanically) series combination of a stiffness element and a mechanical resistance in the Maxwell model of Sect. 4.4.1, and in the Standard Linear Model of *viscoelasticity* in Sect. 4.4.2 introduced the concept of a relaxation time,  $\tau_R$ , that had significant effects on the elastic (in-phase) and dissipative (quadrature) responses as a function of the nondimensional frequency,  $\omega\tau_R$ . Those response curves were “universal” in the sense that causality linked the elastic and dissipative responses through the Kramers-Kronig relations, as presented in Sect. 4.4.4.

That relaxation time perspective, along with its associated mathematical consequences, will be essential to the development of expressions for attenuation of sound in media that can be characterized by one or more relaxation times related to those internal degrees of freedom that make the equation of state a function of frequency. Examples of these relaxation time effects include the rate of collisions between different molecular species in a gas (e.g., nitrogen and water vapor in air), the pressure dependence of ionic association-dissociation of dissolved salts in seawater (e.g.,  $MgSO_4$  and  $H_3BO_3$ ), and evaporation-condensation effects when a fluid is oscillating about equilibrium with its vapor (e.g., fog droplets in air or gas bubbles in liquids).

The *viscous drag* on a fluid oscillating within the neck of a Helmholtz resonator, combined with the *thermal relaxation* of adiabatic temperature changes at the (isothermal) surface of that resonator’s compliance, led to energy dissipation in lumped-element fluidic oscillators in Sect. 9.4.4, producing damping that limited the quality factor of those resonances in exactly the same way as mechanical resistance limited the quality factor of a driven simple harmonic oscillator, which was first introduced as a consequence of similitude (i.e., dimensional analysis) in Sect. 1.7.1.

The *thermoviscous boundary layer* dissipation, summarized in Eq. (9.38), was used to calculate the attenuation of plane waves traveling in a waveguide in Sect. 13.5.5. As will be demonstrated explicitly in this chapter, thermoviscous boundary layer losses provide the dominant dissipation mechanism at low frequencies (i.e., lumped element systems and waveguides below cut-off) for most laboratory-sized objects (including the laboratory itself when treated as a three-dimensional enclosure). For fluid systems that are not dominated by dissipation on solid surfaces in close proximity to the fluids they contain, the dissipation due to losses within the fluid itself (i.e., bulk losses) can be calculated directly from the hydrodynamic equations of Sect. 7.3.

To reintroduce the concepts complex wavenumber or complex frequency that typically characterize the attenuation of sound over space or time, a simple solution of the Navier-Stokes equation will first be derived. That approach will not provide the correct results for attenuation of sound, even in the absence of relaxation effects, because it does not properly take into account the relationship between shear deformation and hydrostatic compression in fluids that are necessary to produce plane waves (see Fig. 14.1). That relationship was used to relate the modulus of unilateral compression for isotropic solids (aka the dilatational modulus) to other isotropic moduli in Sect. 4.2.2 and in Fig. 4.3. The complete solution for bulk losses due to a fluid’s shear viscosity,  $\mu$ ; thermal conductivity,  $\kappa$ ; and the relaxation of internal degrees of freedom (i.e., “bulk viscosity”),  $\zeta$ , will follow that nearly correct introductory treatment and will be based upon arguments related to entropy production, like the analysis in Sect. 9.3.3.

## 14.1 An Almost Correct Expression for Viscous Attenuation

Because we started with a complete hydrodynamic description of homogeneous, isotropic, single-component fluids using the Navier-Stokes equation, we are now well-prepared to investigate the dissipation mechanisms that attenuate the amplitude of sound waves propagating far from the influence of any solid boundaries. A one-dimensional linearized version of the Navier-Stokes equation (9.2) is reproduced below:

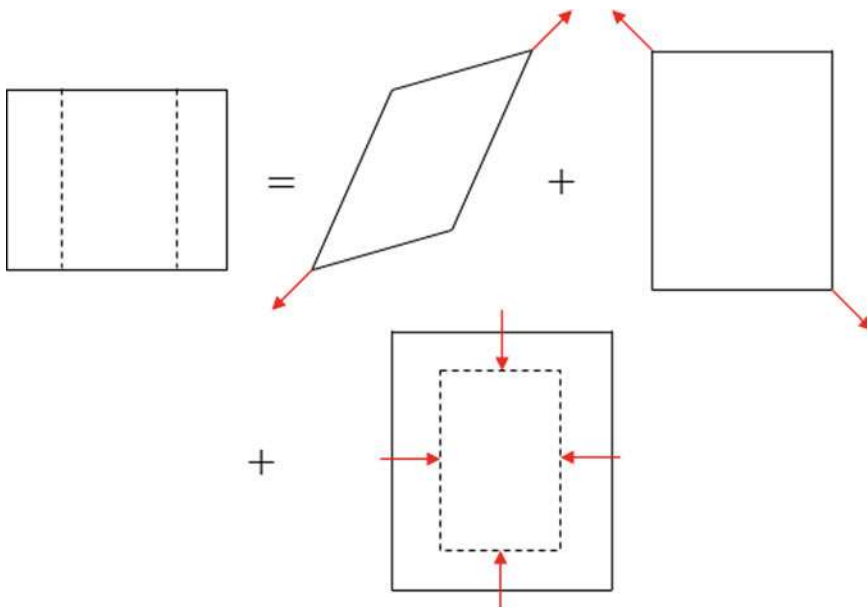


**Fig. 14.1** Schematic two-dimensional representation of the combination of shear and hydrostatic deformations necessary to produce the unilateral compression of a fluid element, corresponding to a plane wave, shown at the *upper left*. If the original fluid parcel at the *upper left* is a square, shown by the *solid lines*, then the compression accompanying a plane wave does not change the upper and lower boundaries, but would require that the two vertical boundary lines contract to the positions indicated by the two *dashed lines*. This deformation can be accomplished by first shearing the square fluid element along one diagonal and then shearing it again along the other diagonal, as indicated by the *arrows*. Those two deformations result in making the square into a rectangle. When the rectangle is subjected to a hydrostatic compression, that rectangle is compressed into the required shape

$$\rho_m \frac{\partial v_1(x, t)}{\partial t} + \frac{\partial p_1(x, t)}{\partial x} - \mu \frac{\partial^2 v_1(x, t)}{\partial x^2} = 0 \quad (14.1)$$

The linearized, one-dimensional continuity equation (10.1) is not affected by the inclusion of viscosity in the Navier-Stokes equation.

$$\frac{\partial \rho_1(x, t)}{\partial t} + \rho_m \frac{\partial v_1(x, t)}{\partial x} = 0 \quad (14.2)$$

Since the thermal conductivity of the fluid is ignored,  $\kappa = 0$ , the linearized version of the adiabatic equation of state can still be invoked to eliminate  $\rho_1(x, t)$  in favor of  $p_1(x, t)$ , allowing expression of the continuity equation in terms of the same variables used in Eq. (14.1).

$$\begin{aligned} \rho_1(x, t) &= \left( \frac{\partial \rho}{\partial p} \right)_s p_1(x, t) = \frac{p_1(x, t)}{c^2} \\ \Rightarrow \quad \frac{1}{\rho_m c^2} \frac{\partial p_1(x, t)}{\partial t} + \frac{\partial v_1(x, t)}{\partial x} &= 0 \end{aligned} \quad (14.3)$$

As done so many times before, the dispersion relation,  $\omega(k)$ , will be calculated by assuming a right-going traveling wave to convert the homogeneous partial differential equations (14.1) and (14.3) to coupled algebraic equations.

$$\begin{aligned} -jkp_1 + (j\omega\rho_m + k^2\mu)v_1 &= 0 \\ j\omega \frac{p_1}{\rho_m c^2} - jkv_1 &= 0 \end{aligned} \quad (14.4)$$

There are now both real and imaginary terms in the coupled algebraic equations, unlike their nondissipative equivalents, such as Eqs. (10.16) and (10.17). The existence of a nontrivial solution to Eq. (14.4) requires that the determinant of the coefficients vanish.

$$\begin{vmatrix} \frac{j\omega}{\rho_m c^2} & -jk \\ -jk & (j\omega\rho_m + k^2\mu) \end{vmatrix} = 0 \quad (14.5)$$

The evaluation of this determinant leads to the secular equation that will specify the complex wavenumber,  $\mathbf{k}$ , in terms of the angular frequency,<sup>1</sup>  $\omega$ .

$$\left(\frac{\omega}{c}\right)^2 = k^2 \left(1 + \frac{j\omega\mu}{\rho_m c^2}\right) \quad (14.6)$$

If  $\omega\mu/\rho_m c^2 \ll 1$ , the binomial expansion can be used twice to approximate the *spatial attenuation coefficient*,  $\alpha$ .

$$\mathbf{k} \cong \frac{\omega}{c} - j \frac{\omega^2 \mu}{2\rho_m c^3} = k - j\alpha_{almost} \quad (14.7)$$

To remind ourselves that this result is not completely correct, this spatial attenuation coefficient has been designated  $\alpha_{almost} = \omega^2(\mu/2\rho_m c^3)$ . The form of this result, specifically the fact that the attenuation is proportional to  $\omega^2/\rho_m$ , suggests that experimental results could be plotted as a function of the square of frequency divided by mean pressure, as shown in Fig. 14.4.

It is also useful to notice that  $\mu/\rho_m c^2$  in Eq. (14.6) has the units of time, so the “small parameter” in those binomial expansions of Eq. (14.6) is of the form  $j\omega\tau_{\bar{\ell}}$ . Equally important is the recognition that such a *relaxation time*,  $\tau_{\bar{\ell}}$ , is on the order of the *collision time* in a gas, based on the *mean free path*,  $\bar{\ell}$ , derived from simple *kinetic theory* of gases in Sect. 9.5.1 [1].

$$\tau_{\bar{\ell}} = \frac{\bar{\ell}}{c} \cong \frac{3\mu_{gas}}{\rho_m c^2} = \frac{3}{\gamma} \frac{\mu_{gas}}{p_m} \quad (14.8)$$

This is different from the relaxation times,  $\tau_R$ , which can characterize the time dependence of the equation of state or the response of a viscoelastic medium described in Sect. 4.4, where  $\omega\tau_R \gtrless 1$ . At frequencies above  $\omega_{\bar{\ell}} \cong (\tau_{\bar{\ell}})^{-1}$ , the assumptions that underlie the hydrodynamic approach are no longer valid (see Chap. 7, Problem 1). For air near room temperature and at atmospheric pressure,  $\tau_{\bar{\ell}} \cong 400$  ps, so  $f = \omega/2\pi \cong 400$  MHz. This is identical with the result obtained in Eq. (9.24) for the critical frequency,  $\omega_{crit}$ , at which sound propagation in air transitions from adiabatic at low frequencies to isothermal at high frequencies. The regime where  $\omega\tau_{\bar{\ell}} > 1$  becomes questionable within the context of a (phenomenological) hydrodynamic theory [1].

<sup>1</sup> The decision to treat  $\omega$  as a real number, thus forcing the wavenumber,  $\mathbf{k}$ , to become a convenience (complex) number, is arbitrary. It leads to a spatial attenuation coefficient that is related to the imaginary component of the wavenumber. Treating the wavelength,  $\lambda = 2\pi/k$ , as a real number forces the frequency,  $\omega$ , to be a convenience number, thus producing a temporal attenuation coefficient. Of course, spatial-to-temporal conversions can be accomplished using the sound speed, as shown in Eq. (14.10).

Unlike the complex wavenumbers of exponentially decaying thermal and viscous waves near boundaries, examined in Sects. 9.3.1 and 9.4.2, where  $\Re[k] = \Im[k]$ , most attenuation mechanisms in bulk fluids far from boundaries have  $\Re[k] \gg \Im[k]$  or  $|k| \gg \alpha$ . If  $k$  is substituted into the expression for the pressure associated with a single-frequency one-dimensional plane wave traveling in the  $+x$  direction,  $p_1(x, t)$ , it is easy to see that  $\alpha$  leads to an exponential decay in the amplitude with propagation distance for the sound wave.

$$p_1(x, t) = \Re[\hat{\mathbf{p}} e^{j(\omega t - kx)}] = \Re[\hat{\mathbf{p}} e^{j[\omega t - (k - j\alpha)x]}] = e^{-\alpha x} \Re[\hat{\mathbf{p}} e^{j(\omega t - kx)}] \quad (14.9)$$

Since space and time can be transformed by the sound speed, a real *temporal attenuation coefficient* can be defined,  $\beta = \alpha c$ , to describe the rate at which the amplitude of the plane wave decays in time.

$$p_1(x, t) = e^{-\beta t} \Re[\hat{\mathbf{p}} e^{j(\omega t - kx)}] \quad \text{where } \beta = \alpha c \quad (14.10)$$

Although the result for  $\alpha_{\text{almost}}$  is not exactly correct, it does exhibit a feature of the correct result for the spatial attenuation coefficient that includes thermoviscous dissipation that is given by  $\alpha_{\text{classical}}$  in Eq. (14.31) where internal relaxation effects are discussed in Sect. 14.5.<sup>2</sup>

Unlike the spatial attenuation coefficient for dissipation of plane waves in a waveguide, given in Eq. (13.78), which is proportional to  $\sqrt{\omega}$ , Eq. (14.7) shows that  $\alpha_{\text{almost}}$  is proportional to the square of the frequency, as is  $\alpha_{\text{classical}}$ .

## 14.2 Bulk Thermoviscous Attenuation in Fluids

Although the previous results for  $\alpha_{\text{almost}}$  are incomplete, it both has provided an introduction to the complex wavenumber,  $\mathbf{k}$ , that determines the attenuation distance and has introduced a relaxation time,  $\tau_{\bar{\ell}}$ , that sets an upper limit to the frequencies above which the continuum model of a fluid is not appropriate. One reason that previous result for the viscous attenuation is not complete is that we have ignored the fact that the fluid deformation corresponding to the passage of a plane wave requires the superposition of two shear deformations and a hydrostatic compression. This superposition of *shear strain* and *hydrostatic strain* is illustrated schematically in Fig. 14.1. Of course, the result for the attenuation coefficient,  $\alpha_{\text{almost}}$ , in Sect. 14.1, also does not yet include the thermal conductivity,  $\kappa$ , of the fluid.

To incorporate all of the dissipative effects in a fluid, it is necessary to start from the complete expression for entropy production in a single-component homogeneous fluid. The mechanical energy dissipation,  $E_{\text{mech}}$ , is the maximum amount of work that can be done in going from a given non-equilibrium state of energy,  $E_o$ , back to equilibrium,  $E(S)$ , which occurs when the transition is reversible (i.e., without a change in entropy) [2].  $\dot{E}_{\text{mech}}$  is the rate at which the mechanical energy is dissipated by the periodic transitions from the non-equilibrium state to the equilibrium state as orchestrated by the wave motion.

$$\dot{\Pi}_{\text{mech}} = -\dot{E}(S) = -\left(\frac{\partial E}{\partial S}\right)\dot{S} = T_m \dot{S} \quad (14.11)$$

The right-most expression in Eq. (14.11) uses the fact that the derivative of the energy with respect to the entropy is the equilibrium value of the mean absolute temperature,  $T_m$ . The entropy equation

<sup>2</sup> Since inert gases have no internal degrees of freedom,  $\alpha_{\text{classical}}$  provides their entire attenuation constant.

(7.43) can be written so that the shear stresses and the hydrostatic stresses can be expressed symmetrically in Cartesian components.<sup>3</sup>

$$\rho T \left( \frac{\partial s}{\partial t} + \vec{v} \cdot \vec{\nabla} s \right) = \nabla \cdot (\kappa \vec{\nabla} T) + \frac{1}{2} \mu \left( \frac{\partial v_i}{\partial x_k} + \frac{\partial v_k}{\partial x_i} - \frac{2}{3} \frac{\partial v_i}{\partial x_i} \right)^2 + \zeta (\nabla \cdot \vec{v})^2 \quad (14.12)$$

The two cross derivatives,  $(\partial v_i / \partial x_k)$  and  $(\partial v_k / \partial x_i)$ , represent the two shear deformations with the hydrostatic component removed:  $\frac{2}{3}(\partial v_i / \partial x_i)$  [3]. The square of the hydrostatic deformation is represented by  $(\nabla \cdot \vec{v})^2$ . The hydrostatic deformation is multiplied by a new positive scalar coefficient,  $\zeta$ , that must have the same units as the shear viscosity [Pa-s].

Having the form of a conservation equation (see Sect. 10.5), the right-hand side of Eq. (14.12) represents the rate of entropy production,  $\dot{S}$ , caused by thermal conduction, viscous shear, and some possible entropy production mechanism (unspecified at this point but eventually related to the time dependence of the equation of state) associated with the hydrostatic deformation. Using Eq. (14.12), the dissipated mechanical power,  $\Pi_{mech}$ , can be evaluated by integrating over a volume element that includes the plane wave disturbance,  $dV$ .

$$\Pi_{mech} = -\frac{\kappa}{T_m} \int (\nabla T)^2 dV - \frac{\mu}{2} \int \left( \frac{\partial v_i}{\partial x_k} + \frac{\partial v_k}{\partial x_i} - \frac{2}{3} \frac{\partial v_i}{\partial x_i} \right)^2 dV - \zeta \int (\nabla \cdot \vec{v})^2 dV \quad (14.13)$$

Since we are still attempting a solution in the linear limit, the lowest-order contribution to the power dissipation must be second order in the wave's displacement from equilibrium; in this case,  $T_1^2$  and  $|\vec{v}_1|^2$ , hence it is positive definite (see Sect. 10.5). For that reason, the absolute temperature,  $T$ , can be taken outside the integral and represented by  $T_m$ , since allowing for acoustical variation of that temperature term would add a correction to the thermal conduction loss that is third order in displacements from equilibrium.

For a plane wave propagating in the  $x$  direction, it is convenient to express  $v_x = v_1 \sin(\omega t - kx)$ , setting  $v_y = v_z = 0$ . Substitution into the last two terms of Eq. (14.13) produces the (nonthermal) mechanical dissipation.

$$-\left(\frac{4}{3}\mu + \zeta\right) \int \left(\frac{\partial v_1}{\partial x}\right)^2 dV = -k^2 \left(\frac{4}{3}\mu + \zeta\right) v_1^2 \int \cos^2(\omega t - kx) dV \quad (14.14)$$

Since we are only interested in the time-averaged power dissipation, the contributions from the nonthermal terms in Eq. (14.13) is  $-(k^2/2)[(4\mu/3) + \zeta]v_1^2 V_o$ , where  $V_o$  is the volume of the fluid under consideration through which the plane wave is propagating.

It is worth comparing the appearance of the factor,  $4/3$ , that multiplies the shear viscosity,  $\mu$ , with the corresponding expression for the modulus of unilateral compression,  $D$  (aka the dilatational modulus), introduced in Sect. 4.2.2, to the shear modulus,  $G$ , and bulk modulus,  $B$ , in Table 4.1:  $D = (4G/3) + B$ . Again, this is a direct consequence of the fact that the distortion produced by a plane wave can be decomposed into two shears (related to  $G$ ) and a hydrostatic compression (related to  $B$ ).

The result in Eq. (14.14), without  $\zeta$ , was first produced by Stokes who expressed the result as the temporal attenuation coefficient [4]. The lack of agreement between his theoretical predictions and experimental measurements provided the starting point for the modern attempts to account for

---

<sup>3</sup>The component form assumes that the equation is summed over the repeated indices,  $i$  and  $k$ . This is known as the “Einstein summation convention.”

attenuation in terms of molecular relaxation [5]. The spatial attenuation coefficient, due to viscous dissipation, was first introduced by Stefan in 1866<sup>4</sup> [6]. The first calculation to include both the effects of thermal conductivity and shear viscosity on the absorption of sound was published by Kirchhoff in 1868 [7].

To evaluate the contribution of thermal conduction to the mechanical dissipation in Eq. (14.13), the temperature change needs to be related to the pressure change to evaluate the one-dimensional temperature gradient,  $(\partial T/\partial x)$ . For an ideal gas, this relation should be familiar, having been derived in Eqs. (1.21) and (7.25).

$$\left(\frac{\partial T}{\partial p}\right)_s = \left(\frac{\gamma - 1}{\gamma}\right) \frac{T_m}{p_m} \quad (14.15)$$

Since we seek an attenuation coefficient that would be applicable to all fluids, a more general expression for  $(\partial T/\partial p)_s$  needs to be calculated to evaluate  $(\partial T/\partial x)$ .

$$\left(\frac{\partial T}{\partial x}\right)_s = \left(\frac{\partial T}{\partial p}\right)_s \left(\frac{\partial p}{\partial v}\right)_s \left(\frac{\partial v}{\partial x}\right)_s = -\rho_m c \left(\frac{\partial T}{\partial p}\right)_s k v_1 \cos(\omega t - kx) \quad (14.16)$$

The derivative of pressure with respect to velocity for a nearly adiabatic plane wave is a direct consequence of the Euler equation:  $p_1 = \rho_m c v_1$ .

The derivative of temperature with respect to density can be evaluated using the *enthalpy function*,  $H(S, p) = U + pV$ , that sums the internal energy,  $U$ , introduced in Sect. 7.1.2 to calculate heat capacities, with the mechanical work,  $W = pV$ . From Eqs. (7.8, 7.9, and 7.10), the internal energy,  $U(S, V)$ , can be transformed into the enthalpy,  $H(S, p)$ , using the product rule for differentiation. In thermodynamics, this operation is known as a *Legendre transformation* [8].

$$\begin{aligned} dU &= TdS - pdV = TdS - d(pV) + Vdp \\ \Rightarrow d(U + pV) &\equiv dH = TdS + Vdp \end{aligned} \quad (14.17)$$

The change in enthalpy,  $dH(S, p)$ , can be expanded in a Taylor series, retaining only the linear terms.

$$dH = \left(\frac{\partial H}{\partial S}\right)_p dS + \left(\frac{\partial H}{\partial p}\right)_S dp \quad (14.18)$$

Comparison of Eqs. (14.17) and (14.18) can be used to evaluate those derivatives.

$$\left(\frac{\partial H}{\partial S}\right)_p = T \quad \text{and} \quad \left(\frac{\partial H}{\partial p}\right)_S = V \quad (14.19)$$

Since the order of differentiation is irrelevant, the mixed partial derivatives must be equal.

$$\frac{\partial^2 H}{\partial p \partial S} = \frac{\partial^2 H}{\partial S \partial p} \quad \Rightarrow \quad \left(\frac{\partial T}{\partial p}\right)_S = \left(\frac{\partial V}{\partial S}\right)_p \quad (14.20)$$

This result is one of several thermodynamic identities known as the *Maxwell relations* [9].

---

<sup>4</sup> Stefan was the thesis advisor of Boltzmann, who was the advisor of Ehrenfest, who was the advisor of Uhlenbeck, who was the advisor of Puterman, who was my advisor, along with Isadore Rudnick, when I was a graduate student at UCLA.

$$\left(\frac{\partial V}{\partial S}\right)_p = \left(\frac{\partial V}{\partial T}\right)_p \left(\frac{\partial T}{\partial S}\right)_p \quad (14.21)$$

The result in Eq. (14.21) can be expressed in terms of tabulated material properties [10] using the definition of the (extensive) heat capacity at constant pressure,  $C_p$ , or the (intensive) specific heat (per unit mass) at constant pressure,  $c_p$ , from Eq. (7.14), and the definition of the isobaric (constant pressure) volume coefficient of thermal expansion,  $\beta_p$ .

$$C_p = T \left( \frac{\partial S}{\partial T} \right)_p \quad \text{or} \quad c_p = T \left( \frac{\partial s}{\partial T} \right)_p \quad \text{and} \quad \beta_p = \frac{1}{V} \left( \frac{\partial V}{\partial T} \right)_p = -\frac{1}{\rho_m} \left( \frac{\partial \rho}{\partial T} \right)_p \quad (14.22)$$

These results can be combined to produce an expression for the temperature gradient required to evaluate the thermal conduction integral in Eq. (14.13) using Eq. (14.16).

$$\frac{\partial T}{\partial x} = c \frac{\beta_p T_m}{c_p} \frac{\partial v_1}{\partial x} = -c \frac{\beta_p T_m}{c_p} v_1 k \cos(\omega t - kx) \quad (14.23)$$

As before, our interest will be in the time-averaged value for evaluation of the thermal conduction term in the integral expression for  $\Pi_{mech}$  in Eq. (14.12).

$$\left\langle -\frac{\kappa}{T_m} \int (\nabla T)^2 dV \right\rangle_t = \frac{-\kappa c^2 \beta_p^2 v_1^2 k^2}{2c_p^2} V_o \quad (14.24)$$

This result can be evaluated in terms of the difference in the specific heats that was shown by thermodynamic arguments to be  $C_p - C_v = \mathfrak{R}$ , in Eq. (7.14), for an ideal gas, or  $c_p - c_v = \mathfrak{R}/M$ , where  $\mathfrak{R}$  is the universal gas constant and  $M$  is the mean molecular or atomic mass of the ideal gas or ideal gas mixture. By the same thermodynamic arguments, the general result for the specific heat difference can be expressed in terms of the fluid parameters in Eq. (14.22) [11].

$$c_p - c_v = T \beta_p^2 \left( \frac{\partial p}{\partial \rho} \right)_T = T \beta_p^2 \left( \frac{c_v}{c_p} \right) \left( \frac{\partial p}{\partial \rho} \right)_s = T \beta_p^2 c^2 \left( \frac{c_v}{c_p} \right) \quad (14.25)$$

The relationship between the square of the isothermal sound speed,  $(\partial p / \partial \rho)_T$ , and the square of the adiabatic sound speed,  $(\partial p / \partial \rho)_s = c^2$ , should be familiar since  $(c_v/c_p) \equiv \gamma^{-1}$ .

Substitution of Eq. (14.25) into Eq. (14.24) provides a compact expression for the time-averaged power dissipation that is valid for ideal gases as well as for all other homogeneous fluids.

$$\left\langle -\frac{\kappa}{T_m} \int (\nabla T)^2 dV \right\rangle_t = -(\gamma/2) \kappa k^2 v_1^2 V_o \left( \frac{1}{c_v} - \frac{1}{c_p} \right) \quad (14.26)$$

Combining Eq. (14.26) with Eq. (14.14) provides an expression for the time-averaged mechanical power dissipation due to all of the irreversible dissipation mechanisms.

$$\langle \Pi_{mech} \rangle_t = -(\gamma/2) k^2 v_1^2 V_o \left[ \left( \frac{4}{3} \mu + \zeta \right) + \kappa \left( \frac{1}{c_v} - \frac{1}{c_p} \right) \right] \quad (14.27)$$

The total energy,  $E$ , of the plane wave occupying the volume,  $V_o$ , can be expressed in terms of the maximum kinetic energy density,  $(KE)_{max}$ .

$$E = (\text{KE})_{\max} V_o = (\frac{1}{2}) \rho_m v_1^2 V_o \quad (14.28)$$

Since the decay rate of the energy is twice that of the amplitude decay rate, the spatial attenuation constant that reflects thermoviscous losses (and whatever  $\zeta$  represents!),  $\alpha_{T-V}$ , can be written in terms of the time-averaged power dissipation,  $\langle \Pi_{\text{mech}} \rangle_t$ , in Eq. (14.27), and the average total energy,  $E$ , in Eq. (14.28).

$$\alpha_{T-V} = \frac{|\langle \Pi_{\text{mech}} \rangle_t|}{2cE} = \frac{\omega^2}{2\rho_m c^3} \left[ \left( \frac{4}{3}\mu + \zeta \right) + \kappa \left( \frac{1}{c_v} - \frac{1}{c_p} \right) \right] \quad (14.29)$$

This final result for  $\alpha_{T-V}$  is valid for all fluids as long as the decrease in the sound wave's amplitude over the distance of a single wavelength is relatively small,  $\alpha_{T-V} \lambda \ll 1$ , since the stored energy was calculated for an undamped sound wave.

We also see that this result is similar to the “almost correct” result,  $\alpha_{\text{almost}}$ , calculated from the Navier-Stokes equation in Sect. 14.1. The dependence on frequency,  $\omega$ ; mass density,  $\rho_m$ ; and sound speed,  $c$ , is identical, but the shear viscosity,  $\mu$ , is no longer the only transport property of the medium that contributes to attenuation of the sound wave; in Eq. (14.29),  $\mu$  has been replaced by the term within the square bracket.

As demonstrated earlier in Eq. (14.8), the expression for attenuation given in Eq. (14.29) will always be valid for sound in gases, since the kinematic viscosity,  $\nu_{\text{gas}} = \mu_{\text{gas}}/\rho_m$ , is on the order of the product of the mean free path,  $\bar{\ell}$ , times the mean thermal velocity of the gas molecules or the sound speed.

$$\frac{\nu_{\text{gas}}\omega}{c^2} \cong \bar{\ell} \frac{\omega}{c} \cong \frac{\bar{\ell}}{\lambda} \ll 1 \quad (14.30)$$

### 14.3 Classical Thermoviscous Attenuation

Before the role of molecular relaxation was appreciated and the associated dissipative coefficient,  $\zeta$ , was introduced, attenuation of sound due to thermoviscous losses was calculated by Kirchhoff [7]. That result is often called the classical absorption coefficient,  $\alpha_{\text{classical}}$ .

$$\alpha_{\text{classical}} = \frac{\omega^2}{2\rho_m c^3} \left[ \frac{4}{3}\mu + \kappa \left( \frac{1}{c_v} - \frac{1}{c_p} \right) \right] = \frac{\omega^2}{2c^3} \left[ \frac{4}{3} \frac{\mu}{\rho_m} + \frac{\kappa}{\rho_m c_p} \left( \frac{c_p}{c_v} - 1 \right) \right] \quad (14.31)$$

For an ideal gas, the classical attenuation coefficient can be expressed more transparently in terms of the kinematic viscosity,  $\nu = \mu/\rho_m$ ; the polytropic coefficient,  $\gamma = c_p/c_v$ ; and the dimensionless ratio of the thermal and viscous diffusion constants, known as the Prandtl number,  $\text{Pr} \equiv (\mu/c_p\kappa) = (\delta_\nu/\delta_\kappa)^2$ , that was introduced in Sect. 9.5.4.

$$\alpha_{\text{classical}} = \frac{\omega^2 \nu}{2c^3} \left[ \frac{4}{3} + \frac{(\gamma - 1)}{\text{Pr}} \right] \quad \Rightarrow \quad \frac{\alpha_{\text{classical}}}{f^2} = \frac{2\pi^2 \nu}{c^3} \left[ \frac{4}{3} + \frac{(\gamma - 1)}{\text{Pr}} \right] \quad (14.32)$$

Most single-component gases and many gas mixtures have  $\text{Pr} \cong 2/3$ . For air at atmospheric pressure and 20 °C,  $\nu = 1.51 \times 10^{-5} \text{ m}^2/\text{s}$ ,  $\text{Pr} = 0.709$ ,  $\gamma = 1.402$ , and  $c = 343.2 \text{ m/s}$ . Under those conditions,  $\alpha_{\text{classical}} / f^2 = 1.40 \times 10^{-11} \text{ s}^2/\text{m}$ . The accepted value of  $\alpha/f^2$  in the high-frequency limit is  $1.84 \times 10^{-11} \text{ s}^2/\text{m}$ . This discrepancy is due to the absence of  $\zeta$  in Eq. (14.32) [12].

Since the difference between the specific heats at constant pressure and constant volume is small for liquids, the viscous contribution to the classical attenuation constant is dominant. For pure water at 280 K,  $\nu_{H_2O} = 1.44 \times 10^{-6}$  m<sup>2</sup>/s and  $\text{Pr}_{H_2O} = 10.4$ , [13] with  $c_{H_2O} = 1500$  m/s, making  $\alpha_{\text{classical}}/f^2 = 1.1 \times 10^{-14}$  s<sup>2</sup>/m for freshwater. The accepted value of  $\alpha/f^2$  in the high-frequency limit is  $2.5 \times 10^{-14}$  s<sup>2</sup>/m, again due to the absence of  $\zeta$  in Eq. (14.32) [14].

## 14.4 The Time-Dependent Equation of State

The distortion of a fluid element caused by passage of a plane wave was decomposed into shear deformations, which changed the shape of the element, and a hydrostatic deformation, which changed the volume of the element, as diagrammed schematically in Fig. 14.1. Each of those deformations introduced irreversibility that increased entropy as expressed in Eq. (14.12), leading to energy dissipation as expressed in Eq. (14.13). Based on the discussion in Sect. 9.4, the shear viscosity,  $\mu$ , was introduced to relate the shear deformations to the dissipative shear stresses.

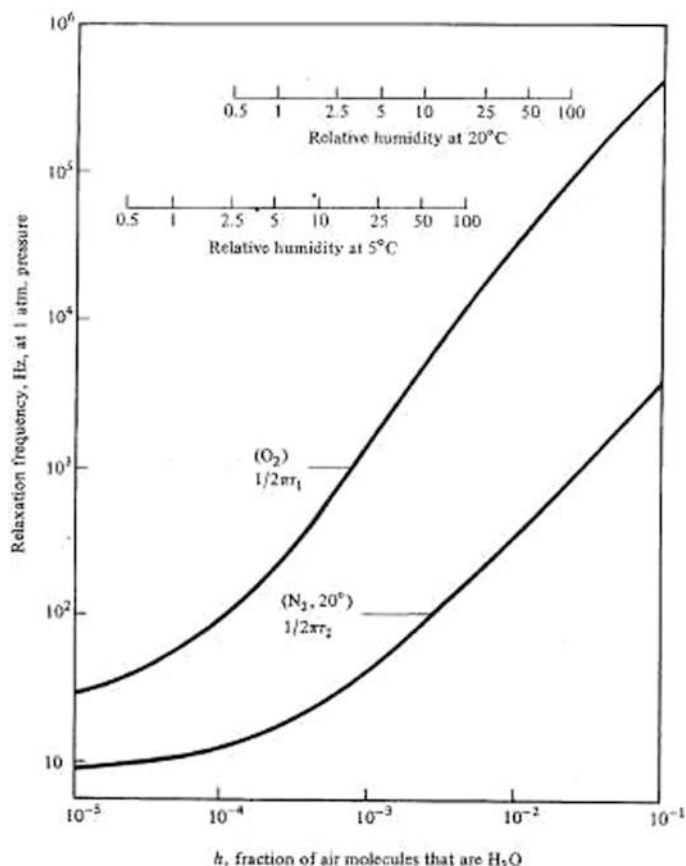
Another coefficient,  $\zeta$ , was introduced to relate entropy production to the divergence of the fluid's velocity field,  $\nabla \cdot \vec{v}$ . The continuity equation requires that when  $\nabla \cdot \vec{v} \neq 0$ , the density of the fluid must also be changing:  $(\partial \rho / \partial t) \neq 0$ . Why should a change in the fluid's density be related to irreversible entropy production?

When the phenomenological model was introduced, it was assumed that only five variables were required to completely specify the state of a homogeneous, isotropic, single-component fluid: one mechanical variable ( $p$  or  $\rho$ ) and one thermal variable ( $s$  or  $T$ ), along with the three components of velocity (e.g.,  $v_x$ ,  $v_y$ , and  $v_z$ ). For a static fluid,  $|v| = 0$ , only two variables were required, resulting in the laws of equilibrium thermodynamics (i.e., energy conservation and entropy increase) rather than the laws of hydrodynamics (that also incorporate thermodynamics). The evolution of those variables was determined by the imposition of five conservation equations (i.e., mass, entropy, and vector momentum). That assertion included an implicit assumption that an equation of state existed and it could be used to relate the thermodynamic variables (mechanical and thermal) to each other *instantaneously*.

For some fluids, the assumption of an instantaneous response of the density to changes in the pressure is not valid. (Noble gases are one notable exception, since they do not have any rotational degrees of freedom.) The microscopic models of gases that were based on the kinetic theory introduced the concept of collision times between the constituent particles (atoms and/or molecules) and the Equipartition Theorem in Eq. (7.2) that stated that through these collisions, an equilibrium could be established that distributed the total thermal energy of the system equitably (on average) among all of the available degrees of freedom. What has been neglected (to this point) was the fact that the collisions take a non-zero time to establish this equilibrium; if the conditions of the fluid element are changing during this time, the system might never reach equilibrium.

How did we get away with this “five-variable fraud” for so long? One answer is hidden in the transition from adiabatic sound speed in an ideal gas to the isothermal sound speed. Equation (9.24) defined a critical frequency,  $\omega_{\text{crit}}$ , at which the speed of thermal diffusion was equal to the speed of sound propagation. At that frequency, the wavelength of sound corresponded to a distance, which was about 20 times the average spacing between particles, known as the mean free path between collisions,  $\bar{l}$ . Since that collision frequency was so much higher than our frequencies of interest, the equilibration between translational and rotational degrees of freedom in gases of polyatomic molecules occurred so quickly that the equation of state appeared to act instantaneously [15]. Even though a vibrating object couples to the translational degrees of freedom in a gas, the translational and rotational degrees of freedom came into equilibrium in much less time than the period of the vibrating object's oscillations.

**Fig. 14.2** Relaxation frequencies,  $f_R = (2\pi\tau_R)^{-1}$ , for equilibration between O<sub>2</sub> or N<sub>2</sub> and water vapor (H<sub>2</sub>O) as a function of the mole fraction of water vapor in air,  $h$ , at  $p_m = 1$  atmosphere. At the top of the graph are scales that can be used to relate the mole fraction of H<sub>2</sub>O on the  $x$  axis to the more popular designation of percent “relative humidity” at 5 °C and 20 °C [16]



That “fraud” was obscured by our use of  $\gamma = 7/5$  in the expression for sound speed which treated the air as instantly sharing energy between the internal translational and rotational degrees of freedom.

When there are other components in a gas or liquid, they may have relaxation times that are sufficiently close to the acoustic periods of interest that their “equilibration” to the acoustically induced changes cannot be considered to occur instantaneously. In air, for example, if there is water vapor present, it will equilibrate with the O<sub>2</sub> and N<sub>2</sub> over times that are comparable to the periods of sound waves of interest for human perception (i.e.,  $20 \text{ Hz} \lesssim f \lesssim 20 \text{ kHz}$ ). Figure 14.2 shows the relaxation frequencies as a function of the mole fraction,  $h$ , of H<sub>2</sub>O and also relative humidity as a percentage [16].

Those equilibration times are dependent upon the gas mixture’s temperature, pressure, and mixture concentration (i.e., mole fraction of water vapor,  $h$ , or relative humidity,  $RH$ ) [17]. It is apparent that the relaxation frequencies in Fig. 14.2 are in the audio range for ordinary values of temperature and humidity [17].

$$f_{ro} = \frac{p_m}{p_{ref}} \left\{ 24 + \left[ \frac{(4.04 \times 10^4 h)(0.02 + h)}{0.391 + h} \right] \right\} \quad (14.33)$$

$$f_{rN} = \frac{p_m}{p_{ref}} \left( \frac{T}{T_{ref}} \right)^{-1/2} \left( 9 + 280h \exp \left\{ -4.170 \left[ \left( \frac{T}{T_{ref}} \right)^{-1/3} - 1 \right] \right\} \right)$$

The relaxation frequencies for water vapor and nitrogen,  $f_{rN}$ , and for water vapor and oxygen,  $f_{rO}$ , assume a standard atmospheric composition with 78.1% nitrogen, 20.9% oxygen, and 314 ppm carbon dioxide at a reference pressure,  $p_{ref} = 101,325 \text{ Pa}$ , and reference temperature,  $T_{ref} = 293.15 \text{ K} = 20.0^\circ\text{C}$ . In Eq. (14.33), the molar concentration of water vapor,  $h$ , is expressed in percent. For ordinary atmospheric conditions near sea level,  $0.2\% \lesssim h \lesssim 2.0\%$ .

To relate  $RH$  to  $h$  (both in %), it is first necessary to calculate the saturated vapor pressure of water in air,  $p_{sat}$ , relative to ambient pressure,  $p_{ref} = 101.325 \text{ kPa}$ , using the triple-point isotherm temperature,  $T_{01} = 273.16 \text{ K} = +0.01^\circ\text{C}$ .

$$\frac{p_{sat}}{p_{ref}} = 10^C; \quad C = -6.8346 \left( \frac{T_{01}}{T} \right)^{1.261} + 4.6151 \quad (14.34)$$

The molar concentration of water vapor,  $h$ , in percent, can then be expressed in terms of the relative humidity,  $RH$ , also in percent [17].

$$h = RH \left( \frac{p_{sat}}{p_m} \right) \quad (14.35)$$

A similar effect is observed in seawater where boric acid,  $\text{B(OH)}_3$ , and magnesium sulfate,  $\text{MgSO}_4$ , have relaxation frequencies of 1.18 kHz and 145 kHz, respectively, at  $20^\circ\text{C}$  [18]. In the case of these salts, the relaxation time represents the pressure-dependent association-dissociation reaction between the dissolved salts and their ions.

## 14.5 Attenuation due to Internal Relaxation Times

*"If a system is in stable equilibrium, then any spontaneous change of its parameters must bring about processes which tend to restore the system to equilibrium."* H. L. Le Châtelier<sup>5</sup>

A new positive scalar coefficient,  $\zeta$ , was introduced in the entropy conservation Eq. (14.12) to scale the irreversibility of hydrostatic fluid deformations. It has the same units as the shear viscosity [ $\text{Pa}\cdot\text{s}$ ]<sup>6</sup> and is usually of about the same magnitude. If the medium does not possess any additional internal degrees of freedom that have to be brought into equilibrium, then its value can be identically zero. That constant is zero for the noble gases (He, Ne, Ar, Kr, Xe, and Rn) that are intrinsically monatomic with atoms that are spherically symmetrical, thus lacking rotational degrees of freedom (see Sect. 7.2). On the other hand, as suggested in Fig. 14.2, if there are processes with relaxation times that are near the frequencies of interest, the value of  $\zeta$  can be orders of magnitude greater than  $\mu$  near those frequencies.

With acoustical compressions or expansions, as in any rapid change of state, the fluid cannot remain in thermodynamic equilibrium. Following *Le Châtelier's Principle*,<sup>5</sup> the system will attempt to return to a new equilibrium state that is consistent with the new parameter values that moved it away from its

<sup>5</sup> Henry Louis Le Châtelier (1850–1936) was a Parisian chemist. This principle is sometimes also attributed to German physicist Karl Ferdinand Braun (1850–1918), the inventor of the cathode-ray tube and the oscilloscope.

<sup>6</sup> Because  $\zeta$  has the same units as shear viscosity, it is commonly called *bulk viscosity* or *second viscosity*, even though its effects are entirely unrelated to shear strains. I find both terms misleading and attempt to avoid their use in this textbook, although acousticians have to be aware that they represent the common nomenclature used to identify losses related to the relaxation of internal degrees of freedom within fluids.

previous state of equilibrium. In some cases, this equilibration takes place very quickly so that the medium behaves as though it were in equilibrium at all times. In other cases, the equilibration is slow, and the medium never catches up. In either case, the processes that attempt to reestablish equilibrium are irreversible and therefore create entropy and dissipate energy.

If  $\xi$  represents some physical parameter of the fluid and  $\xi_o$  represents the value of  $\xi$  at equilibrium, then if the fluid is not in equilibrium,  $\xi$  will vary with time. If the fluid is not too far from equilibrium, so the difference,  $\xi - \xi_o$ , is small (i.e.,  $|\xi - \xi_o|/\xi_o \ll 1$ ), and then the rate of change of that parameter,  $\dot{\xi}$ , can be expanded in a Taylor series retaining only the first term and recognizing that any zero-order contribution to  $\dot{\xi}$  must vanish since  $\xi = \xi_o$  at equilibrium.

$$\dot{\xi} = -\frac{(\xi - \xi_o)}{\tau_R} \quad (14.36)$$

This suggests an exponential relaxation of the system toward its new equilibrium state. Le Châtelier's Principle requires that the rate must be negative and that the relaxation time,  $\tau_R$ , must be positive.

For acoustically induced sinusoidal variations in the parameter,  $\xi$ , at frequency,  $\omega$ , the sound speed will depend upon the relative values of the period of the sound,  $T = 2\pi/\omega$ , and the relaxation time,  $\tau_R$ . If the period of the disturbance is long compared to the exponential equilibration time,  $\tau_R$ , so that  $\omega\tau_R = 2\pi\tau_R/T \ll 1$ , then the fluid will remain nearly in equilibrium at all times during the acoustic disturbance. In that limit, the sound speed will be the equilibrium sound speed,  $c_o$ . In the opposite limit,  $\omega\tau_R = 2\pi\tau_R/T \gg 1$ , the medium's sound speed,  $c_\infty > c_o$ , will be determined by the fluid's elastic response if the internal degrees of freedom cannot be excited by the disturbance. Said another way, the internal degrees of freedom are "frozen out" in that limit; they simply do not have enough time to participate before the state of the system has changed.

One way to think about this effect is to consider the sound speed in a gas of diatomic molecules that possess three translational degrees of freedom and two rotational degrees of freedom. The specific heats of monatomic and polyatomic gases were discussed in Sect. 7.2, and the relationship between the sound speed in such gases and the specific heat ratio,  $\gamma = c_p/c_v$ , is provided in Eq. (10.22). If the rotational degrees of freedom are not excited, then the gas behaves as though it were monatomic, so  $\gamma = 5/3$ . If the rotational and translational degrees of freedom are always in equilibrium, then  $\gamma = 7/5 < 5/3$ , so  $c_\infty = \sqrt{25/21} c_o$ .

The mathematical "machinery" needed to represent the attenuation and dispersion of sound waves in a homogeneous medium with an internal degree of freedom, or a "relaxing sixth variable," has already been developed to describe viscoelastic solids in Sect. 4.4.2. Figure 4.25 could just as well describe the propagation speed (solid line) as a function of the *nondimensional frequency*,  $\omega\tau_R$ , with  $c_o$  being the limiting sound speed for  $\omega\tau_R = 2\pi\tau_R/T \ll 1$  and  $c_\infty$  being the sound speed for  $\omega\tau_R = 2\pi\tau_R/T \gg 1$ . In addition, the *Kramers-Kronig relations* of Sect. 4.4.4 would still apply; the variation in sound speed with frequency requires a frequency-dependent attenuation, shown in Fig. 4.25 as the dashed line, and vice versa.

The transformation of the results derived for the stiffness and damping of a viscoelastic medium simply requires that the sound speed is proportional to the square root of the elastic modulus (i.e., stiffness) as expressed in Eq. (10.21). That substitution allows Eq. (4.67) to produce the propagation speed as a function of the nondimensional frequency,  $\omega\tau_R$ .

$$c^2 = c_o^2 + (c_\infty^2 - c_o^2) \frac{(\omega\tau_R)^2}{1 + (\omega\tau_R)^2} \quad (14.37)$$

The same approach applied to Eq. (4.70) provides the attenuation per wavelength,  $\alpha\lambda$ , as function of the dimensionless frequency,  $\omega\tau_R$ .

$$(\alpha\lambda) = 2\pi \frac{(c_\infty^2 - c_o^2)(\omega\tau_R)}{c_o^2 [1 + (\omega\tau_R)^2] + (c_\infty^2 - c_o^2)(\omega\tau_R)^2} \quad (14.38)$$

Following Eq. (4.71) or Eq. (4.89), the maximum value of attenuation per wavelength in Eq. (14.38) will occur at a unique value of the nondimensional frequency,  $(\omega\tau_R)_{\max}$ .

$$(\omega\tau_R)_{\max} = \frac{c_o}{c_\infty} \quad \text{and} \quad (\alpha\lambda)_{\max} = \pi \frac{(c_\infty^2 - c_o^2)}{c_\infty c_o} \quad (14.39)$$

The consequence of the Kramers-Kronig relations for such single relaxation time phenomena, as emphasized in Sect. 4.4.2, is that the attenuation is entirely determined by the dispersion, and vice versa.

Using these results, it is possible to write simple universal expressions for attenuation due to excitation of internal degrees of freedom in terms of the relaxation frequency,  $f_R = (2\pi\tau_R)^{-1}$ .

$$\frac{\alpha\lambda}{(\alpha\lambda)_{\max}} = \frac{2}{\frac{f}{f_R} + \frac{f}{f_R}} \Rightarrow \alpha(f) = \left[ \frac{2(\alpha\lambda)_{\max}}{cf_R} \right] \frac{f^2}{1 + \left( \frac{f}{f_R} \right)^2} \quad (14.40)$$

The variation in the attenuation per wavelength,  $\alpha\lambda$ , and the propagation speed,  $c$ , as a function of nondimensional frequency,  $\omega\tau_R$ , is plotted in Fig. 14.3 and should be compared to the plot for a viscoelastic solid in Fig. 4.25, which exhibits identical behavior. For relaxation frequencies,  $f_R$ , that are much higher than the frequency of interest,  $f$ , the attenuation constant's quadratic frequency dependence is recovered, as was derived in Eq. (14.7) for  $\alpha_{\text{almost}}$  and in Eq. (14.29) for  $\alpha_{T-V}$ .

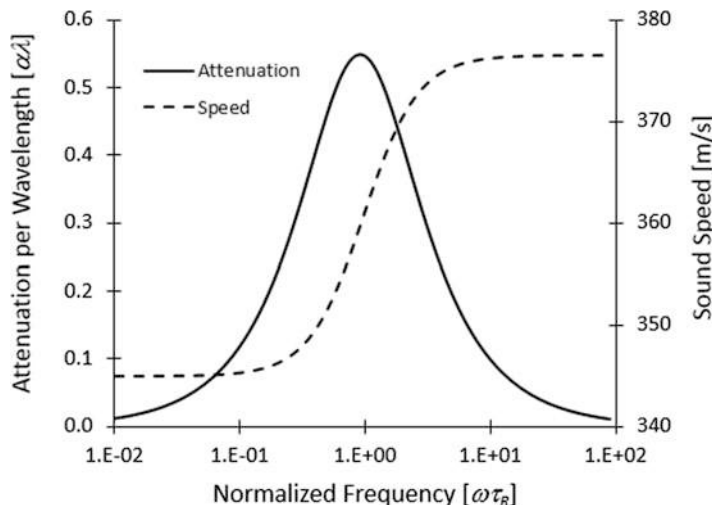


**Fig. 14.3** The attenuation and dispersion for a fluid with  $c_\infty = c_o\sqrt{25/21}$ , where  $c_o = 345$  m/s, as a function of the nondimensional frequency,  $\omega\tau_R$ . Values for the attenuation per wavelength (solid line),  $\alpha\lambda$ , should be read from the left-hand vertical axis, and the values of sound speed (dashed line) should be read from the right-hand axis. This behavior is identical to that of a viscoelastic solid that is shown in Fig. 4.25 since the Kramers-Kronig relations dictate the relationship between the real and imaginary parts of the linear response

### 14.5.1 Relaxation Attenuation in Gases and Gas Mixtures

The first example of the effects of the relaxation of an internal degree of freedom on sound speed and attenuation in gas is taken from the measurements of Shields in fluorine [19]. Halogen vapors (e.g., chlorine, fluorine, bromine, iodine) are unique in that they consist of homonuclear diatomic molecules that have appreciable vibrational energy,  $E_V = (n + 1/2) \hbar\omega_V$ , at room temperature (see Sect. 7.2.2). Because the diatomic molecules behave as simple (quantum mechanical) harmonic oscillators, that internal degree of freedom can be characterized by a single relaxation time corresponding to the radian period of their harmonic oscillations.

Figure 14.4 shows the measured values of attenuation per wavelength,  $\alpha\lambda$ , and sound speed,  $c$ , as a function of frequency (also normalized by pressure), in units of kHz/atm., for fluorine gas

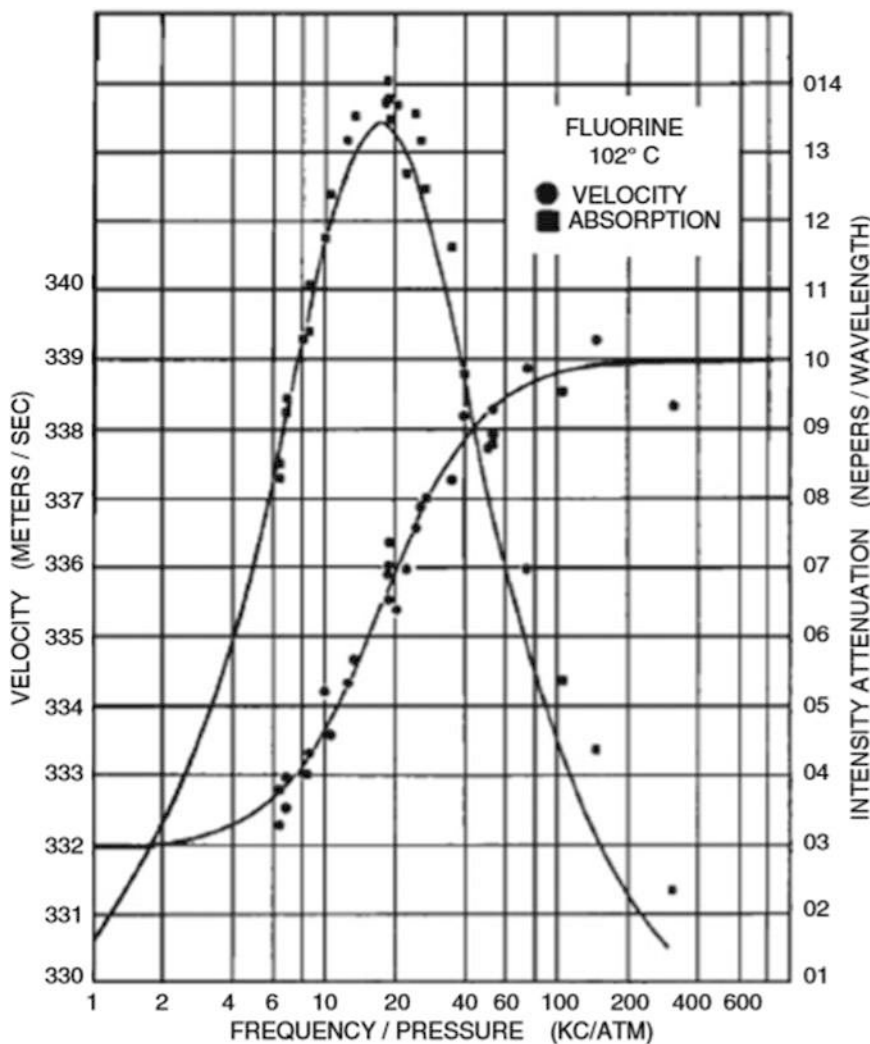


**Fig. 14.4** Measured data for attenuation per wavelength and dispersion (sound speed) in fluorine gas at  $102 \pm 2^\circ\text{C}$  [19]. The sound speed should be read from the left-hand vertical axis, and the attenuation per wavelength,  $\alpha\lambda$ , should be read from the right-hand axis that is labeled “Intensity Attenuation (Nepers/Wavelength).” Nepers is an archaic dimensionless unit that was in common usage at the time this data was published to designate  $\alpha$  in Np/m. It simply refers to the spatial attenuation coefficient, named after John Napier, the inventor of logarithms.  $1 \text{ Np} = 8.69 \text{ dB}$ . The solid lines are fits to the data points that are based on expressions like Eqs. (14.37) and (14.38)

at  $102 \pm 2$  °C, after correction for boundary layer losses at the surface of the tube containing the gas [20].

The *vibrational relaxation time* for diatomic fluorine at 102 °C is  $\tau_R = 10.7$  μs, corresponding to a relaxation frequency,  $f_R = (2\pi\tau_R)^{-1} = 14.9$  kHz. Based on the fit to the sound speed, the limiting speeds are  $c_o = 332$  m/s and  $c_\infty = 339$  m/s. The peak in the attenuation per wavelength,  $(\alpha\lambda)_{\max} = 0.13$ , occurs at  $(\omega\tau_R)_{\max} = 0.98$ , based on Eq. (14.39), in excellent agreement with the data in Fig. 14.4.

The relaxation attenuation in humid air is more complicated since the two relaxation frequencies for equilibration of the water vapor with the nitrogen and with the oxygen are different, as expressed in Eq. (14.33) and plotted in Fig. 14.2. Since energy loss is cumulative, it is possible to express the attenuation constant,  $\alpha_{tot}$ , as the sum of the attenuation caused by the classical value,  $\alpha_{classical}$ , and the contributions from the two relaxation processes.

$$\alpha_{tot} = \alpha_{classical} + \alpha_{O_2} + \alpha_{N_2} \quad (14.41)$$

The pressure, frequency, and temperature dependence for the total attenuation coefficient is provided in combination with the relaxation times of Eq. (14.33) and plotted as a function of the frequency/pressure ratio for various values of the relative humidity in Fig. 14.5 [21].

$$\frac{\alpha_{Air}}{f^2} = 1.84 \times 10^{-11} \left( \frac{p_m}{p_{ref}} \right)^{-1} \left( \frac{T}{T_{ref}} \right)^{1/2} + \left( \frac{T}{T_{ref}} \right)^{-5/2} \times \left\{ 0.01275 e^{-2,239/T} \left[ \frac{f_{rO}}{f_{rO}^2 + f^2} \right] + 0.1068 e^{-3,352/T} \left[ \frac{f_{rN}}{f_{rN}^2 + f^2} \right] \right\} \quad (14.42)$$

The difference between the classical attenuation constant and the total is clearly very large. At 2 kHz and 1 atm.,  $\alpha_{classical} = 0.02$  dB/m, but with 10% relative humidity, the attenuation is  $\alpha_{tot} = 0.80$  dB/m.

Values for the attenuation in dB/km are tabulated in a standard for different values of temperature from  $-25$  °C to  $+50$  °C and  $10\% \leq RH \leq 100\%$  for pure tones with frequencies from 50 Hz to 10 kHz in  $1/3$  -octave increments [17]. A small subset of that data are presented in Table 14.1.

### 14.5.2 Relaxation Attenuation in Fresh and Salt Water

As earlier noted in Sect. 14.3, the measured attenuation of sound in water is greater than  $\alpha_{classical}/f^2$  based on the shear viscosity by more than a factor of two. In the calculation of  $\alpha_{classical}$  for water, the thermal conductivity was neglected. It can be shown that neglect of the thermal conductivity is not the cause of this discrepancy. Measurements of attenuation at 4 °C, where water has its density maximum and the thermal expansion coefficient vanishes, mean that  $c_p = c_v$ , so according to Eq. (14.25), there are no temperature changes associated with the acoustical pressure changes [22].

The excess attenuation has been ascribed to a *structural relaxation* process wherein a molecular rearrangement is caused by the acoustically produced pressure changes. During acoustic compression, the water molecules are brought closer together and are rearranged by being repacked more closely. This repacking takes a non-zero amount of time and leads to relaxational attenuation that makes  $\zeta \neq 0$  [23]. The relaxation time as a function of water temperature for this process,  $\tau_R$ , is on the order of picoseconds and is plotted as a function of temperature in Fig. 14.6.

At 4 °C,  $\tau_R \approx 3.5$  ps, corresponding to a relaxation frequency,  $f_R = (2\pi\tau_R)^{-1} = 45$  GHz, well above experimentally accessible frequencies. For that reason, there are no “relaxation bumps” in the attenuation vs. frequency, as seen in Fig. 14.7. Nonetheless, this structural relaxation makes  $\zeta > \mu$ , accounting for the excess attenuation in pure water.

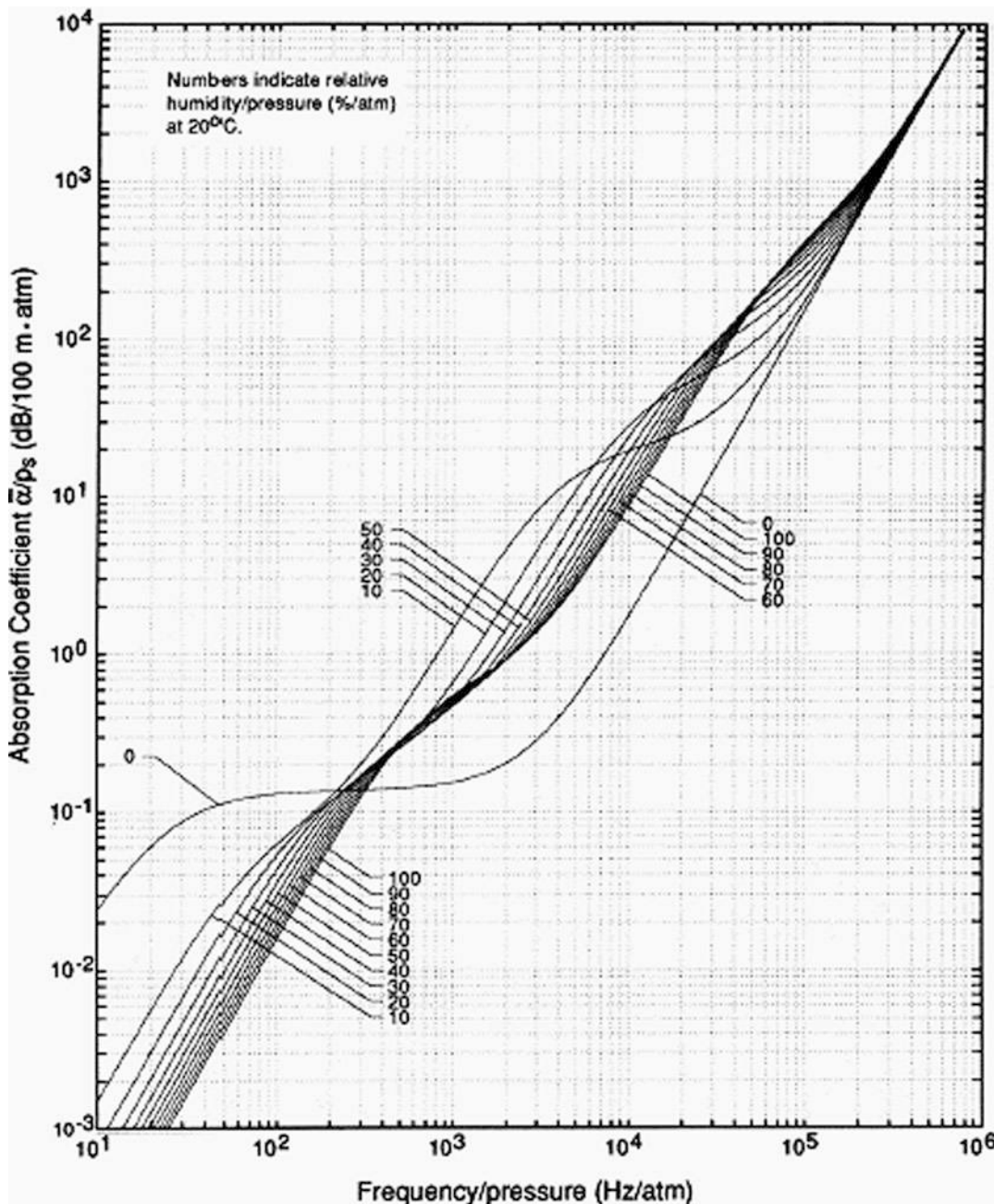


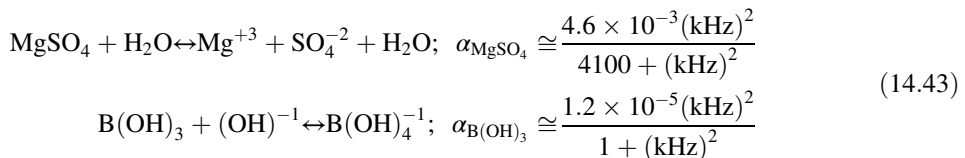
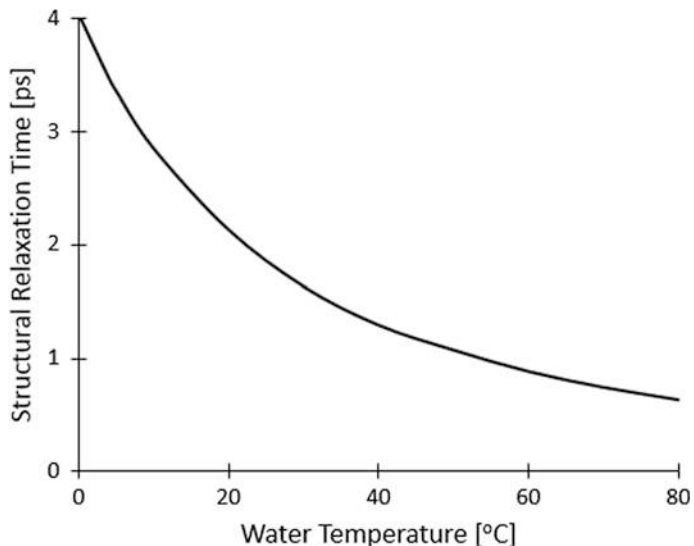
**Fig. 14.5** Sound absorption coefficient per atmosphere in air at 20 °C. The parameter labeling the individual curves is the relative humidity from 0% to 100%. [21] The additional attenuation for dry air ( $RH = 0$ ) is due to collisions between  $N_2$  and  $CO_2$

The attenuation of sound in seawater is similar to that in humid air where the relaxation frequencies are within a frequency range of interest. In seawater, there are two pressure-dependent ionic *association-dissociation reactions* due to the dissolved boric acid,  $B(OH)_3$ , and the dissolved magnesium sulfate,  $MgSO_4$ . Their contributions to the attenuation have the generic form introduced in Eq. (14.40).

**Table 14.1** (Left) Attenuation in dB/km for air at 20 °C with RH = 50%, as a function of frequency. (Right) Attenuation in dB/km at 4.0 kHz, for air at 20 °C, in the relative humidity range of 20% ≤ RH ≤ 70% [17]

Freq. [kHz]	[dB/km]	RH(%)	[dB/km]
1.60	7.37	20	74.4
2.00	9.85	30	48.5
2.50	13.7	40	36.1
3.15	19.8	50	29.4
4.00	29.4	60	25.4
5.00	44.4	70	22.9
6.30	67.8		
8.00	104		
10.00	159		

**Fig. 14.6** Structural relaxation time for the repacking of water molecules caused by acoustical pressure changes [23]



The approximate attenuation values,  $\alpha_{\text{MgSO}_4}$  and  $\alpha_{\text{B(OH)}_3}$ , in Eq. (14.43) are in units of  $[\text{m}^{-1}]$  when the frequency is expressed in kHz.

Those reactions that have relaxation frequencies that depend upon absolute temperature,  $T$ , and salinity,  $S$ , that is expressed in parts per thousand, ‰, and those relaxation frequencies,  $f_{\text{rBH}_3\text{O}_3}$  and  $f_{\text{rMgSO}_4}$ , are in hertz [24, 25].

$$f_{\text{rBH}_3\text{O}_3} = 2,800 \sqrt{S/35} \times 10^{[4-(1,245/T)]} \quad (14.44)$$

$$f_{\text{rMgSO}_4} = \frac{8,170 \times 10^{[8-(1,990/T)]}}{1 + 0.008(S - 35)}$$

For salinity,  $S = 35\text{‰}$ , and  $T = 293 \text{ K}$ ,  $f_{\text{rB(OH)}_3} = 1.58 \text{ kHz}$  and  $f_{\text{rMgSO}_4} = 132 \text{ kHz}$ .

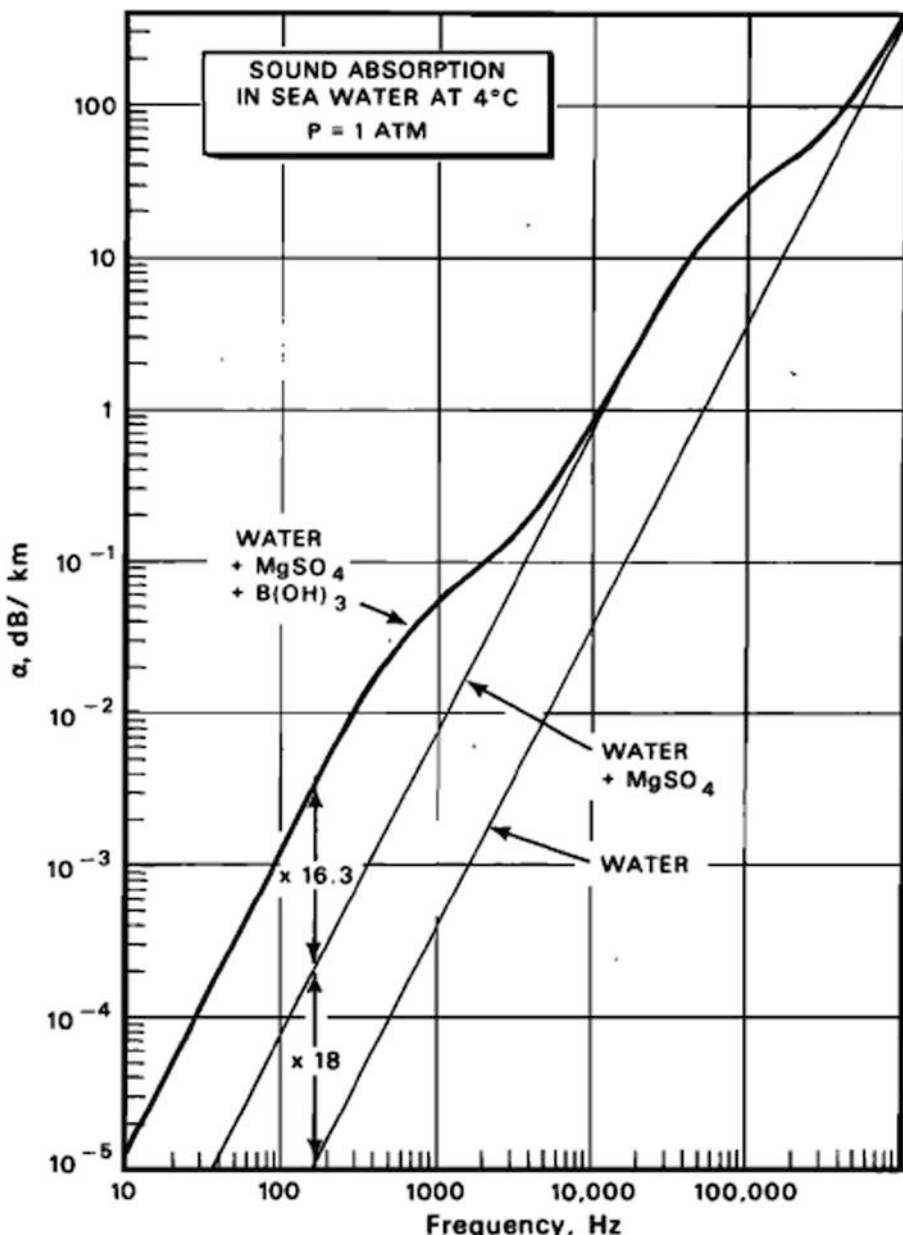


**Fig. 14.7** Attenuation of sound in “standard” seawater [26] with salinity of 3.5% and pH = 8.0 at 4 °C [18]. Below 1 MHz, relaxation attenuation due to association-dissociation of boric acid,  $\text{B}(\text{OH})_3$ , and magnesium sulfate,  $\text{MgSO}_4$ , dominates the “classical” contributions

The attenuation coefficient has the expected form, based on Eq. (14.40), and is plotted as a function of frequency in Fig. 14.7.

$$\frac{\alpha}{f^2} = \frac{A_{\text{B}(\text{OH})_3} f_{\text{B}(\text{OH})_3}}{f^2 + f_{\text{B}(\text{OH})_3}^2} + \frac{P_{\text{MgSO}_4} A_{\text{MgSO}_4} f_{\text{MgSO}_4}}{f^2 + f_{\text{MgSO}_4}^2} + A_o P_o \quad (14.45)$$

Approximate expressions for the coefficients representing the relaxation strengths,  $A$ , and pressure correction factors,  $P$ , are provided by Fisher and Simmons [18] with more accurate values provided by François and Garrison [24, 25].

## 14.6 Transmission Loss

The fact that the bulk attenuation of sound in fluids is quadratic in the frequency has important consequences for ultrasonics ( $f > 20$  kHz) and for long-range sound propagation. At the extremely low frequencies, infrasound in the Earth's atmosphere can propagate around the entire globe, and the sound of breaking waves generated by a storm on the Pacific coast of the United States has been detected by a low-frequency microphone at the Bureau of Standards in Washington, DC. An International Monitoring System with 60 infrasound monitoring stations has been deployed globally to detect violations of the Comprehensive Nuclear-Test-Ban Treaty [27].

### 14.6.1 Short and Very Short Wavelengths

As discussed in Sect. 12.8.1, the Rayleigh resolution criterion implies that the smallest feature that can be resolved in an ultrasonic image will be limited by the wavelength of the sound used to produce the image. Since many ultrasonic imaging systems are used in biomedical applications, we can assume a speed of sound in biological tissue that is approximately equal to the speed of sound in water,  $c_{\text{H}_2\text{O}} = 1500$  m/s [28]. To resolve an object that is about a millimeter would then require sound at a frequency,  $f = c/\lambda \cong 1.5$  MHz. At that frequency, the attenuation of sound in liver tissue is over 2 dB/cm, so a roundtrip transmission loss to go to a depth of 10 cm is 40 dB.

Because the speed of sound in liquids is typically 200,000 times slower than the speed of light, it is possible to achieve optical wavelength resolution of about  $5000 \text{ \AA} = 0.5 \mu\text{m}$  using sound at a frequency of 3 GHz. In addition, acoustical microscopy produces image “contrast” due to variation in the acoustic absorption of the specimens and scattering that arises from the acoustic impedance mismatch between the specimen and the surrounding material due density and compressibility differences (see Sects. 12.6.1 and 12.6.2). Such sources of contrast will reveal completely different information about a specimen than can be deduced due to changes in optical index of refraction or optical reflectance. In addition, sound can penetrate an optically opaque object, and staining is not required for contrast enhancement.<sup>7</sup>

As mentioned, acoustic microscopy is limited by the fact that attenuation is such a strong function of frequency. At 1.0 GHz, the attenuation of sound in water is 200 dB/mm [29]. Despite the high attenuation loss, acoustic microscopes can image red blood cells acoustically at 1.1 GHz with a resolution equivalent to an oil-immersion optical microscope at a magnification of 1000 [30]. Subcellular details as small as 0.1–0.2 μm (e.g., nuclei, nucleoli, mitochondria, and actin cables) have been resolved due to the extraordinary contrast that can differentiate various cytoplasmic organelles [31].

The greatest resolution that has been achieved using acoustical microscopy has been accomplished in superfluid helium at temperatures near absolute zero, which has a sound speed,  $c_I \cong 240$  m/s, a speed that is even lower than the speed of sound in air. Since the dynamics of liquid helium at temperatures below  $T_\lambda = 2.17$  K are determined by quantum mechanics, the attenuation mechanisms

<sup>7</sup> Encapsulated microbubbles are used occasionally to provide the ultrasonic image enhancement equivalent of “staining” in optical imaging.

are different than those for classical fluids, which also gives it a much smaller attenuation. At low temperatures,  $T < 0.5$  K, the phonon mean free path is controlled by scattering from “rotons,” which are quantized collective excitation of the superfluid [32]. Sound wavelengths in liquid helium shorter than  $2000 \text{ \AA} = 0.2 \mu\text{m}$ , in a non-imaging experiment, at frequencies of 1.0 GHz, had been studied before 1970 by Imai and Rudnick [33].

### 14.6.2 Very Long Wavelengths

At the opposite extreme, at much lower frequencies, the absorption can be quite small. Although the worldwide network of infrasound monitoring sites, using electronic pressure sensors and sophisticated signal processing, that is being used to assure compliance with the Comprehensive Nuclear-Test-Ban Treaty has already been mentioned [27], the most famous measurement of long-distance infrasound propagation was made using barometers.

On 27 August 1883, the island of Krakatoa, in Indonesia east of Java, was destroyed by an immense volcanic explosion. The resulting pressure wave was recorded for days afterward at more than 50 weather stations worldwide. Several of those stations recorded as many as seven passages of the wave as it circled the globe:

*“The barograph in Glasgow recorded seven passages: at 11 hours, 25 hours, 48 hours, 59 hours, 84 hours, 94 hours, and 121 hours (5 days) after the eruption.”* [34]

About 4 h after the explosion, the pressure pulse appeared on a barograph in Calcutta. In 6 h, the pulse reached Tokyo; in 10 h, Vienna; and in 15 h, New York. The period of the pulse was between 100 and 200 s corresponding to a fundamental frequency of about 7 mHz. Its propagation velocity was between 300 and 325 m/s [35]. Although that is close to the speed of sound in air near room temperature, the wave was similar to a shallow water gravity wave in which the height of the atmosphere rose and fell with the passage of the wave [36].

---

## 14.7 Quantum Mechanical Manifestations in Classical Mechanics

*“The major role of microscopic theory is to derive phenomenological theory.”* G. E. Uhlenbeck<sup>8</sup>

Although acoustics is justifiably identified as a field of classical phenomenology, there are many acoustical effects that have their origin in the microscopic theory of atoms and therefore manifest macroscopic behaviors that can only be explained in terms of quantum mechanics. The effects of these “hidden variables” have been manifest throughout this textbook starting with the damping of simple harmonic oscillators that connects the “system” to the environment, thus producing Brownian motion [37], which was related to the more general theory coupling fluctuations and dissipation [38] in Chap. 2.<sup>9</sup>

This theme recurred in Chap. 7 when the quantization of energy levels for molecular vibration and rotation influenced the specific heat of gases and in Chap. 9 where a simple kinetic theory of gases was used to determine the pressure and temperature variation of viscosity and thermal conductivity. Now we see in this chapter how structural relaxations in water [23], like those in Fig. 5.23 for the four

---

<sup>8</sup>George Eugène Uhlenbeck (1900–1988) was a Dutch theoretical physicist who, with fellow Dutchman, Samuel Goudsmit (1902–1978), first proposed quantized “spin” as the internal degree of freedom for electrons.

<sup>9</sup>Lars Onsager (1903–1976) was the Norwegian-born physical chemist and theoretical physicist who received the Nobel Prize in chemistry, in 1968, for the reciprocal relations between fluctuations and dissipation that are now referred to as “Onsager reciprocity.”

crystalline structures of plutonium [39], scattering of phonons and rotors in superfluids [32], or molecular vibrations in  $F_2$  [19] and collision times in gas mixtures [15], or chemical reactions [24, 25], manifest themselves in the attenuation of sound.

These internal relaxation effects have been incorporated into our phenomenological theory through the introduction of an additional dissipative process that has been quantified by the introduction of a frequency-dependent parameter,  $\zeta$ , that shares the same units with the coefficient of shear viscosity,  $\mu$ . That coincidence has led to this new parameter being called the coefficient of “bulk viscosity” (or sometimes “second viscosity”), even though it is independent of the shear deformation of the fluid and is not the source of momentum transport.

### Talk Like an Acoustician

Viscoelasticity	Mean free path
Viscous drag	Kinetic theory
Thermal relaxation	Einstein summation convention
Thermoviscous boundary layer	Bulk viscosity
Spatial attenuation coefficient	Second viscosity
Temporal attenuation coefficient	Le Châtelier’s principle
Shear strain	Nondimensional frequency
Hydrostatic strain	Vibrational relaxation time
Collision time	Structural relaxation
Enthalpy function	Association-dissociation reactions
Legendre transformation	Kramers-Kronig relations
Maxwell relations	
Relaxation time	

### Exercises

1. **Bulk attenuation and reverberation time.** An expression was provided in Eq. (13.29) to incorporate the attenuation in air contained within an enclosure into the expression for reverberation time. A “useful correlation” was provided in Eq. (13.30) that was applicable for  $1500 \text{ Hz} \leq f \leq 10,000 \text{ Hz}$  and for relative humidity in the range  $20\% \leq RH \leq 70\%$ .
  - (a) *Average frequency dependence.* Table 14.1 (left) provides the attenuation in dB/km from the ANSI/ASA standard for the frequencies within the range specified at  $20^\circ\text{C}$  for  $RH = 50\%$  [17]. Plot the  $\log_{10}$  of the spatial attenuation,  $\alpha$ , in  $\text{m}^{-1}$  vs. the  $\log_{10}$  of frequency,  $f$ , in kHz, to determine the power law dependence on frequency (see Sect. 1.9.3). Is your result proportional to  $f^{4.7}$  to within the statistical uncertainty of your least-squares fit? Keep in mind that attenuation expressed in [dB/m] must be multiplied by  $0.1151 \cong [10\log_{10}(e^2)]^{-1}$  to convert to  $\text{m}^{-1}$  (sometimes including the dimensionless “Nepers” to report results in Nepers/m).
  - (b) *Humidity dependence.* Table 14.1 (right) also includes the attenuation in dB/km at 4.0 kHz and  $20^\circ\text{C}$  for  $20\% \leq RH \leq 70\%$ . The “useful correlation” claims that the correction to frequency dependence for variations in relative humidity should be linear in  $(50\% / RH)$ . How close is that presumed humidity dependence to values in the table for variation in relative humidity at 4.0 kHz?
2. **The mother of all PA systems.** Shown in Fig. 14.8 is a loudspeaker that can produce 30,000 watts of acoustic power by modulating a pressurized air stream (like a siren) using a cylindrical “valve” mounted on a voice coil, like that used for an electrodynamic loudspeaker. That sound source, located at the apex of the horn, is called a “modulated airstream loudspeaker.” [40]

**Fig. 14.8** A very large horn loudspeaker mounted on an 18-wheel tractor-trailer. (Photo courtesy of Wiley Labs)



Such a public address system was developed to tell illiterate enemy combatants, in their native language, to put down their weapons and surrender from a distance that is greater than the distance that could be traversed by artillery shells. Although the bandwidth of telephone speech for very good intelligibility is generally 300 Hz to 3.4 kHz, for this problem, we will focus on the propagation of a 1 kHz pure tone. Since this system was deployed in desert terrain, assume that  $RH = 10\%$ ,  $T_m = +50^\circ\text{C} = 122^\circ\text{F}$ , and  $p_m = 100 \text{ kPa}$ .

- (a) *Sound level at 100 m.* Assuming hemispherical spreading and no sound absorption, what is the root-mean-square acoustic pressure amplitude if the source produces 30 kW of acoustic power and any nonlinear effects that might cause harmonic distortion (see Sect. 15.2.3) can be neglected? Also neglect any refractive effects due to sound speed gradients caused by temperature or wind as discussed in Sect. 11.3. Report your results as both in r.m.s. pressure amplitude and in dB re:  $20 \mu\text{Pa}_{\text{rms}}$ .
- (b) *Greater distances.* Repeat part *a*, but determine the sound pressure at 1.0 km and 3.0 km, again neglecting attenuation.
- (c) *Include attenuation.* Determine the spatial attenuation coefficient under these conditions at 1.0 kHz and use it to reduce the sound pressure at 0.1 km, 1.0 km, and 3.0 km below that obtained due only to hemispherical spreading.
3. **Pump wave attenuation for a parametric array.** The generation of highly directional sound beams from the nonlinear acoustical interaction of two colinear high-frequency sound beams will be discussed in Sect. 15.3.3. Calculate the exponential attenuation length,  $\ell = \alpha^{-1}$ , of a typical 40 kHz beam in dry air,  $RH = 0\%$ , and moist air with  $RH = 60\%$  using the graph in Fig. 14.5.
4. **Siren.** The siren shown in Fig. 14.9 consumed  $2500 \text{ ft}^3/\text{min}$  of air at a pressure of 5 psi above ambient to produce 50 horsepower of acoustic power at 500 Hz, and did so with 72% efficiency [41].
  - (a) *Hydraulic power.* How much time-averaged power,  $\langle \Pi_{hy} \rangle_t = (\Delta p) |U|$ , is available, in watts and in horsepower, from the specified volume flow rate,  $U$ , and the available pressure drop,  $\Delta p$ ?
  - (b) *Hemispherical spreading.* Assuming the mean temperature during the measurement was  $T_m = 20^\circ\text{C}$  and  $p_m = 100 \text{ kPa}$ , what would be the root-mean-square pressure a distance of

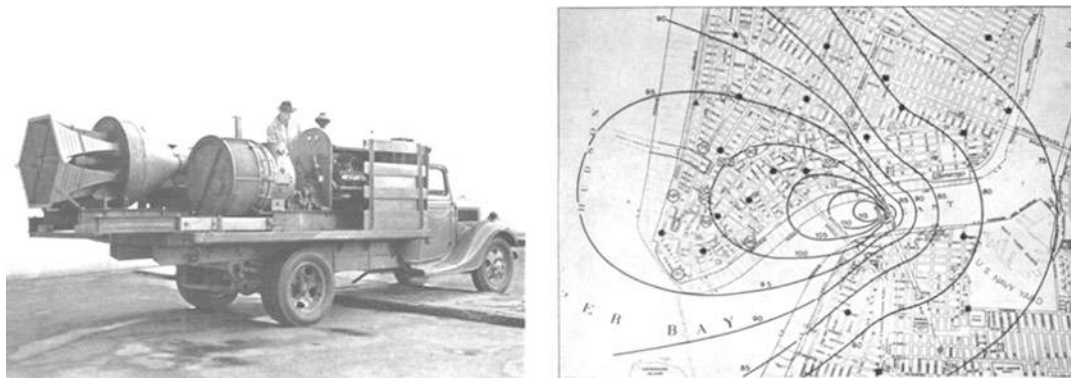


**Fig. 14.9** (Left) Photograph of a 50-horsepower siren and compressor mounted on a truck. The intake filter and compressor are on the near side, and the exponential horn is farther away. (Right) Equal loudness contours measured throughout lower Manhattan when the siren was placed on the Manhattan Bridge facing toward the Financial District. The siren's directivity index was 11.8 dB at 500 Hz (see Sect. 12.8.2) [41]

1000 ft. from the siren if it produced a sound power of 50 horsepower? Report your results both in pressure and dB re:  $20 \mu\text{Pa}_{\text{rms}}$ .

- (c) *Include attenuation.* If  $RH = 50\%$ , how much additional loss, in dB, would be produced by absorption at the same distance?
5. **The SOFAR channel.** One method for locating pilots who crash over the ocean is to drop an explosive sound source that is set to detonate at a depth that is equal to the axis of the deep sound channel that is created by a sound speed profile like the one shown in Fig. 11.8. In that figure, the axis of the sound channel is 1112 m below the ocean's surface. Sound that is trapped in that channel will spread cylindrically, rather than spherically, beyond a transition distance that will be assumed to be much shorter than the distance of interest, so the sound amplitude will decrease in proportion to  $\sqrt{R}$ , where  $R$  is the distance between the source and the receiver.
- (a) *Cylindrical spreading.* What would be the loss, in dB, due to cylindrical spreading over 5000 km relative to the level 1 km from the source?
  - (b) *Include attenuation.* Using the results for seawater in Fig. 14.7, what would be the spatial attenuation, in dB, that would have to multiply the cylindrical spreading loss over 5.0 km calculated in part (a) for sound with a frequency of 100 Hz? Repeat for the loss due to attenuation in seawater after 5000 km.
6. **High-frequency relaxational attenuation constant for air and water.**
- (a) *Limiting frequency dependence.* Using Eq. (14.40), show that for frequencies well above the highest relaxational frequency,  $f_R$ , the attenuation of sound is independent of frequency.
  - (b) *Relaxational attenuation constant (bulk viscosity) of air.* In Eq. (14.42), the measured high-frequency limit of the spatial attenuation constant in air is  $\alpha_{\text{air}}/f^2 = 1.84 \times 10^{-11} \text{ s}^2/\text{m}$ . Calculate  $\alpha_{\text{classical}}/f^2$  for air at atmospheric pressure and  $20^\circ\text{C}$ , and use both high-frequency results (i.e., with and without relaxation effects) to determine the value for  $\zeta_{\text{air}}$  in the high-frequency limit.
  - (c) *Relaxational attenuation constant (bulk viscosity) of pure water.* The measured high-frequency limit of the spatial attenuation constant in pure water at  $4^\circ\text{C}$  is  $\lim_{f \gg f_R} \alpha_{\text{H}_2\text{O}}/f^2 = 2.5 \times 10^{-14} \text{ s}^2/\text{m}$ . Based on  $\alpha_{\text{classical}}/f^2$  for pure water at atmospheric pressure and  $4^\circ\text{C}$ , determine the value for  $\zeta_{\text{H}_2\text{O}}$  in the high-frequency limit.

## References

1. M. Greenspan, Transmission of sound waves in gases at very low pressures, in *Physical Acoustics*, vol. 2A, (Academic Press, 1965), pp. 1–45
2. L.D. Landau, E.M. Lifshitz, *Fluid Mechanics*, 2nd edn (Butterworth-Heinemann, 1987). See §79; ISBN 0-7506-2767-0
3. H. Lamb, *Hydrodynamics*, 6th edn (Cambridge, 1932), reprinted (Dover, 1945). See §30; ISBN 0-486-60256-7
4. G.G. Stokes, On the theories of the internal friction of fluids in motion and the equilibrium and motion of elastic solids. *Philos. Trans. (Cambridge)* **8**, 287–302 (1845)
5. R. B. Lindsay, *Acoustics: Historical and Philosophical Development* (Dowden, Hutchinson & Ross, 1973). p. 261; ISBN 0-87933-015-5
6. M.J. Stefan, Über den Einfluss der inneren Reibung in der Luft auf die Schallbewegung. *Sitzber. Akad. Wiss. Wein* **53**, 526–537 (1866)
7. G. Krichhoff, Über den Einfluss der Warmeleitung in einen Gase auf die Schallbewegung. *Ann. Phys. Chem.* **134**, 177–193 (1868). English translation: On the influence of thermal conduction in a gas on sound propagation, in *Physical Acoustics*, ed. by R.B. Lindsay (Dowden, Hutchinson & Ross, 1974). pp. 7–19
8. A. Bejan, *Advanced Engineering Thermodynamics*, 2nd edn (Wiley, 1997). See §4.4; ISBN 0-471-14880-6
9. F. Reif, *Fundamentals of Statistical and Thermal Physics* (McGraw-Hill, 1965), See §5.5
10. *American Institute of Physics Handbook*, 3rd edn, ed. by D.W. Grey (McGraw-Hill, 1972). ISBN 07-001485-X
11. J.J. Markham, R.T. Beyer, R.B. Lindsay, Absorption of sound in fluids. *Rev. Mod. Phys.* **23**(4), 353–411 (1951). See Eq. (A-13)
12. H.E. Bass, L.C. Sutherland, A.J. Zuckerwar, D.T. Blackstock, D.M. Hester, Erratum: Atmospheric absorption of sound: Further developments. *J. Acoust. Soc. Am.* **97**, 680–683 (1995), *J. Acoust. Soc. Am.* **99**(2), 1259 (1996)
13. J.T.R. Watson, R.S. Basu, J.V. Sengers, An improved representative equation for the dynamic viscosity of water substance. *J. Phys. Chem. Ref. Prop.* **9**(4), 1255–1290 (1980)
14. J.M.M. Pinkerton, A pulse method for the measurement of ultrasonic absorption in liquid: Results for water. *Nature* **160**, 128–129 (1947)
15. M. Greenspan, Rotational relaxation in nitrogen, oxygen, and air. *J. Acoust. Soc. Am.* **31**(2), 155–160 (1959)
16. A.D. Pierce, *Acoustics: An Introduction to its Physical Principles and Applications*, 2nd edn (Acoustical Society of America, 1989). ISBN 0-88318-612-8, pp 554
17. R.J. Peppin, A. Scharine, *Methods for Calculation of the Absorption of Sound in the Atmosphere*, Am. Nat. Standard ANSI/ASA S1.26-2014. See §5.2.1
18. F.H. Fisher, V.P. Simmons, Sound absorption in sea water. *J. Acoust. Soc. Am.* **62**(3), 558–564 (1977)
19. F.D. Shields, Thermal relaxation in fluorine. *J. Acoust. Soc. Am.* **34**(3), 271–274 (1962)
20. F.D. Shields, R.T. Lagemann, Tube corrections in the study of sound absorption. *J. Acoust. Soc. Am.* **29**(4), 470–475 (1957)
21. H. E. Bass, L. C. Sutherland, A. J. Zuckerwar, D. T. Blackstock, and D. M. Hester, Atmospheric absorption of sound: Further developments. *J. Acoust. Soc. Am.* **97**(1), 680–683 (1995), as corrected in the erratum, *J. Acoust. Soc. Am.* **99**(2), 1259 (1996)
22. F.E. Fox, G.D. Rock, Compressional viscosity and sound absorption in water at different temperatures. *Phys. Rev.* **70** (1/2), 68–73 (1946)
23. L. Hall, The origin of ultrasonic absorption in water. *Phys. Rev.* **73**(7), 775–781 (1948)
24. R.E. François, G.R. Garrison, Sound absorption based on ocean measurements. Part I: Pure water and magnesium sulfate contributions. *J. Acoust. Soc. Am.* **72**(3), 896–907 (1982)
25. R.E. François, G.R. Garrison, Sound absorption based on ocean measurements: Part II – Boric acid contribution and equation for total absorption. *J. Acoust. Soc. Am.* **72**(6), 1879–1890 (1982)
26. J. Lyman, R.H. Fleming, Composition of sea water. *J. Mar. Res.* **3**, 134–146 (1940)
27. H.E. Bass, J. Bhattacharyya, M.A. Garcés, M. Hedlin, J.V. Olson, R.L. Woodward, Infrasound. *Acoust. Today* **2**(1), 9–19 (2006)
28. J.C. Bamber, Speed of sound, in *Principles of Medical Ultrasonics*, 2nd edn, ed. by C.R. Hill, J.C. Bamber, G.R. ter Haar (Wiley, 2005). See Fig. 5.3, pg. 178; ISBN 0-470-09396-X
29. R.A. Lemons, C.F. Quate, Acoustic microscopy: Biomedical application. *Science* **181**(4191), 905–911 (1975)
30. C.F. Quate, A. Atalar, H.K. Wickramasinghe, Acoustic microscopy with mechanical scanning – A review. *Proc. IEEE* **67**(8), 1092–1114 (1975)
31. R.A. Johnston, A. Atalar, J. Heiserman, V. Jipson, C.F. Quate, Acoustic microscopy: Resolution of subcellular detail. *Proc. Natl. Acad. Sci. U.S.A.* **76**(7), 3325–3329 (1979)
32. I.M. Khalatnikov, D.M. Chernikova, *Zh. Ekspерим. i Teor. Fiz.* **49**, 1957 (1965), **50**, 411 (1966). Translation: Sov. Phys.-JETP **22**, 1336 (1966), **23**, 274 (1966)
33. J.S. Imai, I. Rudnick, Ultrasonic attenuation in liquid helium at 1 GHz. *Phys. Rev. Lett.* **22**(14), 694–697 (1969)

34. G.J. Symons (ed.), *The Eruption of Krakatoa and Subsequent Phenomena*. Report of the Krakatoa Committee of the Royal Society (Trübner & Co., London, 1888)
35. T.B. Gabrielson, Krakatoa and the Royal Society: The Krakatoa explosion of 1883. *Acoust. Today* **6**(2), 14–18 (2010)
36. G.I. Taylor, Waves and tides in the atmosphere. *Proc. R. Soc. A* **126**(800), 169–183 (1929)
37. G.E. Uhlenbeck, S. Goudsmit, A problem in Brownian motion. *Phys. Rev.* **34**, 145–151 (1929)
38. C.W. McCombie, Fluctuation theory in physical measurements. *Rep. Prog. Phys.* **16**, 266–319 (1953)
39. Y. Suzuki, V.R. Fanelli, J.B. Betts, F.J. Freibert, C.H. Mielke, J.N. Mitchell, M. Ramos, T.A. Saleh, A. Migliori, Temperature dependence of elastic moduli of polycrystalline  $\beta$  plutonium. *Phys. Rev. B* **84**, 064105 (2011)
40. V. Salmon, J.C. Burgess, Modulated airstream loudspeaker. *J. Acoust. Soc. Am.* **29**, 767 (1957)
41. R.C. Jones, A fifty horsepower siren. *J. Acoust. Soc. Am.* **18**(2), 371–387 (1946)

**Open Access** This chapter is licensed under the terms of the Creative Commons Attribution 4.0 International License (<http://creativecommons.org/licenses/by/4.0/>), which permits use, sharing, adaptation, distribution and reproduction in any medium or format, as long as you give appropriate credit to the original author(s) and the source, provide a link to the Creative Commons license and indicate if changes were made.

The images or other third party material in this chapter are included in the chapter's Creative Commons license, unless indicated otherwise in a credit line to the material. If material is not included in the chapter's Creative Commons license and your intended use is not permitted by statutory regulation or exceeds the permitted use, you will need to obtain permission directly from the copyright holder.



---

**Part III**

**Extensions**



# Nonlinear Acoustics

15

## Contents

15.1	<b>Surf's Up</b>	703
15.1.1	The Grüneisen Parameter	705
15.1.2	The Virial Expansion and $B/2A$	707
15.1.3	Anomalous Distortion*	708
15.1.4	The Gol'dberg Number	711
15.1.5	Stable Sawtooth Waveform Attenuation	712
15.2	<b>Weak Shock Theory and Harmonic Distortion</b>	714
15.2.1	The Order Expansion	714
15.2.2	Trigonometric Expansion of the Earnshaw Solution	715
15.2.3	Higher Harmonic Generation	716
15.3	<b>The Phenomenological Model</b>	718
15.3.1	The (Nondissipative) Nonlinear Wave Equation	719
15.3.2	Geometrical Resonance (Phase Matching)	720
15.3.3	Intermodulation Distortion and the Parametric End-Fire Array	721
15.3.4	Resonant Mode Conversion	725
15.4	<b>Non-zero Time-Averaged Effects</b>	729
15.4.1	The Second-Order Pressure in an Adiabatic Compression	729
15.4.2	The Bernoulli Pressure	731
15.4.3	The Rayleigh Disk	733
15.4.4	Radiation Pressure	735
15.4.5	Acoustic Levitation in Standing Waves	736
15.4.6	Adiabatic Invariance and the Levitation Force	738
15.4.7	Levitation Superstability ("Acoustic Molasses")	743
15.5	<b>Beyond the Linear Approximation</b>	746
	<b>References</b>	751

The goal of this chapter is to raise awareness of the limitation of linear analysis, not to create professional expertise in nonlinear acoustics. A fundamental assumption of linear acoustics is that the presence of a wave does not have an effect on the properties of the medium through which it propagates. Under that assumption, two sound waves can be superimposed when they occupy the same space at the same time, but one wave will have no effect on the other wave and once they part company there will be no evidence of their previous interaction. This is illustrated in Fig. 15.1. By extension, the



**Fig. 15.1** Two wave packets pass through each other. (*Left*) The two wave packets are approaching each other. (*Center*) When those wave packets overlap, the disturbances superimpose. (*Right*) After their superposition, they continue their propagation with no evidence of their previous interaction

assumption of linearity also means that a waveform is stable since any individual wave does not interact with itself.<sup>1</sup>

We already know that this assumption of the wave having no influence on the properties of the propagation medium cannot be strictly correct. The wave imparts a small particle velocity,  $v_1$ , to the fluid that adds to the sound speed when that velocity is in the direction of propagation and subtracts from the sound speed when the particle velocity is opposite to the direction of propagation. The local value of the sound speed,  $c(x, t)$ , will vary in time and space due to the wave's convective contribution so that  $c_o + v_1(x, t) \geq c(x, t) \geq c_o - v_1(x, t)$ , where  $c_o$  is the equilibrium (thermodynamic) sound speed:  $c_o = \sqrt{(\partial p / \partial \rho)_s}$ .

The wave also modulates the medium's thermodynamic sound speed. For the case of an ideal gas undergoing adiabatic compressions and expansions, there is an accompanying temperature change of amplitude,  $T_1$ , given by Eq. (7.25), that is related to the amplitude of the pressure change,  $p_1(x, t)$ :  $(\partial T / \partial p)_s = [(\gamma - 1)/\gamma](T_m/p_m)$ . Since the sound speed in an ideal gas is dependent upon the temperature of the gas through Eq. (10.23), this implies that the change in sound speed,  $\delta c$ , due to a temperature change is given by  $(\delta c/c_o) = \gamma(T_1/T_m)$ . In an ideal gas, the local sound speed is slightly faster than  $c_o$  when the acoustic pressure is positive since the gas is warmer and slightly slower than  $c_o$  when the acoustic pressure is negative since the gas is cooler.

As will be demonstrated, these small modifications in the sound speed due to wave-induced fluid convection and to the wave's effect on sound speed through the equation of state can lead to interesting effects that could not be predicted within the limitations imposed by the assumption of linearity. Although their influence on the sound speed may be small, those effects are cumulative. These are called nonlinear effects because the magnitude of the nonlinearity's influence is related to the square of an individual wave's amplitude (*self-interaction*) or the product of the amplitudes of two interacting waves (*intermodulation distortion*).

An additional consequence of the inclusion of nonlinearity is that the time-average of an acoustically induced disturbance may not be zero. In the linear case, the measure of a wave's amplitude will be equally positive and negative around its undisturbed equilibrium value, so that the time-average of the wave's influence will be zero. When the hydrodynamic equations and the equation of state were linearized, the terms in those equations that were discarded could lead to non-zero time-averaged effects. For the linearized continuity equation, the  $\rho_1 v_1$  term was discarded since Eq. (8.19) demonstrated that it was smaller than the  $\rho_m v_1$  term for small values of the acoustic Mach number,  $M_{ac} \ll 1$ . A similar choice was made for the linearization of the Euler equation. The convective portion of the total derivative,  $(\vec{v}_1 \cdot \nabla) \vec{v}_1$ , was discarded when compared to  $\partial \vec{v}_1 / \partial t$  in Eq. (8.38) under the

<sup>1</sup> Although instability requires nonlinearity, nonlinearity does not necessarily always result in instability. Solitons are waveforms that remain stable due to the compensatory influences of nonlinearity and dispersion.

same assumption of small acoustic Mach number. To complete the overall linearization, the Taylor series expansion of the equation of state in Eq. (10.3) was truncated after the first-derivative term.

In this chapter we will recover some of the interesting acoustical phenomena that were lost to the linearization of the phenomenological equations that describe both the dynamics and the medium itself.

## 15.1 Surf's Up

When most people hear the term “wave,” it is likely that word will conjure mental images of surf breaking along a beach. (It is a most pleasant image!) The breaking of waves in shallow water is a dramatic nonlinear effect that is due to both the *convective nonlinearity* and the fact that the height of the wave modulates the propagation speed of a shallow-water gravity wave. The speed of a shallow-water gravity wave represents the competition between the water’s inertia and the restoring force of gravity. Figure 15.2 is a schematic representation of one cycle of such a wave on a fluid of equilibrium depth,  $h_o$ , with a peak wave height of magnitude  $|h_1| \ll h_o$ .

The assumption that the fluid is “shallow” implies that the mean depth of the fluid,  $h_o$ , is much smaller than the wavelength of the disturbance,  $\lambda$ .

$$h_1(x, t) = \Re e \left[ \hat{\mathbf{h}} e^{j(\omega t - kx)} \right] \quad (15.1)$$

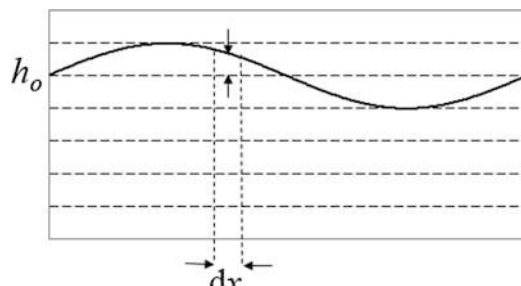
Since there is a free surface, we will assume that the fluid is incompressible. It is much more favorable (energetically) for the free surface to move up than it is for a pressure increase to increase the fluid’s density. The continuity equation can be written by recognizing that the rate-of-change of the fluid’s height,  $\dot{h}_1(x, t)$ , is determined by the difference in the amount of fluid that enters and leaves a “slab” of infinitesimal thickness,  $dx$ , shown in Fig. 15.2.

$$\frac{\partial h}{\partial t} + h_o \frac{\partial v_x}{\partial x} = 0 \quad \Rightarrow \quad \dot{h}_1 = jkh_o v_x \quad \Rightarrow \quad \left| \frac{\dot{h}_1}{v_x} \right| = \frac{2\pi h_o}{\lambda} \quad (15.2)$$

For a shallow-water gravity wave, the fluid’s particle velocity in the direction of propagation,  $v_x$ , is greater than the rate-of-change of height of the free surface if  $h_o \ll \lambda$ . This is an effect most of us have experienced while frolicking in the surf near the ocean’s shore—it is usually the “surge” that knocks us over, not  $\dot{h}_1$ .

Since gravity (not compressibility) provides the restoring force, Euler’s Eq. (7.34) relates the fluid’s velocity in the direction of propagation,  $v_x$ , to the gravitational pressure gradient.

**Fig. 15.2** Schematic representation of a sinusoidal disturbance on the free surface of a liquid that has a mean depth,  $h_o$ . The wave on the surface has an amplitude,  $|h_1| \ll h_o$ , but with a wavelength  $\lambda \gg h_o$



$$\frac{\partial v_x}{\partial t} = -\frac{1}{\rho} \frac{\partial(\rho g h_1)}{\partial x} = -g \frac{\partial h_1}{\partial x} \quad (15.3)$$

The combination of Eqs. (15.2) and (15.3), with the assumption of a rightward traveling wave in Eq. (15.1), leads to a dispersion relation that generates the equilibrium values for propagation speed,  $c_{grav}$ , of a shallow-water gravity wave.<sup>2</sup>

$$\begin{vmatrix} +j\omega & -jh_o k \\ -jgk & +j\omega \end{vmatrix} = 0 \Rightarrow c_{grav} = \frac{\omega}{k} = \sqrt{gh_o} \text{ for } kh_o \ll 1 \quad (15.4)$$

Logarithmic differentiation of Eq. (15.4) provides the relationship between the local wave speed and the instantaneous depth of the fluid.

$$\frac{\delta c_{grav}}{c_{grav}} = \frac{1}{2} \frac{\delta h}{h_o} \Rightarrow \frac{\partial c_{grav}}{\partial h} = \frac{1}{2} \frac{c_{grav}}{h_o} \quad (15.5)$$

We would like to combine the effects of changing depth on the sound speed with the convective contribution to the local sound speed produced by  $v_x$ . The continuity Eq. (15.2) provides that necessary conversion.

$$j\omega h_1 = jkh_o v_x \Rightarrow \frac{h_1}{h_o} = \frac{v_x}{c_{grav}} \equiv M_{ac} \Rightarrow \frac{\partial h}{\partial v_x} = \frac{h_o}{c_{grav}} \quad (15.6)$$

The convective contribution to the local wave speed,  $c(v_x)$ , can be combined with the change in local wave speed due to the changing fluid depth.

$$c(v_x) = c_{grav} + v_x + \left( \frac{\partial c_{grav}}{\partial h} \right) \left( \frac{\partial h}{\partial v_x} \right) v_x = c_{grav} + \frac{3v_x}{2} \quad (15.7)$$

Both convection and the speed's change with depth conspire to increase the local wave speed when  $h_1(x, t) > 0$  and reduce the local wave speed when  $h_1(x, t) < 0$ . The wave's crests travel faster than the zero-crossings (i.e.,  $h_1(x, t) = 0$ ) and its troughs travel slower than the zero-crossings. Figure 15.3 shows the cumulative consequences of the wave's influence on its own local propagation speed. As the wave progresses, the crests will start to overtake the troughs.

In Fig. 15.3, the coordinate system was chosen to move with the equilibrium wave speed,  $c_{grav}$ , so that the distortion becomes evident. At the instant captured in Fig. 15.3, the slope of the zero-crossing has become vertical. To reach that condition, the crest of a sinusoidal waveform must have advanced by one radian length toward the zero-crossing,  $k^{-1} = \lambda/2\pi$  (see Prob. 1), and the trough must have lagged behind by the same amount. The time,  $T_S$ , it takes for the crest to advance by  $k^{-1}$  is given by the speed excess,  $3v_x/2$ , calculated in Eq. (15.7). The distance traveled by the wave once the slope first becomes infinite is known as the *shock inception distance*,  $D_S$ .

---

<sup>2</sup> The exact result for the propagation speed at all depths reduces to  $c_{grav}$  in Eq. (15.4) in the limit that  $kh_o \rightarrow 0$ . Since this result depends upon  $k$ , it is dispersive, so the phase speed,  $c_{grav}$ , will not be equal to the group speed except in the “shallow water”  $kh_o \rightarrow 0$  limit.

$$c_{grav} = \frac{\omega}{k} = \sqrt{\frac{g}{k} \tanh kh_o}$$

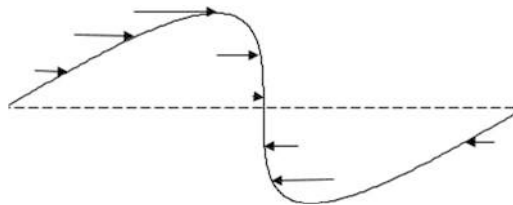


**Fig. 15.3** The local propagation speed of a shallow-water gravity wave depends upon the amplitude,  $|\hat{\mathbf{h}}| \equiv h_1$ , of the wave. As shown by arrows, an initially sinusoidal wave will change shape because the crests are moving faster than the troughs. As shown, this distortion has made the slope at the zero-crossing infinite

$$D_S = c_{grav} T_S = c_{grav} \frac{\lambda/2\pi}{3v_x/2} = \frac{\lambda}{3\pi M_{ac}} \quad (15.8)$$

For surf, the wave can continue beyond  $D_S$ . Since surf has free surface,  $h_1$  can actually become multivalued and will eventually “break,” sometimes with a spectacularly powerful display of sound and foaminess. Stokes was the first to recognize in 1848 that viscosity is the physical mechanism that prevents a sound wave from becoming multivalued. Stokes was also the first to draw a distorted waveform, like the one in Fig. 15.3, which he did in that same paper where he talked about the essential role of viscosity<sup>3</sup> [1].

### 15.1.1 The Grüneisen Parameter

The principles introduced to describe waveform distortion and the creation of a shock front for shallow-water gravity waves are common to all sound waves in fluids. A sound wave will influence the propagation speed of the medium due to a combination of the convective contribution and the fact that the wave’s amplitude also influences the propagation speed. Of course, the nature of that contribution and the relative importance of the convective and equation of state contributions will be differ depending upon the medium. The convenience of representing both contributions in terms of the local fluid particle velocity was demonstrated in the analysis of surf that produced Eq. (15.7). The strength of nonlinear distortion in any medium that supports a plane progressive wave will now be generalized by the introduction of the *Grüneisen parameter*,  $\Gamma$ .

$$c(v) = c_o + \left[ 1 + \frac{\partial c}{\partial y} \frac{\partial y}{\partial v} \right] v \equiv c_o + \Gamma v \quad \text{and} \quad D_S = \frac{\lambda}{2\pi\Gamma M_{ac}} \quad (15.9)$$

The Grüneisen parameter is a designation taken from solid-state physics where it represents the nonlinearity of a solid’s elasticity that is responsible for the non-zero value of a solid’s thermal expansion coefficient.<sup>4</sup> The reader should be cautioned that calling this nonlinear distortion parameter

<sup>3</sup> An excellent history of the early development of nonlinear acoustics is provided by D. T. Blackstock, “History of Nonlinear Acoustics: 1750s–1930s,” as Chap. 1 in *Nonlinear Acoustics*, 2nd ed. (Acoust. Soc. Am., 2008), M. F. Hamilton and D. T. Blackstock, editors; ISBN 0-9-744,067-5-9.

<sup>4</sup> If the elastic potential of a solid depended on only the parabolic potential energy contribution (see Sect. 1.2.1), then as a solid heated up, the amplitude of the motion of the point particles (molecules) would increase, but their equilibrium position would remain unchanged. If there is a cubic contribution to the interparticle potential energy, then as the amplitude of the molecular vibrations increased (with increasing temperature), the equilibrium position would shift causing thermal expansion or contraction of the solid.

the “Grüneisen parameter” and designating it as  $\Gamma$  is not a common choice in other treatments of nonlinear acoustics. For example, in a recent paper by Hamilton [2],  $\Gamma$  represents the Gol'dberg number that is abbreviated as  $G$  in this textbook (see Sect. 15.1.4). In Eq. (15.9), the general amplitude variable is simply written as “ $y$ ,” and the equilibrium sound speed is designated  $c_o$  to distinguish it from the local amplitude-dependent sound speed,  $c(v) = c_o + \Gamma v$ .

If a medium’s sound speed depended upon the density of the medium,  $\rho$ , which obeyed the linear continuity equation, the Grüneisen parameter would be expressed in terms of the sound speed’s variation with density.

$$\frac{\partial \rho}{\partial t} + \nabla \cdot (\rho v) = 0 \quad \Rightarrow \quad \frac{\rho_1}{\rho_m} = \frac{v_1}{c_o} \quad \Rightarrow \quad \Gamma = 1 + \frac{\partial c}{\partial \rho} \frac{\partial \rho}{\partial v} = 1 + \frac{\rho_m}{c_o} \frac{\partial c}{\partial \rho} \quad (15.10)$$

For an ideal gas, the sound speed depends upon the mean absolute temperature,  $T_m$ . As before,  $\delta c$  represents the change in the sound speed due to the change in local temperature.

$$c_o^2 = \frac{\gamma \mathfrak{R} T_m}{M} \quad \Rightarrow \quad \frac{\delta c}{c_o} = \frac{1}{2} \frac{T_1}{T_m} \quad \Rightarrow \quad \left( \frac{\partial c}{\partial T} \right)_s = \frac{1}{2} \frac{c_o}{T_m} \quad (15.11)$$

The Grüneisen parameter for an ideal gas can be expressed in terms of the change in the speed of sound with temperature, the change in temperature with pressure, and the particle velocity amplitude,  $v_1$ , associated with the acoustic pressure amplitude,  $p_1$ , as related by the Euler equation for progressive plane wave propagation:  $p_1 = (\rho_m c_o) v_1$ .

$$c(v) = c_o + v_1 + \left( \frac{\partial c}{\partial T} \right)_s \left( \frac{\partial T}{\partial p} \right)_s \left( \frac{\partial p}{\partial v} \right)_s v_1 \quad (15.12)$$

Using the relationship between temperature and pressure for an adiabatic sound wave in Eq. (7.25), the Grüneisen parameter for an ideal gas can be calculated.

$$\Gamma_{gas} = \left( 1 + \frac{\gamma - 1}{2} \right) = \frac{1 + \gamma}{2} \quad (15.13)$$

For noble gases,  $\gamma = 5/3$  so  $\Gamma = 4/3$ . For diatomic gases and primarily diatomic gas mixtures like air,  $\gamma = 7/5$ , so  $\Gamma_{air} = 6/5$ . In both cases, it is the convective contribution that is most significant contributor for nonlinear distortion in a gas.

To start developing intuition regarding the formation of a shock wave, consider a sound wave in air that has an amplitude at the “threshold of feeling,” 120 dB<sub>SPL</sub>, so  $p_1 = 28$  Pa. If the frequency of the sound wave is 1.0 kHz and the mean gas pressure is 100 kPa, then the acoustic Mach number for such a loud sound can be evaluated using the Euler equation.

$$M_{ac} = \frac{v_1}{c_o} = \frac{p_1}{\rho_m c_o^2} = \frac{p_1}{\gamma p_m} = 2 \times 10^{-4} = 200 \text{ ppm} \quad (15.14)$$

When such a wave propagates down a duct of constant cross-section, the shock inception distance,  $D_S$ , can be expressed in terms of the wavelength of sound using Eq. (15.9).

$$D_S = \frac{\lambda}{2\pi \Gamma_{air} M_{ac}} = \frac{5\lambda}{12\pi M_{ac}} \cong 460 \text{ m} \quad (15.15)$$

At ten times that amplitude (140 dB<sub>SPL</sub>, the “threshold of pain”) and for a frequency of 10 kHz, the shock inception distance would be 4.6 m. In the throat of the horn, for a horn-loaded compression driver [3] or in a brass musical instrument (e.g., trumpet or trombone), the amplitude can be still larger by a factor of ten [4].

### 15.1.2 The Virial Expansion and $B/A$

For the characterization of nonlinear behavior of sound waves in liquids, it is common to expand the equation of state in a Taylor series, known as a *virial expansion*, in powers of the relative deviation of the density from its equilibrium value,  $(\delta\rho/\rho_m) = (\rho - \rho_m)/\rho_m$ .

$$p = p_m + A \left( \frac{\delta\rho}{\rho_m} \right) + \frac{B}{2!} \left( \frac{\delta\rho}{\rho_m} \right)^2 + \frac{C}{3!} \left( \frac{\delta\rho}{\rho_m} \right)^3 + \dots \quad (15.16)$$

The coefficients in that expansion,  $A$ ,  $B$ ,  $C$ , etc. are called the virial coefficients and have the units of pressure. For an adiabatic process, they can be expressed in terms of progressively higher-order thermodynamic derivatives of pressure with respect to density.

$$A = \rho_m \left( \frac{\partial p}{\partial \rho} \right)_{s,\rho_m} = \rho_m c_o^2 \quad (15.17)$$

$$\begin{aligned} B &= \rho_m^2 \left( \frac{\partial^2 p}{\partial \rho^2} \right)_{s,\rho_m} = \rho_m^2 \left( \frac{\partial c^2}{\partial \rho} \right)_{s,\rho_m} = 2\rho_m^2 c_o^3 \left( \frac{\partial c}{\partial p} \right)_{s,\rho_m} \\ \text{or } \frac{B}{A} &= 2\rho_m c_o \left( \frac{\partial c}{\partial p} \right)_{s,\rho_m} = 2\rho_m c_o \left( \frac{\partial c}{\partial p} \right)_{T,\rho_m} + \frac{2\beta_p T_m c_o}{\rho_m c_P} \left( \frac{\partial c}{\partial T} \right)_{p_m,\rho_m} \end{aligned} \quad (15.18)$$

It is useful to notice that  $B$  can be expressed in terms of the derivative of the sound speed with respect to density, which was related to the non-convective contribution to the Grüneisen parameter in Eq. (15.10). The final form for  $B/A$  follows from the expansion of the sound speed derivative with respect to pressure,  $(\partial c/\partial p)_s = (\partial c/\partial p)_T + (\partial T/\partial p)_s (\partial c/\partial T)_p$ , and temperature,  $(\partial p/\partial T)_s = (\partial \rho^{-1}/\partial s)_p = (\partial \rho^{-1}/\partial T)_p / (\partial s/\partial T)_p$ , along with the introduction of the isobaric coefficient of thermal expansion,  $\beta_p = (1/V)(\partial V/\partial T)_p = \rho_m(\partial \rho^{-1}/\partial T)_p$ , and the introduction of the specific heat at constant pressure,  $c_P = (1/T_m)(\partial s/\partial T)_p$  [5].

$$C = \rho_m^3 \left( \frac{\partial^3 p}{\partial \rho^2} \right)_{s,\rho_m} \quad \text{or} \quad \frac{C}{A} = \frac{3}{2} \left( \frac{B}{A} \right)^2 + 2\rho_m^2 c_o^3 \left( \frac{\partial^2 c}{\partial p^2} \right)_{s,\rho_m} \quad (15.19)$$

The sound speed can also be expressed in terms of these virial coefficients [6].

$$\frac{c^2}{c_o^2} = \frac{1}{c_o^2} \left( \frac{\partial p}{\partial \rho} \right)_{s,\rho_m} = 1 + \frac{B}{A} \left( \frac{\delta\rho}{\rho_m} \right) + \frac{C}{2A} \left( \frac{\delta\rho}{\rho_m} \right)^2 + \dots \quad (15.20)$$

This result allows the Grüneisen parameter for liquids to be expressed in terms of  $B/A$ .

$$\Gamma = 1 + \frac{B}{2A} \quad (15.21)$$

Some representative values of  $B/A$  for different substances is provided in Table 15.1. The values of  $B/A$  for liquids are generally greater than 2.0, which means that it is the equation of state's nonlinearity that dominates the convective nonlinearity. This is reasonable since Euler's equation implies that the particle velocity in a liquid is much less than that of a gas for equal pressure changes:  $(\rho_m c)_{liquid} \gg (\rho_m c)_{gas}$ .

**Table 15.1** Some representative values of  $B/A$  for different media [7]

Material	$T [{}^{\circ}\text{C}]$	$B/A$
Monatomic gases (e.g., He, Ne, Ar, Kr, Xe, Rn)		0.667
Diatomeric gases (e.g., O <sub>2</sub> , N <sub>2</sub> , HCl)		0.40
Distilled water	0	4.2
	20	4.985 ± 0.063
	30	5.18 ± 0.033
	40	5.4
	60	5.7
Sea water (3.5% NaCl)	20	5.25
Saturated marine sediment	20	12–19
Isotonic saline	20	5.540 ± 0.032
Ethanol	20	10.52
Methanol	20	9.42
Acetone	20	9.23
Glycerol (4% in H <sub>2</sub> O)	25	8.58 ± 0.34
Ethylene glycol	25	9.88 ± 0.40
Carbon tetrachloride	25	7.85 ± 0.31
Liquid argon	-183.2	5.67
Liquid nitrogen	-195.8	6.6
Liquid helium	-271.4	4.5
Mercury	30	7.8
Sodium	110	2.7
Bovine serum albumin (20 g/100 mL H <sub>2</sub> O)	25	6.23 ± 0.25
Bovine serum albumin (38.8 g/100 mL H <sub>2</sub> O)	30	6.68
Bovine whole blood	26	5.5
Bovine milk	26	5.1
Bovine liver	23	7.5–8.0
Bovine heart	30	5.5

### 15.1.3 Anomalous Distortion\*

Before moving on, it is interesting to consider the role that a non-zero value of  $C$  implies for the formation of shock waves. The behavior that is represented by the Grüneisen parameter causes the sound speed to be increased when the amplitude of the wave is positive and decrease when the amplitude is negative. The  $C$  coefficient makes a contribution that either always increases the sound speed, irrespective of the sign of the wave's amplitude, or always decreases the sound speed, depending upon the sign of  $C$ .

Cormack and Hamilton have investigated shear waves with a cubic nonlinearity,  $C \neq 0$ , using numerical simulations [8]. Figure 15.4 shows two plane waveforms that were initially sinusoidal (dotted lines) that have produced both leading- and trailing-edge shocks (solid lines); two shock fronts per wavelength, unlike Figs. 15.3 and 15.7, where only a quadratic nonlinearity was operative (e.g.,  $1 + B/2A \neq 0$  but  $C/A = 0$ ).

A situation where both the quadratic and cubic nonlinearity play a role in superfluid helium sound propagation near absolute zero was identified for shockwave formation of compressional plane waves where the superfluid component velocity,  $v_s$ , is non-zero, but the (viscous) normal fluid is immobilized,  $v_n = 0$ . That sound wave mode in superfluids is known as 4<sup>th</sup> sound (see Fig. 15.5). This creates a superfluid critical acoustic velocity amplitude,  $v_d$ , which can be defined in terms of the virial

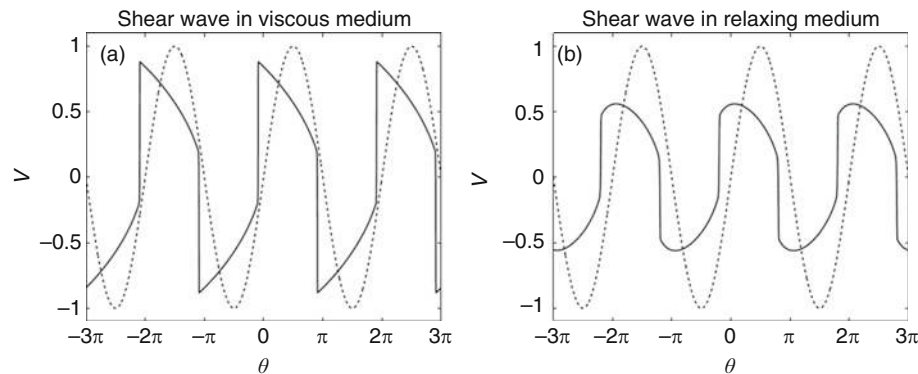
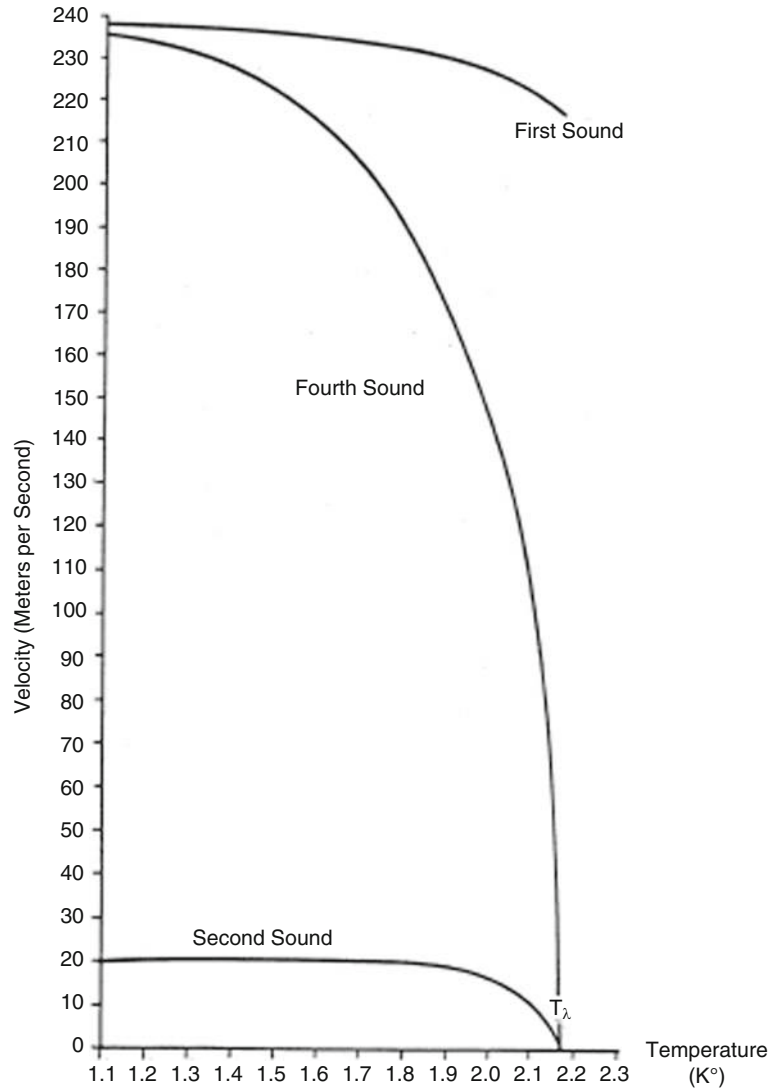


**Fig. 15.4** Waveforms for an initially sinusoidal plane shear wave (dotted lines) in a medium that is dominated by a cubic nonlinearity disturbance far from the sound source with  $C < 0$ . (From [8])

**Fig. 15.5** There are two different sound speeds in liquid  ${}^4\text{He}$  below the superfluid transition temperature,  $T_\lambda \cong 2.14 \text{ K}$ , at saturated vapor pressure. The ordinary bulk compressional wave speed, known as “first sound,” is fairly constant. The speed of thermal waves, called “second sound,” is generally an order of magnitude less than first sound and is a strong function of temperature, vanishing above the superfluid transition temperature,  $T_\lambda$ . Fourth sound is a compressional sound wave in a porous medium that immobilizes the normal fluid so that only the superfluid can oscillate



coefficients, to be the velocity amplitude where the contribution made by the wave distortion due to the  $(B/A)$  term is equal to the influence of  $C/A$  [9].

$$\frac{v_d}{c_o} = \frac{4 + 2(B/A)}{(C/A) + (B/A)[1 - (B/A)]} \quad (15.22)$$

For negative values of  $C$ , the wave is slowed whether the amplitude of the wave is positive or negative.

This double-shock behavior, caused by  $C \neq 0$ , is rather rare for compressional waves. Using values for  $(B/A)$  and  $(C/A)$  for water [10],  $v_d = 1.2c_o$ , corresponding to acoustic pressure swings of 26,000 atmospheres, well over 100 times greater than the highest cavitation threshold ever measured for pure water [11]. This double-shock behavior has been observed for sound propagating through a liquid near its critical point [12].

In an ideal gas, the virial expansion can be expressed in terms of the ratio of specific heats,  $\gamma = c_P / c_V$ , also known as the polytropic coefficient.

$$\frac{p}{p_m} = 1 + \gamma \left( \frac{\delta\rho}{\rho_m} \right) + \frac{\gamma(\gamma-1)}{2} \left( \frac{\delta\rho}{\rho_m} \right)^2 + \frac{\gamma(\gamma-1)(\gamma-2)}{6} \left( \frac{\delta\rho}{\rho_m} \right)^3 + \dots \quad (15.23)$$

For an ideal gas,  $(B/A) = (\gamma-1)$  and  $(C/A) = (\gamma-1)(\gamma-2)$  so the denominator of Eq. (15.22) vanishes making  $v_d/c_o = \infty$ ; double shocks are an impossibility in gases.

Two other unusual results for the Grüneisen parameter arise from the propagation of sound in superfluid helium [13]. Superfluids are analogous to superconductors in that superfluids can flow without viscosity, just like electrical currents flowing without electrical resistance in superconductors. In addition, the superfluid component has both an elastic and a thermal “restoring force” [14]. In superfluid helium, there is a thermal sound mode, known as *second sound*, that is propagating, not diffusive, like the response governed by the Fourier heat diffusion Eq. (9.4) for classical liquids (see Sect. 9.3.1).<sup>5</sup> The temperature dependence of both second sound and the ordinary compressional wave speed (called first sound) are plotted in Fig. 15.5.

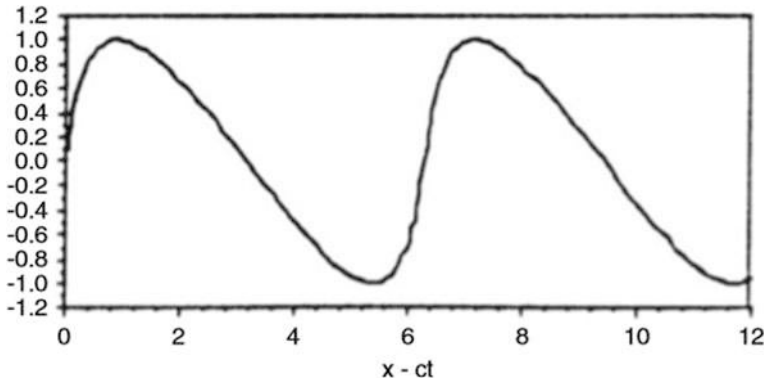
It is clear from the speed of second sound vs. temperature that there is a region where the second sound speed decreases with increasing temperature, behavior that is opposite to that of an ideal gas in Eq. (15.11). In that case, the convective contribution to the nonlinearity is opposite to the equation of state’s contribution. At  $T = 1.884$  K, the two contributions cancel each other, and a large amplitude second sound wave can propagate without distortion [15].

A final anomalous example is provided by third sound in superfluid helium. Because the superfluid can flow without resistance, sound waves can propagate in adsorbed films as thin as two atomic layers of helium.<sup>6</sup> In very thin films, the dominant restoring force is the van der Waals attraction which varies inversely with the fourth power of the distance:  $f = \alpha/h^4$ . Substituting the van der Waals force for the gravitational force in Eq. (15.4) and providing a correction for the thickness-averaged mass density of the superfluid component,  $\langle \rho_s \rangle$ , unlike the surf, the speed of third sound,  $c_3$ , is inversely proportional to the film thickness,  $h_o$ .

<sup>5</sup> In 1962, Lev Landau won the Nobel Prize in Physics for his prediction of the temperature dependence of second sound using his two-fluid theory of superfluid hydrodynamics after the speed of second sound was first measured by Pyotr Kapitza. Kapitza won the Nobel Prize in Physics in 1978 for his measurement of the speed of second sound in superfluid helium.

<sup>6</sup> Prof. I. Rudnick has pointed out that superfluids are interesting because they obey the laws of hydrodynamics on the microscopic scale and obey the laws of quantum mechanics on the macroscopic scale.

**Fig. 15.6** Very thin films of superfluid helium can support surface waves that are restored by the van der Waals attraction between the fluid and the substrate on which the fluid is adsorbed. For films less than  $10 \text{ \AA}$  thick (about three atomic layers), the troughs travel faster than the crests, and the wave bends backward



$$c_3 = \sqrt{\frac{\langle \rho_s \rangle}{\rho} f h_o} = \sqrt{\frac{\langle \rho_s \rangle}{\rho} \frac{3\alpha}{h_o^3}} \quad (15.24)$$

For superfluid films that are less than  $10 \text{ \AA} = 10^{-9} \text{ m}$  thick or about three atomic layers of helium, the equation of state produces troughs that travel faster than the crests so the waves distort backward, as shown in Fig. 15.6, compared to ordinary distortion shown in Fig. 15.3.

### 15.1.4 The Gol'dberg Number

A wave of arbitrary amplitude will not necessarily form a shock. If the sound is attenuated, then the amplitude will decrease with distance, and the tendency to distort will be reduced, since the distortion is amplitude dependent. A dimensionless metric, known as the *Gol'dberg number*,  $G$ , compares the shock inception distance,  $D_S$ , to the exponential attenuation length,  $\ell = \alpha^{-1}$ , where  $\alpha$  is the amplitude exponential attenuation constant that was examined in Chap. 14 [16].

$$G = \frac{\ell}{D_S} = (\alpha D_S)^{-1} \quad (15.25)$$

As an example, the Gol'dberg number can be evaluated for a 2 kHz sound wave with pressure amplitude of  $|\hat{p}| = 900 \text{ Pa}$  (150 dB re:  $20 \mu\text{Pa}_{\text{rms}}$ ) in dry air that propagates down a cylindrical waveguide with an inside diameter of 10.0 cm. For dry air at mean pressure,  $p_m = 100 \text{ kPa}$  and  $T_m = 23^\circ\text{C}$ ,  $c_o = 345 \text{ m/s}$  with  $\delta_\nu = 50 \mu\text{m}$  and  $\delta_\kappa = 59 \mu\text{m}$ . Using Eq. (15.15), with  $M_{ac} = |\hat{p}|/\gamma p_m = 0.64\%$  and  $\lambda = 17.3 \text{ cm}$ ,  $D_S = 3.6 \text{ m}$ . Using Eq. (13.78), the attenuation length in that waveguide is  $\ell = \alpha_{\nu}^{-1} = 20.6 \text{ m}$ . The Gol'dberg number, given in Eq. (15.25), is  $G = 5.7 > 1$ . In this example, the wave will shock before the wave of that initial amplitude suffers sufficient attenuation.

For an initially sinusoidal plane wave in free space, far from any solid boundaries (i.e., not confined within a 10 cm diameter waveguide!), the attenuation length due to classical thermoviscous dissipation, including “bulk viscosity,” at 2 kHz in dry air at one atmosphere would be about 1.2 dB/km  $\cong 1.4 \times 10^{-4} \text{ m}$  (see Fig. 14.5), resulting in an exponential attenuation distance of about 7 km making  $G \cong 200$ . For a plane wave in free space with  $G = 5.7$ , there would be significant distortion, but a fully developed sawtooth shock would not be created. This is because the classical attenuation coefficient is proportional to frequency squared (see Sect. 14.3), so the attenuation of the second harmonic is four times that of the fundamental, rather than just  $\sqrt{2}$  larger for the waveguide, where the attenuation depends upon the square root of the frequency. Mark Hamilton has provided numerical

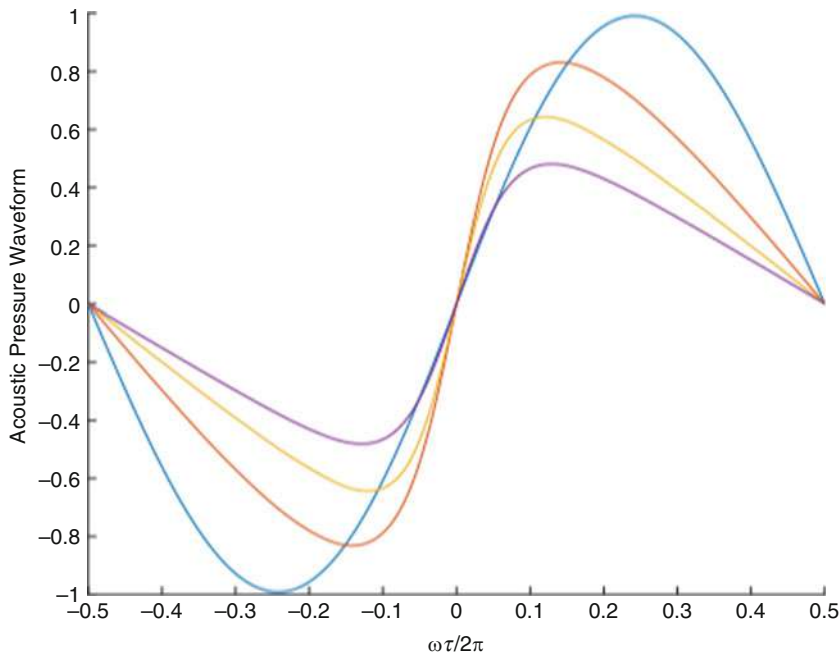


**Fig. 15.7** Numerical simulation of an initially sinusoidal plane wave in free space with Gol'dberg number,  $G = 5.7$ , is shown as the blue sinusoid. As the wave progresses, nonlinear effects cause it to distort, and classical attenuation mechanisms reduce its amplitude. A sawtooth waveform, shown in Fig. 15.8, is not produced. (Figure courtesy of Mark Hamilton)

simulations of the waveforms of such a plane progressive wave in free space for  $G = 5.7$  that are shown in Fig. 15.7.

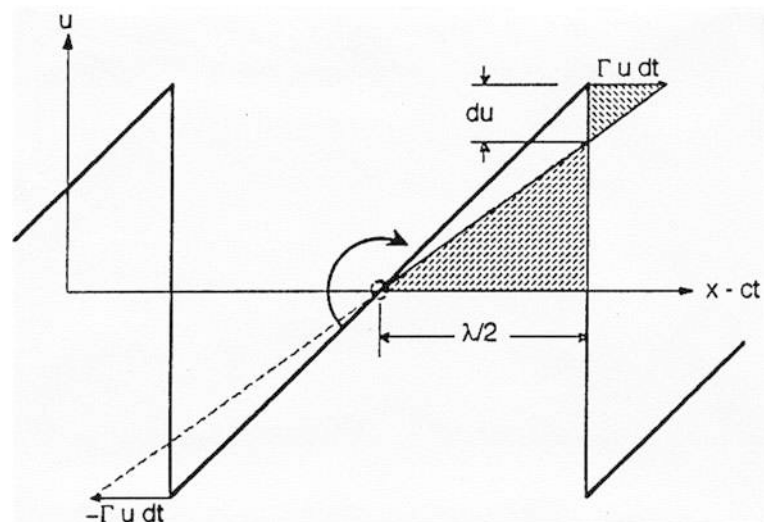
The Gol'dberg number is a dimensionless measure of the importance of nonlinearity relative to dissipation. In some circumstance, dissipation can be entirely ignored. For deepwater gravity waves, the primary source of dissipation is viscosity, and the Gol'dberg number is on the order of one million [17].

### 15.1.5 Stable Sawtooth Waveform Attenuation

For large values of the Gol'dberg number, an initially sinusoidal sound wave propagating in one dimension (i.e., ignoring spherical spreading) will steepen and ultimately become a repeated sawtooth waveform. At sufficiently high Gol'dberg numbers, even spherically spreading waveforms that are initially sinusoidal can form shocks [2]. In fact, any periodic waveform will steepen and ultimately form a repeated sawtooth shape, shown in Fig. 15.8, when the Gol'dberg number is sufficiently large and the wave has propagated well past the shock inception distance.

Once the sawtooth waveform has developed, the shock front produces a gradient in the temperature, particle velocity, and pressure that is very large. Such gradients produce large dissipation due to thermal conduction across the shock front and viscous shear. The amplitude of the sawtooth waveform must decrease due to the resulting energy dissipation. Calculation of the shock wave's attenuation can be made by expressing the discontinuity of the entropy across the shock that is cubic in the pressure discontinuity [18]. For an ideal gas, the difference in entropy across the shock is expressed in terms of

**Fig. 15.8** Any periodic wave of sufficient Gol'dberg number will distort into the sawtooth waveform shown in a coordinate system that is moving along with the wave at the thermodynamic sound speed,  $c_o$ . The “excess velocity” produced by the Grüneisen parameter is proportional to the velocity amplitude,  $u$ , of the wave. The sloping “back” of the sawtooth must then experience solid body rotation since the excess velocity is proportional to the amplitude above its zero-crossing



the universal gas constant,  $\mathfrak{R}$ , and the mean molecular mass of the gas,  $M$ , by use of the Rankine-Hugoniot shock relations [19].

$$s_+ - s_- = \frac{\mathfrak{R}}{M} \frac{(\gamma + 1)}{12\gamma^2} \left| \frac{p_+ - p_-}{p_-} \right|^3 \quad (15.26)$$

Inspection of Fig. 15.8 suggests a simpler geometric approach [20]. If the particle velocity amplitude for the sawtooth waveform is  $u$ , then by Eq. (15.9), each portion of the waveform must advance, relative to the zero-crossing, by  $(\Gamma u dt)$  during a time interval,  $dt$ . The coordinate system, as shown in Fig. 15.8, moves with  $c_o$ , by making the  $x$  axis be  $(x - c_o t)$ . In that frame of reference, the fact that the back of the shock is a straight line, representing a linear increase in  $u$ , requires that the unshocked portion of the waveform undergo solid body rotation, as indicated by the curved arrow in Fig. 15.8.

Since the wave must remain single-valued, the shock front must dissipate sufficient energy to keep the waveform from becoming multiple-valued. The two hashed triangles shown in Fig. 15.8 are similar triangles by Garrett’s First Law of Geometry, so the ratio of their heights to their bases must be equal.

$$\frac{du}{\Gamma u(dt)} = \frac{u}{\lambda/2} \quad (15.27)$$

Setting  $dt = dx/c_o$ , Eq. (15.27) can be integrated from a reference location,  $x_o$ , at which the acoustic Mach number is  $M_o$ , out to some arbitrary distance,  $x$ , from that reference location.

$$c_o \int_{u_o}^u \frac{du}{u^2} = \frac{2\Gamma}{\lambda} \int_{x_o}^x dx \quad \Rightarrow \quad \frac{1}{M} - \frac{1}{M_o} = 2\Gamma \frac{x - x_o}{\lambda} \quad (15.28)$$

This result is both interesting and distinctly different from previous expressions for attenuation. First, the amplitude of the shock does not decay exponentially with distance. Second, although the dissipation is due to thermoviscous losses produced by the steep gradients across the shock front, the attenuation is independent of both the fluid’s shear viscosity,  $\mu$ , and its thermal conductivity,  $\kappa$ , and depends instead upon the Grüneisen parameter.

This sawtooth waveform does not persist. Eventually, it “unshocks,” as shown in Fig. 15.30, as its amplitude decreases to the level where classical attenuation mechanisms are dominant [21].

## 15.2 Weak Shock Theory and Harmonic Distortion

In most fluids, the nonlinearity in the equation of state and the nonlinearity introduced by the acoustically induced convection conspire to cause waves to distort. That distortion increases with the propagation distance, if the amplitude of the wave is sufficient for such nonlinear effects to dominate thermoviscous attenuation (i.e.,  $G \gg 1$ ). For waves of sufficiently large amplitude, this process will turn any periodic wave into a sawtooth wave. In this section, the focus will be on the initial stages of this distortion process.

If a wave is initially a sinusoidal “pure tone,” it will only contain a single Fourier component. That fundamental frequency can be designated  $f_1$ . The distortion will change the wave shape, but the wave will still be periodic with a period,  $T = (f_1)^{-1}$ . The description of the distorted waveform will necessarily require additional Fourier components at harmonic multiples of the fundamental frequency,  $f_n = nf_1$ , with  $n = 2, 3, 4$ , etc. This section will focus on the growth of those harmonic components with distance and their dependence on the initial amplitude of the wave.

### 15.2.1 The Order Expansion

When linear acoustics was first developed in Chap. 8, the parameters that described the acoustic fields were expressed as the sum of an equilibrium value plus a first-order deviation from equilibrium. Equation (8.1) expressed the pressure as  $p(\vec{x}, t) = p_m(\vec{x}) + p_1(\vec{x}, t)$ . Similar expansions were made for the mass density,  $\rho(\vec{x}, t)$ , in Eq. (8.2), temperature,  $T(\vec{x}, t)$ , in Eq. (8.3), and (specific) entropy per unit mass,  $s(\vec{x}, t)$ , in Eq. (8.4). In all cases, the first-order deviations from equilibrium were assumed to be much smaller than the equilibrium values (e.g.,  $p_1 \ll p_m$ ).

This *order expansion* will now be extended to keep track of the effects of nonlinearity on propagation. For example, the particle velocity will be represented as the sum of the fluid’s mean equilibrium velocity,  $v_m$ , and the deviations from equilibrium that are proportional to successively higher powers of such deviations. These deviations will be subscripted to indicate their dependence on the amplitude of the disturbance. A subscript of “1” will indicate a first-order contribution that is linear in the amplitude of the disturbance. A subscript of “2” will indicate a second-order contribution that is quadratic in the amplitude of the disturbance or is the product of two first-order contributions, possibly produced by the interaction of two different waves.

$$v(x, t) = v_m(x) + v_1(x, t) + v_2(x, t) + v_3(x, t) + \dots \quad (15.29)$$

Since our attention will be focused on one-dimensional propagation,  $x$  does not need to be a vector and because the fluids will not be subjected to any externally imposed mean flow,  $v_m(x) = 0$ . As was the case for linear acoustics, the first-order contribution to the acoustical deviation from equilibrium,  $v_1(x, t)$ , will be proportional to the amplitude of the disturbance from equilibrium. The second-order contribution,  $v_2(x, t)$ , will be proportional to the square of the amplitude of the disturbance from equilibrium or to the product of two first-order disturbances, etc.

It will also be assumed that these individual contributions are “well ordered,” in that each successive higher-order contribution will be smaller than its lower-ordered neighbor. In the case of particle velocity, all contributions will also be significantly smaller than the thermodynamic sound speed,  $c_o$ , in the weak shock limit.

$$c_o \gg |v_1| > |v_2| > |v_3| > \dots \quad (15.30)$$

### 15.2.2 Trigonometric Expansion of the Earnshaw Solution

The analysis of the distortion of an initially sinusoidal sound wave can generate a second-order correction by allowing the speed of sound to be dependent upon the amplitude of the disturbance. This result was first exploited by Earnshaw (1805–1888) and was published in 1860 [22].

$$\phi = t - \frac{x - X(\phi)}{\Gamma u(\phi) \pm c_o} \quad (15.31)$$

Here, Earnshaw solved the for a wave launched by a piston located at  $x = 0$  that has a displacement,  $X(t)$ , and velocity  $u(t) = dX/dt$ . The parameter,  $\phi$ , represents the time a given point on a waveform left the piston's face. Earnshaw was also the first to show that  $\Gamma_{gas} = (\gamma + 1)/2$ , for a sound wave in an gas obeying the Adiabatic Gas Law, as we did in Eq. (15.13).

We can exploit Earnshaw's insight to calculate the growth of the second harmonic by successive approximation [23] if the initial disturbance is assumed to be a single-frequency, rightward traveling wave with an initial particle velocity amplitude,  $v'$ .

$$v_1(x, t) = v' \cos(\omega t - kx) = v' \cos \omega \left( t - \frac{x}{c_o} \right) \quad (15.32)$$

A second-order contribution will be generated by substitution of the “local” sound speed, as expressed in Eq. (15.9), for the thermodynamic sound speed that appears in Eq. (15.32), as was expressed by Earnshaw in Eq. (15.31).

$$v_1(x, t) + v_2(x, t) = v' \cos \omega \left( t - \frac{x}{c_o + \Gamma v_1} \right) \quad (15.33)$$

In the weak shock limit,  $M_{ac} = v_I/c_o \ll 1$ , so the denominator of the argument of the cosine function can be approximated by its binomial expansion.

$$v_1(x, t) + v_2(x, t) \cong v' \cos \omega \left[ t - \frac{x}{c_o} \left( 1 - \Gamma \frac{v_1}{c_o} \right) \right] \quad (15.34)$$

The trigonometric identity for the cosine of the sum of two angles,  $a$  and  $b$ , is  $\cos \omega(a + b) = \cos(\omega a) \cos(\omega b) - \sin(\omega a) \sin(\omega b)$ . That identity can be used to separate Eq. (15.34) into two terms.

$$v_1(x, t) + v_2(x, t) \cong v' \cos \omega \left( t - \frac{x}{c_o} \right) - \frac{\Gamma x \omega v_1}{c_o^2} v' \sin \omega \left( t - \frac{x}{c_o} \right) \quad (15.35)$$

Since  $v_1(x, t)$  was defined in Eq. (15.32), the first-order terms on both sides of Eq. (15.35) can be eliminated so that only the second-order contribution remains. The first-order contribution can also be substituted into the second-order expression.

$$v_2(x, t) = -\frac{\Gamma x \omega}{c_o^2} (v')^2 \sin \omega \left( t - \frac{x}{c_o} \right) \cos \omega \left( t - \frac{x}{c_o} \right) \quad (15.36)$$

Using the double-angle sine identity,  $\sin(2a) = 2 \sin(a) \cos(a)$ , it becomes clear that the trigonometric product introduces a second harmonic component that grows linearly with distance,  $x$ , scaled by the wavelength,  $\lambda$ , and is proportional to the square of the initial amplitude,  $(v')^2$ .

$$v_2(x, t) = -\frac{\Gamma x \omega}{2c_o^2} (v')^2 \sin 2\omega \left( t - \frac{x}{c_o} \right) = -\pi \Gamma M_{ac} \frac{x}{\lambda} v' \sin 2\omega \left( t - \frac{x}{c_o} \right) \quad (15.37)$$

The assumption regarding the relative amplitude of the terms in the order expansion, as asserted in Eq. (15.30), will be violated before  $|v_2| = |v_1|$ . To determine the limit of this solution's applicability, those amplitudes can be equated to determine a distance,  $x_{1=2}$ , before which this assumption would be violated.

$$x_{1=2} = \frac{\lambda}{\pi \Gamma M_{ac}} \quad (15.38)$$

It is not surprising that this approximation would fail at a distance that is less than twice the shock inception distance,  $D_S$ . It is also true that this solution assumes that energy is transferred to the second harmonic with no reduction in the amplitude of the fundamental. That is clearly not possible, since the energy that appears as the second harmonic contribution was provided by the energy in the fundamental. The subsequent analysis will correct that difficulty.

### 15.2.3 Higher Harmonic Generation

It would be possible to continue the successive approximation procedure to calculate successively higher harmonics, but that procedure would quickly become algebraically messy. A simple and more intuitive approach is to use Eq. (15.9) to incorporate the local sound speed to deform the wave, as was done initially for shallow-water gravity waves in Fig. 15.3, and then simply use Fourier analysis to extract the amplitudes of the harmonics [24].

An undistorted wave can be parameterized by making its amplitude,  $y$ , be a function of a parameter,  $\theta$ :  $y = \sin(\theta)$ . To distort the wave, the plotted position can be advanced by an amount related to the propagation distance,  $d$ , scaled by the shock inception distance,  $D_S$ .

$$\sigma = \frac{d}{D_S} = 2\pi \Gamma M_{ac} \frac{d}{\lambda}; \quad 0 \leq \sigma < 1 \quad (15.39)$$

In Fig. 15.9, one-half of a sine function has been plotted on the  $x$  axis at two different advanced locations in Eq. (15.40).

$$x = \theta + \sigma \sin \theta \quad (15.40)$$

There is no additional information provided by the negative half-cycle, so the harmonic content of the distorted waveform can be Fourier analyzed between  $0 \leq \theta < \pi$ .

The Fourier coefficients can be projected to obtain the amplitudes of the harmonics using the same procedure as applied to vibrating strings in Sect. 3.5.

$$C_n = \frac{2}{\pi} \int_0^\pi y \sin(nx) dx = \frac{2}{\pi} \int_0^\pi \sin \theta \sin[n(\theta + \sigma \sin \theta)](1 + \sigma \cos \theta) d\theta \quad (15.41)$$

Using the integral definition of Bessel functions of the 1<sup>st</sup> kind in Eq. (C.26), Eq. (15.41) can be expressed as the sum of four Bessel functions.

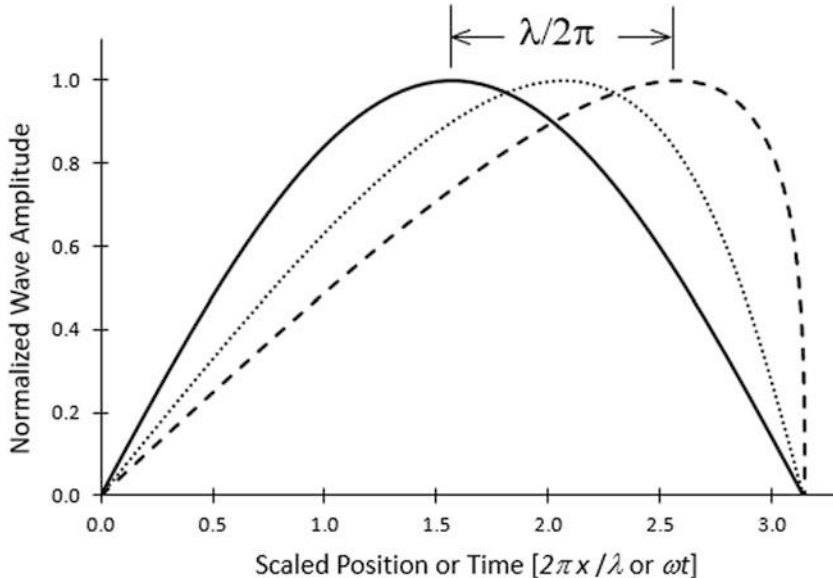
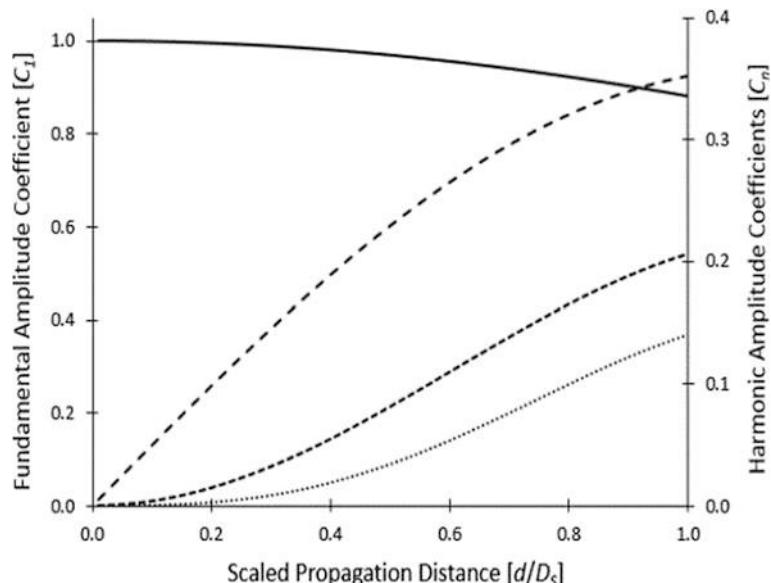


**Fig. 15.9** One-half-cycle of nonlinear distortion. The solid line is the undistorted (sinusoidal) waveform. The dashed line represents the waveform that has propagated to the shock inception distance,  $\sigma = x/D_S < 1$ . The dotted line represents the waveform that has propagated to one-half the shock inception distance

**Fig. 15.10** Fourier coefficients for a nonlinearly distorted sinusoidal wave as a function of the scaled propagation distance,  $\sigma = x/D_S$ . The solid line is the amplitude of the fundamental at  $f_1$  that should be read from the left-hand axis. The long-dashed line is the second harmonic amplitude,  $C_2$ , at  $f_2 = 2f_1$ , the narrow-dashed line is the third harmonic amplitude,  $C_3$ , at  $f_3 = 3f_1$ , and the dotted line is the fourth harmonic amplitude,  $C_4$ , at  $f_4 = 4f_1$ . All  $C_n$  for  $n > 1$  should be read from the right-hand axis



$$C_n = (-1)^{n+1} \{ J_{n-1}(n\sigma) - J_{n+1}(n\sigma) - (\sigma/2)[J_{n-2}(n\sigma) - J_{n+2}(n\sigma)] \} \quad (15.42)$$

Two successive applications of the recurrence relations in Eqs. (C.27) and (C.28) reduce the expression for the harmonic amplitude coefficients,  $C_n$ , to the compact form in Eq. (15.43), which is plotted in Fig. 15.10.

$$|C_n| = \frac{2}{n\sigma} J_n(n\sigma) \quad \text{for } \sigma < 1 \quad \text{and} \quad n = 1, 2, 3, \dots \quad (15.43)$$

This result was originally obtained using algebraic methods by Fubini-Ghiron in 1935 [25].

The initial growth rate of the harmonics with propagation distance can be appreciated by expansion of the Bessel functions for small values of their arguments,  $n\sigma$ , as expressed in Eq. (C.12). As shown in Eq. (C.14), the  $J_l(x)$  Bessel function increases linearly with  $x = n\sigma$ . By Eq. (15.43),  $C_l \propto J_l(\sigma)/(\sigma)$  so it is initially independent of distance. One nice feature of this solution is that as the higher harmonic amplitudes grow, the amplitude of the fundamental decreases. At  $d = D_s$ , the amplitude of the fundamental is only 88% of its original value.

The first terms in the expansion of the higher-order Bessel functions,  $J_n(x)$ , all are proportional to  $x^n$ . As per Eq. (15.43), each Bessel function is divided by  $x = (n\sigma)$ , so that each amplitude coefficient increases in proportion to the  $(n-1)$  power of the scaled distance,  $\sigma = x/D_s$ . This behavior is evident in Fig. 15.10. The second harmonic amplitude,  $C_2$ , initially grows linearly with distance, just as predicted by Airy [23] in the solution by successive approximation that led to Eq. (15.37). The third harmonic amplitude,  $C_3$ , has an initially quadratic dependence on distance, and the fourth harmonic amplitude,  $C_4$ , has an initially cubic dependence on the propagation distance.

A calculation by Fay [26] that included dissipation also produced an expression for the harmonic amplitudes,  $B_n$ , that describe a stabilized waveform where the Gol'dberg number includes thermoviscous attenuation,  $\alpha_{T-V}$ , in Eq. (14.29).

$$B_n = \frac{2}{G \sinh[n(1 + \sigma)/G]} \quad \text{for } \sigma = \frac{x}{D_s} > 3 \quad (15.44)$$

Note that the Fay solution produces the (stable) sawtooth waveform of Fig. 15.8 for distances that satisfy  $G \gg n(1 + \sigma)$ , where the hyperbolic sine function can be replaced by its argument to produce the Fourier amplitude coefficients of a sawtooth waveform (see Fig. 1.22 and Chap. 1, Prob. 12),  $B_n^{\text{sawtooth}} = 2/n(1 + \sigma)$ . As shown by Blackstock [27], the Fay result for the harmonic amplitudes does not reduce to those of Fubini in Eq. (15.43), in the limit of vanishing viscosity since the Fubini coefficients are valid near the source,  $\sigma \leq 1$ , and the Fay coefficients in Eq. (15.44) are valid in the sawtooth region,  $\sigma \geq 3$ . Blackstock provides a solution that connects those two regimes in his paper that has become known as the “Blackstock bridging function.”

### 15.3 The Phenomenological Model

Hydrodynamics provides a complete description of the propagation of sound in fluids. All of the nonlinear behavior that has been introduced in this chapter thus far should be derivable from that hydrodynamic description. As will be demonstrated now, the hydrodynamic approach will also provide additional insights and motivate the description of additional nonlinear phenomena.

As discussed in Sect. 7.3, the dynamics of a single-component homogeneous fluid can be described by two thermodynamic variables (e.g.,  $\rho$  and  $s$  or  $p$  and  $T$ ) and the three components of the velocity field.

$$\vec{v} = v_x \hat{e}_x + v_y \hat{e}_y + v_z \hat{e}_z \quad (15.45)$$

As before,  $v_x$  is the  $x$  component of velocity, and  $\hat{e}_x$  is the unit vector in the  $x$  direction. The “system” is “closed” if there are five independent conservation equations that relate the variables to each other. Those equations should be familiar by now and are reproduced below:

$$\frac{\partial \rho}{\partial t} + \nabla \cdot (\rho \vec{v}) = 0 \quad (15.46)$$

$$\begin{aligned} \frac{\partial(\rho s)}{\partial t} + \nabla \cdot (\rho s \vec{v}) &= \kappa \frac{(\nabla T)^2}{T} + \mu \Phi + \zeta (\nabla \cdot \vec{v})^2 \\ \Phi &= \frac{1}{2} \sum_{i=x,y,z} \sum_{j=x,y,z} \left( \frac{\partial v_i}{\partial x_j} + \frac{\partial v_j}{\partial x_i} - \frac{2}{3} \delta_{ij} \nabla \cdot \vec{v} \right)^2 \end{aligned} \quad (15.47)$$

$$\frac{\partial \vec{v}}{\partial t} + (\vec{v} \cdot \nabla) \vec{v} = -\frac{\vec{\nabla} p}{\rho} + \mu \nabla^2 \vec{v} \quad (15.48)$$

The form of the entropy Eq. (15.47) is rather more general than will be required but includes the square of the viscous shear tensor,  $\Phi$ , and the bulk viscosity,  $\zeta$ , along with thermal conductivity,  $\kappa$ , all as potential sources of entropy production.

As before, those conservation laws contain both  $p$  and  $\rho$  as (mechanical) thermodynamic variables, so that an equation of state,  $p = p(\rho, s)$ , describing each individual fluid's properties, is required to "close" the set. In the absence of dissipation (i.e.,  $\kappa = \mu = \zeta = 0$ ), the equation of state can be combined with the continuity Eq. (15.46), and the entropy conservation Eq. (15.47) to demonstrate that the entropy will be conserved.

$$\frac{Ds}{Dt} = \frac{\partial s}{\partial t} + \vec{v} \cdot \vec{\nabla} s = 0 \quad (15.49)$$

This simplifies the expansion of the equation of state in terms of the density deviation,  $\rho' = \rho - \rho_m$ , since all of the derivatives can be evaluated at constant entropy.

$$p(\rho) = \left( \frac{\partial p}{\partial \rho} \right)_s \rho' + \left( \frac{\partial^2 p}{\partial \rho^2} \right)_s \frac{\rho'^2}{2} + \dots \quad (15.50)$$

### 15.3.1 The (Nondissipative) Nonlinear Wave Equation

As with Earnshaw's solution and the calculation of the harmonic amplitude components in the weak shock limit, this analysis will be restricted to one-dimensional propagation (i.e.,  $v_y = v_z = 0$ ), but at this point, there is no penalty for retaining the vector velocity for evaluation of the hydrodynamic equations and the equation of state up to terms of second-order in the deviation from equilibrium.

$$\frac{\partial \rho_1}{\partial t} + \frac{\partial \rho_2}{\partial t} + \rho_m \nabla \cdot \vec{v}_1 + \rho_m \nabla \cdot \vec{v}_2 + \rho_1 \nabla \cdot \vec{v}_1 + \vec{v}_1 \cdot \vec{\nabla} \rho_1 = 0 \quad (15.51)$$

$$\rho_m \frac{\partial \vec{v}_1}{\partial t} + \rho_m \frac{\partial \vec{v}_2}{\partial t} + \rho_1 \frac{\partial \vec{v}_1}{\partial t} + \rho_m (\vec{v}_1 \cdot \vec{\nabla}) \vec{v}_1 = -\vec{\nabla} p_1 - \vec{\nabla} p_2 \quad (15.52)$$

$$p_2 = \left( \frac{\partial p}{\partial \rho} \right)_s \rho_2 + \left( \frac{\partial^2 p}{\partial \rho^2} \right)_s \frac{\rho_1^2}{2} \quad (15.53)$$

The first-order wave equation is homogeneous.

$$\frac{\partial^2 \rho_1}{\partial t^2} + \left( \frac{\partial p}{\partial \rho} \right)_s \nabla^2 \rho_1 = 0 \quad (15.54)$$

The first-order terms from Sect. 7.2 that were combined to produce that linear wave equation can be subtracted from the combination of Eqs. (15.51), (15.52), and (15.53) to leave a wave equation for the space-time evolution of the second-order sound fields.<sup>7</sup>

$$\frac{\partial^2 \rho_2}{\partial t^2} - c_o^2 \nabla^2 \rho_2 = \nabla^2 \left[ \rho_m \vec{v}_1^2 + \left( \frac{\partial^2 p}{\partial \rho^2} \right)_s \frac{\rho_1^2}{2} \right] \quad (15.55)$$

This wave equation for the second-order deviations of the density from equilibrium is not homogeneous; it has a source term that is driven by quadratic combinations of the first-order sound fields. Using the Euler relation for the first-order fields and Eq. (15.10), this second-order wave equation can be re-written in a more familiar form for plane progressive waves.

$$\frac{\partial^2 \rho_2}{\partial t^2} - c_o^2 \nabla^2 \rho_2 = \frac{c_o^2}{\rho_m} \left[ 1 + \frac{\rho_m}{c_o} \left( \frac{\partial c}{\partial \rho} \right)_s \right] \nabla^2 \rho_1^2 = \Gamma \frac{c_o^2}{\rho_m} \nabla^2 \rho_1^2 \quad (15.56)$$

Not surprisingly, the strength of this nonlinear source term is proportional to the Grüneisen parameter,  $\Gamma$ .

### 15.3.2 Geometrical Resonance (Phase Matching)

The second-order wave equation should reproduce the results obtained for second harmonic distortion in the weak shock limit that were generated by the trigonometric expansion of Earnshaw's solution. That result can be recaptured by squaring the right-going sinusoidal traveling wave,  $\rho_1 = \rho' \cos(\omega t - kx)$ , and then inserting it into the source term on the right-hand side of Eq. (15.56).

$$\Gamma \frac{c_o^2}{\rho_m} \nabla^2 \rho_1^2 = \Gamma \frac{c_o^2}{\rho_m} \frac{\rho'^2}{2} \nabla^2 [1 + \cos(2\omega t - 2kx)] \quad (15.57)$$

The constant will disappear upon operation by the Laplacian, but the  $\cos 2(\omega t - kx)$  term will drive the second-order wave equation. What is crucially important is the recognition that the phase speed of the source term,  $c_{ph} = 2\omega/2k$ , is identical to the phase speed of the second-order density deviations,  $\rho_2$ , which propagates with speed,  $c_o = \sqrt{(\partial p / \partial \rho)_s}$ .

This correspondence between the phase speed of the source and the phase speed of the disturbance it creates is called *geometric resonance*. In this case, the wavevectors representing the first- and second-order fields,  $\vec{k}_1$  and  $\vec{k}_2$ , are colinear. Considering this process as the first-order wave's interaction with itself, the geometric resonance for these colinear propagation directions can be expressed as a wavevector sum.

$$\vec{k}_2 = \vec{k}_1 + \vec{k}_1 \quad \text{where} \quad |\vec{k}_2| = 2|\vec{k}_1| \quad \text{and} \quad \omega_2 = 2\omega_1 \quad (15.58)$$

<sup>7</sup> Do not confuse the wave equation for the second-order deviations from equilibrium with the fact that both the first- and second-order wave equations are both second-order partial differential equations. For the classification of differential equations, second-order refers to the highest-order derivative that appears in the equation.

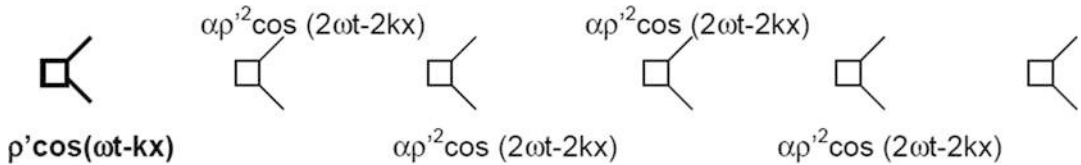


**Fig. 15.11** Conceptual representation of the linear growth of the amplitude of the second harmonic with distance produced by the inhomogeneous source term that drives the wave equation for the second-order acoustic density deviations expressed in Eq. (15.56). The original pump-wave source “loudspeaker” is shown in *bold lines* and *bold fonts* at the far left of this figure

Each infinitesimal fluid volume that is excited by quadratic combinations of the first-order sound fields can be considered a source for the second-order sound field. In Fig. 15.11, those fluid volumes are represented by individual loudspeakers with amplitudes that are proportional to  $\rho'^2$ . Because the phase velocity is also the thermodynamic sound speed,  $c_o$ , each of those “virtual loudspeakers” produces sound that sums in just the same way as the discrete end-fire line array in Sect. 12.7.1. When the sound radiated by the first virtual loudspeaker propagates to the position of the second, the two will be in-phase, and their amplitudes will add coherently. The sum then propagates to the third location and adds in-phase and so on. This coherent addition along the direction of propagation produces the linear growth in the second harmonic’s amplitude that was described in Eqs. (15.37) and (15.43), as well as in Fig. 15.10. It also demonstrates the corresponding quadratic dependence on the amplitude of the first-order field at any location.

### 15.3.3 Intermodulation Distortion and the Parametric End-Fire Array

The distortion of a single, initially sinusoidal plane wave is due to the wave’s own influence on the medium through which it is propagating. The formalism of Eq. (15.56) makes it convenient to consider the nonlinear interaction of two plane waves propagating in the same direction but having different frequencies,  $\omega_\downarrow$  and  $\omega_\uparrow$ . For simplicity, let both sound waves have equal amplitudes,  $\rho_1$ .

At the linear level, they create a sound field that is simply their superposition.

$$\rho'(x, t) = \rho_1 [\cos(\omega_\downarrow t - k_\downarrow x) + \cos(\omega_\uparrow t - k_\uparrow x)] \quad (15.59)$$

The nonlinear source term in Eq. (15.56) is driven by the square of that linear superposition. Letting  $a = (\omega_\downarrow t - k_\downarrow x)$  and  $b = (\omega_\uparrow t - k_\uparrow x)$ , the drive can be expressed as the sum of five contributions.

$$\rho'^2 = (\rho_1^2/2)[2 + \cos(2a) + \cos(2b) + \cos(a+b) + \cos(a-b)] \quad (15.60)$$

Again, the constant term in the square brackets will be eliminated from the driving term by the Laplacian in Eq. (15.56). The  $(2a)$  and  $(2b)$  terms represent the second harmonic distortion of the individual wave produced by their self-interaction. The sum and difference terms,  $\cos(a+b)$  and  $\cos(a-b)$ , are called *intermodulation distortion* products and represent the effect that one wave has on the medium that the other wave is passing through.

Having already analyzed the self-distortion that creates the second harmonic distortion, our interest will now be focused on two interacting waves. Those interacting waves will be called the *pump waves* or *primary waves*. We will assume that their frequencies are closely spaced:  $|\omega_\uparrow - \omega_\downarrow| \ll (\omega_\uparrow + \omega_\downarrow)/2$ . These two colinear waves, as well as the products of their nonlinear interactions, are still all in geometric resonance.

$$c_{ph} = \frac{\omega_{\uparrow}}{|\vec{k}_{\uparrow}|} = \frac{\omega_{\downarrow}}{|\vec{k}_{\downarrow}|} = \frac{2\omega_{\uparrow}}{2|\vec{k}_{\uparrow}|} = \frac{2\omega_{\downarrow}}{2|\vec{k}_{\downarrow}|} = \frac{\omega_{\uparrow} + \omega_{\downarrow}}{|\vec{k}_{\uparrow} + \vec{k}_{\downarrow}|} = \frac{|\omega_{\uparrow} - \omega_{\downarrow}|}{|\vec{k}_{\uparrow} - \vec{k}_{\downarrow}|} = c_o \quad (15.61)$$

In the absence of dispersion, if the two waves are not colinear, then the *phase matching* that is the consequence of geometrical resonance does not occur, and the interaction does not produce waves that propagate beyond the interaction volume [28].

Since the two “pump” or “primary” waves are assumed to be close in frequency, they have about the same thermoviscous spatial attenuation coefficient,  $\alpha_{T.V}$ , resulting in a characteristic exponential decay distance,  $\ell = (\alpha_{T.V})^{-1}$ , as identified before in Sect. 15.1.3 for definition of the Gol’berg number. Since the bulk attenuation coefficient is proportional to the square of the frequency, the two self-distorted second harmonic components will suffer exponential decay over a distance that is only one-fourth of  $\ell$ , as will the wave that is produced by the nonlinear interaction that creates a wave at the sum of the two pump frequencies. The exponential decay of either of the pump waves is represented symbolically in Fig. 10.12 (Left). The growth and subsequent exponential decay of the second harmonics and sum waves are represented symbolically in Fig. 10.12 (right).

Although the waveform instability caused by nonlinear distortion had been understood since the time of the American Civil War, it was not until 1963 that Peter Westervelt recognized that highly directional receivers and transmitters of sound may be constructed by use of the nonlinearity in the equations of hydrodynamics<sup>8</sup> [29]. Although it had been known, both theoretically [30] and experimentally [31], that two plane waves of different frequencies propagating in the same direction generate two new waves at the sum and difference frequencies, it was not until Westervelt’s paper that the practical utility of that difference-frequency wave was recognized.

As we know from the analysis of the radiation from baffled circular pistons in Sect. 12.8, it is impossible to produce a narrow (i.e., directional) sound beam if the circumference of the radiating piston,  $2\pi a$ , is on the order of the wavelength,  $\lambda$ , of the sound being radiated, or smaller. This makes it impossible to produce a directional sound beam at low frequencies from small vibrating surfaces. On the other hand, if  $2\pi a \gg \lambda$ , then the radiated sound will be confined to a narrow beam as quantified in Eq. (12.108). Westervelt recognized that it was possible to use nonlinear acoustics to create a narrow low-frequency beam through the interaction of two narrow high-frequency, high-amplitude sound beams of slightly different frequencies. If the high-frequency beams interacted over a distance that was much longer than the difference frequency wavelength,  $\lambda_{\text{diff}} = 2\pi c_o / (\omega_{\uparrow} - \omega_{\downarrow})$ , then the virtual array, like that depicted symbolically in Fig. 15.11, would produce a directional low-frequency sound beam.

As long as the attenuation distance for the pump waves is longer than the wavelength of the difference frequency wave, the difference frequency will be produced by the end-fire linear array from the nonlinear interaction of the two pump waves and will have the directionality characteristic of the pump wave’s directionality (see Fig. 15.15). The growth of the difference frequency wave will initially be linear with distance (as it was for the second harmonic distortion derived in Sect. 15.2.2), but due to the attenuation of the higher-frequency pump waves, depicted symbolically in Fig. 15.12 (left), the difference wave will reach some limiting amplitude as shown in Fig. 15.13.

An array consisting of 30–40 kHz piezoelectric transducers, shown in Fig. 15.14, was built to demonstrate the directionality of the difference-frequency beam. Fifteen of the transducers were wired electrically in parallel and driven at  $\omega_{\downarrow}/2\pi = 37.5$  kHz, and the other 15 were wired in parallel and driven at  $\omega_{\uparrow}/2\pi = 39.5$  kHz to produce a parametric array that would create a difference wave at

<sup>8</sup> Westervelt first presented his parametric array at a meeting of the Acoustical Society of America in Providence, RI, in 1960, J. Acoust. Soc. Am. **32**, 934 (1960). The abstract for that presentation included an expression for the radiated intensity of the difference-frequency beam.

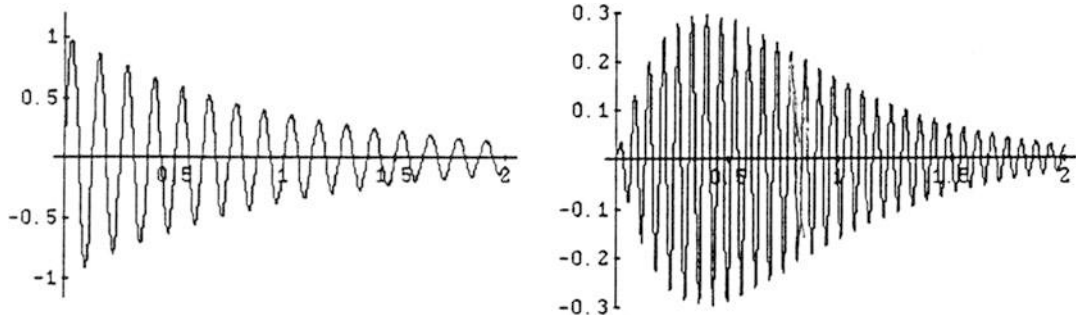


**Fig. 15.12** (Left) Symbolic representation of the exponential decay of the one-dimensional pump wave due to thermoviscous attenuation. (Right) Symbolic representation of the growth and subsequent decay of the second harmonic and sum waves generated by nonlinear processes. Since the frequencies of the second harmonics and the sum wave are approximately twice that of the pump waves, the decay of these nonlinear products takes place over a characteristic exponential decay distance that is one-fourth of that for the pump waves

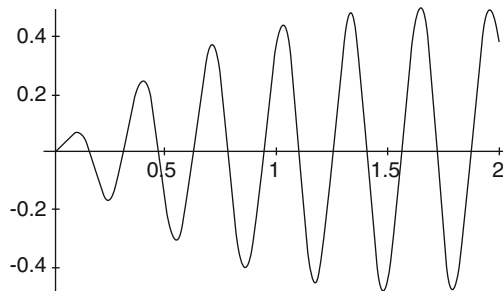


**Fig. 15.13** A directional low-frequency “difference wave” can be created by the nonlinear interaction of two “pump” waves of slightly different frequency, like the wave shown in Fig. 15.12 (left). Since the pump wave attenuates with distance from the source, the difference-frequency wave amplitude initially increases linearly with distance from the source but eventually reaches a maximum amplitude before attenuating or spreading at greater distances

$(\omega_{\uparrow} - \omega_{\downarrow})/2\pi = 2.0$  kHz. These two sub-arrays were interlaced so that the nearest neighbors to any transducers driven at one of the frequencies would radiate at the other frequency.

That array is shown in Fig. 15.14. It has a height,  $h = 5$  cm, and width,  $w = 21$  cm. This produces a circular-equivalent effective radius,  $a_{\text{eff}} = (h + w)/\pi \cong 8$  cm. At 40 kHz, the pump wavelength is  $\lambda_{\text{pump}} \cong 0.9$  cm, so  $ka_{\text{eff}} \cong 60$ , making the pump waves very directional at that frequency. Using the directionality for a baffled piston in Eq. (12.108), the pump wave’s major lobe is confined within about  $\pm 3.6^\circ$ . Since the array is rectangular rather than circular, the 40 kHz beam will be wider than this circular approximation in the vertical direction and narrower in the horizontal direction.

The attenuation of a 40 kHz sound wave in air is strongly dependent upon humidity (see Fig. 14.5). In dry air, the exponential absorption length,  $\ell$  (0% RH) = 23 m, while for a relative humidity of 60%,  $\ell$  (60% RH) = 2 m. The pump amplitude,  $p_1 \cong 20$  Pa, so by Eq. (15.15), the shock inception distance is  $D_S = 8$  m, assuming no spreading. A conservative estimate of the effective low-frequency end-fire array length,  $d_{\text{eff}}$ , might be 2 m, making the virtual line array’s value of  $k_{\text{diff}} d_{\text{eff}} \cong 36$  for the 2.0 kHz difference-frequency wave.

Although the directionality that can be achieved by the parametric array in this example is impressive, the electroacoustic energy conversion efficiency is very poor. The difference-frequency acoustic pressure amplitude, measured at 4 m from the source, was  $p_2 = 0.14$  Pa  $\cong 74$  dB re: 20  $\mu\text{Pa}_{\text{rms}}$ .

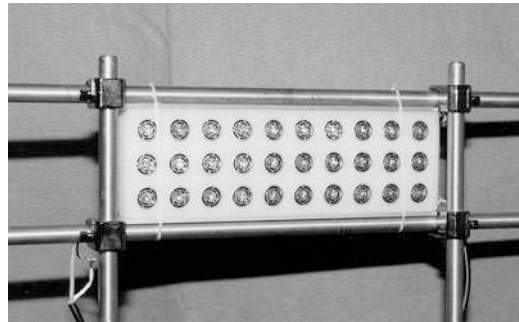


**Fig. 15.14** Photograph of an array of 30 small piezoelectric transducers that is 5 cm tall and 21 cm wide. The array was wired as two interlaced 15-element sub-arrays. One sub-array was driven at  $\omega_1/2\pi = 37.5$  kHz and the other at  $\omega_1/2\pi = 39.5$  kHz to produce a difference-frequency wave at  $(\omega_1 - \omega_2)/2\pi = 2.0$  kHz. [Transducer and photo courtesy of T. B. Gabrielson]

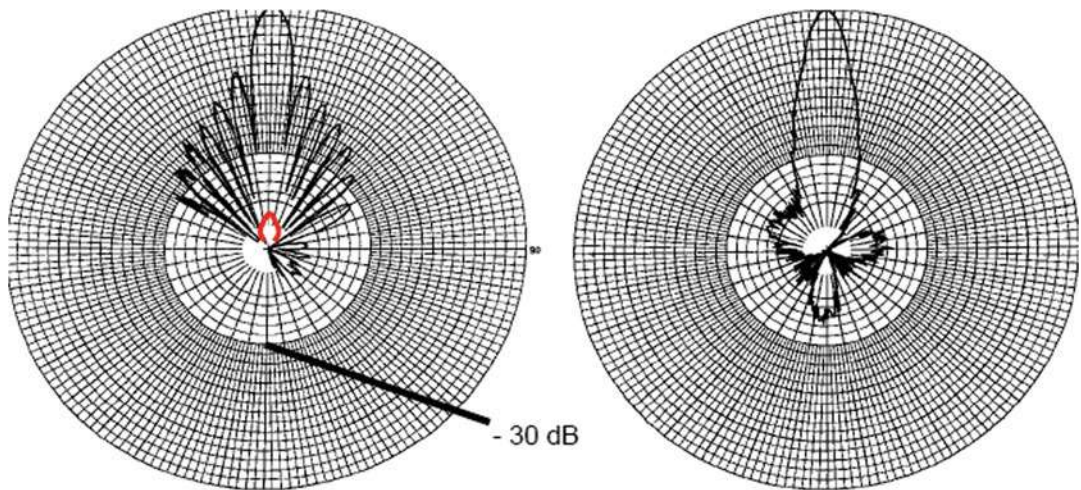


**Fig. 15.15** (Left) The directionality of the pump and of the difference-frequency waves is plotted on the same scale. (Right) When the directionality of the difference-frequency wave is plotted by itself, it is clear that the directionality of the difference-frequency wave is only slightly broader than the directionality of the pump waves

At that distance, the beam's cross-section was about  $1 \text{ m}^2$ . The intensity corresponding to  $p_2 = 0.14 \text{ Pa}$  is  $22 \mu\text{W/m}^2$ . The electrical input power to the array was about 18 watts, so the net electroacoustic conversion efficiency is just about one-part-per-million or approximately 0.0001%.

This increase in difference-frequency directionality and the low conversion efficiency is illustrated in the directionality plots in Fig. 15.15 for a parametric end-fire array operating at pump frequencies of 22 kHz and 27 kHz to produce a 5 kHz difference-frequency wave in water. The efficiency is better than in air due to the higher value of  $\Gamma$  in water and the higher acoustic pressures that could be produced, but the ratio of the amplitude of the difference-frequency to the pump is quite low, as demonstrated when both the pump and the difference frequency waves are plotted together in Fig. 15.15 (left). The smaller-amplitude difference-frequency wave's directionality is plotted by itself in Fig. 15.15 (right). Comparison of the two graphs shows that the difference-frequency beam is only slightly wider than the pump frequency beams.

The low conversion efficiencies of the parametric array are deemed acceptable for some niche applications. Parametric arrays for use in air are being produced commercially, but I have some trepidation about the possibility of detrimental physiological effects due to the very high pump-wave amplitudes at frequencies that are above the normal range of human hearing. I'm not of the opinion that "what you can't hear, can't hurt you."

The ubiquity of such commercially available parametric arrays that are used to produce directional sound in air (i.e., "audio spotlights") has renewed interest in the potentially detrimental health effects of high-amplitude ultrasound exposure and led to the publication of a Special Issue of the *Journal of the Acoustical Society of America* that is focused on this subject [32].

*We are currently in the undesirable situation where a member of the public can purchase a \$20 device that can be used to expose another human to sound pressure levels that are > 50 dB in excess of the maximum permissible levels for public exposure.*

Concern has been exacerbated by reports of the "weaponization" of high-amplitude ultrasound that may have been used to injure diplomats at the US Embassy in Havana, Cuba [33], and elsewhere [34].

When I make measurements near such an ultrasound source (e.g., Fig. 15.14), I wear ear plugs and place sound-attenuating earmuffs over my plugged ears. Other experimentalists who have not taken such precautions have exhibited symptoms like dizziness and nausea.

### 15.3.4 Resonant Mode Conversion

So far, the concept of geometrical resonance has restricted the evolution of harmonic distortion or the production of sum and difference waves to media that do not exhibit significant dispersion, as indicated by Eq. (15.61). If there is dispersion, so  $dc_o/df \neq 0$ , then the some portions of the virtual array will start to become out-of-phase with other portions, and the uniform linear increase in amplitude with distance will become instead a "beating" where the amplitude would start growing and then start diminishing, possibly repeating that alternation if the interaction length were sufficiently long, as some portions of the virtual array subtract from the growth produced by other portions.

In this sub-section, two beams that are not colinear are allowed to interact to produce another wave that travels at a different speed. That beating is illustrated by the measurements made in a waveguide of rectangular cross-section, made by Hamilton and TenCate [38], shown in Fig. 15.16.

**Fig. 15.16** The difference frequency amplitude vs. distance along a waveguide showing the "beating" created by the dispersion caused by the waveguide's frequency-dependent phase speed when the difference frequency,  $f_2 = 165$  Hz, propagates as a plane wave and the two pump waves, at  $f_1 = 2900$  Hz and  $f_- = 2735$  Hz, propagate in the lowest-frequency non-plane wave mode [38]

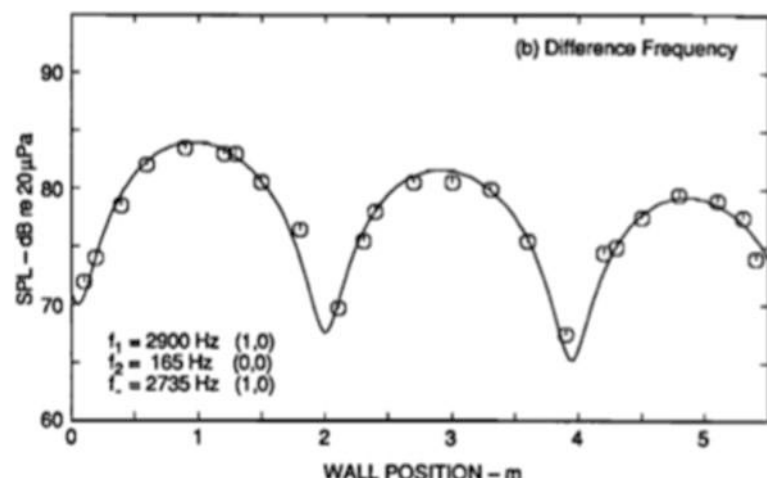
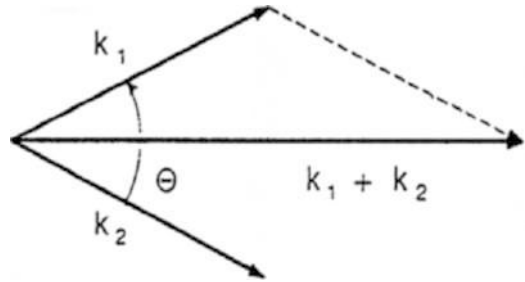


**Fig. 15.17** Two pump waves of the same frequency interact at an angle,  $\theta$ . If  $\theta \neq 0^\circ$ , the vector sum of their wavevectors will be less than the sums of their wavenumbers



If the propagation speed of the nonlinear product is greater than the propagation speed of the pumps and if the pump wavevectors are not colinear, there can be geometrical resonance (i.e., phase matching) at a unique interaction angle. I like to call this a “scissors effect.” If we assume that there are two waves of the same frequency,  $\omega_\uparrow = \omega_\downarrow = \omega$ , but their wavevectors make a relative angle,  $\theta$ , with each other, then the phase speed of the “sum” wave will be higher than the phase speed of either pump (primary) wave. This simple geometry is illustrated in Fig. 15.17.

$$c_{ph} = \frac{\omega_\uparrow + \omega_\downarrow}{|\vec{k}_\uparrow + \vec{k}_\downarrow|} = \frac{2\omega}{2|\vec{k}| \cos(\theta/2)} = \frac{c_o}{\cos(\theta/2)} \geq c_o \quad (15.62)$$

This is similar to a scissors in that the speed of the intersection of the two blades moves faster than the speed at which the tips of the blades approach each other.

As introduced in Sect. 5.1.1, the speed of longitudinal waves in bulk solids is  $c_L = \sqrt{D/\rho}$ , where  $D$  is the dilatational modulus, also known as the modulus of unilateral compression (see Sect. 4.2.2). Shear waves in bulk isotropic solids propagate at the shear wave speed,  $c_S = \sqrt{G/\rho}$ , where  $G$  is the material’s shear modulus (see Sect. 4.2.3). The relationship between the moduli of any isotropic solid, summarized in Table 4.1, allows the relationship between those two sound speeds to be expressed in terms of the solid’s Poisson’s ratio,  $\nu$ , and its Young’s modulus,  $E$ .

$$c_S^2 = \frac{G}{\rho} = \frac{E}{2\rho(1+\nu)} < c_L^2 = \frac{D}{\rho} = \frac{E(1-\nu)}{\rho(1+\nu)(1-2\nu)} \quad (15.63)$$

The stability criterion discussed in Sect. 4.2.3 restricts positive values of Poisson’s ratio to  $\nu < 1/2$ , thus guaranteeing that  $c_L > c_S$ .

Based on the phase speed increase calculated for the interaction of two waves that are not colinear in Eq. (15.62) and the fact that  $c_L > c_S$ , it would be possible to have two shear waves interact through nonlinearity to produce the faster longitudinal wave where the mode-conversion interaction angle,  $\theta_{mc}$ , is determined by the Poisson’s ratio of the solid in which the two shear waves are interacting.

$$\cos\left(\frac{\theta_{mc}}{2}\right) = \frac{c_S}{c_L} = \sqrt{\frac{(1-2\nu)}{2(1-\nu)}} < 1 \quad (15.64)$$

For polycrystalline aluminum,  $\nu_{Al} = 0.345$  [35], so  $\cos(\theta_{mc}/2) = 0.486$ . The required angle between the two shear wavevectors in aluminum must be  $\theta_{mc} = 122^\circ$  to make the interaction phase speed in Eq. (15.62) satisfies geometrical resonance for nonlinear mode conversion that couples two shear waves, each at frequency,  $\omega$ , to a longitudinal wave with frequency  $2\omega$ .

*Resonant mode conversion* in solids was first described theoretically by Jones and Kobett [36] and observed experimentally shortly thereafter in aluminum, by Rollins, Taylor, and Todd, at the interaction angle predicted in Eq. (15.64) [37].

Another opportunity for resonant mode conversion is afforded by inspection of Fig. 15.5. From 1 K to 2 K, second (thermal) sound has a speed,  $c_2$ , of about 20 m/s, while the speed of first (compressional) sound,  $c_1$ , is around 230 m/s. Two second sound waves that are almost anti-colinear could have an interaction phase speed equal to that of first sound. Using the geometry of Fig. 15.16, the mode conversion half-angle, at temperatures below  $T_\lambda = 2.172$  K, depends upon the velocity ratio.

$$\cos\left(\frac{\theta_{mc}}{2}\right) = \frac{c_2(T)}{c_1(T)} \leq 0.10 \quad (15.65)$$

This suggests that  $\theta_{mc}$  will be close to  $180^\circ$ .

A waveguide of rectangular cross-section affords an ideal geometry to provide a long interaction length while also affording precise control of the mode conversion angle for two plane waves of second sound. In a waveguide, the interaction angle of the two traveling plane waves (see Fig. 15.23) is controlled by the ratio of the drive frequency to the cut-off frequency. From Fig. 15.17 and Eq. (13.69), the mode-conversion interaction half-angle,  $\theta_{mc}/2$ , is related to the ratio of the second sound drive frequency,  $\omega$ , to the cut-off frequency of the waveguide's first non-plane wave mode,  $\omega_{co}$ .

$$\cos\left(\frac{\theta_{mc}}{2}\right) = \frac{|\vec{k}|}{\sqrt{k^2 - k_z^2}} = \sqrt{1 - \frac{\omega_{co}^2}{\omega^2}} \quad (15.66)$$

As shown in Fig. 15.18, if the height of the waveguide is  $\ell_z$ , then the cut-off frequency would correspond to a single half-wavelength of second sound being equal to the waveguide's height:  $\omega_{co} = \pi c_2 / \ell_z$ . Substitution of Eq. (15.65) into Eq. (15.66) determines the ratio of the second sound frequency necessary for resonant mode conversion,  $\omega_{mc}$ , to the waveguide's cut-off frequency,  $\omega_{co}$ .

$$\frac{\omega_{co}}{\omega_{mc}} = \sqrt{1 - \frac{c_2^2}{c_1^2}} < 1 \quad (15.67)$$

Of course, it is necessary to do this experiment in superfluid helium at temperatures below  $T_\lambda$ , since second sound provides the pump (primary) waves, as well as to have an adequate nonlinear interaction

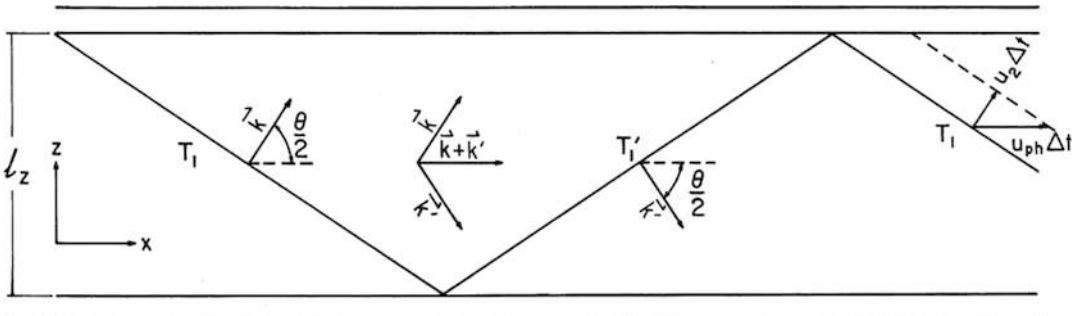


**Fig. 15.18** A waveguide can provide precise control of the interaction angle,  $\theta$ , of the two second sound traveling plane waves that satisfy the waveguide's boundary conditions, since the ratio of the frequency to the cut-off frequency controls the interaction angle

length to observe this resonant mode conversion of second sound to first sound. Those two constraints led to the use of a spiral waveguide shown in Fig. 15.18 (left). Sum and difference waves generated by non-colinear waves in an air-filled waveguide of rectangular cross-section that were not geometrically resonant are shown in Fig. 15.16 that were measured by Hamilton and TenCate [38].

Landau's two-fluid description of superfluid helium requires eight variables [39]. In addition to the two thermodynamic variables, two separate velocity fields are necessary to describe the motion of the superfluid component and of the normal fluid component,  $\vec{v}_s$  and  $\vec{v}_n$ . This makes the second-order wave equation for the nonlinear acoustic interactions more complicated than Eq. (15.56), but the inhomogeneous form, which provides a wave Eq. (15.68) to describe the space-time evolution of the second-order pressure,  $p_2$ , is still driven by quadratic combinations of the first-order sound fields produced by first sound ( $v_1^2$  and  $p_1^2$ ), second sound( $T_1^2$  and  $w_1^2$ ), or their interaction ( $p_1 T_1$ ) [15].

$$\frac{\partial^2 p_2}{\partial t^2} - c_1^2 \nabla^2 p_2 = c_1^2 \left[ \frac{\partial^2}{\partial r_i \partial r_j} \left( \rho v_i v_j + \frac{\rho_n \rho_s}{\rho} w_i w_j \right) - \frac{1}{2} \left( \frac{\partial^2 \rho}{\partial p^2} \right) \frac{\partial^2 p_1^2}{\partial t^2} \right. \\ \left. - \frac{1}{2} \left( \frac{\partial^2 \rho}{\partial T^2} \right) \frac{\partial^2 T_1^2}{\partial t^2} - \left( \frac{\partial^2 \rho}{\partial p \partial T} \right) \frac{\partial^2 (p_1 T_1)}{\partial t^2} - \left( \frac{\partial \rho}{\partial w^2} \right) \frac{\partial^2 (w^2)}{\partial t^2} \right] \quad (15.68)$$

Since there are two velocity fields, Eq. (15.68) expresses the fluid's motion in terms of the center-of-mass velocity,  $\vec{v}$ , which is nearly zero for second sound and  $\vec{w} = \vec{v}_n - \vec{v}_s$ , which is nearly zero for first sound. Because  $w^2$  is a Galilean invariant (i.e., its value is not dependent on the motion of the coordinate system), it is also a thermodynamic variable, as evidenced by the partial derivative in the final term in Eq. (15.68).

Resonant mode conversion of second sound to first sound was observed experimentally from 1.15 K <  $T_m$  < 2.0 K using the spiral waveguide and heater shown in Fig. 15.19 (Right) [40].

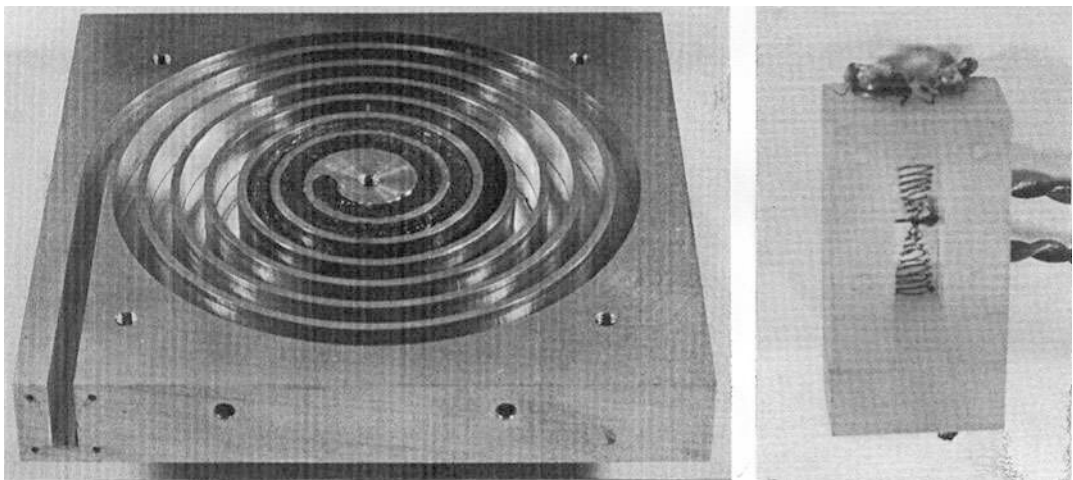


**Fig. 15.19** (Left) A spiral waveguide shown with the lid that housed the first and second sound sensors (microphones) removed. The depth of the waveguide,  $L_z = 14.73$  mm, and the width,  $L_y = 4.8$  mm. The edge length of the square block into which the spiral groove was cut is 12.7 cm. The total length of the spiral is 150 cm, and a wedge absorber, visible near the waveguide's center, occupies the final 60 cm. (Right) Second sound is generated by periodically heating the superfluid. This heater consists of two individual NiCr resistance wire elements with a nearly sinusoidal profile to optimize coupling to the first non-plane waveguide (height) mode. Due to the frequency doubling produced when the heaters are driven with an AC current, the two heater halves were driven 90° out-of-phase (electrically) at one-half the mode conversion frequency

## 15.4 Non-zero Time-Averaged Effects

Nonlinear acoustical effects are driven by quadratic combinations of first-order sound fields. When the first-order sound field was squared to produce Eq. (15.57), the constant term was ignored because it was operated upon by a Laplacian to produce the virtual sources that drove the inhomogeneous wave equation for the propagation of the second-order sound field. In this sub-section, the effects of that constant term will be explored, first with a focus on the square of the first-order particle velocity,  $v_1$ , initially restricting our analysis to one-dimensional propagating plane waves.

$$v_1^2(x, t) = v'^2 \cos^2(\omega t - kx) = \frac{v'^2}{2} [1 + \cos 2(\omega t - kx)] \quad (15.69)$$

Since the first-order acoustic fields have a sinusoidal time dependence, their time-averaged values must vanish over times that are long compared to the periods of such disturbances,  $T \gg 2\pi/\omega$ .

$$\langle p_1 \rangle_t = \frac{1}{T} \int_0^T p_1 \, dt = 0 \quad (15.70)$$

The second-order terms, like the squared velocity in Eq. (15.69), that contain a constant term, will produce time-averaged second-order pressures that will not vanish:  $\langle p_2 \rangle_t \neq 0$ . These second-order non-zero time-averaged pressures can produce substantial forces [41] and torques [42] on objects that are within the sound field. As early as the 1940s, Hillary St. Clair was able to levitate copper pennies ( $\rho_{Cu} = 8.9 \text{ gm/cm}^3$ ) [43]. Using an intense sound field produced by a siren and a reflector, Allen and Rudnick were able to repeat St. Clair's demonstration:

*"When a number of pennies are placed on a stretched silk screen, the parameters can be so adjusted that the pennies do somersaults with "Rockette"-like precision; or so that a penny can be made to rise slowly to a vertical position, appearing all the while to be supporting, acrobatically, another which finally assumes a horizontal position above the first penny touching rim to rim. Also, coins resting on the silk screen can be flipped a distance of a few feet by varying the frequency of the siren rapidly."* [44]

### 15.4.1 The Second-Order Pressure in an Adiabatic Compression

Nonlinear distortion, the generation of harmonics, and the "scattering of sound by sound" were attributed to the fact that a wave will modify the properties of the medium through which it is propagating. To start our investigation of non-zero time-averaged effects, it will be instructive to consider the piston of area,  $A_{pist}$ , in a close-fitted cylinder that is filled with an ideal gas at equilibrium pressure,  $p_m$ . With the piston in its equilibrium position, designated as  $x = 0$ , the equilibrium volume of the gas in the cylinder will be  $V_o = A_{pist} L$ , where  $L$  is the length of the cylinder from the rigid end located at  $x = L$  to the piston's equilibrium position. This arrangement is identical to that depicted schematically in Fig. 8.5.

If the gas inside the cylinder obeys the Adiabatic Gas Law and if the motion of the piston is sinusoidal, with the piston's position given by  $x(t) = x_1 \sin(\omega t)$ , then the pressure within the cylinder will be uniform throughout and given by the Adiabatic Gas Law as long as  $\sqrt{A_{pist}} \ll \lambda/2\pi = c_o/\omega$  and  $L \ll c_o/\omega$ , so that the cylinder can be treated as a "lumped element," where  $c_o = \sqrt{(\partial p/\partial \rho)_s}$  is the speed of sound under equilibrium conditions.

$$\begin{aligned} pV^\gamma = \text{const.} \Rightarrow \frac{p_1(t)}{p_m} &= -\gamma \frac{\delta V}{V_o} = -\gamma \frac{-A_{\text{pist}}x_1 \sin(\omega t)}{A_{\text{pist}}L} \\ \Rightarrow p_1(t) &= \gamma p_m \frac{x_1 \sin(\omega t)}{L} \equiv p_1 \sin(\omega t) \end{aligned} \quad (15.71)$$

This is the familiar “linear” result; a sinusoidal variation in the piston’s position leads to a sinusoidal variation of the pressure within the cylinder. Such a result assumes that  $x_1/L \ll 1$ , so the motion of the piston does not affect the volume,  $V_o$ , that appears in Eq. (15.71). Of course, that is not exactly true. As the ratio of  $x_1$  to  $L$  increases, the importance of the piston’s instantaneous position on the value of the volume of the gas becomes more influential. It is easy to take the change in the cylinder’s volume into account. When the piston moves inward, it sweeps out a volume,  $\delta V(t) = -A_{\text{pist}}x(t)$ , which should be subtracted from the equilibrium volume,  $V_o$ .

$$p(t) = -\gamma p_m \frac{\delta V}{V_o \left(1 - \frac{\delta V}{V_o}\right)} \cong -\gamma p_m \frac{\delta V}{V_o} \left(1 + \frac{\delta V}{V_o}\right) = -\gamma p_m \left[ \frac{\delta V}{V_o} + \left(\frac{\delta V}{V_o}\right)^2 \right] \quad (15.72)$$

Taking the time-average of the pressure over a period,  $T$ , the linear term vanishes, but the quadratic term produces a non-zero time-averaged pressure,  $\langle p_2 \rangle_t$ , since  $\sin^2(\omega t) = \frac{1}{2}[1 - \sin(2\omega t)]$ .

$$\langle p_2 \rangle_t = \frac{\gamma p_m}{2T} \left(\frac{x_1}{L}\right)^2 \int_0^T [1 - \cos(2\omega t)] dt = \frac{\gamma p_m}{2} \left(\frac{x_1}{L}\right)^2 \quad (15.73)$$

The integral over the component oscillating at  $2\omega$  will vanish but the constant component will not. That time-averaged excess pressure will tend to push the piston away from the closed end of the cylinder. This effect produces “piston walk” in Stirling cycle machines.

This time-averaged pressure can be expressed in terms of the first-order pressure calculated in Eq. (15.71):  $x_1/L = p_1/\gamma p_m = p_1/\rho_m c_o^2$ , if the cylinder contains an ideal gas.

$$\langle p_2 \rangle_t = \frac{p_1^2}{2\rho_m c_o^2} \quad (15.74)$$

In this form, it is clear that the non-zero time-averaged pressure is quadratic in the first-order pressure. It is also useful to recognize that this result is equal to the potential energy density as derived from the energy conservation Eq. (10.35).

As with the results of weak shock theory in Sect. 15.2, it is the effects of the piston’s position on the volume that appears in the Adiabatic Gas Law of Eq. (15.72) that produces corrections to the linear result. The creation of a net second-order pressure is due to the asymmetry produced by the fact that the average volume on compression of a piston is smaller than the average volume during expansion.

Application of this result to a one-dimensional standing wave resonator is straightforward. Within the resonator, the first-order pressure can be written as  $p_1(x, t) = \Re e[\hat{\mathbf{p}} \cos(n\pi x/L) e^{i\omega t}]$ . Close to the end at  $x = 0$ , the first-order acoustic pressure is nearly independent of position, just as it is in the piston and cylinder example. By the Euler equation, the longitudinal particle velocity can be written as  $v_1(x, t) = \Re e[j(\hat{\mathbf{p}}/\rho_m c_o) \sin(n\pi x/L) e^{i\omega t}] \equiv -v_1 \sin(n\pi x/L) \sin(\omega t + \varphi)$ , so the particle velocity goes linearly to zero as  $x$  goes to  $L$ , just as it does in the piston and cylinder example. This situation near to the rigid end of the resonator (or close to any standing wave pressure anti-node) can be represented by an imaginary line (i.e., a Lagrangian marker) that moves with the gas, acting as the piston while neglecting the remaining gas in the resonator.

In a sealed resonator, the total mass of the gas cannot change. If the static pressure at the rigid ends (as well as at any pressure anti-node for higher-order longitudinal modes of the resonator,  $n > 1$ )

increases by the amount specified in Eq. (15.74), then the density of the gas must also increase in those locations. For that to happen in a sealed system, the gas density (and pressure) must decrease elsewhere.

In a standing wave, the amplitude of the gas particle velocity at a pressure node (velocity anti-node) is  $v_1 = p_1/\rho_m c_o$ , so if the total mass of the gas cannot change, then the non-zero, second-order, time-averaged pressure at the first-order pressure node must be equal and opposite to the value in Eq. (15.74) and can be re-written in terms of  $v_1$ .

$$\langle p_2 \rangle_t = -\frac{p_1^2}{2\rho_m c_o^2} = -(\tfrac{1}{2})\rho_m v_1^2 \quad \text{at a pressure node} \quad (15.75)$$

In this form, it is clear that the non-zero time-averaged pressure is quadratic in the first-order velocity amplitude. It is also useful to recognize that this result is equal to the kinetic energy density at the velocity anti-node as derived from the energy conservation Eq. (10.35). It also has the functional form of the *Bernoulli pressure*.

The relationship between the second-order time-averaged pressure [45], also known as the *radiation pressure*, and the kinetic and potential energy densities will be derived from the hydrodynamic equations in Sect. 15.4.4 after examining a few examples of the acoustical consequences produced by the Bernoulli pressure in the following sub-section and in Sect. 15.4.3.

### 15.4.2 The Bernoulli Pressure

The first introduction in this textbook to the Bernoulli pressure<sup>9</sup> was provided in the analysis of the Venturi tube (see Sect. 8.4.1) that was intended to aid in the understanding of the convective term in the total hydrodynamic derivative in Eq. (8.33). This resulted in the introduction of a pressure gradient produced in the tube that was driven by the square of the fluid's velocity,  $v^2$ .

$$p = p_m - \frac{1}{2}\rho_m v^2 \quad (15.76)$$

Since the Bernoulli pressure is proportional to the square of the fluid's velocity, it is independent of the direction of flow. For the oscillatory velocities that are produced by sound waves, this means that the time-averaged Bernoulli pressure will be non-zero.

The effects of the Bernoulli pressure for oscillatory flows produced by sound waves were recognized and understood by Lord Rayleigh. The *Kundt's tube* was a popular piece of acoustic apparatus that produced high-amplitude standing waves by stroking a rod that would excite longitudinal vibrations and couple those vibrations to the air contained in a transparent glass tube [46]. Cork dust or lycopodium seeds were commonly used to visualize the sound field by “decorating” velocity anti-nodes. Figure 8.14 shows cork dust striations in the neck of a resonator that is excited in its Helmholtz mode,  $f_o = 210$  Hz (left), and at a frequency,  $f_i = 1240$  Hz, that excited a half-wavelength standing wave in the neck (right) [47].

---

<sup>9</sup>Daniel Bernoulli (1700–1782) was a Dutch physicist and mathematician who published *Hydrodynamica* in 1738 that provided the basis of the kinetic theory of gases which he applied to explain Boyle's law. He was also well known for early development of elasticity theory with Leonard Euler, an effort recognized to this day by the fact that Eq. (5.36) is called Euler-Bernoulli beam equation.

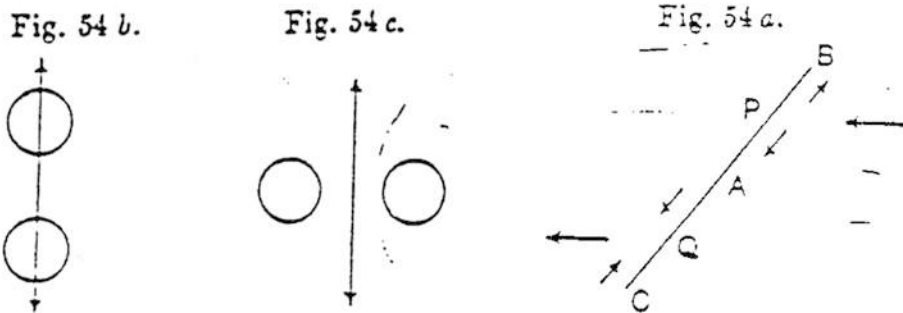


**Fig. 15.20** Three figures taken from Rayleigh's *Theory of Sound*, Vol. II [50]. (Left) In Fig. 54b, two particles are oriented along the direction of oscillatory flow indicated by the double-headed arrow. Since the flow is occluded between the two spheres, the time-averaged pressure is greater between the particles causing them to repel. (Center) When the same two particles are oriented normal to the oscillatory flow in Fig. 54c, the increase in the velocity between the two produces a lower pressure that causes the two particles to attract each other. (Right) A rigid disk is placed at 45° with respect to the oscillatory flow

Rayleigh recognized that two small particles of sufficient mass to remain stationary within the oscillatory flow field, due to their inertia,<sup>10</sup> would be attracted to each other because the oscillatory air flow must accelerate as it passes between the constrictions produced by the adjacent particles. By Eq. (15.76), the increased fluid velocity between the particles results in a lower pressure so that the resultant pressure gradient would drive the particles together.

The figure taken from Rayleigh's *Theory of Sound* that diagrams this attraction is shown in Fig. 15.20 (center). This effect, known as acoustic agglomeration, has been used in several applications where removal of larger clusters of smaller particles from a fluid is easier than the removal of smaller individual particles [48]. More recently, "acoustic agglomeration" has been used for separation of biological cells grown in bioreactors from their nutrient liquid [49].

Rayleigh makes a similar argument, as also illustrated in Fig. 15.20 (left), to explain the striations of the dust particles agglomerated in planes that are normal to the oscillatory flow. When two particles (or planes of particles) are separated along the direction of the oscillatory flow, the stagnation of the fluid between them produces an increase in the time-averaged pressure that causes the particles (or planes of particles) to repel each other, as clearly visible in the striations seen in Fig. 8.14.

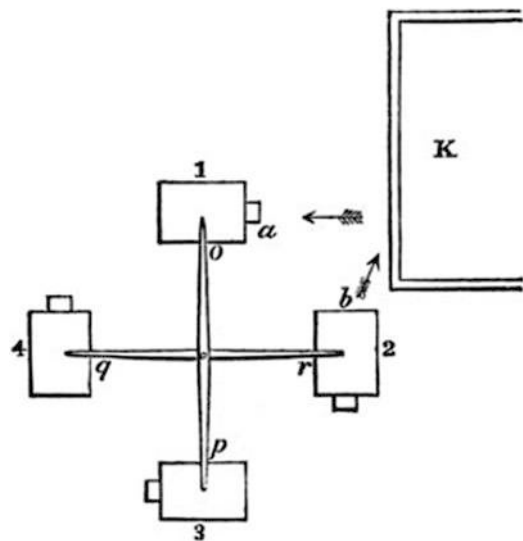
Another interesting manifestation of the Bernoulli pressure was mentioned by Rayleigh in regard to the forces on a Helmholtz resonator. The fluid's velocity in the neck of a Helmholtz resonator is high.

<sup>10</sup>The motion of a small particle in a sound field will depend upon the competition between the particle's inertia (mass), which tends to make it remain stationary in the laboratory frame of reference, and the Stokes drag due to the viscosity of the medium which tends to force the particle to move along with the acoustically oscillating fluid. The inertial force is given by Newton's Second Law,  $F_{inertia} = m (dv/dt)$ , and the Stokes drag force on a spherical particle of radius,  $a$ , (at sufficiently low Reynolds number) is  $F_{drag} = 6\pi\mu av_1$ . Their dimensionless ratio will determine if the particle moves with the fluid or if the fluid moves around the particle. That ratio can be written for a spherical particle with mass density,  $\rho$ , and sound with frequency,  $f$ .

$$\frac{F_{inertia}}{F_{drag}} = \frac{4\pi}{9} \frac{a^2 f \rho}{\mu}$$

For a particle with the density of water ( $\rho = 10^3 \text{ kg/m}^3$ ), in air with  $\mu \approx 1.8 \times 10^{-5} \text{ Pa-s}$ , and then at 100 Hz, that ratio is one for a spherical particle with a radius of about 10 microns. A larger radius particle, like cork dust, coffee whitener, or a seed, will remain nearly stationary in the laboratory frame, and the fluid will oscillate around it, while a much smaller particle, like smoke, will move with the fluid.

**Fig. 15.21** Apparatus drawing, taken from Dvořák [52], showing “four very light paper or glass [Helmholtz] resonators upon two wooden rods,  $o\ p$ ,  $q\ r$ , crossing at right angles, and balanced on a glass cap; all the openings of the resonators fronting one side in the direction of tangents. The whole apparatus is placed before the opening, K, of the resonating box and fork, in the manner indicated”



Based on Eq. (15.76), this suggests that the pressure in the neck must be reduced. Since the neck is in direct contact with an effectively infinite reservoir of atmospheric pressure, the only means by which the required pressure difference can be maintained is if the static time-averaged pressure within the compliance (volume) of the Helmholtz resonator is greater than atmospheric pressure.

This second-order, acoustically induced pressure difference,  $\langle p_2 \rangle_t$ , will lead to a net force on the Helmholtz resonator since the pressure on the surfaces of the volume are unbalanced over the cross-sectional area,  $\pi a_{neck}^2$ , of the neck:  $F_{net} = \pi a_{neck}^2 \langle p_2(v_{neck}^2) \rangle_t$ .

“Among the phenomena of the second order which admit of a ready explanation, a prominent place must be assigned to the repulsion of resonators discovered independently by Dvořák [51] and Meyer [52]. These observers found that an air resonator of any kind when exposed to a powerful source experiences a force directed inwards from the mouth, somewhat after the manner of a rocket. A combination of four light resonators, mounted anemometer fashion upon a steel point, may be caused to revolve continuously.” [53]

Apparently, an acoustical demonstration of the nonlinear force on a resonator that resembles a lawn sprinkler, shown in Fig. 15.21, from [52], was well known to Rayleigh [51]. This effect can be observed in a quantitative way by placing a Helmholtz resonator on a sensitive balance and producing a large amplitude sound field in the vicinity using a loudspeaker driven at the Helmholtz resonance frequency and then observing the increase in the resonator’s apparent weight to do “the rocket.”

### 15.4.3 The Rayleigh Disk

The Bernoulli pressure of Eq. (15.76) can also exert torques,  $N(v_1^2)$ , on an extended object placed in an oscillatory flow field. Rayleigh’s diagram of such a disk that is aligned at about  $45^\circ$  with respect to the

<sup>11</sup> Video demonstrations of several of the non-zero, time-averaged effects in this section were recorded at the 100<sup>th</sup> meeting of the Acoustical Society of America held in Los Angeles, CA, in 1988. This video is included in the second disk of the *Collected Works of Distinguished Acousticians—Isadore Rudnick*, compiled by J. D. Maynard and S. L. Garrett (Acoust. Soc. Am., 2011); <https://www.abdi-e-commerce10.com/ASA/p-230-collected-works-of-distinguished-acousticians.aspx>.

flow field is shown in Fig. 15.20 (right). That figure captures the flow at an instant when it is moving from right to left, as indicated by the arrows. The approaching flow stagnates between A and B where it diverges, and the receding flow stagnates on the other side of the disk between C and Q where it rejoins. On the inflow side of the desk, the flow must accelerate along A-Q-C as the two flows converge on the outflow side at P. The stagnant flow between A and B on the inflow side and between C and Q on the outflow side has a higher pressure than the faster-moving flows at the same locations on the opposite sides of the disk. This produces a net torque that tends to orient the disk perpendicular to the flow, regardless of the flow direction.

An appreciation for the magnitude of this torque can be obtained by calculation of the moment of the Bernoulli pressure in Eq. (15.76) over both sides of a disk having radius,  $a$ , assuming the presence of the disk does not perturb the sound field.<sup>12</sup> The circle in Fig. 4.11 that was used to calculate the radius of gyration for beam flexure will provide the coordinate system for this integration.

$$\begin{aligned} N &= \int_0^a \langle p_2 \rangle_t r \, dS = 4 \int_0^a \frac{\rho_m \langle v_1^2 \rangle_t}{2} h [2h \cos \theta] \, dh \\ &= 4\rho_m \langle v_1^2 \rangle_t \int_0^{\pi/2} (a \sin \theta)^2 a \cos \theta \, d\theta = \frac{4}{3} \rho_m \langle v_1^2 \rangle_t a^3 \end{aligned} \quad (15.77)$$

If the disk is assumed to be suspended by a torsion fiber in the oscillatory flow, then the torque will be zero when the surface of the disk is perpendicular to the flow or when the surface of the disk is aligned with the flow. If the angle between the normal to the disk's surface is designated  $\theta$ , then the torque will be zero when  $\theta = 0^\circ$  (occluding the flow) or when  $\theta = 90^\circ$  (aligned with the flow), except that the  $\theta = 90^\circ$  orientation will be unstable. If the disk is aligned with the flow and its orientation deviates slightly from  $\theta = 90^\circ$ , then the torque will cause the disk to seek the  $\theta = 0^\circ$  orientation. If the disk is in the  $\theta = 0^\circ$ , any small deviation in  $\theta$  will subject the disk to a torque that will tend to restore the  $\theta = 0^\circ$  orientation.

Based on the magnitude of the torque in Eq. (15.77) and the previous stability argument, the torque as a function of the square of the time-averaged oscillatory velocity amplitude,  $\langle v_1^2 \rangle_t$ , and the orientation angle can be written in the form that appears in *Theory of Sound*, which Rayleigh attributes to König [54].

$$N(\theta) = \frac{4}{3} \rho_m \langle v_1^2 \rangle_t a^3 \sin 2\theta \quad (15.78)$$

Rayleigh recognized that “Upon this principle an instrument may be constructed for measuring the intensities of aerial vibrations of selected pitch” and suggests that the disk be a mirror suspended by a silk thread so a light beam could be used as an optical lever (see Sect. 2.4.4) to determine the disk’s orientation [55].

Prior to the introduction of the reciprocity method for calibration of reversible transducers (see Sect. 10.7.2, 10.7.3 and 10.7.4), the Rayleigh disk was a primary technique for determination of acoustic sound field amplitudes [56]. Due to its importance, a detailed analysis of the torque was made by King to include corrections produced by the disk’s influence on the sound field [57]. The torque on a Rayleigh disk located at a velocity anti-node in a standing wave field included wavelength-dependent

---

<sup>12</sup>This assumption is not as bad as it seems since the Bernoulli pressure, as described in Eq. (15.76), is only valid along a streamline. The streamlines in Fig. 15.20 (right) will follow the contours of the disk accounting for the fact that simple results of Eqs. (15.77) and (15.78) are very nearly the correct result.

corrections for the disk's mass,  $m_1$ , as well as the disk's hydrodynamic (inertial) entrained mass,  $m_o = (8/3)\rho_m a^3$ , as calculated in Eq. (12.126).

$$N_{\text{anti-node}}(\theta) = \frac{4}{3}\rho_m \langle v_1^2 \rangle_t a^3 \sin 2\theta \left\{ \frac{m_1 \left[ 1 + \frac{2}{5}(ka)^2 \cos^2 2\theta \right]}{m_1 + m_o \left[ 1 + \frac{1}{5}(ka)^2 \right]} \right\} \quad (15.79)$$

The indifference of the sign of the torque produced by flow in either direction was important in establishing the physical reality of Landau's two-fluid theory of superfluid hydrodynamics.<sup>5</sup> As mentioned briefly in Sects. 15.1.2 and 15.3.4, there are two velocity fields necessary to characterize the dynamics of superfluid flow,  $\vec{v}_s$  and  $\vec{v}_n$ . In a thermally induced second sound wave, the superfluid's center-of-mass velocity is zero, but the counterflow of  $\vec{v}_s$  and  $\vec{v}_n$  is non-zero.

Since the Rayleigh disk responds to the torque of both flow fields without respect to their direction, Pellam and Hanson were able to establish the physical existence of both velocity fields and make the first mechanical measurement of second sound in superfluid helium [58]. Later, Koehler and Pellam were also able to measure the superfluid fraction,  $\rho_s/\rho$ , as a function of temperature using their Rayleigh disk [59]. Both measurements employed a mirror as the disk to detect the disk's deflection optically. Later measurements of torques in superfluids used a nonoptical method to determine the Rayleigh disk's orientation [60].

#### 15.4.4 Radiation Pressure

Restricting attention to one dimension, the Bernoulli pressure can be derived from the Euler Eq. (15.48).

$$\frac{\partial v}{\partial t} + v \frac{\partial v}{\partial x} = - \frac{1}{\rho_m} \frac{\partial p}{\partial x} \quad (15.80)$$

The goal will be to express Eq. (15.80) entirely in terms of the gradient of a scalar, so it is useful to introduce the specific *enthalpy* (heat) function (see Sect. 14.2),  $h = e + pV$ , where  $e$  is the fluid's *internal energy* per unit volume (see Sect. 7.1.2):  $de = dU/V$ .

$$dh = de + p \, dV + V \, dp \quad (15.81)$$

Using the definition of the internal energy from Eq. (7.10),  $de = T \, ds - p \, dV$ , the pressure gradient can be expressed in terms of the specific enthalpy,  $dh = dp/\rho_m$ , and the product rule can be invoked to consolidate the convective contribution.

$$\frac{\partial v}{\partial t} + \frac{1}{2} \frac{\partial v^2}{\partial x} = - \frac{\partial h}{\partial x} \quad (15.82)$$

Having started with the Euler equation, the effects of viscosity have already been eliminated, so the Kelvin circulation theorem guarantees that the velocity field will be curl free; thus it can be expressed as the gradient of a scalar,  $\phi$ , known as the *velocity potential*:  $\vec{v} = \vec{\nabla} \phi$  [61].

$$\frac{\partial}{\partial x} \left( \frac{\partial \phi}{\partial t} + \frac{v^2}{2} + h \right) = 0 \quad (15.83)$$

Since the argument within the gradient in Eq. (15.83) is equal to zero, the function within the gradient must be a constant everywhere throughout the fluid.

$$\frac{\partial \phi}{\partial t} + \frac{v^2}{2} + h = \text{constant} \quad (15.84)$$

This is the “strong” form of Bernoulli’s equation, since it is not restricted only to streamlines, as it was for the version introduced in Eq. (15.76).

To retain accuracy to second-order, the specific enthalpy must also be expanded to second-order.

$$h = h_o + \left( \frac{\partial h}{\partial p} \right)_s (p_1 + p_2) + \left( \frac{\partial^2 h}{\partial p^2} \right)_s \frac{p_1^2}{2} \quad (15.85)$$

These thermodynamic derivatives can be evaluated for adiabatic processes,  $dS = 0$ , from the differential form of the specific enthalpy:  $dh = T \, dS - dp/\rho_m$ .

$$\frac{\partial \phi}{\partial t} + \frac{v^2}{2} + h_o + \frac{(p_1 + p_2)}{\rho_m} - \frac{1}{2} \frac{p_1^2}{\rho_m^2 c_o^2} = \text{constant} \quad (15.86)$$

In this sub-section, we are only interested in the parts of Eq. (15.86) which produce a non-zero time-average. As in Eq. (15.70), the time-average of first-order variations will vanish:  $\langle \partial \phi / \partial t \rangle_t = \langle p_1 \rangle_t = 0$ .

$$\langle p_2 \rangle_t = \frac{1}{2} \frac{p_1^2}{\rho_m c_o^2} - \frac{1}{2} \rho_m v_1^2 + \text{constant} \quad (15.87)$$

The second-order time-averaged pressure is the difference between the potential and kinetic energy densities. In classical mechanics, that combination is known as the Lagrangian density [62].

For a collimated traveling wave of the usual form,<sup>13</sup>  $p_1(x, t) = p_1 \cos(\omega t - kx)$ , the linearized Euler’s equation provides the ubiquitous relationship between the first-order acoustic field variables:  $p_1 = \rho_m c_o v_1$ . That relationship can then be substituted into Eq. (15.87).

$$\langle p_2 \rangle_t = \frac{1}{2} \frac{p_1^2}{\rho_m c_o^2} - \frac{1}{2} \frac{p_1^2}{\rho_m c_o^2} = 0 \quad (15.88)$$

This result is oddly both philosophically significant and trivially obvious. If there were an object in the traveling-wave field, it would scatter some portion of the sound (see Sects. 12.6.1 and 12.6.2), and the sum of the scattered and incident wave fields would produce a standing wave. If the field is entirely a traveling wave, then that wave field cannot include an “object” which would feel the force of a time-averaged second-order pressure based on the object’s density and/or compressibility contrast.

### 15.4.5 Acoustic Levitation in Standing Waves

The result for the time-averaged second-order pressure in Eq. (15.87) can also be evaluated for a standing wave.

---

<sup>13</sup> For a plane wave of infinite extent, the constant in Eq. (15.87) cannot be set to zero as it has to produce Eq. (15.88). This is discussed in C. P. Lee and T. G. Wang, “Acoustic radiation pressure,” J. Acoust. Soc. Am. **94**(2), 1099–1109 (1993).

$$p_1(x, t) = p' \cos(kx) \cos(\omega t) \quad \text{and} \quad v_1(x, t) = \frac{p'}{\rho_m c_o} \sin(kx) \cos(\omega t) \quad (15.89)$$

Substitution of Eq. (15.89) into (15.87) produces the time-averaged second-order pressure distribution for a standing wave in an ideal gas where  $\rho_m c_o^2 = \gamma p_m$ .

$$\langle p_2(x, t) \rangle_t = \frac{1}{4} \frac{p'^2}{\rho_m c_o^2} [\cos^2(kx) - \sin^2(kx)] = \frac{1}{4} \frac{p'^2}{\gamma p_m} \cos(2kx) \quad (15.90)$$

A standing wave produces a time-averaged (i.e., static) second-order pressure distribution. Due to the spatial dependence on  $\cos(2kx)$ , there is a minimum in the second-order pressure at the location of each pressure node, thus at each velocity anti-node and a maximum one-quarter wavelength from that minimum. This is consistent with the second-order piston example used as an introduction to non-zero time-averaged effects in Sect. 15.4.1.

This second-order time-averaged pressure distribution produces pressure gradients that are fixed in space and time and will exert forces on solid objects of non-zero thickness. The force on an object at either the maximum or the minimum in  $\langle p_2 \rangle_t$  will be zero, but that equilibrium will be unstable at the maximum. If a levitated object is displaced slightly from the maximum, it will be forced toward the minimum in  $\langle p_2 \rangle_t$ , that occurs at a first-order velocity anti-node which has the lowest pressure, due to Bernoulli.

The integrated pressure over a small sphere of radius,  $a \ll \lambda$ , will produce a force,  $F_{\text{sphere}}$ , that is, a function of the sphere's location in the standing wave field.

$$F_{\text{sphere}} = \frac{4\pi a^2}{3} \frac{p'^2}{\rho_m c_o^2} (ka) \sin(2kx) = kV_{\text{sphere}} \frac{(p')^2}{2\rho_m c_o^2} \sin(2kx) \quad (15.91)$$

Rudnick provided a clever confirmation of this result in a simple standing wave tube that measured the angle of displacement of small spheres suspended by “a hair” due to the standing wave [63]. The integrated pressure over a small disk of thickness,  $t$ , and radius,  $a$ , will produce a force,  $F_{\text{disk}}$ , that is, a function of the disk's location

$$F_{\text{disk}} = \frac{\pi a^2}{2} \frac{p'^2}{\rho_m c_o^2} (kt) \sin(2kx) = kV_{\text{disk}} \frac{(p')^2}{2\rho_m c_o^2} \sin(2kx) \quad (15.92)$$

To levitate a small sphere made of a material with a mass density,  $\rho_{\text{sphere}}$ , against the force of gravity, the weight of the sphere must be cancelled by the levitation force. This requires that the square of the first-order standing wave pressure field amplitude,  $p'^2$ , exceed a minimum value,  $p'^2_{\min}$ .

$$p'^2_{\min} > \gamma p_m \rho_{\text{sphere}} \frac{g\lambda}{\pi} \quad (15.93)$$

When this criterion is satisfied, then the position of the sphere will adjust itself within the (vertical) standing wave field to make the net force on the sphere be zero at some location below a velocity anti-node. The stability of that equilibrium will be the subject of Sect. 15.4.6.

Of course, the levitated object does not have to be either a sphere or a disk. As shown in Fig. 15.22, almost any small object can be suspended against the force of gravity if the amplitude of the standing wave sound field is sufficient.

**Fig. 15.22** Clockwise from the top left are shown a ladybug, minnow, spider, and ant being levitated by intense standing waves in air. [Courtesy of Northwestern Polytechnical University in Xi'an, China]



#### 15.4.6 Adiabatic Invariance and the Levitation Force

In the previous sub-section, the influence of the object being levitated by the standing wave on the response of the resonator was ignored. As will now be demonstrated, the perturbation of the resonator's normal mode frequency caused by an object will provide an alternative method to predict the levitation force by use of adiabatic invariance and without the necessity of integrating the pressure gradient around the object. In the subsequent sub-section, the feedback between the radiation force and the object's influence on the resonance frequency will also have significant impact on the stability of the levitated object in a resonator that is driven at a constant frequency.

Throughout this text, the concept of adiabatic invariance [64] has been utilized when it was convenient to relate changes in a system's constraints (e.g., boundary conditions) to one or more of that system's normal mode frequencies. Now adiabatic invariance will be applied in the same way (i.e., the “variable constraint” being the position of the object in the sound field) to a one-dimensional standing wave tube's resonance frequencies that are perturbed by an incompressible obstacle that can be placed anywhere within the resonator of length,  $L$ , and cross-sectional area,  $A$ .

It is assumed that the obstacle of volume,  $V$ , shown as a small cube in Fig. 15.23 (left), has dimensions that are all much smaller than the wavelength,  $\lambda_n$ , of any normal mode of interest:  $\sqrt[3]{V} \ll \lambda_n$ . Because the obstacle is located at a pressure anti-node (velocity node) in Fig. 15.23 (left), the excluded (incompressible) volume “stiffens” the gas springiness at that rigid end and raises the unperturbed (empty resonator) frequency,  $f_1$ , of the fundamental ( $n = 1$ ) mode:  $f_1 = c_o/2L$ .

To estimate the increase in frequency caused by the obstacle when it is near a pressure anti-node (velocity node), we can use the same trick that simplified the calculation of the frequency shift caused by the deposition of a thin layer of gold that lowered the fundamental frequency of a quartz microbalance in Sect. 5.1.2 due to its additional mass loading. Let the cube be made of wax. If the wax were melted with the tube in the vertical orientation, then the volume of wax would remain unchanged, but it would be spread uniformly over the resonator's endcap as shown in Fig. 15.23 (right). Since the slope of the pressure at the endcap is zero, the cube and slab versions of the obstacle produce the same

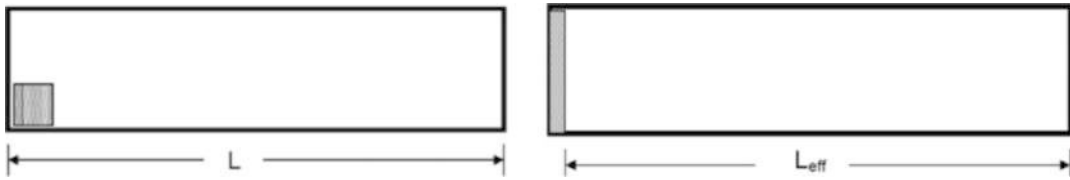


**Fig. 15.23** (Left) A small rigid obstacle (grey square) is placed adjacent to the rigid end of a one-dimensional standing wave resonator of length,  $L$ . (Right) That obstacle has been “melted” so that its entire volume (grey rectangle) has been preserved but is now distributed uniformly over the resonator’s cross-section, producing a decreased effective length,  $L_{\text{eff}}$

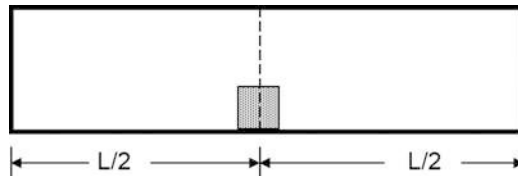


**Fig. 15.24** The same obstacle that was shown in Fig. 15.23 is now located at the center of the resonator. In that position, it lowers the frequency of the fundamental ( $n = 1$ ) normal mode but raises the frequency of the second normal mode ( $n = 2$ )

stiffening of the gas (i.e., exclude the same amount of resonator volume). The perturbed frequency,  $f'_1$ , is then that of the slightly shorter resonator shown in Fig. 15.23 (right):  $f'_1 = c_o/2L_{\text{eff}}$ .

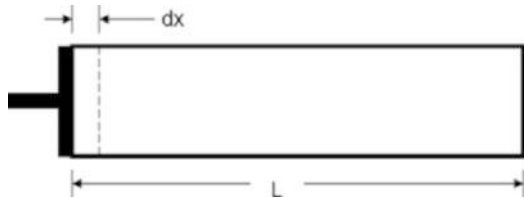
If the same obstacle was moved to the center of the resonator, as shown in Fig. 15.24, then it would lower the resonance frequency below the unperturbed frequency,  $f_1$ . This is because the obstacle has created a constriction in the resonator’s cross-sectional area,  $A$ , at a position within the fundamental mode that is located at a velocity anti-node (pressure node). The high-speed gas near the resonator’s midplane must accelerate to go around the obstacle, thus increasing the kinetic energy without affecting the potential energy stored at the ends of the resonator (see Sect. 13.3.4).

By Rayleigh’s method (see Sect. 2.3.2), this means that the fundamental normal mode frequency must be reduced. The amount of that frequency reduction is dependent upon the shape of the obstacle, so it is not as easy to make a quantitative estimate of the frequency reduction as it was for the case where the incompressible obstacle was located at a pressure anti-node (velocity node). Fortunately, the use of adiabatic invariance provides a method to measure the effect of an obstacle of any shape and any location within the standing wave then relate that frequency shift produced to the levitation force, as described in the next sub-section.

For the resonator’s second mode ( $n = 2$ ), the obstacle is located at a pressure anti-node and thus raises the resonance frequency of that mode. Again, since the resonator’s midplane contributes gas stiffness in the second mode (along with the gas stiffnesses at both ends), the volume exclusion produced by the obstacle increases the gas stiffness. The “melted wax” trick would work again by symmetry, treating the resonator as two half-resonators, each shortened by the appropriate amount:  $L_{\text{eff}}/2 < L/2$ .

It is worthwhile to notice that when this obstacle is located at the center of the resonator, it has ruined the harmonicity of the modes of the closed-closed resonator of uniform cross-section:  $f_n \neq nf_1$ . All of the  $n = \text{odd}$  modes will be “flattened” ( $\flat$ ) (i.e., their normal mode frequencies will be lowered), and all of the  $n = \text{even}$  modes will be sharpened ( $\sharp$ ), as long as the  $\sqrt[3]{V} \ll \lambda_n$  constraint is satisfied so the obstacle can be considered to be “small.” This strategy is regularly employed to suppress the formation of shock waves in standing wave resonators that are used in high-amplitude applications like thermoacoustic refrigerators [65] and sonic compressors [66].

**Fig. 15.25** A simple plane wave resonator with an adjustable left boundary position (piston)



In previous applications of adiabatic invariance, the work that was done against (or by) the radiation pressure was used to estimate normal mode frequencies of resonators with shapes that did not conform to the 11 separable geometries (see Sect. 13.1). It will now be easy, using Eq. (15.87), to demonstrate the connection between frequency changes and work done against the radiation force. If the resonator, shown schematically in Fig. 15.25, has an initial length,  $L$ , the standing wave pressure distribution is related to the velocity distribution that satisfied the rigid (impenetrable) boundary conditions as provided in Eq. (15.89). Here, we will focus on the fundamental mode,  $n = 1$ .

The time-averaged energy in the first mode,  $E_1$ , can be expressed as the time-average of the sum of the kinetic and potential energies, or by the virial theorem (Sect. 2.3.1), as the maximum potential energy,  $(PE)_{\max}$ , by integrating the potential energy density of Eq. (10.35) throughout the resonator's volume.

$$E_1 = \langle PE_{\max} \rangle_t = \int_0^L \frac{[p' \cos(\pi x/L)]^2}{2\rho_m c_o^2} A \, dx = \frac{(p')^2}{4\rho_m c_o^2} AL = \frac{(p')^2}{4\rho_m p_m} AL \quad (15.94)$$

The rightmost result again assumes an ideal gas. The radiation force on the piston at the left of Fig. 15.23 is given by Eq. (15.90). The work increment,  $dW$ , done by the piston against the radiation force is just the force,  $F_{rad} = \langle p_2 \rangle A$ , times the displacement,  $dx$ .

$$dW = A \langle p_2 \rangle_t dx = A \frac{(p')^2}{4\rho_m p_m} dx \quad (15.95)$$

Adiabatic invariance requires that the ratio of the energy in a mode to its frequency remains constant if the system's constraints are changed slowly (i.e., we don't “jerk” the piston).

$$\frac{E_n}{f_n} = \text{const.} \quad \Rightarrow \quad \frac{\delta E_n}{E_n} = \frac{dW}{E_1} = \frac{A \frac{(p')^2}{4\rho_m p_m} dx}{\frac{(p')^2}{4\rho_m p_m} AL} = \frac{dx}{L} = \frac{\delta f}{f_1} \quad (15.96)$$

This is exactly the frequency change that would be due to a decrease in the resonator's length by an amount,  $dx$ , based on the simplest result:  $f_1 = c_o/2 L$ . In fact, the triviality of this result can be interpreted as a check on the expression (or a derivation) of the radiation pressure,  $\langle p_2 \rangle_t$ , in Eqs. (15.87) and (15.90).

It is now possible to combine adiabatic invariance and the normal mode frequency change, related to the change in an obstacle's position in a standing wave resonator, to calculate the levitation force from an alternative perspective [67]. A DELTAEC model of a resonator is provided in Fig. 15.26. The DELTAEC model makes use of a “Master-Slave Link” between Segments #2c and #6c that keeps the total length of the resonator fixed as the constriction, produced by Segments #3, #4, and #5, is moved from one end of the resonator to the other by changing the length of the DUCT in Seg. #2c from 0.0 m to 0.97 m.



```

1 □Levitator Levitation Resonator
2 Equivalent sphere diameter = 4.24 cm
3 Excluded volume = 4 x 10^-5
4 □ 0 BEGIN Initial
5           1.0000E+05 a Mean P Pa
6 Gues      345.55 b Freq   Hz
7           300.00 c TBeg   K
8           2000.0 d |p|    Pa
9           0.0000 e Ph(p) deg
10 Gues     5.2697E-04 f |U|    m^3/s
11           0.0000 g Ph(U) deg
12 Optional Parameters
13 air       Gas type
14 □ 1 SURFACE First end
15 □ 2 DUCT Duct
16           1.0000E-02 a Area   m^2
17           0.3540 b Perim   m
18           0.3000 c Length  m      Mstr
19           4.7241E-02 C |U|    m^3/s
20           -90.104 D Ph(U) deg
21           0.52697 E Htot   W
22           0.36258 F Edot   W
23 Master-Slave Links
24 Optional Parameters
25 ideal     Solid type
26 □ 3 CONE Transition
27 □ 4 DUCT Duct
28           8.0000E-03 a Area   m^2
29           0.3171 b Perim   m
30           1.0000E-02 c Length  m      Mstr
31           4.5302E-02 C |U|    m^3/s
32           -90.151 D Ph(U) deg
33           0.52697 E Htot   W
34           0.34678 F Edot   W
35 □ 5 CONE Transition

```

**Fig. 15.26** Screenshot of a DELTAEC model of a resonator with cross-sectional area,  $A = 1.0 \times 10^{-3} \text{ m}^2$ , and length,  $L = 1.0 \text{ m}$ , filled with dry air at  $300 \text{ K}$  and  $p_m = 100 \text{ kPa}$ . There is a constriction that reduces the cross-sectional area to  $8.0 \times 10^{-3} \text{ m}^2$  that is  $1.0 \text{ cm}$  long and two transitions using CONE segments, each  $1.0 \text{ cm}$  long. That combination of two CONE segments and the constrictive DUCT (Seg. #4) can be positioned anywhere within the resonator. The “Master-Slave Link” in Segments #2c and #6c maintain the total length as the position of the constriction is moved when the DUCT length in Seg. #2c is changed. The “schematic view” at the top of this figure shows the center of the tapered constriction positioned  $31.5 \text{ cm}$  from the driven end

The resonance frequencies of the first and second standing waves that are plotted in Fig. 15.27 as a function of the constriction’s location were produced using DELTAEC’s incremental plotting function (see Sect. 8.6.12). Plots of the normal mode frequency shifts, similar to those in Fig. 15.27, appeared in the literature for the fundamental mode and for the  $n = 2$  mode [68], although it was not recognized at that time that those shifts were related to the levitation forces by adiabatic invariance.

The mobile constriction in the DELTAEC model removes  $40 \text{ cm}^3$  of resonator’s unperturbed  $10 \text{ liter}$  volume ( $10,000 \text{ cm}^3$ ). This is approximately equivalent to a resonator of uniform cross-sectional area,

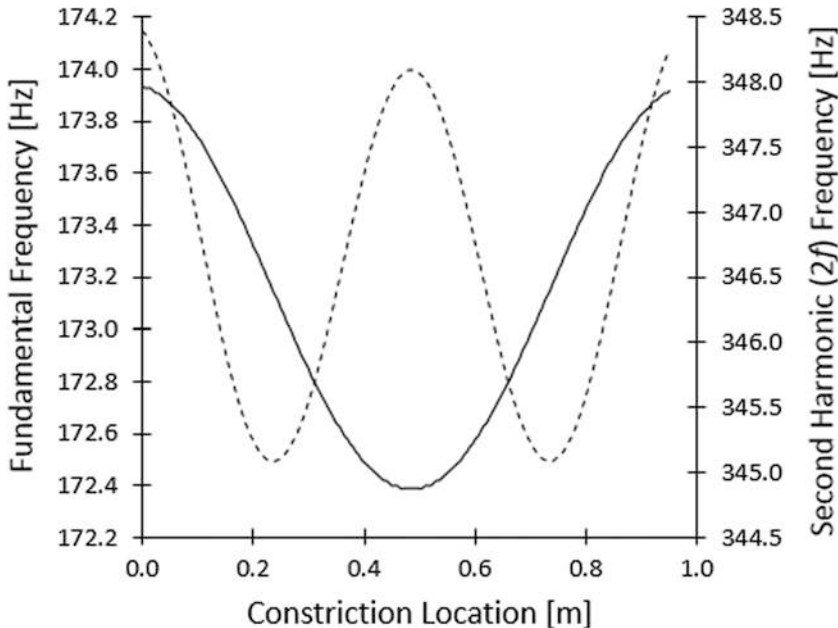


**Fig. 15.27** Resonance frequency of the resonator modeled by DELTAEC in Fig. 15.26 as a function of the position of a constriction that could represent the location of an incompressible sphere or disk. The frequency of the fundamental ( $n = 1$ ) mode is shown as the *solid line* with that frequency to be read from the left axis. The frequency of the second harmonic mode ( $n = 2$ ) is shown as the *dashed line* to be read from the right axis

$A = 1.0 \times 10^{-2} \text{ m}^2$ , that contains an incompressible sphere of radius,  $a_{sphere} = 2.12 \text{ cm}$ , or to a disk of radius,  $a_{disk} = 2.52 \text{ cm}$  and thickness,  $t = 2.0 \text{ cm}$ . Again, the DELTAEC model will not be exact because the shift in the frequency due to a kinetic energy perturbation is shape dependent, even if the obstacle is small compared to the wavelength. Although the constriction in the DELTAEC model is trapezoidal and not a sphere or disk, it provides a plausible approximation of the change in the resonator's cross-sectional area that would be caused by the sphere or disk that provides the same volume exclusion.

Adiabatic invariance requires that the ratio of the modal energy to the modal frequency,  $E_n/f_n$ , be a constant as long as the motion of the obstacle is slow compared to the period of the standing wave,  $T_n = (f_n)^{-1}$ . As shown in Fig. 15.27, the resonance frequency is a function of the constriction's location within the resonator. The energy of the mode must also be a function of position so the radiation force on the sphere,  $F_{sphere}$ , or an obstacle of some other shape must be equal to the gradient in that energy (see Sect. 1.2.1).

$$\vec{F}_{sphere} = -\vec{\nabla}E_n \quad \Rightarrow \quad F_{sphere} = -\frac{dE_n}{dx} = -\frac{dE_n}{df_n} \frac{df_n}{dx} \quad (15.97)$$

Adiabatic invariance guarantees that  $E_n/f_n = \text{constant}$ , so by log differentiation (Sect. 1.1.3),  $dE_n/df_n = E_n/f_n = \text{constant}$ .

The value of  $df_n/dx$  will depend upon the obstacle's position within the resonator. That slope will have its maximum value at locations equidistant between the nodes and the anti-nodes of the first-order standing wave fields. Using the results for the second standing wave mode produced by the DELTAEC model and plotted in Fig. 15.25, the maximum slope is just  $\pi/2$  times the difference between the maximum frequency ( $f_{2+} = 348.4 \text{ Hz}$ ) and the minimum frequency ( $f_{2-} = 345.09 \text{ Hz}$ ), divided by the separation between the location of those two extrema,  $\Delta x = 0.235 \text{ m}$ :  $df_2/dx = 21.1 \text{ Hz/m}$ .

For convenience, the constant,  $E_2/f_2$ , can be evaluated with the obstacle located at the driven end of resonator (i.e., Seg. #2c = 0.0 m), where  $E_2$  is given by Eq. (15.94), with  $p' = 2.0 \text{ kPa}$  (Seg. #0d),  $p_m = 100 \text{ kPa}$  (Seg. #0a),  $\gamma = (7/5)$ , and  $(AL) \cong 0.01 \text{ m}^3$ . At that location,  $f_2 = f_{2+} = 348.4 \text{ Hz}$ , and  $E_2 = 7.14 \times 10^{-2} \text{ J}$ , so  $E_2/f_2 = 2.05 \times 10^{-4} \text{ J/Hz}$ . Substitution of these two results into Eq. (15.97) provides the radiation force due to the constriction,  $F_{\text{rad}}$ , at a position equidistant between the nodes and the anti-nodes of the first-order standing wave fields, which is a consequence of adiabatic invariance for a trapezoidal-shaped obstacle.

$$F_{\text{rad}} = 2.05 \times 10^{-4} \frac{\text{J}}{\text{Hz}} \times 21.1 \frac{\text{Hz}}{\text{m}} = 4.3 \times 10^{-3} \text{ N} \quad (15.98)$$

This result can be compared to the radiation force at the same position for the  $n = 2$  mode, under the same conditions, if the pressure at either anti-node (i.e., rigid end) is set to  $p' = 2.0 \text{ kPa}$ , equivalent to 157 dB *re*:  $20 \mu\text{Pa}_{\text{rms}}$ , for a sphere,  $F_{\text{sphere}}$ , in Eq. (15.91), or a disk,  $F_{\text{disk}}$ , in Eq. (15.92). To make a reasonable comparison, the volume of the sphere is set equal to the volume excluded by the trapezoidal constriction:  $V = 40 \text{ cm}^3$ .

$$F_{\text{sphere}} = V_{\text{sphere}} \frac{(p')^2}{\gamma p_m} \frac{\pi f_2}{c_o} = 3.6 \times 10^{-3} \text{ N} \quad (15.99)$$

From Eq. (15.92), the result would be the same for a disk of the same volume.

Our estimate of the levitation force based on the DELTAE model and adiabatic invariance is reasonably close to that result, given that the frequency shift computation was based on a constriction rather than an obstruction.

At this point, the serious reader will pause to marvel at the elegance and beauty that adiabatic invariance has demonstrated by its ability to circumvent the difficulties of integrals of second-order pressure fields over objects of arbitrary shape in favor of a simple measurement of the resonant frequency shift as a function of position of the object to be levitated within the resonator. Puterman claims that adiabatic invariance is “the cornerstone of modern physics” [69]. Similar results can be obtained for determination of the torque on a Rayleigh disk by measuring the shift in the resonance frequency as a function of the disk’s orientation [60].

### 15.4.7 Levitation Superstability (“Acoustic Molasses”)

Most acoustic levitation systems are driven at a fixed frequency [70]. Since the position of the levitated object can change, the ratio of the drive frequency to the resonator’s resonance frequency,  $\omega/\omega_o$ , will also change. That frequency shift at fixed drive frequency produces an effect referred to as “de-tuning” that is illustrated in Fig. 15.27. The frequency shift causes the amplitude of the standing wave to change resulting in a change in the radiation pressure acting on the levitated object. This modifies the Hooke’s law “stiffness” of the radiation force acting on the object. If the object did not influence the tuning, then the object would be levitated at the equilibrium position within the standing wave where the radiation force and the gravitational force would be equal and opposite. The fact that the object’s position also changes the tuning would change the trapping stiffness constant because its position influences the amplitude of the sound in the resonator when driven at fixed frequency.

This change in stiffness can be understood by examining the three shifted response curves illustrated in Fig. 15.28. All the resonance curves in Fig. 15.28 correspond to a quality factor of  $Q = 10$ . Assume that the resonator is driven at a fixed frequency that was 5% above the resonance frequency of the empty resonator so that  $\omega/\omega_o = 1.05$ . The value of  $v_I^2$  would be 51.2% of the

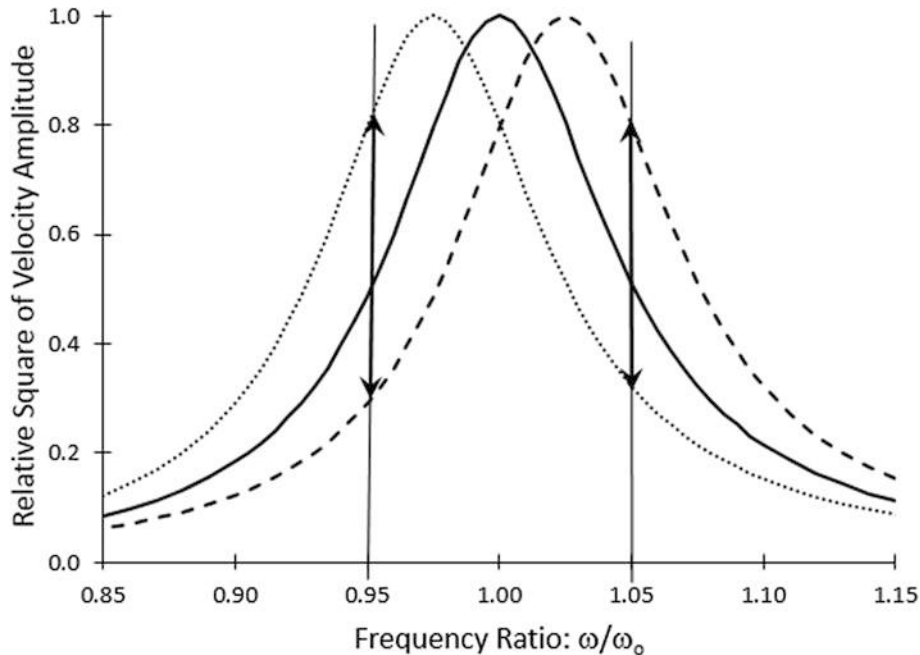


**Fig. 15.28** The presence of the acoustically levitated object changes the resonance frequency of the resonator [68]. The *solid line* is the normalized value of the square of the peak velocity amplitude,  $v_1^2$ , produced when the resonator is driven a frequency relative to the resonance frequency of the empty resonator,  $\omega/\omega_o = 1$ . The *dotted line* corresponds to the resonator's frequency response when the levitated object is located closer to a velocity anti-node. The *dashed line* corresponds to the resonator's frequency response when the levitated object is located closer to a velocity node (i.e., a pressure anti-node)

maximum that occurs at  $\omega/\omega_o = 1.00$ , if the resonator was empty. If the object moved up from its equilibrium position (i.e., toward the closest velocity anti-node), then the resonator's resonance frequency would become lower, corresponding to the dotted resonance curve. The force on the object would decrease because the acoustic standing wave amplitude would decrease, since the value of  $v_1^2$  would be 32.3% of the maximum that occurs at  $\omega/\omega_o = 1.00$ .

If the object moved down from its equilibrium position (i.e., toward the closest velocity node), then the resonator's resonance frequency would become higher, and the drive frequency would be closer to the resonance frequency. The value of  $v_1^2$  in Fig. 15.28 would be 80.4% of the maximum that occurs at  $\omega/\omega_o = 1.00$ , if the resonator was empty. This corresponds to the dashed resonance curve in Fig. 15.28, and the force on the object would increase because the acoustic standing wave amplitude would have increased. The combined effect would be an increase in the stiffness.

If the empty resonator was initially tuned  $\omega/\omega_o = 0.95$ , then the effective stiffness would be less by the same argument except that the object's influence on the sound amplitude would be determined by its “motion” along the vertical line in Fig. 15.28 above  $\omega/\omega_o = 0.95$ , instead of the previous discussion that had the object’s motion causing changes to the acoustic amplitude represented by “motion” along the vertical line above  $\omega/\omega_o = 1.05$  in Fig. 15.28.

If this influence of the object’s position on the effective stiffness of its capture around its equilibrium position in the standing wave occurred instantaneously in response to the object’s change in position, then any displacement of the object would simply oscillate at a slightly different frequency about the equilibrium position than it would if the de-tuning was neglected. Viscous effects (i.e.,

Stokes drag) would eventually damp those oscillations, corresponding to a mechanical resistance,  $R_m$ , in the simple harmonic oscillator equation.

$$m \frac{d^2x}{dt^2} + R_m \frac{dx}{dt} + Kx = 0 \quad (15.100)$$

Because we are considering the standing wave resonator as a driven resonant system with  $Q \neq 0$ , the exponential relaxation time,  $\tau$ , required for the resonator to achieve its steady-state response after its tuning is changed is non-zero (see Sect. 2.5.4):  $Q = (\frac{1}{2})\omega_0\tau$ . The resonator's response time is much longer than the period,  $T = 2\pi/\omega_0$ , of the standing wave:  $\tau = (Q/\pi)T$ . That delay in the resonator's response to the position of the levitated object means that there will be a component of the force modulated by the object's position that will not be in-phase with the object's position but that will be in-phase or out-of-phase with the object's velocity. The influence of the de-tuning will be retarded by a time,  $\tau$ , so the current radiation force acting on the object will depend upon the position of that object at an earlier time,  $t - \tau$ .

If this retardation produces a component of the excess (i.e., de-tuning) force that is out-of-phase with the velocity of the object's displacement from its equilibrium position,  $dx/dt$ , then this force will behave like mechanical damping in addition viscous "Stokes drag," in Eq. (15.100). If this retardation produces a component of the excess (i.e., de-tuning) force that is in-phase with the velocity of the object's displacement from its equilibrium position,  $dx/dt$ , then this force will behave like a negative mechanical resistance.

When the magnitude of that negative resistance is less than the ordinary viscous resistance,  $R_m$ , in Eq. (15.100), then oscillations will take longer to damp out. If the magnitude of that negative resistance is greater than  $R_m$ , then the amplitude of the object's oscillations will grow exponentially with time until some other effect limits the oscillation's amplitude. In some important cases this *de-tuning/de-phasing instability* will throw the levitated object out of the equilibrium position and possibly propel the object against the resonator's boundaries [71].

The two possible scenarios are illustrated symbolically in Fig. 15.29. If the natural frequency of the resonator is lower than the drive frequency,  $\omega/\omega_0 > 1$  (sharp tuning), then motion of the levitated object

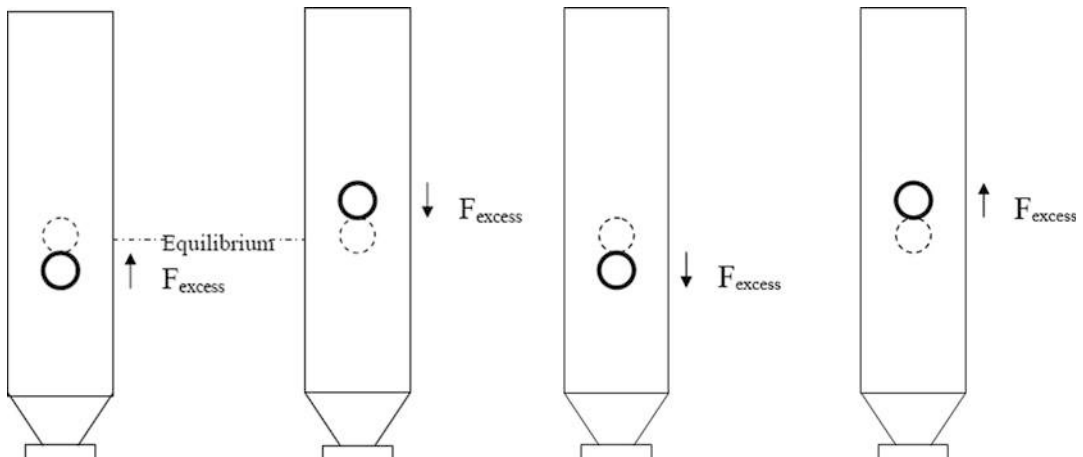


**Fig. 15.29** The de-tuning/de-phasing instability (or superstability) for an acoustically levitated object depends upon whether the resonance frequency of the resonator is above or below the frequency of the sound produced by the loudspeaker. (*Left*) If the drive is tuned "sharp" (i.e.,  $\omega/\omega_0 > 1$ ), then small displacements from equilibrium will increase, and the trapping will become unstable. (*Right*) If the drive is tuned "flat," (i.e.,  $\omega/\omega_0 < 1$ ), then small displacements from equilibrium will damp out faster than if only viscous drag was providing the mechanical resistance making the trapping "superstable"

toward a pressure anti-node (i.e., away from a velocity anti-node) will raise  $\omega_o$  and bring the drive frequency closer to the resonance frequency. This will produce an excess force,  $F_{excess}$ , that will be increased, thus in-phase with the velocity of the object as it is moving up from its lowest position, since the force will depend upon the previous position of the object at a time,  $\tau$ , earlier. When the object reaches its maximum vertical position, the natural frequency of the standing wave resonator will be farther out-of-tune, and the radiation force is reduced, so gravity will provide an excess force. Again, due to the delay, that excess force will be acting in the downward direction and is again in-phase with the (now downward) velocity of the object. This scenario is depicted in Fig. 15.29 (left).

The net effect for the “sharp tuning” case has the excess force doing work on the object, thus increasing the amplitude of its oscillations during each cycle. If the effect is sufficiently large, it can overcome viscous damping making the amplitude of the object’s oscillations grow linearly with time until some other effect limits the amplitude of the oscillations or the object is flung too far from the equilibrium position that it is no longer trapped or bangs against the walls or ends of the resonator.

If the natural frequency of the resonator is higher than the drive frequency,  $\omega/\omega_o < 1$  (flat tuning), then motion of the levitated object toward a pressure anti-node (i.e., away from a velocity anti-node) will raise  $\omega_o$  and bring the drive frequency farther from the resonance frequency. This will reduce the excess radiation force,  $F_{excess}$ , making the influence of gravity more important. That will produce an additional force that is out-of-phase with the velocity of the object as it is moving up from its lowest position, since the force depends upon the previous position of the object at a time,  $\tau$ , earlier.

When the object reaches its maximum vertical position, the natural frequency of the standing wave resonator will be closer to the drive frequency, and the radiation force will be increased. Again, due to the delay, that excess force will be acting in the upward direction and is again out-of-phase with the velocity of the object which will be moving downward. This scenario is depicted in Fig. 15.29 (right).

The net effect for the “flat tuning” case has the excess force adding to the viscous resistance and thus increases the damping. The amplitude of the object’s oscillations, if displaced from equilibrium, will decay more quickly than it would if the damping was due only to the Stokes drag. This additional damping causes superstability [72].

This same damping effect is observed in optics where it is known as “optical molasses” and was responsible for Stephen Chu sharing the Nobel Prize in Physics in 1997 with Claude Cohen-Tannoudji and William Phillips “for development of methods to cool and trap atoms with laser light” [73].

## 15.5 Beyond the Linear Approximation

Most ordinary acoustical phenomena can be analyzed from the linear perspective that has been the focus of every other chapter of this textbook. Linear acoustics and vibrations provide many useful and convenient simplifications. As we have seen, such simplifications are applicable to a large range of interesting problems. That said, this chapter has introduced a few interesting and useful phenomena that are not contained within a linear analysis. Waveform distortion, harmonic generation, shock wave formation and dissipation, parametric end-fire arrays, and mode conversion all rely upon incorporation of effects that a wave has on its propagation medium which are ignored in the linear limit. Inclusion of nonlinear effects leads to an interesting “life cycle” for a large amplitude acoustic disturbance: distortion → shocking → dissipation → classical attenuation [21]. That evolution in an ordinary fluid is depicted symbolically in Fig. 15.30.

By restricting the analysis to one-dimensional propagation of plane wave, many of the nonlinear behaviors have been demonstrated while avoiding more complicated mathematics and still being able to appreciate the cumulative influence of convection and of the medium’s own nonlinearity.

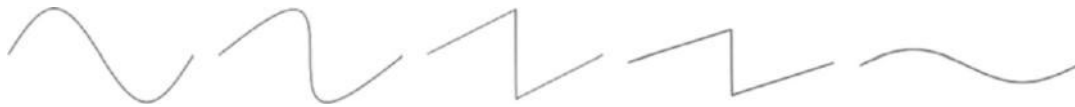


**Fig. 15.30** The simplified life cycle of an initially sinusoidal large amplitude acoustic disturbance propagating as a plane wave in one dimension

The inclusion of nonlinear contributions also provided an introduction to the ability of a sound wave to exert non-zero time-averaged forces and torques on objects that are exposed to high-amplitude sound waves. Acoustic radiation forces are generally much larger than forces that can be exerted by electromagnetic radiation used for trapping atoms [73]. Much of our understanding of these effects can be attributed directly to the Bernoulli pressure that provides an intrinsically second-order contribution to the linear (first-order) pressure field. Once again, exploitation of adiabatic invariance provided a means of avoiding complicated mathematics while providing useful quantitative results.

Finally, it is important to recognize that this chapter was only the “tip of the iceberg.” Many important nonlinear acoustical phenomena have not even been mentioned. Among the most significant are thermoacoustic engines, refrigerators [74], pulse-tube cryocoolers, and sonic mixture separators [75], as well as other important cases of acoustically driven mass streaming [76]. Another area that has been entirely ignored is nonlinear bubble oscillations that can be so violent that they convert sound into light by a process referred to as “sonoluminescence” [77]. The nonlinear distortion of pulses and the propagation of N-waves [78], like those which produce a “sonic boom” [79], are other important phenomena also worthy of investigation.

Topics in the area of nonlinear vibrations also abound. As mentioned in the beginning of this textbook, the inclusion of non-Hookean elasticity leads to the violation of Galilean isochronous independence of period and amplitude. Much like the harmonic distortion produced in high-amplitude wave propagation, a driven nonlinear oscillator will respond at frequencies that are not just the driving frequency. In fact, the response of a nonlinear oscillator can be at sub-harmonic frequencies or can become entirely chaotic rather than deterministic [80].

The purpose of this chapter was to raise awareness of the limitation of linear analysis, not to create professional expertise in nonlinear acoustics. If the reader can recognize the “symptoms” of nonlinear behavior and understand how they arise, then the goals of this final chapter will have been realized.

#### Talk Like an Acoustician

Convective nonlinearity	Phase matching
Self-interaction	Resonant mode conversion
Intermodulation distortion	Pump waves
Shock inception distance	Primary waves
Grüneisen parameter	Bernoulli pressure
Virial expansion	Radiation pressure
Second sound	Kundt's tube
Gol'dberg number	Internal energy
Order expansion	Enthalpy
Blackstock bridging function	Velocity potential
Geometric resonance	Acoustic levitation
Intermodulation distortion	De-tuning/de-phasing instability

## Exercises

- Shock inception distance.** The derivation of Eq. (15.8) used the fact that the crest of a plane sinusoidal wave advances “by one radian length,”  $k^{-1}$ , toward the zero-crossing when the slope of the zero-crossing,  $dv/dx$ , becomes infinite. By using the excess velocity,  $\Gamma v$ , defined in Eq. (15.9), show this is true in the case where dissipation can be neglected, with an initial waveform,  $v(x, t) = |\hat{v}| \sin(\omega t - kx)$ . For the waveform to become the fully developed sawtooth shock, the crest of the initially sinusoidal wave must advance by  $\lambda/4$ , placing the crest directly over the zero-crossing (see Fig. 15.6). Express that distance,  $D_{\text{saw}}$ , in terms of  $D_S$ , again for the case where dissipation can be neglected.
- Waveform distortion.** A 19.2 m long waveguide of circular cross-section with inside diameter,  $D = 5.21$  cm, is shown in Fig. 15.31 and Fig. 15.32 (center). The waveguide is driven by two compression drivers, shown in Fig. 15.32 (left), which can produce large amplitude sound waves.<sup>14</sup> The waveguide is terminated by a porous anechoic cone.

Three  $\frac{1}{4}$ " microphones are flush-mounted at three locations using the fixture that joins smoothly to the PVC pipe to eliminate reflections, shown in Fig. 15.32 (right). One microphone is located



**Fig. 15.31** A U-shaped waveguide made from 2" diameter (nominal) Schedule 40 PVC pipe is suspended from the ceiling to provide an overall propagation path of 19.2 m. At the far end are two compression drivers, and at the near end is a 1.05 m long porous wedge absorber to eliminate reflections. [Waveguide courtesy of Lauren Falco]



**Fig. 15.32** (Left) Two compression drivers. (Center) U-shaped waveguide turn-around section. (Right) Microphone flush-mount holder

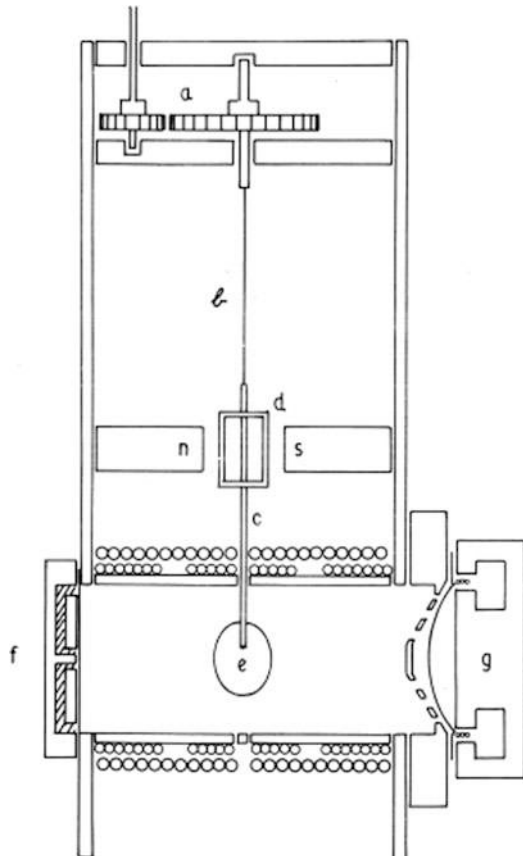
<sup>14</sup>The use of two drivers not only increases the achievable amplitudes but also facilitates measurements of the interaction of two waves of different frequencies.

very close to the drivers at a position designated  $x = 0$ . The second microphone is located at  $x = 3.17$  m, and the third is located at  $x = 17.9$  m.

Assume that the waveguide contains dry air at  $p_m = 100$  kPa with a sound speed,  $c_o = 345$  m/s, and it is driven sinusoidally at  $f_1 = 880$  Hz.

- (a) *Attenuation length.* Using the expression in Eq. (13.78), determine the exponential thermoviscous attenuation length,  $\ell = \alpha_{T-V}^{-1}$ , due to boundary layer dissipation at the fundamental frequency,  $f_1$ . Is that attenuation length shorter or longer for the higher harmonics?
  - (b) *Shock inception distance and Gol'dberg number.* Determine the shock inception distance,  $D_S$ , and using the result of part (a), determine the Gol'dberg number,  $G$ , if  $p_I(0) = 100$  Pa (131 dB re: 20  $\mu\text{Pa}_{\text{rms}}$ ),  $p_I(0) = 300$  Pa (140.5 dB re: 20  $\mu\text{Pa}_{\text{rms}}$ ), and  $p_I(0) = 1000$  Pa (151 dB re: 20  $\mu\text{Pa}_{\text{rms}}$ ).
  - (c) *Harmonic distortion.* Using Eq. (15.43) and neglecting attenuation, determine the amplitude of the fundamental,  $f_1 = 880$  Hz, second harmonic,  $f_2 = 1.76$  kHz, third harmonic,  $f_3 = 2.64$  kHz, and forth harmonic,  $f_4 = 3.52$  kHz, at  $x = 3.17$  m and at  $x = 17.9$  m, assuming  $p_I(0) = 100$  Pa.
  - (d) *More harmonic distortion.* Repeat part (c) assuming  $p_I(0) = 300$  Pa.
3. **Repeated shock.** Determine the ratio of the amplitudes of the harmonics to the amplitude of the fundamental,  $C_n/C_1$ , for a fully developed shock wavelike that shown in Fig. 15.8.
4. **Levitation demonstration resonator.** A ground-based levitator (i.e.,  $g = 9.8$  m/s<sup>2</sup>) is being designed to demonstrate acoustic levitation by levitating the bottoms of Styrofoam coffee cups. Those disks have a diameter of 5.0 cm and a thickness of 1.5 mm, and each has a mass,  $m_{\text{disk}} = 0.15$  gm. Assume that resonator will be constructed from a 1.5 m long, 6" (nominal) diameter, optically clear cast acrylic tube with inside diameter,  $D_{\text{tube}} = 14.0$  cm.
- (a) *Levitation force.* If the resonator is operated in its  $n = 3$  standing wave mode,  $f_3 = 350$  Hz. Determine the pressure amplitude of the standing wave at the rigid end of the resonator so that the levitation force on the disk is three times its weight.
  - (b) *Equilibrium location.* If the tube is oriented so that the speaker is at the bottom and the rigid end is at the top (like those in Fig. 15.29), how far from the top end of the resonator will the disk be levitated at its highest stable location if the standing wave amplitude is that calculated in part (a)?
  - (c) *DELTAECC model.* Make a DELTAEC model of the resonator (without the levitated disk) to determine the volume velocity of a piston that has the same diameter as the tube,  $D_{\text{tube}}$ , which would be required to produce the standing wave pressure amplitude at the rigid end calculated in part (a) for the  $n = 3$  mode. You may make a slight adjustment of the tube's length to force  $f_3 = 350$  Hz. What are the frequencies of the  $f_1$ ,  $f_2$ , and  $f_4$  modes?
  - (d) *Adiabatic invariance.* Use your DELTAEC model in part (a) to estimate the frequency as a function of disk position by moving a constricted DUCT segment that is the same length as the disk (1.5 mm) and has a cross-sectional area equal to that of the empty tube minus the cross-sectional area of the disk. Move that constricted section from the rigid end to about 0.3 m from the driven end of the resonator. Plot  $f_3$  vs. position to produce a graph similar to Fig. 15.27. Repeat for  $f_2$  vs. position.
  - (e) *Advanced DELTAEC model.* Repeat part (c) but explicitly includes the loudspeaker in Fig. 2.43 using the following speaker parameters:  $m_o = 12.0$  gm,  $K = 1440$  N/m,  $B\ell = 7.1$  N/A,  $R_{dc} = 5.2$  Ω,  $L = 0.1$  mH,  $R_m = 1.9$  kg/s, and  $A_{\text{pist}} = 98.5$  cm<sup>2</sup>. The rear of the speaker is enclosed (to protect your hearing!) in a cylindrical enclosure that has an inside diameter of 6" (15.2 cm) and a length of 8" (20 cm). What is the electrical current that must be supplied to the voice coil to produce the  $n = 3$  standing wave amplitude calculated

**Fig. 15.33** Cross-sectional view of a “modern” Rayleigh disk apparatus. [60]



in part (a) at  $f_3 = 350$  Hz? What are the frequencies of the  $f_1, f_2$ , and  $f_4$  modes of the coupled speaker-resonator system (see Sect. 10.7.5)?

Hints: The DELTAEC model of the bass-reflex loudspeaker enclosure in Fig. 8.41 might provide a helpful starting point. An “enclosed current driven speaker” segment, IESPEAKER, will provide a way to incorporate the rear enclosure with the electrodynamic speaker’s excitation of standing waves in the tube.

(5) **Rayleigh disk.** The apparatus in Fig. 15.33 shows a rigid disk (e) suspended at the midplane of a cylindrical resonator from a torsion fiber (b). The resonator has an electrodynamic dome tweeter (g) at one end and an electret microphone (see Sect. 6.3.3) providing a rigid termination at the other end (f). The disk’s angular orientation is detected with the coils surrounding the resonator that incorporates a split-secondary astatic transformer [60]. A gearing system (a) and a coil (d) and magnet structure (n and s) from an analog meter movement can be used to adjust the equilibrium orientation,  $\theta_o$ , of the disk or excite a free-decay oscillation. The maximum occlusion of the resonator occurs when  $\theta_o = 0^\circ$ .

The resonator’s inside diameter is 3.0 cm and its length,  $L = 12.0$  cm. The diameter of the disk is  $D_{disk} = 1.2$  cm. The disk has a mass,  $m_1 = 0.80$  gm and a moment of inertia of about its diameter of  $I_{disk} = 2.0 \times 10^{-8}$  kg-m<sup>2</sup>

Assume the resonator contains dry air at 300 K with  $p_m = 100$  kPa.

- (a) *Fundamental resonance frequency.* What is the frequency of the fundamental half-wavelength mode of the resonator?
- (b) *Torsional stiffness.* If the frequency of disk oscillations is 1.1 Hz, what is the torsional stiffness of the disk's suspension?
- (c) *Standing wave pressure amplitude.* The disk's equilibrium position is adjusted so that  $\theta_o = 45^\circ$ . What is the acoustic pressure amplitude,  $p_1$ , at the surface of the electret microphone if the standing wave causes the disk equilibrium orientation to be  $\theta = 35^\circ$  and the corrections in the curly brackets of Eq. (15.79) are ignored?
- (d) *Scattering corrections.* How large is the correction provided by Eq. (15.79) relative to the simpler expression for the torque in Eq. (15.78)? Express your result as  $N_{\text{antinode}}(35^\circ)/N(35^\circ)$ .
- (e) *Electret microphone sensitivity.* If the open-circuit output voltage of the electret microphone is 285 mV<sub>ac</sub> under the conditions of part (b), what is the microphone's open-circuit sensitivity?

---

## References

1. G.G. Stokes, On a difficulty in the theory of sound. Phil. Mag. (Series 3) 33, 349–356 (1848). Also available in R. T. Beyer, *Nonlinear Acoustics in Fluids* (Van Nostrand Reinhold, 1984)
2. M.F. Hamilton, Gol'dberg number for diverging waves. J. Acoust. Soc. Am. **104**(6), 4419–4427 (2016)
3. I. Rudnick, On the attenuation of high amplitude waves of stable saw-tooth form propagated in horns. J. Acoust. Soc. Am. **30**(4), 339–342 (1958)
4. A. Myers, R.W. Pyle Jr., J. Gilbert, D.M. Campbell, J.P. Chick, S. Logie, Effects of nonlinear sound propagation on the characteristic timbres of brass instruments. J. Acoust. Soc. Am. **131**(1, Pt. 2), 678–688 (2012)
5. R.T.Beyer, “The parameter B/A”, in *Nonlinear Acoustics*, M. F. Hamilton and D. T. Blackstock, eds. (Acoust. Soc. Am., 2008). Ch. 2; ISBN 0-9744067-5-9.
6. R. T. Beyer, *Nonlinear Acoustics* (Acoust. Soc. Am., 1997); ISBN 1-56396-724-3. §3.1.
7. E.C. Everbach, Parameters of nonlinearity of acoustic media, in *Encyclopedia of Acoustics*, ed. by M. J. Crocker, (Wiley & Sons, 1997). Vol. I, Ch. 20; ISBN 0-471-17767-9
8. C.M. Cormack, M.F. Hamilton, Plane nonlinear shear waves in relaxing media. J. Acoust. Soc. Am. **143**(2), 1035–1048 (2018)
9. S.L. Garrett, Nonlinear distortion of 4<sup>th</sup> sound in superfluid helium <sup>3</sup>He-B. J. Acoust. Soc. Am. **69**(1), 139–144 (1981)
10. R.T. Beyer, Nonlinear Acoustics (Experimental), in *American Institute of Physics Handbook*, ed. by D. E. Grey, 3rd edn., (McGraw-Hill, 1972). See Table 30-3, pg. 3–208
11. M. Greenspan, C.E. Tschiegg, Radiation-induced acoustic cavitation: apparatus and some results. J. Res. Nat'l. Bur. Standards, Sec. C **71**, 299–312 (1959)
12. M.S. Cramer, A. Kluwick, On the propagation of waves exhibiting both positive and negative nonlinearity. J. Fluid Mech. **142**(1), 9–37 (1984)
13. I. Rudnick, Physical Acoustics at UCLA in the Study of Superfluid Helium, in *New Directions in Physical Acoustics – Course LXIII, Varenna, Italy*, ed. by D. Sette, (Italian Physical Society and IOS Press, Amsterdam, 1974)
14. S. J. Putterman, *Superfluid Hydrodynamics* (North-Holland, 1974); ISBN 0 7204 030104.
15. S. Putterman, S. Garrett, Resonant mode conversion and other second-order effects in superfluid He-II. J. Low Temp. Phys. **27**(3/4), 543–559 (1977)
16. Z.A. Gol'dberg, Second approximation acoustic equations and the propagation of plane waves of finite amplitude. Soviet Phys. Akust. **2**, 346–350 (1956)
17. A. Larraza, S.L. Garrett, S. Putterman, Dispersion relations for gravity waves in a deep fluid: second sound in a stormy sea. Phys. Rev. A **41**(6), 3144–3155 (1990)
18. L.D. Landau, E.M. Lifshitz, *Fluid Mechanics*, 2nd edn. (Butterworth-Heinemann, 1987). See Eq. 86.1; ISBN 0 7506 2767 0
19. I. Rudnick, On the attenuation of a repeated sawtooth shock wave. J. Acoust. Soc. Am. **25**(5), 1010–1011 (1953)
20. I. Rudnick, On the attenuation of finite amplitude waves in a liquid. J. Acoust. Soc. Am. **30**(6), 564–567 (1958)
21. J.A. Shooter, T.G. Muir, D.T. Blackstock, Acoustic saturation of spherical waves in water. J. Acoust. Soc. Am. **55**(1), 54–62 (1974). See Fig. 1
22. S. Earnshaw, On the mathematical theory of sound. Phil. Tran. Roy. Soc. (London) **150**, 133–148 (1860)

23. G.B. Airy, On a difficulty in the problem of sound. *Phil. Mag.* (Series 3) **34**, 401–405 (1848). Also available in R. T. Beyer, *Nonlinear Acoustics in Fluids* (Van Nostrand Reinhold, 1984). pp. 37–41
24. L.E. Hargrove, Fourier series for the finite amplitude sound waveform in a dissipationless medium. *J. Acoust. Soc. Am.* **32**(4), 511–512 (1960)
25. E. Fubini-Ghiron, Anomalie nella propagazione di onde acustiche di grande ampiezza (Anomalies in acoustic wave propagation of large amplitude). *Alta Frequenza* **4**, 530–581 (1935)
26. R.D. Fay, Plane sound waves of finite amplitude. *J. Acoust. Soc. Am.* **3**(2A), 222–241 (1931)
27. D.T. Blackstock, Connection between the Fay and Fubini solution for a plane sound wave of finite amplitude. *J. Acoust. Soc. Am.* **39**(6), 1019–1026 (1966)
28. J.L.S. Bellin, R.T. Beyer, Scattering of sound by sound. *J. Acoust. Soc. Am.* **32**(3), 339–341 (1960)
29. P.J. Westervelt, Parametric acoustic array. *J. Acoust. Soc. Am.* **35**(4), 535–537 (1963)
30. H. Lamb, *Dynamical Theory of Sound*, 2nd edn. (E. Arnold & Co., 1931). See §63 and §95; reprinted (Dover, 1960)
31. A.L. Thuras, R.T. Jenkins, H.T. O'Neill, Extraneous frequencies generated in air carrying intense sound waves. *J. Acoust. Soc. Am.* **6**(3), 173–180 (1935)
32. T.G. Leighton, Ultrasound in air – Guidelines, applications, public exposure, and claims of attacks in Cuba and China. *J. Acoust. Soc. Am.* **144**(4), 2473–2489 (2018)
33. R.L. Swanson, S. Hampton, J. Green-McKenzie, R. Diaz-Arrastia, M.S. Grady, R. Verma, R. Biester, D. Duda, R.L. Wolf, D.H. Smith, Neurological manifestations among US Government personnel reporting directional audible and sensory phenomena in Havana, Cuba. *J. Am. Med. Assoc.* **319**(11), 1125–1133 (2018)
34. J. Perlez and S. L. Myers, “U.S. issues alert to Americans in China in wake of sonic attack fears,” *New York Times* (June 8, 2018), <https://www.nytimes.com/2018/06/08/world/asia/sonic-attack-china-guangzhouconsulate.html>
35. *Metals Handbook (Desk Edition)*, H. E. Boyer and T. L. Gall, eds. (Am. Soc. for Metals, 1985); ISBN 0-87170-188-X. Table 1, pg. 2–16.
36. G.L. Jones, D.R. Kobett, Interaction of elastic waves in an isotropic solid. *J. Acoust. Soc. Am.* **35**(1), 5–10 (1963)
37. R.R. Rollins Jr., L.H. Taylor, P.H. Todd Jr., Ultrasonic study of three-phonon interactions. II. Experimental results. *Phys. Rev.* **136**(3A), 597–601 (1964)
38. M.F. Hamilton, J.A. TenCate, Sum and difference frequency generation due to noncollinear wave interactions in a rectangular duct. *J. Acoust. Soc. Am.* **81**(6), 1703–1712 (1987)
39. L.D. Landau, E.M. Lifshitz, *Fluid Mechanics*, 2nd edn. (Butterworth-Heinemann, 1987); ISBN 0 7506 2767 0. §139
40. S. Garrett, S. Adams, S. Puterman, I. Rudnick, Resonant mode conversion in He II. *Phys. Rev. Lett.* **41**(6), 413–416 (1978)
41. P.M. Gammel, A.P. Croonquist, T.G. Wang, A high-powered siren for stable acoustic levitation of dense materials in the Earth’s gravity. *J. Acoust. Soc. Am.* **83**(2), 496–501 (1988)
42. F.H. Busse, T.G. Wang, Torque generated by orthogonal acoustic waves – Theory. *J. Acoust. Soc. Am.* **69**(6), 1634–1638 (1981)
43. H.W.S. Clair, Electromagnetic sound generator for producing intense high frequency sound. *Rev. Sci. Inst.* **12**(5), 250–256 (1941)
44. C.H. Allen, I. Rudnick, A powerful high-frequency siren. *J. Acoust. Soc. Am.* **19**(5), 857–865 (1947)
45. B.L. Smith, G.W. Swift, Measuring second-order time-averaged pressure. *J. Acoust. Soc. Am.* **110**(2), 717–723 (2001)
46. J. W. Strutt (Lord Rayleigh), “On the circulation of air observed in Kundt’s tubes, and on some allied acoustical problems,” *Phil. Trans. Roy. Soc. (London)* **175**, 1–21 (1883); *Collected Works*, (Dover, 1964) Vol. II, §108.
47. H. Mukai, S. Sakamoto, H. Tachibana, Experimental study on the absorption characteristics of resonance-type brick/block walls. *J. Acoust. Soc. Japan (E)* **20**(6), 433–438 (1999)
48. M. B. Barmatz, “Acoustic agglomeration methods and apparatus,” U.S. Pat. No. 4,475,921 (Oct. 9, 1984).
49. J.P. Dionne, B. Dutra, K.C. Chitale, G. Ghoshal, C. Leidel, B. Lipkens, A novel acoustic cell processing platform for cell concentration and washing. *J. Acoust. Soc. Am.* **141**(5), 3741 (2017)
50. J. W. Strutt (Lord Rayleigh), *Theory of Sound*, Vol. II (Macmillan, 1896); (Dover, 1945). §253b
51. V. Dvořák, Ueber die akustische Abstoggung. *Ann. Physik* **239**(3), 328–338 (1878)
52. V. Dvořák (with note by A. M. Mayer), “On acoustic repulsion,” *Phil. Mag.* **6**, Series 5, 225–233 (1878); <https://doi.org/10.1080/14786447808639500>.
53. J. W. Strutt (Lord Rayleigh), *Theory of Sound*, Vol. II (Macmillan, 1896); (Dover, 1945). §253a.
54. W. König, Hydrodynamisch-akustische Untersuchungen. *Wied. Ann.* **43**, 51 (1891)
55. J. W. Strutt (Lord Rayleigh), “On an instrument capable of measuring the intensity of aerial vibrations,” *Phil. Mag.* **14**, 186–187 (1882); *Collected Works* (Dover, 1964) Vol. II, §91.
56. L.L. Beranek, *Acoustic Measurements* (Wiley & Sons, 1949), pp. 148–158
57. L.V. King, On the theory of the inertia and diffraction corrections for the Rayleigh disk. *Proc. Roy. Soc. (London)* **A153**, 17–40 (1935)

58. J.R. Pellam, W.B. Hanson, Thermal Rayleigh disk measurements in liquid helium II. *Phys. Rev.* **85**(2), 216–225 (1952)
59. T.R. Koehler, J.R. Pellam, Observation of torque exerted by pure superflow. *Phys. Rev.* **125**(3), 791–794 (1962)
60. S.L. Garrett, Butterfly-valve inductive orientation detector. *Rev. Sci. Inst.* **51**(4), 427–430 (1980)
61. L.D. Landau, E.M. Lifshitz, *Fluid Mechanics*, 2nd edn. (Butterworth-Heinemann, 1987). §8; ISBN 0 7506 2767 0
62. L. D. Landau and E. M. Lifshitz, *Mechanics*, (Pergamon, 1960); See §1 – §5.
63. I. Rudnick, Measurements of the acoustic radiation pressure on a sphere in a standing wave field. *J. Acoust. Soc. Am.* **62**(1), 20–22 (1977)
64. L.D. Landau, E.M. Lifshitz, *Fluid Mechanics*, 2nd edn. (Butterworth-Heinemann, 1987). §49 ISBN 0 7506 2767 0
65. S. L. Garrett, R. W. M. Smith and M. E. Poese, “Eliminating nonlinear acoustical effects from thermoacoustic refrigeration systems,” *Proc. 17<sup>th</sup> International Symposium on Nonlinear Acoustics (ISNA 17)*, pg. 407-415 (Am. Inst. Physics, 2006); ISBN 0-7354-0330-9.
66. Y.A. Ilinskii, B. Lipkens, T.S. Lucas, T.W. Van Doren, E.A. Zabolotskaya, Nonlinear standing waves in an acoustical resonator. *J. Acoust. Soc. Am.* **104**(5), 2664–2674 (1998)
67. S. Puttermann, J. Rudnick, M. Barmatz, Acoustic levitation and the Boltzmann-Ehrenfest principle. *J. Acoust. Soc. Am.* **85**(1), 68–71 (1989)
68. E. Leung, C.P. Lee, N. Jacobi, T.G. Wang, Resonance frequency shift of an acoustic chamber containing a rigid sphere. *J. Acoust. Soc. Am.* **72**(2), 615–620 (1980)
69. S.J. Puttermann, Adiabatic invariance, the cornerstone of modern physics. *J. Acoust. Soc. Am.* **83**(1), S39 (1988)
70. M. Barmatz, Overview of containerless processing technologies, in *Materials Processing in the Reduced Gravity Environment of Space*, ed. by G. E. Rindone, (Elsevier, 1982), pp. 25–37
71. J. Rudnick, M. Barmatz, Oscillational instabilities in single-mode acoustic levitators. *J. Acoust. Soc. Am.* **87**(1), 81–92 (1990)
72. M. B. Barmatz and S. L. Garrett, “Stabilization and oscillation of an acoustically levitated object,” U.S. Pat. No. 4,773,266 (Sep. 27, 1988).
73. S. Chu, Laser manipulation of atoms and particles. *Science* **253**(5022), 861–866 (1991)
74. S.L. Garrett, S. Backhaus, The power of sound. *Am. Scientist* **88**(6), 11–17 (2004)
75. G.W. Swift, Mixture separation, in *Handbook of Acoustics*, ed. by T. D. Rossing, (Springer, 2007). ISBN 978-0-387-30446-7. See §7.6
76. W.L. Nyborg, Acoustic streaming, in *Nonlinear Acoustics*, Acoust. Soc. Am, ed. by M. F. Hamilton, D. T. Blackstock, (2008). See Ch. 7; ISBN 978-0-123-21860-5
77. S.J. Puttermann, Sonoluminescence: Sound into light. *Scientific American* **272**(2), 46–51 (1995)
78. R.T. Beyer, *Nonlinear Acoustics* (Acoust. Soc. Am., 1997). §4.7, ISBN 1-56396-724-3
79. D. J. Maglieri and K. J. Plotkin, *Sonic Boom*, NASA Tech. Report RP-1258 (1991).
80. A. B. Pippard, *The Physics of Vibration* (Cambridge, 1989). See Ch. 8, ISBN 0 521 37200 3

**Open Access** This chapter is licensed under the terms of the Creative Commons Attribution 4.0 International License (<http://creativecommons.org/licenses/by/4.0/>), which permits use, sharing, adaptation, distribution and reproduction in any medium or format, as long as you give appropriate credit to the original author(s) and the source, provide a link to the Creative Commons license and indicate if changes were made.

The images or other third party material in this chapter are included in the chapter's Creative Commons license, unless indicated otherwise in a credit line to the material. If material is not included in the chapter's Creative Commons license and your intended use is not permitted by statutory regulation or exceeds the permitted use, you will need to obtain permission directly from the copyright holder.



---

## Appendices

---

### Appendix A: Useful Physical Constants and Conversion Factors

$\mathfrak{R} = k_B N_A$	8.314462 J/mole-K
$k_B$	$1.380649 \times 10^{-23}$ J/K = $8.617333 \times 10^{-5}$ eV/K
$N_A$	$6.02214076 \times 10^{23}$ mol <sup>-1</sup>
$V_{molar}$	22.4141 l/mol @ 273.15 K, 101,325 Pa
$M_{air}$	28.9644 g/mol
$e$	$1.602176634 \times 10^{-19}$ C
$g$	9.80665 m/s <sup>2</sup>
$h$	$6.62607015 \times 10^{-34}$ J-s = $4.135667 \times 10^{-15}$ eV-s
$\hbar = h/2\pi$	$1.05457182 \times 10^{-34}$ J-s
$c = (\epsilon_0 \mu_0)^{-1/2}$	$2.99792458 \times 10^8$ m/s
$\epsilon_0$	$8.8541878128 \times 10^{-12}$ F·m <sup>-1</sup>
$\mu_0$	$4\pi \times 10^{-7}$ H m <sup>-1</sup>
$2e/h$	483.5978484 MHz/μV
$\sigma$	$5.6697 \times 10^{-8}$ W/m <sup>2</sup> ·K <sup>4</sup> = [ $k_B^4 \pi^2 / 60 \hbar^3 c^2$ ]

As of 20 May 2019 (the 144th anniversary of the Metre Convention), the above values of  $k_B$ ,  $N_A$ ,  $c$ ,  $e$ ,  $h$ ,  $\mu_0$ ,  $\epsilon_0$ , and  $2e/h$  are taken to be exact.

1 psi	6894.8 Pa = 2.307 ft H <sub>2</sub> O	1 psf = 47.88 Pa
1 torr	133.322 Pa = 1.0 mm Hg	
1 atm	101,325 Pa	1" H <sub>2</sub> O = 249.1 Pa
1 bar	100 kPa	
1 ft <sup>3</sup>	28.317 l	
1 gal	3.785411784 l = 231 in <sup>3</sup>	
1 gpm	63.088 cm <sup>3</sup> /s	1 cfm = $4.72 \times 10^{-4}$ m <sup>3</sup> /s
1 cal	4.184 J	
1 W	3.413 BTU/h	
1 ton	3517 W ( $\equiv$ 12,000 BTU/h)	
1 hp	746 W	

## Appendix B: Resonator Quality Factor

*“A man with one watch knows the time; a man with two is never sure.”*

The quality factor ( $Q$ ) of a resonator is a dimensionless measure of the “sharpness” of a resonance. One of the greatest sources of its utility is that we have many equivalent ways of expressing the  $Q$ . This variety allows us to connect the most convenient experimental method to the parameter of interest and provides us with a “second watch” if we want to make a self-consistency check of our results, either theoretically or experimentally.

**Caution** The results summarized below assume that the resonance under consideration is “isolated,” so there are no other resonances that might be sufficiently close in frequency that they would affect the amplitude or phase of the resonance being considered.

**$Q$ -Multiplier** For a given force,  $F$ , or pressure,  $p$ , the magnitude of the response at the resonance frequency of the  $i$ th mode,  $\omega_i$ ,  $i = 0, 1, 2, 3, \dots, \infty$ , will be “amplified” by the quality factor  $Q_i$  of that mode.

$$Q_i = \left| \frac{p(\omega_i)}{p(\omega = 0)} \right| \quad (\text{B.1})$$

**Energy Storage-to-Dissipation Ratio** The time-averaged power dissipated is written as  $\langle \Pi_{\text{dissipated}} \rangle_t$  below.

$$Q = 2\pi \frac{E_{\text{stored}}}{E_{\text{dissipated/cycle}}} = \frac{\omega E_{\text{stored}}}{\langle \Pi_{\text{dissipated}} \rangle_t} \quad (\text{B.2})$$

**Lumped-Element Storage-to-Loss Ratio** For a mass-spring system with natural frequency,  $\omega_o$ ; mass,  $m$ ; mechanical resistance,  $R_m$ ; and stiffness K; or a similar electrical circuit with inductance,  $L$ ; resistance,  $R_{dc}$ ; and capacitance,  $C$ ; or an acoustical compliance,  $C$ , and acoustical inertance,  $L$

$$Q = \frac{\omega_o m}{R_m} = \frac{K}{\omega_o R_m} = \frac{1}{\omega_o R_m C} = \frac{\omega_o L}{R_{dc}}$$

**Half-Power Bandwidth** If the frequencies of the  $-3$  dB points are  $f_+$  and  $f_-$ , then the full  $-3$  dB bandwidth of the resonance,  $\Delta f = f_+ - f_-$ , is related to the quality factor,  $Q$ , by the resonance frequency,  $f_o = (f_+ f_-)^{1/2}$  as written below.

$$Q = \frac{f_o}{f_+ - f_-} = \frac{\omega_o}{\omega_+ - \omega_-} \quad \text{where} \quad f_o = \sqrt{f_+ f_-} = \frac{\sqrt{\omega_+ \omega_-}}{2\pi} \quad (\text{B.3})$$

**Rate of Phase Change with Frequency at Resonance** If the phase shift between force (or pressure) and velocity (or volume flow rate) is expressed as  $\phi$  in radians, or  $\theta$  in degrees, then

$$Q = \frac{\omega_o}{2} \frac{d\phi}{d\omega} \Big|_{\omega_o} = \frac{f_o}{2} \frac{d\phi}{df} \Big|_{f_o} = f_o \frac{\pi}{360^\circ} \frac{d\theta}{df} \Big|_{f_o} \approx \frac{f_o}{114.6^\circ} \frac{d\theta}{df} \Big|_{f_o} \quad (\text{B.4})$$

**Free Decay Rate** If the time required for the amplitude of the oscillations to decay to  $e^{-1} \cong 0.368$  of their value is  $\tau = \beta^{-1} = (2 m)/R_m$ , then

$$Q = \frac{1}{2} \omega_o \tau = \pi \tau f_o = \frac{1}{2} \frac{k}{\alpha} = \frac{\pi}{\alpha \lambda} \quad (\text{B.5})$$

The exponential spatial attenuation constant,  $\alpha$ , is related to the temporal decay rate,  $\tau$ , by the sound speed,  $c$ , where  $k$  is the wavenumber and  $\lambda$  is the wavelength:  $\alpha = \tau/c$ .

Similarly, the  $Q$  is expressed as  $2\pi$  times the number of cycles required for the **energy** to decay by  $e^{-1}$ , or  $\pi$  times the number of cycles required for the **amplitude** to decay by  $e^{-1}$ . More generally,

$$Q = \frac{\pi N}{\ln [x]} \quad (\text{B.6})$$

$N$  is the number of cycles for the amplitude to decay by a factor of  $x$ .

**Reflection Coefficient** In a standing wave resonator, the standing wave can be represented as the superposition of a right- and left-going traveling waves. If the left-going wave is reflected with an amplitude that is  $R < 1$  times the right-going wave amplitude, the coefficient of the right-going wave would be given by the infinite geometric series  $1 + R + R^2 + R^3 + \dots$ , and the left-going wave would have an amplitude that is  $R$  times that infinite sum. The resulting quality factor,  $Q_n$ , of the  $n$ th mode of the resonator can be expressed in terms of the reflection coefficient  $R$  and the mode number  $n$ .

$$Q_n = n\pi \frac{\sqrt{R}}{1 - R} \quad (\text{B.7})$$

**Pole-Zero Resonance Fit** Many modern spectrum analyzers allow a resonance to be fit by a pole-zero function. A single resonance will have two complex poles that are complex conjugates,  $a \pm jb$ . The resonance frequency is  $f = (a^2 + b^2)^{1/2} \cong b$ , if the damping is small ( $a \ll b$ ).

$$Q = \frac{-1}{2a} \sqrt{a^2 + b^2} \cong \frac{-b}{2a} \quad (\text{B.8})$$

**Loss Tangent and Damping Factor** In the characterization of elastomers used as vibration isolators, it is common to define a frequency-dependent, complex elastic modulus  $E^*$ . The complex modulus has a real part,  $E'$ , and an imaginary part,  $E''$ , such that  $E^* = E' + jE'' \cong E(1 + j\delta)$ , where we choose to define a “loss tangent,”  $\tan \delta$ , that is the inverse of the quality factor.<sup>1</sup>

$$Q = \frac{1}{\tan \delta} = \frac{E'}{E''} = \frac{1}{2\zeta} \quad (\text{B.9})$$

The damping factor,  $\zeta$ , is the ratio of the mechanical resistance to the critical value of the mechanical resistance,  $R_m^{crit} = 2(km)^{1/2} = 2m\omega_o$ .<sup>2</sup>

---

<sup>1</sup> For example, see J. C. Snowdon, *Vibration and Shock in Damped Mechanical Systems* (Wiley, 1968).

<sup>2</sup> W. T. Thomson, *Theory of Vibration with Applications*, 2nd edn. (Prentice-Hall, 1981); ISBN 0-13-914,523-0

## Appendix C: Bessel Functions of the First Kind

Bessel's equation

$$\frac{d^2 J_m(x)}{dx^2} + x \frac{d J_m(x)}{dx} + (x^2 - m^2) J_m(x) = 0 \quad (\text{C.1})$$

$$\frac{1}{x} \frac{d}{dx} \left( x \frac{d J_m(x)}{dx} \right) + \left( 1 - \frac{m^2}{x^2} \right) J_m(x) = 0 \quad (\text{C.2})$$

Series expansions

$$J_m(x) = \frac{1}{m!} \left( \frac{x}{2} \right)^m - \frac{1}{1!(m+1)!} \left( \frac{x}{2} \right)^{m+2} + \frac{1}{2!(m+2)!} \left( \frac{x}{2} \right)^{m+4} - \dots \quad (\text{C.3})$$

$$J_0(x) = 1 - \frac{x^2}{2^2} + \frac{x^4}{2^2 \cdot 4^2} - \frac{x^6}{2^2 \cdot 4^2 \cdot 6^2} + \dots \quad (\text{C.4})$$

$$J_1(x) = \frac{x}{2} - \frac{2x^3}{2 \cdot 4^2} + \frac{3x^5}{2 \cdot 4^2 \cdot 6^2} - \dots \quad (\text{C.5})$$

$$J_2(x) = \frac{x^2}{2 \cdot 2^2} - \frac{x^4}{2 \cdot 3 \cdot 2^4} + \frac{x^6}{2 \cdot 3 \cdot 4 \cdot 2^6} - \dots \quad (\text{C.6})$$

Asymptotic forms for large argument

$$\lim_{x \rightarrow \infty} [J_m(x)] = \sqrt{\frac{2}{\pi x}} \cos \left( x - \frac{m\pi}{2} - \frac{\pi}{4} \right) \quad (\text{C.7})$$

Addition theorem

$$1 = J_0(x) + 2J_2(x) + 2J_4(x) + 2J_6(x) + \dots \quad (\text{C.8})$$

Relationships to trigonometric functions

$$\sin x = 2J_1(x) - 2J_3(x) + 2J_5(x) - 2J_7(x) + \dots \quad (\text{C.9})$$

$$\cos x = J_0(x) - 2J_2(x) + 2J_4(x) - 2J_6(x) + \dots \quad (\text{C.10})$$

$$\cos(x \cos \theta) = J_0(x) + 2 \sum_{k=1}^{\infty} (-1)^k J_{2k}(x) \cos(2k\theta) \quad (\text{C.11})$$

$$\cos(x \sin \theta) = J_0(x) + 2 \sum_{k=1}^{\infty} J_{2k}(x) \cos(2k\theta) \quad (\text{C.12})$$

$$\sin(x \sin \theta) = 2 \sum_{k=0}^{\infty} J_{2k+1}(x) \sin[(2k+1)\theta] \quad (\text{C.13})$$

$$\sin(x \cos \theta) = 2 \sum_{k=1}^{\infty} (-1)^k J_{2k+1}(x) \cos[(2k+1)\theta] \quad (\text{C.14})$$

Integral representations

$$J_m(x) = \frac{(x/2)^m}{\sqrt{\pi} \Gamma(m + \frac{1}{2})} \int_0^\pi \cos(x \cos \theta) d\theta \quad (\text{C.15})$$

$$J_0(x) = \frac{1}{\pi} \int_0^\pi \cos(x \sin \theta) d\theta = \frac{1}{\pi} \int_0^\pi \cos(x \cos \theta) d\theta \quad (\text{C.16})$$

$$J_m(x) = \frac{1}{\pi} \int_0^\pi \cos(x \sin \theta - m\theta) d\theta \quad (\text{C.17})$$

Recurrence relations

$$J_{m-1}(x) + J_{m+1} = \frac{2m}{x} J_m(x) \quad (\text{C.18})$$

$$J_{m-1}(x) - J_{m+1}(x) = 2 \frac{dJ_m(x)}{dx} \quad (\text{C.19})$$

$$\frac{dJ_m(x)}{dx} = J_{m-1}(x) - \frac{m}{x} J_m(x) \quad (\text{C.20})$$

$$\frac{dJ_m(x)}{dx} = -J_{m+1}(x) + \frac{m}{x} J_m(x) \quad (\text{C.21})$$

Derivatives

$$\frac{dJ_m(x)}{dx} = \frac{1}{2} [J_{m-1}(x) - J_{m+1}(x)] \quad (\text{C.22})$$

$$\frac{dJ_0(x)}{dx} = -J_1(x) \quad (\text{C.23})$$

$$\frac{d}{dx} [x^m J_m(x)] = x^m J_{m-1}(x) \quad (\text{C.24})$$

$$\frac{d}{dx} [x^{-m} J_m(x)] = -x^{-m} J_{m+1}(x) \quad (\text{C.25})$$

Integrals

$$\int J_1(x) dx = -J_0(x) \quad (\text{C.26})$$

$$\int x J_0(x) dx = x J_1(x) \quad (\text{C.27})$$

$$\int x^{p+1} J_p(x) dx = x^{p+1} J_{p+1}(x) \quad (\text{C.28})$$

$$\int J_0^2(x) x dx = \frac{x^2}{2} [J_0^2(x) + J_1^2(x)] \quad (\text{C.29})$$

$$\int J_m^2(x) x dx = \frac{x^2}{2} [J_m^2(x) - J_{m-1}(x) J_{m+1}(x)] \quad (\text{C.30})$$

$$\int J_m(ax) J_m(bx) x dx = \frac{x}{a^2 - b^2} [b J_m(ax) J_{m-1}(bx) - a J_m(bx) J_{m-1}(ax)] \quad (\text{C.31})$$

### Roots of Bessel Functions (15 Digits)

$n$ th roots of Bessel functions, <sup>3</sup>  $J_m(x) = 0$

$m \setminus n$	$n=1$	$n=2$	$n=3$	$n=4$	$n=5$
$m=0$	2.40482555769577	5.52007811028631	8.65372791291101	11.7915344390142	14.9309177084877
$m=1$	3.83170597020751	7.01558666981561	10.1734681350627	13.3236919363142	16.4706300508776
$m=2$	5.13562230184068	8.41724414039986	11.6198411721490	14.7959517823512	17.9598194949878
$m=3$	6.38016189592398	9.76102312998166	13.0152007216984	16.2234661603187	19.4094152264350
$m=4$	7.58834243450380	11.0647094885011	14.3725366716175	17.6159660498048	20.8269329569623
$m=5$	8.77148381595995	12.3386041974669	15.7001740797116	18.9801338751799	22.2177998965612
$m=6$	9.93610952421768	13.5892901705412	17.0038196678160	20.3207892135665	23.5860844355813
$m=7$	11.0863700192450	14.8212687270131	18.2875828324817	21.6415410198484	24.9349278876730
$m=8$	12.2250922640046	16.0377741908877	19.5545364309970	22.9451731318746	26.2668146411766
$m=9$	13.3543004774353	17.2412203824891	20.8070477892641	24.2338852577505	27.5837489635730
$m=10$	14.4755006865545	18.4334636669665	22.0469853646978	25.5094505541828	28.8873750635304

$n$ th roots of the derivatives of Bessel functions<sup>3</sup> ( $dJ_m(x)/dx = 0$ )

$m \setminus n$	$n=1$	$n=2$	$n=3$	$n=4$	$n=5$
$m=0$	3.83170597020751	7.01558666981561	10.1734681350627	13.3236919363142	16.4706300508776
$m=1$	1.84118378134065	5.33144277352503	8.53631636634628	11.7060049025920	14.8635886339090
$m=2$	3.05423692822714	6.70613319415845	9.96946782308759	13.1703708560161	16.3475223183217
$m=3$	4.20118894121052	8.01523659837595	11.3459243107430	14.5858482861670	17.7887478660664
$m=4$	5.31755312608399	9.28239628524161	12.6819084426388	15.9641070377315	19.1960288000489
$m=5$	6.41561637570024	10.5198608737723	13.9871886301403	17.3128424878846	20.5755145213868
$m=6$	7.50126614468414	11.7349359530427	15.2681814610978	18.6374430096662	21.9317150178022
$m=7$	8.57783648971407	12.9323862370895	16.5293658843669	19.9418533665273	23.2680529264575
$m=8$	9.64742165199721	14.1155189078946	17.7740123669152	21.2290626228531	24.5871974863176
$m=9$	10.7114339706999	15.2867376673329	19.0045935379460	22.5013987267772	25.8912772768391
$m=10$	11.7708766749555	16.4478527484865	20.2230314126817	23.7607158603274	27.1820215271905

<sup>3</sup> <http://wwwal.kuicr.kyoto-u.ac.jp/www/accelerator/a4/besselroot.htmlx>

## Appendix D: Trigonometric Functions

Euler's formula

$$e^{jx} = \cos x + j \sin x \quad (\text{D.1})$$

$$\cos x = \frac{e^{jx} + e^{-jx}}{2}; \quad \sin x = \frac{e^{jx} - e^{-jx}}{2j}; \quad \tan x = \frac{1}{j} \frac{e^{jx} - e^{-jx}}{e^{jx} + e^{-jx}} \quad (\text{D.2})$$

Addition and subtraction

$$\cos \alpha = \pm \sin \left( \alpha \pm \frac{\pi}{2} \right); \quad \sin \alpha = \pm \cos \left( \alpha \mp \frac{\pi}{2} \right) \quad (\text{D.3})$$

$$\sin^2 \alpha + \cos^2 \alpha = 1 \quad (\text{D.4})$$

$$\sin(\alpha \pm \beta) = \sin \alpha \cos \beta \pm \cos \alpha \sin \beta \quad (\text{D.5})$$

$$\cos(\alpha + \beta) = \cos \alpha \cos \beta \mp \sin \alpha \sin \beta \quad (\text{D.6})$$

$$\sin \alpha \pm \sin \beta = 2 \sin \left( \frac{\alpha \pm \beta}{2} \right) \cos \left( \frac{\alpha \mp \beta}{2} \right) \quad (\text{D.7})$$

$$\cos \alpha + \cos \beta = 2 \cos \left( \frac{\alpha + \beta}{2} \right) \cos \left( \frac{\alpha - \beta}{2} \right) \quad (\text{D.8})$$

$$\cos \alpha - \cos \beta = -2 \sin \left( \frac{\alpha + \beta}{2} \right) \sin \left( \frac{\alpha - \beta}{2} \right) \quad (\text{D.9})$$

Products and powers

$$\cos \alpha \cos \beta = \frac{1}{2} [\cos(\alpha - \beta) + \cos(\alpha + \beta)] \quad (\text{D.10})$$

$$\sin \alpha \sin \beta = -\frac{1}{2} [\cos(\alpha + \beta) - \cos(\alpha - \beta)] \quad (\text{D.11})$$

$$\sin \alpha \cos \beta = \frac{1}{2} [\sin(\alpha + \beta) + \sin(\alpha - \beta)] \quad (\text{D.12})$$

$$\sin^2 \alpha = \frac{1}{2}(1 - \cos 2\alpha) \quad (\text{D.13})$$

$$\sin^3 \alpha = \frac{1}{4}(3 \sin \alpha - \sin 3\alpha) \quad (\text{D.14})$$

$$\cos^2 \alpha = \frac{1}{2}(1 + \cos 2\alpha) \quad (\text{D.15})$$

$$\cos^3 \alpha = \frac{1}{4}(3 \cos \alpha + \cos 3\alpha) \quad (\text{D.16})$$

## Appendix E: Hyperbolic Functions

$$e^x = \cosh x + j \sinh x \quad (\text{E.1})$$

$$\cosh x = \frac{e^x + e^{-x}}{2}; \quad \sinh x = \frac{e^x - e^{-x}}{2} \quad (\text{E.2})$$

$$\tanh x = \frac{e^x - e^{-x}}{e^x + e^{-x}} = \frac{e^{2x} - 1}{e^{2x} + 1}; \quad \coth x = \frac{1}{\tanh x} \quad (\text{E.3})$$

Series expansions

$$e^x = 1 + \frac{x}{1!} + \frac{x^2}{2!} + \frac{x^3}{3!} + \dots \quad (\text{E.4})$$

$$\sinh x = x + \frac{x^3}{3!} + \frac{x^5}{5!} + \frac{x^7}{7!} + \dots \quad (\text{E.5})$$

$$\cosh x = 1 + \frac{x^2}{2!} + \frac{x^4}{4!} + \frac{x^6}{6!} + \dots \quad (\text{E.6})$$

$$\tanh x = x - \frac{x^3}{3} + \frac{2x^5}{15} - \frac{17x^7}{315} + \dots \quad \left( x^2 < \frac{\pi^2}{4} \right) \quad (\text{E.7})$$

$$\sinh^{-1} x = x - \frac{x^3}{2 \cdot 3} + \frac{1 \cdot 3}{2 \cdot 4} \frac{x^5}{5} - \frac{1 \cdot 3 \cdot 5}{2 \cdot 4 \cdot 6} \frac{x^7}{7} + \dots \quad (x^2 < 1) \quad (\text{E.8})$$

$$\cosh^{-1} x = \ln(2x) - \frac{1}{2} \frac{1}{2x^2} - \frac{1 \cdot 3}{2 \cdot 4} \frac{1}{4x^4} - \frac{1 \cdot 3 \cdot 5}{2 \cdot 4 \cdot 6} \frac{1}{6x^6} - \dots \quad (x^2 < 1) \quad (\text{E.9})$$

$$\tanh^{-1} x = x + \frac{x^3}{3} + \frac{x^5}{5} + \frac{x^7}{7} + \dots \quad (x^2 < 1) \quad (\text{E.10})$$

Addition and subtraction

$$\cosh^2 \alpha - \sinh^2 \alpha = 1 \quad (\text{E.11})$$

$$\sinh(\alpha \pm \beta) = \sinh \alpha \cosh \beta \pm \cosh \alpha \sinh \beta \quad (\text{E.12})$$

$$\cosh(\alpha \pm \beta) = \cosh \alpha \cosh \beta \pm \sinh \alpha \sinh \beta \quad (\text{E.13})$$

$$\tanh(\alpha \pm \beta) = \frac{1 + \tanh \alpha \tanh \beta}{\tanh \alpha + \tanh \beta} = \frac{\sinh 2\alpha \pm \sinh 2\beta}{\cosh 2\alpha + \cosh 2\beta} \quad (\text{E.14})$$

$$\sinh \alpha \pm \sinh \beta = 2 \sinh \left( \frac{\alpha \pm \beta}{2} \right) \cosh \left( \frac{\alpha \mp \beta}{2} \right) \quad (\text{E.15})$$

$$\cosh \alpha \pm \cosh \beta = 2 \cosh \left( \frac{\alpha + \beta}{2} \right) \cosh \left( \frac{\alpha - \beta}{2} \right) \quad (\text{E.16})$$

$$\cosh \alpha - \cosh \beta = 2 \sinh \left( \frac{\alpha + \beta}{2} \right) \sinh \left( \frac{\alpha - \beta}{2} \right) \quad (\text{E.17})$$

## Products and powers

$$\sinh \alpha \sinh \beta = \frac{1}{2} [\cosh(\alpha + \beta) - \cosh(\alpha - \beta)] \quad (\text{E.18})$$

$$\cosh \alpha \cosh \beta = \frac{1}{2} [\cosh(\alpha + \beta) + \cosh(\alpha - \beta)] \quad (\text{E.19})$$

$$\sinh \alpha \cosh \beta = \frac{1}{2} [\sinh(\alpha + \beta) + \sinh(\alpha - \beta)] \quad (\text{E.20})$$

$$\sinh 2\alpha = 2 \sinh \alpha \cosh \alpha \quad (\text{E.21})$$

$$\sinh 3\alpha = 3 \sinh \alpha + 4 \sinh^3 \alpha \quad (\text{E.22})$$

$$\cosh 2\alpha = 2 \cosh^2 \alpha - 1 \quad (\text{E.23})$$

$$\cosh 3\alpha = 4 \cosh^3 \alpha - 3 \cosh \alpha \quad (\text{E.24})$$

$$\sinh^2 \alpha = \frac{1}{2} (\cosh 2\alpha - 1) \quad (\text{E.25})$$

$$\sinh^3 \alpha = \frac{1}{4} (\sinh 3\alpha - 3 \sinh \alpha) \quad (\text{E.26})$$

$$\cosh^2 \alpha = \frac{1}{2} (\cosh 2\alpha - 1) \quad (\text{E.27})$$

$$\cosh^3 \alpha = \frac{1}{4} (\cosh 3\alpha + 3 \cosh \alpha) \quad (\text{E.28})$$

## Functions of complex arguments

$$\begin{aligned} \sin jx &= \cosh x & \sinh jx &= j \sin x \\ \sin x &= -j \sinh jx & \sinh x &= -j \sin jx \end{aligned} \quad (\text{E.29})$$

$$\begin{aligned} \cos jx &= \cosh x & \cosh jx &= \cos x \\ \cos x &= \cosh jx & \cosh x &= \cos jx \end{aligned} \quad (\text{E.30})$$

$$\tan jx = -j \tanh jx \quad \tanh jx = -j \tan jx \quad (\text{E.31})$$

---

# Index

## A

- Absolute (reciprocity) calibration, 476–482  
Absolute temperature, 337  
Absorption of sound  
    air (dry), 681–682  
    air (humid), 682–684  
    boundary layers, 396, 438–440  
    classical thermoviscous, 681–682  
    fresh water, 681–682, 688–692  
    Helmholtz resonator, 415–416, 440–443  
    narrow tubes, 435–436, 438–440, 660–662  
    relaxation in gases and gas mixtures, 687–688  
    room, 632, 694  
    seawater, 688–692  
    spatial, 674–677  
    surfaces and walls, 660–662  
    thermal conduction, 660–662, 677–681  
    temporal, 674–677  
    transmission loss, 692  
    viscosity, 660–662, 674–677, 681–682  
Absorption graphs  
    air (dry and humid), 689  
    sea water, 691  
Absorptivity (Sabine), 627–632  
Accelerometer, 102–103, 231  
    compressional and shear piezoelectric, 188–190  
Acoustic admittance ( $Y$ )  
    branch, 490–492  
    DELTAECC “softend”, 387  
    Helmholtz resonator, 492–494  
Acoustic approximation, 359–361, 363–364, 370–371  
Acoustic compliance, 366  
    gas spring, 366–367  
Acoustic energy flux (intensity), 464–465  
    intensity level (IL), 466–467  
Acoustic filters, 492–495  
Acoustic impedance ( $Z_{ac}$ ), 366  
Acoustic inertance, 372–373  
Acoustic intensity, 464–465  
Acoustic levitation, 738–743  
Acoustic Mach number ( $M_{ac}$ ), 364, 370, 704–705  
Acoustic power ( $\Pi_{ac}$ ), 396, 464–465  
Acoustic power dissipation  
    in boundary layer, 396, 432–433, 438–440, 660–662  
    by chemical relaxation (sea water), 688–692  
    classical thermoviscous attenuation ( $\alpha_{classical}$ ), 681–682  
    in a Helmholtz resonator, 440–443  
    in plane wave resonator (quality factor), 472–473  
    by relaxation, 684–686  
    by thermal relaxation, 427–430, 432–433, 660–662, 677–680  
    by viscosity, 438–440, 674–660, 677–662, 681–682  
Acoustic pressure, 359  
Acoustic transfer impedance ( $Z_t$ )  
    coupler, 481–482  
    double Helmholtz resonator, 482  
    free-field, 481  
    planewave resonator, 474–475, 482  
    planewave tube, 482  
Active noise cancellation, 667  
Added (hydrodynamic) mass  
    baffled circular piston, 602–603  
    general multipole, 573  
    piston at the end of a tube, 607–610  
    pulsating sphere (monopole), 551–552  
    sphere executing translational oscillations (dipole), 573  
Adiabatic compliance, 366  
Adiabatic compression, 729–731  
Adiabatic equation-of-state (ideal gas), 341–342  
Adiabatic invariance  
    acoustic levitator, 738–743  
    enclosure, 648–651  
    membrane, 300–302  
    pendulum, 71–73  
    resonator obstacle, 738–743  
    Space Shuttle Cargo Bay, 648–651  
Adiabatic sound speed ( $c$ )  
    ideal gas, 457  
    liquid, 460  
Adiabatic temperature change  
    ideal gas, 5–6, 342–343  
    solid, 181  
Adiabatic-to-isothermal transition ( $\omega_{crit}$ ), 433–434  
African thumb piano (M’biria), 278  
Air-concrete interface, 514–516  
Altec 21-C microphone, 328

- American Society for Testing and Materials (ASTM)  
     significant figures, 37
- Amplitude decay, 47, 73–76, 674–677
- Amplitude reflection coefficient ( $R$ )  
     cross-sectional discontinuity, 490–492  
     fluid interface (normal incidence), 514–518  
     fluid interface (oblique incidence), 528–529  
     three media (normal incidence), 518–519
- Amplitude shading (discrete line array), 591–593
- Anechoic chamber (spherical spreading), 611–612
- Angle  
     critical, 526–528  
     grazing, 533  
     incidence (Snell's law), 523–526  
     intromission, 528–529  
     reflection (Snell's law), 523–526  
     refraction (Snell's law), 523–526  
     transmission (Snell's law), 523–526
- Angular frequency (radian frequency,  $\omega$ ), 61
- Anisotropic elasticity, 225–227  
     auxetic materials, 186  
     physical constants, 225–227  
     polycrystalline materials, 227  
     stiffness matrix, 226–227
- Anti-node, 143, 470–472
- Antireflective coating, 520
- Anthropomorphic frequency weighting, 468–470
- Architectural acoustics  
     critical distance, 633  
     density of modes, 626–627  
     mode characterization, 624–625  
     reverberation time, 630–632  
     Schroeder frequency, 633–634
- Argand plane, 18–19
- Association-dissociation (chemical) relaxation  
     (salt water), 688–692
- Atmospheric lapse rate, 367–368
- Atmospheric pressure, 733
- Atomic bomb blast wave, 52–53
- Atomic mass unit, 337, 462
- Attenuation  
     at boundaries, 396, 432–433, 438–440, 660–662  
     bubble, 557–560  
     bubble cloud, 586–588  
     classical thermoviscous attenuation, 681–682  
     in ducts, 435–436, 438–440  
     molecular effects, 684–686  
     nonlinear effects (sawtooth shock waves), 712–713  
     in planewave resonators, 472–473  
     by relaxation effects, 684–686  
     of sawtooth waveform, 712–713  
     in seawater, 688–692  
     by thermal conduction, 427–430, 432–433, 677–680  
     by viscosity, 438–440, 660–662, 674–677, 681–682
- Auditory threshold, 467
- Auxetic materials, 186
- Average power, 21–22
- Avogadro's number, 337
- A-weighted sound pressure level (dB<sub>A</sub>), 468–470
- Axial modes, 624
- B**
- Baffled piston  
     directionality, 595–599  
     far-field radiation, 604–607  
     first null and piston diameter, 597–599, 604–607  
     radiation impedance, 602–604  
     radiation mass, 603  
     radiation resistance, 602–604
- Baffled rectangular piston, 604
- Ballistic propagation, 433–435
- Band-pass filter, 494–495
- Band-stop filter, 492–494, 521–522
- Bandwidth  
     equivalent noise bandwidth ( $\Delta f_{EQNB}$ ), 81  
     half-power bandwidth ( $\Delta f_{-3\text{ dB}}$ ), 87–90
- Bar (normal modes in flexure)  
     clamped-clamped, 253–254  
     clamped-free, 252–253  
     free-free and tuning fork, 254–256
- Basis functions, 13–16, 107–108, 155–157
- Bass-reflex speaker enclosure, 405–412
- Beam steering, 591–593
- Bending moment, 193–198
- Bernoulli, Daniel, 297
- Bernoulli pressure, 731–733  
     levitation force, 737–738  
     torque on a Rayleigh disk, 732, 734–735  
     Venturi tube, 369–370
- Bessel, F.W., 297
- Bessel functions  
     first kind, 295–298, 642  
     graphs, 298  
     identities, 679, 758–759  
     integrals, 759  
     modified, 321–322  
     power series solution, 295–298  
     recursion relations, 759  
     second kind (Neuman functions), 298  
     spherical, 554–555, 653  
     tables, 300, 639, 641, 760  
     zeros, 639, 757
- Bessel's differential equation, 295–298, 638
- Binomial distribution, 32
- Bipole, 560–564
- Black, Harold S., 466
- Blackstock's bridging function, 718
- Boltzmann distribution, 346
- Boltzmann's constant ( $k_B$ ), 76–82, 337, 653
- Boric acid in seawater, 688–692
- Bodine, Albert, 242–244
- Boundary conditions  
     for bar, 250  
     for circular membrane, 294  
     for flexible string, 138–144, 158–160  
     no-slip (viscosity), 434  
     on normal velocity component, 514–518  
     on pressure, 514–518  
     at pressure-release surface, 518  
     for rectangular membrane, 286  
     for rectangular waveguide, 655

- for rigid-walled enclosure, 623, 645–636, 645, 652, 656
- Boundary layer thickness  
  thermal ( $\delta_\theta$ ), 427–430  
  viscous ( $\delta_v$ ), 436–438
- Boyle's law, 731
- Broadside direction, 561
- Brunt–Väisälä frequency, 414
- Bubble in water  
  dissipation, 430–433, 557–560  
  multiple scattering from bubble cloud, 586–588  
  resonance (Minnaert) frequency, 555–557, 612–613  
  sound scattering, 584–586  
  surface tension (Laplace's formula), 555–557  
  quality factor, 557–560
- Buckingham  $\Pi$ -theorem, 23–29
- Buckling  
  Euler force, 200–202  
  slenderness ratio ( $L/a$ ), 200–201  
  transverse deflection, 200–201
- Bulk modulus  
  adiabatic ( $B_s$ ), 182–183, 460, 506  
  relation to other isotropic moduli, 187
- Bulk viscosity ( $\zeta$ )  
  air 677–679, 682–684, 696  
  water, 688–692
- B-weighted sound pressure level (dB), 468–470
- C**
- Calibration of microphones, 476–482
- Cantilever spring  
  uniform beam, 193–198  
  triangular (tapered) beam, 198–200
- Capacitance microphone, *see* Condenser microphone
- Capacitive reactance, 366
- Capillary force (Laplace force), 50, 248, 555–557
- Cardioid directionality, 574–575
- Cardioid microphone, 575–577
- Cartesian coordinate systems, 284–286, 291, 292, 294
- Catenoidal horn, 499–500
- Causality sphere, 526–548
- Cavitation effects, 517, 710
- Cavitation threshold, 710
- Celerity, 115, 360
- Central forces (virial theorem), 67–68
- Characteristic equation (secular equation), 107, 676
- Characteristic impedance (specific acoustic impedance), 463–464  
  air, 514–515  
  string, 164–166, 174
- Characteristic modes of 3-D enclosures  
  cylindrical enclosure, 635–641  
  rectangular room, 623–625
- Space Shuttle cargo bay, 648–651
- spherical enclosure, 651–654
- toroidal enclosure, 644–646
- Chemical relaxation  
  fluorine, 687–688  
  sea water, 688–692
- Chromatic scale (equal temperament), 146–147
- Circular membrane, 294–302  
  adiabatic invariance, 300–302  
  annular membranes, 302–304  
  effective piston area, 304–306  
  kinetic energy, 327  
  Laplacian operator, 295  
  modal frequencies, 299–300  
  modal density, 300  
  musical instruments, 283, 294  
  power series solution (Frobenius method), 295–298  
  pressure-driven, 308–310  
  tympani, 306–308  
  wedges, 302–303
- Circular piston in baffle  
  axial pressure field ( $p_{ax}$ ), 604–607  
  directionality and directivity, 599–602  
  near-field radiation (on-axis), 604–607  
  radiation impedance, 602–604
- Circular plate vibration, 321–324
- Climate change, 505
- Closed tube resonance (rigid termination), 470–474  
  closed-open tube, 474  
  quality factor ( $Q$ ), 472–473
- Circular waveguide, 659–660
- Cloud of bubbles, 586–588
- Coefficient of nonlinearity  
  Grüneisen parameter ( $\Gamma$ ), 705–706  
  virial expansion ( $B/2A$ ), 707–708
- Coherent sound sources, 468
- Coil spring  
  coupling stretch and twist (Wilberforce pendulum), 204–205  
  double-start helical, 206  
  stiffness, 203–204  
  twist and tilt, 205–206
- Collision time (mean-free-path), 443–444
- Compact scatterers, 580–584
- Compact source, 544
- Compactness criterion, 545
- Complex conjugate, 21
- Complex elastic moduli, 211–213
- Complex exponential, 17, 21
- Complex numbers, 16–22  
  algebraic operations, 19–21  
  Argand plane, 18–19  
  Euler's formula, 18  
  imaginary number ( $j$ ), 17  
  phasor notation, 19  
  time-averaged power (multiplication), 21–22
- Complex plane, 18–19
- Complex roots, 20–21
- Conductivity  
  electrical, 424–425  
  thermal, 425–427
- Confounding variables, 40
- Conical horn, 495
- Condenser microphone  
  breakdown (ionization) bias voltage, 315–316

- Condenser microphone (*cont.*)  
 constant charge, 312–313  
 electret, 317–320  
 electret equivalent bias voltage, 319–320  
 electrical equivalent circuit, 312  
 electrostatic collapse, 316–317  
 electrostatic force, 316  
 lumped-element model, 327–328  
 MEMS device, 328–329  
 “1-inch” microphone diagram, 311  
 open-circuit sensitivity, 314–315  
 optimal backplate radius, 313–315  
 optimal sensitivity, 313–315  
 polarization voltage ( $V_{bias}$ ), 312–313  
 pre-amplifier, 312  
 pressure-driven membrane, 308–310  
 pressure equilibration (relaxation time), 450, 451  
 typical “1-inch” microphone, 311
- Conservation equation  
 energy, 464–465  
 entropy, 351–352  
 mass, 348, 350  
 momentum, 350
- Conservative force, 8
- Consonance and dissonance (musical), 144–147
- Constant sound speed gradients  
 construction point, 534  
 piecewise linear approximation, 529  
 propagation delay, 536–537  
 refraction of sound, 529  
 solid body rotation, 531–532  
 sound channels, 534–536  
 sound focusing, 538–539  
 under Arctic propagation, 537
- Continuity equation  
 energy, 464–465  
 fluid mass (mass conservation), 363  
 heat, 425–427  
 horn, 496–497  
 mass, 348, 350  
 momentum, 350  
 nonlinear, 719  
 surface gravity wave, 504, 703
- Continuous line array, 593–595
- Conservation equation, 348, 352
- Convective derivative, 361
- Convective nonlinearity, 370, 703
- Conversion factors (units), 755
- Corner horn, 502
- Correlated/uncorrelated errors, 35–37
- Correlation coefficient, 39–42
- Coupled Helmholtz resonators, 402–405  
 DELTAE model, 403  
 schematic view, 403
- Coupled oscillators, 105–115  
 coupled algebraic equations, 106–107, 109–110, 113–115  
 coupled pendula, 126  
 identical masses and springs, 106–107, 112–115
- level repulsion, 110–111  
 loudspeaker in a bass-reflex enclosure, 409–412  
 nearest-neighbor interactions, 112–115  
 normal coordinates, 107–108  
 speaker-resonator coupling, 482–488, 664–665, 749–750
- Covariance, 35–37
- Crest factor, 467
- Critical angle, 526–528
- Critical damping, 76
- Critical distance, 633
- Cross-sectional area change  
 branching, 491–492  
 constrictions and expansions, 521–523  
 horns, 495–501
- Cutoff frequency  
 exponential horn, 495–499  
 waveguide, 655–656
- C-weighted sound pressure level (dB<sub>C</sub>), 468–470
- Cylindrical coordinates, 295
- Cylindrical enclosure, 635–644  
 azimuthal functions, 637  
 Bessel functions ( $J_n$ ), 295–298, 638–639, 758–759  
 mode shapes, 640, 642–643  
 Neumann solutions ( $N_n$ ), 298, 644–646  
 nodal circles and diameters, 641–643  
 periodic boundary conditions, 637  
 radial functions, 642  
 speaker-driven resonator, 664–665
- Cylindrical resonator, *see* Cylindrical enclosure
- Cylindrical waveguide, 659–660, 666, 667
- D**
- d’Alembertian operator, 136
- Damping  
 critical damping, 76  
 equivalent noise bandwidth ( $\Delta f_{EQND}$ ), 81  
 free-decay frequency, 75–76  
 frictional (Coulomb) damping, 82–83  
 mechanical resistance ( $R_m$ ), 74  
 overdamped, 76  
 quality factor ( $Q$ ), 25, 75–76, 87–90, 756–757  
 thermal equilibrium and thermal fluctuations, 77–81  
 underdamped, 76  
 viscous damping, 73–75
- Dashpot, 73–75
- Decay curve for sound in rooms, 630–632
- Decibel, 465–468  
 addition, 468, 505  
 definition, 88  
 half-power, 88  
 history, 465–466
- Decrement (logarithmic), 74
- Deep isothermal layer (ocean), 530, 534
- Deep sound channel (ocean), 534–536
- Degenerate modes  
 enclosures, 624–625, 640, 646–648  
 membranes, 288–290
- Degrees-of-freedom, 105, 108

- DELTAEAC (Design Environment for Low-amplitude Thermoacoustic Energy Conversion)  
 downloading, 382  
 incremental plotting (\*.ip), 397–401  
 \*.out files, 384–390, 392–394  
 reverse Polish notation (RPN) segments, 394–395  
 state variable plots (\*.sp), 391  
 thermophysical properties, 382–384
- Density  
 acoustic, 360  
 energy, 464–465  
 equilibrium, 360, 367–368  
 linear, 135  
 mass, 237, 337–338  
 surface, 285  
 volume, 337–338
- Density of modes  
 three-dimensions, 626–627, 641–644  
 two-dimensions, 291–294
- De-tuning/de-phasing instability, 743–746
- DI (directionality index), 602
- Dielectric constant, 311, 318–320
- Dielectric breakdown, 315–316
- DIFAR directional sonobuoy, 578
- Differential, 4–5
- Diaphragm  
 across a duct, 520  
 microphone, 310–311
- Difference frequency wave, 721–725
- Diffuse sound field, 633–634
- Diffusion equation, 422–424
- Dilatational modulus (a.k.a. Modulus of Unilateral Compression), 183–185, 240  
 relation to other isotropic moduli, 187
- Dimensional homogeneity, 22–23
- Dimensionless groups, 25–26  
 Grüneisen parameter ( $\Gamma$ ), 705–706  
 Gol'dberg number ( $G$ ), 711–712  
 Mach number ( $M_{ac}$ ), 364, 370, 704–705  
 Prandtl number (Pr), 383, 447–448, 681  
 Reynolds number, 436  
 Strouhal number, 27  
 Wakeland number ( $\beta$ ), 488–490
- Dipole  
 dipole strength, 572–573, 580  
 directionality, 567–570  
 hydrodynamic mass, 573  
 near pressure-release boundary, 568  
 out-of-phase monopoles, 567–570  
 small incompressible body's translational oscillations, 578–580
- Dipole strength, 572–573, 580
- Directivity, 599–602
- Directivity index, 598, 602
- Dispersion, 247–249, 684–686  
 capillary waves, 248  
 exponential horns, 498  
 flexural waves, 249–250  
 fluorine gas, 687–688  
 gravitational surface waves, 248
- Kramers-Kronig relations, 213–216, 684–686
- waveguide, 656–658
- Dispersion relation, 459–462
- Dissipation  
 dissipation function, 465  
 by internal relaxation, 684–692  
 at repeating (sawtooth) shock front, 712–713  
 by shear viscosity, 661–638, 662–439, 674–679  
 by thermal conduction, 432–433, 661–662, 679–681  
*See also* Bulk viscosity ( $\zeta$ )
- Distortion (nonlinear), 714–720
- Doppler mode splitting, 647–648, 663–664
- Double Helmholtz resonator, 402, 416–417, 450–451
- Double shock waves, 708–710
- Driven circular membrane, 308–310
- Driven systems  
 displacement-driven SHO, 100–102  
 electrodynamic microphone, 99–100  
 force-driven SHO, 83–86  
 mass-controlled response regime, 85  
 mechanical impedance, 84  
 moving-coil (electrodynamic) loudspeaker, 95–98, 126–128  
 Rayleigh line shape, 85–86  
 resistance-controlled response regime, 84  
 resonance bandwidth, 87–88  
 resonance tracking (phase-locked loop), 90–92  
 stiffness-controlled response regime, 85  
 transient response, 92–94  
 transmissibility, 102
- Ducts  
 absorption at walls, 472–473, 660–662  
 coupling to loudspeakers, 482–490  
 with discontinuous cross-section, 490–492  
 guided modes in circular ducts, 659–660, 666–667  
 guided modes in rectangular ducts, 655–656, 658–659, 665–666  
 resonances in ducts, 470–475, 482–488  
 side-branch in ducts, 492–494  
 transient pulse propagation, 667–668
- Dynamic loudspeaker, 95–98, 126–128
- Dynamic microphone, 99–100
- Dynamic range, 260
- Dynamic (or absolute) viscosity ( $\mu$ ), 434  
 ideal gas (kinetic theory), 446
- Dynamical equation, 334, 373
- E**
- Earnshaw, Samuel, 715
- Echo satellite, 669–670
- Effective bandwidth  
 equivalent noise bandwidth ( $\Delta f_{EQNB}$ ), 81  
 half-power bandwidth ( $\Delta f_{-3\text{ dB}}$ ), 87–90
- Effective length  
 flanged piston, 602–604  
 Helmholtz resonator neck (DELTAEAC), 396–397  
 Helmholtz resonator neck (experimental), 378–381  
 unflanged piston, 607–610
- Effective mass, *see* Entrained mass
- Effective modulus (rubber springs), 217–218
- Efficiency  
 dipole radiation, 573

- Efficiency (*cont.*)  
     dipole scattering, 582  
     electroacoustic coupling, 488–490  
     monopole radiation, 553–554
- Einstein, Albert, 335, 546, 617
- Elastic suspension (thermoacoustic resonator), 617–618
- Elasticity  
     Anisotropic (crystalline), 225–227  
     isotropic, 179–187
- Elastic moduli  
     bulk ( $B$ ), 182–183, 187  
     complex, 211–213  
     dilatational ( $D$ ), 183–185, 187  
     effective modulus (rubberlike materials), 217–218  
     Lamé ( $\lambda$ ), 187  
     Poisson’s ratio ( $\nu$ ), 181, 183, 184, 187  
     relations among isotropic moduli, 187  
     shear ( $G$ ), 185–187, 262  
     unilateral compression ( $D$ ), 183–185, 187  
     Young’s ( $E$ ), 180–181, 260–262
- Electret microphone, 317–320
- Electrical impedance ( $Z_{el}$ ), 51
- Electroacoustic reciprocity, 477–482
- Electrodynmic loudspeaker, 95–98, 126–128
- Electrodynmic microphone, 99–100
- Electromagnetic cross-talk, 260
- Electrostatic levitation oscillations, 123
- Electrostatic potential energy, 316
- Enclosure  
     bass-reflex loudspeaker, 405–412  
     cylindrical, 635–644  
     rectangular room, 623–635  
     spherical, 651–655  
     toroidal, 644–646, 663–664
- End correction, *see* Effective length
- End-fire array  
     discrete, 591–592  
     parametric, 721–725
- End-fire direction, 561, 591
- End-to-end calibration, 34
- Energy  
     bar, 242–244, 264–265, 276  
     enthalpy, 679, 735–736  
     heavy chain, 154  
     internal (thermodynamic), 339–340, 344  
     kinetic, 66–67, 150, 337, 441, 472  
     kinetic energy density in fluids, 465  
     oscillator, 66–67  
     potential, 6–10, 150, 276, 475, 740  
     potential energy density in fluids, 465  
     string, 147–149, 157–158
- Energy balance equation, 630
- Energy density, 465
- Enthalpy function, 679, 735–736
- Entrained mass  
     for baffled piston, 603  
     for dipole, 573  
     for monopole, 552  
     for multipole source, 573
- for piston at the end of a tube, 608  
     for pulsating sphere, 552  
     for quadrupole, 615  
     for translating sphere, 573
- Entrance length (for Poiseuille flow), 436
- Entropy, 339  
     production of, 350, 678  
     dissipation function, 465  
     flux, 348, 678  
     discontinuity at shock front, 713  
     production of, 350  
     wave (second sound in superfluids), 709
- Equal-loudness contours (Fletcher-Munson curves), 467–468
- Equal temperament (musical scale), 144–147
- Equipartition theorem, 76–82  
     electrical noise (in resistors, Johnson noise), 82  
     ideal gas laws, 336–338  
     fluctuations, 80  
     thermal noise, 81, 88  
     thermal velocity, 80
- Equivalent noise bandwidth ( $\Delta f_{EQNB}$ ), 81, 88–90
- Equation of state, 352  
     adiabatic fluid, 341–342  
     dynamic, 682, 684–686  
     isothermal gas, 338  
     virial expansion, 707
- Ergodic hypothesis, 31
- Error propagation, 35–37  
     covariance, 35–37
- Eucken formula, 447
- Euler-Bernoulli beam equation, 247
- Euler equation, 349–350, 369  
     linearized, 370–372, 456–457, 464, 504, 549, 637, 638, 704  
     nonlinear, 719
- Euler force (buckling), 202
- Eulerian coordinate system, 350, 361
- Eulerian volume (fluid element), 362, 371
- Euler, Leonhard, 18, 297, 334
- Euler’s formula, 18
- Evanescent wave, 428
- Experimental errors, 29–32  
     correlated or uncorrelated, 35–37
- Exponential horn, 495–500
- Extensive variables, 337, 461
- Eyring-Norris equation, 663
- F**
- Faraday’s law, 98
- Far-field  
     axial pressure (baffled piston), 604–607  
     radiation pattern, 613–614
- Fermat’s principle, 525–526
- Ferroelectric ceramic, 188–189
- Feynman, Richard P., 7, 325, 334
- Field-effect transistor, 318
- Fifth (musical interval), 144–147
- Filter

- band-pass, 494–495  
 band-stop, 492–494, 521–522  
 high-pass (stub) filter, 494–495  
 low-pass (constriction or expansion), 521–523
- Finite string  
 displacement driven, 167–169  
 efficient driver-load interaction, 170–171  
 force-driven, 170  
 mechanical impedance of mass, 169
- First Law of Thermodynamics, 339–341
- First sound (superfluid helium), 709, 728
- Flare constant (horns), 497
- Flat tuning (levitation superstability), 746
- Fletcher-Munson curves, 467–468
- Flexible string (wave equation), 134–135
- Flexural modes (thin bar)  
 dispersion, 247–249  
 Euler-Bernoulli beam equation, 247  
 lowest-frequency mode, 262  
 mode shapes, 252–256  
 normal mode frequencies, 251–255  
 Rayleigh waves, 256  
 wave functions, 249–250
- Flexural rigidity, 321
- Flexural wave speed, 247
- Fluid parcel/particle, 333, 348–350, 361
- Focusing (sound)  
 by graded speed, 539  
 by marine mammals, 538
- Force  
 drag due to viscosity, 434  
 due to potential gradients, 9, 742  
 on a sphere in a standing wave, 743
- Force-driven fixed string, 175
- Forced vibration, 83–87, 100–102
- Fourth sound (superfluid helium), 709
- Fourier analysis, 13–16
- Fourier coefficient  
 harmonic distortion, 716–717  
 sawtooth wave, 53–54  
 square wave, 15–16  
 triangle wave, 16
- Fourier diffusion equation, 423, 426
- Fourier, Jean-Baptiste Joseph, 22, 297
- Fourier's theorem, 14
- Fourier synthesis, 13–16
- Fourth (musical interval), 145–147
- Free boundary conditions, 138, 140, 166
- Free decay frequency, 75–76
- Frequency (angular), 14, 61
- Frequency weighting (sound level meters), 468–470
- Frictional (Coulomb) damping, 82–83
- Frobenius, Ferdinand Georg, 296
- Frozen sound speed, 685
- Fubini-Ghiron solution (nonlinear wave distortion), 716–718
- Fundamental frequency, 143
- Fundamental Theorem of Calculus, 5, 8, 343
- G**  
 Gamma function, 597  
 Garrett's First Law of Geometry, 22, 524, 713  
 Galilean invariance, 728  
 Galileo, 12, 121  
 Gas constant (Universal), 337, 713  
 Gases  
 adiabatic temperature change, 342–343  
 bulk viscosity ( $\zeta$ ), 678, 681–682  
 diatomic, 344–347  
 dry air (standard), 462  
 ideal, 336–338, 341–342, 354  
 internal degrees-of-freedom, 347, 684–686  
 molecular weight (mass), 338  
 monatomic, 344  
 polyatomic, 344–347  
 polytropic coefficient, 341–342, 355–356  
 sound speed, 383, 457, 460–461, 707  
 sound speed in gas mixtures, 460–462  
 specific-heat ratio, 341
- Gas spring, 354–355, 366–367
- Gas stiffness ( $K_{\text{gas}}$ ), 354, 367
- Gauge invariance, 9
- Gaussian distribution, 32–33
- Generalized susceptibility, 213
- Geometric resonance, 720–725
- Geophone, 102–104, 129
- Gerber scale, 61, 64
- Gibbs phenomena, 15, 16
- Glass transition temperature, 218–220
- Glockenspiel, 255
- Gol'dberg number, 711–712
- Gradient microphone, 575–577
- Gradient operator, 8, 423, 549–550, 638–639, 653, 735–736, 742
- Gravitational potential energy, 68–70
- Grazing angle, 533
- Greenspan viscometer, 450–451
- II-Groups, 25–29
- Group speed, 658, 660, 667–668
- Grüneisen parameter ( $\Gamma$ ), 705–706
- Guided waves, 654–662
- H**  
 Half-power beam width, 615  
 Half-width, 87  
 Half-wit, *see* Donald J. Trump  
 Hanging chain, 153–155  
 Harmonic analysis, 277, 359, 364  
 Harmonic distortion (nonlinear), 714–718  
 Harmonic series, 143–145, 158, 160  
 Heake, John, 206  
 Heat capacity (ideal gas)  
 constant pressure, 340–341  
 constant volume, 340, 344–347  
 isobaric, 340–341  
 isochoric, 340, 344–347  
 ratio, 346

- Helmholtz equation, 622  
 Helmholtz resonator, 358, 415, 416, 438–440, 557, 732, 733  
 High-pass (stub) filter, 494–495  
 Homogeneous media, 338  
 Hooke’s law, 61, 180  
 Horn  
   catenoidal, 499–500  
   conical, 495  
   corner, 502  
   exponential (semi-infinite), 495–499  
   finite length, 500–502  
   flare constant, 497  
   historical photos, 496  
   resonances, 502  
   Salmon, 499–500  
 Humidity, effects of, 632, 663, 683, 684, 688, 700, 723  
 Huygens principle, 523–524  
 Hydrodynamics  
   bulk viscosity ( $\zeta$ ), 422, 677–679, 682–684, 688–692  
   conservation equation, 348, 352  
   entropy equation, 350–351  
   equation of state, 352  
   equilibrium thermodynamics, 347  
   macroscopic models, 352  
   Navier-Stokes equation, 349–350, 358, 367, 423, 674–675  
   time reversal invariance, 422–424  
 Hydrophones, 481, 536, 578  
 Hydrostatic pressure, 367–368  
 Hydrostatic strain (volumetric strain), 182–183  
 Hyperbolic functions, 762–763
- I**
- Ideal gas laws  
   adiabatic, 341–342  
   isothermal, 338  
 Images, method of, 564–567  
 Imaginary part, 21  
 Imaginary unit ( $j$ ), 17  
 Impedance, *see* Specific type  
 Impedance matching (antireflective) layer, 520  
 Impedance transformer, 168–169  
 Incoherence, 468  
 Incompressible sphere  
   dipole behavior, 579  
   equivalent cylinder (dipole strength), 580  
   multiple scattering, 586–588  
   scattering (compact density contrast), 580–583  
   translational oscillations, 579  
 Inductive reactance, 372  
 Inert (noble) gas, 345  
 Inertance, 372–373  
 Inertia coefficient, 150, 152, 154  
 Infrasound, 482, 692, 693  
 Inhomogeneous differential equation, 308–310, 719–720  
 Inhomogeneous media (scattering)  
   bubble cloud, 586–588  
   compressibility contrast, 583–584  
   density contrast, 580–583  
   single (resonant) bubble, 584–586  
 Initial conditions  
   for coupled harmonic oscillators, 108–109  
   for simple harmonic oscillator, 61–63  
   for string, 155–156  
 Instantaneous value, 359  
 Integration by parts, 5  
   *See also* Product rule  
 Intensity  
   Acoustic, 465  
   level (IL), 466–470  
   reference ( $I_{ref}$ ), 470–471  
 Intensive variables, 338  
 Interface between fluids, 514–519  
 Intermodulation distortion, 721–725  
 Internal energy, 339–340, 735  
 International Organization for Standards (ISO)  
   anthropomorphic level weighting, 468  
   broadband sound sources, 456  
   one-third octave band frequencies, 456  
 Interval (musical), 144–147  
 Intromission angle, 528–529  
 Isobaric heat capacity, 341  
 Isochoric heat capacity, 340  
 Isothermal boundary layer, 432  
 Isothermal equation of state (ideal gas), 338  
 Isothermal sound speed, 433–434  
 Isotropic, 338  
 Isotropic elasticity  
   bulk modulus ( $B$ ), 182–183  
   dilatational modulus ( $D$ ), 183–185  
   elastic constants, 187  
   elastic materials, 181  
   modulus of unilateral compression ( $D$ ), 183–185  
   relationship between moduli, 187  
   shear modulus ( $G$ ), 185–187  
   superposition, 13, 181–182, 610  
 Isotropic fluid, 348
- J**
- Joining conditions, 373  
 Joule heating, 104, 128, 166, 424, 439, 488–490  
 Jug hustler, 129  
 Just intonation (musical scale), 145–147
- K**
- Kepler’s third law (planetary motion), 68  
 Kettledrum (Tympani), 306–308, 327  
 Kinematic viscosity ( $\nu$ ), 437  
 Kinetic theory of gases, 336, 338, 353, 443, 676  
   mean free path, 443–444  
   microscopic model, 336–338, 443  
   Prandtl number, 447–448  
   quantum mechanical effects, 443  
   shear viscosity ( $\mu$ ), 443  
   thermal conductivity ( $\kappa$ ), 444–446  
   viscosity ( $\mu$ ), 446–448  
   viscous shear, 443

- Kramers-Kronig relations  
attenuation and dispersion in fluorine, 687–688  
single relaxation time systems, 684–686  
spring-damper systems, 213–216  
Standard Linear Model (SLM), 210–211  
viscoelastic materials, 206–207, 210–211
- Kronecker delta, 14
- k*-space (Reciprocal space), 291–292
- Kundt's tube, 731
- L**
- Laboratory frame-of-reference, 361
- Laennec, René Théophile Hyacinthe, 655
- Lagrangian coordinates, 361
- Lagrangian density, 736
- Lamé constant ( $\lambda$ ), 187
- Laplace's formula (capillarity), 555–557
- Laplacian operator, 286, 349, 549, 622, 636
- Layered fluids (refraction), 515–516, 518–519, 529–530
- Least-squares fitting, 37–38  
adjustable parameters, 46–47  
correlation coefficient, 39–42  
error estimates, 42–43  
linear correlation coefficient, 39–42  
linearized least-squares fitting, 43–46  
relative error in slope ( $\delta m/m$ ), 42–43  
more than two coefficients, 46–47
- Le Châtelier's Principle, 684
- Lead zirconium titanate (PZT), 189, 193
- Legendre transformation, 679
- Lennard-Jones potential, 49, 50, 123, 446
- Lenz's law, 96
- Le système international d'unités*, 23
- Level repulsion, 111, 412, 484–485
- Levitation, acoustic, 737–746  
superstability, 743–746
- Linear array  
continuous, 593–595, 614  
discrete, 544, 588–591, 610  
shaded, 593  
steered, 591–592
- Linear operator, 12–13
- Linear relationship, 12
- Linear response theory, 207–211, 213–216
- Linear superposition, 13  
compact monopole and dipole, 610  
continuous line source, 614  
four-element line array, 614
- Linearity, 12
- Linearized continuity equation, 363–366
- Linearized Euler equation, 370–372
- Loaded membrane (point mass), 290, 327
- Loaded string (point mass), 152–153, 161–163, 169, 177
- Logarithmic decrement ( $\delta$ ), 75
- Logarithmic differentiation, 5–6
- Long line array, 615
- Longitudinal modes of a thin bar, 236–239, 278
- Longitudinal waves in bulk solids, 240
- Losses, *see* Absorption, Attenuation, and Dissipation
- Loss factor/damping factor, 218–219
- Loss modulus, 218–219
- Loss tangent ( $\tan \delta$ ), 218
- Loudness, 467–470
- Loudspeaker  
in bass-reflex enclosure, 409–412  
electrodynamic, 95–98, 126–128  
enclosure (woofer), 545
- Low-pass filter (constriction or expansion), 521–523
- Lumped element approximation, 63–64, 358
- Lyapunov stability, 6
- M**
- Mach number ( $M_{\infty}$ ), 364, 370, 704–705
- Macroscopic variables, 334–335, 338
- Magnitude (complex number), 19
- Main thermocline (ocean), 530
- Mass, 23
- Mass conservation law, 348, 352
- Mass controlled regime, 85
- Mass law (for partitions), 520–521
- Mass-loaded string, 121, 126, 161–163, 169, 177
- Master curve, 269–270
- M'bira, 278
- Maxwell model (relaxation time), 207–210
- Maxwell relations, 679–680
- Mean field approximation, 586–588
- Mean free path, 443–444, 449–450
- Mean value, 30
- Mechanical impedance, 83–85, 87, 92, 101
- Mechanical reactance, 84, 552, 602–603
- Mechanical resistance, 22, 73–74, 163–165, 207, 522, 602, 603
- Medium density fiberboard (MDF), 417
- Mersenne's laws, 174
- Membrane  
annular, 302–304  
circular, 294–300  
effective piston area, 304–305  
forced motion, 308–310  
hexagonal, 302–303  
rectangular, 284–294  
tension per unit length, 285  
triangular (equilateral), 302–303, 326
- Method of images, 138–140, 564–568
- Microphone  
Altec 21-C, 328  
cardioid, 574–577  
condenser, 310–317  
electret, 317–320  
electrodynamic, 99–100  
MEMS, 80, 328–329  
moving-coil, 99–100
- Microphone vibration isolator, 230–231
- Microscopic models  
atoms, 336, 337  
Boltzmann's constant ( $k_B$ ), 337  
Equipartition theorem, 76–82, 336, 337
- Mirrored galvanometer, 78–80

- MKS units, 23  
 Mixed layer (ocean), 530  
 Modal degeneracy, 284, 288–290  
 Modal density, *see* Density of modes  
 Modal excitation
  - cylindrical resonator, 664–667
  - driven waveguide (rectangular), 658–659, 667–668, 670
  - rectangular enclosure, 625–626
 Mode splitting
  - cylindrical enclosure (Doppler), 647–648
  - cylindrical enclosure (incompressible obstacle), 646–647
  - square membrane (point mass), 290
  - toroidal enclosure (Doppler), 647–648, 663–664
 Modes (thin bar)
  - elastic moduli (*see* Elastic moduli)
  - flexural waves (*see* Flexural modes)
  - harmonic analysis, 277
  - longitudinal waves (*see* Longitudinal modes)
  - torsional waves, 245–246
  - stiff string, 274–277
 Modified Bessel functions ( $I_m$  and  $K_m$ ), 321–324  
 Modulus, *see* Elastic moduli  
 Modulus of unilateral compression ( $D$ ), 183–185
  - relation to other isotropic moduli, 187
 Mole (unit), 23, 337, 344  
 Molecular relaxation
  - equation of state, 682–686
  - vibrational, 687–688
 Monopole
  - compactness criterion, 544–545
  - hydrodynamic mass, 552
  - radiated power, 553
  - radiation impedance, 550–554
 Motor parameters, 490  
 Multipole expansion, 554–555  
 Musical intervals, 144–145  
 Musical scales, 145–147
- N**  
 Navier-Stokes equation, 349–350, 358, 367, 423, 674  
 Near field (baffled piston), 604–607  
 Nearest neighbor interactions, 113–114  
 N-element discrete line array
  - beam steering and shading, 591–595
  - geometric series, 589
  - inter-element separation, 589
  - straight-line path, 588
 Neper (unit), 687  
 Net force, 8–9  
 Neumann function ( $N_n$ ), 298, 303  
 Neutral equilibrium, 7  
 Neutral plane, 194–195  
 Newtonian fluids, 434  
 Newton's Law of Cooling, 424–425, 434  
 Newton's Second Law of Motion, 66, 333, 336, 348, 372, 373, 517  
 Nodal circle, 299, 303  
 Nodal diameter, 297, 299  
 Nodal line, 287  
 Noise
  - community equivalent level ( $L_{eq}$ ), 470
  - day-night level ( $L_{dn}$ ), 470
  - equivalent bandwidth ( $\Delta f_{EQNB}$ ), 81, 88–90
  - thermal noise voltage (Johnson noise), 82
  - thermal noise, 76–81
 Nondimensional frequency
  - flow (Strouhal number), 27–28
  - relaxation time ( $\omega\tau_R$ ), 207–211, 269–270, 684–686, 690
 Nondissipative lumped elements
  - acoustical compliance, 366
  - acoustical inertance, 358, 372–373
  - acoustical mass, 373
  - double-Helmholtz resonator, 416–417
  - electrical circuit element, 358
  - gas spring, 366–367
  - Helmholtz resonator, 358
  - linearized continuity equation, 363–365
  - linearized Euler equation, 370–372
  - lumped elements, 412
  - oscillations about equilibrium, 359–361
  - pistonphone microphone calibrator, 414–415
  - pressure oscillations, 358
 Nonlinear acoustics
  - anomalous distortion, 708–711
  - continuity equation, 703
  - convection (speed change), 704
  - convective nonlinearity, 703
  - Earnshaw solution, 715–716
  - equation of state, 702
  - Euler equation, 702
  - Gol'dberg number, 711–712
  - Grüneisen parameter, 704–705
  - harmonic distortion, 714
  - higher harmonic distortion, 716–718
  - hydrodynamic equations, 702
  - levitations superstability (acoustic molasses), 743–746
  - linear analysis, 701
  - linear approximation, 746–747
  - order expansion, 714
  - shallow-water gravity wave, 703–705
  - sinusoidal disturbance, 703
  - stable sawtooth waveform attenuation, 712–713
  - trigonometric expansion (2nd harmonic distortion), 715–716
  - virial expansion, 707
  - weak shock theory, 714
 Nonlinear effect, 365, 702  
 Nonlinear wave equation, 719–720  
 Non-reflecting termination, 166  
 Non-slip boundary condition, 435  
 Non-separable coordinate geometries
  - adiabatic invariance, 648
  - azimuthal modes, 650–651
  - nuclear reactor coolant pool, 668–669
  - Space Shuttle cargo bay, 648–651

- Nonuniform string, 152–153, 176, 177  
 Non-zero time-averaged effects  
   acoustic levitation, 737–743  
   adiabatic compression, 729–731  
   adiabatic invariance, 738–743  
   Bernoulli pressure, 731–733  
   inhomogeneous wave equation, 729  
   levitation superstability, 743–746  
   radiation pressure, 735–736  
   Rayleigh disk, 734–735  
   second-order pressure, 729–731  
   standing waves, 737–738  
 Normal coordinates, 107–108  
 Normal modes  
   anti-nodes, 143  
   boundary conditions, 141–144  
   coupled oscillators, 107–108  
   fundamental frequency, 143  
   harmonic series, 143  
   standing waves, 143  
   “string of pearls,” 141  
   Wavenumber, 141–143  
 Norris-Eyring reverberation time, 663  
 Nuclear explosion wave, 52–53
- O**  
 Oblique modes, 624  
 Ohm’s law, 22, 424–425  
 “Old-age limit” of waveforms, 746–747  
 Omnidirectional source  
   causality sphere, 546–548  
   compact monopole, 550–553  
   monopolar acoustic transfer impedance, 553–554  
 One-dimensional propagation  
   abrupt discontinuities, 490–492, 514–523  
   acoustic energy, 464–465  
   cavitation effects, 517  
   characteristic impedance, 464  
   complex pressure reflection coefficient, 519  
   conservation equation, 465  
   continuity equation, 464  
   duct constriction/expansion low-pass filters, 521–522  
   energy densities, 465  
   Euler equation, 464  
   Fermat’s principle, 523–526  
   harmonic plane waves, 463–464  
   horns of finite length, 500–503  
   hydrodynamic equations, 464  
   impedance matching (anti-reflective) layer, 520  
   inhomogeneous medium, 513–514  
   intensity, 465  
   limp diaphragm, 520  
   lumped-element model, 454–456  
   mass law (for partitions), 520–521  
   planar interface, 513  
   planewave, 514, 515, 519  
   power transmission coefficient, 519  
   pressure release boundary, 518  
   Rayleigh reflection coefficient, 528–529  
   reflection, 516  
   Salmon horns, 499–500  
   semi-infinite exponential horns, 495–499  
   Snell’s law, 523–526  
   specific acoustic impedance, 464  
   stub tuning, 494–495  
   superposition of sound levels, 468  
   thermal relaxation losses, 515  
   total internal reflection, 526–528  
   transmission, 516, 518  
 One-dimensional wave equation, 136, 238, 245, 246, 457–458, 499, 720  
 Onsager reciprocity, *xiv*  
 Open-circuit microphone sensitivity, 315, 320, 328, 476, 480  
 Optimum efficiency, 489  
 Order expansion, 714  
 Orthogonal functions, 13, 155–156  
 Oscillator output impedance, 51  
 Oscillatory plug flow, 438  
 Outgoing (spherical) wave, 546–550  
 Overtones, 143
- P**  
 Packard, Richard E., 198  
 Paddle-driven rectangular waveguide, 667–668  
 Parametric arrays, 725  
 Particular solution, 307–309  
 Pascal’s law, 338, 374  
 Paschen’s law (breakdown voltage), 315–316  
 Parameter of nonlinearity  
   B/A coefficient, 707–708  
   C/A coefficient, 707  
   Grüneisen parameter ( $\Gamma$ ), 705–707  
 Pendulum  
   adiabatic invariance, 71–73  
   data analysis, 51–52  
   heavy chain, 153–155  
   simple pendulum, 10–11, 70–71  
 Penetration depth, *see* Boundary layer thickness  
 Period ( $T$ ), 14, 61, 142  
 Periodic boundary condition, 296, 637–638  
 Permittivity of free space ( $\epsilon_0$ ), 311, 755  
 Peruvian whistling bottles, 375–376  
 Phase-locked-loop (PLL), 91–92  
 Phase matching, 722  
 Phase speed ( $c_{ph}$ ), 45, 248–249, 275, 459–460, 498, 656, 658, 660, 665, 668, 722, 726  
 Phasor, *xix*, 62, 74, 84, 87, 93, 95, 100–102, 165–167, 308–310, 363–367, 370, b372–373, 471–472, 475, 476, 479–480, 483, 488–489, 491–492, 497–498, 508, 514–519, 523, 528, 544–550, 552–556, 558–559, 562, 568, 575–585, 595–597, 600, 602, 660–661  
 Phasor notation, 19  
 Phenomenological models  
   adiabatic, 339  
   conservation laws, 338, 718–719  
   Einstein’s quotation, 335

- Phenomenological models (*cont.*)  
 entropy, 339, 340, 719  
 geometrical resonance (phase matching), 720–721  
 homogeneous and isotropic properties, 338  
 intermodulation distortion, 721–725  
 isobaric heat capacity ( $C_P$ ), 341  
 isochoric heat capacity ( $C_V$ ), 340  
 macroscopic variables, 338  
 single-component fluid, 339  
 thermodynamics, 338  
 thermodynamic temperature, 339
- Phon, 467
- Physical constants, 755
- Piecewise linear approximation, 529–530, 534
- Piezoelectric accelerometers, 118
- Pi-Groups, 25–29
- Piston angular null, 616
- Pi-theorem (similitude), 23–26
- Pixiphone, 255
- Planck distribution, 346
- Planck's constant ( $h$  or), 276–277, 345–347, 755
- Planck's equation, 71, 111
- Piano string (with stiffness), 276–277
- Piston (circular) in an infinite baffle, 595–604
- Pistonphone (calibrator), 414–415
- Plane wave, 523
- Point particles, 336
- Point mass, 60, 112, 117
- Point source, *see* Monopole
- Poiseuille's formula, 436
- Poisson's ratio ( $\nu$ ), 181  
 relation to other isotropic moduli, 187
- Poisson, Simone Denis, 181
- Polar coordinates, 294–295
- Polar moment-of-inertia, 245, 246
- Polarizing voltage ( $V_{bias}$ ), 313–317, 319
- Pole-zero fitting, 757
- Polyatomic gases  
 ball-and-stick model, 344  
 Boltzmann factor, 346  
 bulk viscosity ( $\zeta$ ), 347  
 diatomic molecule, 344–345  
 Equipartition theorem, 344  
 heat capacity, 347  
 molar heat capacity, 346, 347  
 nitrogen (N<sub>2</sub>), 346  
 optical spectroscopy, 346  
 Planck's constant ( $h$  or), 345, 755  
 quadratic degrees-of-freedom, 345  
 vibrational degrees-of-freedom, 346  
 vibrational frequency, 346
- Polyatomic molecules, 344–347
- Polytropic coefficient ( $\gamma$ ), 306, 308, 342
- Potential (velocity), 735
- Potential energy  
 and forces, 8  
 density (in fluids), 465, 736  
 gravitational, 7, 10, 69–70  
 Hooke's law, 9
- standing wave, 472, 740
- Power transmission coefficient ( $T_{II}$ ):  
 constriction or expansion chamber, 521–523  
 partition (mass law), 520–521
- Power, time-averaged, 21–22
- Prandtl number (Pr)  
 classical attenuation, 681  
 DELTAEC thermophysical properties, 383  
 ideal gas mixtures, 447–448
- Precision, 29–30
- Pressure  
 acoustic, 359  
 equilibrium ( $p_m$ ), 359  
 instantaneous, 359  
 reference sound pressure level, 467–468
- Pressure gradient microphone  
 Bauer's approach, 575  
 electrical signal, 576  
 equivalent circuit, 577  
 front-to-back propagation delay, 577  
 popular implementation, 575  
 transduction mechanism, 576
- Pressure reflection coefficient, 518, 528
- Pressure release boundary, 568
- Pressure transmission coefficient ( $T$ ), 518
- Principle of reciprocity, 477–478
- Principle of superposition, 13–16, 181–184, 289–290, 468, 560, 567, 588, 610
- Product rule, 5, 44–45, 49
- Proof mass, 188, 189
- Propagation constant, *see* Wavenumber
- Pulsating spherical source, 546–548, 553–554
- Pump wave attenuation, 695
- Pump waves, 721–722
- Pythagorean scale (musical), 147
- Q**
- Q (quality factor)  
 definitions (multiple), 75, 756–757  
 DELTAEC, 394, 402  
 driven plane wave resonator, 474–475, 482, 745  
 from similitude, 25  
 geophone, 104  
 Helmholtz resonator, 440–443, 451, 482  
 simple harmonic oscillator, 75–76, 86–89, 93–94, 118, 129  
 standing wave (cylindrical) resonator, 472–473
- Quadratic degree-of-freedom, 77
- Quadratic quadrupole radiation impedance, 615
- Quadrature output, 268
- Quadrupole, 615
- Quarter-wavelength open tube, 474, 494–495
- Quartic degree-of-freedom, 77
- Quartz microbalance, 240–242
- Quasi-static approximation, 63–66
- R**
- Radian frequency (angular frequency,  $\omega$ ), 61
- Radiation efficiency (monopole), 442, 553, 554

- Radiation force, 743  
 Radiation impedance, 166  
     baffled circular piston, 602–604  
     bipole, 560, 562, 563, 571–573  
     compact spherical source (monopole), 544, 550–553  
     dipole, 568–574  
     monopole, 544, 550–553  
     quadrupole, 573, 615  
     unbaffled piston, 607–610  
 Radiation mass, 192, 379  
     *See also* Radiation reactance  
 Radiation pressure, 735–736, 740  
 Radiation reactance  
     baffled circular piston, 602–603  
     baffled rectangular piston, 604  
     dipole, 573  
     general multipole, 573  
     monopole, 550–552  
     unbaffled circular piston, 607–608  
 Radiation resistance  
     baffled circular piston, 602–603  
     baffled rectangular piston, 604  
     dipole, 573  
     monopole, 550–553  
     semi-infinite string, 165, 166  
 Radius of curvature, 135, 194  
 Radius of gyration, 195  
 Random errors, 30  
 Rate of sound decay, *see* Reverberation  
 Rationalization (of a complex number), 20  
 Rayleigh disk, 734–735  
 Rayleigh resolution criterion, 599–600  
 Rayleigh scattering, 582  
 Rayleigh waves, 256  
 Rayleigh's method, 68–69, 152–153, 263–266, 290, 739  
 Ray tracing, 531  
 Reactance, *see* Specific type  
 Real springs  
     buckling, 200–202  
     bulk material, 187–188  
     cantilevered beams, 193–194  
     coil (*see* Coil springs)  
     elastic energy, 187  
     flexure springs, 193–194  
     Hooke's law, 187  
     reduced mass, 192  
     rubber springs (*see* Rubber springs)  
     solids as springs, 188–193  
     stiffness, 192–193  
     torsional springs, 202–203  
     triangularly tapered cantilevered beams, 198–200  
     vibration isolators, 188  
 Receivers, *see* Source  
 Reciprocal space (*k*-space), 291  
 Reciprocity  
     acoustic, 477  
     calibration, 507–509  
     coupler, 481  
     double Helmholtz resonator, 482  
     electroacoustic, 478–481  
     free-field, 481  
     planewave tube, 482  
     planewave resonator, 480, 482  
     reversibility, 477  
 Rectangular membrane, 284–294  
 Rectangular room  
     density of modes, 626–627  
     modal excitation, 625–626  
     modes, 623–625  
     reverberation time ( $T_{60}$ ), 630–632  
     separation of variables, 622–623  
     statistical energy analysis, 627–630  
 Rectangular waveguide  
     general solution, 655–656  
     group velocity ( $c_{gr}$ ), 656–658  
     mode excitation, 658–659  
     phase velocity ( $c_{ph}$ ), 658  
 Recursion formulæ for Bessel functions, 760  
 Reduced frequency, 269  
 Reduced mass, 124, 193, 345  
 Reference  
     intensity level (in air), 467  
     sound pressure level (in air), 467  
     sensitivity, 315  
 Reflection coefficient  
     changing cross-section, 491–492  
     normal incidence, 518  
     oblique incidence, 528  
     three media, 519  
 Refraction, 523–526, 529–539  
 Relative humidity, 632, 663, 683–684, 689, 694, 723  
 Relative uncertainty, 30–32, 37, 43, 49, 97, 130, 262, 266,  
     279, 356, 417, 665  
 Relaxation attenuation  
     attenuation maximum (per wavelength), 686  
     chemical, 689–692  
     in fresh and salt water, 688–692  
     in gases and gas mixtures, 687–688  
     molecular, 443–444, 687–688  
     relaxation time (equation of state), 684–686  
     sound speed (vs. frequency), 685, 687  
     structural, 273, 688, 690  
     thermal, 430–433  
 Residual (statistical), 38  
 Resistance, *see* Specific type  
 Resistance controlled regime, 84, 98  
 Resonance  
     bubble, 555–557  
     double-Helmholtz resonator, 402, 416–417, 450–451  
     “down 3 dB” bandwidth ( $\Delta f_{-3 \text{ dB}}$ ), 88  
     driven system, 83  
     equivalent noise bandwidth ( $\Delta f_{EQNB}$ ), 89  
     Helmholtz resonator, 378, 380, 389–390, 415–417  
     loudspeaker's frequencies, 96  
     mechanical resistance, ( $R_m$ ), 84  
     phase vs. frequency, 91, 756  
     sharpness, 87  
     simple harmonic oscillator, 83–87

- Resonance (*cont.*)  
 standing wave in tube, 470–472, 474  
 standing wave on string, 141–144, 158–163, 167–169  
 3-dimensional enclosures, 623–624, 640–643, 645,  
 650, 653–654
- Resonant mode conversion  
 beating, 725  
 geometrical resonance, 725  
 geometry, 727  
 mode-conversion interaction, 727  
 polycrystalline aluminum, 726  
 “scissors effect,” 726  
 shear waves, 726  
 solids, 726  
 superfluid helium, 727–728  
 thermodynamic variable (Galilean invariant), 728  
 two pump waves, 726  
 waveguide, 725, 727
- Resonant ultrasound spectroscopy (RUS), 270–274
- Resonator quality factor  
 driven planewave resonator (cylindrical), 474–475  
 Helmholtz resonator, 402, 440–443  
 open-closed planewave resonator (cylindrical), 474  
 planewave resonator (cylindrical), 472–473
- Resonator-transducer interaction  
 Bass-reflex loudspeaker enclosure, 409–412  
 DELTAEAC model, 484, 486  
 driver parameters, 484  
 driver-resonator interaction, 484  
 electrodynamic loudspeaker, 482  
 gas pressure oscillations, 483  
 ISPEAKER segment, 486, 487  
 isolated closed-closed resonator, 485  
 level repulsion, 412, 484–488  
 motor mechanism, 483  
 Newton’s Second Law of Motion, 482, 483  
 planewave resonator, 483  
 speaker’s mechanical resonance, 484–487  
 steady-state conditions, 483
- Retarded time, 745
- Reverberation, 631–632
- Reverberation time  
 architectural design, 630–632, 662–663  
 Eyring-Norris equation, 663  
 humidity effect, 632, 694  
 Sabine equation, 630–632
- Reverse Polish notation (RPN), 382, 394–395, 408, 410
- Reversible transducer, 99, 478–481
- Reynolds number, 436
- Ribbon microphone, 576
- Rigid-walled spherical resonators, 653–654, 670
- Rigid-walled toroidal enclosure  
 azimuthal modes, 645–646  
 trigonometric functions, 644
- Ring down, 43–44, 47, 75–76, 93
- Roark’s Formulas for Stress and Strain*, 196
- Rooms  
 cylindrical, 635–644  
 non-separable geometry, 648–651
- rectangular, 623–627  
 spherical, 652–654  
 toroidal, 644–646, 663–664
- Root-mean-square (rms), 467–468
- Rotational internal energy, 345
- Rubber springs  
 damping, 216  
 effective modulus, 216–218  
 natural frequency (isolator), 216  
 Poisson’s ratio ( $\nu$ ), 217  
 rubber-to-glass transition, 218–220  
 shape factor ( $S$ ), 217  
 transmissibility (Type I and Type II), 222  
 vibration isolation, 216
- viscoelastic transition frequency, 225  
 viscoelastic transmissibility, 224
- Rüchardt’s method (polytropic coefficient), 354
- S**
- Sabine, Wallace C., 630–631
- Sabine equation, 630–632
- Salinity, 529, 690
- Salmon horns, 499–500
- Sawtooth waveform  
 attenuation (nonlinear), 712–713  
 Fourier components, 53–54
- Scale of just intonation (musical), 146
- Scaling laws, *see* Similitude
- Scattering strength  
 single bubble or swim bladder, 584–586  
 compact compressibility contrast, 583–584  
 compact density contrast, 581–583
- Schroeder frequency, 634, 663
- Schlagwetter-pfeife*, 505
- Sea water  
 attenuation of sound, 689–692  
 speed of sound, 529
- Second harmonic distortion, 715–718
- Second Law of Thermodynamics, 339, 351, 678
- Second-order correction, 714
- Second-order wave equation, 719–720
- Second sound, 709
- Second viscosity ( $\zeta$ ), 347, 350, 351, 422, 465, 678,  
 680–681  
*See also* Bulk viscosity
- Secular equation, 107
- Seismic mass, 188, 189
- Seismometer, 103
- Self-interaction (nonlinear), 720–723
- Semi-infinite half-space, 564–567, 598, 601
- Semitone (musical), 147
- Separation condition, 287, 622–623
- Separation-of-variables, 286, 295, 622–623, 636–637
- Series approximation, 2–4, 48–49, 160, 296, 536–537,  
 714–716
- Shaded array, 591–593
- Shadow zone, 532–533
- Shallow water gravity wave (surf), 504, 703–705
- Shape factor (rubber springs), 217–218

- Shear (or dynamic or absolute) viscosity, 434–435, 443, 446  
Shear modulus ( $G$ ), 185–186, 245  
    relation to other isotropic moduli, 187  
Shear strain, 185–186  
Shear waves, 245–246  
Shear wave speed, 245  
Shock inception distance ( $D_S$ ), 704–706, 711, 716  
Shock wave  
    attenuation, 712–713  
    equal-area rule, 713  
    formation, 711–712  
    thickness, 713  
Shure microphones  
    Model 55 “Unidyne®”, 100  
    Model SM58, 100, 575–577  
Side branch  
    Helmholtz resonator, 492–494  
    stub, 494–495  
Silly Putty®, 210  
Similitude, 23–29, 50–51  
Simple harmonic oscillator, 24–25, 60–61, 158–161  
Simple pendulum, 10–11  
Simple source, *see* Monopole  
Single relaxation time model  
    chemical equilibrium, 688–692  
    equation-of-state (bulk viscosity), 684–686  
    fluorine gas, 687–688  
    structural (water), 690  
    viscoelastic solids, 207–211, 266–270  
Siren, 494–495, 695–696  
SI System of units, 22–23  
Skin depth (electromagnetic), 438  
Skip distance, 534–536  
Slenderness ratio, 200–202  
Slow waves (in a compliant waveguide), 506  
Small signal approximation, 359–361, 715–716  
Small-Thiel parameters (loudspeakers), 410  
Smith, Robert W. M., 206  
Snell’s law  
    grazing angle, 533–536  
    normal angle, 523–526  
SOFAR channel, 536, 696  
Solid angle ( $d\Omega$ ), 600–601  
Solid body rotation, 531–533, 713  
Solomongo, 325  
Sonic gas analysis, 460–462, 505–506  
“Sonic hammer,” 242–244  
Sonic hydrogen detector design, 505–506  
Sonoluminescence, 747  
Sound absorption, *see* Attenuation and Dissipation  
Sound channels, 534–536  
Sound decay, *see* Reverberation  
Sound level  
    A-weighted, 468–469  
    B-weighted, 469  
    C-weighted, 469  
    day-evening-night averaged ( $L_{den}$ ), 470  
    day-night averaged ( $L_{dn}$ ), 470  
    daytime average, 470  
    equivalent ( $L_{eq}$ ), 470  
    reference sound pressure level (SPL), 468  
Sound level meter, 469  
Sound radiation, 544–548  
Sound speed profile  
    linear, 531–532  
    piecewise linear, 529–530  
Sources and Receivers  
    Altec-Lansing Model 21C, 328  
    baffled piston, 595–607, 616  
    bipole, 560–564, 614  
    cardioid (unidirectional) microphone, 574–575  
    compact spherical, 544–554  
    condenser microphone, 310–317  
    continuous line, 593–595, 614  
    discrete line, 588–593, 614, 615  
    DIFAR sonobuoy, 578  
    dipole, 567–573, 578–580  
    electret condenser microphone, 317–320  
    electrodynamic loudspeaker, 95–98, 126–128, 616–617  
    electrodynamic microphone, 99–100  
    end-fire array, 591–593  
    line array, 588–595, 614, 615  
    MEMS microphone, 328–329  
    monopole, 544–554, 611  
    multipole, 554–555  
    parametric array, 721–725  
    point, 544–554, 611  
    pressure gradient, 575–577  
    quadrupole, 615  
    ribbon microphone, 576  
    Shure Model 55 (Unidyne®) and Model SM58, 100  
    spherical (pulsating), 544–554  
    spherical (translating), 578–580  
    thermoacoustic, 617–618  
    thermophone, 506–507  
    unbaffled piston (at end of a tube), 607–610  
    unidirectional (*see* cardioid)  
Source strength, 553–555  
Space Shuttle cargo bay, 230, 649, 650, 670  
Spar buoy oscillations, 119–120  
Spatial attenuation coefficient, 676  
Speaking length (for piano strings), 276–277  
Specific acoustic impedance, 463, 516–519, 527–529  
    *See also* Characteristic impedance  
Specific heat ratio (ideal gas) ( $\gamma$ ), 342  
Specular reflection, 525  
Speed of sound ( $c$ )  
    air, 462  
    DETAEC, 382–384  
    gas mixtures, 460–462  
    ideal gas, 460–461  
    liquid nitrogen, 460  
    liquids, 460  
    local, 705–706  
    seawater, 529–530  
    thermodynamic, 460, 707

- Speed of transverse waves on a string, 135, 137, 161  
 Spherical coordinates, 549  
 Spherically diverging sound waves  
   acoustic impedance, 550  
   gradient operator, 549–550  
   harmonic bubble oscillations, 552  
   monopolar sound source, 551  
   monopole acoustic transfer impedance, 553–554  
   multipole expansion, 554–555  
   space and time evolution, 549  
   spherical source, 552  
 Spherical enclosure, 651–654  
 Spherical harmonics, 554–555  
 Spherical resonators  
   pressure-released, 652–653  
   rigid-walled, 653–654  
 Spherical sound waves, 548–550  
 Spherical spreading, 611–612  
 Springs  
   automotive valve spring, 227  
   cantilever, 121–122, 197–200, 229–230  
   coil, 10, 203–206  
   design, 187, 199, 202  
   flexure springs, 193–200  
   gas, 354–355, 366–367  
   hardening nonlinearity, 10  
   in parallel combinations, 65  
   potential energy, 65  
   rubber (*see* Rubber springs)  
   in series combinations, 64  
   softening nonlinearity, 10–11  
   strain transformer, 231  
   torsion spring, 229, 246  
   *See also* Real springs  
 Spring constant (K), 9, 227  
 Square membrane, 288–290  
 Square wave, 15–16  
 Stability coefficient, 150, 152, 154  
 Stable equilibrium, 6  
 Stagnation point, 732  
 Standard (dry) air, 462, 755  
 Standard deviation, 33, 36, 42  
 Standard linear model (SLM) of viscoelasticity, 210–211  
 Standing waves  
   annular membranes, 302–304  
   circular membranes, 299–300, 306–308  
   cylindrical enclosures, 635–644  
   non-separable geometries, 648–651  
   quality factor ( $Q$ ), 472–473  
   rigid tubes, 470–472  
   rectangular membranes, 286–290  
   rectangular rooms, 623–624  
   speaker-driven resonator, 482–488  
   spherical enclosures, 651–654  
   strings, 141–144  
   thin bars (flexural), 250–256  
   thin bars (longitudinal), 236–239  
   thin bars (torsional), 245–246  
   toroidal enclosures, 644–646  
 Statistical energy analysis, 627–630  
   absorbed energy, 629–630  
   acoustic energy, 628–629  
   critical distance, 633  
   energy balance approach, 628  
   Sabine equation, 630–632  
   sound energy, 629  
   steady-state sound level, 628  
   time-averaged acoustic power, 627  
 Statistical fluctuations, 31, 76–82  
 Steady state  
   driven oscillator, 83–90  
   driven room, 625–626, 663  
 Steady-state radiation, 545  
 Steradian, 600–601  
 Stiff string, 274–277  
 Stiffness, 8–10  
   acoustic levitation, 738–743  
   coil spring, 203–204  
   cantilever beam, 198, 228–230  
   torsional, 202–203, 229, 245–246  
   triangular cantilever, 198–200, 228  
 Stiffness-controlled regime, 84–85  
 Stiffness-loaded string, 177  
 Stiffness matrix, 225–227  
 Stokes drag, 732  
 Storage modulus, 218–220  
 Strain ( $\epsilon$ ), 180–181  
 Strain transformer, 231  
 String vibrations  
   consonance and dissonance, 144–145  
   consonant triads and musical scales, 145–147  
   electrical stringed instruments, 283  
   Fourier series, 155  
   Gaussian pulse, 137  
   infinitesimal string segment, 135  
   imperfect boundary conditions, 173  
   initial conditions, 155–157  
   “lumped-element” model, 158, 160, 173  
   mass-loaded boundary conditions, 161–163  
   plucked string, 155  
   resistance-loaded boundary conditions, 163–165  
   struck string, 155  
   total modal energy, 157–158  
   transcendental equation, 159  
   vertical force, 138  
   whirling, 177  
 Strouhal number, 26–29  
 Struve function, 602–604  
 Streaming, 364–365  
 Stress ( $\sigma$ ), 180–181  
 Stress tensor  
   crystalline, 225–227  
   viscous, 351–352  
 Structural relaxation  
   plutonium, 273  
   water, 690  
 Substitution (mathematical), 22  
 Superconducting quantum interferometer (SQUID), 239

- Superfluid helium, 711  
Superposition  
  Fourier synthesis, 15–16  
  orthogonal functions, 13  
Surface tension, 50, 555–556  
Sum and difference frequencies (intermodulation), 721–725  
Symmetric mode, 106, 110–111  
Systematic (bias) error, 34–35
- T**  
Taylor series, 2–4, 48–49, 707, 758, 762  
Tangential modes, 624  
Temperament (musical), 145–147  
Temperature change (adiabatic) due to sound, 5–6, 342–343  
Temporal absorption coefficient, 73–75, 677, 757  
Thermal boundary layer  
  adiabatic compression, 430–432  
  adiabatic temperature oscillations, 429  
  adiabatic vs. isothermal propagation, 433–444  
  boundary condition, 429  
  bounded volume, 430–432  
  condenser microphone, 450  
  diffusion equations, 449  
  energy loss, 432–433, 660–662  
  evanescent wave, 429  
  Greenspan viscometer, 450–451  
  microscopic model, 449  
  mean-free-path, 443–444, 449–450  
  solid-gas interface, 429  
  thermal penetration depth ( $\delta_\kappa$ ), 428  
  vacuum insulation, 449–450  
Thermal conductivity, 423  
Thermal diffusion wave, 427–430  
Thermal energy, 340  
Thermal expansion coefficient, 383, 705  
Thermal fluctuations, 77–79  
Thermal penetration depth ( $\delta_\kappa$ ), 428  
Thermal noise, 78–81  
Thermal noise voltage (Johnson noise), 82  
Thermocline (ocean), 530  
Thermodynamics  
  Einstein quotation, 335  
  First law, 339  
  Second law, 339  
Thermophone, 506–507  
Thermoviscous boundary layer dissipation, 433, 439, 440, 660–662  
Three-dimensional enclosures, *see* Enclosures  
Thiel-Small parameters (loudspeakers), 410  
Thin-plate model, 321–324  
Time-averaged energy, 740  
Time reversal invariance, 422–424  
*Tonpilz* transducer (underwater projector), 191–193, 228  
Toroidal resonator, 644–646, 663–664  
Torsional (bar) modes  
  Fitzgerald effect, 258  
  polar moment-of-inertia, 245  
            stiffness-length product, 246  
            torsional wave speed, 246  
Torsional rigidity, 246  
Torsional stiffness, 202–203, 229  
Torsional wave speed (thin bars), 245–246  
Total internal reflection, 526–528  
Trace velocity, 524–525  
Trace wavelength, 524  
Transducer  
  accelerometer, 103–104, 188–190  
  Altec-Lansing Model 21C, 328  
  bass-reflex loudspeaker, 405–412  
  calibration, 476–482  
  cardioid (unidirectional) microphone, 574–575  
  condenser microphone, 310–317  
  DIFAR sonobuoy, 578  
  dynamic, 99–100  
  electret condenser microphone, 317–320  
  electrodynamic loudspeaker, 95–98, 126–128, 616–617  
  electrodynamic microphone, 99–100  
  electrostatic, 311–320  
  end-fire array, 591–593  
  geophone, 103–104  
  line array, 588–595, 614, 615  
  horn, 495–501  
  loudspeaker, 95–98, 126–128, 616–617  
  MEMS microphone, 328–329  
  moving-coil, 99–100  
  piezoelectric, 188–193  
  pressure gradient, 575–577  
  reciprocal, 477–478  
  reversible, 477–478  
  ribbon microphone, 576  
  sensitivity, 476–477  
  Shure Model 55 (Unidyne®) and Model SM58, 100  
  thermoacoustic, 617–618  
  thermophone, 506–507  
  *See also* Sources and Receivers  
Transient response, 92–94  
Translating sphere (dipole radiation), 578–580  
Translational internal energy, 337, 685–686  
Transmissibility, 100–102, 220–225  
Transcendental equations, 159, 163, 164, 169  
Transmission coefficient  
  changing cross-section, 491–492  
  constriction/expansion low-pass filter, 521–522  
  Helmholtz side-branch, 492–494  
  Mass law (partition), 520–521  
  normal incidence, 518  
  three media, 519  
Transmission loss  
  short and very short wavelengths, 692–693  
  very long wavelengths, 693  
Transmission unit (TU), 466  
Transverse wave speed (string), 135  
Travel time, 536–537  
Trial function (Rayleigh's method), 149–155, 263, 365  
Trigonometric functions, 4, 761

- Tsunami, 504
- Tubes
- area discontinuities, 521–523
  - driven and rigidly terminated, 482–488
  - end correction (unbaffled), 607–610
  - junctions, 490–492
  - rigidly terminated, 470–473
- Tube wall boundary layer attenuation, 660–662
- Tube wall boundary layer dissipation, 472–474
- Tuning, 225, 278, 456, 743
- Tuning fork, 255–256
- Two degree-of-freedom oscillators, 105–111
- Two in-phase monopoles
- acoustic pressure, 566
  - axial symmetry, 564
  - bipole, 562
  - directionality factor, 563
  - equatorial plane, 561
  - image source, 567
  - interference effects, 565, 567
  - light sources (Young's double-slit), 565
  - phantom sources, 564
  - pressure distribution, 562
  - SONAR array applications, 560
  - two-dimensional projection, 564
  - Young's original diagram, 565
- See also* Bipole
- Two out-of-phase compact sources
- acoustic pressure, 568
  - anti-phase sources, 569
  - beam pattern, 569, 570
  - directionality, 569–570
- Taylor series approximation, 568
- See also* Dipole
- U**
- Ultrasound
- Unbaffled piston, 607–610
- Undamped harmonic oscillator, 60–63
- Universal gas constant, 337, 341, 344, 755
- Units, 22–23
- Unstable equilibrium, 7–8
- U. S. Environmental Protection Agency (EPA), 470
- U. S. Standard Atmosphere, 334, 462
- U-tube oscillations, 118
- V**
- Väisälä-Brunt frequency, 414
- Vapor pressure of water, 684
- Variable constraint, 738
- Vector identities, 464
- Velocity of sound, *see* Speed of sound
- Velocity potential, 735
- Velocity profile (ocean), 529–530
- Vibrating reed electrometer, 319–320
- Vibrational internal energy, 346
- Vibrational relaxation temperature, 346
- Vibration isolation, 70, 100, 121
- Vibration sensors, 102
- accelerometer, 104
  - geophones, 103–104
  - piezoelectric accelerometers, 104
  - seismometers, 103
  - transduction mechanism, 102–103
- Vibrations of thin plates
- flexural vibration, 321
  - modified Bessel functions ( $I_m$  and  $K_m$ ), 321–322
  - normal modes (clamped circular plate), 322–324
  - Poisson's ratio ( $\nu$ ), 320
- Virial expansion (equation-of-state), 707–708
- Virial theorem, 67–68
- Viscoelasticity
- complex stiffnesses and moduli, 211–213
  - generalized susceptibility, 207
  - K-K relations (*see* Kramers-Kronig relations)
  - linear response theory, 207
  - Maxwell (relaxation time) model, 207–210
  - quasi-static approximation, 206
  - rubberlike materials, 206
  - single relaxation time model, 206–207
  - SLM (*see* Standard Linear Model)
- Viscosity
- absolute ( $\mu$ ), 435
  - boundary layer (oscillatory), 436–438
  - bulk ( $\zeta$ ), 677–679, 682–684, 688–692, 696
  - dynamic viscosity ( $\mu$ ), 435
  - kinematic viscosity ( $\nu$ ), 435
  - Navier-Stokes equation, 434
  - Newtonian fluids, 434
  - Ohm's law, 434
  - Poiseuille flow, 435–436
  - Quality factor ( $Q_{vis}$ ), 440–443
  - Second viscosity (*see* Bulk viscosity)
  - Shear viscosity ( $\mu$ ), 434
- Viscous boundary layer ( $\delta_v$ ), 436–438
- Viscous drag, 674
- Viscous penetration depth ( $\delta_v$ ), 436–438
- Viscous stress tensor, 351, 353
- Void fraction, 587
- Voigt notation, 226
- Voltage-controlled oscillator (VCO), 267–268
- Volume velocity, 363, 365, 366, 372, 377, 546–548, 553–555
- Volumetric strain, 49, 183
- W**
- Wakeland number, 489–490
- Wall losses (thermoviscous), 661–662
- Water vapor in air, 684
- Wave equation
- angular frequency ( $\omega$ ), 458
  - arbitrary function of ( $x \pm ct$ ), 458
  - continuity equation, 456
  - equations of hydrodynamics, 456
  - first-order partial differential equations, 456–457
  - gases and liquids, 457

- linearized continuity, 458  
“linear operator” form, 135  
longitudinal waves in thin bars, 238  
mass conservation, 456  
one-dimensional, 135–136, 154, 238, 245, 274,  
    456–458, 499, 720  
second-order partial differential equation, 458  
speed of transverse waves, 135  
three-dimensional wave equation, 549, 622, 636  
time and space dependence, 458  
transverse waves, 458  
    two-dimensional wave equation, 286, 295
- Waveform distortion, 748–749
- Waveguides
- cylindrical (*see* Cylindrical waveguides)
  - driven, 658
  - phase speed ( $c_{ph}$ ), 656–657
  - rectangular cross-section, 655
  - square cross-section, 659
  - wavenumber ( $k$ ), 656
  - wavevector, 657
- Wavelength ( $\lambda$ ), 142
- short and very short, 692–693
  - very long, 693
- Wavenumber ( $k$ ), 141–143, 165, 173
- Wavenumber space ( $k$ -space), 291–294, 626–627
- Weak shock theory, 703–705, 714–728
- Weber bars, 239
- Weighting network, 468–470
- Whirling string, 177
- Width of a resonance ( $\Delta f_{\text{3 dB}}$ ), 87–90
- Wiedemann-Franz law, 447
- Wilberforce pendulum, 204–205
- Williams-Lendel-Ferry (WLF) equation, 270
- Work
- and conservative force, 8
  - and energy, 8
  - evaluation (work done), 50
- X**
- Xylophone, 255
- Y**
- Young’s modulus, 180
- constant of proportionality, 181
  - PZT, 192–193
  - relation to other isotropic moduli, 187
  - rubberlike materials, 217
  - steel, 192–193
- Z**
- Zero crossings, 116, 150